

AD-A283 898



AFDTC-TR-93-06  
VOLUME I

**SIXTEENTH BIENNIAL  
GUIDANCE TEST SYMPOSIUM**

**PREPARED BY  
CENTRAL INERTIAL GUIDANCE TEST FACILITY  
GUIDANCE TEST DIVISION**

**46TH TEST GROUP  
1644 VANDERGRIFT ROAD  
HOLLOMAN AFB, NEW MEXICO 88330-7850**

**5, 6, & 7 OCTOBER 1993**

**DTIC  
ELECTE  
SEP 01 1994  
S G D**

Publication of this report does not constitute approval or disapproval of the ideas or findings. It is published in the interest of exchanging scientific and technical information.

**DISTRIBUTION STATEMENT:** Approved for public release; distribution is unlimited.

The Public Affairs Office has reviewed this report, and it is releasable to the National Technical Information Service where it will be available to the general public, including foreign nationals.

94 8 31 221

94-28373



252



# REPORT DOCUMENTATION PAGE

Form Approved

OMB No. 0704-0188

Public reporting burden for this collection of information is estimated to average 1 hour per response, including the time for reviewing instructions, searching existing data sources, gathering and maintaining the data needed, and completing and reviewing the collection of information. Send comments regarding this burden estimate or any other aspect of this collection of information, including suggestions for reducing this burden, to Washington Headquarters Services, Directorate for Information Operations and Reports, 1215 Jefferson Davis Highway, Suite 1204, Arlington, VA 22202-4302, and to the Office of Management and Budget, Paperwork Reduction Project (0704-0188), Washington, DC 20503.

1. AGENCY USE ONLY (Leave blank)		2. REPORT DATE OCTOBER 1993	3. REPORT TYPE AND DATES COVERED SYMPOSIUM PAPERS 5-7 OCT 93	
4. TITLE AND SUBTITLE SIXTEENTH BIENNIAL GUIDANCE TEST SYMPOSIUM (VOLUME I)			5. FUNDING NUMBERS JON: 9993NGTS PE: 65708F	
6. AUTHOR(S) The authors names are indicated on the individual papers.				
7. PERFORMING ORGANIZATION NAME(S) AND ADDRESS(ES) 46th Guidance Test Squadron/CC (AFMC) 1644 Vandergrift Road Holloman AFB NM 88330-7850			8. PERFORMING ORGANIZATION REPORT NUMBER AFDTC-TR-93-06 Volume I	
9. SPONSORING / MONITORING AGENCY NAME(S) AND ADDRESS(ES) 46th Guidance Test Squadron/CC (AFMC) 1644 Vandergrift Road Holloman AFB NM 88330-7850			10. SPONSORING / MONITORING AGENCY REPORT NUMBER AFDTC-TR-93-06 Volume I	
11. SUPPLEMENTARY NOTES				
12a. DISTRIBUTION / AVAILABILITY STATEMENT Approved for public release; distribution is unlimited.			12b. DISTRIBUTION CODE	
13. ABSTRACT (Maximum 200 words)  These proceedings contain papers which were presented at the Sixteenth Biennial Guidance Test Symposium. This symposium, hosted by the 46th Guidance Test Squadron, Central Inertial Guidance Test Facility, Holloman Air Force Base, New Mexico, on 5-7 October 1993, was directed toward the exchange of information, stimulation of new ideas, and discussion of current techniques associated with the development and evaluation of inertial guidance and navigation systems and global positioning systems. The papers presented included such topics as new test and calibration techniques for guidance systems, advances in flight references systems, global positioning system integrations, and software developments.  Volume I contains papers which are unclassified and have no distribution restriction.				
14. SUBJECT TERMS			15. NUMBER OF PAGES	
			16. PRICE CODE	
17. SECURITY CLASSIFICATION OF REPORT UNCLASSIFIED	18. SECURITY CLASSIFICATION OF THIS PAGE UNCLASSIFIED	19. SECURITY CLASSIFICATION OF ABSTRACT UNCLASSIFIED	20. LIMITATION OF ABSTRACT UNCLASSIFIED	



**THIS PAGE LEFT BLANK INTENTIONALLY**

## FOREWORD

The Sixteenth Biennial Guidance Test Symposium was held at Holloman Air Force Base, New Mexico, on 5, 6, and 7 October 1990. This symposium was hosted by the Central Inertial Guidance Test Facility (CIGTF) of the 46th Guidance Test Squadron, 46th Test Group.

The purpose of the symposium was to provide a forum for approximately 350 people from industry, universities, foreign governments, Department of Defense, and other Government agencies to exchange technical information. Papers covered a wide spectrum of topics related to the test and evaluation of systems and components for missile guidance and aircraft navigation applications with emphasis on advances and new information.

Fifty-three excellent papers were presented at this symposium; however, due to time constraints, only a portion of those papers submitted could be included in the program.

The Paper Selection Committee included Darwin G. Abbott, Aerometrics, Inc.; Dominic Brienza, Naval Air Warfare Center; Richard E. Clark, The Analytic Sciences Corp.; Sam George, OCA/ALC/LIIRN; Richard Greenspan, Charles Stark Draper Laboratory, Inc.; Tom Hancock, ASC/YOG; Richard Holdeman, TRW-Ogden; Boyd E. Holsapple, WL/A&AI-3; Gene Hymas, TRW-Ogden; Paul Olson, AMSEL-RD-C2-TS; Lt Col Randy Paschall, AFIT/EN; Lt Col Robert N. Riggins, AFIT/ENG; and Len Sugerman, Physical Science Laboratory.

In addition to those mentioned above and the contributing authors, a large number of people contributed to the success of this symposium. I wish to express my appreciation to each of them for their efforts. Special thanks go to our Symposium Manager, Frederick R. Schreiber, and our Technical Managers, Robert S. Kelher and Reese C. Sturdevant, and to the Symposium Coordinator, Dora B. Walker.

Publication of this report does not constitute approval or disapproval of the ideas or findings stated within. It is published in the interest of exchanging scientific and technical information.

  
MICHAEL P. DICKER, Lt Col, USAF  
Commander, 46th Guidance Test Squadron

Accession For	
NTIS CRA&I	<input checked="checked" type="checkbox"/>
DTIC TAB	<input type="checkbox"/>
Unannounced	<input type="checkbox"/>
Justification	
By	
Distribution /	
Availability Codes	
Dist	Avail and/or Special
A-1	

**THIS PAGE LEFT BLANK INTENTIONALLY**

**TABLE OF CONTENTS**  
**SIXTEENTH BIENNIAL GUIDANCE TEST SYMPOSIUM PROCEEDINGS**  
**VOLUME I**  
**UNCLASSIFIED**

	PAGE
<b>REPORT DOCUMENTATION PAGE</b>	i
<b>FOREWORD</b>	iii
<b>TABLE OF CONTENTS</b>	v
<b>SESSION I-A: OPENING SESSION</b>	
<i>GPS Update</i> Major Joseph T. Sanford, SMC/CZUT, Los Angeles AFB CA	3
<i>A Superconducting Six-Axis Accelerometer for Platform Control and Space Applications</i> E.R. Canavan and H. J. Paik, Department of Physics and Center for Superconductivity Research, University of Maryland, College Park MD	19
<i>Low Cost Quartz Rate Sensors Applied to Tactical Guidance</i> S. W. Hammons, Systron Donner Inertial Division, Concord CA	33
<i>A Systems Approach to Gyro Modeling</i> George Erickson, Sperry Marine, Inc., Charlottesville VA	49
<i>Inertial Navigation Performance of an IFOG Over Dynamic Environments</i> Ralph A. Patterson, Erick L. Goldner, Amado Cordova, and David M. Rozelle, Litton, Inc., Guidance & Control Systems Division, Woodland Hills CA	65
<b>SESSION II-A: MINUTEMAN</b>	
<i>Minuteman II and Minuteman III Guidance Computer Test Process Automation</i> William H. Crigger, Aerospace Guidance & Metrology Center, Newark AFB OH	79
<i>A Concept for Sled Testing Minuteman III Guidance Systems</i> Hossny El-Sherief, Dave Knight, Dan Simon, and Myron Teeter; TRW, Ballistic Missiles Division, San Bernardino CA	91
<i>Minuteman III Guidance Computer Expert System</i> William H. Crigger and Michael W. Murasky, Aerospace Guidance and Metrology Center, Newark AFB OH	115
<b>SESSION II-B: INTEGRATED GPS</b>	
<i>Embedded GPS / INS - The Advantage</i> Gary W. Linn, Navigation Products Engineering; Captain Mikel M. Miller, USAF - Education with Industry, Honeywell, St. Petersburg FL; and Lawrence C. Vallot, Honeywell Systems and Research Center, Clearwater FL	131

***Test of an Integrated GPS / INS System for Precision Velocity*** 151  
 Brian Mitchell, IEWCS Navigation System Upgrade, CECOM Command/Control and System Integration, Ft Monmouth NJ; and Joseph McGowan, Project Manager, Intermetrics, Inc., Oceanport NJ

***Test and Evaluation of a New, Tightly-Coupled GPS / INS*** 159  
 Donald T. Knight, Knight Systems, San Pedro CA; Allen (Skip) W. Osborne and Robert W. Snow, Allen Osborne Associates, Westlake Village CA; and Don G. Kim, Inertial Science Inc., Newbury Park CA

### **SESSION III-A: STRATEGIC SYSTEMS**

***Use of a High Performance Aircraft and GPS to Evaluate the Accuracy of the Peacekeeper Inertial Measurement Unit*** 169  
 Captain Roger Evans, 6595th Aerospace Test Group, Vandenberg AFB CA; Angelo Truncale, Rockwell International Corp., Anaheim CA

***Guidance and Control Expert System Shell (GCESS) Applications*** 183  
 Charles F. Saffle, Jr., Aerospace Guidance and Metrology Center, Newark AFB OH

***Stellar Radiometry and Astrometry Supporting Development and Test of Advanced Guidance Systems*** 197  
 James A. Hand and Michael E. Ash, Draper Laboratory, Cambridge MA

### **SESSION III-B: DIFFERENTIAL GPS**

***New Horizons in Differential GPS*** 229  
 B. A. Kumar Babu and Dr. Greg M. Robbins, Del Norte Technology Inc., Euless TX

***INS / DGPS Trajectory Determination*** 241  
 Pierre-Eric Pommellet and Pascal Dutot, Laboratoire de Recherche Balistiques et Aerodynamiques, Vernon, France

***Applications of Accurate Terrain Referenced Navigation*** 251  
 Martin V. Couch and G. A. Wilkinson, British Aerospace (Systems and Equipment) Ltd., Plymouth, England

### **SESSION IV-B: TEST BEDS**

***Effect of Noise in Precision Centrifuge Testing of Accelerometers*** 269  
 George H. Neugebauer, Sun City CA; Presenter Dr. Michael D. Hooser, CIGTF, Holloman AFB NM

***High Accuracy Inertial Test Table*** 283  
 Dr. Louis A. DeMore, Robert Anticole, Hans Riegenbach, Frank Almendinger, and Michael Swamp, Contraves Inc., Pittsburgh PA; Dr. Michael D. Hooser, CIGTF, Holloman AFB NM

***High Stability Large Centrifuge Test Bed*** 305  
 Dr. Louis A. DeMore, Robert Anticole, and Hans Riegenbach, Contraves Inc, Pittsburgh PA; Dr. Michael D. Hooser, CIGTF, Holloman AFB NM

## **SESSION V-A: WEAPONS TESTING**

- Low Cost Quartz Rate Sensors Applied to Tactical Guidance IMUs* 325  
Richard N. Silva and Glenn W. Murray, Rockwell International Corp., Defense Electronics, Anaheim CA

## **SESSION V-B: FIBER OPTIC GYROS (FOG)**

- A Tactical Fiber Optic Gyro with All-Digital Signal Processing* 337  
Michael S. Perlmutter, Northrop Corporation, ESD, Norwood MA
- Resonant Fiber Optic Gyro (RFOG) Technology Development* 351  
John R. Haavisto and Todd Kaiser, Draper Laboratory, Cambridge MA;
- A Fiber-Optic Rotation Sensor for NASA Space Missions* 363  
O. Laznicka, R. Gauthier, R. Magee, J. Haavisto, K. Kissa, and R. Tumminelli, Draper Laboratory, Cambridge MA; R. Bartman, Jet Propulsion Laboratory, Pasadena CA

## **SESSION VI-B: STELLAR SYSTEMS**

- Test and Evaluation Aspects of Integrated Pointing and Tracking Systems for Future Manned Space Flight* 375  
Alfred Anderman, Rockwell Space Systems Division, Downey CA
- Pointing Stabilization System Using the Optical Reference Gyro* 389  
Jerold P. Gilmore, Tze T. Chien, Dale T. Woodbury, Michael F. Luniewicz, and Stephan J. Feldgoise, Draper Laboratory, Cambridge MA
- Inertial Pseudo Star Reference Unit* 409  
Michael F. Luniewicz, Dale T. Woodbury, Jerold P. Gilmore, Tze T. Chien, Draper Laboratory, Cambridge MA

## **SESSION VII-A: ADVANCED SYSTEMS**

- The Advantages of a Long Range Precision Strike Weapon* 429  
Thomas E. Reed, Consultant, Charlton MA
- Sled Testing of the Advanced Inertial Measurement Units* 445  
Maria Reta and Robert Lawrence, 46th Guidance Test Squadron/GDSG (CIGTF), Holloman AFB NM
- Alignment Transfer in a Modular Guidance System* 453  
Leonard S. Wilk, Draper Laboratory, Cambridge MA

## **SESSION VII-B: ACCELEROMETERS**

- Inertial Grade SiAc<sup>TM</sup> Silicone Accelerometer* 461  
Dan McLane, Litton Guidance and Control Systems, Woodland Hills CA
- The Microwave Resonator Accelerometer for Strategic System Application* 477  
Anthony Petrovich, R. Gels, and J. Kutchmanich, Draper Laboratory, Cambridge MA

- Results of Testing Linear Accelerometers on a Low Cost Centrifuge Using "IEEE STD 836-1991"** 489  
R. D. (Sam) Marquess, Applied Motion Technology, Inc., Concord CA

#### **SESSION VIII-A: MEASUREMENT METHODS**

- High Accuracy, Short Term Trajectory Measurement of an Airborne Vehicle for Control of Inverse Synthetic Aperture Radar Image Formation** 549  
John W. Sisak and ERIM staff, ERIM, Ann Arbor MI

- RLG Bias or Random Walk?** 585  
M. M. Tehrani, Litton Guidance and Control Systems, Woodland Hills CA

- Methods for Improved Estimation and System Integration for Time-Space-Position Information** 591  
James Chaffee, Arrowsmith Technologies Inc., Austin TX; Barbara McQuiston, Systronics Inc., Dayton OH; Jonathan Abel, Abel Innovations, Palo Alto CA

- An Adaptive Kalman Filter to Improve Micromechanical Inertial Instrument Performance** 603  
Jonathan Kossuth and Charles Kochakian, Draper Laboratory, Cambridge MA

#### **SESSION VIII-B: TEST FACILITIES**

- Improved Synchronization Capabilities of the Little Mountain Pulserad 958 Gamma Simulator** 629  
S. S. Spring and R. D. May, Rockwell International, Ogden UT; B. H. Bernstein, Bernstein Design Services, Livermore CA

- Navigation / Survey Test Van** 641  
Brian E. Fly and Blake F. Lenett, Honeywell Military Avionics (GNO), St. Petersburg FL

- Configurable Data Acquisition Test Software, PC Based MIL-STD-1553B Multiplexed Data Bus Test Software** 649  
David R. Hollingsworth, Honeywell Inc., MAVD/GNO, St. Petersburg FL

- Advanced Magnetic Azimuth Detector (AMAD) Development** 659  
Michael A. Friday, Oklahoma City Air Logistics Center OK;  
John N. Hericks, Honeywell MAVD, Minneapolis MN; Heather Jewett, Lear Astronics Corp., Santa Monica CA; Gordon F. Rouse, Honeywell Systems & Research Center, Minneapolis MN

#### **SESSION IX-A: NAVIGATION SYSTEMS**

- B-1B GSS Replacement Program** 693  
Michael A. Friday, Avionics Reliability Center, OC-ALC OK; Charles T. Bye and Daniel J. Murphy, Honeywell Inc., MAVD, St Louis Park MN

- CIGTF Verification Testing of the SNU 84-1/E. The USAF Enhanced Accuracy Standard Navigation Unit** 703  
Mark E. Petersen, B. T. Stiles, Honeywell MAVD, St. Petersburg FL; Larry Boykin, 46th Guidance Test Squadron (CIGTF), Holloman AFB NM

- Air Alignment for the Base Inertial Navigation System - LINS 300** 719  
R. H. W. Reilly, British Aerospace (Systems and Equipment) Ltd., Plymouth, England

## **SESSION IX-B: GPS TESTING**

***Test and Evaluation Status of the Honeywell H-764G Embedded GPS / INS at CIGTF*** 733  
**Joseph J. Elchynski, Honeywell MAVD, St. Petersburg FL; Dave Syse,**  
**46th Guidance Test Squadron (CIGTF), Holloman AFB NM**

***Neural Net-Directed Complementary Filters and Applications to GPS Data*** 753  
***and Acoustic Signal Enhancement***  
**Bal N. Agamata, Naval Command Control and Ocean Surveillance Center (NCCOSC),**  
**NISE West, San Diego CA**

***Test Results of a GPS Translator Post-Test Processing System*** 785  
**David E. Reed and Peter Brown, NAVSYS Corp., Colorado Springs CO**

## **STANDBY PAPER**

***High Accuracy Performance Capabilities of the Military Standard Ring Laser Gyro*** 805  
***Inertial Navigation Unit***  
**George Gilster, Litton Inc., Guidance & Control Systems Division, Woodland Hills CA**

**ATTENDANCE LIST** 817



**THIS PAGE LEFT BLANK INTENTIONALLY**

16th Test Group

I N T E R O F F I C E   M E M O R A N D U M

Date: 22-Nov-1993 07:26am MDT  
From: Bob Kelher  
KELHER  
Dept: GDS  
Tel No: 679-2195

TO: GUIDANCE TEST DIVISION

( GD )

Subject: Conflict Management Course

The Conflict Management Course will be 11-12 Jan 1994. Times and place are TBD. This is for 25 people. We need to forward a 1556 and a proposed list of attendees to Mr Lillibridge. The list of names is not real important because the official will be the sign-in sheet.

Bob Kelher  
22 Nov 1993

46th Test Group

I N T E R O F F I C E   M E M O R A N D U M

Date: 22-Nov-1993 09:59am MDT  
From: GUIDANCE TEST DIVISION  
GD  
Dept: GD  
Tel No: 679-2123

TO: Joy Means

( MEANS )

Subject: Conflict Management Course

**SESSION I-A**  
**OPENING SESSION**

***CHAIRMAN***

**FREDRIC R. NADEAU**

***46TH GUIDANCE TEST SQUADRON***  
***CIGTF***

**THIS PAGE LEFT BLANK INTENTIONALLY**

**GPS UPDATE**

***MAJOR JOSEPH T. SANFORD***

***SMC/CZUT, Los Angeles AFB CA***



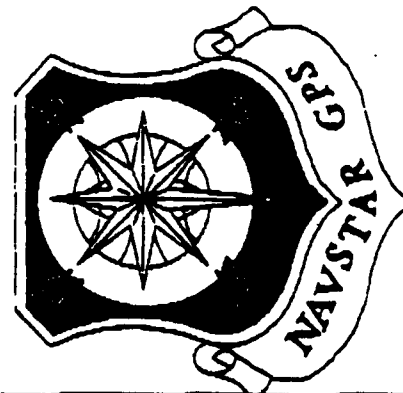
SUPPORT



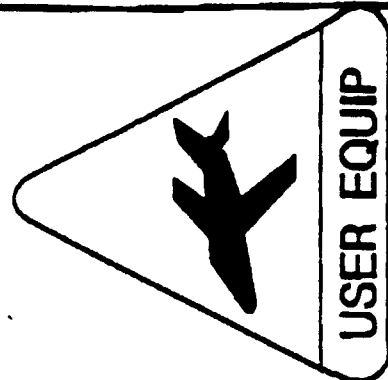
SUPPORT

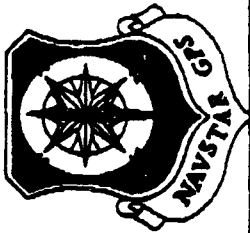
SUPPORT

# GPS USER EQUIPMENT TEST & EVALUATION ROADSHOW

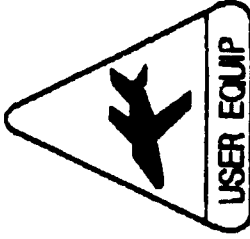


SUPPORT





**SPACE & MISSILE SYSTEMS CENTER  
GPS USER EQUIPMENT  
TEST & EVALUATION ROADSHOW**



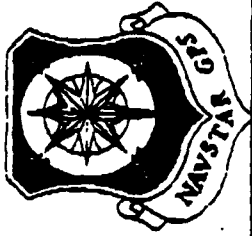
**PURPOSE**

**FACILITATE THE**

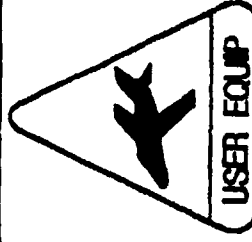
**EXPLOITATION OF GPS IN**

**DoD WEAPON SYSTEMS**



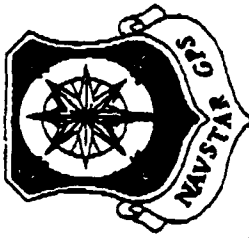


**SPACE & MISSILE SYSTEMS CENTER  
GPS USER EQUIPMENT  
TEST & EVALUATION ROADSHOW**

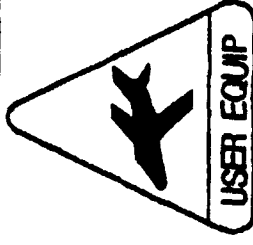


## **GPS AS A FORCE ENHANCER**

- ⊙ **PROVIDES PRECISE POSITION, VELOCITY, AND TIME INFORMATION FOR USE IN OPERATIONAL/SUPPORT MISSIONS**
  - e.g.: AIR TO GROUND WEAPONS DELIVERY, LOGISTICAL AIR DROPS AND GROUND DELIVERY, RENDEZVOUS, SUPPORT WEAPONS POSITIONING, PRECISION AND NON-PRECISION APPROACH
- ⊙ **ENHANCES NAVIGATION ACCURACY**
- ⊙ **PROVIDES A PRECISE TIME STANDARD FOR SECURE COMM**
  - e.g.: HAVEQUICK
- ⊙ **PROVIDES A COMMON REFERENCE FOR BOTH TIME AND POSITION FOR JOINT FORCES INTEROPERABILITY**
- ⊙ **IS CONTINUALLY AVAILABLE IN ALL WEATHER, 24 HRS/DAY, WORLD-WIDE**

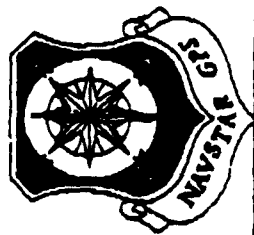


**SPACE & MISSILE SYSTEMS CENTER  
GPS USER EQUIPMENT  
TEST & EVALUATION ROADSHOW**

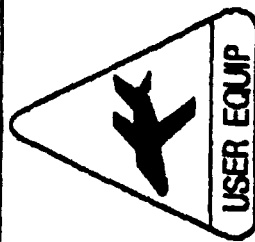


## **JPO TEST AND EVALUATION ROLE IN REQUIREMENTS GENERATION/ VALIDATION PROCESS**

- ❖ **ASSESS USE OF CURRENT UE TO MEET USER REQUIREMENTS AND SCENARIOS AND CHARACTERIZE TOTAL SET CAPABILITIES FOR USER INFORMATION**
- ❖ **RECOMMEND MODS TO EXISTING UE TO MEET CURRENT OR NEW USER REQUIREMENTS AND SCENARIOS**
- ❖ **RECOMMEND NEW UE CHARACTERISTICS TO MEET NEW USER REQUIREMENTS**



**SPACE & MISSILE SYSTEMS CENTER  
GPS USER EQUIPMENT  
TEST & EVALUATION ROADSHOW**



**CENTER OF EXPERTISE FOR GPS TESTING  
TEST AGENCY MEMBERSHIP**

**JPO**

**46th TEST GROUP**

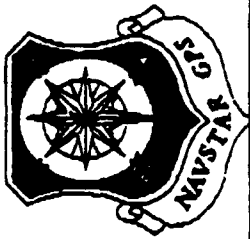
**NAWC-AD PAX**

**NRaD**

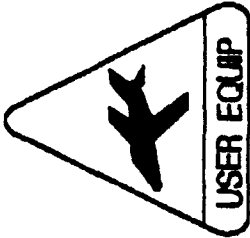
**NISE-WEST**

**USAEPG**

**NRL**



**SPACE & MISSILE SYSTEMS CENTER  
GPS USER EQUIPMENT  
TEST & EVALUATION ROADSHOW**

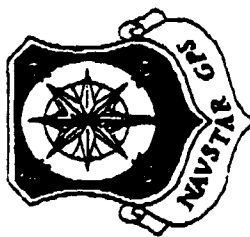


# **CENTER OF EXPERTISE FOR GPS TESTING**

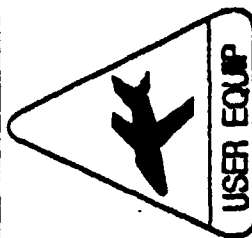
**JPO**

## **★ TEST MANAGEMENT**

- BUDGETING**
- MULTISERVICE TESTING  
ASSESSMENT AND REPORTING**
- DoD GPS TEST CLEARING HOUSE**



**SPACE & MISSILE SYSTEMS CENTER  
GPS USER EQUIPMENT  
TEST & EVALUATION ROADSHOW**



# **CENTER OF EXPERTISE FOR GPS TESTING**

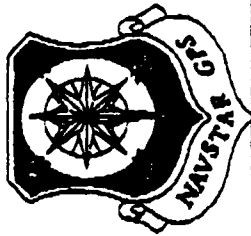
## **46th TEST GROUP**

### **⊙ RESPONSIBLE TEST ORGANIZATION (RTO)**

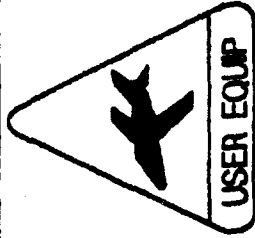
**➤ FIELD TESTING OF LOW-,  
MEDIUM-, AND HIGH-  
DYNAMIC AIR PLATFORMS  
IN BENIGN, JAMMING,  
AND/OR SPOOFING  
ENVIRONMENTS**

**➤ DIFFERENTIAL TESTING**

**REPRESENTATIVE  
PICTURE**



**SPACE & MISSILE SYSTEMS CENTER  
GPS USER EQUIPMENT  
TEST & EVALUATION ROADSHOW**



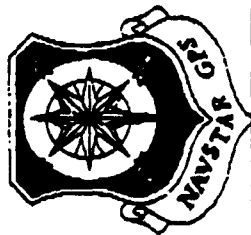
# **CENTER OF EXPERTISE FOR GPS TESTING**

**NRaD**

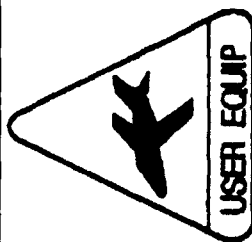
**◎ PARTICIPATING TEST  
ORGANIZATION (PTO)**

- LABORATORY TESTING OF  
RECEIVER AND ANTENNA  
SYSTEMS TO  
SPECIFICATION  
REQUIREMENTS FOR ALL  
GPS ENVIRONMENTS  
INCLUDING JAMMING AND  
SPOOFING**

**REPRESENTATIVE  
PICTURE**



**SPACE & MISSILE SYSTEMS CENTER  
GPS USER EQUIPMENT  
TEST & EVALUATION ROADSHOW**



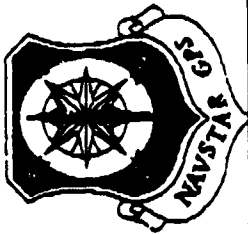
# CENTER OF EXPERTISE FOR GPS TESTING

**USAEPG**

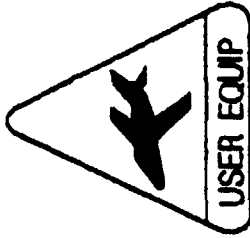
**◎ PARTICIPATING TEST ORGANIZATION  
(PTO)**

- **FIELD PERFORMANCE AND HUMAN  
FACTORS TESTING FOR  
PERSONNEL AND GROUND AND  
WHITE WATER PLATFORMS IN  
BENIGN, JAMMING, AND/OR  
SPOOFING ENVIRONMENTS**
- **ENVIRONMENTAL AND FIELD  
PERFORMANCE TESTING OF  
RECEIVER AND ANTENNA  
SYSTEMS**

**REPRESENTATIVE  
PICTURE**



**SPACE & MISSILE SYSTEMS CENTER  
GPS USER EQUIPMENT  
TEST & EVALUATION ROADSHOW**



# **CENTER OF EXPERTISE FOR GPS TESTING**

## **NAWC-AD PAX**

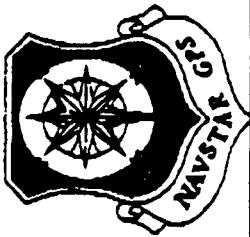
### **◎ PARTICIPATING TEST ORGANIZATION (PTO)**

- **FLIGHT SIMULATION FOR  
AIRCRAFT INTERFACE  
EVALUATION,  
PERFORMANCE  
CHARACTERIZATION, AND  
HOST VEHICLE  
INTEROPERABILITY**

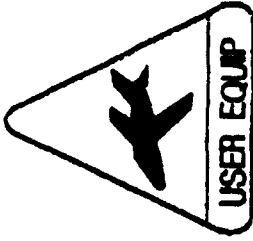
- **EMI/EMC**

**REPRESENTATIVE  
PICTURE**





**SPACE & MISSILE SYSTEMS CENTER  
GPS USER EQUIPMENT  
TEST & EVALUATION ROADSHOW**



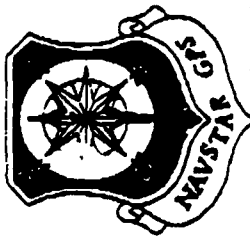
# **CENTER OF EXPERTISE FOR GPS TESTING**

## **NISE-WEST**

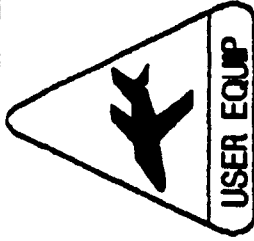
**✪ PARTICIPATING TEST  
ORGANIZATION (PTO)**

- **LABORATORY AND BLUE  
WATER TESTING OF GPS  
SEA SETS**
- **SPECIAL FORCES  
INTERFACE TESTING**

**REPRESENTATIVE  
PICTURE**



**SPACE & MISSILE SYSTEMS CENTER  
GPS USER EQUIPMENT  
TEST & EVALUATION ROADSHOW**



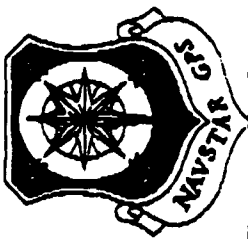
# **CENTER OF EXPERTISE FOR GPS TESTING**

**NRL**

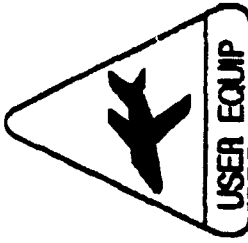
★ PARTICIPATING TEST  
ORGANIZATION (PTO)

- LABORATORY TESTING OF  
RECEIVER SYSTEMS FOR  
PRECISE TIME AND  
PRECISE FREQUENCY

**REPRESENTATIVE  
PICTURE**



**SPACE & MISSILE SYSTEMS CENTER  
GPS USER EQUIPMENT  
TEST & EVALUATION ROADSHOW**



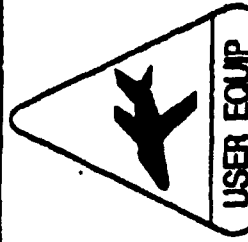
## **DoD TEST CLEARINGHOUSE**

### **OBJECTIVES**

- ✧ **Coordinate the electronic exchange of information to ensure that DoD GPS users stay informed of new applications and technologies.**
- ✧ **Ensure the availability and accessibility of existing test data, characterization and investigative information to the GPS user or potential users by functioning as a centralized repository of information.**



**SPACE & MISSILE SYSTEMS CENTER  
GPS USER EQUIPMENT  
TEST & EVALUATION ROADSHOW**



## **DoD TEST CLEARINGHOUSE**

### **OBJECTIVES**

- ✧ **Increase user and test agency participation in GPS test planning to ensure future UE acquisitions will satisfy the customer.**
- ✧ **Eliminate the potential for duplication of effort.**
- ✧ **Improve coordination of test infrastructure activities.**
- ✧ **Increase user awareness of new technologies and applications.**

**THIS PAGE LEFT BLANK INTENTIONALLY**

# **A Superconducting Six-Axis Accelerometer for Platform Control and Space Applications**

**E. R. Canavan and H. J. Paik**  
*Department of Physics and  
Center for Superconductivity Research  
University of Maryland  
College Park, MD 20742*

Approved for public release; distribution is unlimited.

## **Introduction and Background**

Continued advancement in inertial navigation, platform stabilization and gravity survey depends on the ability to resolve ever smaller accelerations. Further progress in this direction depends on a clear understanding of the basic physical limitations on the resolution of accelerometers. One of the most critical limitations is imposed by the Fluctuation - Dissipation Theorem, which states that any dissipation in a system causes random fluctuations, with amplitude proportional to the square root of temperature, in the variables describing its state (Brownian motion in mechanical systems; Johnson noise in electrical systems).

Physicists working on probably the most challenging motion measurement problem, the detection of gravitational waves, realized a few decades ago that this restriction can be circumvented by cooling instruments to the boiling point of liquid helium (4.2 K). Not only are all fluctuations reduced by a factor of ten from room temperature values, assuming fixed dissipation, but in many cases the dissipation in the system can be made drastically lower. This is particularly true for low frequency electrical subsystems, in which superconducting materials can be used to effectively eliminate dissipation.

Additionally, a new device becomes available: the Superconducting QUantum Interference Device (SQUID), an extremely low-noise magnetic-flux-to-voltage amplifier. The magnetic flux in a superconducting loop is quantized. However, if the loop is broken by two superconductor-insulator-superconductor junctions and a bias current is applied through the junctions, the voltage across the junctions is a periodic function of the number of flux quanta in the loop. The Johnson noise on this voltage is low enough that a very small fraction of one flux quantum may be resolved. In the laboratory, SQUIDs have demonstrated energy resolutions per unit bandwidth approaching the Heisenberg uncertainty limit,  $\Delta E \Delta t > h/2\pi$ , where  $h$  is Planck's constant. Although commercially available SQUIDs are about a thousand times noisier, they are still by far the quietest amplifier, and SQUID manufacturers are making steady progress toward matching the performance achieved by researchers.

How can the unsurpassed magnetic flux sensitivity of the SQUID be exploited for high resolution acceleration measurements? Typically, these devices are operated in closed-loop, or "flux-locked", mode: a room temperature controller feeds current back to a small coil to cancel flux changes in the SQUID loop. A second small coil (the input coil), inductively coupled to the loop, induces

a flux proportional to its current. In this configuration, the system acts as a linear, high gain, extremely low noise current-to-voltage amplifier. Because of the controller, commercial systems have small-signal bandwidths on the order of a few tens of kilohertz and dynamic ranges (the ratio of the maximum input signal to the power spectral density of input referred noise) of  $10^8 \text{ Hz}^{1/2}$  below 100 Hz. The input coils are relatively small (typically  $2 \mu\text{H}$ ), so SQUID systems are optimally matched to low impedance devices. The signal source must also have very low resistance to keep Johnson noise small. Thus, SQUIDs are usually used with superconducting transducers.

The Meissner effect, the exclusion of all magnetic field from the interior of superconductors, allows the construction of a very simple superconducting displacement transducer. A superconducting coil connected to the input coil of a SQUID forms a superconducting loop. If the loop carries a large current, it contains a large, fixed number of flux quanta. Now, if a large piece of superconductor in the vicinity of the coil moves toward the coil, it effectively pushes flux quanta out of the coil and into the SQUID input coil, where the change is detected. Transducers of this type used in gravitational wave detectors typically achieve displacement sensitivities (power spectral density of noise referred to displacement) smaller than  $10^{-16} \text{ m Hz}^{-1/2}$ . By using such a technique to measure the displacement of a relatively compliant mass-spring system, extremely good acceleration sensitivity can be obtained.

Although the prime motivation for using cryogenic devices is the reduction of noise, low temperatures offer another important benefit: greatly enhanced dimensional stability. Coefficients of thermal expansion must

go to zero at 0 K. For most materials, the coefficients at 4.2 K are approximately three orders of magnitude lower than at room temperature. Furthermore, creep is caused primarily by thermally activated processes which are frozen out at these temperatures. Additionally, many internal friction mechanisms are also frozen out, allowing very low loss springs.

Building on the experience of the gravitational wave detection community, the University of Maryland group developed the Superconducting Gravity Gradiometer (SGG), currently the most sensitive gravity gradiometer. However, because of residual sensitivity to platform motion, the most demanding applications of the gradiometer, such as global gravity mapping from orbit, require extremely good platform control in all six rigid-body degrees of freedom. In order to provide a sensitive, compact and cryogenically compatible readout device for such a controller, we invented the Superconducting Six-Axis Accelerometer. To keep the instrument relatively simple and compact, it uses only a single proof mass, which is magnetically levitated to provide good compliance in all degrees of freedom.

## Physical Description

Figure 1 shows an exploded view of the sensor. The 144 g proof mass is formed by three intersecting, orthogonal square slabs, 50.2 mm on a side and 2.39 mm thick. The proof mass fits into a cavity formed by mounting the eight cubical coil-forms inside the cubical cavity (50.8 mm (2") on a side) in the housing. Three sides of each coil-form face the proof mass; mounted on each of these sides are two concentric, spiral niobium coils. We use the inner coils for sensing and the

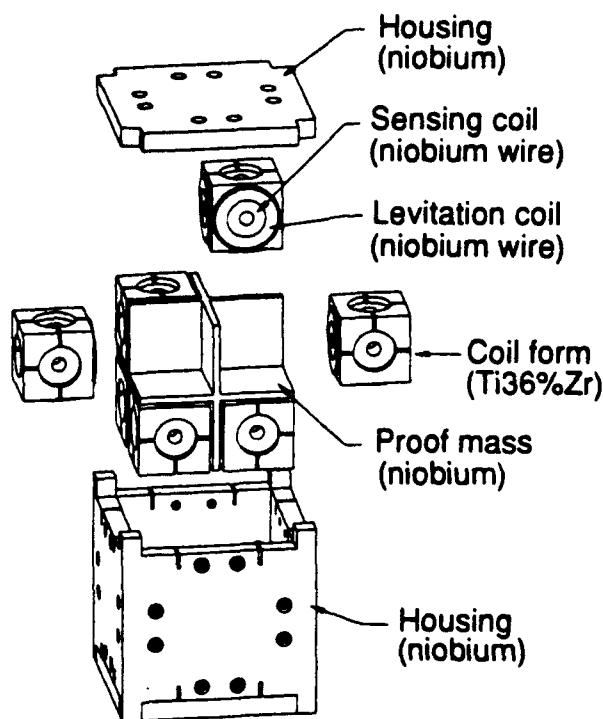


Figure 1. Exploded view of the SSA.

outer coils for levitation. When the proof mass is levitated, there is a 0.3 mm (0.012") gap between it and the coils, but small stops on the coils prevent it from moving more than 0.1 mm (0.004"). Although it is not displayed this way on the figure, the SSA is usually mounted in the "umbrella" orientation, that is, with the center of the housing and two diagonally opposed vertices along a vertical line. This makes all circuits symmetric with respect to  $g_e$ , the gravitational field of the earth, thus reducing the maximum magnetic field required for levitating the mass. In this orientation, coils in three planes are "below" the proof mass and coils in the three other planes are "above" it.

Naturally, selection of the proper materials is critical to the performance of the device. The proof mass and all superconducting wires are pure niobium, because niobium has the highest known first critical field,  $H_{c1}$ .  $H_{c1}$  is

the highest field a superconductor can tolerate while completely excluding magnetic flux. (High  $T_c$  superconductors all have extremely low  $H_{c1}$ , and thus would not provide the same performance.) When using niobium, particularly for the manufacture of fine wire, it is important to avoid any processing step that might increase the concentration of interstitial impurities, especially oxygen, since these increase the ductile-to-brittle transition temperature. Each junction between superconducting circuit elements must be carefully welded to maintain a high quality superconducting path through the circuit.

## The Magnetic Spring

We connect the four coils in each of the three planes below the proof mass to form three translational levitation circuits, which provide linear levitation force along three orthogonal axes. As Figure 2 shows, the four coils are simply connected in series with a transformer. The sets of coils above the proof mass are connected to form rotational levitation circuit, which provides torques about the three axes. Figure 3 shows that the coils on one side of the torque axis and the coils on the

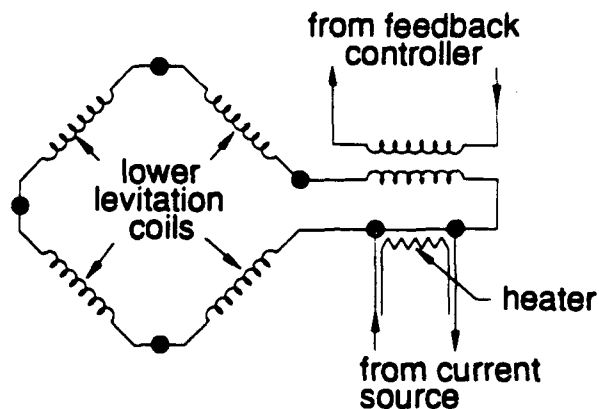


Figure 2. Translational levitation circuit.



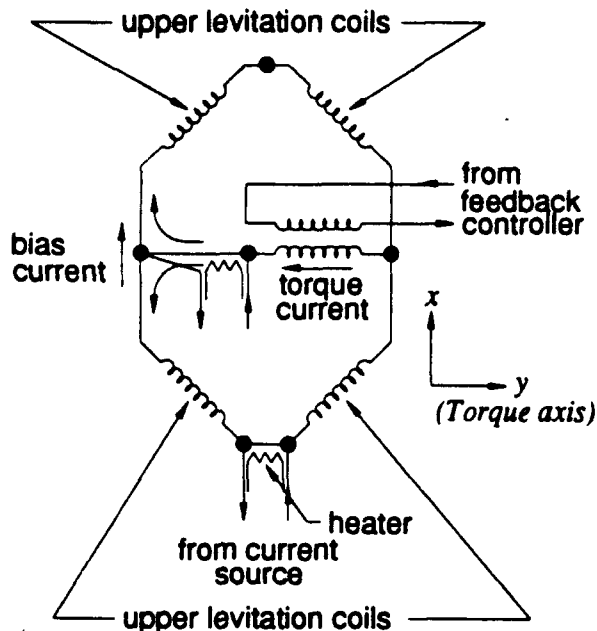


Figure 3. Rotational levitation (torquing) circuit.

other side of axis are connected in parallel with a transformer.

We use the heaters shown in the two figures to trap flux or "store current" in the circuits. By applying a heat pulse large enough to momentarily raise the temperature of a small section of wire above the critical temperature, we break the superconducting path and force any current passing through the charging leads (labeled "from current source") to pass through and induce a flux in the inductors. When the warm section becomes superconducting again, the flux in these inductors is trapped and remains absolutely constant after the current source is removed.

Storing current in a translational circuit or in the outer loop of the rotational circuit ("bias current") creates a force normal to the plane of the coils. The rotational circuit has an additional heater which allows us to store current through the central branch of the circuit ("torque current"). This current adds to the

bias current on one side of the circuit and subtracts from it on the other, creating a torque. Normally, the currents in the rotational circuits are an order of magnitude smaller than those in the translational circuits.

The force between a superconductor and a current-carrying wire comes from the interaction of surface currents on the superconductor and the current in the wire. The superconductor sets up surface currents to cancel any field in its interior. The force between the surface currents on a superconducting plane and the current,  $I$ , in a nearby coil is  $\Lambda I^2/2$ . The force provided by the four translational levitation coils,  $2\Lambda I^2$ , must cancel the component of the proof mass weight normal to the coils,  $mg_E \cdot \hat{n}$  (plus a small force, which we ignore here, due to the bias current in the coils above the proof mass). The current required in each translational circuit to lift the proof mass is then

$$I_{lev} = \sqrt{\frac{mg_E}{2\sqrt{3}\Lambda}} \quad (1)$$

The force coefficient  $\Lambda$  is proportional to the turns density squared. The wire-wound coils of the present SSA have a turn-to-turn spacing of approximately 100  $\mu\text{m}$ , giving  $I_{lev} = 5.5$  A. Such currents are rather easily generated and handled. Furthermore, the current is only needed for several brief ( $\sim 1$  min) periods during the initial setup of the device. In contrast, capacitive levitation schemes generally require thousands of volts to levitate significant masses against the Earth's field. If photolithographic techniques were used to make the coils, a reduction in the line spacing, and hence the required current, by an order of magnitude could easily be achieved.

For a flat spiral coil parallel to a superconducting plane, the force coefficient is a function of the gap,  $x$ , but as  $x$  becomes small

compared to the coil diameter,  $\Lambda(x)$  approaches a constant value. In this case, the coil inductance is  $L = x \Lambda$ . If the coil is connected to a fixed inductor,  $L_f$ , then the total flux trapped in the circuit is  $(x \Lambda + L_f) I$ . Because of flux quantization, this quantity must remain fixed even if the gap changes by  $\delta x$ :

$$(x \Lambda + L_f) I = [(x + \delta x) \Lambda + L_f] (I + \delta I). \quad (2)$$

Thus,

$$\delta I = -I \frac{\Lambda \delta x}{\Lambda x + L_f}, \quad (3)$$

where we have dropped the small quadratic  $(\delta x \delta I)$  term. Therefore, if  $L_f \gg \Lambda x > \Lambda \delta x$ , the change in current, and thus the change in force, with a change in gap is very small. In other words, the mass will act as though it is supported by a spring with very small spring constant.

Unfortunately, the gap dependence of  $\Lambda(x)$  puts a lower bound on the spring constant. If we approximate  $\Lambda(x)$  with a linear function of  $x$ ,

$$\Lambda(x + \delta x) = \Lambda(x) - \gamma(x) \delta x, \quad (4)$$

then the force on a superconducting plane displaced by a small amount  $\delta x$  from the equilibrium position is

$$\begin{aligned} \delta F(x + \delta x) &= F + \delta F \\ &= [\Lambda(x) - \gamma(x) \delta x] I^2 / 2. \end{aligned} \quad (5)$$

Therefore, even if  $L_f$  is large enough to make  $\delta I$  negligible, there is still a change in force,  $\delta F = -\gamma(x) I^2 \delta x / 2$ , giving an effective spring constant of  $\gamma(x) I^2 / 2$ .

This minimum spring constant sets the minimum realizable resonance frequency for the translational modes of the SSA proof

mass. Taking the spring constant of a circuit with four such coils and substituting the levitation current given by Eq. (1) yields

$$\omega_{\min} = \sqrt{\frac{k}{m}} = \sqrt{\frac{g \epsilon / \sqrt{3}}{\Lambda(x) / \gamma(x)}}. \quad (6)$$

This is the frequency of a pendulum with length  $\Lambda(x) / \gamma(x)$ . The quantities  $\Lambda(x)$  and  $\gamma(x)$  are not calculable in closed form. However, numerical computations show that the length  $\Lambda(x) / \gamma(x)$  is a weak function of the gap. It is also a weak function of the coil geometry; for example, a solenoid and a pancake coil with the same maximum diameter and number of turns have values that differ by less than 30%. For the present SSA,  $\omega_{\min} / 2\pi = 11.3$  Hz.

The derivation of the complete expression for the rotational mode frequencies is rather lengthy [1], but the following heuristic argument provides the proper expression for the dominant term. Consider the coordinate system shown in Figure 4. The coils of the  $y$  translational levitation circuit are on the  $-y$  side of the  $x$ - $z$  plane. To first order, the total inductance of this circuit remains unchanged with a rotation of the proof mass about the  $x$  axis, because the inductance of the two coils on the  $-z$  side increases by the same amount as

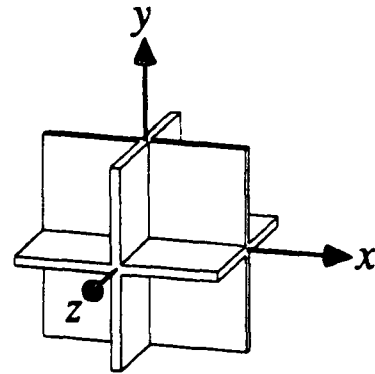


Figure 4. The proof mass coordinate system.

the inductance of those on the  $+z$  side decreases. The same is true for rotations about the  $z$  axis. Since the total flux is fixed, the current does not change with rotation.

With fixed current, the effective spring constant is  $\gamma(x)I^2/2$ . If we assume that the force of a coil acts at its center, a distance  $c$  from the axis of rotation, and that the displacement at this point due to a rotation by an angle  $\delta\theta$  is  $c\delta\theta$ , then the torque due to the four coils is

$$\delta T = c\delta F = c[4(\gamma I^2/2)(c\delta\theta)]. \quad (7)$$

A rotation about one axis affects coils in two planes. (A rotation about the  $z$  axis changes inductances in the  $y$ - $z$  and  $x$ - $z$  planes.) Therefore, the total angular spring constant is  $\tau = 4c^2\gamma I^2$ . Again substituting Eq. (1), we obtain

$$\omega_{rot} = \sqrt{\frac{\tau}{J}} = \sqrt{\left(\frac{2mc^2}{J}\right)\frac{gE}{\Lambda(x)/\gamma(x)}}, \quad (8)$$

where  $J$  is the moment of inertia of the proof mass. Using the values for the present SSA,  $\omega_{rot}/2\pi = 9.1$  Hz. As mentioned above, this is only an approximation; the actual frequency is approximately 60% higher.

Up to this point, we have considered motion in only one degree of freedom at a time, but the position and orientation of the proof mass with respect to each coil is affected by motion in several degrees of freedom. The force due to the magnetic fields always acts perpendicular to the proof mass surface. This causes the force in one degree of freedom to be proportional to displacements in other degrees of freedom. Thus, the action of the levitation circuits must be described by a spring constant matrix with non-zero off-diagonal terms. A full analysis of the proof mass motion is presented elsewhere [1]; here we pres-

ent only an intuitive derivation of these cross terms.

Consider small motions of the proof mass with respect to the coordinate system defined by Figure 4. The coils in the  $y$ - $z$  plane, the  $x$  translational levitation circuit and the  $\theta$ , rotational levitation circuit normally apply a force along the  $x$  axis. The total force,  $F_{dc} = 2\Lambda(I_{lev}^2 - I_{bias}^2)$ , cancels the  $x$  component of the proof mass weight. In the umbrella orientation,  $F_{dc}$  is the same for all three axes. A small rotation about the  $z$  axis,  $\delta\theta_z$ , will cause a component of this force,  $F_{dc} \sin(\delta\theta_z) \approx F_{dc} \delta\theta_z$ , to appear in the  $y$  direction. Similarly, the same rotation  $\delta\theta_z$  will cause a small component,  $-F_{dc} \delta\theta_z$ , of the force from the coils in the  $x$ - $z$  plane to appear in the  $x$  direction.

A translation of the proof mass places a torque on an orthogonal axis because of a change in the effective moment arms. Consider the coils in the  $x$ - $z$  plane, which produce a force  $F_{dc}$  in the  $y$  direction. We assume that the force from a coil acts on a single point on the proof mass directly above the center of the coil, a distance  $c$  from the  $z$  axis. The coils on the  $+x$  side generate a torque  $cF_{dc}/2$  about the  $z$  axis, and those on the  $-x$  side generate  $-cF_{dc}/2$ , so the total is zero. Now, if we displace the proof mass by a small distance  $\delta x$  along the  $x$  axis, the coils on the  $+x$  side produce a torque  $(c - \delta x)F_{dc}/2$  (relative to the center of the proof mass) and those on the  $-x$  side produce  $-(c + \delta x)F_{dc}/2$ , so the total is  $-F_{dc}\delta x$ . The same displacement  $\delta x$  causes the coils in the  $x$ - $y$  plane to generate a torque  $F_{dc}\delta x$  about the  $y$  axis.

Applying the same reasoning to displacements in all degrees of freedom, we find that the spring constant of the levitation circuits can be represented as

$$\mathbf{k} = \begin{pmatrix} k\mathbf{I} & F_{dc}\mathbf{S}^T \\ F_{dc}\mathbf{S} & \tau\mathbf{I} \end{pmatrix}, \quad (9)$$

where  $k$  and  $\tau$  are the linear and angular spring constants, respectively,  $\mathbf{I}$  is a  $3 \times 3$  identity matrix, and  $\mathbf{S}$  is the unit antisymmetric matrix,

$$\mathbf{S} = \begin{pmatrix} 0 & 1 & -1 \\ -1 & 0 & 1 \\ 1 & -1 & 0 \end{pmatrix}. \quad (10)$$

The cross-coupling terms due to these off-diagonal spring constants can be strongly suppressed by applying feedback.

An important property of a precision accelerometers is the stability of its spring constant. The spring constants of the SSA depend solely on purely geometric quantities such as  $L$ ,  $\Lambda(x)$  and  $\chi(x)$ . As mentioned in the introduction, creep and thermal contraction are negligible in most materials at liquid helium temperature. However, to this point we have been treating superconducting bodies as perfect diamagnetic objects, with zero field just inside the surface and a large field just outside. In actuality, the field drops exponentially with distance inside the surface. The length scale of the exponential decrease is called the *penetration depth*,  $\lambda$ , and it has a temperature dependence given by

$$\lambda(T) = \frac{\lambda(0)}{\sqrt{1 - (T/T_c)^4}}. \quad (11)$$

where  $\lambda(0)$  is the penetration depth at 0 K. For niobium,  $\lambda(0) = 47$  nm and  $T_c = 9.2$  K.

For the field, the effective gap is the distance between the plane passing through the center of the coil wire and a plane approximately  $\lambda(T)$  inside the surface of the proof mass. It is this effective gap that remains fixed, so if  $\lambda(T)$  increases, the position of the

proof mass drops by an equal distance. Well below the mass-spring resonance frequency,  $\omega_0$ , the acceleration  $a$  and the displacement  $x$  are related by  $a = \omega_0^2 x$ . Thus, the temperature coefficient of acceleration is

$$\begin{aligned} \frac{da}{dT} &= \omega_0^2 \frac{d\lambda}{dT} \\ &= \frac{\lambda(0)}{T_c [1 - (T/T_c)^4]^{3/2}} \left( \frac{T}{T_c} \right)^3. \end{aligned} \quad (12)$$

At  $T = 4.2$  K, this coefficient is  $4 \times 10^{-9}$  m s<sup>-2</sup> K<sup>-1</sup> for the present SSA. This implies that if we require an acceleration sensitivity of  $10^{-11}$  m s<sup>-2</sup>, we must keep the temperature noise below 2.5 mK Hz<sup>-1/2</sup>. Temperature control at this level can be provided by commercially available instruments. If we attain higher acceleration sensitivity, we will need tighter temperature control. Cryogenic devices with temperature noise levels around 1  $\mu$ K Hz<sup>-1/2</sup> are routinely constructed. Furthermore, the temperature coefficient can be lowered by an order of magnitude by reducing the temperature to below the superfluid helium transition temperature (2.17 K), a measure that has additional benefits for temperature control.

## Displacement Sensing

We showed in the introduction that a large superconductor, a superconducting coil, and a SQUID can be configured as an extremely sensitive displacement transducer. If the superconducting surface and the coil are flat and separated by a small gap, the change in the current of a closed circuit is directly proportional to the gap, as given by Eq. (3). Since a (flux locked) SQUID is a linear voltage-to-current amplifier, the voltage out of the SQUID controller is linearly proportional to the displacement. This type of sensing

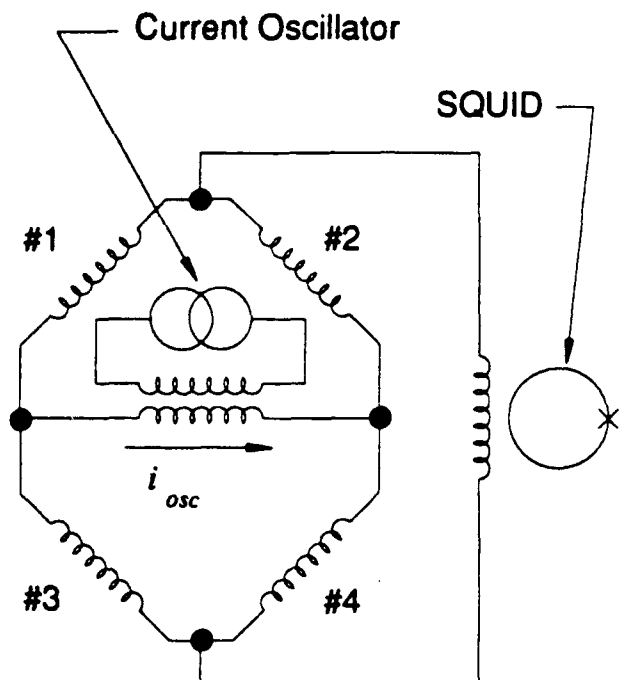


**Figure 5.** Displacement sensing circuit. For translational sensing, coils #1 and #4 are below the proof mass; #2 and #3 are above.

circuit is used in the SGG and in gravitational wave antennas. Unfortunately, the closed-loop behavior of the SQUID system gives this configuration an undesirable feature. If the signal exceeds the slew rate of the controller, or if rf interference causes a temporary loss of the SQUID voltage, the controller "loses lock." When the system resettles, the output voltage offset by an amount equivalent to an integral number of flux quanta. Even if the dc level is unchanged, the number of flux quanta in the SQUID loop, and thus the dc displacement, may have shifted. This property is especially objectionable when the output is the input of a feedback controller, such as for platform stabilization.

For this reason, the SSA uses an ac inductance bridge, as shown in Figure 5. An oscillator with a current output stage, coupled through a superconducting transformer, provides a sinusoidal current across two vertices of the bridge. In the translational sensing

circuit, the coils labeled #1 and #4 are below the proof mass and those labeled #2 and #3 are above it. If the coils are identical, then when the proof mass is centered between the upper and lower coils, all the inductances are equal and no current flows through the SQUID input coil. An upward or downward displacement unbalances the bridge, forcing current  $i_{SQ}$  through the input coil.

More quantitatively, we can represent the variation of inductance with displacement,  $\delta x$ , using a truncated Taylor expansion:

$$L(\delta x) = L_0 + \Lambda_0 \delta x - \frac{\gamma}{2} (\delta x)^2. \quad (12)$$

$L_0$ ,  $\Lambda_0$ , and  $\gamma_0$  are the inductance and its first and second derivatives with the proof mass centered. Solving the circuit equations for  $i_{SQ}$  and expanding to third order yields

$$i_{SQ} = i_{osc} \frac{\Lambda_0}{L_{SQ} + L_0} \delta x + O[(\delta x)^3], \quad (13)$$

where  $i_{osc}$  is the current through the secondary of the transformer. For proper impedance matching,  $L_{SQ} = L_0$ . Since  $L_0 = x_0 \Lambda_0$ , where  $x_0$  is the gap, Eq. (13) reduces to

$$i_{SQ} \approx i_{osc} \frac{\delta x}{2x_0}. \quad (14)$$

The rotational sensing circuits differ only in the position of the coils. They are arranged so that #1 and #4 increase with rotation about the appropriate axis and #2 and #3 decrease. In this configuration, the SQUID output is proportional only to rotation about the axis, to first order.

Thus, the signal from the SQUID, after demodulation, provides a voltage proportional to displacement of the proof mass from the centered position. This has an important advantage for the SSA: centering the proof mass, first at dc by choosing the proper set of

currents to store in the various levitation circuits, then over a wide bandwidth by applying feedback, is simply a matter of minimizing the SQUID output. The proof mass must be centered as well as possible in order to minimize cross coupling and certain other dynamical errors. Furthermore, any shift in the dc level due to SQUID unlocks appears after demodulation as a pulse, so the feedback controller can set the proof mass back to its proper position following such an event. The scheme has an additional benefit: because it is sensitive only to the difference between the upper and lower gap, it is insensitive to changes in the penetration depth caused by a change in the average temperature of the proof mass. Only changes in temperature gradients, which are small, cause a response.

The frequency  $f_{osc}$  of the oscillator that drives the bridge circuit, typically around 1 kHz, is a compromise between bandwidth and dynamic range. Demodulation of a signal in a band around  $f_{osc}$  produces a band of equal magnitude around  $2f_{osc}$ . This must be reduced by filtering before the signal enters the SSA controller. However, filters introduce low frequency poles which limit the bandwidth of the closed loop system. Thus, a modulation frequency at least an order of magnitude above the closed loop bandwidth ( $\sim 100$  Hz) is desirable. On the other hand, with the SQUID controller presently in use, the maximum tolerable sine wave amplitude, and thus the dynamic range, decreases with frequency. At 1 kHz, the dynamic range is  $\sim 3 \times 10^6$  Hz<sup>1/2</sup> with a frequency dependence of approximately  $f^{-1}$ . This is not an inherent limitation; systems having a constant dynamic range of  $2 \times 10^7$  Hz<sup>1/2</sup> up to 6 kHz have been built [2]. A previous version of the SSA used a single SQUID coupled to all six sensing circuits. In this case, the oscillator frequencies had to be widely spaced in frequency, so some of the

axes had a significantly lower dynamic range than others. The present design uses one SQUID for each circuit to avoid this problem.

## Acceleration Sensitivity

As we discussed in the introduction, thermally induced mechanical and electrical fluctuations limit the resolution of an accelerometer. In the SSA, the dissipation of the superconducting magnetic springs is low enough that the noise of the SQUID amplifier generally dominates over the Brownian motion noise. The noise of SQUID can be modeled as a simple current noise source across its input coil with a constant power spectral density of  $P_{i_{sq}}$ .  $P_{i_{sq}}$  shows 1/f frequency dependence below approximately 0.1 Hz, but because the signal is modulated, it is unaffected by this red noise. Well below the mass-spring resonance frequency, we can estimate the equivalent acceleration noise by combining Eq. (14) and the relationship between displacement and acceleration,  $\delta x = a/\omega_0^2$ . We substitute  $2P_{i_{sq}}$  for  $i_{sq}$ . (Demodulation causes the SQUID noise to contribute twice.) Using Eq. (6) for  $\omega_0$ , we obtain an expression for the equivalent acceleration noise:

$$P_a = 4x_0\omega_0^2 \frac{P_{i_{sq}}}{i_{osc}} = \frac{4g_E}{\sqrt{3}} \left( \frac{\gamma_0 x_0}{\Lambda_0} \right) \frac{P_{i_{sq}}}{i_{osc}} \quad (15)$$

For a given coil diameter, the dimensionless quantity  $(\gamma_0 x_0/\Lambda_0)$  is a weak function of gap and geometry. Thus, for a given SQUID and coil size, minimizing  $P_a$  depends primarily on maximizing  $i_{osc}$ .

Unfortunately, there is an inherent limitation on  $i_{osc}$ . The current through the sensing

coils produces a force on the proof mass proportional to  $i_{osc}^2$  at dc (and  $2f_{osc}$ , but the proof mass does not respond at this frequency). At zero displacement, the net force is zero (assuming perfectly matched coils). When the proof mass moves up, the impedance of the lower coils increases and that of the upper coils decreases, so more current flows through the upper coils, increasing the downward force. Hence, the sensing circuit provides an additional spring constant which tends to lower the acceleration sensitivity. By including the spring constant due to the sensing circuit in the calculation of  $P_a$ , we find that  $P_a$  reaches a minimum when  $i_{osc}$  is large enough to double the initial spring constant. This optimum  $i_{osc}$  is on the order of the levitation currents. With the present SQUIDs (S.H.E. rf SQUIDs), for which  $P_{ISQ} \approx 10^{-11} \text{ A Hz}^{-1/2}$ , the optimum  $i_{osc}$  would give an acceleration noise of approximately  $2 \times 10^{-11} \text{ m s}^{-2} \text{ Hz}^{-1/2}$ . For a more modern system, the Quantum Design dc SQUID,  $P_{ISQ} \approx 6 \times 10^{-13} \text{ A Hz}^{-1/2}$ , after reflection through an impedance matching transformer. This is equivalent to an acceleration noise of  $2 \times 10^{-12} \text{ m s}^{-2} \text{ Hz}^{-1/2}$ . The equivalent angular acceleration noise is  $2 \times 10^{-10} \text{ rad s}^{-2} \text{ Hz}^{-1/2}$ . In a low g background, the acceleration sensitivity is at least an order of magnitude lower.

A practical limitation prevents us from using the optimum current. The coils are not perfectly matched. Because of this, the force on the proof mass is not zero when it is at a position which balances the bridge. This dc force is a problem because it depends on the amplitude of the oscillator. Drift in the oscillator will cause a changing force on the proof mass, and hence a drift in the acceleration output. We can estimate this acceleration by calculating the total force on the proof mass when the parameter  $\Lambda$  for two lower coils

differs from that of the two upper ones by  $\delta\Lambda$ . Simple circuit analysis gives this force as  $\delta\Lambda i_{osc}^2$ . If  $i_{osc}$  changes by a small amount  $\delta i$ , the resulting shift in the acceleration output is  $\delta a = 2\delta\Lambda i_{osc} \delta i / m$ , or in terms of relative errors,

$$\delta a = 2 \left( \frac{\delta\Lambda}{\Lambda} \right) \left( \frac{\delta i}{i_{osc}} \right) \frac{\Lambda i_{osc}^2}{m}. \quad (16)$$

We want to set  $i_{osc}$  low enough so that oscillator noise does not dominate over SQUID noise in the useful bandwidth of the device. Because of the temperature dependence of critical components in the voltage-to-current output stage, even a well designed current oscillator will have significant red noise. The SQUID output, after demodulation, has little excess red noise above the millihertz regime. Thus, the worst oscillator noise is at the lowest frequency that we expect to use, approximately 1 mHz. We estimate that at this frequency, a current source using the best available components should be stable to 10 ppm. The force coefficients  $\Lambda$  are matched to about 1%. Setting Eq. (16) equal to Eq. (15) (times the square root of frequency) gives a limiting  $i_{osc}$  of 90 mA. Even with this limitation, performance is quite good. Substituting  $i_{osc} = 90 \text{ mA}$  back into Eq. (15) yields an acceleration noise of  $8 \times 10^{-10} \text{ m s}^{-2} \text{ Hz}^{-1/2}$  and an angular acceleration noise of  $6 \times 10^{-8} \text{ rad s}^{-2} \text{ Hz}^{-1/2}$ , using the current SQUIDs. Of course, if the signal frequencies of interest are higher than this, the limitation is relaxed. For frequencies above a few Hertz, the noise of the oscillator is white and low enough not to matter (assuming the present SQUIDs are used).

This limitation on  $i_{osc}$  is purely a technological one. The dimensions of the present wire-wound coils cannot be controlled to better about 100  $\mu\text{m}$ . Using standard photolithographic techniques, thin film coils with

dimensional tolerances close to 1  $\mu\text{m}$  should be easily manufacturable. In this case,  $\delta \ln \Lambda$  would be small enough that this error source will no longer be relevant. Thin film devices of high quality niobium (such as the SQUIDs) are routinely manufactured, although making reliable, high current (hundreds of milliamps) superconducting junctions between the films and wires will require some development.

The noise levels calculated for the current design are a substantial improvement over those of a previous version of the device. In that model, all six bridge circuits were connected in series directly with the SQUID input coil. Unfortunately, the impedances are not correctly matched in this configuration. Additionally, the secondary of the feedback transformer was not large enough to minimize the resonance frequency of the translational modes; resonance frequencies were typically 21 Hz. Improving the impedance matching and lowering the resonance frequency will reduce the acceleration noise in the current device by approximately one order of magnitude. For example, the measured acceleration noise of first model of the device was  $3 \times 10^{-9} \text{ m s}^{-2} \text{ Hz}^{-1/2}$ , using  $i_{osc} = 0.23 \text{ A}$  in one of its translational sensing circuits. This matches the value calculated from its parameters to within 25%. An angular acceleration noise of  $7 \times 10^{-8} \text{ rad s}^{-2} \text{ Hz}^{-1/2}$  was measured on an angular sensing circuit with  $i_{osc} = 0.48 \text{ A}$ . For the same current, the acceleration noise of the current design should be  $3.0 \times 10^{-10} \text{ m s}^{-2} \text{ Hz}^{-1/2}$ . The improvement in angular acceleration noise will only be by about a factor of 4, because the dominant term in the angular spring constant depends only on the coil geometry, which is approximately the same.

## Controller

Many of the characteristics of the SSA can be improved by using feedback. Because of the low dissipation of the magnetic levitation, the open-loop acceleration-to-voltage transfer function of the SSA has an undesirable large peak at the resonance frequency. In addition, the levitation force is a nonlinear function of position. Feedback flattens the response and increases the bandwidth from  $\sim 13$  to  $\sim 100 \text{ Hz}$ . It also reduces displacement, particularly at low frequencies where the controller gain is high, and thus improves linearity and reduces displacement-related dynamical errors. One of the most important dynamical errors is the cross-axis sensitivity introduced by the off-diagonal terms of the spring constant matrix (Eq. (9)). Although ordinary single-input, single-output feedback reduces cross coupling substantially, the SSA controller uses a sophisticated multiple-input, multiple-output (MIMO) design to further suppress these terms [3], [4].

There are several important considerations in the design of the controller. One of the main challenges when designing a room-temperature controller for an extremely low noise cryogenic instrument is making sure that the controller does not eliminate the advantage of using a cryogenic system by introducing noise that greatly exceeds the SQUID noise. Satisfying this criterion requires careful attention to the output stage of the controller, which takes the voltages from the signal conditioning stage and produces a current that is coupled into the levitation circuits to produce the feedback force. Any noise due to this stage appears as an equivalent acceleration noise. By choosing the voltage-to-current conversion ratio to be low enough, the equivalent acceleration noise can be made to match that of the SQUID. However, a low V-to-I



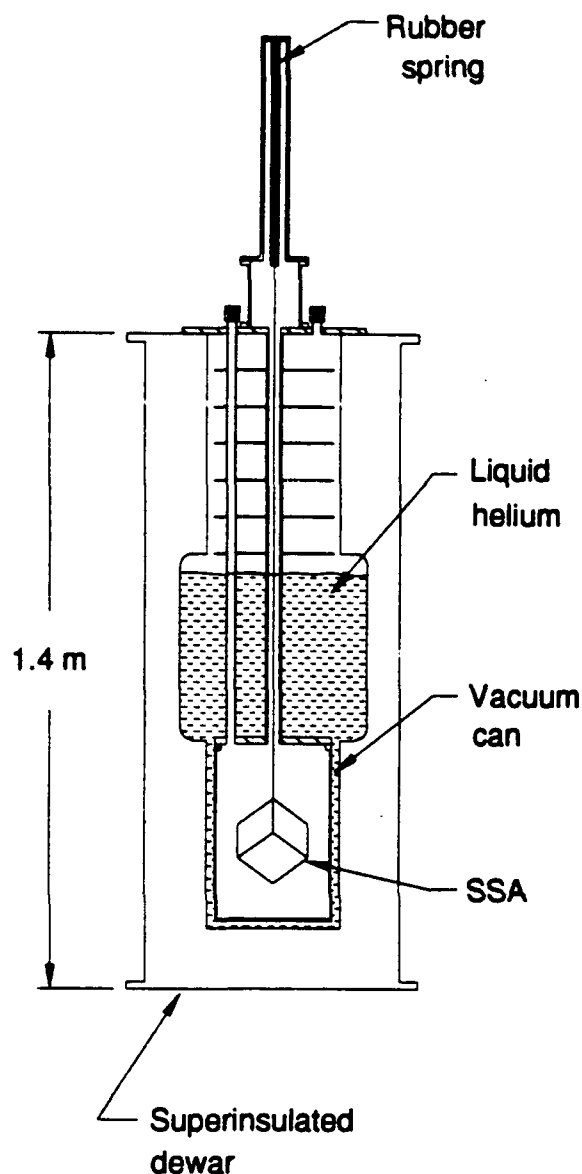


**Figure 6.** Schematic drawing of the SSA in a typical cryostat used for testing. A shaker, used for applying accelerations, is not shown.

ratio implies that the maximum tolerable signal is small. Increasing the ratio increases the maximum signal, but at the cost of greater noise. Equivalently, the controller can displace upward (not increase) the dynamic range of the system.

The controller must also not diminish the dynamic range. Because of the relatively

large dynamic range of available SQUID controllers (on the order of  $10^7 \text{ Hz}^{1/2}$ ), as well as the sensitivity of the SQUID to rf noise (such as produced by digital systems), we choose to implement the controller with analog circuits. With this type of device we must choose the various gains throughout the system to avoid saturation in any stage when accelerations are below the design maximum. We have also designed the SSA controller to be stable and robust against changes in the accelerometer parameters.

## Ancillary Equipment

Although the proof mass of the SSA is only 5 cm on a side, the overall system, including all electronics and cryogenic hardware, is presently quite large. With modest effort, it can be substantially reduced. Figure 6 schematically portrays the SSA in a cryostat similar to one recently built for a gravity gradiometer. The accelerometer and its superconducting circuitry hang inside a vacuum can from a long rubber spring that provides isolation from high-frequency ( $> 2 \text{ Hz}$ ) seismic noise. For applications in a quiet environment, the device could be mounted with a much stiffer suspension directly to the inside of the vacuum can. The vacuum can fits into a liquid helium dewar. The one shown here is 1.4 m high and 0.4 m in diameter. With careful design, one could reduce the dewar height to less than 1 m.

The extreme sensitivity of SQUIDs to electromagnetic fields that makes them so desirable also makes it necessary to use great care to shield them from undesirable fields. We use several stages of isolation. First, the SSA housing and connection boxes are superconducting, and all critical leads pass through superconducting tubes. We have used a

resistive titanium alloy for the coil forms and for the oscillator transformers because these will strongly damp rf signals. The vacuum can is also superconducting. The inner wall of the dewar around the vacuum can and the entire outer wall are of aluminum. In addition, we use two concentric mu-metal shields inside the dewar's vacuum space to reduce the background magnetic field. Finally, all leads entering the cryostat pass through EMI filters.

## Applications

The extremely low noise of the SSA will allow it to extend the state of the art in several important applications. The initial impetus for its development came from the need to meet the extremely demanding platform motion requirements on the proposed Superconducting Gravity Gradiometer Mission [5]. The drag-free satellite contemplated for this mission would contain an SGG that would map the Earth's gravity with unprecedented resolution [6], [7]. Because the SSA is also a cryogenic instrument, it can be mounted directly on the SGG. More importantly, although the SSA can be operated and fully tested in the one-g background field on Earth, in orbit only small levitation currents are needed to provide a bias for the feedback current. Therefore, the effective spring constant, and thus the equivalent acceleration noise level, will be several orders of magnitude lower than on Earth.

Using the SSA, actively controlled terrestrial platforms could offer unprecedented quiet seismic environments. Active quiet platforms are under investigation for a number of uses. The Seismically Stable Platform (SSP) at Holloman Air Force Base is intended for testing of inertial guidance systems. Similar devices could be used in laser interferometer

gravitational-wave antennas. The mirrors of the interferometer must be mounted on seismically quiet platforms. Particularly at low frequencies ( $<100$  Hz), the level of allowed platform motion is extremely small. Active control of the SGG platform in the laboratory could reduce several motion-related error sources, and so improve measurements of the inverse-square law of gravity [8].

Although gravity survey from orbit has the advantage of providing complete global coverage, resolution of features substantially smaller than 50 km is not likely in the foreseeable future. However, at an altitude of 1 km, geological features with a size on the order of 1 km produce gravity gradient signals that even a much less sensitive gradiometer can detect. Unfortunately, an airplane is a hostile environment for sensitive motion detectors. An actively controlled platform can remove angular and high-frequency translational motion. However, control of translational motion at low frequencies is not possible (using existing autopilots), because the displacements needed exceed the dimensions of airplane interiors. An SGG/SSA package could be mounted on a platform controlled by standard instruments, and the SSA could be used to remove errors from low-frequency translational motion and residual angular motion of the platform.

The SSA could also be used alone for airborne gravity survey. In this case, the SSA would be mounted on a simple passive isolation platform along with a GPS receiver. Subtracting the acceleration of the vehicle, obtained using the GPS data, from the acceleration measured by the SSA will give the variation in local gravity. This technique has been successfully tried in airplanes [9] and unmanned balloons [10] using single-degree-of-

freedom gravimeters. Because the SSA provides the motion in all six degrees of freedom, it would allow the local gravity vector to be mapped. An SSA to be used in such a seismically noisy environment would have to be optimized to maximize its dynamic range.

## Acknowledgements

This work was supported by the Air Force Phillips Laboratory under contract F19628-87-K-0053.

## References

- [1] Paik, H.P., Parke, J.W., and Canavan, E.R., "Development of a superconducting six-axis accelerometer", Final Report to the Air Force Geophysics Laboratory, Report No. GL-TR-89-0181 (1989).
- [2] Wellstood, F., Heiden, C., and Clarke, J., "Integrated dc SQUID magnetometer with a high slew rate", *Reviews of Scientific Instruments* 55(6):952-957 (1984).
- [3] Bachrach, B., *Control of a superconducting six-axis accelerometer*, Master's Thesis, University of Maryland (1990).
- [4] Bachrach, B., Canavan, E.R., and Levine, W.S., "Diagonalizing controller for a superconducting six-axis accelerometer", *Proceedings of the 29th IEEE Conference on Decision and Control*, Honolulu, HI (1990).
- [5] Paik, H.J., et al., "Global gravity survey by an orbiting gravity gradiometer", *EOS* 69(48): 1601, 1610-1611 (1988).
- [6] Paik, H.J., "Superconducting tensor gravity gradiometer for satellite geodesy and inertial navigation", *Journal of the Astronautical Sciences* 29(1):1-18 (1981).
- [7] Moody, M.V., Chan, H.A., and Paik, H.J., "Superconducting gravity gradiometer for space and terrestrial applications", *Journal of Applied Physics* 60(12):4308-4315 (1986).
- [8] Moody, M.V. and Paik, H.J., "Gauss's Law test of gravity at short range", *Physical Review Letters* 70(9): 1195-1198 (1993).
- [9] Brozena, M. and Peters, M.F., "An airborne gravity survey of eastern North Carolina", *Geophysics* 53(2): 245-253 (1988).
- [10] Lazarewicz, A., et al., "Balloon-borne high altitude gravimetry: The flight of DUCKY II", Environmental Research Papers, No. 988, Air Force Geophysics Laboratory (1987).

# LOW COST QUARTZ RATE SENSORS APPLIED TO TACTICAL GUIDANCE

**S. W. Hammons  
Systron Donner Inertial Division  
2700 Systron Drive  
Concord, CA 94518**

## ABSTRACT

With the production of over 11,000 Quartz Rate Sensors (QRS) since July 1991, this Systron Donner product has proven itself a low cost alternative to conventional gyroscopes, both optical and spinning mass. Programs ranging from Maverick to the Northrop BAT IMU have taken advantage of the QRS's distinctive combination of performance and producibility to meet their system product goals.

This paper presents both technical background and data showing the current and projected performance capabilities of the QRS and how it is now being applied in 3 and 6 degree of freedom guidance packages with accuracy requirements from 10°/hr. This data is especially noteworthy in the light of the production proven low cost capability of the QRS resulting from its single piece, micromachined sensor element.

## INTRODUCTION

This section highlights six years of activity at Systron Donner Inertial Division in understanding and maturing the Quartz Rate Sensor (QRS), bringing it into production, and adapting it to a new range of applications.

In these days of significantly reduced governmental financial support to industry, a clear case has to be established for the investment of millions in company research and development dollars into a particular gyro technology where there is no guarantee that the end product will make the returns necessary within a predetermined timescale.

The principle behind the QRS are not unique and are discussed later; however, the inherent simplicity, and potential ease of manufacture promised an extremely low-cost sensor.

The QRS is a single degree of freedom 'solid state' open loop rate gyro capable of capturing rates up to and exceeding 7,000 degrees/second

with linearity better than 25 ppm. Short term bias stability is better than  $\pm 2$  degrees/hour.

Drive and signal processing electronics are typically contained within an Application Specific Integrated Circuit (ASIC) chip providing a d.c.-in d.c.-out capability for ease of interfacing.

There are, even today, many thousands of conventional spinning wheel rate gyros manufactured every year for a wide range of applications. Many of these systems were designed 20 or more years ago, when the subminiature, one inch diameter by two inches, long sensor was reaching maturity.

While the subminiature rate gyro represented a considerable advance at the time, and became the mainstay of numerous stability and control applications, a number of problems still existed.

Depending on the application, problems for the traditional rate gyro may include:

- High power consumption/heat dissipation
- Need to excite the gyro every 18 months to redistribute wheel lubricants
- Ultra fast start only by driving momentarily with high power

- Fragile mechanisms, sensitive to vibration
- Support electronics equal or greater in size than gyro itself
- Need to generate various amplitudes and phases of a.c. supply

The Quartz Rate Sensor addresses both the above and many other concerns in an ideal manner.

## **BACKGROUND**

The principles behind the QRS are long established. A pendulum, freely suspended, when set in oscillation will swing with respect to a spatial reference, as demonstrated in many museums by Foucault's pendulum.

Vibrating structures, be they hemispherical, wine glass, or tuning fork shaped, have the same property. Once set resonating, an attempt to rotate them about their reference axis causes a Coriolis force to be generated. This force is an analogue of the applied rotation rate.

Around 1942 the Sperry Gyroscope company commenced work on a tuning fork angular rate sensor known as the Gyrotron (Fig. 1).

Although the concept was proven, the device was not put into production due mainly to:-

- Instability of balance due to instability of materials
- Need for temperature stabilization
- Large size
- Need for rather complex electronics (for 1952)

Nonetheless, the Gyrotron did demonstrate a sensitivity of around 2 deg/hr.

The technology of micromachining opened up the latent potential of utilizing single crystal structures as the complete sensor element. Hundreds of thousands of quartz oscillators, as used in digital watches, calculators and computers, are now produced daily.

The Quartz Rate Sensor is a logical technological step since the manufacturing process is based on use of the same photolithographic techniques, as used in the manufacture of quartz watch crystals. Refinement of the design and positioning of the electrodes onto the piezoelectric quartz facilitates consistency of mechanical structure and manufacture with a high yield/performance factor.

### BASICS OF OPERATION

Consider the "H" fork layout in Fig. 2. The drive tines are driven at their resonant frequency of nominally 10 KHz by a closed loop constant gain oscillator circuit.

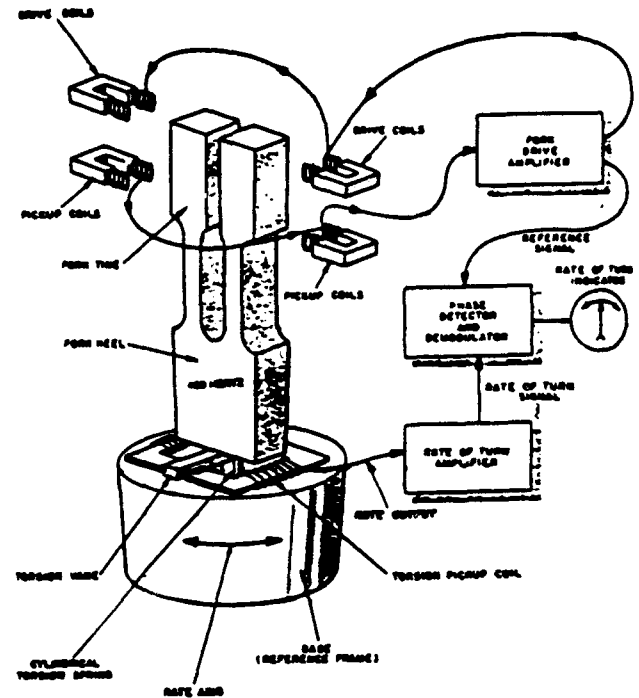


Fig. 1. SPERRY GYROTRON

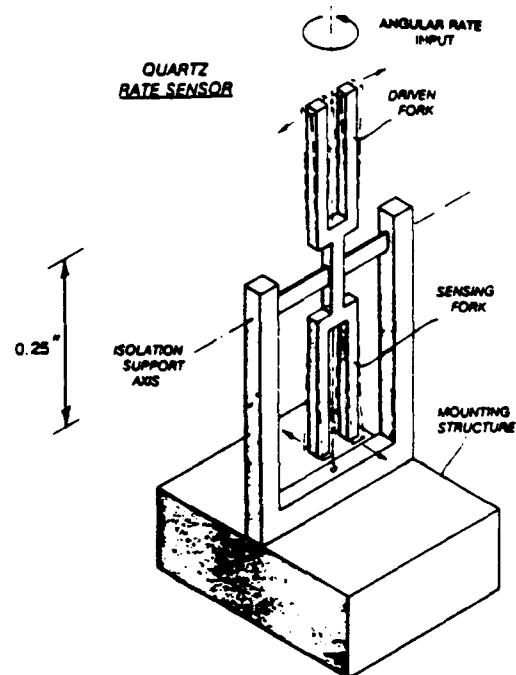


Fig. 2. Double-Ended Tuning Fork

The mount needs to be strong since it has to be capable of supporting the quartz element, yet isolated so as to maximize the Coriolis coupling torque into the pick-off tines. Drive and pick-up voltages are also routed via the mount. Finite Element Analysis (FEA) of the quartz element and its mount with various vibration stimuli have yielded invaluable insights into optimizing the mount area, which has enabled the company to model the behavior of the forks to external stimuli about all axes. The use of FEA has been extended to combine the computed mechanical performance with the anisotropic quartz properties to predict the electrical output of a specific configuration of fork and mount.

## ELECTRONICS

The electronics around the QRS are straightforward and depicted in Fig. 4.

An AGC loop around the drive tines ensures that the amplitude of the drive tines is kept constant over temperature. The start-up time of the QRS includes the time required to stabilize this loop, which is typically 600 - 800 mSecs. A status indication line is taken from this loop, output as a discrete signal. This is a confidence check that at least 60% of the QRS is fully operational. This discrete, termed the 'Tine Motion Detector' (TMD signal) clamps the output of the QRS during initial activation, holding the output signal at zero during the start-up interval.

The signal charge voltage appearing on the pick-up tines due to the Coriolis coupling torque signal is fed into an a.c. charge amplifier, whence it is amplified, shaped and synchronously demodulated at the reference frequency to produce the output signal.

The majority of the ASIC is analog in bipolar technology; however, a digital tracking filter is used to suppress subharmonics of the demodulation which occur in the bandpass.

The decision was taken early on to move directly from the initial discrete electronics to an ASIC. The development cost of this alone has been considerable, yet much valuable experience has been gained.

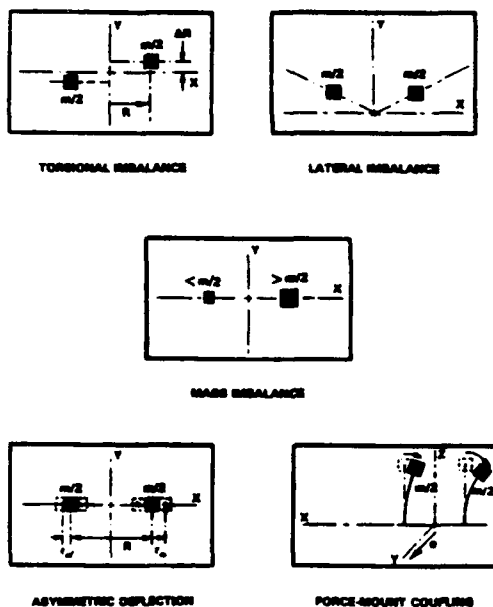


FIG. 3: ILLUSTRATION OF POSSIBLE ERROR SOURCES

When the tines are rotated at a rate  $\Omega$  about the input axis, a Coriolis torque, reciprocating and in phase with the tine mass velocity is produced. The torque manifests itself as a "walking" motion of the pick-off tines perpendicular to the vibration plane of the drive tines. (More complete analyses are to be found in the references at the end of this paper.)

The Coriolis force on the radially moving mass is given by:

$$F = 2 m \Omega v_R \quad (1)$$

where  $\Omega$  is the input rotational speed to be measured,  $m$  is one of the tine masses, and  $v_R$  is the radial velocity of the moving mass.

Each tine of the tuning fork oscillates with amplitude  $r$  sinusoidally at a frequency  $\omega$  about a radius  $R$  from the fork axis:

$$R(t) = R + r \sin(\omega t) \quad (2)$$

Differentiating (2) and inserting in (1) gives:

$$F = 2 \Omega m \omega r \cos(\omega t) \quad (3)$$

Multiplying the force by the instantaneous radius gives the Coriolis torque on the system. This can be closely approximated using  $R$  as the radius, ignoring the small harmonic content of the torque:

$$T = 2 \Omega m \omega R r \cos(\omega t) \quad (4)$$

This torque is applied to the output resonant system consisting of the support torsional stiffness  $k$  and the total fork structure moment of inertia  $J$ . The output system differential equation from basic physics is:

$$J \ddot{\theta} + b \dot{\theta} + k \theta = T \quad (5)$$

The output inertia can be represented as an equivalent mass that is  $A$  times larger than  $m$  at the radius  $R$ :

$$J = A m R^2 \quad (6)$$

When the output system is damped to a quality factor of  $Q$ , the standard solution to (5) is:

$$\theta(t) = T \cos(\omega t + \phi) / J \sqrt{(\omega^2 - \omega_0^2)^2 + (\omega \omega_0 / Q)^2} \quad (7)$$

When the output system is tuned to the drive,  $\omega = \omega_0$  and, substituting for  $J$  and  $T$  from (4) and (6):

$$\theta(t) = 2 m r R \Omega Q \cos(\omega t) / (A m R^2) \quad (8)$$

For small angles, the sideways deflection at the mass is:

$$y(t) = R \theta(t), \text{ therefore } \quad (9)$$

$$y(t) = 2 r \Omega Q \cos(\omega t) / (A \omega) \quad (10)$$

An evaluation of (10) for a typical tuning fork, comparing  $y(t)$  to the minimum motion detectable by a sensitive capacitor microphone, indicates that theoretically, rotation rates as small as 0.0001 earth rate (ER) should be measurable by such a



device. In practice, the lower measurement limit is not determined by the tuning fork itself but by self-generated noise in the electronic signal processor; careful measurements with optimized forks have yielded a "random walk" noise level of some 0.06 degrees/root-hour, in the same region as that of small laser gyros.

Theoretically, the tuning fork gyro has zero bias and a very stable scale factor. It is insensitive to such things as acceleration, magnetic fields and angular velocity normal to the input axis. Whilst imperfections in the gyro should have no effect on the rate output signal, they do produce a quadrature signal which does interfere with the discrimination of the rate signal. In practice, the bias performance of the gyro is limited by the residual response to the quadrature signal. The success Systron Donner has achieved is largely due to the analysis of the sources of error and controlling their combined effect under a wide range of environmental conditions.

The main error sources are:

- **Torsional Imbalance.**  
Where the drive tines vibrate parallel to the X axis, but are offset as shown in Fig. 3A.

- **Lateral Imbalance.**  
The drive tines vibrate at an angle to the X axis as shown in Fig. 3B.
- **Mass Imbalance.**  
Where the drive tines are vibrating along the X axis, but have different mass. Fig. 3C.
- **Asymmetric Deflection.**  
Where each drive tine vibrates at a different amplitude. Fig. 3D.
- **Force - Mount Coupling.**  
The tuning forks are suspended by beams attached to the mount. Imperfections can produce asymmetry which causes one side of the mount to be "stiffer" than the other. See Fig. 3E.

While how the QRS operates is itself of importance, of equal importance is how it is packaged to be a useful instrument. Were it possible to simply attach wires to the quartz and use the device, the performance attainable would be spectacular in terms of bias stability. Considerable analysis has been undertaken on the optimum method of mounting the fork to take account of thermal interaction, acceleration, vibration and shock.

Inevitably, customer tend to want specific dynamic performance, so provision is made for external components to set full range (scale factor) and to capacitively bypass the internal output amplifier, limiting the signal bandwidth to nominally 100 Hz.

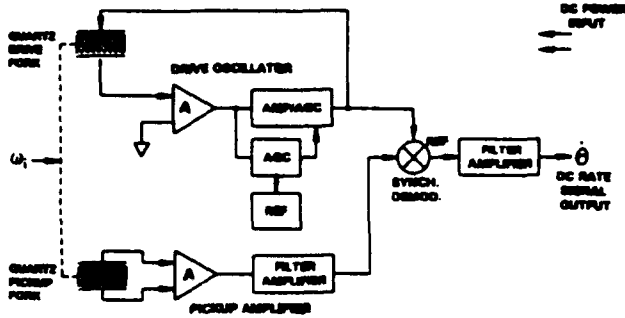


Fig.4. Quartz Rate Sensor Electronics

### TARGET SPECIFICATION

The initial target was to match the performance of a typical spring-restrained subminiature rate integrating-gyro, but with improvements in size, ruggedness, reliability and price. A typical specification is shown in Fig. 5; - these specification parameters have been met and exceeded in many cases for special applications.

#### Full Scale Output

Traditional rate gyros rely on different thicknesses of spring elements to achieve different full scale rate ranges. The QRS and contemporary solid state rate sensors achieve this purely by electronic gain control, since the signal processor controls the sensor range and signal bandwidth. Components are added during calibration around the ASIC to set the full range, which can be as small as  $\pm 5$  degrees/second or as large as 5,000 degrees/second.



#### QRS-11 SUMMARY SPECIFICATIONS (Typical)



The System Donner Quartz Rate Sensor (QRS) is a 'solid-state' replacement for rate gyroscopes. Inertial angular rate is sensed using a subminiature oscillating quartz element. The QRS is directly powered by a DC voltage input and provides a high-level analog DC rate signal output, with a wide bandwidth frequency response. The small size, excellent performance, low power requirements, and long operating life make the QRS superior to conventional rate gyroscopes.

#### POWER REQUIREMENTS

Input Voltage:  $\pm 5\text{VDC} \pm 5\%$   
Input Power: less than 0.8 watts

#### PERFORMANCE

Range:  $\pm 5^\circ/\text{s}$  to  $1000^\circ/\text{s}^*$   
Full Scale Output:  $\geq 2.5\text{ VDC nominal}$   
Bandwidth ( $-90^\circ$ ):  $> 100\text{ Hz}$   
Damping:  $0.7 \pm 0.3$  equivalent  
Start-up Time:  $< 1\text{ second}$   
Scale Factor Calibration:  
-temperature coefficient:  $< 1.0\%$  of value  
-temperature coefficient:  $< 0.03\%/^\circ\text{C}$   
Bias (Null) Set:  
-temperature coefficient:  $< 0.5^\circ/\text{sec}$   
-temperature coefficient:  $< 0.005^\circ/\text{sec}/^\circ\text{C}$   
-long-term (1 year):  $< 0.2^\circ/\text{sec}$   
-g sensitive:  $< 0.02^\circ/\text{sec}/\text{g}$   
Resolution/Threshold:  $< 0.002^\circ/\text{sec}$   
Linearity:  $< 0.05\%$  of full range  
Output Noise (Typ.):  $0.01^\circ/\text{sec per root Hz}$   
Operating Life: 10 years, typical  
Pressure Sensitivity:  $< 0.01^\circ/\text{s}/\text{psi}$

#### ENVIRONMENTS:

Temperature:  
-Operating:  $-40^\circ\text{C}$  to  $+85^\circ\text{C}$   
-Storage:  $-55^\circ\text{C}$  to  $+100^\circ\text{C}$   
Vibration Survival: 20 g rms, 20 to 2 kHz random  
Shock: 200 g, 2 milliseconds  
Pressure: 0 to 2 atmosphere

\* Performance test for  $\geq 100^\circ/\text{s}$  range

Fig.5. Data Sheet for Typical QRS

#### Bias Set/Repeatability/Stability/Over Temperature

This parameter needs careful interpretation, since there are a number of elements which affect it.

Bias set refers to the output at ambient temperature. This can be some percentage of full scale; however, normal practice is that the user incorporates a bias-set adjustment facility within his buffering electronic circuitry to 'remove' any factory bias set residual.

Repeatability is the turn-on to turn-on change in output of the gyro after repeated applications of power. Unlike spinning wheel gyros in the Quartz Rate Sensor, there is no mechanism relating to mechanical central position or spin motor pole synchronization.

Stability is typically broken down into short term (the first few minutes after turn-on), medium term (day to day) and long term (over a year). In-run stability of the QRS is typically better than  $25^\circ/\text{hr.}$  at constant temperature.

Bias stability over temperature is the key parameter to rate sensor performance. Development of the spinning wheel single degree of freedom rate gyro has resulted in a typical performance of around  $\pm 3\%$  full scale over temperature. The Quartz Rate Sensor is unique among vibrating sensors of this type in being able to match, or better this figure. For one ongoing contract, large numbers have been manufactured and shipped meeting a specification of less than 0.2% full scale over temperature.

This is achieved by close attention to detail in the design process, and by calibration during the manufacturing phase. All QRSs are thermally cycled on a multiple jig (Fig. 6) and the bias data recorded. This data is subsequently compared with an algorithm to derive values of discrete components to optimize the temperature dependency of the individual sensor. No thermistor or active temperature control is used.

### Scale Factor/Linearity

Scale factor stability and linearity are excellent in the QRS due primarily to the fact that there is no equivalent to gimbal displacement in this type of sensor. Carefully performed rate linearity runs demonstrate linearities in the tens of ppm, far better than that of an equivalent spinning wheel gyro.

### Dynamics

The dynamic performance of the QRS is mainly dictated by the electronics in the synchronous demodulation loop. Unlike spinning wheel sensors, where bandwidth is largely influenced by full scale rate capability of the sensor, bandwidths in excess of 100 Hz are achievable by the QRS regardless of full scale range.

Noise, gain and bandwidth are inter-related. Since compromises had to be made in order to utilize ASIC electronics in the QRS, self-generated noise can be reduced by adding selected discrete components to the present ASIC electronics. A new QRS variant will soon be available with low-noise circuitry for certain applications.

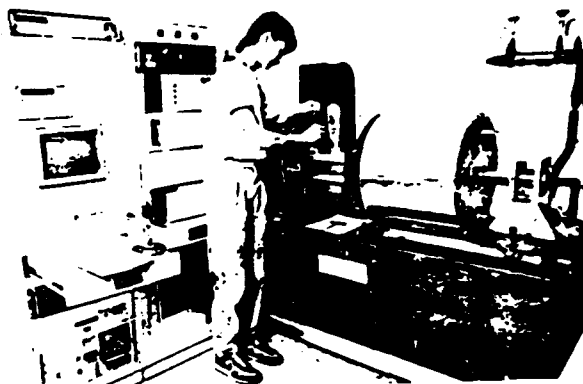


Fig.6. Multiple Unit Test Equipment

## Vibration

One of the more significant results of Systron Donner's design maturation of the Q.R.S. is its ability to provide superb performance during the direct application of high level vibration. Typical vibration offsets are less than 0.003 degrees/second per applied g rms of vibration.

## Environmental

The QRS has been designed to meet the stringent requirements of military applications, and has been qualified in missile, airborne and naval applications.

## THE QRS MATURES

The design of the vibrating fork can have an almost infinite combination of size, thickness, and electrode pattern. The main constraints in the initial versions were the size of the wafer of Z cut swept quartz, the number of forks per wafer and the final size of the QRS as an end item.

In order to guarantee overall build quality, Systron Donner decided to micromachine and process the quartz in house, which necessitated the generation of appropriate specifications to maintain strict control of the raw quartz material. The dedicated clean room and in-process handling equipment also needed to be designed consistent with the 2" x 1" quartz wafers.

The manufacturing process is essentially a photolithographic process (see Fig. 7) where gold is deposited on the wafer, a mask is overlaid to create the outline, the whole is then etched under controlled conditions. Side face electrodes are electro-deposited using special techniques.

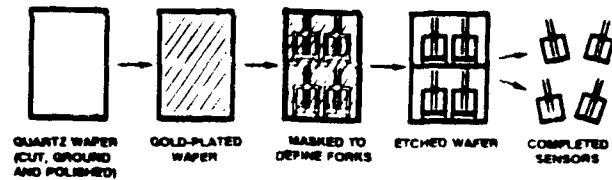


FIG. 7: QRS QUARTZ PROCESSING  
PHOTOLITHOGRAPHIC FLOW

The QRS clean room is shown at Fig. 8, which has a capacity of 1,000 wafers a month on a single shift basis.

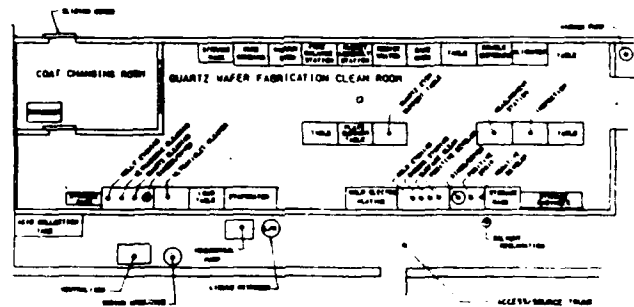


Fig.8. Quartz Fabrication Clean Room

The first production sensor, the QRS 10, became available around 3 years ago; the internal configuration is shown in Fig. 9. The key feature is the "nugget" assembly which contains the quartz element and suspension held in position by special adhesives, then laser welded into the capsule. Four terminals access the drive and pick-off electrodes. The QRS 10 found applications in a number of areas, particularly in the WSC-6 ("Whiskey 6"), satellite antenna stabilization which is now a standard installation on U.S. Navy, Danish and Dutch ships. The package is interchangeable with the previous spinning gyro unit, but has the main advantage of long life since there are no wearout modes.

The QRS 10 created considerable interest, due to its versatility in being able to fit where no other type of gyro could be considered. For example, Fig. 10 shows a two axis package for a missile seeker, complete with all electronics in a thickness of 8 mm. With lightweight and flexible interconnect cabling, there is minimal inertial loading on the missile scanning system.

In the continual drive at Systron Donner to achieve higher performance and lower cost for given applications, a working party, which included outside consultants IBM and Bechtel Corporation, reviewed the QRS 10 design and its cost of manufacture; as a result, the QRS 11 was evolved using a larger fork, effectively including its own decoupling gimbal assembly (see Fig. 11 cut away QRS 11) and simplified construction.

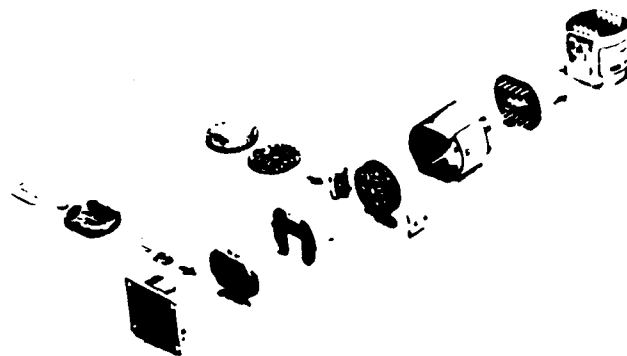


Fig.9. Exploded View of the Quartz Rate Sensor - Model QRS-10

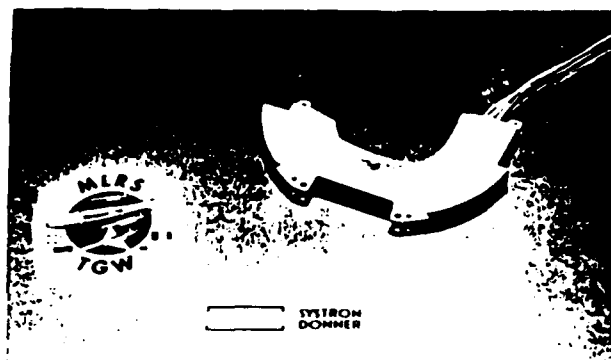


Fig. 10. TWO AXIS QUARTZ RATE SENSOR (Cover Removed) for GIMBALLED SEEKER STABILIZATION

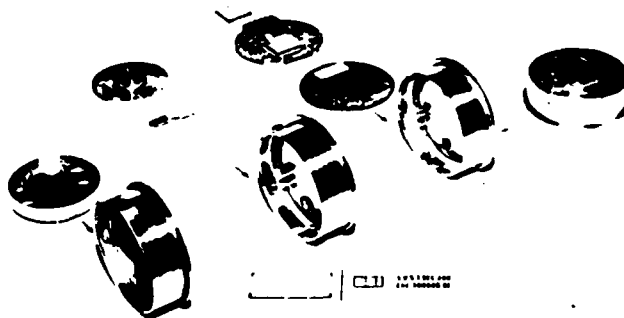


Fig.11. Exploded View of the Quartz Rate Sensor - Model QRS-11

The QRS 11 has been in production since early 1992, manufactured at rates in excess of 800/month. The main application has been in a missile autopilot, but it has also been supplied for line-of-sight stabilization, instrumentation and automotive stability control. Over 10,000 units have now been supplied.

Many shapes and sizes of forks have been fabricated, and the capability exists to model, in software, the design and performance of a given design in a few days. A new variant can be designed and simulated, the manufacturing masks computer-generated, and prototype units made in 4-6 weeks. This capability is being used to create OEM designs for specific applications, which include high shock, maximized performance and ultra low-cost.

The QRS 10 and 11 share the same ASIC; however, modifications continue to optimize the performance in terms of lower noise, increased power supply and noise rejection, and reduced complexity.

#### QRS IN INERTIAL MEASUREMENT UNITS (IMU)

The small inherent size of the QRS make it ideal for a compact 6 Degree-Of-Freedom IMU.

The package (Fig. 12) shows three orthogonally oriented QRS elements in an envelope diameter of 1½ inches by 2 inches long. This forms the basis of a missile body gyro

package where the complete package, some 4 inches overall, incorporates analog-to-digital conversion and memory mapping of rate sensor bias, scale factory and alignment against temperature to further improve the overall accuracy of the system.

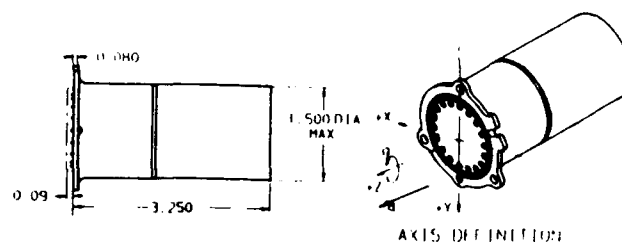


Fig.12. Micro Quartz Inertial Measurement Unit

An interesting point is that the roll gyro has two sets of electronics around the one sensor, providing a signal of high roll rate during deployment and de-spin, and a lower range of vehicle control afterwards.

A full IMU requires three accelerometers for attitude/velocity measurement. This is accomplished as shown in Fig. 13 where the gyro cluster incorporates the Vibrating Quartz Accelerometers (VQA), which utilizes the change in resonant frequency of a quartz vibration element when under compression or tension to provide a direct digitally-compatible acceleration measurement.

The IMU has a unique, simple architecture. The internal block diagram is shown in Fig. 14. The IMU does not incorporate a processor of any kind, since customer systems have computing power available for flight control and signal processing, and the relatively small additional capacity required for IMU sensor modelling and coordinate transformation algorithms makes the scheme extremely viable.

With a production run, it is more economic to build the system accuracy into software which is a one-time cost, rather than building inherent accuracy into every sensor.

The Systron Donner scheme relies on the data recorded during final system test, with data being analyzed and coefficients of up to third order memory mapped against temperature to compensate for bias, scale factor and alignment changes of all six sensors.

On system activation, the host processor accesses the EEPROM and downloads the mapped data, whereupon the IMU commences to output a digital stream of "raw" digital data comprising pitch, roll and yaw delta angles plus x, y, z, delta velocities. A digital temperature sensor output is provided as the reference to the memory mapping.

Since the IMU temperature changes relatively slowly, an update in the raw-compensated data need to be carried out only every second or so. The data compensation flow is shown in Fig. 15.

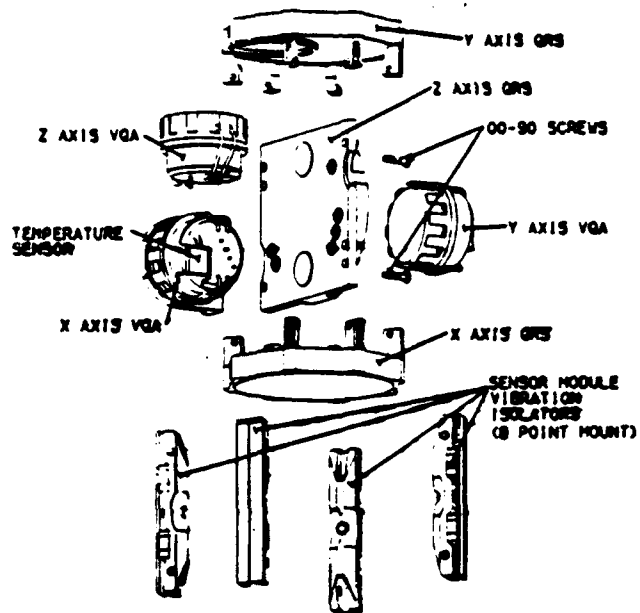


Fig.13. Exploded View of the Inertial Cluster Assembly

#### MICRO QUARTZ IMU SIMPLIFIED BLOCK DIAGRAM

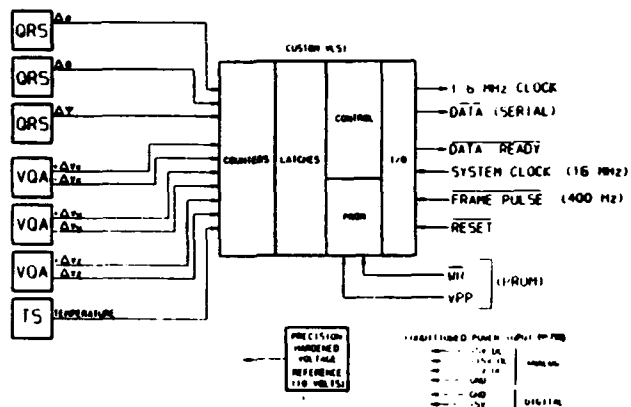
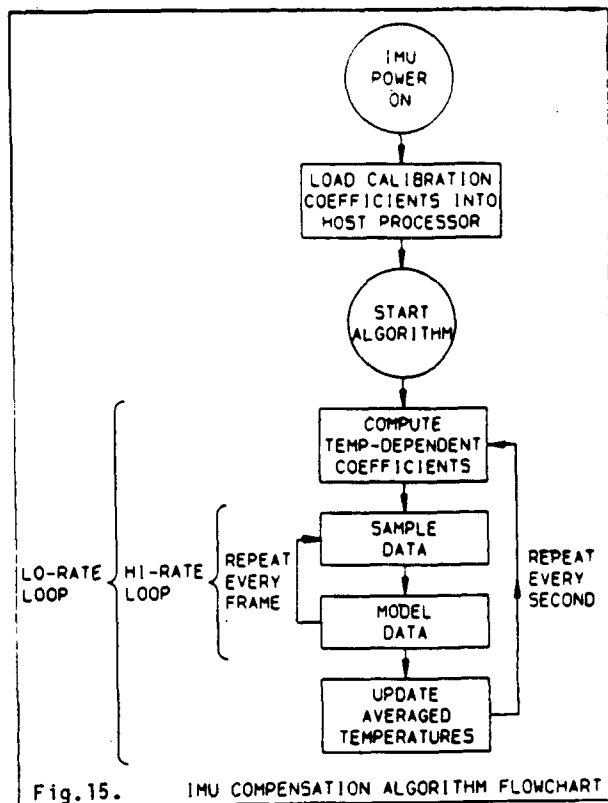
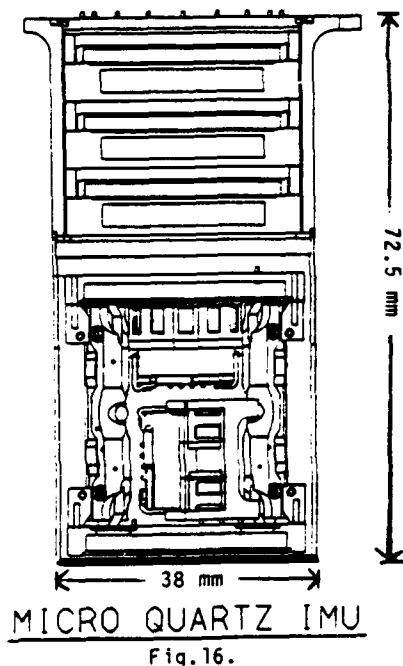


Fig.14. IMU Block Diagram



This scheme using the host processor avoids system duplication of power and weight, as well as possible incompatibilities between dual computing elements. Accuracy in the order of  $10^\circ/\text{hr}$  and better is achievable, as shown by the data in Figs. 19 and 20 where single channel from a 6 DOF IMU, is displayed.

A requirement for an ultra compact IMU resulted in the configuration shown in Fig. 16. The 6 D.O.F. sensor element remains as previously shown, but the electronics are now packaged onto three ceramic multilayer circuit discs. Each disc has a "button board" containing up to four ASICs which slot into the ceramic circuits. Interconnection between the layers and the outside is via an annulus of 140 pins around the circumference of the discs.



This package, built in prototype form, unless manufactured in considerable volume, incorporates an electronics packaging technology which is simply too expensive for low/medium use. Current IMU programs utilize a package similar to that in Fig. 17, where the same inertial instrument package is used alongside more conventional surface mount technology electronics.



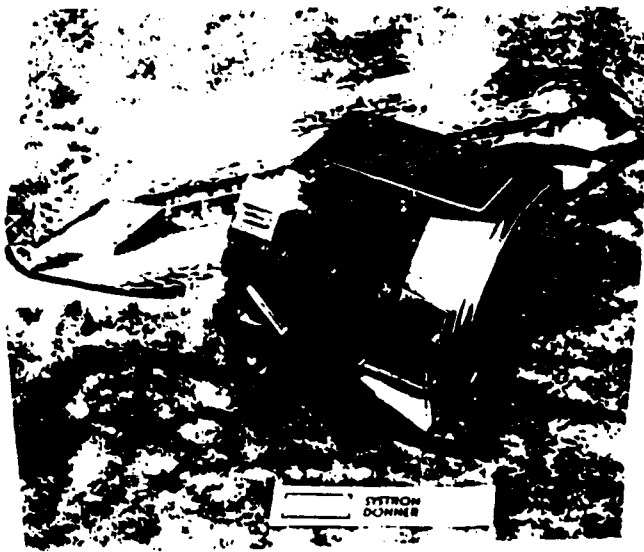


Fig.17. IMU

## FUTURE

Our customers, who typically operate within the constraints of military/aerospace control, are themselves under pressure from lower budgets and reduced production runs. This, in turn, increases the commercial pressure on inertial equipment manufacturers to produce lower priced equipment with resulting smaller margins to recover the development costs.

The QRS, and QRS/VQA based IMU are uniquely able to provide users both military and civil, with an optimum solution due to the inherent simplicity of the sensing mechanism. For civil users a new low-cost version of the QRS has been made available, called the "GYROCHIP". User acceptance has been rapid, and numerous new applications are being served.

The low mass of the inertial element makes the QRS ideal for high shock applications, with current programs looking for a 30,000 g shock capability.

Under a co-operative agreement with a manufacture of Global Positioning System OEM electronics, the 6 Degree Of Freedom Inertial Sensor Assembly (ISA) (see Fig. 18) cluster is being integrated to produce a highly compact navigation system, the "long term" reference being the GPS, the ISA providing wide-bandwidth dynamic and instantaneous inertial positional data.

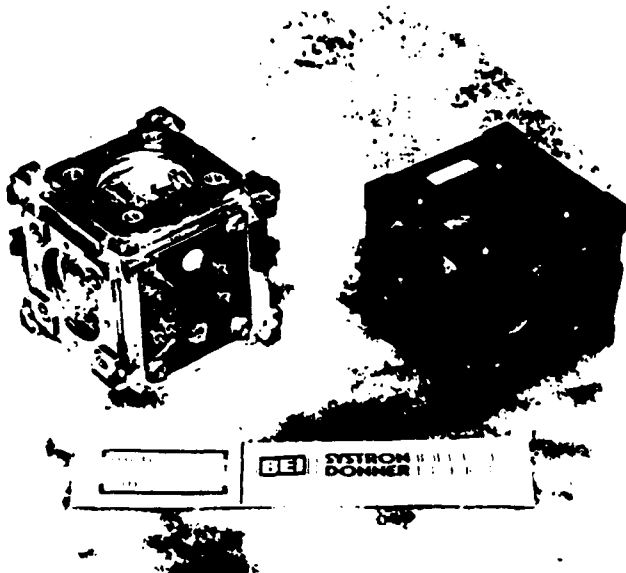


Fig.18. Inertial Sensor Assembly (ISA)

Manufacturing and micromachining in quartz is already a mature technology. The cost reductions sought, and needed for automotive and robotic applications will come from improved manufacturing and test methods, plus simpler and totally digital electronics.

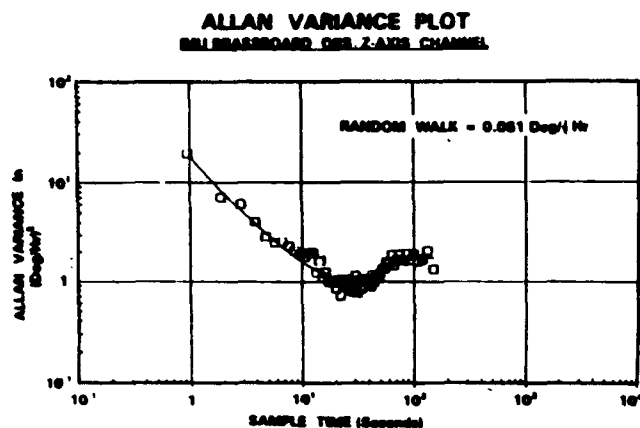


Fig.19.

### 18Hr Breadboard Stability Test

600Hz Aq, .1Hz St, IS \*1 Z

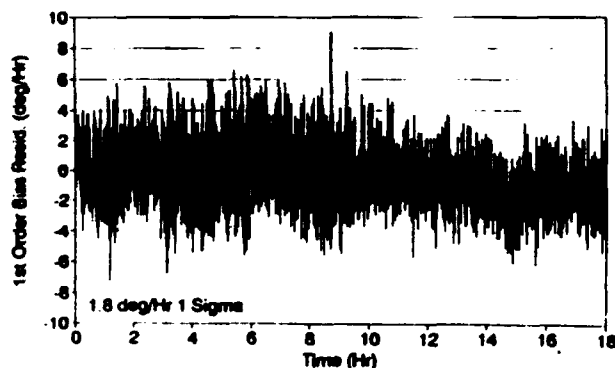


Fig.20.

**THIS PAGE LEFT BLANK INTENTIONALLY**

**A Systems Approach to Gyro Modeling**  
by  
**George Erickson**  
**Sperry Marine Inc.**  
**1070 Seminole Trail**  
**Charlottesville, VA 22901**  
**804-974-2454**

**Presented at**  
**Sixteenth Biennial Guidance Test Symposium**  
**October 5 - 7, 1993**

**Approved for Public Release; distribution is unlimited.**

# A SYSTEMS APPROACH TO GYRO MODELING

by  
George W. Erickson  
Sperry Marine Inc.

## ABSTRACT

To encourage broader use and standardization of methods for determining gyro model equation parameters, the IEEE/AESS Gyro and Accelerometer Panel is introducing an organized approach to modeling based on the most popular methods, to be first presented in the revised IEEE Std 647, Specification Format Guide and Test Procedures for Single Axis Laser Gyros.

An overview of dynamic and stochastic modeling is presented. Applications include gyro modeling, simulation, Kalman filter design, error analysis, performance specification, prediction and evaluation.

A general model consists of a mathematical statement of the physical plant equations; an error model consisting of a perturbation model and environmental sensitivities; a stochastic model describing random drift behavior; and a measurement model consisting of a linear combination of the output states and additive measurement noise. The gyro model equation, consisting of the response to inertial inputs, environmental sensitivities, drift rate and scale factor error contributors is organized in this format.

Methods of determining input/output characteristics are discussed. Stochastic modeling via time series analysis is introduced. Emphasis is placed on application of the Allan Variance and PSD. An approach to test and analysis is presented. Data acquisition, data reduction, preprocessing, and evaluation of results are discussed.

## INTRODUCTION

The general (non-linear) modeling problem was posed by Norbert Wiener during the early 1940s [2]. He defined the unidentified system in terms of a "black box," which he sought to identify and characterize in terms of bodies of known structures, or what he called "white boxes." The solution to the linear problem uses various time and frequency domain techniques to find an operational equivalent of the black box, which may then be constructed by combining certain canonical forms of these white boxes. Although the model structure may be different from the true structure, the input-output properties are to be equivalent.

The non-linear problem, discussed in Papoulis [6], and extensively in Bendat [41], will not be addressed here.

## Unit Model

The term "unit" refers to an operational entity which performs a well defined, unique function. The unit model consists of several parts, as illustrated in Figure 1. The plant, or physical model, is described by differential or algebraic equations which express the physics of its operation. This is the deterministic part of the plant that is addressed with dynamic modeling techniques.

The second part, the error model, consists of a perturbational model, which includes the sensitivity to the variation of parameters in the plant equations, and an environmental model, which includes the sensitivities to environmental disturbances.

The third part is the Stochastic model, which includes the random drift observed under otherwise benign operating conditions. The measurement model consists of a linear combination of the system states and additive output noise.

Optimal filtering, based on accurate models, can reduce system error to the limit of minimum residual white noise. The model also can be used for performance prediction and evaluation relative to a specification [10, 11, 17, 20].

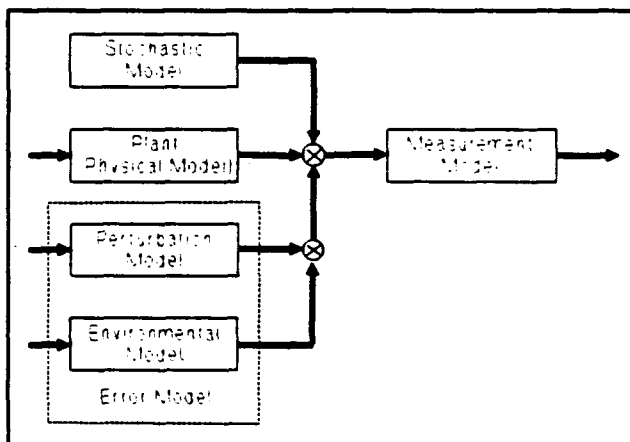


Figure 1. System Model

## Gyro Model Equation

A generic model equation which applies to many types of sensors is shown in Figure 2. It consists of inertial, environmental, and random contributors.

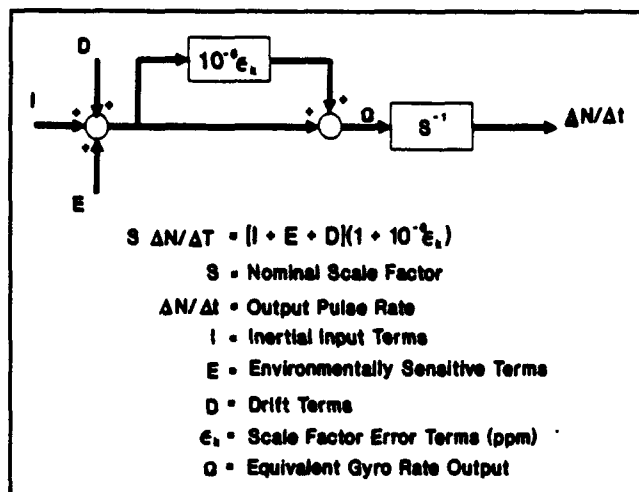


Figure 2. Generic Model Equation

This approach to compartmentalizing gyro model equations is introduced in IEEE Std 647 to organize the various contributors. The model equation for some gyros, such as the Dynamically Tuned Gyro (DTG: IEEE Std 813) contains many terms.

## MODELING

Important applications of modeling occur in simulation studies, performance evaluation, and Kalman filter design. In dynamic modeling, given one or more inputs and one or more outputs, the input/output relationships are usually determined from both time series. Applications include those where random noise is summing at the output.

In Stochastic modeling, there is usually no direct access to an input. A model is hypothesized which, as though excited by white noise, has the same output characteristics as the unit under test. Such models are not generally unique, so certain canonical forms are chosen. For example, David Allan of the National Institute of Standards and Technology (NIST) used a power series for the Power Spectral Density (PSD) and the corresponding variance analysis in the time ( $\tau$ ) domain for the analysis of oscillator stability [8]. This type of variance analysis is discussed in Annex C of the IEEE Std 647.

The idea is that one or more hypothetical white noise

sources of strength  $N_i^2$  drive the canonical transfer function(s), resulting in a response with the same statistical and spectral properties as the actual device (black box model). This is also the objective of the gyro drift analysis.

## Dynamic Modeling

The most significant terms in an optical gyro model equation include scale factor, bias and misalignment. The model coefficients are conventionally determined using regression methods, with the gyro being forced with deterministic inputs.

Spinning wheel gyroscopes such as a two-degree-of-freedom gyro, or single-degree-of-freedom gyros that exhibit substantial two-degree-of-freedom effects [13, 15], are more interesting subjects for dynamic modeling. The resulting two-degree-of-freedom model is similar to the model equation for the dynamically tuned gyro (DTG). The dynamics have a fourth order characteristic response. The four eigenvalues can have significant dependency on the angular momentum of the gyro. The resulting frequency-dependent transfer function may be analyzed by methods described below.

Many methods of estimating transfer functions are presented in Sinha and Kusztá [33]. Of the classical approaches, for example, the frequency response method is one of the earlier methods used [9]. Prior to development of the FFT, the input signal was stepped through discrete frequencies while measuring the relative amplitude and phase from input to output. With current methods, white noise is inserted usually at a rate proportional summing point. The open and closed loop transfer functions are computed using digital signal processing. This method allows for estimation in the presence of uncorrelated additive noise.

Time response methods are another classical means (using step and impulse response) to estimate the transfer function. One method, called deconvolution [33], determines the impulse response from the input and output by using the convolution integral (discrete form) in terms of the sampled data. A matrix equation describes the output at each point of time as a function of the input. The solution to the equation is the impulse response of the black box unit under test.

Another approach to using the impulse (or step) response method models the discrete form of the transfer function (Z-transform) as the ratio of two power series [33]. Two

matrix equations are derived which express the coefficients in terms of the output impulse response. The denominator coefficients may be solved in terms of the impulse response data, and the numerator coefficients may then be solved in terms of the denominator coefficients and the output data.

Several approaches model the output in terms of a difference equation corresponding to the discrete time transfer function [33]. The output is expressed parametrically in terms of its past values (the autoregressive part) together with present and past values of the input (the moving average part). A matrix equation relates the parameter vector, which comprises the transfer coefficients, to a concatenated set of the input, output data (expressed in a matrix) and output vector comprising another set of the sequential output data. The problem has been variously formulated for noisy data, using least-squares or maximum likelihood estimation (LSE, MLE) methods. Recursive forms exist for on-line estimation.

Another technique is to introduce a white noise input, and analyze the output relative to the input. This time-domain method is called the correlation method [9, 33]. The cross correlation between the input and the output is computed, from which the impulse response is deduced. This method is limited to stationary time series from linear time invariant systems. The main problem with this approach is that as the model becomes more complicated, it is harder to identify the cross correlation function. The contributors are particularly difficult to decompose into constituent parts when they cover a large dynamic range or overlap significantly in frequency content. If the form of the model is unknown, identification is a difficult job. This is one problem with the Box-Jenkins approach and most of the other methods of dynamic modeling.

Frequency domain approaches (spectral decomposition) [12] are usually a better tool for detailed model investigation. The PSD in particular is a fundamental tool for characterization of signals and plays an important role in time series analysis and statistical communications. Canonical forms of decomposed spectra are more recognizable over wider dynamic range and increased complexity of signal compared to time domain methods.

The PSD is uniquely related to the correlation function by way of the Fourier Transform. Means of calculating the PSD from the raw data using the FFT are, however, more commonly used. Real time processing with ensemble averaging has considerably improved the ability to estimate signal spectra and transfer functions.

With the frequency domain approach, the transfer function may be estimated from the cross-power spectral density (XPSD) of the output with the input divided by the PSD of the input [9]. This gives both the magnitude and phase of the transfer function.

### Stochastic Modeling

The idea of applying white noise and constructing the transfer function in this manner is important to stochastic modeling. The reason for that is, if the input is white noise, you can estimate the transfer function of a linear, minimum phase, time invariant system simply from the power spectrum of the output. Instead of getting the cross PSD between input and output, the transfer function can be estimated from the power spectrum of the output alone. The phase information is uniquely determined from the magnitude response.

Thus, for a linear time-invariant system, by having knowledge of the output only, and assuming white noise inputs, it is possible to characterize the unknown model. Many of the methods are very similar to some of the dynamic modeling methods except that the input is unobservable. The frequency domain approach of using the power spectral density to estimate transfer functions is straightforward. Even certain pathological cases, such as bias instability [8, 25, 26, 34, 35], which appears as a  $1/f$  process [32], (flicker rate noise), and angle quantization noise (characteristically different from continuous white angle noise) [6, 31, 35] can be discerned, with careful analysis technique.

As in the case of dynamic modeling, several time domain methods have been devised for stochastic modeling. The correlation function approach [5, 6, 9, 33] is the dual of the PSD approach, being related as Fourier Transform pairs. Similar to the corresponding dynamic modeling method, the equivalent impulse response may be deduced from the autocovariance sequence computed from the output data. One approach models the covariance function as sums of exponentials and damped sinusoids, using least squares estimation to obtain model parameters. This is analogous to expressing the frequency response function in terms of a partial fraction expansion.

Another correlation method relates the autocovariance sequence to coefficients of a difference equation, expressed as an auto regressive moving average (ARMA) process. This method was expounded by Box-Jenkins [14, 20, 33]. Correlation methods are very model sensitive and not suited to dealing with odd power law processes, higher

order processes or wide dynamic range. They work best with apriori knowledge based on a model of few terms.

Several variance function methods have also been devised. They are very similar, primarily differing in the ancillary signal processing. Weighting functions, window functions, etc., are incorporated into the analysis algorithms in order to achieve a particular desired result of improving the model characterizations. Many of these are discussed in Rutman [25]. The two simplest are the Allan Variance and Modified Allan Variance [29, 40], which are discussed in the next section together with the PSD.

The adaptive Kalman filter is another means of system identification [20]. The noise covariance and dynamics may be estimated if the form of the model is known. This may be combined with a model adjustment or learning model approach for more flexibility.

### Gyro Random Drift Model

Noise contributors in typical gyro models [11, 20, 24, 26, 27, 34, 35] include white angle noise, quantization noise [6, 20], white rate noise, correlated (Markov) random drift, bias instability (1/f or flicker rate), rate random walk, flicker rate ramp (ramp instability), and random rate ramp. Correlated (Markov) drift rate has been recently reported in optical rotation sensors, but is more common in spinning wheel gyros. White angle noise has also been observed in dithered RLGs at both the gyro and system level. Bias instability (flicker rate) and ramp instability (flicker ramp, flicker acceleration) behave like evolutionary (non-stationary) processes.

Normally, the PSD of a random process is expected to exhibit even order log-log slopes of -2, 0, +2 and so on, indicating even powers of frequency (+2 slope corresponds to +6 Db per octave). However, the 1/f flicker process has a -1 slope PSD (-3 Db per octave). It occurs in certain types of distributed parameter models; for example, a hypothetical R-C transmission line excited with white noise current will exhibit a 1/f noise voltage at the input [32]. Because flicker noise is not readily expressed in terms of ordinary state equations, it is sometimes approximated by a Markov model or more precisely by multiple stage ARMA (autoregressive moving average) model. Rate random walk is a long term, very low frequency phenomena. Even lower frequency is flicker ramp, which can be thought of as instability in the slope of rate ramp, is equivalent to the integral of a 1/f noise.

Other model contributors include random ramp (a

"deterministic" process whose slope is random initial condition), usually removed together with the bias prior to processing, and periodic signals which ought to be removed through filtering, better selection of oscillator frequencies, EMI reduction, etc.

### FAVORED METHODS

The PSD and Allan Variance methods of time series analysis are less restrictive and have more general application to investigation of stochastic models than most other approaches. They are thus among the preferred means of analysis adopted by the inertial systems community in cases where real time processing or adaptive identification are not needed. Specialized algorithms exist which are used to test dominant model terms as part of gyro acceptance testing, and may be used effectively once the model and acceptance limits have been established. These are not discussed here.

### Power Spectral Density (PSD)

The PSD is the standard representation of the spectral decomposition of a time series. It is a powerful tool for analyzing or characterizing data, and stochastic modeling. The PSD, or spectrum analysis, is also better suited to analyzing periodic or aperiodic signals than other methods.

To summarize the basic relationships for stationary processes the two-sided PSD,  $S(\omega)$  and covariance,  $K(\tau)$  are Fourier Transform pairs related by:

$$S(\omega) = \int_{-\infty}^{+\infty} e^{-j\omega\tau} K(\tau) d\tau$$

$$K(\tau) = \frac{1}{2\pi} \int_{-\infty}^{+\infty} e^{j\omega\tau} S(\omega) d\omega$$

$$\begin{aligned} K_{xy}(\tau) &= \langle x(t)y(t+\tau) \rangle \\ &= \overline{x(t)y(t+\tau)} \end{aligned}$$

It can be shown [6] that for nonstationary process, the average covariance  $\bar{K}(\tau)$  and average power spectrum  $\bar{S}(\omega)$  are related in the same way.

The transfer function form of the stochastic model may be estimated directly from the PSD of the output data (on the



assumption of an equivalent white noise driving function). Similar to methods for curve-fitting a Bode plot, the transfer function may be estimated using the pole-zero form, partial fraction expansion, power series, ARMA model spectral estimation, etc.

### Useful Properties

For linear systems, the output PSD is the product of the input PSD and the magnitude squared of the system transfer function. If state space methods are used, the PSD matrices of the input and output are related by the system transfer function matrix by:

$$S_{yy}(\omega) = H(j\omega)S_{xx}(\omega)H^*(j\omega)$$

For the special case of unit white noise input, the output PSD directly gives the system transfer function magnitude.

The PSD and autocorrelation function are Fourier Transform pairs. The Fourier Transform representation of the PSD is directly related to the Bilateral Laplace Transform derived from the transfer function of the corresponding stochastic model. The corresponding Allan Variance of a stochastic process may be uniquely derived from its PSD; however, there is no general inversion formula. The same is true of the relationship between the probability density function and the corresponding PSD.

The white noise covariances of process and measurement noise pertaining to the (continuous) Kalman filter theory are identically the corresponding two-sided PSD's white noise strengths expressed in units squared per hertz.

For a process to have finite power its PSD must eventually terminate in a negative slope at high frequencies. This property must be provided to satisfy the Nyquist sampling criteria for sampled data. This is discussed further in the data acquisition section. Likewise, a PSD cannot continue to rise (without limit) toward zero frequency (over a finite time interval). In practice, this is limited by the finite length of the time series.

Certain processes, such as periodic, "narrow band," or quantization noise are better described by their energy spectrum or an integrated PSD, since their PSD amplitudes are dependent on the resolution bandwidth, a function of sampling rate. This property is used to distinguish, for example, quantization noise from white angle noise. Both have a +2 slope rate PSD, but whereas the amplitude of the white angle noise PSD is independent of the sample rate (resolution bandwidth), the amplitude of the quantization noise PSD is directly proportional

(approximately) to the sample period (at the lower frequencies), as can be seen by rewriting the expression for quantization noise from IEEE Std 647, Annex C, as:

$$S(\omega) = \omega^2 Q^2 T \left( \frac{\sin \omega \frac{T}{2}}{\omega \frac{T}{2}} \right)^2$$

$$= \omega^2 Q^2 T \text{ for } T < \frac{1}{\omega}$$

The time average PSD of a nonstationary process has the properties of a PSD of a stationary process [6]. With present "real-time" PSD analysis, evolutionary spectra can be represented as either two-dimensional or time varying PSDs. For nonstationary processes, the covariance function is a function of two time variables (e.g., the "age" variable and the "running time" variable). In the frequency domain, a two-dimensional PSD is defined as the Double Fourier Transform of the covariance function and is a function of two frequency variables. For reference, the relationships are given by:

$$K_{xy}(t_1, t_2) = \overline{x(t_1) y(t_2)}$$

The two-sided, two-dimensional PSD  $\Gamma(\omega_1, \omega_2)$  and the general covariance function  $K(t_1, t_2)$  are double Fourier Transform pairs related by:

$$\Gamma(\omega_1, \omega_2) = \int_{-\infty}^{\infty} \int_{-\infty}^{\infty} K(t_1, t_2) e^{-j(\omega_1 t_1 - \omega_2 t_2)} dt_1 dt_2$$

$$K(t_1, t_2) = \frac{1}{(2\pi)^2} \int_{-\infty}^{\infty} \int_{-\infty}^{\infty} \Gamma(\omega_1, \omega_2) e^{j(\omega_1 t_1 - \omega_2 t_2)} d\omega_1 d\omega_2$$

For further discussion on nonstationary processes, see Papoulis [6].

For certain types of spectra, where wide dynamic range is required, such as when periodic content is present, application of a "window" function as part of the FFT processing can improve resolution. Windows, such as the Hamming and Von Hann (Hanning) windows reduce the impact of Gibb's phenomenon resulting from truncation of a time series. Thus, for example, two adjacent spectral peaks of significantly different amplitudes may be separated at the expense of somewhat broadening them.

These issues are discussed further in the next section, Allan Variance and [9, 22, 25]. PSD properties of the various contributors are given in Figure 4 and Table 1.

## Allan Variance

The two sample (a.k.a. first difference) Allan Variance was developed in the mid 60's and adopted by the time and frequency standards community for the characterization of phase and frequency instability of precision oscillators. Because of the close analogies to inertial sensors, the method has been adapted to random drift characterization of a variety of devices. Annex C of IEEE Std 647 treats this subject in more detail than the discussion below.

The old method of specifying drift in terms of a single RMS number, even when associated with a correlation time, was inadequate for predicting system performance, leading to some very conservative means of specification. Later, frequency domain methods proved superior for evaluating performance, but difficult for non-system analysts to interpret.

The Allan Variance is a compromise. Simply put, it is a method of representing RMS random drift error as a function of averaging time. It is simple to compute, much better than having a single RMS drift number to apply to a system error analysis, relatively simple to interpret and understand. Its most useful applications are in preliminary model investigation, and the specification and estimation of random drift coefficients.

The basic Allan Variance relations are summarized as follows:

$$\theta(t) = \int_0^t \Omega(t') dt'$$

$$\overline{\Omega}_k(\tau) = \frac{\theta(t_k + \tau) - \theta(t_k)}{\tau}$$

Then the Allan Variance is defined by:

$$\sigma_a^2(\tau) = \frac{1}{2} (\overline{\Omega}_{k+1} - \overline{\Omega}_k)^2$$

and is related to the two-sided PSD,  $S_{\Omega}(f)$  by:

$$\sigma_a^2(\tau) = 4 \int_0^{\infty} S_{\Omega}(f) \frac{\sin^4 \pi f \tau}{(\pi f \tau)^2} df$$

There is no inversion formula.

One of the most notable deficiencies of the standard Allan Variance is the non-unique characterization of white angle, flicker angle and quantization noise at the high frequency end, and random rate ramp versus flicker ramp at the low frequency end. These, however, may be sorted out by using the Modified Allan Variance and/or prewhitening methods discussed in the Post-Processing section. Other approaches include applying a prefilter to the time series (such as a triangular filter), or alternatively incorporating it into the Allan Variance computation, or applying it as a "window." The theory and use of windows is discussed by Hamming [22]. This approach is equivalent to some of the other variance methods discussed by Rutman [25].

If the standard Allan Variance is viewed as an application of a variable "rectangular window" to the time series, then the Modified Allan Variance may be viewed as the application of a variable "triangular window" to the time series. Maximum efficiency is obtained by using an algorithm that uses maximum overlap. Some of these issues are discussed in Stovall [39], where a triangular prefilter with maximum overlap is suggested. The more obvious advantage of the higher order filtering is in dealing with these "high pass" processes (those with positive PSD slopes) by terminating the filtered process in a controlled low pass characteristic, insuring a finite variance.

Allan Variance properties of the various contributors are given in Table 1.

## TEST, DATA PROCESSING and ANALYSIS

This section discusses the methods of test, data acquisition, data processing and analysis. Several suggestions are made to improve the efficiency of these operations and the subsequent analysis.

### Approach

General test conditions and equipment are discussed in Section 9 of IEEE Std 647. Test procedures are discussed in Section 10.11. It is important to control the influence of external environments on the test. External sources of

Table 1. Properties of Random Processes

Nomenclature	Stochastic Model Contributor		Asymptotic Properties PSD S(f)			Asymptotic Properties Allan Variance $\sigma_a^2(\tau)$		
	Generic	Equivalent White Noise Input	Other Name	$\theta$	$\Omega$	$S_{\omega}(f)$	$\theta$	$\Omega$
White Angle	$N_{\omega}^2$	$\Phi^2$	Angle Measurement Noise	0	+2	$(2\pi f)^2 \Phi^2$	-1/2	-1 (-3/2)*
Angle Quantization	---	$Q^2$	White Angle Energy Spectrum	0	+2	$\frac{4Q^2}{f} \sin^2 \pi f \theta$	0	-1
Flicker Angle	$N_{f\omega}^2$	---	Pink Angle Noise	-1	+1	$2\pi f N_{f\omega}^2$	0	-1
Angle Random Walk, White Rate Noise	$N_{\omega}^2$	$N^2$	Red Angle Noise	-2	0	$N^2$	+1/2	-1/2
Rate Quantization	---	---	Discrete White Rate Noise or White Rate Energy Spectral Density	-2	0	---	+1	0
Flicker Rate	$N_{f\omega}^2$	$B^2$	Bias Rate Instability or Pink Rate Noise	-3	-1	$\frac{B^2}{2\pi f}$	+1	0
Markov Rate	$N_{\omega}^2$	$q^2$	Correlated Drift Rate	-2, -4	0, -2	$\frac{(q, f)^2}{1 + (2\pi f)^2}$	+1/2, +1/4	+1/2, +1/4
Rate Random Walk	$N_{\omega}^2$	$K^2$	Red Rate Noise	-4	-2	$\frac{K^2}{(2\pi f)^2}$	+1/2	+1/2
Flicker Acceleration	$N_{f\omega}^2$	$R^2$	Ramp Instability of Pink Acceleration Noise	-5	-3	$\frac{R^2}{(2\pi f)^3}$	+2	+1
Random Bias	$\Omega(0)$	$B^2$	Bias or Fixed Drift	**	**	$B^2 \delta(f)$	**	**
Random Ramp	$\dot{\Omega}(0)$	$R^2$	Rate Ramp	**	**	---	**	**
Periodic Rate	$\Omega_0$	---	Harmonic	Discrete Line Spectra	Discrete Line Spectra	$\frac{1}{2} \Omega_0^2 \delta(f - f_0)$	**	**
						$\cdot \delta(f - 1)$		

\* mod  $\sigma_a^2(\tau)$  (Modified Allan Variance), \*\* Remove by regression or filtering

error should be removed or compensated for in an appropriate prefilter. Differential techniques (such as back-to-back sensor test) are also effective. Error detection/correction is also an important step of the data acquisition process.

Sample rates, anti-aliasing filtering, and record lengths are to be chosen with regard to various system considerations [9]. The longer term effects of random drift on performance with regard to the mission profile should be separated using signal processing techniques prior to data acquisition, and the high frequency data should be analyzed separately.

### Data Acquisition

Efficiency is achieved by combining data reduction methods into the data acquisition process thus transforming the data into a more useful form. Choice of sampling rates, record lengths, data editing, prefiltering, etc., are important to the economy and quality of the subsequent analyses.

Generally, the data sample rate is selected to be at least twice the signal bandwidth limited by filtering to the highest frequency of interest. However, Papoulis [6] shows that six samples per bandwidth cycle are required to characterize a signal from its past values only. The record length should be at least several times the required performance interval as dictated by the mission profile. Coverage of too large a temporal dynamic range is imprudent; collecting 0.1 ms data for 1000 hours yields an unnecessarily large data set.

The recommended approach is to limit the time/frequency domain dynamic range (of record length to sample period) to about three orders of magnitude. This is done by dividing up the total range into overlapping intervals of geometrically increasing lengths. Thus, the high frequency data is acquired for a short period of time. Lower frequency data is filtered (integrated) and acquired for a longer period. Signal processing is used to remove the undesired effects outside the bandwidth of interest. The appropriate sampling rates/record lengths should be chosen to overlap about one decade of frequency (time), consideration being given to the particular characterization of the process when practical.

Approximate prior knowledge of the process is beneficial to determination of data acquisition parameters. One approach is to choose the geometric means of the record length and sample period to correspond to the geometric

mean of the corresponding frequency or time domain range of the dominant characteristic of interest. Another aspect of this idea relates to "prewhitening," which is usually done as part of a post-processing operation after the data is collected but prior to detail analysis.

Quantization "noise," discussed in Britting, et al. [31] and Papoulis (as random binary transmission) [6], can be a limiting factor in the ability to estimate model coefficients efficiently. It can also have a deleterious effect on short term performance. Since quantization is often times dictated by sensor design consideration, such as RLG scale factor, or otherwise constrained to unsatisfactory levels, its effect must be handled externally by signal processing. This can be done as part of the data acquisition/reduction process, or in post processing. It usually entails processing through a second or higher order digital filter, with calculations scaled to higher precision.

### Post-Processing

Post-processing of the acquired data includes the "quick look," data editing, trend removal, digital filtering of other deterministic signal (i.e., periodic) and other prewhitening signal processing.

The "quick-look" is a cursory visualization of each record of the data in the form of graphical times series. Bad data is edited out and replaced by interpolated or simulated data. Trends are observed for removal and separate analysis by Least Squares Estimation techniques. Periodic content is removed by filtering. This is the first step in the prewhitening process.

Best estimates are achieved when the estimation error (residuals or innovations process) is reduced to a white noise process. An adaptive Kalman filter can be designed to do this, for example. Another approach requires apriori knowledge of the nominal stochastic model.

In this approach, an inverse filter is mechanized in the signal processing to prewhiten the data (see Figure 3). This may simply entail applying either an integration operation (as with angle white noise) or a differencing operation (as with rate random walk). As a practical matter, additional high frequency poles must be added to band limit the resulting dynamic range required for subsequent analysis.

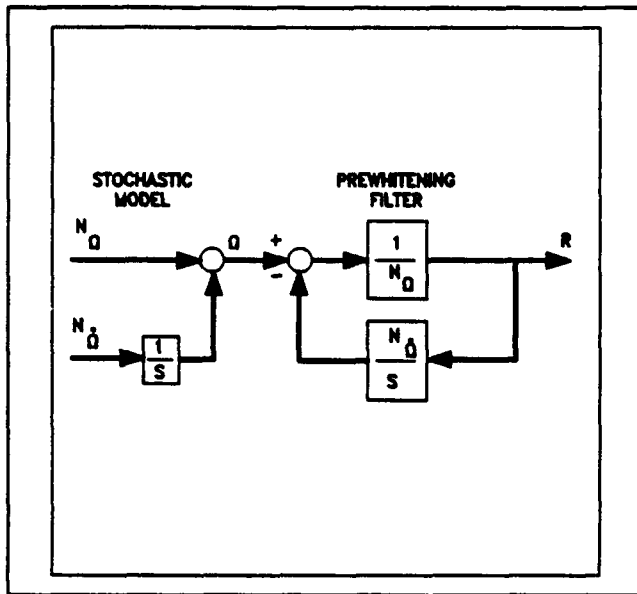


Figure 3. Example of Prewhitening

$$S_Q(\omega) = N_Q^2 + \frac{N_{\dot{Q}}^2}{\omega^2}$$

$$H(s) = \frac{\frac{s}{\hat{N}_{\dot{Q}}}}{1 + s \frac{\hat{N}_{\dot{Q}}}{\hat{N}_Q}} = \frac{1}{\hat{N}_Q + \frac{\hat{N}_{\dot{Q}}}{s}}$$

$$S_R(\omega) = H_{RQ}(\omega) S_Q(\omega) H_{RQ}^*(\omega) = |H_{RQ}|^2 S_Q$$

$$= \left[ \frac{1}{\hat{N}_Q^2 + \frac{\hat{N}_{\dot{Q}}^2}{\omega^2}} \right] \left[ N_Q^2 + \frac{N_{\dot{Q}}^2}{\omega^2} \right] = 1 \quad \text{if} \quad \begin{cases} \hat{N}_Q = N_Q \\ \hat{N}_{\dot{Q}} = N_{\dot{Q}} \end{cases}$$

### Time Series Analysis Considerations

Subsequent to data acquisition and post-processing, the resulting processed data records are prepared for time series analysis. Each data record constructed as described above contains piece-wise information to be extracted and

re-assembled in a composite analysis, which will then display the full dynamic range of the desired result. In re-assembling the computed information in the appropriate chart, it may be necessary to reverse operations to put the output data into the proper format and proper units. If, for example, prewhitening was applied, the corresponding post-darkening operation is necessary to reconstruct the characteristic signatures of the analyzed data.

Prior to this step the model coefficients must be estimated. A first approximation (second approximation if prewhitening has been performed) can be estimated by sketching in the asymptotes to the charted data analysis (PSD or Allan Variance) and computing approximate model coefficients. The prewhitening filter may be derived and applied to the data in a second pass, and the error coefficients from the residuals may be re-estimated. Alternatively, a more rigorous weighted least squares procedure, which weighs by the inverse error covariance, may be used. Error bounds on the coefficient should also be computed to establish the goodness-of-fit.

With the coefficients thus determined and the composite data analysis assembled on the appropriate chart, the resulting characteristic curve fit can be superimposed on the charted data, together with the error bounds to give a detailed representation of the stochastic model characterization. The coefficients are also used to construct a block diagram and generate the detailed state equations describing the stochastic model. The following figures illustrate the resulting piecewise asymptotic representations of the corresponding Allan Variance (Figure 5) and PSD (Figure 6) of a hypothetical gyro with parameters:

N = 0.001 °/√h	rate white noise
B = 0.001 °/h	bias instability
K = 0.0001 °/h/√h	rate random walk
Q = 0.557 " (q=2")	quantization noise

### CONCLUSION

This paper has provided a brief introduction and "roadmap" to the study of dynamic and stochastic modeling. Through a better understanding of the modeling process and standardization of test and reporting of data, the inertial system and gyro designer can more effectively meet their goals.

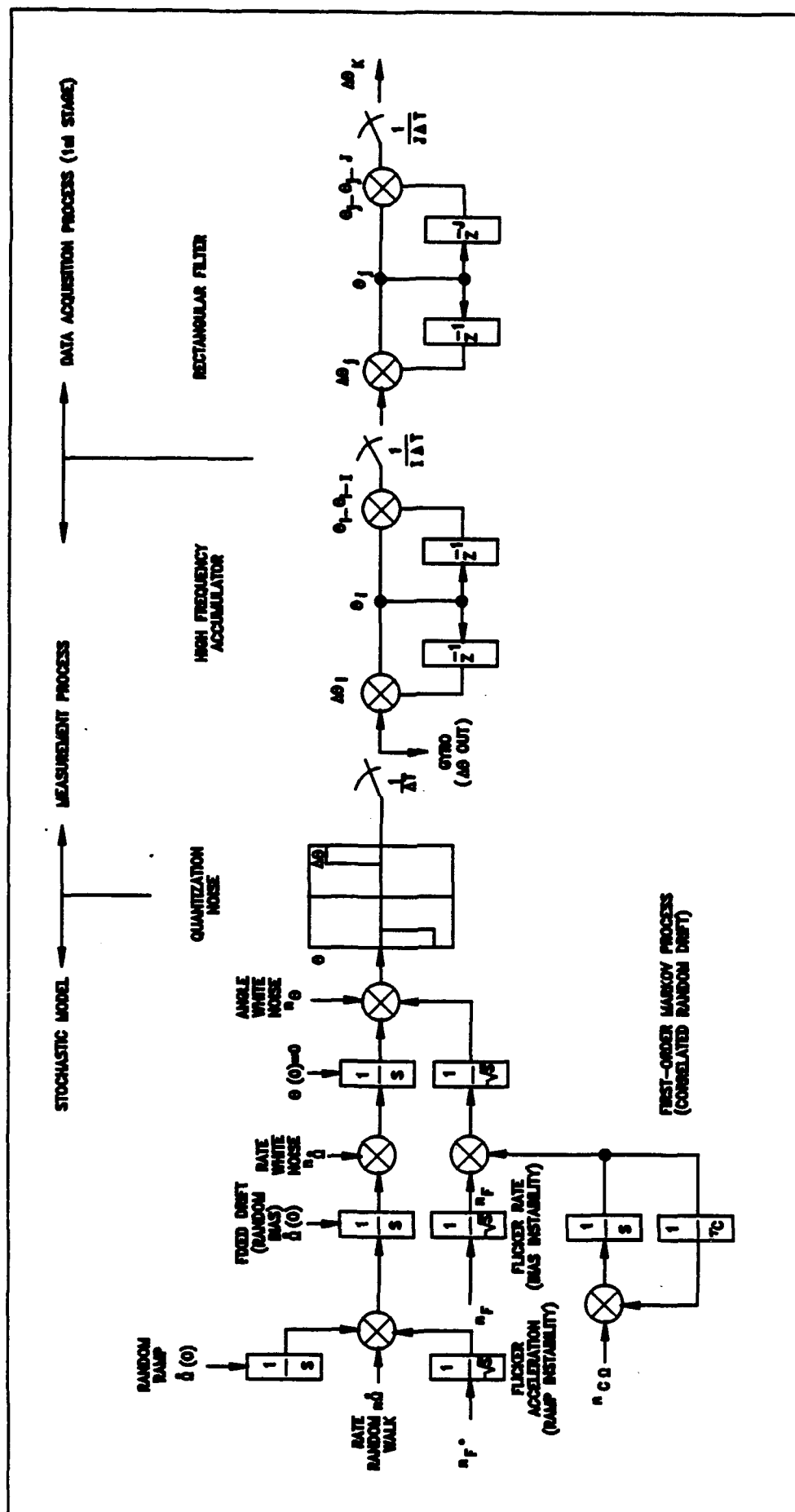


Figure 4. Block Diagram of Stochastic Model Through Data Acquisition

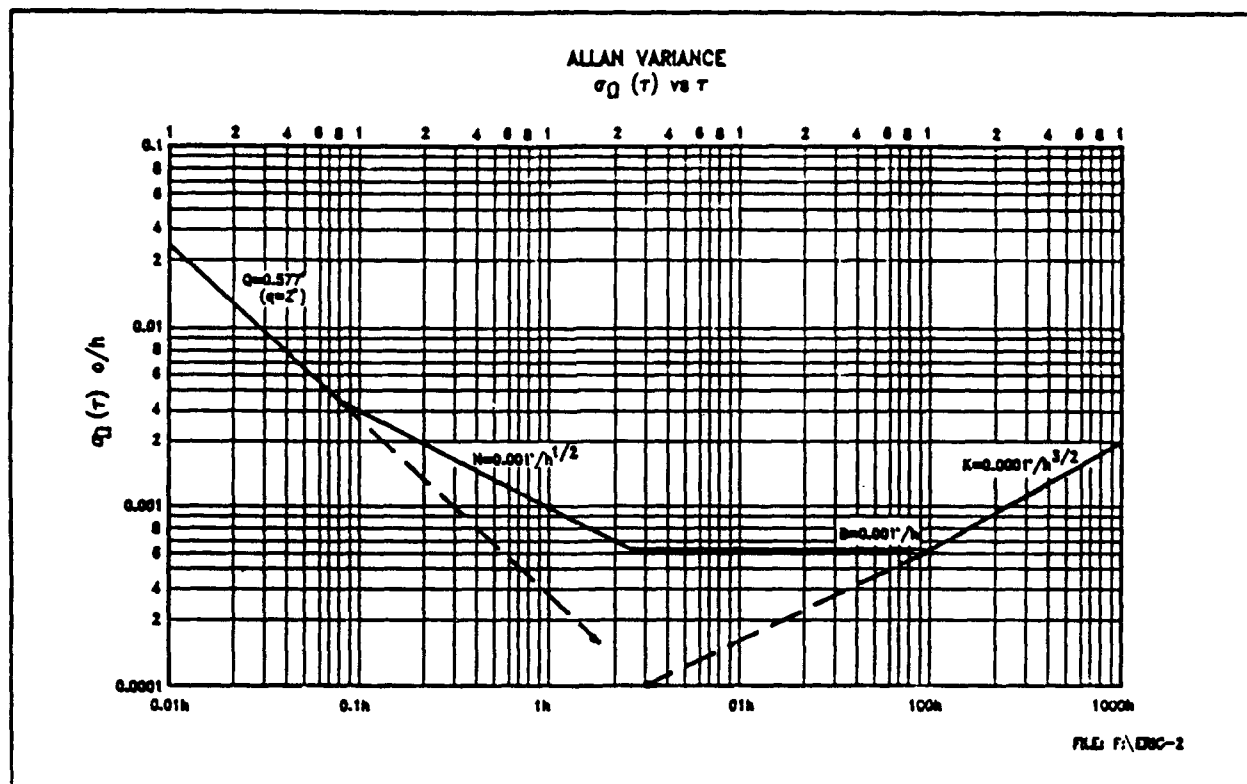


Figure 5. Allan Variance

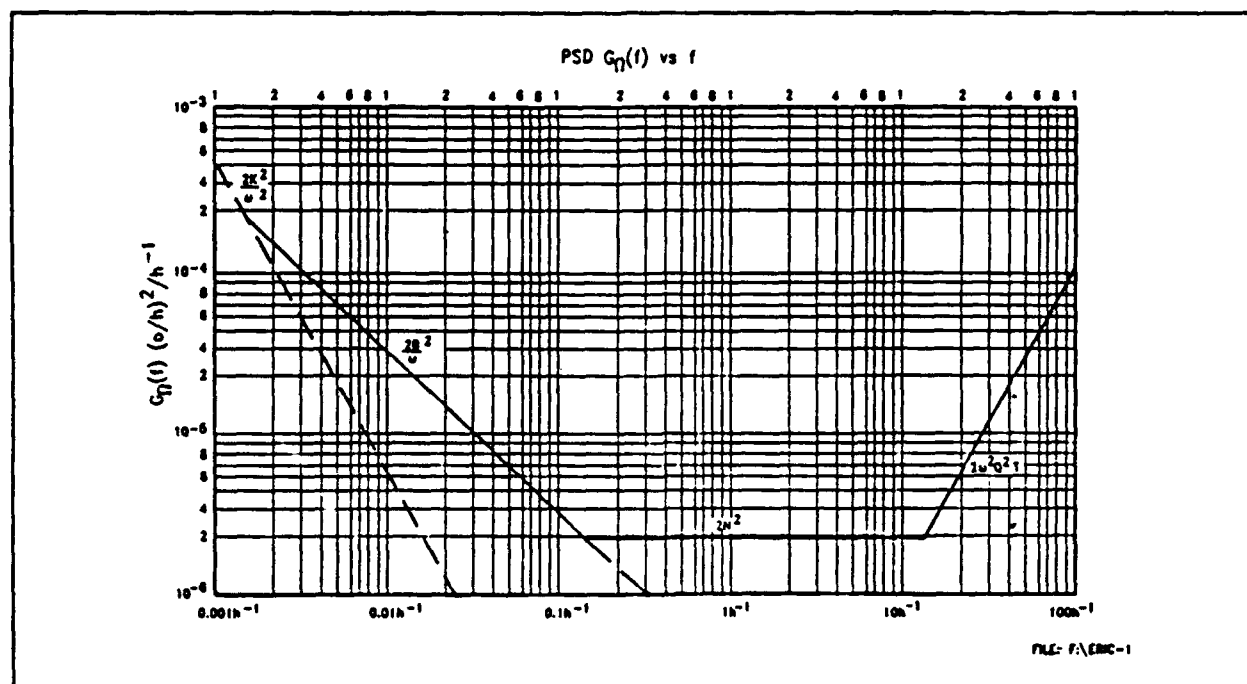


Figure 6. PSD

## **ACKNOWLEDGMENTS**

This paper has been revised and amended from a presentation [41] to the Institute of Navigation (ION), and is based upon a series of informal tutorials presented over several meetings of the IEEE/AESS Gyro and Accelerometer Panel.

## **BIOGRAPHY**

George Erickson has a B.E.E. degree from RPI and an M.S.E.E. jointly from SMU and TCU. He has worked in controls, signal processing and inertial systems for 28 years. At Sperry Marine Inc. he has managed several IR&D programs in the inertial systems/sensors area. Mr. Erickson received an Outstanding Technical Achievement Award in 1975.



## CHRONOLOGICAL BIBLIOGRAPHY

- [1] Von Neuman, J. and Morgenstern, O., *Theory of Games and Economic Behavior*, N.Y., reprint John Wiley and Sons, 1967, Copyright Princeton University Press, 1944.
- [2] Wiener, N., *Cybernetics: or Control and Communication in the Animal and the Machine*, Cambridge, MA: MIT Press, 1948, second edition 1961.
- [3] Kalman, R. E., "A New Approach to Linear Filtering and Prediction Problems," *ASME Transactions*, vol. 182D, Mar 1960, pp 35-45.
- [4] Hannan, E. J., *Time Series Analysis*, Great Britain: Science Paperbacks and Methuen and Co LTD, 1960, Reprinted 1967.
- [5] Parzen, E., *Stochastic Processes*, San Francisco, CA: Holden-Day, 1962.
- [6] Papoulis, A., *Probability, Random Variables and Stochastic Processes*, New York: McGraw-Hill, 1965.
- [7] Machol, R. E., *Systems Engineering Handbook*, New York: McGraw-Hill, 1965.
- [8] Allan, D. W., "Statistics of Atomic Frequency Standards," *Proceedings of the IEEE*, vol. 54, No. 2, pp. 221-230, Feb 1966.
- [9] Bendat, J. S. and Piersol, A. G., *Measurement and Analysis of Random Data*, New York: John Wiley and Sons, 1966.
- [10] Gelb, A. and Sutherland, A. A. Jr., "Design of Strapdown Gyroscopes for a Dynamic Environment," *TASC report TR101-1*, 1967.
- [11] Sutherland, A. A. and Gelb, A., "Applications of the Kalman Filter to Aided Inertial Systems," *NWC-TP-4652*, China Lake, CA, Aug 1968.
- [12] Van Trees, H. L., *Detection, Estimation, and Modulation Theory, Part I*, John Wiley and Sons, 1968.
- [13] Wrigley, Hollister, and Denhard, *Gyroscopic Theory, Design, and Instrumentation*, Cambridge MA: M.I.T. Press, 1969.
- [14] Box, G. E. P. and Jenkins, G. M., *Time Series Analysis: Forecasting and Control*, San Francisco, CA: Holden-Day, 1970, Revised 1976.
- [15] Britting, K., *Inertial Navigation Systems Analysis*, New York: Wiley-Interscience, 1971.
- [16] Barnes, J. A., Richi, L. S., Cutler, D. J., Healy, D. B., Leeson, T. E., McGunigal, J. A., Mullen, J. A., Smith, W. L., Sydnor, R. L., Vessot, R., and Winkler, G. M. R., "Characterization of Frequency Stability," *IEEE Transactions on Instrumentation and Measurement*, vol. IM-20, pp 105-120, May 1971.
- [17] Coffman, V., "On-Line Estimation of Parameters Using Experimentally Developed Gyro Models, and Other Applications," *Ph.D. Dissertation*, Stanford University, SUDAAR No. 467, Dec 1973.
- [18] Lesage, P. and Audoin, C., "Characterization of Frequency Stability: Uncertainty Due to the Finite Number of Measurements," *IEEE Transactions on Instrumentation and Measurement*, vol. IM-22, No. 2 pp. 157-161, Jun 1973.
- [19] Brogan W., *Modern Control Theory*, New York: Quantum Publishers, 1974.
- [20] Gelb, A., TASC Staff, *Applied Optimal Estimation*, Cambridge MA: M.I.T. Press, 1974.
- [21] Giacoletto, L. J., *Electronics Designers' Handbook* (Second Edition), New York: McGraw-Hill, pp. 16-20, 1977.
- [22] Hamming, R. W., *Digital Filters*, Englewood Cliffs, NJ: Prentice Hall, 1977.

- [23] Lindsey, W. C. and Chie, C. M., "Identification of Power-Law Type Oscillator Phase Noise Spectra from Measurements," *IEEE Transactions on Instrumentation and Measurement*, vol. IM-27, No. 1, pp. 46-53, Mar 1978.
- [24] Sargent, D. and Wyman, B. O., "Least Squares and How They Give Us Fits," Second Printing, *TRW Report 32143-61010TU-00*, 9 Jun 1978.
- [25] Rutman, J., "Characterization of Phase and Frequency Instabilities in Precision Frequency Sources: Fifteen Years of Progress," *Proceedings of the IEEE*, vol. 66, No. 9, Sep 1978.
- [26] Kochakian, C. R. "Time-Domain Uncertainty Charts (Green Charts): A Tool for Validating the Design of IMU/Instrument Interfaces," *Proceedings of the AIAA Guidance and Control Conference*, Aug 11-13, 1980.
- [27] Sargent, D. and Wyman, B. O., "Extraction of Stability Statistic from Integrated Rate Data," *Proceedings of the AIAA Guidance and Control Conference*, Aug 11-13, 1980.
- [28] Cadzon, J. A., "High Performance Spectral Estimation - A New ARMA Method," *IEEE Transactions on Acoustics, Speech, and Signal Processing*, vol. ASSP-28, No. 5, pp. 524-528, Oct 1980.
- [29] Allan, D.W. and Barnes, J. A., "A Modified 'Allan Variance' with Increased Oscillator Characterization Ability," *Proceedings of the 35th Annual Frequency Control Symposium*, pp. 470-475, May 1981.
- [30] Howe, D. A., Allan D.W. and Barnes, J. A., "Properties of Signal Sources and Measurement Methods," *Proceedings of the 35th Annual Frequency Control Symposium*, pp. 441-447, May 1981.
- [31] Britting, K., Rombalski, W., Marcus, F., Smith, R., "Statistical Description of Quantization Error", *Northrop, PPD*, unpublished paper, 1982.
- [32] Keshner, M. S., "1/f Noise," *Proceedings of the IEEE*, vol.70, No. 3, pp. 212-218, Mar 1982.
- [33] Sinha, N. K. and Kusza, B., *Modeling and Identification of Dynamic Systems*, New York: Van Nostrand Reinhold, 1983.
- [34] Tehrani, M. M., "Ring Laser Gyro Data Analysis with Cluster Sampling Technique," *Proceedings of SPIE*, vol. 412, 1983.
- [35] King, A. D., "Characterization of Gyro In-Run Drift," *Symposium Gyro Technology 1984*, pp. 10.0-10.56, Oct 1984.
- [36] Mark, J. and Brown, A., "Laser Gyroscope Random Walk Determination Using a Fast Filtering Technique," *Symposium Gyro Technology 1984*, pp. 9.0-9.21, Oct 1984.
- [37] Vallot, L., Stein, G., Dinter, H., and Enns, D., "Short Acceptance Test Procedures for Ring Laser Gyros," *12th Biennial Guidance Test Symposium*, pp. 1-12, 22-24 Oct 1985.
- [38] Walls, F. L., and Allan, D. W., "Measurements of Frequency Stability," *Proceedings of IEEE*, vol.74, No. 1, Jan 1986.
- [39] Stovall, S. H., "Analysis of Ring Laser Gyro Noise Measurement Techniques," *China Lake CA: NWC Technical Report*, 1987.
- [40] Allan, D., Hellwig, H., Kartaschoff, P., Vanier, J., Vig, J., Winkle, G.N.R., Yannoni, F., "Standard Terminology for Fundamental Frequency and Time Metrology," *Proposed IEEE Standard Para-P-1139*.
- [41] Bendat, J.S., *Nonlinear System Analysis and Identification From Random Data*, New York: John Wiley & Sons, 1990.
- [42] Erickson, G.W., "An Overview of Dynamic and Stochastic Modeling of Gyros," *Proceedings of the 1993 National Technical Meeting of the ION*, Jan 1993.

**THIS PAGE LEFT BLANK INTENTIONALLY**

## **Inertial Navigation Performance of an IFOG Over Dynamic Environments**

Ralph A. Patterson, Eric L. Goldner, Amado Cordova and David M. Rozelle  
Litton, Inc., Guidance and Control Systems Division  
5500 Canoga Ave.  
Woodland Hills, CA 91367

Inertial navigation performance of an interferometric fiber optic gyro has been demonstrated over extended environments. Bias uncertainty, angle random walk, scale factor and input axis alignment errors consistent with inertial navigation requirements have been achieved under static and dynamic conditions. The IFOG technology is shown to be viable for many inertial grade applications where high performance, low cost and high reliability are critical factors.

### **I. INTRODUCTION**

The measurement of rotation is crucial for attitude control and navigation of vehicles and for stabilization and pointing control of such objects as antennae and optical imaging systems. The traditional instruments for sensing body rotation of high performance aircraft, missiles and spacecraft have been spinning mass, and more recently, ring laser gyros. Typical performance requirements for such instruments include  $<0.01$  deg/hr bias stability,  $<0.005$  deg/ $\sqrt{\text{hr}}$  angle random walk,  $<50$  ppm total scale factor error and  $<2$  arc-sec axis alignment stability, all over extended environments. The number of applications for rotation sensing under adverse environments (such as temperature, vibration, ionizing radiation) has been increasing, especially within military and space programs. The fiber optic gyro (FOG) has, in recent years, become regarded as a potential alternative technology for such applications, especially where cost, environmental stability and reliability are key considerations. Litton has been developing inertial navigation interferometric FOG (IFOG) technology for use in its inertial measurement units (IMU) since 1986. Figure 1 illustrates the technological changes inertial measurement systems have been undergoing since 1980. The changing weight, power consumption and reliability associated with the advancement of optical gyros is evident, with IFOG-based systems being an attractive alternative for the next generation. The instruments under development, the methods for characterizing their performance and typical performance data are presented. The advantages of this optical fiber technology over older rotation sensing techniques are discussed. Predictions for IFOG performance improvements in the future are also presented.

## II. INSTRUMENT DESIGN

The physics upon which the fiber optic gyro operates is the Sagnac effect [1]. In short, the relative phase between two counterpropagating waves of light within a closed path is proportional to the path's rotation rate. The IFOG is an instrument which utilizes this phenomenon in an optical fiber interferometer. One possible architecture is shown in Fig. 2. The light leaves the optical source at left. Some of the light is transmitted toward the interferometer at the multiplexing directional optical fiber coupler (MUX). The light propagates to the second, loop coupler. This coupler serves both as a beam splitter and beam combiner, and divides the light into two roughly equal amplitude waves. The waves counter propagate around the fiber coil and interfere coherently as they leave the interferometer through the loop coupler. Finally, some of the light propagates to the photodetector after reaching the MUX.

In the past, the dominant bias errors of concern for optical fiber gyros have been: 1) polarization-type errors over temperature; and 2)  $dT/dt$  errors (where  $dT/dt$  represents the time rate of change of temperature gradients across the optical fiber sensing coil) of the type described by Shupe [2]. Scale factor errors have been mostly dominated by source wavelength variations. Alignment of the input axis is primarily dependent upon the mechanical design of the sensing coil and its supporting structure. In addition to minimizing performance errors, the design of the gyro needs to be both inexpensive to produce in large volume quantities and reliable.

The instruments tested for this work were single-axis gyros. Each contained a 1 km fiber sensing coil with an average diameter of about 5.8 cm. This results in an absolute open loop scale factor (the ratio of the phase angle between the two waves within the interferometer to the rate of rotation of the instrument) of  $3.7 \mu\text{Rad/deg/hr}$ .

Litton's design has been developed to achieve three main goals: high performance, low cost and high reliability. To achieve high performance relative to polarization errors, a broadband source and a reciprocal optical architecture are used. The source offers the advantages of low cost and high reliability of a solid state technology and relative insensitivity of its output wavelength to ambient temperature.

Borrowing from the microelectronics industry, the integrated optics (IO) technology takes advantage of standard integrated circuits wafer processing methods and hardware to produce low cost IO chips that include a polarizer, y-junction coupler and phase modulators on a single device. The low loss IO waveguides, 55+ dB polarizer extinction ratio and low phase modulator intensity modulation further enhance the high performance, low cost and extended reliability capability of the IFOG.

The sensor coil has been designed to enhance the instrument's performance. The design combines low loss, low polarization cross-coupling fiber (for minimal polarization-type bias errors [3]) with a quadrupole winding pattern for minimal thermal sensitivity under fast thermal ramp rate conditions [4]. Careful management of heat flow about the coil also helps minimize bias non-modelability.

To minimize the random walk of the instrument, a very low noise receiver module comprised of PINFET detector followed by a transimpedance amplifier is used. High output power from the gyro's light source and low loss optical components also contribute to reducing the gyro's random walk.

A closed loop local signal modulation/demodulation scheme is employed to achieve high rate sensitivity with high linearity and environmental stability of the gyro's scale factor. A block diagram of the signal processing electronics of the type used for obtaining the data presented is shown in Fig. 3. A signal creating an artificial  $\pm\pi/2$  radian relative phase difference between the counterpropagating waves is applied to the phase modulator once every  $\tau$  (where  $\tau$  is the loop transit time of light around the sensing coil) to achieve the high rate sensitivity and bias the gyro transfer function to an operating point that is essentially linear. An additional signal is applied to the phase modulator to constantly null the rotation-induced relative phase shift between the waves. This signal is hence proportional to the rotation rate of the gyro, and is output for further signal processing. This closed loop operation offers several advantages over open loop demodulation techniques. It allows high scale factor linearity over the full rotation rate range of interest (due to operating within a linear region of the gyro's transfer function). This signal processing scheme provides for high thermal stability of the instrument scale factor. The closed loop operation also ensures relative insensitivity to optical power fluctuations.

## EXPERIMENT

An on-going effort has been made to characterize the performance of Litton's IFOGs. The test program has the dual purpose of assessing the current status of the design and determining the accuracy limitations imposed by the gyros upon the inertial navigation system operation. The data reported in this paper were obtained using the closed loop demodulation technique described with the gyros mounted on a Contraves rate table secured to a seismic isolation pier. The gyro's thermal environment was precisely controlled for all tests using a computer controlled oven enclosing the rate table's rotating platform.

Data were collected under computer control at intervals from one to sixty seconds per sample. Quantization reduction (triangular) filtering was performed to show the gyro's level of performance and determine sensitivities. However, for the data presented, no compensation algorithms were applied. Typical test results are presented in the following sections for the major performance areas of bias, scale factor and input axis alignment. Vibration test results for inertial navigation IFOGs are also discussed.

## **Bias**

Three primary bias performance areas were evaluated:

- 1) Angle random walk (ARW)
- 2) Bias stability under constant thermal conditions
- 3) Bias uncertainty after modeling under dynamic thermal conditions

ARW measurements consist of collecting several hours of one second bias data while the instrument temperature is maintained constant. These data are then analyzed using the Allan variance technique implemented in the program 'AUTOFIT' [5] to separate the measurement noise (quantization) effects from the angle random walk (bias white noise) effects. An example of the ARW determined for a typical IFOG is shown in Fig. 4. The Allan variance analysis indicated an ARW of 0.0027 deg/ $\sqrt{\text{hour}}$  with a standard measurement error of 0.0003 deg/ $\sqrt{\text{hour}}$ . It should be noted that there is no measurable *rate* random walk or trend in the bias.

Bias stability under constant thermal conditions was determined by collecting 43 hours of bias, sampled every 60 seconds while controlling the gyro temperature at 25 deg C. The gyro performance measured under these conditions was 0.007 deg/hour one sigma (Fig 5) with a 1 hour filter applied to the data to distinguish the bias from random walk effects.

The bias uncertainty of IFOGs is routinely measured under dynamic thermal conditions over the range -55 to +71 deg C. The profile of the gyro temperature versus time shown in Fig. 6a, is representative of that expected for typical inertial navigation applications. For the testing whose results are presented in Figs. 6b and 6c, the gyro was subjected to thermal ramp rates up to 0.5 deg C/min. The gyro output and temperature measurements were collected at ten second intervals. The bias residual data shown in Fig 6b was determined by fitting the gyro output to a temperature model. A 30-minute time constant filter was then applied to the data to reduce the ARW effects. The result of this is shown in Fig 6c and was shown to have a standard deviation of 0.0092 deg/hour.

## **Scale factor (SF)**

Three areas of SF performance were investigated:

- 1) SF stability at constant temperature
- 2) SF linearity
- 3) SF uncertainty after modeling under dynamic thermal conditions

SF stability under constant thermal conditions of a Litton IFOG was shown to be 0.7 ppm one sigma (Fig 7). The gyro output data were taken with a 100 deg/sec rate table rotation rate. To remove the effects of bias variation from the scale factor data, the direction of rotation was reversed every 15 revolutions. This allowed a measurement of the scale factor once every

minute. Data were collected for three hours and the standard deviation determined. This data demonstrates the inherent stability of the overall instrument and the light source.

To determine the scale factor linearity, gyro output data were taken at 5 deg/sec steps in rotation rate over the -500 to +500 deg/sec rotation rate range, and reduced by linear regression analysis. The scale factor of the gyro tested was linear to within 1.5 ppm, one sigma, as illustrated in Fig 8.

The gyro SF under dynamic thermal conditions was shown to be 9.1 ppm, one sigma, over a -55 to 71 deg C range (Fig 9). This was measured by rotating the gyro at 100 deg/sec while subjecting the gyro to a dynamic thermal environment. The temperature of the gyro versus time are shown in Fig 9a. As in the SF stability testing, the rotation direction was reversed every 15 revolutions so that the effects of bias variations on the results could be eliminated. The residual scale factor variation after modeling the gyro output for temperature is shown in Fig 9b versus time, and is 9.1 ppm, one sigma, with a 5 minute filter applied to the data.

### **Input axis (IA) alignment**

The IA alignment uncertainty of the gyros under dynamic thermal conditions is measured by mounting the gyro with its input axis perpendicular to the rate table rotation axis and spinning the rate table at 100 deg/second. For the data presented, the gyro temperature was ramped from -55 to +71 deg C. Fig. 10 shows the IA alignment versus temperature during such a test. After application of a model based upon the coil temperature, the one sigma of the IA alignment during the test was 0.38 arc-seconds.

### **Vibration Performance**

In addition to bias, scale factor and input axis alignment measurements, the response of Litton's IFOGs to vibration input was evaluated. As pointed out by Chin [6], experimental results obtained with attitude and heading reference system (AHRS) grade IFOGs have shown no bias sensitivity due to rectification of the vibration input. Litton's inertial navigation IFOGs incorporate the same significant coil design features (winding pattern, etc.) as the AHRS grade IFOG. The inertial navigation IFOG vibration performance was measured to exceed the requirements for 0.01 deg/hr applications in tests at the gyro level. System level tests are planned for early 1994.

## **CONCLUSIONS**

Inertial navigation performance has been demonstrated over dynamic environments with an IFOG. The measured random walk was 0.0027 deg/ $\sqrt{\text{hr}}$ . This can potentially be further reduced by use of a correlation technique [7, 8]. Both stable temperature and dynamic temperature condition bias uncertainties were shown to be less than 0.01 deg/hr. Alternative spool materials and improved thermal management of the sensor coil may further decrease fast thermal ramp bias errors. Although the scale factor stability (0.7 ppm), linearity (1.5 ppm) and temperature sensitivity (9.1



ppm) were better than those required for many inertial navigation applications, enhancement can be expected as improved techniques are implemented to control and compensate for source temperature sensitivity. The current mechanical design provides for IA errors (less than 0.4 arc-sec) well within the requirements of typical navigation-grade applications. Instrument level vibration tests of Litton IFOGs have shown excellent results. System level tests are planned for early 1994.

To reduce the life cycle cost of inertial measurement systems, Litton has chosen optical components and a mechanical design that will provide high instrument reliability, and hence, high system reliability. For example, routing of the optical fiber has been controlled such that fiber bend radii exceed fiber manufacturers' minima with sufficient design margin to meet the reliability and dormancy requirements of inertial navigation applications. Solid state light sources are used to enhance the instrument reliability. Much of the Litton IFOG design and fabrication processes exploit mature telecommunication and electronics technologies - optical fiber fabrication, integrated circuit manufacturing, fiber interconnect technology, mass production of components such as solid state sources, directional couplers and optical detectors. Inertial navigation performance over dynamic environments as well as the potential for low manufacturing cost and high reliability make IFOG technology a viable, low cost alternative to traditional rotation-sensing technologies.

### ACKNOWLEDGMENTS

The authors wish to express their appreciation to Mr. Charles Thorsen for his assistance in testing the IFOGs and Mr. James Steele for providing the closed loop electronics used for testing the gyros.

Some of the data presented was produced under contract with the Naval Command, Control and Ocean Surveillance Center's Research, Development, Test and Evaluation Division, and the Advanced Research Projects Agency on the GGP Program.

### BIBLIOGRAPHY

- [1] S. Ezekiel and H.J. Arditty, Eds., Fiber Optic Rotation Sensors, Springer Series in Optical Sciences, 32, Springer-Verlag, NY (1982).
- [2] D.M. Shupe, "Thermally induced nonreciprocity in the fiber-optic interferometer," Appl. Opt., 19, 654 (1980).
- [3] W.K. Burns et al., "Fiber-optic gyroscope with polarization-holding fiber," Opt. Lett., 8, 540 (1983).
- [4] N.J. Frigo, "Compensation of linear sources of nonreciprocity in Sagnac interferometers," Proc. SPIE, 412, 268 (1983).

- [5] D. Sargent and B.O. Wyman, "Extraction of stability statistics from integrated rate data," AIAA Guidance and Control Conference, Danvers, MA (1980).
- [6] G. Chin, A. Cordova and E. Goldner, "Extended environmental performance of attitude and heading reference grade fiber optic rotation sensors," Proc. SPIE, 1367, 107 (1990).
- [7] P.R. Morkel et al., "Elimination of excess photon noise from fiber superradiant sources," Conference on Lasers and Electro-optics, CTUH76, 154 (1990).
- [8] R.P. Moeller and W.K. Burns, "1.06- $\mu\text{m}$  all-fiber gyroscope with noise subtraction," Opt. Lett. 16, 4902 (1991).

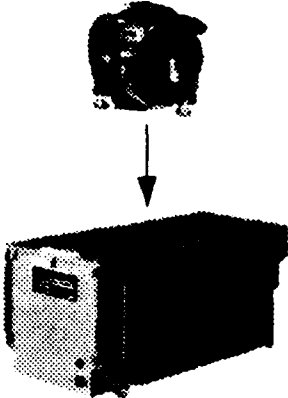
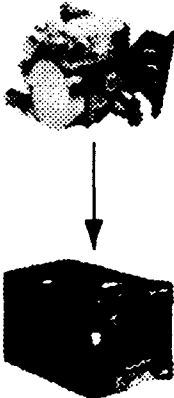
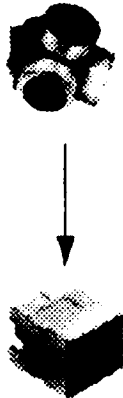
YEAR	1980	1990	2000
FEATURES	FIRST GENERATION RING LASER GYROS & MECHANICAL ACCELS	SECOND GENERATION RLG (ZLG™)1980 & MECHANICAL ACCELS	INTERFEROMETRIC FIBER OPTIC GYROS & SILICON ACCELS
			
WEIGHT	46 LBS	19 LBS	7 LBS
POWER CONSUMPTION	140 WATTS	27 WATTS	15 WATTS
RELIABILITY	3,800 HRS MTBF	8,000 HRS MTBF	20,000 HRS MTBF

Figure 1. Evolution of Litton's Navigation Systems from 1980 through 2000 (forecast). With the advancement of optical gyros has come a series of lighter, more reliable systems.

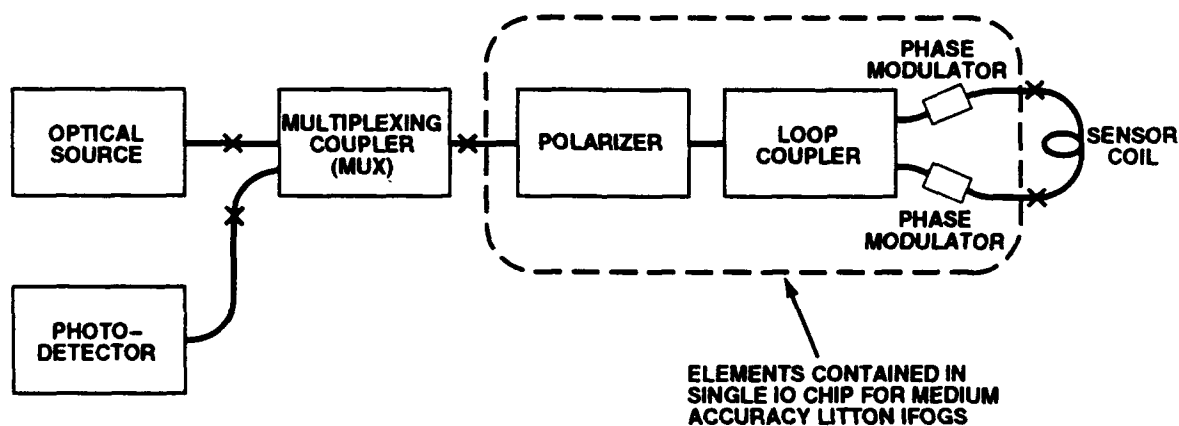


Figure 2. IFOG block optical architecture used in Litton inertial navigation systems. X indicates a fiber-optic splice.

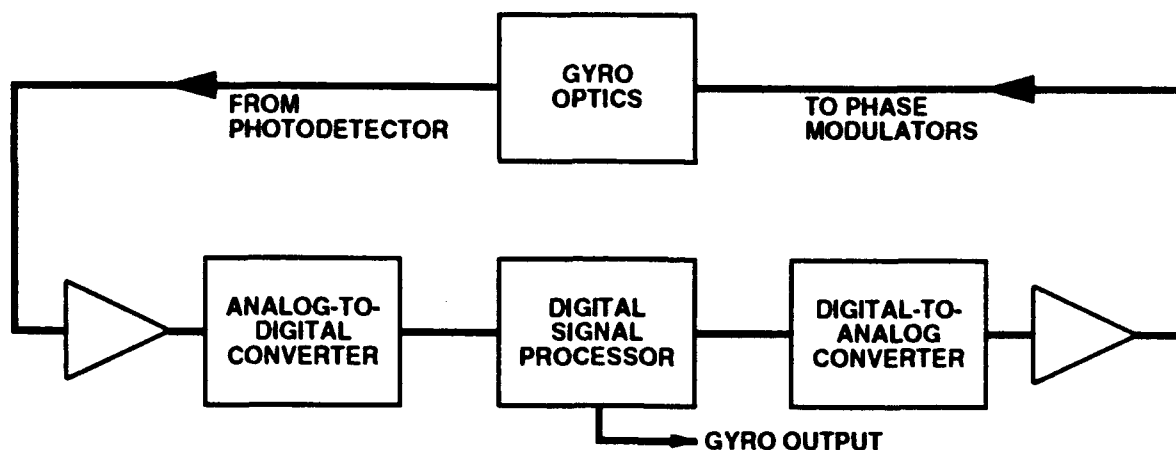
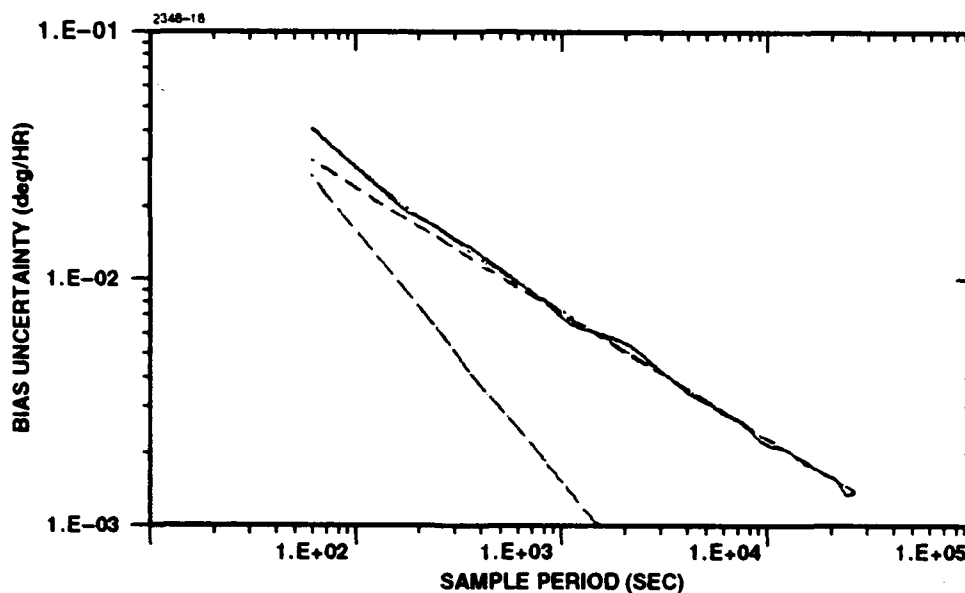


Figure 3. Closed loop modulation/demodulation electronics block diagram. Loop closure drives FOG output to null.



NO.	COEFFICIENT	ESTIMATE	STD. ERR.	ERR/EST RATIO
1	TREND	0.00000	DEG/HR/HR	
2	RT RNDM WALK	0.00000	DEG/HR/RT-HR	
3	ANGLE RW	.00269	( $\pm$ .00028) DEG/RT-HR	10.26%
4	MEAS NOISE	.63	( $\pm$ .19) ARC-SEC	29.63% ARC-SEC
RMS ERROR OF LOG FIT: .048				

Figure 4. AUTOFIT analysis of bias of a typical 1-km IFOG. The angle random walk of this instrument, the dominant source of the bias uncertainty, was 0.00269 deg/root-hour. The duration of the test was 15 hours.

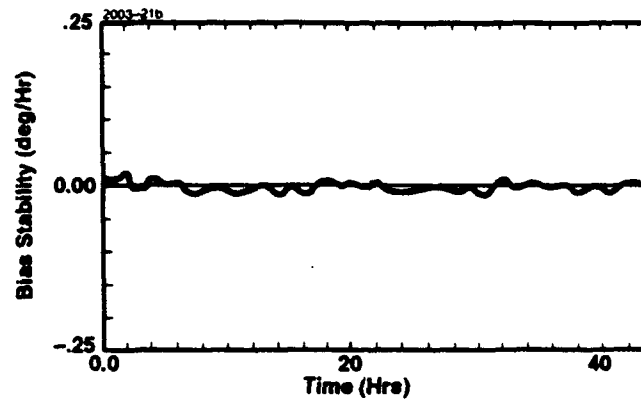


Figure 5. IFOG bias at constant temperature. The one sigma bias with a one hour filter applied to the data obtained during a 43 hour test was 0.007 deg/hour.

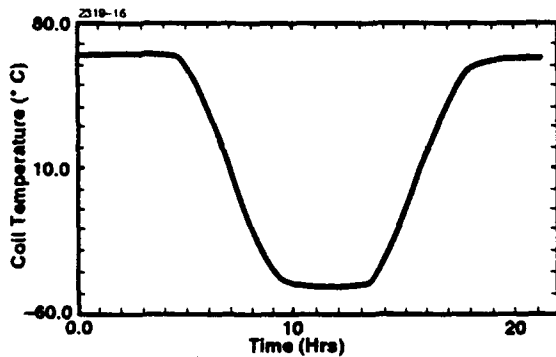


Figure 6a

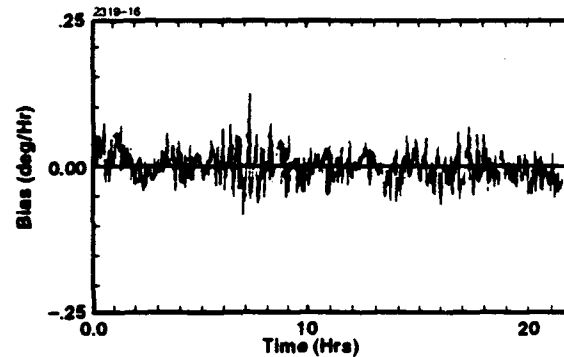


Figure 6b

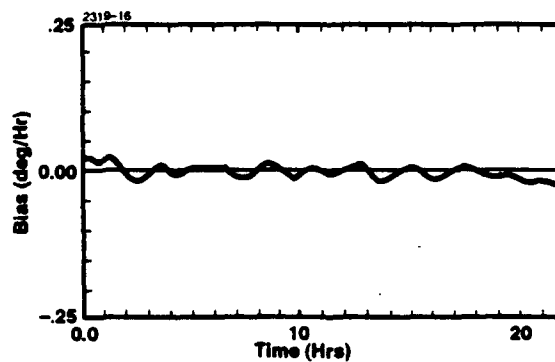


Figure 6c

Figure 6. IFOG bias uncertainty during dynamic thermal conditions. *Fig 6a* illustrates the temperature profile measured at the sensor coil. *Fig 6b* is the residual of the bias after applying a regression in  $T$  and  $dT/dt$  to the data with a 2-minute filter applied. After applying a 30-minute filter to the data (to separate ARW) the standard deviation is 0.0092 deg/hour as shown in *Fig 6c*.

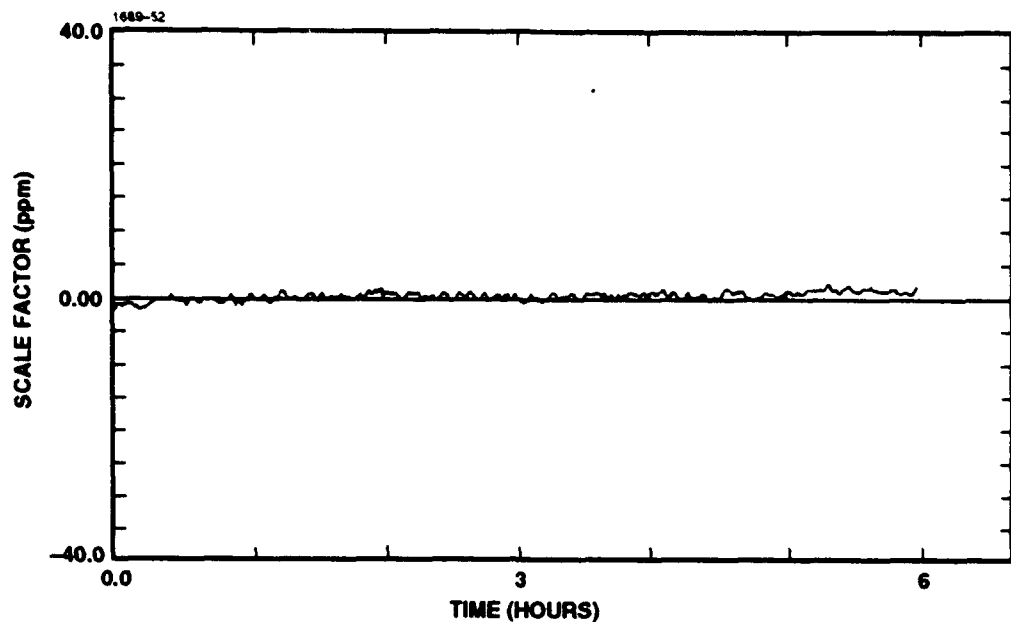


Figure 7. IFOG scale factor stability at constant temperature. The one sigma uncertainty is 0.7 ppm. The run duration was six hours.

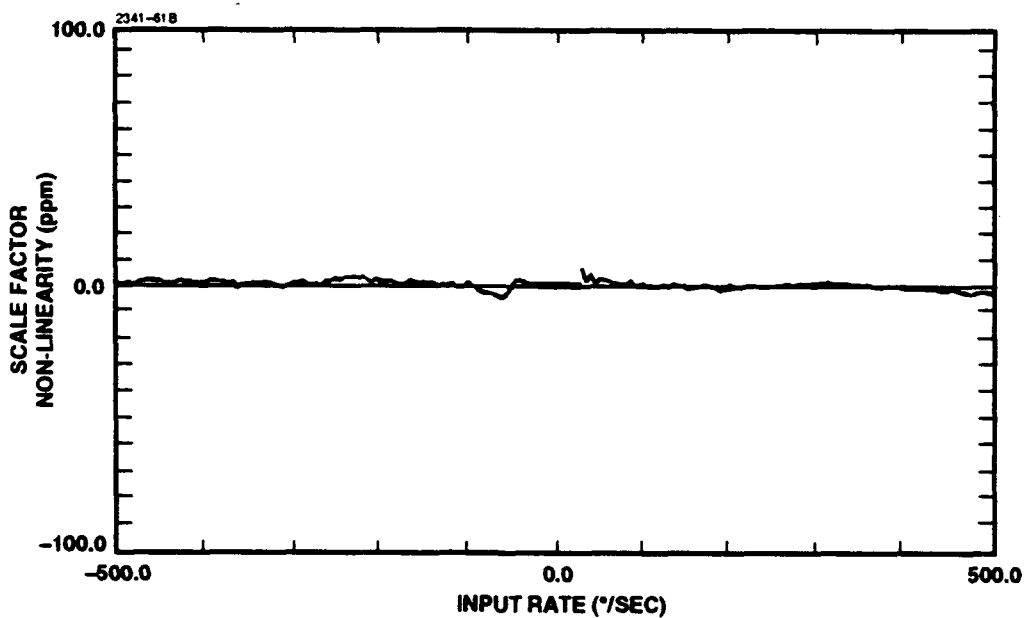
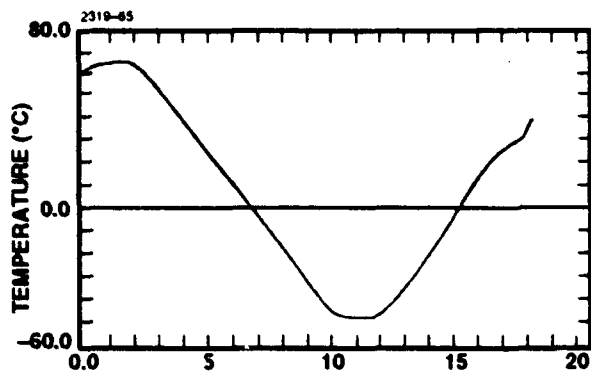
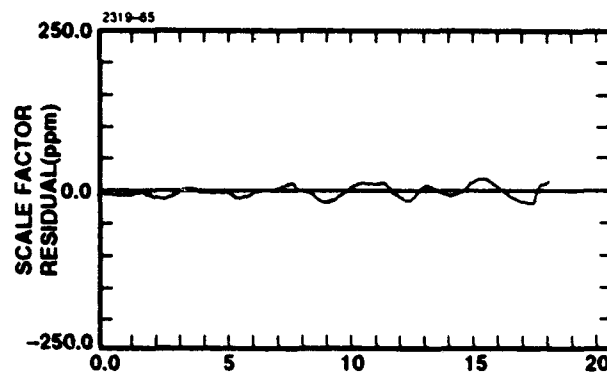


Figure 8. IFOG scale factor linearity. A linear fit was applied to the data from -500 deg/sec to +500 deg/sec input rotation rate. The residual is plotted versus rotation rate. The standard deviation was 1.5 ppm with samples obtained in increments of 5 deg/sec input rate.



TIME (HRS)  
Figure 9a.



TIME (HRS)  
Figure 9b.

Figure 9. IFOG scale factor uncertainty driving dynamic thermal condition. *Fig 9a* is the temperature profile measured at the gyro and used for modeling the data. *Fig 9b* is the residual of the scale factor after modeling. The one-sigma value was 9.1 ppm.

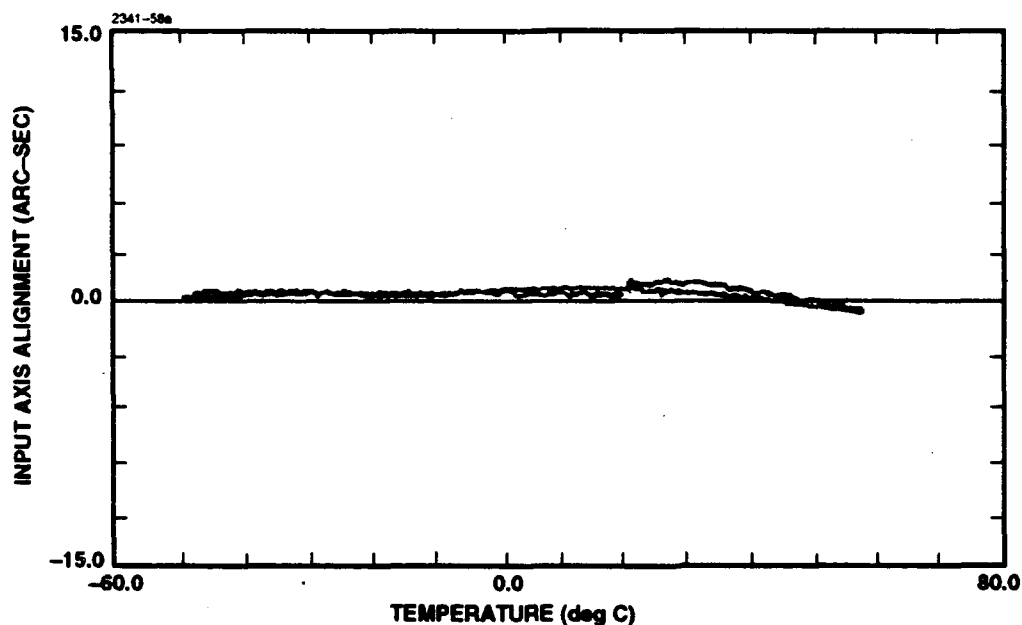


Figure 10. IFOG IA response to temperature. The one sigma uncertainty was 0.38 arc-second with a total excursion of less than 3 arc-seconds before modeling. A linear temperature model was applied to the data.

**SESSION II-A**

**MINUTEMAN**

***CHAIRMAN***

**ELDON PETERSON**

***NORTHROP CORPORATION***



**THIS PAGE LEFT BLANK INTENTIONALLY**

**Minuteman II and Minuteman III  
Guidance Computer  
Test Process Automation**

**by  
William H. Crigger**

**AEROSPACE GUIDANCE & METROLOGY CENTER  
MISSILE AUTOMATIC TEST EQUIPMENT BRANCH  
813 Irvingwick Drive W.  
Newark AFB, OH 43057  
Unclassified**

## Table of Contents

<u>Title</u>	<u>Page</u>
Abstract	3
Background	3
Requirements	4
Requirements Resolution	5
Process Automation Benefits	8
Process Automation Portability	9
Conclusions	10
Definitions of Terms	11

## Tables

<u>Table</u>	<u>Title</u>	<u>Page</u>
1	Minuteman MGC Automatic Test Processes	4

## Figures

<u>Figure</u>	<u>Title</u>	<u>Page</u>
1	Automatic Processing Block Diagram	6
2	Automatic Processing Mode Selection Prompt	8
3	Process Starting Point Selection	8

## **Minuteman II and Minuteman III Guidance Computer Test Process Automation**

### **ABSTRACT**

Malfunction Verification, Diagnostic Processes, and Functional Testing of MM II and MM III guidance computers was a manual process. A Computer Test Station (CTS) operator was required for each phase of the Minuteman computer production process.

These processes have been automated, so that one CTS operator may now simultaneously operate three stations. This automation has been accomplished using personal computers, and readily available software compilers. This paper will provide an overview of the techniques utilized to achieve this automation. Additionally, suggestions will be provided for the adoption of this technique for other workloads.

### **BACKGROUND**

Five CTSs were received at Newark Air Force Base during the period July 1985 through March 1986. Each CTS contained an embedded IBM PCXT personal computer, an off-the-shelf circuit card providing an interface to the CTS electronics, the CTS interface electronics, MM II/MM III memory motor and twenty-eight volt dc primary power supplies, power supplies for the CTS electronics, the Computer Test Station Operating System program (CTSOSP), and software packages for the MM II and MM III Missile Guidance Computers (MGCs).

Each CTS was designed to provide required test environments for MM II and MM III MGCs. The test environments included, but were not limited to, malfunction verification testing, diagnostic testing, repair verification testing, vibration testing, and functional testing. Other test environments could, for example, be a series of special tests mandated by analysis of Minuteman computer field performance data, or tests which fell outside the normal spectrum of malfunction verification and repair.

Prior to the development of the process automation capability, any process (i.e., malfunction verification testing, repair verification testing, etc.) was in essence a manual operation. A CTS operator was required to follow well-defined manual procedures in order to accomplish any designated task. Such procedures included, but were not limited to, keyboard inputs for various purposes, observations of results data, monitoring a procedure's performance execution, responding to results, and maintaining records of such activities for historical purposes.

A major difficulty with manual production processing (in this case the product was a Minuteman Guidance Computer) was that each CTS required an operator to provide all of the manual inputs to the CTSOSP via the personal computer in order to produce the required result. Unnecessary delays were thereby introduced into the manual production process by such normal events as breaks, lunch, shift changes, time required to read and comprehend test data, nonavailability of personnel, etc. Additionally, there is within such a group of manual operations a definite probability that necessary steps and tests will be overlooked or performed in an erroneous manner on occasion.

Downsizing, increasing costs, competition for workloads, and other factors were presenting increasing difficulties when the manual production method was utilized.

Therefore, it seemed prudent to scrutinize all CTS operations with a view to process automation. This in-depth analysis began in December of 1989.

#### REQUIREMENTS

An initial system requirements analysis disclosed that process automation should be extended to the processes listed in table 1.

Table 1  
Minuteman MGC Automatic Test Processes

MM II Pre-vibration Functional Testing.
MM II Post-vibration Functional Testing.
MM II Malfunction Verification Testing.
MM II Diagnostic Testing.
MM III Pre-vibration Functional Testing.
MM III Post-vibration Functional Testing.
MM III Malfunction Verification Testing.
MM III Diagnostic Testing.

The system requirements analysis was extended to include all applicable Operating Instruction Specifications. These were reviewed to completely define the manual operations necessary for comprehensive performance of all identified processes by a CTS operator. Techniques utilized most often in malfunction verification and diagnostic testing were screened to provide similar results. These analyses provided the basis for the development of the automatic processing software models. The requirements analysis yielded the following assessment of IBM compatible personal computer resources necessary to successfully provide automatic processing wherever required for the CTS/MGC workload.

- CTSOSP Source Files.
- Compatible Compiler.
- Compatible Overlay Linker.
- 40 Mbyte Fixed Disk (minimum).
- 640 kbyte RAM memory.

#### REQUIREMENTS RESOLUTION

Given the memory constraints of the personal computers involved, it was decided that software overlay techniques would be used to achieve the desired process automation objectives. This would mean that the process automation module would become resident in the personal computer only when required. The unused memory would be available for other purposes at all other times. Figure 1 illustrates this technique.

In order to produce this result, the CTSOSP program module, tasked with correctly responding to manual inputs in the performance of any MGC test (UUT module in Figure 1), was screened to identify all specific functions exercised during such manual responses. These were then moved into a library (Library module in Figure 1). Each function was then assigned a unique identifying name. This process accomplished the following objectives:

- Reduced the size of the UUT program module to acceptable limits.

- Provided a means for the performance of every function when required by a manual, operator supplied input to the UUT program.

- Provided a means for the performance of every function when required by an automatic process being performed by the process automation overlay.

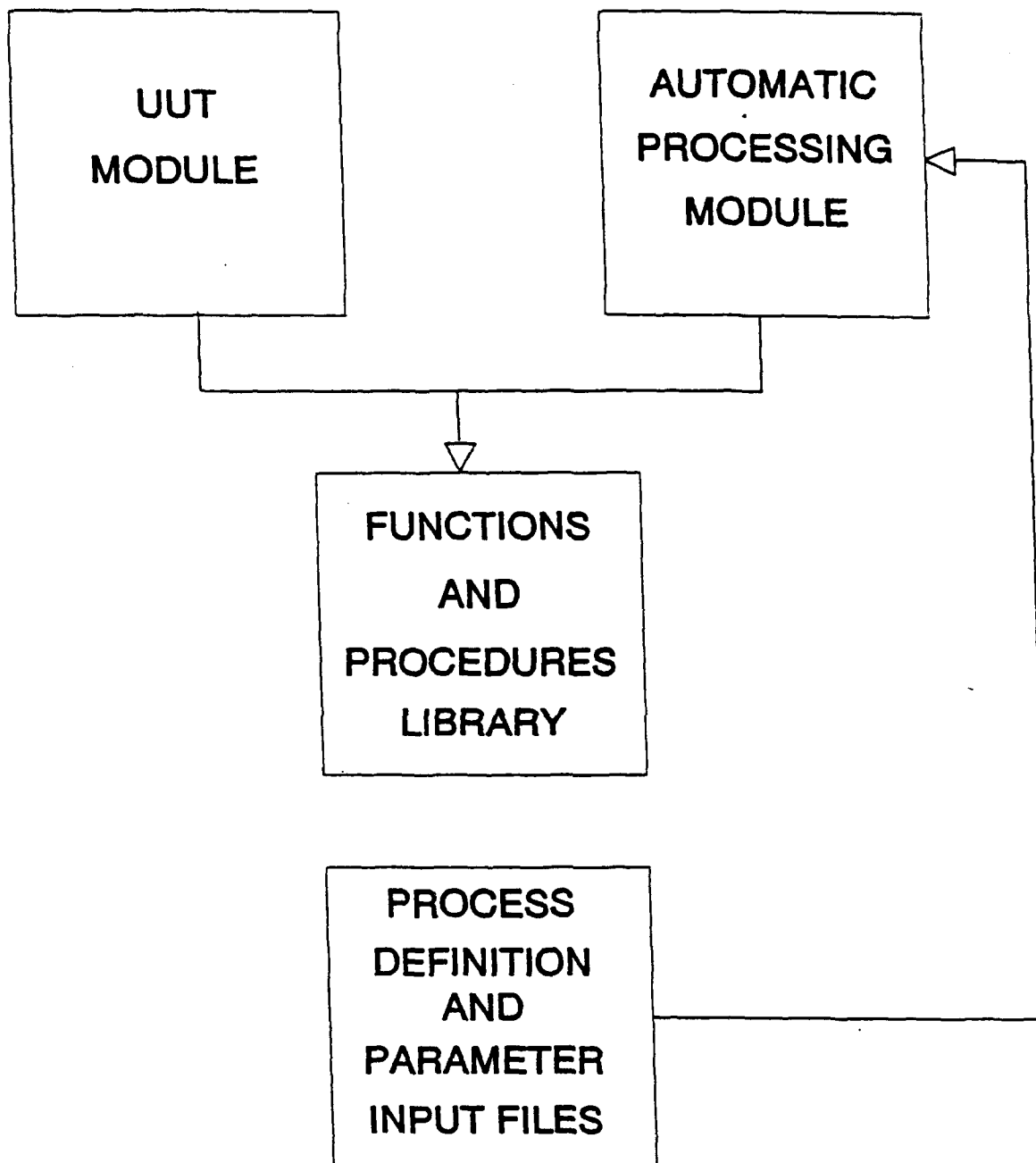


Figure 1, Automatic Processing Block Diagram

Provided greater readability of CTSOSP software flow and development.

The final design was validated and placed into production status on all CTSs in April 1991. Design simplicity yielded a short maturity cycle for the system. Current operation is as described by Figure 1.

The Automatic Processing overlay is loaded as a result of one keystroke by the CTS operator. A menu (Figure 2) is provided to permit selection of the required process. The menu, shown with the MM III MSC Post-vibration Final Functional Test process selected, is removed from the active display after the operator selection is received.

A display (similar to Figure 3) is provided containing the tests available with the selected process. The operator may select an appropriate process starting point. This precludes a requirement to resume a sequence of tests from the beginning, in the event that an MGC needed to be moved to another CTS due to equipment failure. MGC software constraints necessitate limiting the number of valid beginning points in these processes. These are indicated by the dashes (-) preceeding the test names in Figure 3.

Each test component of a particular process was performed manually by a series of keystrokes, measurements, or various types of performance observations. A macro language was developed to enable automatic performance of each test component step. Each automatic process test component was then developed using the required macro code. These automatic process test component macro files were saved and became inputs to the Automatic Process Overlay Module (ref. Figure 1, parameter input files).

Each defined automatic process (ref. table 1) is defined by available test data. A process definition file (PDF) for each process was constructed using commercially available word processors. The files were then saved using the form **name.pdf**. Two key elements of **name** are MGC type (MM II or MM III), and process series type (Previb, Final, or Diagnostic series). Each record of the PDF contains both the test title, and a reference number. This reference number becomes the basis of a parameter input file (PIF). This PIF contains all macro code necessary to perform the test automatically. These files are provided as inputs to the automatic process overlay (figure 1). The automatic process overlay begins by opening the PDF file at the selected starting point, extracting the test name and reference number, and converting the macro code to library calls (figure 1) to execute the test.



Progress reports are provided in unique disk files as well as hardcopy, so that evaluation of performance data may be accomplished at a later date. The automatic processor module continues to process test input records from the PDF until the process is complete, or until a failure is detected. System failure data is saved in cases where such data is available.

#### Automatic Processing Mode Selection Prompt

```
[ ] MANUAL [ ] PREVIB [*] FINAL [ ] DIAGNOSTIC SERIES
```

Figure 2

#### D37D Previbration Test AL81514 Starting Point Selection

Title	Paragraph
-Master Reset Test	6.5.4
-Manual Keyboard Test	6.5.5
-Hot and Cold Channel Preservation Test	6.6.1
-Computer Output Timing Test	6.6.2
-Speed and Stability Test	6.6.3
-Computer Analog Accuracy Setup	6.7.1
Voltage Input Accuracy Test	6.7.2
-Voltage Output Accuracy Test	6.7.3
-DAC Dump/Recovery Test	6.7.4
-Voltage Input Interaction Test	6.7.5
-Computer Power Supply Voltage Test	6.7.6
-Power Supply Response Test	6.7.7
-Computer Secondary Power Supply Setup	6.8.1
-Memory frequency Variation Test	6.8.2
Computer Burn-In Test	6.8.3
-Preliminary Operations Test	6.9.1
-FSC Disable Test	6.9.2

Figure 3

#### PROCESS AUTOMATION BENEFITS

Process automation applied to the MM II and MM III MGC workloads provided a capability to virtually eliminate production process delays. A single CTS operator could now operate three CTSs with

ease. This provided a potential for significant labor cost savings. Slight modifications to the CTS hardware further reduced the number of manual inputs to the process automation software, and thereby increased the MM MGC throughput.

Additionally, process automation assured that a thorough test of each MM II and MM III MGC was performed. This factor translates into better quality testing in all automated processes.

#### **PROCESS AUTOMATION PORTABILITY**

A significant feature of this process automation system is its portability. For example, subsequent to the validation and delivery it became necessary to develop various types of automatic diagnostic and malfunction verification processes to accommodate varying malfunction verification and diagnostic requirements.

The incorporation of the new tests into the automatic processing environment was simply a matter of defining the requirements, developing the process file, and incorporating the macro code for each additional test in the process. Additional solutions could thereby be achieved with ease, often in a matter of a few hours.

The potential application of this type of process automation technology to other workloads is dependent on several factors. If a personal computer is currently a component of the workload test environment, then the following considerations apply:

- availability of program source file data.

- availability of software support tools (i.e., compilers, linkers, etc.).

- availability of knowledgeable personnel to define the required macro code.

- availability of knowledgeable personnel to develop the required software modules interfacing the macro code and the existing software.

If a personal computer is not available, then in addition to the preceding requirements, a study must be done to ascertain the practicality of installing one and developing the required software and hardware interfaces.

This type of assessment is currently being accomplished at Newark AFB, with a view to automating a previously manual test station which is becoming unsupportable due to the non-availability of critical parts.

The initial assessment is that these types of circuits and circuit components may be replaced with standard logic devices. A preliminary personal computer/test station interface design has been developed. Many of the existing software techniques are directly applicable to this workload. cursory inspections reveal several other workloads at Newark Air Force Base which may be automated in a manner similar to that described in this paper.

## **CONCLUSION**

Process automation is relatively easy to achieve in many cases. The cost/benefits ratio is such that Air Force managers can be provided these types of process enhancements with assurance of high payback, improved product quality and reliability, and greater flexibility with respect to diminishing manpower resources.

## Definitions of Terms

Term	Definition
Byte	Eight bits of digital computer data
CTS	Minuteman II & Minuteman III Missile Guidance Computer Test Station
CTSOSP	CTS Operating System Program
KB	Abbreviated form of kbyte
KBYTE	1024 bytes of digital computer data
MGC	Missile Guidance Computer
MBYTE	Megabyte, one million bytes of computer data
MM	Minuteman (Minuteman II or Minuteman III Intercontinental Ballistic Missile)
PIF	Parameter Input File
PDF	Process Definition File
RAM	Random Access Memory

Author: William Crigger  
Commercial: (614) 522-8068  
DSN: 346-8068  
FAX: (614) 522-7991

Mailing Address: William H. Crigger  
AGMC/MAEL(2)  
813 Irvingiwick Drive W  
Newark AFB, OH 43057-0005

**A Concept for Sled Testing Minuteman III  
Guidance Systems**

**Hossny El-Sherief,  
Dave Knight, Dan Simon, and Myron Teeter**

**TRW Ballistic Missiles Division  
Systems Integration Group  
P.O. Box 1310  
San Bernardino, CA 92402-1310**

**Approved for Public Release; distribution is unlimited.**

## ABSTRACT

Rocket sled testing has proven to be a useful tool for evaluating the functional performance and accuracy of inertial navigation systems. Sled testing can be used to evaluate the performance of new prototype system designs as well as the performance degradation or design enhancement of mature systems.

This paper describes the status of a conceptual study that is underway for sled testing the Minuteman III, NS-20 Guidance System. Although the NS-20 has an extensive in-flight and ground test history, rocket sled testing has not been conducted on this system. In this paper, the basic advantages and limitations of sled testing the NS-20 system are compared to other forms of ground tests and flight tests. Specific benefits of sled testing this mature guidance system are identified. Potential sled test show stoppers, guidance error observability, the sled test vibration environment, and the necessary sled test equipment and software modifications are discussed.

## I. INTRODUCTION

Rocket sled testing has proven to be a useful, non-destructive test for evaluating inertial navigation systems in a highly dynamic environment [Bunce, Nielson]. Figure 1 depicts a typical sled test space-time system, and Figure 2 shows the tracksite configuration. Although the Minuteman III guidance system (NS-20) first became operational over 22 years ago and has an extensive in-flight and ground test history, rocket sled testing has not been conducted on this system. This contrasts with many other ICBM guidance systems which have undergone extensive sled testing.

The predecessor to the NS-20, the Minuteman II NS-17 Guidance System, underwent a total of 21 sled tests in 1973 and 1974. These tests were conducted to augment a reduction in Minuteman II flight tests. The Peacekeeper Advanced Inertial Reference Sphere (AIRS) guidance system has undergone a total of 72 sled test runs dating back to 1977 [Cuevas], including a series of nine test runs in 1993. The AIRS was tested for a variety of reasons, although the common objective was to evaluate alignment accuracy and overall system performance. AIRS sled tests are currently scheduled through 1999. The AIRS guidance system also underwent 12 sled tests as part of the Rail Garrison program in 1989 and 1991 [Cuevas].

The two candidate designs for the Small Intercontinental Ballistic Missile guidance systems, the Alternate Inertial Navigation Systems (AINS), were sled tested as part of their design evaluation and part of the procedure to select from competing

designs. The two versions of the Advanced Inertial Measurement Unit (AIMU) brassboard units (high acceleration reentry guidance systems) also underwent sled tests as part of the design assessment and to compare competing designs.

Sled tests are currently planned for the new Advanced Inertial Measurement System (AIMS) in early 1994 to compare competing designs [Hand].

Given the significant benefits derived from sled tests conducted on many other guidance systems, could sled testing have value for the mature NS-20 guidance system? This paper discusses a conceptual study that has been performed to answer that question. The possibility of using sled testing as a method to detect age-related degradation in accuracy, reliability and functional performance is discussed. Augmentation of the current NS-20 flight test program through sled testing is addressed. Specifics of an NS-20 sled test program are discussed, including the potential show stoppers, and the equipment needed for the test facility and the NS-20 guidance system. The software needed for sled testing is described, and the observability of the guidance error terms in a sled test are discussed. Sled testing of the NS-20 is compared to other tests, e.g. flight tests, vibration tests, and centrifuge tests.

## **II. POTENTIAL SHOW STOPPERS**

At the inception of this study, three areas were identified as potential show stoppers—that is, concerns that could be serious enough to prevent a worthwhile NS-20 sled test program. The first was a concern that the sled test environment would seriously damage the NS-20 gyrocompass assembly (GCA) or degrade its accuracy. The second was the availability of guidance system support equipment suitable for sled testing, and the third was the lack of spare memory in the NS-20 Guidance System computer.

### **II-A. NS-20 GYROCOMPASS ASSEMBLY**

The concern regarding the GCA's ability to withstand the sled test environment was based upon the knowledge that the GCA is used only for pre-flight azimuth alignment. It has no purpose after launch. Since it does not matter if it is damaged in flight (it will obviously never be used again), its ability to withstand the flight environment (or simulated flight environment in sled tests) without damage or degradation was suspect. The cost of repairing or replacing the GCA after sled test induced damage would make sled testing unacceptable. Damage to the GCA would also compromise a major sled test benefit - repeated tests on the same guidance set.



The Minuteman II NS-17 Guidance System sled test program answered this concern. At the time this study was initiated, it was not known that NS-17 systems had been sled tested. This discovery and subsequent review of the test documentation revealed that multiple sled test runs had been conducted on four NS-17 systems. Extensive functional and performance data were taken before and after each run. Analysis revealed no evidence of GCA damage or accuracy degradation. Although the NS-17 and NS-20 GCAs differ slightly, these differences are not in areas that would affect the NS-20 GCA's ability to withstand the sled test environment. Consequently, it can be stated with confidence that sled testing will not damage or degrade the accuracy of the NS-20 GCA.

## **II-B. GUIDANCE SYSTEM SUPPORT EQUIPMENT**

The second concern was the possible lack of suitable NS-20 Guidance System sled test support equipment. This concern was based upon the prospect that the NS-20 Factory Test Equipment (FTE) would have been required for NS-20 sled tests, just as the NS-17 FTE had been the guidance support equipment for the NS-17 sled tests. Concerns about the NS-20 FTE included its age (over 20 years old), its obsolescence (based on old IBM 1800 computer technology), its questionable reliability, and the fact that it is large and difficult to transport, set up and debug. On top of these concerns, there was uncertainty regarding the availability of the NS-20 FTE. Fortunately, alternatives for guidance system support equipment fulfilling NS-20 sled test requirements have been identified, thus eliminating this concern. The comparisons between alternatives are discussed later in this paper.

## **II-C. GUIDANCE SYSTEM COMPUTER SPARE MEMORY**

The third concern, extremely limited spare memory in the NS-20 computer, was also eliminated as a show stopper. It was thought that added instructions would be needed in the resident NS-20 Operational Ground Program (OGP) and Operational Flight Program (OFF) for the sled test functions. It was concluded that overwriting the OFF with a sled test program can solve the memory needs. Other potential solutions are also being investigated. It is concluded that this is not a show stopper, but it is a challenging area for an NS-20 sled test program. This subject is addressed in more detail later in this paper.

## **III. GUIDANCE ERROR OBSERVABILITY**

This section discusses results of a covariance analysis which was conducted to determine the observability of guidance errors.

A Kalman filter has been implemented in a simulator program to estimate NS-20 guidance errors based on simulated sled test data. The start of the simulated sled track is located at 34 degrees latitude, and the track runs due north (although in reality the track runs 4 degrees off of true north). The x-platform axis of the NS-20 points along the sled track. Figure 3 shows the NS-20 geometry. The sled test software applies a constant torque to the NS-20 to maintain it in a locally level orientation (with respect to the launch point). One important result of this torquing is that acceleration-sensitive NS-20 errors are driven by real acceleration (with respect to inertial space) rather than by the acceleration which is sensed by the accelerometers (which includes acceleration due to gravity). The simulated sled acceleration lasts for 80 seconds, although the acceleration during the last 50 seconds or so is fairly low, as the sled is simply coasting to a stop. The acceleration varies between -5.6 and 6.7 g's, and the velocity reaches a maximum of 850 miles per hour. By the time the sled stops moving, it has travelled slightly over 4 miles. The sled test includes 60 seconds of pre-run and 60 seconds of post-run data collection sandwiched around the 80 seconds of hot-run data collection, for a total of 200 seconds of test time. The sled trajectory acceleration which was used is shown in Figure 4, and was obtained from an analytical approximation found in [Aiyawar].

The covariance part of the Kalman filter was propagated during the 200 seconds of the sled test at a 100 Hz rate to determine the increase of information that would result from a sled test. The state of the Kalman filter is composed of NS-20 errors [Rockwell]. Since the errors are assumed to be constant during the duration of the sled test, the state transition matrix of the linear system is the identity matrix and the process noise is zero. The measurement of the system is the difference between the NS-20-indicated velocity and the track-indicated velocity. The measurement matrix is therefore the sensitivity of the NS-20-indicated velocity to the NS-20 errors [McAllister]. The Kalman filter covariance is thus propagated as follows [Gelb]:

$$K_k = P_{k-1} H_k^T (H_k P_{k-1} H_k^T + R_k)^{-1}$$

$$P_k = (I - K_k H_k) P_{k-1}$$

where K is the Kalman filter gain, R is the covariance of the measurement noise, H is the measurement matrix, I is the identity matrix, and P is the covariance of the state estimate. The square roots of the diagonal entries of P are the standard deviations of the state estimates. Note that the actual state estimate does not need to be computed in order to compute the covariance matrix P.

The measurement noise values employed came from a PIGA noise mitigation method developed by Rockwell and currently used to

evaluate IMU performance during NS-20 vibration tests. In this method the precise time of each PIGA pulse is determined thereby reducing pulse quantization standard deviation from 0.0346 feet per second to noise that can be modelled by the equation

$$\sigma = \max (0.003, 0.0029 * g) \quad (\text{ft/sec}).$$

This equation means the standard deviation of the PIGA noise is the maximum of either 0.003 or 0.0029 times the absolute magnitude of sensed acceleration in g's. Similarly, by this equation, the noise can not be less than 0.003 feet per second.

The information gained about NS-20 error terms can be quantified by recovery ratios. The recovery ratio for an error state is the final standard deviation of the state estimate divided by the initial standard deviation, so a low recovery ratio corresponds to a better estimate and a greater increase in information. A recovery ratio less than approximately 0.5 generally indicates that a significant amount of new information has been gained about the error state under consideration.

Table 1 shows the NS-20 recovery ratios for one standard deviation magnitudes of the NS-20 error terms. It can be seen from Table 1 that nine NS-20 errors are recoverable from an NS-20 sled test if a slight latitude is extended in the 0.5 ratio criteria. Interpretation of this result, however, requires an understanding of which error terms are important contributors to impact miss. Observability of an error term that is insignificant to the NS-20 CEP is of no value; observability of errors that are major miss contributors, however, is crucial to the determination of whether or not sled tests can be used as a method to assess guidance system accuracy.

The NS-20 Error Model Document [Rockwell] identifies the major sources of impact miss to be:

- (1) Azimuth alignment error
- (2) Calibration error
- (3) Gyro  $g$ - and  $g^2$ -sensitivities (primarily B and S coefficients);
- (4) PIGA scale factor errors
- (5) Accelerometer input axis misalignments due to flight vibration and shock; and
- (6) Deployment errors.

**Table 1 - NS-20 Recovery Ratios**

<b>NS-20 Error</b>	<b>One-sigma Recovery Ratios</b>
<b>Initial Conditions</b>	
Azimuth	0.17
West Alignment	0.23
North Alignment	0.53
<b>Accelerometer</b>	
x bias	0.54
y bias	0.72
z bias	0.72
x scale factor	0.31
y scale factor	0.82
z scale factor	0.82
x input $g^2$	0.44
y input $g^2$	0.83
z input $g^2$	0.83
<b>Gyro</b>	
x bias	0.80
y bias	0.43
z bias	0.92
g-sensitive	
SB2	0.92
SA1	0.90
SB1	1.00
C2	0.82
C1	0.98
D2	1.00
D1	0.89
$g^2$ sensitive	
B2	0.52
B1	0.73
E2	1.00
E1	0.17
FB2	0.96
FA1	1.00
FB1	1.00

Clearly, item (6) cannot be monitored with sled testing.

Item (5) will be observable by comparison of calibration data before and after the sled test run.

When the analysis indicated some of the important error terms were not observable at one standard deviation, additional analyses were run with each of these unobservable errors increased to a three standard deviation magnitude one at a time.

Item (4), PIGA scale factor, is observable, at one sigma on the x PIGA and three sigma on the y and z PIGAS (both y and z ratios dropped to 0.43 at three sigma).

For item (3), the B2 error term is observable at one sigma and B1 becomes observable at three sigma (ratio 0.34). The S coefficients ratios (0.62 and 0.57 respectively) indicate they might become observable at slightly larger values.

Many of the elements of the calibration error, item (2), are due to misalignment between the alignment reference block and the flight instruments (PIGAS and G6 gyros). These errors manifest as azimuth alignment and level alignment errors, which have good observability in sled test.

Azimuth alignment, item (1), is readily observable even at one standard deviation.

#### IV. POTENTIAL BENEFITS OF CONDUCTING AN NS-20 SLED TEST PROGRAM

As mentioned in the Introduction, the purpose of this study is to determine if there is benefit to be gained by sled testing the mature NS-20 Guidance System. There is little incentive to conduct sled tests to improve accuracy and/or reliability since the NS-20 currently meets its requirements on both. It is postulated that NS-20 sled tests could be used, however, as a monitor to identify age-induced degradations in accuracy, functional performance, and/or reliability. As such, sled tests could augment the monitoring provided by the NS-20 flight test program which is currently limited to three flights per year after having been six flights a year for a considerable period. Problems could be detected and corrected as much as a year earlier than with flight tests alone.

For a sled test program to be a credible monitor for accuracy degradation of an aging system, however, the major flight errors must be excited by the sled test trajectory. The analysis

described in Section III was conducted to determine if this is the case. It was shown that with the exception of the RV deployment error, most of the major in-flight errors are observable in sled tests if a three standard deviation magnitude is permitted for some of the error terms. For an accuracy degradation monitor this would probably be acceptable. It thus appears that rocket sled testing would be an effective test method to monitor NS-20 accuracy degradation.

If it is decided to initiate an NS-20 sled test program, it is envisioned that this program might be patterned after the successful AIRS sled test program, where each year three test runs each have been conducted on three guidance systems. Conducting sled tests on three NS-20 guidance systems would thus double the sample size of guidance systems tested in a dynamic environment (combining sustained acceleration, vibration, and shock), compared to flight tests alone. The three runs per system provide insurance against being unduly influenced by a single anomalous test run; combining each systems' three test results would produce more representative performance than a single test.

The accuracy monitoring would be accomplished by comparing the total sled test guidance system error with the total guidance system error predicted by the NS-20 Error Budget. As long as the guidance system accuracy stayed within the one standard deviation boundaries predicted by the error budget, no further analysis would be performed. Test results exceeding the boundaries would be analyzed to determine their cause. Test results indicating a pattern of accuracy degradation with the passage of time, as might be expected with this aging system, would also be analyzed as to cause.

Functional performance would be monitored under a sled test program by reviewing functional signals for aberrant behavior. Reliability monitoring would be achieved by analyzing any guidance system failures.

## **V. SLED TESTING VERSUS OTHER TEST METHODS**

There are several methods other than sled testing which can be used for testing a given guidance system. Some of these methods are flight testing, centrifuge testing, vibration testing, and subsystem/component testing. This section discusses the pros and cons of sled testing as compared to each of these alternatives.

### **V-A. SLED TESTS COMPARED TO FLIGHT TESTS**

Minuteman III flight tests from Vandenberg Air Force Base (VAFB) are unquestionably more realistic approximations to an operational mission than are rocket sled tests. A test flight

trajectory is quite similar to an operational trajectory. The acceleration, vibration, and shock environments approximate those of operational launches.

Sled tests, however, offer the advantages that they cost much less than flight tests. In addition, the guidance system is not expended in a sled test so the same unit can be tested repeatedly to obtain multiple measurements which has many advantages. A test procedure can be modified and the test repeated on the same unit. Furthermore, calibration can be conducted before and after the sled run to precisely measure any changes. The sled track provides a very precise reference for accuracy evaluation. The guidance systems can be oriented to improve error term observability and changes can be readily made to obtain additional data. Although the rocket sled test is a significantly less realistic approximation of an actual operational Minuteman III mission than a VAFB flight test, it is the closest test to a flight test that can be done on the ground. It provides a unique combination of flight-like environments of sustained acceleration with some application of vibration and shock.

#### **V-B. SLED TESTS COMPARED TO CENTRIFUGE TESTS**

Centrifuge tests could also be used to investigate NS-20 performance [Peters2], but sled tests are the best ground test approximation to flight tests. The centrifuge rotational method of obtaining sustained g's departs significantly from an ICBM trajectory simulation with a greater time to maximize acceleration. As a consequence, centrifuge tests aggravate gyro drift errors that persist for a shorter time during the ICBM boost phase of a flight trajectory. This significantly complicates the use of centrifuge tests as a method of assessing guidance system performance. In addition, existing centrifuges which are capable of testing the NS-20 lack sufficient accuracy for performance assessment. This is due to such things as arm stretch and wobble, and the lack of precise position and velocity measurements for comparison to NS-20 measurements. Centrifuge tests are less costly than sled tests.

#### **V-C. SLED TESTS COMPARED TO VIBRATION TESTS**

Vibration tests can provide a closer approximation to the flight test vibration environment [Burnett,Peters1], but cannot produce the sled test linear acceleration which is key in assessing the response of the guidance accelerometer under simulated flight and the platform gimbal structures and gimbal servos performance under inertial loading. Sled test vibration levels vary from test to test, but these levels are on the same order of magnitude as flight levels. Vibration testing is much less costly, however, than sled testing, and requires less test time. As a consequence,

many more systems can be tested in a given time frame and for a given dollar cost.

#### **V-D. SLED TESTS COMPARED TO SUBSYSTEM/COMPONENT TESTS**

When comparing sled tests to guidance subsystem/component tests, sled testing has the advantage that the tests are on the entire guidance system in an environment that more realistically approximates the mission. Tests at levels lower than the full guidance system have the inherent risk that they may produce results not fully representative of the guidance system as a unit. In addition, tests on the full guidance system may help identify unmodelled or inadequately modelled error terms. These error terms may not be revealed in lower level testing, because either the environment cannot be duplicated, or the test procedure is not properly designed to excite the error terms (since their existence is either unknown or inadequately understood).

On the other hand, subsystem and component testing are much less expensive than sled testing. Subsystem/component tests also have greater versatility in that more components can be tested and larger sample sizes are easier to obtain.

Given the strengths and weaknesses of sled tests versus subsystem/component tests, the two test methods could be employed in conjunction. Subsystem/component tests could be used to analyze problems or anomalies found in sled tests.

#### **VI. SLED TEST EQUIPMENT REQUIREMENTS AND SOFTWARE MODIFICATIONS**

A major concern regarding the viability of NS-20 sled tests is the identification of available guidance support equipment (GSE) that can meet the sled test requirements with few or no modifications. If major modifications are required or new equipment has to be designed and built, the development time and cost will weigh heavily against the value of the test.

As mentioned earlier, the NS-17 sled test program had used the Factory Test Equipment (FTE). At the time of the NS-17 tests in 1973 and 1974, this FTE was fairly new and up-to-date. However, the NS-20 FTE is now relatively antiquated and is showing its age with unreliability. It lacks many of the features of modern GSE and would consume a great deal of space in the sled track blockhouse. The debugging of the test equipment software would also be difficult, and the availability of the NS-20 FTE is in doubt.



## **VI-A. HARDWARE**

Before alternatives to the NS-20 FTE could be sought, the major GSE requirements had to be defined. These requirements and the GSE candidates are summarized in Table 2 and discussed below.

The Operational Support Equipment (OSE) option consists of the programmer group, coupler, power supplies and chiller from the standard launch facility. The launch control center function would be supplied by the Squadron Data Simulator (SDS). The SDS can copy software overlay modifications from a test site launch control center, thereby maintaining configuration with the current ground program. The primary advantage of this option is the low cost. A disadvantage is that the sled software would need to utilize a set of operational commands to respond and execute sled unique functions.

The Reentry System Launch Program (RSLP) equipment has capabilities similar to the OSE. However, items such as ground program overlays are embedded in firmware, and changes could be prohibitively costly. The cost of a new set is unknown at this time. Two sets of this equipment now exist at Vandenberg Air Force Base in California, and are scheduled for use in supporting RSLP test launches.

The Depot Support Equipment (DSE) and its emulator cannot communicate directly with the operational ground program. This option would be most advantageous if the objectives of the sled test were consistent with the use of the factory functional software in the MM III flight computer.

A recent candidate not shown on the matrix is the hardness surveillance system control unit (HSSCU) which is also based upon a very mature HP-1000 processor. This unit is now being evaluated as to its potential in supporting a sled test software program envisioned for the D-37.

The ability to load software and change the loaded software is a required feature of the test equipment. The ability to support direct memory addressing is also a desirable feature, but it is not a firm requirement if sufficient laboratory support for software troubleshooting exists at another site.

# NS-20 SLED SUPPORT EQUIPMENT REQUIRED CAPABILITIES

	D-37 SLED S/V	GSE OPTIONS FOR THE STUDY			
		OSE W/SDS (NOTE)	RSLP (NOTE)	DSE (NOTE)	1800 EMULATOR (CCT)
POWER		X	X	X	X
COOLING		X	X	X	X
CONTROL	X	X	X	X	X
COMMUNICATION WITH D-37	X	X	X	X	X
MONITORING	X				
AUTO SAFING	X		X	X	X
SUPPORTABILITY		X	X		X**
MAINTAINABILITY		X	X		X**
BLOCKHOUSE FLOOR SPACE		X	X		X
FME INDICATOR	X				
FLIGHT INITIALIZATION DATA AND STATE VECTORS NEAR T=0 ON TELEMETRY	X				
ALIGNMENT DATA	X				
CALIBRATION DATA	X				
REENTER CAL FROM LAUNCH W/O POWER CYCLE	X				
MAINTENANCE STATUS	X				
UNINTERRUPTABLE POWER		?	?	?	?
SHORT TIMELINE CAL AND ALIGN	X				
SOFTWARE LOADING	X	X*	X*	X*	X*

TABLE 2. GSE REQUIREMENTS VERSUS CANDIDATE EQUIPMENT  
PAGE 1 OF 2

# NS-20 SLED SUPPORT EQUIPMENT REQUIRED CAPABILITIES

	D-37 SLED S/W	GSE OPTIONS FOR THE STUDY			
		OGE W/SDS (NOTE)	RSLP (NOTE)	DSE (NOTE)	1800 EMULATOR (CCT)
STRIP CHART DISPLAYS					
DATA RECORDING					
SPACE-TIME DATA ACQUISITION					
SLED ENVIRONMENTS DATA					
OPERATOR DISPLAY AND STATUS			X		X
PLACE GSP IN FREE INERTIAL TORQUE MODE FOR LAUNCH	X				
OUTPUT TELEMETRY AND DISCRETE DATA PRE AND POST LAUNCH	X				
OP CODE RESPONSES TO ACCOMMODATE OSE UP-LINK COMMANDS	X				
INHIBIT/ENABLE CONTINUOUS MONITORING	X				
MAINTAIN SA MODE	X				
SUPPORT S/W OVERLAYS		X	X		

## NOTE-

THE INCLUSION OF THE THREE GENERAL SYSTEMS IS TO SHOW THE RELATIVE MERITS OF EACH AS RELATED TO THE TOPIC AND ONLY ONE APPROACH IS TO BE PURSUED.

\* - BY ADDING A STANDARD CARTRIDGE TAPE UNIT (CTU)

\*\* - COMPUTER CABLE TECHNOLOGY (CCT) NOT AVAILABLE

TABLE 2. GSE REQUIREMENTS VERSUS CANDIDATE EQUIPMENT  
PAGE 2 OF 2

The test equipment must be supportable and easily maintainable by non-specialized contractor personnel and, upon occasion, test track personnel. Equipment which is not supported or not common has in the past presented problems. The equipment must afford the operator sufficient visibility and convenience for monitoring the test progress, the general health of the test article, and critical items of the test equipment. This visibility is normally in the form of computer-generated displays, printouts, strip charts and meters/readouts. A means of emergency power and cooling removal is also required. Most of the equipment considered to date and shown in Table 2 meet or can be easily adapted through the use of peripheral items to meet these requirements.

The conclusion to date regarding the selection of the GSE is that its cost will be highly sensitive to the type of sled test software used in the D-37. If the software chosen resembles the operational ground program, then the OSE or RSLP suites can be used without modifications. The remainder of the candidates would require software modification and would contain the attendant development costs.

#### **VI-B. SLED SUPPORT EQUIPMENT**

In addition to the GSE needed to support the guidance system for sled testing, there is a category of equipment needed for the test itself, referred to herein as sled support equipment (SSE). This includes equipment such as the sled forebody, the rockets, cooling systems, etc. A review was conducted by the Central Inertial Guidance Test Facility (CIGTF) personnel to identify and assess the effort required to provide SSE needed for NS-20 sled tests. Although this was a preliminary analysis, CIGTF experience with other guidance system sled test programs enabled them to identify with confidence the major items such as the forebody, the sled test instrumentation, the telemetry unit, miscellaneous ground equipment and the sled-borne coolant system.

The forebody would be a refurbished and modified unused asset from a previous program. This minimizes the cost and effort to provide this major element of SSE. The remaining SSE can be provided by modifying equipment used on other programs as well. CIGTF foresees no obstacles or major cost items in any of the SSE needed for the NS-20 sled tests.

The mechanical fixtures which attach and secure the test article would be chosen to simulate the vibration and attitude flight environments. These fixtures would also be designed to provide environmental protection, power, cooling, and data routing during the testing. Data would be telemetered during the sled test by a radio frequency link, and simultaneously recorded on board the sled vehicle.

## **VI-C. SOFTWARE**

The NS-20 software should be representative of the software aboard an operational MM III missile. Of paramount importance is the capability to calibrate before and after the sled run without power interruptions. In addition, the achievement of the launch-ready status for the sled test should replicate that of the operational flight in order to avoid ambiguities in the results. These software operations should be identical in coding, and should reside on an identical NS-20 computer.

The sled launch mode for at least one run on each system should also replicate the missile flight mode in the torquing of the guidance instruments. Simulated flight navigation during the sled test allows the navigation data to be obtained in a position frame, thereby smoothing the raw accelerometer data.

There are also other features to be incorporated in the software in order to support the many different possible test objectives. For example, control of and communication with the guidance platform and the test support equipment should be provided. The platform and computer hardware should be monitored, and the self-test features of the software should be used to determine the overall health of the system and to avoid any potential damage. In response to a discrete issued by the sled test program, power and cooling must be automatically removed to prevent damage. This feature is commonly referred to as auto-safing and will sometimes involve monitoring the communications. A loss of communication is interpreted as failure of either the NS-20 or the GSE computer to service the communications link, and under certain conditions is cause to terminate power and cooling. An auto-safing summary of the critical events should be output in order to effect the application and removal of the power and cooling sources. An indication of the change from launch-ready to launch mode should be telemetered in order to assist the post-test analysis.

A software feature should be provided to allow rapid entry to launch mode. This will support simulated sled launches in order to practice activities which ensure launch team readiness. This so-called "short time line to launch" mode allows for practicing of normally lengthy sequences.

A method of re-entering calibration without power cycling should also be a feature of the test software. This feature will allow the assessment of any shifts of the instrument parameters across the sled launch without risking parameter shifts which frequently occur with power cycling.

The ability to position the platform in an arbitrary attitude is a candidate (unverified requirement) software feature. The

observability of platform errors may be enhanced by varying the platform orientation.

In order to avoid a potentially lengthy qualification of the now nonexistent sled software, a candidate software jump-off point involving an existing qualified software program should be determined. The first of these candidates is the current operational ground program. This software would yield the most realistic attainment of strategic alert. Memory in the flight computer required for the sled software changes can be made available by deleting the operational flight program. The second candidate for a jumping off point is the ground program previously used in the Fly-2 flight tests. The Fly-2 program had two NS-20 platform/D-37 computers aboard a single missile.

Other software candidates for the jumping off point are also under consideration, but appear to contain calibration and alignment perturbations as compared to the operational ground program. This would result in an extensive verification effort. One of these candidates is the vibration test software, which contains the option to return to calibration and alignment after the test without power cycling. Another candidate is the factory functional software which contains more extensive diagnostics than any derivative of the operational ground program. Upon identification of specific items or subsystems to be examined for degradation post-test, this software could be an integral part of achieving that objective. The pre and post-test execution of this software on a sled test unit does not necessarily have to occur at the sled test location, but could occur at either depot or factory sites.

## VII. SUMMARY AND CONCLUSIONS

The status of a conceptual study of sled testing the Minuteman III Guidance System (NS-20) has been presented. Sled testing has proven to be of benefit to many ICBM guidance systems. Analytical findings show that sled testing will be of benefit to the NS-20 as well. It appears that the primary benefit of sled testing would be as a monitor to identify age-induced degradation, primarily in accuracy, but would also provide degradation information concerning functional performance and reliability. As a consequence, it is possible that problems could be detected as much as a year earlier with NS-20 sled tests and flight tests combined than with flight tests alone.

Three serious concerns which could prevent a worthwhile sled test program were addressed. Guidance system error observability was determined by a covariance analysis. It was shown that, with the exception of RV deployment error, the major error terms affecting the guidance system CEP are observable in sled test

(although some error terms have to increase to three times their error budget values).

An area which is under investigation that may enhance error term observability during sled testing is to include different NS-20 orientations.

It was mentioned that functional performance could be monitored in sled tests by reviewing functional signals for aberrant behavior. Reliability monitoring could be achieved by analyzing guidance system failures which occur during the test. In this way, sled tests would augment the NS-20 flight test program, which is currently limited to three flights per year. Sled tests would thus double the sample size of guidance system tests in a dynamic environment (combining acceleration and vibration).

The advantages and disadvantages of sled testing as compared to other test methods were discussed. It was seen that sled testing is unique, because it is the ground test which is most like a flight test. It is much less expensive, however, than flight testing. Finally, the hardware and software requirements for an NS-20 sled test program were presented.

#### **VIII. ACKNOWLEDGEMENTS**

This work has been performed in support of LTC Stu Flood, Guidance PMT Chief of the Sustainment Support Organization of the Air Force Systems Command, under contract number F04704-92-C-0005. The authors would like to thank the following personnel for their useful technical support during the course of this work: Captain Curtis Coffman and Bob Lawrence of the 46th Test Group; Gerry Grimaldi and Tom Williams of Rockwell International; and Gene Hymas, Bruce Brown, Benjamin Frint, Bob Jezik, Nick Kfoury, Dave Larson, Richard Holdeman, and Ken Kosaka of TRW.

#### **IX. REFERENCES**

[Aiyawar] R. Aiyawar, R. Boylan, and E. Graves, "AIRS/Sled Test Sensitivity Analysis Report," Cambridge, MA: The Charles Stark Draper Laboratory, June 1977.

[Bunce] K. Bunce and G. Grachis, "Utilization of Velocity Residual Signatures to Determine Error Terms of Inertial Components and Systems in a Sled Test Environment," Fourteenth Biennial Guidance Test Symposium, pp. 349-385, October 1989.

[Burnett] R. Burnett and R. Macary, "Design of Precision Vibration Test Station for High Accuracy Accelerometer Calibration,"

Fifteenth Biennial Guidance Test Symposium, pp. 259-270, September 1991.

[Cuevas] J. Cuevas "The History of AIRS Rocket Sled Testing MPMS Through Peacekeeper", 21st Joint Services Data Exchange for Guidance, Navigation and Control Symposium, October 1992.

[Gelb] A. Gelb (editor), Applied Optimal Estimation, Cambridge, MA: The MIT Press, 1974.

[Hand] J. Hand and A. Harris, "Development of Stellar Tracking Requirements for Rocket Sled Testing of Advanced Inertial Measurement System", 21st Joint Services Data Exchange for Guidance, Navigation and Control Symposium, October 1992.

[McAllister] D. McAllister and J. Wilcox, "Digital Computer Program for Generalized Inertial Guidance System Error Analysis," Redondo Beach, CA: TRW Systems Group, March 1969.

[Nielsen] R. Nielsen, B. Cosentino, R. Lawrence, and S. Doyle, "Reverse Velocity Sled Test Simulations to Determine Uncertainties in Accelerometer Model Coefficients," Fourteenth Biennial Guidance Test Symposium, pp. 427-477, October 1989.

[Peters1] R. Peters and S. Foote, "Determination of Nonlinear Coefficients in a Dry Accelerometer by Vibration Testing," Fifteenth Biennial Guidance Test Symposium, pp. 237-258, September 1991.

[Peters2] R. Peters and R. Marquess, "A Practical Three Axis Balancing System for Precision Centrifuge Applications," Fifteenth Biennial Guidance Test Symposium, pp. 225-235, September 1991.

[Rockwell] Minuteman III G & C Error Model Update, Rockwell International, Anaheim, CA, November 21, 1989.



# SPACE-TIME SYSTEM

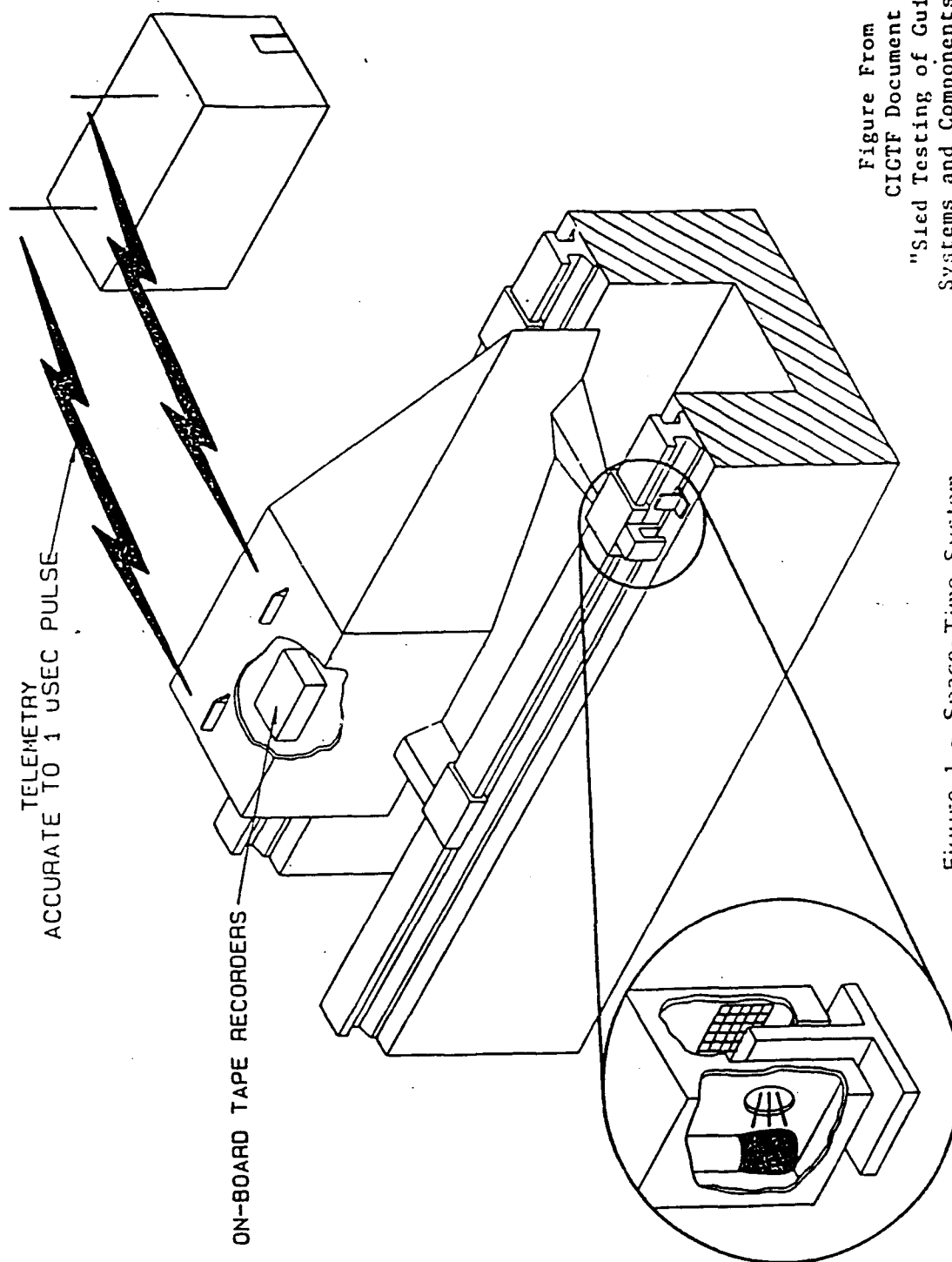


Figure 1 - Space-Time System

Figure From  
CIGTF Document  
"Sled Testing of Guidance  
Systems and Components" 1987

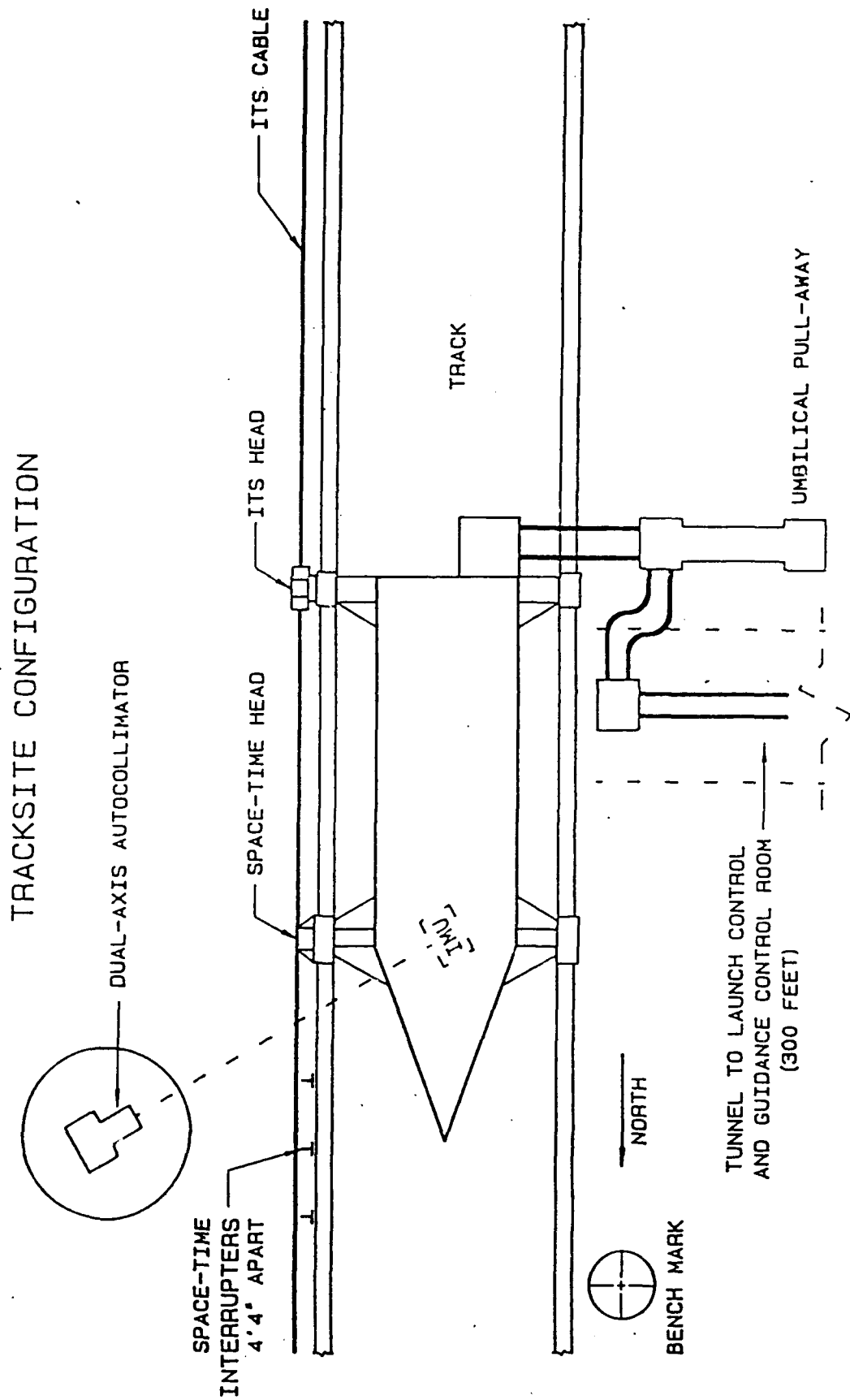


Figure From  
CIGFF Document  
"Sled Testing of Guidance  
Systems and Components" 1987

Figure 2 - Tracksite Configuration.

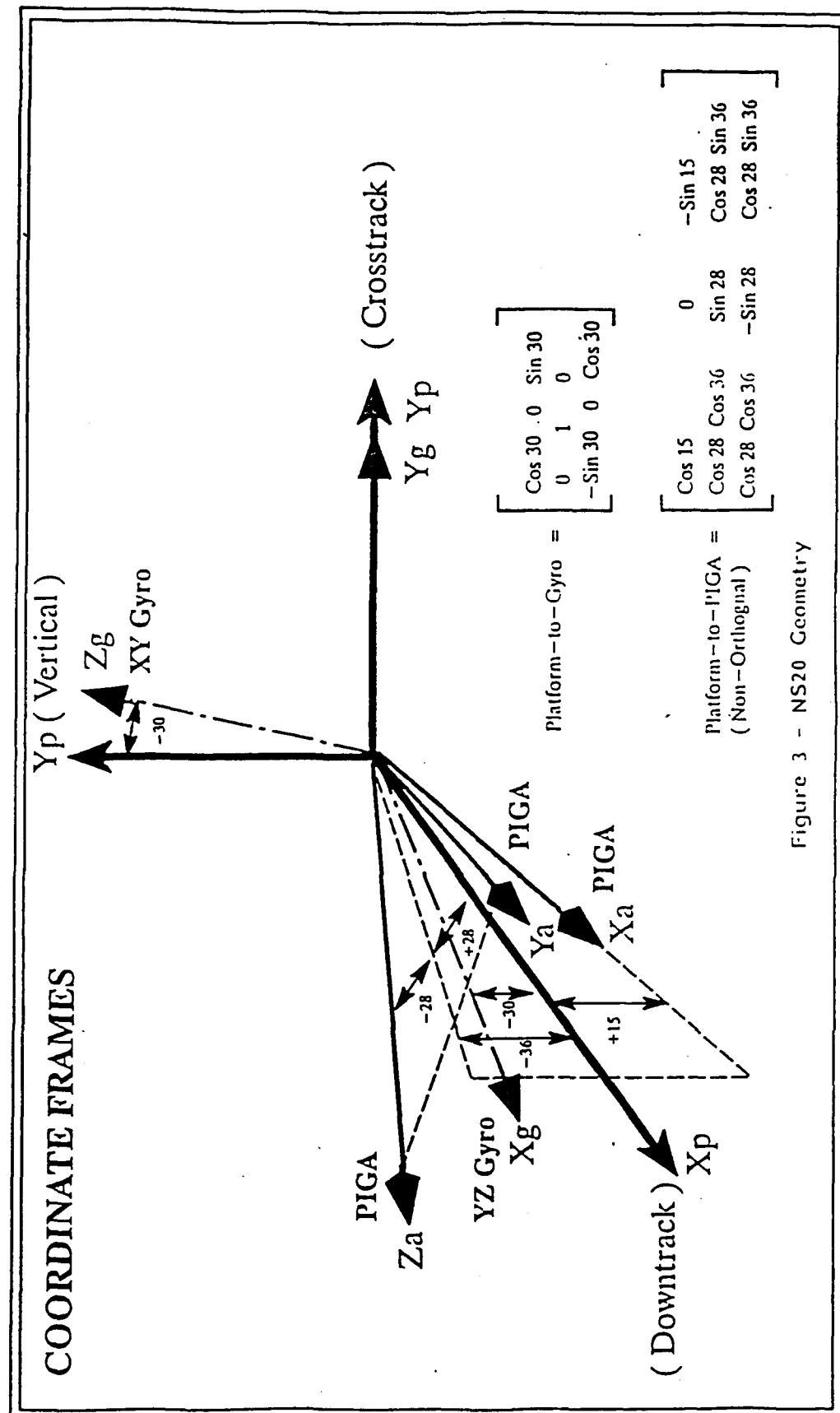


Figure 3 - NS20 Geometry

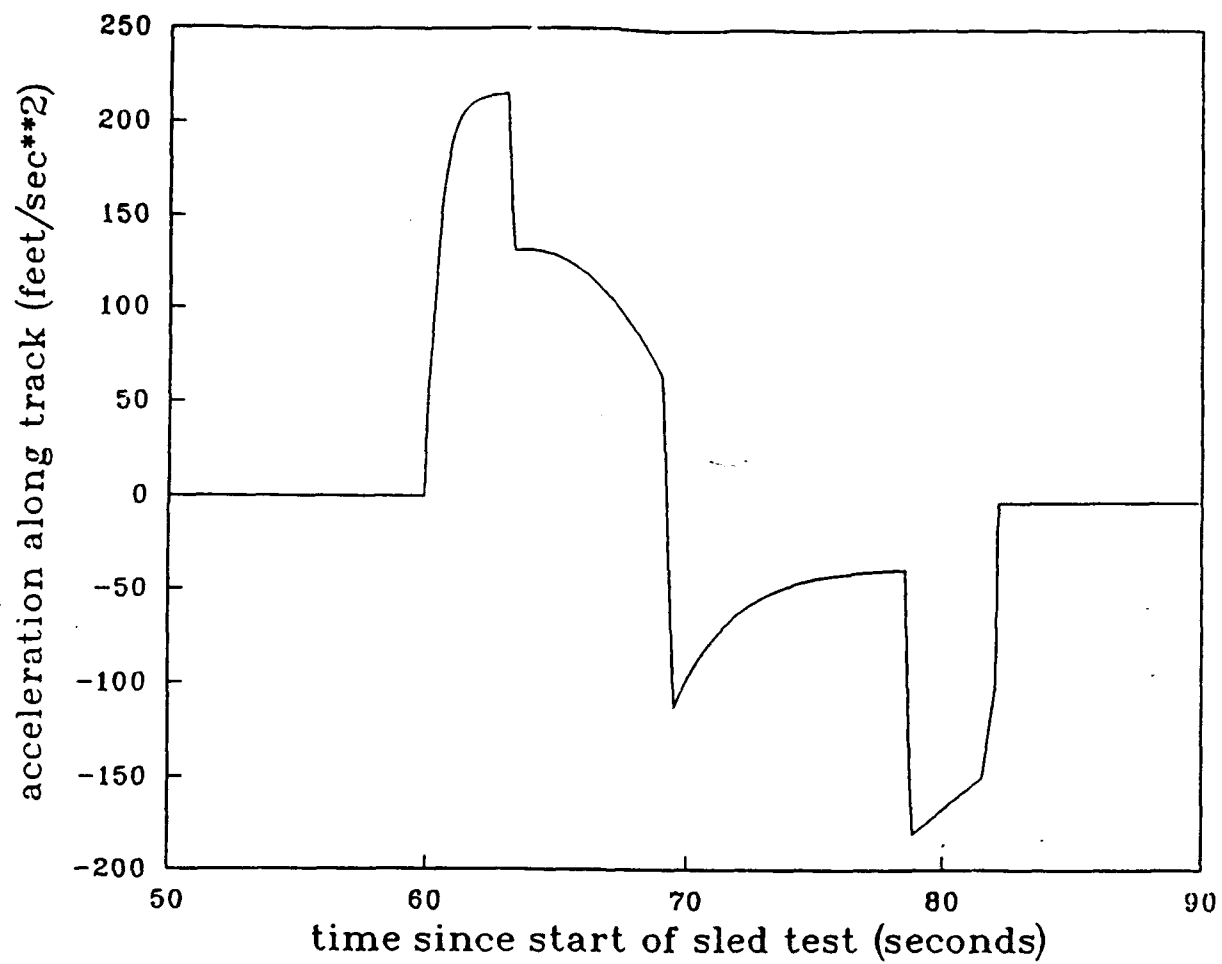


Figure 4 - Sled Test Acceleration Profile

**THIS PAGE LEFT BLANK INTENTIONALLY**

# **Minuteman III Guidance Computer**

**Expert System  
by**

**William H. Crigger  
&**

**Michael W. Murasky**

**AEROSPACE GUIDANCE & METROLOGY CENTER  
MISSILE AUTOMATIC TEST EQUIPMENT BRANCH**

**813 Irvingwick Drive W.**

**Newark AFB, OH**

**Unclassified**

## Table of Contents

<u>Title</u>	<u>Page</u>
Abstract	3
Requirements	4
Requirements Resolution	5
Fault Isolation Overlay Module	6
Diagnostic Overlay Module	7
Definitions of Terms	13

<u>Figures</u>	<u>Title</u>	<u>Page</u>
1	CTS EXPERT SYSTEM BLOCK DIAGRAM	9
2	FIM FAULT TREE, MM III MGC COMPUTER SYSTEMS TEST PROGRAM	10
3	FIM FAULT TREE, MM III MGC COMPUTER SYSTEMS TEST PROGRAM	11
4	DM, HIGH RESOLUTION GRAPHICS DISPLAY, MM III MGC EXPERT SYSTEM	12

## **Minuteman III Guidance Computer Expert System**

### **ABSTRACT**

Loss of expertise with respect to the Minuteman III guidance computer is a concern at Newark Air Force Base. The effect of this loss may be minimized by the development and installation of an expert system which captures the experience necessary to effectively troubleshoot, repair and test this complex missile guidance computer.

This paper will provide an overview of this expert system development and operation. Additionally, guidelines will be provided for the utilization of these techniques with respect to other workloads.

### **BACKGROUND**

Malfunction verification, fault isolation, and repair of a MM III MGC has been a manual operation. If an MGC failed during the execution of a program, the technician is required to utilize program description documents, program listing documents, knowledge of MM III MGC logic and general electronic fault isolation techniques to isolate the failure. The technician may occasionally be required to develop and load the failing MGC with a short program to stimulate suspected defective circuitry. Intermittent conditions present special requirements with respect to fault isolation techniques. Further difficulties are presented when the MGC fails during a vibration environment.

The MM III MGC is a very complex device. A learning curve of two years to reach a level of competence necessary to perform fault isolation and repair of faulty MM III MGCs is not unusual for new technicians.

The reliability of the MM III MGC is such that several years may elapse before one encounters a particular type of MM III MGC fault. Therefore, a technician new to the MM III MGC maintenance program may easily require many years to develop a broad experience base. This factor alone causes such an experienced MGC technician to be a valuable asset to the MM III MGC program. Downsizing, attrition, and other factors are causing an alarming loss of such expertise.

MM III MGC intermittent failures are not a frequent occurrence. However, when they do occur, such problems require careful analysis and response if repair costs are to be maintained at a reasonable level. Correlation of current and historical failure data may point to a failure cause or failure trend. This type of analysis may be accomplished only by experienced personnel.



MM III MGC asset management is becoming more of a concern with the passage of time. Premature aging of MM MGC components may be induced by excessive and improper handling. These factors provide justification for increased emphasis with respect to correct and accurate fault isolation techniques, problem diagnosis, and repair. Additional justification for increased emphasis in these areas is also motivated by decreasing quantities of available critical parts.

These and other factors make expert system technology a vital maintenance tool. Realization of these facts contributed to the decision to develop the expert system described in this paper.

## REQUIREMENTS

The CTS expert system must be dynamic in operation. It must function as an integral part of the CTSOSP. Product safety and environmental concerns do not permit a static, off-line design.

The CTS expert system therefore must be modular as depicted by figure 1.

A MM III MGC failure often is very sensitive to variations in temperature, supply voltage levels, vibration, environmental pressure, memory motor speed, and other less obvious factors. These constraints require the CTS expert system to maintain environmental integrity for purposes of failure mode preservation as well as product safety.

A MM III MGC converts a + 28 VDC supply output into twelve individually regulated DC voltage levels. Certain CTS test environments for the MM III MGC require specific levels of voltage variation from the normal supply levels. The CTS expert system must be capable of accurate, dynamic measurement of such supplies to assure that the CTS voltage variation levels have been established within defined limits.

These twelve voltage supplies may be varied at selected levels above or below the nominal value. This yields 4096 possible voltage combinations. The CTS expert system must be capable of selecting, verifying, and maintaining any of the 4096 possible combinations.

A TCU circulates coolant through the MGC coolant jacket to provide temperature control. MGC test environments establish three temperature bands in the range 41°F to 68°F. The MGC may exhibit a tendency to fail at certain temperatures and function properly at others. The CTS expert system must therefore be capable of maintaining a failing coolant temperature with an accuracy of  $\pm 1^\circ\text{F}$ .

Inserting specific fault isolation software into a failing MGC is a technique used often by knowledgeable technicians. This software is designed to stimulate selected sections of MGC logic in such a manner as to permit rapid and accurate fault isolation. The CTS expert system must be capable of inserting this type of software into the MGC when required, evaluating the software performance, and providing notification of software failures when such software fails to stimulate the required logic, or does so in an incorrect manner.

An observed failure may possibly be caused by one or more of any number of MGC faults. This variance is due to the different logic circuits being exercised at the point where the fault occurs. A fault class file is built for each identified failure group. Each group record must point to a different fault isolation approach to a given problem. This expert system must occasionally sort these fault class files to keep the expert system up-to-date with current failure trends.

Newark AFB has five CTSS. After having updated its fault class files the expert system must assure that the other CTSS are kept current with such developments. The expert system accomplishes this through a LAN. This permits automatic CTS software configuration management.

#### **REQUIREMENTS RESOLUTION**

Figure 1 provides a block diagram of the CTS expert system. The UUT program module is permanently resident in the CTS personal computer RAM whenever an MGC is being tested. This module provides software linkages to the various library procedures and functions utilized for normal CTS operation. The other modules are loaded as overlays when needed.

The CTS operator causes The ESM overlay to be loaded into the personal computer RAM whenever MGC fault isolation is required. This is accomplished by a single personal computer keystroke. The ESM performs an initial environment screen. The primary intent is to provide assurance that the MGC is actually failing, and that a knowledge base is available for the failure.

The twelve MGC secondary power supplies are screened to assure that initialization requirements for the current test have been met. This screen may involve nothing more than a test of the level of each supply if the current test requires them to be set to their nominal values. If the secondary supplies are required to be varied from nominal, then an additional check is done to assure that the CTS operator performed the required initialization correctly. If the current MGC program was automatically varying the twelve supplies through the possible 4096 voltage settings, then the current setting is logically locked by the ESM to assure that the MGC secondary

supply environment is intact throughout the fault isolation procedure. MGC program execution failures may be induced if certain supply limits are not strictly observed. These kinds of induced failures are flagged to the CTS operator.

The MGC temperature is noted and locked by the ESM to the failing temperature  $\pm 1^{\circ}\text{F}$ . This assures that a temperature sensitive failure will not be lost during the fault isolation process through MGC temperature variation.

#### **FAULT ISOLATION OVERLAY MODULE**

The ESM now loads the appropriate FIM overlay. The FIM overlays are developed to respond to particular types of MMIII MGC failures. a partial list of these FIMs would perform fault isolation on such types of problems as MGC power supply, synchronization, mode control, program load, analog to digital conversion, digital to analog conversion, or memory preservation during 28 VDC primary power cycling for example.

The major emphasis at this time is development of the FIM being designed for an MGC program used during random vibration testing, as well as functional sell-off (CSP). This particular MGC program has approximately 750 failure points, and 4,500 contributing causes. The MGC program is not a structured program. That is, it does not begin testing the simple MGC functions and move to the more complex. Rather, it is totally unstructured. It was designed to execute a maximum number of MGC instructions in a minimum amount of time. A learning curve of two or three years with respect to fault isolation of MGC failures with respect to the CSP is not unusual. Manual fault isolation of MGC/CSP failures often requires several hours to accomplish. The ESM & FIM overlays capture this experience and provide rapid failure point and failure class identification in milliseconds. The experience built into these software modules represents approximately fifty-five man-years of experience.

The FIM provides a dynamic interface to the MGC. This dynamic interface is a vital component of this expert system. The MGC undergoing fault isolation testing may well be failing only in a random vibration environment. The MGC will cease failing when the vibration is removed.

During such times the FIM may be required to verify the value of a particular MGC memory location. The FIM will examine a selected memory location several times, requiring that all such memory location samples be equal. A variance in value may indicate a memory channel which is sensitive to vibration, voltage variation, or temperature. The FIM will have found the problem in this case.

Figure 2 illustrates the initial portion of the fault tree for the CSP. The fault path is isolated in approximately 100 milliseconds. The FIM fault tree search at this level is accomplished by dynamic analysis of MGC memory data. That is, the MGC fault environment is preserved, thereby allowing the FIM to perform the same examination which would be accomplished by a skilled technician. The FIM, however, accomplishes these examinations with the speed of the personal computer, and the wisdom of fifty-five man-years of experience.

The FIM requires ten successive MGC memory read operations of a single location to be equal, in order for the MGC memory circuitry to be considered valid. This is due in part to the MGC memory design, and also to MGC memory failure characteristics. The MGC memory data is stored on a rotating magnetic disk. Approximately ten milliseconds are required for one such disk revolution. Many MGC memory channels contain 128 data words, and occupy one track on the disk. This means that the FIM requires ten milliseconds between MGC memory read operations from such channels. Ten such MGC memory read operations require approximately 100 milliseconds.

Figure 3 illustrates the next fault isolation iteration. The values are actual valid MGC memory values when a failure occurs in the ST/14 branch. The MGC instruction register is examined for one of these valid failures. Should a non-valid S/T 14 failure be indicated, then the fault is known to be due to an MGC program execution error. A different fault isolation branch is taken in this event.

The FIM now performs a series of MGC dynamic memory inspections, comparing the actual values to predicted values. The differences between the actual and predicted memory values define a unique fault class. The analytical techniques used to arrive at the correct fault class represent the capture of approximately fifty-five man-years of MM III MGC experience.

#### DIAGNOSTIC OVERLAY MODULE

Fault isolation control is now passed to the DM (ref. figure 3). The DM utilizes special MGC software to provide stimuli to the failing MGC logic. Figure 4 provides a typical operator prompt. Note that instructions are provided with respect to the MGC module affected, where to look, and what one would expect to see. These are standard techniques developed using the fifty-five man-years of experience with the MM III MGC. Decisions are made by the expert system based on CTS operator observation. The expert system isolates the failure to perhaps one to three components in most cases.

The failure data, and fault isolation results are then provided to the CTS network file server, which archives this data for future

reference. A data base is being built which contains records of MGC module replacement and repair activity. This data is used to keep the expert system on each station up-to-date with respect to component replacement activity.

It is expected that future analysis of this data will yield an abundant harvest of valuable information with respect to the MM III MGC.

# COMPUTER TEST STATION (CTS)

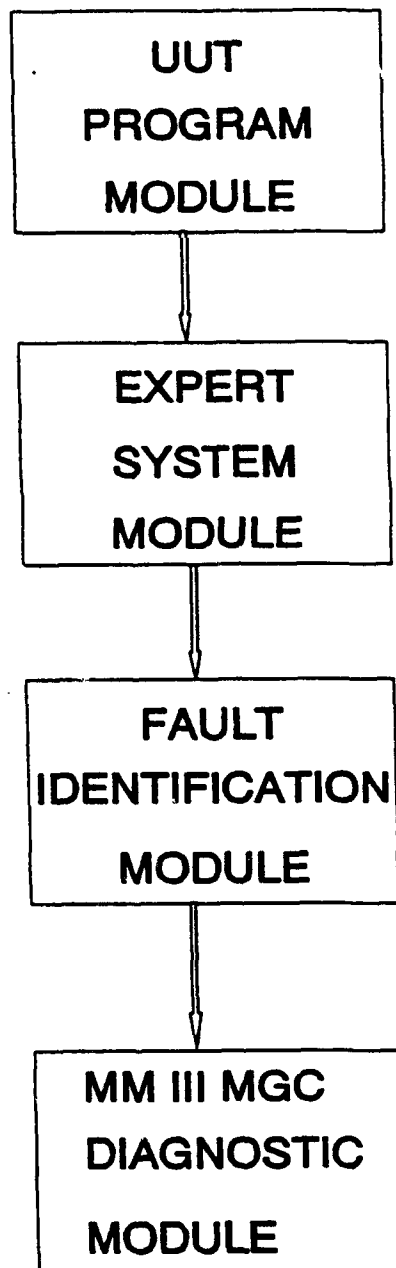


FIGURE 1, CTS EXPERT SYSTEM BLOCK DIAGRAM

# FIM FAULT TREE, MM III MGC COMPUTER SYSTEMS TEST PROGRAM

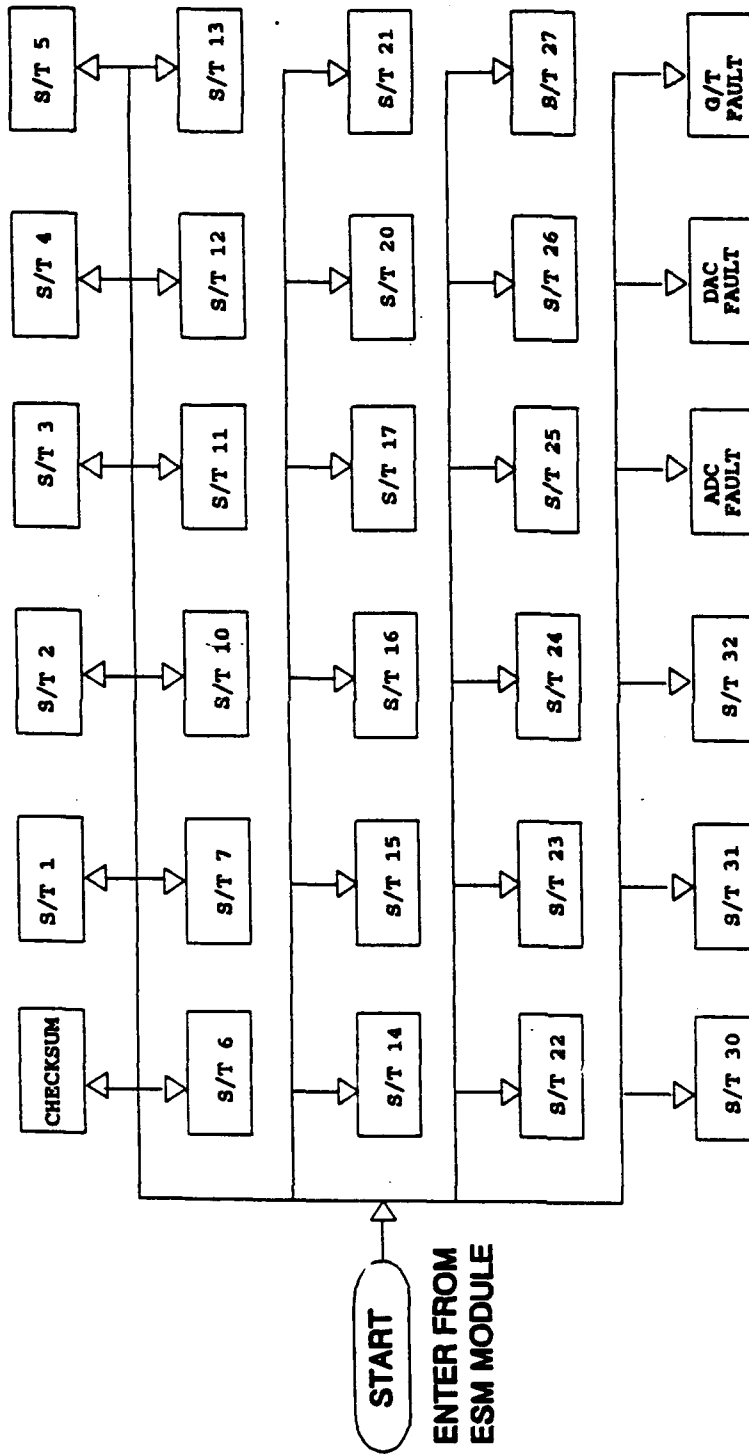


Figure 2, CTS EXPERT SYSTEM

# FIM FAULT TREE, MM III MGC COMPUTER SYSTEMS TEST

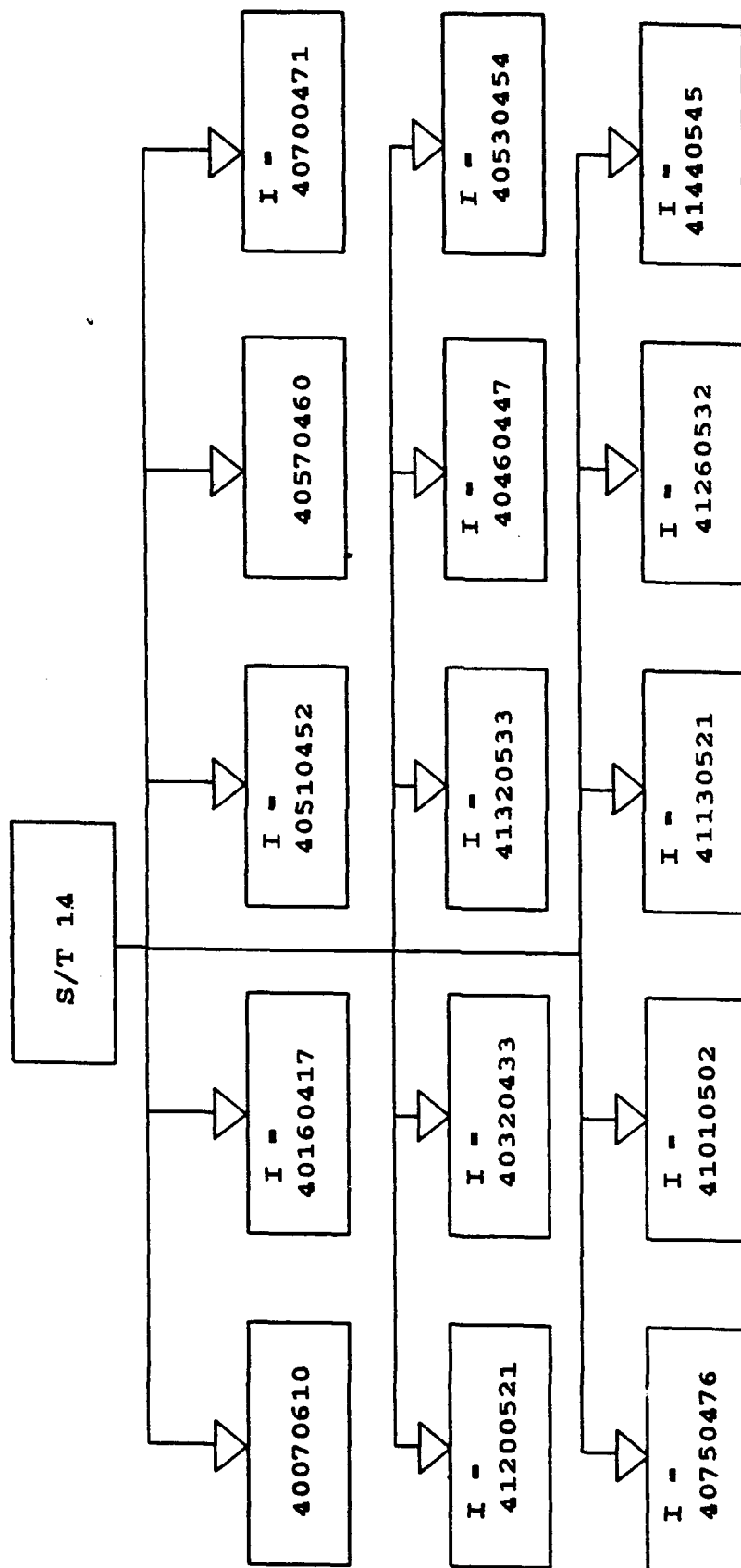


FIGURE 3



# DM, HIGH RESOLUTION GRAPHICS DISPLAY, MM III MGC EXPERT SYSTEM

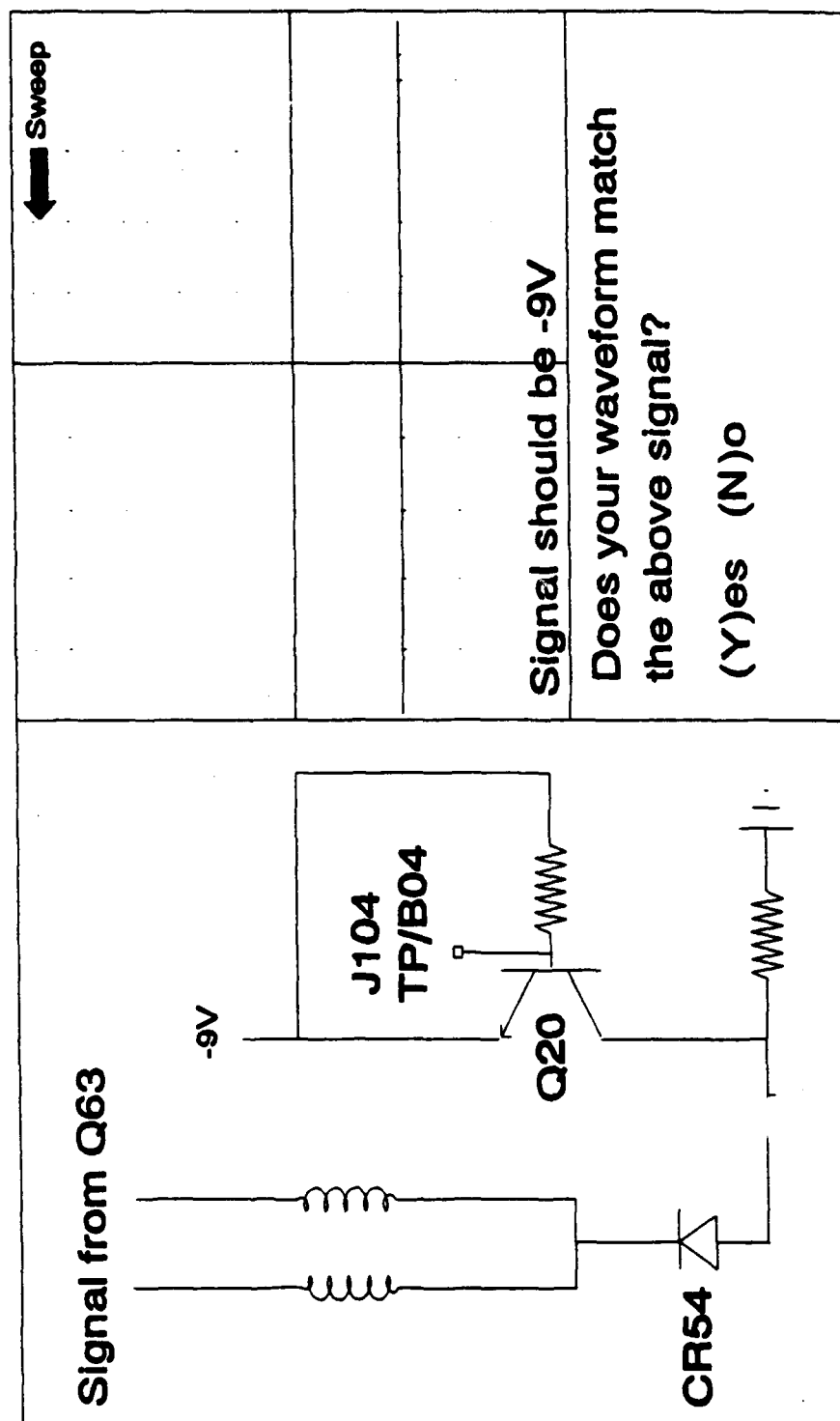


FIGURE 4

## Definitions of Terms

Term	Definition
CTS	Minuteman II & Minuteman III Missile Guidance Computer Test Station
CSP	Minuteman III MGC Computer Systems Test Program
CTSOSP	Computer Test Station Operating System Program
DC	Direct Current
DM	Expert System Diagnostic Module
ESM	Expert System Module
FIM	Expert System Fault Isolation Module
LAN	Local Area Network
MGC	Missile Guidance Computer
MM III	Minuteman III Missile Guidance Computer
RAM	Random Access Memory
TCU	Temperature Control Unit VDC Volts Direct Current

Author: William Crigger  
Commercial: (614) 522-8068  
(DSN): 346-8068  
FAX: (614) 522-7991

Mailing Address: William H. Crigger  
AGMC/MAEL(2)  
813 Irvingwick Drive W.

**SESSION II-B**  
**INTEGRATED GPS**

***CHAIRMAN***  
**Lt Col DAVE EIDSAUNE**  
***LOS ANGELES AFB CA***

**THIS PAGE LEFT BLANK INTENTIONALLY**

---

# **Embedded GPS/INS — The Advantage**

---

by

**Gary W. Linn**  
Project Staff Engineer - Navigation  
Products Engineering  
Honeywell Military Avionics Division

**Mikel M. Miller**  
Captain, USAF - Education With  
Industry Student  
Honeywell Military Avionics Division

**Lawrence C. Vallot**  
Research Staff Scientist  
Honeywell Systems and Research Center

Approved for public release; distribution is unlimited.

# **Embedded GPS/INS — The Advantage**

by

**Gary W. Linn**  
Project Staff Engineer - Navigation Products  
Engineering  
Honeywell Military Avionics Division

**Mikel M. Miller**  
Captain, USAF - Education With Industry  
Student  
Honeywell Military Avionics Division

**Lawrence C. Vallot**  
Research Staff Scientist  
Honeywell Systems and Research Center

## **I. ABSTRACT**

Mankind's ability to determine where they are—especially in relation to where they want to be—has been of interest since time began. Whoever could "navigate" the best had a distinct advantage in a competitive (peace or conflict) environment. The stars, the sextant, the compass, and "experience" have all played major roles in this ancient problem. Within the past several decades, advances in navigation technology have played a significant role in reducing the magnitude of this problem. Major advances started with the development of Inertial Navigation Systems (INSs) and radio navigation systems (most recently the Global Positioning System (GPS)). These systems have played a major role in land, sea, air, and space navigation. However, individual system error sources preclude "perfect navigation." An INS will provide accurate short-term information but degrades over time due to uncompensated sensor errors and/or mechanical misalignments. The GPS provides an accurate navigation solution; however, aircraft dynamics, antenna shading, and jamming cause noisy measurements and can prevent reception of the GPS navigation signal.

The solution is obvious and has been well documented—integrate the two systems. This paper goes a step further and discusses the advantages of embedding a GPS receiver into an INS. The advantages are numerous and include technical, performance, operational, and cost benefits. This paper will discuss various "integration" options and Honeywell's approach for their tightly-coupled embedded H-764G GPS/INS. The H-764G blends raw INS and GPS pseudo-range and delta-range data into a single Kalman Filter. A brief discussion is also presented concerning Differential GPS (DGPS) implementations and potential applications using a tightly coupled embedded DGPS/INS.

## **II. INTRODUCTION**

There are many factors which would influence a decision "to embed" or "not to embed" a Global Positioning System (GPS) receiver within the Inertial Navigation System (INS). A number of papers, prepared by both Government<sup>1,2</sup> and industry sources<sup>3,4</sup>, have discussed advantages and rationale for selection of the embedded GPS/INS configuration and use of pseudo-range and delta-range satellite data. Some of the more important benefits derived from embedding are summarized in Table 1 and will be discussed in this paper. These benefits are available in the Honeywell H-764G GPS/INS shown in Figure 1. The relative importance of any one item over another is obviously dependent upon the results of trade studies accomplished on the particular mission and host vehicle application under consideration. We will conclude with a brief discussion of potential applications for an embedded DGPS/INS system.

Table 1. Embedded Benefits.

- More accurate navigation solution
- No cascading of Kalman filters or positive feedback loops
- Error bounding with fewer than four satellites in view
- Improved resistance to jamming
- Faster reacquisition after jamming
- Less costly antenna installation
- Smaller size and weight
- Security Consideration: No requirement to provide a secure data bus for transmission of pseudo-range and delta-range data
- Data time-tagging, data transmission rates, not critical
- Retrofitting less costly: Physically simpler
- Retrofitting less costly: Less impact to mission computer
- Usable on multiple aircraft/vehicle types without development of a unique Kalman filter for each
- Changes to GPS/INS after fielding less likely to impact mission computer software
- Improved reliability and reduced Life Cycle Cost (LCC) due to use of fewer Line Replaceable Units (LRUs), components
- Additional retrofitting options due to small size

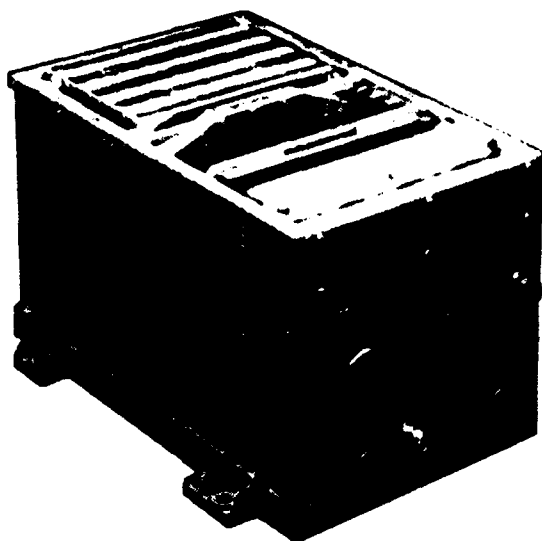
### III. DISCUSSION OF EMBEDDED VS. STAND ALONE

This section discusses two options for integrating GPS with inertially based navigation systems. First, a discussion on the multiple line replaceable unit (LRU) configuration using a separate INS and a separate GPS receiver is presented. This is followed by a description of the embedded GPS/INS configuration.

#### **Separate INS and Separate GPS Configurations**

There are significant architectural differences between an installation using an INS with embedded GPS and one using a separate INS and separate GPS receiver. Figure 2 shows a typical installation where a separate INS and separate GPS receiver LRU is used. Position and velocity (PV) data from each LRU is sent to the mission computer via the 1553B multiplex data bus. The PV data from these two sources is integrated in a Kalman filter typically implemented within the mission computer and results in an "aided" (blended) navigation solution. The





Blended GPS/INS Performance	
Position Accuracy	< 16 m SEP
Velocity	< 0.03 m/s

Form Factor	7 x 7 x 11 inches
Weight	≈ 17 pounds *
Power	≈ 40 watts *

\* These parameters will vary from application to application depending on the configuration of the four expansion slots.

Figure 1. Honeywell's H-764G Embedded GPS/INS

blended solution is more accurate than the navigation solution derived from a typical stand alone INS aided with standard sensors such as an Air Data Computer. This is true as long as valid GPS data is available for the mission computer Kalman filter.

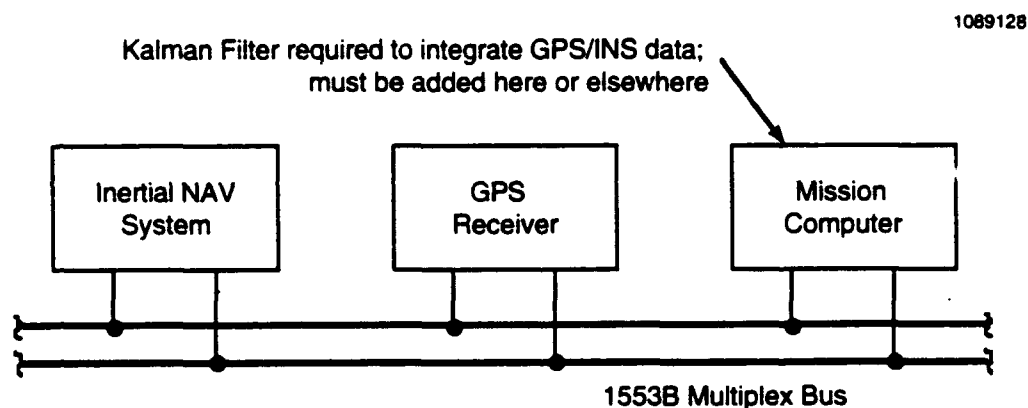


Figure 2. Separate INS and Separate GPS Receiver

The configuration shown in Figure 3 is commonly referred to as a "closely coupled" system. Figure 3 shows the interconnection and data flow typical of a closely coupled installation. Note that there are three Kalman filters, one in each LRU. Development of the aided navigation solution in the multiple LRU configuration requires very careful time-synchronized data processing by these three Kalman filters to prevent corruption of the navigation solution.

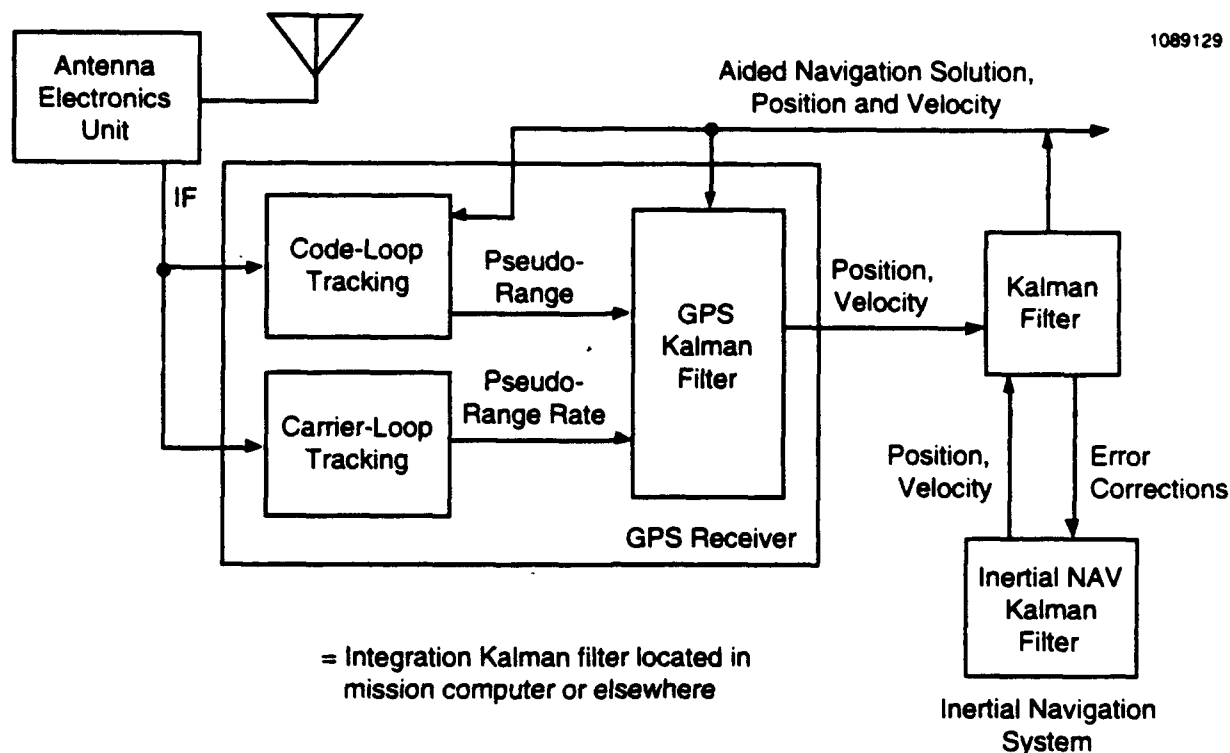


Figure 3. Closely Coupled Multiple LRU Configuration

In addition to bounding output errors, the mission computer Kalman filter may feed aided velocity data back to the GPS receiver to assist in satellite tracking. Tracking loop aiding becomes important during vehicle dynamics and during satellite reacquisition after jamming. Figure 3 shows velocity aiding of the GPS "code tracking" loop.

A major limitation of the separate INS and separate GPS receiver configuration is that GPS receiver output data cannot be used to bound INS errors when fewer than four satellites are in view. In fact, when fewer than four satellites are in view, useful GPS data is generally unavailable. This is a major concern when approaching targets where there is an increased likelihood of jamming.

### INS With Embedded GPS Configuration

Figure 4 shows an INS with embedded GPS configuration. In this configuration, there is only one Kalman filter which is embedded within the GPS/INS. For this configuration, satellite pseudo-range and delta-range data (raw measurement data) is used to bound INS errors. This is to be contrasted with the approach used in the multiple LRU configuration shown in Figure 2, where position and velocity data from the GPS Kalman filter are used by the mission computer Kalman filter to bound INS errors.

The embedded configuration shown in Figure 4 is inherently simpler than the multiple LRU configuration shown in Figure 2 since it requires fewer LRUs and less data communication between LRUs. In the embedded configuration, all navigation solution data processing is performed within the single GPS/INS LRU. The mission computer is only involved with GPS/INS moding and Input/Output (I/O), neither of which usually require careful time synchronization.

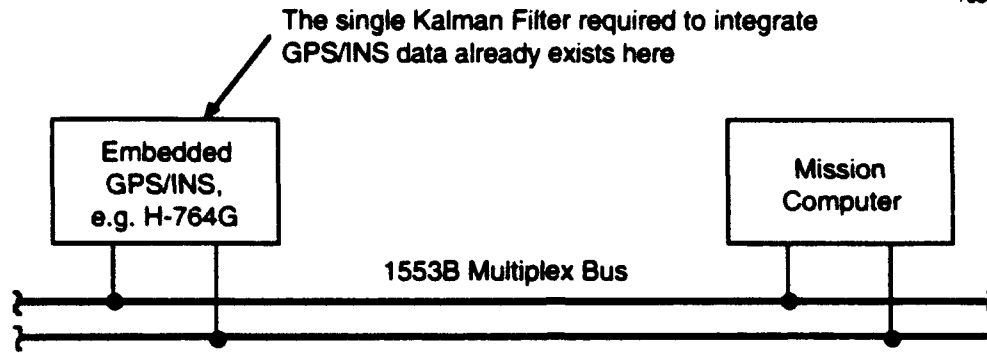


Figure 4. GPS Receiver Embedded in the INS

The embedded configuration shown in Figure 4 is referred to as "tightly coupled." Figure 5 shows the interconnection and data flow typical of a tightly coupled installation.

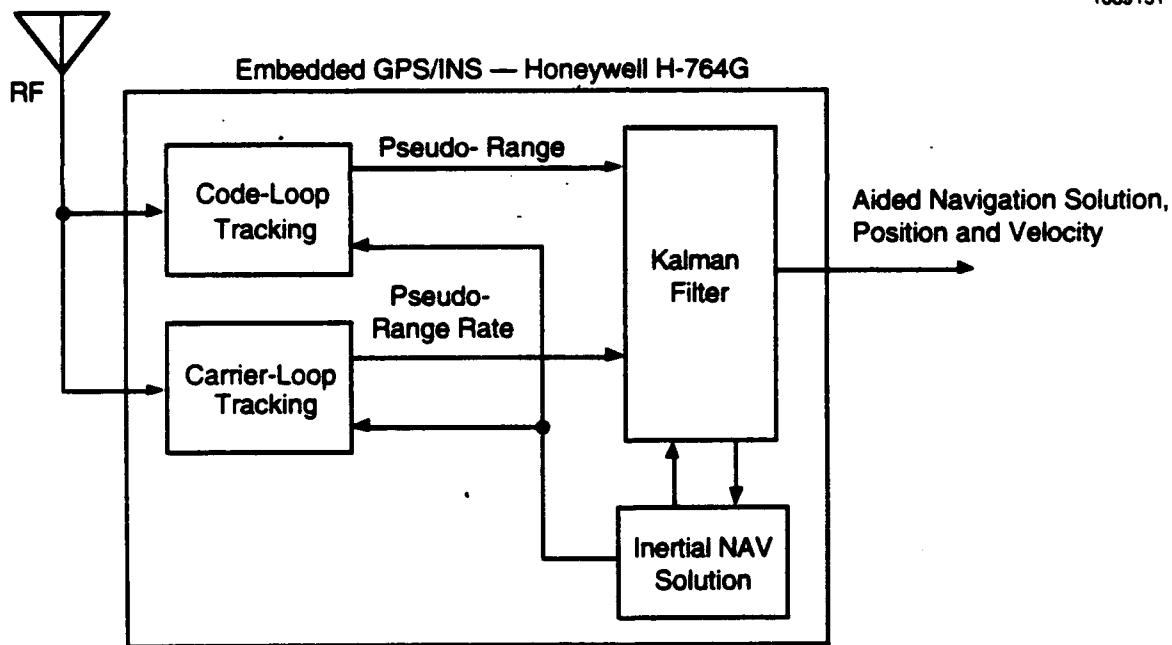


Figure 5. Tightly Coupled INS With Embedded GPS Configuration

Note that in this configuration both the code and carrier tracking loops are aided. Aiding the carrier tracking loop results in a higher resistance to jamming and reduced satellite tracking loss due to high vehicle dynamics. Although it is possible to aid the carrier tracking loop in the multiple LRU configuration, it is more difficult due to timing and data latency problems.

## **IV. BENEFITS**

### **More Accurate Navigation Solution Using Embedded GPS/INS**

Direct use of satellite pseudo-range and delta-range data can result in a more accurate navigation output solution. As shown in Figures 3 and 5, both configurations use pseudo-range and delta-range data but not in the same way. In the multiple LRU configuration, pseudo-range and delta-range data are used by the GPS-resident Kalman filter to generate the position and velocity data sent to the mission computer Kalman filter. The GPS Kalman filter therefore "pre-filters" or removes information from the raw satellite data needed by the mission computer Kalman filter to properly model GPS errors. This then results in a less accurate navigation solution than can be obtained by an INS with an embedded GPS configuration. Since there is only one Kalman filter in the INS with embedded GPS configuration, there is no "double" filtering and therefore improved output accuracy.

Use of pseudo-range and delta-range results in a more accurate and robust navigation solution<sup>3</sup>. Security regulations, however, prevent transmission of pseudo-range and delta-range between a stand-alone GPS receiver and other LRUs (see Section VI, Security Considerations).

### **Data Time-Tagging And Data Transmission Rates**

If pseudo-range and delta-range data could be transmitted from the stand-alone GPS receiver to the mission computer, the accuracy benefits described for the embedded system could theoretically be achieved. However, this would require very careful handling and time-tagging of the data transferred from the INS and GPS which are operating asynchronously with each other. That is, in order to accurately combine the separate INS and GPS data in the mission computer Kalman filter, it is necessary to know the point in time when each sample was valid. The uncertainty and jitter of the time-tagging process in the multiple LRU implementation greatly degrades system performance during high dynamic conditions. This is not a concern in embedded GPS/INS system because synchronization of internal hardware and software processes can be forced by slaving inertial navigation data processing and Kalman filter operation to the GPS receiver clock. Another option is to have a one oscillator for the entire GPS/INS system.

### **Kalman Filter Benefits**

*No Cascading Of Kalman Filters Or Positive Feedback Loops.* When delta-range data is not available in the stand-alone GPS receiver due to jamming, shading, or fewer than four satellites being viewed, GPS receiver velocity output data can become heavily correlated with (look very much like) the velocity data fed to it from the mission computer Kalman filter. This can result in an undesirable positive feedback situation which, worst case, can result in a totally divergent mission computer Kalman filter solution and unusable output data<sup>5</sup>. To prevent positive feedback from occurring, the GPS receiver data is either not used, or the rate that the data is used in the mission computer Kalman filter is reduced. In the embedded configuration there can be no positive feedback and GPS data can be used by the single embedded Kalman filter as often as it is available.

*Applicability For Other Platforms.* In general, the Kalman filter design for a multiple LRU configuration will be unique for each aircraft/vehicle installation and will require extensive flight testing at a very precisely instrumented test range to ensure proper operation. Because operation of the Kalman filter in the INS with embedded GPS will have already been verified by system manufacturers and other users, extensive flight testing will not be required and overall aircraft/vehicle integration costs should be much less. Therefore, use of the INS with embedded

GPS approach on multiple aircraft/vehicle types will be greatly simplified because it will not be necessary to develop a unique Kalman filter for each aircraft/vehicle.

*Changes To Fielded Equipment* After fielding, any performance enhancement changes to either the stand-alone INS or the stand-alone GPS receiver will likely necessitate changes to the mission computer Kalman filter design as well. Such changes will expose the entire mission computer flight software to some amount of risk and require recertification of this software as well. Updating of the INS with embedded GPS for performance enhancements will not necessarily require updating of mission computer software since any Kalman filter changes will be accommodated within the embedded system.

### **Error Bounding With Fewer Than Four Satellites In View**

"Aiding" of an inertial navigation output solution is the bounding (restriction) of the position and velocity output errors inherent in any INS. These errors are due to uncompensated sensor errors and/or mechanical misalignments which may exhibit a bounded error characteristic or grow slowly without limit. Obviously, one way to limit inertial system errors is to specify a higher precision system — a costly approach.

Output errors can be bounded by using GPS data (or data from another source) as a reference and integrating the reference data with INS output data in a Kalman filter. During aiding, it is also possible to determine what the uncompensated INS errors are and then compensate for them either in the mission computer Kalman filter or in the INS. It would be nice if INS output errors remained low after compensation since this would eliminate the requirement for continual compensation. However, in the real world this is not possible because some INS error sources are dynamic, i.e., they change their value with time, temperature, or some other variable. Additionally, compensation values are calculated using a model of the INS. Models are only approximations and will never be able to perfectly predict INS performance. Continual compensation is required to minimize INS error growth. When the compensation process ceases, INS output errors will begin to grow.

In the multiple LRU configuration there can be no compensation when fewer than four satellites are in view since useful GPS position and velocity data will be unavailable. Due to the use of pseudo-range and delta-range in the INS with embedded GPS configuration, some compensation will continue as long as there is at least one satellite in view<sup>6</sup> since Line-of-sight (LOS) data from each satellite is processed as an independent observable in the navigation Kalman Filter.

### **Improved Resistance To Jamming**

Resistance to jamming may be defined as the ability to track satellites in the presence of jamming signals. As previously noted, tracking ability, and therefore jamming resistance, is improved by aiding the carrier loop in the embedded configuration with data fed back from the embedded Kalman filter. Carrier loop tracking also helps in satellite reacquisition if tracking lock is lost<sup>6</sup>.

The effect of a higher jamming resistance is the bounding of INS errors for a longer period of time in an increasing jamming environment. Figures 6 and 8 illustrate resistance to jamming for four different system configurations. In Figure 6, an aircraft is flying toward a target located at the left side of the plot with a 2,000 watt broad band noise jamming source located at the target. For simplicity, and also as a worst case, it is assumed that the earth is "bald" and that the aircraft is "transparent." With these assumptions, the GPS receiver feels the full effect of the jammer without benefit of terrain or aircraft structure blockage. The curved line in Figure 6 shows the jamming to signal ratio (db) which increases as the target is approached.

The following four system configurations are considered in Figure 6:

- Stand-alone GPS receiver and stand-alone INS with a Fixed Reception Pattern Antenna (FRPA)
- INS with embedded GPS with a FRPA
- Stand-alone GPS receiver and stand-alone INS with a Controlled Reception Pattern Antenna (CRPA)
- INS with embedded GPS with a CRPA

Figure 6 shows that the multiple LRU configuration with an FRPA will be jammed out at about 190 km (12 minutes @ mach 0.8) from the target. The embedded configuration with an FRPA will not be jammed out until the aircraft has penetrated to within approximately 95 km (6 minutes @ mach 0.8) from the target. This is a significant increase in jamming resistance achieved through use of the INS with embedded GPS configuration.

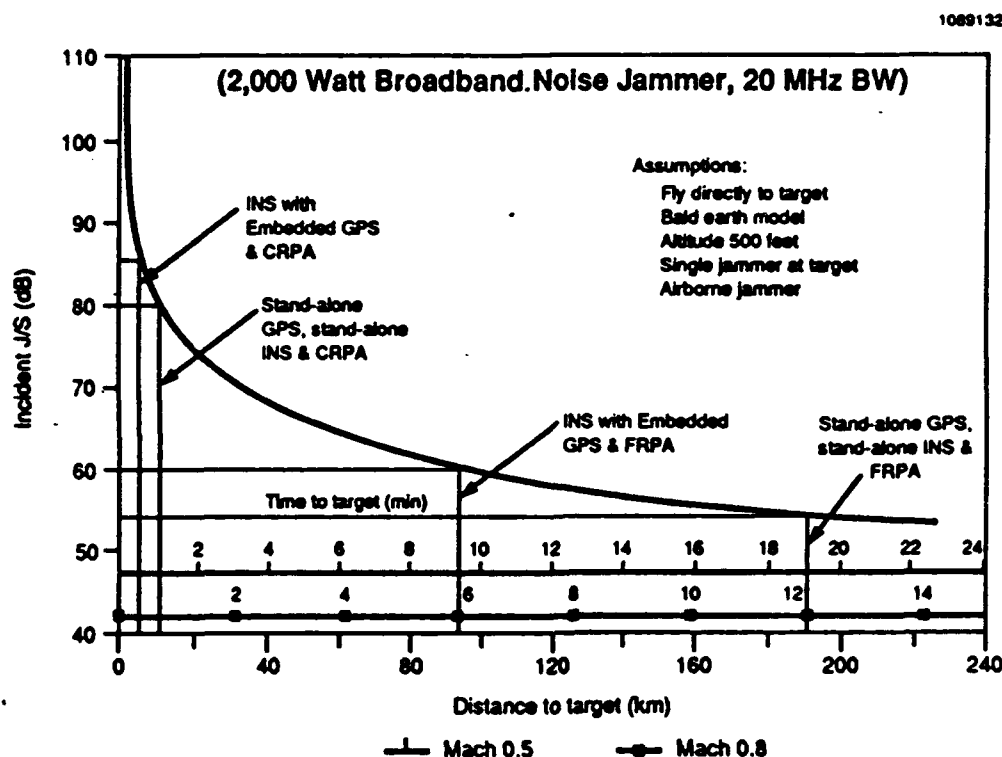


Figure 6. Jamming Resistance

The final two configurations shown in Figure 6 show the effect of replacing the FRPA with a CRPA resulting in still higher jamming resistance. Use of a CRPA would be preferred if the only consideration were jamming resistance. However, two significant trade-offs, size and cost, may be made between an FRPA and a CRPA installation. CRPA installations are larger and cost several times more than an FRPA installation. Depending upon mission requirements, and the user must obviously determine these requirements, the increased jamming resistance of an INS with embedded GPS system when used with an FRPA may meet navigation performance requirements when exposed to jamming. If the INS with embedded GPS configuration and an FRPA were used, there would also be a significant reduction in hardware requirements as illustrated in Figure 7.

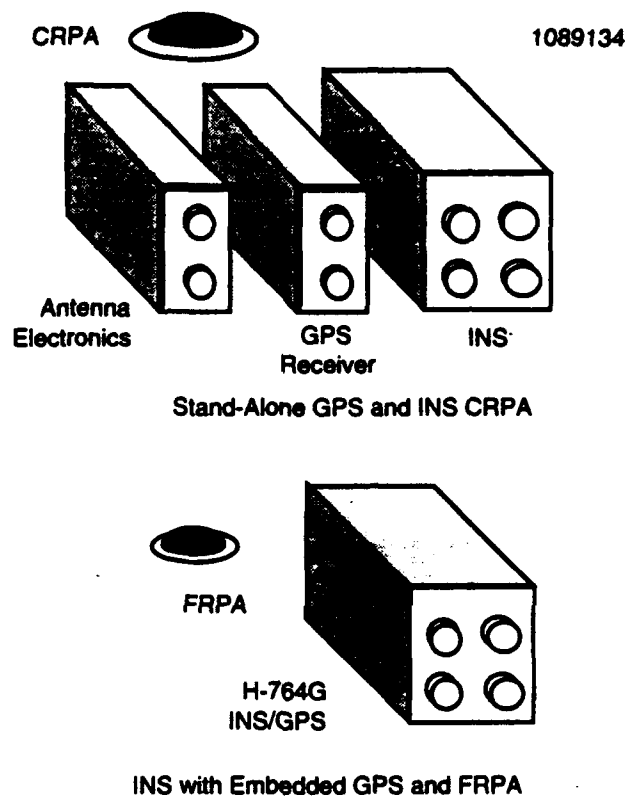


Figure 7. Antenna Configuration

To illustrate how performance is related to jamming resistance, Figure 8 shows position error growth when the GPS receiver is completely jammed out for the jamming scenario assumed for Figure 6. In Figure 8, it is assumed that, prior to being jammed completely out, GPS data had been available for a period long enough to trim the INS to the best extent possible. The INS, either stand-alone or embedded, is assumed to be a medium accuracy, 1 nmi/hr (Circular Error Probable (CEP)) INS.

When the multiple LRU configuration is used with an FRPA, position error will be over 400 feet by the time the target is reached. When the INS with embedded GPS configuration is used with an FRPA, the position error at the target will be approximately 175 feet. There is a significant difference in error growth between the embedded and multiple LRU configurations when both configurations are used with an FRPA.

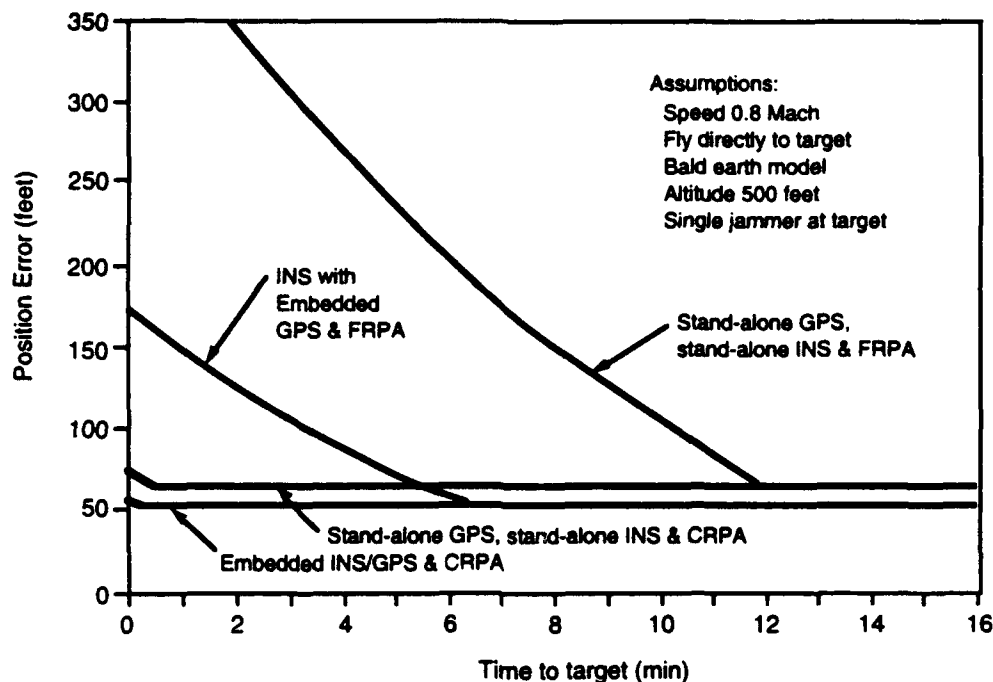


Figure 8. Jamming Performance

### Retrofitting Less Costly

**Physically Simpler.** Replacement of the existing INS with an embedded GPS/INS system may significantly reduce the cost of physically modifying the aircraft/vehicle. The small size of the GPS/INS may allow fitting it completely within the envelope of the INS it replaces. Conversely, use of the multiple LRU configuration, depending upon jamming requirements, requires that physical space be found for two additional LRUs, a GPS Receiver and the Antenna Electronics Unit, as well as for a CRPA which is much larger than an FRPA. Additionally, the antenna electrical interface for an INS with embedded GPS - FRPA installation will be simpler since only a single Radio Frequency (RF) antenna line is required to interface the GPS/INS with the FRPA. If the distance between the FRPA and the GPS/INS is long and a preamplifier is required, power for the preamplifier can be provided by the GPS/INS via the single RF line. The Antenna Electronics Unit, used with a CRPA installation, requires three coax lines plus two power lines, a significant weight penalty in wiring alone. Wiring comparisons are shown in Figure 9.

**Less Impact to Mission Computer.** Development of the mission computer Kalman filter required for the multiple LRU configuration shown in Figure 2 can be quite costly from an integration point of view and is often accompanied by significant technical challenges imposed by existing aircraft constraints.

Since the INS with embedded GPS configuration shown in Figure 4 has the Kalman filter necessary for INS and GPS integration embedded within a single LRU, initial aircraft integration costs are reduced. Mission computer software changes will be necessary for I/O changes, but these changes should be much less extensive (and less expensive) than development of a Kalman filter in mission computer software.



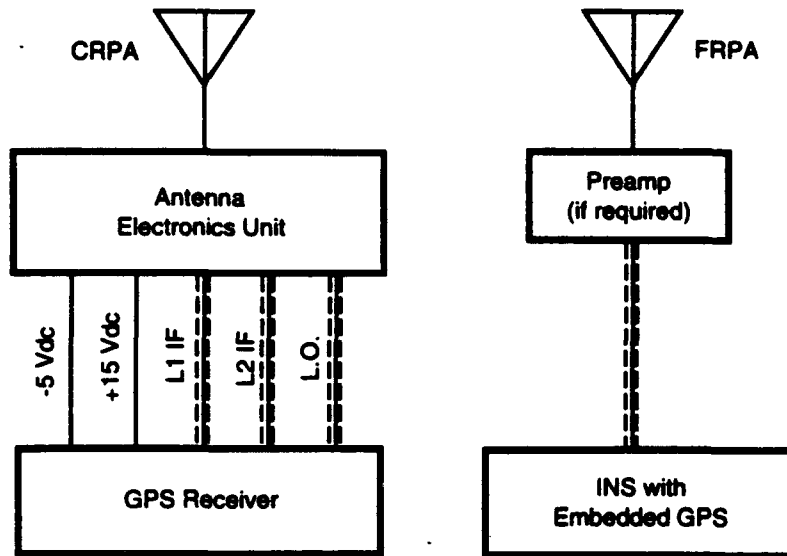


Figure 9. GPS Receiver to Antenna Wiring Comparison

**Kalman Filter Processing Requirements.** In older aircraft/vehicles, there may not be sufficient mission computer memory and/or spare computer processing time to implement the required Kalman filter within the mission computer.

**Data Bus Rate, Duty Cycle, and Time-Tagging of Data.** When considering the multiple LRU architecture, 1553B multiplex bus duty cycle considerations may impose constraints on the amount of data which can be passed and maximum data transfer rates. Perhaps the most difficult part of the required Kalman filter design is to account for the lack of time synchronization between the individual INS and GPS systems.

**Additional Retrofitting Options** The small size of an INS with embedded GPS provides the integrator with more options when retrofitting:

- Instead of replacing the existing INS with an INS with embedded GPS system, the existing INS could be retained and the Attitude Heading Reference System (AHRS), if used, replaced. This would provide a backup inertial navigation capability.
- If a dual INS system with an AHRS is being updated, the two INSs could be replaced with two higher reliability INS with embedded GPS systems and the AHRS could be deleted.

### **Hover Mode Drift Accuracy Improvement Using INS With Embedded GPS**

Helicopters require a unique mode of flight, the Hover mode, which automatically maintains helicopter position relative to a desired point. An integrated GPS/INS system can produce the extremely low output drift required for this mode. An integration scheme using delta-range has been shown to result in half the hover drift and significantly higher mission effectiveness in a target handover operation<sup>3</sup>. Because the INS with embedded GPS configuration continues to bound errors as long as at least one satellite is in view, Hover mode drift will remain lower than possible with the multiple LRU configuration as the number of satellites in view decreases. As

previously noted, there is no usable navigation output data from the stand-alone GPS receiver when fewer than four satellites are in view.

This Hover mode capability, coupled with the small size and weight of an INS with embedded GPS, such as the H-764G, suggests the use of an INS with embedded GPS for helicopter applications. The H-764G INS with embedded GPS system is an excellent, non-emitting replacement for the lower reliability Doppler inertial systems typically used for helicopter navigation.

#### **Suspending Constellation Changing During Hovering, Weapon Initialization**

During helicopter hovering and weapon initialization, it is desirable to not have "steps" in navigation output data. Steps can be caused by changes in the constellation of satellites being tracked or by receipt of new almanac data. The Honeywell H-764G INS with embedded GPS system may be commanded to a "hover hold" or "attack" mode that prohibits constellation changing and downloading of new almanac data. Satellites that can no longer be tracked are dropped from the constellation without replacement.

Additionally, the H-764G will accept commands to select or deselect any visible satellite. This would allow user specification of the same constellation for all aircraft/vehicles in the area.

#### **Size, Weight, And Reliability**

For applications where weight is extremely critical, including helicopter and carrier-launched vehicle applications, the small size and weight of available INS with embedded GPS systems may cause size and weight to be one of the most important trade-offs. The following two tables show size and weight for both the INS with embedded GPS configuration and a Standard Navigation Unit (SNU) 84-1 INS-based, multiple LRU configuration. Not included is the weight of cabling between the antenna or antenna electronics unit and the GPS receiver. As discussed in Section IV, the CRPA installation requires five signal lines, three coax and two power, compared to just one coax line for an FRPA installation. Depending upon length of run, cabling weight could be very significant in a CRPA installation.

Table 2. Embedded Configuration.

Embedded Configuration			
LRU	Size (inches) H x W x L	Weight	Notes
INS	7 x 7. x 11	17 pounds	H-764G GPS/INS
FRPA	5 (dia) x 1.5	0.5 pound	FRPA *
	<b>TOTAL:</b>	17.5 pounds	

Table 3. Multiple LRU Configuration

Multiple LRU Configuration			
LRU	Size (inches) H x W x L	Weight	Notes
INS	7.6 x 7.9 x 18.1	48 pounds	SNU 84-1 RLG INS
GPS Receiver	7.6 x 3.6 x 12.8	15 pounds	
AE	8 x 2.3 x 12	8.5 pounds	Antenna Electronics
CRPA-2	14.1 (dia) x 2	4.5 pounds	CRPA
	<b>TOTAL:</b>	<b>76 pounds*</b>	

\* The total weight would be reduced by 12.5 pounds (Total = 63.5 pounds) if a FRPA was used. However, jamming resistance as shown in Figure 6 is reduced.

*Improved Reliability, Reduced LCC* The use of fewer LRUs (and therefore fewer parts) in the INS with embedded GPS configuration should result in an increase in reliability. Since fewer LRUs and Shop Replaceable Units (SRUs) will need support, a lower LCC should also be expected.

### **Security Considerations**

Currently, the National Security Agency (NSA) will not allow transmission of pseudo-range and delta-range data from a GPS receiver to another system unless that transmission is via a secure (TEMPEST) data bus. In fact, system configurations which pass classified or sensitive pseudo-range and delta-range data from the GPS receiver to the INS are not encouraged under Joint Program Office (JPO) GPS guidelines<sup>2</sup>. If a secure bus were implemented, the entire system would be classified when keyed with cryptovariables and would require special handling; data would remain classified for 48 hours.

The INS with embedded GPS configuration is unclassified when keyed with cryptovariables and the Honeywell H-764G INS/ GPS design has been approved by the NSA.

## **V. DIFFERENTIAL APPLICATIONS**

A navigation system with 16 meter SEP accuracy will satisfy the majority of users. However, for those users requiring accuracy in the centimeter to 5 meter range, the incorporation of differential GPS (DGPS) to the embedded GPS/INS system provides a viable opportunity. The motivation for differential operation is that many of the largest GPS error sources, such as satellite clock and ephemeris errors, ionospheric and tropospheric delays and selective availability (found in Standard Positioning Service (SPS) receivers) are common to two or more receivers operating in spatial proximity. These common errors can be nearly eliminated in the differential mode, greatly enhancing navigation performance.

In those situations which allow post-processing of data (such as test range instrumentation applications), the DGPS corrections based on the reference GPS data can simply be recorded and applied later to correct the measured pseudoranges at the mobile GPS receiver. However, many DGPS applications; such as aircraft precision approach applications, need real-time accuracies in the range of a few meters or less. These cases require a data link to broadcast the corrections to the mobile receiver. Many different communication links have been evaluated and/or used, such as VHF and UHF radio links, marine radio beacons, and GPS-like L1 band transmissions. Extensive efforts are underway, particularly in the civil aviation and marine DGPS areas, to establish standards for the DGPS correction messages (i.e., the Radio Technical Commission for Maritime Service (RTCM-104)) and correction link media.

### **Basic DGPS Operation**<sup>7</sup>

*Pseudorange Corrections.* The basic differential GPS (DGPS) concept is illustrated in Figure 10. A reference GPS receiver's antenna is installed at a surveyed site. Predicted pseudoranges to all satellites being tracked are computed based on the GPS satellite positions and the known reference station coordinates. Differences between predicted and observed pseudoranges are filtered to remove high frequency receiver-unique errors, and then transmitted over a differential correction link to user vehicles in the vicinity of the reference station. The corrections are then applied to the pseudoranges measured by the user vehicle's GPS receiver prior to performing the navigation calculations.

*Position Corrections.* An alternative DGPS approach is to measure the GPS position errors (i.e. latitude, longitude, and altitude) at the reference station, and to apply these measured errors as position corrections at the mobile GPS user's receiver. However, this approach requires that the reference and mobile GPS receivers track the same set of satellites, which is a significant limitation in a dynamic environment. Aircraft dynamics and antenna shading can often cause satellites to temporarily drop out of the mobile receiver's active constellation. For this reason, the "position correction" DGPS concept is less attractive than the commonly used range correction approach.

### **Kinematic Carrier Phase DGPS**

DGPS is commonly used in surveying applications to achieve centimeter level positioning. In contrast to real-time aircraft navigation, the surveying problem is somewhat easier because of its very low (often zero) dynamics, and because data post-processing is generally acceptable. Extension of the GPS processing methods used by the survey community to real-time, low-to-moderate dynamics applications is an area of active research today. This extension to dynamic environments is usually described by the term "kinematic DGPS."

The key feature of kinematic DGPS is that the position calculations are primarily based on carrier phase measurements, rather than the pseudoranges. The carrier phase is essentially a high-quality range measurement; however, the phase data gives only the fractional-wavelength portion of the range. To use the phase ranges for positioning, it is necessary to determine the integer number of wavelengths associated with a particular carrier phase measurement. This process is normally referred to as "ambiguity resolution." Once the ambiguities have been determined, the phase ranges are used to provide centimeter level position accuracies.

A variety of methods can be used to perform the carrier ambiguity resolution function. The methods tend to rely on redundancy in the GPS observations (7 or more satellites visible), changes in the satellite/user constellation geometry over time (several minutes to tens of minutes), or the use of pseudolites to augment constellation geometry. Although the kinematic

GPS methods are currently applied in some surveying problems, much work remains before they can be reliably used in aircraft applications.

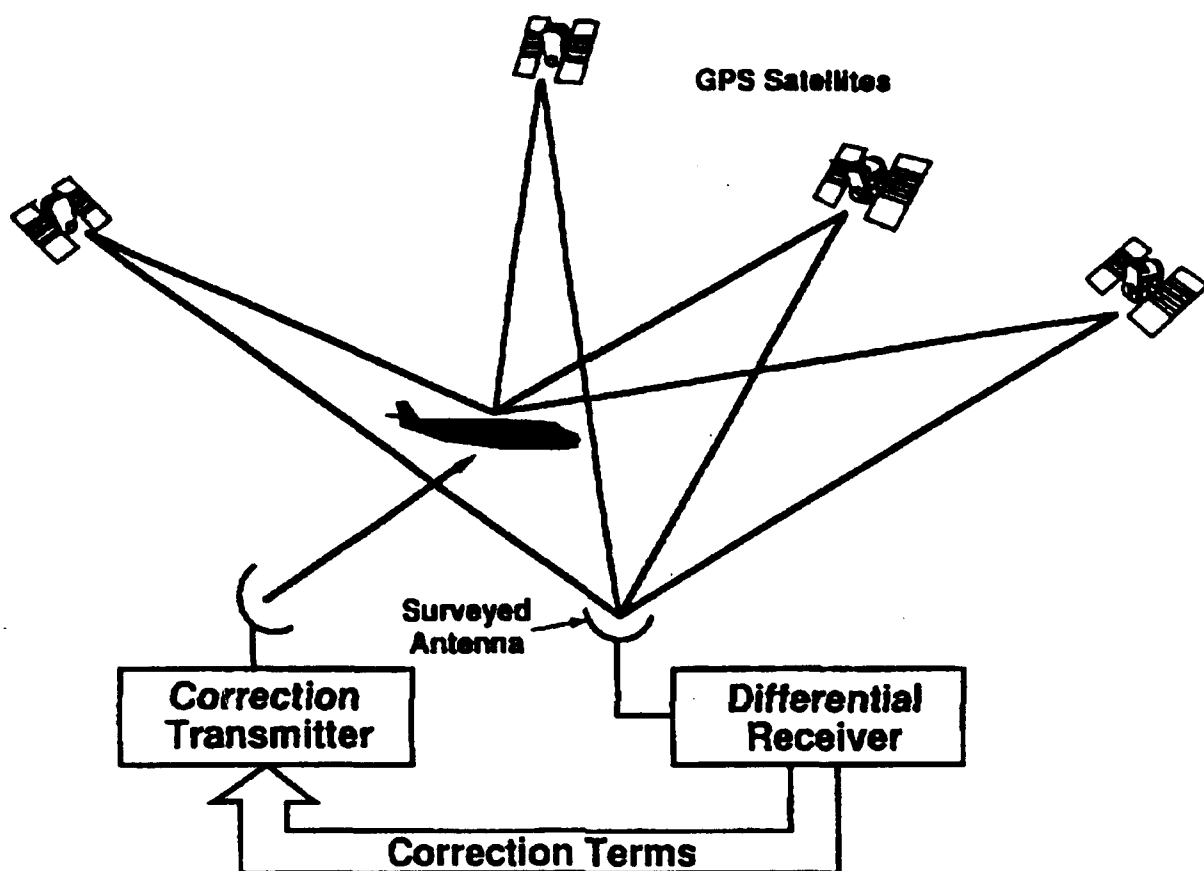


Figure 10. Differential GPS Operation.

### **DGPS Accuracy**

DGPS and DGPS/inertial accuracies can range from the centimeter level on up to a few meters depending on the particular application, the type of GPS receiver hardware, and the methods used to process the GPS data. Most reported results for conventional code DGPS (that is, DGPS navigation with pseudorange corrections) are in the range of 1 to 5 meters. An example of DGPS/inertial accuracy with this type of mechanization is shown in Figure 11. This figure shows the ensemble statistics of lateral position error for a set of 71 approaches and touchdowns flown in a Boeing 737 test aircraft<sup>8</sup>. The "truth reference" position data was provided by a laser tracker. Root mean square lateral error was about 9 feet. Multipath error affecting the reference GPS receiver was probably the principal source of error in these tests. Due to the inherently poorer GPS constellation geometry in the vertical direction, vertical channel errors were about twice as large as the lateral errors.

It should be noted that the DGPS/inertial performance shown in Figure 11 was obtained using a 2-channel, C/A-code standard positioning service GPS receiver. Better performance is achievable through use of multi-channel receivers which dedicate a channel of tracking

electronics full-time to each satellite being tracked, such as the receiver module used in the H-764G. Other paths to improved performance are the use of P-code or the so-called "narrow-correlator" C/A code designs, both of which provide low pseudorange measurement noise (on the order of 0.1 meter) and better multipath rejection characteristics than conventional C/A code receivers. "Code DGPS" based on carrier-smoothed differentially corrected pseudoranges can provide 1 to 2 meter (one sigma) position accuracies.

### **Embedded DGPS /INS**

The major areas of concern in kinematic carrier phased DGPS lie in resolving the carrier ambiguity problem, and the dynamic environment issues of cycle-slips and intermittent loss of lock on the carrier phase.

*Ambiguity.* Ambiguity resolution is currently achievable under stationary conditions by post-processing the data. Research is underway to develop and test algorithms for reliable real-time carrier phase ambiguity resolution in a dynamic environment where seven or more satellites are visible. An embedded GPS/INS system is a potential approach to resolving the carrier ambiguity by using tightly coupled inertial aiding to overcome data degradation common in a dynamic environment. A code-based blended DGPS/INS solution can help define a small position uncertainty volume using the best set of four satellites to define a 3-D grid of potential solutions based on the measured carrier phases from the set of four satellites, see Figure 12. Finally, a hypothesis test on redundant satellite phase residuals will allow a rapid pruning of false solutions. Table 4 summarizes the ambiguity resolution approach.

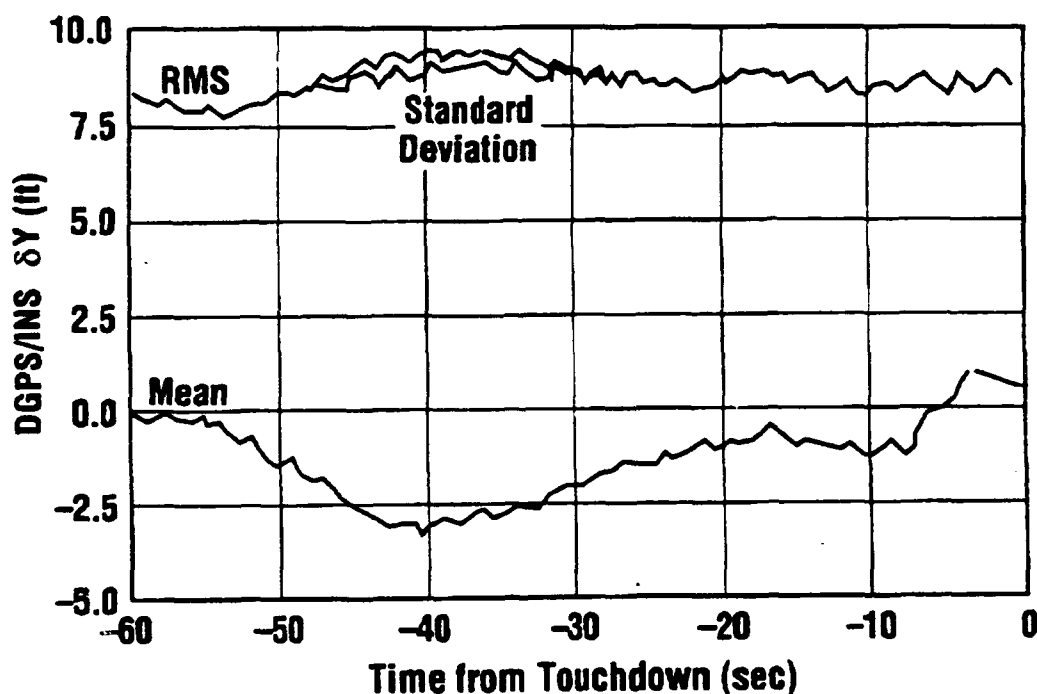


Figure 11. DGPS/INS Lateral Errors

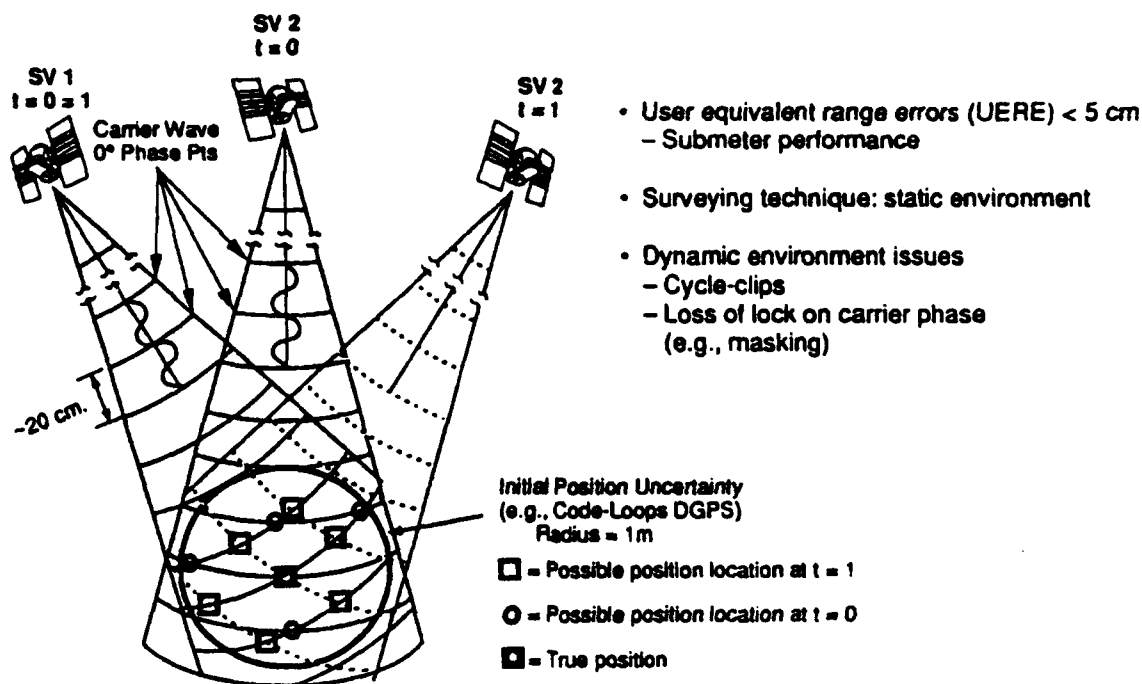


Figure 12. Carrier Phase Differential Kinematic Carrier Ambiguity Resolution

Table 4. Ambiguity Resolution Approach

1. Define search volume using code DGPS solution and uncertainty measure.
2. Choose best set of four satellites.
3. Generate 3-D grid of all potential solutions within the search volume based on the measured carrier phases from the set of four satellites.
4. Using redundant (5,6,...,n) satellites, compute the mean square phase residual test statistic:

$$S_k = \frac{1}{j(n-4)} \sum_{t_1}^{t_j} \sum_{i=5}^n (\phi_i - \phi_i)^2$$

for each of the potential solutions.

5. Edit out false solutions with threshold test: Is  $S_k > T$  ?
6. If more than one potential solution remains, collect another set of phase data and go to Step 4. If only one solution, ambiguity has been resolved.

*Cycle Slips and Loss of Lock.* The greatest risk to this approach of ambiguity resolution lies in the excessive number of carrier cycle slips and the intermittent loss of lock on the satellite signal. However, we believe the use of a tightly coupled embedded GPS/INS will resolve this problem. The highly accurate, high frequency solution of a high performance inertial should provide the GPS carrier tracking loop aiding information required to enable the receiver to "coast" through the loss of lock and cycle slip problem. This difficult concept is currently being researched using a separate INS and will easily transition to the embedded GPS/INS configuration.

## **VI. SUMMARY**

An INS with embedded GPS configuration, such as the Honeywell H-764G GPS/INS, offers many significant advantages over a stand-alone GPS and INS installation. Ease of integration retrofitting, fewer LRUs, less security concerns, and the performance, cost, and physical benefits should be important considerations when adding GPS capability to any aircraft/vehicle.

For those users with greater navigation accuracy requirements, an embedded DGPS/INS offers a viable solution. An embedded DGPS/INSs tightly coupled inertial aiding should overcome the data degradation caused by cycle slips and the loss of signal lock common in a dynamic environment. The applications of a tightly coupled, embedded DGPS/INS system with sub-meter accuracy in a dynamic environment are numerous. Besides the use in precision approach applications, the potential use as a highly accurate independent reference system for evaluating other navigation and guidance systems in any environment are tremendous. The kinematic carrier phase DGPS solution will provide submeter position accuracy, and the embedded system will also provide attitude and GPS based time.



## **REFERENCES**

1. Lewantowicz, Zdzislaw H.. 1992. "Architectures and GPS/ NS Integration Impact on Mission Accomplishment." Proceedings, Position Location and Navigation Symposium (PLANS).
2. NAVSTAR GPS Joint Program Office (JPO). 1992. "Guidelines for NAVSTAR GPS Embedded Receiver Applications."
3. Coffee, John R.. "GPS-INS Integration Requirement for Robust NOE Helicopter Navigation."
4. Franklin, Marty and Pagnucco, Steve. 1991. "Integrated GPS/INS for Cruise Missile Applications." Proceedings of the Cruise Missiles Technology Symposium.
5. Lewantowicz, Zdzislaw H. and Keen, D.W.. 1992. "GPS Aided Navigation Performance for Weapon Release With Fewer Than Four Satellites." Proceedings, PLANS.
6. Griffin, James R., et. al.. 1991. "Performance Enhancements For Inertially Aided GPS Navigation Systems." Proceedings of the Cruise Missiles Technology Symposium.
7. NAVSTAR GPS Joint Program Office (JPO). 1991. "NAVSTAR GPS User Equipment Introduction."
8. Vallot, L., Snyder, S., Schipper, B., Parker, N., and Spitzer, C. 1991. "Design and Flight Test of a Differential GPS/Inertial Navigation System for Approach/Landing Guidance," Navigation: Journal of the Institute of Navigation, Vol. 38, No. 2.

## **Test of an Integrated GPS/INS System for Precision Velocity**

**Brian Mitchell**

**IEWCS Navigation System Upgrade Project Leader  
CECOM Command/Control and Systems Integration Directorate (C<sup>2</sup>SID)  
System Technology Division  
Fort Monmouth, NJ**

**Joe McGowan**

**IEWCS Navigation System Upgrade Project Manager  
Intermetrics, Inc  
108 Main Street  
Oceanport, NJ 07757**

### **Abstract**

Recent performance testing, conducted at the Holloman, AFB test track, of a hybrid navigation system consisting of an enhanced Miniature Airborne GPS Receiver (MAGR) and a SNU-84-1 USAF Standard Inertial Navigation Unit (INU) was conducted to qualify a configuration for use in an electronics warfare family of host vehicles. The results show that this combination of navigation sensors can support the stringent navigation accuracy requirements imposed by mission equipment, essentially a velocity accuracy of .01 m/s RMS. This paper will describe the test configuration, methodology and results.

### **Introduction**

Emerging developments in the ARMY's emitter location capabilities are placing increasingly stringent accuracy requirements on the host vehicle navigation systems, particularly in the velocity components. This was recognized in the early 1980's by the ARMY and several analyses were conducted to determine the level of accuracy required and identify potential sensor suites that could satisfy these accuracies<sup>1</sup>. In 1987, C<sup>2</sup>SID lead the integration of a two channel GPS receiver with a 0.4 NM/HR inertial navigation system that achieved 0.02 meters/sec velocity accuracy under benign flight dynamics<sup>2</sup>. This work was conducted in support of the Guardrail/Common Sensor (Gr/CS) program. Enhancements to the emitter location capabilities of Gr/CS are currently in development under the Intelligence and Electronic Warfare Common Sensor (IEWCS) Program, and will provide improved location accuracies, greater coverage of the frequency spectrum, a more robust repertoire of recognized signal types, and the capability to be hosted on both air and ground vehicles.

The position and velocity accuracy requirements of the IEWCS family of mission equip-

	Horizontal (Each Axis)	Vertical
Position (Meters RMS)	8.00	8.00
Velocity (Meters/Second RMS)	0.01	0.10

Table 1. IEWCS NSU Performance Requirements

ments are shown in Table 1. The very high velocity accuracy is achievable by virtue of the benign dynamics present in the IEWCS mission profile.

### Background

Work on the IEWCS Navigation System Upgrade (NSU) began in 1990 with a study phase whose objectives were to identify existing candidate components for the navigation system, subject to the following criteria:

1. Performance - the component must support the accuracy objectives without unacceptable degradation in the high vibration environment of a helicopter.
2. I/O Compatibility - the component must provide the necessary data I/O to support a hybrid navigation architecture with a Kalman Filter providing an optimal navigation solution, as well as the informational needs of the mission platform. Implicit in this requirement is the need for all output parameters to be time tagged, and for the component to support time synchronization with other components.
3. Design Issues - the extent to which existing components would require modification in order to support the performance objectives.

The study stressed the evaluation of standard components toward the recommendation of a navigation system with minimum life cycle costs. In this context, "standard" was defined to mean components that are currently maintained in the DOD inventory, have existing logistics support networks, and for which experience and lessons learned from previous application would serve to minimize the non-recurring engineering costs. Although the MAGR did not strictly meet this definition, at that time the MAGR NDI acquisition was in progress, making it the de facto standard 5 channel GPS receiver.

After applying criteria 2 and 3 above the field of candidates was narrowed to include the USAF Standard Inertial Navigation Systems as defined by the ENAC-77 and SNU-84-1 specifications as well as the DOD GPS receivers which are compatible with the MIL-STD-1553B Multiplex Data Bus (i.e. the AN/ASN-149 (V)2 and MAGR). Covariance analysis was then conducted to make a final selection. The results of this analysis, shown in Table 2, lead to the recommendation that the MAGR and SNU-84 class INUs be adopted as the primary navigation components<sup>3</sup>.

	5 Channel GPS SNU-84-1 INU	2 Channel GPS SNU-84-1 INU	5 Channel GPS ENAC-77 INU	2 Channel GPS ENAC-77 INU
Filter Complexity	11 State	Optimal	11 State	Optimal
Pos. Error (m)				
Horizontal	4.5	3.8	4.5	3.2
Vertical	8.0	6.0	8.0	6.5
Vel. Error (m/sec)				
Horizontal	0.007	0.013	0.010	0.015
Vertical	0.020	0.015	0.020	0.020

Table 2. NSU Study Covariance Analysis Results

## Test Design

The tests were conducted at the Sled Test Facility of the 46th Test Group of the Central Inertial Guidance Test Facility (CIGTF) at Holloman AFB, New Mexico. This test facility was chosen because it is the only available government range that could readily provide the velocity reference quality necessary to support testing against the 0.01 meters/sec IEWCS performance requirement. The range instrumentation provides position reference data better than 1 meter and velocity accuracy of 0.001 meters/sec, measured at the wheel of the test vehicle and 0.005 meters/sec when applied at the system-under-test installation location<sup>4,5</sup>.

Test vehicles at this facility operate on a set of instrumented tracks (similar to railroad tracks) that run roughly North-South. Test runs in the forward (North) direction were conducted at a nominally constant 30 mph (13.4 meters/sec), while those in the reverse direction were at 20 mph (8.9 meters/sec). During the period of the testing, the track was instrumented for about 25,000 feet (7620 meters), yielding approximately 600 seconds of data in the forward runs, and 900 seconds in the reverse runs. A typical test trajectory is shown in Figure 1.

Each test run represented a short (10-15 minute) snapshot of the performance of the integrated navigation solution. To ensure that the ensemble of test runs was representative of the wide variety of external errors sources that affect GPS performance (e.g. atmospheric propagation effects, control segment errors), 3 to 6 of these snapshots were taken at various times of the day for each of the 5 days of data collection.

## Performance Results

This section presents the results of the quantitative performance scoring applied to the integrated MAGR/INU navigation solution from each test run. Fifteen test runs were

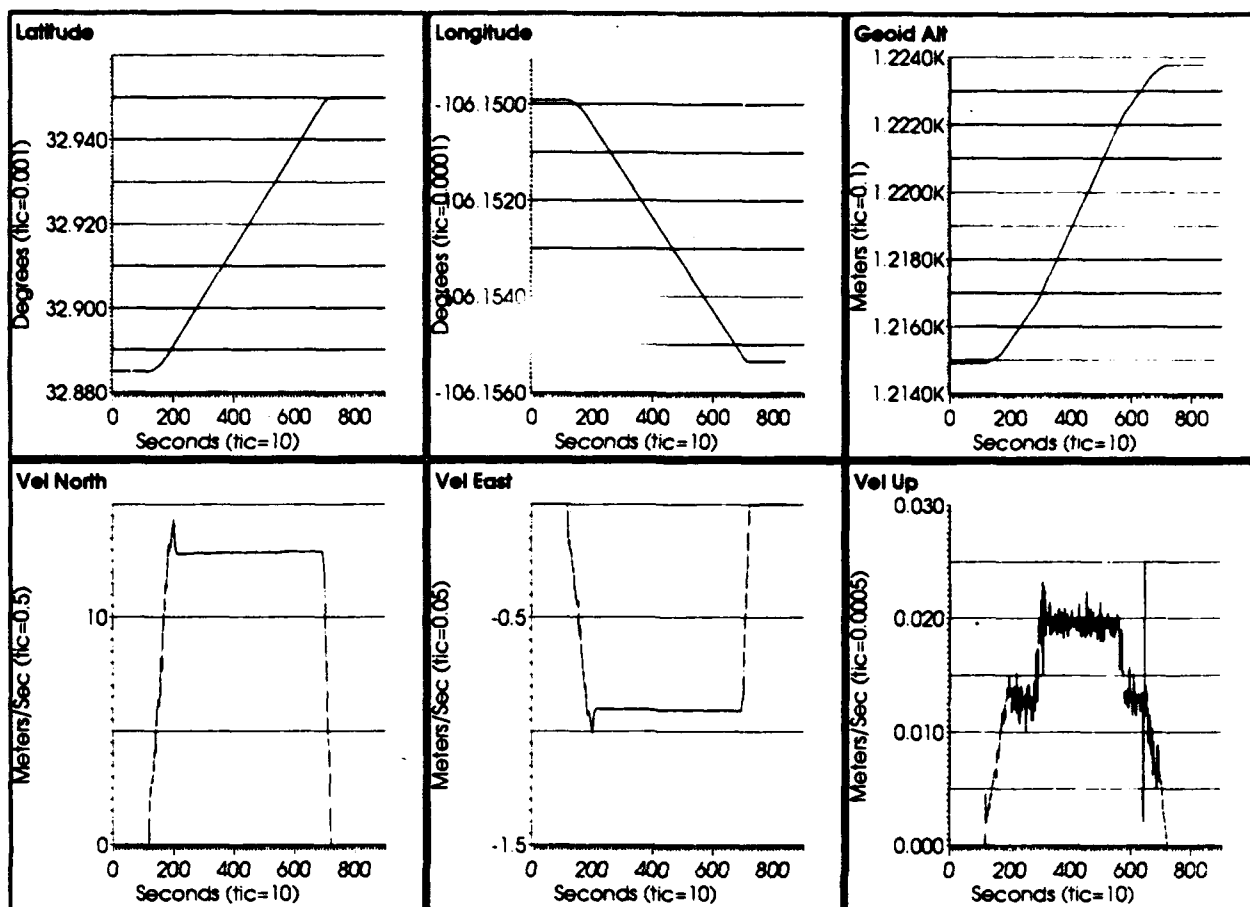


Figure 1. Typical Test Profile

processed to determine the RMS errors being committed by the system in position and velocity. From the ensemble RMS statistics, an expected level of performance was established. An appreciation for the mission-to-mission variability in the performance was also obtained by comparing the performance exhibited in each run to the ensemble performance.

In developing the performance results, the error histories were generated by differencing the MAGR/SNU integrated navigation solution with the reference solution supplied by CIGTF. The RMS statistic of the error history was then calculated over the entire interval of the test run. A typical error history is shown in Figure 2. The offset in position error at time 392430 is a known characteristic of GPS position errors that accompanies a satellite switch.

Figure 3 shows a bar graph of the RMS position errors for each of the test runs in the East, North, and Up directions. The ensemble of the RMS statistic, shown on the extreme right in Figure 3, is approximately 5 meters in each of the horizontal coordinates and 8 meters in the vertical. Comparing these results to the requirements in Table 1, the ensemble performance exhibited over all of the test runs achieved or exceeded the

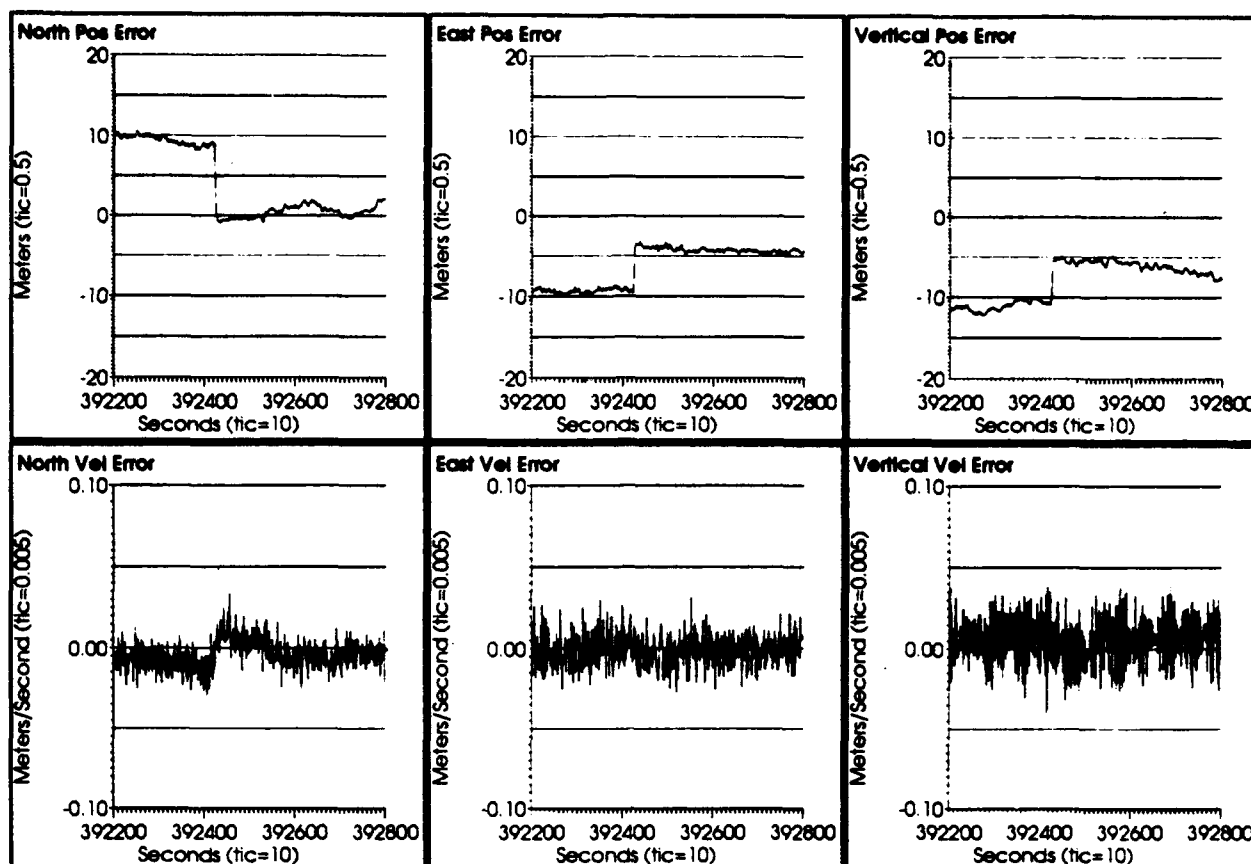


Figure 2. Typical SUT Error History (Test Run 2282RSV2)

desired position accuracy. The wide variability between any particular run and the ensemble is an expected characteristic of GPS based systems. The GPS errors that affect position are largely bias-like in nature and vary considerably between individual satellites. The position performance in each run was generally better than 9 meters in each coordinate. In the two runs in which a component exceeded 10 meters, it was found that the bias component of the error was unusually large.

Figure 4 shows a bar graph of the RMS velocity errors for each of the test runs. The ensemble is 0.01 meter/sec in the horizontal coordinates and 0.018 in the vertical. Referring again to Table 1, it can be seen that the desired performance levels have been met. Only relatively small variation is exhibited across all of the data sets. This is also an expected characteristic, particularly in continuously tracking receivers such as the MAGR.

## Conclusion

Data has been presented that demonstrates that the navigation performance requirements of the IEWCS mission platforms can be satisfied by the combination of a MAGR and a SNU-84-1 compliant INU.

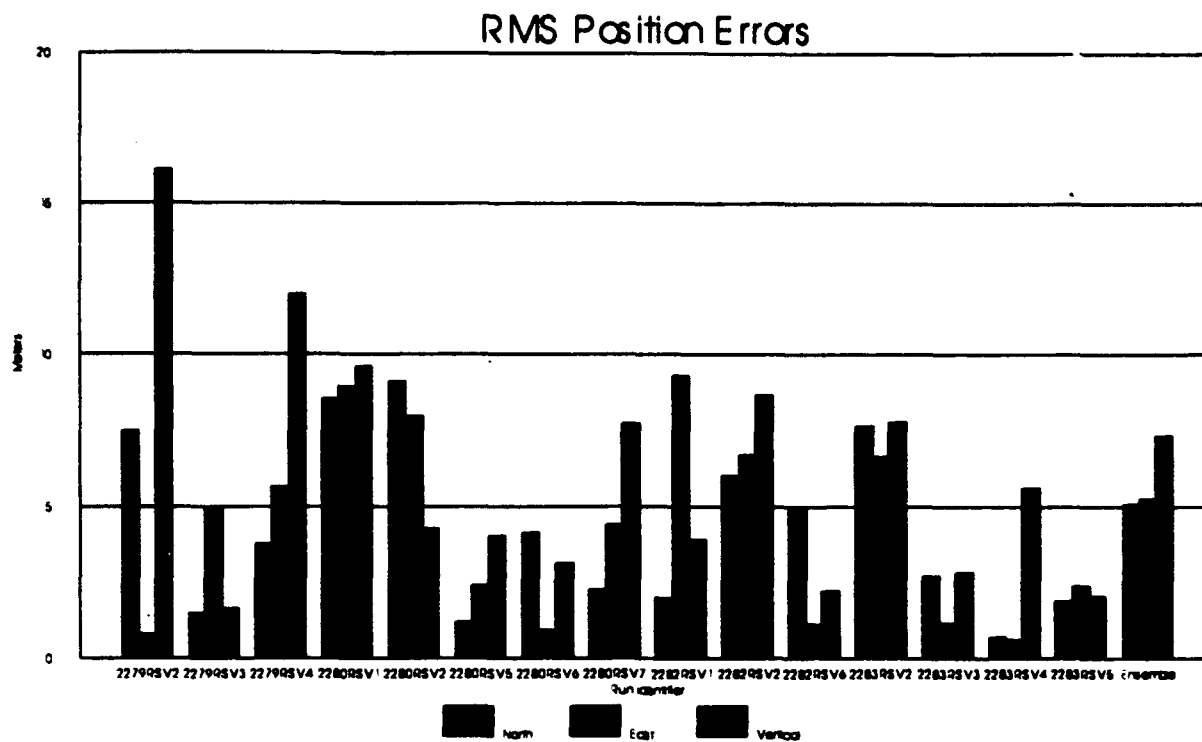


Figure 3. MAGR/SNU RMS Position Errors

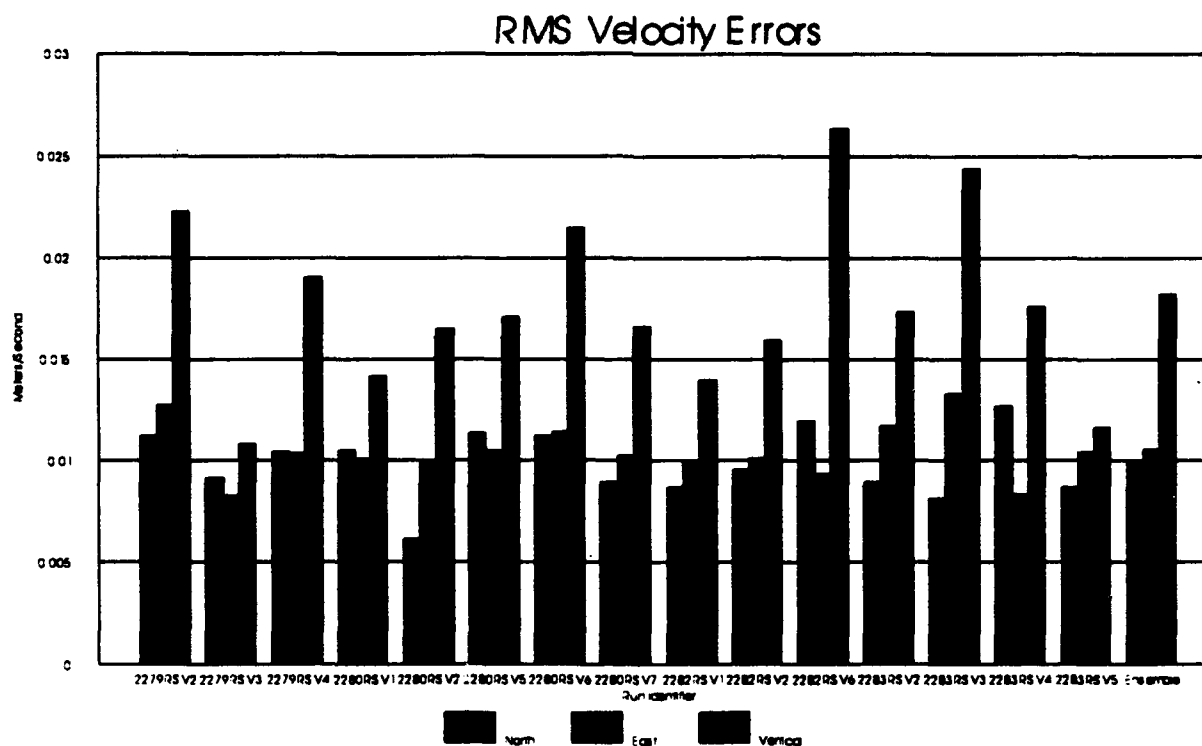


Figure 4. MAGR/SNU RMS Velocity Errors

The performance of the integrated navigation solution produced by the MAGR with aiding inputs from a SNU-84-1 compliant INU can be summarized as follows:

1. With a high degree of confidence the navigation system will support the IEWCS mission to the levels shown in Table 1.
2. Variations in the GPS operating environment will contribute to a high degree of mission-to-mission variability in the position performance and relatively low variability in velocity. The variability frequently provides better performance, but system errors may sometimes modestly exceed the desired performance.

The observed position accuracy of the integrated solution was consistently within the desired 8 meters (RMS per axis). In those cases where the error exceeded this limit, it was found that the GPS pseudorange error exhibited larger than expected bias errors. Attempts to isolate the cause of the high pseudorange errors were not conclusive.

The observed velocity accuracy was consistently around 0.01 meters/sec (RMS per axis) in the horizontal axes and was always well within the 0.1 meters/sec vertical axis requirement. This performance was achieved in spite of some surprisingly high velocity bias errors. It is suspected that the bias can be treated within the receiver and therefore represents an area likely to yield performance improvement, should the need arise.

In summary, the results presented herein support a very satisfying conclusion - the stringent performance requirements of the IEWCS mission can be met utilizing standard navigation units. Since the performance potential is inherent in the equipment tested, mission platforms need only supply the MID-STD-1553 bus control function to execute the timely transfer of information between them, and implement a scheme that allows the individual 1553 time tag clocks to maintain synchronization with each other. Acquisition and life cycle costs of these units will be minimized through the economy-of-scale benefit obtained from the existing acquisition strategy of coordinated tri-service procurement and the existing logistics support networks.

## References

1. Niemela, J. and Pinto, R., "Analysis of Positioning and Navigation Requirements for Airborne Emitter Location Systems", 28th Annual Joint Electronic Warfare Conference, Quantico, VA, May 1983
2. McGowan, J., "Velocity Accuracy Measurement of GPS User Equipment", AGARD Conference Proceedings No. 411, London, United Kingdom, October 1986
3. Intermetrics, Inc, "EH-60 Navigation Upgrade Study", October 1990



#### References (cont.)

4. Central Inertial Guidance Test Facility, Guidance Test Division, 46th Test Group, "Miniaturized Airborne GPS Receiver (MAGR) Sled Test Data Package", CIGTF-DP-93-03, March 1993
5. Intermetrics, Inc., "IEWCS Navigation System Upgrade Test Preliminary Report", April 1993

# TEST AND EVALUATION OF A NEW, TIGHTLY-COUPLED GPS/INS

Donald T. Knight  
Knight Systems  
973 12th Street, #3  
San Pedro, CA 90731  
(310) 833-5889

Allen (Skip) W. Osborne and Robert W. Snow  
Allen Osborne Associates  
756-J Lakefield Road  
Westlake Village, CA 91361  
(805)495-8420

Don G. Kim  
Inertial Science, Inc.  
3533 Old Conejo Road #104  
Newbury Park, CA 91320  
(805)499-3191

Approved for public release; distribution is unlimited.

## Abstract

A TurboRogue GPS receiver built by Allen Osborne Associates, Inc., and an AHRS-grade INS built by Inertial Science, Inc., have been integrated and tested using a new, tightly-coupled GPS/INS integration concept developed by one of the authors. Goals of the effort included a demonstration of modularity, accuracy and significantly reduced cost of GPS/INS integration. This paper mainly deals with test and evaluation that was done to verify that the combined GPS/INS system was working, and that its accuracy goals were being met. Van testing was conducted, resulting in a verification of functionality and performance. The primary evidence is the consistency of GPS/INS system performance relative to GPS receiver measurements collected in the van, combined with overdetermined GPS data that allow verification of TurboRogue performance using the same recorded field data. GPS/INS testing could be compressed because of the accuracy of GPS measurements; any glitch in the system that would have caused the computed GPS antenna position to jump by three inches would easily have been detected, because the TurboRogue was measuring differential delta ranges to an accuracy of an eighth of an inch. The combined system made predictions that fit the measured data to within the measurement accuracies. System features demonstrated included solving for a seven-foot lever arm from INS to GPS antenna that coupled van angular dynamics into the prediction of satellite-to-user range rates without corrupting the accuracy of range rate measurements. The second major piece of evidence is the ability of the system to calibrate and align the INS during combined GPS/INS operation, then to turn the INS loose and watch it navigate by itself with an accuracy that is extremely unlikely unless its prior calibration was successful. Again, testing could be compressed because system accuracy affords a rapid INS alignment during combined GPS/INS operation.

## Summary

The purpose of the test and evaluation effort reported here was to demonstrate an approach to tightly-coupled GPS/INS integration that is faster and less expensive than previous approaches, and to prove out the major hardware and software components by demonstrating an actual prototype. Currently, in the US, only about half a dozen large companies and corporate teams have succeeded in developing a tightly-coupled GPS/INS. Most GPS/INS systems are loosely coupled, being easier to integrate but lacking the performance of their optimal, tightly-coupled counterparts. Associated with the difficulties of tightly-coupled integration are development delays, lengthy test programs and inflexibility of finished designs. A great many potential uses for GPS/INS go unfilled because of the high

cost of integration. If a way could be found to reduce the difficulty of GPS/INS optimal integration, then both the potential users and suppliers would benefit by expanding the diversity and number of systems in use, at a price that users could afford, and at a development pace that would keep up with changing needs. A GPS/INS tight integration concept was developed by Don Knight stressing modularity of components and ease of integration. The concept is presented in a paper (1) given at PLANS '92. Subsequently, the authors of the present paper contributed their respective capabilities to the demonstration of a prototype.

GPS receiving and INS components were placed in a van. The INS was synchronized to measure acceleration and angular rate over intervals that coincided with GPS integer seconds. The raw measurements of each INS and GPS device were recorded with the van moving, and the recorded data were subsequently combined in post-processing software that computes the GPS/INS integrated solution.

Verification of performance was based on overdetermination of GPS data, and on functional and statistical tests that are the subject of this paper. The chief conclusion from this effort is that the GPS and INS components, and their integration into a tightly-coupled prototype, are working. The configuration tested was not intended to be representative of any particular application. Rather, the intent was to prove out a core capability. Having accomplished that, it can be said with confidence how one derivative system or another will work when a version is tailored to a specific application. What has not been accomplished at this point is executing the whole system in real-time, and feeding INS-derived GPS Doppler predictions back into the receiver to improve the receiver's noise rejection and to speed the receiver's re-acquisition of GPS signals that have been interrupted. Also not accomplished at this point is the verification of Kalman filter accuracy estimates by comparison with a dual-state covariance analysis. The significance of the work reported here is in finding a simpler, more effective way to optimally integrate GPS receivers with inertial navigation systems.

## Test Equipment Configuration

Figure 1 shows the equipment configuration used for van testing. Navigation signals broadcast by GPS satellites were processed in a TurboRogue GPS receiver. A GPS antenna was mounted on a luggage rack, and the TurboRogue was physically situated on a workbench within the van. The TurboRogue acquired GPS signals, read orbital ephemeris parameters that were modulated onto satellite broadcasts, and navigated autonomously as if no other

equipment were in the van. TurboRogue measurements of carrier phase and pseudorange, at both L1 and L2 frequencies, were recorded at 1 Hz on a 4-megabyte FLASH EEPROM card. The measurements were subsequently transferred to floppy disks for post processing. An atomic clock was available in the van during some of the testing. TurboRogue had the ability to use either its own internal crystal oscillator, or the external Rubidium frequency standard. The TurboRogue synchronized its range measurements to occur on integer seconds of GPS time, and then it output a one-pulse-per-second (1PPS) timing signal coincident with those measurements, to an accuracy of 0.1  $\mu$ sec. A base-station TurboRogue receiver (not shown) also synchronized with GPS integer seconds, and recorded carrier and code phase measurements from a known, surveyed site, coincident with measurements recorded in the van. A strapdown inertial navigation system (INS) was bolted down to the same workbench, and was connected to the GPS receiver 1PPS timing signal. That enabled the INS to synchronize its measurement of angular rate  $\Delta\theta$  and linear acceleration  $\Delta V$  to occur in 10 millisecond intervals that exactly divide a GPS second into 100 equal intervals, with the first such interval beginning on a GPS integer second. A laptop PC connected to the INS recorded six channels of 100 Hz  $\Delta V$  and  $\Delta\theta$  information, and subsequently this information was transferred to floppy disks for post processing. Recording two hours of INS raw data required about 13 megabytes of hard disk space, and the information could be transferred for post processing on about ten floppy disks. The INS recorded a sync bit demarcating GPS integer seconds in its raw data. GPS time of the sync bits was then established in post processing by correlating the onset of van motion as seen in the GPS and INS data files. The hardware and software components used in the demonstration are described next.

#### TurboRogue GPS Receiver

The Allen Osborne Associates, Inc. (AOA) TurboRogue tracks up to eight satellites without time multiplexing among satellites or channels, simultaneously measuring both pseudorange distances to satellites and the phase of received carrier signals for each of three channels (L1-C/A, L1-P and L2-P). In the absence of multipath and antenna errors, the TurboRogue is specified to measure L1-P pseudorange with a precision of 0.4 cm and a systematic accuracy of 1.0 cm. Carrier phase measurements of L1-P, the signal used here, are specified to a precision of 0.2 mm and a systematic accuracy of 0.1 mm. That essentially means that the TurboRogue receiver does not contribute anything to a system error budget that includes multipath, antenna errors, and some vagaries of the earth's atmosphere. As is described below, the actual, demonstrated accuracy of differential delta ranges seen in two hours of operation with the van moving, was better than 2 mm, RMS. That included the errors in four separate measurements of carrier phase, taken by two different receivers, and included multipath and environmental errors with 14 miles separating the two receivers. Delta ranges were computed in post processing software by differencing carrier phase measurements sampled on integer GPS seconds, and represent a measure of relative velocity of the satellites.

#### Digital Miniature Attitude Reference System (DMARS)

The inertial navigation system (INS) used was a DMARS, built by Inertial Science, Inc. The DMARS is a

fully-featured INS, capable of autonomous navigation when configured with inertial-grade sensors and digitizer modules. The system includes two 2-axis tuned-rotor gyros, three accelerometers, A/F digitizer modules and a computer, all housed in a cylindrical case 4.3 inches in diameter and 6.5 inches long. A strapdown sensor configuration was used. More than 70% of the resident computer capability is reserved for user programs which may be programmed into resident EEPROM. A single 65-pin connector provides all the necessary interface. The DMARS is a second-generation system, having originated in a Roll-Isolated Inertial Navigation System (RIINS). A variety of gyros, accelerometers, and digitizer modules can be used interchangeably in DMARS. Options include Bell Incosym's Mod-17 and Mod-20 gyros, and Condor Pacific's T-100 gyros. For the GPS/INS work described here, a version of DMARS was configured with AHRS-grade sensors and digitizers.

#### GPS/INS Integration Software

Most of the actual GPS/INS integration was accomplished in post processing software. The only electrical connection in real-time was the 1PPS timing signal from TurboRogue to the INS. The only physical connection was through the frame of the van, holding the GPS antenna fixed relative to the INS instrument cluster. Post processing software used the INS recorded data to drive a strapdown navigation solution, and used the GPS recorded pseudoranges, carrier phase measurements, and orbital parameters in a GPS/INS integration Kalman filter. For a fully real-time demonstration, it would only be necessary to host this same software under a real time executive in the laptop PC or in the DMARS computer, to pass the GPS data through an RS-232 interface to the laptop or DMARS computer, and to send real-time GPS differential corrections from the base station to the van via a modem or FM data link. The GPS/INS integration software was developed by Knight Systems. Mr. Knight has been working on GPS for the past 18 years, and has successfully (2) flight tested earlier GPS/INS tightly-coupled Kalman filters of his own design.

#### Data Collection Effort

February 4 and 5, 1993 We assembled the equipment configuration shown in Figure 1 and drove the van out onto rural highways in an attempt to record field data. There were multiple problems with the data recorded on those two days, including recorder problems that limited the total amount of data collected to about half an hour. Analysis of the data that was obtained, however, led to some useful conclusions. We were able to diagnose a timing problem. Also, processing a few minutes of the GPS data, we found that we could look forward to some spectacular accuracies. The distances that the TurboRogue measured simultaneously to seven or eight satellites came together at a single point, once per second with the van moving, with an accuracy on the order of 25 centimeters (ten inches) of residual range error. The velocities that the TurboRogue measured with respect to all seven or eight satellites converged on a solution for van speed and heading with an accuracy that was conservatively placed at 3 millimeters per second, or about 0.006 mph (six one thousandths of a mile per hour.) That performance was accomplished without any special techniques such as filtering the reference station data to reduce multipath error, or switching over to a kinematic

technique which would improve the ranging accuracy several-fold. Next, the TurboRogue data were used to plot ground traces, and it could clearly be seen that the ground traces correlated with maps of the area. At one point, we drove into a residential area, weaving through surface streets, and then drove back out the same way we had gone in. That produced two parallel ground traces neatly separated by the width of one lane of traffic. Finally, a sensitive statistical test was devised to look for error in TurboRogue measurements. Only one mechanism was found to produce noticeable glitches in the data; there were frequent signal interruptions caused by trees, highway signs and other obstructions, and most of those interruptions simply led to a small gap in recorded data as was expected. It occasionally happened, however, that the TurboRogue could report an erroneous carrier phase measurement during the last fraction of a second before the receiver detected that the signal it had been tracking had vanished. Catching those errors in the recorded data was easy, because the rare occurrence of such an error prevented the range rate measurements from all agreeing with one another to an accuracy of 0.006 miles per hour.

**March 11** On our second attempt at recording field data, problems with the recording equipment again limited the amount of usable data to about ten minutes. That ten minutes, however, turned out to contain much more information than was at first expected; it provided the first clear indication that we had a success on our hands and that the combined GPS/INS system was working. In post-processing, it was found that the receiver, INS and integration software all worked together beautifully, producing a combined GPS/INS solution that looked a lot like simulation results we had seen earlier. The whole system held together and made predictions that fit the measured data to within the measurement accuracies. Error plots and statistics looked good. All of the system features appeared to be working, including a solution for a two-meter lever arm from INS to GPS antenna that coupled van angular dynamics into the prediction of range rates, without degrading the accuracy expected of the range rate measurements. Very strong evidence was obtained that the system was working, as is described below.

**April 8 and 9** We solved the problem with the recording equipment and collected an hour and 20 minutes of data during an interval with about 5 satellites in view.

**April 13** On our fourth and final outing, we got a clean recording during a two-hour interval with up to eleven satellites in view. All the information recorded on this date from turn-on to shut-down was included in the final statistics described below, except for five outliers that were associated with signal interruptions, as before. The main value of the data recorded on this date was in solidifying the demonstration, and in adding statistical heft to the conclusions we had reached earlier based on the March 11 data.

#### System Functionality Verified

The quality of the data recorded on March 11 enabled us to conclude that the system was working, even with only a ten-minute sample. Any glitch in the INS data, or integration software, that would have caused the computed GPS antenna to jump by three inches would easily have been detected, because the test receiver was measuring differential delta ranges to an eighth of an inch. The quality and

abundance of satellite data also made INS and other system errors rapidly observable in the GPS/INS integration Kalman filter, so that just the simple act of backing out of a parking space, waiting for traffic to clear, and then speeding up onto a rural highway was sufficient to separate the error effects and calibrate the system. The sequence of events in the Kalman filter enabling it to recognize the different errors in the system occurred rapidly and followed our expectations. Subsequent to calibration, the INS could be turned loose to navigate on its own with an accuracy that agreed with Kalman filter predictions. Overall, the combined GPS/INS system was seen to be doing what it was supposed to be doing.

Figure 2 shows a ground trace of the van backing out of a parking space, turning northward, waiting for traffic, and then speeding up on a highway. A similar ground trace (not shown) was obtained using only the GPS data. Superimposing the two ground traces on the same graph produces two parallel traces separated by the antenna lever arm, the displacement from the INS to the GPS antenna. The separation was expected because the GPS-only solution describes antenna position, whereas the mixed GPS/INS solution describes INS position. Also, right at the point where the van backs up and then turns, at the bottom left corner of Figure 2, the INS traces out a small loop due to being situated behind the van's rear axle. An enlargement of the figure shows that loop clearly.

Figure 3 shows heading and ground track of the GPS/INS solution superimposed on the same graph. Track is the direction of the van's motion, whereas heading indicates where the van is pointed. It can be seen that the two are highly correlated, as would be expected for a land vehicle. This is evidence that the system is working, because nothing was done to inform the software that this correlation would occur; the same software works on aircraft and ships which are often pointed one way and moving another due to cross winds and cross currents. There is no significance to the two degree bias in Figure 3. The bias simply reflects the fact that the INS was bolted to a workbench within the van, and the workbench was not aligned to point in the same direction as the van's wheels.

The system was able to solve for the lever arm from INS to GPS antenna. Initial estimates for the lever arm were obtained with a tape measure, and were assumed to be accurate to about a foot. Even if the lever arm could be measured exactly, relative to the van, the information still had to be expressed in an XYZ coordinate system defined by the INS sensor cluster, and it was never intended that the cluster would be aligned with the van to better than a couple of degrees. The initial estimates of 73 inches forward, 29 inches right, and 34 inches up were reasonably accurate. The Kalman filter reduced the initial uncertainty of 30 cm (a foot) to 3 cm, as can be seen in Figure 4. Later, with two hours of data recorded on April 13, the filter brought that down to 3 mm in each horizontal axis, and 6 mm in the vertical axis. It can be seen in Figure 4 that the lever arm uncertainty remains on a 30 cm plateau as long as the van is not moving. This was expected since it is not possible for the filter to separate lever arm error from INS position error until the van turns. Subsequent to the turn, the filter can tell the difference between lever arm error and INS position error because lever arm error turns with the van whereas INS position error does not. The filter knew the sum of lever arm error and INS position error, so it could say with precision where the GPS antenna was located, but it couldn't say where the INS was

located, to better than 30 cm, until the van turned. Figure 5 shows the Kalman filter position uncertainty. It can be seen that the position uncertainty sits on the same 30 cm plateau, caused by the lever arm uncertainty, until the van turns.

Similar plots were generated for velocity, clock, tilt/azimuth, accelerometer biases and gyro drifts estimated by the 20-state Kalman filter. In every case the behavior was as expected.

#### TurboRogue Performance Verified

GPS receiver performance was verified independently of the INS, using the two hours of field data collected on April 13, and other data collected earlier. It was found that there was no "grey zone" in the TurboRogue performance. Either its data were present to full accuracy, or else the TurboRogue was not reporting anything for a given channel. The only exception was the error mechanism identified in the February 4 and 5 data where the TurboRogue would report an erroneous carrier phase measurement during the last fraction of a second before the receiver detected that a signal it had been tracking had vanished. Error detection was easy. A composite weighted fit error would jump from a typical value of about ten to an error value of several thousand. Based on that error test, five samples were deleted from the April 13 data. All the remaining 3758 samples collected in the two-hour session were included in performance statistics described below.

With the GPS solution heavily overdetermined, pseudorange measurement errors were estimated by summing the squares of pseudorange fit errors over all  $N = 3758$  measurement epochs, and over each measurement, with an average of  $n = 6.683$  measurements at each epoch, then dividing by  $N(n - 3)$ , and then taking the square root. Fit error is the discrepancy between a pseudorange measurement and the position solution obtained using all the pseudorange measurements collected at the same epoch. The term  $(n - 3)$  appears in the denominator because three pseudoranges were required to compute position on April 13, with an atomic clock in the van. Equivalent results were obtained on March 11 using  $(n - 4)$  without an atomic clock in the van. The base-station receiver was connected to an atomic clock at all times. The actual differential pseudorange measurement accuracy obtained for April 13, including multipath, environmental effects, and all errors in the post processing software, was 22.7 cm (9 inches, RMS). Accuracy of the differential delta ranges, obtained by the same procedure, was 1.92 mm (a little over 1/16 of an inch). In other words, the TurboRogue was measuring range rates to an accuracy of 2 mm/sec, or 0.0043 miles per hour as seen in over 25,000 measurements.

#### GPS/INS Consistency Verified

In the foregoing, pseudorange and delta range fit errors were determined against a solution for van position that was based only on the GPS data. The same error statistics can be computed for the case where van position is computed from both the GPS and INS data that have been combined into an optimal GPS/INS solution. That was done for April 13 data, using the same 3758 two-second measurement epochs. The results are shown in the table, below. The fit errors are expected to be larger in this case, and they are. The increase occurs for two reasons. First, the INS smooths the

GPS position and velocity solution, which is another way of saying that the system loses some of its freedom to bounce the solution around in order to accommodate errors in the GPS data. The solution from any given measurement cycle is carried forward by the INS and is included in the optimal solution on the next two-second measurement cycle. The value of "3" used above might be reduced if there was some way of establishing this loss of freedom, but the "3" was left alone. Second, all of the errors of INS sensing and post-processing are included in the new fit errors. If the workbench was vibrating with an angular amplitude of one milliradian, then that effect, coupled with the two-meter lever arm from INS to GPS antenna, would introduce 2 mm of delta range prediction error due to that mechanism alone. Had there been any glitch or gross systematic error effect in the INS sensors and electronics, or in the post processing software that accomplishes strapdown navigation and predicts the GPS antenna position, that effect would have been visible in the plots of fit errors versus time, shown in Figures 6 and 7. The only effects visible in Figure 7 are the five outliers, each of which is associated with a drop in the number of satellites being tracked. The delta range fit errors are still only 4.7 mm (about 3/16 of an inch). It cannot be concluded from this that the INS agrees with its system-level error model, but it is fairly safe to say that there are no gross implementation errors anywhere in the system. The magnitude of a jump in antenna position required to be detected would be on the order of 6 cm (2.4 inches). Right after the Kalman filter has processed all the measurements at a given epoch, the filter's velocity uncertainty is typically about 0.4 cm/sec in each axis. Velocity estimates are then extrapolated to the next measurement epoch using INS data, and the accuracy of the predicted velocity at the start of the next measurement epoch is typically about 1 cm/sec. In order to be detected as more than  $6\sigma$  random noise, a glitch in the system would have to substantially degrade this 1 cm/sec prediction accuracy, and a jump in computed antenna position of 6 cm would be sufficient to do that.

	Delta Range	Pseudorange
GPS Only	2 mm	23 cm
GPS/INS	4.7 mm	28 cm

#### Free Inertial Performance Verified

It is also possible to calibrate and align the INS during combined GPS/INS operation, then to turn the INS loose and watch it navigate by itself with an accuracy that is extremely unlikely unless its prior calibration was successful. To demonstrate this ability, a post-processing run was conducted in which the Kalman filter was denied the use of GPS measurements some of the time. The system error growth in the absence of GPS measurements is indicative of free-inertial performance. Free-inertial error was determined by comparison with a trajectory in which all the GPS data were included. A repetitive route was driven on April 13 in order to support this demonstration. Shown in Figure 8, the route consists of approximately 4.5 minutes of southerly travel on a rural highway, followed by a return trip back up

the same road. The round trip took about 9 minutes and was repeated 13 times. In post processing, GPS data were used in the Kalman filter for about the first 110 seconds of each northerly or southerly trip, and were then denied for the following 160 seconds. The "closed-loop/open-loop" cycle was repeated 26 times within the two hours and five minutes of recorded data. Figures 9, 10, and 11 show RMS errors that resulted for free-inertial performance. Also shown are typical Kalman filter error covariances. Errors are projected onto the east, north and vertical directions. It can be seen that the north/south and vertical errors are within about one standard deviation, and that the east/west error is within about 1.7 standard deviations, an acceptable random error. The magnitude of free-inertial drift is about as expected for the AHRS-grade sensors that were used. The 110 seconds is a short interval to align the INS, calibrate its errors, and solve for position and velocity, but the system accuracy affords a rapid INS alignment during combined GPS/INS operation.

#### Remaining Work

A dual-state covariance analysis will be done to verify Kalman filter accuracy estimates. The filter's free-inertial curves in Figures 9 through 11, and the filter's estimate of position accuracy in Figure 5, have to be confirmed by other methods. A real Kalman filter has a limited error state model and a lot of intentional mis-modeling in order to be able to operate in real-time.

The results shown here were obtained without any special techniques other than using a reference receiver at a known location. There was no filtering done to reduce multipath error at the reference station, and kinematic techniques have not been tried as of this writing. Just plain pseudoranges and delta ranges were used. The results shown here are the starting point for another round of improvements that should be possible by re-processing the same data with increasing sophistication. The goal at this time was proving out system components and verifying the core GPS/INS capability, without necessarily pushing for the limit in performance potential. It would be desirable to know what that potential is.

Finally, a real-time demonstration could be done. When executed in real time, the GPS/INS integration software only requires 55% of the computing capacity of a 20 MHz 386 PC with a math coprocessor, so it could easily execute in a laptop PC or in the DMARS computer's spare capacity. Receiver aiding is already built into the integration software. To use the feature, the receiver provides a list of satellites and gets back 100 Hz Doppler increments for each satellite. Adding together a long string of increments gives GPS Doppler at any time to within the accuracy of the INS. The increments even arrive synchronously with the receiver's own clock.

#### Acknowledgements

Allen Osborne Associates, Inc., outfitted a van, put a GPS antenna on the luggage rack, built a workbench in the van, provided base-station and mobile TurboRogue receivers, provided battery power supplies, provided personnel to operate the equipment, and provided two atomic clocks.

Inertial Science, Inc., contributed their DMARS inertial navigation system, made modifications to

synchronize the INS to GPS integer seconds, provided a laptop PC and data compression software to record the INS 100 Hz data, and provided personnel to operate the equipment.

Don Knight developed the GPS/INS integration concept, developed the GPS/INS integration software, performed data reduction and analysis, and was the chief author of this paper.

Finally, sincere appreciation is expressed to Lee Baum, and Bor Chang of AOA, and to Yoon Kim of ISI for their help in bringing all the equipment together and making it work.

#### References

1. Donald Knight, Achieving Modularity with Tightly-Coupled GPS/INS, Proceedings of the IEEE PLANS '92 Position Location and Navigation Symposium, Monterey, CA, March 23-27, 1992.
2. Donald Knight, GPS Integration with Low-Cost Inertial Navigation Unit, Proceedings of the Institute of Navigation, Satellite Division First Technical Meeting, Colorado Springs, CO, September 1987.

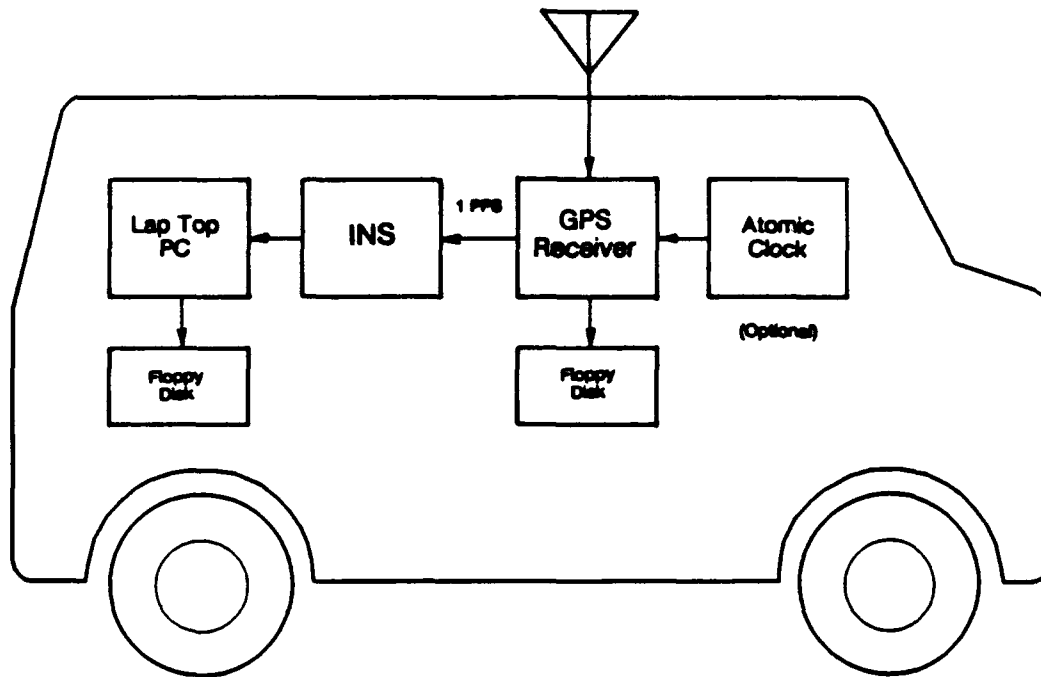


Figure 1. Test Equipment Configuration

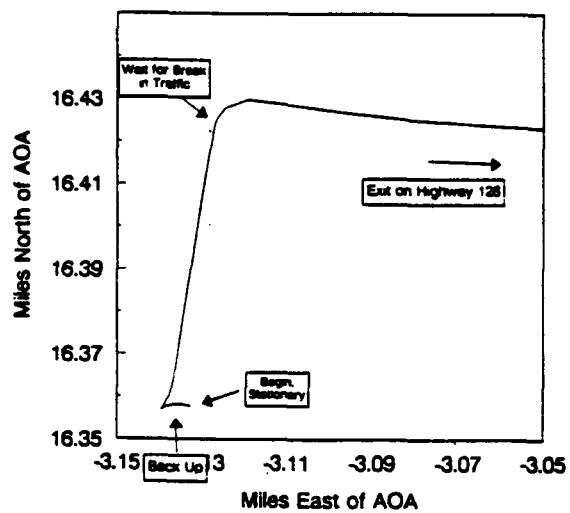


Figure 2. Ground Trace, March 11

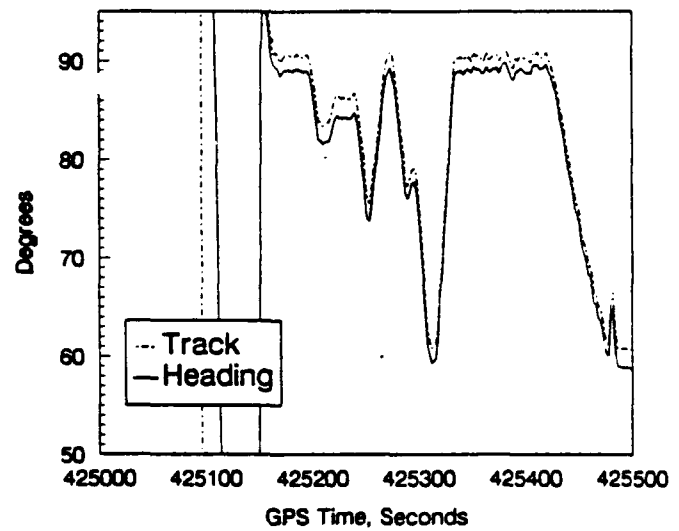


Figure 3. Heading Correlates with Track

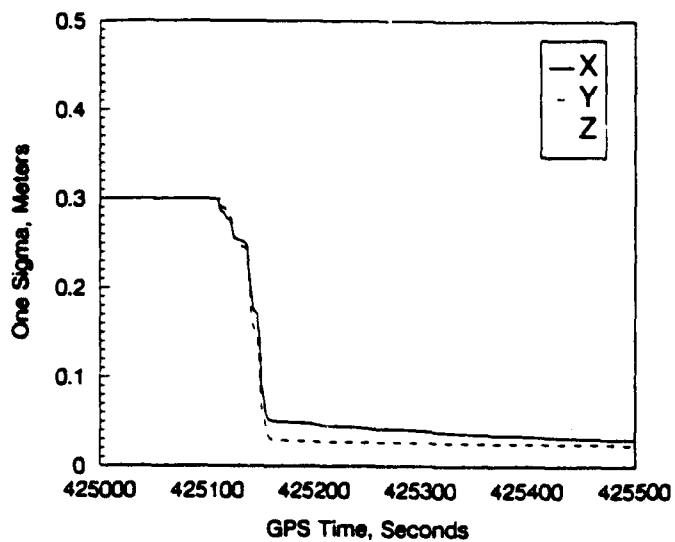


Figure 4. Lever Arm Uncertainty

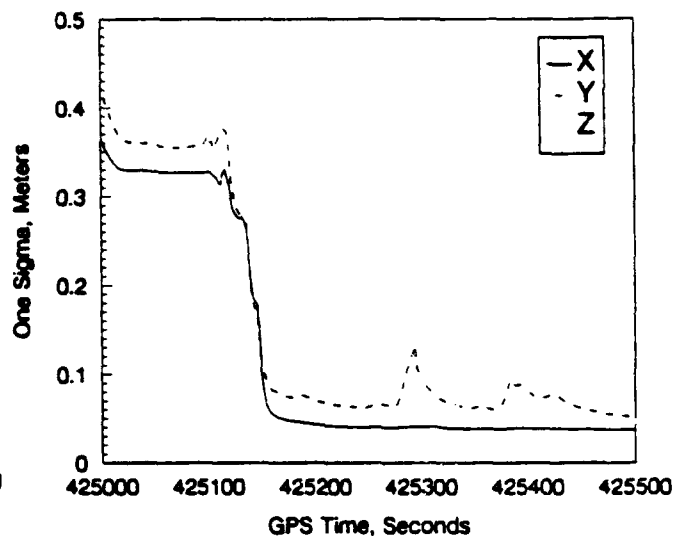


Figure 5. Position Uncertainty

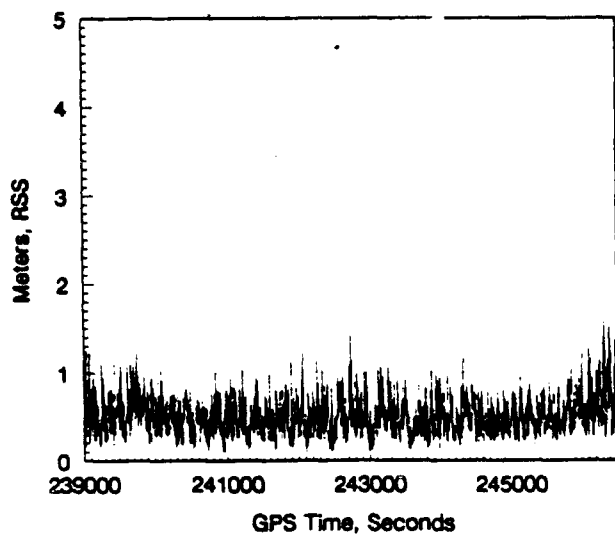


Figure 6. Pseudorange Fit Errors

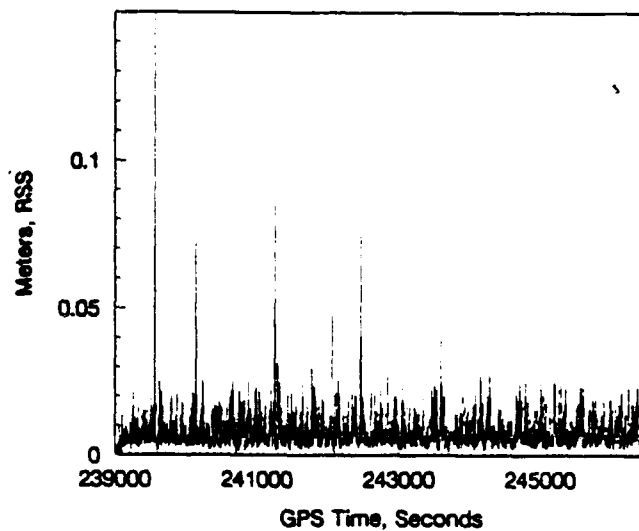


Figure 7. Delta Range Fit Errors



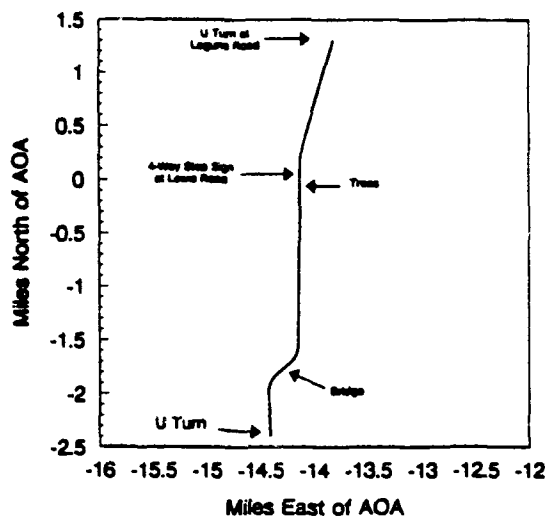


Figure 8. Ground Trace, April 13

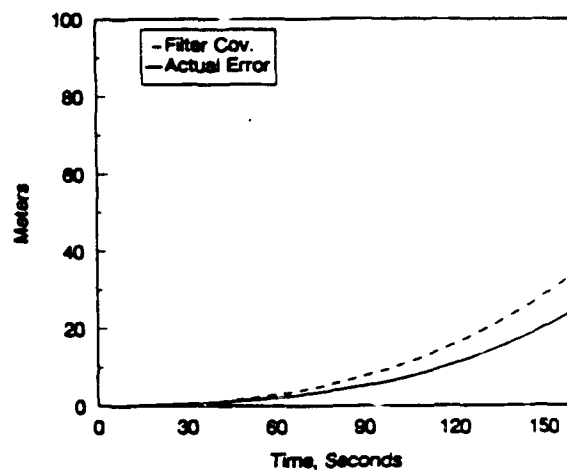


Figure 9. North/South Position Error Growth

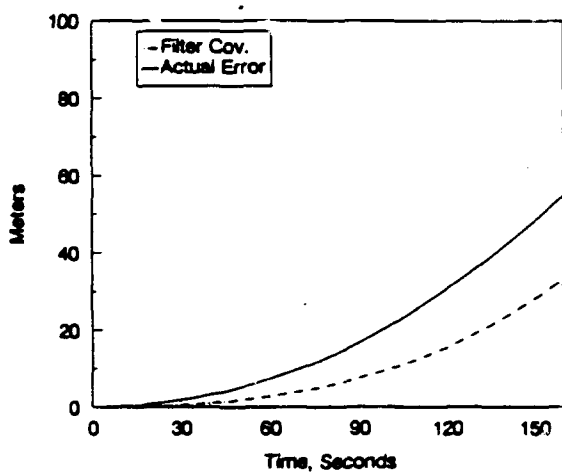


Figure 10. East/West Position Error Growth

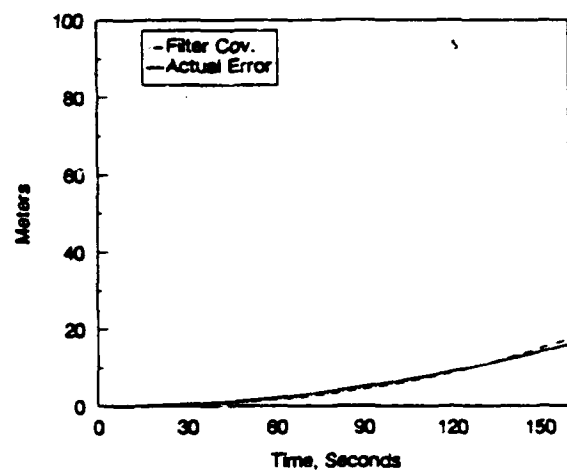


Figure 11. Vertical Position Error Growth

**SESSION III-A**  
**STRATEGIC SYSTEMS**

***CHAIRMAN***  
***SY LEVINE***  
***NORTHROP CORPORATION***

**THIS PAGE LEFT BLANK INTENTIONALLY**

# USE OF A HIGH PERFORMANCE AIRCRAFT AND GPS TO EVALUATE THE ACCURACY OF THE PEACEKEEPER INERTIAL MEASUREMENT UNIT

A paper written for presentation at the  
Sixteenth Biennial Guidance Test Symposium  
Holloman Air Force Base, New Mexico  
October 5-7, 1993

Captain Roger Evans, USAF  
6595th Aerospace Test Group  
Vandenberg AFB, California

Angelo Truncale  
Rockwell International Corporation  
Autonetics Electronic Systems Division  
Anaheim, California

## INTRODUCTION

Doc Draper enjoyed telling how, when he was first involved in designing gyroscopic instruments, a modification he introduced working late into the night, was tested the following morning in an aircraft flown by his friend, Jimmy Doolittle, using the tracks of the Long Island Railroad as a straight-line reference. At the time of these tests, the Long Island Railroad tracks were an adequate reference for the job of evaluating the accuracy of those early instruments. As the accuracy of the item under test improved, or the dynamics of the test environment increased, or when the test was conducted over a larger test area, assuring the accuracy of the reference system became more critical. Clearly, the ability to instrument and accurately measure reference quantities has traditionally established the area over which tests can be performed:

- In the laboratory, accurate measures of azimuth, the value of gravity and the latitude angle are enough to gather relatively accurate data from 1-g tests on inertial components and systems.
- Centrifuge tests require not only accurate measurements of arm length and angular rate, but arm stretch and droop must also be carefully measured or controlled if part per million accuracies are to be realized.
- For the Holloman sled test to be of any value, it has had to be surveyed and instrumented such that its azimuth and level are known to better

than a second of arc over its entire 50,000 foot length.

- Missile tests, such as to the Kwajalein Atoll are very costly in that they require establishing accurate references over long distances. Launch and landing sights must be carefully surveyed, gravity maps generated, and radar installations along the 4000 mile flight distance must be installed, carefully aligned and calibrated.

The availability of a Global Positioning System (GPS) brings about new possibilities for developing an extremely accurate reference system for the testing of inertial instruments and systems. If GPS can be shown to be sufficiently accurate, then the size of the laboratory or the length of the centrifuge arm or sled track need no longer constrain the planning of instrument or system tests. This paper addresses this possibility.

## Motivation

As part of a Peacekeeper\* (MX) guidance system accuracy improvement effort, the Air Force Development Support Organization (DSO) located

*\* The Peacekeeper (MX) [11] guidance system is the most accurate purely inertial guidance system in the world, with accuracy demonstrated by tests in the laboratory, on the sled track at Holloman AFB, and in over 30 missile flight tests from Vandenberg AFB, CA, to the Kwajalein Atoll in the Pacific Ocean. Since its first flight in 1982, its accuracy has been further improved as a result of the introduction of several modifications recommended by the associated-contractor supported Accuracy Working Group.*

at Norton AFB, CA, chartered the Rockwell Autonetics Electronic Systems Division (AESD) in Anaheim CA, to determine if individual instrument terms, currently not modeled in the on-board computer's Kalman filter, could be extracted in tests of the Missile Guidance and Control Set (MGCS), using a high performance aircraft with velocity and position information provided by GPS.

The motivation for this study was an ongoing investigation into gyro higher order acceleration sensitive drift terms ( $g^3$  and  $g^4$ ), which could have their origins in the gyro's gas bearing. Accuracies of interest were in the  $<0.0001^\circ/\text{hr}/g^n$  region. Although computer analyses of the bearings and a planned series of gyro level tumble and vibration tests in the laboratory were expected to provide initial insights, aircraft tests, if accurate enough, could be a valuable tool for investigating these terms at the system level. Furthermore, once the aircraft/GPS program was implemented, a new guidance test tool would be available to do accuracy assessment or to investigate other sources of suspected instrument mismodeling in the MGCS. Aircraft testing would permit the community to bridge the gap between laboratory tests and missile flight tests in a quasi-linear-g environment with tests that could be tailored to excite the coefficients of interest, and repeated as necessary to achieve credible statistics.

With details of an aircraft test capability defined, other applications for this approach became obvious. For fielded systems, as in the case of Peacekeeper or Minuteman, aircraft tests could be used to supplement missile flight tests while preserving assets. An obvious advantage of aircraft tests is that the system is not destroyed and returns to be tested again and again. This feature provides the ability to track the accuracy of a group of systems, and to investigate the drivers of any accuracy degradation that may be observed over time. Further, in the development of the next generation of systems, aircraft tests could provide valuable performance information early-on in the program, providing a precursor to subsequent missile flight tests.

In presenting the evaluation of an aircraft/GPS capability, this paper describes the assumptions made, and summarizes the results of various studies and analyses. GPS accuracy assumptions were based on post-processed, real Trident and Peacekeeper (w/GPS) missile flight data. As an

example of these data, results of Peacekeeper tests with GPS on board are presented. The results of our analyses support the conclusion that aircraft tests are a viable approach to assessing guidance system accuracy. With the viability of the approach established, the paper goes on to discuss a possible strawman GPS/Aircraft Test program.

This paper begins with an overview of several reference systems currently used to test inertial instruments and systems. From this, one may conclude that testing a guidance system in a high performance aircraft using GPS is the next logical step in developing the next-generation reference system for the testing of inertial hardware.

## TYPICAL REFERENCE SYSTEMS

To put high-accuracy aircraft tests in perspective, the following paragraphs briefly describe three test environments; sled, aircraft and operational missile flight tests. Each has its unique set of reference requirements, and each requires a considerable investment by the sponsor.

### Rocket Sled Test

Rocket Sled Testing allows for high accelerations and decelerations in a tightly controlled environment over a precise track. The 50,788 foot linear sled track at Holloman AFB, NM, has been managed by the 46th (formerly the 6585th) Test Group since the track became operational in 1950. The sled system has achieved a remarkable level of success as the forerunner to testing of inertial systems in their operational environments, or for testing new system hardware and software. Sled testing an inertial guidance system spans the gap between laboratory testing and operational missile flight testing [10,12]. Laboratory testing provides information on individual inertial instrument errors in specific orientations and under specific inputs, while operational flight testing provides the ultimate validation of a system's overall performance. As with missile flight testing, sled testing provides insights into the capability of the complete system; but the test article is retrievable after a sled test allowing further evaluation or additional sled testing of the system. Although sled testing is not a substitute for operational flight testing, it has been used very successfully to supplement missile flight tests in the evaluation of critical system performance characteristics; e.g., self-alignment accuracy.

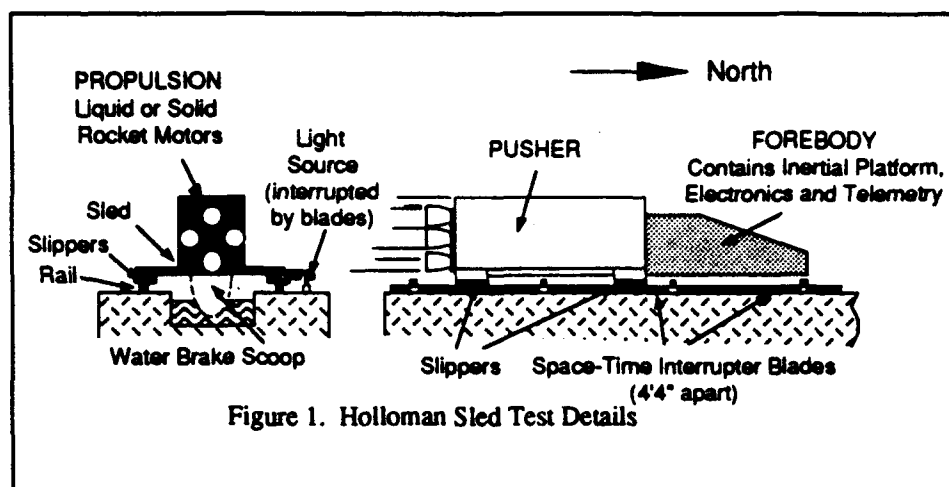


Figure 1. Holloman Sled Test Details

As shown in Figure 1, the sled test system consists of two pieces of equipment: the sled forebody, which houses the unit under test; and the solid rocket pusher, which provides the propulsion for the test. The sled forebody and the pusher are mounted to the test track with steel shoes (slippers), which are in sliding contact with the rails. The test track consists of heavy-duty rail sections, welded and precision ground to form two continuous steel rails, which are supported by a reinforced concrete base. A water trough below the track is used to create a high-g deceleration when the water scoop from the sled pusher breaks through the corrugated water barriers down the track. During a test run, exact time and position data are recorded using a light signal on the sled, which is interrupted by precisely surveyed "interrupter" blades positioned along the test track. These time data are compared to the data from the inertial components under test to provide observables for evaluating system performance. The sled track has proven to be very useful in evaluating missile guidance systems, such as the Peacekeeper Advanced Inertial Reference

Sphere. The accuracy of the track azimuth is known to better than 0.5 arcsec.

### Aircraft Test (using CIRIS)

The 46th Test Group at Holloman AFB, NM, has provided an Aircraft test capability to some of its tactical and aircraft inertial guidance system customers using the Completely Integrated

Reference Instrumentation System (CIRIS). CIRIS consists of precisely surveyed ground-based transponders positioned along the flight routes between Holloman AFB, San Diego, CA, and Dallas, TX; and north to the Canadian border (Figure 2). The transponders are used to determine the realtime position of the aircraft at any given time in the flight. This reference position information is then compared realtime with the position information from the test article to determine its navigation error. Aircraft testing using CIRIS is performed in Air Force C-141 and C-130 cargo aircraft, F-15 fighter aircraft, and helicopters. The helicopter testing is done over the White Sands Missile Range (WSMR), which also uses the CIRIS transponder system. The accuracy of the CIRIS system is in the 0.1 nautical mile region (0.0015 degrees/hour).

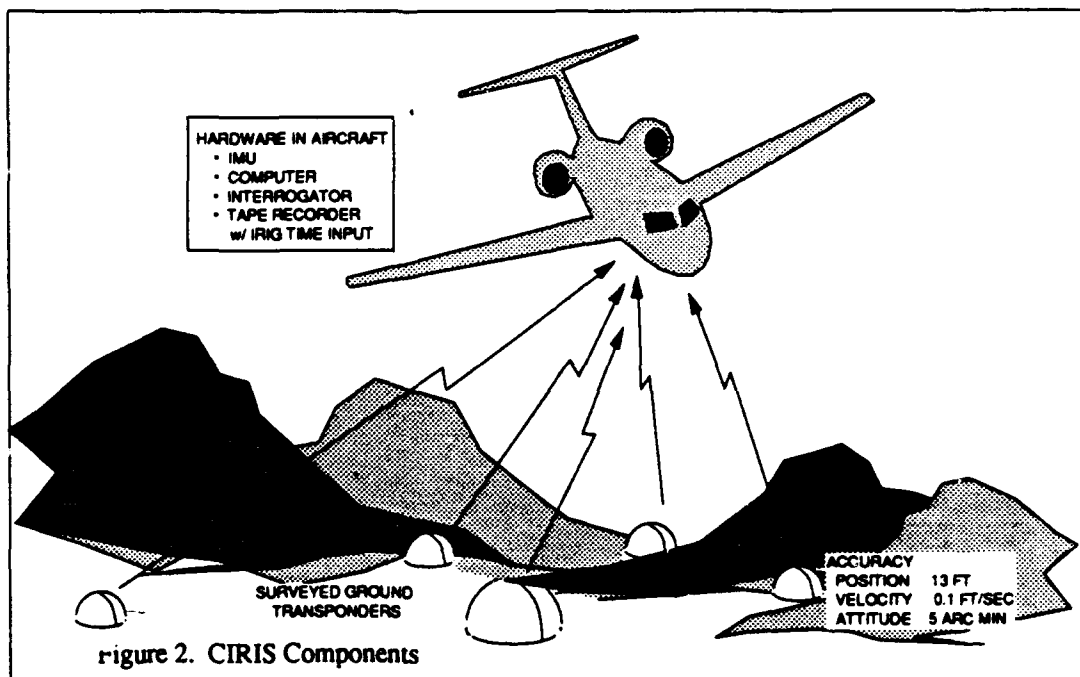


Figure 2. CIRIS Components

## Operational Missile Flight Test (Using Radar)

The final determination of the performance of ICBM and SLBM guidance systems is in the operational environment. Typically, a series of missile flight tests are planned during the development of a new missile or guidance system. In support of Air Force programs, development and operational test launches have been conducted from Vandenberg AFB, CA since the early 1950s. The reference system used for scoring the trajectory of the missiles has been radar and the splash location of the missile's unarmed warhead at a predetermined downrange target. Because of the long tracking distances involved, tracking a missile using radar requires the radar to have power in the Megawatt range. Since land is not always available in optimum locations, radar tracking often lacks the best geometry needed to track a missile during its flight. Radar tracking of missiles has been shown to be a reliable (albeit expensive) system for scoring the performance of missile guidance systems. As an example, the Air Force Peacekeeper program conducted 18 missile flight tests to prove the missile and its guidance system before it was deployed. Following its operational deployment, periodic missile test launches are conducted as part of a continuing accuracy and reliability surveillance program. Radar tracking of the flight trajectory permits the separation of flight errors to the total IMU (level 1) and when errors are large, to the individual gyro, accelerometer or initial conditions (level 2). Radar tracking is not accurate enough to permit characterizing individual instrument coefficient errors (level 3).

## Space Shuttle Test (Using GPS/GBS)

As the costs of missile flights have increased, an alternative method to test the Peacekeeper inertial guidance system was studied to supplement missile flight tests. In 1990, under a contract with the Air Force DSO, the Charles Stark Draper Laboratory (CSDL) submitted a proposal to test missile guidance systems using the Space Shuttle [8]. The reference system for these tests (Figure 3) consisted of GPS and a Ground Beacon System (GBS). The Space Shuttle is equipped with GPS/GBS antennas and receivers. The GPS/GBS data would be recorded along with the guidance system data during the Space Shuttle flight, and post-processed following the mission. The Space Shuttle/GPS reference system, when compared to the traditional ground radar reference system, was estimated to improve re-entry vehicle scoring by 30 percent. Additionally, significant improvement in observability into the guidance system error terms modeled in the Kalman filter was predicted over the use ground-based radars.

### PEACEKEEPER GPS EXPERIMENT

In June and September 1991, the Air Combat Command (formerly the Strategic Air Command) and the DSO of the Silo-Based ICBM SPO of the Air Force Material Command (formerly Systems Command) launched Peacekeeper missiles from Vandenberg AFB, CA 3500 miles downrange to the Kwajalein Atoll in the Pacific Ocean. These two reliability test flights of the operational system differed from previous test flights in that

each carried a GPS translator system. These two Peacekeeper/GPS operational test flights were code named GT-06 (Glory Trip) and GT-07. Elements of the test are shown in Figure 4 on the next page.

These two flights were an Air Force experiment to test the feasibility of using GPS satellite data and a Kalman filter post-processing scheme to more accurately score missile test flights and to investigate if results could be accurate enough to identify individual instrument coefficient impact miss contributors. Although the methodology was new to the Air Force, the concept of using a GPS translator and post-processing the re-

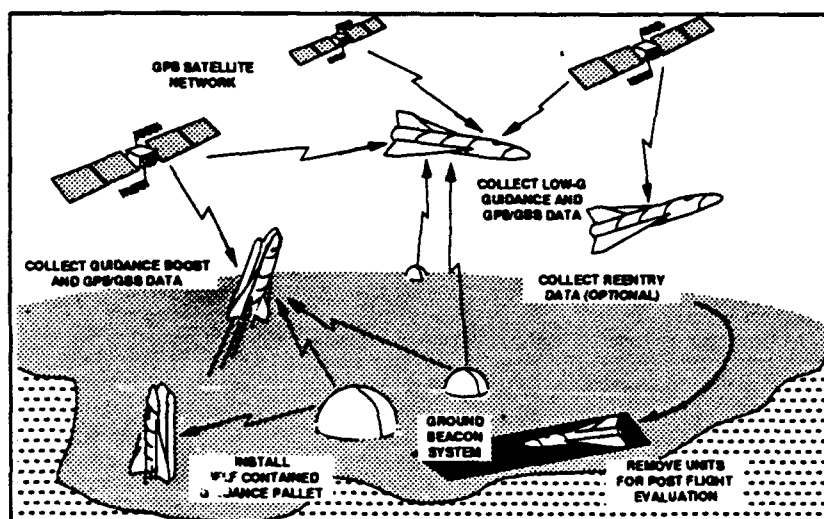
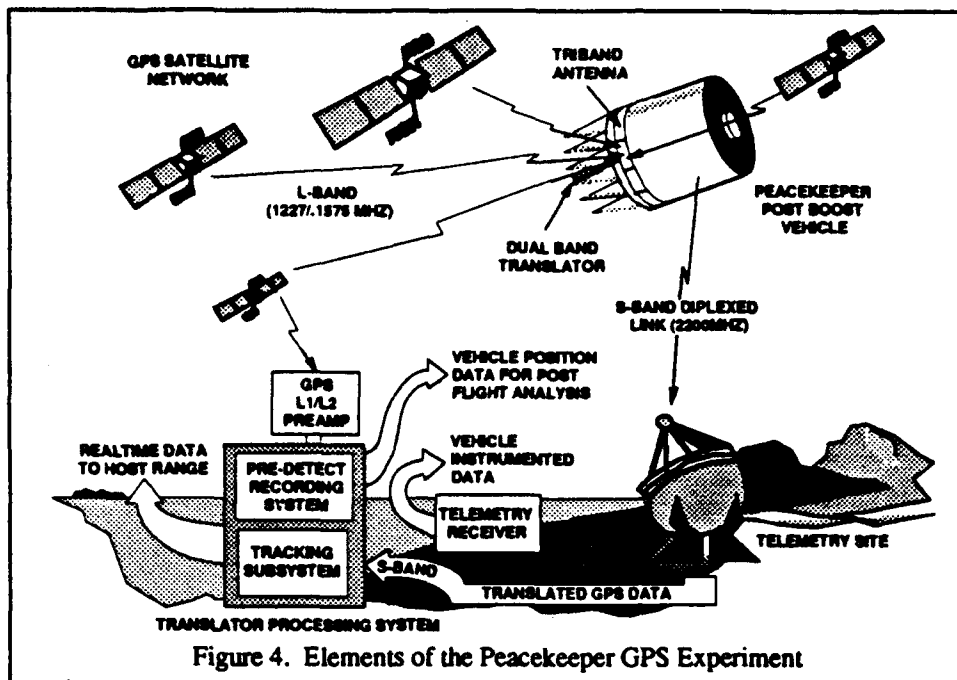


Figure 3. Proposed Gathering of GBS/GPS Data in Shuttle Tests



recorded satellite data to obtain velocity and position references was familiar to the Johns Hopkins Applied Physics Laboratory (APL)[4]. APL has been providing support and gaining experience in post-processing C-Band Radar, Telemetry Doppler, and GPS data on the Navy Poseidon and Trident Programs since 1976 [1,4].

### Test Objectives and Description.

The primary objectives of the Peacekeeper GPS experiment were:

- Demonstrate ground and flight hardware performance,
- Demonstrate the ability to use "crammed" L2 signals (the 20 MHz L2 P code data was crammed into a 2 MHz bandwidth during translation) for Ionospheric corrections,
- Demonstrate the feasibility of us-

ing GPS for range safety; and,

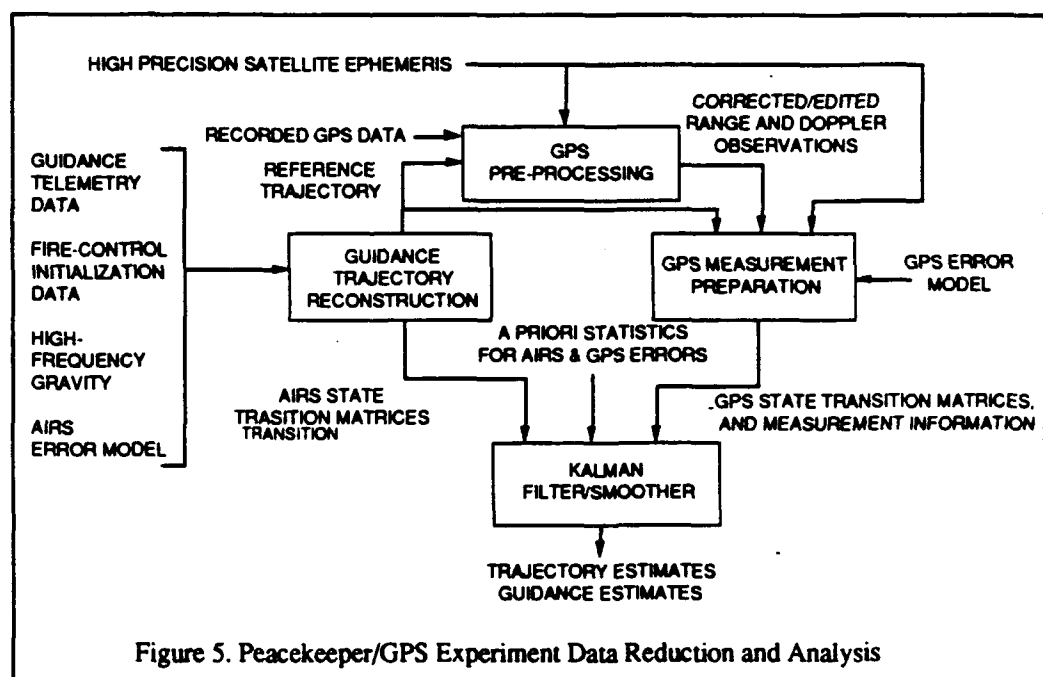
- Evaluate the GPS capability as compared to ground based radars in analyzing guidance hardware errors.

The translator system on board the missiles received "all" available GPS data on L-band and transmitted the information realtime to ground stations on S-band. The reference system was developed post-flight using the GPS and guidance data with Kalman filtering techniques, then it was com-

pared to the post-flight generated, guidance system indicated trajectory.

### Test Results

The Peacekeeper/GPS experiment was extremely successful in achieving all of the stated objectives for both flights. The results indicated that the accuracy of GPS data exceeded that of radar data for evaluating guidance system accuracy performance. The major portion of the effort involved data handling as shown in Figure 5. Note that the Kalman filter/smoothing acts on corrected





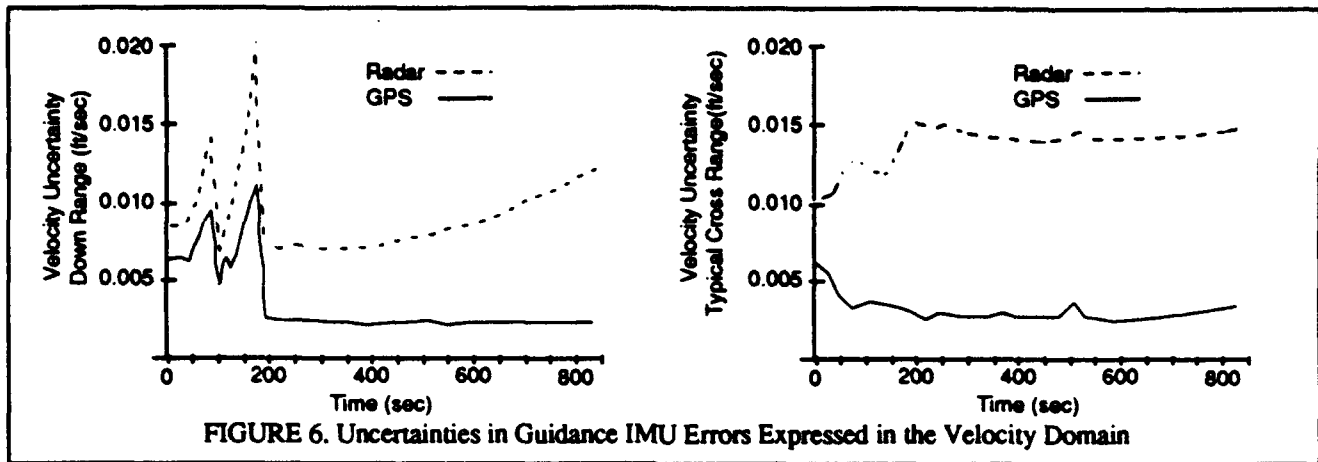


FIGURE 6. Uncertainties in Guidance IMU Errors Expressed in the Velocity Domain

GPS and guidance system data and contains models of both GPS and the AIRS system. Figure 6 indicates that the uncertainties in estimating guidance system (IMU) errors, expressed in the velocity domain, were two to three times better when using GPS rather than radar data, and for the most part were below 0.005 ft./second.

By demonstrating the levels of velocity uncertainties achievable, the Peacekeeper/GPS data provided a baseline with which tests in an aircraft could be analyzed and investigated.

### AIRCRAFT TESTING WITH GPS

The goal of the Peacekeeper accuracy community, in its analysis of IMU testing in an aircraft, was to determine whether these tests could achieve the levels of accuracy necessary to extract individual instrument coefficients, with acceptable

uncertainties, and if such a test capability was feasible. Beginning with the concept shown in Figure 7, the issues addressed in the study ranged from whether the necessary hardware could be supported and mounted in a high performance aircraft, to whether the 0.005 ft./second GPS accuracy, demonstrated on Peacekeeper was adequate.

### Computer Simulations

The first step was the performance of a computer analysis to determine the feasibility of estimating the values of instrument error coefficients including gyro higher order, acceleration sensitive terms. The three-step analysis is summarized in Figure 8. It includes the following subtasks:

- A PC-based aircraft simulator program was developed that would generate velocity and acceleration profiles for various input trajectories,
- A model of the system containing instrument error coefficients was excited with the three-axis acceleration profiles and the response of the system determined.
- Covariance analysis techniques, which combined simulated Guidance

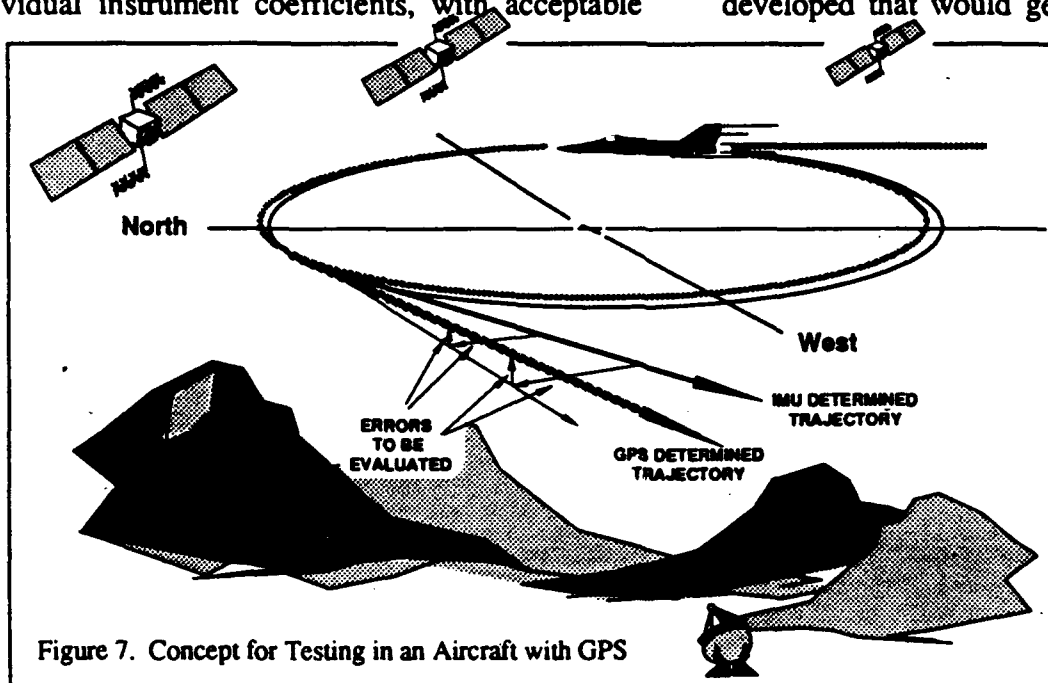
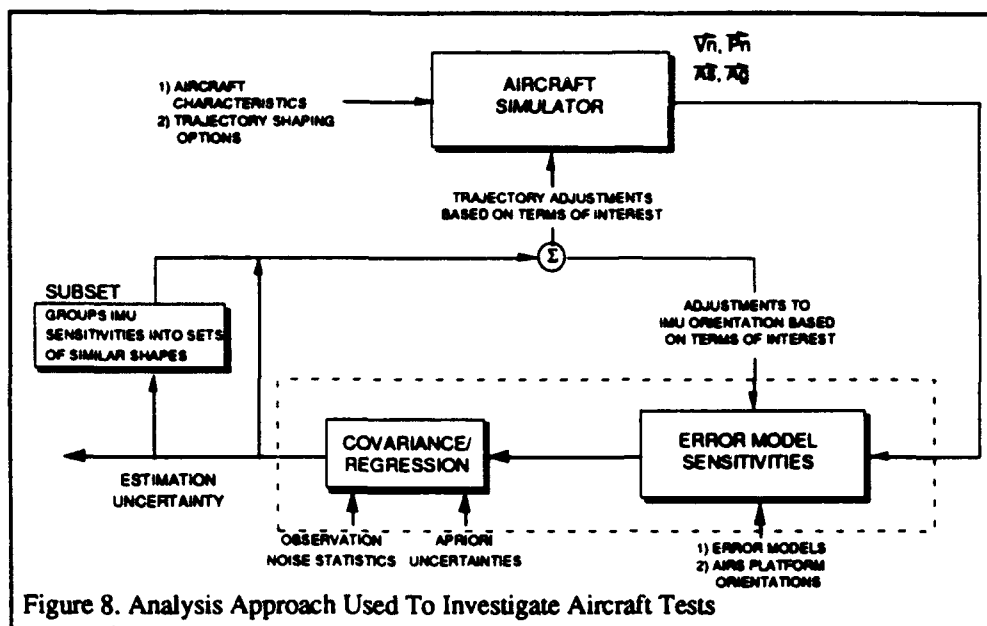


Figure 7. Concept for Testing in an Aircraft with GPS



erating and decelerating segments. The flight parameters outputted included sensed acceleration, velocity, position, rates and coordinate transformations. Initially, dizzying trajectories were evaluated with little regard to particular aircraft or pilot capabilities. In subsequent discussions with Air Force pilots at CIGTF, they suggested that perhaps some Navy pilots could be convinced to fly the sets of continuous 6g, 360 degree vertical and hori-

and GPS data were used to evaluate whether, and by how much, the initial uncertainties in Kalman filter estimates of coefficient values could be reduced as a flight progressed.

## The Aircraft Trajectory Generator

A PC-based aircraft simulator program was developed which used aircraft characteristics and various trajectory shaping options to give aircraft velocities and accelerations at 0.01 second intervals. Typical trajectories included combinations of coordinated horizontal turns, vertical turns including loops, and straight line accel-

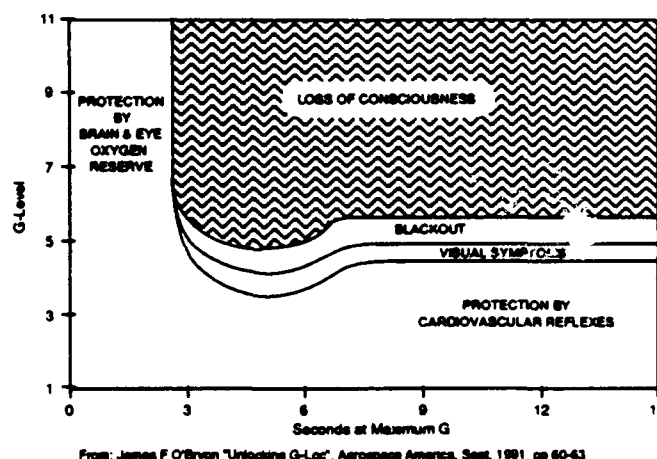
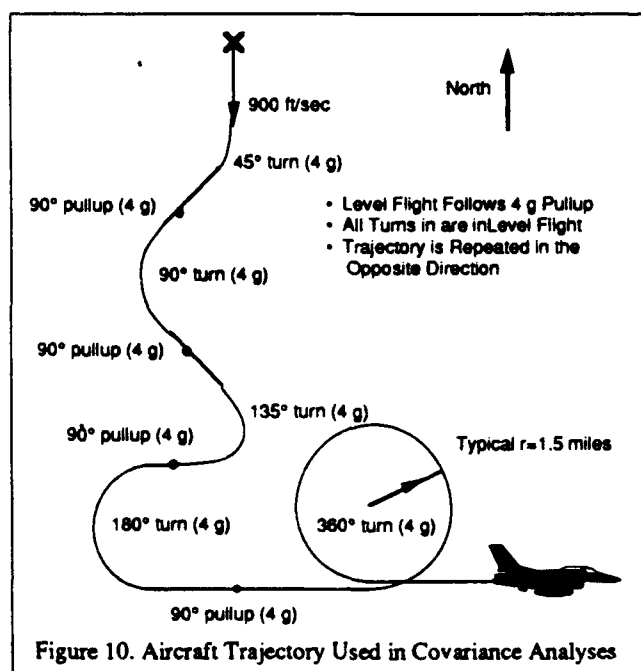


Figure 9. Pilot Physiological Response to High Accelerations

zontal turns that were contained in the original trajectories; however, Air Force pilots would be limited by the body's ability to tolerate high gs for extended periods of time. Figure 9 provides insights into these limitations.

As a result of these conversations, the more realistic, but still demanding, trajectory shown in Figure 10, was defined and used in the covariance analyses. It contains the following maneuvers:

- Straight line acceleration segment to 900 ft./sec.,
- 45° right horizontal turn pulling 4 g,
- 90° pull up - 4 gs, then level,
- 90° left horizontal turn - 4 gs,
- 90° pull up - 4 gs, then level,



- 135° right horizontal turn - 4 gs,
- 90° pull up - 4 gs, then level,
- 180° left horizontal turn - 4 gs,
- 90° pull up - 4 gs, then level,
- 360° left horizontal turn, level, repeated in the opposite direction.

### Covariance Analyses

A covariance analysis program was developed to apply a Kalman filter to the IMU and GPS data and to track the behaviour of the individual instrument coefficient estimate uncertainties as the IMU was subjected to the flight trajectory. Briefly, the Kalman filter is a maximum likelihood estimator, which estimates flight error contributors from comparisons of the IMU-defined flight path to the GPS-determined flight path. The estimated flight error contributors include the modeled instrument coefficients. The better the Kalman filter is able to perform this process, the lower the uncertainty in the values of coefficients determined.

A 69 state Kalman Filter was used to perform this analysis. The filter states were:

- 66 IMU coefficients:
  - Three each position, velocity and attitude errors,
  - Thirty seven Gyro errors: 3 Biases, 9 G Sensitive, 15 G<sup>2</sup> Sensitive, 3 G<sup>3</sup> Sensitive, and 6 G<sup>4</sup> Sensitive terms.
  - Nine SFIR errors: 3 Biases, 3 Scale Factor, 3 Input Axis Alignment
- 3 States of position measurement bias errors,
- Values of initial uncertainties were based on current accepted IMU error models.

Uncertainties for the GPS-determined velocity and position are also included in the model. For these numbers two organizations with extensive experience in using post processing techniques to improve GPS data were consulted; APL and Interstate Electronics (IEC), in Anaheim, CA. The latter supplies the hardware for the acquisition of GPS data to both the Navy and Air Force and also has experience in the reduction and correction of GPS data[5,6,7].

Following discussions with individuals from these organizations, three sets of conditions for GPS measurement noise were used in the covari-

ance analyses.

- Model 1  
Position Error = 10 ft (1 $\sigma$ ) White Noise  
Velocity Error = 0.005 ft/sec (1 $\sigma$ ) White Noise  
Filter Update Interval = 15 sec
- Model 2  
Position Error = 7 ft (1 $\sigma$ ) Bias  
White Noise = 0.01 ft (1 $\sigma$ )  
Filter Update Interval = 1 sec
- Model 2S - Sensitivity to increased noise  
Position Error = 7 ft (1 $\sigma$ )  
White Noise = 0.1 ft (1 $\sigma$ )  
Filter Update Interval = 1 sec

For the analysis, the platform orientation at the start was inertially fixed and oriented to local level, pointing north, with the aircraft pointing south. The results of several computer runs are tabulated in Table 1. Note in the table, that when a 7 ft. bias and 0.01 ft. (1 $\sigma$ ) white noise was assumed for the GPS error, in most cases the initial uncertainty was reduced substantially, in many cases well below 10% of its initial value. The fact that during a flight not all gyros (or accelerometers) will see the same g's is responsible for the spread in the final uncertainties. To evaluate the coefficients of all three instruments, several tests, with the Stable Member at different initial orientations, will be necessary in order to expose each instrument to comparable flight g's. This ability to optimize the orientation of the Stable Member, and to define beforehand an optimum trajectory, is a key to why aircraft tests can be so productive. Contrast this with a missile test where there is little control over the orientation of the Stable Member at launch, or the acceleration profile relative to the various instrument axes.

The results of these analyses indicated that the aircraft test approach would work, the next step was to confirm that the hardware necessary to implement a flight test program could be assembled. The final step was to lay out the elements of a successful test program.

### GPS Errors

Much was learned in meetings with individuals from TRW, CSDL, APS, IEC, and CIGTF. In realtime navigation system tests, CIGTF's experiences indicate that accuracies in the 0.1 ft./sec.,

13 foot region are achievable. Those who have repeatedly shown that the 0.005 ft./sec number can be met through post processing of data, spoke of the care necessary in addressing every detail of the experiment, from antenna selection to the model of the system under test. In this post processing, known GPS errors are removed from the data before they are used in the filter. Errors that remain become modeled states in a Kalman filter solution that includes convergence on GPS, as well as IMU errors.

Before the GPS data are used in the Kalman Filter they are corrected for the following:

- Ionospheric and Tropospheric effects impact the data that reach the aircraft. These effects can be removed from the data by collecting an additional set of satellite data at a ground station in the vicinity of the test area. Since the error drivers reside in high altitudes, these errors will be virtually the same in the aircraft data as well as in the ground data. With the position of the ground station known, errors in its GPS-derived position are assumed to also be in the aircraft GPS position and are removed.
- Antenna Phase Center Migration refers to velocity (and position) variations that result from the relationship between the antenna and
- the instantaneous position of the satellites. For example, a stationary antenna often measures velocity variations in the 0.01 ft./second region simply because the satellites are moving across the sky overhead. This effect can be minimized with proper antenna design and the remaining error modelled as a function of satellite position relative to the antenna.
- Lever Arm Effects describe the error between the location of the aircraft as defined by the GPS antenna and the location described by the IMU. While the test set up can be designed so as to minimize this distance, the optimum set up, co-location of the two points, is not achievable. The trigonometry of lever arm effects can be accurately modeled and compensated for in the data.
- Cycle slips describe those instances in which data are lost for any of several reasons. To correct for cycle slips the data are currently corrected by hand; i.e., an analyst identifies the incorrect datum and inserts what is believed to be the correct value based on interpolation between surrounding points.
- Finally, precision ephemerides for each satellite are used to correct the position of the satellite at the time of the experiment.

Kalman Filter Error State	Units	Initial Condition	GPS Model 1 10 ft.(1 $\sigma$ ) 0.005 ft./sec.(1 $\sigma$ )		GPS Model 2 7 ft. bias(1 $\sigma$ ) 0.01ft (1 $\sigma$ )		GPS Model 2S 7 ft. bias (1 $\sigma$ ) 0.01ft (1 $\sigma$ ) WN	
Position	ft.	15	1.0	.07*	1.0-2.6	.17	1.6-3.7	.1-.25
Velocity	ft./s	0.01	<0.002	.2	<0.0001	.01	<.00024	.018-.024
Attitude	asec	1	0.1-0.2	.2	<0.01	.01	.024-.038	
Gyro Bias	°/Hr	0.001	5.0-8.4x-4	.5-.8	1.3-3.4x-4	.13-.34	3.7-7.0x-4	.37-.7
G-Sens	(°/hr./ft./s <sup>2</sup> )	1.4-4.5x-5	0.14-4x-4	.88-1.0	1-11x-6	.07-.24	6.7-34x-6	.48-.76
G <sup>2</sup>	°/hr./ft./s <sup>2</sup> ) <sup>2</sup>	8-33x-8	8-33x-8	1.0	5-100x-9	.06-.3	1.6-26x-8	.2-.8
G <sup>3</sup>	u°/hr./g <sup>3</sup>	200	90-176	.45-.88	17-52	.09-.26	70-121	.35-.61
G <sup>4</sup>	u°/hr./g <sup>4</sup>	200	45-155	.23-.78	<20	.10	22-59	.11-.3
Accl bias	ug	0.25	0.23	.92	.075-.16	.3-.64	.14-.20	.56-.8
SF	ppm	0.5	.26-.42	.52-.84	<.05	.1	.06-.12	.12-.24
FI1	ug/g <sup>2</sup>	.05	.042-.049	.86-.98	.0025-.012	.05-.24	.015-.03	.3-.6
FX1	ug/g <sup>2</sup>	.05	.035-.046	.7-.92	.002-.0135	.04-.27	.009-.021	.18-.42
FOX	ug/g <sup>2</sup>	.05	.048-.05	.96-1	.005-.026	.1-.52	.042-.047	.84-.94
FSX	ug/g <sup>2</sup>	.05	.048-.05	.96-1	.004-.016	.08-.32	.02-.044	.4-.88
GPS pos Bias	ft.				1.0-2.5	.14-.36	1.5-3.7	.21-.53

\* indicates the ratio of final over the initial value; i.e., a 0.1 indicates that the initial uncertainty was reduced to 10% of its initial value - this is good, 0.9 indicates that the uncertainty was reduced to 90% of its initial value - not very good.

Table 1. Results of Covariance Analyses Indicating Reduction in Initial Uncertainty as a Function of GPS Characteristics

While not related to GPS, but very important, Gravity Disturbance Estimates must be carefully compensated. As a start, a gravity map of the test area is essential; however, the accuracy of the Peacekeeper system suggests that in preparation for a series of experiments, repeated tests with very benign acceleration profiles could be performed to extrapolate the value of gravity over areas of the map that may be less detailed. In support of such an effort, the Coast and Geodetic Survey group has experience with the use of laser altimeters and retroreflectors that permit the knowledge of altitude to 6 inches ( $\sim 0.05$  micro-g).

### Hardware Requirements

Another aspect of the feasibility study was to determine what hardware would be needed to support a system, and assure that it would fit in a high performance aircraft that is available to the test group at CIGTF. The hardware necessary to support an MGCS in an aircraft includes:

- The MGCS test article,
- The Guidance Cooling and Condensing Unit (GCCU), which provides and circulates Freon to the pressure and temperature requirements needed to maintain precise MGCS temperature and extract its almost 1200 watts of power.
- Aircraft Power Conversion Unit - needed to convert aircraft 400 Hz to the 67 VDC required by the MGCS and the various other voltages required by the test hardware,
- MGCS on board data recorder,
- MGCS status transmitter for real time assessment of MGCS health and status,
- GPS Antenna,
- GPS Translator - The translator was selected because it does not eliminate any of the information contained in the original GPS data as would be the case with a Receiver,
- Assorted cables and hoses required to interface the various items with each other and a truck which would be used to control the MGCS while on the ground, and,
- Various mounting brackets and trusses.

MGCS tests on the Holloman sled have been performed for several years, as a result, much information is available to provide insight into the relative size of most of these items. In meetings with personnel at CIGTF, various options were discussed. Although an F-16 was initially considered, it was decided that an F-111, although not as hot as an F-16, would be adequate, and its large ordnance bay would reduce the demands on the hardware designer. At first it was anticipated that the entire sled forebody could be raised directly into the ordnance bay. A subsequent review of aircraft drawings indicated that the ordnance bay was not large enough to accommodate the entire sled forebody and that the required hardware would be re-mounted on a pallet designed to fit into the available space. An existing test van that contains ground support equipment and computers for MGCS tests on the sled could be applied directly to aircraft tests.

### A Flight Test Program

With the feasibility of the approach established, a two-phase program was recommended that would permit achieving goals with minimum risk. In the first phase, flight test data would be gathered in a C-141 transport. This would provide a pathfinder for later tests conducted in an F-111. First phase efforts include:

- Expand Covariance analysis to include detailed GPS and gravity error models,
- Address GPS processing concerns, including:
  - Processing through data drop outs
  - Handling of gravity model,
  - Lever arm corrections,
  - Antenna phase center migration
- Update test support and post-processing software
- Procure and modify required hardware, including,
  - GPS translator
  - High-speed data recorder
  - Aircraft power converter
- Define F-111 antenna requirements,
- Define F-111 aircraft modifications.

C-141 transports are assigned to Holloman

and are available to support testing at the base. These are certified for continuous 2 g turns, making it possible to collect data and check out software and test approaches while using MGCS support hardware that are currently operating in support of Holloman sled tests. The size of the C-141 makes it possible to mount the entire sled forebody containing the MGCS and its environmental control hardware, and the test van that supports the testing into the aircraft with only minor modifications. An appropriate GPS antenna would be added and its distance to the IMU accurately measured.

Existing post-test tools and techniques, developed to support Peacekeeper and Minuteman sled and/or flight tests, including the GPS flights would be used. In the data reduction software the function of the sled space/time reference system would be replaced by GPS data. A gravity field covering over 140 square miles, mapped by DMA for the 46th Test Group at Holloman is available. By first flying on the C-141, actual aircraft test data, supporting verification of all techniques and software, could be accumulated in a matter of months. Tests in an F-111 modified to its final, optimized configuration would then permit the gathering of system data in a high-g environment. The tasks leading to the second phase, F-111 tests include:

Modifying the aircraft to carry the hardware necessary to support an MGCS:

- Integrate the MGCS onto a pallet that could be raised and lowered into the aircraft weapon's bay.
- A telemetry system for transmitting MGCS and translator data to a ground station,
- A closed loop MGCS coolant unit similar to the design that is used on sled tests,
- Power conversion capability to convert on-board 400Hz power to the 67 VDC required by the MGCS,
- Provisions for hot transfer from van power and control to aircraft power and control. While batteries are not allowed in aircraft, a battery in the van would parallel the ground power unit as it was being disconnected to assure a transient-free transfer of power,

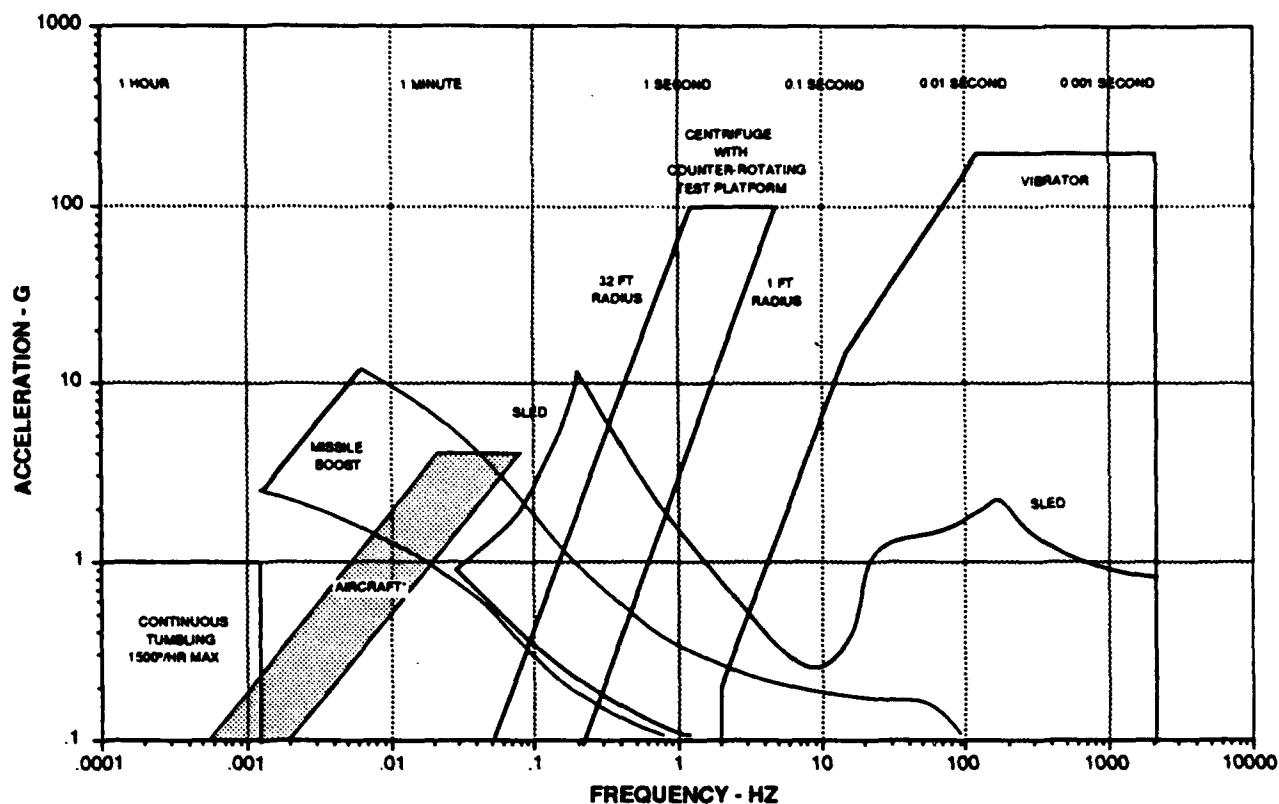
- Provisions for monitoring and telemetering real-time MGCS health to a ground station while the tests are under way, enabling ground control to direct the pilot to return to base in the event a test must be aborted,
- Design of an antenna configuration that assures continuous satellite monitoring over the full breadth of aircraft attitudes during the flight tests. For example, the Peacekeeper missile was fitted with a specially designed segmented antenna that provides 360 degree coverage. For the aircraft version a special antenna may have to be designed. This would require analyses of flight profiles to assure that signals from the necessary number of satellites are captured throughout the entire flight profile.

Specify, procure, integrate and check out the various items of ground support equipment:

- Receiver and high-rate magnetic recorder to record translated-satellite and MGCS data.
- A translator data processing station to perform the post flight signal tracking.
- Modifications to the van that is used to support MGCS tests on a sled.

It will be necessary to document all the details needed to support an individual flight test:

- Defining the trajectories that permit visibility into the coefficients of interest,
- Analyze satellite ephemerides to identify the best time of day for testing to assure that satellites are in view of the aircraft and are not shadowed by various aircraft parts as the aircraft executes the designated maneuvers,
- Definition of test time lines, beginning with system turn-on, followed by calibration on the ground, followed by the performance of a series of test flights. Each flight may be of 30 to 45-minute duration, returning to the starting point so that the IMU can be reinitialized and re-oriented for the next test,
- Pilot instructions for the different flight trajectories will have to be documented and briefed.



\*Aircraft testing based on a 4 g limit at air speeds of 900fps and 250fps

Figure 11. Acceleration and Frequency Characteristics of Commonly Used Inertial System Test Environments  
[Aircraft characteristics added to Tom Reed's plot from Reference 9]

Finally, the data collected would be reduced and analysed and, if necessary, any subsequent series of tests defined.

## CONCLUSIONS

From the results of this study the authors draw the following conclusions:

1. Aircraft testing, involving GPS, is a viable approach to gathering performance data on high precision missile guidance systems without losing the test asset.
  2. The risks associated with developing the aircraft test capability described are low since no part of the effort requires any advancement in the current state of the art.
  3. Figure 11 above shows the acceleration and frequency characteristics of the various environments used for inertial system and component testing. Aircraft testing permits extraction of individual instrument characteristics while best approximating the missile environment.
- In this figure note how:
- a. Laboratory tests, while providing a time-proven vehicle for expanding our knowledge of the instrument models, do not fall anywhere near the missile use environment; results must be extrapolated to the use environment.
  - b. Vibration tests cover only a small part of the missile's higher frequency region, and require that assumptions be made about the frequency in-sensitivity (or sensitivity) of individual instrument coefficients in order to extrapolate results to the lower frequency use environment.
  - c. Centrifuge tests also cover only a small portion of the missile environment. Historically, attempts at extracting high-performance system data from centrifuge tests have resulted in more questions than answers being generated.
  - d. Sled tests provide a test environment that

covers a large portion of the missile profile. However, while successful in extracting azimuth information and generating a "lumped" accuracy assessment, the ability to extract individual instrument coefficients is limited by the short duration of the test and the inability in that short time to resolve platform drift to the required accuracies.

4. Although the Peacekeeper all-attitude stable platform can operate through the maneuvers described, some minimal modifications to these trajectories could adapt them to a limited rotation, gimballed system, such as the one contained in Minuteman.
5. The process of correcting GPS data is currently very time consuming. This process must be automated if GPS is to be used to its full advantage by future generations of test engineers.
6. In today's fiscal environment the expense of developing an aircraft test capability could be considered high, yet the investment is quite small when compared to the cost of on-going missile test programs in which the multi-million dollar assets flown are lost forever.

## ACKNOWLEDGEMENTS

The authors wish to acknowledge the many individuals from organizations around the country who contributed to the body of information presented in this paper.

Many individuals at Rockwell supported the effort. Tasos Gianotas was fast and accurate in writing the necessary programs and performing the many computer analyses described in the paper. Continuing conversations with his manager, Jerry Grimaldi, Rockwell's Guru of flight radar data regression analyses, made sure that our results were congruent and our conclusions made sense. Gerry Kimball, and Tom Williams were always available to discuss an idea and to share their technical experiences and in-sights. From Rockwell's group of GPS experts, Ed Martin and Richard Sfier, spoke on the issues of hardware capability, limitations and concerns.

APL's Larry Levy, gave us the benefit of his experience with Trident flight data analysis, providing information on the handling of GPS

data. Richard Brooks, Bob Crane and Robert Snow of IEC gave us suggestions for data reduction approaches and the hardware necessary to collect the flight data.

Finally, Grady Nickelson and the other folks at CIGTF, shared their experiences with CIRIS while their Flight Test Engineer, Lt Robert Rice provided insights into the real test situation, aircraft drawings and characteristics.

## REFERENCES

1. Captain T. Rude, etal, "Peacekeeper Guidance Error Estimation using the Global Positioning System", AIAA Missile Sciences Conference, Monterey, CA, February 1993.
2. TRW, Draper, RI and APL, "GPS Experiment on Peacekeeper Flight Test GT-06 PA", June 1 1992.
3. TRW, Draper, RI and APL, "GPS Experiment on Peacekeeper Flight Test GT-07 PA", June 1 1992.
4. Levy, L.J. and Porter, D.W., Johns Hopkins Applied Physic Laboratory, "Application of Maximum Likelihood Parameter Identification to Test and Evaluation of Inertial Navigation Systems". Proceedings of the Fifteenth Biennial Guidance Test Symposium, September 24-26, 1991.
5. K.M. Blankshain, Interstate Electronics, "Accurate Tracking of High Dynamic Vehicles with Translated GPS". The Institute of Navigation, Satellite Division, International Technical Meeting, September 19-23, 1988
6. A.J. Kanyuck, Interstate Electronics, "Tracking Accuracy of the GPS Translator Processing System", Tenth Joint Range Instrumentation Accuracy Improvement Group Meeting, Western Space and Missile Center, February 1991
7. R. Crane, R. Brooks, K. Blankshain, R. Snow, Interstate Electronics, "Post-Mission Processing of Translated GPS Tracking Data", Tenth Joint Range Instrumentation Accuracy Improvement Group Meeting, Western Space and Missile Center, February 1991
8. J. Hand, "CSDL-R-2262 Space Shuttle as National Test Bed for Guidance Subsystems,"



Inertial Instruments and Components", Charles Stark Draper Laboratory, August 1, 1990

9. T.E. Reed, "C-4721 Missile Inertial Guidance System Model Validation by Centrifuge Testing", Charles Stark Draper Laboratory, July 1976

10. "The High Speed Test Track - Facilities and Capabilities", Munitions Systems Division, 3246th Test Wing, 6585 Test Group, Test Track Division, Holloman Air Force Base, April 1989

11. A. Truncale, "Evolution of Peacekeeper Inertial Guidance Components and System Design", AIAA Guidance, Navigation and Control Conference, August 12-14, 1991.

12. J. Cuevas, "CSDL-C-6311 The History of AIRS Rocket Sled Testing MPMS Through Peacekeeper", Joint Services Data Exchange, October 26-29, 1992.

# **Guidance and Control Expert System Shell (GCESS) Applications**

**Charles F. Saffle Jr.**

**Aerospace Guidance and Metrology Center  
Missile Automatic Test Equipment Branch  
Newark AFB Ohio 43057-0005**

**01 June 1993**

**Unclassified**

## **ABSTRACT**

The development of diagnostic applications using the Guidance and Control Expert System Shell (GCESS) is presented. GCESS is a government owned, engineering software tool used to develop and run automated diagnostic applications. The shell uses a Fault Tree Paradigm approach for diagnosis, and was originally designed for use by the Peacekeeper Missile Guidance and Control repair depot and contractor personnel. Additional applications have been developed using this shell.

This paper will give an overview of the operation of GCESS, pertaining to application development. The focus will be on the Inertial Measurement Unit (IMU) Expert System, the Stable Member Assembly Expert System, and the 8569B Spectrum Analyzer Expert System applications, at the Aerospace Guidance and Metrology Center (AGMC), Newark AFB OH.

## **GCESS BACKGROUND**

The Aerospace Guidance and Metrology Center (AGMC) in Newark, Ohio, is responsible for diagnosing and repairing faults in the Guidance and Control (G&C) equipment used in the Peacekeeper Missile. Diagnostic and repair support is provided to AGMC by four major G&C associate contractors (ASCONs): Northrop Corporation (Inertial Measurement Unit and gyros), Rockwell International (Missile Electronic Computer Assembly), Honeywell, Inc. (gyros and accelerometers), and Litton Industries (accelerometers). The support provided to AGMC by the ASCONs includes custom-designed software programs to diagnose faults in both airborne and ground support equipment. These programs are uniquely designed and maintained for different levels of diagnostic support from the major assembly to the circuit card.

Two fundamental problems were being experienced with this approach to the G&C maintenance task. The first problem was the high ongoing cost of maintaining a variety of diagnostic software that had been developed by the ASCONs using conventional software development methods. Different high-level languages, diagnostic architectures, and user interfaces have required extensive involvement of experienced personnel to improve diagnostic accuracy and coverage. The second problem was the continuing involvement of ASCON experts who were occasionally still required to help AGMC diagnose the causes of G&C equipment faults. It became evident that the troubleshooting methods employed by the experts had not been sufficiently mechanized within the then present deployed diagnostic software programs.

Expert system solutions to these problems were investigated. An off-the-shelf commercial shell could not be found which fully satisfied Air Force requirements. Therefore, Inference Corporation's ART-IM (Automated Reasoning Tools for Information Management), a commercial, general purpose, PC based, expert system shell, was chosen as the host shell for

GCESS. ART-IM was chosen as the expert system shell upon which to base GCESS because it provided a number of integrated facilities that were believed to be important to the GCESS shell (Figure 1). Inference Corporation and the Peacekeeper ASCONs worked together to develop GCESS.

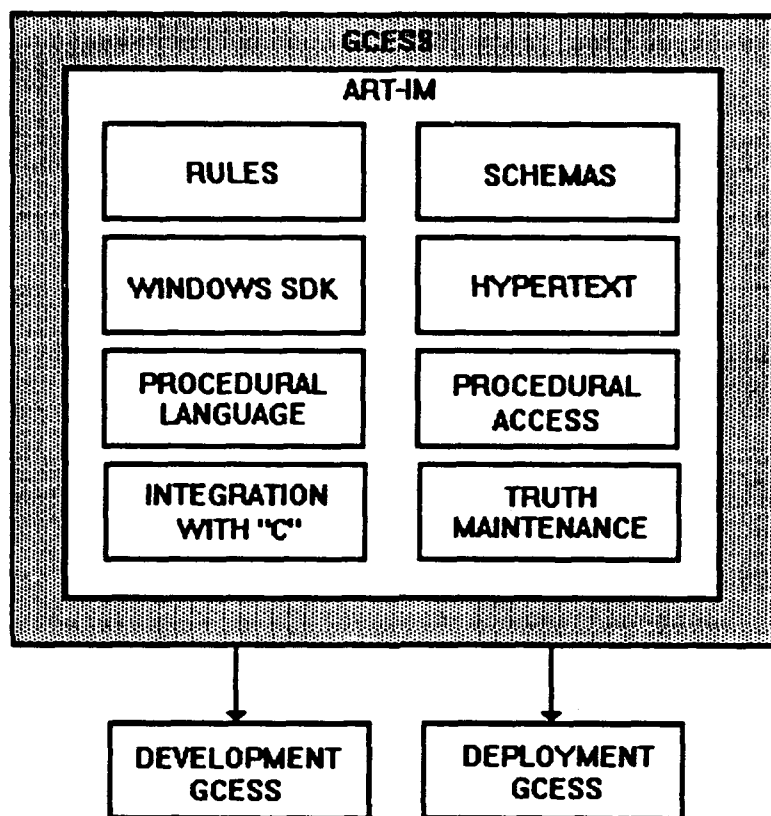


Figure 1

GCESS runs in a Microsoft Windows environment and was designed as an application program of ART-IM. In reality, GCESS is a shell within a shell. Simply stated, GCESS is a friendly user interface to the ART-IM expert system shell. GCESS is both a delivery and development tool. It is for programmers, engineers, and diagnosticians who want to build an automated diagnostic system. It is also an end user tool for technicians to run diagnostic applications, view, and interpret their results. Using GCESS, developers can create diagnostic applications based on the fault tree paradigm. GCESS provides editing and debugging facilities for incrementally creating the fault tree, defining the interfaces to outside systems, loading and running applications, viewing recommendations, and generating reports.

## INTRODUCTION

An overview of the processes involved in application development with GCESS will first be discussed. This will include the major components of GCESS: fault tree based diagnostic system creation and configuration, Automatic and Interactive operating modes, and creation of deployment versions. The focus will then turn to three expert system applications at AGMC which use GCESS: the Inertial Measurement Unit (IMU) Expert System, the Stable Member Assembly Expert System, and the 8569B Spectrum Analyzer Expert System. An overview of what each application does, and the process through which each application was developed will be discussed.

## APPLICATION DEVELOPMENT WITH GCESS

When the GCESS development version is first started in Windows, the main screen is displayed (Figure 2).

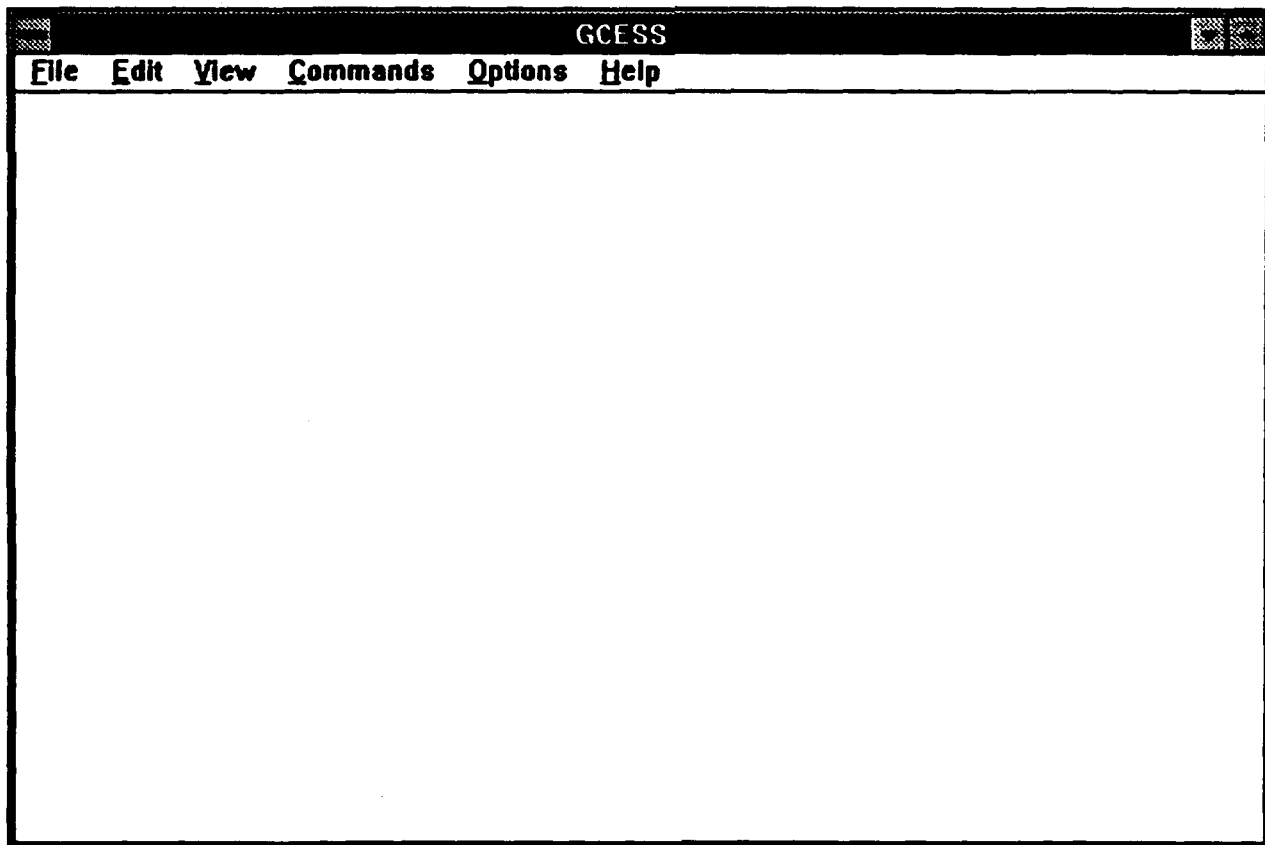


Figure 2

From this screen a new knowledge base may be created, or an existing knowledge base may be edited. Creation of a new knowledge base begins by selecting "New Knowledge Base" from the "File" menu bar option. The developer then names the application which is being created. GCESS applications may operate in Automatic or Interactive modes. Normally, GCESS will be used in Automatic mode. This requires GCESS to be connected to an external data server which will retrieve test data from Automatic Test Equipment (ATE) stations. The external data server is used as a repository for symptoms and measurement data needed by the application. The name and location of the data server is declared to the application during the configuration process.

GCESS provides a default configuration for all applications, but most, if not all, applications will require modifications to the configuration files. This information is accessed by selecting "Configuration" from the "Options" menu bar option. The configuration information which the user is able to modify consists of default values governing GCESS behavior, the definition of various filename paths, and definitions for pre- and post-processing functions.

GCESS uses fault classes organized into fault trees to support diagnosis. A fault class expresses a diagnostic rule in the form: "if these conditions are true, then take this action". Within a fault tree, there are three basic types of fault classes. They are initial, intermediate, and terminal. Each fault class may exhibit the characteristics of only one type, or any combination of the three.

A fault tree based diagnostic system is a program which performs an orderly decomposition of a problem from a generalized class of faults to a single fault. In GCESS, an external data server attached to a test station generates symptoms which indicate that something is wrong in the entity being diagnosed. These symptoms are then sequentially processed by matching them to a top level node in the fault tree. Using the model for a fault tree below (Figure 3), each node of the fault tree represents a distinct test from least restrictive at the top of the tree to most restrictive at the bottom. A fault tree acts very much like a filter in which symptom information enters the fault tree at the top, filters through the nodes, which are called fault classes, eventually passing through to a terminal fault class at the bottom of the fault tree. Each terminal fault class then produces recommendations when the problem has been identified.

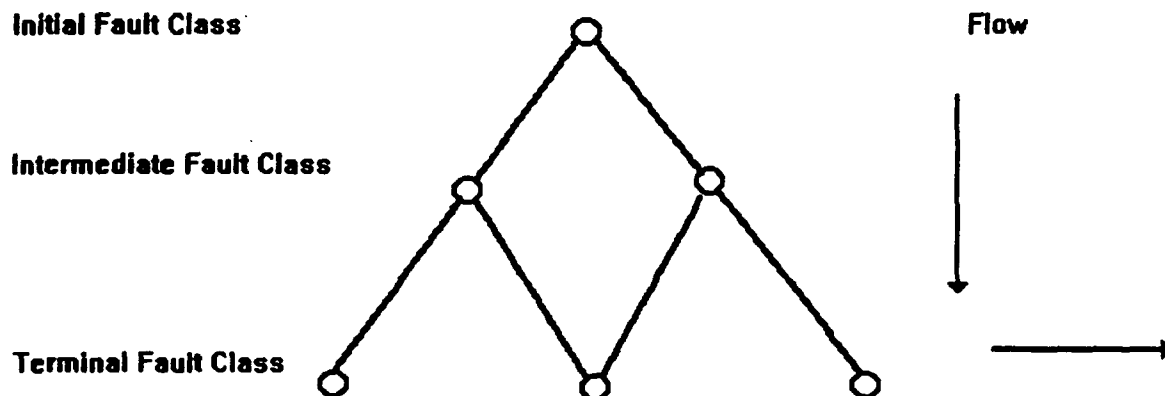


Figure 3

At the top level GCESS performs the following loop during a diagnostic run:

1. Select a symptom to process.
2. Determine the initial fault class.
3. Iterate through the fault tree anchored by the initial fault class.

In every node of the fault tree, tests are performed which can result in one of three outcomes:

1. The determination is made that further exploration along the current fault tree path is unnecessary.
2. The problem is decomposed into multiple hypotheses.
3. The fault is identified resulting in the generation of a recommendation.

As previously stated, GCESS provides the capability for creating two types of applications: Automatic and Interactive. To construct an automatic application you would normally go through the following steps:

1. Identify the types of symptoms and measurements.
2. Create a data server.
3. Identify replicated units, name, and identify value variables needed to support them.
4. Identify and determine the relationships of the fault classes needed to perform the diagnosis, and the roots of the diagnostic trees.
5. Create a new GCESS knowledge base.
6. Edit the initial fault class mappings.
7. Edit the measurements, name, and identify value variables to be used.
8. Edit the fault classes.
9. Configure for using the data server.
10. Save the knowledge base.
11. Create hypertext help files.
12. Run the knowledge base, test it, edit it, and rerun it until satisfied, during one or several sessions, saving after changes.
13. Deploy the application.

As step 2 above implies, to keep GCESS independent of particular data formats, an application specific data server may be necessary. This is constructed as a separate module (Dynamic Link Library or DLL) in the Windows environment. A DLL is a window library of functions that are linked at program execution time. These libraries help reduce the overall size of a program by being loaded in memory when called. The data server required by GCESS will perform all the functions that an application will require which GCESS cannot perform. Applications which operate in a fully Interactive mode may use a generic GCESS default data server called "default.dll". For applications which operate in either a fully or partially Automatic mode, an application specific data server must be developed. This is a programming function and is accomplished outside of GCESS in a C language environment.

To construct an interactive application you would normally go through the following steps:

1. Plan a diagnostic decision tree and name all fault class nodes including the first, or root node, that asks the first question.
2. Create a new GCESS knowledge base.
3. Edit the initial fault class map to choose the root fault class for the dummy symptom (in the default.dll).
4. Create the fault classes.
5. Configure for using the default.dll data server.
6. Save the knowledge base.
7. Create hypertext help files.
8. Run the knowledge base, test it, edit it, and rerun it until satisfied, during one or several sessions, saving after changes.
9. Deploy the application.

GCESS applications may operate in an Automatic state, an Interactive state, or a combination of the two states. Applications that operate in the Automatic state may be optioned to load and operate on any one symptom or all symptoms. These symptoms are diagnosed sequentially. In the Interactive state, a default symptom is entered which allows the application to enter its fault tree and thus query the user for answers to its questions. Within the Automatic and Interactive states, applications usually run in a Data Mode, but may also be run in a Tutorial Mode. In Data Mode, fault class conditions are evaluated by GCESS. In Tutorial mode, the fault class conditions are displayed to the user, who must determine whether they are to evaluate TRUE or FALSE. This reveals the methods and processes of the applications diagnoses to the user.

The last step after an application's knowledge base is complete, is to create a deployment version. This is accomplished by selecting "Deployment" from the pull down File menu. GCESS responds by creating a series of C source files with extension '.C' and '.H' along with a makefile named 'makefile' for creating the deployment executable. GCESS requires that the user have the Microsoft C Compiler Version 7.0 installed prior to compiling the deployment code. An executable is created by changing the default directory to the deployment directory and issuing the nmake utility called 'nmake' from the DOS command line. The result is a C language program representing the application, compiled and linked for the Windows environment. This process requires additional disk space but assures that diagnostic knowledge is truly "compiled in" to deployed applications. For this reason, GCESS application development requires Windows C development tools.



## **IMU EXPERT SYSTEM**

The IMU Expert System was developed by Northrop to aid AGMC engineers and technicians in the troubleshooting and repair of the Peacekeeper IMU. In keeping with the aforementioned steps of application development in the automatic state, the process of building the IMU Expert System is as follows:

1. Identify the types of symptoms and measurements: Functional testing of the IMU on its ATE stations provides large amounts of measurement data in the form of datasets and a results file. From the types of measurements being made in any given test, corresponding symptom names were applied to the measurements. The symptom names became the initial fault classes of the fault tree.
2. Create the data server: A data server was created that would read the format of the datasets and results file. This data server recognizes when a failure flag has been set in the data, and will transport the failing measurement to its corresponding initial fault class. From there, the expert system will diagnose the symptom by propagating it through the fault tree to an eventual terminal fault class.
3. Identify replicated units, and name, and value variables needed to support them: By accomplishing this step, the size of the expert system may be reduced.
4. Identify and determine the relationships of the fault classes needed to perform the diagnosis, and the roots of the diagnostic trees: The IMU knowledge base currently contains well over 1000 fault classes. Approximately 400 fault classes are "root", or initial fault classes. This results in a fault tree network that is approximately 400 fault classes in width and varying from 1 to 5 fault classes in depth.
5. Create a new GCESS knowledge base: This is the actual use of the GCESS development program. Up to this point only the data server has been created and the logistics of the knowledge base have been laid out. The new knowledge base is now named and configured. If the data server (from Step 2) is not yet complete, the configuration may be updated upon its completion.
6. Edit the initial fault class mappings: The initial fault classes (i.e. symptom names) are entered into the knowledge base.
7. Edit the measurements, name, and value variables to be used: The types of measurements, their names, and their value variables are entered for all the presently known fault classes being created in the knowledge base. This creates the entire fault tree.

8. Edit the fault classes: Now that the fault tree has been created, information for fault diagnosis is entered into each fault class. This information may include the rules and functions that act upon the symptoms presented to the fault class, textual explanation of why the specific rules and functions are used, textual explanation of any diagnosis, any graphics files that would be applicable.
9. Configure for using the data server: If not already accomplished the data server should be configured into the knowledge base.
10. Save the knowledge base
11. Create hypertext help files.
12. Run the knowledge base, test it, edit it, and rerun it until satisfied, during one or several sessions, saving after changes.
13. Deploy the application: By deploying the application, the knowledge base is compiled and linked, producing an executable program. This reduces the amount of disk drive and memory space required, the amount of time the application requires to come on line and then run, and eliminates the possibility of the knowledge base inadvertently being changed.

## **STABLE MEMBER ASSEMBLY EXPERT SYSTEM**

The Stable Member Assembly Expert System was developed by AGMC to aid engineers and technicians in the troubleshooting and repair of the Peacekeeper Stable Member Assembly. With the Peacekeeper IMU Expert System in place at AGMC, the next logical step was to develop an expert system for a Peacekeeper related component. Since the Stable Member Assembly is a lower level assembly of the IMU, and the testing of the two assemblies is similar, it was selected as the next expert system to be developed.

The Stable Member Assembly ATE functional testing produces datasets and results files in the same format as the IMU. In addition, over 50% of the testing done on the Stable Member Assembly is similar to testing accomplished at the IMU level. As a result, the pre- and post-processors and the knowledge base for the IMU Expert System could be modified and used for creating the Stable Member Assembly Expert System.

The IMU Expert System was used as a template for creating the Stable Member Assembly Expert System. The process used to construct this expert system deviates somewhat from the process that would be used to construct a new expert system. This process went as follows:

The types of symptoms and measurements in the datasets and results file were first identified and compared to the IMU Expert System's. The differences found would later become modifications, additions and/or deletions in the initial fault class map. The IMU Expert System's data server (i.e. pre- and post-processors) was then renamed and modified to accept the differences in the Stable Member Assembly's datasets and results file.

The IMU Expert System's knowledge base was then entered in GCESS and renamed the Stable Member Assembly Expert System. All initial fault classes (i.e. symptom names) that were not Stable Member Assembly related were deleted. An example would be a set of fault classes that represent a functional test that is run at IMU level testing but not at Stable Member Assembly testing. The resulting "orphaned fault classes" (i.e. fault classes without an initial fault class) were then assessed to determine if they could be easily modified and used in new fault classes representing new tests that were not performed at IMU level testing. If the assessment was positive, the fault classes were retained and modified. If the assessment was negative, the "orphaned fault classes" were deleted. New initial, intermediate, and terminal fault classes, were then created for Stable Member Assembly specific tests. All of the fault classes in the fault tree were then edited and modified to reflect the Stable Member Assembly functional testing. This include changing the rules and functions that act upon the symptoms presented to the fault class, the textual explanation of why the rules and functions are what they are, the textual explanation of any diagnosis, any graphics files that would be applicable, and the hypertext help files.

When the knowledge base was completed, the new data server was configured into the knowledge base, and the knowledge base was saved. It was tested and debugged, and the final version saved and deployed. The Stable Member Assembly knowledge base currently contains well over 900 fault classes. Approximately 300 fault classes are "root", or initial fault classes. This results in a fault tree network that is approximately 300 fault classes in width and varying from 1 to 5 fault classes in depth.

## **8569B SPECTRUM ANALYZER EXPERT SYSTEM**

The 8569B Spectrum Analyzer Expert System was developed by AGMC to aid Test Measurement and Diagnostic Equipment (TMDE) technicians in the troubleshooting and repair of the 8569B Spectrum Analyzer. This spectrum analyzer was a relatively new TMDE area workload at AGMC. The TMDE technicians were experiencing problems troubleshooting this piece of equipment. No one technician intimately knew the complete operation of this spectrum analyzer. Different technicians were knowledgeable, or experts, on various sections of the spectrum analyzer. This was an ideal situation for applying an expert system. The knowledge and experience of the different technicians were input and combined into a single cumulative knowledge base. This expert system can now be used by any technician to aid in the troubleshooting and repair of the spectrum analyzer.

Time, manpower restraints, and workload requirements, mandated that an expert system be deployed, in as little time as possible, that would help technicians who were untrained in spectrum analyzer operation, to troubleshoot spectrum analyzer faults. It was determined that a fully interactive expert system would best meet the above requirements. The 8569B Spectrum Analyzer is functionally tested on an ATE station. The 8569B Spectrum Analyzer Expert System was designed as an off-line, stand alone, fully interactive system. The expert system's fault tree attempts to follow the flow of the ATE functional testing. When an ATE functional test failure occurs, the spectrum analyzer is removed from the ATE, freeing the ATE for continued use, and the expert system is activated to aid in troubleshooting.

This expert system was designed following the steps listed for construction of interactive applications. The expert system begins with one initial fault class which queries the user to select from one of two types of failure modes. Depending on the mode selected, the expert system then asks the user to perform various tests and measurements in response to a series of questions. These questions propagate through the fault tree network to an eventual terminal fault class which will produce either repair recommendations or further test recommendations. This expert system was built in the manner that a knowledgeable technician would troubleshoot a spectrum analyzer fault. Depending on the location and nature of the fault, the technician would troubleshoot in one of two ways. In the first method, the technician would selectively troubleshoot back through the modules from the failure output until the origin of the fault was found. In the second method, the technician would go to the start of the section in which the failure output occurred and selectively troubleshoot forward through the modules until the origin of the failure was found.

Three GCESS functions were used in this interactive expert system to propagate down through the fault tree. They are: QUESTION\_YES\_OR\_NO, QUESTION\_MULTIPLE\_CHOICE, and QUESTION\_FOR\_VALUE. Answering yes or no to a question, selecting a choice, or entering a value in response, would determine the path in which one would take to propagate through the fault tree to a final recommendation.

This expert system was developed and deployed in less than 300 total man-hours using one engineer to extract the "expert knowledge" from two TMDE technicians. When initially deployed, this expert system contained over 400 fault classes and the depth of the fault tree varied from 4 to 26 fault classes. Since deployment of this expert system to TMDE, it has been used to help familiarize and train other technicians in the operation, and troubleshooting of faults, with the 8569B Spectrum Analyzer.

## **SUMMARY AND CONCLUSION**

GCESS operating in the ART-IM environment is a versatile tool which has found many applications at AGMC. With the addition of GCESS operating in the ART Enterprise environment, many more future applications are envisioned.

GCESS is currently being upgraded and ported from Inference Corporation's ART-IM shell (GCESS Version 2.0) to its ART Enterprise shell (GCESS Version 2.2). GCESS in ART Enterprise will provide a state-of-the-art tool for efficient creation of hybrid intelligent systems. The advantages of operating in the ART Enterprise environment, compared to the ART-IM environment are as follows:

1. Simple applications require no programming.
2. Point-and-click screen building.
3. Query, join, and update of data in distributed databases.
4. Key word retrieval of unstructured information.
5. Streamlined application development.
  - Rapid creation of proof-of-concept demonstrations.
  - Decreased development time.
6. Object-oriented architecture facilitates code re-use.
7. Portable among different platforms.
8. Integrates with procedural code for maximum flexibility.
9. Runtime applications created without a compiler.

With the IMU Expert System and the Stable Member Assembly Expert System in operation at AGMC, diagnosis of ATE functional test failures, which once required engineers spending hours sifting through stacks of data, is now completed in mere minutes. Both of these expert systems are continually updated to reflect the corresponding updates to the ATE functional test software/hardware.

The 8569B Spectrum Analyzer Expert System has served its purpose of aiding technicians in troubleshooting spectrum analyzer faults, and familiarizing and training new technicians with spectrum analyzer operation. After approximately four months of use in the TMDE area, the knowledge of the technicians responsible for the spectrum analyzer has equaled, or exceeded, that of the expert system. When the expert system's knowledge is exceeded, the new information is input from the technician to the expert system's knowledge base, and an updated version of the expert system is deployed. If determined to be cost effective, future updates of this expert system would be to evolve it into an automated system which would retrieve test data from the ATE to perform failure diagnosis, similar to the IMU and Stable Member Assembly expert systems. However, with looming workforce reductions and realignments, the 8569B Spectrum Analyzer Expert System in its present form will remain a valuable asset.

## **REFERENCES**

- Fischer, R. L. A Guidance and Control Expert System Shell for Peacekeeper Missile Maintenance Applications. Proceedings of the Fifteenth Biennial Guidance Test Symposium, 1991.**
- Fischer, R. L. A Guidance and Control Expert System Shell for Peacekeeper Missile Maintenance Applications. Proceedings of the Twenty-first Joint Services Data Exchange for Guidance, Navigation and Control, 1992.**
- Inference Corporation. GCESS Application Developer's Guide Version 2.0  
Prepared for Northrop Electronic Systems Division, 1992.**

**THIS PAGE LEFT BLANK INTENTIONALLY**

**CSDL-P-3309**

**Stellar Radiometry and Astrometry  
Supporting Development and Test  
of Advanced Guidance Systems**

**by**

**James A. Hand and Michael E. Ash**

**October 1993**

*to be presented at  
The CIGTF Sixteenth Biennial Guidance Test Symposium  
Holloman Air Force Base, NM  
October 1993*

**"APPROVED FOR PUBLIC RELEASE; DISTRIBUTION IS UNLIMITED."**



**555 Technology Square  
Cambridge Massachusetts 02139**



## **ABSTRACT**

One stellar-inertial guidance system that is under development requires accurate knowledge of star "colors" (irradiance in wavelength bands) to aid acquisition in high background noise. The challenges in the star color observations covered in this paper are performance of precise, multicolor, multistar measurements from several independent observatories, and then achieving close agreement among the data such that accuracy of results can be inferred from the ensemble.

Another stellar-inertial guidance system being developed requires accurate analysis of endoatmospheric star angular positions that are to be used for independent evaluation of a test system's capability to update its navigated position from star sightings immediately after a "hot run" on Holloman's rocket sled. The challenges in this effort are to estimate very accurate, in-atmosphere multistar position agreements among independent analyses, and then to permit the tested system to demonstrate its best performance in a constrained star tracking situation from the rocket sled.

This paper describes the limits and methods of the star radiometry measurements and analyses, and the astrometry analyses that are being used to support development of two advanced guidance systems.

## **ACKNOWLEDGMENTS**

This paper was written and produced by The Charles Stark Draper Laboratory, Inc. in support of the Navy's Stellar System Upgrade (SSU) for the Trident Program, and in support of the Air Force's Advanced Inertial Measurement System (AIMS) Advanced Technology Transition Demonstration. Several persons at Draper have supported the development of the paper, either directly or indirectly. Special thanks are given by the authors to Peter Howard, program manager of SSU, and to Ralph Walker, Sled Test Manager Advanced Inertial Measurement System (AIMS), for their review and comments. Thanks for financial support are given to David Burke, Engineering Vice President of Draper, and Philip Felleman, Director of the System Engineering Group. Thanks also to Capt. Ronald Perry of the Ballistic Missile Organization (BMO) for his review, and to Mr. Andrew Weber, of SP for his review.

## TABLE OF CONTENTS

### Section

- 1.0 BACKGROUND AND INTRODUCTION
  - 1.1 Star Radiometry Experiment Supporting Stellar Subsystem Upgrade
  - 1.2 Star Position Verification Exercise Supporting Advanced Inertial Measurement System
- 2.0 EXECUTIVE SUMMARY
  - 2.1 Star Radiometry Experiment Concepts and Results
  - 2.2 Star Position Verification Exercise
- 3.0 DETAILED DISCUSSIONS
  - 3.1 Star Radiometry Experiment
  - 3.2 Star Position Verification Exercise
    - 3.2.1 Star Position
    - 3.2.2 Precession Correction
    - 3.2.3 Parallax Correction
    - 3.2.4 Nutation Correction
    - 3.2.5 Site Position
    - 3.2.6 Wobble Correction
    - 3.2.7 Earth Rotation Correction
    - 3.2.8 Aberration Correction
    - 3.2.9 Azimuth-Elevation Calculation
    - 3.2.10 Refraction Correction
- 4.0 REFERENCES
- 5.0 LIST OF ACRONYMS

## LIST OF ILLUSTRATIONS

### Figure

- 2.1-1 Star sightings in atmosphere through air masses from zenith to horizon.
- 2.1-2 Comparison of star sightings
- 2.1-3 Known less measured color bands visible, Harvard Observatory, 2/25-26/93.
- 2.2-1 Rocket sled forebody.
- 2.2-2 Rocket sled position transducers.
- 2.2-3 Hot run and star sighting sequence.
- 2.2-4 Rocket sled test orientation.

## LIST OF TABLES

### Table

- 2.1-1 Achievable precision in stellar photometry [1].
- 2.1-2 Achieved precision in star radiometry experiment.
- 2.1-3 Harvard Observatory data compared with Naval Observatory data and "known" catalog values.
- 3.2-1 Magnitude of corrections to obtain apparent star positions.

## **1.0 BACKGROUND AND INTRODUCTION**

### **1.1 Star Radiometry Experiment Supporting Stellar Subsystem Upgrade**

Draper Laboratory is leading the development of an SSU for the MK 6 Guidance System employed in the Trident II strategic missile. This work, under the U.S. Navy Strategic Systems Program (SSP) Office, is being conducted in cooperation with several Industrial Support Contractors (ISCs), principally Hughes Corporation, Kearfott Corporation, and Martin Marietta Corporation (formally GE Aerospace Division). The Star Radiometry Experiment (SRE) described in this paper is a small part of the overall development effort.

The SSU requires accurate knowledge of star spectral irradiance (femto-watts/cm<sup>2</sup>-nm) in three band passes divided into low, medium and high, over the range of roughly 350 to 1100 nanometers in order to support star acquisition and centroiding in a high-noise background (radiation). A preliminary design budget has been assigned for the irradiance accuracy value (not disclosed in this paper). An important impetus for this experiment was that there are certain relatively dim stars having advantageous locations used with the Charge Coupled Device (CCD) star sensors, for which existing catalogs lack complete data in all of the needed band passes. The first half of this paper describes the in-process experiment toward determining the accuracy of star irradiance that can be achieved endoatmospherically among three independent observatories. Also, comparisons with the "known" star catalogue values for selected irradiance bands, or colors, such as the Cousins 13-color bands and the Johnson 13-color, and Johnson five-color bands: visual (V), ultraviolet less blue (U-B), visual less red (V-R) and red less infrared (R-I) are shown. In order to provide a nonsensitive and unclassified report, the data discussion and results will be limited to standardized magnitude descriptions and five-color comparisons, rather than the current output required by the CCD.

Star color observations that agree among the observatories in the bandwidths of interest can be used to add to the observational database. Of course, these observations must be also underpinned by differential photometry to known reference stars of various colors to demonstrate that the observational procedures, processing, etc., are valid. The paper will describe the equipment, procedures, mathematics, and results of the SRE work conducted to date, including the measurements from two of the three observatories, and the comparisons with the known catalogue data.

### **1.2 Star Position Verification Exercise Supporting Advanced Inertial Measurement System**

Draper is technically supporting the development of an AIMS under direction of the Air Force/BMO. The AIMS inertial measurement systems are being developed in two stellar inertial versions by competing industrial contractor teams; namely, Litton with Hughes and Northrop, and Martin Marietta with Honeywell. As a part of the overall development, the candidate stellar inertial systems will be subjected to rocket sled testing at Holloman Air Force Base through the Air Force Central Inertial Guidance Test Facility (CIGTF). Draper is Test Director, CIGTF is Test Conductor, and the contractors are participants on the test team in a competitive arrangement.

In order to substantiate (i.e., bound) the performance of the AIMS immediately after having been subjected to each rocket sled "hot run" test, each unit will automatically sight on two preselected stars. Post-processing and analysis of the inertial and stellar data will be used to substantiate the performance, i.e., properly functioning inertial instruments, and stellar angular measurements corresponding to position updates to the guidance systems sufficient for correcting an actual flight trajectory. The overall performance level of the AIMS will not be disclosed in this nonsensitive, unclassified document.

One of the limits on the testing is the accuracy (not precision) with which the direction to the preselected stars can be determined by endoatmospheric star sightings. Considering error sources such as ephemerides (angular positions) of the stars from the star catalogue, precession of the equinoxes, velocity aberration, atmospheric refraction residual, and so forth. Also, of course, the proper computations and software programs to conduct the theoretical stellar pointing determinations are required in order to arrive at known pointing vectors for the star sensors on the AIMS. By post-processing the accurately known star directions versus those measured values by each AIMS candidate, the performance of the candidates can be substantiated.

As a part of the overall sled test program, a Star Position Verification Exercise (SPVE) is being arranged for performance among those organizations that may post-process and analyze the sled test data from the candidate AIMS. These organizations include TRW, Inc. (TRW), Defense Mapping Agency (DMA) with CIGTF, the industrial competitors named above, and Draper. As Sled Test Director, Draper is designing and coordinating the SPVE for the Air Force. The purposes of this SPVE are to verify that the organizations can precisely determine star positions required, and that the ensemble data from all sources agree to a level defined as the limiting accuracy on the star position knowledge. This report covers the general design of the SPVE - our expectations are that results will be reported in a later paper. The latter half of this paper describes the general procedures and mathematics required to determine the star directions in an altitude and azimuth frame of reference suitable for sled testing.

An executive summary of the SRE and the SPVE is provided in the next section of the paper in order to provide conceptual descriptions free of the mathematics required for describing each of the experiments being conducted. In the sections that follow the executive summary, the mathematics used for each of the experiments are described.

## 2.0 EXECUTIVE SUMMARY

### 2.1 Star Radiometry Experiment Concepts and Results

Essentially, the purposes of the SRE are 1) to perform independent star sightings at multiple independent observatories and 2) to verify the agreement among the data for close consistency. These data, where they agree, and given that the observations are surrounded by the appropriate calibration sightings, can then be used to confirm (deny) irradiance data from known stars, or can be used to add data in the star colors catalogues where needed. Generally, among the shortcomings of existing catalogues addressed by these types of experimental sightings are: insufficient data on certain stars, or individual colors, outdated catalogue data where additional observations are available, catalogue misprints or erroneous star data, and questionable minimum or maximum brightness (irradiance) due to star variability. Long-term sightings are required for stars with long-term periods of variability (e.g., months to years). This variability issue is beyond the scope of the SRE in that the sighting sets of the cost-limited SRE were a few nights at each observatory.

One set of sightings reported on here was performed at the U.S. Naval Observatory, Flagstaff Station, under the direction of Dr. H. Guetter (arranged through the Navy, Mr. A. Weber, and Kearfott Corporation, Mr. L. Gordy and Mr. J. Bevelock). Another sighting set was designed by Draper (Mr. J. Hand), performed at the Harvard-Smithsonian Observatory, Harvard, MA, under the direction of Dr. Robert Stefanic, and with measurements by Mr. Joseph Zejac of Harvard-Smithsonian, Mr. Mark Nasson of Draper and Mr. Hand. The third sighting set, in progress, is being conducted at the Cape Canaveral Eastern Test Range by Mr. G. Bertiaux of Draper. These data are not yet included in the interim results reported here.

In describing the general approach, we will concentrate on a description of the SRE sightings performed at the Harvard-Smithsonian Observatory. Generally, this part of the overall experiment was conducted in accordance with the equipment, procedures, mathematics, and analysis described in Henden and Kaitchuck's excellent text, Astronomical Photometry [1].\*

In summary, the star sightings are performed to known calibration stars and to the test stars ("program stars") viewing through a calibrated set of filters (e.g., Johnson five-color UVBRI), and a detector assembly mounted on the telescope, such as the OPTEC Model SSP solid-state photometer [2]. The sightings are essentially differential photometry to the extent that comparative sightings are made to reference stars, rather than absolute photometry to a standard black body radiator source. Historically, the calibration stars were originally chosen for their color characteristics and were calibrated relative to a known black body source [3, 4]. The summary of this process is covered by the Johnson list of standard stars, including the measurement errors estimated by Johnson and Mitchell in their original work.

Conceptually, the star measurements are first done in an instrumentation system, using the telescope and the OPTEC photometer, thereby resulting in measurements that can be compared, one star versus another, in that instrumentation system. Specifically, these

---

\* Radiometry refers to the parts of spectrum including and beyond the visible light band of approximately 400 to 700 nanometer wavelength. "Photometry" is the common term used in texts for the star observations even though, strictly speaking, they extend on both the shorter wave bands and the longer bands relative to the visible spectrum.

results provide good comparison of the magnitude differences among calibration stars, which are provided by various sets of standard stars in UBV and UBVRI [Ibid. 1; see also 5] and differences among the selected program stars where colors are given in the references. By using a careful sighting procedure to the preselected stars at high and low altitudes above the horizon through the atmosphere, and of proper colors, both the linear extinction effects (absorption) of the atmosphere and the linear color effects (differential absorption) are estimated by linear regressions (Figure 2.1-1).

As shown in Figure 2.1-1, more atmospheric absorption occurs as a function of viewing stars through more air in viewing toward the horizon. Secondary extinction coefficients can also be computed from such data. This procedure permits the star brightness in the various colors to be estimated on an exoatmospheric standardized basis. Thus, the measurements are intended to estimate extinction and transformation coefficients such that the standardized values can be compared with similar values from other observatories. Briefly, the measurement procedure involves three sightings each through each of the standardized color filters, and with background light suitably subtracted for each sighting by sighting onto a nearby region not containing the target star.

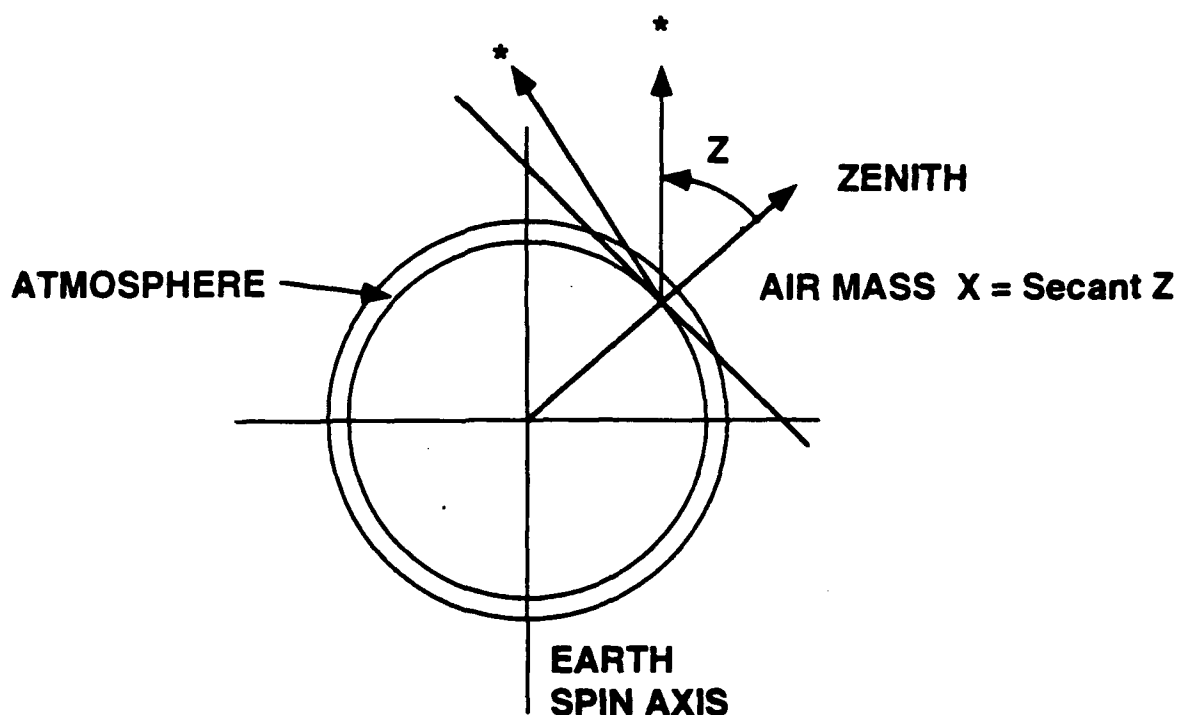


**Figure 2.1-1. Star sightings in atmosphere through air masses from zenith to horizon.**

Our goal is to provide the photometry to achievable limits in order to support the IMU development program. The question immediately arose as to the level of measurement consistency achievable from the standard star catalogues and from the sighting procedures. Table 2.2-1 below gives some estimates of achievable photometry as extracted from Reference 1 and as traceable to original photometry system developments by Mitchell and Johnson [Ibid. Ref. 3, page 14]. For these purposes the logarithmic brightness differences are approximately the same as the percentage differences, i.e., 0.01 to 0.03 magnitude @ 1 to 3%, one sigma.

**Table 2.1-1. Achievable precision in stellar photometry [1].**

Photographic plate photometry	2%	(page 7)
Johnson list of standard stars	2 to 3%	(page 94)
Errors in (U-B) due to Balmer discontinuity	2 to 3%	(page 39)
Extinction measurements by professionals	2 to 3%	(page 89)
Transformation coefficient	2 to 3%	(Estimate)

Given these limitations on individual error contributors, we are pleased with the sighting results achieved at the Harvard Observatory-Smithsonian with two sighting nights, and with the comparisons of that data with the results from the Flagstaff Observatory and with National Aeronautics and Space Administration (NASA) data. For example, if for the second night of observations we root sum squared (RSS) the standard stars uncertainty and the extinction measurement alone, and apply the same limit for transformation, i.e., all three items at 3%, we have a limit of 5.2%. This compares well with the known-less-measured-values for extinction and transformation coefficients (5%) shown in Table 2.1-2. In other words, the measurements of the calibration stars (5%) match well the expected tolerance (5.2%).

The results do remind us of why radiometry along the east coast is comparatively difficult - high atmospheric moisture content and relatively low altitude above sea level - compared with the dry, high altitude observatories in the western parts of the country.

**Table 2.1-2. Achieved precision in star radiometry experiment.**

**Harvard-Smithsonian Observatory**

Known less measured calibration stars (Extinction and transformation, second night)	5%	(Fig. 2.1-2)
All stars (calibration and program)	8%	(Fig. 2.1-3)
Comparisons with Flagstaff [6] and NASA [7]	6% avg.	(Table 2.1-3)

Figure 2.1-2 summarizes the known-less-measured colors of the calibration stars versus the color bands for UBVRI. The data results indicate that the large difference with the (R-I) data in the first night of sightings was solved by the improved procedures (longer integration time of each sighting) of the second night. The plot also shows that the results in Visible, (B-V) and (U-B) and (V-R) are acceptable results for either night.

Figure 2.1-3 summarizes the Harvard-Smithsonian results in terms of each data point for the second night of observations (i.e., the average of three sightings in each filter with the background removed). The results indicate that the data generally fall well within the  $\pm 9\%$  bound. That is, by comparing the individual data points with the boundary lines for each color, one can determine comparison with known values. The star ID number is normalized so that the exact stars sighted are intentionally not listed.

Table 2.1-3 summarizes the comparison of a subset of the Flagstaff data and a subset of the data from Harvard-Smithsonian. Also, a limited set of data from NASA are shown. The summary indicates:

- Generally good agreement among observations.
- Generally dimmer data from Harvard-Smithsonian (negative in this type of comparison), because of more moisture in the air mass, which requires secondary coefficients to be modeled more fully.

Our preliminary conclusions from these results are:

- The results are acceptable, and refinement of the measurement procedures is practical, if needed in the future.
- The star data could be improved with additional sightings to reduce statistical scatter, and by measuring secondary extinction effects with special star selections.
- All star measurements and comparisons with other observatories could be improved with additional sightings to reduce statistical scatter and with the same stars for comparison at all observatories. The results are acceptable considering that the Flagstaff sightings were done in the narrow-band Cousins system and the Harvard-Smithsonian sightings were done in the wide-band Johnson system. Narrow-band measurements at Harvard-Smithsonian would be useful.



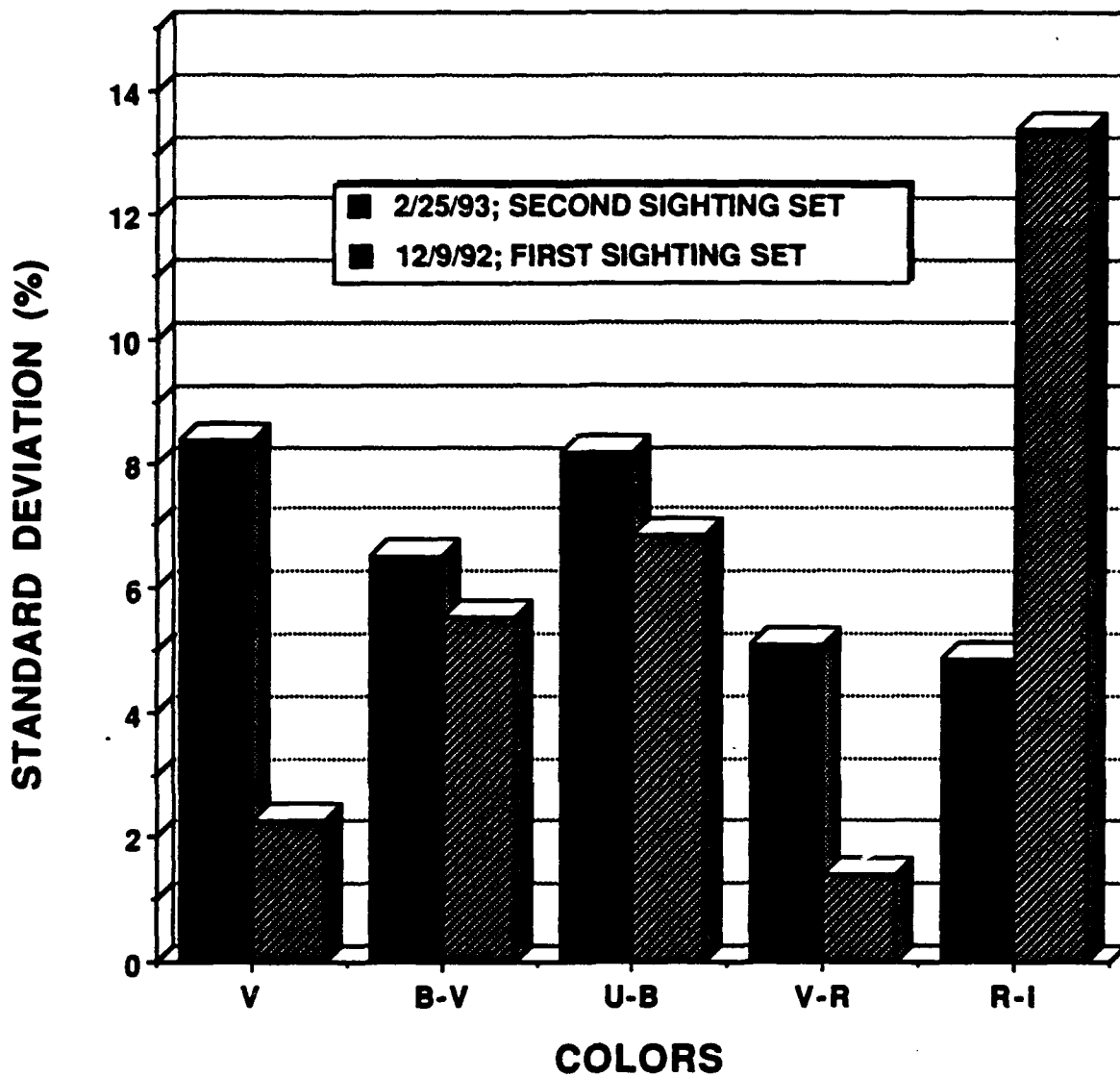


**Figure 2.1-2. Comparison of star sightings: known less measured brightness Harvard Observatory 12/9/92 versus 2/25/93.**

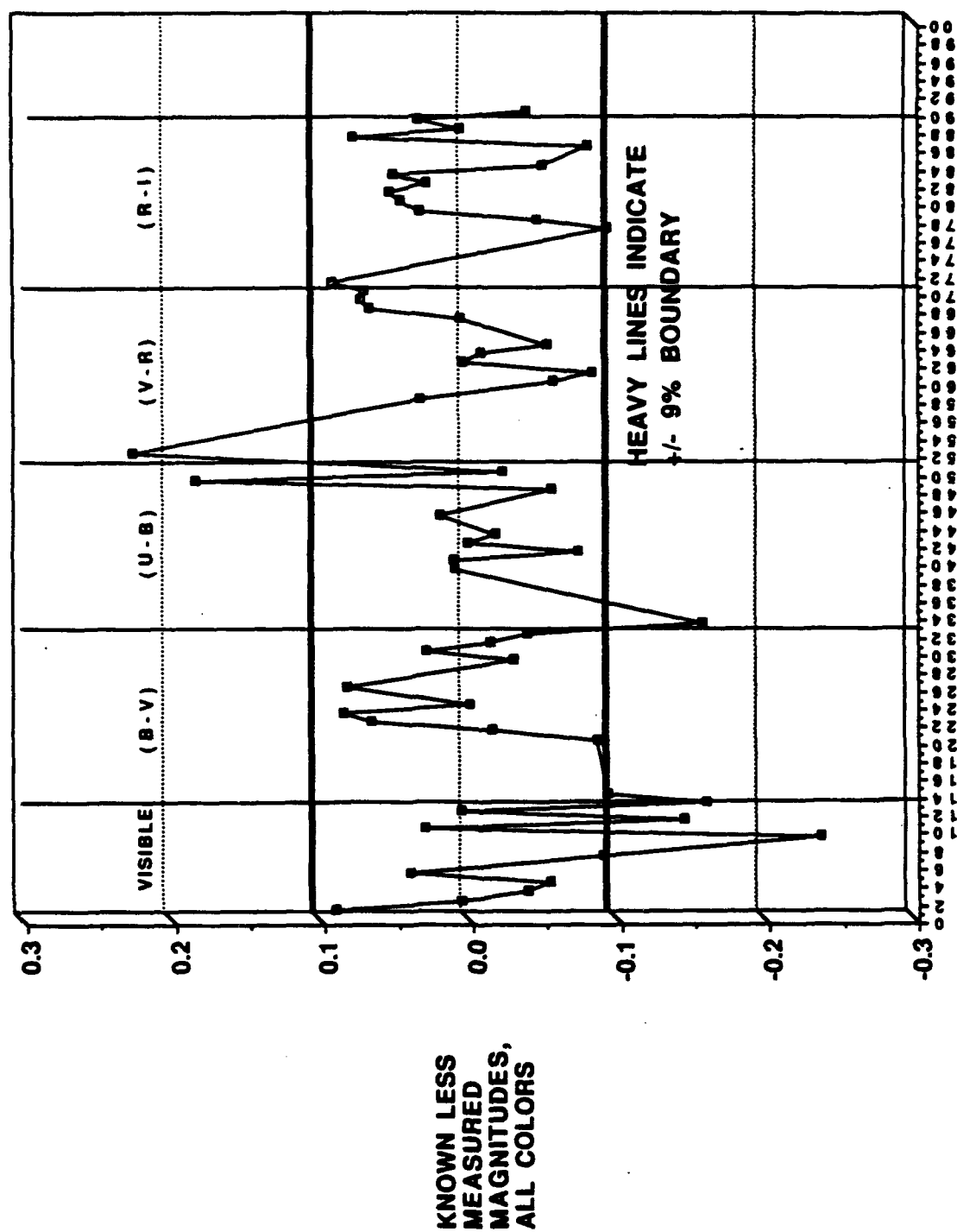


Figure 2.1-3. Known less measured color bands visible, Harvard Observatory, 2/25-26/93.

**Table 2.1-3. Harvard Observatory data compared with Naval Observatory data and “known” catalog values.**

[illegible]

**Table 2.1-3. Harvard Observatory data compared with Naval Observatory data and “known” catalog values (cont.).**

[illegible]

## 2.2 Star Position Verification Exercise

The rocket sled testing of the competing AIMS candidate IMUs is scheduled for late 1994 and early 1995 on the Holloman track. The two-star stellar updates that will be performed by each IMU immediately at the end of the hot runs obviates the need for precise initial azimuth alignment by providing alignment sighting data proportional to integrated navigation errors. By use of the Space-Time System on the track to measure sled position as a function of time during the hot run, and by knowing the exact angular positions of the preselected stars when they are sighted by the IMU, data will be sufficient to check both the functional integrity of the IMU during the run and the accuracy at the conclusion of the hot run. Hence, in order to assess the performance of the candidate IMU, the star positions must be known exactly at the times of sighting. The purpose of the SPVE is to demonstrate that the required knowledge can be computed accurately for assessing the performance of the candidate IMUs.

A paper on the details of the rocket sled testing was presented to the Joint Services Data Exchange last year [7]. A brief overview of the sled testing description from that paper will be provided here in order to place the SPVE in perspective.

The IMU is mounted in the rocket sled and is provided integrated electronics, cooling, vibration isolation, data recording, timing, and telemetry support. Figure 2.2-1 is a skeleton view of the rocket sled, including its various support sections. The rocket sled accelerates and then decelerates the IMU down the track. The track instrumentation provides measurements of position along the way at precisely known intervals by means of position transducers, which are detected onboard the sled by means of interrupter blades (Figure 2.2-2). These positions are recorded on the sled high-speed data recorders along with the IMU data and a reference time signal. At a known position along the track, the sled is brought to a stop by means of a deceleration water break system, and star sightings commence (Figure 2.2-3).

Prior to the hot run and thereafter, a set of independent star sightings will be accomplished by a team of observers from the DMA. The purpose of these sightings is to provide an independent estimate of atmospheric refraction changes during the testing. In the event there are sudden changes to the atmospheric refraction, such as a cold front, then the testing will be held off until a stable atmosphere is assured.

In deriving the star pair sets for the sled testing, a compound set of criteria were met. The final star pairs selected and measured will include:

- Stars high enough in altitude to avoid inordinate atmospheric refraction error
- Low enough star altitude to provide good azimuth observability
- Wide enough angular separation to provide good cross product definition to the third degree of angular definition
- Preselected stars at the proper orientations relative to the sled track at the required test times
- Brightness and spectral class of stars adequate for candidate detectors

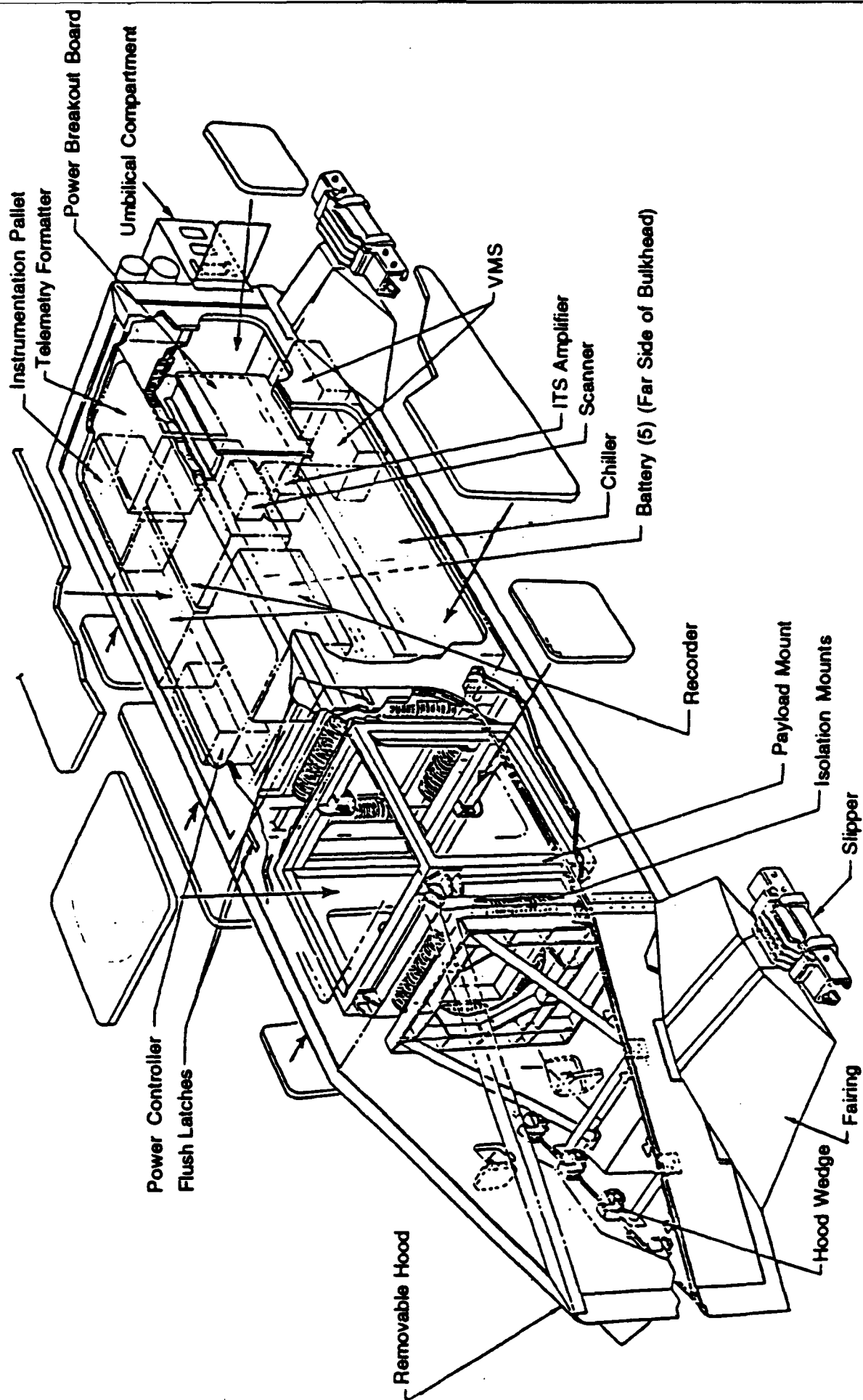


Figure 2.2-1. Rocket sled forebody.

Reference: AF/CIGTF, 6585th Test Group Facilities and Capabilities, ADTC OI 78-148

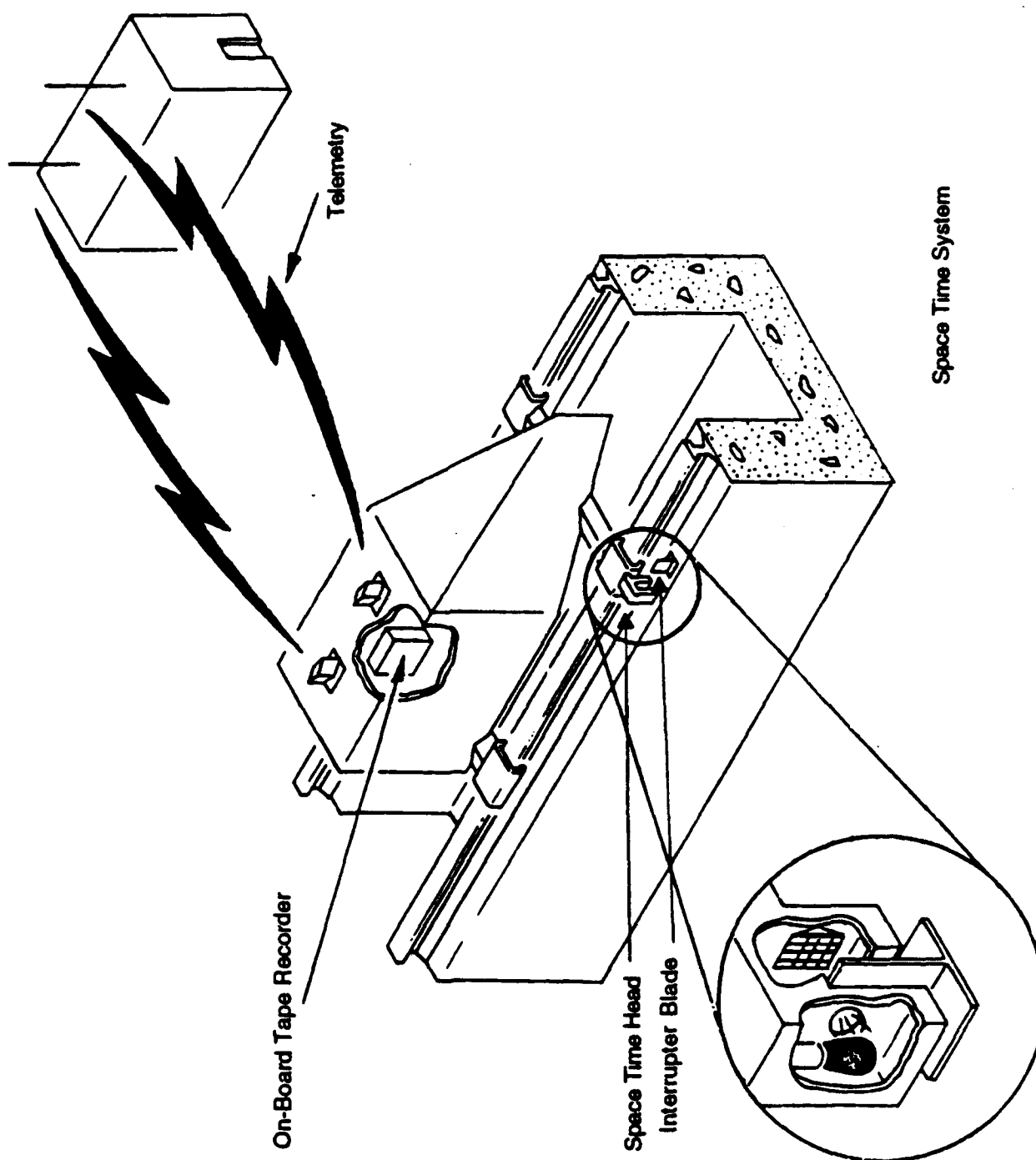
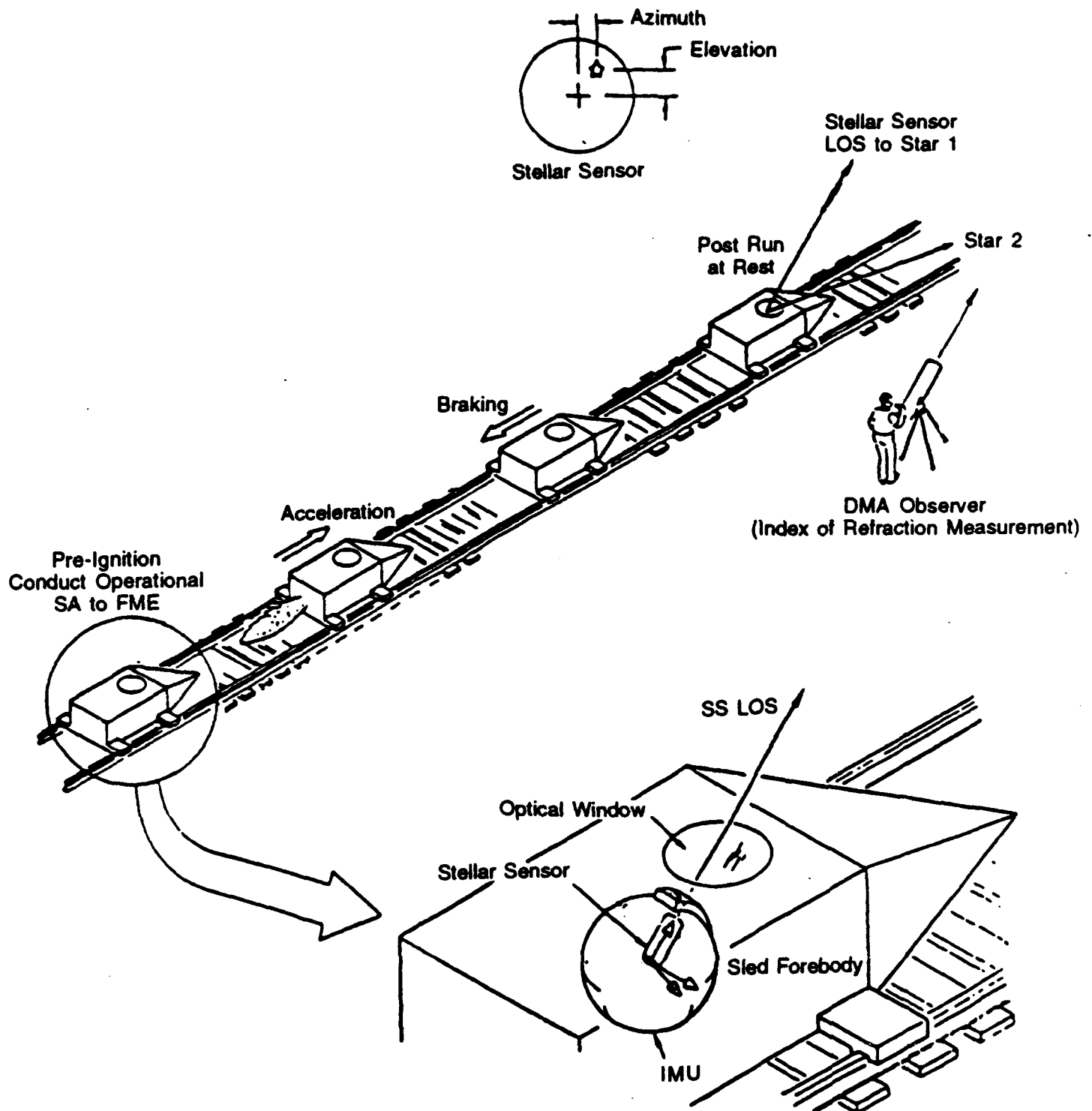


Figure 2.2-2. Rocket sled position transducers.

Reference: AF/CIGTF, 6585th Test Group Facilities and Capabilities, ADTC OI 78-148



**Figure 2.2-3. Hot run and star sighting sequence.**



- Adequate number of star pairs to support sled test schedule for approximately eight months
- No detectable double or variable stars
- Stable refraction environment during star sightings
- Adequate viewing time within sled two-window limits
- Fast rotary table motion from first to second star in order that elapsed time between stars does not degrade sightings
- Accurately known star positions relative to altitude and azimuth such that performance can be assessed.

The star sensor on the IMU will automatically commence the two-star sighting sequence after the sled is stopped. Figure 2.2-4 shows a side view of the earth to give a perspective of how star sensor field relates to the astronomic vertical and local horizontal system at the sled track. Included in the two-star sighting sequence will be a turn about one of the star lines of sight such that the integrity of the alignment to the inertial instruments can be checked. When the second star is sighted, sufficient data will have been collected for the navigation update. Additional star pair sightings may be collected during the sequence in order to provide additional engineering data. Also included in the sequence will be the IMU measurement of the included angle between the two stars. This measurement can be used to augment the sled engineering data since the exact angles between the preselected stars are known.

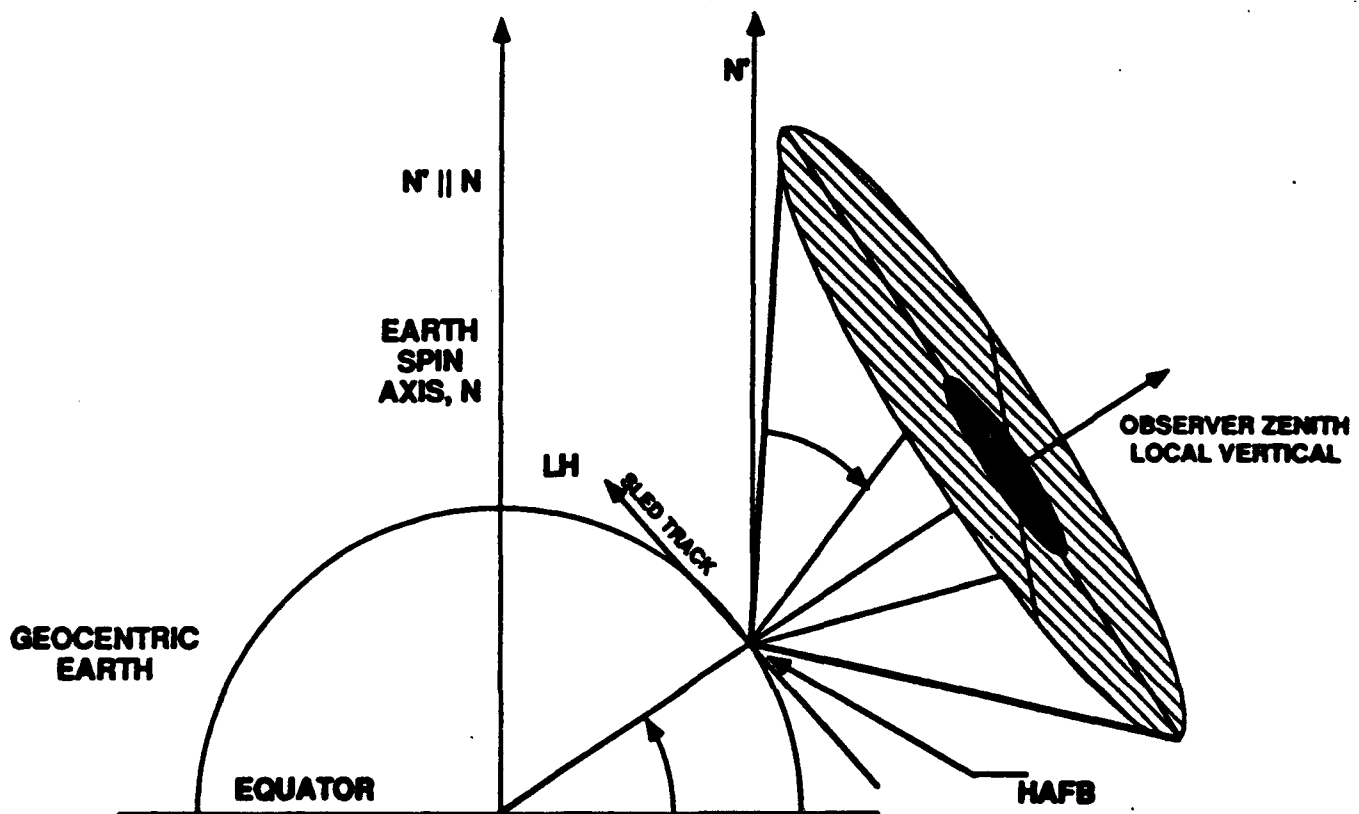


Figure 2.2-4. Rocket sled test orientation.  
(Note: track is approximately North)

The task at hand in performing the SPVE is to reduce several theoretical star observations to apparent altitude and azimuth in the local astronomic (North and local vertical) frame of reference and then to compare them among the inputs from the participating organizations. Here we summarize the definitions of the star positions reduction in English prior to the mathematical reductions in a later section of the paper. Also, the magnitude of the effects are listed in order to give the reader an estimate of the size of the uncompensated errors that are being corrected.

- Change from FK4 to FK5 catalogues - There were relatively large (approx. 1 arcsec) systematic errors made in the development of the FK4 catalogue [8]. These errors, including those due to choice of equinox line and precession constant, were detected and corrected by the development of the FK5 catalogue.
- Star position and Proper motion - Star position is the true position, outside of the atmosphere, at a specific point in time (e.g., Epoch J2000.0 = noon on Jan. 1 year 2000). Proper motion is the movement of the star at right angles to the line of sight between the earth and star, measured in right ascension and declination (h, m, s and deg, ', "). Position errors are up to approximately 0.1 arcsecond for the fundamental stars in the FK5. Proper motions are in the range of approximately 0 to 13 arcseconds per year.
- Parallax - This term is the apparent change in the position of a star due to change in the location of the observer, specifically, half the angular shift of a star's apparent position as seen at opposite ends of the earth's orbit. The magnitude of this correction is in the range of 0.0 to 0.7 arcseconds.
- Precession of the equinoxes - The slow westward motion of the equinox point in the sky relative to the stars of the zodiac because of the mean inertial motion of the earth's spin axis; magnitude of effect 50 arcseconds per year.
- Nutation - Oscillations in the earth's rotation pole about the mean pole; magnitude of effect is 20 arcseconds.
- Gravitational deflection of light - Bending of light near the sun due to gravity. Negligible bending of light for situations where the star line of sight is more than 30° from the sun line of sight.
- Wobble - Polar motion of the earth's rotation axis relative to the international pole of figure of the earth fixed in the earth's crust. The magnitude of effect is 0.3 arcseconds.
- Earth rotation correction - An error of 0.01 s in knowing the time of an observation causes a 0.15 arcsecond angle error.
- Velocity aberration correction - An apparent displacement of the observed position of a star from its geometrical position due to the finite velocity of light and the motion of observer. The magnitude of effect is 0.3 arcseconds for the earth rotational velocity and 20 arcseconds for the earth's orbital velocity.
- Atmospheric refraction - A displacement of the apparent star position caused by the lens-effect bending of the star light as it passes through the earth's atmosphere. The magnitude of this effect is approximately 100 arcseconds, maximum, for the angles at which the stars are being viewed in the AIMS testing.

The section following describes the SRE and the SPVE in some detail.

### 3.0 DETAILED DISSUSSIONS

#### 3.1 Star Radiometry Experiment

In this section of the paper, we describe some of the procedural details and mathematical approach used for measuring the colors of the stars in the UBVRI. In addition to Reference [1] already cited, two experiments in the application of these procedures are referenced for those who may wish to proceed with observational work in photometry [9, 10]. For brevity, we shall concentrate on only the Visible and (B-V) "channels" of the mathematics, since the other measurements are essentially of the same type and processing.

The essential procedures are to choose the calibration stars for their known colors and positions in the sky, and to sight the program stars interspersed with the calibration stars. Achieving a good range of air mass through which the calibration star sightings are made is assured by the judicious choice of those stars from the standards listing [op cit. 1, page 281 and onward]. The sighting procedure involves three 10-second integrations of the star signal through the appropriate filter, and the same for the background light when the telescope is moved slightly away from the star line of sight. These data are then averaged and subtracted to arrive at the star-only counts. Having done the same type of sighting procedures for the calibration stars and the program stars, the data can then be processed as follows [op cit. 1, page 312 and onward].

$$v_0 = v - k_v X \quad (1)$$

$$b_0 = b - k_b X \quad (2)$$

where  $v_0$ ,  $b_0$  are the instrumental magnitudes after accounting for atmospheric absorption. The  $v$  and  $b$  are instrumental raw magnitudes, such as

$$v = -2.5 \log (\text{visual filter star counts})$$

$$k_v = \text{linear extinction coefficient}$$

Also,

$$X = \sec z \quad (\text{zenith angle}) \quad (3)$$

$$\sec z = (\sin \phi \sin \delta + \cos \phi \cos \delta \cos H)^{-1} \quad (4)$$

where,

$\phi$  = observer's latitude

$\delta$  = declination of the star

$H$  = hour angle, =  $15 \times (\text{Local Sidereal Time} - \text{Right Ascension})$ , in degrees.

This  $X$  value is the number of air masses through which the observation is made.

Similar to equation (2),

$$(b-v)_0 = (b-v) - k'_{bv} X \quad (5)$$

and

$$k'_{bv} = k'_b - k'_v. \quad (6)$$

The method for determining the extinction terms is simply to find the linear regression  $k$  value by plotting  $v$  versus  $X$  and  $b$  versus  $X$ . Then, the exoatmospheric values  $v_0$  and  $b_0$  can be computed.

Differences in colors between the program star (subscript  $p$ ) and the calibration star (subscript  $c$ ) can be readily computed by

$$\begin{aligned} \Delta(b-v) &= (b_p - v_p) - (b_c - v_c) \\ &= (v_p - b_c) - (v_p - v_c) \\ &= \Delta b - \Delta v \end{aligned} \quad (7)$$

In the event that the stars are far apart in the sky, we can account for the different air masses by

$$(\Delta v)_0 = \Delta v - k'_v(X_p - X_c) \quad (8)$$

$$(\Delta b)_0 = \Delta b - k'_b(X_p - X_c) \quad (9)$$

Now, by the observing procedure that has standard A-type stars from the standards list (i.e.,  $(B-V) = 0$ ), the standard value for the star can be computed (caps indicate standardized value)

$$V = v - k'_v X + \epsilon(B - V) + Z \quad (10)$$

where

$\epsilon$  is the unknown transformation coefficient

$Z$  is the instrumentation zero value from the calibration stars.

For early A-type stars  $(B-V)$  is small, and  $\epsilon$  is small; the product is very small. Therefore, to good approximation

$$V - v = Z_v - k'_v X \quad (11)$$

A plot of  $V - v$  versus  $X$  yields a straight line with slope  $k'_v$ , and the intercept is the zero value.

Similarly, to good approximation,

$$(B - V) - (b - v) = -k'_{bv}X + Z_{bv} \quad (12)$$

A plot of  $(B - V) - (b - v)$  versus  $X$  yields a straight line with a slope of  $-k'_{bv}$ .

Observation for the second-order extinction coefficient  $k''_{bv}$  involves viewing two closely spaced stars of very different colors at various air masses; a measurement that is needed once or twice a year because the term is small and fairly stable. Because the air masses are approximately equal, the algebra reduces to

$$\Delta(b - v)_0 = \Delta(b - v) - k''_{bv} X \Delta(b - v) \quad (13)$$

Because  $\Delta(b - v)_0$  is constant, a plot of  $\Delta(b - v)$  versus  $X \Delta(b - v)$  gives a straight line with slope  $k''_{bv}$ .

Having determined the extinction coefficients,  $k'_v$  and  $k'_b$ , the transformation coefficients for standardizing any unknown star can be estimated. Thus far, we know  $V$  and  $B - V$  from the standard star tables, and  $v_0$  from equation (1). Therefore, a plot of  $V - v_0$  versus  $(B - V)$  yields a linear least squares fit slope of the transformation coefficient  $\epsilon$  and a zero intercept of  $Z_v$  by

$$V - v_0 = \epsilon(B - V) + Z_v \quad (14)$$

Then, to determine the  $\mu$  and  $Z_{bv}$  terms, a plot of  $[(B - V) - (b - v)]$  versus  $(B - V)$  is required. The relationship from the slope so determined is

$$\mu = 1/(1 + \text{slope}) \quad (15)$$

and,

$$Z_{bv} = \text{intercept} * (\mu). \quad (16)$$

Finally, for any star we have the standardized magnitude,

$$(B - V) = \mu(b - v)_0 + Z_v \quad (17)$$

and, by rearrangement of equation (14),

$$V = v_0 - \epsilon(B - V) + Z_v. \quad (18)$$

These standardized values can now be compared with standardized values from other observatories because they have been corrected for atmospheric extinction and have been transformed from the instrumentation system used. For additional details on corrections such as the Balmer spectral discontinuity at 364.7 nm, the reader is referred to the often-cited photometry text and handbook [op cit. 1].

### 3.2 Star Position Verification Exercise

Here we discuss some of the mathematical details of the determination of star position in terms of altitude and azimuth at the rocket sled track. We use a second set of incremental equation numberings for purposes of keeping track of this set of equations.

Table 3.1.2-1 lists the magnitude of corrections that are made to star catalogue right ascension (h m s) and declination ( $^{\circ}$  ' ") to obtain apparent azimuth-elevation values accurate to 0.1" given the date, universal time coordinated (UTC) time, and site of an observation. A vector approach for carrying out the corrections is now described.

**Table 3.2-1. Magnitude of corrections to obtain apparent star positions.**

Quantity	Magnitude of Effect	Quantity	Magnitude of Effect
Proper motion		Aberration	
Typical	0.2"/year	annual circular	20"
Large	2"/year	annual elliptic	0.34"
Maximum	13"/year	diurnal	< 0.3"
Parallax	< 0.7"	Refraction	
Precession	50"/year	60° elevation	34"
Nutation	20"	45° elevation	59"
Wobble	0.3"	25° elevation	124"
UT1-UTC  < 1 sec	< 15"	15° elevation	214"
Deflection of vertical	5"	0° elevation	2189"

#### 3.2.1 Star Position

The FK5 [8] or other star catalogue gives the right ascension (RA), declination (Decl), and proper motion of a star at the J2000.0 epoch referred to the mean equinox and equator of J2000.0, where J2000.0 is 2000 January 1 12<sup>h</sup> TDB (Time Dynamical Barycentric, Julian Date 2451545.0). Let  $t$  be the date and UTC (Greenwich) time of a star observation, and let the time in Julian ephemeris centuries from J2000.0 be

$$T = \frac{t + \Delta t - J2000.0}{36525 \text{ days}} \quad (1)$$

where the current difference between UTC and TDB is  $\Delta t \approx 60$  sec. Then the star coordinates in the J2000.0 frame corrected for proper motion per century are

$$\left. \begin{aligned} \text{RA} &= (\text{catalogue RA}) + (\text{proper motion in RA}) \times T \\ \text{Decl} &= (\text{catalogue Decl}) + (\text{proper motion in Decl}) \times T \end{aligned} \right\} \quad (2)$$

For a star in a double star system, RA and Decl could be further corrected for the motion of the star relative to the center of mass of the double star system. The unit vector to the star in the J2000.0 frame is then

$$\vec{X}_a = \begin{bmatrix} \cos(\text{Decl}) \cos(\text{RA}) \\ \cos(\text{Decl}) \sin(\text{RA}) \\ \sin(\text{Decl}) \end{bmatrix} \quad (3)$$

### 3.2.2 Precession Correction

The earth precession angles from the mean equinox and equator of J2000.0 to the mean equinox and equator of the given date  $t$  are [11]

$$\left. \begin{aligned} \zeta &= 2306.2181'' T + 0.30188'' T^2 + 0.017998 T^3 \\ z &= 2306.2181'' T + 1.09468'' T^2 + 0.018203 T^3 \\ \theta &= 2004.3109'' T - 0.42665'' T^2 - 0.041833 T^3 \end{aligned} \right\} \quad (4)$$

The orthogonal precession matrix  $P$  is [12], [13]

$$\begin{aligned} P_{11} &= \cos \zeta \cos \theta \cos z - \sin \zeta \sin z \\ P_{12} &= -\sin \zeta \cos \theta \cos z - \cos \zeta \sin z \\ P_{13} &= -\sin \theta \cos z \\ P_{21} &= \cos \zeta \cos \theta \sin z + \sin \zeta \cos z \\ P_{22} &= -\sin \zeta \cos \theta \sin z + \cos \zeta \cos z \\ P_{23} &= -\sin \theta \sin z \\ P_{31} &= \cos \zeta \sin \theta \\ P_{32} &= -\sin \zeta \sin \theta \\ P_{33} &= \cos \theta \end{aligned} \quad (5)$$

The transformation to a star position vector referred to the mean equinox and equator of date is

$$\vec{X}_b = P \vec{X}_a \quad (6)$$

### 3.2.3 Parallax Correction

Let  $\vec{Z}_b$ ,  $\vec{Z}'_b$  be the position and velocity of the earth relative to the sun at the epoch  $t$  referred to the mean equinox and equator of date. These are calculated using the mean elliptic orbit of the sun relative to the earth-moon barycenter referred to the mean equinox and ecliptic of date [12] and then rotating by the mean obliquity  $\epsilon$  of the ecliptic [11]:

$$\epsilon = 23^\circ 26' 21.448'' - 46.8150'' T - 0.00059'' T^2 + 0.001813'' T^3 \quad (7)$$

Let  $R$  be the distance from the sun to the star. The unit vector pointing from the earth to the star corrected for parallax is

$$\vec{X}_c = \frac{R \vec{X}_b - \vec{Z}_b}{|R \vec{X}_b - \vec{Z}_b|} \quad (8)$$

If  $R = 4.3$  light years for Alpha Centauri, the parallax correction is  $\pm 0.7''$  over a year. For a distant star, it is essentially zero. The parallax due to the displacement of the observing site from the center of the earth and of the center of the earth from the earth-moon barycenter is ignorably small.

### 3.2.4 Nutation Correction

Let  $\Delta\psi$  and  $\Delta\epsilon$  be the nutations in longitude and obliquity of approximate magnitudes 20" and 9", respectively, evaluated using at least 30% of the 106 and 64 terms, respectively, in the International Astronomical Union IAU trigonometric series [11]. The orthogonal nutation matrix  $N$  is [12], [13]

$$\begin{bmatrix} N_{11} & N_{12} & N_{13} \\ N_{21} & N_{22} & N_{23} \\ N_{31} & N_{32} & N_{33} \end{bmatrix} = \begin{bmatrix} 1 & -\Delta\psi \cos \epsilon & -\Delta\psi \sin \epsilon \\ \Delta\psi \cos \epsilon & 1 & -\Delta\epsilon \\ \Delta\psi \sin \epsilon & \Delta\epsilon & 1 \end{bmatrix} \quad (9)$$

where the square of small angles in radians are ignored (0.001" error).

The transformation to a star position vector referred to the mean equinox and equator of date is

$$\vec{X}_d = N \vec{X}_c \quad (10)$$

### 3.2.5 Site Position

The earth-fixed vector from the center of the earth to an observing site is

$$\vec{Y}_\alpha = \begin{bmatrix} r \cos \phi' \cos \theta \\ r \cos \phi' \sin \theta \\ r \sin \phi' \end{bmatrix} \quad (11)$$

where  $r$  is the radius from the center of the earth,  $\theta$  the east longitude, and  $\phi'$  the north geocentric latitude, related to the geodetic latitude  $\phi''$  (angle between the normal to the reference ellipsoid and the equator) by standard formulas [12].

Let  $\phi$  be the astronomic latitude (angle between local vertical and the equatorial plane), differing from  $\phi''$  due to gravity anomalies. The unit vector along the local vertical is

$$\vec{N}_\alpha = \begin{bmatrix} \cos \phi \cos \theta \\ \cos \phi \sin \theta \\ \sin \phi \end{bmatrix} \quad (12)$$

The 0.03" variation in the local vertical due to the lunar-solar earth tides is ignored.

Let  $\vec{P} = [0 \ 0 \ 1]^T$  be the unit vector pointing along the pole of figure of the earth. Then the unit vector along the meridian to the north is

$$\vec{M}_\alpha = \frac{\vec{P} - (\vec{P} \cdot \vec{N}_\alpha) \vec{N}_\alpha}{|\vec{P} - (\vec{P} \cdot \vec{N}_\alpha) \vec{N}_\alpha|} \quad (13)$$



### 3.2.6 Wobble Correction

Let  $x, y$  be the wobble angles (of the order of  $0.3''$ ) of the pole of rotation relative to the conventional international pole of figure of the earth. The orthogonal wobble matrix  $W$  in terms of the wobble angles in radians is [14]

$$\begin{bmatrix} W_{11} & W_{12} & W_{13} \\ W_{21} & W_{22} & W_{23} \\ W_{31} & W_{32} & W_{33} \end{bmatrix} = \begin{bmatrix} 1 & 0 & x \\ 0 & 1 & -y \\ -x & y & 1 \end{bmatrix} \quad (14)$$

The transformation of vectors with subscript  $\alpha$  referred to the pole of figure to vectors with subscript  $\beta$  referred to the pole of rotation is

$$\vec{Y}_\beta = W^T \vec{Y}_\alpha, \quad \vec{N}_\beta = W^T \vec{N}_\alpha, \quad \vec{M}_\beta = W^T \vec{M}_\alpha \quad (15)$$

where  $W^T$  is the transpose of  $W$ .

The International Earth Rotation Service (IERS) determines the wobble angles and the UT1-UTC time correction using Very Long Baseline Interferometer and lunar and satellite laser ranging observations. The  $x, y$  wobble angles and UT1-UTC can be predicted to some accuracy a few weeks ahead in time, but the most accurate values would be published by the IERS a few weeks after a rocket sled experiment has taken place.

### 3.2.7 Earth Rotation Correction

Given the UTC time of an observation using a clock synchronized to a time service radio station, the UT1 time is determined from the published or extrapolated UT1-UTC value, where UT1-UTC is kept less than a second by retarding UTC by a leap second as needed (approximately once a year). An error of 0.01 sec in timing or knowledge of UT1-UTC causes an error of  $0.15''$  in angle.

Given the UT1 time, sidereal time  $s$  is determined as follows. The mean sidereal time (Greenwich hour angle of the mean equinox of date, first point of Aires) at  $0^h$  UT1 time on a given calendar date is [11]

$$s_0 = 6^h 41^m 50.54841^s + 8640184.812866^s \tau + 0.093104^s \tau^2 - 6.2^s \times 10^{-6} \tau^3 \quad (16)$$

where  $\tau$  is the time in Julian centuries of 36525 days elapsed from  $0^h$  UT1 on that date since 2000 January 1  $12^h$  (Julian Date 2451545.0).

The rate of UT1 time relative to the rate of sidereal time on the given date is [11]

$$\frac{dUT1}{ds} = 0.997269566329084 - 5.8684 \times 10^{-11} \tau + 5.9 \times 10^{-15} \tau^2 \quad (17)$$

The true sidereal time at a given UTC time on the given date is [12]

$$s = s_0 + \frac{UTC + (UT1 - UTC)}{dUT1/ds} + \Delta\psi \cos \epsilon \quad (18)$$

The orthogonal earth rotation matrix  $S$  is [13]

$$S = \begin{bmatrix} \cos s & \sin s & 0 \\ -\sin s & \cos s & 0 \\ 0 & 0 & 1 \end{bmatrix} \quad (19)$$

where  $s$  is in radians. The transformation of vectors with subscript  $\beta$  fixed in the earth referred to the pole of rotation to vectors with subscript  $d$  referred to the true equinox and equator of date is

$$\vec{N}_d = S^T \vec{N}_\beta, \quad \vec{M}_d = S^T \vec{M}_\beta \quad (20)$$

The velocity of the observing site relative to the center of the earth referred to the true equinox and equator of date is

$$\vec{Y}'_d = \frac{dS^T}{dt} \vec{Y}_\beta \quad (21)$$

where because there are 86400 seconds in 24 hours or  $2\pi$  radians

$$\frac{dS}{dt} = \begin{bmatrix} -\sin s & \cos s & 0 \\ -\cos s & -\sin s & 0 \\ 0 & 0 & 1 \end{bmatrix} \frac{2\pi/86400}{dUT1/ds} \quad (22)$$

### 3.2.8 Aberration Correction

The velocity of the earth relative to the sun referred to the true equinox and equator of date is

$$\vec{Z}'_d = N \vec{Z}'_b = \vec{Z}'_b \quad (23)$$

The velocity of the observing site relative to the sun is

$$\vec{V} = \vec{Z}'_d + \vec{Y}'_d \quad (24)$$

To first order in  $V/c$  ( $c$  = velocity of light = 299792.458 km/sec), the classical physics or special relativity aberration correction is like raindrops striking the windshield of a moving automobile at a different angle than they do for a stationary automobile. The unit vector pointing from the observer to the star corrected for aberration is

$$\vec{X} = \frac{\vec{X}_d + \frac{\vec{V}}{c}}{\left| \vec{X}_d + \frac{\vec{V}}{c} \right|} \quad (25)$$

The second order  $(V/c)^2$  term in the special relativity aberration correction is ignored, as it is a 0.002" effect compared to the first order aberration effects of 20" due to the 30 km/sec earth orbital velocity and 0.3" due to the earth rotation.

The velocity of the earth relative to the earth-moon barycenter causes a 0.008" aberration effect, and the velocity of the sun relative to the center of mass of the solar system causes a 0.002" aberration effect, so both are ignored.

Star catalogues before FK5 were constructed without the elliptic part of the aberration taken into account, i.e., the earth's orbit was assumed circular, causing a 0.34" aberration bias. If star coordinates are taken from an older star catalogue, the velocity of the earth relative to the sun should be computed assuming a circular orbit.

The general relativity bending of light is 1.8" for light passing close to the sun, but only 0.004" 90° from sun [11]. Since sled test star observations will be at night (>40°), the general relativity bending is less than 0.02" and is ignored.

### 3.2.9 Azimuth-Elevation Calculation

The altitude or elevation of a star with unit vector  $\vec{X}$  in the coordinate system referred to the true equinox and equator of date is

$$\text{elevation} = \arcsin(\vec{X} \cdot \vec{N}_d) \quad (26)$$

Let  $\vec{X}_p$  be the projection of  $\vec{X}$  onto the horizontal plane:

$$\vec{X}_p = \vec{X} - (\vec{X} \cdot \vec{N}_d) \vec{N}_d \quad (27)$$

The azimuth of the star (positive north to east) is

$$\text{azimuth} = \arctan \left[ \frac{(\vec{X}_p \times \vec{M}_d) \cdot \vec{N}_d}{\vec{X}_p \cdot \vec{M}_d} \right] \quad (28)$$

with proper choice of quadrant depending on the signs of the numerator and denominator.

### 3.2.10 Refraction Correction

Let  $z$  be the zenith angle (90° minus the elevation angle from Equation (26)). Then an approximate expression for the refraction correction to be added to Equation (26) to obtain the apparent elevation is [1]

$$\text{refraction correction} = 60.4'' \tan z - 0.06688'' \tan^3 z \quad (29)$$

Refraction tables specific to the sled test site should be used, even taking into account local atmospheric pressure, temperature and relative humidity. For example, a detailed refraction model is given in Reference [14]. The refraction correction will be primarily in the vertical dimension, or altitude dimension.

#### 4.0 REFERENCES

- [1] Henden, A. A., and Kaichuck, R. H., Astronomical Photometry, Wilmann-Bell, Inc., Richmond, Va.
- [2] OPTEC, Inc., Lowell, MI., Manual for SSP-3 Solid State Photometer, undated.
- [3] Mitchell, and Johnson, H. L., Thirteen Color Narrow-Band Photometry of One Thousand Bright Stars, Communications of the Lunar and Planetary Observatory, University of Arizona, Vol. 8, Part 1, 1969.
- [4] Johnson, H. L., and Mitchell R. I., Thirteen Color Photometry of 1380 Bright Stars. Steward Observatory, University of Arizona, 1975.
- [5] The Astronomical Almanac for the Year 1993, U.S. Naval Observatory, Washington, DC.
- [6] Letter, Warren, W., Hughes STX Corp. at NASA Godard Space Flight Center, to James A. Hand, "Photoelectric Data for Six Stars," 21 September 1992.
- [7] Hand, J. A. and Harris, R. A., Development of Stellar Tracking Requirements for Sled Testing of the Advanced Inertial Measurement System, Sept. 1992, Presented at the Joint Services Data Exchange, Palm Springs, CA.
- [8] Fifth Fundamental Catalogue (FK5) Part 1 The Basic Fundamental Stars, Astronomisches Rechen-Institut, Heidelberg, Verlag G. Braun, Karlsruhe, Germany, 1988.
- [9] Sanders, W. H., and Persha, G., "Determination of Extinction and Transformation Coefficients, BVR and I Bands, using SSP-3," Undated, Argo National Observatory, Lowell, MI.
- [10] Adams, B. H., Data Reduction Techniques for Differential Photoelectric Photometry, 1989, Dept. of Physics, Kansas State University.
- [11] "Improved IAU System," Supplement to the Astronomical Almanac for the Year 1984, U.S. Government Printing Office, 1983.
- [12] Explanatory Supplement to the Ephemeris, H. M. Nautical Almanac Office, London, 1961.
- [13] Mueller, Ivan I., Spherical and Practical Astronomy Applied to Geodesy, Frederick Ungar Publishing Company, New York, 1969.
- [14] Quasius, G. and McCanless, F., Star Trackers and Systems Design, 1966, Spartan Books, MacMillan and Co., London.

## **5.0 LIST OF ACRONYMS**

<b>AIMS</b>	<b>Advanced Inertial Measurement System</b>
<b>BMO</b>	<b>Ballistic Missile Organization</b>
<b>CCD</b>	<b>Charge Coupled Device</b>
<b>CIGTF</b>	<b>Central Inertial Guidance Test Facility</b>
<b>Decl</b>	<b>Declination</b>
<b>DMA</b>	<b>Defense Mapping Agency</b>
<b>IAU</b>	<b>International Astronomical Union</b>
<b>IERS</b>	<b>International Earth Rotation Service</b>
<b>IMU</b>	<b>Inertial Measurement Unit</b>
<b>ISC</b>	<b>Industrial Support Contractors</b>
<b>NASA</b>	<b>National Aeronautics and Space Administration</b>
<b>RA</b>	<b>Right Ascension</b>
<b>RSS</b>	<b>Root Sum Squared</b>
<b>SPVE</b>	<b>Star Position Verification Exercise</b>
<b>SRE</b>	<b>Star Radiometry Experiment</b>
<b>SSP</b>	<b>Strategic Systems Program</b>
<b>SSU</b>	<b>Stellar System Upgrade</b>
<b>TDB</b>	<b>Temps Dynamic Barycentric</b>
<b>TRW</b>	<b>TRW, Inc.</b>
<b>UTC</b>	<b>Universal Time Coordinated</b>

**SESSION III-B**  
**DIFFERENTIAL GPS**

***CHAIRMAN***  
**DIRK DeDOES**  
***INTERMETRICS, INC.***

**THIS PAGE LEFT BLANK INTENTIONALLY**

## **NEW HORIZONS IN DIFFERENTIAL GPS**

**Paper Number: 93-30**

**B.A. Kumar Babu, Senior Scientist**

**Dr. Greg M. Robbins, Vice President**

**Del Norte Technology, Inc.  
1100 Pamela Drive  
Euless, TX 76040**

**Prepared for:**

**Sixteenth Biennial Guidance Test Symposium  
5-8 October 1993  
Holloman AFB, New Mexico**

**Approved for Public Release; distribution is unlimited.**



## **NEW HORIZONS IN DIFFERENTIAL GPS**

**B.A. Kumar Babu & Dr. Greg M. Robbins  
Del Norte Technology, Inc.**

### **ABSTRACT**

Differential GPS (or DGPS) has found widespread use in commercial navigation applications. Though applicable to P-code, C/A code and dual code systems, cost and other constraints restrict many users to only the C/A code. The principal sources of error in a C/A system are Selective Availability, atmospheric and other deterministic errors. Typically, a reference station situated at a known location generates various corrections that are broadcast to users over a given geographic area. These corrections are known as differential corrections and when used properly enable a C/A code system to provide accuracies rivalling and sometimes exceeding authorized dual frequency, non differential, P-code GPS systems. Del Norte Technology, Inc (DNIT) believes that providing an accurate navigation solution, in realtime, is just the beginning of what can be accomplished with Differential GPS. The fusing of data from other sensors, the ability to monitor in real time the quality of the navigation solution being provided, and providing the platform for integration of third party Personal Computer software with a GPS system can expand the power and scope of Differential GPS significantly. All of these issues have been addressed by the authors and their associates to greatly extend the power of DGPS and has resulted in a line of highly powerful, and relatively inexpensive, DGPS and Trisponder systems from DNIT. This paper details some of the development work being done and discusses the results of initial field trials.

### **INTRODUCTION**

The Standard Positioning Service will offer non-military users accuracies of about 100 meters. Those users requiring higher accuracies will need Differential GPS (DGPS). A reference receiver is placed at a known site. The information available from the satellites typically consists of code phase, carrier frequency, satellite ephemeris and coefficients that enable an estimation of atmospheric delays and other error sources. The reference compares satellite derived information with estimates of these based on its known location. The differences are used to generate correction parameters for each satellite. These correction parameters are transmitted over a radio link to mobile GPS receiver systems in the area. The mobile systems use these corrections in their navigation computation to offset Selective Availability induced errors as well as errors caused by atmospheric delays. The latency inherent in the generation of these corrections and their

subsequent use is a critical factor. The industry has standardized the format of the transmitted differential data; this format is known as RTCM. Though it is an adequate format for most accuracy requirements, it still leaves a lot to be desired for the sophisticated user. Del Norte GPS systems currently are providing sub meter accuracies both under static and dynamic conditions using proprietary algorithms and data formats for differential correction transmission. Del Norte Technology, Inc. also designs and manufactures microwave precise positioning equipment using X-band frequencies for ranging. Sensor fusion algorithms developed at DNTI enable the fusing of data from the X-band systems with the raw GPS receiver measurements to provide extra robustness to the DGPS system by providing an independent measurement source. In the interests of easy readability, Del Norte DGPS systems will be hereinafter be referred to as DNTI systems.

## SENSOR FUSION

When the full constellation of satellites is deployed, twenty four hour, three dimensional coverage is assured for most places on the earth. The scenario, unfortunately, assumes that there would be no physical (obstacles) or electronic (interference and jamming) obscuration of satellites. For surveying applications it is not enough that there are a minimum of four satellites visible. The dilution of precision of these satellites is a critical factor in maintaining good accuracy. In places like harbors, the constant movement of ships results in intermittent satellite dropouts which cause continuous interruptions to the survey work. In other places both man made and natural obstacles result in less than ideal surveying and navigation conditions. In both of the above situations the addition of an external sensor (or sensors) that is totally independent of the satellites can provide meaningful performance enhancement even during satellite obscuration. Many military systems fuse Inertial Navigation Systems with GPS. However the costs of these units tend to be prohibitive and even then INS systems will drift in the absence of adequate GPS information making them unsuitable for surveying applications. Del Norte has had considerable experience with shore based microwave ranging systems (Trisponders) that can provide ranging information to better than a meter (one sigma) accuracy. When range information to more than one station is available an independent position solution can be obtained. However, the blending of data from the Trisponders with GPS observables in a Kalman filter results in the ability of the DNTI system to operate with incomplete sets of data from each of the sensors as long the combination of sensors provides a complete set. Thus, for instance, the system can generate a two dimensional survey quality position solution using just two satellites and a Trisponder measurement. The system user has control over where to locate a Trisponder station (or stations). A user will typically locate the station(s) such that Trisponder obscuration does not occur often; this will

result in uninterrupted surveying being possible in spite of intermittent satellite and or Trisponder obscuration. Field tests at the Aberdeen Harbor (Scotland) and at ports in Wales (United Kingdom) have been very successful in validating both accuracy and uninterrupted navigation claims. Figure 1 shows the Del Norte scheme to integrate GPS measurements with Trisponder measurements.

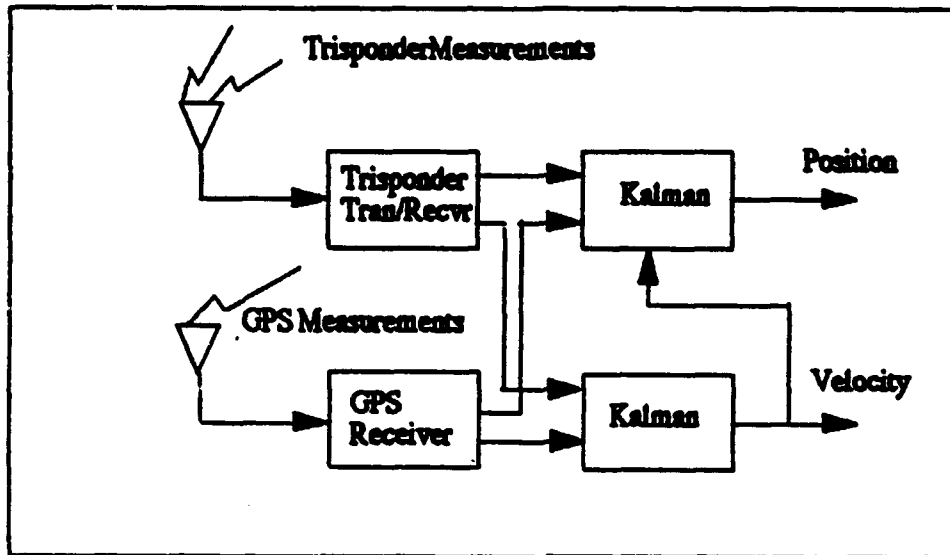


**Figure 1. Del Norte Sensor Fusion Technique**

The Transmitter/Receiver pair provides range and range rate information to the Kalman filters which process the data along with GPS measurements. The sensors can either operate autonomously or together in a synergistic way. GPS code phase and carrier frequency measurements are processed in separate filters to prevent corruption of velocity estimates by noisy pseudorange differences. This decoupling of code phase and carrier frequency processing also allows for easy integration of other sensors. Furthermore, decoupled filters take far less throughput than coupled filters resulting in a position solution being made available with the minimum of latency after measurements are obtained. The DNII system provides the ability to synchronize the Trisponder measurements with the GPS 1 part per second signal.

In field trials it was seen that sensor fusion not only improved the robustness of the system by minimizing "no solution" times but also improved solution accuracy even when a sufficient number of GPS satellites were visible. This was especially apparent when GPS satellite geometry (HDOP, VDOP) was bad. The addition of even a single Trisponder station in many cases improved the HDOP sufficiently to make a qualitative difference. Figure 2 shows how the addition of a single ranging measurement from a Trisponder reduces the GPS uncertainty ellipse.

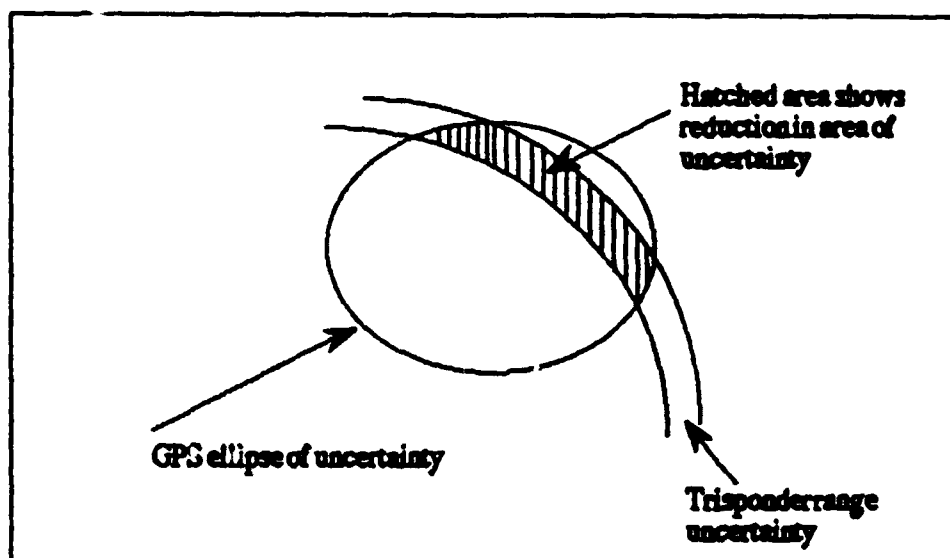


**Figure 2. Reduced error due to sensor fusion**

The integration of data from these sensors in effect slides the ellipse of uncertainty into the region circumscribed by the Trisponder arcs such that the magnitude of error and its uncertainty shrinks. The fused position is located in the hatched area. As more Trisponder measurements or additional satellites become available the hatched area changes shape and becomes smaller and smaller.

Figure three shows some of the results of a survey done at Newport (Wales, Great Britain) on June 28th, 1993 using sensor fusion. A Del Norte 1008 GPS/Trisponder system was used in the survey and was installed on a survey boat operated by the Associated British Ports (ABP) survey crew.

A reference station had previously been set up at the Newport tide hut. Six Trisponder stations were available but three of the stations were out of range of the boat. Of the other three only two of the stations were activated for use in sensor fusion. The survey took three hours. Many obstructions (like passing ships) were encountered during the survey resulting in the number of visible satellites dropping frequently to three and a few times to two. However, because of the sensor fusion capabilities of the 1008 and the availability of Trisponder measurements, the entire survey was accomplished satisfactorily without losing even a second of time. It can be seen from Figure 3 that no difference in positioning is discernible between periods when four or more satellites were visible and when fewer than four were visible. Similar tests were conducted in early July 1993 at Aberdeen Harbor with very similar results.

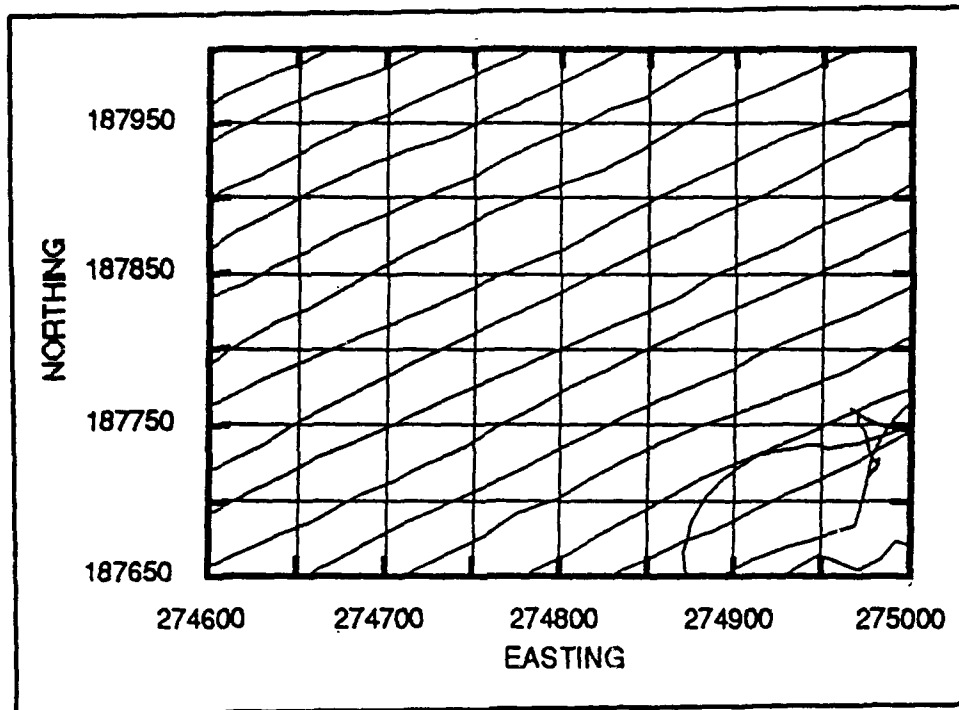


**Figure 3. Survey lines (using sensor fusion)**

## **QUALITY MONITORING**

An increasing number of users depend on DGPS as the principal, if not the only, means of position determination. Under these circumstances a user may be justified in wondering about the quality of the solution being generated. Since a DGPS system is composed of at least one reference station and one mobile station there are at least two factors to consider. The first factor involves the quality of the corrections being generated at the reference station, since an error in the corrections being generated at the reference has a direct bearing on the quality of the position solution at the mobile station. The second involves events happenings at the mobile station. We will discuss each of these two issues below.

The causes for error in the corrections generated at the reference station are many. For instance, one of the sources of error is the fact that in the present version of the RTCM format there is only one bit assigned to indicate the scale factor for both the pseudo range correction as well as the range rate correction. A fast varying range rate correction will introduce errors in the transmitted pseudo range corrections by virtue of poor resolution. This problem is resolved by Del Norte by using a proprietary format that will allow for independent scale factors. A second mechanism for the introduction of error in the reference is that caused by sudden

variation in SA correction rate. This variation acts like an impulse function on the reference Kalman filter, and the nature of the impulse response can be a contributor to error. DNTI systems address this problem by phase locking the corrections generated to the innovations sequence of the Kalman filter resulting in near instantaneous response to such impulses. Other DGPS users [3] like Michael Jensen have proposed using a Monitor station (or stations) at known locations that use the differential corrections from a reference and determine from their own solutions if there are any problems with the corrections. Any deviation between the generated solution and the known solution is an indicator of a potential problem with the differential corrections being received and can be used as the mechanism for either identifying or correcting the problem. DNTI systems currently under design will be capable of operating in this mode.

At the mobile station, apart from the error in the received differential corrections, the primary sources of error are (a) the geometry of the satellites with respect to the user, (b) multipath effects, (c) signal to noise ratios of the satellites being tracked, (d) dropout of differential corrections, and (e) the inadequacy of the number of satellites being tracked. In order to correctly assess the performance of the mobile system a user will need access to all the above information. DNTI systems therefore provide numbers that represent the DGPS system's position accuracy in each axis. These numbers are derived as a function of (a) the satellite DOP (Dilution of Precision), (b) receiver signal to noise ratio, (c) quality of differential correction estimates obtained from the reference, (c) the User Range Accuracy information broadcast by the satellites and (d) differential drop out criteria. Since all available satellite information is processed, any "spurious" measurement is automatically screened out of the navigation solution by comparing the measurement residual with the square root of the Kalman filter computed line of sight residual variance. Other quality assessment indicators are also provided. For instance when measurements from at least two Trisponders are available, another level of confidence is obtained by simultaneously displaying Trisponder and DGPS generated positions and the difference between them. Sensor fusion provides an independent assessment of the quality of the satellite measurements via the use of the highly accurate ranging information provided by the Trisponders.

In many cases, a mission may have to be aborted when the differential data link is lost (temporarily or permanently) and secondary positioning sources are not available. This can be a severe handicap especially when the mission is being conducted at a large distance from land. A solution to this problem is available in the form of "Deldif" post processing software. Raw data is collected at a reference station and the mobile station; after completion of a mission "Deldif" software processes both the reference and mobile data and generates differentially corrected solutions that are accurate, even under dynamics, to tens of centimeters. The post

processed solution can be used in lieu of the real time position data collected or can be used in conjunction with the latter as a "solution quality" check.

A test was conducted in Arlington, Virginia where the distance between six stations was computed using (a) Deldif estimates of the positions of those stations and (b) a laser range finder. In the Table 1 below the distance, in meters, between pairs of stations is represented as S1/S2, S1/S3 etc., where S1, S2, ... S6 are the six stations.

**Table I - Delta between Laser Range Finder and Deldif Processing**

	S4/S5	S5/S6	S1/S2	S2/S4	S4/S6	S2/S5	S1/S4	S2/S6	S1/S5	S1/S6
Laser	15.35	17.26	19.47	24.28	32.25	38.63	42.96	55.93	57.82	75.03
Deldif	14.94	17.55	19.35	24.96	32.06	38.99	43.88	56.50	58.12	75.59
Delta	0.41	-0.29	0.12	-0.68	0.19	-0.34	0.92	-0.57	-0.30	-0.56

The row heading "Delta" represents the difference in ranges as determined by the laser range finder and that obtained by using Deldif post processing software. All units are meters. It is seen that the mean of the absolute values of the delta is 0.44 meters. The realtime solution obtained by the DGPS system compared favorably with the Deldif solution thus validating the concept of using Deldif not only as an enhancer of the solution accuracy but also as a "quality check".

## **INTEGRATION OF THIRD PARTY SOFTWARE WITH DGPS**

Many users have commercial PC based navigation software that can significantly augment and extend the capabilities of a DGPS system if it were possible to run that software in the GPS "box". Del Norte GPS Hardware/Software architecture makes a major extension to the DGPS capabilities possible, by providing an easy means of integrating third party PC software with DNTI systems. Current DNTI DGPS systems are centered around the 80486/80487 PC/AT and ISA bus architecture. The DNTI system has multiple serial and parallel ports, two display controllers with separate memory spectrums that can control both an internal front panel display and an external VGA monitor through a back panel connector, floppy and hard drives.

Figure 4 depicts the software architecture in the "Unix ring" diagram. The DGPS application software consists of a real time operating system that co-exists with DOS. Several tasks, including GPS and Trisponder processing, run concurrently.

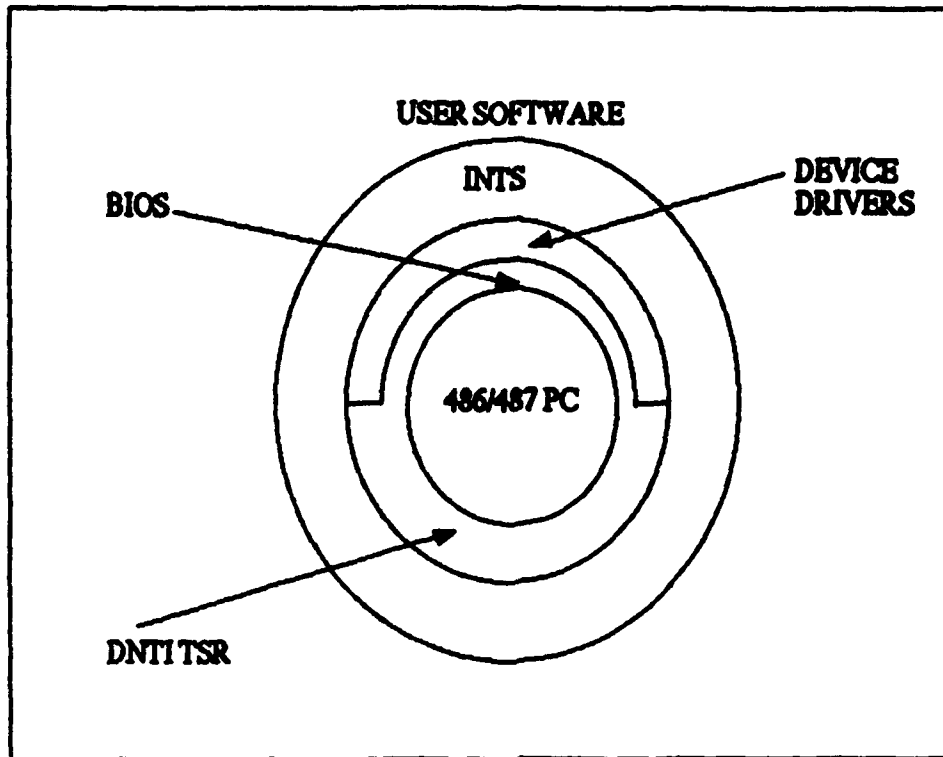


**Figure 4. DNTI TSR Architecture**

The main software task controls all traffic through the various ports and calls appropriate tasks for position computation, logging, output control, and other processes. These tasks are configured as a "Terminate and Stay Resident" (TSR) program so that DNTI software can act as the bridge between user software and the DNTI system hardware. A user's software can then access hardware mechanisms for control over ranging, Trisponder calibration, and GPS functions. An example of this is the integration of Coastal Oceanographics HYPACK software with the Del Norte Model 586/1008 system.

## **CONCLUSION**

Many reasons exist for wanting to fuse data between Trisponder range-range systems and GPS, not the least of which is to provide positioning from two known reliable systems with the consequent increase of confidence in the resulting position. Another possible reason may be that an embedded base of Trisponder equipment is in use and well understood by operators. Under this condition the introduction of GPS as a new sensor can be accomplished for low marginal cost, since the same GPS equipment can also support Trisponder. By obtaining a dual purpose instrument, retraining costs can be minimized. Operationally, even with a full GPS



constellation, fusing Trisponder and GPS can make sense in ports and harbors when passing ships or nearby structures can cause line of sight obstructions.

Several pieces of information in the Del Norte line of GPS systems provide quality control indications. Whenever the system displays position, sigma values of the estimated position can also be displayed. Other indicators of quality are available to the user and include dops, differential corrections available, and the number of satellites in use. In the fusion mode both Trisponder and GPS uncertainties are blended into the positional sigma value. Also in this mode is the position difference calculation between that obtained by the Trisponder alone and that obtained by GPS alone. Thus a user of the equipment has many indications to use in assessing the quality of his navigation solution.

The ability to run third party software on the DNII platform enables a user to take advantage of sophisticated graphics and analysis programs and integrate their capabilities with the DGPS output. Thus, for instance, there would be no need to buy additional PC's to post process the data collected during a survey. The processing can be done right on the Del Norte DGPS systems.

This paper has described major extensions to the DGPS horizon made possible by sensor fusion, quality monitoring/control and integration of third party PC software with DGPS on a DNII platform.

## **ACKNOWLEDGEMENTS**

The writers would like to express appreciation to Mr. Andy Zienkiewicz (Chief Surveyor) of the Associated British Ports for providing the survey boat , for conducting the survey (using DNII sensor fusion ) at Newport, Wales and for allowing us to use the results of the survey. Appreciation is also expressed to Dr. Alan Krulisch of Arete Associates for collecting Deldif data and providing corresponding laser range information. And, last but not least, appreciation is given to the various designers at Del Norte who contributed to the system design and concept validation. These include John Kovach, Paul Dano, Pat Hennessey, Wendell Brooks , Danny Mitchell and Nathan Dunson.

## **REFERENCES**

- 1)Babu, Kumar., " Sensor Fusion via Decentralized Kalman Filters", Del Norte Technology internal memorandum, February 1993.

- 2) Dunson, Nathan., "Del Norte's Hardware and Software Platform for Third Party Vendor Software Development", Del Norte Technology internal memorandum, February 1993.
- 3) Jensen, Michael H.B., "Quality Control for Differential GPS in Offshore Oil and Gas Exploration", GPS World, September 1992.
- 4) Wong, Hennessey, Babu., " Integration of DGPS Correction Message on an X-Band Ranging System", ION GPS Conference, January 1993.
- 5) Robbins, Greg M. and Pointon, John G., "Method and Advantages of Using Microwave Ranging Signals for Differential GPS Data Transfer ", Differential Satellite Navigation Symposium, Amsterdam, March-April 1993.

**THIS PAGE LEFT BLANK INTENTIONALLY**

## **INS/DGPS Trajectory Determination**

**Pierre-Eric Pommellet & Pascal Dutot**  
*Laboratoire de Recherche Balistiques et Aérodynamiques*  
27207 Vernon, France

Approved for Public Release  
Distribution is unlimited

### **Biographies**

Pierre-Eric Pommellet is currently the GPS & Navigation Department Manager at L.R.B.A. He graduated from Ecole Polytechnique in 1987, from Ecole Nationale Supérieure de l'Aéronautique et de l'Espace in 1989. He received a Master Degree in Aeronautics and Astronautics from MIT in 1990. He is an associate member of Sigma Xi. He has been involved in navigation studies since 1990.

Pascal Dutot is engineer at L.R.B.A. He received a Master of Science in Electrical Engineering from the University of Caen in 1986. He has been involved in trajectory determination since 1990 as a software engineer.

### **Abstract**

In order to test small and medium size navigation systems, L.R.B.A. has designed test vehicles and has integrated sensors able to determine a "true" position or reference trajectory.

The reference trajectory is computed in post processing through a Kalman smoother, using information coming from an inertial unit (UNI 52A from Sagem) and two Ashtech XII GPS receiver in differential mode.

LRBA has implemented an optimal two stages DGPS software, which was evaluated by comparison with surveyed points during static tests, and by comparison with radars and cinetheodolites at the French Flight Test Center. Accuracy of the system was shown to be 3m at 95% in 2D and 5m at 95% in 3D. Velocity and attitude's accuracy are estimated to be better than 0.05 cm/s and 1 millirad.

Optimization for long baselines (up to 1000 km) is currently studied with the identification of a local ionospheric model derived from bi-frequencies' measurements.

### **1. Introduction**

L.R.B.A. was created in 1946 by the French DoD in order to develop the French space and ballistic programs. Its realizations range from Véronique and

Diamant rockets to the navigation software of missile launcher nuclear submarines. In 1971, the industrial activity was separated from the laboratory to create the Société Européenne de Propulsion (S.E.P.) which is now in charge of Ariane's engines. L.R.B.A. main activities are now concerned with satellites and missiles guidance equipments, algorithms and integration, from theoretical studies to environmental tests.

In 1973, LRBA was designated by the French DoD to be the reference test center for inertial navigation systems, and, in 1993, the GPS was added to this mission. In order to be able to study and test highly accurate navigation systems, LRBA has had to develop specific test beds, and a family of trucks and test vans has then been equipped with autonomous power supply and laboratory capabilities. The newest ones are called VEXIN (Inertial and Navigation EXperiment Vehicle) and VETT (All Terrains test Vehicle) (reference 5).

The outputs of the tested systems are synchronized with a trajectory determination system which combine an INS and a GPS receiver. The navigation accuracy is given in post processing by comparing stored measurements and a reference trajectory issued from DGPS and a INS/DGPS smoother.

### **2. Hardware support**

The hardware integrated on board the vehicle for trajectory determination consists of three distinct parts: The inertial navigation system, the GPS receiver and the data storage equipment.

The INS is an UNI52A from the ULISS family of SAGEM. It's a gimbaled navigation unit, based on 0.02°/h class gyros named S040, and 10<sup>-3</sup> class accelerometers. This class of inertial equipment is used massively in the French Air Force and the Naval aviation. It provides positions at 6.25 Hz, velocities and attitudes at 50 Hz, and performance class is 1.2 N/h in drift, 1.2 m/s in horizontal velocity, and 5 arc-minutes in attitudes.

The GPS receiver being used is a C/A code Ashtech XII (12 channels), providing raw

measurements (pseudo-ranges, delta-ranges and integrated Doppler) along with ephemeris data and a 1 PPS output for synchronization purpose. Two receivers are used for trajectory determination, 1 on a fixed location which was surveyed in WGS84, and one on the mobile vehicle.

The control and data storage equipment consist of a computer based system, able to control the data bus interface of the INS, and to store all the measurements that are necessary for trajectory determination (meaning pure INS data and GPS raw-measurements).

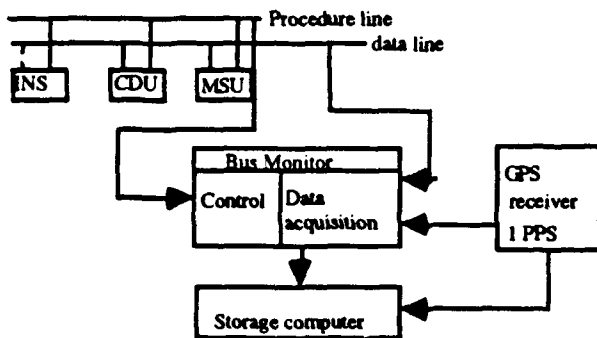


Figure 1: Data control and storage equipment

The reference trajectory is driven in post processing on Spark workstations. First, the DGPS solution is realized with an optimal two-stages' algorithm, combining elementary parallel Kalman filters and weighted least squares. Second, a 16 states Kalman smoother uses the INS values and the DGPS outputs to realize an optimal complementary filter, based on a classical INS error propagation model

### 3. Differential GPS Implementation

It is well known (reference 6) that GPS sources of errors such as Selective Availability, ionospheric and tropospheric delays, ephemeris and satellite clock errors are strongly correlated for two receivers within few hundreds of kilometers of each other. For that matter, a receiver located on a surveyed point can elaborate an estimate of the global error budget, by comparing its raw measurements with what it should be with respect to its known location and the satellite position. This error estimate, or differential correction, can then be used by a remote receiver to improve dramatically its navigation accuracy: This technique is well known now as differential GPS.

We use three kinds of GPS raw-measurements: Pseudo-ranges, or ranges derived with time

measurements, delta-ranges or relative velocities derived by Doppler effect, and integrated Doppler. First, an optimal filter between the pseudo-ranges and the integrated Doppler is implemented, then differential corrections are derived at the static receiver. The position and clock bias at the remote receiver are calculated through an iterated least square algorithm using corrected pseudo-ranges. Finally, velocity and clock drift are issued from the corrected Doppler measurements and a linear least square.

### 4. INS/DGPS Filter

Since the dynamic of the INS error propagation is well understood, we have chosen to implement a complementary filter to compute the reference trajectory, in other words:

$$X_{ref} = X_{INS} + \delta X$$

and  $\delta X$  is estimated by a Kalman smoother which uses INS outputs to linearize the error propagation model, and DGPS updates in position and velocity.

The propagation of  $\delta X$  takes the following form:

$$\delta \dot{X} = G(X) \cdot \delta X + v, \quad v \sim N(0, Q)$$

where

$$X = [Lat \ Lon \ Vn \ Ve \ \phi \ \theta \ \psi]$$

with

Lat	INS latitude in radian
Lon	INS longitude in radian
Vn	INS north velocity in m/s
Ve	INS east velocity in m/s
$\phi, \theta, \psi$	INS attitude angle in radian

The state vector  $\delta X$  includes the errors on the X components, along with the errors on the inertial sensors (gyros and accelerometers).

$$\begin{aligned} \delta X &= [\delta Lat \ \delta Lon \ \delta Vn \ \delta Ve \ \delta \phi \ \delta \theta \ \delta \psi \ A1 \ A2] \\ A1 &= [Bx \ By \ Dx \ Dy \ Dz] \\ A2 &= [fx \ fy \ b1 \ b2] \end{aligned}$$

in above

$\delta Lat$	latitude error
$\delta Lon$	longitude error
$\delta Vn$	north velocity error
$\delta Ve$	east velocity error
$\delta \phi \ \delta \theta \ \delta \psi$	attitude errors
$Bx, By$	accelerometers bias

Dx,Dy,Dz  
fx,fx  
b1,b2

gyros drifts  
accelerometers scale  
factors  
gyros g sensitive  
coefficients

The details of the error propagation model are given in the Appendix.  
When DGPS is available (at least 4 satellite in view and GDOP smaller than a tunable threshold), we get a linear measurement on the state vector  $\delta X$ , which is:

$$y = \begin{bmatrix} \text{Lat}_{\text{INS}} - \text{Lat}_{\text{DGPS}} \\ \text{Lon}_{\text{INS}} - \text{Lon}_{\text{DGPS}} \\ \text{Vn}_{\text{INS}} - \text{Vn}_{\text{DGPS}} \\ \text{Ve}_{\text{INS}} - \text{Ve}_{\text{DGPS}} \end{bmatrix} = H \cdot \delta X + v$$

$$H = \begin{bmatrix} 1 & 0 & 0 & 0 \\ 0 & 1 & 0 & 0 \\ 0 & 0 & 1 & 0 \\ 0 & 0 & 0 & 1 \end{bmatrix} [0]$$

and  $v \sim N(0, V)$

In above, the DGPS values are corrected from the level arm between the inertial sensors and the GPS antenna, using attitudes and attitude velocities from the INS.

The implementation of the linear Kalman smoother is then straightforward (reference 3). The update rate was chosen to be 10s, which is enough because of the good quality of the inertial sensors. A  $3\sigma$  test is performed on the DGPS data to screen out bad measurements.

These algorithms were implemented in C on unix workstations.

## 5. DGPS Accuracy

### 5.1 Position Accuracy

The accuracy of the DGPS software was evaluated in dynamic with the French Flight Test Center. A test bed was implanted on a Caravelle jet airplane. Two means were used to give a "true" trajectory: First a radar based system, accurate at 0.5m at 1 sigma, second an optic based system, or cinetheodolites, accurate at 1m at 1 sigma. A total of 9 flights was conducted, giving more than 3300 measurements. Only (PDOP<6) GPS results were kept. Typical baseline during those tests was of the order of 10 kilometers, and two fixed stations were used for two test flights providing results for baselines up to 100 kilometers. Those flights have

included accelerated maneuvers along with 2g turns.

flight number	baseline (km)	2D at 95 % (m)	3D at 95 % (m)	meas. number
0	~10	2.00	3.33	232
1	~10	2.37	2.81	529
2-1	~10	2.48	3.56	310
2-2	~100	3.37	4.13	310
3-1	~10	3.78	4.96	382
3-2	~100	4.00	5.61	414
4	~10	2.67	4.38	300
5	~10	1.35	1.98	270
total	-----	3.08	4.25	2747

Figure 2: Radar referenced flights

flight	2D at 95% (m)	3D at 95% (m)	meas. number
1	1.44	3.28	296
2	1.91	3.02	207
3	1.77	3.35	176
total	1.79	3.33	679

Figure 3: Optic referenced flights

The accuracy demonstrated during those tests turned out to be in the order of 3m in 2D at 95 % and better than 5m in 3D at 95 %, for baseline less than 100 km.

As an example, we give the differences between DGPS and cinetheodolites in Figure 4\_1 and 4\_2 along with the histogram of the 2D results.

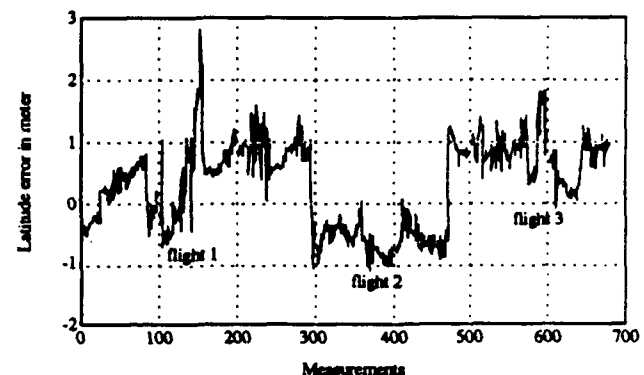


Figure 4\_1: Latitude error of DGPS

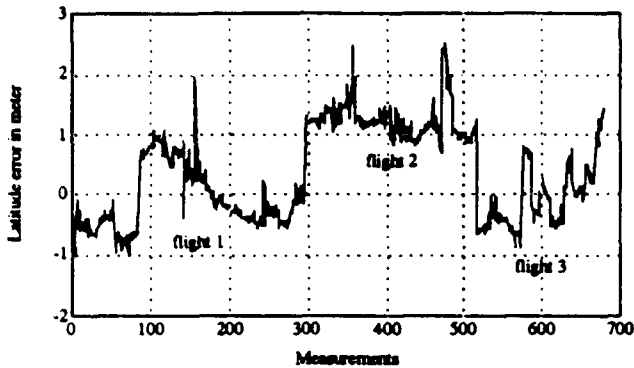


Figure 4\_2: Longitude error of DGPS

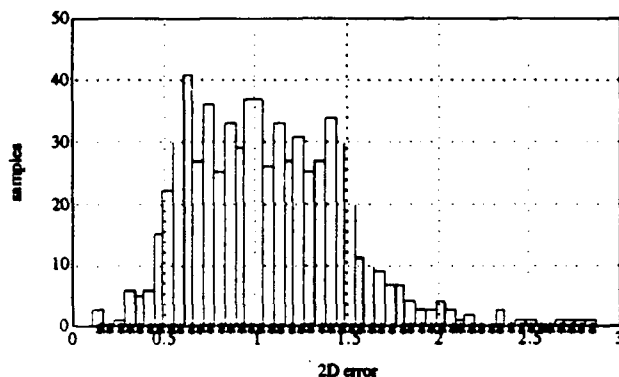


Figure 4\_3: 2D error histogram

Long distance tests were driven to evaluate the accuracy of the DGPS as a function of the baseline. For that purpose, two receivers were used on surveyed point with distance between them varying from 0 to 800 km. Each test lasted at least 2 hours. Even if only static results are available, they give a good idea of the potentiality of long distance differential GPS.

Results in 2D and in 3D are as follow:

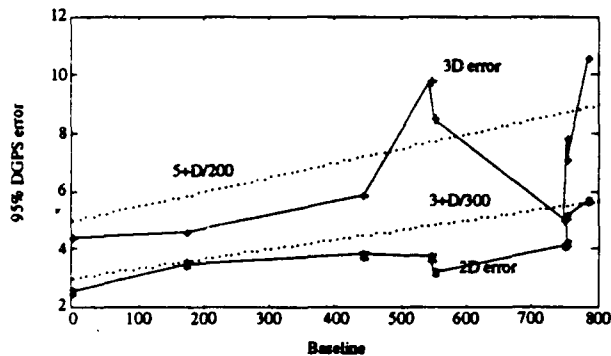


Figure 5: Long distance tests

Figure 5 shows the degradation of the accuracy as approximately a linear function of the baseline. If P2 is the 2D accuracy at 95% and P3 the 3D accuracy at 95%, and if D is the baseline between the two receivers (in kilometers), we showed that:

$$P2 \sim 3 + D/300 \text{ (in meters)}$$

$$P3 \sim 5 + D/200 \text{ (in meters)}$$

## 5.2 Velocity Accuracy

As no precise references are available to evaluate velocity accuracy, only static tests can give an idea of what is achievable at low dynamics. Actually, as the satellites are moving quite fast, and as the relative velocity between a static receiver and the satellites is in the order of several hundred meters/second, the static case is still representative of a low dynamic motion (ie non accelerated but not necessary low speed).

On those tests, DGPS turned out to be extremely precise, in the order of 2cm/s at 95%, whatever the baseline.

## 6. INS/DGPS Results

The INS/DGPS smoother has been tested during several flights with a Transall aircraft. We present here an example of those tests.

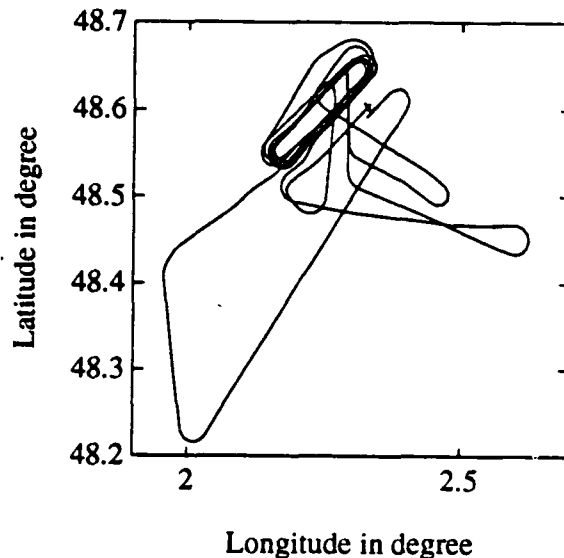


Figure 6: Pure INS

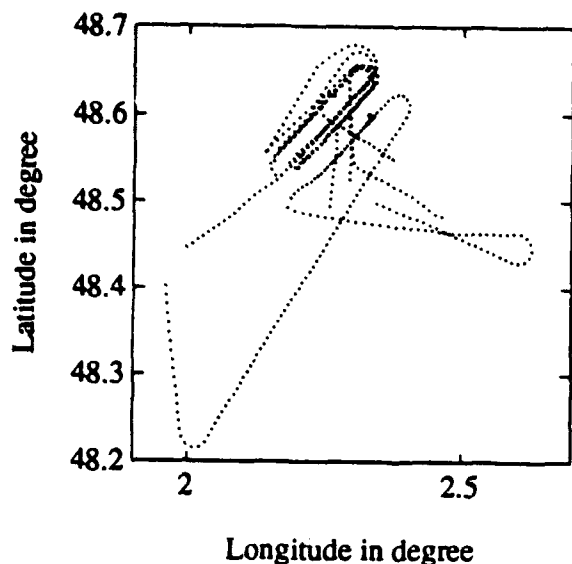


Figure 7: DGPS

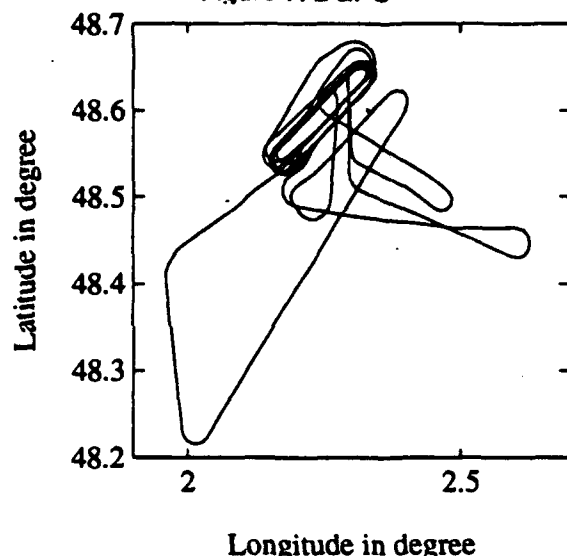


Figure 8: Filtered INS

Figure 6 shows the pure inertial trajectory during the flight (The drift of the INS is clearly shown). Figure 7 presents the DGPS trajectory and we see that GPS is not always available. Figure 8 shows the filtered trajectory which is precise (DGPS accuracy) and continuous (from the INS).

As the general behavior of the filter was correct (the innovation vector is a white noise), a good way to evaluate its accuracy and robustness is to simulate a lack of GPS during maneuvers (such as turns). Actually, as DGPS is available during that time, but not used into the filter, a reference trajectory exists with the optimum accuracy. We can then compare the outputs of the new filter with this "true" trajectory. This was done for various amplitudes of the GPS mask, from 10s to 1200s.

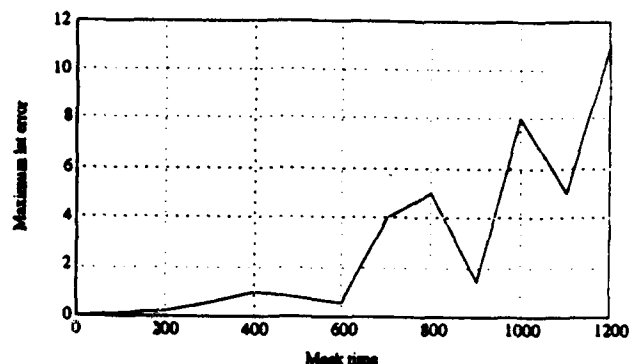


Figure 9: Latitude error during mask

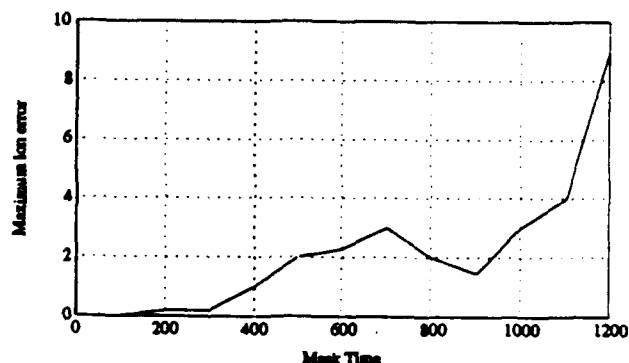


Figure 10: Longitude error during mask

Figure 9 and 10 show the maximum error that was encountered as a function of the mask duration. We remark that if the lack of GPS does not exceed 10 minutes (which is generally the case), the accuracy degradation stays below 3m. The filter was tuned in order to correlate those results with the covariance matrix.

Concerning velocities, the Kalman smoother has a strong smoothing effect on the raw DGPS velocities, that is showed by Figure 11 and 12. Actually, as the attitude velocities are quite noisy on this kind of INS, the level arm corrected DGPS velocity become noisy (in the order of 0.1 m/s at  $1\sigma$ ). Once filtered, the velocity accuracy comes back to few centimeters/second.



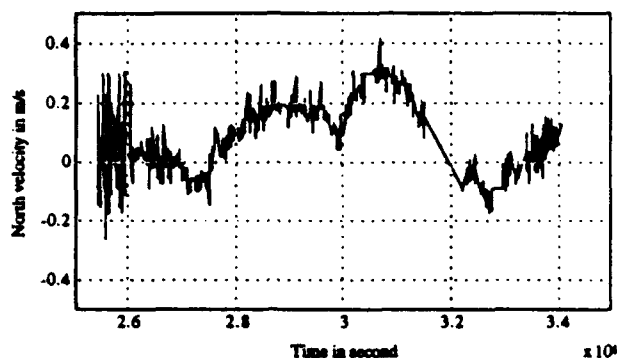


Figure 11: INS-DGPS velocity

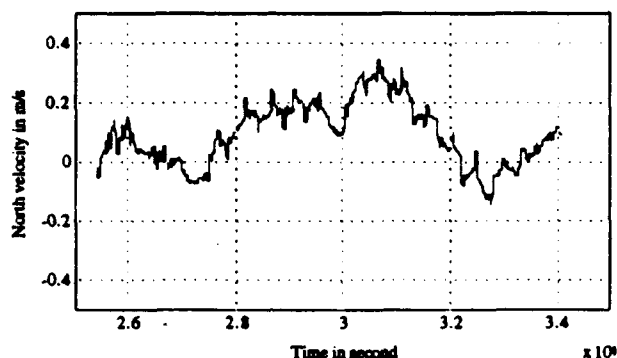


Figure 12: INS-filter velocity

## 7. Conclusion

The hardware integration and the software development done by LRBA for trajectory determination provide precise and continuous position and velocity information in the 3 axis. An aeronautic class INS and an Ashtech XII GPS receiver are used in post processing to proceed an optimal two stages DGPS filter and a Kalman smoother. Accuracy and robustness demonstrated with flight tests turned out to be very good, in the order of 3m at 95% in 2D (5m in 3D) with a graceful degradation function of the baseline, staying better than 10m for 800 km. LRBA is currently working on an improvement of the DGPS software, using bi-frequencies measurements on the reference station, so that a local ionospheric model can be identified during the test. Autonomous integrity module will also be implemented in a near future.

## 8. Acknowledgments

The authors would like to thanks all the GPS and Navigation department. They would also like to thanks the French Flight Test Center for their collaboration in the accuracy evaluation.

## 9. References

1. North Atlantic Treaty Organization, Military Agency for Standardization, STANAG 4294, Navstar Global Positioning System (GPS) Characteristics, 1991
2. Faure P., "Navigation Inertielle et Filtrage Optimal", Dunod 1971.
3. Gelb A. (editor), "Applied Optimal Estimation", MIT Press, Cambridge Ma. 1974
4. Salomon A., "Restitution des erreurs de la centrale UNI40 du VASI, Définition de la méthode", LRBA 258/85/SYI 1985.
5. Pommellet P. and Panefieu B., "Trajectory Determination of a Test Vehicle", Proceeding of the National Technical Meeting of the ION, San Diego 1992.
6. Pommellet P. and Panefieu B., "Analyse du GPS Différentiel", LRBA /93/SIN/473/NC

## 9. APPENDIX

### A. DGPS Algorithm

We define:

$X$	true receiver location (fixed and mobile)
$X_i$	satellite location based on the ephemeris parameters
$c$	speed of light in vacuum
$b$	receiver clock bias (in meters)
$a$	receiver clock drift (in meter/s)
$d$	error delay (weather clock, ephemeris, iono, tropo, multipath)
$N$	ambiguity (wave-length multiple)
$\epsilon_c$	code error
$\epsilon_p$	phase error

We then have:

True pseudo-range (not known)

$$(1) \quad PR_i = \|X - X_i\| + b$$

Measured pseudo-range

$$(2) \quad mPR_i = \|X - X_i\| + b + d_{\text{clock}} + d_{\text{ephe}} + d_{\text{iono}} + d_{\text{tropo}} + d_{\text{mult}} + \epsilon_c$$

Non noisy pseudo-range (not known)

$$(3) \quad pPR_i = \|X - X_i\| + b + d_{\text{clock}} + d_{\text{ephe}} + d_{\text{iono}} + d_{\text{tropo}}$$

Integrated Doppler measurement

$$(4) \quad mDli = \|X - X_i\| + b + d_{\text{clock}} + d_{\text{ephe}} - d_{\text{iono}} + d_{\text{tropo}} + N + \epsilon_\phi$$

True Delta range

$$(5) \quad DR_i = \frac{(\dot{X} - \dot{X}_i) \cdot (X - X_i)}{\|X - X_i\|} + a$$

Delta range measurement

$$(6) \quad mDR = \frac{(\dot{X} - \dot{X}_i) \cdot (X - X_i)}{\|X - X_i\|} + a + d_{\text{ephe}} + d_{\text{clock}} - d_{\text{iono}} + d_{\text{tropo}} + \epsilon_d$$

As the noise level introduced by multipath and by the code tracking loop error is high relative to the level of accuracy we are looking for, we filter the pseudo-ranges with the integrated Doppler through a one state Kalman filter. Actually, if  $k$  and  $k+1$  represent time indices, we can write:

(from (3) and (4))

$$(7) \quad pPR^{k+1} - pPR^k = mDl^{k+1} - mDl^k + 2\delta d_{\text{iono}} + w$$

(from (3) and (2))

$$(8) \quad mPR^{k+1} = pPR^{k+1} + d_{\text{mult}} + \epsilon_c$$

$$\text{with } w = \epsilon_\phi^{k+1} - \epsilon_\phi^k \\ \delta d_{\text{iono}} = d_{\text{iono}}^{k+1} - d_{\text{iono}}^k$$

If we assume that the noise are white and non correlated, and under gaussian assumptions, we can estimate pPR with respect to a least square criterion by a classical 1 state Kalman filter:

$$fPR_0 = mPR^0, P_0 = R, \\ R = E((d_{\text{mult}} + \epsilon_c)^2), \\ Q = E((2\delta d_{\text{iono}} + w)^2)$$

$$fPR_{k+1/k} = fPR_{k/k} + mDl^{k+1} - mDl^k \\ P_{k+1/k} = P_{k/k} + Q \\ K = P_{k+1/k} (P_{k+1/k} + R)^{-1} \\ fPR_{k+1/k+1} = fPR_{k+1/k} + K \cdot (mPR^{k+1} - fPR_{k+1/k}) \\ P_{k+1/k+1} = (1 - K) \cdot P_{k+1/k}$$

This provides a filter measurement (or fPR) with its error covariance that will be used in place of the raw pseudo-range for the fixed and remote receivers.

Except for strong multipath, the basic assumptions that are made for the filtering problem turn out to be correct, and this kind of algorithm gives very good results in terms of accuracy and of robustness.

For each satellite in view, the differential correction computed by the fixed receiver, is:

$$\delta PR = fPR - PR \\ = b + d_{\text{horiz}} + d_{\text{ephe}} + d_{\text{iono}} + d_{\text{tropo}} + fr$$

$$\delta DR = mDR - DR \\ = a + d_{\text{ephe}} + d_{\text{horiz}} - d_{\text{iono}} + d_{\text{tropo}} + \epsilon_d$$

The differential corrections contain the spatially correlated errors plus the common biases.  $fr$  is a filtering residual that depends mostly on the level of multipath.

Next, we compute for the remote receiver:

$$(9) \quad PR_i = fPR_i - \delta PR_i - \|X - X_i\| + b$$

$$(10) \quad DR_i = fDR_i - \delta DR_i - \frac{(\dot{X} - \dot{X}_i) \cdot (X - X_i)}{\|X - X_i\|} + a$$

Finally, as soon as 4 measurements are available,  $X$  and  $b$  are calculated by an iterated least square algorithm weighted by the filter covariances. Once this is done, the velocity and clock drift are derived by a linear least square. The output rate of the position and velocity delivery is 1 Hz.

We assume an initial guess for position,  $X_0$ ,  $b_0$  then, at the first order:

$$PR_i = \|X_0 - X_i\| - \frac{X_0^T}{\|X_0 - X_i\|} \cdot (X_0 - X) + b_0 - b - b_0$$

or

$$PR_i - \|X_0 - X_i\| + b_0 = - \frac{X_0^T}{\|X_0 - X_i\|} \cdot (X_0 - X) + b_0 - b$$

when putting all those equations together in a matrix form, we get:

$$Y = H \begin{bmatrix} X_0 - X \\ b_0 - b \end{bmatrix}$$

with

$$Y = \begin{bmatrix} \vdots \\ PR_i - \|X_0 - X_i\| + b_0 \\ \vdots \end{bmatrix}, \text{ and } H = \begin{bmatrix} \vdots & \vdots \\ -X_0^T & 1 \\ \vdots & \vdots \end{bmatrix}$$

$X$  and  $b$  can then be computed with the minimization of a criterium that weights the measurements with respect to their covariance matrix issued from the Kalman filter, ie:

$$(X, b) = \operatorname{argmin} \left( (Y - H \begin{bmatrix} X_0 - X \\ b_0 - b \end{bmatrix})^T \cdot W \cdot (Y - H \begin{bmatrix} X_0 - X \\ b_0 - b \end{bmatrix}) \right)$$

$$\text{with } W = \begin{bmatrix} \ddots & 0 & 0 \\ 0 & \frac{1}{P_i} & 0 \\ 0 & 0 & \ddots \end{bmatrix}$$

finally

$$\begin{bmatrix} X_0 - X \\ b_0 - b \end{bmatrix} = (H^T \cdot W \cdot H)^{-1} \cdot H^T \cdot W \cdot Y$$

This algorithm is iterated until  $X - X_0$  converge to 0. Once the  $X$  vector is known, equation (10) become linear in  $\dot{X}$  and  $a$ , and therefore can be solve with a classical linear least square.

## B. INS Propagation Model

The derivation of the error propagation equation is classical and can be found in references 2 and 4. Inertial components errors are modeled as first order Markovian processes. The vertical channel is decoupled from the horizontal channel with a baro-inertial loop. We hence get

$R$	semimajor axis of the WGS-84 ellipsoid
$f$	flattening of the WGS-84 ellipsoid
$\Omega$	earth rotation rate
$\alpha$	mechanization angle
$\gamma_n$	north acceleration
$\gamma_e$	east acceleration

$$\Omega_n = \Omega \cdot \cos(\text{Lat}) + E_v / R_e$$

$$\Omega_e = -V_n / R_n$$

$$\Omega_z = \Omega \cdot \sin(\text{Lat}) - V_e / R_e \cdot \tan(\text{Lat})$$

$$R_n = R \cdot (1 - 2 \cdot f + 3 \cdot f \cdot \sin^2(\text{Lat}))$$

$$R_e = R \cdot (1 + f \cdot \sin^2(\text{Lat}))$$

$$\frac{d}{dt} \delta \text{Lat} = \frac{V_n}{R_n}$$

$$\frac{d}{dt} \delta \text{Lon} = \frac{\sin(\text{Lat})}{R_n \cdot \cos^2(\text{Lat})} \cdot V_e \cdot \delta \text{Lat} + \frac{1}{R_e \cdot \cos(\text{Lat})} \delta V_e$$

$$\Delta f_n = g \cdot \delta \psi + \gamma_e \cdot \delta \theta + B_x \cdot \cos(\alpha) - B_y \cdot \sin(\alpha) + f_x \cdot \cos(\alpha) \cdot (\gamma_n \cdot \cos(\alpha) - \gamma_e \cdot \sin(\alpha)) + f_y \cdot \sin(\alpha) \cdot (\gamma_n \cdot \sin(\alpha) + \gamma_e \cdot \cos(\alpha))$$

$$\Delta f_e = -g \cdot \delta \phi - \gamma_n \cdot \delta \theta - B_x \cdot \sin(\alpha) - B_y \cdot \cos(\alpha) + f_x \cdot \sin(\alpha) \cdot (-\gamma_n \cdot \cos(\alpha) + \gamma_e \cdot \sin(\alpha)) + f_y \cdot \cos(\alpha) \cdot (\gamma_n \cdot \sin(\alpha) + \gamma_e \cdot \cos(\alpha))$$

$$\frac{d}{dt} \delta V_n = -V_e \cdot (2 \cdot \Omega \cdot \cos(\text{Lat}) + \frac{V_e}{R_e \cdot \cos^2(\text{Lat})}) \cdot \delta \text{Lat} +$$

$$2 \cdot \Omega_z \cdot \delta V_e + \Delta f_n$$

$$\frac{d}{dt} \delta V_e = V_n (2 \cdot \Omega \cos(Lat) + \frac{V_e}{R_e \cos^2(Lat)}) \cdot \delta Lat +$$

$$(\Omega \sin(Lat) - \Omega z) \cdot \delta V_n + \frac{V_n}{R_e} \tan(Lat) \cdot \delta V_e + \Delta f_e$$

$$\frac{d}{dt} \delta \phi = -\Omega \sin(Lat) \cdot \delta Lat + \frac{\delta V_e}{R_e} + \Omega z \cdot \delta \theta -$$

$$\Omega e \cdot \delta \psi + \cos(\alpha) \cdot Dx - \sin(\alpha) \cdot Dy + b1 \cdot \gamma_n - b2 \cdot \gamma_e$$

$$\frac{d}{dt} \delta \theta = \frac{\delta V_n}{R_n} - \Omega z \cdot \delta \phi + \Omega n \cdot \delta \psi - \sin(\alpha) \cdot Dx$$

$$- \cos(\alpha) \cdot Dy + b1 \cdot \gamma_e + b2 \cdot \gamma_n$$

$$\frac{d}{dt} \delta \psi = -(\Omega \cos(\phi) + \frac{V_e}{R_e \cos^2(Lat)}) \cdot \delta Lat -$$

$$\frac{\tan(Lat)}{R_e} \cdot \delta V_e + \Omega e \cdot \delta \phi - \Omega n \cdot \delta \theta - Dz$$

All the other states have a first order markovian error propagation model.

$$\dot{x} = -\frac{1}{T} \cdot x + w, \text{ with } w \sim N(0, W)$$

**THIS PAGE LEFT BLANK INTENTIONALLY**

# APPLICATIONS OF ACCURATE TERRAIN REFERENCED NAVIGATION

M V COUCH & G A WILKINSON

BRITISH AEROSPACE (SYSTEMS & EQUIPMENT) LTD  
PLYMOUTH, ENGLAND, PL6 6DE

---

## 1 ABSTRACT

A number of vital functions can be added to a high speed military aircraft if its position relative to the terrain is known precisely. Digital Terrain Systems, such as the British Aerospace TERPROM<sup>1</sup> system, provide these functions as a consequence of the high accuracy of the Terrain Referenced Navigation (TRN) capability.

The precise, drift-free navigation accuracy of TERPROM's TRN function enables it to provide the pilot with such information as a predictive Ground Proximity Warning (GPW), covert Terrain Following (TF) and passive Target Ranging.

These functions have been thoroughly flight tested over hundreds of hours in a number of aircraft including the USAF F-16 and the RAF Tornado. Various terrain types, INS types and map qualities have been covered during this testing. The system has proven to be consistently accurate and robust and this has culminated in it now being under contract for a production USAF F-16 programme.

## 2 INTRODUCTION

Today's military aircraft frequently have to fly at very low levels, by day and night, in all weathers, and low-level attacks often have to be carried out without reference to external navigational aids. Very few aircraft can achieve this effectively and, in doing so, use ground mapping and terrain following radars which are heavy, expensive and, when operated, may alert an enemy. However, over a number of years, British Aerospace (Systems and Equipment) Ltd (BASE) has developed TERPROM, a Digital Terrain System (DTS), which provides highly accurate navigation plus weapon aiming, passive terrain following and ground collision avoidance with no requirement for external aids or forward electronic emissions. Furthermore, this is achieved with proven reduction in pilot/crew workload.

---

<sup>1</sup>TERPROM is a registered trademark in Great Britain and worldwide trademark applications have been filed.

The Terrain Referenced Navigation (TRN) function provides aircraft position relative to the terrain using a multi-state Kalman filter. Radar altimeter measurements and a digital map are used to calibrate the inertial reference system errors. In addition, the position estimate is continually adjusted to account for local variations in the map database, effectively calibrating the errors in the database.

The Terrain Following (TF) function interrogates the terrain ahead of the aircraft and generates commands to enable the pilot to maintain a flight path as close as possible to his selected height above the terrain. With the advantage of 'over-the-hill' visibility, database TF enables the maximum possible penetration into valleys to be achieved. This function operates at all attitudes and, at present, speeds up to M1.0.

The Ground Collision Avoidance System (GCAS) uses the aircraft dynamic information and response to predict the aircraft flight path. The local terrain is examined and, for standard recovery manoeuvres, the ground proximity that will occur is predicted. Warnings are then issued to the pilot based on this predicted proximity.

The aircraft Target Ranging is enhanced with impact point information relative to the terrain being continuously updated by TERPROM. Weapon delivery accuracy better than air-to-ground radar ranging has been demonstrated in flight using practice bombs.

This paper describes the above functions and gives an indication of the significant amount of flight testing carried out on them to date. In addition, current developments, contained within Advanced Terrain Avoidance Cuing (ATAC), of the TERPROM system are discussed.

### **3     SYSTEM DESCRIPTION**

A Digital Terrain System can, potentially, provide the following functions in addition to drift-free Navigation: predictive Ground Collision Avoidance, covert Terrain Following, Terrain Avoidance, Threat Avoidance and passive Target Ranging. The limiting factor to the ability to supply these functions is, and always will be, an accurate knowledge of aircraft position relative to the terrain.

The TERPROM DTS currently provides the following capabilities.

### 3.1 Terrain Referenced Navigation (TRN)

The core of the DTS is a software suite with a bulk memory store which contains a terrain map in digital form. The TRN function uses this map, together with the aircraft navigation system, to predict aircraft height above the ground. It then compares this prediction with the true height as measured by the radar altimeter and uses the difference between its prediction and reality as the measurement to its Kalman filter to provide corrections to navigation system outputs. In this way, drift-free navigation accuracy typically better than 40m CEP horizontal and 3m rms vertical, over terrain with slopes as low as 2%, can be achieved.

Through the Kalman filtering techniques, an error-corrected model of the aircraft navigation system (normally INS based) can be built. The effects of INS errors are then significantly reduced and the robustness of the system model is such that, once established, the high accuracy degrades only slowly towards raw INS performance, even on long over-water passages or during total radio silence. Conversely, once radar altimeter information is again available, system performance can quickly recover to better than 40m accuracy.

TERPROM has two modes of TRN operation:

- a) Continuous or Track mode which updates at approximately 3Hz to provide the confidence and safety levels essential for operational and training use. This is the primary operating mode, where each radar altimeter reading is used as a measurement into the Kalman Filter.
- b) Single Fix or Acquisition mode which is used only when the system is initialised in the air, when recovering from extended operations over water or when the system is unsure of position for any other reason. In this mode, a batch of radar altimeter readings is used as a measurement into the Kalman Filter.

These modes are selected automatically by the mode control software and require no crew intervention.



### **3.2 Terrain Following**

Using the terrain database and a kinematic model of the aircraft, terrain following signals can be generated and fed directly to an autopilot or to the HUD (Head Up Display) flight director for the pilot to follow. Since the DTS knows the shape of the terrain beyond the immediate horizon, intelligent terrain following algorithms can be implemented, reducing aircraft exposure. Database TF permits unrestricted manoeuvring in terrain following flight.

For aircraft already equipped with, or requiring, a Terrain Following Radar (TFR), the DTS TF algorithms can be integrated or embedded into the TFR, enabling it to operate in a much more covert fashion. Power output can be selectively reduced, transmissions can be scheduled and sectors intelligently blanked.

### **3.3 Ground Collision Avoidance**

Again, using the terrain database and a kinematic model of the aircraft, "intelligent" or predictive ground collision avoidance warnings can be generated. They are predictive in that they do not rely on current radar altimeter inputs and will give warnings if the aircraft tries to fly or bank into a vertical cliff face or, indeed, if the aircraft approaches the ground inverted. Although reliant on radar altimeter information in the long term, in the short term, measured in minutes rather than seconds, full performance is maintained with no radar altimeter information at all. If required, commands to initiate automatic pull-up or recovery manoeuvres can be generated. Obstacle warnings, from stored DVOD (Digital Vertical Obstruction Data), are also provided.

### **3.4 Passive Target Ranging**

Target co-ordinates can be entered before flight or passed, in flight, by a target handover system and with this information an accurate range to target can be provided. Also, because target height is accurately calculated from the database and aircraft height is known, target relative height is continually available for weapon aiming calculations. Thus weapon aiming accuracy is significantly improved, whilst remaining totally covert.

A DTS can also supply passive ranging algorithms which provide absolute and relative target position for any, pilot-designated, target of opportunity. This technique, known as look-aside ranging, can readily be used in conjunction with Helmet Mounted Displays or any off-boresight target designating equipment.

### **3.5 TERPROM Hardware Configuration**

TERPROM can be implemented in a number of ways, depending upon the aircraft system architecture. The current host hardware for the TERPROM algorithms for the USAF production contract is the Fairchild Defense Mega Data Transfer Cartridge with Processor (MDTC/P). This unit is 19cm x 12cm x 4cm, currently contains sufficient solid state memory for 200,000sq nm of map data and has a Texas Instruments C30 Digital Signal Processor on which the TERPROM software (100% Ada source code) is hosted. This configuration has been flight tested on F-16s in Texas, New Mexico and Utah.

## **4 TERRAIN FOLLOWING**

### **4.1 Design Aims**

Terrain Following (TF) is generally designed to provide a vertical steering cue (incremental vertical acceleration demand) to the pilot's HUD (or, alternatively, to the aircraft autopilot) to enable him to fly the aircraft covertly at his selected clearance height above the terrain. The aims are to:

- a) minimise aircraft height above the set clearance
- b) prevent aircraft penetrations below the set clearance
- c) clear peaks and ridge lines with zero vertical velocity.

The advantages that the DTS TF algorithm has over a terrain following radar are that:

- a) it is covert, even to the extent that the radar altimeter can be turned off for several minutes without significantly degrading the accurate navigation required for TF.
- b) terrain several kilometres ahead of the aircraft can be interrogated via the database, thereby minimising aircraft exposure. Hence, the aircraft can be pulling down as it clears a peak, rather than after having cleared it, since the DTS has prior knowledge of the terrain over the peak.

## 4.2 Scan Area

The TERPROM TF algorithm is, at present, designed for subsonic aircraft speed and runs at approximately 12.5Hz (ie the output changes at 12.5Hz). The first step is the definition of the "scan area" ahead of the aircraft. In non-turning flight this is a "pencil beam" centred on the aircraft's forward velocity. The semi-width of the beam is proportional to the TRN across-track position uncertainty, derived from the navigation filter covariance matrix. This ensures that the scanning of the terrain ahead takes into account all likely aircraft positions in the terrain database. For additional safety, TERPROM disables its TF calculations if its radial uncertainty in aircraft position exceeds a preset threshold; such a condition would generally occur, however, only during extended flight over flat terrain or water.

For turning flight, for which the rate of turn is deduced from the INS velocities and accelerations, the scan area is centred on the predicted aircraft forward velocity three seconds into the future and the edges of the beam are opened out by an amount proportional to the rate of turn (see Fig 1).

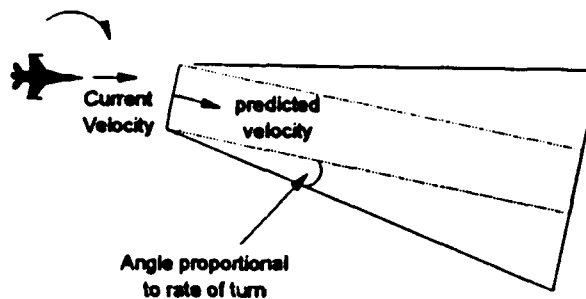


Figure 1. TF Scan Area in Turning Flight

The beam is divided along its length into equal "range bins". The length of the bins is increased with aircraft speed, and tuned to the rate at which the TF algorithm is running. The total length of the beam varies between 4km and 9km, dependent on aircraft speed.

#### **4.3 Worst Case Profile (WCP)**

Having defined the scan area and divided it into range bins along its length, the next step is the generation of the Worst Case Profile (WCP) of terrain and obstructions in the scan area. This is achieved by scanning across each range bin to find the highest terrain height or vertical obstruction in that bin. Again, to increase safety, the terrain and obstruction data are "spread" along the beam's length either side of their nominal locations by an amount proportional to the TRN along track position uncertainty. Therefore, any significant terrain height or obstruction will generally appear in more than one range bin. This ensures that pull-up commands before ridges are not cued too late and that pull-down commands over ridges are not cued too early.

The WCP is therefore an array containing, for each range bin, the highest "peak" (terrain height or obstruction) that could reasonably lie in that bin. Effectively, the most significant terrain and obstructions around all the likely immediate aircraft flight paths have been collapsed down into a two-dimensional (range/height) profile.

#### **4.4 Computation of TF Command**

To compute the TF command, the first step is to form an initial "preprocessed profile" which is simply the WCP raised by the pilot-selectable set clearance height. This initial profile is then modified to form the preprocessed profile by simulating an aircraft trajectory (see Fig 2) which "fills in" the initial profile and which gives zero vertical velocity,  $V_z$ , over significant peaks. The initial vertical acceleration,  $a_0$ , for this trajectory is then the acceleration demand. In deriving the aircraft trajectory, climb and dive angle and manoeuvre constraints are applied as are pilot-selectable ride hardness parameters. For safety, a "worst case height" of the current aircraft position above the terrain is assumed; this effectively raises the terrain and obstruction database (or lowers the aircraft position in the database) and is derived from the navigation filter covariance matrix. The incremental acceleration demand (TF command) output to the HUD is obtained by differencing the acceleration demand derived above with either the INS vertical acceleration or, if available, the pilot's filtered analogue stick command.

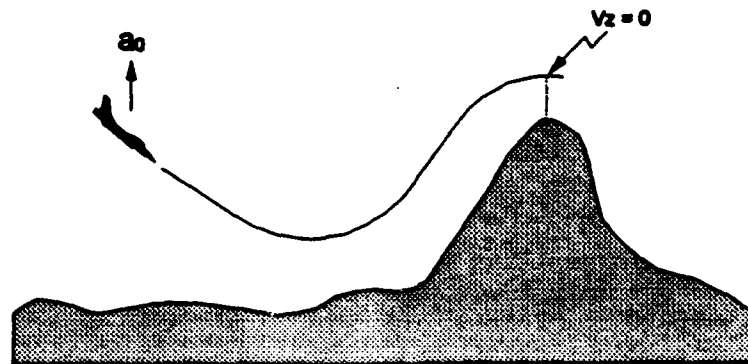


Figure 2 TF Simulated Aircraft Trajectory

## 5 GROUND COLLISION AVOIDANCE SYSTEM (GCAS) AND OBSTRUCTION CUIING

### 5.1 Ground Collision Avoidance System (GCAS)

As currently implemented, TERPROM's predictive Ground Collision Avoidance System (GCAS), which runs at 12.5Hz, provides a warning (a "Break-X") to the pilot's HUD if a simple kinematic model of the predicted aircraft trajectory penetrates the pilot-selected GCAS set clearance height above the terrain. The kinematic trajectory is derived from a 2-second forward projection of the current aircraft velocity from its worst case height followed by a 3g vertical pull-up to a distance 3km ahead of the current aircraft position. The terrain used for the GCAS is the same WCP generated for TF but raised by the GCAS set clearance height.

### 5.2 Obstruction Cuing

The database of vertical obstructions (DVOD) can be used to issue a warning to the pilot's HUD if an obstruction is detected in the aircraft's flight path. The function runs at 12.5Hz. The area scanned ahead of the aircraft is the initial 4km of the TF pencil beam extended outwards either side by 7 degrees (see Fig 3).

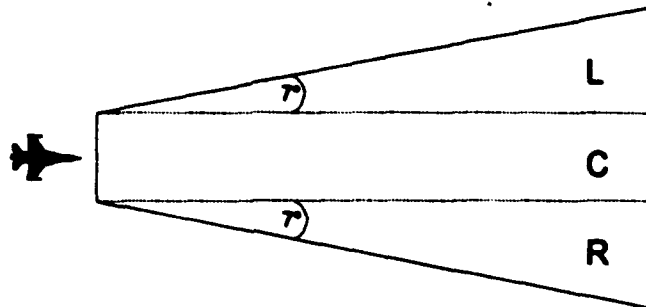


Figure 3. Obstruction Cuing Scan Area

As currently implemented, the algorithm finds the "most significant" obstruction, if any, in the scan area and then determines whether it is to the "left", "centre" or "right" (corresponding to regions L, C and R respectively in the Figure). The most significant obstruction is found by projecting forward the current aircraft velocity from its worst case height to the range from the aircraft of each obstruction. Each obstruction in the scan area is "raised" by the TF set clearance height (or a default height if TF is not selected). The most significant obstruction is that which gives the greatest penetration above the projected velocity vector. If none of the obstructions penetrates the flight path then, of course, no warning is given.

## 6 ADVANCED TERRAIN AVOIDANCE CUING (ATAC)

The latest development of the TERPROM DTS is the addition of an Advanced Terrain Avoidance Cuing (ATAC) function. This function provides graded, ground-stabilised, directional terrain avoidance warnings.

The description given in this paper is the current version of this function. Discussions are continuing concerning the exact implementation of ATAC, but what is clear, however, is that there are significant benefits to be gained from the addition of such a function.

## 6.1 Graded Warnings

The addition of a graded ground proximity warning gives the pilot a "heads-up" to indicate that the aircraft is getting close to the terrain but the situation, as yet, is not critical. In this way, it becomes possible for a pilot to "play" the warning as he feels relevant, depending on the flight conditions.

The graded warnings are generated using three prediction curves (rather than the single one used by GCAS). These curves are based on a 1 second forward projection of the current aircraft velocity from its worst case height followed by a 1.5g, 2.5g and 3.5g incremental vertical pull-up respectively, to a distance 3km ahead of the current aircraft position. Figure 4 illustrates these curves and the associated warnings which might be displayed on the pilot's HUD.

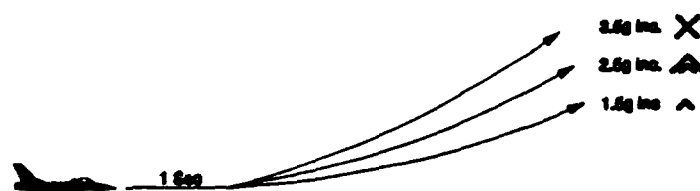


Figure 4 ATAC Graded Warning Curves

## 6.2 Directional Indication

Whereas a single Worst Case Profile is used by GCAS, the ATAC function uses three such profiles. The scan area described in section 4.2 is divided into Left, Centre and Right regions. Terrain within each of these regions is then used to produce a WCP for Left, Centre and Right. These profiles are then raised by the ATAC set clearance height selected by the pilot.

The curves given in Figure 4 above are now "overlaid" on each of the WCP's.

Depending upon which, if any, of these curves intersects with the terrain profile the appropriate grade or level of warning is issued for each of the directional profiles. Figure 5 shows an example in which no warning is generated by the terrain to the left of the aircraft, the lowest level warning is generated for terrain directly ahead of the aircraft, and the second level warning is produced by the terrain to the right of the aircraft.

Should any of the terrain profiles cause the third level warning to be generated then a "Break X" is displayed as in the standard GCAS function.

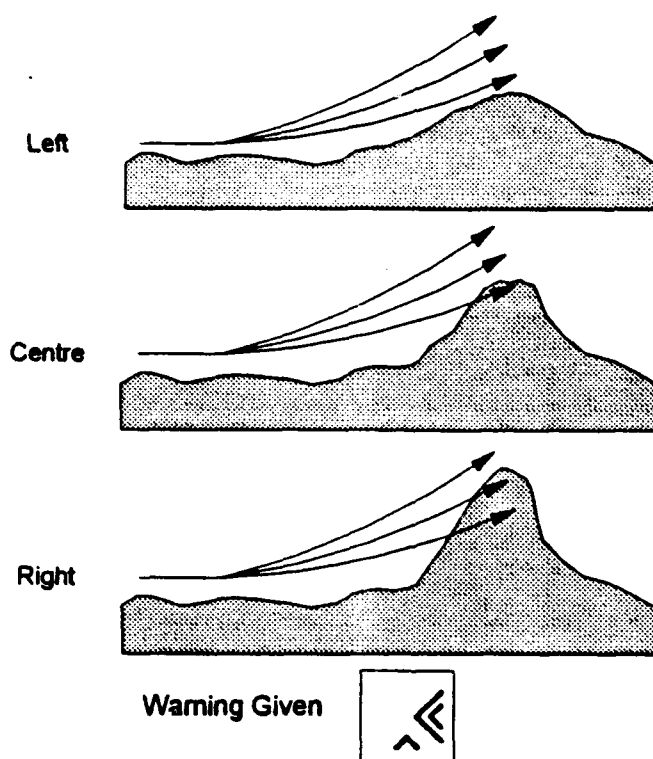


Figure 5. Typical ATAC Warning



Ground stabilisation of these warnings, in terms of the symbology displayed on the HUD, completes the functionality of the Advanced Terrain Avoidance Cues. The effects and benefits of the graded, directional, ground-stabilised warnings provided by ATAC are illustrated in Figure 6.

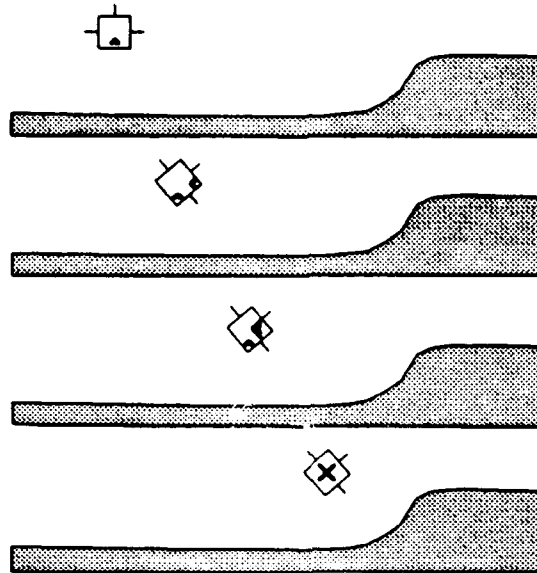


Figure 6. Ground Stabilised ATAC Warnings

## 7 RANGING FUNCTIONS

With accurate knowledge of aircraft position relative to the terrain it becomes possible for a DTS to effectively replace air-to-ground radar or laser ranging and provide a covert, passive target ranging function.

## 7.1 Passive Ranging

TERPROM's Passive Ranging (PR) function returns the height of the terrain at a point with given East and North offsets from the aircraft, the offsets being provided by the Flight Control Computer (FCC). Used iteratively in this way, accurate target ranging is achieved covertly by continually computing the predicted impact point of the weapon. This computation is performed at 12.5Hz.

The method is illustrated in Figure 7, where, for simplicity, the aircraft is assumed to be stationary. The FCC computes the bomb fall line to give  $I_1$  as the first predicted impact point. To do this, a flat earth is assumed and the height above ground,  $h$ , is provided to the FCC by the radar altimeter or from TRN. The FCC then provides TERPROM with the offset,  $R_1$ , and the height of the terrain at  $I_1$  is returned. A new impact point,  $I_2$ , is now computed by the FCC from both the fall line and a new height. A new offset,  $R_2$ , is then provided to TERPROM, which returns the terrain height at  $I_2$  and the process continues. It can be seen that the iterative process is converging on the point where the bomb fall line intersects the terrain (point  $I$ ).

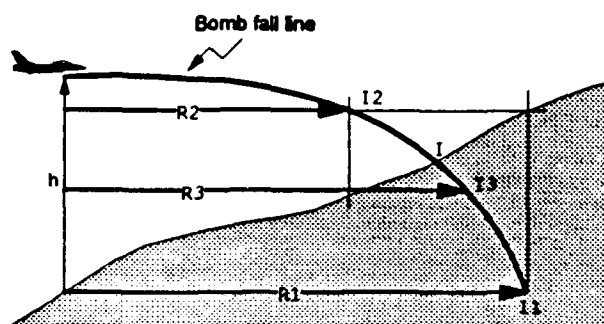


Figure 7. Passive Ranging Principle

## 7.2 Look Aside Ranging

TERPROM's Look Aside Ranging (LAR) function is also passive and was originally developed for use with a helmet-mounted sight, whereby a pilot "designates" a point on the ground by looking at it. The LAR function is provided with a line of sight (LOS), in aircraft axes, from the FCC and returns the latitude, longitude and terrain height of the point of intersection of the LOS with the ground (the "target") together with the "target" range in platform axes. This information can then be used for weapon aiming purposes or can be used iteratively to continually compute an impact point.

The iterative process is illustrated in Figure 8. The FCC computes the bomb fall line to give the "flat earth" impact point  $I_1$ . The LOS  $L_1$  is provided to TERPROM, which returns the terrain height at  $T_1$  by computing the intersection of  $L_1$  with the terrain using its database. The FCC now computes  $I_2$  using this height and the bomb fall line and provides LOS  $L_2$  to TERPROM, which returns the terrain height at  $T_2$ . The process continues and it can be seen that the impact points  $I_1$ ,  $I_2$ , ... are converging on the point  $I$  where the bomb fall line intersects the terrain.

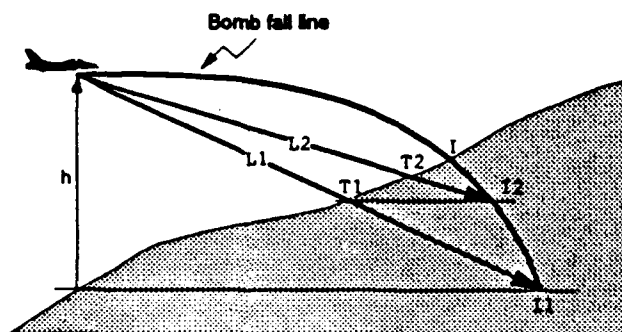


Figure 8. Look Aside Ranging Principle

## **8      FLIGHT TESTING**

Flight testing of TERPROM began in 1979 on an instrumented Jetstream aircraft. These tests proved both the concept and its accuracy throughout eighty sorties in all types of weather and over a variety of terrain.

In 1985, at Fort Worth in Texas, the system was thoroughly tested in a General Dynamics (GD) F-16 and achieved all performance aims in navigation, ground collision avoidance, terrain following and weapon aiming.

Following the initial series of trials on an F-16 aircraft, the system was flight trialled on a Panavia Tornado, with the aim of demonstrating safe, low level navigation and terrain following in the European theatre. The sorties were successfully flown over varying terrains at operational heights and speeds and included automatic terrain following at 350ft and 450kts.

TERPROM has also been assessed by the Royal Netherlands Air Force in an RNLAf F-16. The trials took place over the very flat terrain of Holland and Belgium and proved that TERPROM performs well even in this most demanding of situations. As a result of these trials, the RNLAf have specified that a Digital Terrain System should be part of the baseline upgrade to the EuroClub F-16 fleet.

Extensive qualitative performance analysis has been performed by Lockheed test pilots, in particular the late Joe Bill Dryden (senior test pilot) who had been flying the TERPROM system for over eight years, and who continuously commented favourably on its performance and operational benefits. A sample of his conclusions from this analysis is given in Reference 1.

In 1991 the USAF completed rigorous trials of TERPROM using an instrumented F-16 aircraft and range. TERPROM provided highly accurate navigation, was shown to be totally robust in terms of GCAS, OC and TF functions, and demonstrated a weapon aiming accuracy improvement over radar ranging modes. Following these instrumented flight trials Lockheed (then GD) , Fort Worth Division, produced a performance evaluation report (Reference 2). This document records both quantitative and qualitative analysis of the TERPROM DTS flight performance. The quantitative analysis was carried out by Lockheed engineers and the qualitative analysis was performed by a number of USAF and Lockheed F-16 test pilots.

The F-16 and Tornado trials programmes have proved the effectiveness of TERPROM and its capability to provide safe and accurate flight guidance at the low levels and high speeds essential for operations over the modern battlefield.

TERPROM continues to fly on a Lockheed F-16 at Fort Worth, Texas, and is now flying with F-16 USAF Reserves at Hill AFB, Utah.

## **9      SUMMARY**

It is clear that significant benefits can be gained by high-speed, military aircraft with the addition of a proven Digital Terrain System. A greatly reduced pilot workload (little or no navigation effort required) and major safety improvements via the ground proximity/terrain avoidance warnings are, in themselves, important contributions to any aircraft system (including civil aircraft). In addition, military jets can also benefit from improved target ranging and covert terrain following.

The extensive and thorough flight testing of the BASE TERPROM DTS has been discussed. As a direct result of the success of this flight testing the TERPROM DTS is now under contract for an F-16 programme. An example of the continuing development of the system has been illustrated with the description of the ATAC function.

## **REFERENCES**

- 1      General Dynamics magazine: Code One  
October 1988  
Volume 3, Number 3
- 2      Engineering Report: Digital Terrain System F-16 A/B  
TERPROM Performance Evaluation  
General Dynamics, Fort Worth Division  
16 PR10331, 8 February 1993

**SESSION IV-B**

**TEST BEDS**

***CHAIRMAN***

**RALPH PATTERSON**

***LITTON***

**THIS PAGE LEFT BLANK INTENTIONALLY**

EFFECT OF NOISE IN PRECISION  
CENTRIFUGE TESTING OF ACCELEROMETERS

by

George H. Neugebauer, Ret.

Sun City CA

Presented by

Michael D. Hooser, Ph.D.

46th Guidance Test Squadron, Holloman AFB NM



EFFECT OF NOISE IN PRECISION  
CENTRIFUGE TESTING OF ACCELEROMETERS  
by GEORGE H. NEUGEBAUER

ABSTRACT

In precision centrifuge testing of accelerometers to obtain their nonlinear performance coefficients, it has been accepted dogma by most engineers that averaging the outputs over several revolutions of the centrifuge would substantially reduce the errors in the coefficients due to noise in the output. Computer simulations prove this concept to be false. For example, to reduce the errors due to noise by one order of magnitude, it appears necessary to average the outputs over about 400 revolutions. Averaging the outputs over that many revolutions might introduce errors due to heating effects.

Depending on the noise level and the input acceleration range, the errors in the coefficients may be as great or greater than the coefficients themselves and thus a serious problem.

At a centrifuge facility, the standard deviation of the noise vs input acceleration must first be determined, then with the data furnished in this paper, the maximum errors in each coefficient may be determined.

Though this paper has been written specifically for precision centrifuge testing of accelerometers, the same general conclusions would apply to any type of measurements.

INTRODUCTION

Before proceeding further, let me define exactly what I mean by noise in this context. NOISE IS THE STANDARD DEVIATION OF THE OUTPUT OF AN ACCELEROMETER FROM REVOLUTION TO REVOLUTION WHILE THE CENTRIFUGE IS MAINTAINED AT A NOMINALLY CONSTANT ANGULAR VELOCITY. ANY VARIATION IN SPEED DURING A MEASUREMENT WOULD CONTRIBUTE TO THE NOISE.

Next, let me define the coefficients I have been writing about. For these studies I have adopted a commonly-used model equation for the accelerometer. See Ref.(1) (rearranged order).

$$A_o = K_3 a_i^3 + K_{oq} a_i |a_i| + K_2 a_i^2 + a_i + K_o \quad (1)$$

where:  $A_o$  = accelerometer output - g  
 $K_3$  = cubic coefficient - g/g<sup>3</sup>  
 $K_{oq}$  = odd-quadratic coefficient - g/g<sup>2</sup>  
 $K_2$  = quadratic coefficient - g/g<sup>2</sup>  
 $a_i$  = input acceleration - g  
 $K_o$  = Bias - g

Because of uncertainties in the estimated radii to the equivalent center-of-mass (ECM) of the seismic element and misalignment of the accelerometer input axis with respect to the radius to the ECM, the centrifuge data reduction equation requires terms additional to those in Eq.(1), Ref.(1).

$$A_o - a_i = K_3 a_i^3 + K_{oq} a_i |a_i| + K_2 a_i^2 + c_n a_n + c_p a_p + K_{on} + K_{op} \quad (2)$$

where terms with subscript "n" apply only when  $a_i$  is negative and terms with

subscript "p" apply only when  $a_1$  is positive. A Coriolis term may also be added when appropriate.

Some five or six years ago, the Gyro and Accelerometer Panel of the IEEE was trying to decide which of two competing centrifuge data reduction equations was superior. Ref.(1) & (2). The Panel decided to generate centrifuge data with known coefficients and see which procedure recovered the coefficients more accurately. The Panel wanted to inject noise into the output to make it more realistic. I contended that injecting noise would simply confuse the issue. The noise would introduce errors in the coefficients and it would be impossible to tell whether those errors were due to the noise or to the data-reduction procedures. In addition, I proved by computer simulation that given the noise-acceleration distribution, I could accurately determine the errors in the coefficients due to the noise.

The Panel ignored my contention and generated artificial centrifuge data with a noise level of 300ug or 500ug, I don't recall which. The noise completely swamped the coefficients which made it impossible to determine which procedure was superior. It did show that noise of that magnitude would cause a very serious problem.

After further discussion, the Panel did adopt the data-reduction procedure of Ref.(1). This procedure has the advantage of having only one equation, instead of three, to cover the full range of input acceleration, positive and negative. It also proved to be adaptable to an iteration procedure, Ref.(3), which largely eliminates the errors due to uncertainties in measuring the radius to the ECM of the seismic element and also those due to the horizontal component of the misalignment of the input axis with respect to the radius to the ECM. It is my belief that the principal advantage of the iterative procedure is that it obviates the necessity of trying the impossible task of accurately measuring the radius to the ECM. The computer can do it more accurately and faster.

As noted above, the iterative procedure largely eliminates the errors due to the horizontal component of the misalignment but it cannot correct for the vertical component of the misalignment. Fortunately, it is easy to control the vertical misalignment by comparing the static output when mounted on the centrifuge arm with the static bias obtained in a precision dividing head test and adjust the vertical angle.

The vertical misalignment affects only the even powered terms. The errors in  $K_{oq}$  and  $K_2$  due to the vertical component of misalignment are:

$$\Delta K_{oq} = 1.5(\phi_p + \phi_n)K_3$$

$$\Delta K_2 = 1.5(\phi_p - \phi_n)K_3$$

where  $\phi_p$  and  $\phi_n$  are the vertical components of the misalignment with positive and negative input accelerations, respectively. Knowing the approximate value of  $K_3$ , One can determine the limits on the vertical misalignment. I first noted these errors in some computer simulations which I was later able to confirm by analysis.

In my computer simulations on the effect of noise, I am only interested in determining the errors in the accelerometer coefficients and not the coefficients themselves. Therefore the equation I used is:

$$\mathcal{J}_i = k_3 a_i^3 + k_{oq} a_i |a_i| + k_2 a_i^2 + c_n a_n + c_p a_p + k_{on} + k_{op} \quad (4)$$

where  $\mathcal{J}_i$  is the noise in the output when the input acceleration is  $a_i$ . As before, the terms with subscripts "n" and "p" apply when  $a_i$  is negative and positive, respectively. For simplicity, I shall hereafter refer to  $k_3$ ,  $k_{oq}$ ,  $k_2$  etc. as the noise coefficients. The noise output at a whole series of input accelerations are recorded and Eq.(4) is solved by the method of least squares.

For generating the noise " $\mathcal{J}_i$ " I used the random number function of the computer and the Central Limit Theorem. For those who may have forgotten how the Central Limit Theorem is used in this connection, let me give a short description. If we were to draw all possible samples of size N from a population and record the mean value of each sample, the sample being immediately returned to the population, we would have a frequency distribution of  $\bar{X}$  which would have a mean value  $\mu_{\bar{X}} = \mu_x$  and a standard deviation  $\sigma_{\bar{X}} = \sigma_x / \sqrt{N}$ , where  $\mu_x$  and  $\sigma_x$  are the mean and the standard deviation, respectively, of the population.

If X has a normal distribution, then  $\bar{X}$  will have a normal distribution. More importantly, the sampling distribution approaches a normal distribution for N sufficiently large even though the population distribution differs radically from normal. In the case of the random numbers  $0 \leq R \leq 1$ , we have a rectangular distribution and  $f(\bar{X})$  will be nearly normal for N as low as five and be essentially normal for N equal to ten.

Using  $N = 10$  and  $X = R - 0.5$ , we will have a central distribution with:

$$\begin{aligned} \mu_{\bar{X}} &= 0 \\ \sigma_{\bar{X}} &= \sigma_x / \sqrt{10} \end{aligned}$$

To have a unit standard deviation, we must multiply  $\sigma_{\bar{X}}$  by  $\sqrt{10}$ . Then this, in turn, must be multiplied by the desired standard deviation.

Considering the accuracy with which the accelerometer coefficients are usually wanted, I thought that a standard deviation of 100ug which I had used in my early studies, was excessive. So I asked Dr. Michael Hooser of the CIGTF facility at Holloman AFB what he considered typical at his facility. He replied that it was of the order of a few ug. Assuming that the noise at a commercial facility would be greater than that at a research facility such as CIGTF, I arbitrarily adopted the following noise function:

$$\mathcal{J}_i = \sigma_b + \sigma_l a_i = 10\text{ug} + (1.5\text{ug/g})a_i \quad (5)$$

where  $\sigma_b$  is the standard deviation of the bias component of the noise and  $\sigma_l$  is the linear component of the noise function.

Adopting the above specific numbers for the noise does not limit the generality of my results since, as I will show, one can closely estimate the noise coefficients for any combination of bias and linear noise parameters at any given confidence level.

# CORRECTING FOR NOISE LEVEL AND ACCELERATION RANGE

Since it is critical in the application of my results to facilities with different noise levels and input acceleration ranges, I will show how the noise coefficients are affected by each variable. Let me interpolate here that I can repeat the same series of random numbers by using the same seed number  $0 \leq S \leq 100$ . Therefore I can repeat the same series of noise in the output. The seed numbers need not be integers though I happened to use integers.

First, let us compare results with different bias noise levels. Let the bias noise levels be  $10\mu g$  and  $20\mu g$  with seed number  $S = 3$ . The input acceleration range is  $\pm 10g$ . The data is taken at forty uniformly-spaced input accelerations starting at  $+10g$  and ending at  $-10g$ . The results given in TABLE I show that when the bias noise is doubled, the noise coefficients are doubled.

TABLE I

Coef.	$\sigma_b = 10\mu g$	$\sigma_b = 20\mu g$
$k_3$	-3.322481-08	-6.644962-08
$k_{oq}$	4.418514-07	8.837028-07
$k_2$	1.803903-07	3.607806-07

Next, let us look at the results when the linear noise factor is doubled. The input acceleration range is the same  $\pm 10g$  and the seed number is  $S = 3$  for both cases. The results given in TABLE II show that when the linear factor is doubled, the noise coefficients are doubled.

TABLE II

Coef.	$\sigma_L = 1.5\mu g/g$	$\sigma_L = 3.0\mu g/g$
$k_3$	8.039878-09	1.607976-08
$k_{oq}$	-1.235462-07	-2.470924-07
$k_2$	1.380232-07	2.760464-07

Acceleration range is another parameter which varies not only between facilities but also from contract to contract at a given facility. Let us first check how the noise coefficients vary with acceleration range due to bias noise alone. In each case the data is taken at forty uniformly-spaced input accelerations. The bias noise standard deviation is  $10\mu g$  and with  $S = 3$ .

TABLE III

$\sigma_b = 10\mu g$			
Coef.	$\pm 10g$	$\pm 20g$	$\pm 50g$
$k_3$	-3.322481-08	-4.153100-09	-2.657984-10
$k_{oq}$	4.418514-07	1.104628-07	1.767405-08
$k_2$	1.803903-07	4.509758-08	7.215611-09

TABLE III shows that  $k_2$  varies inversely as the cube of the acceleration range whereas  $k_{oq}$  and  $k_3$  vary inversely as the square of the range due to bias noise alone.

The effect of acceleration range with linear noise only is shown in TABLE IV. Here we find that  $k_3$  varies inversely as the square of the acceleration. The  $k_{og}$  and the  $k_2$  terms vary inversely as the first power of the acceleration range. Note the difference in the effects of acceleration range for bias noise and for linear noise.

Coef.	Acceleration Range		
	+/-10g	+/-20g	+/-50g
$k_3$	8.039878-09	2.009970-09	3.215951-10
$k_{og}$	-1.235462-07	-6.177308-08	-2.470923-08
$k_2$	1.380232-07	6.901158-08	2.760463-08

It does appear that increasing the acceleration range is a very effective way of reducing the effect of noise. However, this avenue of improvement is limited by the design of the accelerometer and of the centrifuge.

Another series of runs was made with a bias noise of 10ug and a linear noise of 1.5ug/g. The acceleration range and the seed number are the same as for the previous runs. The results are shown in TABLE V.

Coef.	Acceleration Range		
	+/-10g	+/-20g	+/-50g
$k_3$	-2.518492-08	-2.143130-09	-5.579675-11
$k_{og}$	3.183051-07	4.868975-08	-7.035179-09
$k_2$	3.184134-09	1.141092-07	3.482024-08

As expected, the numbers in TABLE V are equal to the sums of the corresponding ones in TABLES III and IV.

#### EFFECT OF AVERAGING

Now that the necessary preliminaries are over, let me get down to the crux of this paper which is to determine if averaging the output of an accelerometer over several revolutions of the centrifuge will effectively reduce the noise coefficients. Recall that what I call noise coefficients are the errors in the accelerometer coefficients due to noise.

Using  $\sigma_b = 10\text{ug}$ , see Eq.(5), I made three series of 100 computer simulation runs with seed numbers from 0 to 99. The acceleration range was +/-10g with data taken at forty uniformly-spaced input accelerations. One series averaged the output over one ( $n = 1$ ) revolution of the centrifuge. A second series averaged the outputs over ten ( $n = 10$ ) revolutions while a third series averaged the outputs over fifty ( $n = 50$ ) revolutions. A portion of the results is shown in TABLE VI. The  $\sigma$  columns are the standard deviations of the output noise at the forty input accelerations of each run. The last two rows are the means and the standard deviations of each column.

All calculations were carried out to thirteen (13) significant figures. In order to make it easier to compare results of the three series, I have multiplied the noise coefficients by  $10^9$  and displayed only four significant figures. The mean noise for  $n = 1$  is 9.922ug which is within one percent of

TABLE VI  
NOISE COEFFICIENTS  $\times 10^9$  with BIAS = 10ug

SEED	n = 1					n = 10					n = 50				
	$k_3$	$k_{og}$	$k_2$	$\int ug$	$k_3$	$k_{og}$	$k_2$	$\int ug$	$k_3$	$k_{og}$	$k_2$	$\int ug$	$k_3$	$k_{og}$	$\int ug$
0	15.24	-455.0	111.8	10.260	34.78	-604.5	80.53	3.688	-9.810	79.48	-35.93	1.562	-9.810	79.48	1.562
1	-13.47	214.4	101.8	10.126	35.55	-543.1	-210.4	3.311	9.360	-134.7	56.94	1.429	9.360	-134.7	1.429
2	71.10	-1019	-6.802	10.176	-5.725	80.96	-74.47	3.073	-2.099	35.62	11.31	1.435	-2.099	35.62	1.435
3	-33.22	441.9	180.4	10.702	-17.99	210.3	-29.66	2.948	-19.35	274.1	59.04	1.515	-19.35	274.1	1.515
4	-86.70	1620	-227.7	9.871	51.15	-735.5	32.48	3.130	-6.765	111.1	1.754	1.562	-6.765	111.1	1.562
-	-	-	-	-	-	-	-	-	-	-	-	-	-	-	-
96	-13.15	218.0	-11.79	10.150	5.196	-106.3	-168.1	3.491	-3.607	63.14	60.46	1.465	-3.607	63.14	1.465
97	60.02	-1039	-46.74	10.716	-7.367	145.5	-65.98	3.673	5.517	-97.74	42.86	1.455	5.517	-97.74	1.455
98	-20.77	20.08	230.3	10.343	-39.29	538.4	-36.78	3.027	-10.85	147.7	58.24	1.582	-10.85	147.7	1.582
99	-19.70	311.2	-156.6	7.773	25.97	-319.6	86.64	3.653	1.926	-2.289	20.95	1.485	1.926	-2.289	1.485
Mean	1.003	-17.00	0.336	9.922	0.292	-3.636	0.272	3.183	0.075	-0.928	0.356	1.385	0.075	-0.928	1.385
Sigma	83.80	1367	176.1	1.971	35.09	529.7	67.18	0.577	11.44	174.1	31.52	0.214	11.44	174.1	0.214

the desired 10ug. The mean noise levels for  $n = 10$  and  $n = 50$  are within two percent of the expected  $10\text{ug}/\sqrt{n}$ .

The standard deviation (sigma) of the noise coefficients differ widely from the expected inverse square root of  $n$  relationship. The reason for this misbehavior becomes evident when we look at the great range in values from run-to-run. At  $n = 1$ , the noise coefficient  $k_3$  varies in magnitude over a range of 840:1; the coefficient  $k_{oq}$  varies over a range of 68:1; and  $k_2$  has a range in magnitude of 216:1. This wide range in values accounts for the fact that some noise coefficients when  $n = 10$  and  $n = 50$  are greater in magnitude than the corresponding coefficients when  $n = 1$ . However, on the average there is a distinct improvement but not as great as  $1/\sqrt{n}$ .

Another series of 100 computer simulation runs were made with a linear noise of 1.5ug/g replacing the bias noise. A portion of the results are shown in TABLE VII. Essentially the same comments may be made about these three series of runs as were made about the results in TABLE VI.

Still another series of three runs were made with both bias and linear noise components. A portion of the results are shown in TABLE VIII. It is seen that the coefficients in TABLE VIII are equal to the sum of the corresponding coefficients in TABLES VI and VII to at least six significant figures.

Next, I checked on how the standard deviations of the coefficients changed with increasing sample size. With  $n = 1$ ,  $\sigma_p = 10\text{ug}$  and an input acceleration range of  $\pm 10g$ , as before, the means with sample size 100, 200, 400 and 800 are shown in TABLE IX.

TABLE IX  
Mean St'd Deviation of  
Noise Coefficients  $\times 10^9$   
Sample Size

Coef.	100	200	400	800	Mean
$k_3$	83.80	86.07	85.02	87.50	86.
$k_{oq}$	1367.	1401.	1372.	1401.	1390.
$k_2$	176.1	206.1	220.5	211.4	213.

With a sample size of 200 or more, each coefficient seems to have reached a plateau. The means in the last column exclude sample size 100.

Similar runs were made with a linear noise of 1.5ug/g. The results are given in TABLE X. Again the standard deviation appear to have reached a plateau with a sample size of 200 or more. The means in the last column exclude sample size 100.

TABLE X  
Mean St'd Deviations of  
of Noise Coefficients  $\times 10^9$   
Sample Size

Coef.	100	200	400	800	Mean
$k_3$	71.00	74.23	76.77	77.95	76.
$k_{oq}$	1046.	1072.	1079.	1097.	1082.
$k_2$	172.7	211.6	206.1	203.6	207.

TABLE VII  
NOISE COEFFICIENTS  $\times 10^9$  with RAMP = 1.5ug/g

Seed No.	n = 1					n = 10					n = 50					
	k <sub>3</sub>	k <sub>Oq</sub>	k <sub>2</sub>	Σ ug	k <sub>3</sub>	k <sub>Oq</sub>	k <sub>2</sub>	Σ ug	k <sub>3</sub>	k <sub>Oq</sub>	k <sub>2</sub>	Σ ug	k <sub>3</sub>	k <sub>Oq</sub>	k <sub>2</sub>	Σ ug
0	-121.0	1844	-258.7	9.835	7.924	-68.22	9.175	3.052	1.719	-48.27	-47.17	-48.27	1.719	-48.27	-47.17	1.347
1	-34.37	679.2	40.87	9.069	-37.40	441.6	49.13	3.050	10.86	-132.6	11.29	-132.6	10.86	-132.6	11.29	1.296
2	56.14	-988.9	159.9	9.570	12.86	-197.6	-6.240	2.601	13.24	-186.0	-7.132	-186.0	13.24	-186.0	-7.132	1.177
3	8.040	-123.5	138.0	11.36	21.20	-366.0	-57.76	3.040	14.81	-157.5	-18.50	-157.5	14.81	-157.5	-18.50	1.559
4	7.651	-333.6	86.36	8.753	5.787	-97.27	102.5	3.142	0.918	-34.87	-15.24	-34.87	0.918	-34.87	-15.24	1.497
-	-	-	-	-	-	-	-	-	-	-	-	-	-	-	-	-
96	-3.690	183.1	-12.48	8.379	8.305	-261.2	-19.55	3.525	-5.233	114.2	-13.76	114.2	-5.233	114.2	-13.76	1.200
97	23.61	-436.8	-80.43	9.784	2.439	-20.02	11.42	3.099	14.81	-157.5	-18.50	-157.5	14.81	-157.5	-18.50	1.559
98	87.02	-1203	74.85	10.53	4.438	-122.8	-108.2	2.877	7.252	-47.04	-14.56	-47.04	7.252	-47.04	-14.56	1.539
99	-71.41	857.7	10.55	7.243	60.94	-858.7	70.61	3.551	5.062	-72.18	-49.26	-72.18	5.062	-72.18	-49.26	1.480
Mean	0.946	-13.46	0.616	9.066	-0.266	4.122	1.672	2.900	0.095	-1.022	0.189	-1.022	0.095	-1.022	0.189	1.249
Sigma	71.00	1046	172.7	1.669	23.20	329.2	86.45	0.418	10.89	155.7	30.29	155.7	10.89	155.7	30.29	0.266



TABLE VIII  
NOISE COEFFICIENTS  $\times 10^9$  with BIAS = 10ug and RAMP = 1.5ug/g

Seed No.	n = 1						n = 10						n = 50					
	$k_3$	$k_{Og}$	$k_2$	$\bar{y}$ ug	$k_3$	$k_{Og}$	$k_2$	$k_3$	$k_{Og}$	$k_2$	$\bar{y}$ ug	$k_3$	$k_{Og}$	$k_2$	$\bar{y}$ ug	$k_3$	$k_{Og}$	$k_2$
0	-105.8	1389	-147.0	13.937	42.71	-672.7	89.70	-8.091	31.21	-83.10	4.887	-8.091	31.21	-83.10	2.047	-8.091	31.21	-83.10
1	-47.85	893.6	142.6	13.034	-1.843	-101.5	-161.2	20.22	-267.3	68.23	4.360	20.22	-267.3	68.23	2.243	20.22	-267.3	68.23
2	-47.85	893.6	142.6	13.034	7.138	-116.6	-80.71	11.14	-150.3	4.182	4.199	11.14	-150.3	4.182	1.969	11.14	-150.3	4.182
3	-25.18	318.3	318.4	12.220	3.215	-155.7	-87.43	-4.543	116.6	40.54	4.578	-4.543	116.6	40.54	2.329	-4.543	116.6	40.54
4	-79.05	1286	-141.3	13.116	56.93	-832.8	135.0	-5.848	76.23	-13.49	4.148	-5.848	76.23	-13.49	2.640	-5.848	76.23	-13.49
96	-16.84	401.0	-24.27	13.821	13.50	-367.5	-187.6	-88.39	177.4	46.69	5.122	-88.39	177.4	46.69	2.104	-88.39	177.4	46.69
97	83.63	-1476	-127.2	15,202	-5.198	125.5	-54.56	20.18	-292.9	32.38	4.404	20.18	-292.9	32.38	2.015	20.18	-292.9	32.38
98	66.25	-1002	305.2	13.677	-34.85	415.6	-145.0	-3.601	100.7	43.68	4.733	-3.601	100.7	43.68	2.328	-3.601	100.7	43.68
99	-91.11	1169	-146.0	12.185	86.91	-1178	157.3	3.136	-74.47	-28.31	4.837	3.136	-74.47	-28.31	2.435	3.136	-74.47	-28.31
Mean	1.949	-30.46	0.952	13.379	0.027	0.485	1.944	0.171	-1.950	0.545	4.426	0.171	-1.950	0.545	1.915	0.171	-1.950	0.545
Sigma	118.7	1835	232.5	2.931	45.77	667.1	114.2	15.22	227.8	43.24	0.711	15.22	227.8	43.24	0.347	15.22	227.8	43.24

In jest, Dr. Hooser called the means in TABLES IX and X by the fanciful name of cosmic numbers because of the use I make of them. Though at times I take my work seriously, I don't believe these numbers are quite in the same category as the speed of light or the charge on an electron.

Reviewing the noise coefficients with  $\sigma_p = 10\mu g$  and those with  $\sigma_e = 1.5\mu g/g$  when  $n = 10, 20$ , and  $50$  (not all shown) I found that about 30 percent of them exceeded 1.2 times the appropriate cosmic numbers of TABLES IX and X divided by the square root of  $n$ . There was a slight indication that the factor 1.2 decreases as  $n$  increases.

#### APPLICATION TO A PRECISION CENTRIFUGE FACILITY

I have shown that even with the low noise function  $S_i = 10\mu g + (1.5\mu g/g)a_i$  (best fit st'd deviation) there can be serious errors in the recovery of the accelerometer coefficients from precision centrifuge data. It is quite certain that some centrifuge facilities will be found to have noise levels which are at least one order of magnitude worse with corresponding greater errors.

Also shown is that whether or not an accelerometer model equation includes an odd quadratic term, there will be a very substantial odd quadratic term due to the noise alone. Even if an accelerometer truly does not have an odd quadratic coefficient, one should be included in the centrifuge data reduction equation: otherwise the odd quadratic error due to noise will appear as errors in the linear and the cubic coefficients.

One should be able to determine if the odd quadratic term is real or an artifact due to noise. If the odd quadratic term is real for a given model of accelerometer, the mean value of a series of tests on one or several accelerometers should statistically be significantly different than zero.

From the non-existence of data on noise in the literature, I must conclude that most test engineers do not fully appreciate how serious a problem this could be. I am quite sure that there is some data available, it just hasn't been recognized. The first thing that has to be done is to take measurements of the noise.

Some of the noise may be attributable to the accelerometer being tested, therefore it is imperative that noise measurements be made with the type of accelerometer to be tested. Much of the necessary noise data could probably be taken during the regular accelerometer test program. Both the bias and the linear noise components must be determined.

Record the output of the accelerometer for each of fifty or more revolutions of the centrifuge and at each of sixteen or more acceleration levels covering the full input range, positive and negative. Calculate and plot the standard deviation of the variation in output vs input acceleration. Hopefully, the data points will lie approximately on a straight line. If so, determine the best fit straight line by any of the standard methods. This line will have a bias coefficient,  $\sigma_p$ , and a linear coefficient,  $\sigma_e$ , so that the noise function is  $S_i = \sigma_p + \sigma_e a_i$ , where  $a_i$  is the input acceleration. This noise function is for averaging the output over one revolution, i.e. for  $n = 1$ .

We are now ready to determine the limits on the probable errors in the accelerometer coefficients due to noise at some specified confidence level when averaging the output over  $n$  revolutions. Then it can be decided if those

errors are acceptable or not based on contractual obligations.

Let me now show by an example how the data given herein along with the noise function found for the facility may be used to determine limits on the errors in the accelerometer coefficients at a specified confidence level.

EXAMPLE. At a certain centrifuge facility, the noise function was found to be  $S_i = 15\mu g + (2.5\mu g/g)a_i$ . The input acceleration range is  $\pm 8g$  and the

output is averaged over 30 revolutions at each acceleration level. Determine the limits on the errors of each accelerometer coefficient due to noise at a 95 percent confidence level.

Consider the bias noise first. From TABLE IX we find that for  $n = 1$ , an acceleration range of  $\pm 10g$  and a bias noise of  $10\mu g$ , the noise coefficients are:

$$\begin{aligned}k_3 &= 0.086\mu g/g^3 \\k_{oq} &= 1.390\mu g/g^2 \\k_2 &= 0.213\mu g/g^2\end{aligned}$$

As previously stated, these coefficients must be multiplied by the factor 1.2 and then corrected for the higher noise level and the reduced input acceleration range to get their one sigma values.

$$\begin{aligned}k_3 &= 1.2(0.086)(15/10)(10/8)^3/\sqrt{30} = 0.0552\mu g/g^3 \\k_{oq} &= 1.2(1.390)(15/10)(10/8)^2/\sqrt{30} = 0.714\mu g/g^2 \\k_2 &= 1.2(0.213)(15/10)(10/8)^2/\sqrt{30} = 0.109\mu g/g^2\end{aligned}\tag{6}$$

Next consider the errors due to the linear component of the noise. From TABLE X with  $n = 1$ , acceleration range  $\pm 10g$  and a linear noise of  $1.5\mu g/g$ , the standard deviation of the noise coefficients are:

$$\begin{aligned}k_3 &= 0.076\mu g/g^3 \\k_{oq} &= 1.082\mu g/g^2 \\k_2 &= 0.207\mu g/g^2\end{aligned}$$

These standard deviations must be multiplied by 1.2 and corrected for the higher noise level and the reduced acceleration range.

$$\begin{aligned}k_3 &= 1.2(0.076)(2.5/1.5)(10/8)^2/\sqrt{30} = 0.0434\mu g/g^3 \\k_{oq} &= 1.2(1.082)(2.5/1.5)(10/8)/\sqrt{30} = 0.494\mu g/g^2 \\k_2 &= 1.2(0.207)(2.5/1.5)(10/8)/\sqrt{30} = 0.0945\mu g/g^2\end{aligned}\tag{7}$$

The values in Eq.(6) and (7) are the corrected standard deviations of the noise coefficients due to the bias and the linear components, respectively. To obtain the combined effect of the bias and the linear noise components, we must resort to the theorem: The variance (square of the standard deviation) of the sum of two independent variables is equal to the sum of their individual variances. Therefore, the standard deviations of the noise coefficients due to the combined bias and linear components are:

$$s_3 = \sqrt{0.0552^2 + 0.0434^2} = 0.0702\mu g/g^3$$

$$s_{oq} = \sqrt{0.714^2 + 0.494^2} = 0.868 \text{ug/g}^2$$

$$s_2 = \sqrt{0.109^2 + 0.0945^2} = 0.144 \text{ug/g}^2$$

Next we must determine the 95 percent confidence interval for the noise coefficients. In this case we want to bracket the errors in the accelerometer performance coefficients so we must use the two-sided Student t statistic. Since in any precision centrifuge test we should have at least 36 data sets we may use the approximation  $t = 2$ . Therefore, we may be 95 percent confident that the errors in the accelerometer coefficients due to noise will be no more than the following:

$$K_3 = \pm 0.140 \text{ug/g}^3$$

$$K_{oq} = \pm 1.736 \text{ug/g}^2$$

$$K_2 = \pm 0.288 \text{ug/g}^2$$

Since I wrote the above, I have shown these pages to several engineers for their comments. Some of them have stated that my assumed noise function is too optimistic and that the bias noise should be around 100ug. There was no suggestion for the magnitude of the linear noise component, which did not surprise me. In view of their comments, I am adding a second example with higher noise levels.

EXAMPLE 2. At another centrifuge test facility, the noise function was found to be  $\hat{f}_i = 100\text{ug} + (8\text{ug/g})a_i$ . All other parameters are the same as in the first example.

Consider the effect of the bias noise first. Using TABLE IX and correcting for the higher noise level and the lower acceleration range, we get:

$$k_3 = 1.2(0.086)(100/10)(10/8)^3/\sqrt{30} = 0.552 \text{ug/g}^3$$

$$k_{oq} = 1.2(1.390)(100/10)(10/8)^2/\sqrt{30} = 7.14 \text{ug/g}^2 \quad (8)$$

$$k_2 = 1.2(0.213)(100/10)(10/8)^2/\sqrt{30} = 1.09 \text{ug/g}^2$$

Next consider the errors due to the linear component of the noise. Using TABLE X and correcting for the higher noise level and the reduced acceleration range, the standard deviation of the noise coefficients with  $n = 30$  are:

$$k_3 = 1.2(0.076)(8/1.5)(10/8)^2/\sqrt{30} = 0.139 \text{ug/g}^3$$

$$k_{oq} = 1.2(1.082)(3/1.5)(10/8)/\sqrt{30} = 1.580 \text{ug/g}^2 \quad (9)$$

$$k_2 = 1.2(0.207)(3/1.5)(10/8)/\sqrt{30} = 0.302 \text{ug/g}^2$$

The values in Eqs.(8) and (9) are the corrected standard deviations of the noise coefficients due to the bias noise of 100ug and the linear noise 8ug/g, respectively. The standard deviations due to the combined bias and linear noise are:

$$s_3 = \sqrt{0.552^2 + 0.139^2} = 0.569 \text{ug/g}^3$$

$$s_{oq} = \sqrt{7.14^2 + 1.580^2} = 7.312 \text{ug/g}^2$$

$$s_2 = \sqrt{1.09^2 + 0.302^2} = 1.13 \text{ug/g}^2$$

As in the first example, for the 95 percent confidence level, we may use a Student t statistic  $t = 2$ . Then the errors in the accelerometer coefficients may have a variation of :

$$\begin{aligned}K_3 &= 1.14u\alpha/\alpha^3 \\K_{0\alpha} &= 14.6u\alpha/\alpha^2 \\K_2 &= 2.26u\alpha/\alpha^2\end{aligned}$$

#### REFERENCES

- (1) Neugebauer, George H., Precision Centrifuge Testing of an Accelerometer. Sixth Biennial Guidance Test Symposium. Holloman AFB. October 1972.
- (2) B. H. Evans and Thomas Fuhrman., Determination of Accelerometer Nonlinearities from Precision Centrifuge Testing, Second Inertial Guidance Test Symposium, Holloman AFB, 1964.
- (3) Neugebauer, George H., An Improved Data Reduction Procedure for Accelerometer Centrifuge Data, Thirteenth Biennial Guidance Test Symposium, Holloman AFB, 1987.

High Accuracy  
Inertial Test Table

Louis A. DeMore, Ph.D.\*  
Michael D. Hooser, Ph.D.\*\*  
Robert Anticole\*  
Hans Riegenbach\*  
Frank Almendinger\*  
Michael Swamp\*

\*Contraves Inc., Pittsburgh, PA  
\*\*Central Inertial Guidance Test Facility,  
Holloman AFB, NM

July, 1993

---

## ABSTRACT

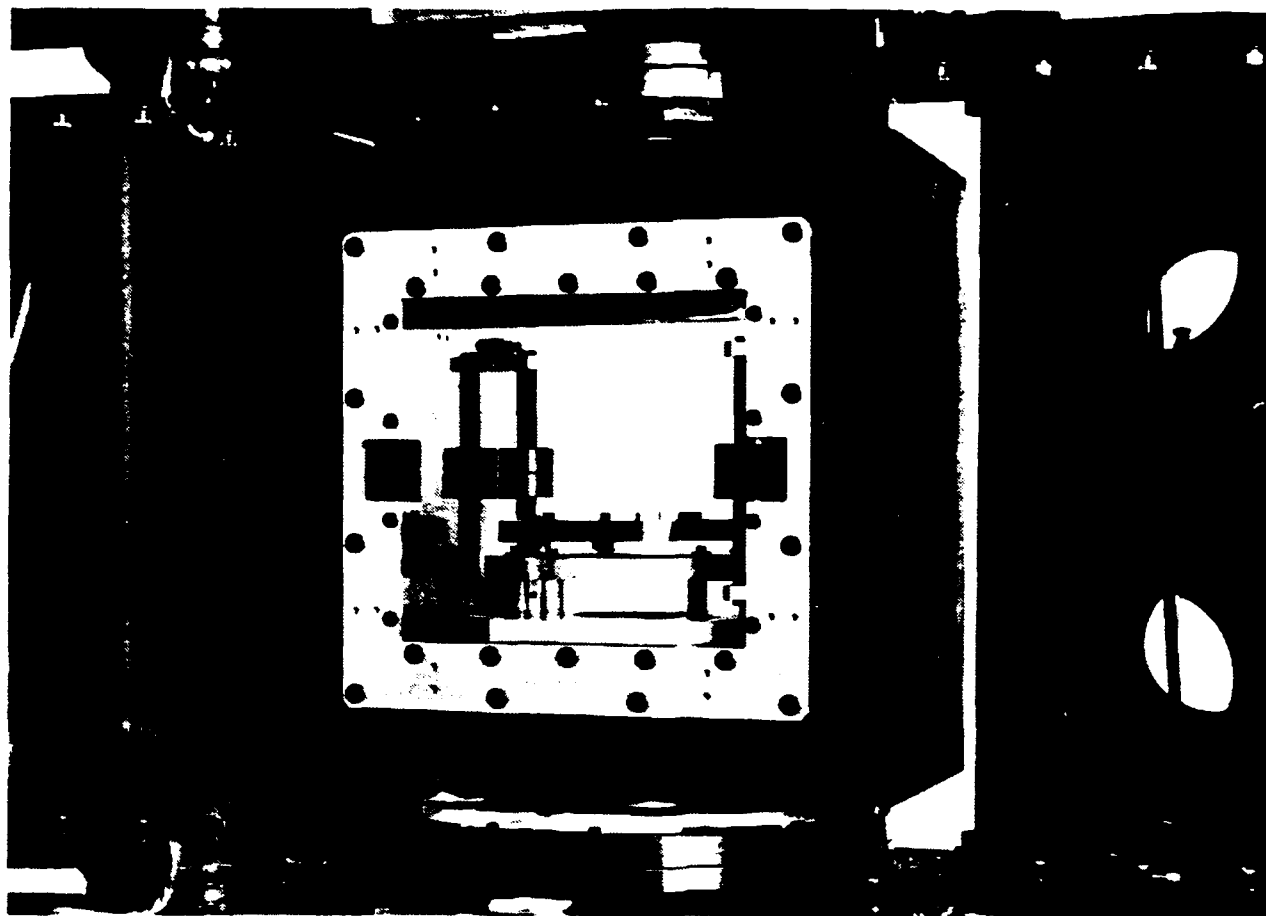
Contraves, Inc. under contract with the Central Inertial Guidance Test Facility at Holloman Air Force Base, has completed a feasibility study, a conceptual design, and has built a single-axis proof-of-principle prototype test table. This effort is being conducted to provide the USAF with a state-of-the-art rate and positioning fixture capable of 0.1 arc second pointing accuracy and 1.0 PPM rate stability.

This paper presents design goals and performance data from several technology enhancement options such as carbon-fiber gimbals, magnetic bearings, state-space based digital axis control system, dual back-to-back Inductosyns, fiber optic rotary joints, and roll rings. The system, even in the preliminary stage, has demonstrated the technologies necessary to achieve the desired positioning accuracy and rate stability. Data are presented to show that the system currently exceeds the state-of-the-art in motion simulators.

## INTRODUCTION

The Improved Three-Axis Test Table (ITATT) program represents an order of magnitude improvement in pointing accuracy and rate stability over present state-of-the-art test tables. Many new technologies were studied in the conceptual design of this table. These technologies covered the entire gamut of test table engineering and manufacturing disciplines and involved gimbal material and structure, the bearing configuration, axis sensors and calibration techniques, actuators, signal transmission to the test package, and the instrumentation and control. All of these technologies were ultimately employed in the fabrication of the inner-most axis of the table, which is the first phase in the overall development of the three-axis table. Reference (1) describes the ITATT conceptual design.

Figure 1 is a photograph of the single-axis table undergoing initial testing at Contraves. The first phase, single-axis subsystem uses a carbon fiber reinforced plastic gimbal instead of the more conventional aluminum for improved gimbal stiffness-to-weight performance and improved geometrical stability under thermal stress. Active magnetic bearings, which are used for both radial and thrust load support, significantly improve the axis wobble, stiffness and alignment characteristics over the most precise mechanical ball bearings and air bearings. Dual back-to-back Inductosyn\*, instead of a single-axis sensor, are the core of the axis position sensor system; which, coupled with an on-line, automated, real-time calibration routine, provides an order of magnitude



92-121-4

Figure 1. Prototype Single-Axis Table

\*Inductosyn is a registered trademark of Farrand, Inc., Valhalla, New York.

\*\*Roll Rings is a product developed and marketed by Honeywell, Inc., Satellite System Operations, Glendale, AZ.



## SINGLE-AXIS TEST TABLE

improvement in axis position accuracy. The brushless, toroidally surface wound and slotless AC motor and drive reduces motor cogging effects, thus practically eliminating disturbances to the axis rate. The test article signal transmission subsystem uses a combination of a fiber optic rotary joint, roll rings\*\* and low friction slip rings as opposed to conventional slip ring design in order to increase life, reduce axis frictional disturbances and improve rate stability. Finally, the state-space based all digital axis control system is the platform which supports the control system strategies such as state and disturbance estimation, disturbance rejection, axes decoupling, and optimal command generation for overall improved system response.

When completed, ITATT will be instrumental in the development of next generation inertial guidance test components and measurement units. Figure 2 is a conceptual drawing of the complete three-axis test table.

The overall requirements of ITATT form the basis for the design and performance requirements of the single axis system. Table 1 lists the performance requirements of the single axis table.

Table 1. Requirements

Gimbal Deflections	0.0015 arc sec
Axis Wobble	0.02 arc sec
Position Range	Continuous
Position Accuracy	0.02 arc sec
Position Resolution	0.019 arc sec
Axis Rate Range	0.001 to 1000 deg/sec
Axis Rate Stability	1 ppm

Contraves has just completed the design and fabrication of the single axis test table shown in Figures 1 and 3. Figure 3 is a collage of photographs of the complete system including all control and power electronics.

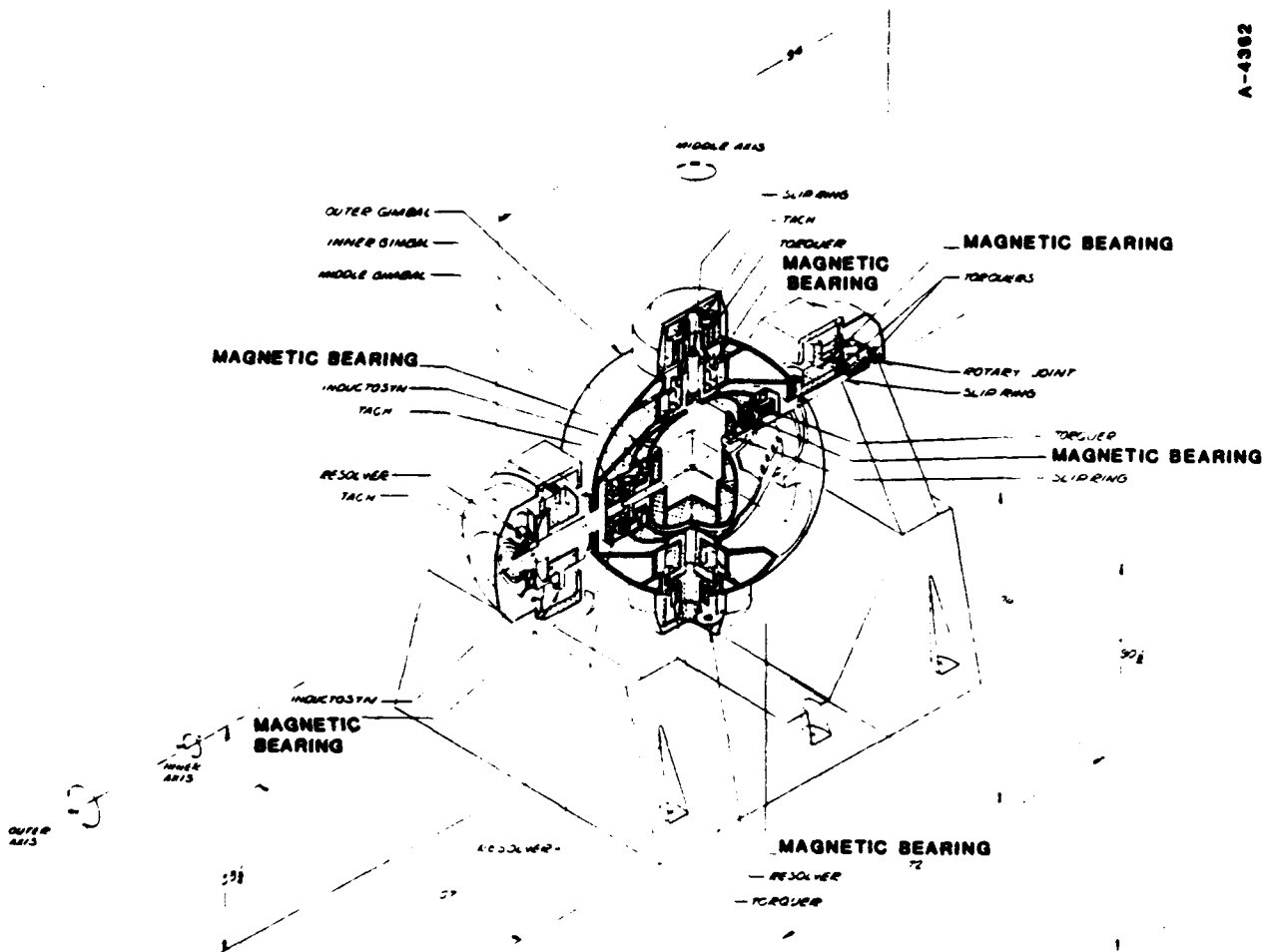
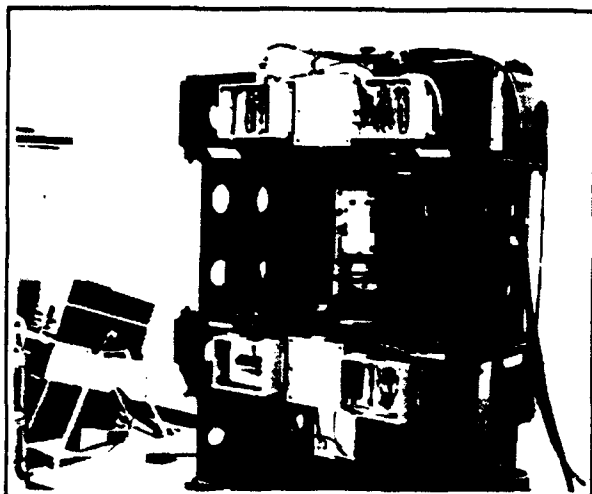
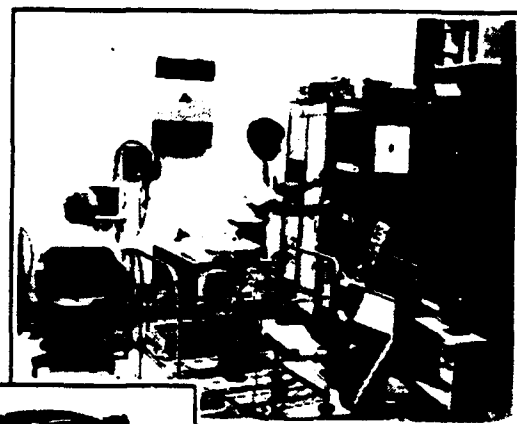


Figure 2. Improved Three-Axis Test Table (ITATT) Concept

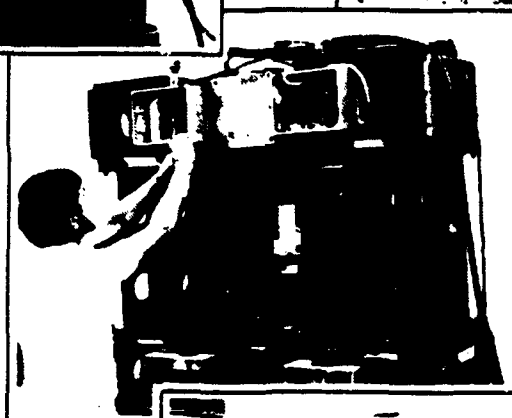


92-127-10



92-127-8

A 19428



92-127-11



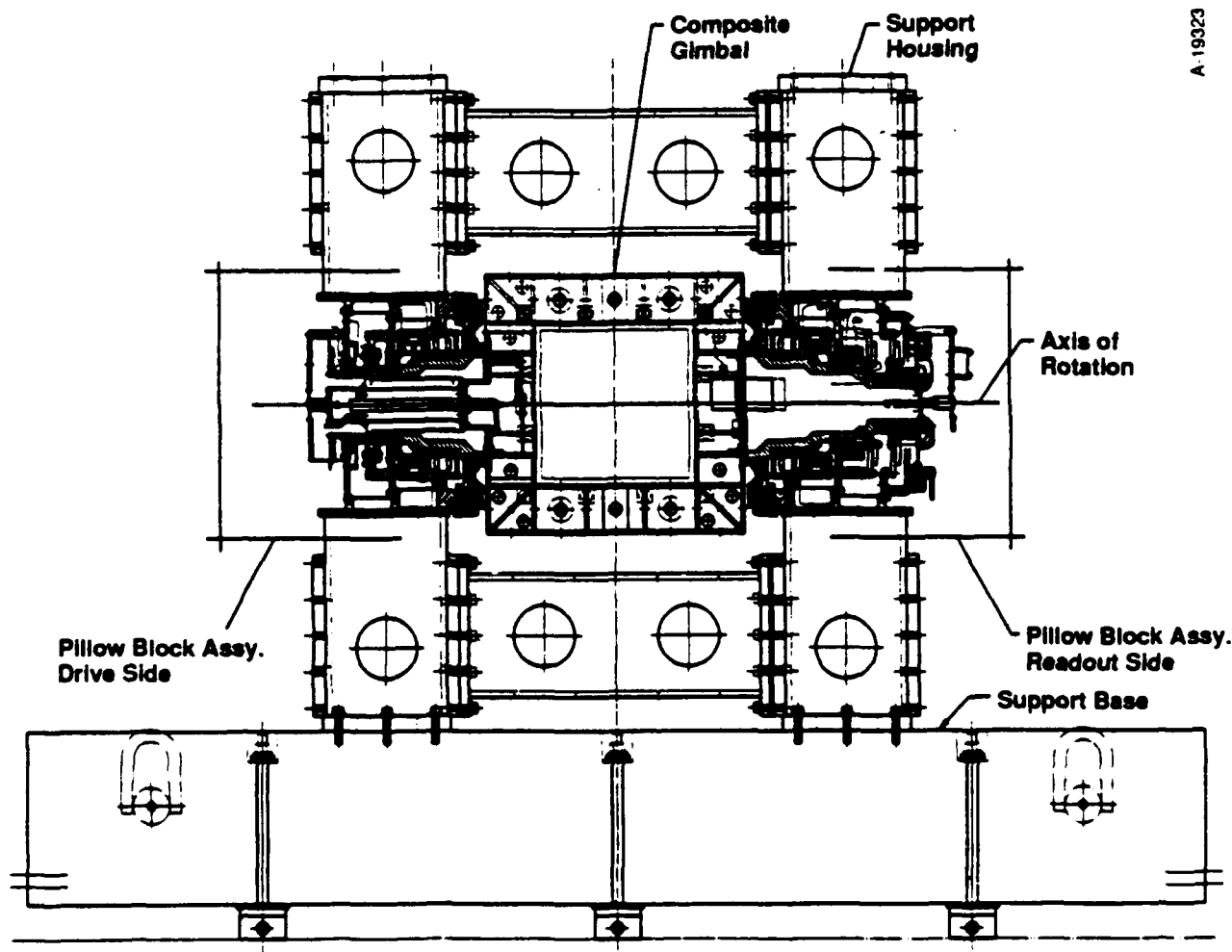
92-127-9

Figure 3. Single Axis Test Table (including Control and Power Electronics)  
Undergoing Tests at Contraves

## GIMBAL STRUCTURE AND MATERIAL

Figure 4 is a top assembly drawing of the test table and fixtures as it exists in the laboratory. The figure shows the composite gimbal supported by two pillow block assemblies which are, in turn, supported by a steel fixture and a granite base. The axis of rotation is shown in a horizontal attitude; the fixture may be positioned to place the axis in a vertical orientation to measure gravitational effects. Figures 5 and 6 are the assembly drawings for the drive side and readout side pillow blocks respectively. Each side has a radial and axial active magnetic bearing set with back-up mechanical bearings. Individual radial and axial position sensors are used in the magnetic bearing servo loops. The drive motor, resolver, fiber optic rotary joint and roll rings are shown on the drive side of the pillow block. The dual Inductosyns and slip ring assembly are shown on the readout side.

Both traditional and advanced composite materials were considered and evaluated for specific stiffness, coefficient of thermal expansion, thermal conductivity, dimensional stability, fabrication problems, and cost. Using the candidate materials, several gimbal configurations were evaluated with respect to the test table's system performance goals for angular pointing accuracy and angular rate stability. Specific gimbal design parameters affecting the system performance goals for angular pointing accuracy and angular rate stability include the angular payload deflections due to torsional wind-up and asymmetrical stiffness, the linear payload deflections that cause torque disturbances and shaft wobble, and the natural frequencies affecting the control system bandwidths. Detailed finite element models of each configuration were used to predict the performance characteristics and demonstrate the advantages of the graphite/epoxy composite design.



A 19323

Figure 4. Top Assembly of the Single Axis Test Table

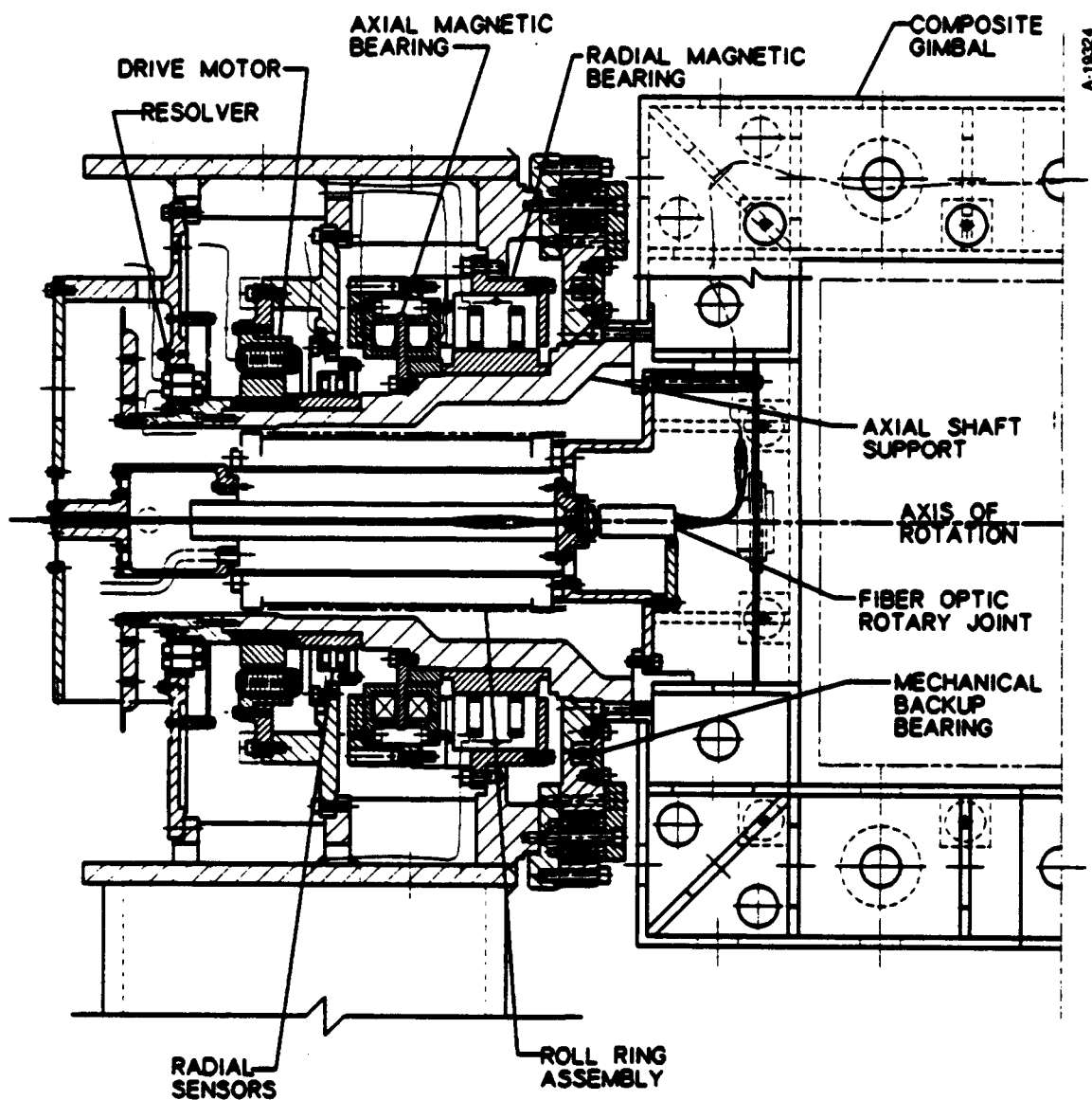


Figure 5. Single Axis Test Table Drive Side Assembly Drawing

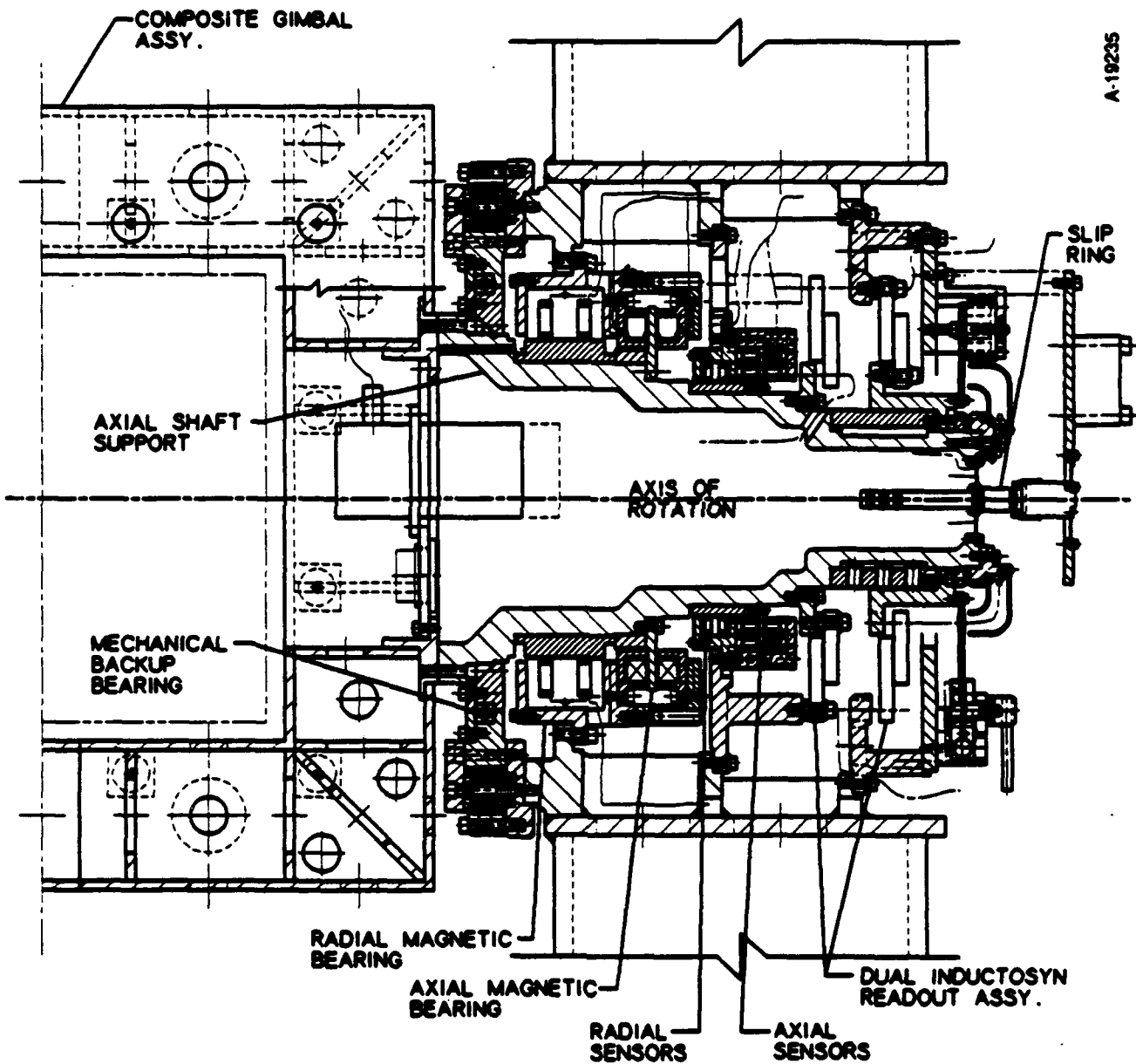


Figure 6. Single Axis Test Table Readout Side Assembly Drawing

The overall ITATT system performance requirements place stringent requirements on the gimbal structure. The flow down of these ITATT system requirements to the gimbal is shown in Table 2. The essential gimbal requirements are high specific stiffness, high absolute stiffness, high stiffness symmetry, and high dimensional stability for both the construction material and the configuration. These attributes are needed to make the gimbal act as close to a rigid body as possible. For example, the gimbal stiffness must be sufficient to make all elastic payload angular deflections negligible under any gimbal load orientation. In addition, the dimensional stability must be sufficient to make long and short term gimbal angular distortions negligible. Reference (2) presents the details of the gimbal design.

The final gimbal design is constructed of graphite/epoxy with Invar fittings in a rectangular honeycomb configuration. This assembly is shown in Figure 7 and is summarized in Table 3.

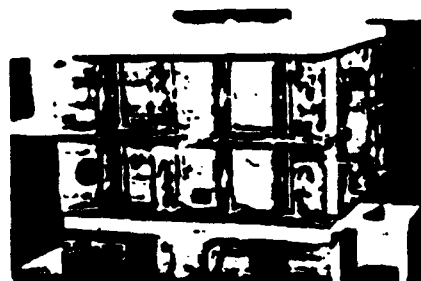
**Gimbal Material** - The graphite/epoxy material was selected because of its outstanding thermal distortion index and superior specific stiffness. The thermal properties of graphite/epoxy justify the additional costs and manufacturing complexity. The CTE (coefficient of thermal expansion) in PPM/°F is 8 for the steel, 13 for the aluminum and only 1 for the graphite/epoxy. The Invar fittings are used for the machining interfaces because they have a CTE close to the graphite/epoxy. The laminate thickness is a constant 0.25 inch throughout the part to maintain symmetric hydroscopic expansion.

**Gimbal Configuration** - The rectangular gimbal shape was selected because it provides essentially the same sectional stiffness and symmetry properties as a spherical shape yet offers a superior mechanical interface to the cubic test payload. The stiffness and symmetry properties of the spherical and rectangular shapes are equivalent because the inner gimbal must provide an opening for installation of the test payload. This opening truncates the spherical gimbal and negates its axisymmetric properties.

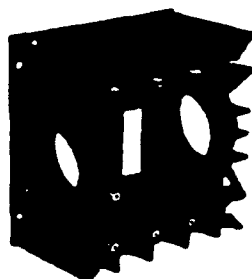
Due to symmetry and the honeycomb structure, the angular deflection at the payload is nominally zero for gravitational induced loadings. Position errors of the payload, relative to the encoder, can still arise as the required drive torque will vary at a 2 per revolution frequency if the gimbal's linear deflection (sag) is not uniform for any gravitational load orientation. The drive torque variation can be related to the work required to change the height and hence the potential energy of the payload and deflected structure between the most compliant and the least compliant orientations. This situation is shown schematically in Figure 8 where it is apparent that a potential energy differential exists between the vertical and horizontal load cases. Torque variations and the resulting payload angular errors were computed for all gimbal configurations. It has been determined that these non-constant linear gimbal deflections are not a significant error source as the position and rate errors do not exceed 0.00021 arc second and 0.002 ppm.

**Table 2. Flow Down of ITATT System Performance Requirements to the Gimbal**

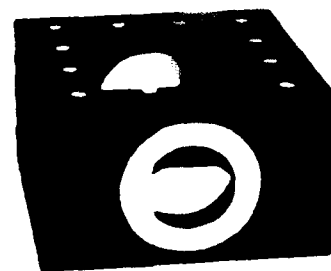
System Requirements	Gimbal Requirements	Specific Performance Requirements
Pointing Accuracy	Support payload with: (100 lbs, 12-inch cube) • Stiffness Symmetry • High Stiffness • Dimensional Stability	Negligible angular distortion achieved by:  • Low Modulus Variations • High Specific Modulus • High Absolute Modulus • High Transient Thermal Distortion Index • Negligible Hydroscopic and Microcreep Effects • Tight Manufacturing Tolerances
Rate Stability	Support payload with: • High Torsional Stiffness • Stiffness Symmetry • High Torsional Resonances	Negligible rate errors achieved by:  • Low Modulus Variations • High Specific Modulus • High Absolute Modulus • Close Manufacturing Tolerances



Gimbal in assembly fixture



Gimbal partially assembled



Final assembly

Figure 7. Single Axis Table Gimbal in Various Stages of Assembly

Table 3. Single Axis Table Gimbal Design Summary

Shell Material .....	Pitch carbon fiber/epoxy (Amoco P55S/ERL 1962)
Insert Material .....	Invar
Configuration .....	Rectangular
Weight .....	70 lbs
Modulus Symmetry .....	Within 5%
Manufacturing Tolerances .....	Flatness, parallelism, squareness less than 0.010 inch
Encoder Location .....	Opposite motor
First Major Torsional Resonance .....	Above 600 Hz
Linear Deflections at Center	
Gimbal Vertical .....	50 $\mu$ inches
Gimbal Horizontal .....	204 $\mu$ inches
Shaft (Trunnion) Deflection	
Average Shaft Angular Deflection .....	3.06 $\mu$ rad (0.6 arc sec)
Variation in Shaft Angular Deflection .....	1.32 $\mu$ rad (0.26 arc sec)

Other errors may be introduced by excessive trunnion shaft rotation (i.e., trunnion bending that is inherent with gimbal sag) since the encoder accuracy is effected by trunnion shaft deflections. The magnitude of shaft angular deflections at the encoders is reduced by using large diameter shafts and by minimizing the space between the radial bearings. In conjunction with the high stiffness of the composite gimbal, these design features make it possible to hold shaft rotation at the encoders to 3.7 microradians.

Imbalance and other asymmetries result in angular deflections of the payload (i.e., windup of the gimbal) that vary with a once per revolution frequency. Imbalance about the inner axis results in a sinusoidally varying imbalance torque when the inner gimbal is rotated with the axis horizontal. Since the torque motor is on the opposite side of the gimbal from the encoder, the effect of torque variations on position and rate accuracy is quite low: 0.0004 microrad/in-lb of imbalance and 0.002 ppm/in-lb of imbalance

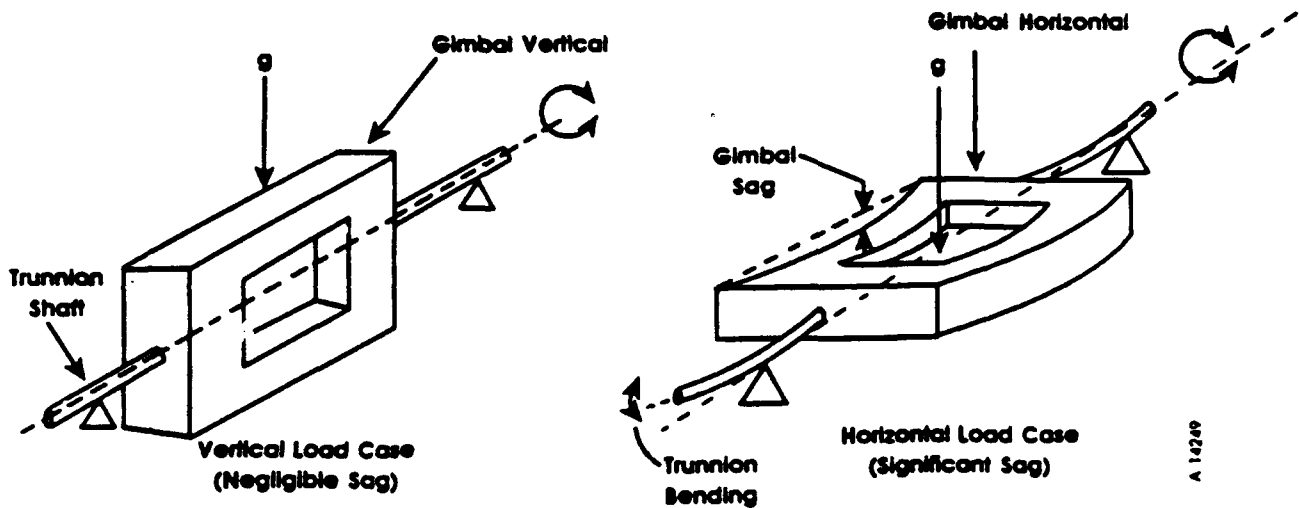


Figure 8. The Anisoelastic Gimbal Effect (Non-Constant Deflections)

respectively. A 1 in-lb imbalance due to a mass shift along the inner axis was found to result in a position error of 0.0023 arc second and a rate error of 0.0044 ppm.

Asymmetric mass distributions in a balanced axis can also result in payload position errors. This condition could arise if an unbalanced payload was installed in the gimbal, and then weights were attached to the gimbal to balance the system. This effect was evaluated by running several cases in which an imbalance moment was applied to the payload package and equipollent forces were applied to likely counterweight mounting points on the gimbal as shown in Figure 9. It was determined that the composite gimbal design can tolerate 5 in-lb of payload imbalance with net position and rate errors of 0.0035 arc second and 0.017 ppm, respectively.

**Manufacturing Considerations** - Three distinct areas were addressed in the final design manufacturing tolerance evaluation:

1. Flatness requirements for a single unsupported plate section.
2. General dimensional tolerances.
3. Material uniformity requirements.

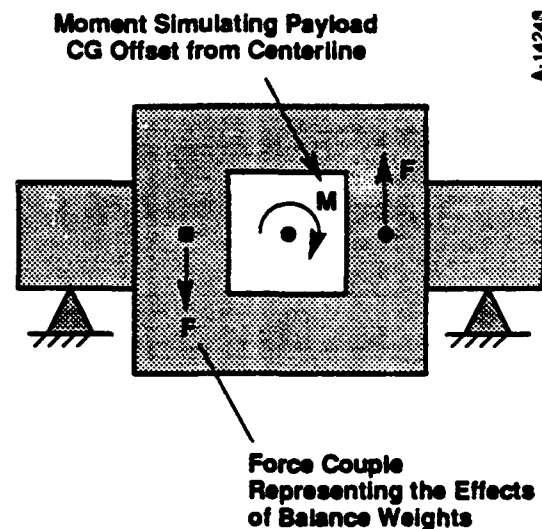


Figure 9. Simulation of Mass Asymmetries

The effect of unsupported panel flatness deviations of 0.010 inch is a payload rotation of 0.000006 arc second. The effect of gross dimensional deviations of 0.020 inch is a payload rotation of 0.0015 arc second. The effect of a 5% elasticity modulus change in one panel is a rotation of 0.0003 arc second.



The manufacturing tolerance requirements proved to be an important link between the gimbal material and configuration decisions. The rectangular gimbal is constructed from flat stock graphite/epoxy laminate glued together to form the shells and stiffeners. This construction technique proved to be the most practical method for achieving 5% elasticity modulus symmetry and 0.010-inch geometric tolerances.

## ACTIVE MAGNETIC BEARING

The active magnetic bearing consists of a ferromagnetic rotor suspended in the magnetic flux of electromagnets fixed to the stator. The axis employs both thrust and radial bearings, the bearing system must apply magnetic forces along five independent axes. Figure 10 depicts the five controlled axes: two perpendicular axes at each shaft end and a fifth axis parallel to the shaft rotational axis. The radial and axial active magnetic bearings use Contraves proprietary "E" stator design which minimizes drag friction. The rotor material undergoes only 4 partial flux excursions vs. 4 complete reversals; this reduces the magnetic retentive moments by about a factor of 4.

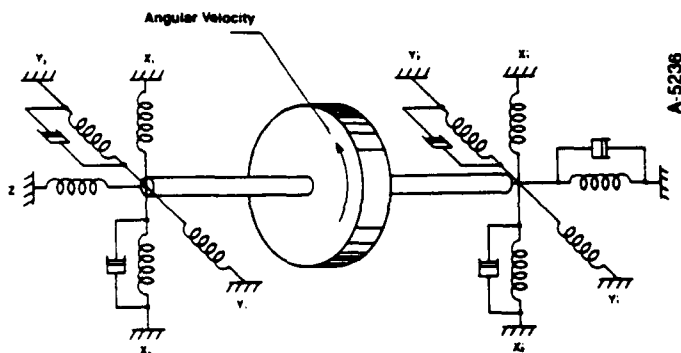


Figure 10. Active Magnetic Bearing Model, Springs Represent Electromagnets

The magnet assemblies for the radial and thrust bearings have the following characteristics:

- Force @ saturation = 860 lbs
- Current @ saturation = 4.84 amps
- Current @ 150 lbf = 2.02 amps
- Total Coil power loss @ 200 lbf, 25°C = 6 watts
- Coil inductance = 0.086 H
- Air gap = 0.007 to 0.0075 inch

**Control and Instrumentation** - Active feedback control systems are employed to both stabilize and accurately position the rotor in space. The control systems are Type 3 servos (when electronically linearized) employing a position sensor in the outer loop. The active magnetic bearing is non-linear and open loop unstable. A control strategy was developed to stabilize and linearize the loops. A computer model was developed and sensitivity analysis performed to uncover the factors most sensitive in the linearization technique. Figure 11 is a schematic block diagram of the bearing control system. The position sensor is an inductive type (magnetic coils and reference ring) sensing impedance (air gap) variations. There are two, differential, radial gap sensors located near each bearing 180 degrees apart. The separation between the radial bearings is 35 inches which produces a scale factor of 0.02 arc sec = 1.7  $\mu$ inches. The radial reference ring has a roundness of 10  $\mu$ inches and a finish of 8  $\mu$ inches. There are differential axial gap sensors on either side of the target disc for thrust position feedback. Finish and flatness of the disc are commensurate with the radial reference ring. Table 4 gives the characteristics of the sensor system.

Table 4. Bearing Radial and Axial Sensor Characteristics

Core Material	Permalloy - 0.004 in. thick (lamination)
Air Gap	0.015 inch nominal

The original design concept for the radial position sensor was to sense over a wide arc to average out defects in the rotor surface. It was assumed this approach would relieve by a factor of 10 the tight machining tolerances required to achieve the 0.02-arc sec wobble; this assumption did not prove to be true

for low frequency (cycles/revolutions) machining errors. Tighter machining tolerances were eventually imposed. The original roundness of 50  $\mu$ inches was improved to 40  $\mu$ inches; and, with diamond turning techniques, this roundness should be reduced by a factor of 10.

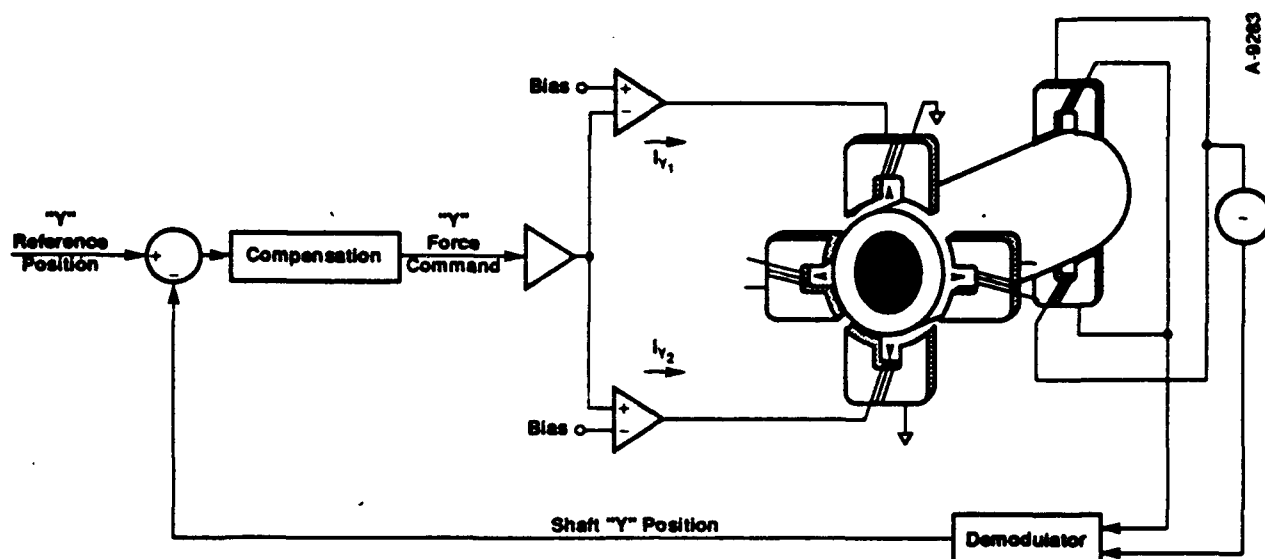


Figure 11. Bearing Control System Block Diagram

**Wobble** - The most important specification of the Active Magnetic Bearing is 0.02 arc sec wobble, which is 10 times better than the prevailing state-of-the-art. A precision air bearing has about 0.3 to 0.5 arc sec wobble. The best ITATT wobble measurements were as low as 0.18 arc sec, peak-to-peak as shown in the wobble test data of Figure 12. The shaft machining error which is 40  $\mu$ inches at present, is the major source of the wobble error. ITATT sensor spacing of 35 inches requires <4  $\mu$ inches of shaft runout to achieve 0.02 arc sec wobble. Shaft remachining to tighter tolerances will ultimately achieve the specification objective. Actual (mechanically measured) shaft runout was compared to runout measured by the shaft position sensor for position sensor shafts made of various materials. Material selection minimized the variance between the sensor readout and the shaft runout, thus minimizing sensor induced wobble.

Once the SPS targets are machined to better than 4  $\mu$ inches or error reduction techniques are employed, the most important factors in achieving the wobble specification are temperature control and shaft position sensor (SPS) stability.

Wobble measurement in the 0.02 arc sec range strains the state-of-the-art and requires tight temperature control in addition to careful measurement techniques. For example, less than 0.01 arc sec standard deviation of the measurements is required to produce confidence in the results. Thermocouples, tiltmeters and

retroreflectors are useful in uncovering the source of measurement errors.

Computer programs were developed to amplify the wobble error curve shown in Figure 12, to assure repeatability of the error profile and closure.

Considerable effort was expended on shaft position sensors and the new third generation sensors now meet the resolution, accuracy, temperature coefficient and drift necessary to achieve the specification.

A data acquisition system with computer automated testing and analysis are essential to produce measurements in the 0.01 to 0.1-arc sec range.

**Disturbance Torques** - The disturbance torques produced by the bearing at low speed are predominantly due to hysteresis iron losses. Theoretically, this torque disturbance is independent of rate, constant beyond a certain threshold and quite linear for small displacements about zero (up to twice the air gap value). The design running torque for the ITATT outer axis is approximately 1.2 oz-in.

Preliminary tests show (inner) axis static friction as low as 6 oz-in when measured by a spring scale. Motor vendor data attributes about 4 oz-in to the motor and the slip ring friction was measured at 1 oz-in leaving about 1 oz-in for the bearing.

# WOBFMINP

Rev 1

minimizes  
p-p wobble

yoff=8.447  
xoff=-5.33

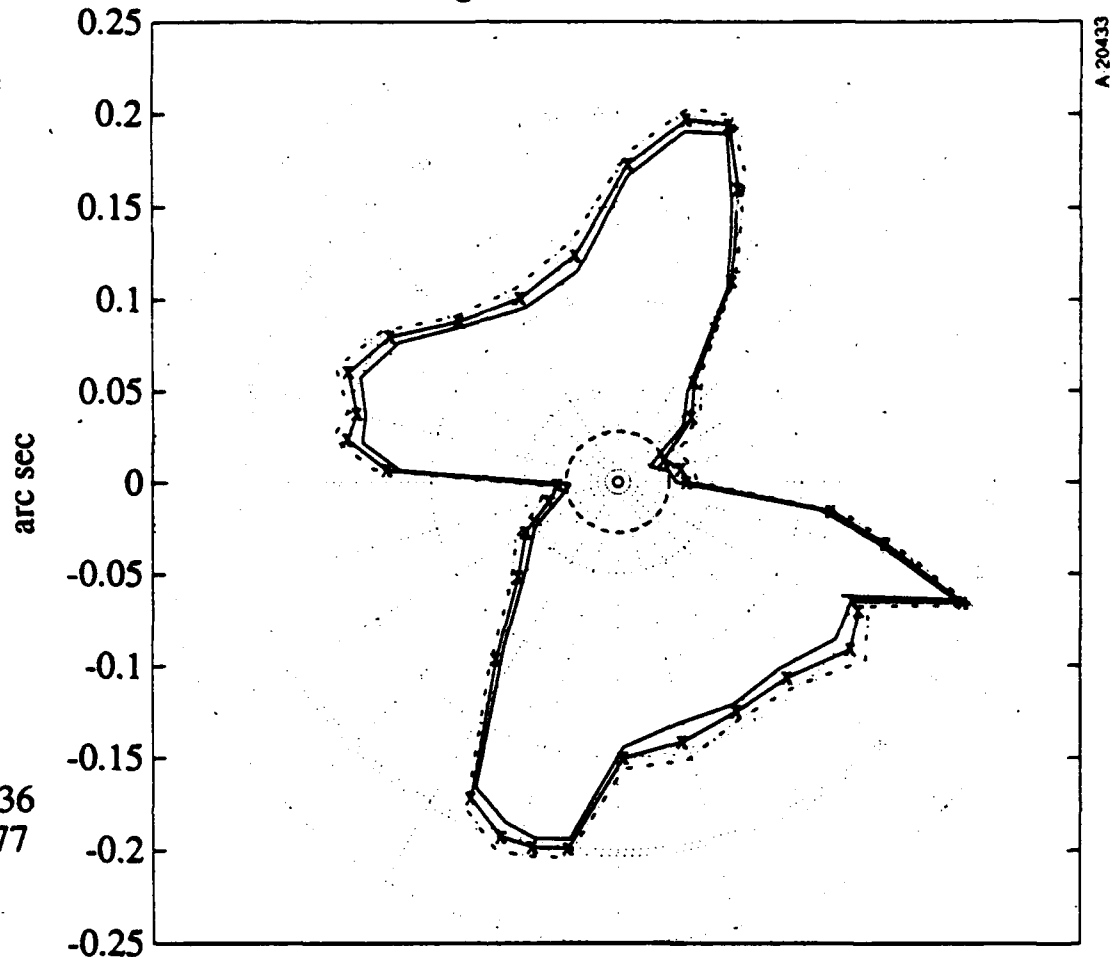
rmax=0.2036  
rmin=0.0277

mean s.d.=0.00643

wobble = 0.0545 arcsec rms

wobble = 0.1759 arcsec p-p

Wobble Reading  $\pm 1$  worse case s.d. for wo524105



after warmup

27-May-93 A20000 ISATT

Figure 12. Single-Axis Table Bearing Wobble Measurement (0.12 arc sec)

**Stiffness** - Since the bearing system is essentially an integral type servo loop, the bearing stiffness is governed by the typical (Type III) torque rejection curve and, as such, is a function of excitation (torque disturbance) frequency. Figure 13 is a typical stiffness curve. For low frequencies the stiffness is dominated by the control system dynamics; the high frequencies are dominated by the axis inertia or mass.

Tests were done with a 100-pound force. 0.1  $\mu$ inch resolution position sensors were used to measure shaft deflection while the force was applied to the gimbal. The measured static stiffness was  $>100 \times 10^6$  lbf/in. A typical air bearing static stiffness is about  $10 \times 10^6$  lbf/in.

**Bearing System Electronics** - The active magnetic bearing electronics are housed in a separate console and consist of:

- Control Electronics Card Rack
  - Control cards
  - Control loop compensation
  - Linearization circuits
  - Low voltage power supplies for cards
- 10 power amplifiers
  - Linear unipolar current amplifiers
- Power supply for power amplifiers

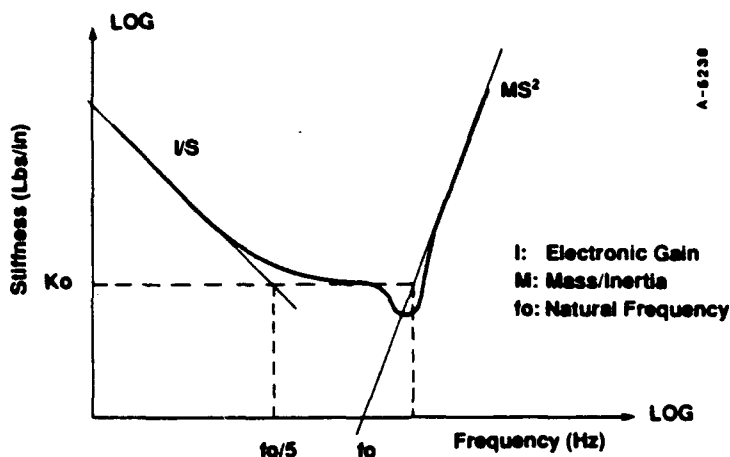


Figure 13. Typical Stiffness Curve for Tests, Active Magnetic Bearing

## MOTOR AND DRIVE SYSTEM

**Motor Considerations** - The primary motor design consideration was the requirement to meet a high small signal bandwidth while holding motor cogging and ripple disturbances to a small fraction of the disturbance budget. Thermal protection of the motor from accidental abuse, winding, and pole selection were less important, but required consideration. Contraves selected a 5 lb-ft brushless, permanent magnet, surface wound motor and three phase linear amplifier for the axis actuator.

Cogging torque is probably the most significant motor disturbance. The torque disturbance necessary to achieve 1 ppm angular rate stability is:

$$T_d \leq \frac{4.5 \omega_1^2 J}{N} \times 10^{-6}$$

where:

$T_d$  = disturbance torque, lb-ft

$\omega_1$  = one-half the open loop crossover, rad/sec

$J$  = total inertia, lb-ft-sec<sup>2</sup>

$N$  = disturbance frequency, cycle/rev

The parameters were estimated conservatively at:

$\omega_1 = 2 \times 15$  (30 Hz crossover and 50 Hz BW)

$J = 5$

$N = 48$  (48-pole motor)

resulting in a 0.0042 lb-ft maximum disturbance target. Vendor testing showed an actual cogging torque of 0.003 lb-ft on the ITATT motor.

A motor disturbance of lesser importance was torque ripple. Our specification control drawing called for a 1% torque ripple but our testing showed the vendor had 2% fifth harmonic distortion.

Although the motor peak torque capability was 5 lb-ft, the continuous capability was estimated (not measured) at 2 lb-ft. Motor winding parameters were chosen to obtain a flat torque (5 ft-lb) vs. speed curve up to 500 deg/sec with the proposed amplifier. A thermistor was included in each motor phase to provide protection monitoring.

**Amplifier Considerations** - Electromagnetic interference is an important factor in sub-arc sec accuracy systems and the power amplifier is usually the main noise source. Since a linear amplifier was chosen for noise considerations, power dissipation was also a concern. Commutation for a brushless motor is important because of its effects on disturbances, peak torque, and efficiency. The most important disturbance source in a brushless PM amplifier is drift or offset current. A DC offset on the AC motor current produces a disturbance torque proportional to the offset current and the motor torque constant at a frequency of Pole/2 cycles per revolution. The motor design goal of less than 0.004 lb-ft of torque disturbance is equivalent to an amplifier offset current of less than 10 milliamperes with the motor  $K_t$  of 0.35 lb-ft/amp. A floating current sense circuit was designed with low drift operational amplifiers to eliminate the offset current disturbance.

A second source of disturbance considered was torque ripple due to unbalanced current gains. The motor commutation software allows independent selection of Phase A and Phase B current gains; unmatched gains produce  $P$  (number of motor poles) cycle per revolution torque disturbances proportional to the product of gain unbalance and output torque.

The total noise goal is less than  $5 \times 10^{-5}$  ft-lb rms, which reduces to about 1  $\mu$ A rms for the power amplifier. Linear amplifiers were the only choice for this application. A low drift current sensor and a three-phase linear amplifier were designed from three Contraves Model 40-CG-160 linear amplifiers. The selection of a linear amplifier, for noise considerations,

required an analysis of the power dissipation requirements and capability of the amplifier. Power dissipation of a single phase (one 40-CG-160) amplifier varies linearly with operating speed during acceleration and deceleration; the continuous dissipation capability of the 40-CG-160 is 160 watts.

## BI-DIRECTIONAL SIGNAL TRANSMISSION SYSTEM

The ITATT will provide signal transmission to the test package with all gimbals under continuous rotation. Traditionally, slip rings were the transmission device of choice. For the single axis table, Contraves selected a combination of slip rings, roll rings and a fiber optic rotary joint. This combination provides both power and low level signal transmission with minimum axis friction (both starting and running) and minimum transmission noise.

**Slip Rings** - The slip ring assembly transfers signals or power to a rotating ring through a stationary brush-like device which pushes against the ring. This sliding motion causes friction and wear in both the ring and the brush. Slip ring technology is relatively mature. Its biggest drawbacks are its somewhat high starting and running friction torques.

A low friction slip ring with a design life of 10 million revolutions has been provided. Twenty circuits are provided for customer use and 25 for operating the Inductosyns and other axis components. Friction has been minimized by reducing the brush contact pressure and ring diameter, by reducing the current carrying capacity, and by proper selection of ring and brush materials. Torque disturbances are minimized by keeping the structural compliance and the stick-slip as low as possible. Low noise is a result of positive contact pressure between the ring and brush and the self cleaning nature of the assembly, i.e., the brushes tend to wipe away any debris on the rings.

A summary of the preliminary slip ring test results is:

- Dielectric resistance specification of 500 VRMS, 60 Hz was met.
- Insulation resistance specification of 500 VDC was met.

- Starting torque was measured at 0.97 oz-in. Specification is 1.1 oz-in maximum.
- Dynamic resistances are within the 25 milliohms or less specification.

**Roll Rings** - The rolling transmission device is a relatively new item that replaces the brushes and rings of a slip ring with a rolling flexure element and two tracks. Figure 14 is a photograph of roll ring components.

A 120-circuit roll ring, designed for a life of 10 million revolutions, is included on the axis. Advantages of roll ring technology are minimal torque for high current capacity, low maintenance, long life and minimal wear debris. High current slip rings require large pads with stiff springs, which produces high friction and stiction at low rates. Roll rings do not have this disadvantage but they have been shown to have higher noise. ITATT uses roll rings for high current capability and low friction slip rings for low level signals. To minimize roll ring random noise spikes and opens, two roll ring circuits are wired in parallel to provide one customer circuit. A summary of the preliminary test results of this assembly is:

- 100 of the 120 circuits have less than 100 milliohm of dynamic noise.
- Starting torque was 0.38 oz-in.
- Running torque was 0.2 oz-in.
- Insulation resistance was within the 1000-Mohm specification on 117 of the 120 circuits.
- All circuits have -70 dB minimum (circuit to circuit) isolation at 1 kHz into a 50-ohm load.

**Fiber Optic Rotary Joint** - Twenty fiber optic channels are provided for transmission of test item data. These 20 bi-directional channels are multiplexed and transmitted via one fiber optic rotary joint (FORJ). Both electrical multiplexing and wavelength division multiplexing are used to multiplex the 20 signals before they are transmitted across the FORJ. The FORJ is non-contacting with inherently low noise. The device is designed for a life of 10 million revolutions. Figure 15 is a block diagram of the system showing the signal transmission flow.

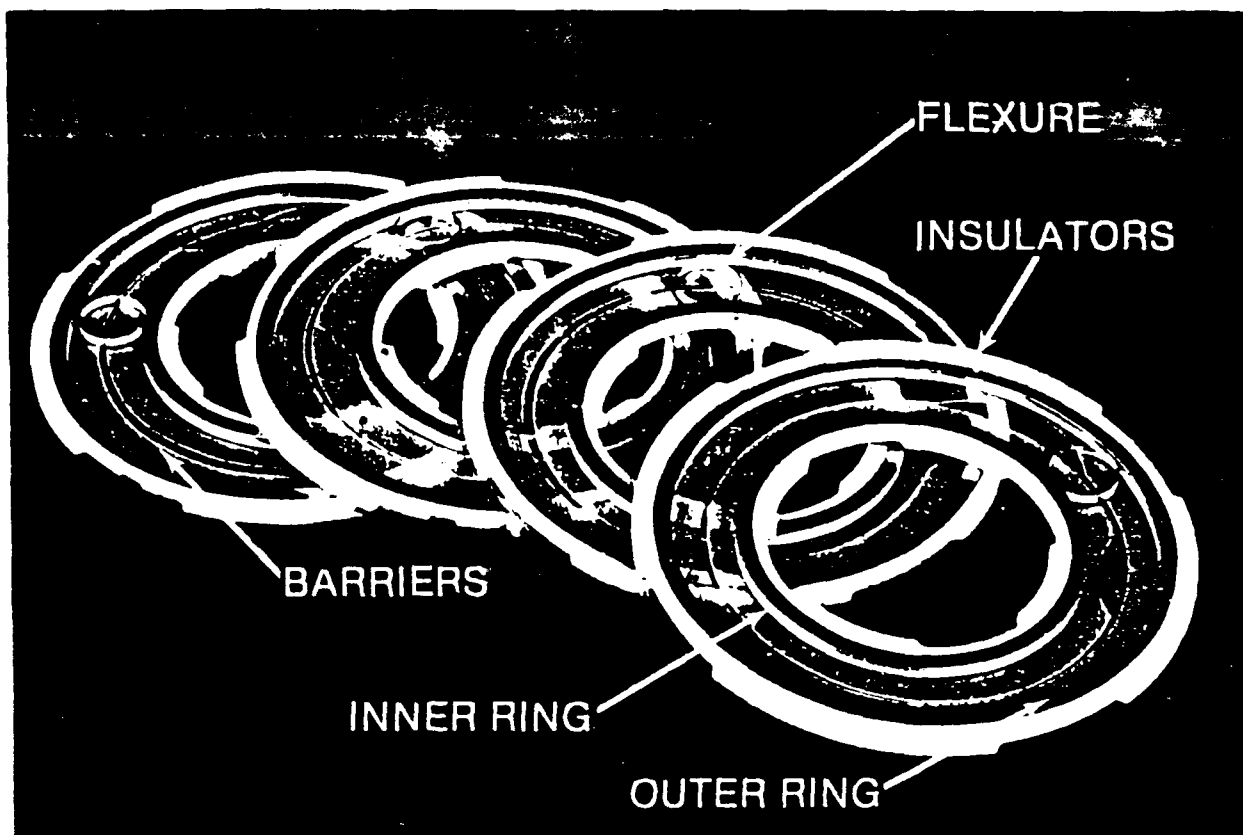


Figure 14 Roll Ring Components

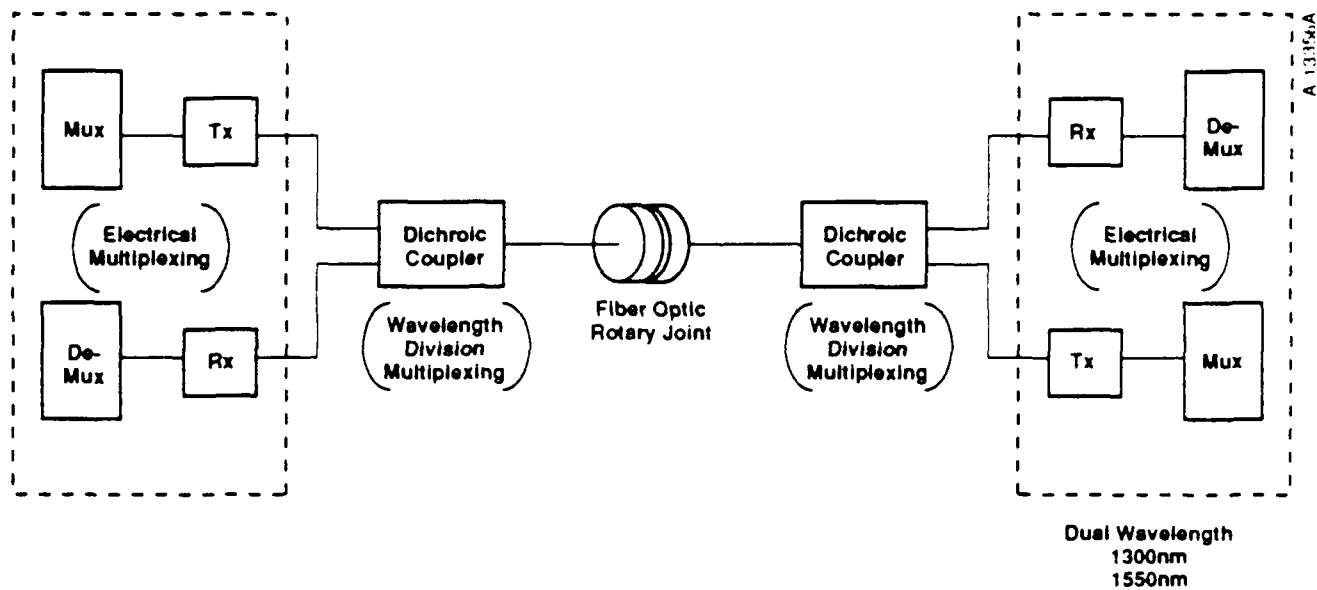


Figure 15 Fiber Optic Rotary Joint Signal Transmission Block Diagram

A summary of the preliminary test results for the fiber optic rotary joint system are:

- Break away friction was 0.01 oz-in.
- Running friction was 0.02 oz-in.
- The transceiver was expected to have a maximum bit error rate (BERT) of  $1 \times 10^{-9}$ . Preliminary testing with a bit error rate test set (the Hewlett-Packard HP3762/3) showed no errors at certain data rates. However, at a 5-Mbps data rate the test set would not synchronize to the pseudo-random data. At a 5-Mbps data rate the test set's error output was used to trigger an HP16500A logic analyzer that showed there were no errors. This test was run for 16 hours and sampled nearly  $31 \times 10^6$  bits. It would require 2000 hours to sample  $1 \times 10^9$  bits.

## AXIS CONTROL AND INSTRUMENTATION

**Axis Control System Description** - The control system performs all the functions associated with the normal command and control of the axis. Some of the functions and features of the system are:

- Digital control system with fixed sampling rate of 1.0 kHz,
- State estimator provides rate signal feedback using only a position transducer,
- Servo compensator provides stable and deterministic system response. Compensation constants are modifiable,
- Multiple control modes which encompass:
  - Position versus rate control
  - Encoder versus estimator feedback
  - Single versus dual feedback loop,
- Real-time low-level command generator for computing trapezoidal velocity profiles from user or host high-level motion commands,
- Position encoder correction per stored error curve,
- Torque disturbance correction for ripple and cogging, and
- Interlock monitor assures safety of personnel and equipment.

The digital encoding and control hardware consists of the components shown in Figure 16: one Intel SBC 386 single board computer (supervisor and control processor), two encoder input/output processors (EIOP), and a 386SX PC (user interface processor) connected to the Intel SBC through an RS-232 and a GPIB communication link. The functions of each component are shown in Table 5.

The control system uses two 720-pole Inductosyns, one as the primary feedback sensor and the other for calibration. Data are processed through a 16-bit A/D converter and a continuous calibration scheme in the EIOP. The result is a drift free feedback resolution of better than 0.02 arc sec.

**Single-Axis Controller** - Digital control design techniques were used in the design of the single-axis controller which consists of a position compensator and rate compensator. Both compensators are digital filter equivalents of stopped integrators. An error signal, calculated from the command and state estimate, enters each compensator. Figure 17 is a block diagram of a single axis controller. The position compensation (K1, A, B) and rate compensation (K2, C, D) are calculated by using classical design techniques to compute the gain and compensation. Tustin's approximation is then used to compute the appropriate parameters in the Z-plane. The sample time (T) was chosen sufficiently small (1 millisecond) to alleviate any potential problems with the controller or estimator operating at too slow a sample rate. The rate feedforward torque ( $\tau_{ff}$ ) is summed in after the rate compensator.

The control system has five operating modes:

1. POSN 1 Mode
  - Type III position loop.
  - No state estimator.
  - High bandwidth.
2. RATE 1 Mode
  - Type III position loop.
  - No state estimator.
  - High bandwidth.
  - Position commands derived from rate command.
3. POSN 2 Mode
  - Type II position loop around Type II rate loop.
  - State estimator used for position and rate feedback.
  - Low bandwidth/noise.

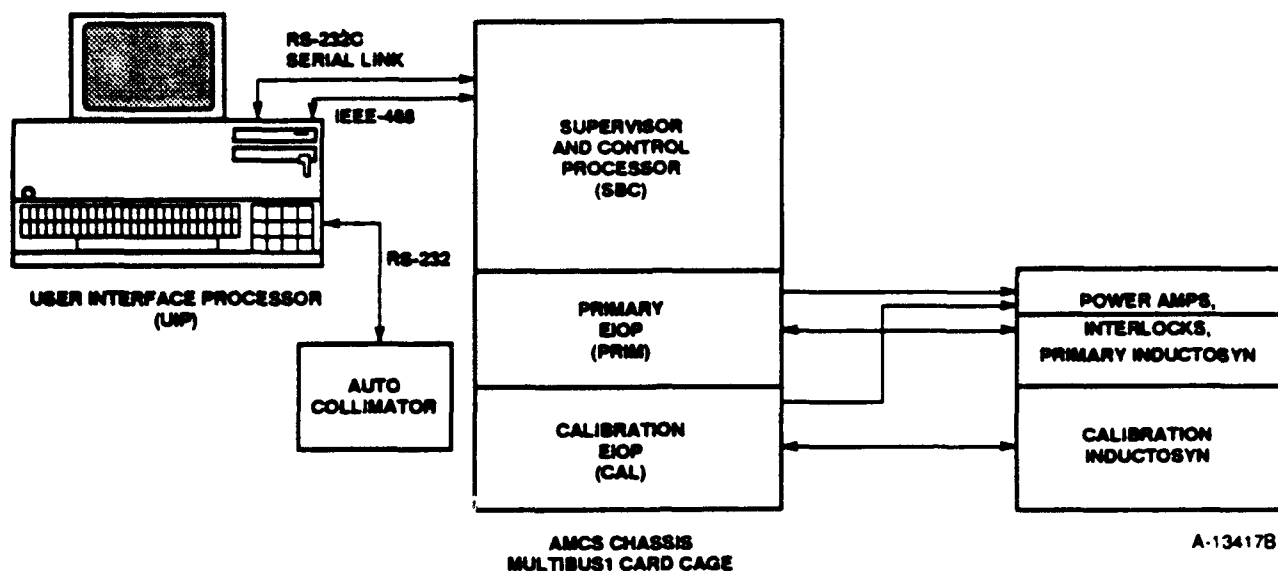


Figure 16. Axis Digital Encoding and Control Hardware

Table 5. Axis Digital Encoding and Control Component Functions

Component	Description	Function
User Interface Processor	ZEOS 386SC 16 MHz PC with 2 MB memory and hard disk	<ul style="list-style-type: none"> <li>User interface.</li> <li>System software storage for download power-up.</li> <li>Software development and test.</li> <li>Test result storage.</li> </ul>
Supervisor and Control Processor	Intel ISBC386/21 16 MHz Multibus I single-board computer	<ul style="list-style-type: none"> <li>Overall system coordination.</li> <li>Present user interface.</li> <li>Realtime command generator.</li> <li>Encoder and torque correction.</li> <li>Interlock monitor and control.</li> <li>Motor commutation.</li> <li>State estimation of axis model.</li> <li>Servo compensation.</li> <li>Disturbance correction.</li> </ul>
Primary I/O Processor	Contraves encoder I/O processor (EIOP)	<ul style="list-style-type: none"> <li>Primary Inductosyn I/O.</li> <li>Interlock and power amp I/O.</li> <li>Provide 1 kHz system sample clock.</li> <li>Output Phase A motor current command.</li> </ul>
Calibration I/O Processor	Contraves encoder I/O processor (EIOP)	<ul style="list-style-type: none"> <li>Calibration Inductosyn I/O.</li> <li>Output Phase B motor current command.</li> </ul>



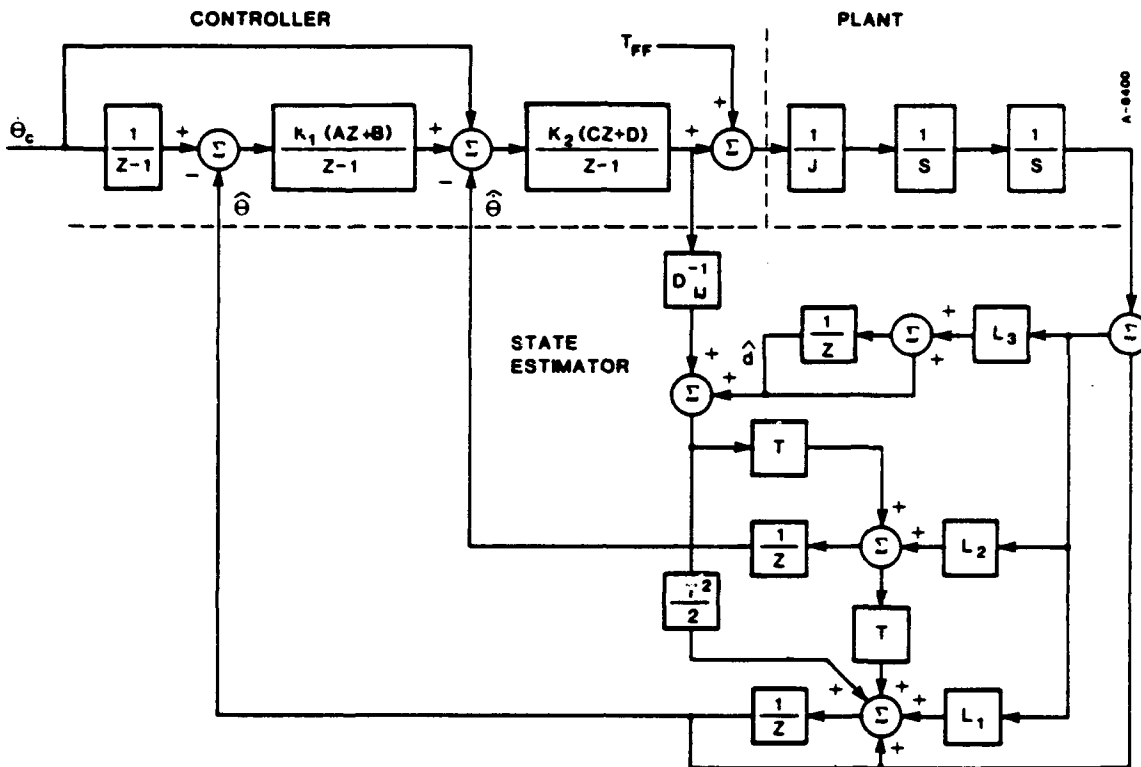


Figure 17. Single Axis Controller and State Estimator

#### 4. RATE 2 Mode

- Type II rate loop.
- State estimator used for rate feedback.
- Low bandwidth/noise.
- Best for rate stability.

#### 5. RATE 3 Mode

- Type II position loop around Type II rate loop.
- State estimator used for position and rate feedback.
- Low bandwidth/noise.
- Best for position tracking.

The POSN 1 and RATE 1 modes are intended for high bandwidth operation while the other modes have lower bandwidth and noise. The other low bandwidth, state-estimator modes are able to filter encoder noise and produce a quieter system with better rate stability.

**Test Software** - The Improved Three-Axis Test Table required new and better test methods and procedures. Programs were written to run on the PC and perform automatic tests for:

- Lo Speed Rate Stability
- Axis Wobble
- Position Accuracy
- Position Accuracy using Back-to-Back (BTB), (Dual) Inductosyn

The programs are written in Quick Basic, except for a FORTRAN routine to perform the FFT on the BTB testing.

The Low Speed Rate Stability program is a new test method developed for ITATT to overcome the limitation of poor low frequency (below 1 Hz) direct measurement capability. This method reduces the effect of random noise and measures the RMS rate stability over selectable intervals by calculating the standard deviation of the average rates over a series of intervals.

The Axis Wobble program automates the standard Contraves procedure for determining axis wobble using discrete angle measurements from a two-axis digital autocollimator. One hundred readings are taken for

each axis at 10-degree intervals; peak and RMS wobble are calculated, and wobble can be plotted.

The Position Accuracy program automates Contraves' standard manual procedure for determining the angular position accuracy. The total error is the RSS of the coarse error (once per revolution) and the fine error (once per Inductosyn cycle) using an autocollimator.

The BTB Inductosyn Calibration and Position Accuracy program is the centerpiece of the ITATT test software, and automates time consuming procedures: calibrating or measuring an Inductosyn error curve, validating the error correction algorithm, and measuring the angular position accuracy. The program is first used to measure the error curves of the primary and calibration Inductosyns. It then calculates Fourier coefficients necessary for error correction: magnitude, frequency, and phase. After these coefficients are entered into the control system Inductosyn error tables, the program validates their effectiveness and calculates residuals of the corrected error curves. These tests take about 12 hours and are usually run overnight, unattended. Much quicker runs to check position accuracy can be made when the error curve is not required.

## CONCLUSIONS

This single axis gimbal system, even in the preliminary stage, has demonstrated the technologies necessary to achieve 0.1 arc sec positioning accuracy and 1 ppm rate stability. The system has been, and continues to be, a test bed for magnetic suspension, composite gimbals, on-line Inductosyn calibration, low disturbance actuators, advanced signal transmission and digital axis control. Preliminary test results in each of the identified technological areas are very encouraging and are already better than the state-of-the-art.

## REFERENCES

- (1) "Design Study for a High-Accuracy Three Axis Test Table", L.A. DeMore, et. al., Journal of Guidance, Control and Dynamics, p. 104, January - February, 1987.
- (2) "Development of a Composite Gimbal for a High Precision Inertial Guidance Test Table", B. Cuerden and D. Henderson, SPIE vol. 1303, Advances in Optical Structure Systems, 1990.

**THIS PAGE LEFT BLANK INTENTIONALLY**

---

**High Stability  
Large Centrifuge Test Bed**

**Louis A. DeMore, Ph.D.\*  
Michael D. Hooser, Ph.D.\*\*  
Robert Anticole\*  
Hans Riegenbach\***

**\* Contraves Inc., Pittsburgh, PA**

**\*\* Central Inertial Guidance Test Facility, Holloman AFB, NM**

**July, 1993**

---

## **ABSTRACT**

This paper is a historical perspective of the development of the world's most precise, large diameter, centrifuge test bed. Included are discussions and data regarding the original design goals, the recovery from an installation accident, the rebuilding effort, and the final test results. The design and installation of the machine, located at Holloman Air Force Base, New Mexico, represents a large cooperative effort between the manufacturer, Contraves, Inc., and Air Force personnel.

The final results are impressive even though the system was almost completely rebuilt following the installation accident. Data are presented showing the success of the main axis air-bearing rebuild effort, and the final performance of the machine in rate and "g"-stability. The achieved performance coupled with the unique feature of a two-axis, gimballed positioner at the boom tip, provides a test bed of unparalleled performance and versatility for acceleration sensitive instruments.

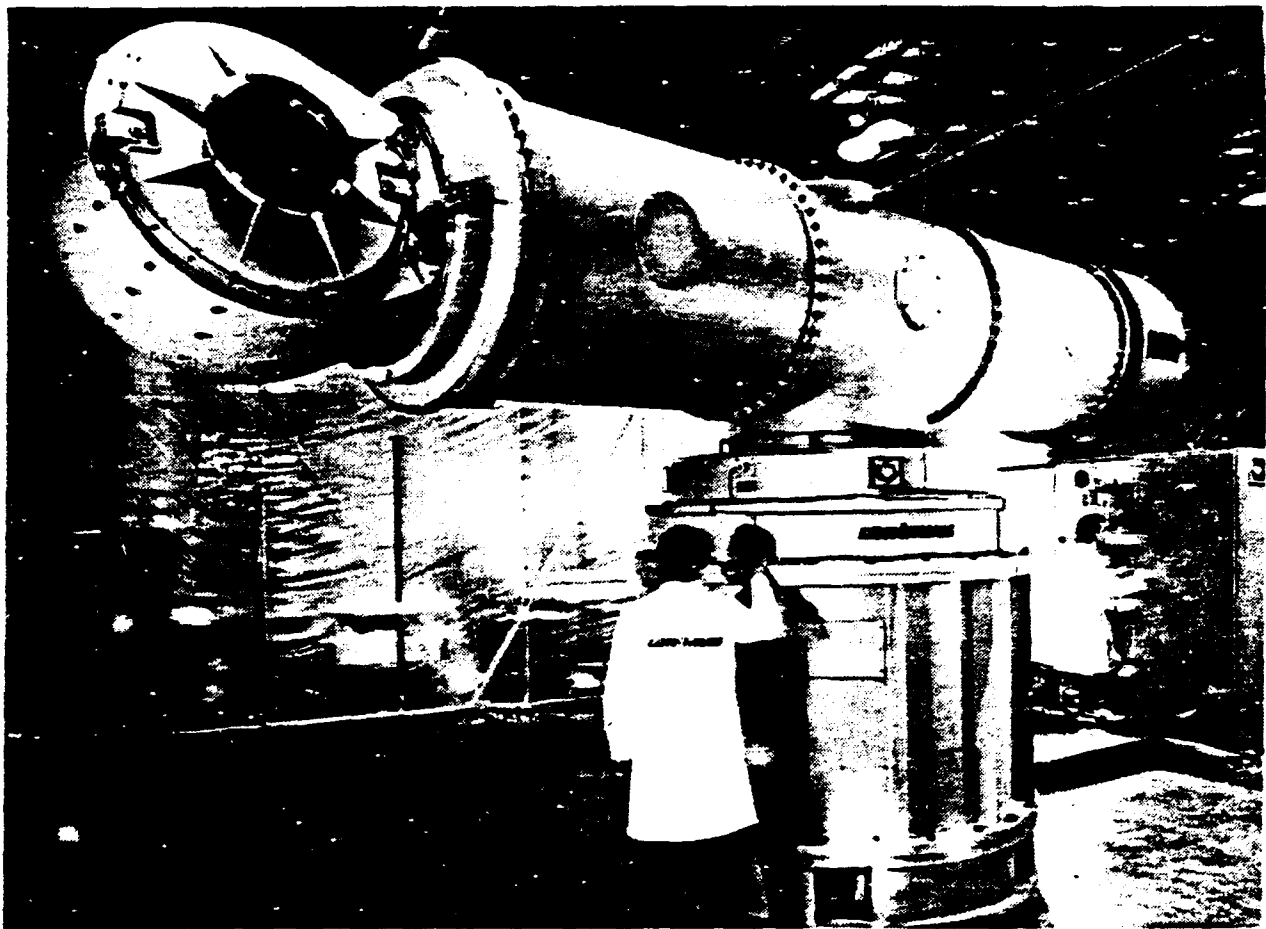
## Introduction

The centrifuge, shown in Figure 1, has a 10-foot radius boom and can accommodate a test package weighing 100 pounds with a volume of an 18-inch cube. It produces an acceleration field of from 0.5g's to 50g's at rates of 72 deg/sec to 720 deg/sec with extremely high stability. Rate stabilities of less than 0.5 ppm and g stabilities of 1.0 ppm were achieved throughout the operating envelope, an order of magnitude better than the present state-of-the-art! This extremely high stability coupled with the unique feature of a two-axis, gimbaled positioner at the boom tip, provides a test bed of unparalleled performance and versatility for precision acceleration test items.

The development of this system truly challenged the prevailing state-of-the-art. From the initial design study

to the final acceptance test, a significant amount of creativity, innovation, skill, judgement, care and hard work went into this monumental effort. The system was almost completely rebuilt following an accident at site installation. In spite of this, the final results are truly impressive. References (1), (2), and (3) have previously described particular parts of the centrifuge development. Some of the sections which follow rely on these references.

Figure 2 is a collection of photographs which show the centrifuge manufacturing and final assembly stages prior to the accident. These photographs demonstrate dramatically the manufacturing and assembly skills needed to build this machine.



88-101-20

Figure 1. Model 445 Centrifuge

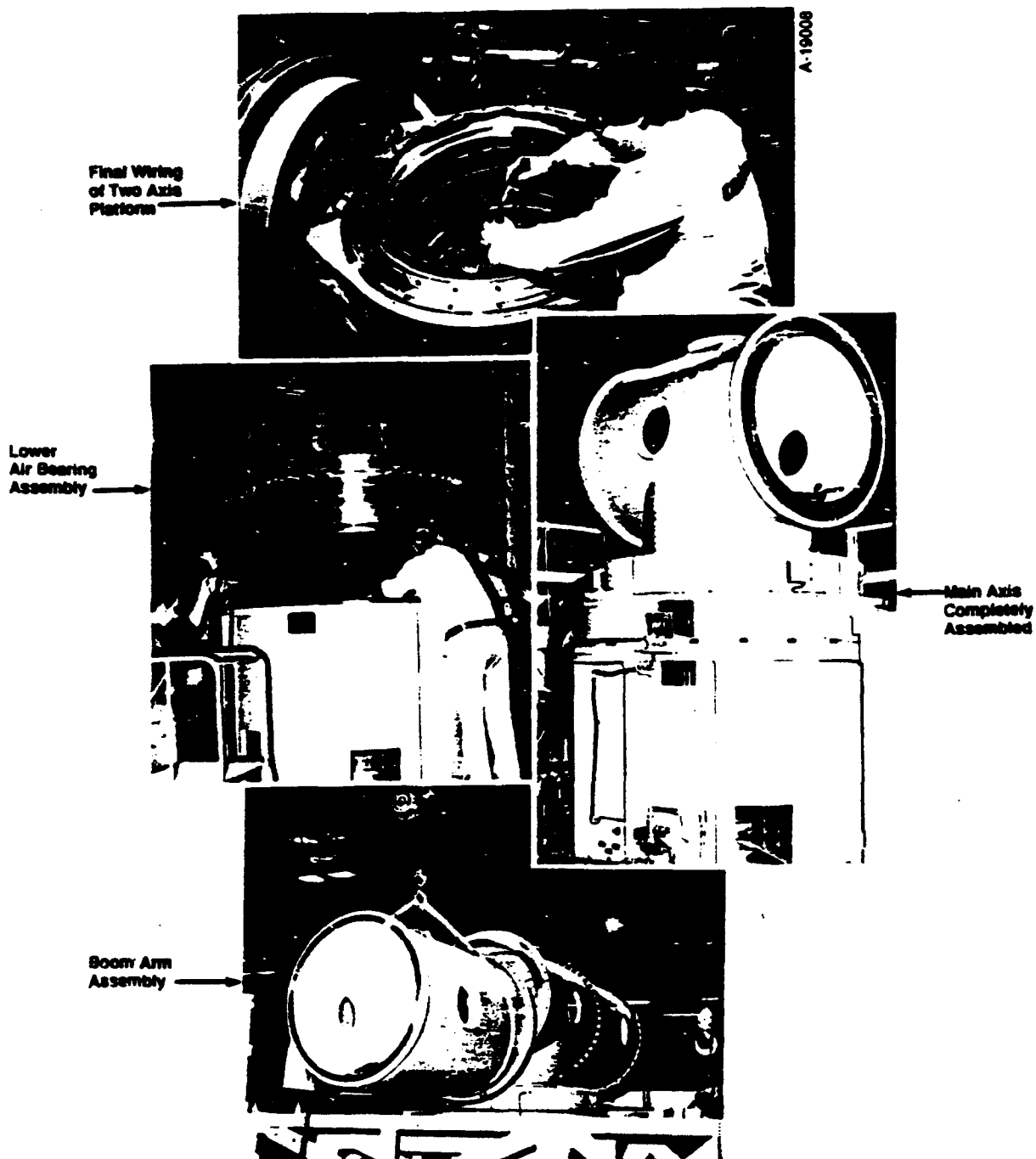
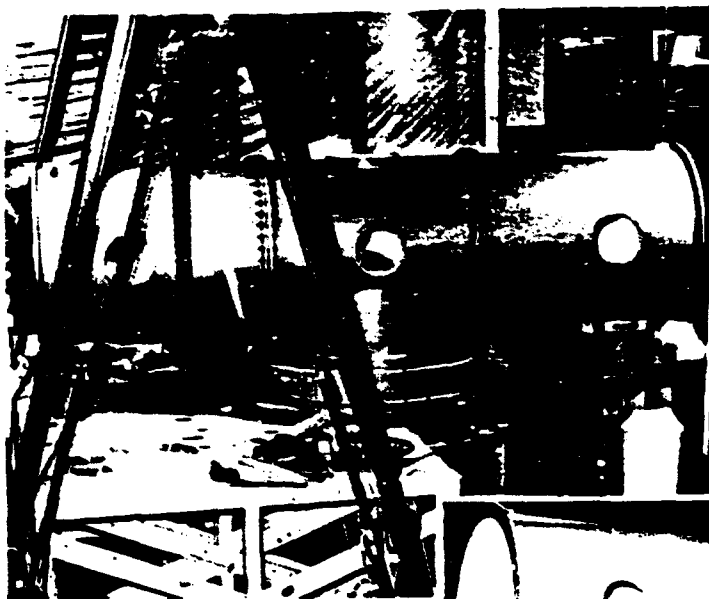
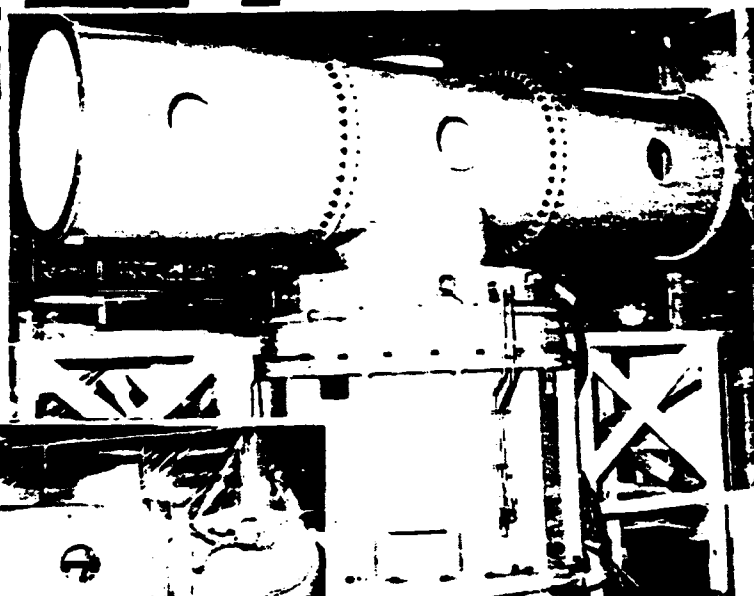


Figure 2. Centrifuge's Manufacturing and Final Assembly Stages

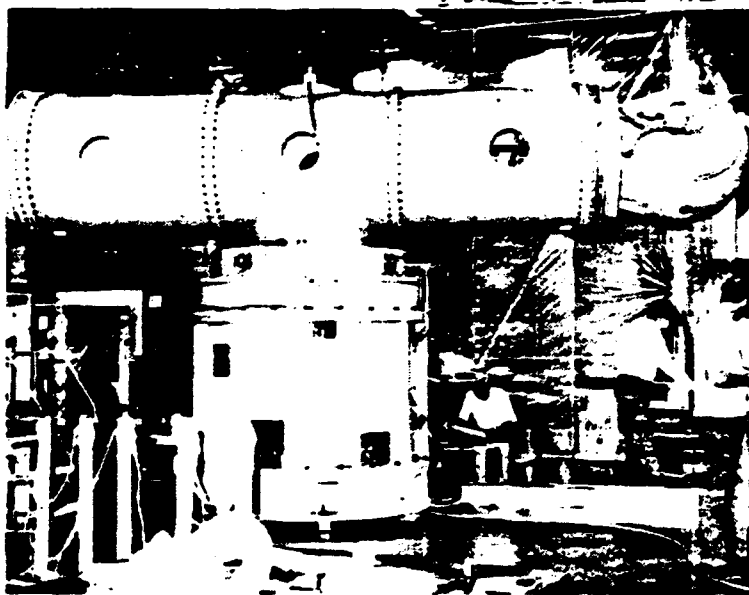


A-19009

Positioning Boom  
Arm Pieces



Boom Arms and  
Main Axis  
Completely Assembled



Two Axis Platform  
Installed at Boom Top

Figure 2. Centrifuge's Manufacturing and Final Assembly Stages (Cont'd)



## Physical Configuration

The centrifuge system configuration consists of the main axis structure with circular boom, two-axis platform, balance assembly, and an enclosure provided for safety. The symmetric main axis design balances the aerodynamic loading, makes mechanical balancing of the system easier, and allows for the use of common components. The circular boom reduces aerodynamic drag and maximizes bending and torsional stiffness.

The worst case moment loads shown in Table 1 are produced with all axes rotating at 720 deg/sec.

**Table 1. Worst Case Moment  
(Gyroscopic) Loads**

Axis	Bearing Load (ft-lb)	Motor Load (ft-lb)
Main	13,000	3,500
Outer	13,000	2,600
Inner	3,000	1,700

The rotating weight of the main axis is 20,000 pounds and the two-axis platform weighs 2500 pounds. Finally, 1000 ft-lbs of aerodynamic drag are generated by the boom as the main axis rotates in the enclosure.

**Two-Axis Platform** - The two-axis platform (TAP) mechanical configuration is shown as a three dimensional cross section in Figure 3 with major components labeled.

The basic centrifuge design features and operating constraints for the TAP include the following:

1. The TAP operates under a high centrifuge acceleration; 50 g's at a 120-inch radius with a 5 g per foot gradient and a 1 g gravitational acceleration perpendicular to the centrifugal acceleration.
2. The inner and outer axes can rotate in phase with the main axis at a maximum of 720 deg/sec.
3. Standard non-exotic structural materials are used (aluminum, magnesium, steel, etc.).

4. The bearings are mechanical anti-friction type; no other type of bearing has the necessary load capacity-to-weight ratio.
5. Each axis has stiffness symmetry so that, under 50 g centrifugal loading, the radial deflections are constant for any angular orientation of the inner or outer axis.
6. Permanent magnet DC brushless, frameless motors are used to drive each axis because of their high torque-to-weight and power-to-weight performance.
7. Components such as Inductosyns®, resolvers, and slip rings are incorporated in each axis for position readout and feedback, rate feedback, signal transmission, and power transmission.
8. Optical access (2-1/2 inch diameter) from the center of the main axis to the test package center is provided for the laser interferometer radius measurement system.
9. Test package interface is simple and easy to work with to minimize operator set-up and test time.

The most important design feature is the minimal TAP rotating weight. The structure, bearings, and motors are as small and light as possible to minimize the centrifugal and gyroscopic loads. The non-constant gyroscopic torques are further reduced by balancing the three orthogonal inertia values of each axis as closely as possible. The optimal solution was the smallest and lightest configuration which had acceptable safety and reliability margins. This optimization yielded these benefits:

- Small bearings (and small loads) which produce less friction and heat.
- Small torque motors which produce less heat.
- Small gyroscopic torques which deflect the boom less and, therefore, increase g-stability and/or reduce the stiffness requirements of the main axis.
- Small TAP and boom cross sectional area and radius and, therefore, results in low windage friction torque on the main axis.

®Trademark of Farrand, Inc.

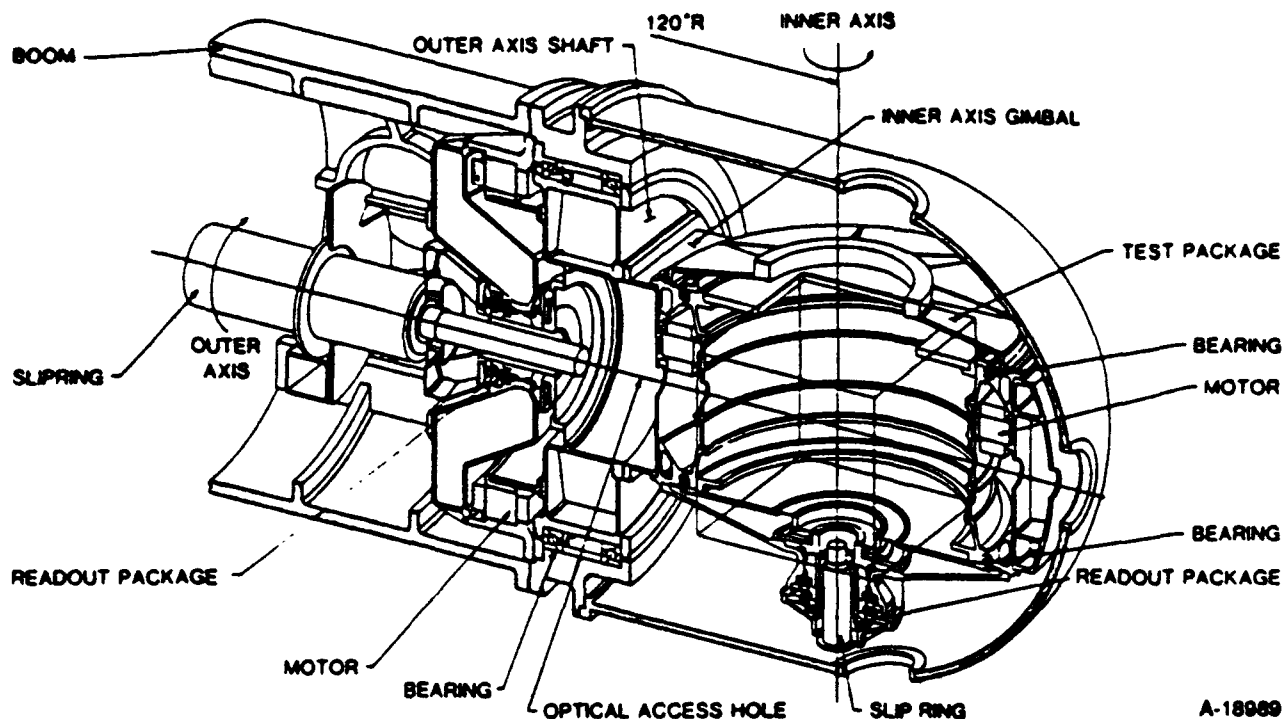


Figure 3. Model 445 Two-Axis Platform

- A lightweight TAP produces a lightweight symmetric counter-balance assembly and reduces the total weight the main axis must support.

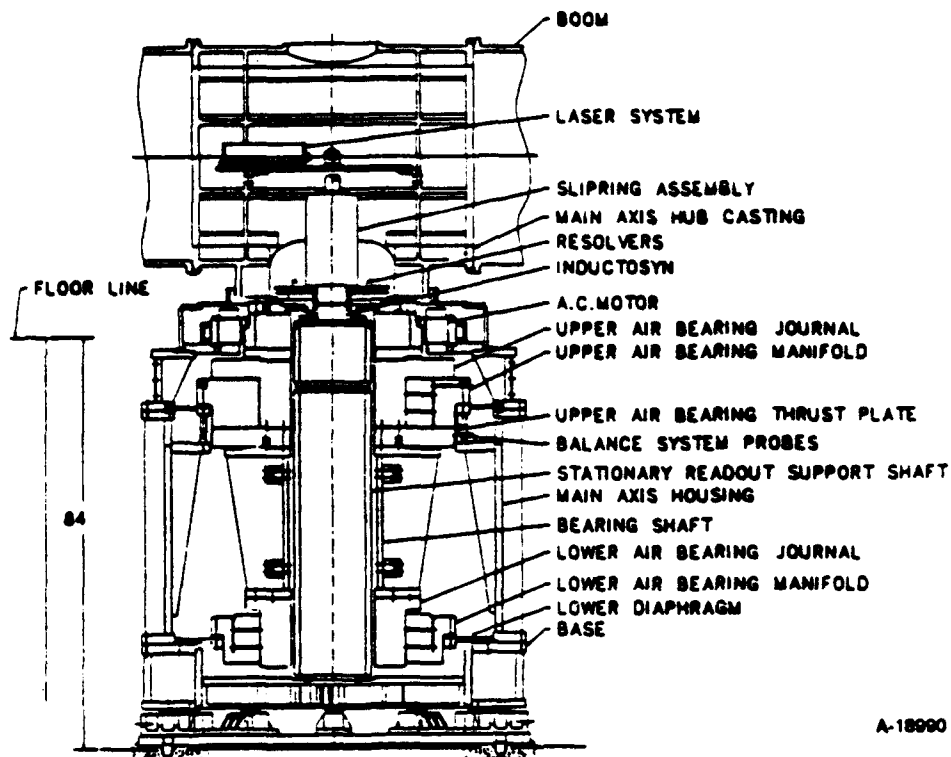
**Main Axis** - The main axis design requirements were derived from the g-stability error budgets and the expected loads. First, the rigid body error budget (i.e., dynamic motion variation due to the bearings) required the following performance characteristics:

- wobble  $< 0.3$  arc second
- run out  $< 20$  microinches
- main axis bearing moment stiffness of 13,000 ft-lbf/arc second

Second, the structural angular variation budget required that the main axis structure, bearings, base, boom, and bolted joints rotate no more than 14 arc seconds at 120-inch radius when loaded with the maximum non-constant gyroscopic moment. Finally, the main axis and boom had to support a large (240,000 lbf) tension load produced when operating the centrifuge structure at maximum g levels.

Figure 4 shows the cross sectional view of the main axis. A pair of large diameter hydrostatic air bearings are used to support the rotating weight and provide moment stiffness. The design essentially decouples the bearings from the 240,000 lbf centrifugal load. A DC brushless torque motor is mounted close to the boom to provide the stiffest possible drive shaft. The slip ring and position transducer are mounted between a stationary readout shaft and the center boom casting. Proximity probes are provided to dynamically measure the system imbalance and provide this information to the system console and the operator for further action. The entire main axis is housed in a rigid steel weldment and placed in a pit to lower the main axis and allow easy access to the test package.

A pair of bearings separated by a fixed distance provides the required moment stiffness in the most efficient manner. Careful alignment is required during assembly, but the required bearing capacities and stiffness are much smaller for this configuration than for a single air bearing. The main axis bearing stiffness can be approximated using the free body diagram and



A-18990

Figure 4. Model 445 Main Axis Assembly

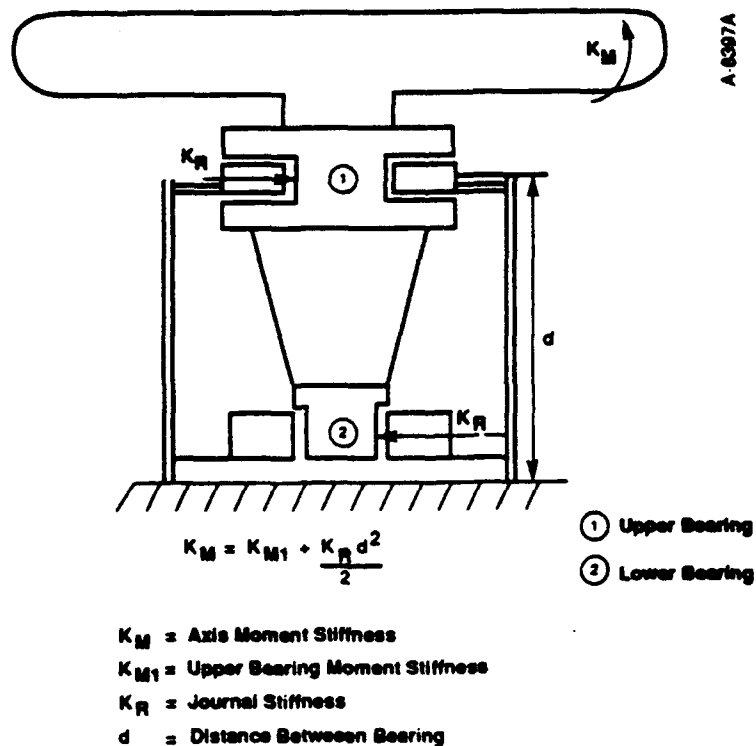


Figure 5. Main Axis Moment Stiffness

the equation in Figure 5. The diaphragm mounting arrangement, required for easier alignment, greatly reduces the impact of the individual bearing moment stiffnesses leaving a dominant radial stiffness term. The journal stiffness of  $28 \times 10^6$  lbf/inch is determined using the equation in Figure 5, with a 48-inch separation distance (d), the required 13,000 ft-lbf/arc sec axis moment stiffness ( $K_M$ ), and ignoring the upper bearing moment stiffness ( $K_{M1}$ ).

The position of the bearings with respect to the boom was determined to decouple the centrifugal force from the air bearing. Decoupling of the force is required as the 240,000 lbf centrifugal load would deform the bearings into an elliptical shape causing the air gap of less than 0.001 inch to close. The cylindrical motor shaft perpendicular to the centrifugal force's direction separates the bearing from the radial tensile loads. The centrifugal force acting on the top of the motor shaft causes deflections at the top of the shaft but has essentially no effect at the bottom near the bearing, thus efficiently decoupling the force from the bearing.

The centrifuge is an excellent application of the reduced preload double thrust bearing. The analysis indicates a thrust diameter of approximately 50 inches is required with a bearing pressure of 140 psig. The force vs. gap curve is calculated as shown in Figure 6. The reduced preload feature saves a gap reduction of 10% which permits larger imbalance deflections and manufacturing tolerances. The total stiffness is calculated from the sum of the slopes at the operating point. Stability of the bearing around the operating point is confirmed and the stability region is shown in Figure 6.

Table 2 summarizes the design and analysis results and compares them with actual air bearing measurements and data taken during fabrication and assembly.

**Manufacturability** - All manufacturing tolerances were very carefully considered for these large air bearing pieces. It was critical to hold flatness, roundness and perpendicularity variations to less than 10% of the 0.0007-inch gap.

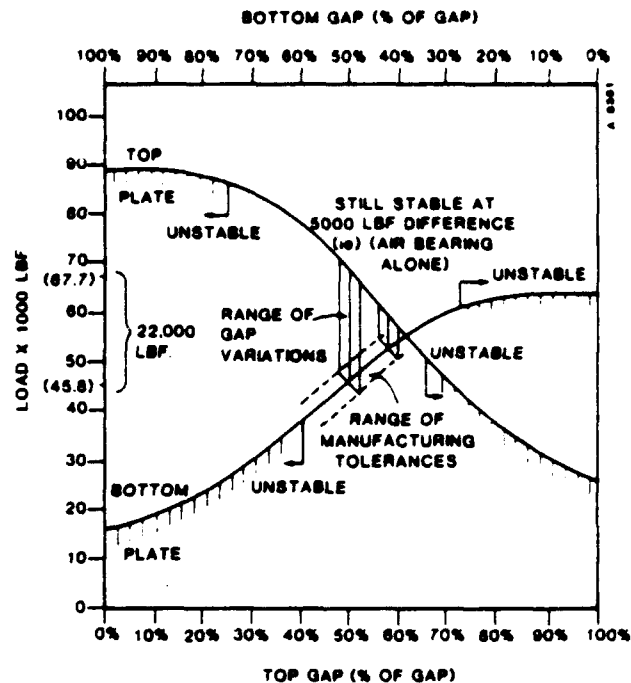


Figure 6. Final Load vs. Gap for Bottom and Top Plate Thrust Bearings

The small gaps on the air bearings required that the two bearings be aligned to a very stringent (0.0001 inch) concentricity and perpendicularity tolerance and hold this tolerance over the expected 5 °F operational temperature range. The tolerance was selected to keep the variations of the air bearing gap, due to the misalignment of the two bearings, to less than 10% of the original gap.

The main axis includes several aids for alignment. Both the upper and lower bearing supports use a diaphragm approach. The diaphragms have moment stiffness equal to half the moment stiffness of the bearing; however, angular misalignments can be twice as large for the same gap variation as a misalignment that will bend the diaphragm. The diaphragm has the desired characteristics of small moment stiffness to allow for angular misalignments with large radial stiffness to provide resistance to the 13,000 ft-lbf gyroscopic moment. The upper diaphragm can not support all the weight of the axis so, six vertical stiffeners are added to help support the weight. Figure 4 shows the overall mounting approach and the individual bearing supports.

**Table 2. Air Bearing Design/Analysis and Measured Results**

<b>Parameter</b>	<b>Design/Analysis</b>	<b>Measured</b>
Thrust Dimensions	50 x 30 inch diameter top 47 x 32 inch diameter bottom	-
Thrust Stiffness	72 x 10 <sup>6</sup> lbf/inch	83.7 x 10 <sup>6</sup> lbf/inch
Journal Dimensions	30 inch diameter x 10 inches long	-
Journal Stiffness, upper	25 x 10 <sup>6</sup> lbf/inch, min.	26.0 x 10 <sup>6</sup> lbf/inch
Journal Stiffness, lower	25 x 10 <sup>6</sup> lbf/inch, min.	36.9 x 10 <sup>6</sup> lbf/inch
Upper Bearing Moment Stiffness	2700 ft-lbf/arc sec (goal)	2700 ft-lbf/arc sec
Main Axis Angular Stiffness	13,000 ft-lbf/arc sec	16,900 ft-lbf/arc sec (calculated value, includes Upper Bearing Moment Stiffness)
Gross Weight Capacity with No Gap Reduction	20,000 lbf	21,350 lbf
Weight of Double Acting Thrust Journal and Thrust Plate	5000 lbf	-

The diaphragm mounting approach also helps solve another difficulty commonly encountered with large precision machines. The 5° F room temperature variation can cause a thermal gradient of 5 degrees from one side of the main axis to the other. The gradient will cause the distance between the bearings to be different on one side of the axis. The result will be an angular misalignment that uses 10% of the upper thrust bearing and 20% of the radial bearing gaps if the axis is rigidly mounted. Instead, the diaphragms bend and less of the gap is used.

**Balance System** - A balance system at the opposite end of the boom from the two-axis platform is provided as shown in Figure 7. The same outside outline as the TAP is maintained to keep the aerodynamic load balanced. The counter balance system was custom machined at assembly to balance the factory installed TAP equipment. Additional Counterweights may be added to balance the test package.

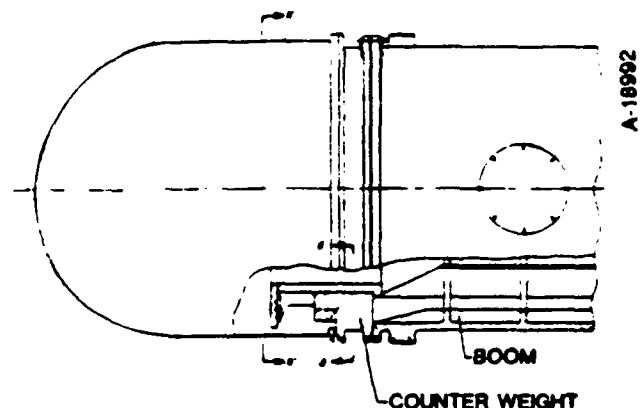


**Figure 7. Model 445 Balance Assembly**

As with most precision rotational test equipment, the system must be balanced for each test package. A measurement system is provided by the control system to assist the operator with balancing. Proximity probes monitor the motion of the upper air bearing (see Figure 4). A rotating imbalance will cause deterministic motion of the bearing that will be measured and used by the control system to calculate the balance weights required. The proximity probes have sufficient resolution and repeatability to balance the 20,000 lbf rotating weight to within 3 lbf at 10 feet. The resulting angular displacement of the main axis due to this imbalance is 0.34 arc second.

**Safety Features** - The rotating centrifuge boom represents a tremendous amount of energy when traveling at top speed. For this reason an enclosure was provided for both operator and equipment safety. The enclosure provided a side benefit of reducing the aerodynamic drag torque. Other safety features include:

- A break-away diaphragm designed to break and guide the axis if the air bearings should seize.
- An imbalance sensor on the main axis.
- Multiple mount disable switches to protect maintenance and operating personnel.
- Cover interlocks preventing operation with the TAP covers off.

## Control and Instrumentation

The control and instrumentation system performs all the functions associated with the control of the centrifuge. Some of these functions include:

- Position and Rate Calculations and Profiles
- State Estimation
- Gyroscopic Motion Calculations
- Torque Commands
- User Input/Output
- Mechanical and Electrical Interlocks
- Actuator Drive
- Test and Calibration System
- Deterministic Disturbance Reductions

The control system consists of three single board computers and three encoder input/output processor boards housed in a Multibus card cage chassis. The control console contains all the power supplies, control electronics, and power control switches.

The centrifuge control system has three main components: (1) three-axis coupling model, (2) single-axis controllers, and (3) state estimators. The overall model is shown in Figure 8. The inputs to the axis controllers are the error signals generated from the axis commands and the state estimates ( $\hat{p}, \hat{\dot{p}}$ ). The axis command consists of a position and rate command for each individual axis. The output of the controllers are torque commands ( $\tau_c$ ) that feed the plant and the torque decoupling matrix. The plant supplies the position outputs ( $\theta$ ), used to drive the error signals in the state estimators. The decoupling matrix converts the torque commands into three decoupled acceleration estimates ( $\hat{\ddot{\theta}}$ ). The acceleration estimates are the driving input to the state estimators. The three-axis coupling model generates feedforward torque commands ( $\tau_{ff}$ ) that are added to the controller torque commands.

**Three-Axis Coupling Model** - The three-axis coupling model is a computer model of the centrifuge reaction torques based on Euler's equations. The coupling model is given in Equation 1.

$$\tau = D_{ij}^{-1}(\theta, \dot{\theta}) * \ddot{\theta} + C_k(\theta, \dot{\theta}) \quad (\text{Eq. 1})$$

The torques ( $C_k$ ) are large gyroscopic torques, produced when all three axes are rotating simultaneously. The three-axis coupling model counteracts the torque effects by generating torque feedforward signals ( $-C_k$ ). The torque decoupling matrix ( $D_{ij}^{-1}$ ) decouples the acceleration estimates from the torque commands. The decoupling of the accelerations enables the axis controllers to be designed on an individual basis.

**Single-Axis Controller** - Digital control design techniques were used in the design of the single-axis controllers. Each controller consists of a position compensator and a rate compensator; both compensators are digital filter equivalents of stopped integrators. An error signal, calculated from the command and state estimate, enters each compensator. Figure 9 is a block diagram of a single-axis controller. The position compensation (K1, A, B) and the rate compensator (K2, C, D) are calculated using classical design techniques to compute the gain and compensation. Tustin's approximation is then used to compute the appropriate parameters in the z-plane. The sample time (T) was chosen sufficiently small (1 millisecond) to alleviate problems associated with the controller or estimator operating at slow sample rates. The rate feedforward torque ( $\tau_{ff}$ ) is summed in after the rate compensator.

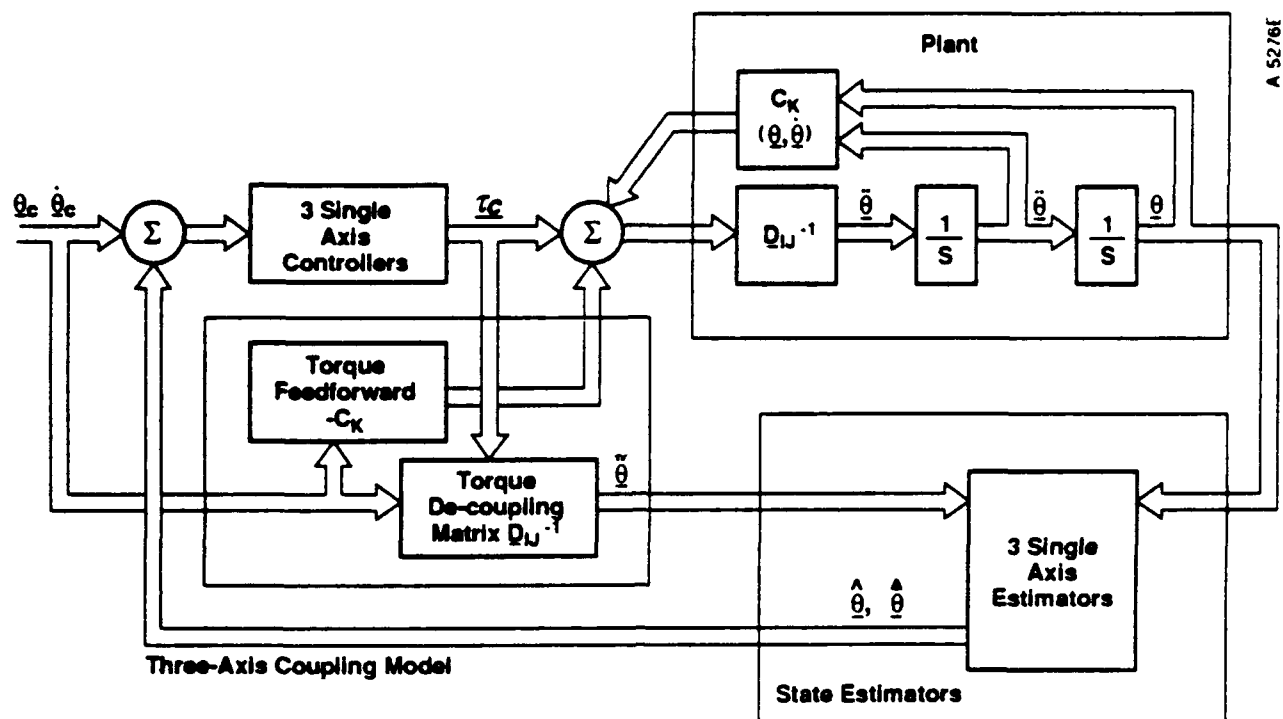


Figure 8. Multi-Axis Control System

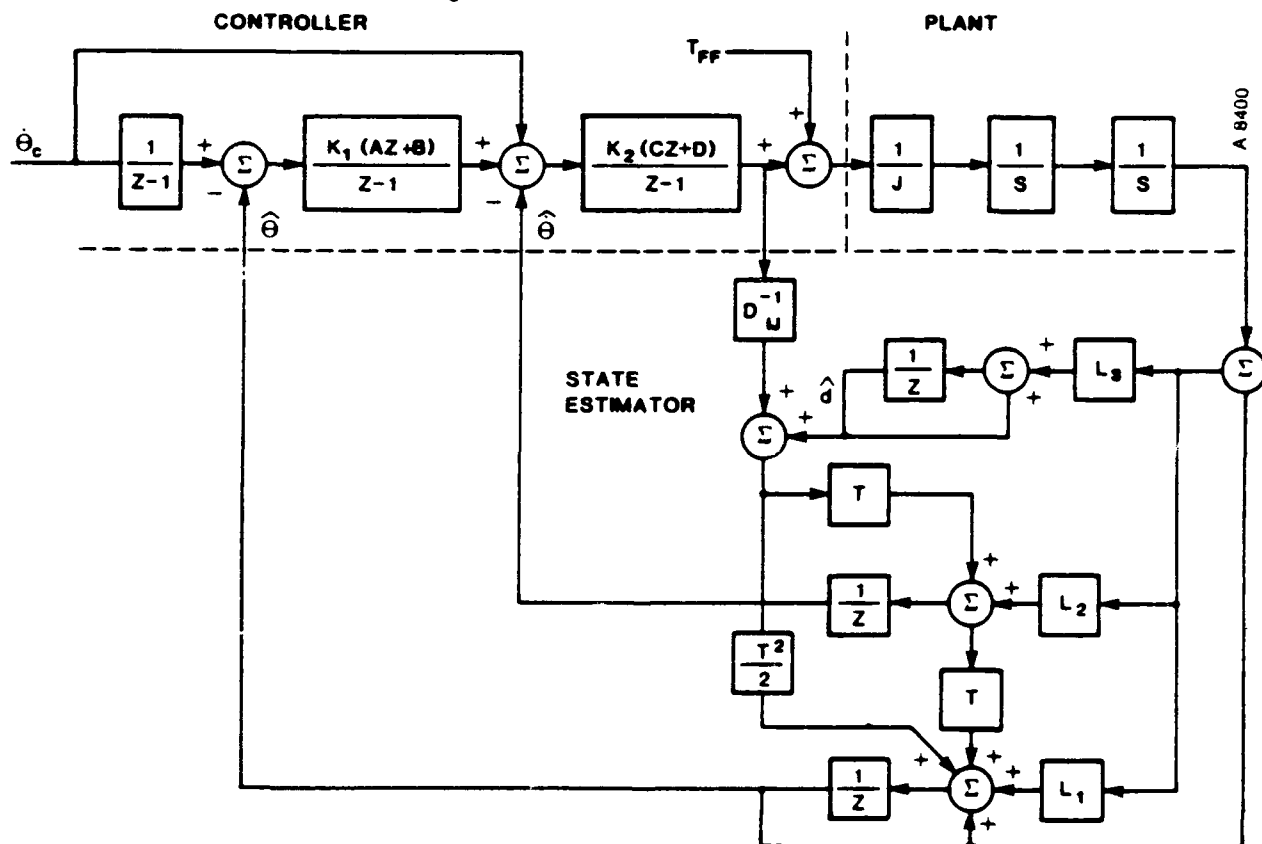


Figure 9. Single Axis Controller and State Estimator

**State Estimators** - The feedback for each axis is generated by a Luenberger Observer with an appended tracking system. The tracking system consists of a single integrator driven by the observer error. This will estimate any first order disturbance corrupting the plant after the power amplifier. Equation 2 is the observer and Equation 3 describes the disturbance estimator. A and M are the system matrices, B is the input vector, C and N are the output vectors, L and D are the estimator gain matrices, and  $\hat{X}$  and  $\hat{d}$  are the state and disturbance estimates, respectively.

$$\hat{X}(k+1) + A * \hat{X}(k) + b * u(k) + b * \hat{d}(k) + L * (\theta_m(k) - C * \hat{X}(k)) \quad (\text{Eq. 2})$$

$$\begin{aligned} P(k+1) &= M * P(k) + D * (\theta_m(k) - C * \hat{X}(k)) \\ d(k) &= N * P(k) \end{aligned} \quad (\text{Eq. 3})$$

**Actuator Drive System** - Brushless DC torque motors and power amplifiers provide the high torques necessary to overcome the large gyroscopic reaction torques when operating under simultaneous rates. The brushless motors provide a much higher torque-to-inertia ratio than standard motors while contributing minimal torque disturbance to the centrifuge rate.

Figure 10 shows a block diagram of the power amplifier and torque motor. The power amplifier sinusoidally excites the motor windings to orient the electromagnetic field. This requires knowledge of the absolute motor shaft position which is provided by a resolver. The amplitude of the electromagnetic field is modulated in proportion to the torque command. The angle of the field is maintained perpendicular to the permanent field of the magnets (rotor). This keeps the torque sensitivity at its peak regardless of shaft position, and minimizes the torque ripple due to commutation errors.

**Centrifuge Test and Calibration** - Two common centrifuge errors are:

1. Test item radius and angular variation and
2. Rate instability

Measurements are made on line and off line to calibrate out these main sources of error.

**Radius and Angular Measurements** - The radius measurement system uses a laser interferometer (illustrated in Figure 4), which is mounted directly to the centrifuge arm. Optical access is available so that radius growth can be measured at the test article with the output available on a continuous basis. To reduce the sensitivity of the laser system to temperature and pressure, an environmental tube is placed between the laser head and the retroreflector. Angular deflection in either the vertical or horizontal plane may be measured by installing angular measurement optics on the laser interferometer system.

This system allow radius measurements within 1 microinch and angular measurements within 1 arc second to be made and transferred for off-board recording in real-time.

**Rate Measurement** - The average centrifuge rate is determined by measuring the time required for the centrifuge to rotate through a known angle. This is done by measuring the point-to-point time required for an integer number of revolutions. The time is measured with a counter which has a precision time source as its input. The counter is triggered by an event marker which occurs once per centrifuge revolution. The accuracy of this measurement is limited only by the accuracy of the time source and the position repeatability of the event marker.

## Accident, Repair and Re-Installation

In February, 1989, during the initial installation, a portion of the centrifuge enclosure roof collapsed causing major damage to the system. The enclosure is a 12-sided containment chamber constructed on a 24-foot diameter. The 12 chamber wall segments are prestressed, steel reinforced concrete panels six feet high, six feet wide, and eight inches thick. The roof consists of six steel panels, weighing approximately 3500 pounds each, and two steel I-beams which support the roof panels on the walls in the final welded configuration.



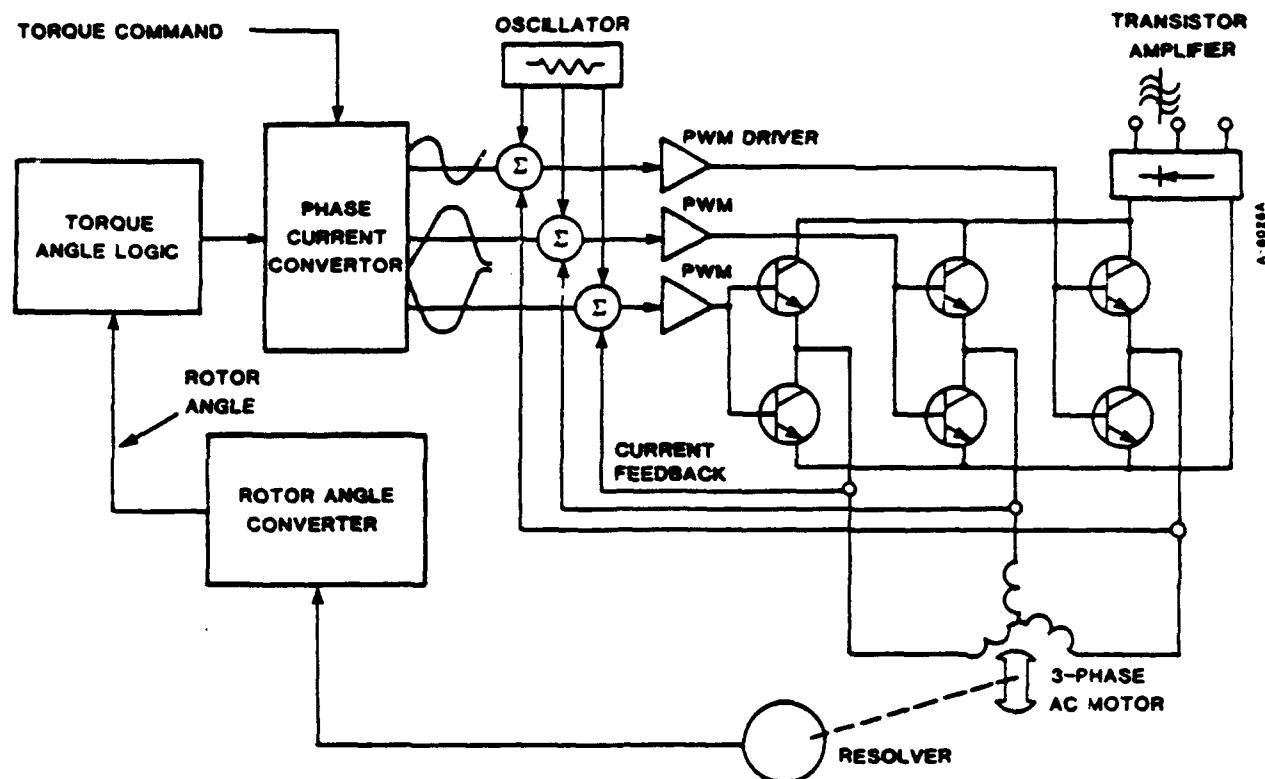


Figure 10. Brushless AC Servo Drive Block Diagram

The accident occurred during the placement of the final roof panel. With the centrifuge already installed in the pit inside the chamber, the roof panel slid off the wall and I-beam supports and crashed into, and came to rest upon, the boom tip containing the TAP. Figures 11, 12 and 13 are photographs of the accident shortly after it occurred. Figure 11 is a perspective view of the enclosure showing the roof pieces tilted and translated from their original alignment. Figure 12 is a closer view through the chamber doorway showing the collapsed roof pieces. Figure 13 is a close-up showing the roof panel resting on the boom tip.

The centrifuge was removed from the enclosure, disassembled, and shipped back to Contraves where it was completely disassembled and inspected. The accident damaged one boom piece and hub, the TAP outer axis bearing housing and bearing retainer, the TAP cover and, most significantly, the main axis lower air bearing. The critical tasks of regrinding and sizing the lower air bearing manifold and journal practically constituted a complete remanufacturing effort. In fact, after replacing damaged material, the tasks of reassembly, realignment and reintegration were essentially a repeat of the entire initial work and took months to complete. In-process and final factory floor

tests of the remanufactured centrifuge indicated no degradation of the mechanical or control system performance from the pre-accident condition. These tests were limited to low rotational rates; the final performance tests would have to wait until the centrifuge was reinstalled at CIGTF. The system was shipped back to CIGTF and successfully reinstalled inside the enclosure.

### Final Test Results

After reinstallation and preliminary checkout of the system, an extensive series of tests was conducted. A comprehensive Acceptance Test Plan (ATP) which had been developed by Contraves and approved by the Air Force was initiated and conducted on-site. It provided the basis for final disposition of the contract. The ATP was comprised of a large number of sub-system tests designed to measure the operational effectiveness of the centrifuge.

The operating specifications measured during the ATP that will be discussed here are those which measure the accuracy of the machine as it would most often be used in the test environment. In this case,

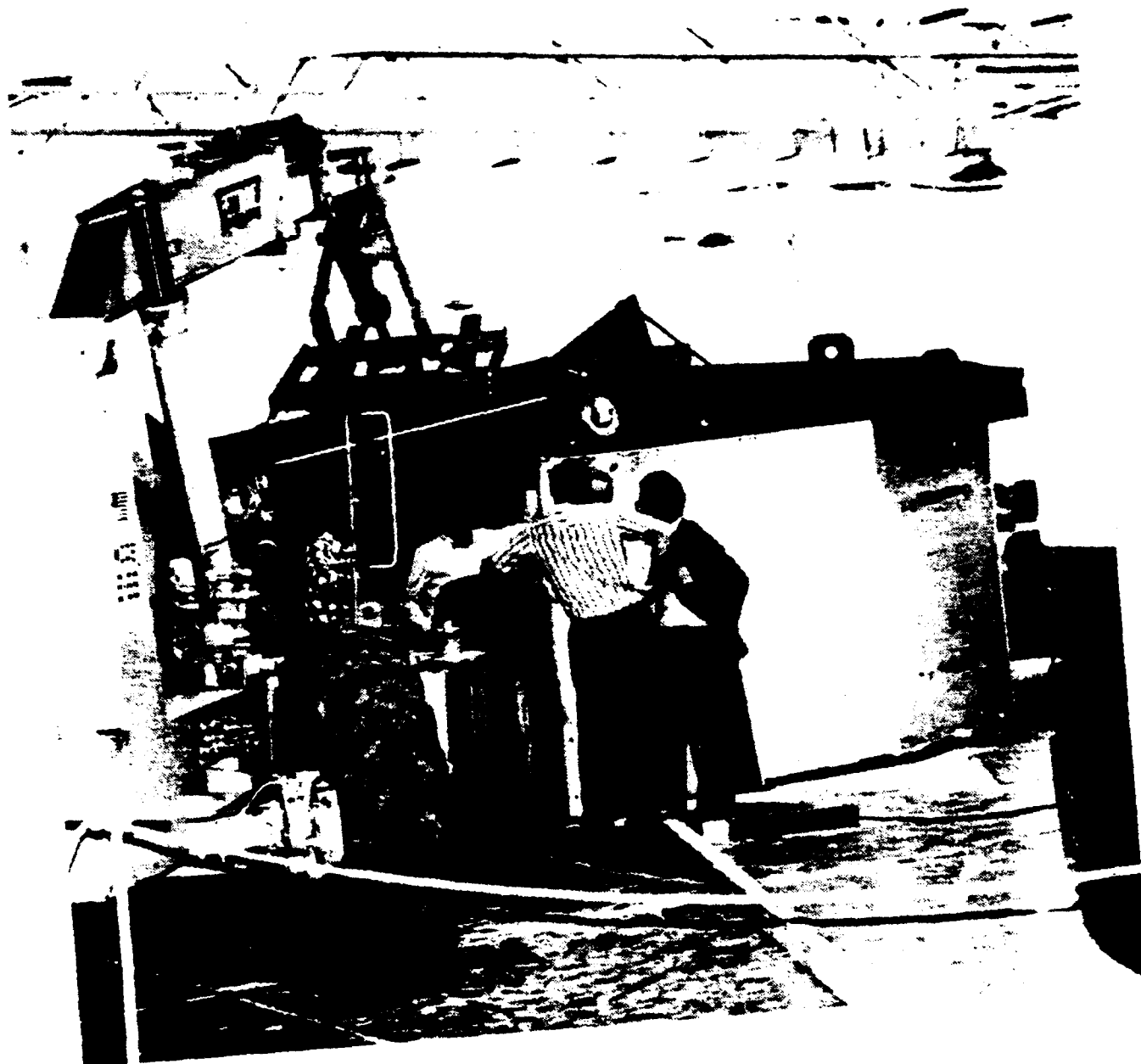


Figure 11. Perspective View of Accident

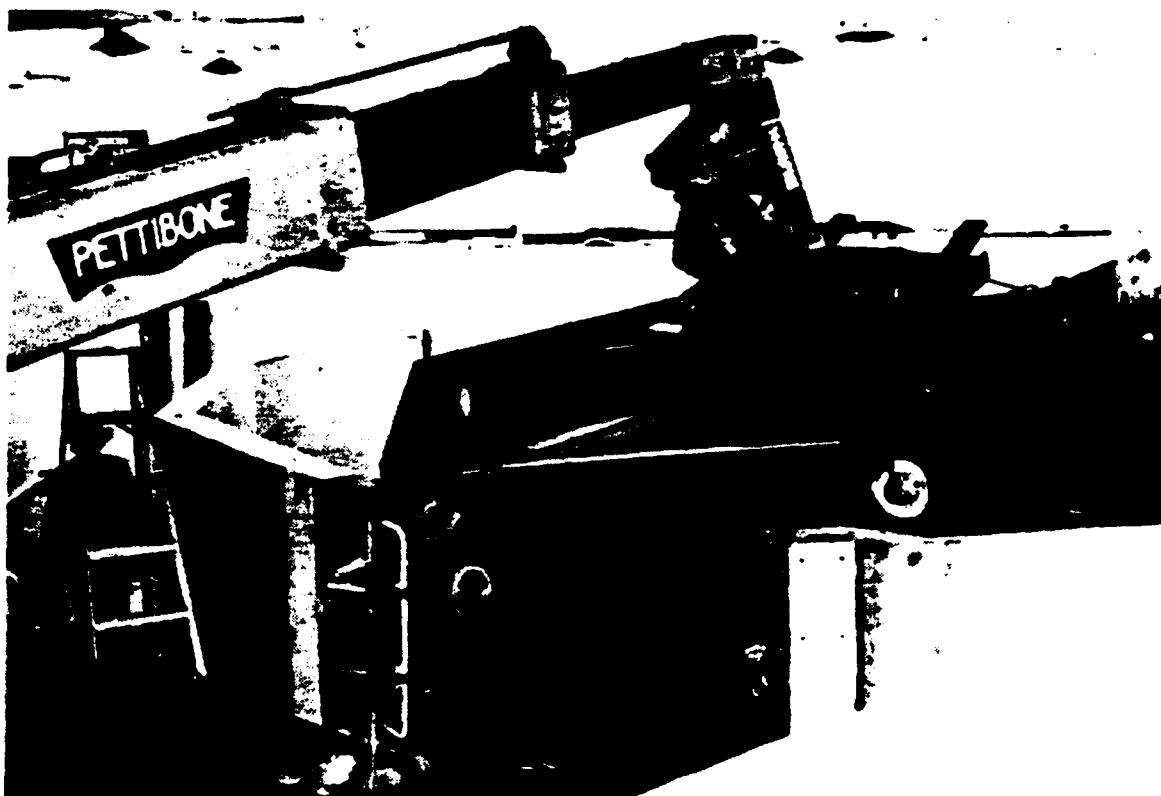


Figure 12. Close Up View of Accident Showing Collapse of Roof

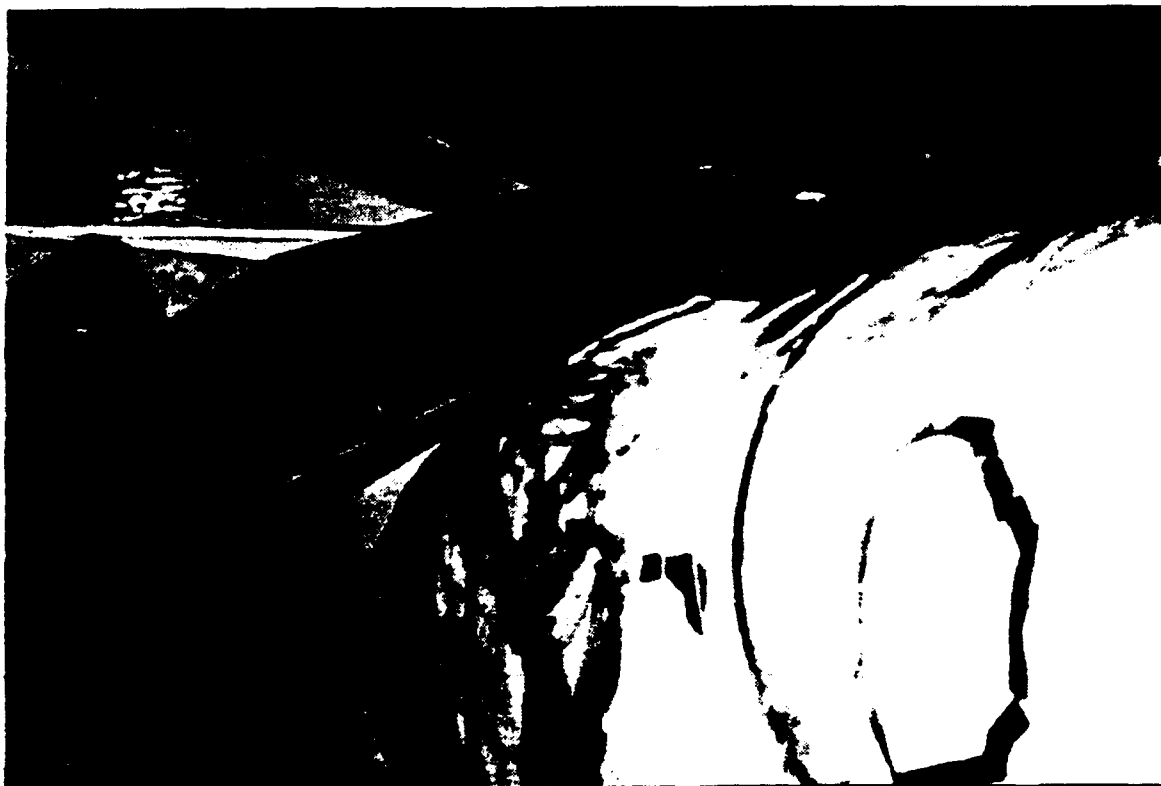


Figure 13. Close Up View of Accident Showing Roof Piece Resting on Boom Tip

overall g-stability is the most critical operating parameter, as the machine would be used to provide precise accelerations to a test item.

Total g-stability, defined herein as the revolution-to-revolution stability of the centripetal acceleration seen by a test item mounted inside the two-axis platform, is a very difficult measurement to make as there are a large number of contributors to the error. Reference (4) presents an exhaustive list of these contributors and how best to handle them. Total g-stability errors can be divided into radius and rate errors. This machine was built with an optical reference system (laser interferometer) whose function is to measure radius variations and therefore allow for post-test compensation. Radius variations are to be measured and compensated for each individual test, and therefore, for the purposes of this ATP, are not considered "centrifuge" errors. Once radius variations have been accounted for, rate variations are the major contributor to errors in overall g-stability. The g-stability measurement of this machine therefore became a problem of measuring the rate stability.

The rate stability was quantified, as mentioned earlier, by measuring the time for the centrifuge to rotate through a given angle. Various angles up to and including 360 degrees were used to measure rate stability. The sub-revolution angles were chosen so once per revolution periodic errors would not be masked. The time source was a temperature controlled 10 MHz crystal oscillator. Two unique angle markers were used in an effort to separate the angle marker error from the true centrifuge rate instability. The methods used were: (1) a CIGTF installed fiber-optic unit providing 72 pulses-per-rev, and (2) the Contraves fine resolution pulse output (approximately 500,000 pulses-per-rev). Both methods gave similar results to within the expected uncertainty of their measurements (0.2 PPM, 1-sigma). In addition to the time for angle measurement, CIGTF monitored the outputs of three Bell XI-82 accelerometers mounted on the centrifuge for

the duration of the ATP. A careful examination of their outputs provided another indication of rate instability, which correlated nicely with the two period measurements.

During the final set of tests conducted during August, 1992, Contraves engineers made control system modifications until the centrifuge achieved a rate stability of <0.5 PPM (1-sigma) over its entire operational range of 72 to 720 degrees/sec (0.5 to 50 g). This level of performance was achieved day-after-day in 1992, as it has periodically since then, indicating this machine is as rotationally stable, if not more so, than any other large diameter centrifuge in the world. This rate stability coupled with the ability to measure radius growth and test item tilts to 1 microinch and 1 arc second, respectively, make this machine unparalleled in its ability to provide stable, repeatable, predictable accelerations to a test item.

## REFERENCES

- (1) "Design Study for a Large Centrifuge Test Bed", L. DeMore, et.al., AIAA Guidance Navigation and Control Conference, August 18-20, 1986.
- (2) "Control Test and Validation for a Large Diameter High Stability Centrifuge", S. Willis, et. al., AIAA Guidance, Navigation and Control Conference, August 17-19, 1987.
- (3) "Detailed Mechanical Design of a Large Diameter High-Stability Centrifuge", D.A. Henderson, C.J. Woolheater, AIAA Fall Conference, August 19-20, 1987.
- (4) IEEE Std 836-1991, IEEE Recommended Practice for Precision Centrifuge Testing of Linear Accelerometers, The Institute of Electrical and Electronics Engineers, Inc., 1991.

**THIS PAGE LEFT BLANK INTENTIONALLY**

**SESSION V-A**  
**WEAPONS TESTING**

***CHAIRMAN***  
**DR. JOHN NIEMELA**  
***FORT MONMOUTH NJ***

**THIS PAGE LEFT BLANK INTENTIONALLY**

# **LOW COST QUARTZ RATE SENSORS APPLIED TO TACTICAL GUIDANCE IMUs**

Prepared by

Richard N. Silva and Glenn W. Murray

ROCKWELL INTERNATIONAL CORPORATION, DEFENSE ELECTRONICS  
3370 Miraloma Avenue  
Anaheim, CA 92803

Approved for Public Release; Distribution is Unlimited



## ABSTRACT

The military has shifted its emphasis from strategic weapons, which are characteristically high performance, low volume and very expensive, to tactical weapons, which are low to moderate accuracy, high volume and low cost. The challenge in meeting the needs of this shift is to develop a small, low-cost Inertial Measurement Unit (IMU) with sufficient accuracy to meet the needs of modern precision tactical weapons. New instruments, new digital signal processing techniques and the Global Positioning System (GPS) have redefined the cost and performance capability achievable with tactical IMUs.

Rockwell International is developing a Digital Quartz IMU (DQI) to meet the needs of this new generation of IMU requirements. The DQI is being designed around an Inertial Sensor Assembly (ISA) being jointly developed by Rockwell International and the Systron Donner Inertial Division of BEI. The ISA utilizes small, batch-fabricated quartz inertial sensors to achieve low cost and small volume. Traditional analog processing of the output of this class of sensor has been replaced with digital processing based on sigma delta analog-to-digital converters to achieve improved performance. This combination of low-cost batch processed sensors with the stability of high-speed digital signal processing produces an IMU that meets the needs of a wide variety of tactical weapons with attractive performance/cost ratios.

Prototypes of the DQI design will be completed and evaluated in early 1994. This paper provides an overview of the DQI design and status. A description of the performance objectives and design approach used for the Inertial Sensor Assembly, digital signal processing and mechanical packaging of the DQI are presented.

## INTRODUCTION

Traditionally, precision tactical weapons required the use of expensive medium-to-high performance inertial systems to achieve their objectives. The inertial navigation system (INS) was solely responsible for guiding the weapon to the target or sufficiently close for other non-inertial systems to take over. In these weapons, the role of the INS was dictated by the need for precision and the desire for autonomous operation.

The accuracy and low cost of GPS receivers has helped to redefine the traditional role of the INS in the tactical arena. Advances in GPS technology have continued to improve the performance while reducing the size and cost to the point that GPS/INS solutions become viable and attractive for tactical applications. Solutions using GPS as a stable positional reference coupled with an IMU to provide continuous velocity and attitude output, create a GPS/INS system that is accurate, difficult to jam and economical. This shifts the focus of an IMU from high accuracy to low cost.

With the advent of new solid state inertial sensors, one can consider formulating an IMU product that has tactical grade inertial performance, low cost, and when integrated with a GPS receiver can provide the precision navigation required. Such is the case with the Digital Quartz Inertial Measurement Unit (DQI) currently in development.

Rockwell International has teamed with the Systron Donner Inertial Division of BEI Electronics to co-develop an Inertial Sensor Assembly (ISA) using Systron Donner's Quartz technology. The ISA is integrated into the DQI by Rockwell to provide a tactical grade IMU. The mechanization is digital, thus eliminating the bulk of the temperature sensitive parts that have been used in past implementations.

The DQI product is currently in the brassboard stage of development with a form, fit, and function unit fabricated and in the integration and test phase. Prototype units will be available in the first quarter of calendar year 1994. The DQI is designed as a standard product capable of satisfying the needs of a variety of stand-alone as well as GPS/INS implementations. Both configurations have their place in tactical applications such as missiles, aircraft, and guided munitions. Eventually the plan is to introduce these systems into a variety of commercial markets.

## PRODUCT DEFINITION

Once the decision had been made that both the market and the technology existed for a low cost tactical grade IMU, the next step was to establish the specific design requirements for the DQI product. This was done based on a number of considerations and evaluations. Primary among these considerations were :

1. Time to market
2. Unit production cost
3. Performance and system characteristics needed for the class of application to be addressed
4. Capability of the proposed technologies to be utilized
5. Capability and cost of potential competing technologies

Clearly, many of these considerations are in conflict. For example, improved performance might be achievable but only at the expense of time-to-market or production cost. Therefore the design considerations were prioritized as shown above and decisions made according to this order.

To converge on an optimum set of requirements, preliminary requirements were established at the start of the program based on the initial assessment of the market to be addressed and projected technology capability. Availability at an affordable price was clearly the primary considerations derived from the initial market evaluation. Based on this, a time to market goal of two years (2/94) and a unit production price of \$5000 were identified as the key design drivers.

During the preliminary design phase, these requirements were constantly reevaluated based on preliminary design studies, candidate mission analyses and Quality Function Deployment (QFD) processes. Decisions were weighted by placing highest priority on production cost and time to market while maintaining a core level of performance required for GPS-aided tactical missile and ground based weapon applications. This preliminary design phase of the program then led to the definition of a set of detail performance, physical and environmental requirements as summarized in Tables I and II.

Table I - Physical / Environmental Requirements

Operating Temperature	
Steady State	-54 deg C to +71 deg C
Intermittent	-54 deg C to +85 deg C
Random Vibration	
Operating	12 grms
Non operating	19 grms
Shock	150 g
Weight	2.3 pounds
Volume	40 cubic inches

Table II - Performance Requirements

Rate Channel	
Bias Stability Over Life	10 deg/hr
Short Term Bias Stability	0.5 deg/hr
Scale factor Stability	200 ppm
Noise	0.06 deg/rt hr
Maximum Rate	1000 deg/sec
Acceleration Channel	
Bias Stability Over Life	1.5 millig
Short Term Bias Stability	0.5 millig
Maximum Acceleration	70 g
Scale Factor Stability	300 ppm
Input Axis Stability	0.5 milliradians
Data Rate	
Auto pilot (acceleration/rate)	600 Hz
Inertial ( $\Delta V/\Delta \text{angle}$ )	100 Hz
Bandwidth	50 Hz
Power	
Voltage Level	+28 VDC
Power Consumption	20 watts

## SIMPLICITY OF DESIGN

Starting with the initial design goals discussed in the previous section, the detail design of the DQI was evolved. The concept developed for the Digital Quartz IMU is comprised of two major functions consisting of the co-developed ISA containing inertial sensors and sensor electronics and the IMU specific functions including digital signal processing electronics, Input/Output function and power conversion. Since the DQI design objective is to produce a unit which meets the requirements of a broad range of applications centered around the basic requirements, a system architecture was developed that is primarily software driven and therefore flexible enough to adapt to various signal processing needs, data rates and I/O protocol without hardware impact.

The resulting design is illustrated in the block diagram of Figure 1. This figure provides a block diagram illustrating the major elements of the DQI and their functional relationships. A description of each of these major functions is provided in the following sections.

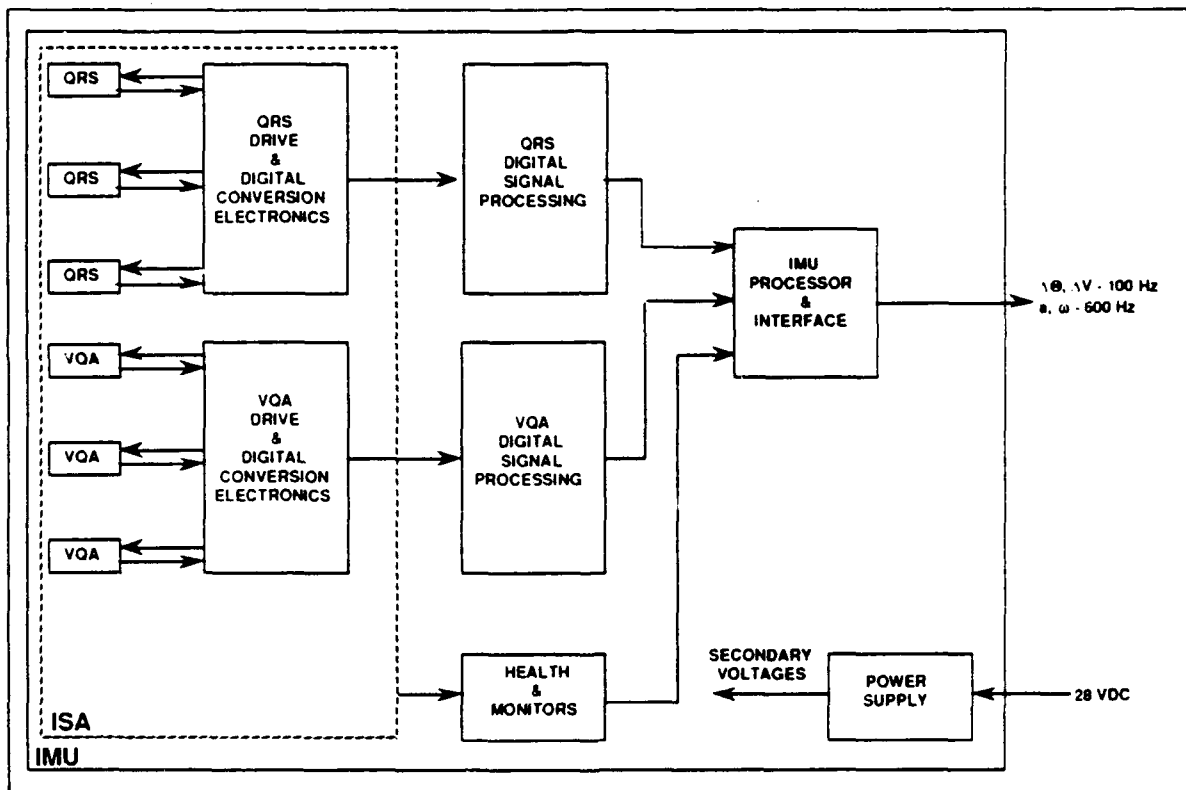


Figure 1. DQI Functional Block Diagram

### Inertial Sensor Assembly

The heart of the DQI is the ISA, which contains a sensor cluster assembly and the ISA electronics. The cluster supports the inertial sensors in an orthogonal set and provides for shock isolation. The electronics convert the raw analog signals from the sensors to digital information.

### Inertial Sensors

The rate and acceleration sensors used in the DQI are batch-fabricated quartz sensors manufactured by the Systron Donner Inertial Division of BEI Electronics. Rate sensing is

provided by three Quartz Rate Sensors (QRSs). The QRS is a tuning fork device that operates on the Coriolis effect to generate angular rate information. Batch processing is the key to the very low cost of these tactical grade rate sensors. This aspect of the Systron Donner proprietary design is essential in achieving our goal of \$5000 per unit cost.

Similarly, Systron Donner's Vibrating Quartz Accelerometers (VQAs) are used as the acceleration sensing devices. These dual crystal quartz devices operate in a push-pull mode when subjected to an input acceleration yielding two output frequencies. The difference in the output frequencies is proportional to input acceleration. The VQAs are also batch processed and, for that reason, are very low cost.

### **Inertial Sensor Performance**

The accelerometer was characterized using a battery of tests, including tumble tests through a 1 g field, centrifuge tests over temperature, and turn-on tests. The results of these tests show that the VQA performance meets or exceeds the DQI requirements. Table III displays measured values for some of the most critical performance parameters.

Table III - VQA Measured Performance Parameters

Performance Term	Value	Units
Short term Bias	.018	mg
Velocity random Walk	.014	mg/rt Hz
Turn On Time	200	ms

The VQA output was sampled at 488 Hz and filtered to provide one point every 10 seconds. The known table angle was then subtracted from the data yielding the bias error as a function of time. The results of this run show a stable bias and no detectable higher ordered G sensitivity. The RMS bias over a 1.2 hr test is .018 mg against a system performance requirement of 1.5 mg.

The VQA also exhibited acceptable performance when tested to the 11 G limit of a centrifuge while operating over the full thermal environment of -55C to + 75C. Noise measurements taken over 12 minute periods demonstrate the stability and low noise characteristics of the VQA. An analysis of this data verifies that the sensor noise is well below the requirement. Testing also verified that the accelerometer has acceptable input axis stability.

Another outstanding characteristic of the VQA is its performance immediately after voltage is applied to the sensor and its associated electronics. Tests show the VQA is functioning within 200 ms with no turn on transient.

The data presented above demonstrates that the VQA is capable of meeting the performance goals of the DQI. In addition improvements are being developed to enhance producibility and yield. Test data on these improved sensors was not available at the time of publication.

The Quartz Rate Sensor was characterized utilizing both static and rated tests with its input axis mounted both normal and perpendicular to the spin axis of a rate table in a thermally controlled environment. Table IV summarizes the results.

Table IV - QRS Measured Performance Parameters

Performance Term	Value	Units
Short term Bias	0.57	deg/hr
Angle Random Walk	.088	deg/rt-hr
Turn On Time	< 1	sec
Short Term Scale Factor	28	ppm
Input Axis Stability	.02	mrad

Bias and scale factor were derived from a series of rotating tests. The rate table was rotated at  $\pm 100$  deg/sec for 30 sec in each direction and repeated for the length of the test. The gyro output was sampled and demodulated at 600 Hz and triangular filtered to a storage rate of 1 Hz. The bias and scale factor residuals after thermal compensation demonstrate that the QRS is a viable technology to meet the DQI performance requirement.

Testing revealed that the QRS has excellent input axis stability and extremely low angle random walk over temperature. Input axis stability was demonstrated with the gyro mounted in a cluster with the sensor's input axis orthogonal to the spin axis of the rate table. Angle random walk measurements of .088 deg/rt hour were consistently obtained. These values are comparable to small Ring Laser Gyros and Fiber Optic Gyros which cost considerably more. Data was taken at 600 Hz as temperature was slewed from -55C to +75C in both tests.

Similar to the VQA the QRS has demonstrated its suitability for rapid reaction systems, because of its short turn-on time and its small turn-on transient. The QRS and its associated electronics were able to provide data within 1 second with only small turn-on transient effects that were completely gone after 1 min.

### ISA Cluster

The ISA cluster serves the two main functions of mounting and shock isolation for the inertial sensors. Mounting for the sensors is provided by a metal cube with one of the six inertial sensors mounted on each surface of the cube. The cube is installed in a structural shell suspended at each corner by elastomeric shock isolators.

### Inertial Sensor Electronics

The inertial sensor electronics converts the analog outputs from the inertial sensors to digital signals for further processing within the DQI. The goal is to maximize the use of digital electronics to eliminate the many error sources associated with analog electronics. This allows the DQI mechanization to be more software intensive and thus more flexible than previous implementations with similar inertial instrument technologies.

### IMU Electronics

The IMU electronics perform the two main functions of digital signal processing, and central processing. The digital signal processing function extracts the useful information from the inertial sensor signals and passes it on to the central processor. The central processing function performs thermal compensation of the inertial information, input/output formatting and control, and Built-in-Test (BIT). These functions are partitioned into three

modules which are interconnected via a master interconnect board that also contains the power conversion electronics.

The key to the electronics mechanization is the use of high speed, programmable digital signal processors that operate on the rate sensor data. High speed is essential in meeting throughput and bandwidth requirements. Programmability offers the flexibility to develop and improve algorithms quickly, accommodate planned improvements and fully exercise the complex algorithms before committing to Application Specific Integrated Circuits (ASICs).

The DQI accepts 28 volts DC and uses an internal power converter to generate the necessary secondary voltages. The design will accommodate use of external secondary voltages if required by specific application making it possible to achieve even lower cost.

### **IMU Packaging**

The primary packaging requirements for the DQI are: (1) low cost, (2) minimum volume and weight, (3) necessary structure to provide the required alignment to the vehicle and to withstand the shock and vibration environments. A high fidelity mock-up of the design to meet these requirements has been produced and is in test. A picture of the mock-up is shown in Figure 2.

The DQI housing is made up of an extruded aluminum body, a stamped lid and a machined aluminum base. The design requires a minimum of machining to insure proper alignment and fit. The extrusion process provides an inexpensive means of manufacturing a combined body and a card guide set. The three parts are welded into a complete housing using proprietary batch processing techniques.

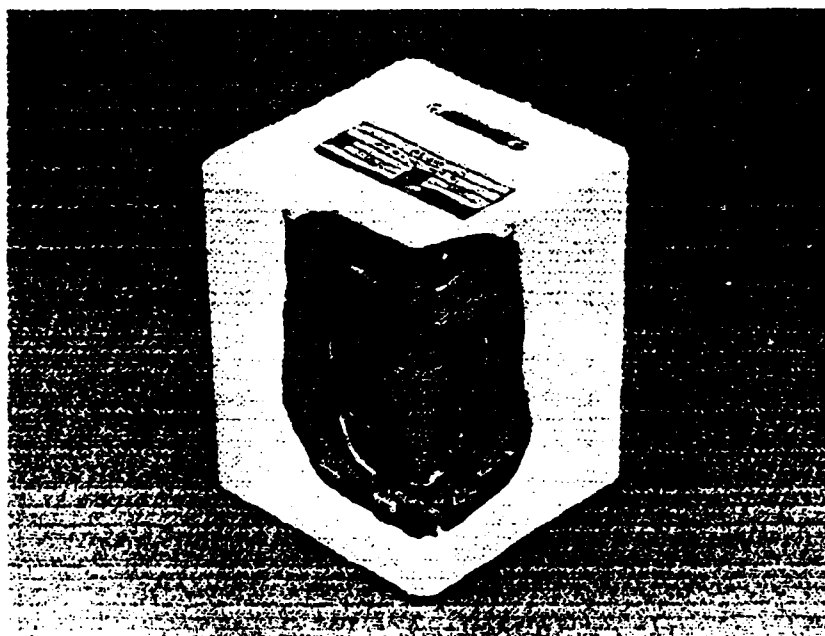


**Figure 2.**



The ISA cluster assembly mounts in the center of the aluminum base plate and is surrounded by electronic modules on each of its four sides and by the master interconnect board on the top. The power supply and input/output connector are located on the master interconnect board (MIB) and physically attached to the housing lid. All four electronic modules interface via the MIB.

The electronic modules are multi-layer, printed wiring boards populated on both sides with surface mount components. The modules are retained in card guides by spring clips which also serve as the heat conduction path.

## **DQI PRODUCT DEVELOPMENT TIMELINE**

The DQI product development was initiated in February 1992 with a target for prototype availability in February 1994. All sensor, cluster and brassboard ISA development testing has been completed. Brassboard hardware which is form, fit and function equivalent to the prototypes is currently undergoing evaluation testing. Prototype IMUs will complete fabrication in late 1993 to support the February 1994 availability.

**SESSION V-B**  
**FIBER OPTIC GYROS (FOG)**

***CHAIRMAN***  
**KATHY CLIETT**  
***WRIGHT-PATTERSON AFB OH***

**THIS PAGE LEFT BLANK INTENTIONALLY**

## **A Tactical Fiber Optic Gyro With All-Digital Signal Processing**

**Michael S. Perlmutter  
Northrop Corporation  
Electronics Systems Division - Norwood Site**

### **ABSTRACT**

Northrop's Electronics System Division has built and tested a tactical fiber optic gyro (FOG) with all-digital signal processing. The Northrop FOG uses 160 meters of polarization maintaining optical fiber wound on a spool 29 mm in diameter. Without any data compensation, this FOG has demonstrated excellent scale factor stability and non-linearity ( $< 100$  ppm) over a high dynamic range ( $\pm 1400^\circ/\text{s}$ ), low random walk ( $< 0.02^\circ/\sqrt{\text{hr}}$ ), and outstanding bias stability over temperature and day-to-day ( $< 1^\circ/\text{hr}$ ).

An Inertial Measurement Unit (IMU) utilizing a FOG/MSA (Micro Silicon Accelerometer) cluster has been developed and integrated with a GPS receiver. Testing was done to demonstrate performance of the sensor and IMU over the military environment.

### **INTRODUCTION**

The Norwood site of Northrop's Electronics Systems Division has continued development of a fiber optic gyroscope (FOG) for a low cost inertial measurement unit (IMU), designed specifically for tactical weapons applications. The Northrop FOG is based on the successful single axis FOG-50 design developed by Photonetics S.A (of Marly Le-Roi, France) over the past five years. Northrop is completing the development of this sensor for military-type applications, and has integrated it with a micro silicon accelerometer (MSA) and Global Positioning System (GPS) receiver into a tightly integrated, low cost, solid-state IMU.

Northrop's FOG uses the simplest optical configuration necessary for very demanding applications employing a sensor coil that is 5.5 mm thick, with an outside diameter of 36 mm, and an inside diameter of 29 mm, constituting a volume of less than  $2 \text{ cm}^3$  ( $0.12 \text{ inch}^3$ ). We believe that the gyro using this sensor coil has the highest performance to volume figure of merit of any fiber or ring laser based gyroscope.

The FOG signal processing and closed loop operation use completely digital electronics. This proprietary, all-digital processing scheme differentiates the Northrop gyro from all other FOGs with similar optical components; it also imparts significant advantages to this design in terms of performance, cost, and volume. The all-digital processing scheme permits this FOG to operate free of the electronic bias drift sources intrinsic to FOGs using analog demodulation

schemes. The absence of electronic bias drift eliminates the necessity for electronic adjustments and output data compensation.

### PRINCIPLE OF OPERATION

The principle of a FOG is quite simple. It is based on the phenomenon that a circual system has different optical path lengths in the two propagation directions when it is rotated. The difference in the propagation properties of the two directions provides a measure of rotation. This phenomenon was first described by Sagnac in 1913<sup>1</sup>. This non-reciprocal effect can be easily derived by a simple argument. If two coherent light beams emanating from a common source travel in opposite directions around a stationary circular path (or ring) of radius R (with the source fixed on the ring), they are in phase when they return to the source. If the ring is now rotated with a tangential velocity  $v$ , the beam rotating with the ring has an optical path longer than the counter-rotating beam by a distance  $\Delta L$  given by

$$\Delta L = \frac{4\pi Rv}{c}$$

where  $c$  is the speed of light in vacuum.

For monochromatic light of wavelength  $\lambda$ , this change in optical path length results in a non-reciprocal Sagnac phase difference

$$\Delta\phi = \frac{8\pi^2 Rv}{\lambda c}$$

between the two beams after a single pass around the ring. For a single ring (loop) enclosing an area  $A$  and rotating with an angular velocity  $\Omega$ , the phase difference is given by

$$\Delta\phi = \frac{8\pi A\Omega}{\lambda c}$$

It is important to note that the resultant phase shift is independent of the medium and of the exact shape of the loop. This compliant property of the sensor portion of a FOG is advantageous when designing FOG sensors to fit the volume constraints of specific applications.

The resultant phase shift can be increased by additional loops (turns of fiber). If we wind an  $N$  turn fiber coil, the resultant phase shift becomes

$$\Delta\phi = \frac{8\pi A\Omega N}{\lambda c}$$

Alternatively, we can express the resultant phase shift in terms of coil diameter and fiber length by noting that

$$A = \frac{\pi D^2}{4}$$

$$L = N\pi D$$

and

We can now rewrite the resultant Sagnac phase shift as

$$\Delta\phi = \frac{2\pi LD}{\lambda c} \Omega$$

It is important to note that a constant angular velocity yields a constant phase difference. We can thus think of a FOG as a rate gyro i. e., the output is proportional to rate.

As with any two wave interferometer where two waves overlap in space, the response obtained is cosinusoidal. Thus, the optical intensity can be written as

$$I = I_0 (1 + \cos \Delta\phi)$$

Unfortunately, the Sagnac phase shift due to rotation is exceedingly small for modest rotation rates.

Shortly after Sagnac's original demonstration, A. Michelson constructed an interferometer, using about eight kilometers of evacuated sewer pipes, to detect the Earth's rotation. Employing instruments available at that time, Michelson was just able to measure the phase shift produced by Earth's rotation - only about a tenth of a fringe.

Today, FOGs can easily measure a phase difference of a micro-radian; fiber interferometers of relatively small size can measure the earth rotation with great accuracy. For example, the gyro described in this paper, operating at a wavelength of 830 nm, using 160 meters of fiber wound on a coil with an average radius of 16 mm, can measure a rotation rate of 2°/h per micro-radian of induced phase shift.

Since the output response of a FOG is cosinusoidal, it is worthwhile to calculate the unambiguous range of rotation rate measurement corresponding to a phase shift of  $\pm \pi$  radians. For Northrop's FOG, this unambiguous range of input rates is more than 1500°/s, resulting in an unambiguous dynamic range of more than 10<sup>6</sup>.

## GYROSCOPE OPTICAL DESIGN

The idea of using optical fibers to make a rotation sensor based on the Sagnac effect was first demonstrated by Vali and Shorthill in 1976<sup>2</sup>. During the next seventeen years many advantages of the FOG were recognized and exploited, and during this long development period, the optimum operating conditions have also been almost universally recognized and implemented. A majority of the FOGs targeted for the 0.1 to 1°/h performance range are thus operated in a closed loop mode, using a broadband source, an integrated optic circuit for the phase modulation, and a coil made with polarization maintaining fiber<sup>3</sup>.

Northrop's FOG, targeted for this type of "tactical" performance, uses the simplest optical configuration consistent with its objectives: five optical elements and electronic circuitry for operation of the FOG in a closed loop mode. A schematic is presented in figure 1.

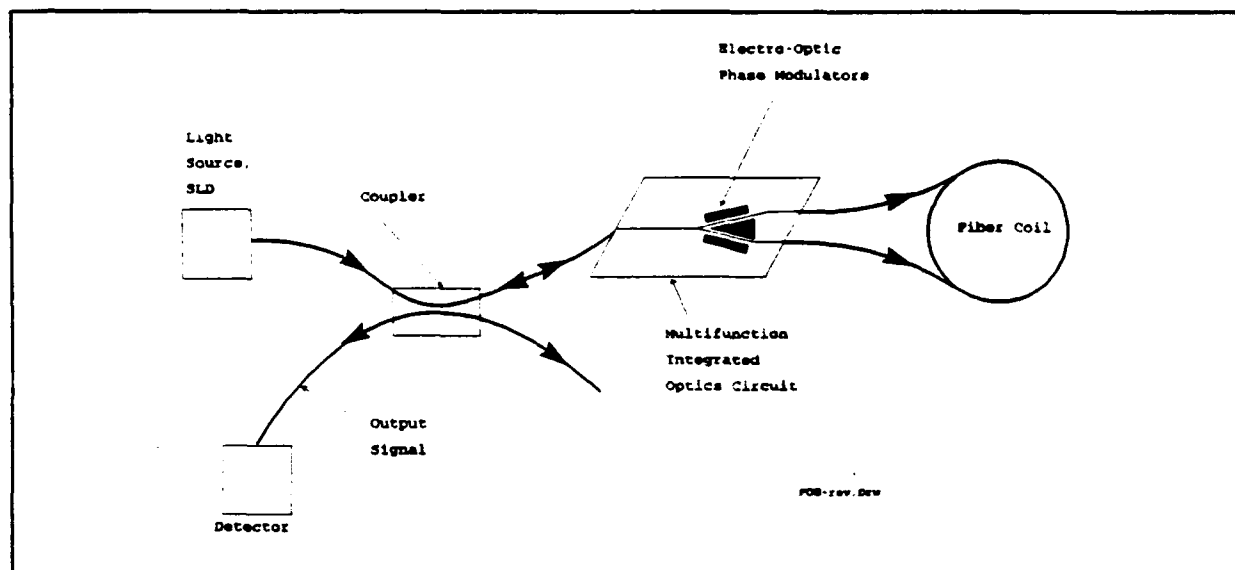


FIGURE 1. Schematic of the Northrop FOG

The operating wavelength of the Northrop FOG was chosen to be in the near infrared, between 800 and 850 nm, predominately because of the extensive availability of components at this wavelength (with the consequence of lower cost) and the packaging benefits achieved from using components at a short wavelength (size of optical components is usually proportional to wavelength).

The optical elements and electronic circuitry of the Northrop FOG are briefly described in the following section.

A superluminescent diode (SLD) operating at approximately 840 nm was selected as the source for Northrop's FOG because it is readily available, has a high optical output power

(required for low noise applications), and because this type of broad band, short coherence length light source eliminates interference effects of backscattered light<sup>4</sup>. The selected SLD couples approximately 400  $\mu$ Watts of linearly polarized optical power into a fiber pigtail at a diode current of 50 mA. Spectral modulation is typically less than 5 percent.

Recent advances in the fabrication of SLDs have led to high optical output power diodes with very long life and low spectral modulation<sup>5</sup>. Devices based on an angled active stripe geometry using a strained layer quantum well InAlGaAs/AlGaAs structure have demonstrated thousands of hours of failure-free operation. Thus, bulk degradation effects consisting of the formation and expansion of dark line and dark spot defects, believed to be the dominant failure mechanism in SLDs, have been virtually eliminated with these devices.

An SLD shifts its operating wavelength with temperature at a rate of about 300 parts per million (ppm) per degree C. Since the Sagnac phase and the compensating phase have the same wavelength dependence, phase ramp feedback should be globally wavelength independent. This is however only true if the effect of the reset is gated out, however, and the basic wavelength dependence of the Sagnac effect is retrieved with the signal processing scheme used in the Northrop FOG<sup>6</sup>.

In order to achieve a scale factor stability of less than 100 ppm, without any data compensation, temperature control of the SLD is required. This is accomplished by mounting the diode chip on a solid state thermo-electric cooler capable of maintaining the chip at a constant temperature. Highly reliable, rugged single and double stage coolers are now readily available. Fiber optic pigtailed SLDs with thermistors and monitor photodiodes are packaged in industry standard 14 pin packages.

A polarization preserving 2 x 2 coupler is used to couple out some of the returning signal<sup>7</sup>. Fabrication techniques for making polarization-preserving 3 dB couplers have been refined over the past twelve years with two types of couplers commercially available today. Both the fused biconic taper and the side polished techniques have produced couplers with very low cross talk (less than -25 dB), low optical loss (less than 0.3 dB) and stable coupling ratio (less than  $\pm 3\%$ ) through a temperature range of -55°C to +85°C.

We have successfully used both types of couplers in our FOG design, and it appears that both couplers have comparable performance over the environment, and are of comparable cost in small quantities. Side polished couplers have the advantage of being able to fit into a smaller volume than those made by the fused biconic taper method. Ultimately, the cost of a polarization preserving coupler in large quantities will dictate the preferred manufacturing method.

A multifunction integrated optic circuit (IOC) is used for three functions in our FOG:

1. to split the light into two equal components which counter-propagate around the fiber coil, and are recombined in the "Y" branch,
2. to polarize the transmitted light,
3. to apply an alternating (biasing) phase shift along with a phase shift to the counterrotating beams offsetting the Sagnac induced phase shift due to applied angular velocity.



Single crystal lithium niobate ( $\text{LiNbO}_3$ ) has become the most common substrate material used in integrated optical circuit (IOC) manufacture due primarily to its excellent electro-optic waveguide properties. Two different technologies have emerged for producing waveguides in  $\text{LiNbO}_3$  for FOG applications: titanium indiffusion and proton exchange. Both techniques are based on chemical techniques, and both are readily available from a number of manufacturers. The proton exchange method is the more recent technology; it appears to produce waveguides with a higher polarization extinction (greater than 60 dB) and lower optical loss (less than 3 dB/chip), as compared to waveguides made using the titanium indiffusion technique.

FOGs of the type described in this paper have incorporated IOCs manufactured using either technique with comparable results. Proton exchange waveguide IOCs have been chosen for the FOGs built by Northrop during the past year because of their higher performance and lower cost. These IOCs use an x-cut and y-propagating crystal orientation with the two phase modulators operated in a push-pull mode. Again, the critical discriminator for the waveguide manufacturing technology is the ultimate cost of the device, since both techniques yield devices of adequate performance for our design.

A 160 m polarization preserving fiber coil wound on a bobbin having a diameter of 29 mm and a width of 5.5 mm comprises the sensing element. In order to minimize the size of the sensing coil, we selected a fiber with a single acrylate jacket of 125 microns diameter. This fiber has a cladding diameter of 80 microns, a mode field diameter of 5.5 microns, a beat length of 1.1 mm, and attenuation of 3.2 dB/km.

Thermal transients and vibrations can produce parasitic signals since reciprocity is only valid for time invariant systems. We have adopted the quadrupole coil winding technique in our FOGs to get the best common mode rejection for thermal and vibration perturbations<sup>8</sup>.

A low cost PIN silicon photodetector is used to detect the rotation induced Sagnac phase shift. This diode is located with the electronics, and is optically connected to the FOG by a fiber optic cable. This arrangement has the advantages of keeping the optical sensor small, keeping the optical diode close to its preamplifier, minimizing cross talk from IOC modulation, and minimizing errors arising from inappropriate ground loops.

### PRINCIPLE OF THE ALL-DIGITAL SIGNAL PROCESSING

Digital demodulation has been characterized as a means of making a perfect gyro with imperfect components<sup>9</sup>. The Northrop design operates the FOG in closed loop mode using a proprietary digital demodulation technique and a digital phase ramp to obtain exceptional performance from a very compact sensor coil.

To get high sensitivity from our FOG, a square wave phase modulation between  $+\pi/2$  and  $-\pi/2$  radians is applied at the eigen frequency of the sensing coil. (Eigen frequency is defined as  $1/2T$  where  $T$  is the group delay through the fiber coil.) When an angular velocity

is applied to the gyro, the Sagnac induced phase shift unbalances the modulated signal, producing a square wave modulation of the output signal at the eigen frequency. This signal (on the photodiode) is converted directly into digital form at each half period. The value of the second half period is subtracted digitally from that obtained during the first half period. This type of digital demodulation is completely free of electronically induced bias drift, since it does not use any DC amplification.

To take full advantage of this all-digital approach, a digital phase ramp is used to offset the Sagnac induced phase shift. This has the effect of creating a phase difference between the counter-rotating waves (one direction sees it before passing through the coil, the other after passing through the coil) that is equal and opposite (using a digital loop) to the Sagnac induced phase shift. Thus, the voltage applied to the phase modulators is the digital sum of the digital phase ramp and the square wave modulation. By taking advantage of the fact that the system has to work only over a given length (the length of the fiber coil), this digital approach avoids the two main drawbacks of analogue approaches: flybacks of finite duration, and non- $2\pi$  resets.

In FOGs using a phase ramping technique, the standard readout is to count the  $2\pi$  resets. With this digital approach, the rate (value of the phase shift induced by rotation) is stored in a register, and a sub-multiple value is generated without waiting for a complete  $2\pi$  reset. Using a four bit parallel output, the electronics provide a pulse for each 0.91 arc-seconds of rotation. In addition, the electronics also provide a procedure to count the  $2\pi$  resets, each corresponding to 7.3 arc-seconds of rotation.

This digital modulation/demodulation, and signal processing technique is the ideal FOG "signal extraction" approach since it provides low noise, drift free, and high dynamic range operation at a low cost, using standard electronic components. The following section, describes the exceptional performance obtained utilizing this type of all-digital electronics.

## PERFORMANCE

A comprehensive characterization of the performance of a FOG requires tests of scale factor and bias stability. The scale factor relates the output counts to the actual input rotation of the gyroscope. Ideally, the scale factor is independent of angular rate, time, and orientation and is also insensitive to environmental fluctuations. The bias stability test characterizes the drifts in the indicated rotation rate of the gyroscope for a constant (near zero) input rotation rate. Ideally, the bias of the gyroscope is also independent of time and orientation, and is insensitive to environmental fluctuations. Rate noise on the output signal limits the resolution to which the rotation rate may be determined for a given integration time. These performance issues are discussed in the following section, together with characteristic data from the Northrop tactical FOG with its all-digital signal processing.

To test the low-rate scale factor of our FOG, we placed the gyroscope on a slowly rotating table with the input axis aligned perpendicular to the rotation axis of the rate table, and

pointing south. The table was then rotated at  $0.06^\circ/\text{s}$  for two hours, with the FOG input axis slowly rotating through south, west, north and east directions. The rotation rate corresponds to a complete table revolution each 100 minutes. When the gyro is pointed north it should measure a rate of  $11.1^\circ/\text{h}$  (the component of earth's  $15^\circ/\text{h}$  rotation at latitude of  $42^\circ 11'$ ) and  $-11.1^\circ/\text{h}$  when it points south. The gyro output vs. time test results are plotted in figure 2 and re-plotted vs. the input rate in figure 3.

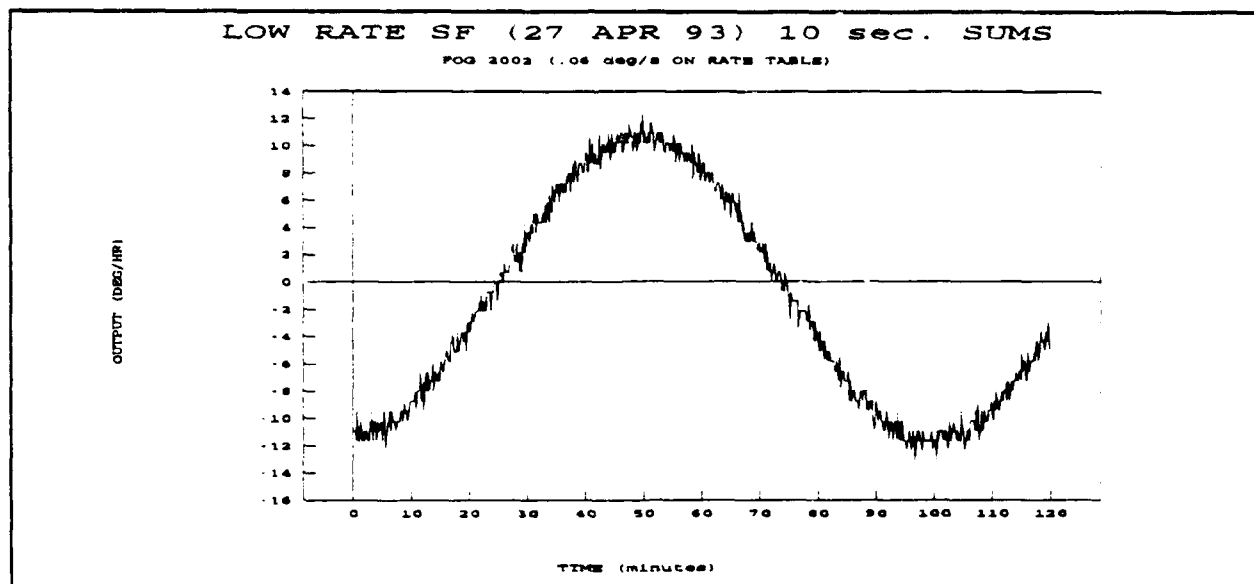


FIGURE 2. GYRO OUTPUT VS. TIME - MEASUREMENT OF EARTH ROTATION

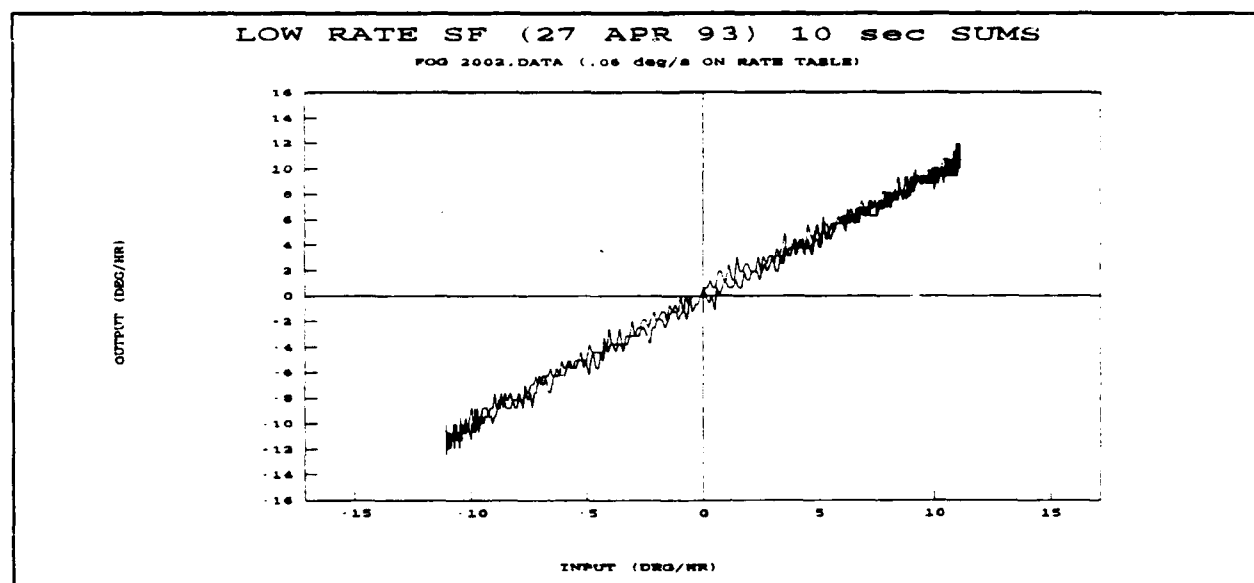


FIGURE 3. LOW RATE SCALE FACTOR LINEARITY

The data shown in the two graphs conclusively demonstrates the excellent low rate scale factor characteristics of our sensor. There is no evidence of a scale factor non-linearity, nor of

low rate lock-in at input rates close to zero.

Scale factor linearity for an input angular rate test range of  $\pm 1000^\circ/\text{s}$  is shown in figure 4. The uncompensated data is plotted as the deviations of the indicated scale factor from the mean. The scale factor data is based on averaging the gyroscope signal over 10 table revolutions. The maximum deviation was measured as 13 ppm, and the standard deviation was measured at

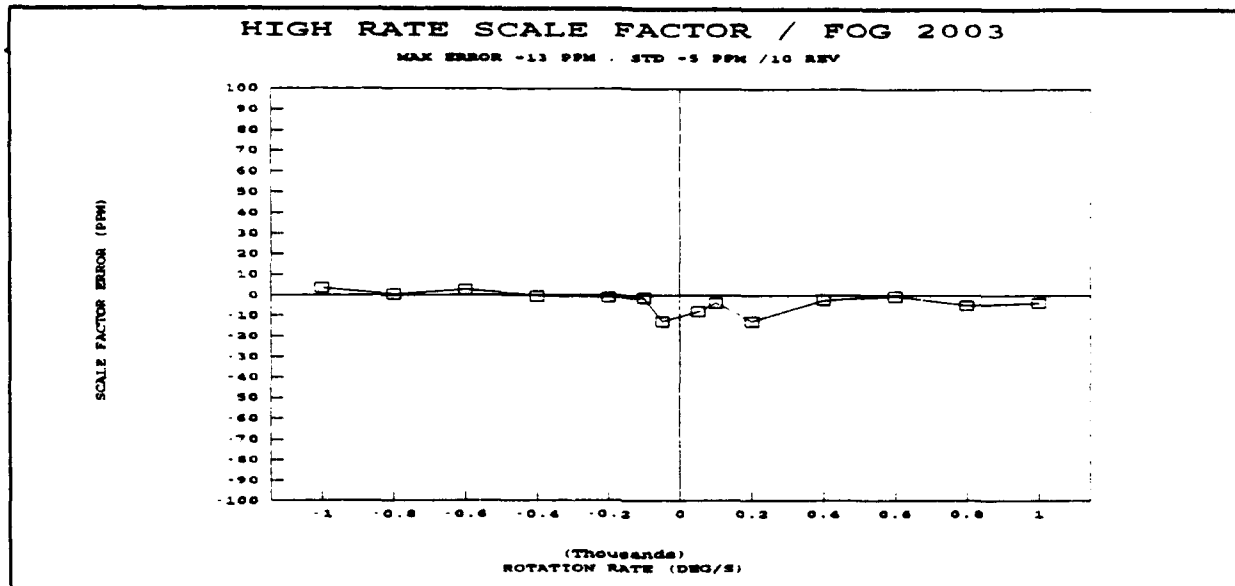


FIGURE 4. HIGH RATE SCALE FACTOR LINEARITY

less than 10 ppm.

Numerous environmental fluctuations influence the stability of a tactical gyroscope; of these, temperature variations are the most pervasive. Instruments insensitive to rapid temperature variations are desirable for many applications. Thus, is very advantageous to use instruments that do not require any temperature compensation because they can be tightly integrated in a variety of applications without the use of numerous temperature sensors, microprocessors, and compensation algorithms. Our tactical gyroscope has been designed to be temperature insensitive.

Figure 5 displays the uncompensated bias drift performance of our FOG, as a function of gyroscope temperature which was varied between  $-35^\circ\text{C}$  and  $+75^\circ\text{C}$  at a rate of  $5^\circ\text{C}/\text{minute}$  (thermal chamber rate of change). The resultant gyroscope measured rate was plotted as a function of gyro temperature. Earth rate (with input axis horizontal and pointing north) of  $11.1^\circ/\text{hr}$  and null bias were not subtracted from the data of figure 5. The bias stability (computed by taking the standard deviation of all data points) was calculated to be  $0.7^\circ/\text{h}$ . Again, we emphasize that this data is entirely uncompensated.

Null bias data summed over fixed sample time typically contain three kinds of noise: quantization noise, wide band white noise and long term drift. Quantization noise results from

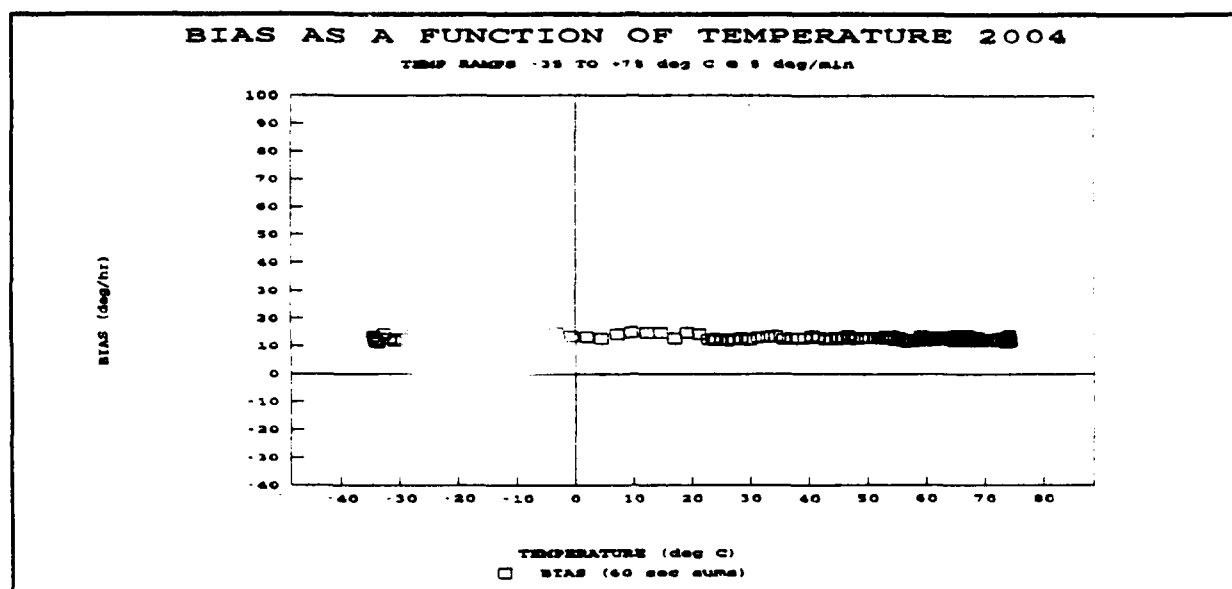


FIGURE 5. UNCOMPENSATED BIAS DRIFT AS A FUNCTION OF TEMPERATURE

the fact that the four bit parallel output of the sub-multiple rate stored in the register provides a pulse for 0.91 arc-seconds of rotation. The resultant one count uncertainty per sample period produces an error in rate that is inversely proportional to sample time. Thus, as we sample at shorter time intervals, we find an increase in noise inversely proportional to sample time. (At one second this is only about  $1/\sqrt{6^\circ/\text{h}} \sim 0.4^\circ/\text{h}$  which is small compared to the white noise.

White noise originates from two sources: photon (shot) noise and thermal (Johnson) noise. Photon noise is caused by statistical fluctuations of the current in the photodiode pre-amp current -voltage feedback resistance due to the finite nature of the charge quantum. The photon noise generated on this resistance has an rms value  $\sigma_i$  given by

$$\sigma_i = \sqrt{2qIB}$$

where  $q$  is the electron charge,  $I$  is the mean signal photodiode current, and  $B$  is the measurement bandwidth.

Thermal noise in the charge resistor  $R$  of the amplifier at temperature  $T$  is given by  $\sigma_v$

$$\sigma_v = \sqrt{4kTRB}$$

where  $k$  is Boltzmann's constant and  $B$  is, as before, the measurement bandwidth.

In this FOG where a silicon PIN photodiode is used and the returning optical power is several micro-Watts, sensor noise is limited by photon shot noise. This (flat spectrum) noise

(white noise) corresponds to a random walk angle. The units of the error coefficient are expressed as  $^{\circ}/h^{1/2}$ . A characteristic null bias test of this FOG with one second sample time is shown in figure 6.

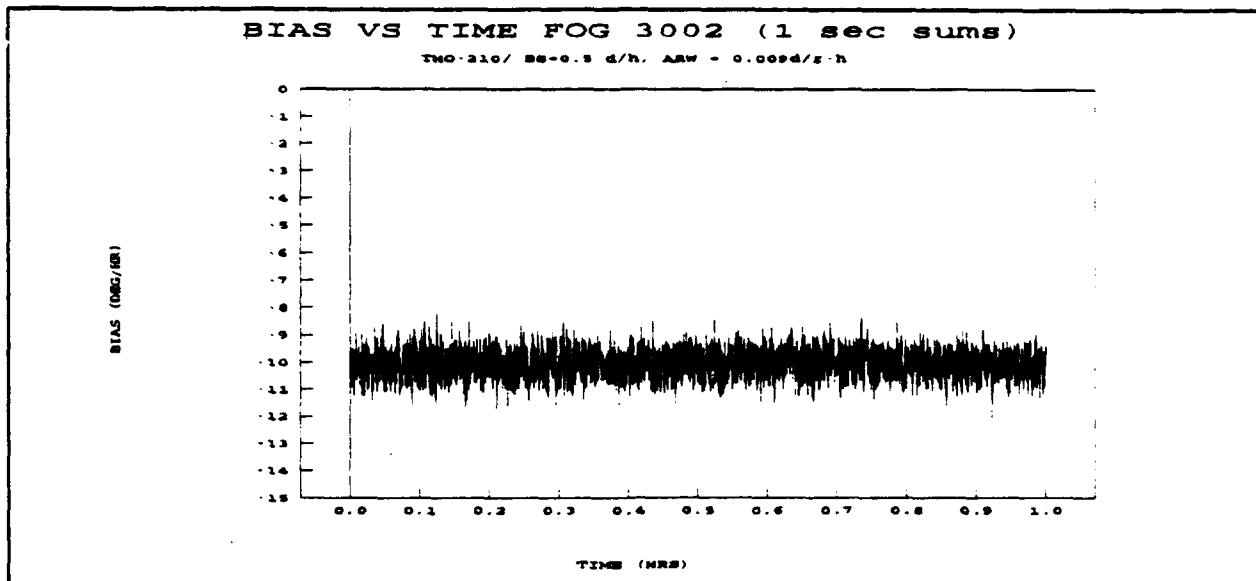


FIGURE 6. BIAS VS TIME FOG 3002, (1 second SUMS)

By calculating the standard deviation of these data points we get the random walk in angle of  $0.009^{\circ}/h^{1/2}$ . This result matches the results of the TRW AUTOFIT program for calculating standard deviations of output rate as a function of sampling time. The calculated rate ramp is  $0.106^{\circ}/h/h$ . A plot of the standard deviation as a function of sample time and the best fit of the data using AUTOFIT is shown in figure 7.

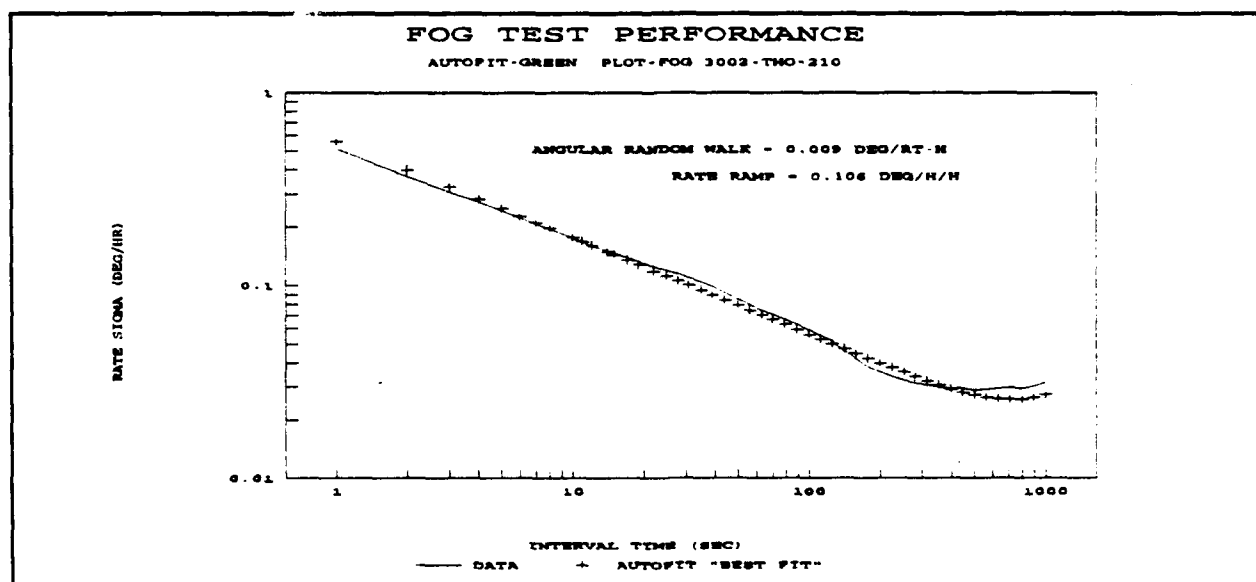


FIGURE 7. AUTOFIT ANALYSIS OF FOG BIAS DATA

## SYSTEM CONSIDERATIONS

Present day FOGs are being seriously considered for various medium and low accuracy inertial measurement units (IMUs) for attitude and heading reference systems (AHRS), aircraft avionics, and missile guidance systems. Gyro performance in demanding environments and their cost are major concerns for these systems. This FOG, with its high performance-to-size figure of merit, low cost potential, and numerous other advantages, satisfies many current requirements, and extends the range of FOG applications to additional medium and high grade applications.

Northrop's FOG has several features that provide advantages when integrated into an IMU. Due to its very robust and high design margin, a single light source can be shared by all three gyros in a three axis cluster (TAC). This configuration results in significant cost savings, since the additional couplers (splitters) are less expensive than additional pigtailed light sources. Furthermore, because of its very high performance to volume ratio, FOGs of this design can be packaged in very compact configurations. Northrop has combined three FOGs of the performance described in this paper into a miniature three-axis cylindrically shaped cluster, with a diameter of 2.8 in and a height of 1.6 in. The total volume of this modular TAC configuration is less than 10 in<sup>3</sup>.

The all-digital processing of the Northrop FOG permits very efficient multiplexing of the gyro signal in a three-axis IMU. Additionally, this all-digital signal processing leads to signal processing electronics that need no adjustments or data compensation (as demonstrated in the gyro bias as a function of temperature plot). Since data compensation is not required for this FOG (and IMUs based on it), it can be combined in very tightly integrated systems and in various specialized applications, without requiring the additional microprocessors used exclusively for gyro compensation.

We have also integrated three of these FOGs with Northrop's micro silicon accelerometers (MSA) and a GPS receiver, forming a FOG GPS/I navigator. This FOG GPS/I navigation set (NAVSET) provides continuous digital outputs to convey vehicle heading, position, velocity, acceleration, attitude, attitude rates and status information. The NAVSET functions either as an aided inertial navigation system (INS), using GPS to enhance its accuracy by bounding gyro drift errors, or as a stand-alone INS, if the GPS is unavailable. The NAVSET has been tested with a Northrop GPS receiver, as well as with a six-channel single board GPS receiver supplied by a major military GPS producer.

Northrop's closed loop acceleration sensor is micro-machined in silicon. The device is very economical to produce since mass production is common to the IC industry. Our MSA has a 3 kHz bandwidth, a  $\pm 50$  g performance range, with a 1 mg day-to-day bias stability, better than 10  $\mu\text{g/g}^2$  non linearity error, a resolution of less than 1  $\mu\text{g}$ , and a shock failure level greater than 12,000 g.

## CONCLUSION

Fiber optic rate sensors are true solid-state devices. There are no mechanical moving parts, no gaseous or liquid components, no high voltage, and no physical interfaces that require outstanding seals to separate the "inside" from the "outside". These solid state rate sensors have true ruggedness, simplicity, and a low cost potential almost as a physical given.

The Northrop FOG uses 160 meters of polarization maintaining optical fiber wound on a spool 29 mm in diameter. Without any data compensation, it has demonstrated excellent scale factor stability and non-linearity ( $< 100$  ppm) over a high dynamic range ( $\pm 1400^\circ/\text{s}$ ), low random walk ( $< 0.02^\circ/\sqrt{\text{hr}}$ ), and outstanding bias stability over temperature and day-to-day ( $< 1^\circ/\text{hr}$ ).

Northrop has continued to develop an advanced FOG with all-digital signal processing for a low cost inertial measurement unit designed specifically for tactical weapons applications. This FOG is based on the successful single axis FOG-50 design developed over the past five years by Photonetics S.A (of Marly Le-Roi, France). Northrop is completing the development of this sensor for military type applications, as well as integrated it with a micro silicon accelerometer and GPS receiver into a tightly integrated, low cost, solid state FOG GPS/I navigator.

## ACKNOWLEDGEMENT

The author is grateful to the members of the Optical Instrument group at Northrop Corporation's Electronics Systems Division - Norwood Site for their outstanding contributions to the advancement of this FOG. The author also wishes to thank the members of Photonetics' FOG team for their hard work, dedication and friendship during this project. Finally, the author wishes to thank Northrop's management for their support and commitment to this program.

## REFERNECES

1. Sagnac, G., "L'ether lumineux demontre par l'effet du vent relatif d'ether dans un interferometre en rotation uniforme", xxes rendus de l'Academie des Sciences, Vol. 95, 1913, pp 708-710
2. Vali, V. and R. W. Shorthill, "Fiber Ring Interferometer", Applied Optics, Vol. 15, 1976 pp. 1099-1100
3. The most significant papers on FOGs published between 1976 and 1989 have been collected in : "Selected Papers on Fiber Optic Gyroscopes", edited by R. B. Smith, SPIE Milestone Series, Volume MS 8, (1989)



4. W. K. Burns, C. L. Chen, and B. I. Moeller, "Fiber-optic gyroscopes with broad band sources", J. Lightwave Technol., vol. LT-1, p. 98, 1983
5. G.A. Alphonse, D. B. Gilbert, M.G. Harvey and M. Ettenberg, "High-Power Superluminescent Diodes", IEEE Journal of Quantum Electronics, Vol. 24, No.12, pp. 2454-2457, December 1988
6. This important point is discussed in more detail by H. Lefevre in chapter 8 of his book "Fiber Optic Gyroscope" Artech House , 1993
7. R. A. Bergh, H. C. Lefevre and H. J. Shaw, "All Single Mode Fiber Optic Gyroscope", Opt. Lett., Vol. 6, No. 4. pp 175 - 177, 1981
8. N. J. Frigo, "Compensation of Linear Sources of Non-Reciprocity in Sagnac Interferometers", SPIE Proceedings, Vol. 412, 1983, pp 268-271
9. H. C. Lefevre, P. Martin and J. Morisse, "High Dynamic range Fiber Gyro With All-Digital Signal Processing", SPIE Vol. 1367 pp. 72- 80, 1990

# RESONANT FIBER OPTIC GYRO ( RFOG ) TECHNOLOGY DEVELOPMENT

J. Haavisto, T. Kaiser<sup>1</sup>,

## Abstract

The Resonant Fiber Optic Gyro ( RFOG ) has been under development at Draper Laboratories for several years. Significant advances in the state -of-the-art of photonics components for the RFOG have been accomplished in Draper's photonics laboratories. Progress has also been made in reducing gyro error sources and demonstrating gyro performance in the laboratory. First we will describe the RFOG and outline the relationship between performance and the component requirements. Then we will review the improvements in critical components accomplished at Draper, including narrow linewidth solid state lasers, low loss fiber resonators and low noise integrated optics circuits ( IOC's ). We will then describe the theoretical models and experimental results which led to the identification and reductions in gyro error mechanisms and present laboratory test results on RFOG breadboards.

## Introduction

The RFOG senses rotation via the Sagnac effect by comparing the resonant frequencies of the clockwise (CW) and counterclockwise (CCW) light beams traversing a fiber optic resonator. The light originates from a solid state laser source with a frequency tunable, narrow linewidth output. Light is split into two channels to excite the CW and CCW directions in the resonator. An integrated optics circuit ( IOC ) provides modulation and frequency shifting to the CW and CCW inputs. The RFOG is shown in Figure 1.

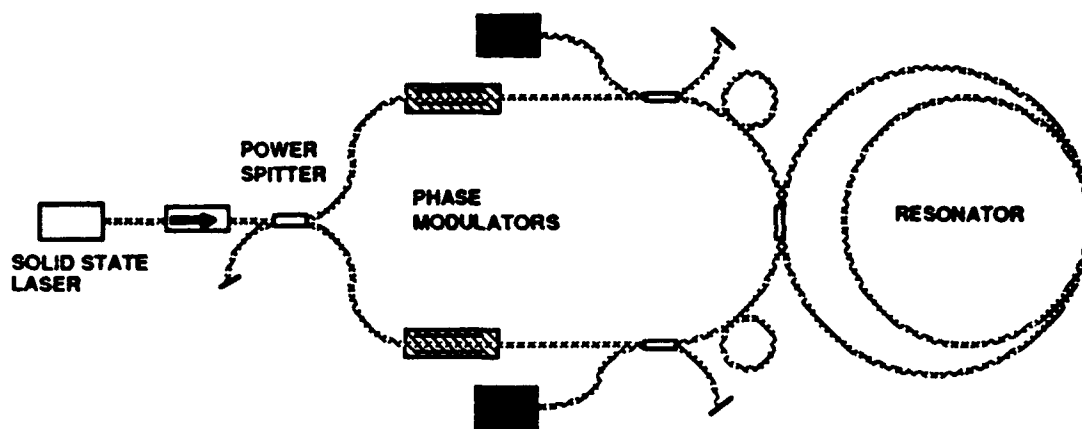


Figure 1 RFOG

---

<sup>1</sup>The Charles Stark Draper Laboratory, Cambridge, MA

A comprehensive model was established categorizing all known error sources. Parametric forms of the error sources using baseline parameters were used to project the feasibility of meeting various performance goals. Component and gyro experiments were used to expand the original model and quantify error source parameters.

Component technology was developed suitable for moderate to high performance ( 1 to .01 deg/hr ) applications. In collaboration with MIT Lincoln Laboratory, a miniature diode pumped crystal laser was developed for the RFOG. Wide bandwidth tuning and very narrow laser linewidth , less than 100 Hz, was demonstrated. Very narrow linewidth ( < 20 kHz ) polarization maintaining fiber resonators were fabricated and tested at Draper. Stable polarizing resonators were made and evaluated in breadboard gyros. Efficient, low loss integrated optics circuits ( IOC's ) were fabricated and low AM and crosstalk circuits developed.

A systematic experimental program has identified the primary causes of gyro drift and noise and demonstrated techniques for its reduction. A demonstration gyro was assembled incorporating several improvements. Drift of 0.5 deg/h was demonstrated with the gyro breadboard in the laboratory, a factor of 20 improvement over the initial results. Subsequent gyro and component experiments, coupled with related analysis, identified additional errors and defined a path to further performance improvements. Performance in the .01 deg/hr regime is projected based on incorporation of the advanced component technology and improvements in the gyro electronics.

## Component Activities

### Microcrystal Laser

In collaboration with MIT Lincoln Laboratory (MITLL), their diode pumped Nd:YAG microcrystal lasers were developed to meet RFOG requirements. Lasers were evaluated by Draper for linewidth and frequency tuning were tested to be within performance specifications for high performance RFOG's at both MITLL and at Draper. Draper also developed an in-house capability to fabricate the lasers, and developed a packaging design to incorporate the lasers in a 3-in gyro. Lasers were characterized for output power, temperature dependence, and wavelength. A plot of optical output power versus pump power is plotted in Figure 2.

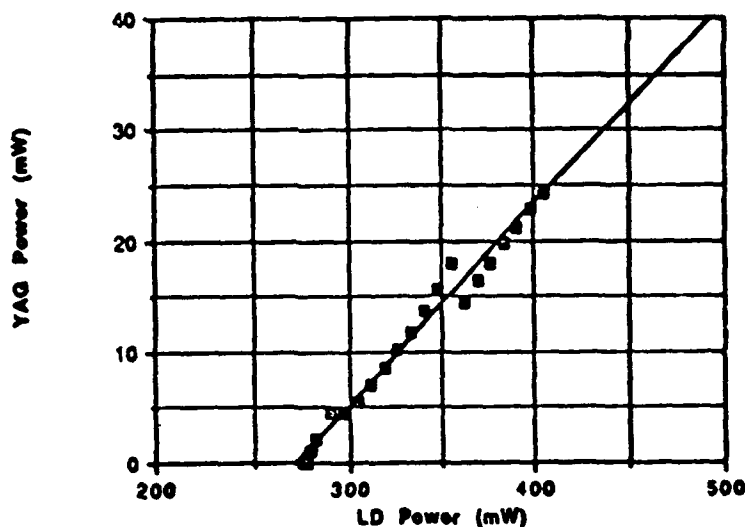


Figure 2. Optical output power vs pump power.

Additional testing included a heterodyne experiment to measure linewidth performed by beating two free-running lasers. The results showed an instrument limited linewidth of 400 Hz (Figure 3).

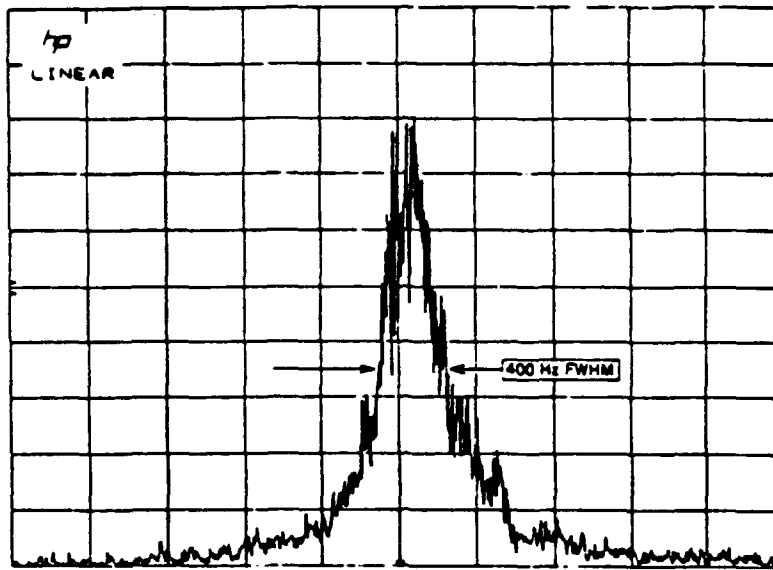


Figure 3. Laser Linewidth

Using an improved experimental setup, the observed beat signal was further reduced to a 50-Hz linewidth. The two lasers are run from two independent power supplies. The beat signal from the heterodyne optical output is detected and referenced to a microwave oscillator. The reference oscillator maintains the center frequencies of the lasers a fixed frequency apart. This is essentially equivalent to the RFOG operating conditions. A startup company to manufacture lasers has been set up by former Draper and MITLL personnel, which will be a potential source of packaged devices for the RFOG.

#### Integrated Optics Circuit (IOC)

Draper established the capability to fabricate integrated optics circuits (IOC's) suitable for RFOGs. Complete devices were fabricated, packaged, and tested. LiNbO<sub>3</sub> was the baseline material used for all development work based on its high electro-optic coefficients and material stability. X-cut crystals were used because of the simplicity of configuration for efficient electro-optic devices. The IOC's met all the specifications in the baseline model. The baseline integrated optical circuit (IOC) for the RFOG performs three functions: (1) formation of the cw and ccw propagating waves via an on-chip beam splitter; (2) phase modulation to form the modulation signals; and (3) frequency shifting to compensate for the nonreciprocal rotation-induced Sagnac shift. These processes define the basic form of the RFOG IOC; namely, a channel waveguide with a Y-branch power splitter with three phase modulators (Figure 3). The IOC was fabricated in x-cut lithium niobate by the proton exchange method.

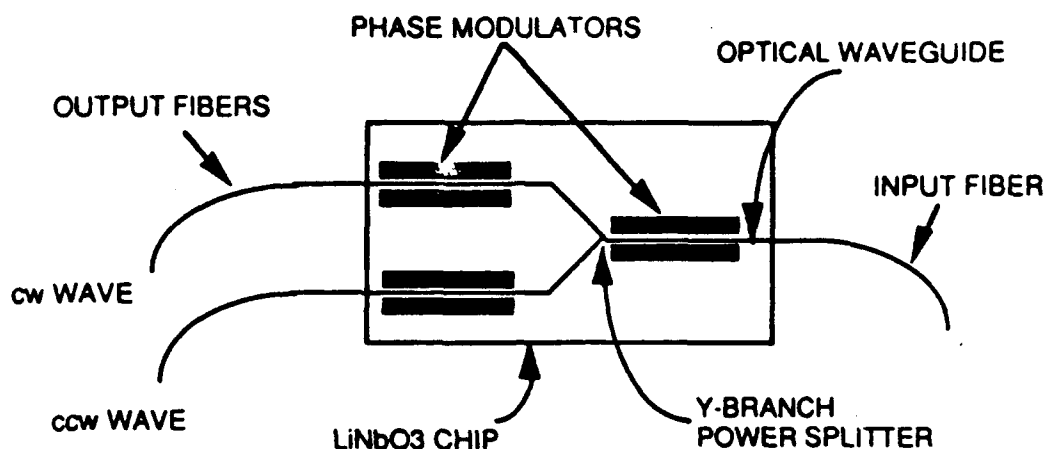


Figure 3. Schematic of 3-port RFOG IOC device.

The waveguides were formed by proton exchange (PE) technique, which yields low-loss, highly polarizing waveguides. The PE technique, by which protons from a benzoic acid bath are chemically exchanged with lithium ions in the LiNbO<sub>3</sub> material (Figure 4), raises the LiNbO<sub>3</sub> index of refraction along only one crystallographic axis so that only one polarization may be supported.

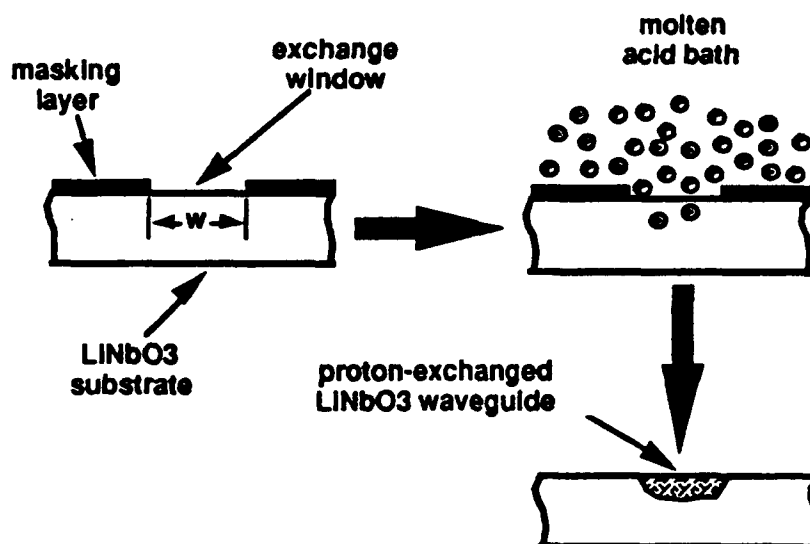


Figure 4 Proton Exchange waveguide process.

### 1.2.3. Fiber Optic Resonator

Draper established fiber optic coupler and resonator fabrication capability for RFOG device fabrication including low loss couplers, splices, and resonators. Resonators with lengths ;from 20 to 400 meters were fabricated. Linewidths as low as 20 kHz were demonstrated Typical parameters for spliced PM resonators are shown in the table.

Serial Number	Finesse	Dip Depth (%)	Cross-Coupling (dB est)	FSR (MHz)	Back-scatter (dB)	Dip Symmetry (%)
41/42	65	99	-20	8.9	-43	$\approx 2$
54/55	145	99	-25	9.1	-53	$\approx 3$

Figure 5 shows the absorption dips for one of the spliced PM resonators.

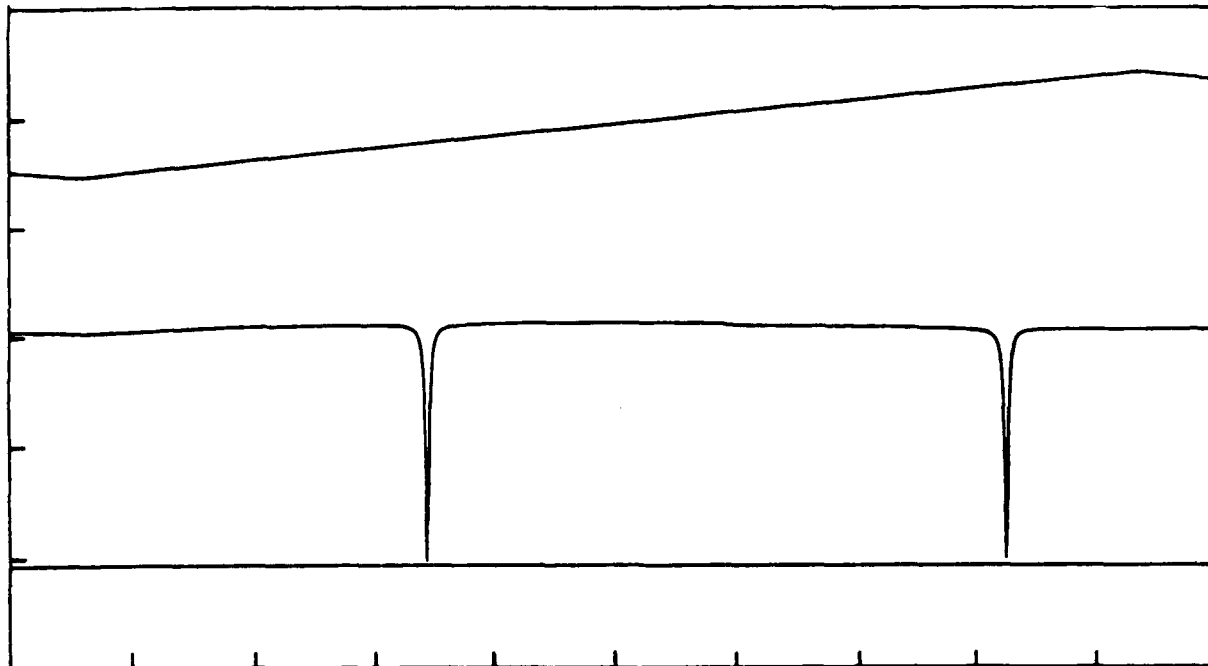


Figure 5. Spliced resonator absorption curve.

A spliceless resonator was fabricated out of a 20-m coilform of Fujikura PM fiber. It was polished and assembled, and was adjusted to obtain dips with an approximate finesse of 320 and a modulation depth of 93 percent. The preliminary data for the variable coupler ring showed a linewidth of less than 32 kHz with crosstalk of less than -25 dB. A spliced resonator incorporating a polarizer in the ring was also fabricated which resonated in only one polarization, and was used in gyro testing.

### Gyro Experiments

Preliminary gyro experiments tested all major error sources. We identified the hierarchy of errors, consequently eliminating the Kerr effect and Brillouin scattering as significant errors. We identified backscatter as the dominant error mechanism, with polarization as a second major error source, but workable for the short-term experiments needed. We developed a systematic diagnostic technique to localize backscatter sources. Complementary component testing and experimental techniques were developed in parallel.

We uncovered a shortcoming in the integrated optical circuit (IOC) modulation, and identified a large amplitude modulation (AM) component and problems in carrier suppression. Systematic experiments identified two AM sources, both limiting carrier

suppression. A detailed theoretical model was developed that included both a description of the physical origin of the AM mechanism and a calculation of the manner in which the AM manifested itself in the limitation of full carrier suppression. The IOC efforts were important because the observed effects vary short and long term, depending on both temperature and frequency. The effects are difficult to measure directly in component tests and tend to be overlooked in typical acceptance and qualification testing. In a gyro configuration, however, the effects cause errors.

The first gyro test results were performed with a carefully constructed gyro that met the baseline specifications, with the exception that a short fiber resonator was used. The breadboard contained diagnostics for predemonstration testing. The first drift results were discouraging, with greater than 10 deg/h bias drift long term due to coherent backscatter. Diagnostic experiments eliminated the components and preresonator optics, and indicated that the resonator was the major source of the backscatter. Modulation of selected parts of the fiber verified that the error source was resonant backscatter. We demonstrated modulation techniques to average the drift, which resulted in measurements below 1 deg/h.

Limitations observed in the gyro IOCs led to an experiment using two separate IOCs. The largest error source was attributed to the crosstalk between the phase modulators on the Y-branch gyro device. Signals on one phase modulator created fields that coupled over to the adjacent phase modulator. This leaked signal modulates the light on the other branch in the waveguide, contaminating the separate discrete channels required for gyro performance.

To test for IOC crosstalk in gyro operation, new separate integrated optics circuits were spliced into the gyro, one in each direction. The old IOC with Y-branch and phase modulators was left in the gyro so that a direct comparison of the two operations could be obtained (see Figure ). An improvement of a factor of six was then seen between the one-chip operation (with IOC crosstalk) and the two-chip operation (without IOC crosstalk).

One of the separate phase modulator integrated optics chips added had a slightly higher amplitude modulation than the other. The device with the higher AM was not able to suppress the carrier as well as the other device in gyro operation. It was later shown that the amplitude modulation in the device was the ultimate limiting factor in the level of carrier suppression that could be obtained.

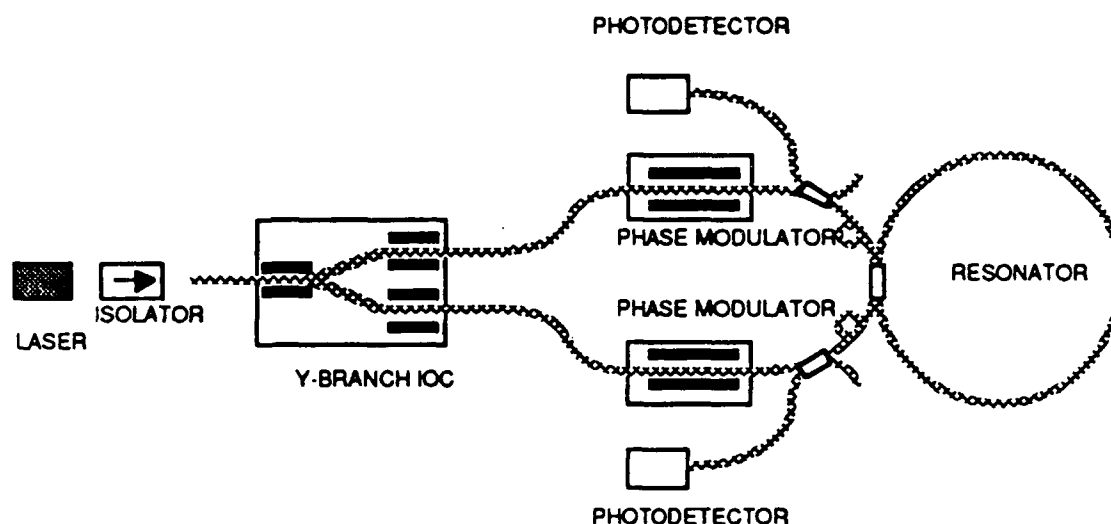


Figure 7. Experimental gyro setup.

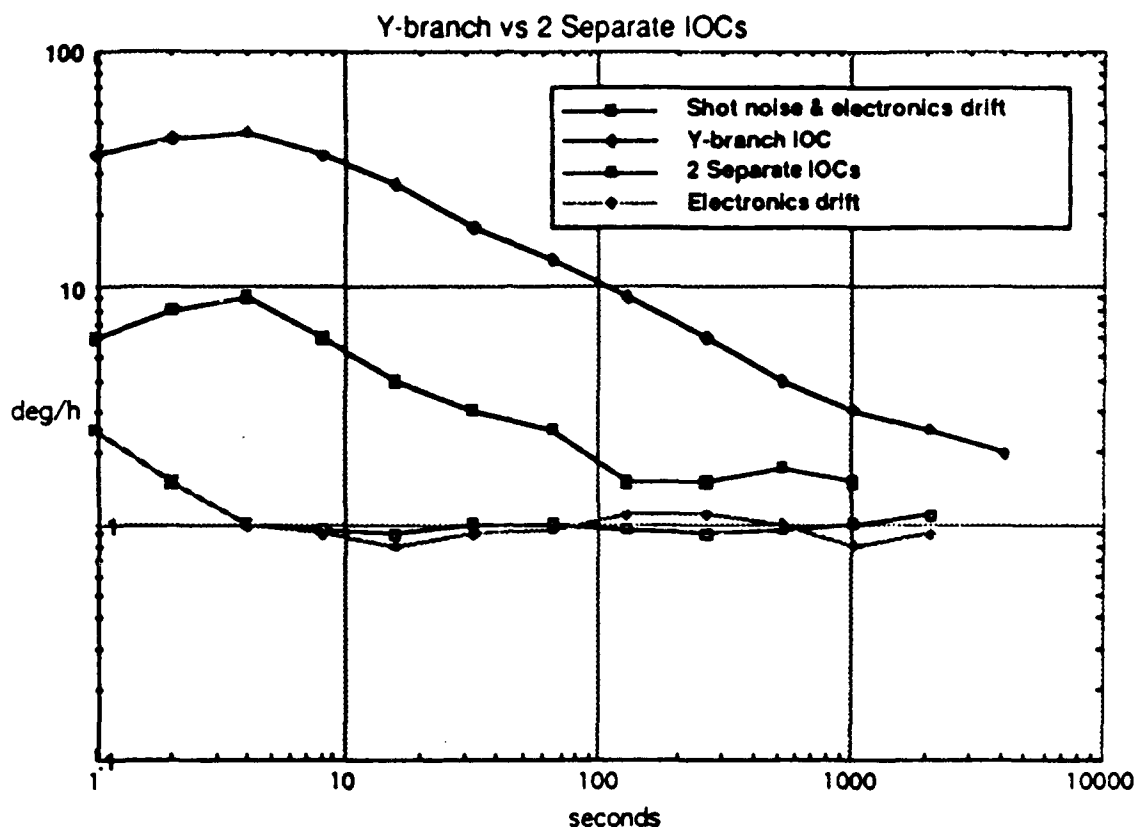


Figure 8 Experimental data.

### Gyro Test Setup

The gyro demonstrations used a breadboard instrument. The optics were laid out on a 8 X 16 inch plate. Figure 5-1 shows a block diagram of the gyro. The open blocks near the center of the diagram are the optical components. The laser was a diode-pumped ring laser with frequency tuning by either temperature or PZT flexing of the laser cavity. This coherent source was then isolated by a Faraday rotator and launched into the optical fiber portion of the gyro. The overall intensity into the resonator could be adjusted by changing the launch efficiency. At times, a tunable coupler was used, and the relative intensity between the two channels could be varied.

The final gyro configuration used two separate integrated optics to minimize the possibility of crosstalk between the two channels. The IOCs were proton-exchange lithium niobate devices bought off-the-shelf from UTRC. The required drive signals were summed electronically before exciting the waveguide. The waveguides were angle polished to reduce backreflections, then pigtailed with a polarization-maintaining fiber. No discernible reflections could be measured. Measured IOC AM was 5 percent.

The input/output couplers were made with PM fiber. They were bought commercially from Canadian Instruments and are the lapped optical contact bond type devices. The unused ends were angle polished and tested for backreflections. These ends could then be monitored to study the intensities entering the ring resonator. The delicacy of the polished bare fiber required great care, and when the input intensities were not needed, the fiber ends were immersed in an index-matching oil that protected the ends and guaranteed that they were reflectionless.



Several ring resonators were tested. The final gyro used a polarizing coil spliced to a polarization-maintaining coupler. This resonator was built at Draper. It had no unwanted polarization, a finesse of about 20, a dip depth of 98 percent, but an asymmetry of 5 percent. The asymmetry caused by modal loss mismatch was the source of several bias offsets. The transmission-designed resonator using two couplers in the ring resonator was never tested.

The photodetectors were custom-made by RCA Canada. The photodetector and preamplifier are standard components, but the package and pigtail were specially designed to eliminate backreflections into the gyro. This was done with limited success. The photodetectors were tested independently on an OTDR, and the lowest reflecting devices were hand-selected.

The data acquisition used a four-channel stripchart recorder to monitor analog signals and a computer to store both analog and digital data. The computer system used a Mac II with Labview software and acquisition boards. The system could take and store four analog channels and two digital channels for almost indefinite periods. It was finally limited by the size of the hard drive. Acquisition runs of several days were commonly taken. The analog channels had a resolution of 5 mV, and low signals were sometimes gained before introducing them into the acquisition system. A digital channel was used to take all gyro bias output. In preparation for closed-loop operation, the open-loop data was sent through a voltage-to-frequency converter, then fed to the computer. The V to F had a bias of 50 kHz; hence, all open-loop data was centered around the 50-kHz output of the V to F.

The resonator up to this point was a polarization-maintaining design. The resonator was temperature-controlled such that the unwanted polarization was held away from the operating point. This was done with limited success. The set point on the controller drifted with room temperature (millidegrees), which was sufficient to allow the polarization effect to bias the gyro data (Figure 8).

This did not allow for long drift runs on the gyro performance. Several methods were considered to alleviate this effect. The chosen implementation at Draper was to insert a polarizer in the resonant coil. This was done by taking single-polarization fiber and winding it on mandrel, then splicing polarization-maintaining coupler halves to the coil. A resonator was then produced that has a polarizing coil and the stability of a polarization-maintaining coupler. The ring resonator was measured to have a finesse of 20 and a free-spectral range of 9.8 MHz, sufficient for gyro operations.

The polarizing resonator was spliced into the gyro brassboard. The gyro could then be run without temperature control on the resonator. No observable second polarization was seen when the laser was ramped in frequency through several free-spectral ranges. The gyro was then operated with this ring resonator and no discernible polarization effects could be observed.

## Gyro Test Results

The experimental test results are presented as an Allan variance of output data. This is a statistical estimate of the data dispersion, or in this case, a graphical representation of the instrument uncertainty as a function of the averaging time. The Allan variance (time domain) can be thought of as the Fourier transform of the power spectral density (PSD) (frequency domain). Figure 9 shows the characteristics of various stochastic processes for both PSDs and Allan variances.

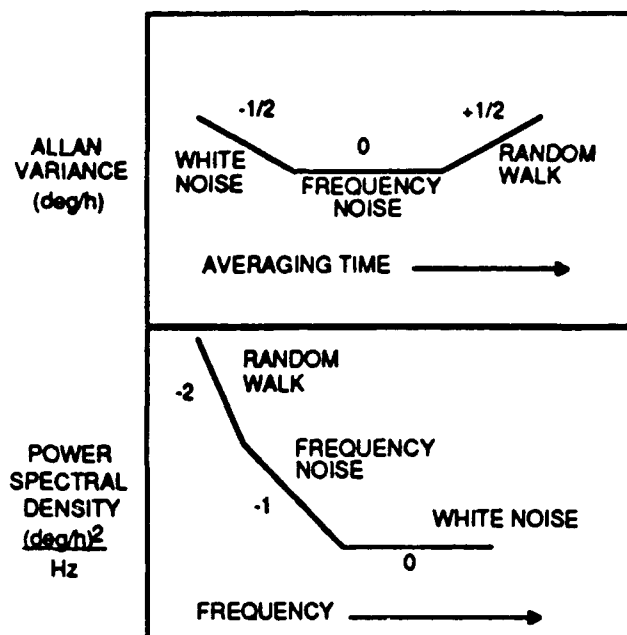


Figure 9. Gyro bias output characteristics

The results of the demonstration gyro tests show a performance of 0.5 deg/h. a performance improvement by a factor of 20 from the experimental gyro results obtained at the outset of testing. The latest results are shown in Figure . The lowest line shows the electronics floor of the data. This was taken by blocking the laser light and leaving all the electronics on. The white noise of the electronics was low enough to measure the optical shot noise of the system, but began to interfere with long-term bias stability measurements.

The optical shot noise, the second curve from the bottom, was measured by unblocking the laser, allowing the light to reach the photodetector, and demodulating the signal off resonance. The shot noise gets overshadowed by the electronics drift after a couple of hundred seconds when both follow the electronics drift curve.

The factor of 20 in performance improvement was obtained by reducing the effects of the coherent interference from backscatter. The residual amplitude modulation in the integrated optics still limited the gyro performance. The data shows a white noise level only a factor of 2 above the shot noise level. Two gyro performance curves taken over four months apart are shown (Figure 10). The last performance improvement by a factor of 5 was delivered by applying a Draper technique in the modulation that reduced the effects of the coherent interference from backscatter. The residual amplitude modulation in the integrated optics was still limiting gyro performance. The data shows a white noise level only a factor of 3 above the shot noise level. The instrument performed at an 0.5 deg/h level for the entire 3-h acquisition run. New electronics with better long-term stability would be required to demonstrate much better performance, since the 2000-s point of the electronic curve is nearing the gyro curve.

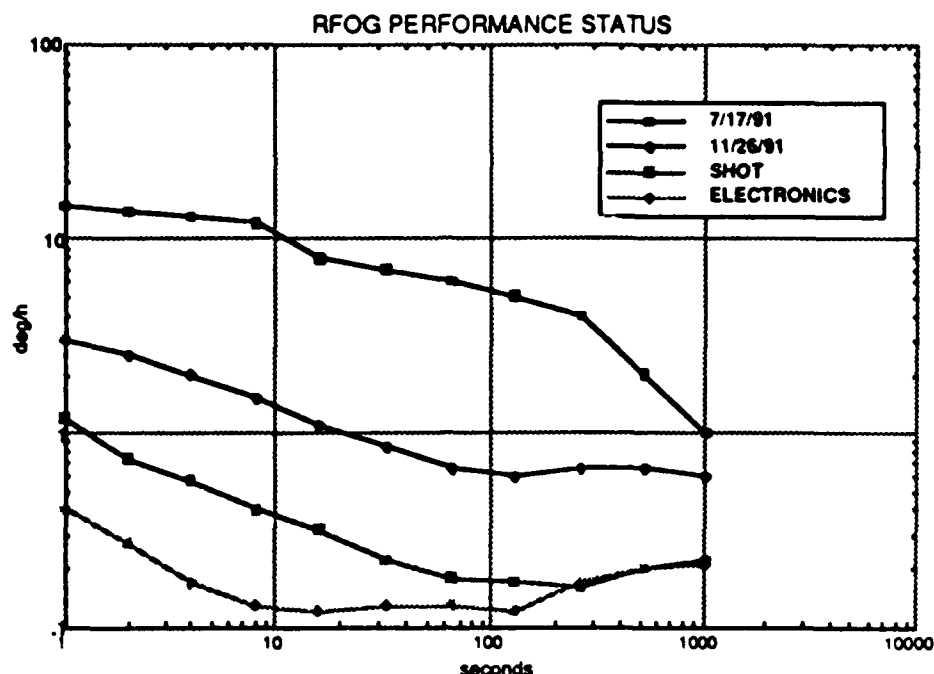


Figure 10.

### Conclusions and Recommendations

The gyro test revealed that no fundamental limit has been found in the RFOG down to 0.5 deg/hr. The current bias drift in the demonstration gyro has been isolated to residual coherent backscatter. This was verified by modulating the fiber, and hence, the relative interference terms with PZT fiber stretchers at various positions in the gyro. When properly terminated fiber ends were modulated, no effect on gyro performance was seen. When the fiber inside the resonator was modulated, however, the bias was driven and proved to be bounded. The stretching of the fiber in the resonator changed the relative phase and amplitude of the backscattered signal and caused the gyro bias to shift. Had the suppressed carrier modulation been more efficient, this error would have eliminated or reduced. Due to residual amplitude modulation in the integrated optics, the projected suppression could not be obtained.

The high-frequency white noise in the demonstration gyro was almost entirely shot noise. The ability to reach this performance level shows that the method for locking the laser to the resonator was very successful. No significant changes are needed. The reduction of the resonator polarization errors by inserting a polarizing element in the resonator proved successful. This was done with polarizing fiber, but alternative methods could be tried, e.g., polarizing couplers, metal film polarizers, and 90-deg splices. The Kerr effect and double backscatter were not evident to the 0.1-1.0 deg/h performance level of this experiment. Improved methods of gain and intensity control would allow definitive experiments to be performed to quantify these effects in the 0.01 deg/h regime.

The gyro performance was limited by the components used. A redesigned integrated optics with reduced crosstalk and amplitude modulation would improve the gyro performance. Both factors proved to hamper gyro performance, but were partially circumvented by using alternative designs or modulation schemes. Improved devices supplemented by these techniques should yield significant improvements. Low-crosstalk and low-amplitude-modulation IOC have been demonstrated using Draper's IOC technology. Alternate designs and lower-loss resonators would also aid in developing the

RFOG's potential. The technology clearly exhibits the ability to perform to below 0.1 deg/h better with the improvement of the critical components.

Currently, the limiting error sources are those arising from backscatter, the optical signal-to-noise (S/N) level, and frequency asymmetry. The unsuppressed backscatter is still the largest, and is limited by crosstalk and amplitude modulation on the IOC. The overall S/N level, determined by laser power and resonator linewidth, defines the bias drift arising from fundamental optical and electronics noise. The frequency asymmetry, due both to AM and ring asymmetry, allows intensity and electronics drifts to cause bias shifts. Test results indicate that these are the only error sources that are observable in the performance data and can be reduced by improvements in the components.

While RFOG performance still lags behind that of the interferometric fiber-optic gyro (IFOG), the resonator approach holds sufficient advantages to warrant further development. The shorter fiber length required still offers a significant cost advantage for navigation-grade performance applications. At current prices, this savings is significant. Other potentially significant advantages of an RFOG are lifetime and reliability. The shorter fiber length means simpler coil winding and less fiber handling, which reduces the risk of damage to the fiber during gyro assembly and improves reliability. The use of diode-pumped crystal laser in the RFOG also improves reliability, as the typical broadband source used for IFOGs is operated at high currents to obtain sufficient output power, which seriously impacts reliability. In the RFOG, the lasers typically have excess power capabilities and can be run at low-power levels to enhance reliability. The potential for the RFOG to fill a niche, particularly in high-reliability systems, is still there. Short experimental runs show the capability of the instrument. More development is required for the instrument to reach its potential, but our work indicates that it has yet to reach it or even push it.

#### Acknowledgments

Resonant Fiber-Optic Gyro ( RFOG ) development at Draper has been supported by several government contracts and Draper IR & D. Much of the photonics component technology and basic gyro research was supported by company IR & D. Some of the specific component and gyro development described here was performed under a WRDC/DARPA-sponsored RFOG Technology Development Program, a multiyear research and development effort aimed at demonstrating the feasibility of Draper's Resonant Fiber-Optic Gyro (RFOG) for navigation systems.

**THIS PAGE LEFT BLANK INTENTIONALLY**

# A FIBER-OPTIC ROTATION SENSOR FOR NASA SPACE MISSIONS

O. Laznicka, R. Gauthier, R. Magee, J. Haavisto, K. Kissa, R. Tumminelli\*

R. Bartman\*\*

We describe the status of a fiber optic rotation sensor ( FORS ) under development by Draper Laboratory and Jet Propulsion Laboratory (JPL). Brassboard FORS have demonstrated the performance levels required for precision pointing and control of spacecraft, platforms, telescopes and advanced NASA Space systems. Preliminary tests of FORS solid-state opto-electronic components indicate that they will meet the reliability characteristics required for long duration space usage. We outline the design of the FORS, the status of optoelectronic qualification testing and the results of current instrument performance tests.

## INTRODUCTION

In the late 1970's, the Jet Propulsion Laboratory (JPL) initiated the development of interferometer gyro technology denoted the fiber-optic rotation sensor (FORS). During the 10 year developmental activities breadboard instruments demonstrated significant performance potential including a 0.07 deg/h bias drift. Based upon these encouraging results, Draper Laboratory and JPL formed a joint effort to convert the FORS breadboard technology into a packaged instrument suitable for long duration space missions. In the first year of the effort we began assembly of FORS brassboards, performed system requirements analysis, and system configuration studies. In the second year, we completed assembly of several FORS brassboard instruments, conducted rate table testing of an assembled FORS instrument with closed loop electronics, and completed system Inertial Reference Unit (IRU) conceptual trade studies. In the third year, we concentrated on additional rate table performance and characterization tests on the FORS brassboard instrument(s) with high performance FORS closed loop electronics, developed space qualified gyro optical components and designed a single-axis engineering model gyro capable of undergoing performance and environmental testing. This paper summarizes the results of the third year's efforts.

## FORS DESIGN

### Gyro Requirements

We have derived a set of gyro requirements from a preliminary set of platform pointing control requirements of a NASA mission (CRAF - CASSINI) by establishing the corresponding IRU requirements and flowing these down to the instrument level. The FORS requirements specify the allowable pointing error over short intervals (seconds or fractions of a second), and long intervals (minutes to hours). Over short intervals, platform stability is dominated by limit cycling, transient disturbance response, and other dynamic effects. For longer intervals, accumulated IRU errors due to scale

---

\*Draper Laboratory, 555 Technology Square, Cambridge, Massachusetts 02139

\*\*Jet Propulsion Laboratory, Pasadena, California 91109

factor and gyro input axes alignment uncertainty and bias drift error dominate the platform stability error.

The total pointing knowledge error budget for the IRU can, to first order, be allocated among bias drift, scale factor, input axes misalignment, and random walk. Based upon three separate pointing requirements, a gyro error allocation analysis was completed (Table 1). Clearly, the driving requirement is the 1 mrad total error over a two hour period.

**Table 1**  
**GYRO ERROR REQUIREMENTS (3s)**

Specification	(1)	(2)	(3)
Bias uncertainty (°/hr)	1.28	0.11	0.016
Scale factor uncertainty (ppm)	320	125	85
Misalignment uncertainty (μrad)	100	100	95
Angle random walk (°/√h)	$2.5 \times 10^{-3}$	$2.1 \times 10^{-3}$	$2.5 \times 10^{-3}$

(1) 4.5 μrad total error over 0.5s and 0.5 deg integrated slew angle.

(2) 85 μrad total error over 100s and 20 deg integrated slew angle.

(3) 1 m rad total error over 2h and 300 deg integrated slew angle.

## FORS DESCRIPTION

### Principle of Operation

The FORS is an Interferometric Fiber Optic Gyro (IFOG) measuring rotation rate via the Sagnac effect. The Sagnac effect creates a differential phase shift between two beams of light counter-propagating in a rotating optical fiber coil proportional to the rotation rate. The phase shift is given by:

$$\Delta\phi_s = \frac{4\pi RL}{\lambda c} \Omega$$

where R is the radius of the coil, L is the length of the optical fiber,  $\lambda$  the vacuum wavelength of the optical source, c the speed of light in the medium, and W the input rate component parallel to the fiber coil axis.

The standard IFOG includes a light source, a fiber coil interferometer and signal processing optics and electronics. The fiber optic gyroscope configuration for the Draper-JPL engineering model ( EM ) uses a Source Integrated Detector (SID), Integrated Optic Circuit (IOC), fiber coil and electronics and is shown in Figure 1. ( An earlier version, the FORS brassboard instrument used a more complex IOC and discrete source, coupler, and detector. )

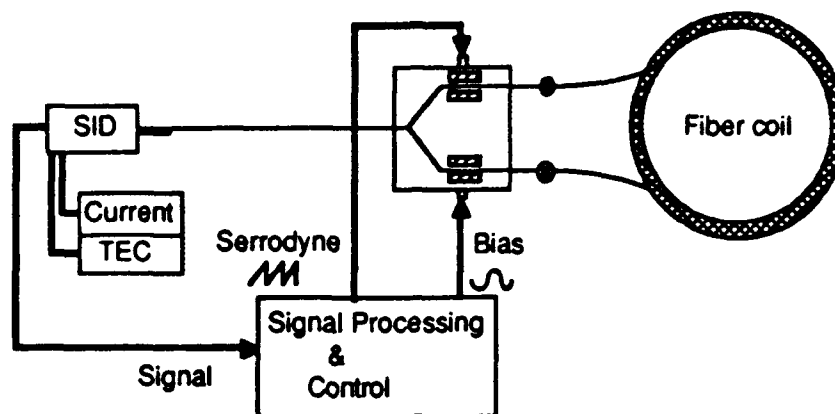


**Figure 1. IFOG With SID and X-Cut Integrated "Y" Junction Optical Circuit.**

The SID uses a low coherence optical source to minimize coherent noise. The SID module combines the optical source and photo detector and associated optical splitting without the penalty of the 50/50 coupler. The output of the SID is coupled into the integrated optic circuit (IOC) for optical processing.

The IOC splits the light into two components, one for CW one for CCW propagation. It provides electro-optic signal processing for optimum rate detection sensitivity and provides mode filtering to minimize noise effects. The wave guides on the IOC are inherently single mode and single polarization. The "Y" junction wave guide splits the input light into the clockwise (CW) and counterclockwise (CCW) waves both passing through IOC modulators.

The outputs of the IOC are fed into the two ends of the fiber coil and circulate in opposite directions. After the light waves pass through the fiber coil, they reenter the IOC, pass through the electro-optic modulators, recombine at the Y-junction and are coupled back into the SID module. The light is directed onto the detector and used to extract the phase information proportional to the input rotation rate.

The signal processing electronics detects the modulation signals on the optical signal providing control signals to the IOC's electro-optical serrrodyne modulator. With no rate input, the serrrodyne modulator introduces no frequency shift into the counter propagating beams. When a rate induced phase shift is present the serrrodyne modulator raises or lowers the frequency of the counter propagating beams (thereby adjusting their accumulated phase) to null out the Sagnac induced phase shift.

The synchronous detection feature that is provided by the sinusoidal bias modulator results in a more sensitive output less susceptible to  $(1/f)$  flicker noise. The closed loop operation that is achieved using the serrrodyne modulation provides a wide dynamic rate range capability with improved scale factor stability and linearity.

#### Source - detector module ( SID )

The SID combines the optical source, photo detector and optical coupler functions into a single compact module. By eliminating one of the standard IFOG's two couplers, substantial optical power savings (6 dB) are realized. The design of a SID is shown in Figure 2.



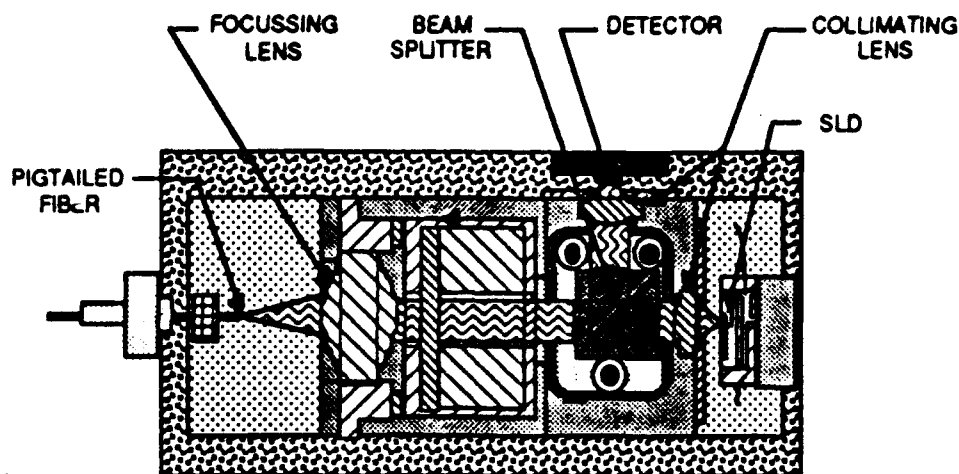


Figure 2: SID Configuration.

The output from a broad band superluminescent diode ( SLD ) source is collimated by the first lens then fed through a polarizing beam splitter ( PBS ) and a Faraday rotator. The PBS transmits the desired polarization reflecting the unwanted polarization to a beam dump. The transmitted polarization is rotated 45 degrees by the rotator and focused by a second lens into the output fiber. After transiting the IOC and fiber coil the return optical beam reenters the SID and is now collimated by the second lens. The rotator rotates the polarization an additional 45 degrees so that it is now orthogonal to the original beam and is reflected by the PBS onto the photodetector. This configuration not only saves 6 dB over the standard approach but also serves to isolate the source from feedback maintaining the quality of its output.

### Integrated Optics Circuit

The integrated optical circuit (IOC) is fabricated in x-cut lithium niobate (  $\text{LiNbO}_3$  ). The overall geometry of the device is shown in Figure 1. The wave guide pattern is delineated using an aluminum diffusion mask and the waveguides formed using a proton exchange process followed by high-temperature anneal. The y-branch power splitter uses an abrupt bend with a  $1^\circ$  half-angle with the output arms separated by  $250\mu\text{m}$ . The total device length is 40mm. The end faces of the device are angled at  $10^\circ$  to reduce back-reflection. The fiber end faces are angle polished to  $15^\circ$  to maximize coupling and individually aligned for power throughput and polarization cross-talk. Fiber pigtails are attached using UV-curable adhesive.

### Gyro Electronics

The control loop architecture for FORS is similar to that for a spinning wheel gyro, the difference being mainly in the outputs. As with any interferometric device, the output from the photo detector is the sum of a DC component proportional to the average optical power incident on the detector and an AC component proportional to the phase difference  $\phi_d$  between the gyro's two counter propagating waves. This phase difference is the sum of three components, a rotation-induced Sagnac phase difference and two phase differences added by the gyro IOC's electro-optical phase modulators one for bias and the other a serrodyne frequency shift. The bias phase modulation is analogous to the mechanical gyro's signal generator excitation and the

serrodyne phase modulation provides a feedback phase shift analogous to the rebalance torque generator. After the DC term is removed, the photo detector output is synchronously detected via full-wave demodulation with the bias modulation reference. The synchronously detected output is then proportional to the sine of  $f_d$ . The control loop electronically drives the serrodyne plates on the IOC to null the loop, i.e., force  $f_d$  to zero. In the nulled condition, the phase differences induced by the Sagnac effect and the serrodyne signal exactly balance each other; hence, the incremental angle of rotation about the gyro's input axis is proportional to the serrodyne phase shift. Angular rate input to the gyro is proportional to the slope of the serrodyne signal.

### Brassboard Gyro

We have made and tested three brassboard gyros. All use 1 km of PM fiber configured in a 6.8 inch diameter coil, a lithium niobate IOC and commercially-available 1300-nm ELEDs and PINFETs for the source and detector. A fused PM fiber coupler is used for the input 3 dB splitter. Figure 4 is a picture of FORS Gyro Brassboard #3 (GB #3) for which test results are reported in the rate table testing section.

The fiber coil form was configured to hold a minimum of one kilometer of  $250 \pm 15 \mu\text{m}$  diameter fiber optic cable. In order to reduce thermal gradients, the coil form was made from aluminum and the coil was "quadrupole wound."

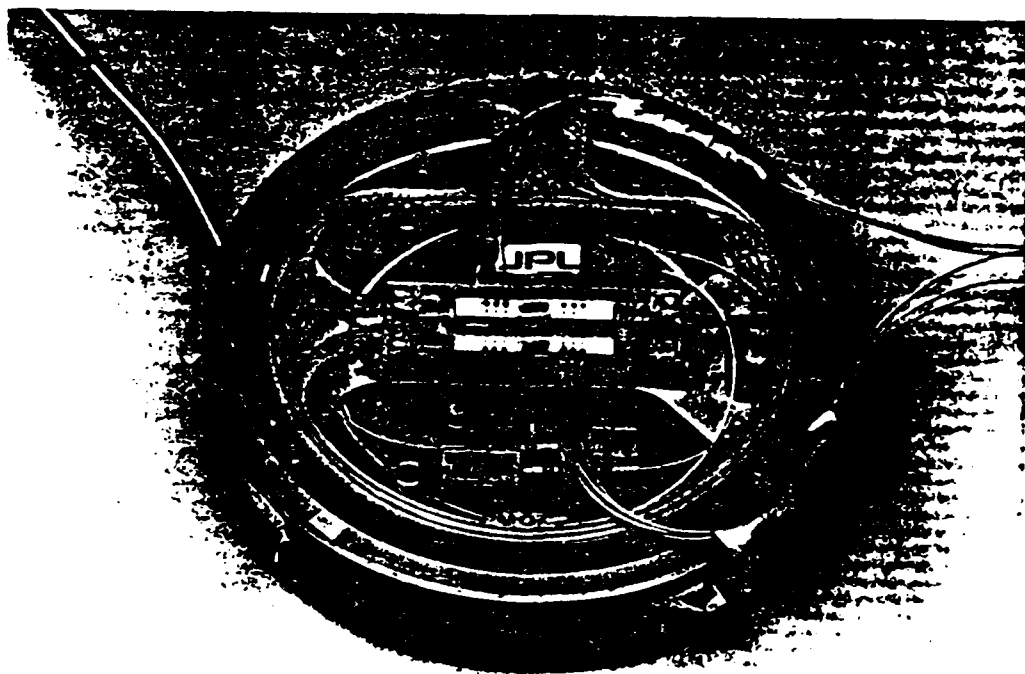


Fig. 4. Gyro Brassboard #3.

Inside the coil form, a center web made from "torlon," a graphite impregnated plastic is used. This web is strong yet lightweight and a very good thermal insulator. The IOC and fused coupler are mounted on the top side of this web, insulated from thermal inputs from the gyro related electronics mounted on the reverse side. The two optical components which dissipate heat, the edge light emitting diode (ELED) and photo detectors, are isolated from the web member and heat sunk directly to the electronic circuit board and its heat sink plate. The finished gyro is then covered with a "mu-metal," magnetic shielding cover and placed in a thermally controlled enclosure.

An Engineering Model Gyro (EM #1) has been built that incorporate a more robust mechanical design directed toward meeting the spacecraft environmental requirements as well as incorporating the SID replacement for separate source, detector, and coupler. The first of these instruments is planned to be under test in June of 1993.

The initial testing of this instrument will focus on the gyro noise characteristics followed by a series of drift and scale factor measurements. Analysis and component testing indicate that with the reduced losses in the engineering model and the higher power optical source, the ARW should improve by approximately a factor of 3.

Bias and scale factor of this engineering model should also reflect improvement due to the improved thermal design and optical improvements.

After the completion of the performance testing, the instrument will enter thermal control capability and sensitivity testing. This instrument incorporates internal thermal control as well as thermal isolation of the components that are most sensitive. The brass-board instrument had no temperature control or isolation; all testing was performed with the gyro in a temperature controlled enclosure.

A second engineering model (EM #2) instrument is currently planned to be built identical to EM #1. After a nominal test sequence to verify performance characteristics, this instrument will undergo an environmental testing. Of primary interest is the survivability and performance over vibration.

## COMPONENT QUALIFICATION

Draper, in conjunction with JPL, is in the process of addressing optoelectronic component lifetime and reliability issues. The end result will be analyses, test data and a component qualification plans for space qualified optical components for the FORS. Two questions are being addressed: (1) can the components survive in the space environment, basically a packaging question, and (2) will the components continue to meet the required specifications for the mission lifetime. This is a performance question, i.e., how will the environmental conditions and the mission length effect the performance.

### Source/Detector

Reliability issues for the SID involve both the source and detector dies and the packaged assembly. Plans for the LED source and pin photo detector chips include

both an experimental determination of the lifetime of the devices and radiation tests while the devices are under life test.

Lifetime tests performed on the unpackaged chips will subject the devices to high temperature accelerated aging. The dies will be characterized weekly. Relevant specifications for system performance (i.e., optical output power, emission spectrum for the LED and dark current for the detector) will be monitored to insure that the dies continue to meet system requirements. A device failure is defined as the inability to meet one of the above specifications. Based on the number of failures and an estimation of the activation energy, one can use the Arrhenius relationship and the log normal distribution to calculate lifetimes at system temperatures.

Environmental testing examines the effect of space environmental conditions, primarily radiation, on the lifetime and specifications of the chips. The unpackaged devices will face gamma, electron, and proton radiation and then be placed on life testing.

### Fiber and Coil

The prime concern in the qualification of fiber is lifetime prediction. The failure mechanism of fibers under the action of stress and environment has been studied extensively with significant data available as telecommunications grade fiber. The FORS uses polarization maintaining Panda fiber with limited data pertaining to strength. We have initiated specific lifetime and reliability tests to perform a complete strength and mechanical analysis of the Panda fiber. The data generated from this analysis will enable lifetime predictions to be made under the full range of conditions of stress and environment.

An equally important fiber reliability issue is handling during the coil winding operation, gyro components and gyro build process. Damage sustained by the fiber during any of these operations greatly reduces the life expectancy of the gyro. Draper has reviewed the handling procedures used by component vendors and is working with them to develop a set of safe fiber handling practices. For some components, a strength/mechanical analysis will be performed to generate a lifetime prediction model for the fiber pigtail. For the coil, the winding process will be qualified by doing an analysis on fiber that has been subjected to the winding process.

Since splices are necessary to build the gyro, it is important to recognize that special procedures must be used in order to assure a high strength splice. The use of stripping tools and/or other mechanical coating removal methods can weaken the fiber by as much as an order of magnitude. In addition, the quality of the cleave, cleanliness of the fiber, the splice machine and the environment in which the splice is made have an effect on splice strength. The fiber industry has developed high strength splice processes for use with standard telco fibers and have documented the factors that affect splice strength. Draper is developing a similar process to achieve a high strength splice with Panda fiber.

In addition to reliability, there are issues concerned with optical performance over a range of environmental conditions. Tests are underway to characterize the coil under temperature, mechanical shock, and vibration. Radiation effects is one of the most important considerations. Radiation tests on the Panda fiber are now underway at JPL. The fiber will be characterized for attenuation and polarization maintenance (cross-talk) as a function of dose.

### IOC

Possible IOC component failure modes can be grouped into two categories: material related failures in proton-exchanged lithium niobate and adhesion related failures at the material interfaces. We have initiated a series of experiments and analyses to address both principal material failures, e.g. micro-crack propagation, proton diffusion, inter-diffusion of metals in IOC electrodes, and failure of wire bond, adhesive, and solder materials, and interface failures, e.g. loss of adhesion at the fiber-IOC, IOC electrode de-lamination, loss of wire bond adhesion, and loss of adhesion at mounting surfaces.

The potential for material failure is being addressed through a series of material and accelerated aging studies. For example, intrinsic or process induced defects in lithium niobate can act as initiation sites for micro-crack propagation. The crack size and velocity of crack growth will be determined from fatigue testing. The mobility of protons in the lithium niobate at mission temperature will be determined using Secondary Ion Mass Spectrometry (SIMS) which measures hydrogen concentration vs. depth. Movement of hydrogen will be measured after accelerated aging at several elevated temperatures, in order to accurately determine the activation energy for proton diffusion.

We have begun accelerated aging studies on unpackaged IOC devices. Any degradation of IOC performance after exposure to elevated temperature and radiation will be correlated to lifetime using the experimentally determined activation energies for proton and metal diffusion. The SIMS studies will provide the proton diffusion activation energy, and the metal inter-diffusion activation energies will be determined from profiles of the electrode composition, taken at different aging temperatures.

Adhesion failure is a critical reliability issue. In particular, the reliability of the fiber-IOC butt joint must be established because of the vulnerability of the butt-joint and lack of lifetime data in the literature. Accelerated aging of the joint will be done by applying elevated temperature and humidity to test samples. Sensitivity of the joint to environmental factors such as thermal cycling, shock, vibration, and radiation will be investigated. Both thermal cycling ( $-50^{\circ}$  to  $+150^{\circ}$  C) and static mechanical loading ( $>6000$  G) have been applied to similar pigtailed without failure. Environmental testing will eventually be performed on devices that have been aged at an accelerated rate.

## RATE TABLE TESTING

Considerable rate table testing of the FORS brassboard gyros has been performed and the results have been reported in previous papers. We summarize the results and present the latest results on angle random walk. Performance tests on the FORS brassboard gyro were designed to demonstrate the capability of this instrument to meet the performance requirements in the three defined regimes (Table 1). In particular, the tests were geared to obtain bias and scale factor data in a laboratory environment.

### Bias Drift

Bias drift tests on the instrument were normally overnight (15 hours) and long weekend runs. The gyro axis was oriented vertical parallel to the rotary table axis. Gyro data and monitor signals (i.e., temperatures, voltages, etc.) were

simultaneously sampled and stored to disk in real-time. Allan variance analysis and time plots were used to determine gyro drift uncertainty as a function of averaging time. Gyro rate data was integrated to form angle data, and these data analyzed for pointing accuracy.

### Scale Factor

Scale factor tests were performed over the range of  $+2.5^\circ/\text{s}$  to  $-2.5^\circ/\text{s}$  about the gyro's input axis. High resolution gyro output data was acquired simultaneously with various monitor signals at each one degree table increment. Data from a full rotation of the table is acquired at each rate, for a total of 360 points per rate. From this data, bias and the angle scale factor magnitude (pulses/degree of table rotation) and their uncertainties are determined.

A summary of the performance parameters that were measured is contained in Table 3. This table also lists the performance levels required for the space craft mission described earlier. As can be seen from this table, the current performance of the brass board instruments is consistent with the requirements of the space mission.

Parameter	Measured (1 s)	Requirement (1 s)
Demonstrated pointing error :		
0.5 seconds	$< 1 \mu \text{ rad}$	$1.5 \mu \text{ rad}$
2 hours	$< 50 \mu \text{ rad}$	$333 \mu \text{ radian}$
Scale factor stability (day to day)	$< 10 \text{ PPM}$	$28 \text{ PPM}$
Scale factor stability (2 hour stability)	$\approx 1 \text{ PPM}$	
Bias Stability (2 hour integration)	$< 0.002 \text{ deg/hour}$	$0.005 \text{ deg/hour}$
Angle random walk	$0.0010 \text{ deg}/\sqrt{\text{hour}}$	$0.0025 \text{ deg}/\sqrt{\text{hour}}$

Table 3. Measured vs. Required Performance (1 sigma values)

Bias stability has been demonstrated to be essentially the same on all three brassboard instruments and scale factor testing has been performed on two brassboards. Both instruments tested for scale factor stability have produced similar results.

Recent investigations utilizing these instruments have focused on the angle random walk (ARW) capability of the brass-board gyro and the possible performance enhancements to be realized when an engineering model instrument is completed in May 1993. These tests indicated that the instrument is shot noise limited and the

nominal current capability of the brass-board instrument is  $1.0 \times 10^{-3} \text{ }^\circ/\sqrt{\text{hr}}$  or  $4.0 \times 10^{-3} \text{ (}^\circ/\text{hr)}^2/\text{Hz}$  (see figure 5).

## CONCLUSIONS

Laboratory test results achieved to date have demonstrated the viability of FORS technology meeting the high performance goals of NASA's interplanetary spacecraft applications, e.g. the Cassini mission to Saturn. Gyro electro-optic components technology needed for these inertial instruments exists in the marketplace and is being strongly driven by the needs of the communication industry. Developmental funds are presently being allocated and work undertaken to refine some packaging issues so that they can operate over the planned long life missions (>16 years). Plans are to verify an engineering model FORS instrument not only in a laboratory environment but through the contemplated operational environmental disturbances and to develop a plan for the space qualification of the optical components.

## Acknowledgments

We acknowledge the significant contributions of the technical team responsible for the results of this program particularly M. Fontanella, P. Ward, N. Sarma, and D. Goodwin of Draper Lab and L. Dorsky and B. Youmans of JPL.

This activity has been supported by funding from NASA and Draper IR&D.

**SESSION VI-B  
STELLAR SYSTEMS**

***CHAIRMAN***  
**FERDINAND F. KUHN**  
***SYSTEC***



**THIS PAGE LEFT BLANK INTENTIONALLY**

# Test and Evaluation Aspects of Integrated Pointing and Tracking Systems for Future Manned Space Flight

Alfred Anderman  
Rockwell Space Systems Division  
12214 Lakewood Blvd., Downey, CA, 90241

## Abstract

Test and evaluation aspects of implementing precise pointing and tracking capabilities for the proposed NASA Advanced Manned Launch System/ Personnel Launch System (AMLS/ PLS) are presented in this paper. Alternate combinations of sensors are considered, with special reference to autotrack, autoland, space rendezvous, berthing, and docking techniques. Integrated INS/GPS sets, using GPS in the differential or relative mode, can save weight and power in future vehicles, and eventually eliminate the need for MLS and/or rendezvous radars. Integration of the Navstar GPS and the GLONASS systems is technically feasible. This was demonstrated by the development of integrated GPS/GLONASS receivers, with increased availability and reliability of the combined satellite system, to meet FAA and ICAO commercial aviation safety requirements.

Both the US Global Positioning System (GPS), and the CIS Global Navigation Satellite System (GLONASS) will provide users with consistent global coverage position fixing. However neither system, by itself, can be certified as a sole source navigation system because not enough satellites will be in view of vehicular receivers at any one time to satisfy the requisite redundancy and system monitoring standards of the FAA and ICAO. A hybrid receiver using signals from the combined satellites of both GPS and Glonass will overcome the coverage shortage of either system.

Alternately, the NASA/GSFC developed Tracking and Data Relay Satellite System (TDRSS) Onboard Navigation System (TONS) will provide another potential source of onboard knowledge of high-accuracy navigation products to users of the TDRSS and its successor, TDRSS-II, autonomously, using only fixed-frequency forward-link TDRSS signals.

Besides providing high accuracy position data, GPS, using interferometric differential carrier doppler phase measurements, can also provide an attitude reference of accuracy compatible with the flight control system. Star trackers capable of providing attitude precision measured in arc-seconds may be required for optical telescope pointing. However 10-minute attitude accuracies are adequate for most manned space vehicles and their payloads, for flight control and uplink/downlink antenna-pointing at least up to S-Band frequencies. Summaries of flight and simulation test results of GPS-based attitude measurement accuracies are included in the paper.

## INTRODUCTION

NASA, in consultation with representatives of the space launch and satellite industry, is designing a program for support of research into launch system component technologies to achieve higher performance and lower costs of delivering payloads into orbit. The report of the Commercial Space Transportation Advisory Committee (COMSTAC) specifically recommends the use of "low cost GPS based guidance". One nanosecond of time error is equivalent to 30 cm of range error, so that precision timing and frequency control available to GPS navigation can be integrated into the avionics system for other functions.

The complexity of future mission control systems can be significantly reduced by integrating GPS into telemetry, tracking and command (TT&C) to maintain accurate time, frequency, and ephemeris, and into guidance, navigation, and control (GN&C) to maintain accurate attitude, location, and tracking. Any application requiring access to Coordinated Universal Time (UTC) can be served, including telecommunications, space tracking, antenna pointing, electronic intelligence, metrology, navigation, and data acquisition.

## TEST & EVALUATION ASPECTS OF POINTING AND TRACKING

Test and Evaluation are essential components at every stage of any major development program, not only in DESIGN DECISIONS early in the cycle, in FUNCTIONAL FLOWS for mission scenarios, but also THROUGHOUT THE LIFE CYCLE, for managing risk, as illustrated in Figures 1- 3 respectively.

## **FUTURE MANNED TRANSPORTATION & SPACE SHUTTLE GPS TEST PLANS**

Future manned space transportation will probably depend on a mix of vehicles, as indicated in Figure 4. On-going NASA studies have resulted in preliminary designs of Advanced Manned Launch Vehicle (AMLS) and Personnel Launch System (PLS), while anticipating continued use of the Shuttle Fleet through the first quarter of the 21st Century [16]. A comparison of vehicle sizes is shown in Figure 5.

The Shuttle on-board real-time computations can benefit from GPS for accuracy of vehicle state vectors, spacecraft navigation, satellite delivery, experiment positioning, resource mapping, payload deployment and retrieval, propellant economics, data processing, and mission planning, including functions requiring pointing and tracking.

Space Shuttle bridging plans call for GPS Developmental Flight Test (DFT) during 1993, and for Shuttle Fleet retrofit with GPS during the 1990s. The DFT flight profile will include ascent and two initial orbits, and also orbit, deorbit burn, and entry through touchdown, as shown in Figure 6. There are no present plans to add GPS attitude correction to the list of additional "Shuttle Evolution" functions, primarily due to integration complexities, although there is the potential for eliminating the need for star trackers. GPS and non-GPS attitude determination accuracies are compared in Figure 7 [15].

## **EXISTING AND POTENTIAL SHUTTLE AVIONICS CAPABILITIES:**

### **1. ONBOARD PRECISE TIME & FREQUENCY REFERENCES**

The Space Shuttle stable crystal-controlled master timing unit provides a serial time reference to the onboard computers, and other subsystems, with stability better than 1 part in  $10^9$  per day long term, and  $10^{10}$  short term, but requires 72 hr. stabilization time after power-off at 35 deg. F.

GPS time, determined by the USNO Master Clock (MC), can provide UTC(USNO) time to within 100 ns, after correcting for the difference from UTC by an integral number of seconds. GPS system time is on a continuous time scale, referenced to midnight 5 Jan 1980, whereas UTC and GLONASS time contain leap seconds to allow for the deceleration of the earth rotation. This number is provided as part of the navigation message, because it changes every time there is a leap second. GPS onboard time can also provide ephemeris for antenna pointing and target tracking.

### **2. NAVIGATION PERFORMANCE**

Three-sigma position and velocity errors at main engine cutoff (MECO) of about 4600 ft and 20 ft/sec could be updated in the post-MECO state to about 100 ft and 0.6 ft/sec in about 2 minutes, using GPS.

On-orbit TDRSS provides adequate state vectors using two-way range rate (Doppler) data through both satellites within one revolution, in about 60-90 minutes. With only one relay satellite available, the 1.5 pass minimum tracking interval is about 115 minutes. An integrated time line suggests that 120-195 min. are required from the start of tracking to maneuver execution. With a full GPS constellation the state could be determined within about 2 minutes, as for the post-MECO state. Updating and resetting externally requires use of the data processing system.

For ground entry navigation, using C-Band radar, the mission control center (MCC) updates onboard knowledge of position after blackout at about 150 kft. altitude. GPS could provide accurate post-blackout navigation capability to about 200 ft and 1.2 ft/sec, or much better in differential mode.

### **3. PRECISE EPHEMERIS INFORMATION**

Precise ephemeris data is important onboard for mission success, status monitoring, also for rendezvous and docking. TDRS measures to better than 100 m accuracy, but does not give instantaneous position fixes, as does GPS. Presently time measured in hours is needed for the ranging data to be processed on the ground to obtain or update orbital ephemeris elements. In low earth orbit, unpredictable atmospheric drag is the largest limit on prediction. Continuous onboard filtering and orbital element updating based on GPS can eliminate ground-based tracking and processing and reduce communications bandwidth.

#### 4. TDRSS ONBOARD NAVIGATION SYSTEM (TONS)

TONS, under development by NASA/GSFC, is claimed to provide one-sigma orbit determination to 10 m, time to 1 microsec, and frequency to 1 in  $10^{12}$  via onboard extraction of tracking measurements from a forward signal by augmenting the transponder with an ultrastable onboard oscillator, as an alternative to the current ground-based orbit, frequency, and time determination. This technique is claimed to involve lower cost, power, weight, and volume impacts than GPS, primarily for small low earth orbit satellites, but there are no present plans for use on manned vehicles.

#### ATTITUDE MEASUREMENTS

##### 1. SPACE SHUTTLE INTEGRATED IMU/STAR TRACKER ATTITUDE CONTROL

Star trackers (STs) are used to align the inertial measurement units (IMUs), can provide attitude precision measured in arc-seconds and are required for optical telescope pointing. However arc-minute attitude accuracies are adequate for most manned space vehicles and their payloads, for flight control and uplink/downlink antenna-pointing at least up to S-Band frequencies.

Enhanced GPS can eliminate the need for redundant star trackers, with all the complications imposed by optical windows and the associated accessories. Space Shuttle accessories include 1) Light shade assemblies defining the field-of-view (FOV) of the tracker, 2) Shutter mechanisms, automatically opened/closed by 3) Bright object sensor, to prevent damage by an object such as the sun or moon, and 4) Redundant electric motors for door-opener mechanisms.

##### 2. ATTITUDE BY INTERFEROMETRY

GPS interferometric attitude measurement accuracies, using three or four antennas, are dominated by the noise of the carrier tracking phase lock loop (PLL) of the GPS receiver. Some error sources, contributed by 1) GPS receiver, 2) GPS satellite, 3) GPS satellite ephemeris, 4) Common mode multipath, and 5) Selective availability effects, can be removed through differencing techniques. New approaches to remove phase ambiguity and cycle slip errors, as recently verified by C. S. Draper Labs and elsewhere, could enable considerable commonality to be achieved between navigation and flight control sensors.

From measurements using the precisely known antenna phase-center locations in the user vehicle, most recently the following interferometric GPS attitude determination techniques have been used: 1) "Carrier Doppler Phase Difference", on orbit assuming periodic attitude variations, 2) "Phase Time Triple Difference" on orbit, as well as 3) "Thrust Vector Determination" during powered flight, and 4) "Ambiguity Modeling", treating carrier cycle ambiguity as a continuous valued random bias to be estimated by statistical filtering of GPS carrier phase measurements augmented by an integrated INS.

Phase ambiguity and cycle slip error removal was pioneered by C.S. Draper Labs [5] but until recently, the smoothing of GPS attitude data was considered "troublesome" [2]. Shipboard experiments on the USS Yorktown gave 2, 5.5 and 7 degree accuracies in azimuth, pitch, and roll respectively, using 60cm baselines. Extrapolating to a 25 m baseline, the azimuth value would drop to 0.1 degree, 1-sigma.

Approach 1 simulation used by Texas Instruments [14], resulted in 0.2 and 0.26 mrad Space Station and Space Shuttle smoothed attitude errors respectively, using 5m baselines, 7 second averaging, an assumed 40 dB-Hz carrier to noise power ratio, 3 dB receiver noise figure, and 7 Hz carrier loop tracking bandwidth. Phase errors caused by multipath reflections were modeled, but all other error sources were assumed to cancel in the double differencing process.

The assumed periodic attitude variation results in angular measurement errors inversely proportional to averaging time. Straight lines of negative slope in Figure 8 represent "constant averaging time" lines under this assumption, as shown in Figure 9 [13].

Azimuth pointing information of 1.2 mrad accuracy for aiming field artillery was also obtained, using Approach 1, a commercial receiver, 0.84 m baseline, and 300 seconds integration time, by Adroit Systems, for the U.S. Army Engineer Topographic Labs. [10].

ESA ESTEC Radio-Navigation Test Bed Laboratory used Approach 2 and two commercial GPS C/A code receivers and 2m fixed platform baselines, getting 2 mrad attitude accuracies relative to the baseline [13].

"Phase Time Triple Differences" were measured in General Dynamics space transfer vehicle GPS/INS studies [11]. Carrier phase "single difference" measurements from two antennas eliminates satellite clock

error source. The "double difference" for two satellites eliminates receiver error sources such as receiver clock error. The "triple difference" for two different time instances resolves carrier cycle ambiguity between measurements from the two antennas to a satellite, by extending the single, double and triple difference measurements to four satellites, and solving sets of simultaneous equations.

Assuming 2 mm carrier phase measurement accuracy, calculated pitch/yaw theoretical maximum attitude accuracies were 0.27 & 1.29 mrad for 7.2 & 1.5 m baselines respectively. Under worst-case error assumptions, RSS'ed with carrier measurement errors, attitude accuracies degrade to 0.29 & 1.38 mrad respectively. Ambiguity resolution time, of the integer carrier cycles, solving simultaneous equations, using Least Squares Estimate (LSE), exceeds 100 seconds.

Approach 2, used by Ashtech Inc. in the 3-dimensional direction-finding (3DF) 24-channel GPS Attitude Measuring System gave calculated attitude angles of 1 mrad accuracy for 1 m spacings, and determined phase ambiguities using 4 antennas, and at least one epoch of data from 4 satellites, in a double differenced carrier phase search algorithm [7].

Approach 3 was used by Mayflower Communications Co in a MSFC sponsored Orbital Maneuvering Vehicle (OMV) study that showed that pitch and yaw attitude determination required a single roll axis thrust, but that thrusting in more than one direction is required for 3-d attitude determination, preferably near orthogonal. For a 45 milli-"g" thrust, an 8 mrad accuracy required 200 sec. averaging time [11].

In Approach 4, as used by Mayflower Communications Co.[17], instead of search algorithms resolving cycle ambiguities, each ambiguity modeled as a random process is included as a statistical filter error state, with integer constraints, guided by residual/variance threshold monitors. Orientation is obtained by interpreting baseline-difference phase measurements as orientations of antenna baselines relative to line-of-sight vectors.

With zero body rotation in inertial space, attitude estimation depends on the antenna baseline motion relative to the received satellite line-of-sight, and is only that caused by the relative orbital motion between the GPS satellite and the user space vehicle. Performance was improved by means of a second-order approximation to a higher order nonlinear

filtering algorithm, a Modified Gaussian Second-Order (MGS) Filter, instead of the more commonly used Extended Kalman Filter (EKF). Simulations resulted in attitude error reductions from 90 to 5 and 1 mrad using the EKF and MGS algorithms respectively, at 3 mrad/sec attitude rotation rates in 100 seconds, using 1.4 m antenna baselines [17].

### 3. INTERFEROMETRY ATTITUDE ERRORS

Results reported in the various simulations, and in some test programs, are shown approximately in Figure 10, superimposed on the "GPS attitude error versus antenna base vector length" chart, previously used in Figures 8 and 9. Some are test points, while others represent simulations with different noise assumptions, but they do provide a graphical overview.

The basic interferometric observables are the doppler phase differences between various antenna phase centers, with respect to the local oscillator time reference, using measurements from two carrier tracking loops. Correlated local oscillator phase common mode noise cancels out in difference measurements.

Similarly errors common to each GPS satellite cancelled by differencing the phase measurements between two different antenna phase centers include clock and ephemeris radial prediction errors, short-term oscillator noise, and highly correlated ionospheric errors for closely spaced antenna phase centers.

Both the antenna phase-center determination and signal jitter on board the GPS satellites are not regarded as the major error sources, provided the physical structure for measuring attitude is sufficiently symmetrical, using identical antenna elements and symmetrical alignment and mounting.

With 3 antennas mounted on a rigid structure, the relative positions determine 3-dimensional attitude. Using 4 antennas differential phase ambiguities can be removed. Other major error sources, including receiver clock error, satellite clock error, low levels of satellite ephemeris error, common mode multipath, and effects due to Selective Availability (SA), can also be removed by the differencing techniques [7].

The remaining attitude determination errors are functions of geometry, baseline length, multipath, number of satellites visible, and also dynamic/kinematic effects. The feasibility of achieving the simulated

GPS attitude determination results, as briefly summarized above, operationally by successfully interfacing GPS into an integrated INS/GPS GN&C system, remains to be verified in flight tests. However Space Shuttle Developmental Flight Test (DFT) objectives exclude validation of GPS attitude determination.

## DIFFERENTIAL GPS USAGE

The GPS signal basic coarse/ acquisition (C/A) code was intended for commercial, and the encrypted precise (P) code for military, users, but receiver resolution equivalent to P-code can be obtained by use of a ground-based transmitter in a precisely known position, a "pseudosat", which can also eliminate most selective availability (SA) effects.

When only relative position and velocity information is of concern, such as for landing or space rendezvous, differential GPS use only requires "pseudosat" positioning to tape measure accuracy from a reference point. The two basic ways of processing GPS data to determine the relative position of two users: 1) "independent" and 2) "simultaneous" processing method, are shown in Figure 11.

## SPACE STATION RENDEZVOUS AND PROXIMITY OPERATIONS

Rendezvous, docking, and other proximity operations will require the Space Station to function as a traffic control center for enroute, terminal area, and approach control. Representative future control zones, and ranges of application of different relative motion sensors, are shown in Figure 12. A star tracker is used for far field sighting and a rendezvous radar at smaller distances. GPS receivers on both the Space Station and approaching manned vehicles will allow autonomous capabilities by providing more accurate and updated proximity information using the differential GPS mode.

Recent analyses and simulation studies have shown that the "0.1% rule" (range rate equal to 0.1% of the range) used by the Space Shuttle is overly conservative, and considerably reduced docking times and costs can be achieved by the use of differential GPS, supplemented by either laser or other electro-optical docking devices, or by manual docking procedures optimized for human factors.

## TEST AND EVALUATION FACILITIES

Special facilities essential to the development of new or improved avionics, include the Shuttle Avionics Integration Laboratory (SAIL), providing means for testing both new or modified flight hardware, and flight software (Figures 13 and 14), and the Avionics Development Laboratory (ADL), providing means of testing new components, interconnections, and network protocols (Figure 15).

Also the Bevalac Radiation Test Facility provides for single event effect (SEE) radiation tests at the Lawrence Berkeley Laboratory (LBL). GPS receivers not designed for the space environment were exposed to beams of ionizing radiations to predict the in-flight failure rates due to radiation. Such tests will become of increasing importance as the need for economy makes commercial off-the-shelf (COTS) subsystems and components more attractive.

## SUMMARY AND CONCLUSIONS

For future manned space vehicles, the objective of safety comparable to commercial aviation requires meeting FAA/ICAO requirements for vehicles like the AMLS and PLS. ICAO's GPS integrity monitoring requires use of a) ground-based stations to monitor satellite signals and transmittal of information messages on a GPS Integrity Channel (GIC), via commercial satellites if faulty signals are found, or b) Receiver Autonomous Integrity Monitoring (RAIM), allowing on-board equipment to determine signal integrity. RAIM requires simultaneous reception of four satellites to be certain of detecting a malfunction.

GPS 24-channel receivers, such as the Ashtech 3DF [7], can provide attitude, and can potentially benefit from a combination of the GPS and the Soviet Union GLONASS systems, that are now cooperating to provide civil aviation NAV-AID.

Stand-alone Instrument Flight Rule (IFR) satellite navigation requires a minimum of 6 satellites in view. A hybrid receiver using signals from the combined 48 satellites of both GPS and GLONASS systems, with built-in self-test and fault management, will overcome the coverage shortage of either system, and provide adequate reliability and availability, as well as integrity.

Some of the special Test and Evaluation facilities required for space were also described.

## ACKNOWLEDGEMENTS

The author thanks Carl F. Ehrlich, AMLS/PLS Program Manager at the Rockwell Space Systems Division, and Howard Stone, of the AMLS/PLS Program Office at NASA Langley Research Center, for permission to include Figures 4 and 5, based on NASA Study Contract NAS1-18975[16]. However the views expressed in this paper are for information only, and have not been endorsed by RIC or NASA.

## REFERENCES

- [1] Project Paper 743A, "Global Positioning System Sensor (GPS/GLONASS)", *Aeronautical Radio Inc. (ARINC), Annapolis, MD, 21401*
- [2] Agamata B.N. et al, "A Proposal for a Dynamic Test Platform for Inertial Units and/or GPS", *Proc. ION National Technical Meeting, Phoenix, AZ, January 1991, P. 371-381*
- [3] Anderman A., "Integrated INS/GPS/GLONASS Navigation Aid for Manned Space Flight", *Proc. ION National Technical Meeting, Phoenix, AZ, January 1991, P. 277-286*
- [4] Anderman A., "Integrated INS/GPS Attitude Determination for Manned Space Flight", *Proc. ION GPS-91, Albuquerque, NM, September 1991, P. 161-170*
- [5] Counselman C.C., & Gourevitch S.A., "Miniature Interferometer Terminals for Earth Surveying: Ambiguity and Multipath with Global Positioning System (GPS)", *Trans IEEE on Geoscience and Remote Sensing, Vol. GE-19, No. 4, October 1981, P. 244-252*
- [6] Cox K.J.(Ed), "Proc. Strategic Avionics Technology Working Group (SATWG) Meeting for November 1990", *NASA-JSC, Houston, TX*
- [7] Ferguson K. et al, "Three-Dimensional Attitude Determination with the Ashtech 3DF 24- Channel GPS Measurement System", *Proc. ION National Technical Meeting, Phoenix, AZ, January 1991, P. 35-41*
- [8] Fisher H.L. et al, "Autonomous All-Stellar Attitude Determination Experiment: Ground Test Results", *14th Annual AAS Guidance & Control Conference, Paper AAS-91-025, Keystone, CO, February 1991*
- [9] Garcia T.B., "Space Shuttle Orbiter (SSO) Operational Level C Functional Subsystem Software Requirements (FSSR):- Guidance, Navigation, and Control (GN&C), Part E: Star Tracker Subsystem Operating Program (SOP)", *Rockwell SSD Report STS 83-0014C, 01-20, Vol.2, Downey, CA, August 1990*
- [10] Jurgens R.D. et al, "GPS Azimuth Determining System (ADS) Cycle Resolution, System Design, and Army Test Results", *Proc. ION National Technical Meeting, Phoenix, AZ, January 1991, P. 45-51*
- [11] Keierleber K.D. & Maki S.C., "Attitude Determination for Space Transfer Vehicles Using GPS", *Proc. ION National Technical Meeting, Phoenix, AZ, January 1991, P. 85-101*
- [12] Klemperer C., "Long-Baseline Radio Interferometry", *Proc. IEEE, May 1972, P.600-621*
- [13] Martin-Neira M. et al, "Attitude Determination with GPS: Experimental Results", *IEEE AES Magazine, Vol. 5, No. 9, September 1990, P. 24-29*
- [14] Rath J. & Ward P., "Attitude Estimation Using GPS", *Proc. ION National Technical Meeting, San Mateo, CA, January 1989, P. 169-178*
- [15] RIC85-329, 3-28-85, "Spacecraft Applications of Advanced GPS Technology Study", Vol. 1, Para 2.4: "Attitude Control", *Downey, CA*
- [16] Rockwell SSD, "Personnel Launch System/Advanced Manned Launch System (PLS/AML) Study": a) "AML Final Technical Review", & b) "PLS Hardware/ Software Design Description", *Downey, CA, August 1991*
- [17] Satz H.S. & Cox D.B., "GPS Inertial Attitude Estimation via Carrier Accumulated Phase Measurements and Statistical Filtering of Phase Cycle Count Ambiguity", *Proc. ION National Technical Meeting, Phoenix, AZ, January 1991, P. 289-294*

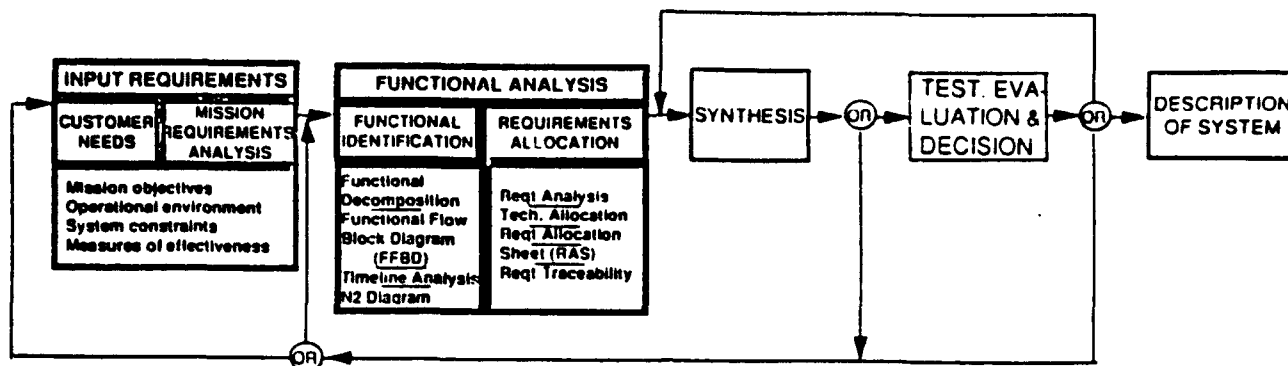


**Figure 1. Test and Evaluation of Pointing & Tracking in Design Decisions (Functional Analysis & Requirements Allocation)**

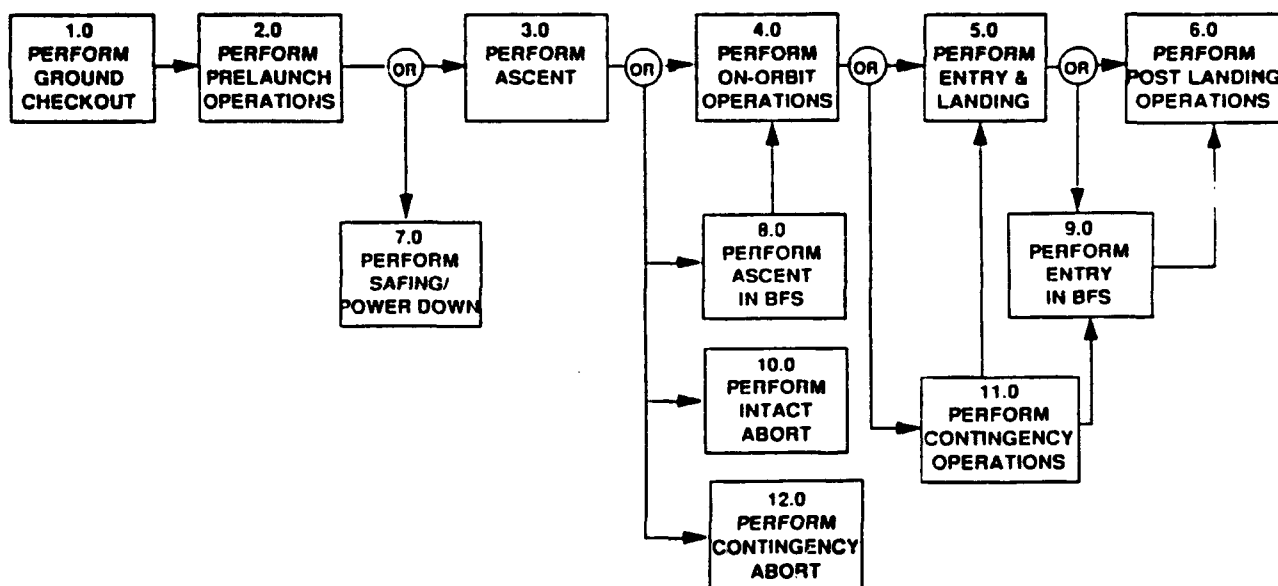


**Figure 2. Test and Evaluation of Pointing & Tracking in Scenario Functional Flow**



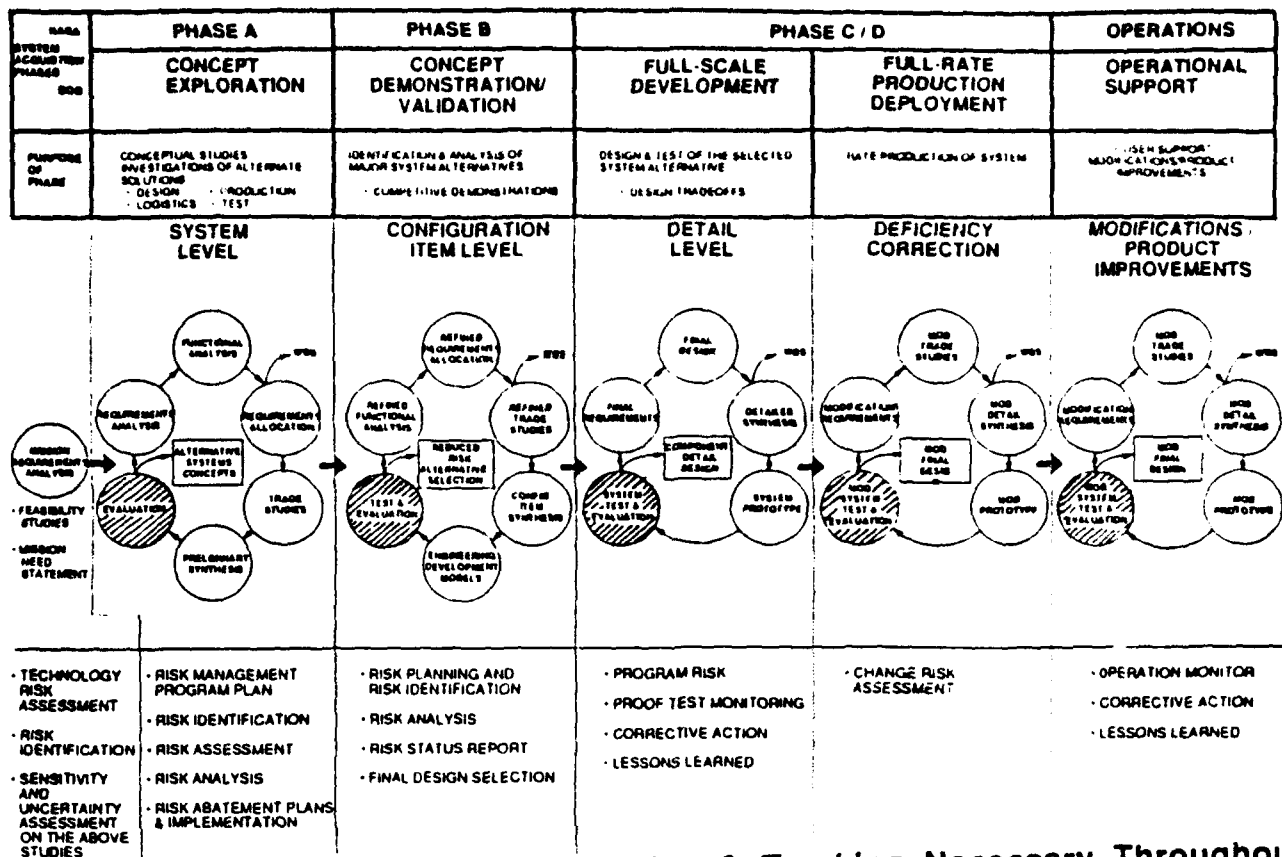


**Figure 3. Test and Evaluation of Pointing & Tracking Necessary Throughout The Life Cycle as Part of Risk Management**

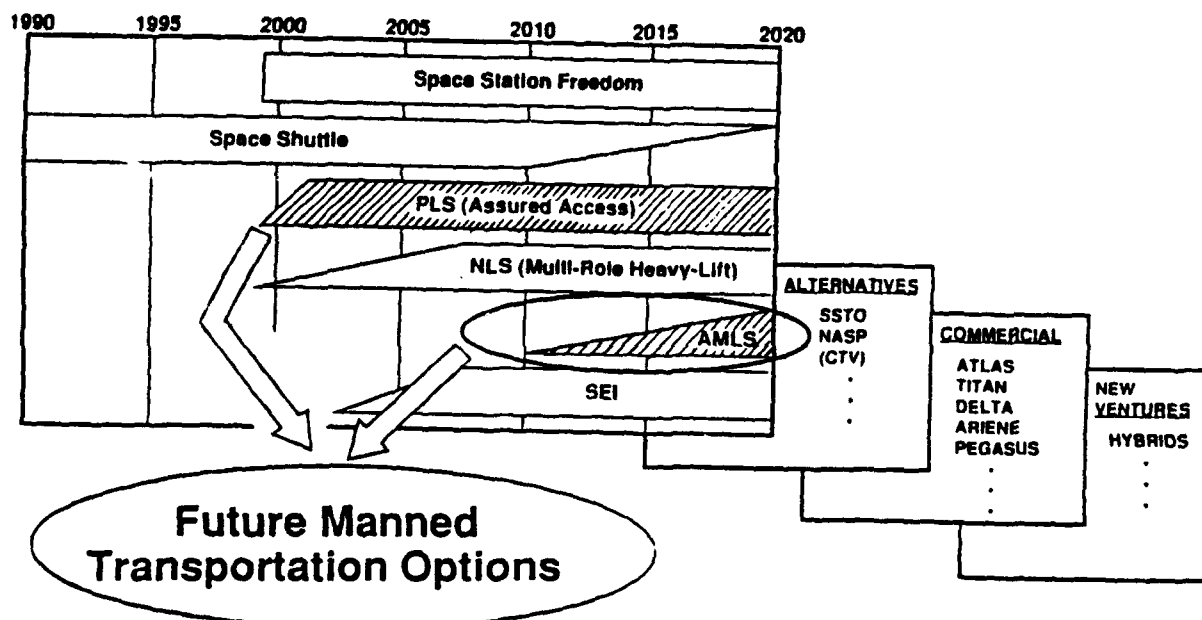


**Figure 4. Role of the AMLS and PLS in the Future Manned Space Transportation System**

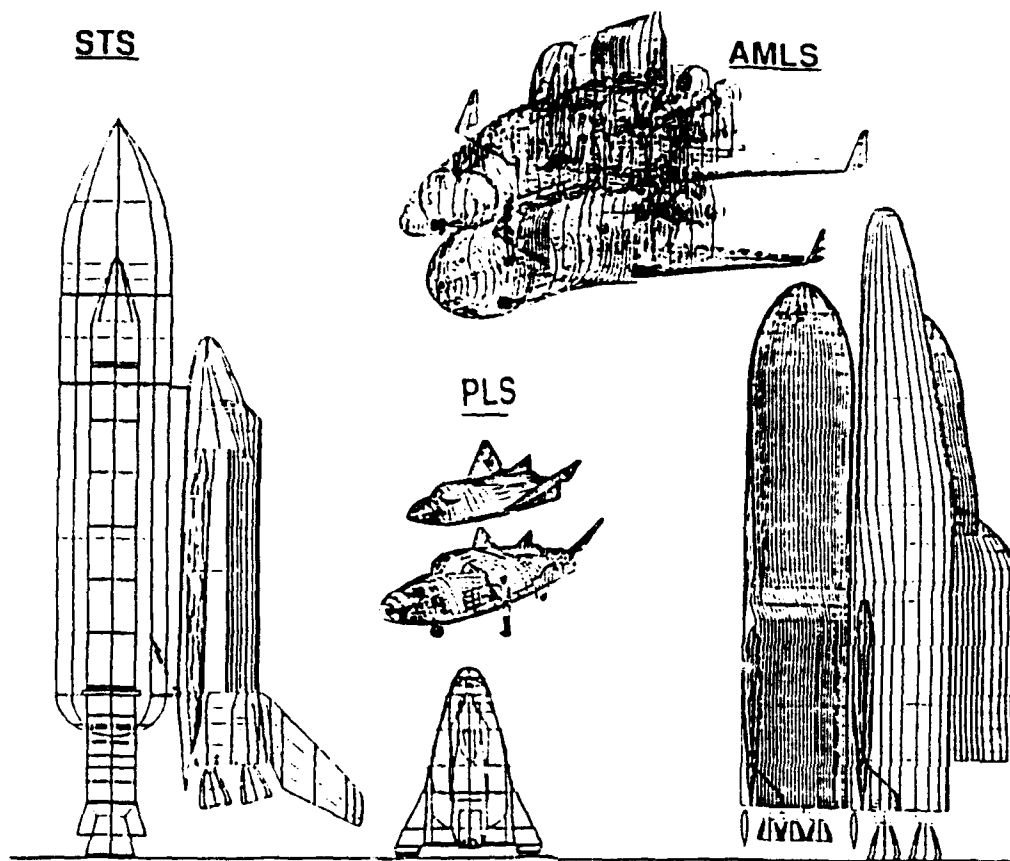


**Figure 5. Relative Sizes of Space Shuttle Orbiter (STS), AMLS, and PLS**

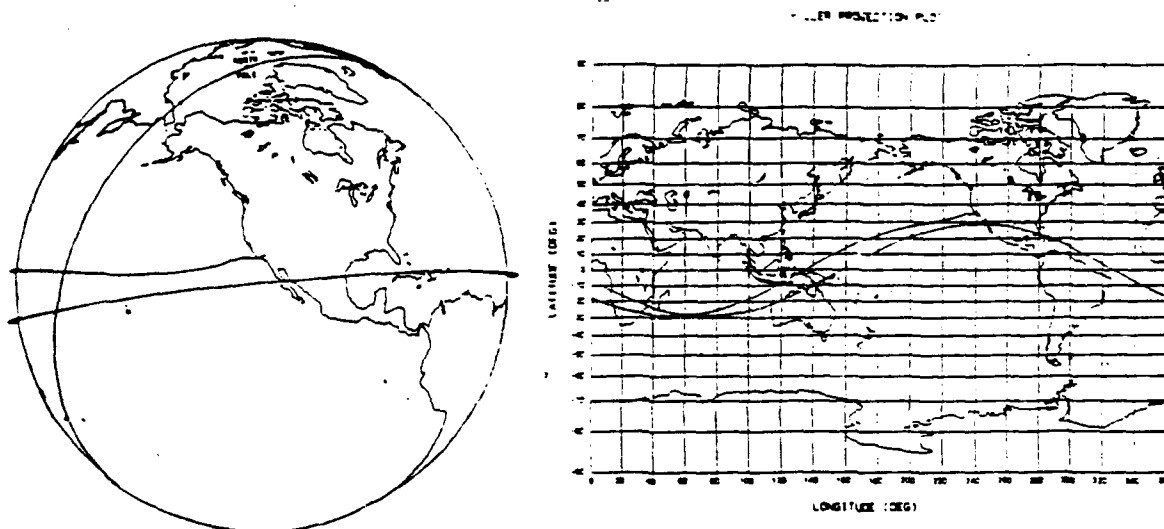
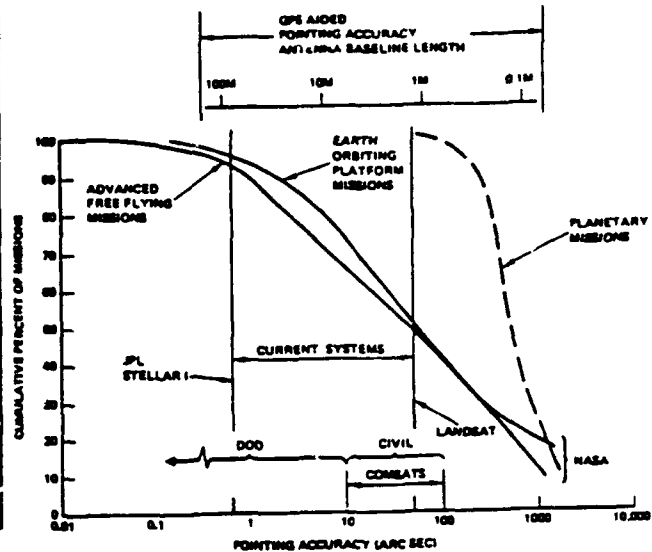


**Figure 6. Space Shuttle GPS Developmental Flight Test (DFT) Profile: Orbit, Deorbit, and Entry**

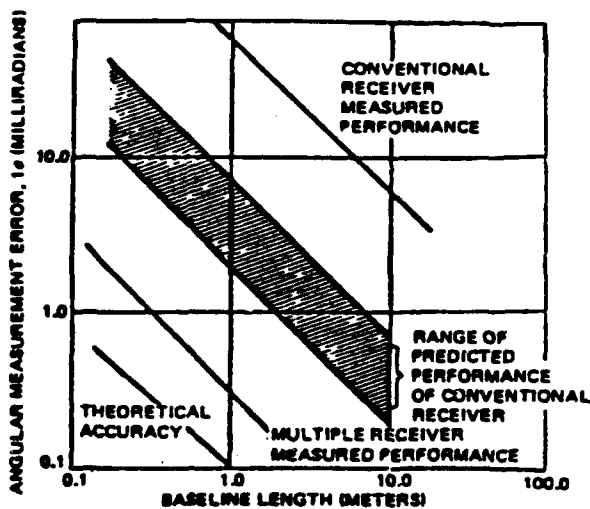
METHOD	1 $\sigma$ ACCURACY (ARC SEC)	CONSTRAINTS/LIMITATIONS	USE
ANDED-INERTIAL			
• Star Tracker	1-100	• Headoff from earth system	Space Station, Shuttle, Satellites
• Star Scanner	10-100	• Headoff from earth system	DMSP, PDS-1
• S-band Interferometer	10-100	• Headoff from earth system	DMSP, PDS-1
• Laseraltimeter	100	• Headoff from earth system	DMSP, PDS-1
• Star Scanner	200	• Headoff from earth system	DMSP, PDS-1
ALL STELLAR	10-100	• Headoff from earth system	DMSP, PDS-1
SYNCHRONIZATION	20-1000	• Headoff from earth system	DMSP, PDS-1
EARTH/STAR MEASUREMENT	100-3000	• Headoff from earth system	DMSP, PDS-1
SURVEILLANCE/MEASUREMENT	2000-7200	• Headoff from earth system	DMSP, PDS-1
GPS SENSOR	2000-7200	• Headoff from earth system	DMSP, PDS-1
RF SENSOR	720	• Headoff from earth system	DMSP, PDS-1
ANTENNA PATTERN/MEASUREMENT	10000	• Headoff from earth system	DMSP, PDS-1
LASER	21-2000	• Headoff from earth system	DMSP, PDS-1



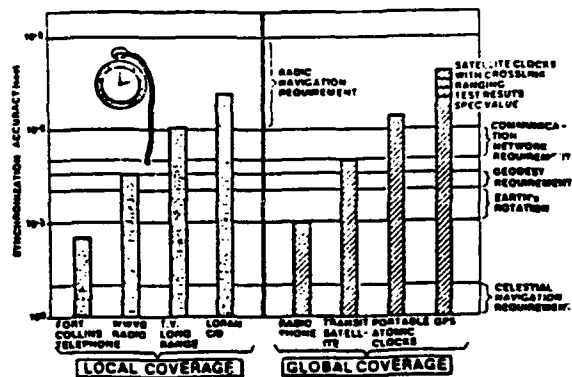
Non-GPS Attitude Determination Approaches

GPS Attitude and Pointing Applications/Capability

**Figure 7. Comparison of Non-GPS and GPS Attitude Determination Accuracies**



Accuracy vs. Base Vector Length



Time Synchronization Capabilities of Various Systems

**Figure 8. GPS Angular Measurement and Time Synchronization Performance**

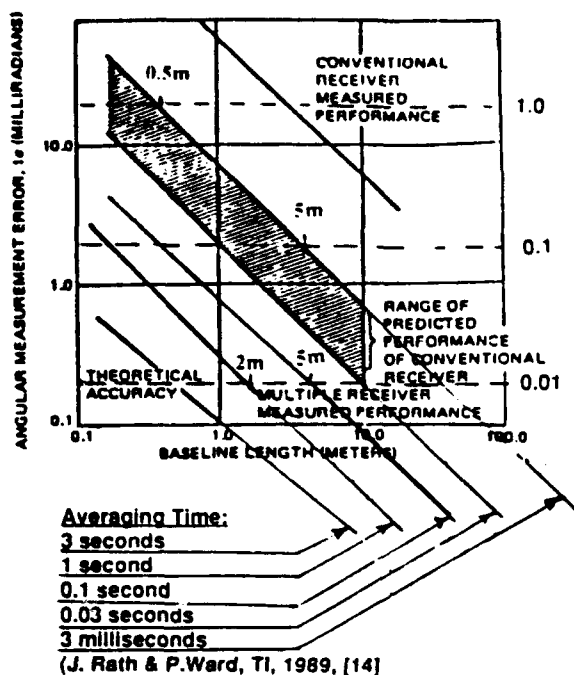
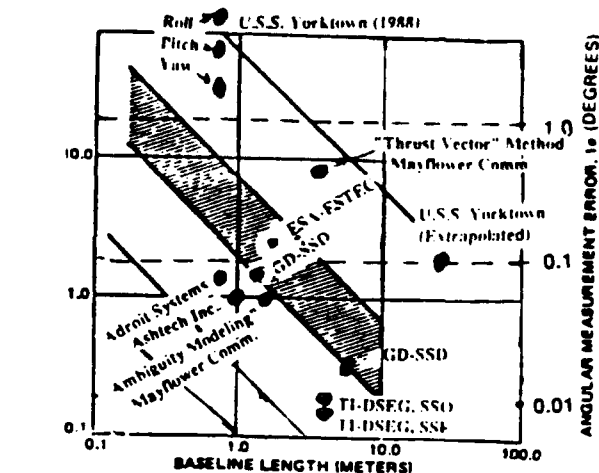


**Figure 9. "Constant Averaging Time" Lines of GPS Angular Measurement Performance [14]**

(Drawn on Attitude Error Vs Base Vector Length Chart. [15])



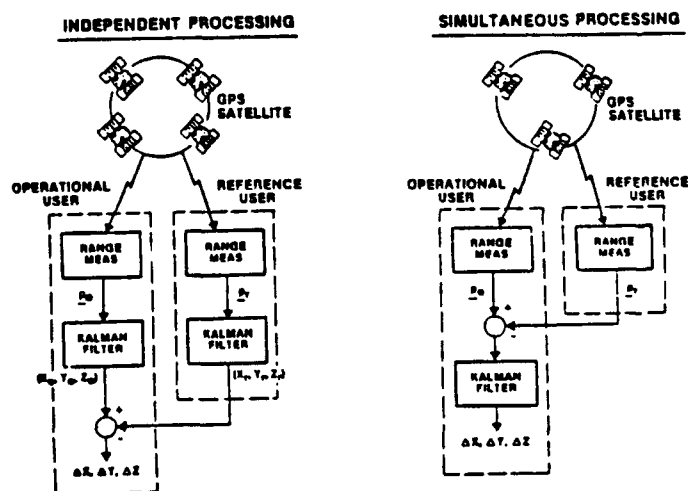
#### RECENT GPS ATTITUDE DETERMINATION METHODS

- 1) "Carrier Doppler Phase Difference",  
 TI-DSEG, SSF Sim., Jan.'89 [14]  
 TI-DSEG, SSF Sim., Jan.'89 [14]  
 Adroit Systems, Jan.'91 [10]
- 2) "Phase Time Triple Difference",  
 ESA-ESTEC, Sept.'90 [12]  
 GD-SSD, Jan.'91 [11]  
 Ashtech Inc., Jan.'91 [7]
- 3) "Thrust Vector" Method,  
 Mayflower Comm., Jan.'91, [11]
- 4) "Ambiguity Modeling",  
 Mayflower Comm., Jan.'91 [17]

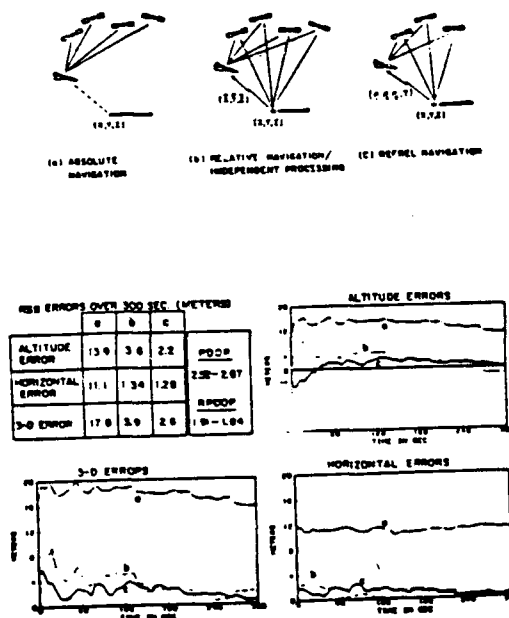
**Figure 10. Summary of GPS Attitude Determination Results**

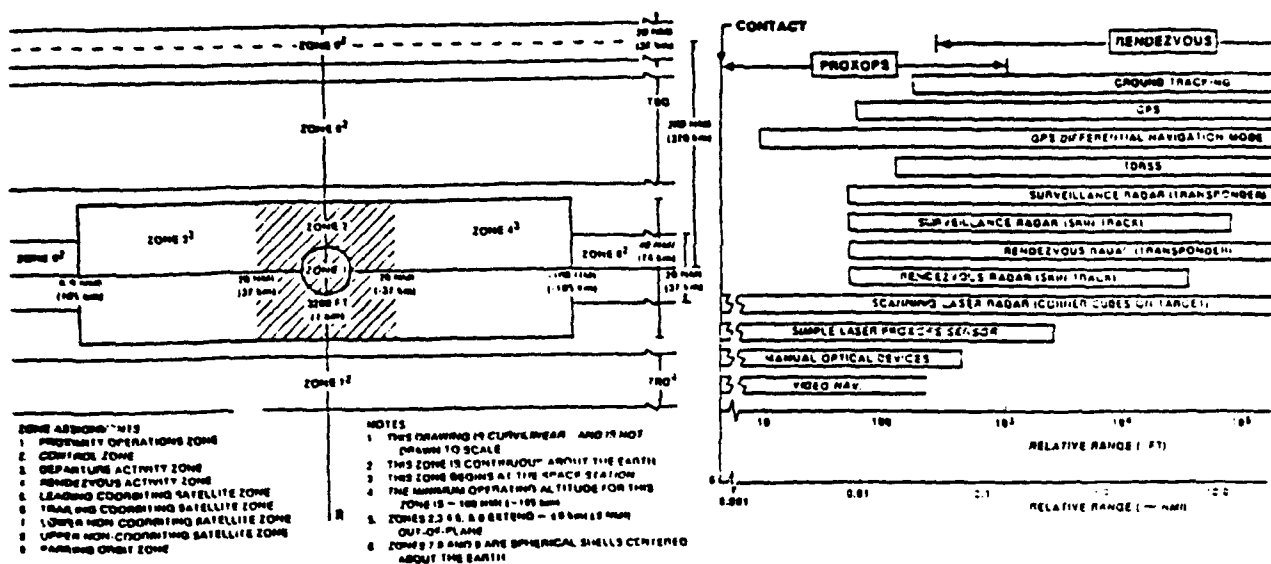
(Drawn on Attitude Error Vs Base Vector Length Chart. [15])

#### Two Methods of Differential GPS Solution Processing



**Figure 11. Navigation Errors in Aircraft Landing Versus GPS Mechanization**





A. Space Station Operational Control Zones

B. Range of Application of Relative Motion Sensors

**Figure 12. Space Station Rendezvous Zones & Relative Motion**

## SAIL CONFIGURATION

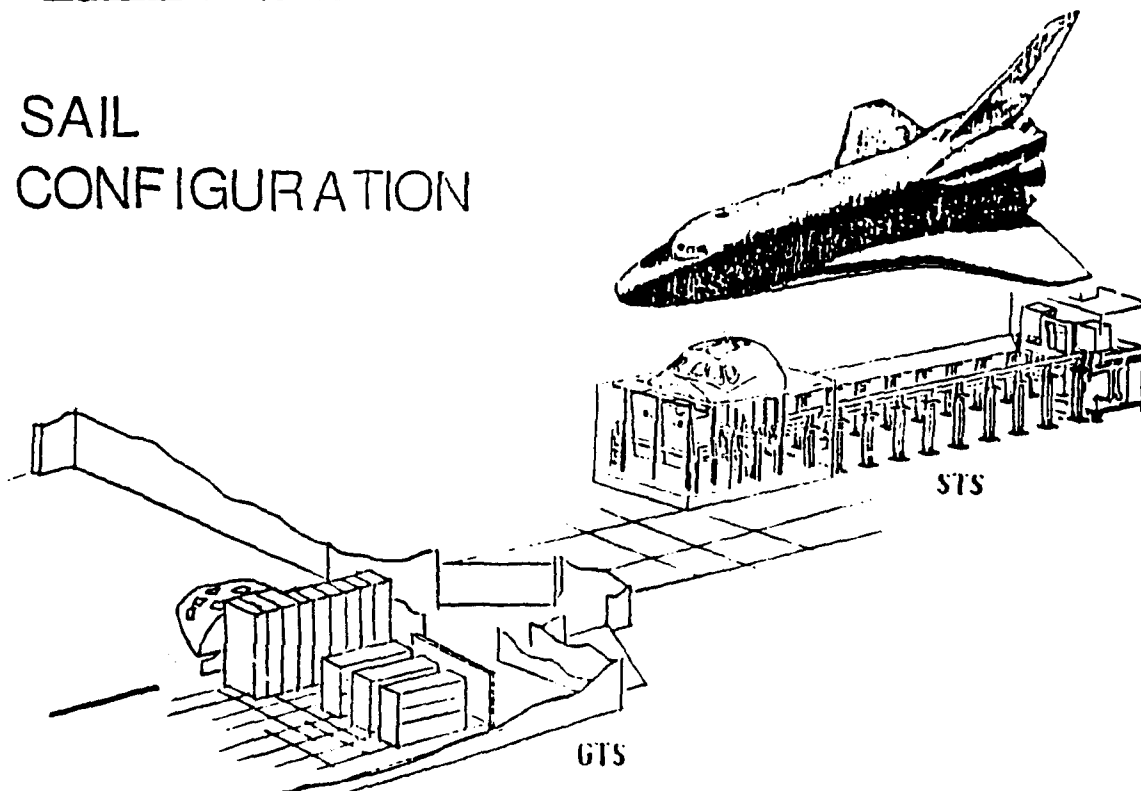


**Figure 13. Shuttle Avionics Integration Laboratory (SAIL)**  
**STS = Space Transportation System (Shuttle Mockup)**  
**GTS = Guidance, Navigation, & Control (GN&C) Test Station**



**THIS PAGE LEFT BLANK INTENTIONALLY**

## POINTING STABILIZATION SYSTEM USING THE OPTICAL REFERENCE GYRO

Jerold P. Gilmore, Tze T. Chien,

Dale T. Woodbury, Michael F. Luniewicz, and Stephan J. Feldgoise

The Charles Stark Draper Laboratory, Inc.

### ABSTRACT

Stabilization technology is critical to the performance of precision pointing and tracking systems. In surveillance systems, a stabilization system is required for image jitter suppression. In intersatellite communication systems, stabilization is required for receiver detector disturbance isolation, so as to enhance the received beam signal-to-noise ratio for dim target acquisition.

This paper presents a closed-loop pointing stabilization system using an inertially stabilized reference beam and a fast steering mirror. The inertially stabilized reference beam is provided by an optical reference gyro (ORG). The ORG is a dry-tuned gyro implemented with a fiber-coupled light source and collimating optics on the spinning rotor to produce a stabilized reference beam. It is a compact, light-weight device. A testbed facility using a prototype ORG is presented to demonstrate the pointing stabilization system performance. Both analytical modeling and hardware test experiments were performed to evaluate the system residual jitter error in a disturbance environment. The analytical prediction was validated by the hardware test results. Based on the test and analytical results, an enhanced ORG design with an improved isolation capability and a higher spin speed was characterized. It is projected that an enhanced ORG system will achieve a submicroradian stabilization jitter performance over a 0.1-100 Hz base disturbance environment. A pointing, stabilization, alignment, and attitude determination system using the enhanced ORG is configured. Projected sizing, weight and power consumption are presented.

### INTRODUCTION

Advanced space systems for surveillance, strategic defense applications, and optical communication require stabilization subsystems that provide extreme jitter suppression in wide band vibration disturbance environments. Potential applications include target/scene surveillance systems, airborne and space laser pointing systems, and laser intersatellite communication systems.

In surveillance systems, stabilization systems are required for image jitter compensation and sensor agility enhancement. Agility refers to speed for acquisition and settling in tracking and retargeting. Speed can be significantly improved when the image can be stabilized in the presence of structural settling by using a high bandwidth fast steering mirror (FSM) loop. In airborne and space laser pointing systems, a stabilized beam can be used as an alignment reference for jitter stabilization of the outgoing marker laser beam. The stabilization system can also be applied to facilitate acquisition of a dim laser beam in intersatellite communication. In the communication system the receiver satellite focal plane disturbance should be stabilized to less than 1 pixel size to enhance the received beam signal-to-noise ratio (SNR) for spatial acquisition.

This paper presents a line-of-sight (LOS) pointing stabilization system implemented by closing a high bandwidth FSM loop on an inertially stabilized reference beam. The inertially stabilized reference beam is produced by the ORG developed at Draper Laboratory. This prototype ORG is a two-degree-of-freedom dynamically tuned gyro equipped with a fiber-coupled light source and a collimating lens assembly on the spinning rotor. Because the rotor spin-axis is inertially stabilized by the gyro dynamics, the beam projected from the rotor-mounted



optics is also inertially stabilized. More detail on the ORG is given in a later section.

## APPLICATION CONCEPT

A pointing and stabilization application concept using the ORG reference beam is presented in Figure 1. In this application, the reference beam is injected into the telescope via an extended corner cube. As shown in Figure 1, both the ORG beam and the communications beam link LOS pass through the same optical path: a telescope, an FSM, and a beam splitter to their respective detectors. Since both the ORG beam quad-detector and the imager are mounted rigidly on a common focal plane assembly, the imager smear can be corrected by nulling the reference beam quad-detector error using the FSM.

Pointing acquisition is accomplished using the focal plane detector (FP) and a pointing loop. The target image offset error, whose SNR has been enhanced by the ORG stabilization loop, is applied through  $T(s)$  to the ORG torque generator (TG) to precess the ORG rotor. The rotor-mounted reference beam direction is therefore steered to provide the error signal at the quad detector to control the FSM loop. Thus, a pointing loop is closed to null the target image offset on the focal plane and align the target LOS to the receiver.

As the FSM moves from its center position as required by the pointing stabilization loop, the FSM motion measured by Kaman position provides an error signal to the follow-up loop through  $S(s)$  to realign the spacecraft.

In Figure 1, 3-axis attitude determination is achieved using a second roll-axis gyro on the optical bench. Encoding of the two torque inputs of the ORG provide the pitch and yaw axis inputs.

## OPTICAL REFERENCE GYRO

The ORG is a two-degree-of-freedom dynamically tuned gyro (DTG) with an on-board laser light source to furnish a collimated inertially stabilized LOS reference. The ORG rotor is supported on the gyro spin shaft through a double gimbal cylindrical hinge which decouples the rotor from the shaft through the dynamic "tuning" effect. The tuned spin rate of the prototype ORG is 89.5 Hz.

The laser light source is fixed to the ORG case and aligned to emit the optical beam along the gyro rotor spin axis. The laser beam diffracts through a pinhole on the rotor; the central lobe of the

diffraction field is collimated by a large output lens on the rotor (Figure 2). The collimated output serves as the optical LOS reference beam. This design decouples the laser beam from the case and effectively places the source on the rotor, because the pinhole is as small as the diffraction limited spot size of the output lens.

The ORG has a permanent magnetic torque generator (TG) and an inductive electromagnetic signal generator (SG) for rotor torquing and angle measurement. A permanent magnet motor provides the gyro spin axis drive. The drive shaft is supported on a high reliability, low noise spin axis bearing to minimize spin axis runout and rotor angle noise.

The prototype ORG was built at Draper Lab. in 1981 with Army and internal IR&D funding. A cross-section view of this unit is shown in Figure 3. In 1989, with IR&D funding, this ORG was refurbished with a fiber-coupled light source and improved electronics.

The ORG beam wobble at the rotor spin speed was successfully nulled with a discrete noise eliminator. This eliminator employs phase-locked and automatic gain control loops to torque the ORG rotor such that the large beam jitter, rotor wobble at spin-speed is canceled by the closed-loop discrete noise eliminator circuit. Moreover, the eliminator provides a very narrow notch with practically no phase and gain distortion beyond a  $\pm 5$  Hz band around the spin speed frequency.

Figure 4 illustrates the noise characteristics of the ORG reference beam (ORG) as detected on a quad-sensor. Two noise power spectra are shown. The top figure shows the beam noise of 10.8  $\mu R$  rms without the use of the discrete noise eliminator. With discrete noise eliminator, the reference beam noise performance is improved to 0.244  $\mu R$  rms, as shown in the lower plot.

Another critical ORG performance characteristic is isolation of the reference beam from case motion. This isolation is directly measured as a transfer function from the ORG case motion to the reference beam jitter output. Figure 5 shows that this prototype ORG provides a base motion isolation capability of -32 dB over a measured frequency range of 0.1 - 100 Hz. During the measurement process, it was observed that the reference beam isolation is not only a function of the gyro dynamic mistuning effect, but it is also a function of translation motion coupling due to divergence of the reference beam.

The measured performance of this prototype ORG is summarized in Table 1.

Table 1. Prototype ORG parameters.

Angle noise (optical)	244 nR rms, 0.1-100 Hz
Drift Stability	<0.020 deg/h
Spin speed	89.5 Hz
Rotor/case isolation	-32 dB, 0.1-100 Hz
Slew capability @ 2.5W	8 deg/s
G-capacity (@ hinge)	100 g
Motor power	0.8W
Light source	Fiber-coupled laser diode
Wavelength	670 nm
Optical power out	15 $\mu$ W
Optical power at source	5 mW
Beam exit diameter	0.25 in filled 0.7 in clear aperture
Pinhole diameter	8 $\mu$ m
Wavefront quality	NA
Beam divergence	NA
Size	2.5 in dia x 6 in length
Weight	28 oz

## POINTING STABILIZATION TESTBED

A pointing stabilization testbed facility was developed at Draper Lab to demonstrate the pointing performance using the optical reference gyro. This facility configuration as shown in Figure 6 was designed to emulate the application concept in Figure 1.

A collimated light source, simulating a distant target is mounted on a stable reference pier. The target LOS, passing through an optical mirror system, is sensed by a scoring quad angle sensor mounted on the test table. When the test table is driven with a dynamic base disturbance environment, the scoring quad sensor output is distorted by the base motion.

To stabilize the jitter distortion, the inertially stabilized ORG reference beam is injected through the same optical mirror system to its quad angle sensor which is mounted on the same test table. When a base disturbance environment is applied, this quad senses an error signal that drives the FSM through a high bandwidth closed-loop servo to compensate for the disturbance. Since the FSM operates on both the target LOS and the ORG reference beam, the LOS jitter (or image smear) on the scoring quad detector will also be stabilized. The residual LOS jitter is measured by the scoring quad detector output. This measurement, when correlated to the base motion

input,  $\theta_{BI}$ , (measured by an autocollimator), provides a measure of the image system base motion isolation capability.

Pointing performance for an offset target is demonstrated in this test bed with a photopot detector. As mentioned in the application concept, the target image offset error drives the ORG torquer through a pointing control loop to point the ORG beam such that the FSM nulls the target image offset in closed loop. The acquisition and settling time are measured by the error signal at the photopot detector and the CCD camera display.

In addition, in simulating the spacecraft control loop, a 0.1 Hz follow-up loop is implemented to align the test table to the offset target. The follow-up transient response is measured by the FSM position sensor output. In this case, the slew response is limited by the low bandwidth of the table servo loop. By closing an ORG pointing loop, the target offset can be nulled with much faster response by the high bandwidth FSM loop. This enhancement of the sensor agility will be demonstrated in the pointing transient tests.

The pointing and stabilization system test facility is shown in Figure 7.

## ANALYTICAL MODELING

A pointing and stabilization system block diagram for performance analysis is presented in Figure 8. This figure shows the signal flow of the control loops of the test facility in Figure 7. In the figure,  $\theta_{TI}$  corresponds to the target, a collimated inertial light source.  $\theta_{BI}$  is the base motion disturbance input (injected by the test table). The ORG reference beam error is composed of two terms: the beam noise  $n_{RI}$  and the ORG residual base motion coupling error  $H(s) \theta_{BI}$ .  $H(s)$  represents the ORG base motion isolation transfer function which was measured to be a pure gain of -32 dB.  $F(s)$  and  $G(s)$  are the FSM and servo compensator transfer functions, respectively.  $B(s)$  is the equivalent base motion coupling into the FSM.  $T(s)$  represents the pointing servo compensator transfer function.

The system performance is evaluated as the receiver residual jitter error,  $e_4$ , in Figure 8. There are two main error sources contributing to the receiver jitter error. They are the base motion disturbance  $\theta_{BI}$  and the ORG sensor noise  $n_{RI}$ . This system performance is computed by deriving the transfer functions of these two critical error sources.

The results are summarized in Equations (1) and (2):

$$\frac{e_4}{n_{RI}} = \frac{1}{D(s)} \left( \frac{2F(s)G(s)}{1 + 2F(s)G(s)} \right) \quad (1)$$

$$\frac{e_4}{\theta_{BI}} = \frac{1}{D(s)} \left( \frac{2F(s)B(s) - 1}{1 + 2F(s)G(s)} + \frac{2H(s)F(s)G(s)}{1 + 2F(s)G(s)} \right) \quad (2)$$

where

$$D(s) = \left( 1 + \frac{T(s)}{s} \frac{2F(s)G(s)}{1 + 2F(s)G(s)} \right)$$

As analysis of Equation (1) indicates the residual jitter error due to the ORG sensor noise is bounded by its noise of 0.244  $\mu$ R, rms, 0.1 - 100 Hz. In comparison, the residual jitter error due to the base disturbance is much more significant. The analysis is therefore focused on the base disturbance isolation.

Two cases of base disturbance isolation are analyzed. The first case is to evaluate the ORG-FSM stabilization system jitter performance. In this case, the pointing controller is open ( $T(s) = 0$ ), and Equation (2) simplifies as  $D(s)$  becomes unity. This transfer function is simulated and plotted in Figure 9. At low frequencies, the isolation performance is governed by the ORG isolation capability  $H(s)$  (-32 dB). This corresponds to the second term in Equation (2). At higher frequencies, the isolation performance is limited by the closed-loop bandwidth represented by the first term in Equation (2). Because the spin rate of this prototype ORG is 89.5 Hz, the stabilization system is implemented with a closed-loop bandwidth at 110 Hz. Increasing the spin rate of the ORG will permit design of a higher bandwidth FSM loop providing higher bandwidth closed loop isolation. Improving the base motion isolation,  $H(s)$ , and increasing the ORG spin rate are the two key design parameters for the ORG performance enhancement.

In the second case, the pointing loop is closed. As shown in Equation (2), the transfer function is cascaded by the characteristic equation  $\left( \frac{1}{D(s)} \right)$ . As a result, within the pointing loop bandwidth, the ORG residual isolation error  $H(s)$  is further attenuated by the pointing loop. This is shown by the transfer function plotted in Figure 10.

The analytical simulation results will be validated by hardware test results in the next section.

## TEST RESULTS

Base motion stabilization test results and pointing transient response test results are presented.

### Base Motion Stabilization Evaluation

The stabilization evaluation is demonstrated by two system performance test results: a stabilization transfer function measurement and residual jitter spectrum measurement.

### Pointing Stabilization Transfer Function Measurement

As in the analytical simulation, two system transfer functions are measured. The ORG-FSM stabilization transfer function measurement is presented in Figure 11. It is shown with the corresponding coherence for measurement validation. Except in two frequency bands which are related to the FSM flexible modes and the 89.5 Hz eliminator notch, the measured transfer function matches closely the analytical result in Figure 9. At low frequencies, the isolation performance is governed by the ORG isolation, which was measured at -30 dB in this test run. At higher frequencies, the isolation performance is limited by the FSM closed loop bandwidth of 110 Hz. The second stabilization transfer function incorporates the pointing loop using the photopot sensor. The transfer function measurement in Figure 12 represents the residual jitter error measured at the photopot with respect to the base disturbance. The measurement again is matched closely to the analytical simulation in Figure 10. Finally, again with the pointing loop closed, a second transfer function was measured. Figure 13 shows the transfer function of the residual jitter error measured at the scoring quad with respect to the base disturbance. The transfer function measurement in Figure 13 is corrupted by the photopot sensor noise over the low bandwidth while the analytical simulation is derived based on an ideal photopot without sensor noise.

### Pointing Stabilization System Jitter Error

The second performance test evaluates the pointing stabilization system residual jitter error when a representative base disturbance environment is applied. A Ball Aerospace test environment model was selected as the case study which has an rms disturbance of 30  $\mu$ R, 0.1 - 100Hz with significant disturbance power over a bandwidth of 0.1 - 10 Hz as shown in Figure 14.

The residual jitter error of the ORG-FSM stabilization system with the pointing loop open was first measured. The result is presented in Figure 15. This figure shows the end-to-end closed loop stabilization performance achieved with a base disturbance environment of 30.7  $\mu$ R rms applied to the test table. As shown, the residual stabilization jitter error measured at the scoring quad is 2.13  $\mu$ R rms, 0.1 - 100 Hz, as shown in the lower figure. This residual stabilization jitter represents the total error contributed by both the residual base disturbance error and the intrinsic ORG sensor noise.

Performance is further improved by the addition of the pointing loop as illustrated in Figure 16. In this case, with an input disturbance of 31.5  $\mu$ R rms, 0.1 - 100 Hz, the residual jitter error measured at the scoring quad is 1.73  $\mu$ R rms, 0.1 - 100 Hz.

Table 2 summarizes the analytical and test results of the pointing-stabilization system residual jitter error. The results match consistently, validating this analytical model for performance projections. Differences between the analytical projection and test data are the results of test facility error sources which are not covered in the analytical model. These sources include the ORG and photopot sensor noises, the ORG isolation capability mismatch (-30 dB in system test runs vs. -32 dB in instrument test runs), the flex modes in the FSM, the ORG eliminator and the 60 Hz electrical grounding noise.

Table 2. Pointing stabilization system performance.

Configuration		Test Results	Analytical Projections
Stabilization System $H(s) = -32$ dB FSM Loop BW = 110 Hz	Input Disturbance rms, 0.1-100 Hz	30.7 $\mu$ R	30.3 $\mu$ R
	Residual Jitter rms, 0.1-100 Hz	2.13 $\mu$ R	1.54 $\mu$ R
Pointing Stabilization System $H(s) = -32$ dB FSM Loop BW = 110 Hz Pointing Loop BW = 4 Hz	Input Disturbance rms, 0.1-100 Hz	31.5 $\mu$ R	30.3 $\mu$ R
	Residual Jitter rms, 0.1-100 Hz	1.73 $\mu$ R	1.46 $\mu$ R

## Pointing Transient Response

To demonstrate the pointing system agility for acquisition and settling in tracking and retargeting, the pointing transient response was measured. Two system tests were performed.

The first test was to measure the transient time response to a target offset of 0.2 mR. Because of the field-of-view limitation of the scoring quad ( $\pm 4$   $\mu$ R), the transient error was measured by the photopot error signal. The result is presented in Figure 17 showing a transient time of 0.43 sec. The jitter superimposed on the transient response is due to the photopot noise. For comparison, an analytical transient response is simulated in Figure 18 (with an ideal photopot). The close correlation between the analytical and test results are clearly demonstrated.

To demonstrate the agility of the FSM loop with respect to a simulated spacecraft 0.1 Hz follow-up loop, the transient response measurement of the follow-up loop is presented in Figure 19. The 0.1 Hz follow-up loop shows a transient time of 10.68 sec. A factor of 25 improvement in the response agility with the ORG-FSM pointing stabilization loop was achieved.

A second transient response test is demonstrated by the image stabilization display on a CCD camera. In Figure 20, the image was smeared by a base motion disturbance superimposed by an image offset. The image smear was effectively suppressed, but the offset remained, when the ORG-FSM stabilization loop was activated. This is demonstrated in Figure 21. Finally, with the pointing loop activated, the image offset was nulled and its blur essentially eliminated. This display is shown in Figure 22.

## ENHANCED ORG PROJECTIONS.

A program was initiated in 1992 to upgrade the prototype ORG design to satisfy the performance requirements of high performance pointing and stabilization applications. The enhanced ORG design incorporates recent developments in Draper Lab DTG technology to yield improved inertial stability of the optical line-of-sight reference. The enhanced ORG hinge gimbal assembly has been extensively modeled to establish design specifications to ensure that isolation "tuning" performance goals are satisfied. In addition, the light source optics system has been improved to provide a higher optical output power and a pinhole mechanization insensitive to the case motion and rotor wobbling.

The projections for the enhanced ORG performance parameters are summarized in Table 3.

Table 3. Enhanced ORG Design Parameters

Angle noise (Optical)	100 nR rms, 0.1 - 100Hz
Drift stability	0.005 deg/h
Spin speed	200 Hz
Rotor/case isolation	-50 dB, 0.1 - 100 Hz
Slew capability	15 deg/s
G-capability (@ hinge)	100 g
Motor power	0.95 W
Torquer power	2.5 W (@15 deg/s)
Light source	Monolithic laser diode
Wavelength	670 nm
Optical power out	1 mW
Optical power at source	2.5 mW
Beam exit diameter	0.7 in
Pinhole diameter	4.5 $\mu$ m
Wavefront quality	$\lambda/6$ P-V
Beam divergence	40 $\mu$ R
Size	3.25 in dia. x 7 in
Weight	35 oz

As projected by analysis and validated by test results, the most critical parameters for pointing stabilization system performance enhancement are the ORG isolation capability  $H(s)$  and the FSM loop bandwidth which is limited by the ORG spin rate. With the enhanced ORG design, both parameters have been improved. For an estimation of performance improvement, the analytical model, which was validated by test results, is applied to derive the pointing stabilization system transfer functions and residual jitters using an enhanced ORG of a -50 dB isolation and a 200 Hz FSM loop bandwidth. The results are shown in Figure 23 and 24. For comparison, the results are overlaid with the transfer functions corresponding to the prototype ORG parameters. The improvement in base motion isolation is significant. For a quantitative evaluation, analytical projection of the residual stabilization jitter error was recalculated using the enhanced ORG parameters. In a disturbance environment of 30.3  $\mu$ R rms, 0.1 - 100 Hz, the projected residual jitter error is 0.35  $\mu$ R rms, 0.1 - 100 Hz for the ORG-FSM stabilization system, and is 0.32  $\mu$ R rms, 0.1 - 100 Hz for the pointing stabilization system.

In summary, the performance analysis of the stabilization system using the enhanced ORG indicates that a residual jitter of 0.35  $\mu$ R rms, 0.1 - 100 Hz can be achieved in a disturbance environment of 30  $\mu$ R rms, 0.1 - 100 Hz. This stabilization

system, when corrected for contributions by other error sources, including the ORG sensor noise, is projected to achieve a residual jitter of <0.5  $\mu$ R rms, 0.1 - 100 Hz.

For potential space applications, a pointing, stabilization and attitude determination system using the enhanced ORG is presented in Figure 25. This self-contained instrument and electronics assembly unit can provide an inertially stabilized reference beam to be used for pointing, stabilization and alignment control applications. In addition, with the addition of a second gyro to provide attitude sensing of the LOS axis, this unit can provide a full self-contained inertial attitude determination package. In Figure 25, a Draper-developed interferometric fiber-optic gyro is used for the LOS-axis sensing. For airborne applications, incorporation of an accelerometer triad can provide data for g-compensation.

The size, weight and power estimates for the ORG/IFOG instrument package and its electronics assembly are summarized in Table 4.

Table 4. Projected ORG/IFOG pointing system characteristics.

Parameters	Instrument Package	Electronics Assembly
Size (L" x W" x H")	9.4 x 4.0 x 4.2	8.4 x 6.2 x 7.0
Weight (lbs.)	6.1	10
Power* (W)	2	22

\*Fixed power (heater and gyro torquing power not included)

## CONCLUSION

This paper presents a closed-loop pointing and stabilization system using an inertially stabilized reference beam and a fast steering mirror. The inertially stabilized reference beam is provided by an ORG. The ORG is a dry-tuned gyro implemented with a laser diode light source and collimating optics on the spinning rotor to provide a stabilized reference beam.

A testbed facility using a prototype ORG was developed to demonstrate the pointing stabilization system performance. Both analytical and hardware test experiments were conducted to evaluate the system residual jitter error in a disturbance

environment. The analytical prediction was validated consistently by the hardware test results.

Based on the test and analytical results, it was concluded that the most critical parameters for the pointing and stabilization performance enhancement are the ORG isolation capability and the FSM loop bandwidth which is limited, in turn, by the ORG spin rate.

An enhanced ORG design with an isolation capability of -50 dB and a spin-rate of 200 Hz was characterized. It is projected that with the enhanced ORG,  $<0.5 \mu\text{R}$  stabilization jitter performance over 0.1-100 Hz can be achieved in a representative base disturbance environment of  $30 \mu\text{R rms}$ .

A pointing, stabilization, alignment and attitude sensing unit configuration using the enhanced ORG is presented. The size, weight and power consumption for the ORG instrument package and electronics assembly are projected.

#### ACKNOWLEDGMENTS

The authors wish to acknowledge Greg Cappiello for his work on the optical system design.

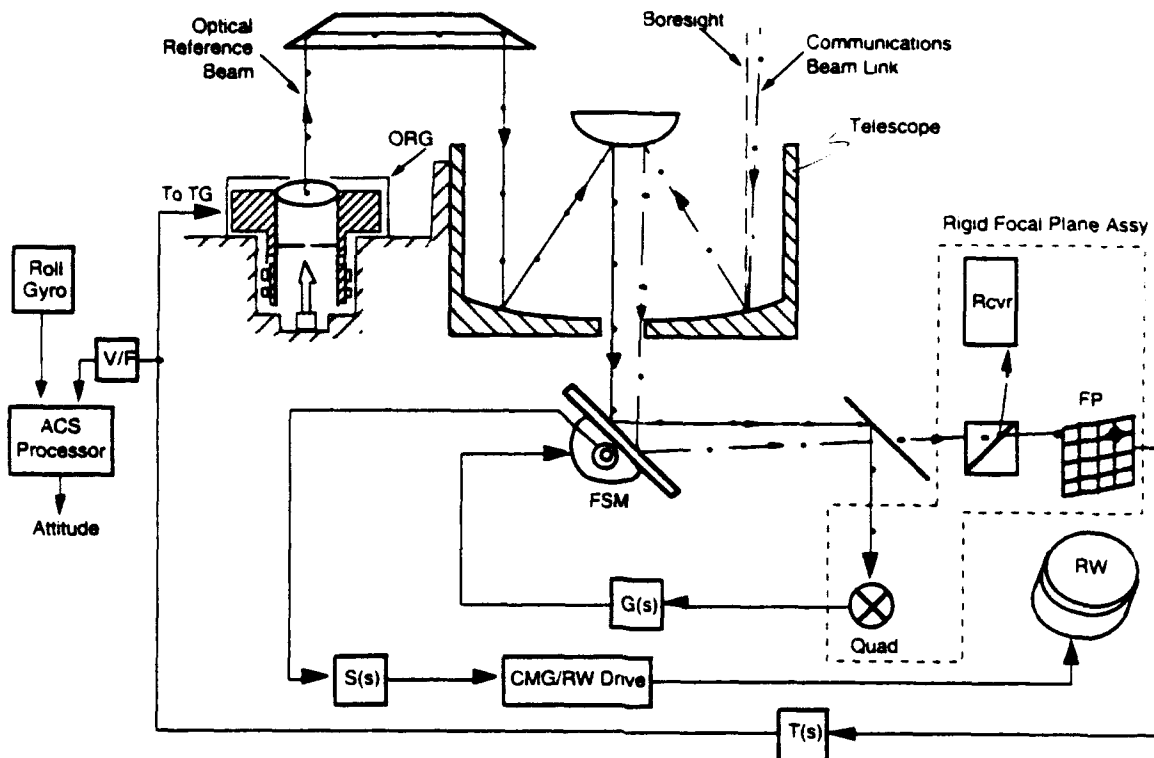


Figure 1. Pointing stabilization system application concept.

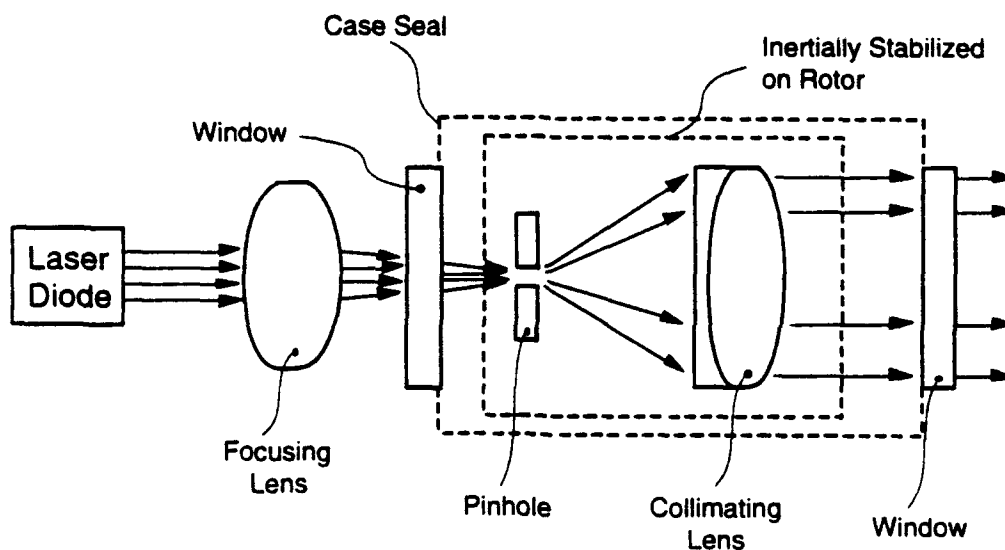


Figure 2. Optical Reference Gyro optics schematic.

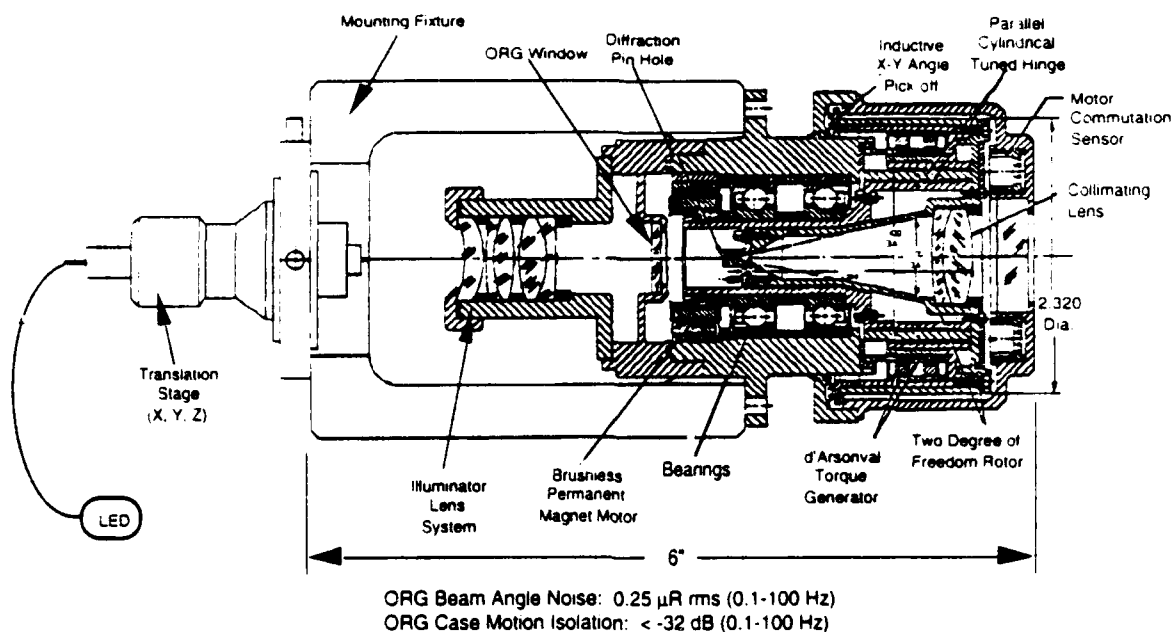


Figure 3. Prototype ORG assembly.

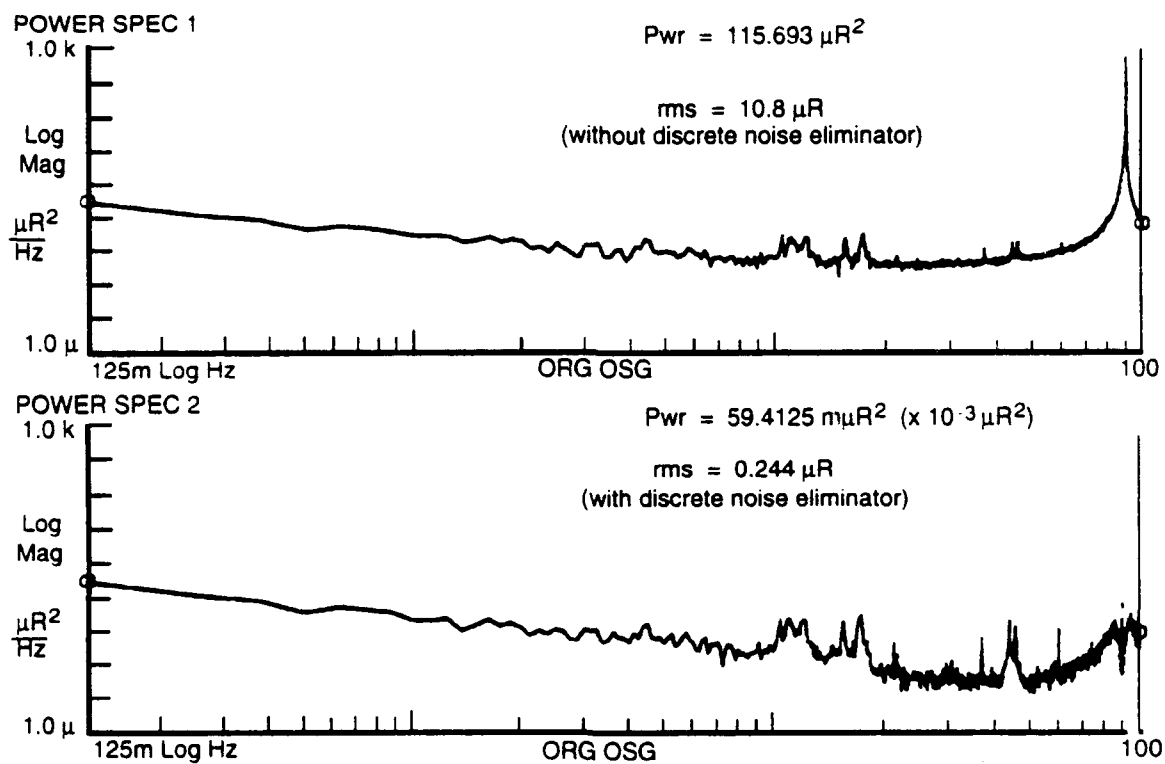


Figure 4. ORG beam noise measurement.



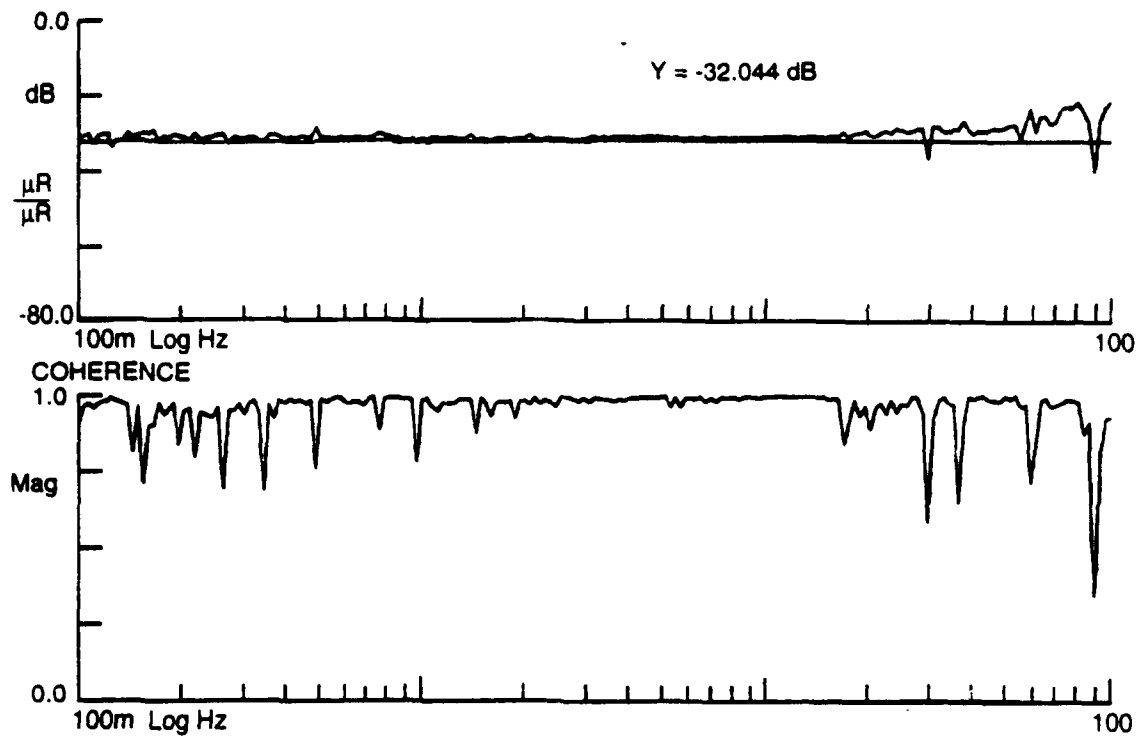


Figure 5. ORG beam isolation measurement.

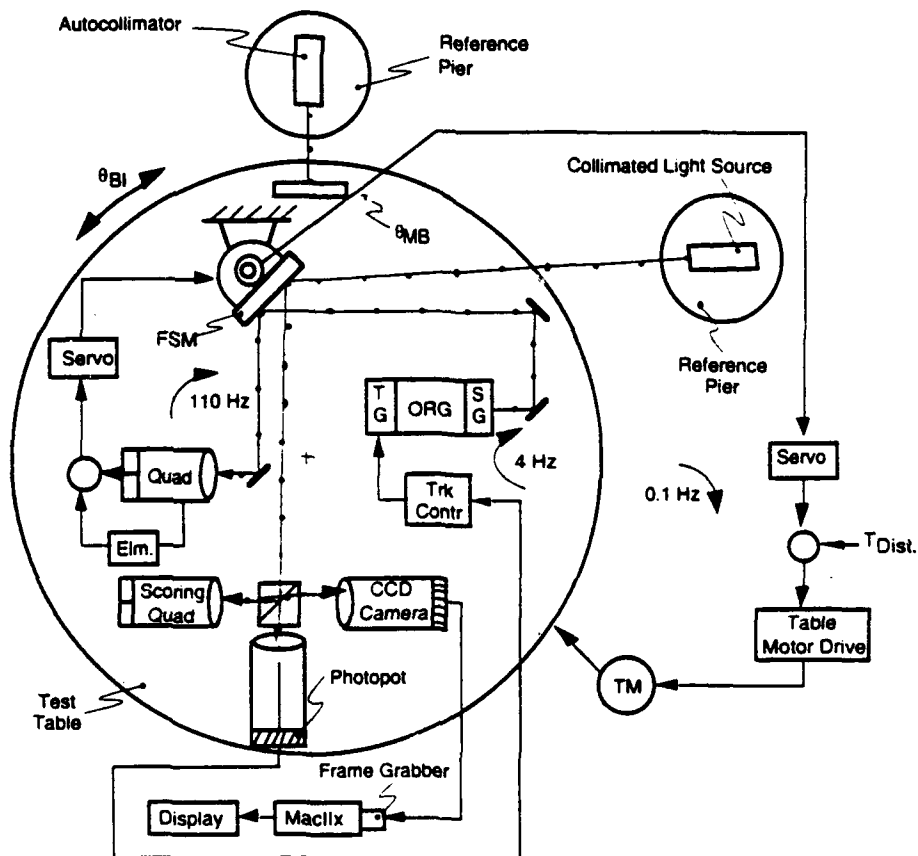


Figure 6. Pointing stabilization testbed configuration.

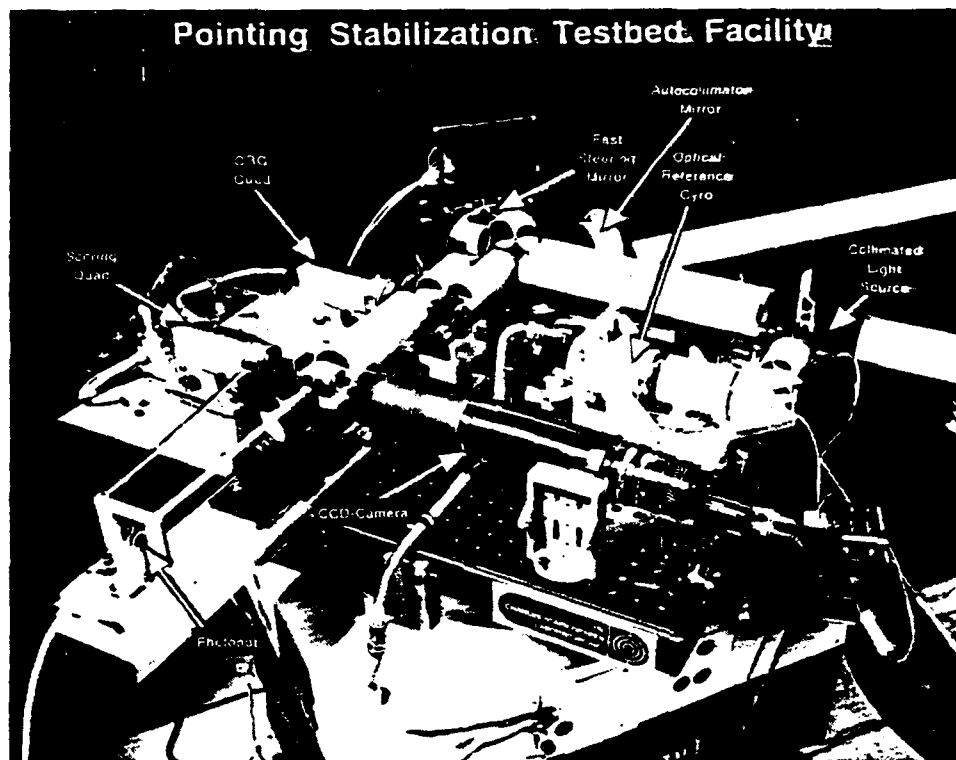


Figure 7. Pointing stabilization testbed facility.

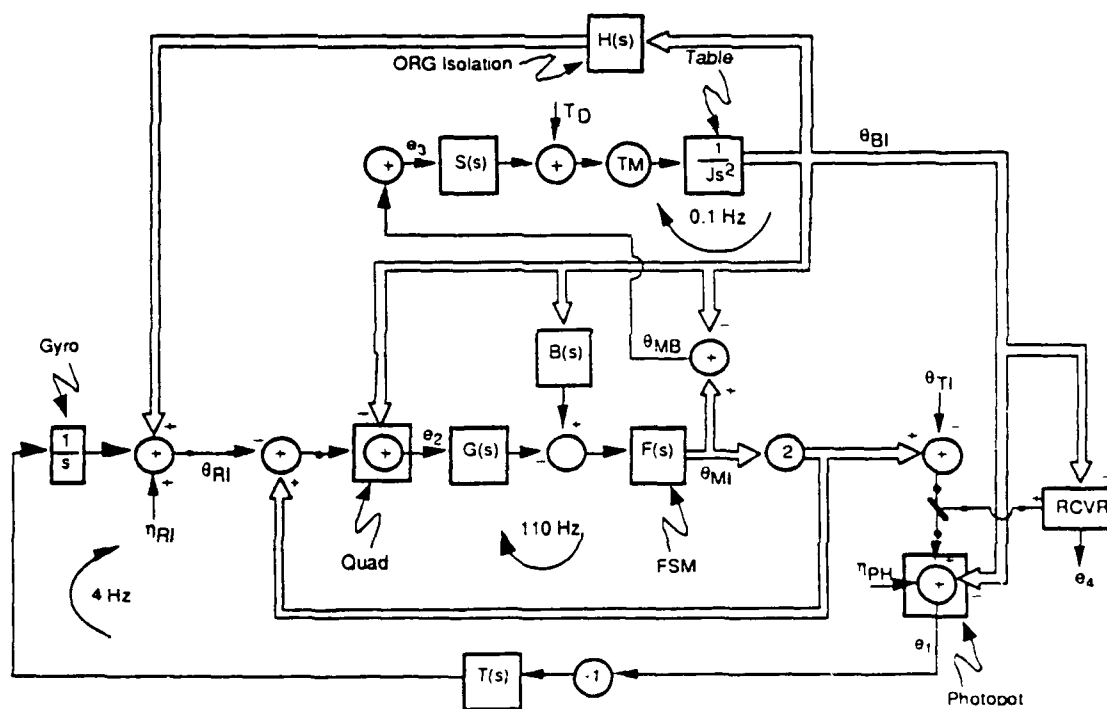


Figure 8. Pointing stabilization control system.

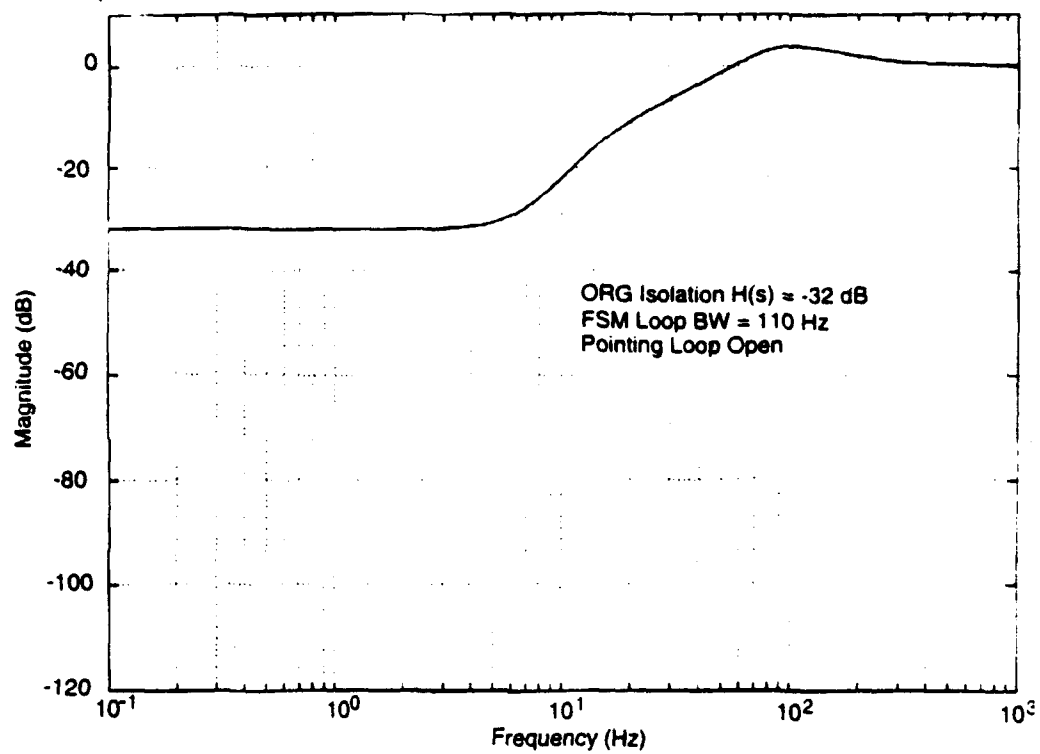


Figure 9. Analytical stabilization system transfer function.

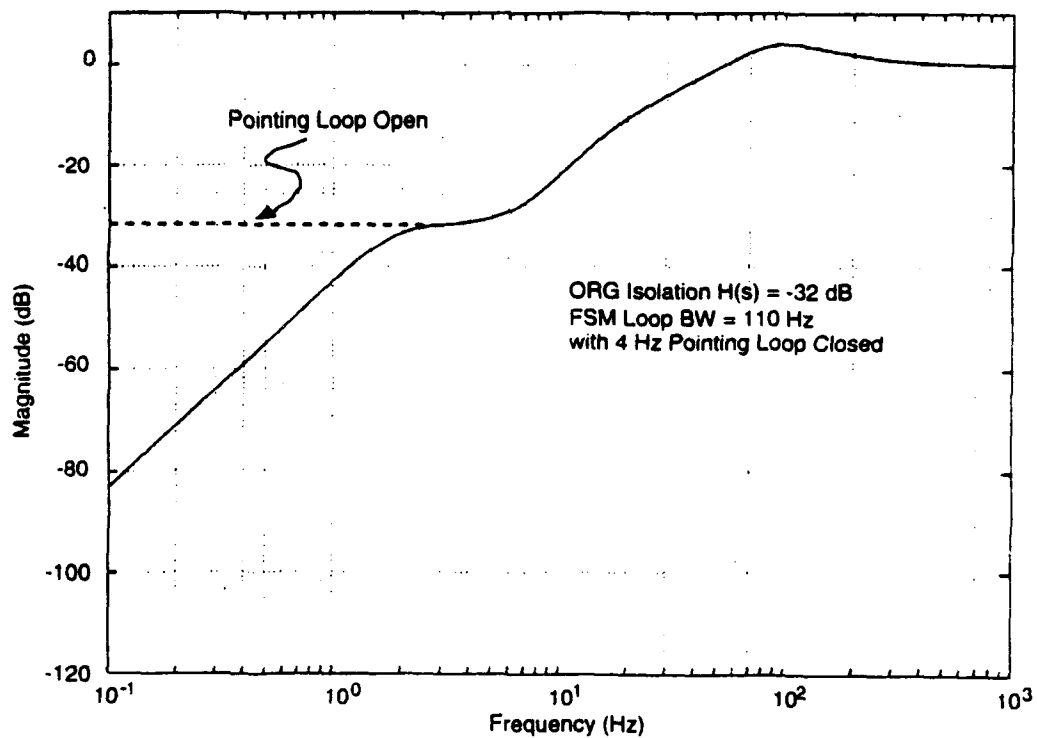


Figure 10. Analytical pointing stabilization system transfer function.

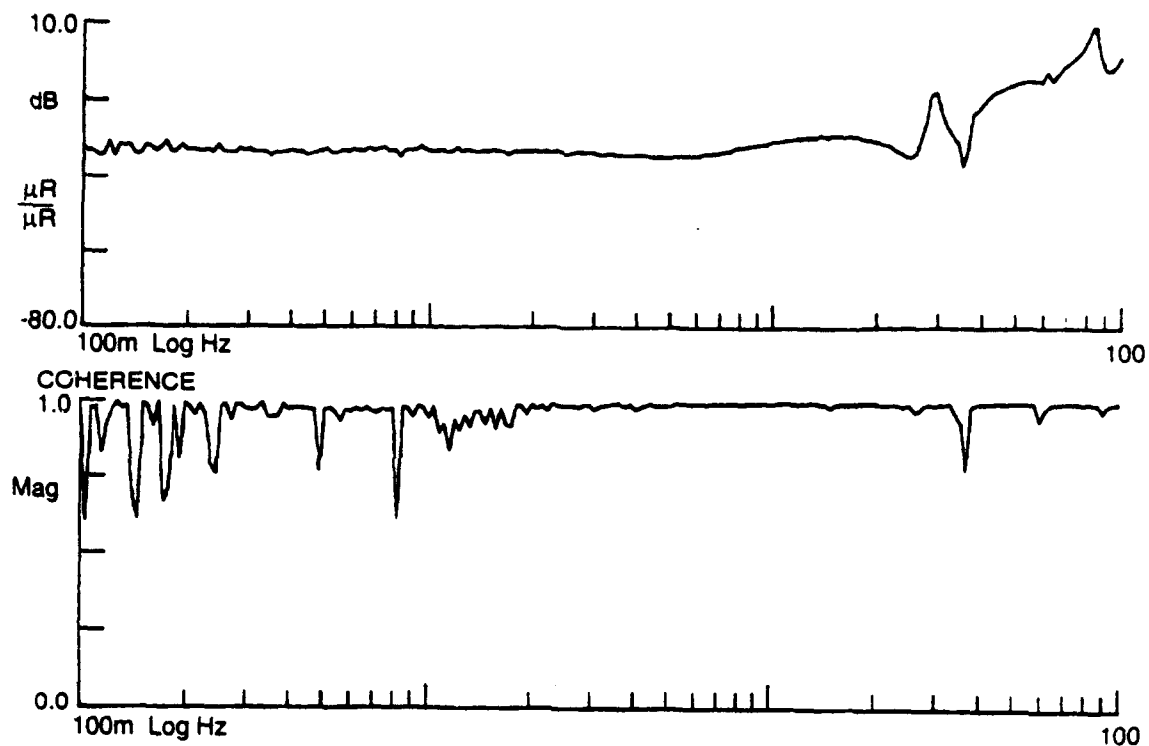


Figure 11. Stabilization system transfer function measurement.

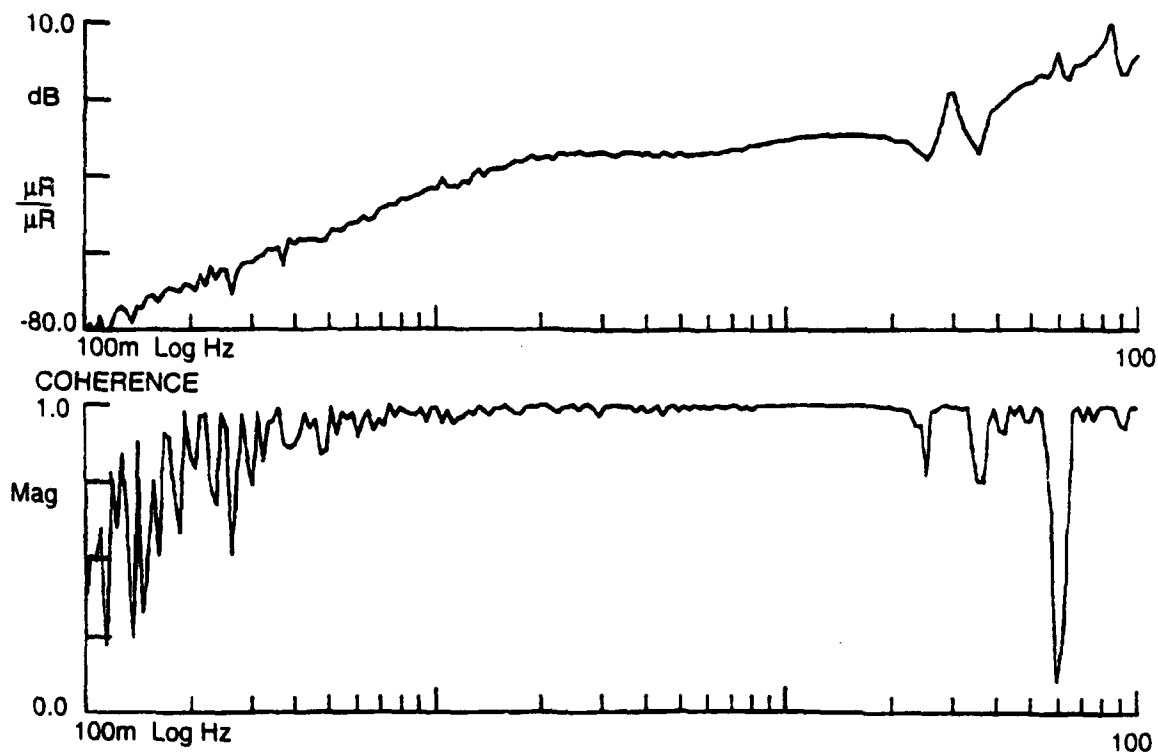


Figure 12. Pointing stabilization system transfer function measurement (measured at Photopot sensor).

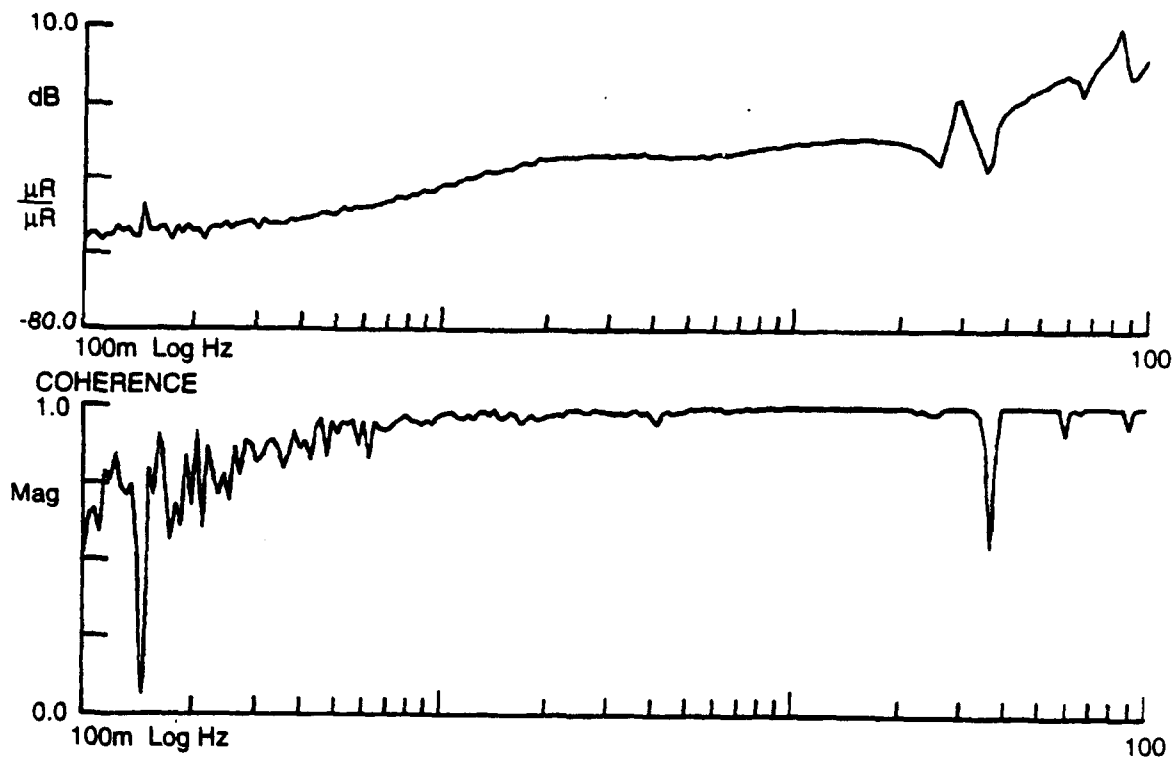


Figure 13. Pointing stabilization system transfer function measurement (measured at scoring quad).

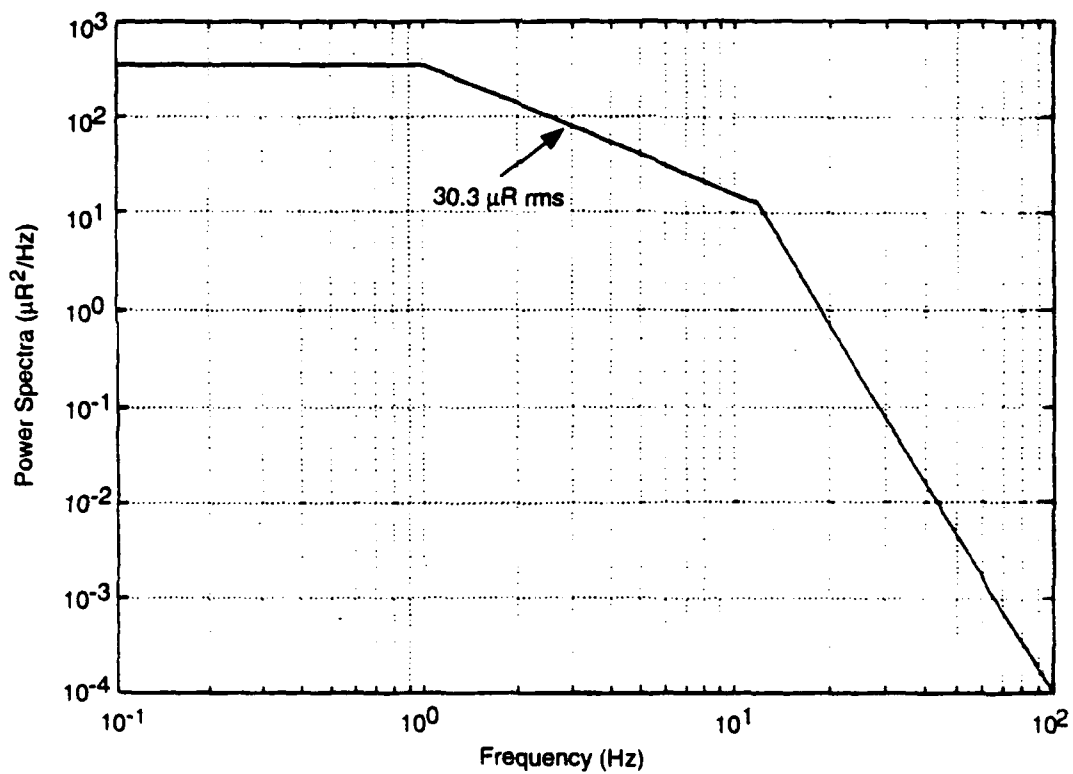


Figure 14. Base motion disturbance spectrum.

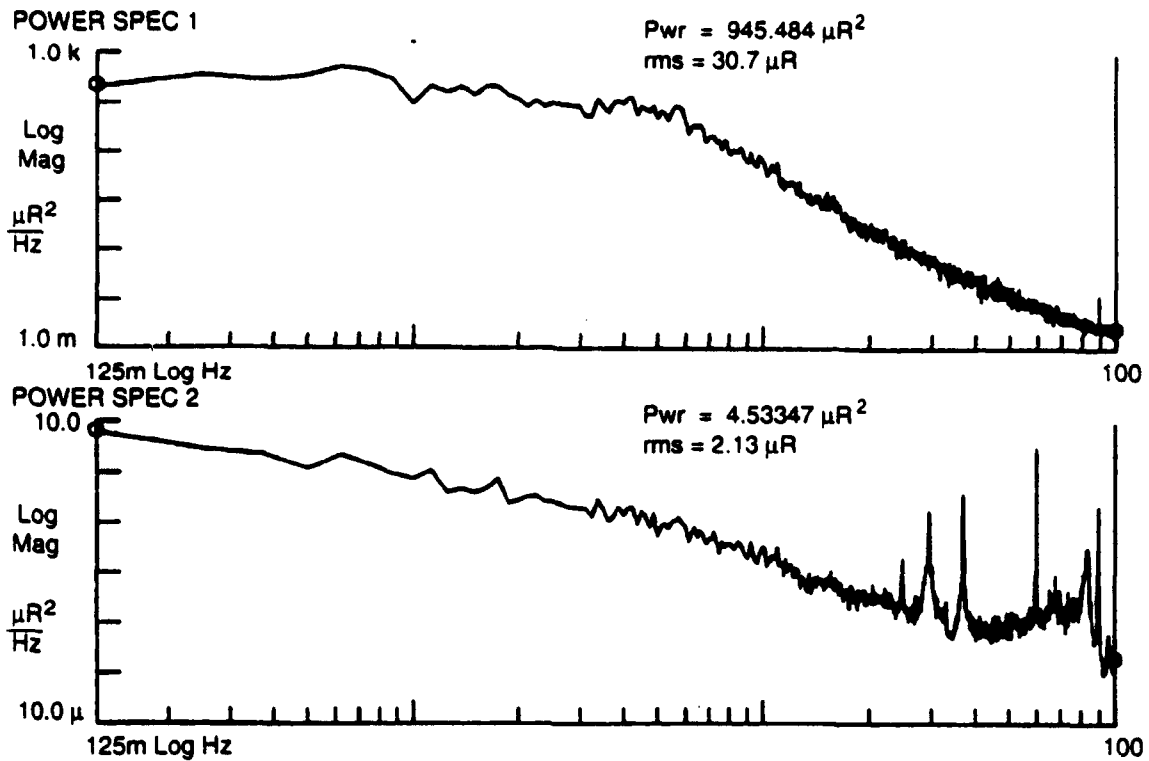


Figure 15. Stabilization system residual jitter measurement.

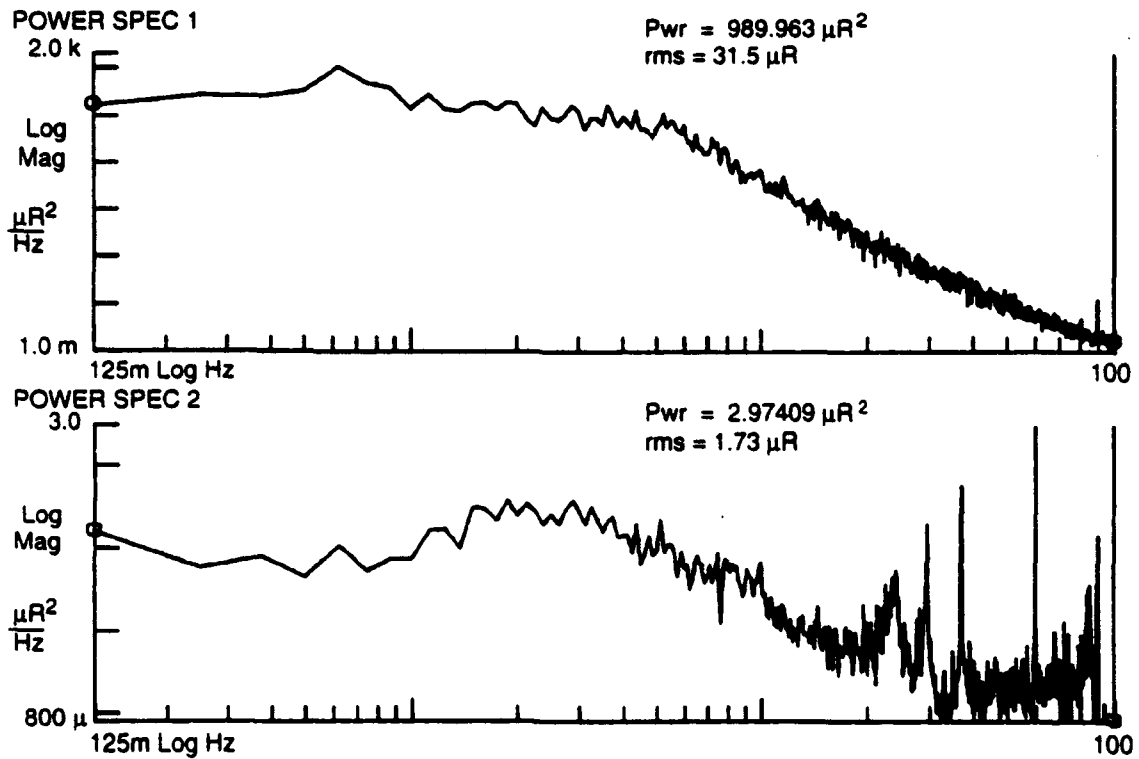


Figure 16. Pointing stabilization system residual jitter measurement.

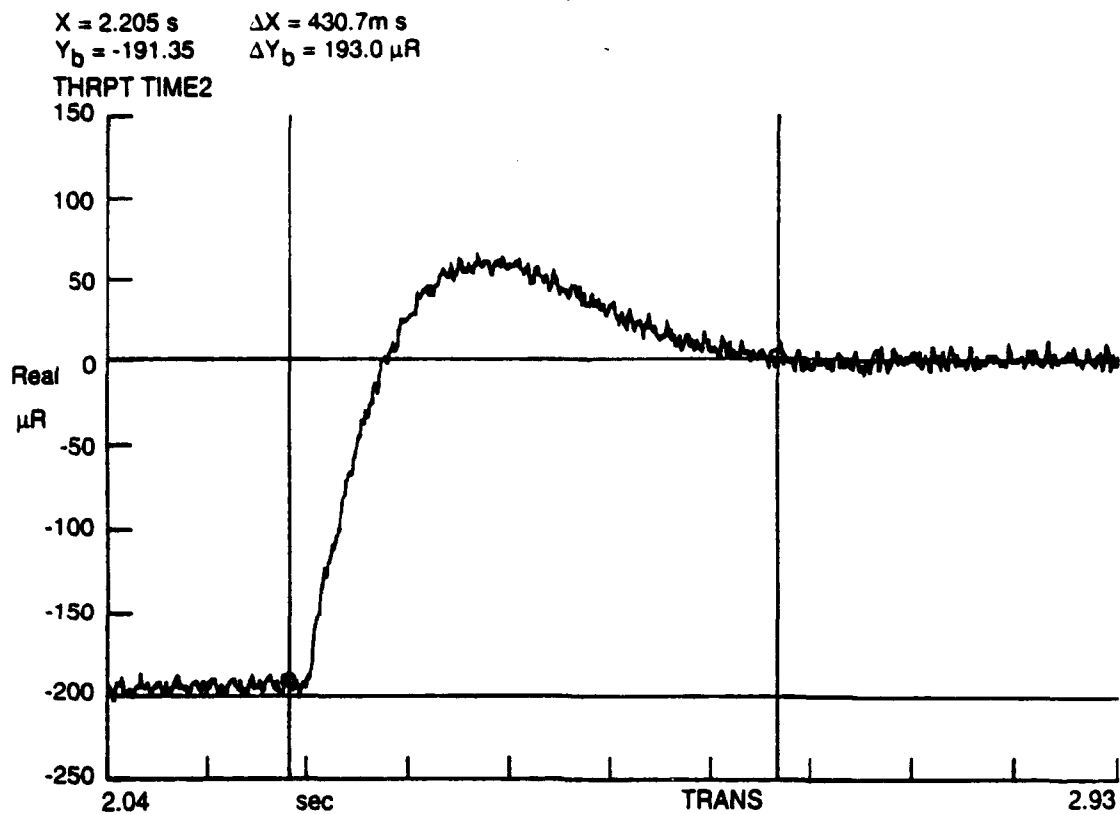


Figure 17. Pointing stabilization system transient response measurement.

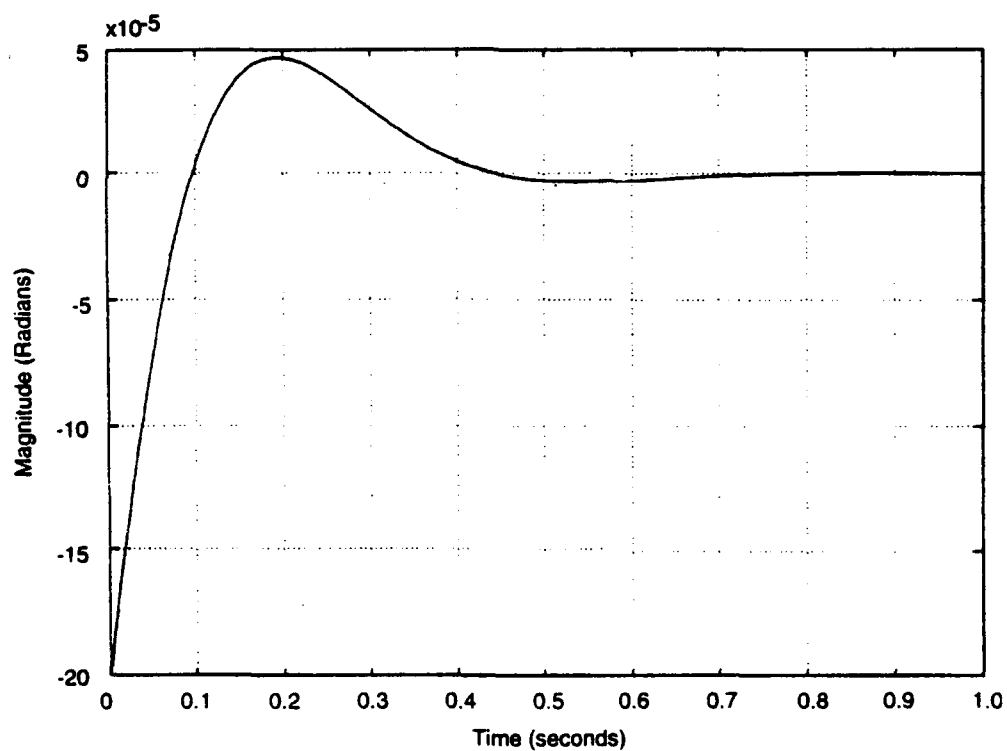


Figure 18. Analytical pointing transient response.

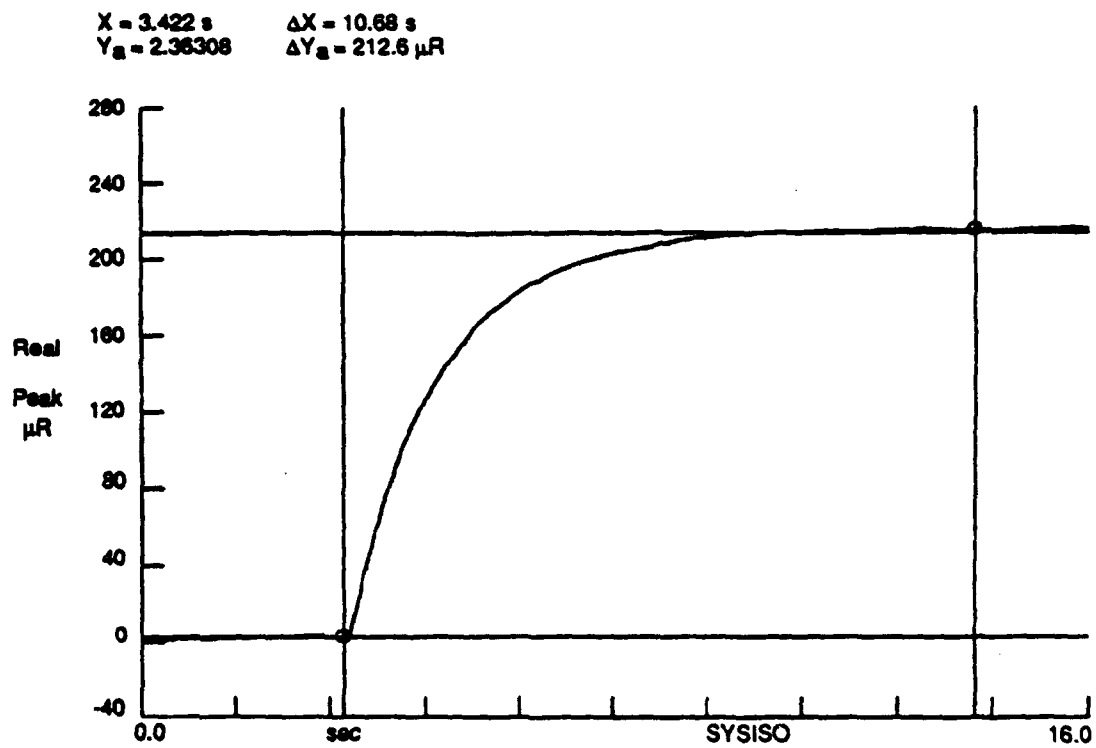


Figure 19. Test table follow-up transient response measurement.

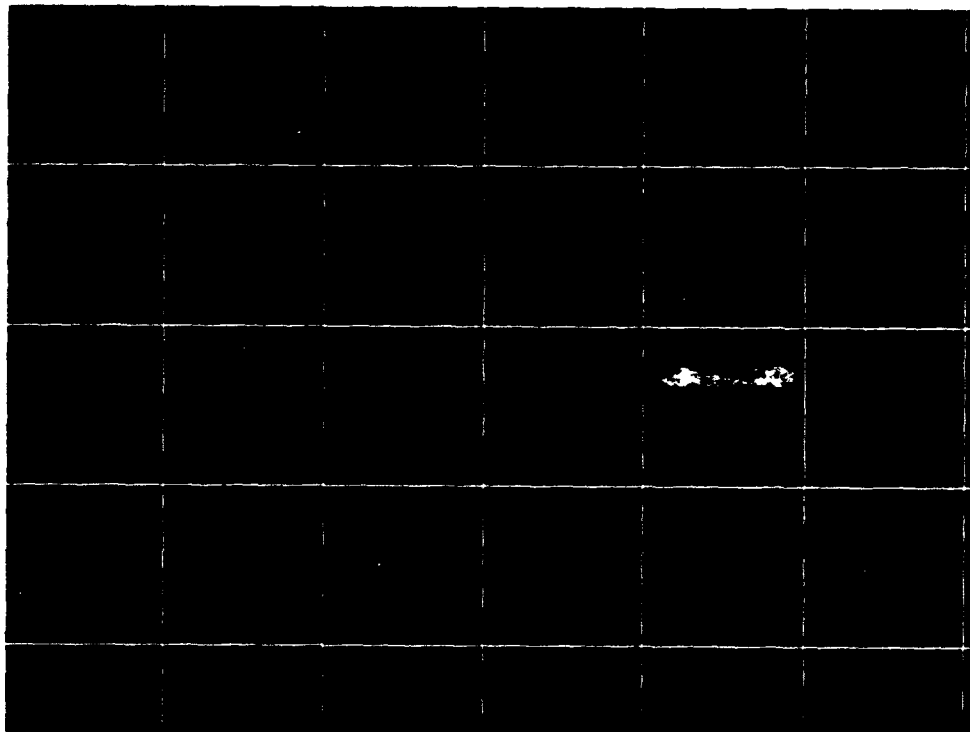


Figure 20. Image display with base motion and offset.



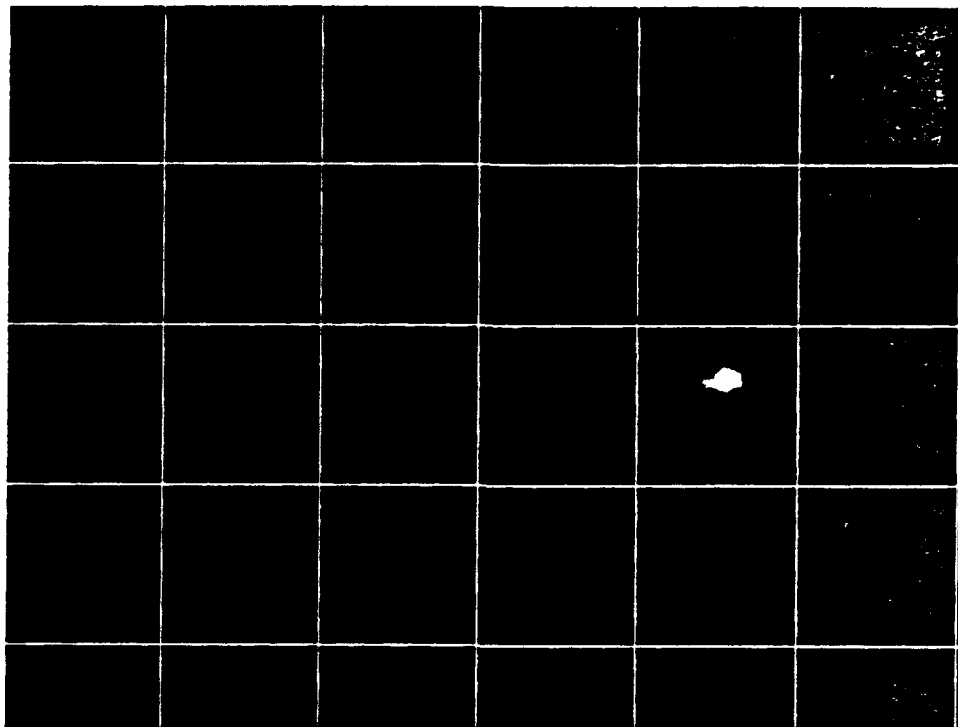


Figure 21. Image display with stabilization (*blur suppressed, offset remains*).

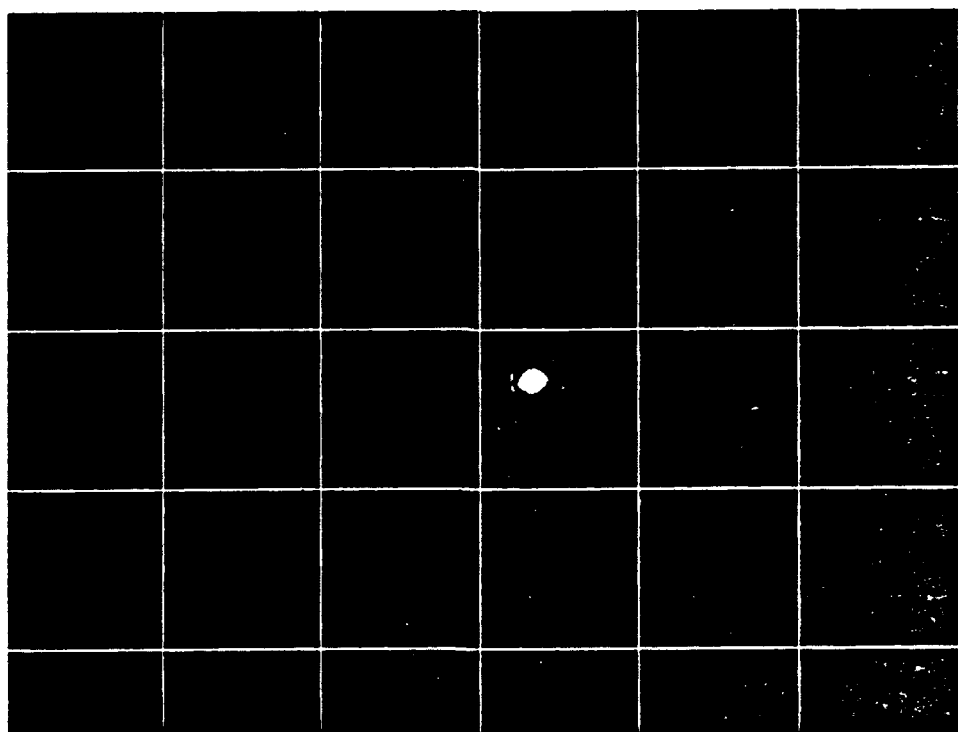


Figure 22. Image display with pointing and stabilization (*blur eliminated and offset nulled*).

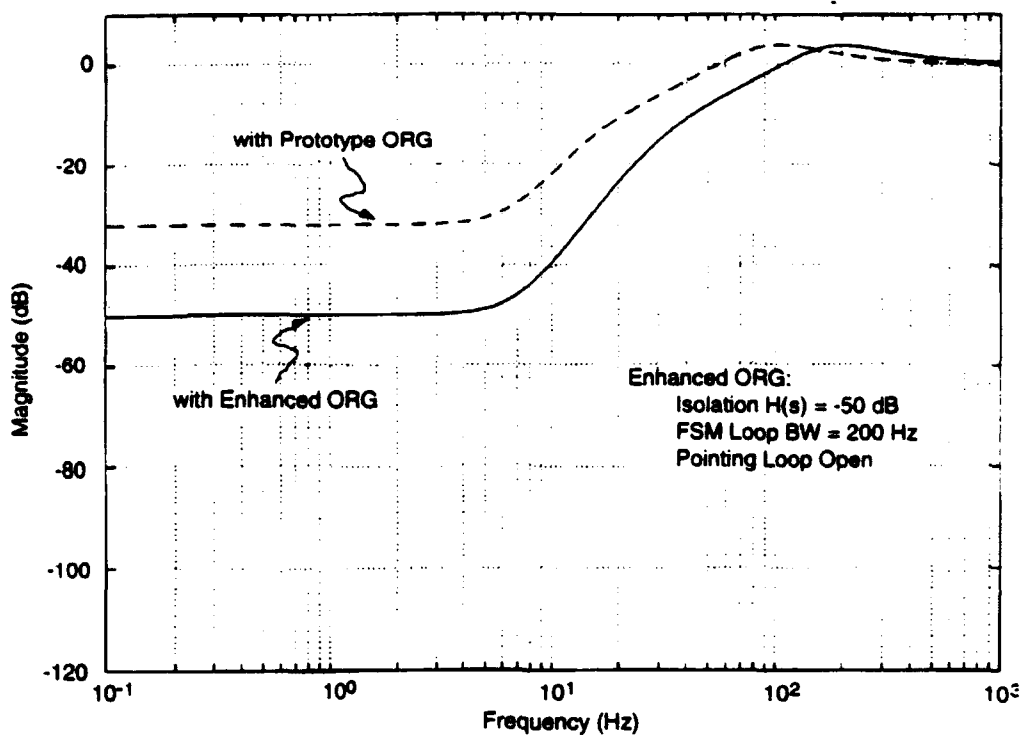


Figure 23. Analytical stabilization system transfer function (with enhanced ORG).

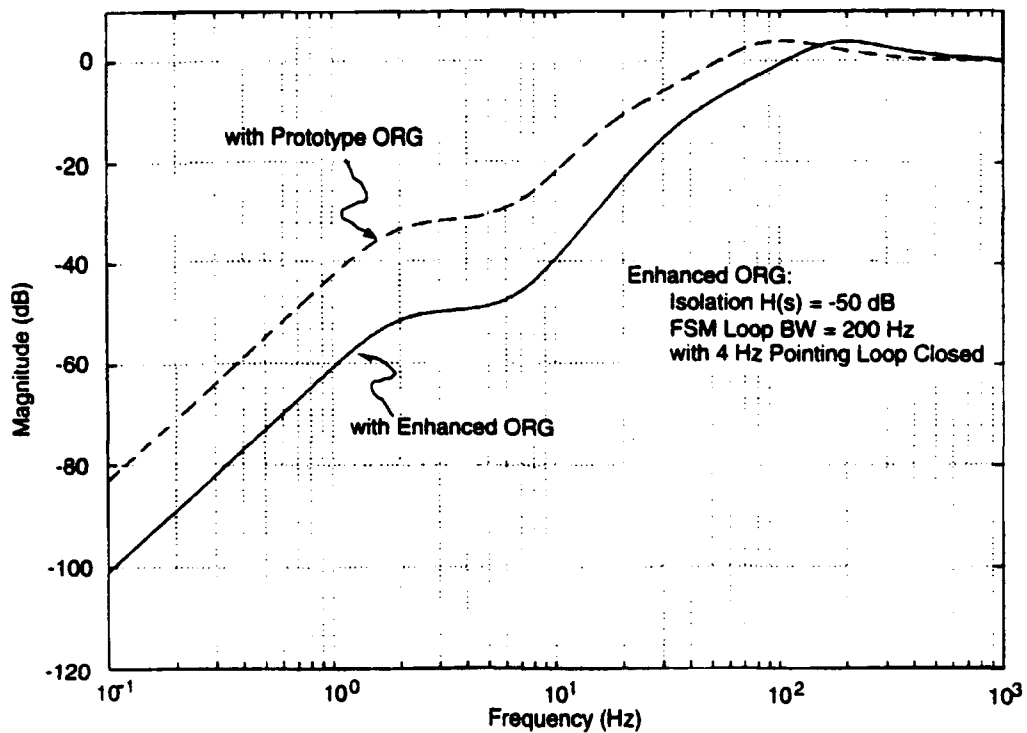


Figure 24. Analytical pointing stabilization system transfer function (with enhanced ORG).

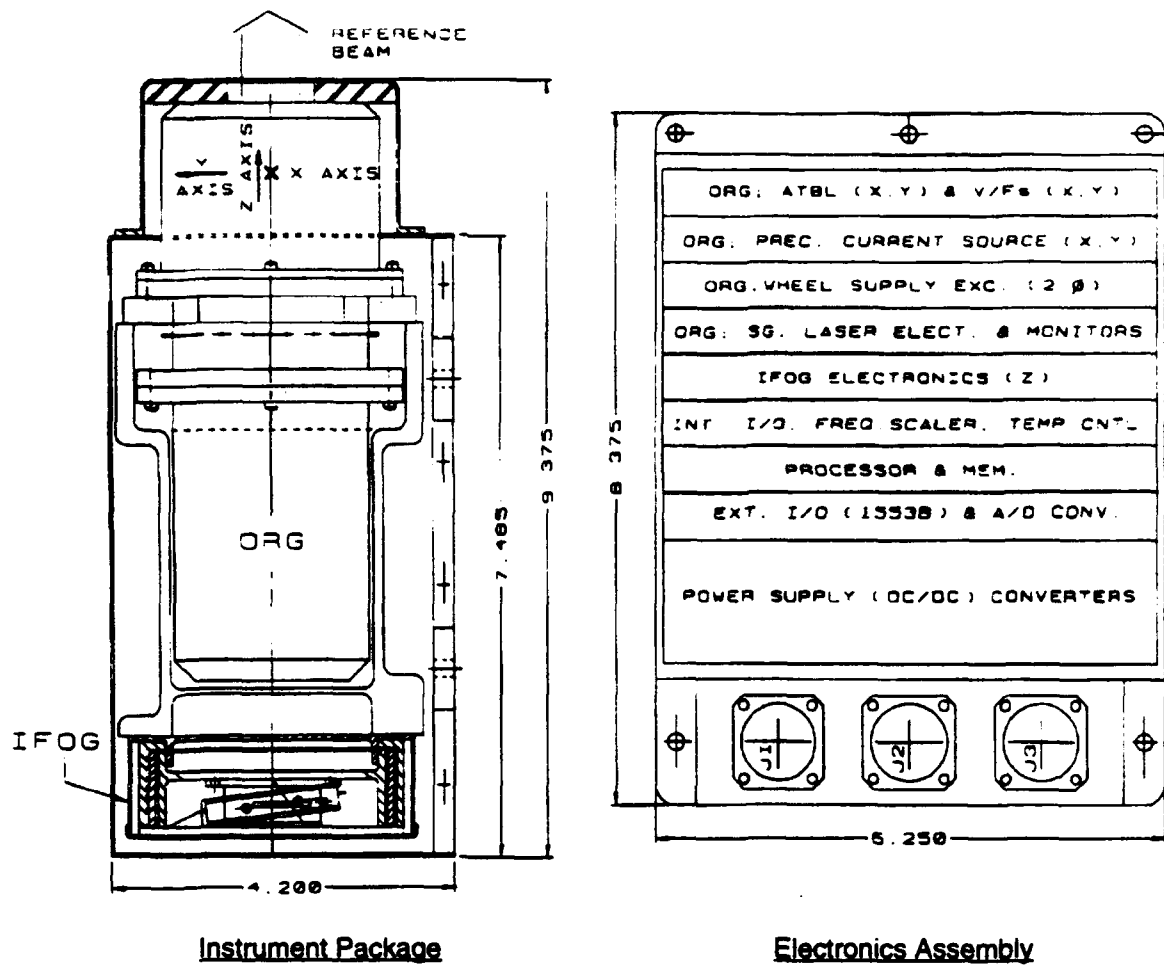


Figure 25. Projected ORG/IFOG pointing system configuration.

# **INERTIAL PSEUDO STAR REFERENCE UNIT**

by

**Michael F. Luniewicz  
Dale T. Woodbury  
Jerold P. Gilmore  
Tze T. Chien**

**of Draper Laboratory**

**Sixteenth Biennial Guidance Test Symposium**

**5-7 October 1993**

**Holloman Airforce Base, New Mexico**

**Approved For Public Release  
Distribution Unlimited  
Case # PL-93-0343 Dated 25 June 1993**



# INERTIAL PSEUDO STAR REFERENCE UNIT

Michael F. Luniewicz  
Dale T. Woodbury  
Jerold P. Gilmore  
Tze T. Chien

DRAPER LABORATORY

## INTRODUCTION

Advanced space systems for earth observation sensing and defense applications share a common objective: high-resolution monitoring. They require subsystems that accurately provide precise line-of-sight (LOS) pointing of the monitoring sensor with extreme jitter suppression and a precision attitude control system. To address this objective, Draper has developed a pointing system, the Inertial Pseudo Star Reference Unit (IPSRU). The IPSRU effort is a DARPA and SDI sponsored program at Draper under contract with the USAF Phillips Laboratory. The IPSRU implements a collimated light source mounted on a wide-band, extremely low-noise inertially stabilized platform. The collimated light beam becomes, in effect, a jitter-stabilized pseudo star. In addition, its direction in inertial space can be pointed at a precise rate by commands applied to the platform.

## APPLICATION CONCEPT

An application concept for the IPSRU reference probe beam is presented in Figure 1. In this application, the probe beam is injected into the telescope via an extended corner cube. As illustrated in the figure, both the probe beam and the scene LOS pass through the same optical path: a telescope, a fast-steering mirror (FSM), and a beam splitter to their respective detectors. Since both the IPSRU probe beam quad-detector and the scene imager are mounted rigidly on a common focal plane assembly, the scene imager smear can be corrected by nulling the quad-detector pseudo star error using the FSM.

In this image stabilization mechanization, the imager error is stabilized in a closed-loop implementation using the reference beam quad-detector. The

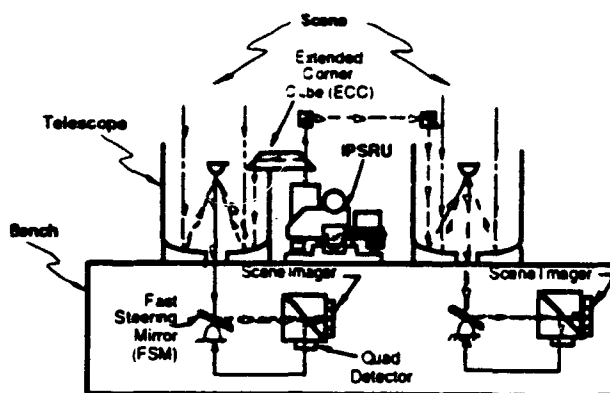


Figure 1. IPSRU application concept.

quad-detector has a high signal-to-noise ratio due to the high-intensity reference beam. Stabilization of the imager requires both effective attenuation of the base motion and low probe beam noise. Given base motion and probe beam noise spectra, an optimal stabilization loop can be designed to minimize the overall image jitter error by trade-off analysis between the residual base motion and the probe beam noise error. Ultimately, image jitter error minimization is bounded by the beam noise error.

The IPSRU concept provides closed-loop base motion error nulling for image stabilization in comparison with the alternate open-loop strapdown base motion error subtraction methods. This stabilized reference beam closed-loop approach provides the following advantages.

- The IPSRU probe beam closed-loop base motion compensation approach is desensitized from inertial sensor scale-factor errors, which are critical error sources in an open-loop implementation.
- The IPSRU inertially-stabilized probe beam error also permits correction for telescope

flexing that introduces common-mode errors to the probe beam and scene LOS.

- The stabilized implementation, in contrast, is free from the following open-loop strap-down implementation error sources:
- The strapdown gyro senses full base motion dynamics, resulting in large coupled errors.
- The strapdown gyro transfer function has large phase distortion due to torque-rebalanced limitations. Even composite strap-down sensor implementations exhibit higher residual errors due to phase mismatching.

## IPSRU DESIGN FEATURES

The IPSRU Platform is illustrated in Figure 2. A collimated fiber coupled light source is mounted on a two-degree-of-freedom stabilized platform. The signal flow mechanization is illustrated in the functional block diagram, Figure 3. The platform inertial sensing is achieved by configuring a composite wide-band inertial sensor that combines the sensed outputs of a dynamically-tuned, two-degree-of-freedom gyro (DTG) with the output of two angular displacement sensors (ADS). The platform is controlled by pointing and stabilization loops. The composite inertial sensors via servo electronics drive four differentially operated moving-coil actuators to provide inertial stabilization. Precision currents are applied to the gyro torquer by the torque drive electronics in response to control processor commands to effect platform slew, tracking, and bias compensation control. The IPSRU mechanical system is supported by a compact 2-axis central hinge that provides LOS rotational freedom and a stiff suspension in translation. The hinge implements a two-degree-of-freedom flexure that provides low rotational spring rates about the LOS stabilization axes. In addition, platform position sensors provide follow-up spacecraft attitude control in an inertial reference frame. The probe beam is implemented by coupling a laser diode light source through a single-mode optical fiber into a collimating lens assembly mounted on the stabilized platform.

A recent functional expansion of the IPSRU configuration is also illustrated in Figure 3. A second gyro mounted on the base provides a third axis of attitude sensing, nominally about the probe beam LOS. Combining the outputs of the platform and base-mounted gyros provides complete self-contained inertial attitude determination of the LOS. This capability permits the IPSRU configuration to operate for both jitter stabilization and attitude sensing for spacecraft applications.

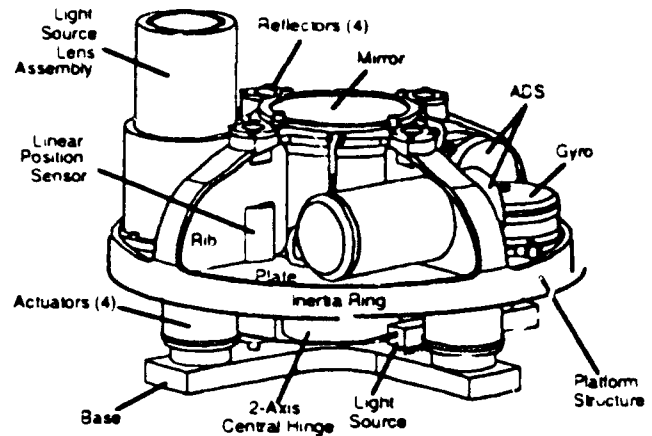


Figure 2. IPSRU functional diagram (2-axis configuration).

Provisions for monitoring an add-on accelerometer triad enables g-compensation in aircraft applications. Depending on the quality of the accelerometers and the level of integration desired, the 3-axis attitude capability and accelerometer sensing could be configured via software processing to implement navigation. An additional DQ accumulator is also implemented in the processor I/O. Software provisioning in addition to the platform mode and initialization functions include the implementation of an attitude algorithm and provisions for attitude matrix and gyro compensation updates based on stellar observations. Figure 4 illustrates the location of the second gyro on the IPSRU platform.

## IPSRU PERFORMANCE

The IPSRU platform performance projections are presented in Table 1. In this table, critical parameters are specified, including the rms jitter over the listed bandwidth, slew dynamics, base motion rejection, and platform drift are presented. Also tabulated are mechanical system parameters, including dimensions and weight, and optical parameters including wavelength and wavefront quality. Two platform bandwidths were assessed. A 20-nrad jitter is projected for the high-bandwidth version (0.1 to 300 Hz). As presented in the IPSRU performance summary (Table 1), the measured beam jitter ranges from 30 to 38 nrad rms. This higher noise level is directly traceable to the higher sensor noise of the gyro (28 nrad compared to 13 nrad). Also, air turbulence may have degraded the beam jitter measurement, as in-vacuum testing has not been completed.

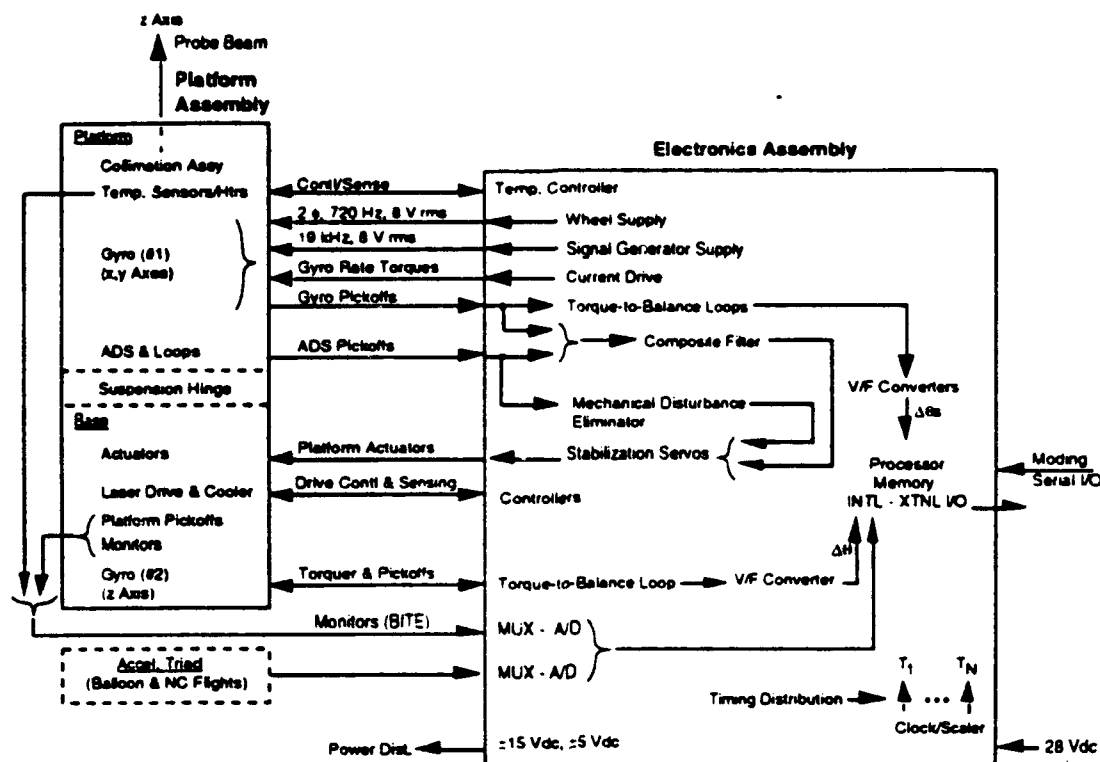


Figure 3. IPSRU functional block diagram.

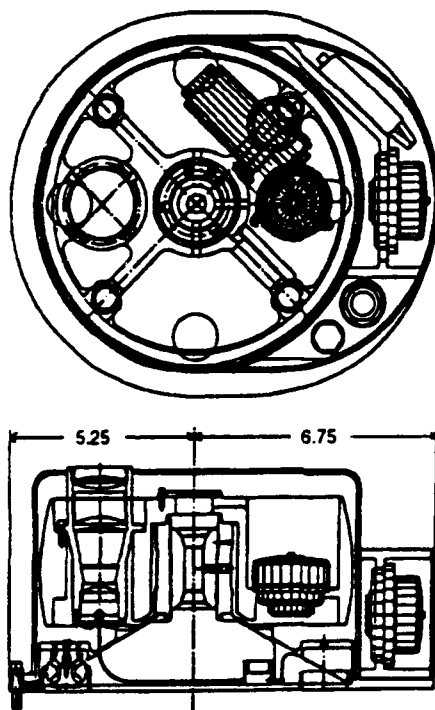


Figure 4. IPSRU platform (addition of second gyro).

These IPSRU platform performance projections are based on an analysis that considered the flow-down error model presented in Figure 5. This error model is focused on the evaluation of jitter errors.

There are five main error sources contributing to the platform jitter estimate: the base motion disturbance, the actuator noise, the inertial sensor noise, the DTG mechanical noise, and the light source inherent jitter and its measurement system noise. Each of the error source contributions to platform jitter was evaluated by deriving the corresponding transfer function and characterizing the error spectrum of disturbance and noise. Whenever available, the error characterization was based on test data.

#### INERTIAL SENSOR EVALUATION

The critical issue in defining ultimate jitter stabilization performance rests with the intrinsic performance of the inertial sensors. This section specifically addresses the test and evaluation of these critical inertial sensors.

#### GYRO SENSOR CHARACTERIZATION

A Kearfott Guidance and Navigation (KG&N) MOD II E/S gyro (S/N 542E)\* was evaluated for the IPSRU system application in June 1991. More

\* Draper wishes to express its appreciation to KG&N for their consignment of the MOD II E/S S/N 542E and S/N 266.

Table 1. IPSRU Platform Performance Projection

PERFORMANCE	UNITS	PROJECTION		Measured Results X-axis	Measured Results Y-axis
Dynamic Environment	$\mu\text{rad rms}$ (0.4-312 Hz)	320		417	366
Jitter (rms)	nrad	16	20	37(1)	34
Bandwidth	Hz	0.1-100	0.1- 300	0.4-312	0.4-312
Angular Acceleration	$\text{deg/s}^2$	5		>5	> 5
Angular Rate	$\text{deg/s}$	5		N/A	N/A
Base-Motion Rejection	dB				
@ 0.1 Hz		$\geq 100$		113	112
1-100 Hz		>50		>55	>55
Drift Rate	$\text{deg/h}$	$\leq 0.005$		0.005	0.004
Stability (1 h, 1s)					
Scale Factor (1 $\text{deg/s}$ , 1s)	ppm	<15		14(4)	N/A
Gyro Torque Loop	BW-Hz	>30		N/A	N/A
Attitude DQ LSB	$\mu\text{rad}$	1.8		N/A	
Optics					
• Wavefront Quality (Peak-to-Valley)		1/10		<1/10	
• Wavelength	nm	830		<1/10	
• Power	mW	$\geq 10$		14	
Physical Dimensions	in	8.75D x 6.3 hgt (2)		8.75D x 6.3 hgt (2)	
Weight	lb	<18		17.03	
Power on Platform	W	3.7 + 7.5 (3)		N/A (5)	

- (1) During one scoring run, the X-axis jitter measured 41 nrad. This appeared to be due to ground motion coupling into the reference pier.
- (2) Not including thermal shroud for spacecraft sun incidence, etc., and second gyro.
- (3) Heater power at midrange control point.
- (4) Measurement conducted at 0.1  $\text{deg/s}$ .
- (5) Vacuum testing not completed.

recently, the delivered KG&N MOD II E/S gyro, S/N 266 was evaluated. In this section, gyro output signal noise is quantified. Signal generator (SG) measurements were performed with an aligned ADS (S/N 147) as a correlating reference. In addition,

for earth rate and bias error elimination, the MOD II E/S was implemented with a low-bandwidth (0.1 Hz) rebalance loop. The measured gyro S/N 542E angle noise at the SG is presented in Figure 6 in the form of power spectrum density (PSD) over a bandwidth of 0.125 to 100 Hz. The measurement shows a



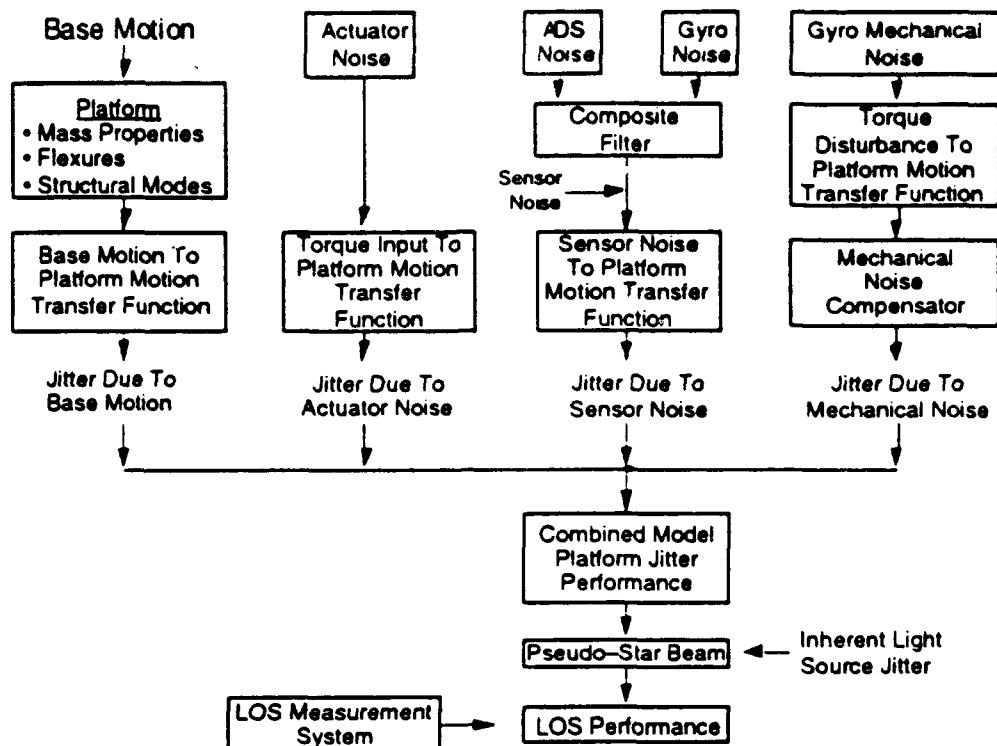


Figure 5. IPSRU flow down error model.

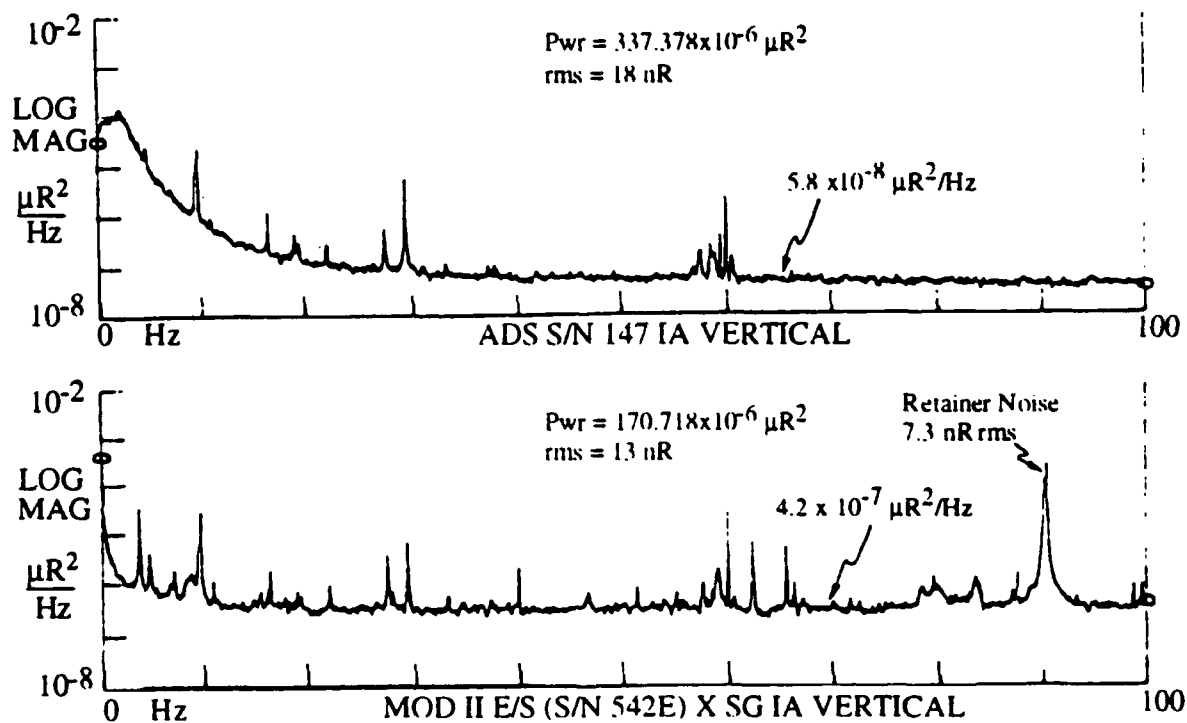


Figure 6. MOD II E/S and ADS sensor data.

MOD II E/S angle noise floor of  $4.2 \times 10^{-7} \mu\text{rad}^2/\text{Hz}$  and an rms noise of 13 nrad.

Discrete noises are also observed in Figure 6. Specifically, a significant discrete noise of 7.3 nrad is observed at the mechanical bearing retainer frequency of 90 Hz. Other discrete noises at 9.8 Hz and 29.4 Hz can be identified as cultural disturbances by correlation with the aligned ADS noise spectrum data. Additionally, as shown in the figure, the ADS sensor noise floor of  $5.8 \times 10^{-8} \mu\text{rad}^2/\text{Hz}$  is almost an order of magnitude lower than the gyro noise floor.

For further comparison of the DTG S/N 542E and ADS performance, an overlay of their sensor noise data is presented in Figure 7. The data shows a crossover of the two sensor noise level around 10 Hz. This illustrates one of the motivations for blending the gyro with an ADS into a composite sensor to provide further noise improvement. In the final design, a 15-Hz mixing frequency was selected, allowing the ADS to meet the desired 5-deg/s<sup>2</sup> acceleration goal.

An identical set of noise PSD measurements was performed on the delivered MOD II E/S gyro S/N 266. The results in an overlay form with the ADS data are shown in Figure 8. The indicated rms noise level on this gyro is 28 nrad over 0.1 to 100 Hz, approximately twice as high as the level obtained in June 1991 on S/N 542E.

The combination of both sets of gyro data (S/N 542E and 266) when operated on in the composite filter are then illustrated in Figure 9. In this case, each of the respective gyro data sets are combined with the ADS signal at a 15-Hz crossover. As shown in Figure 9, the composite sensor using gyro S/N 542E resulted in a 9-nrad rms level over 0.1 to 100 Hz, while the composite sensor using gyro S/N 266 resulted in a 24-nrad noise level.

## ADS CHARACTERIZATION

In this section, the ADS sensor noise measurement data are presented, and its slew acceleration response is evaluated.

### ADS Noise Measurement

Two sets of ADS noise data have been evaluated. The Systron-Donner ADS with a torque loop break frequency of 2 Hz shows an rms noise of 21 nrad over 1 to 100 Hz, while the Draper-modified ADS with a break frequency of 15 Hz shows an improved rms noise performance of 3 nrad. For comparison, both noise data are overlaid in Figure 10. It has been consistently observed that the ADS sen-

sor shows noise improvement when implemented with a torque loop of a higher break frequency.

### ADS Slew Acceleration Response

In addition to increasing the ADS high-pass corner frequency from 2 Hz to 15 Hz for sensor noise reduction, the higher frequency corner also prevents the ADS from saturating under slew accelerations greater than 5 deg/s<sup>2</sup>. In performance testing, the IPSRU has been subjected to 10 deg/s<sup>2</sup> without saturating the ADS.

## COMPOSITE SENSOR MECHANIZATION

Based on sensor transfer function analysis, it is apparent that no single inertial sensor can provide the desired wide-band platform stabilization capability. The DTG's limitation for a wide-band, high-fidelity sensor results from its large phase distortion, wheel noise and cross-axis coupling errors. On the other hand, the ADS does not provide adequate signal sensitivity below its corner frequency.

Draper has implemented a composite sensor mechanization for the IPSRU application that provides:

- A composite sensor with extremely low sensor noise.
- A wide-band composite inertial sensor with "zero" phase error and "unity" gain over (dc to 100 Hz) bandwidth.
- A composite sensor compatible with the slew dynamics requirement.

The composite sensor originated in an April 1985 Draper IR&D program to implement a wide-band, low-jitter stabilization platform. The loop composite sensor was mechanized with gyro and ADS blended at 10 Hz.

The IPSRU composite sensor configuration using the MOD II E/S gyro and ADS blended at 15 Hz was evaluated using the test configuration shown in Figure 11, and its measured composite sensor transfer function is shown in Figure 12. Its magnitude is essentially a constant gain with a maximum peak-to-peak error of 0.25 dB. More significantly, the measured phase angle shows a maximum error of 2 deg. This data indicates the implementation of a precisely blended composite sensor that exhibits a nearly perfect transfer function with "unity" gain and "zero" phase angle error. Moreover, analysis indicates that this transfer function performance is relatively insensitive to expected variations in ADS, gyro, and filter parameters.

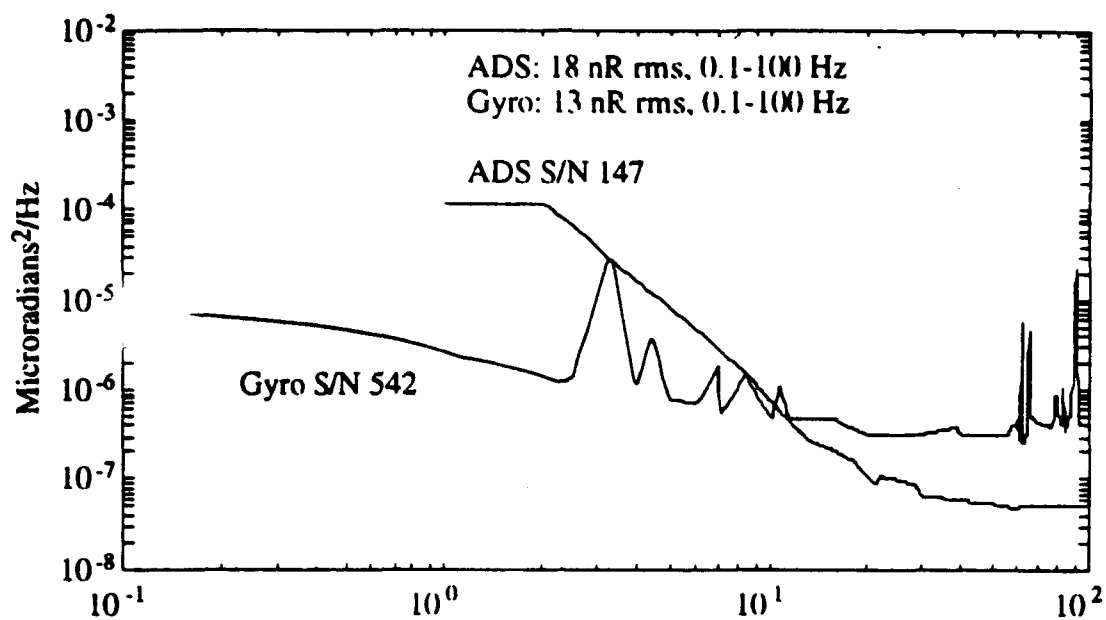


Figure 7. Noise PSDs of Gyro S/N 266 and ADS S/N 147.

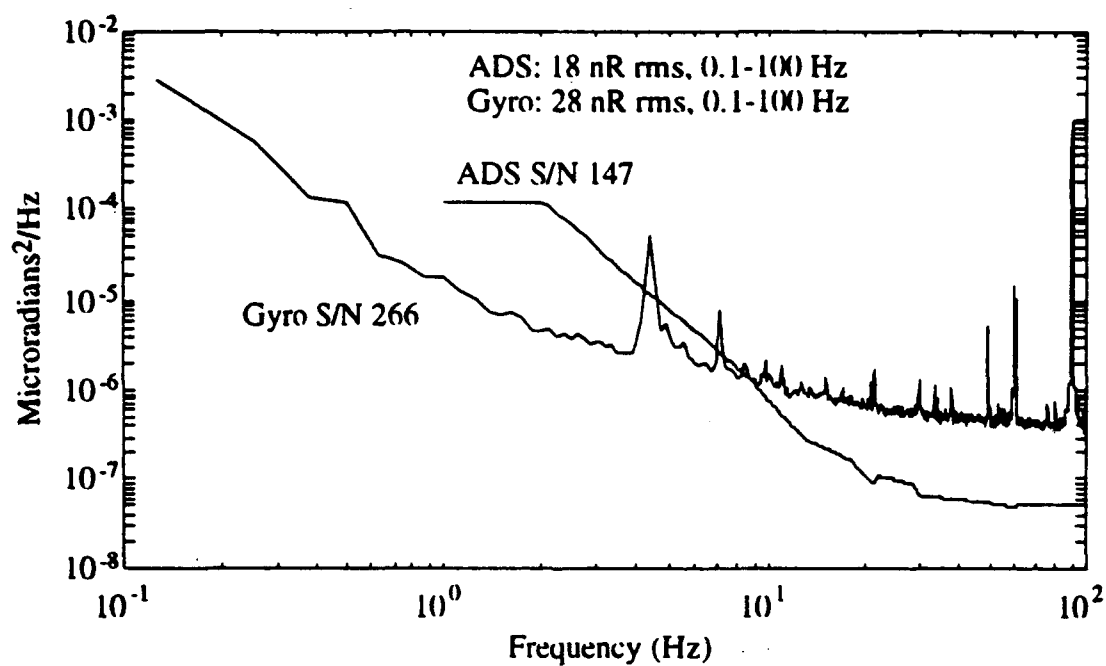


Figure 8. Noise PSDs of Gyro S/N 266 and ADS S/N 147.

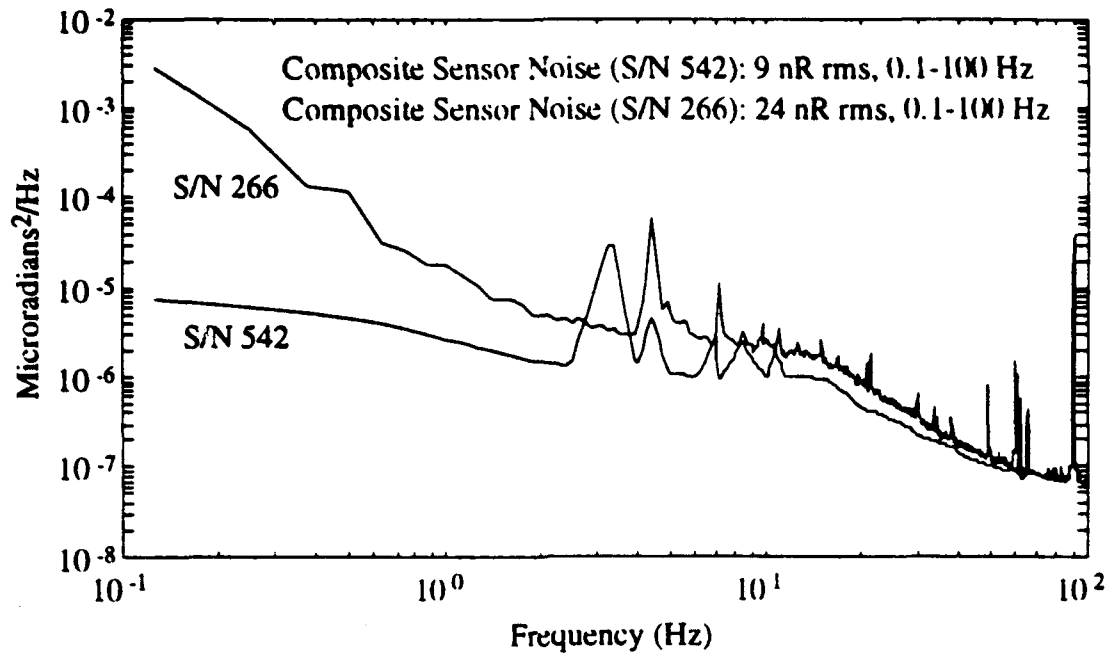


Figure 9. Composite Sensor Noise.

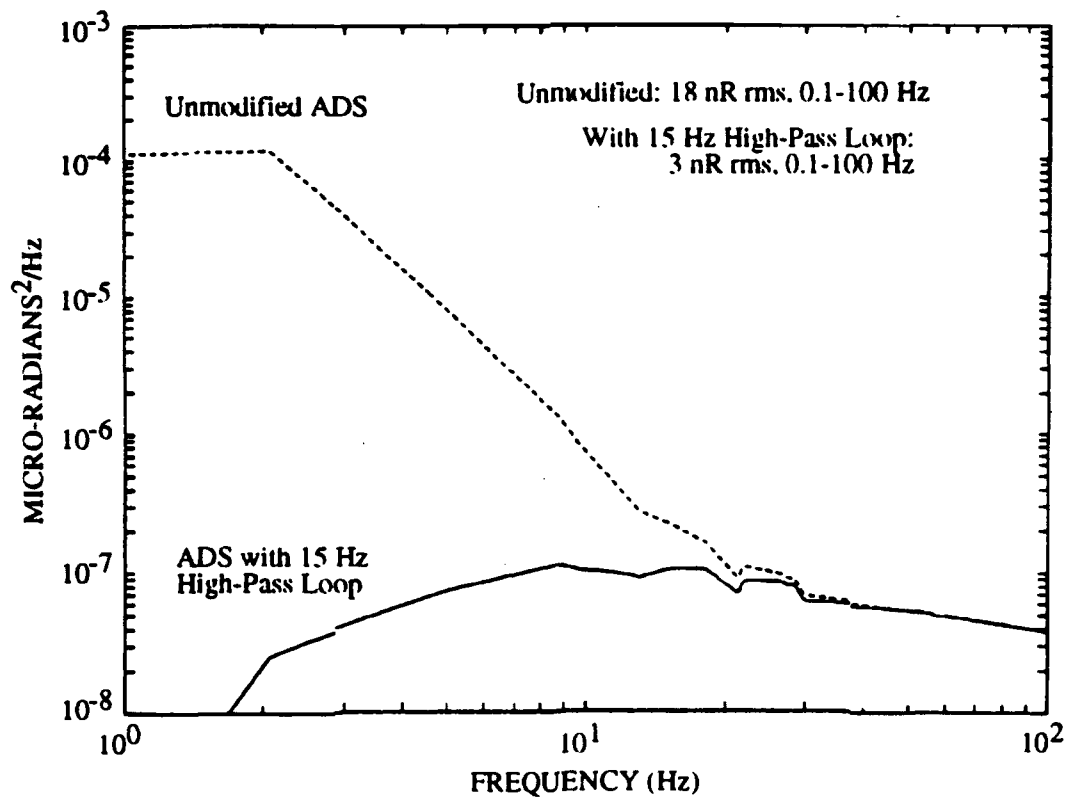


Figure 10. ADS noise with 15 Hz high-pass loop.



## IPSRU SYSTEM PERFORMANCE EVALUATION

### Platform Stabilization Jitter Evaluation

Two performance parameters of IPSRU determine the IPSRU reference beam jitter. One is the intrinsic noise of the IPSRU beam due to inertial sensor noise, servo characteristics and light source optical noise. The other is the coupling of base motion to the IPSRU platform. These two contributors to total beam jitter have been measured separately and together. Beam jitter with no base disturbance applied to the test table provides a measure of intrinsic noise. A transfer function measured between table motion and beam motion quantifies the base motion isolation of IPSRU. Finally, beam jitter measured when the test table is driven with a validation test input spectrum indicates the combined end-to-end IPSRU performance.

### Base Motion Isolation Performance

The integrated base motion isolation performance is determined by the platform stabilization loop and at frequencies beyond the closed-loop bandwidth, the inertia, damping, and spring restraint characteristics of the platform. Closed-loop stabilization is the result of the combined transfer function characteristics of the composite sensor (gyro, ADS, and composite filter), the servo controller electronics, the drive actuators, and the platform physical parameters and structural flexure modes. The design effort synthesized these elements using detailed multidegree-of-freedom transfer function models for each sensor and a detailed finite-element model of the platform structure and central hinge. Figure 13 depicts the overall IPSRU platform modal model.

The finite-element analysis produced a model with 30 flexible modes to 5 kHz. The integrated system analysis resulted in robust stability across the platform flexible modes with >12 dB attenuation of the first mode at 2850 Hz. Moreover, good high-bandwidth inner-loop (300 Hz) stability margins were realized with a 13-dB gain margin and 34-deg phase margin. The system, in addition, exhibits 2-axis stability robustness in that stability margins remain unchanged by simultaneous changes to both orthogonal stabilization axes.

The design effort resulted in a stabilization loop with a 100-Hz bandwidth. The corresponding base isolation performance analysis is reflected by the base-angle input to the platform angle output magnitude response shown in Figure 14, e.g., approximately 120 dB attenuation at 0.1 Hz and 55 dB at 100 Hz. The platform inertia provides isolation at higher frequencies as reflected by  $1/f^2$  rolloff in

Figure 14. Measured IPSRU base motion isolation from 1 Hz to 100 Hz is overlaid in Figure 14. The limited frequency range is due to low measurement coherence outside this band.

To quantify performance, the IPSRU model was exercised across two representative but distinctively different spacecraft base motion environments, the "OLJS" and the "Ball" simulation test PSDs. The OLJS environment exhibits a 320- $\mu$ rad rms input from 0.1 to 1 kHz, with the dominant disturbance energy in the 0.1 to 1-Hz band. The "Ball" test environment exhibits 35  $\mu$ rad rms over 0.1 to 1 kHz, but the disturbance energy is much higher at frequencies above 10 Hz.

The IPSRU isolation performance was calculated for both base disturbance models with rms error contributions of 1 and 4 nrad, respectively. Also, a validation base disturbance was applied to the test table and the resulting IPSRU beam jitter was measured. As shown in Figure 15, the validation disturbance exceeds both the OLJS and Ball models over the entire frequency range. Table 2 summarizes the jitter of the IPSRU beam with and without the base disturbance driving the test table. Also, Figure 16 shows the PSDs of the table disturbance and the resulting IPSRU beam jitter for the case when the validation base disturbance is applied. The beam jitter PSD remains essentially unchanged when the test table is not driven with the validation input.

Table 2. IPSRU beam jitter with and without validation base disturbance applied to test table.

Axis	Test Table Drive	Base Disturbance	Reference Beam Jitter
X	Benign	< 3 $\mu$ rad <sup>(1)</sup>	35 nrad
	With Disturbance Input	417 $\mu$ rad	37 nrad
Y	Benign	< 3 $\mu$ rad <sup>(1)</sup>	32 nrad
	With Disturbance Input	366 $\mu$ rad	34 nrad

(1) Measurement system ZLG sensor noise ~3  $\mu$ rad rms (0.4 to 312 Hz).

### PLATFORM SLEW RESPONSE EVALUATION

In the slew mode, an acceleration command profile through the computer generates a current input into the DTG torquer to slew command the IPSRU platform. The test table is used as a spacecraft simulator and is controlled through the platform position sensors in a follow-up mode.

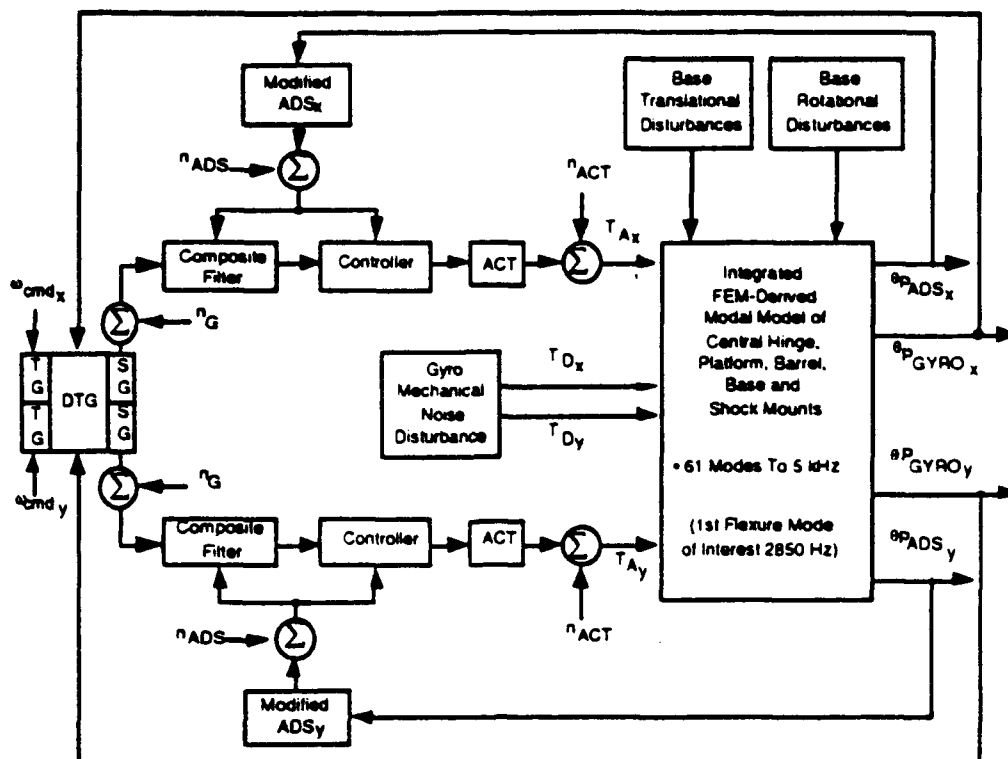


Figure 13. Integrated stabilization and platform modal model.

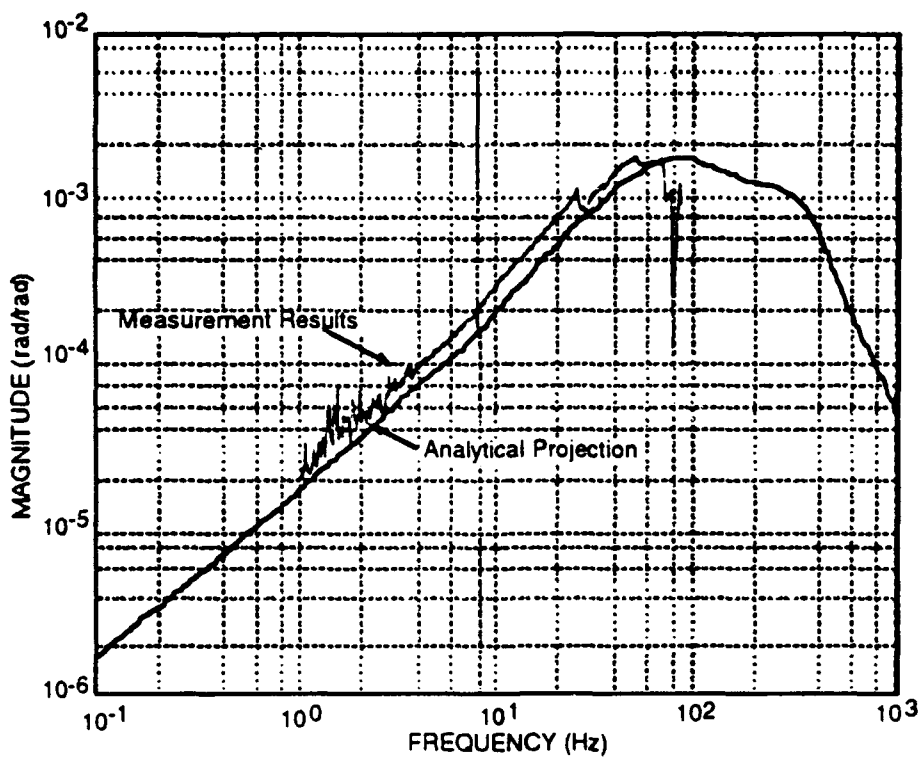


Figure 14. Base angle input to platform angle output.

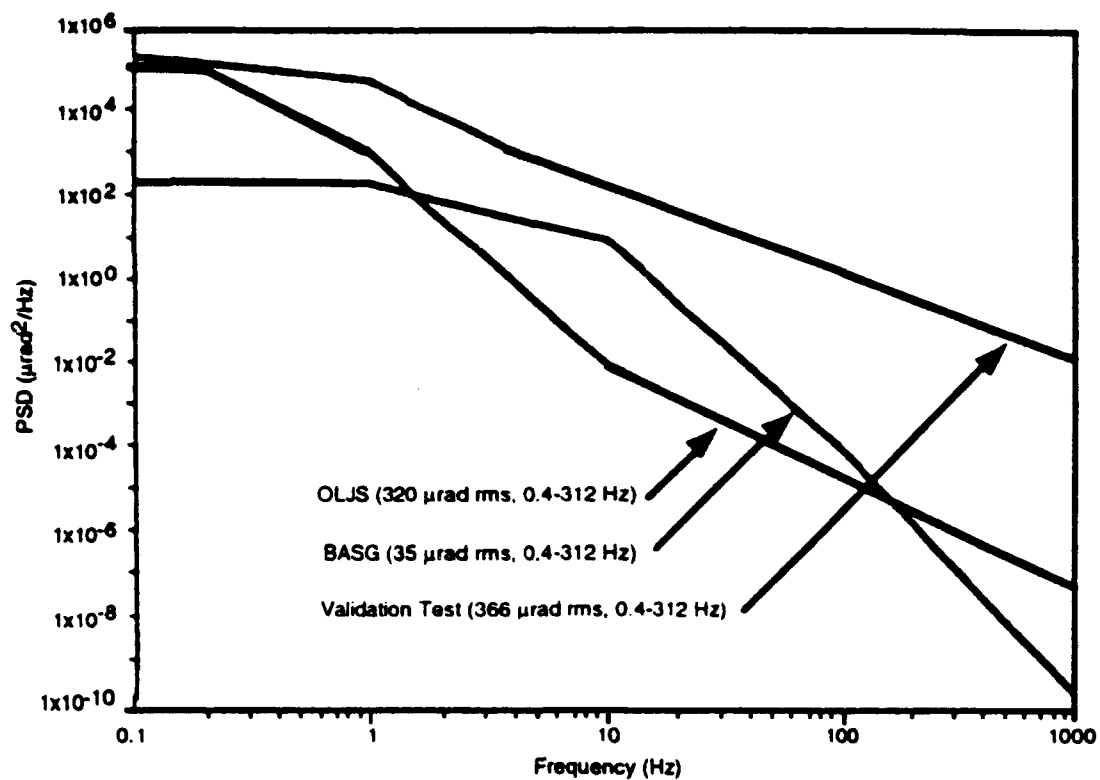


Figure 15. Input base disturbance spectrum.

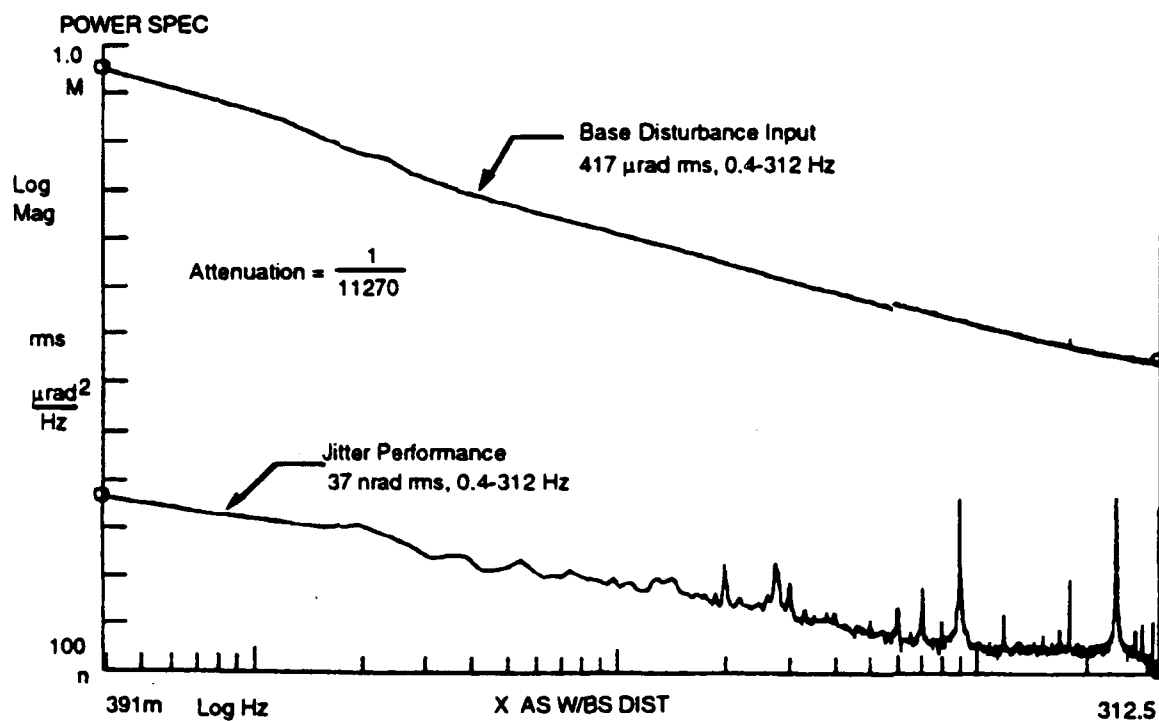


Figure 16. Jitter performance measurement I (with base disturbance, X-axis).



For slew mode evaluation, the precision current source and the gyro scale factor must be precisely compensated for stability and bias error to achieve the projected accuracy across the dynamic range of 5 deg/s and 5 deg/s<sup>2</sup>. IPSRU platform response is measured by the enhanced laser interferometer, 6.8 nrad/bit. In addition, the laser interferometer measurement system provides a measurement range of  $\pm 2$  deg, sufficient to cover a representative slew angle range. Over the 2-deg range, an arcsine correction is applied to the interferometer output. The difference between the synchronous measurements of the laser interferometer and the slew command input provides the platform error response. Table 3 summarizes the results from a slew response test. Over a total 8-deg maneuver, in a bang-bang 5°/s<sup>2</sup> mode, the end-point error is only 3  $\mu$ rad, corre-

scoring devices are described. A precision pointing scoring system was developed based on a Draper IR&D program. The key performance scoring devices are an enhanced laser interferometer system and a precision angle sensor.

#### Enhanced Laser Interferometer

An enhanced laser interferometer system was developed at Draper to provide the measurement capability of precision pointing performance. This system was developed by enhancing the electronic resolution module of a Hewlett-Packard angular laser interferometer system (5501A). This laser interferometer system provides an enhanced resolution of 5.8 nrad/bit. It has a measured sensor noise of 6.2 nrad rms over (0.4 to 100 Hz) with a rate capability of  $\pm 1.65$  deg/s. The current Draper laser interfer-

Table 3. IPSRU slew response test results.

Maneuver	Total Angle of Maneuver	Platform Pointing Error Transient	Open-Loop End - Point Offset	Scale-Factor Error
$\pm 2$ -deg, 5-deg/s <sup>2</sup> bang-bang, 2 cycles	8 deg	60 $\mu$ rad	3 $\mu$ rad	21 ppm
$\pm 2$ -deg, 0.1-deg/s constant rate, 2 cycles	8 deg	12 $\mu$ rad	2 $\mu$ rad	14 ppm

sponding to a scale-factor error of 21 ppm.

#### PLATFORM DRIFT RATE EVALUATION

A tracking loop was closed from the output of the enhanced angle sensor measuring the IPSRU reference beam to the gyro torquer slew inputs, forcing the IPSRU to track a fixed component of earth rate. The value of the rate command was recorded over a 1-h period, and the mean and standard deviation of this data were calculated. The results of these measurements are given in Table 4.

Table 4. IPSRU drift rate stability test results.

Parameter (Over 1-h duration)	X-Axis (vertical)	Y-Axis (east-west)
Mean Bias (deg/h)	-8.445	-0.2287
Standard Deviation (deg/h)	0.004375	0.004974

#### SYSTEM INTEGRATION TEST PRECISION POINTING SCORING SYSTEM

Measurement capabilities consistent with IPSRU performance projection represent a significant technology challenge. In this section, key performance

ometer system is being revised to provide a  $\pm 5$ -deg/s

rate capability. This interferometer system has a resolution of 6.8 nrad/bit due to smaller optics, and a 2-deg field of view (with arcsine correction).

#### Enhanced Angle Sensor

For IPSRU light source jitter measurement, an enhanced 2-axis angle measurement sensor has been constructed. The measured performance of this angle sensor is 6 nrad rms 0.1 to 300 Hz with a range of 4  $\mu$ rad peak-to-peak.

#### INTEGRATION TEST CONFIGURATION

The integration test configuration for IPSRU evaluation is presented in Figure 17 to illustrate the test concepts. The IPSRU evaluation is performed on a 3-axis test table. The test table inner gimbal serves as a spacecraft simulator. It is controlled by a follow-up servo using the IPSRU platform position sensor outputs. Two scoring instrumentation systems are implemented. A laser interferometer system is used to evaluate IPSRU platform performance, and an angle sensor for an end-to-end evaluation of the IPSRU system beam jitter performance, including the light source inherent jitter error. The integration test is supported by a data acquisition and computer control system.

Several features of test setup are important to note. Test performance scoring consistent with the performance projections identified in Table 1 requires an extremely quiet test pier and reference base implementation and the suppression of air turbulence effects between the various LOS sources and their measurement detectors. The Draper test pier assigned to the IPSRU program has been selected for its low vertical-axis cultural noise levels ( $\sim 5$  nrad, ADS measurement over 300 Hz). High-performance jitter scoring will be accomplished with one IPSRU reference axis aligned with the vertical table axis shown in Figure 17. The reference base is a 9000-lb black granite block, which exhibits high intrinsic damping.

Critical to the IPSRU base motion isolation measurements is that the reference pier holding the scoring instrumentation (angle sensor and laser interferometer) be isolated from test table motion. High isolation was validated by measuring the transfer function between the test table motion (measured with a ZLG) and the inertial motion on the reference pier (measured with an ADS). The table drive amplitude used was the same for this test as for the IPSRU base motion isolation transfer function measurement. The test table to reference pier coupling transfer function is shown in Figure 18. No measurable coupling exists except between 30 and 60 Hz, as indicated by the coherence function. Here, the maximum coupling is -78 dB, which is sufficiently smaller than the IPSRU base motion isolation in that same frequency band, and thus does not corrupt the IPSRU isolation measurement.

A table-mounted vacuum chamber encloses the IPSRU to prevent air turbulence from degrading the IPSRU beam jitter measurement and the laser interferometer measurement. Thermal experiments indicate that when the IPSRU is maintained at 135°F (the set point for a satellite application), jitter measurements would be overwhelmed by air turbulence unless enclosed in a vacuum. The vacuum chamber and optical parts are shown in Figure 17.

Note that the testing conducted on IPSRU to date has been in air with the IPSRU set point temperature reduced to 82°F. Shrouds were installed around the optical beams to reduce air turbulence effects. It may be that some remaining air turbulence has corrupted the low-frequency jitter measurements (below 2 Hz), and jitter performance may be better than current measurements indicate.

## CONCLUSION

This paper presents a precision pointing inertial pseudo star reference unit (IPSRU) system. An

application concept on image stabilization is illustrated. The IPSRU platform performance projected analytically is compared to measured performance data. The IPSRU implements a collimated light source mounted on a wide-band, extremely low-noise, inertially-stabilized platform. The collimated beam, in effect, becomes a jitter-stabilized pseudo star.

A critical issue in defining the ultimate IPSRU jitter stabilization performance rests with the relative performance intrinsic to the inertial sensors. In this paper, the test and evaluation of a MOD II E/S dynamically-tuned gyro (DTG) and an angular displacement sensor (ADS) are addressed. The measurement over 0.1 to 100 Hz showed a MOD II E/S on a rms noise level that ranged between 28 and 13 nrad (depending on the gyro used). The ADS torque loop was modified to increase its break frequency to 15 Hz to achieve IPSRU 5-deg/s<sup>2</sup> slew acceleration capability. The modified ADS sensor showed an even lower angle noise floor of  $5.8 \times 10^{-8}$   $\mu\text{rad}^2/\text{Hz}$ .

Based on sensor transfer function analysis, it was concluded that no single inertial sensor can provide the desired wide-band platform stabilization capability. Draper has implemented a composite sensor mechanization by blending a DTG with two ADSs at a mixing frequency of 15 Hz for the IPSRU platform application. Tests demonstrated a composite sensor implementation with a nearly unity transfer function and less than 2-deg phase error. In addition, the composite sensor provides further noise improvement. The composite sensor implementation using the DTG and ADS data could contribute as low as 10 nrad in the platform jitter budget, yielding a projected 16 nrad over a bandwidth of 0.1 to 100 Hz. However, the only available gyro for incorporation in the first deliverable IPSRU is gyro S/N 266, so the composite sensor noise level of 24 nrad would be expected, yielding a correspondingly higher platform jitter budget, and a platform jitter ranging from 30 to 38 nrad was measured. It is also noted that in addition to the higher sensor noise of gyro S/N 266, jitter measurements were made in air rather than in a vacuum. Air turbulence may have degraded jitter performance measurements below about 2 Hz where the jitter floor is high. The measured base motion isolation essentially matches the analytically predicted performance.

Critical performance scoring instrumentations for evaluating the IPSRU precision performance were reviewed. These include a Draper-enhanced laser interferometer system with a 6.8-nrad resolution and further enhancements of the Draper-developed angle sensor with a measured rms noise of 6 nrad over a 100-Hz bandwidth.

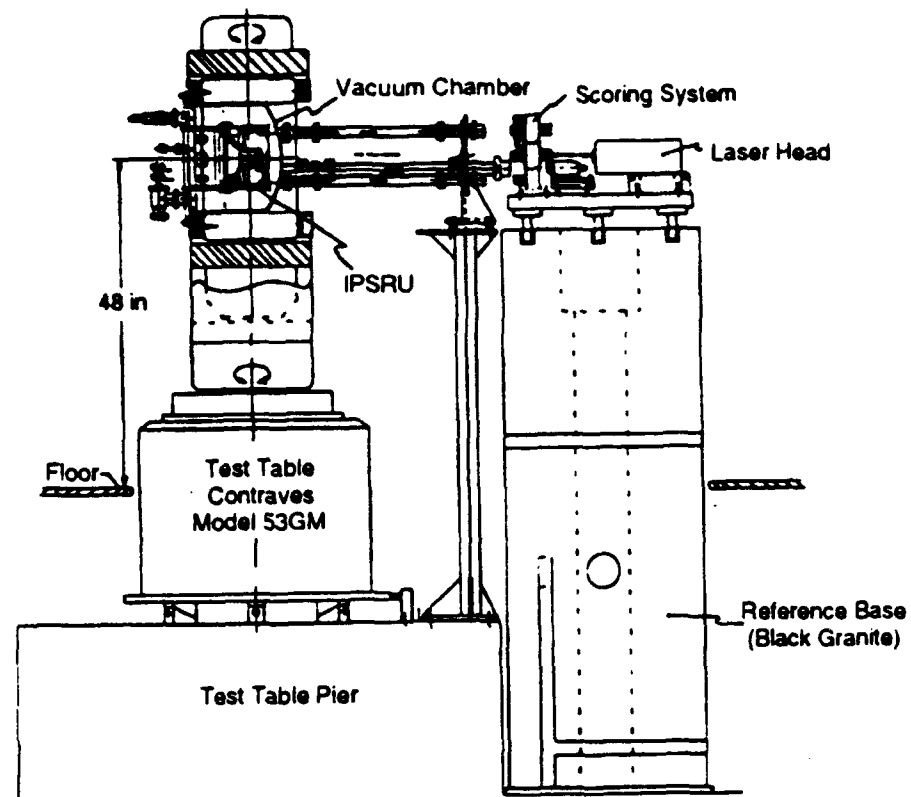


Figure 17. Integrated test facility layout.

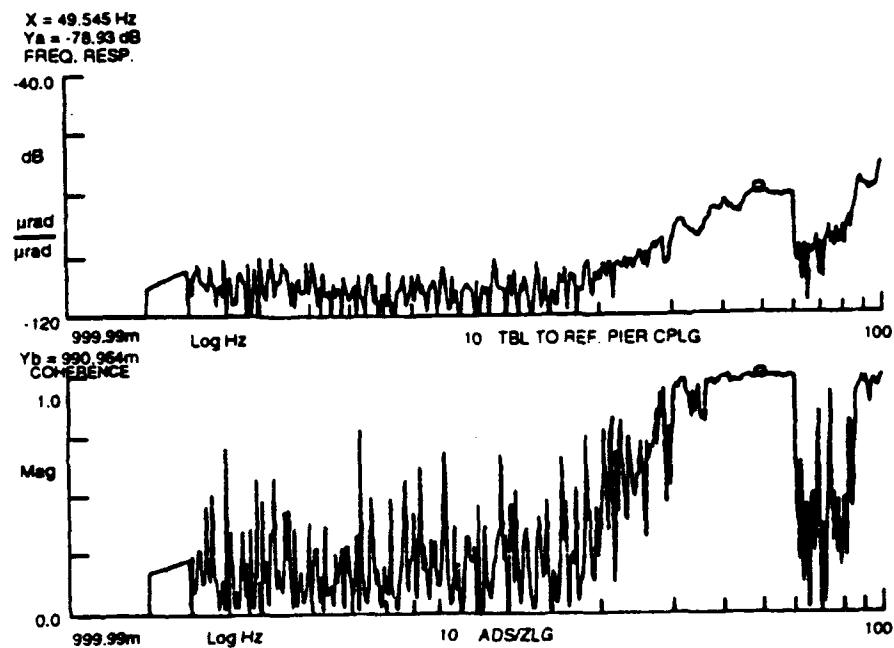


Figure 18. Table base - reference pier motion transfer function.

## REFERENCES:

Gilmore, J., et al., "Inertial Pseudo-Star Reference Unit," *IEEE Proceedings, PLANS Symposium*, Monterey, California, 23-27 March 1992.

Luniewicz, M., et al., "Comparison of Wide-Band Inertial Line of Sight Stabilization Reference Mechanizations," *SPIE Aerospace Sensing, Acquisition, Tracking and Pointing VI Symposium Proceedings*, Orlando, Florida, 21-24 April 1993.

**THIS PAGE LEFT BLANK INTENTIONALLY**

**SESSION VII-A  
ADVANCED SYSTEMS**

***CHAIRMAN***  
**BOYD E. HOLSAPPLE**  
***WRIGHT-PATTERSON AFB OH***

**THIS PAGE LEFT BLANK INTENTIONALLY**

# **THE ADVANTAGES OF A LONG RANGE PRECISION STRIKE WEAPON**

By  
Thomas E. Reed  
Consultant

Presented at  
The Sixteenth Air Force Guidance Symposium  
Holloman Air Force Base

October 5, 6, 7, 1993



## ABSTRACT

The present world situation requires a renewed look at the strategic weapons in our country's inventory. Our present national goals include the development of a non-nuclear precision strike weapon in the form of guided bombs and cruise missiles. The addition of a long range, land based, non-nuclear weapon capable of precisely hitting any target in the world would greatly increase our country's capability in this area by allowing essentially invulnerable surgical strikes at high value targets without jeopardizing our personnel and with a minimum amount of collateral damage. This paper will elaborate on the advantages and limitations of this type of weapon, comparing it to other methods of precision strike delivery systems. It will also describe the methods of obtaining the high precision accuracy, define the risk areas and present an outline of the program required for full development.

## **ACKNOWLEDGEMENTS**

The authors would like to acknowledge various members of the BMT office, TRW and C. S. Draper Laboratory for their helpful suggestions. This paper is written strictly for the stimulation of ideas and is the expressed opinion of the author. This paper does not necessarily reflect the views or opinions of the Air Force, TRW, Draper Laboratory or any agency — public or private.

## TABLE OF CONTENTS

INTRODUCTION	1
PRECISION STRIKE GUIDANCE	2
OTHER PRECISION STRIKE DELIVERY SYSTEMS	2
LRPW DESCRIPTION	2
Range Capability	2
Warhead	4
Launch Sites	4
LRPW ADVANTAGES	4
Low Maintenance Cost	4
Invulnerability	4
Humane	4
Increased Destruction	5
Fast Reaction	5
Psychological Impact	5
Better Domestic Acceptance	5
Minimal Foreign Influence	5
Low Development and Deployment Costs	5
LRPW OPERATION	5
DEVELOPMENT & OPERATIONAL ISSUES	6
Definition of Targets	8
Target Locations	8
Mission Support	8
Launch Readiness	8
GPS Ionosphere Distortion	9
Time Management	9
INS Parameter Update during Boost	9
Changing Satellites	9
Satellite Integrity	9
Reentry Velocity Vector Matching	10
Plasma Attenuation of GPS Signals	10
Anti-Jamming Techniques	10
Reacquisition after Plasma or Jamming	10
Differential or Relative GPS	10
Terminal Dynamics	11
CONCLUSIONS & RECOMMENDATIONS	11

# THE ADVANTAGES OF A LONG RANGE, PRECISION STRIKE WEAPON

## INTRODUCTION

In July 1992, the office of the Director of Defense Research and Engineering (DDR&E) issued a report entitled, "Defense Science Technology Strategy". The purpose of this report was to focus the nation's defense technology to better fit the post cold war realities. To quote:

"The core of this strategy is to (1) provide for the early, intensive and continued involvement of warfighters, (2) fuel and exploit the information technology explosion, and (3) conduct extensive and realistic technology demonstrations."

The report provides focus by generating seven science and technology thrusts:

1. Global Surveillance and Communication
2. Precision Strike
3. Air Superiority and Defense
4. Sea Control and Undersea Superiority
5. Advanced Land Combat
6. Synthetic Environments
7. Technology for Affordability

This paper will focus primarily on thrust #2, Precision Strike, but will be influenced in varying degrees by the others. The report gives the following definition:

"Precision Strike is a set of integrated, multi-Service capabilities for locating, identifying and killing high-value, time-sensitive military targets. This detection-engagement cycle must be executable in all weather conditions, day or night, with precision accuracy<sup>1</sup>, and in timely response to the commander's operational needs. *Success in Precision Strike depends on achieving a seamless interface with Global Surveillance and Communications systems..*" [Italics theirs]

There are essentially six basic methods<sup>2</sup> of delivering a Precision Strike weapon, with other sub-sets. This report will attempt to show the advantages, disadvantages and roles that we believe are suitable for each of these delivery systems. The primary goal of this paper is to show that a Long Range, home based Precision Strike Weapon system, hereafter called the LRPW, can have a unique and major role in this nation's total Precision Strike capability.

---

<sup>1</sup> The stated accuracy goal is 3 meters.

<sup>2</sup> A space platform weapon could be considered the seventh method but will not be covered here.

## **PRECISION STRIKE GUIDANCE**

All Precision Strike weapons will need some type of terminal aid in order to obtain the required accuracy. The different methods for terminal aiding are beyond the scope of this paper. The assumption is that terminal aids are a common denominator for all precision strike capabilities and the only distinction between precision strike weapons is the acquisition and maintenance cost of the weapon versus target value.

The method described by this paper is an advanced GPS/IMU using differential update methods for accuracy enhancement. This method, once developed, should be a cost effective terminal aid. It will require improvements in target location technology and the development of better anti-jam GPS methods -- all of which appear to be technically feasible.

## **OTHER PRECISION STRIKE DELIVERY SYSTEMS**

There are other precision strike weapons either operational or in various stages of development by the Air Force, the Navy or the Army. They are:

1. Field Artillery
2. Joint Direct Attack Mission (JDAM, aircraft bombing)
3. Air Launched Cruise Missile (ALCM)
4. Sea Launched Cruise Missile (SLCM)
5. Sea Launched Ballistic Missile (SLBM)
6. Intercontinental Ballistic Missile (ICBM)

These different methods of precision strike have different operational advantages and disadvantages as shown in Table 1. There is, and will continue to be, an interchange of technical information between these services to minimize the duplication of effort and deliver a broad precision strike capability to our country at a minimum of cost. In the development and operational section of this paper, an attempt is made to define the pertinence of the ICBM weapon system issues to the other services and government agencies.

## **LRPW DESCRIPTION**

The following description is the author's strawman design. It is assumed that the final weapon will not deviate significantly from this description. It is further assumed that this weapon is designed for non-nuclear confrontations and will not require hardening of itself, its launch facilities or its C<sup>3</sup>I facilities.

This non-nuclear LRPW will consist of a reentry vehicle enclosed in a cone shaped shroud mounted atop a Minuteman booster. The reentry vehicle, weighing approximately 1400# will consist of a high lift to drag ratio ( $\approx 4$ ), controllable body containing an integrated GPS/INS guidance navigation and control (GN&C) system and an approximately 500# warhead. The GN&C system will control both the missile, during the boost stage, and the reentry vehicle during the reentry and terminal flight.

TABLE 1. PRECISION STRIKE DELIVERY SYSTEMS

PARAMETER	JDAM	ALCM	SLCM	SLBM	ICBM
REACTION TIME	Depends on distance to target.	If based in US will require long range flight with refueling.	Within minutes if ship is in position, otherwise it could take days.		Always less than one hour!
HUMAN JEOPARDY	Delivery aircraft can be shot down over enemy territory.	Low risk as weapons are released outside enemy territory.		Low risk of hostile action from all but the most sophisticated enemies.	Absolutely none for friendly forces. Also enemy can be warned and allowed to evacuate.
PROCUREMENT COST	The actual weapon is relatively inexpensive. The aircraft is not, but most are in inventory.	The actual weapon is moderately expensive. The aircraft is also, but most are in inventory.	The actual weapon is moderately expensive. The ship is very expensive but available.	The weapon is expensive, but the launch vehicle is in current inventory.	
PEACETIME COST	Personnel, training and maintenance of aircraft are relatively high.		Ship maintenance and personnel makes this cost high.		These weapons can be kept dormant with essentially no maintenance.
COST PER KILL	Actual weapon costs are relatively inexpensive.	Actual weapon costs are moderately expensive. Also long expensive flight hours.	Actual weapon costs are moderately expensive. Ship expenses per shot are relatively low.	Weapon costs are very high. Would only be used on high priority targets.	
FRIENDLY AIRSPACE INTRUSION	No intrusion if tactical airfield is near border.	Usually the flight path will take the aircraft over "friendly" territory.	Possible if enemy is landlocked.	Weapon will fly far above defendable airspace.	
VULNERABILITY	Delivery system (aircraft) must fly over enemy defenses.	The cruise missile is subsonic and moderately vulnerable.			High much reentry will make this weapon essentially invulnerable.

Items in bold indicate a definite advantage.

## **Range Capability**

The LRPW will have a ballistic range of approximately 4500 nm and a range extension using the high L/D vehicle of approximately 3000 nm.

## **Warhead**

Different types of targets, from 'soft' to very 'hard' will require different types of warheads. The warhead will consist of one of the following general types:

1. High Explosive, Penetrator -- This will allow the HE to detonate within semi-hard structures. This type of warhead will limit the impact velocity to some where below mach 4.
2. High Explosive, Impact or Airburst -- Used to maximize over-pressure for use on 'soft' targets
3. High Kinetic Energy Penetrator -- This will be used against hardened targets with its primary purpose to do damage with the pierced ceiling splaying.

## **Launch Sites**

The LRPW will be based within the contiguous USA at either the Western Test Range (WTR at Vandenberg AFB, California) or the Eastern Test Range (ETR at Cape Canaveral, Florida) using available launch facilities, either above or below ground. In order to reduce reaction time there will be a small number of armed but dormant missiles on launch pads ready for immediate activation while having reserves in nearby storage.

## **LRPW ADVANTAGES**

The LRPW will give provide this nation with an affordable capability that will complement other weapon systems. This missile weapon system would be based in this country, using present launch sites, and be capable of hitting targets worldwide with an accuracy that would allow surgical damage with conventional high explosives or non-explosive high kinetic energy penetrators. Here are some of its unique advantages:

### **Low Maintenance Cost**

This weapon, being essentially unmanned, has inherently the lowest maintenance cost of all precision strike methods. As this is not a mass attack weapon, only a few are required to be in launch position. This reduces the number of launch personnel. The use of GPS allows fast warm-up allowing the entire weapon system to be in a fully dormant state. This reduces the number of maintenance personnel as well as depot repair facilities. The primary continuing costs of the military is in personnel and any weapon that can maintain its effectiveness while operating with reduced manpower should be given top priority.

### **Invulnerability**

It can be dangerous to assign the capabilities of past adversaries to future ones. The cruise missile, at this time, is the only alternative to the precision strike missile. It remains sub-sonic and therefore a much more vulnerable weapon and will become more vulnerable as countries obtain more sophisticated countermeasures. It is also crucial to maintain more than one capability against any given threat.

### **Humane**

Because of its lack of vulnerability, less sophisticated enemies can be told when the strike will occur, allowing them to evacuate the area.

### **Increased Destruction**

The destructive effects of a warhead impacting at mach 4, or higher, is considerably more than a sub-sonic impact. The use of differential GPS, which can be available using present technology, will allow a hit accuracy well below twenty feet, dramatically increasing the surgical effectiveness and decreasing the possibility of collateral damage.

### **Fast Reaction**

The fast reaction time will make it very effective against "volatile" targets (e.g. temporary terrorist stockpiles, docked ships, etc...). This weapon could hit any target in less than 90 minutes.

### **Psychological Impact**

You do not fight wars with Tomahawks or these missiles. Their costs relegate them to very specific roles. This missile will have a much higher psychological impact on future adversaries, being essentially a "bolt from heaven", less than two hour away from the "go" decision. This, in itself, may someday eliminate the need to ever use it!

### **Better Domestic Acceptance**

The fact that this can be done without loss of life -- on both sides -- reduces the moral opposition. The knowledge that some situations can develop to the point of requiring future direct military intervention enhances the argument for "nipping" dangerous situations "in the bud".

### **Minimal Foreign Influence**

The basing of these weapons on sovereign ground eliminates the possibility of foreign influence. The loss of foreign bases is a definite possibility as this "safer" world turns inward and isolationism increases. The ability of our aircraft or cruise missiles to fly over "friendly" territory may be severely curtailed, making strike paths longer or impossible.

The cost of that single air strike on Libya, both from the military and the State Department, could deploy many of these missiles, which can produce the same effect without the chance of pilot loss and with none of the international agreements that were required prior to that raid.

### **Low Development and Deployment Costs**

The total cost of deploying these missiles is minimal considering its unique effectiveness. The use of surplus boost vehicles, MM II and MM III, and presently available above or below ground launch sites significantly reduces deployment costs and essentially reduces the development costs to that of the reentry vehicle and its interface.

### **LRPW OPERATION**

The following operational scenario covers three methods of operation for a precision strike high lift to drag reentry vehicle containing an GPS aided with an INS.

The GPS/INS is actuated prior to liftoff, and, with the accurate knowledge of the launch site position, the current satellite errors are corrected. Upon liftoff both the GPS and the



INS will be monitoring position and velocity with the computer maintaining the best estimate based on the a priori uncertainties of the INS and the computed uncertainty of the GPS<sup>3</sup>. At the same time, using a Kalman type filter, it is correcting the observable INS parameters.

This process continues during freefall except the attitude errors built up in the INS, due to gyro drift, which are not observable. In fact the only INS navigational parameters observable during this period are accelerometer biases and gravity errors. Also when the GPS changes satellites it will use the stored best positional information to estimate the new GPS bias<sup>4</sup>.

Once the RV enters the atmosphere and develops drag, i.e. deceleration, then cross 'g' axis INS misalignments and other parameters can be obtained. To obtain all three misalignments there needs to be a yaw or pitch maneuver. These misalignments are critical, as accurate misalignment information is needed to maintain frequency lock during the plasma stage when the GPS signal is attenuated or blocked.

As the RV enters denser atmosphere, the outer RV skin becomes extremely hot and the hottest sections start to burn away or ablate, emitting ionized particles called plasma. This plasma is conductive and therefore attenuates the GPS satellite signals until they are no longer useful. During this period the INS must accurately maintain the RV position. This change over from GPS/INS control to INS control is handled automatically in the Kalman filter. The rapid reacquisition of GPS after the plasma region is over depends on the INS and Kalman filter's ability to "navigate" through the plasma. This is a major constraint on the INS specifications.

In the terminal phase of the mission the RV is guided to the target by one of these three methods:

#### Unaided GPS

This method relies on having accurate RV position on board during the terminal phase. The positional accuracy relies on the stability of the satellite errors and the accuracy by which the satellite errors are recalibrated as "new" satellites are picked up and "old" satellites are dropped.

#### Differential GPS

This method relies on having a surveyed ground receiver<sup>5</sup> nearby that is receiving GPS information from the same satellite set as the RV GPS/INS unit. It sends three simple scalar numbers to the RV indicating the current GPS errors.

#### Relative GPS

This method relies on having a ground station receiving the same satellites as the RV GPS/INS and at a known position in relation to the target. It transmits the target offsets directly to the RV in the instantaneous GPS coordinate set. [Note: Doesn't require absolute target location.]

---

<sup>3</sup> This assumes that there is an independent signal to noise indication available.

<sup>4</sup> This will only be used only for the unaided GPS method. (Explained later).

<sup>5</sup> It was reported that differential GPS has a theoretical accuracy of one millimeter per kilometer of offset!

## **DEVELOPMENT & OPERATIONAL ISSUES**

While the booster and the launch facilities are available this totally new weapon will require a development program. The following is a partial list of areas in which there will be issues to be resolved. Table 2. shows which of the following issues are common to other agencies.

**TABLE 2. LEVERAGE POSSIBILITIES**

ISSUE	JDAM	SLCM	ALCM	SLBM
Mission Support	NO	NO	NO	NO
Launch Readiness	NO	YES	NO	YES
Ionosphere Distortion	YES	YES	YES	NO
Time Management	YES	YES	YES	YES
Parameter Update	YES	YES	YES	YES
Velocity Vector Match	YES	NO	YES	YES
Changing Satellites	YES	NO	YES	YES
Plasma Attenuation	NO	NO	NO	YES
Anti-Jam; Anti-Spoof	YES	YES	YES	YES
GPS Reacquisition	YES	YES	YES	YES
Differential GPS	YES	YES	YES	YES
Relative GPS	NO	YES	YES	YES
Vehicle Control	YES	YES	YES	YES

### **Definition of Targets**

The selection of applicable targets needs to be realistically constrained to those worthy of using a multi-million dollar weapon. The limiting of targets to only high priority targets should allow the convergence of guidance methods, trajectories, mapping requirements and warhead types.

### **Target Location**

Target location uncertainty is currently one of the largest error sources. This is primarily a DMA responsibility, with some help from tactical aircraft, but its success is critical to the entire program. DMA should be kept informed of future SEP requirements as well as current high priority targets.

If unaided or differential GPS is used then the target must be accurately known in GPS coordinates. If relative GPS is to be used then the target to ground receiver must be accurately surveyed -- probably a job for tactical aircraft. If the target is time critical (i.e. relocatable), it may require rapid resurveying -- <24 hour?

Mapping methods include imaging by satellites, aircraft SAR, aircraft IF and aircraft visual. In all of these methods the accurate positional knowledge of the satellite or aircraft is required. This accuracy can be obtained from GPS information, corrected on-line or off line by differential GPS methods.

### **Mission Support**

Mission Support is defined as the operations that must take place between the point in time when the political or military target has been selected and the missile being properly programmed for that target.

The effectiveness of this weapon is dependent on its ability to react rapidly to international threats. This will require that the pre-flight decision method be streamlined with the ability to design a trajectory for any target selected in a manner of minutes.

One major problem will be the prior acquisition, storage and later retrieval of target coordinates and/or images. If a terminal sensor is required the radar, IR or visual image must be stored with either multiple aspect angles or full three dimensional images. Targets stored should also include information on the viability of the data, uniqueness and type of warhead.

The trajectory will need to be defined to assure sufficient range extension, safe third stage splashdown, proper attack angle, adequate evasive maneuvers and, probably, a safe abort area. All of this information must then be properly transmitted to the launch vehicle.

A goal of thirty minutes is not unreasonable but will require a seamless C<sup>3</sup>I operation.

### **Launch Readiness**

It will be assumed that a particular missile with a proper warhead is on a launch pad awaiting a command to begin an active countdown, which includes the loading of the mission parameters. During this wait period the GPS/INS is turned on and pre-launch GPS updates are obtained. The launch is then initiated after the mission parameters are loaded and the final approval has been received.

The ability to receive GPS signals on the ground in the launch position will be a factor in the antenna/shroud design. The trajectory upload speed and integrity as well as the warmup time of the INS may be critical parameters in the response time.

### **GPS Ionosphere Distortion**

The ionosphere can deviate the RF waves from the satellites producing varying transmission paths and therefore erroneous position and velocity information. This is compensated to a degree by having two frequencies (L1/L2) which are affected differently by the ionosphere, allowing the majority of this distortion to be calibrated. Initial errors can be eliminated by the use of an accurately surveyed nearby GPS receiver. The GPS/INS system must be able to receive and act on information from this ground based receiver.

## **Time Management**

All guidance information, GPS position, GPS velocity, INS attitude and INS velocity gained must be properly time tagged ( $< 1$  millisecond) to assure proper operation in real time. Independent verification using dynamic ground testing (centrifuge or rocket sled) will be required to validate the adopted system timing technique.

## **INS Parameter Update During Boost**

As the missile is guided through the powered boost trajectory, some of the inertial instrument parameter errors become apparent as the GPS is continuously determining velocity and position. These parameters can then be continuously upgraded as the flight progresses. Boost maneuvers may be required to update other important INS parameters. The accuracy of these updates is dependent on the actual and assumed uncertainties of both the GPS and the INS, as well as the observability afforded by the boost trajectory.

Analyses will be required to determine parameter hit sensitivities, parameter observability during boost, and parameter extraction accuracy for a set of typical boost trajectories. Note: This will probably be a strapdown INS requiring knowledge of long term parameter inaccuracies.

## **Changing Satellites**

When a new satellite signal is received the GPS/INS must recognize it and obtain a bias value for this new satellite by using the existing navigation information. The ability to obtain these biases can be obtained by analysis and ground testing.

## **Satellite Integrity**

The GPS will track as many satellites as possible to increase accuracy and it requires at least five satellites to be able to detect a soft failure in one satellite<sup>6</sup>. The system algorithm must include fault detection methods.

## **Reentry Velocity Vector Matching**

During freefall the only visible INS parameter is accelerometer bias, assuming no thrust commands during update. Attitude information of the guidance unit can drift due to gyro inaccuracies. During the deceleration of reentry, these misalignments can be calibrated by velocity matching between the INS and GPS. Rotational errors about the flight path are not observable so the reentry trajectory needs some optimizing maneuvers to make these parameters observable.

Analysis is required to design proper trajectories so as to maximize the attitude update accuracy while minimizing the loss of range due to the added maneuvers. Update accuracy is effected primarily by accelerometer noise.

---

<sup>6</sup> Ref. "GPS RAIM: Screening Out Bad Geometries Under Worst Case Bias Conditions" Navigation Vol. 39 No. 4 Pg. 407.

## **Plasma Attenuation of GPS Signals**

When the reentry vehicle is above a certain speed and the atmosphere is above a certain density then the vehicle becomes enclosed in a cone of ionized, conductive particles known as plasma. This plasma can attenuate or even blackout the GPS satellite signals.

The effect of plasma on the navigation accuracy can be minimized by either designing the trajectory to avoid the plasma velocity/altitude region or by adjusting filter gains to allow the INS to do full navigation during GPS blackout.

## **Anti-Jamming Techniques**

If the enemy knows the reentry vehicle is coming then they can jam helicopters with GPS jammers that are highly effective against nearby GPS receivers.

Anti-jam methods include GPS receiver filter techniques, post receiver techniques and directional antenna design. All or any of these methods will provide varying degrees of effectiveness.

Surprise might be the most effective countermeasure against jamming.

## **Reacquisition After Plasma or Jamming**

If the GPS temporarily loses the satellite signals, it can reacquire when the signals return. The speed at which this reacquisition can occur is dependent on the tracking loop bandwidths and the degree of velocity (GPS frequency) and position (GPS phase) error. During this GPS outage, the INS can be used to track the vehicle velocity and maintain the loops essentially in a pseudo-lock condition.

The ability to rapidly reacquire in a dynamic environment can be tested on the ground using high velocity sled runs.

## **Differential & Relative GPS**

Differential GPS can be used when the target and ground GPS coordinates are accurately known. Relative GPS can be used when the target location is known in relation to the ground based GPS receiver. Both require an up (satellite biases) and down (for interrogation) information link, direct or through a third unit relay.

The accuracy depends on the number of satellites that the ground station is tracking that are common to the ones being tracked by the vehicle.

## **Terminal Dynamics**

The GPS/INS will be sending guidance commands to the vehicle attitude control unit. These signals constitute the closed loop commands and must be dynamically compatible with the required SEP and the angular stability of the entire system, which becomes a function of atmospheric density and vehicle speed. The lower bandwidth (estimate: 5 to 10 Hz) of the vehicular control loops will require that the trajectory just prior to impact, within a mile or so, must be void of any significant maneuvers.

The terminal maneuver will most likely be a transition from near horizontal flight to near vertical impact. This maneuver must be planned and controlled to remain within the dynamic limits of the vehicle and its guidance units.

## **CONCLUSIONS & RECOMMENDATIONS**

This weapon system is designed for the "new" world, using new thinking, as an inexpensive addition to our present worldwide military presence. It will allow the President the option of surgically removing certain threats to world peace at an early stage with a minimum of domestic and foreign repercussions.

The ICBM technology that produced a successful deterrent to nuclear war in the past can now be used to help reduce the chance of warfare and nuclear proliferation in the future.

This program needs to go forward with the full support of the military, the Congress and the people with a priority commensurate with its potential for 'nipping' world dangers 'in the bud' and thereby minimizing the need for more drastic military actions in the future.

**THIS PAGE LEFT BLANK INTENTIONALLY**

# **Sled Testing of the Advanced Inertial Measurement Units**

**Maria Reta  
Robert Lawrence**

**46th Guidance Test Squadron  
46th Test Group  
Holloman AFB, New Mexico**

## **Abstract**

This paper describes some of the unique sled test methodology innovations developed at the 46th Test Group, Holloman AFB for system testing reentry vehicle maneuvering inertial measurement units for the Advanced Inertial Measurement Unit (AIMU) development program. The AIMU systems were performance and environmental response tested through a combination of ground tests. Sled testing verified the performance and functional integrity of the systems in a high-g dynamic environment. This paper summarizes the rocket sled capability and results from testing on the high speed test track which continues to be one of the best tools for conducting dynamic tests of inertial guidance systems in simulated operational environment.



## **1.0 Introduction**

The objective of the Advanced Inertial Measurement Unit (AIMU) development program was to demonstrate the reentry performance technology for ICBM maneuvering reentry vehicle applications. The AIMU was a strapdown configuration using temperature compensated Bell XI accelerometers and Ring Laser Gyroscopes (RLG). High speed sled testing was one aspect of the ground tests conducted to verify and evaluate the AIMU functional integrity, performance and error model in a dynamic environment.

## **2.0 Test Description.**

The sled test consisted of integrating the AIMU into a monorail sled which was subjected to the acceleration profile shown in Figure 1. Test preparation consisted of detailed test planning, facilities and test bed build up, environmental tailoring and verification, instrumentation checkout, test procedures development and verification, and system integration. The test sequence to characterize the environment and integrate AIMU laboratory tests with three system sled tests were as follows:

1. Sled Test – Environmental( AIMU Mass Simulator )
2. Laboratory Test – Calibration( Initial), Simulation Flights
3. Sled Test #1 – System
4. Laboratory Test – Calibration / Calibration Check, Simulation Flights
5. Sled Test #2 – System
6. Laboratory Test – Calibration / Calibration Check, Simulation Flights
7. Sled Test #3 – System
8. Laboratory Test – Calibration / Calibration Check, Simulation Flights

Alignment and navigation functions were performed prior to the sleds first motion and maintained throughout the dynamic and post sled test sequence. Recorded system and track space-time reference data were compared to generate post processing error functions for regression analysis. Laboratory tests, calibrations and simulation flights, were performed on the three-axis table before and after each system sled test to quantify results.

### 3.0 Sled Tests

**3.1 Sled Test Bed.** The test bed was a monorail sled capable of accepting up to five ZAP rocket motors, which generated 130,000 pounds of total thrust, and a rail mounted water brake. The 220 pound payload consisted of a specially designed pallet which was vibration isolated and comprised an installation of power, instrumentation, mounting fixture and the AIMU. The nominal profile (approximately 150 g maximum acceleration, 3200 ft/sec velocity and 60 g water brake) varied depending upon the actual payload weight and ambient temperature.

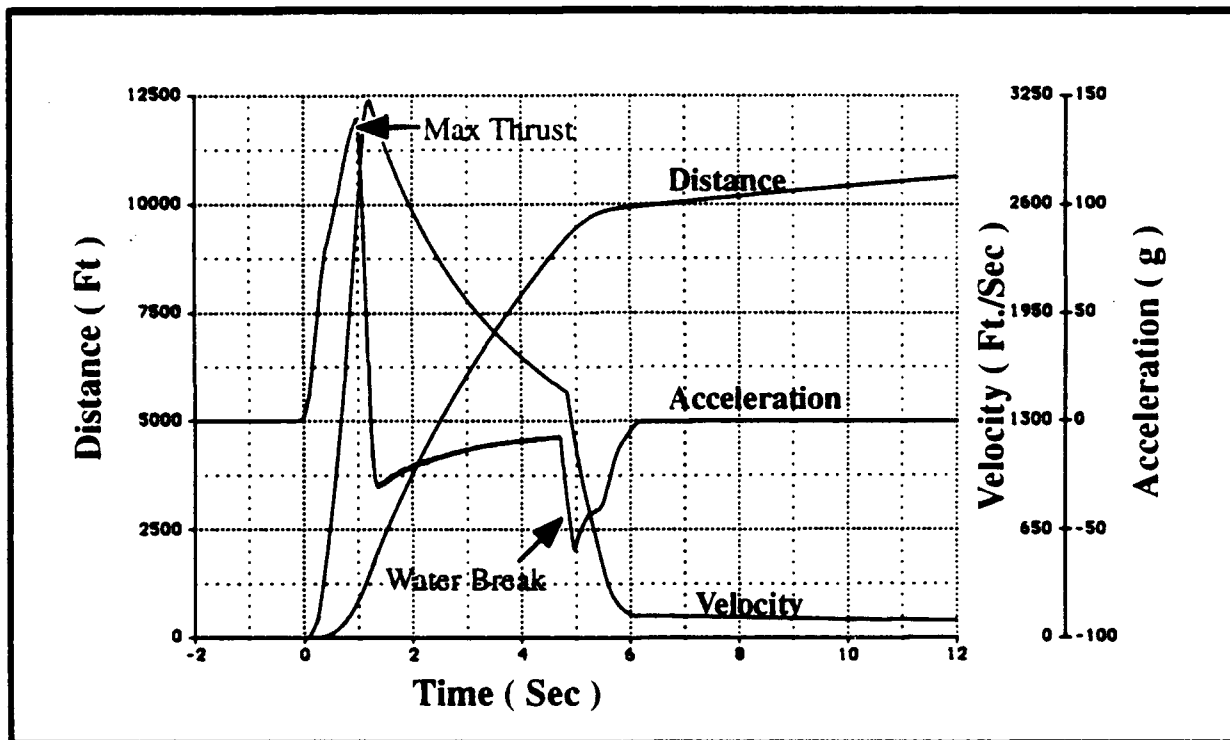


Figure 1. Sled Test Profile

**3.2 Sled Reference System.** The track space-time reference system consisted of a series of surveyed, bevel-edged interrupter blades positioned at nominal intervals of 4.33 feet along the track. An infrared beam in a sled-borne sensing head was interrupted each time the sensing head passed an interrupter, thus generating a series of pulses as the sled moved along the track. The accuracy of the reference was dependent upon the Defense Mapping Agency (DMA) and laser interferometer survey and the space time measurements.

The DMA survey was considered the reference standard and was derived from surveys of the downtrack interrupter control (IC) benchmarks distances (nominally 2,600 feet), downtrack benchmark distances (nominally 100 feet), crosstrack and vertical survey data, deflection of the vertical, gravity, elevations, and track azimuth ( $<0.5$  arcsec). The laser interferometer survey constituted the measured intervals between all interrupters. The interrupters located adjacent to the IC benchmarks were mathematically adjusted to coincide with the IC positions using the DMA survey as reference. The pulses generated by the space-time sledborne sensing head and the time at which each pulse occurred were recorded to permit computation of sled position with respect to time ( $<0.001$  ppm).

The reference position vector functions were generated from space-time measurements after associating the time each interrupter station was passed with its surveyed downtrack, crosstrack, and vertical position. The result was a three-dimensional location of each interrupter station in a Launched Centered Earth Fixed (LCEF) reference frame. To account for Coriolis and gravitational acceleration, distance corrections were computed and added to the position vector. This equates to the output obtained from an ideal triad of doubly integrating accelerometers in a LCEF coordinate system to the accuracy shown in Table 1.

Table 1 – Sled Space Time Reference Accuracy

Direction	Position ( ft ) 4.33 ft Interval	Velocity ( ft/sec ) 2 sec Avg Interval
Downtrack ( X )	0.0025	0.0013
Crosstrack ( Y )	0.006	0.003
Vertical ( Z )	0.006	0.003

**3.3 Sled Environmental Tests.** The environmental test satisfied the requirement to verify the sled profile, vibration environment and data acquisition system and the functionality of the Launch Support Equipment (LSE). The sled test used an AIMU mass simulator and data were collected from environmental transducers (linear vibration triads and linearly variable differential transformers) located on the sled forebody, pallet, AIMU mounting fixture and mass simulator. The vibration accelerometers provided peak vibration levels (g rms) with associated power and

frequency content. Relative motion of the pallet with respect to the sled was measured using the differential transformers. Reference space-time data quantified the sled profile and performance characteristics of the primary reference data.

**3.4 Sled System Test.** The system sled test was the quantitative evaluation of the AIMU performance in a dynamic environment. Commanded by LSE before umbilical release the AIMU entered boost navigation from alignment (pre-run) prior to sled launch, was subjected to the dynamic profile(hot-run) shown in Figure 1 and continued static navigation to power shutdown from sled stop(post-run) point. System and sled (environmental/space-time reference) data were telemetered and recorded throughout the test.

## 4.0 Laboratory Test

**4.1 Laboratory Test Bed.** The test bed was a Contraves Model 53Y-30H three-axis rate table equipped with a temperature chamber ( -55 deg C to +85 deg C). Position accuracy and attitude resolution (1 arcsec) can be maintained with the maximum angular accelerations and rates given in Table 2.

Table 2 - Three Axis Table Angular Acceleration and Rate

Axis	Acceleration(max) (deg/sec/sec)	Rate (max) (deg/sec)
Inner Gimbal	1100	800
Middle Gimbal	400	750
Outer Gimbal	250	750

**4.2 Calibrations.** The calibration was a procedure which solved for the compensation coefficients required by strapdown systems based upon gyro and accelerometer outputs and knowledge of the test conditions. The tests were conducted using the rate table and contractor specific procedures in the static and dynamic modes at three specific temperatures (45, 75, and 110 deg F). The initial calibration prior to the first sled test established a baseline

of the systems compensation coefficients. Calibrations there after were repeats of the initial calibration or an abbreviated version (Calibration check) to monitor coefficient changes and validate the regression analysis results.

**4.3 Simulation Flights.** The simulated flight tests verified the calibration parameters by determining the attitude, position, and velocity errors of the AIMU under controlled conditions which simulate the rotational motions and environmental temperatures expected during flight. The tests were conducted using the rate table at three rates (180, 540, and 720 deg/sec) and three temperatures (45, 75, and 110 deg F) selected by the reference trajectory.

## **5.0 Data Processing and Analysis**

The majority of the test objectives were verified by regression analysis, which is a procedure using error functions and a Kalman filter mechanization to isolate, identify and estimate system errors. The distance domain error functions were generated by differencing the system, transformed from the Earth Centered Inertial coordinate frame, and reference position vector distance data ( system minus reference ) in the track (LCEF) coordinate frame. The velocity domain error functions were computed by generating a smoothed derivative ( 0.25 to 2.0 second average interval) of the distance error functions. Specific error signatures were verified and unanticipated errors modeled to quantify system performance.

The Kalman filter algorithm was used to obtain the most optimal estimates throughout the sled test sequence with a fixed point smoothing algorithm operating recursively forward in time to obtain initial launch point smoothed estimates. The velocity domain was chosen for the filter measurement error update because it provided improved separability over the position domain and significantly less noise in the acceleration domain. Filter weighting and tracking control was accomplished by changing the measurement noise values for the pre-, hot-, and post-run segments. Attaining an adequate filter model that yielded the best possible estimation performance required a substantial amount of engineering insight and sled test experience. The error model (25 states) was a deterministic generation of the AIMU compensation modeled and unmodeled error functions selected

by a correlation and observability study based upon the platform/instrument orientation and dynamic of the sled profile. Initial estimates and filter uncertainties were based upon calibration results, component tests and filter tuning. The laboratory calibrations/simulation flights provided the quantification needed to monitor system/coefficient changes and validate the regression estimates.

## **6.0 Conclusions**

The performance and functional integrity of the AIMU in dynamic environment were demonstrated. Compared to a flight test the system was recoverable and available for comprehensive post test analysis. Analysis based upon two or more sled tests verified the test objectives and uncovered unanticipated problems. Acceleration sensitive, second and third order nonlinearity, accelerometer error terms were observable and modeled. Therefore, the high average acceleration and accuracy of reference system makes sled test a very valuable tool for evaluating guidance system performance and instrument error terms.

## References

1. "Advanced Guidance Technology Advanced Inertial Measurement Unit Sled Test Plan",AFDTC-TP-91-05,6585th Test Group, Guidance Test Division,Holloman AFB, New Mexico 88330-5000, dated July 1991.
2. "Honeywell Advanced Inertial Measurement Unit Flight Qualification Unit Rate Table Tests",AFDTC-TP-92-02, 6585th Test Group, Guidance Test Division,Holloman AFB, New Mexico 88330-5000, dated February 1991.
3. "Honeywell Advanced Guidance Technology Advanced Inertial Measurement Unit Laboratory and Sled Test",AFDTC-TP-92-38, 6585th Test Group, Guidance Test Division,Holloman AFB, New Mexico 88330-5000, dated August 1992.
- 4."Rockwell Advanced Inertial Measurement Unit Sled Test", AFDTC-TP-92-85, 6585th Test Group, Guidance Test Division, Holloman AFB, New Mexico 88330-5000, dated November 1992.

## Alignment Transfer in a Modular Guidance System

Leonard S. Wilk  
Principal Member Technical Staff  
The Charles Stark Draper Laboratory, Inc.  
Cambridge, Massachusetts

### Abstract

One of the requirements for a modular, integrated guidance system, is to determine and maintain the angular alignment between and among some of its various subsystems. Whether the purpose of the modularity is to permit substitutions of the units, or to permit a distributed placement of the units on the vehicle, the relative angular alignments among the sensors can have an impact on the accuracy of the guidance system. These angular alignments have traditionally been maintained by rigid structure, but this can place severe constraints on the overall design. An alternative is to measure these alignments and use the measurements in a compensation scheme.

### Introduction

In a company-sponsored demonstration of an advanced modular guidance system at the Draper Laboratory, we plan to incorporate an alignment device to measure the misalignment between an Inertial Measurement Unit (mounted on shock mounts) and a Stellar Sensor. This device is based on a concept known by the acronym AXIS, which is taken from Alignment Transfer by Integrated Strain. The alignments are sensed by measuring the integrated strains on the surface of a connecting rod. The device, which has been under development for two years, will measure all three degrees of freedom to a resolution of 0.4 arc second and over a range of 25.6 arc seconds. It has a total length of about 6 inches and is "L" shaped with a right-angle bend. The measurements are made with optical fibers. The concept of the device is described in this paper.

In general, the angular or positional orientation of one subsystem with respect to another is determined by a structure. One subsystem, for example a sensor, is usually located with respect to another measurement subsystem by the structural frame of the vehicle supporting it. Of course, at installation (and perhaps periodically afterward) various tools may be used to adjust or check this rigid alignment. In cases where this alignment is critical, this may be an "expensive" way to do it. For example, in the Apollo Command Module the critical alignment between the IMU, the telescope and the sextant was maintained by mounting all these elements on a navigation base which was a large structure machined out of a solid piece of beryllium.

When the structure is not sufficiently stable, alignment is frequently transferred by optical means, usually with

mirrors, lenses, etc. An example of this is the Optical Alignment Group on a ballistic missile carrying submarine where azimuth information is transferred from the SINS to the missile guidance system by a system of mirrors and a traveling optical cart. In these cases, the alignment transfer is usually done on an occasional or periodic basis, where the orientation is sampled and either presumed to remain constant between samplings or else the subsequent misalignment is not important.

Described in this paper is a method of monitoring the alignment between two or more units continually and with high bandwidth. This can be done with high resolution (nanoradians) using optical fibers, or less expensively using resistive wires although with resistive wires the measurement resolution will be reduced. The method requires that the units be connected with a flexible member (a thin rod or pole) on which the fibers or wires are attached. (In some circumstances the supporting structure itself can be used for attaching the fibers or wires.) In many aspects, this approach is much more tolerant of the environment than mirrors and lenses, e.g. fog and vibration. Also, it has much flexibility in that it can be placed around corners, pass through bulkheads, etc.

The concept is called AXIS which is an acronym for "Alignment Transfer by Integrated Strain". This device is being investigated at the Draper Lab., and has been for several years (Ref. 1). We have several designs under development currently. The objective of one of these efforts is to demonstrate the transfer of alignment on a Patriot or ERINT Launcher for the U. S. Army Missile Command. We will transfer the orientation of the Gunner's Quadrant, on the base of the launcher, to a reference near the guidance systems of the erected missiles, transferring all three angles continually with a sub-milliradian accuracy.

I believe that this concept and its development has many applications; in the civilian as well as the military market. I characterize it as a solution looking for more problems.

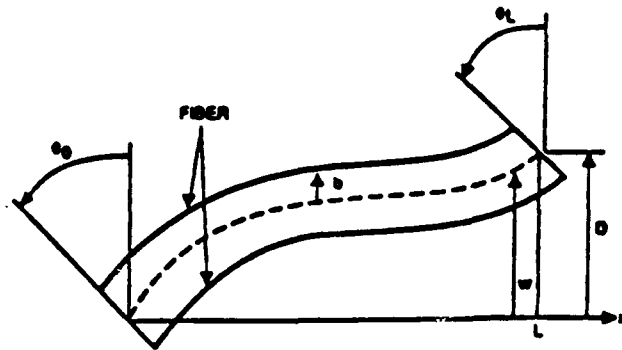
### Alignment Transfer by Integrated Strain (AXIS)

If one considers the strains on the surface of a long thin uniform rod, one comes to the heuristic conclusion that the change in length of a longitudinal surface line is directly proportional to change in angle of one end of the rod with respect to the other. Specifically, the change in length is equal to the change in angle times the distance of the line from the neutral axis. (Here, the bending, the neutral axis and the



surface line all lie in the same plane). A more rigorous examination, as shown in Figure 1 supports this conclusion and also indicates how a displacement measurement of one end with respect to the other can be instrumented.

$P$  = sensor weighting (uniform)  
 $b(x)$  = half diameter  
 $w''(x)$  = rod curvature  
 $x$  = distance along rod



OUTPUT OF INTEGRATING STRAIN SENSOR  
WITH WEIGHTINGS FUNCTION  $p(x)$

$$-\Delta L = \epsilon = \int_0^L P b(x) w''(x) dx$$

$$= P b(x) w'(x) \Big|_0^L - P b'(x) w(x) \Big|_0^L + \int_0^L P b''(x) w(x) dx$$

$$\text{If } b(x) = B$$

$$\epsilon = P B [w'(L) - w'(0)] = P B (\theta_L - \theta_0) \text{ (ANGLE OUTPUT)}$$

$$\text{If } b(x) = K (1 - x/L)$$

$$S = -K P w'(0) + K P/L [w(L) - w(0)]$$

$$= -K P (\theta_0 - D/L) \text{ (DISPLACEMENT OUTPUT)}$$

Figure 1. AXIS Analysis.

If the line element is at a constant distance ( $B$ ) from the neutral axis, the change in length is given directly by:

$$\Delta l = B (\theta_L - \theta_0) \quad (1)$$

(Figure 1 also shows how the line element can be selected to provide a displacement indication, but that is not the subject of this paper.) Note that in the analysis shown on Figure 1, the change in length of the line element is independent of the length and shape of the rod.

This concept provides the basis for a very powerful method of transferring angular orientation (and displacement) of one end of the rod to the other end, where the line element is represented by a physical fiber whose length, or change in length, can be measured.

This change in length can be troublesome to measure directly, and, as is frequently the case, the differential length

between two fibers, providing common mode rejection, is a substantially better method. These ideas can be utilized to effectively implement the transfer of all three rotation angles between units. Figure 2 below shows a three-axis AXIS arrangement to accomplish this.

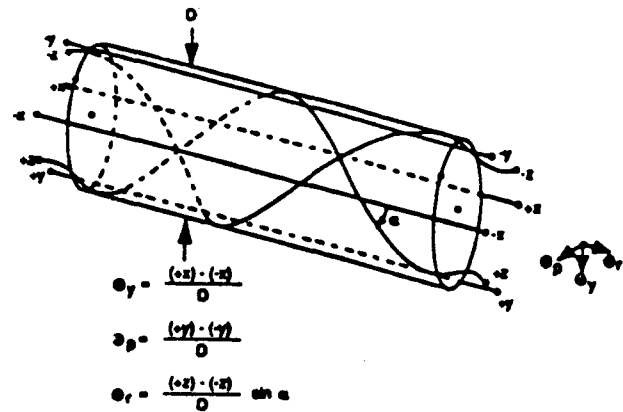


Figure 2. Three-Axis Angular Transfer Arrangement.

As shown in Figure 2, a pair of fibers in the (nominally)  $yz$  plane will provide a measure of the relative rotation about the  $x$  axis (e.g. the pitch angle):

$$\theta_p = \Delta L_y / D \quad (2)$$

The pair of fibers in the (nominally)  $xz$  plane provide the yaw angle,

$$\theta_y = \Delta L_x / D \quad (3)$$

while a clockwise helical fiber compared to a counterclockwise helical fiber provides the roll (twist) angle,

$$\theta_r = \Delta L_z \sin \alpha / D \quad (4)$$

where  $\alpha$  is the helix angle,  $D$  is the diameter separating the pairs of fibers, and  $\Delta L$  is the difference in length between the fibers of a pair.

Some topological comments are in order. (1) The above configuration will provide the three angles independently given that the magnitude of the angles does not get too large (of order 30 degrees). (2) Bending and twisting that is constrained to one plane can be accommodated to large angles without topological limit. (3) Several rods can be joined in series: if the rods are joined at fixed right angles in cardinal directions, then the fiber pairs, rod to rod, can be joined so as to provide the proper angular transformations; if the rods are constrained to lie in cardinal planes, but at (fixed) arbitrary angles in these planes, and a double set of fibers implemented, the double pairs of fibers can be proportionally combined for proper transformations; with a triple set of fibers, the rods can be at any arbitrary fixed angles, and proportional combinations among the fiber pairs will provide the correct transformations. Further analytical work remains to be done to fully understand the limitations of three

dimensional large angle bending. One further topological comment: the characterization of the rod as long and thin is meant to denote that the rod does not have any significant transverse shear.

### Implementation

The primary implementation question is how to measure the change in length between the pairs of line elements. At Draper we have pursued two main directions; optical and electrical. The optical approach utilizes optical fibers which are bonded to the rod and the difference in length is sensed interferometrically. The electrical approach utilizes conductive wires bonded to the rod and the difference in length is sensed by measuring the resistance change. Both of these methods have been successfully demonstrated and each has its own unique characteristics. Other approaches, and variations from those described below, are under development at the Draper Laboratory.

#### Optical

The interferometric fiber-optic approach provides great sensitivity, wide bandwidth and a large dynamic range. The fundamental configuration is shown in Figure 3 below. The output from narrow line width laser is split by a 50/50 coupler. This provides coherent light to the two optical fibers which are bonded to the rod. The output light from these two fibers is caused to form an interference pattern which is sensed as described below. The sensed fringe pattern is digitized and summed into a register. The accumulated net sum from the time that the process is started then represents the net angular change of one end of the rod from the other.

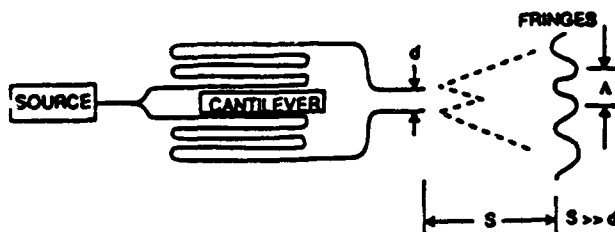


Figure 3. Interferometer Scheme.

This optical approach can be designed to be extremely sensitive – both by the nature of the basic interferometer scheme itself and also by virtue of the fact that the length of fiber bonded to the rod can be very great. By laying multiple traverses, back and forth, each traverse will measure the surface integrated strain. The basic sensitivity is given by:

$$\Delta \Theta / \Delta \Phi = N \lambda / 2 \pi D \eta \quad (5)$$

where

- $\Delta \Theta$  = Angle change (radians)
- $\Delta \Phi$  = Fringe angle (radians)
- $N$  = Number of traverses of optical fiber
- $\lambda$  = Free space wavelength of light
- $D$  = Diameter between fibers of a pair
- $\eta$  = Strained index of refraction of fiber (includes photo elastic effect)

For an experimental measurement, partial results are shown in Figure 4 below, the calculated scale factor is 1.5043 arc sec/fringe-count. The measured scale factor shown in Figure 4 is 1.235 arc sec/fringe-count.

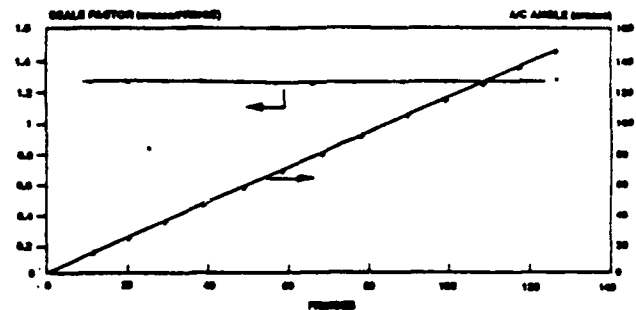
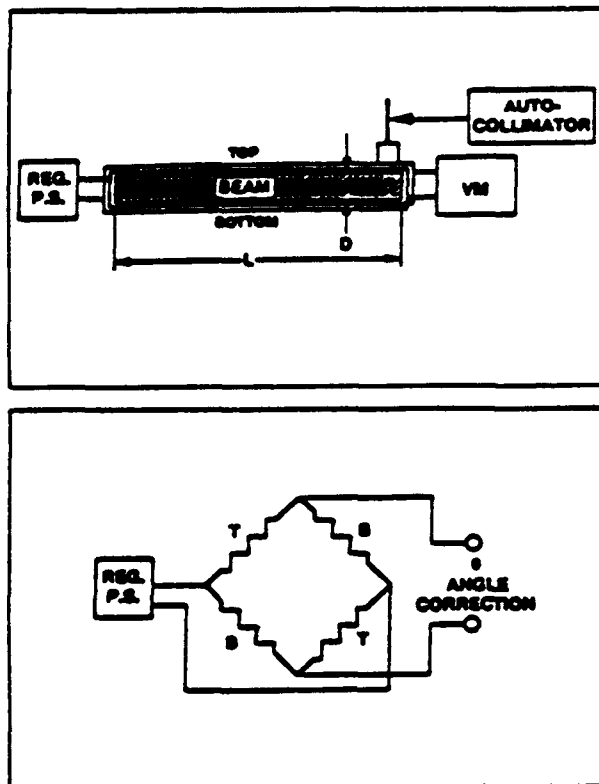


Figure 4. Test Configuration 2 Results.

#### Electrical

An alternative method of measuring the integrated strain is to use resistive wires bonded on the rod. As the wires are stretched or compressed, the change in resistance is measured and the change is a measure of the strain. Typically, multiple wires are used so that they can be placed in a full Wheatstone bridge configuration. This technique is similar to strain gage technology, although instead of discrete sensing at a small area, the wires are laid along the length of the rod. Although this approach is not nearly as sensitive as the optical method, it has some significant advantages. The two main advantages are: (1) it is considerably less expensive; and (2) it provides a whole angle readout during all operation. One of the major differences with the optical approach is that the sensitivity is now inversely proportional to length. This is due to the properties of the Wheatstone bridge configuration, whose sensitivity is proportional to  $\Delta R/R$ . Adding more turns of wire does not change this ratio. This approach is indicated in Figure 5.



$$\delta\theta = \frac{\Delta L}{D} = \frac{\Delta L/L}{D/L} = \frac{\delta R/R}{D/L}$$

Figure 5. Resistive AXIS Concept.

The sensitivity of the configuration is given by:

$$\Theta / \Delta E = 2 L / f D E \quad (6)$$

where;

- $\Theta$  = Angle of one end of the rod with respect to the other (referenced to an initially calibrated value)
- $\Delta E$  = Voltage output from bridge
- $L$  = Length of rod
- $f$  = Strain gage factor of wire
- $D$  = Diameter separating wires of a pair
- $E$  = Excitation voltage applied to bridge

In Figure 6 we show some early experimental results. With 30 volts applied to the Wheatstone bridge, we achieved a sensitivity of 1.46 millivolt / milliradian.

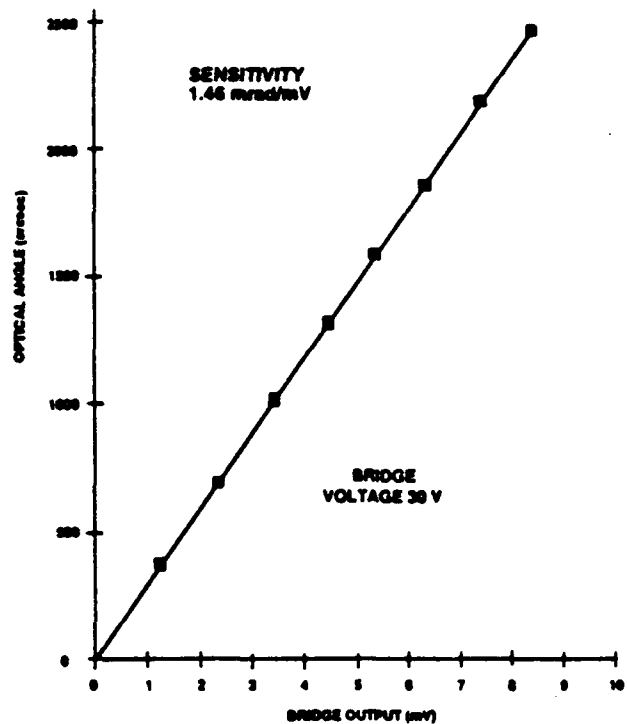


Figure 6. Resistive AXIS Test Results.

#### Strapdown System Demonstration AXIS Subsystem

The Draper program to demonstrate the operation of a Stellar-Inertial Strapdown System is described elsewhere. In this paper is outlined the design parameters of the AXIS alignment transfer subsystem.

The AXIS subsystem to provide the alignments between the AIMU and the Stellar Sensor is based on the technology described above. In this case the integrated strains are measured only by the photonic method. In particular, all three degrees of freedom are measured twice, each with a different scale factor. This technique is analogous the two speed resolver method of achieving a large dynamic range along with fine resolution.

The scale factors are chosen to provide one of the speeds with a sensitivity of 3.200 arc seconds per fringe, while the other has a sensitivity of 3.657 arc seconds per fringe. By interpolating fringes to 1/8 of a fringe, we achieve a resolution of 0.4 arc second over a dynamic range of 25.6 arc seconds.

Each speed is implemented by a 1.3  $\mu\text{m}$  5 mW dfb laser feeding a 60 dB optical isolator, driving a 1 x 8 splitter (only 6 outputs used). Each pair provides one channel of measurement on the AXIS substrate, and then connected to a fringe

generator, which is described in Ref. (2). These fringe generators, however will incorporate 4 in-line element detectors in place of the dual detectors. By properly summing and differencing the outputs of the four detector elements, the fringe pattern can be resolved to 1/8 by sensing the sign of these signals only.

The AXIS substrate is basically made in three sections, which will be bolted together. Two of the sections are spool-like arms with machined grooves to guide the laying of the optical fibers. The central section is a precision cube, which serves to position the arms at precisely 90 degrees.

#### References

- (1) U. S. Patent No. 4,788,868: 1988.
- (2) "Wide Dynamic Range Fiber-Optic Alignment Transfer Device," L. S. Wilk, R. P. Dahlgren, SOLID STATE OPTICAL MATERIALS SYMPOSIUM, AMERICAN CERAMIC SOCIETY, MAY 1991.
- (3) "Dynamic Missile Reference Alignment," L. S. Wilk, AIAA MISSILE SCIENCES CONFERENCE, FEB. 1993.

**THIS PAGE LEFT BLANK INTENTIONALLY**

**SESSION VII-B  
ACCELEROMETERS**

***CHAIRMAN***  
**ROY FARMER**  
***DELCO ELECTRONICS CORPORATION***

**THIS PAGE LEFT BLANK INTENTIONALLY**

**Inertial Grade SiAc™ Silicon Accelerometer**

**Dan McLane**

**Litton Systems  
Guidance and Control Systems Division  
5500 Canoga Ave  
Woodland Hills Ca, 91367  
phone (818) 715-2747  
FAX (818) 715-4351**

**20 July 1993**



## **Inertial Grade SiAc™ Silicon Accelerometer**

### **Abstract**

A unique silicon accelerometer has been developed at Litton to satisfy a wide range of performance requirements from low cost expendable munitions to inertial navigation systems. This paper describes the silicon accelerometer design and presents performance data. Unique methods for testing the silicon accelerometer including real-time error compensation and self-calibration techniques used to enhance performance are also described.

The silicon accelerometer chips are micromachined from silicon wafers. The precision micromachined accelerometer structure is a very accurate, rugged accelerometer capable of over 100 g operating range which can survive high shock and overrange accelerations. The SiAc™ silicon accelerometer chip is packaged with an electrostatic digital servo which results in a closed loop, pendulous mass, force-to-balance accelerometer.

The silicon accelerometer is the first instrument with embedded capability for performing internal digital compensation to enhance performance. An on-board microcontroller provides precision servo control and also implements auto-ranging, real-time error compensation, auto-calibration features and self-test. Special tests implementing real-time torquer scale factor compensation which minimize vibration errors are described. Data presented in the paper supports inertial grade accuracy requirements over the full military temperature range.

### **SiAc™ Silicon Accelerometer**

Litton has developed a new family of silicon accelerometers which are ideally suited for the demanding environments required by emerging applications in smart munitions, tactical missiles and aircraft navigators. The SiAc™ silicon accelerometer has inertial grade accuracy, can measure greater than 100g inputs in the presence of high vibration and yet is quite small, low weight, with low power consumption and low cost. The unique all silicon accelerometer structure which incorporates the accelerometer proofmass and support structure in one piece of single crystal silicon has high g and high shock capability - over 40,000 g static loading without damage and beyond 2000g shock without failure - and proven performance levels previously impossible with mechanical or resonating structure designs. The SiAc™ silicon accelerometer truly represents the next step in accelerometer technology for inertial navigation systems.

Interim performance goals for the inertial grade accelerometer are summarized below.

Requirement	
g range	70 g
bias stability	50 $\mu$ g
scale factor	50 ppm
temperature range	-54 to 85 deg C

The batch assembly, and automated processing methods used for the silicon accelerometer are targeted to allow the accelerometer to achieve a factor of five cost improvement over current accelerometers.

The silicon accelerometer has been under continuous development at Litton using internal research and development funds since 1983. Development after initial prototypes continued with demonstration units flown in test vehicles on several tactical grade programs including SCIT, Compass/AHRS, and AMRAAM. Litton currently has the LN200 silicon accelerometer in production to support contracts on tactical grade programs including AMRAAM, LH, JDAM and Clementine space vehicle. The LN200 production accelerometer is capable of performance better than 200  $\mu$ g, 300 ppm stability and 40g input range. Continuing research has yielded key developments in chip design and electronics which have resulted in the evolution from a tactical grade to a navigation grade accelerometer with 70 g range and 50  $\mu$ g, 50 ppm stability performance. Initial inertial grade accelerometers are being delivered for systems integration in the GGP systems during 3Q '93. Further development during 1994 will result in an accelerometer with 100g range and 25  $\mu$ g, 25 ppm performance.

### **Silicon Accelerometer Chip Fabrication**

The silicon accelerometer is a pendulous mass, closed loop force-to-balance instrument controlled by an electrostatic digital forcing servo. Figure 1 shows an exploded view of the accelerometer structure. The accelerometer pendulum is supported by a pair of hinges in a very small gap between the two outer glass layers to form the sensing pendulum. The pendulum forms a pair of capacitors with the top and bottom electrodes plated on the glass layers which change differentially with pendulum motion. The servo electronics uses the differential capacitance to measure the pendulum position and also to electrostatically force the pendulum back to a null position.

The basic process steps for making the accelerometer chips are :

- micromachining the proofmass assemblies
- anodically bonding the proofmass to top and bottom glass layers
- chip level testing

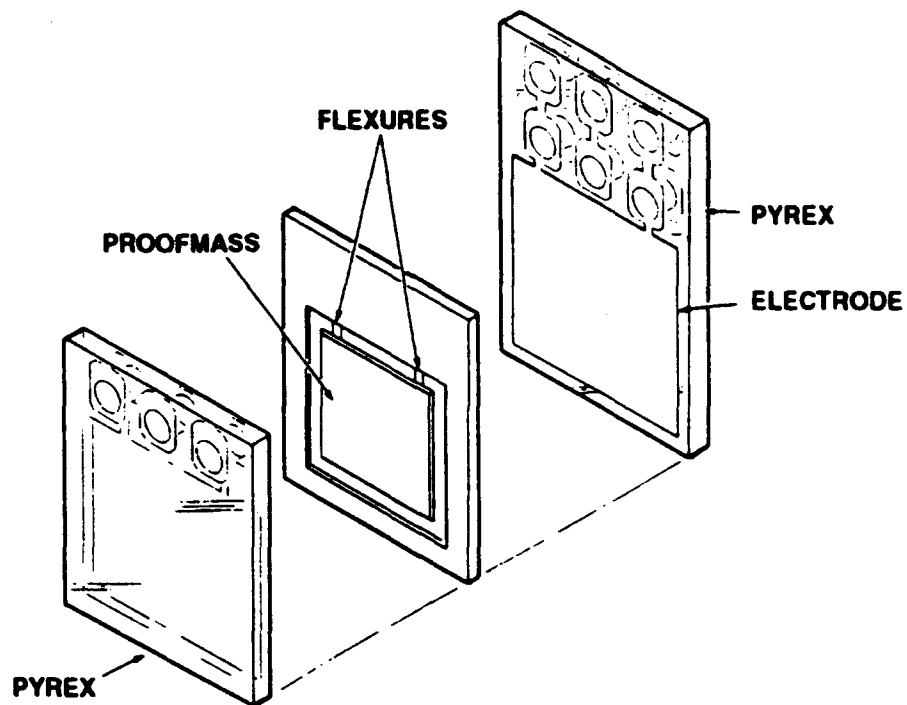


Figure 1. Silicon Accelerometer - Exploded View

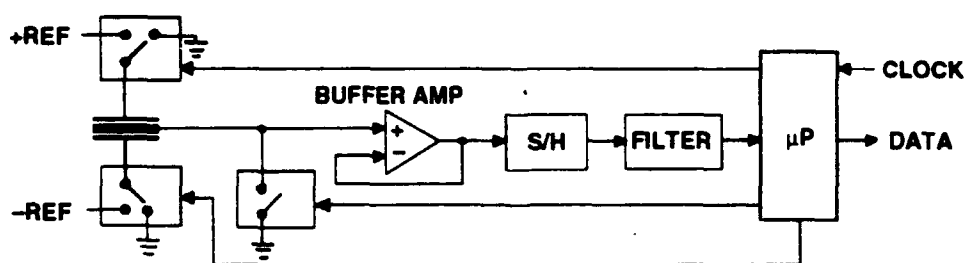


Figure 2. Servo Technique

The accelerometer proofmass is made by micro machining (anisotropic chemical etching) silicon wafers to form the working pendulum in the instrument. The silicon layer is a complete proofmass structure with pendulum, hinges and frame all etched from a single crystal piece of silicon. The proofmass assemblies are etched from a wafer of silicon in a batch process with more than 100 proofmass assemblies per wafer. Batch production of the accelerometer chips results in low cost and repeatable instrument performance.

The glass layers on each side of the silicon proofmass have metalized electrodes to form the capacitor plates on top and bottom which are used as plates for the forcing and sensing capacitors. Each glass layer wafer is anodically bonded to the silicon wafer and forms a very strong chemical bond without the use of any epoxies or organic materials. This is achieved by a process in which free oxygen in the glass is driven to the silicon-glass interface where it can attach the silicon to the glass by chemically bonding. The bond strength exceeds the tensile strength of the glass. The three layer wafer is then diced into accelerometer chips ready for testing. Each finished accelerometer chip is 0.300 inches long by 0.250 inches wide and is 0.052 inches thick. Accelerometer chips are tested in batches on a semi-automatic tester for pendulum freedom, scale factor and bias characterization.

The silicon accelerometer has proven itself to be ideal for harsh environments as a result of the fabrication technique. Shock testing up to 2000g and centrifuge testing up to 10,000 g have been conducted which showed no failures. Arbor press loading of up to 40,000 g failed to damage the accelerometer. Damage by handling mishaps is greatly reduced relative to older mechanical accelerometers. The secret of the high shock and g loading capability is the large damping, small gaps, and properties of silicon as a structural material. Silicon is a perfectly elastic material and will not retain a permanent deformation like metals when loaded. With a properly designed hinge and gap size, the accelerometer pendulum bottoms out against the outer glass plates and prevents over-extension of the hinge thus allowing for survivability in overrange high g conditions. The small gap also results in squeeze film gas damping which damps structural resonances, prevents excess motion from out of band vibration inputs and gives about 1 g-second of velocity storage.

### **Servo Electronics**

Performance of the silicon accelerometer is tightly linked to the servo control method. Litton has developed special electrostatic servo control techniques which minimize the error forces generated by the servo and result in the best performance. Electrically the accelerometer appears as a differential capacitor with three terminals - top plate, pendulum and bottom plate. The capacitances between the top and bottom glass metalized electrode and the silicon pendulum vary as the pendulum moves in the gap. The silicon accelerometer uses electrostatic attraction forces to control the proofmass to a null position for closed loop operation.

The accelerometer is controlled by a set of three switches surrounding the proofmass which switch signals for position sensing and control signals to control the accelerometer

pendulum. A basic block diagram is shown in figure 2. The servo operates in two phases: pendulum position sensing phase and torquing phase. During the pickoff phase, the pendulum position is detected by observing the pendulum voltage when the top and bottom plates are switched to a precision voltage level. The position of the pendulum in the voltage gradient between the top and bottom electrode plates is sensed by holding the pendulum node at a very high impedance. No error forces are generated by the servo control using this method if the pendulum electrical impedance is high. At the null position, the pendulum voltage is nominally zero for equal voltages on the top and bottom plates. The pendulum voltage measured during this pickoff phase is used as the error signal to the servo. The servo uses a proportional-integral-derivative control compensation to calculate the force required to pull the pendulum back to the null position based on the position error signal.

After the force is calculated, the servo begins the torquing phase of the control cycle. Torque on the pendulum is produced when either the top or bottom plate switches to ground while the other stays on and pendulum is grounded. This voltage from the active forcing plate to the pendulum causes torque from electrostatic attraction. The error signal specifies a precision time for the application of the torquing force after which the torquing plate is turned to ground and the servo awaits the next servo period. The servo cycle is nominally 4 kHz. The servo timing is generated using a small microcontroller which commands the plate switching, calculates the forcing time and reports the applied force representing measured acceleration over a digital serial link.

### **Unique Design Feature of the SiAc™**

The main advantage of the Litton accelerometer servo is the elimination of servo induced error forces on the pendulum. Most electrostatic servos use a fixed bias field to linearize the square-law relationship of voltage to force. This tends to induce a large, fixed attractive force on the pendulum which must be compensated for by the servo. Any variation in null point stability results in poor accelerometer bias stability. By contrast, the Litton servo applies only the control force required for control using a fixed force level applied for a variable time period and eliminates the fixed bias field. Servo induced spring rates are over *1000 times* less with the Litton servo approach. Bias stability due to null point variation is thereby greatly improved and bias stability of better than  $40 \mu g$ ,  $1\sigma$  for 6 hours has been demonstrated.

The servo has several other features which enhance performance including

- dual ranging operation
- auto-calibration
- built-in test

All of these features are made possible by the unique embedded all-digital data interface between the accelerometer and the user. A full duplex, high speed (1M baud), synchronous digital data link from the accelerometer to the system has been implemented.

For the first time, the accelerometer becomes an intelligent part of the system which allows for real-time error compensation and calibration procedures. The digital data link is also virtually impervious to data corruption and is easier to use than traditional analog data which must be digitized with precision quantizers or pulse width modulation controllers.

The servo design accommodates multiple ranges and may be easily modified for different g capabilities unlike resonating structure accelerometers by changing the control voltages. The current inertial grade design is dual ranging and has 20g and 80g ranges. The 20g low range is suitable for manned vehicles and most spacecraft, while the high range is used for high dynamic vehicles like missiles. This improves performance greatly by increasing resolution in low range, decreasing servo-induced error forces and decreasing transients within the accelerometer electronics when the highest accuracy is required in low range. The servo electronics with the accelerometer monitors the current g level and automatically switches when the duty cycle level in high range falls below 20% of the high range or whenever commanded by the system. The algorithm prevents the accelerometer from switching ranges too often to reduce range switching errors.

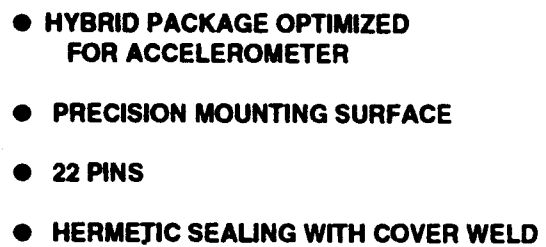
The microprocessor is used to calibrate the accelerometer scale factor and bias by using an auto-calibration feature allowing for in-situ accelerometer asymmetry testing. The system may periodically check the calibration by commanding an asymmetry test and adjust the bias or scale factor calibration. This special test consists of the microprocessor adding extra control pulses to those required for normal servo control and observing the accelerometer output. By adding pulses to each side alternately, the scale factor asymmetry may be calculated by the microprocessor and the scale factor and bias calculated for best vibration performance.

Built-in test functions in the accelerometer circuitry are performed at each turn-on and under command of the system. The built-in tests check the reference voltage level, A/D operation, microcontroller as well as perform sanity checks on the temperature sensor and accelerometer servo value. Error conditions are reported to the user to allow unit level isolation of faults.

The software consumes about 100 bytes of volatile memory for variables and 500 bytes of program code embedded in non-volatile on-board memory. The memory is reprogrammable even after the accelerometer is built to accommodate code updates and application specific code modifications using the built-in bootloader on the microcontroller. The software duty cycle is about 50 % of the processor capability.

### **Accelerometer Packaging**

The accelerometer proofmass and hybrid servo electronics are packaged in a compact housing as a fully integrated, power in - digital data out, instrument. The housing has been designed to provide a precision mounting for alignment and proper heat sinking for the electronics. The housing is hermetically sealed with a dry nitrogen environment inside



468

to protect the electronics and accelerometer chip. The finished accelerometer package is 1.30 inches wide, 1.46 inches long and 0.125 inches thick (33 mm by 36.5 mm by 3.2 mm thick) with 22 pins as shown in figure 3. Finished weight is 24 grams for the current package. Figure 4 shows an open accelerometer module prior to hermetic sealing. Size and power may be significantly reduced with further electronics miniaturization with custom chips.

## **Performance**

The SiAc™ silicon accelerometer has evolved through design refinements and newly developed control techniques into an instrument suitable for inertial grade performance systems. Table 1 shows the test results for the inertial grade silicon accelerometer.

Excellent bias and scale factor stability of 40  $\mu\text{g}$ ,  $1\sigma$  and 45 ppm,  $1\sigma$  respectively were achieved. Alignment stability was shown to be less than 2 arc-sec,  $1\sigma$ . Turn-on bias repeatability of 28  $\mu\text{g}$ ,  $1\sigma$  was also demonstrated. See figures 5, 6 and 7 for typical stability test results. Residuals to a second order compensation for temperature were 50 ppm and 90  $\mu\text{g}$  over the temperature range of -54 to +71 °C as shown in figures 8 and 9.

Vibration and dynamic performance also met the performance goals of the program. Figure 10 shows the frequency response of the SiAc™ with a smooth response and the -3 dB bandwidth point at 150 Hz. Phase lag at 20 Hz is 4.5 degrees. The lack of any resonant frequencies is due to the high damping in the accelerometer chip.

Vibration rectification testing showed very low rectification with only 25  $\mu\text{g}$  error for a 2 grms random vibration input with a flat spectrum from 20 to 2000 Hz. In fact, 8 grms input resulted in only 100  $\mu\text{g}$  vibration rectification error. Figure 11 shows a vibration test for rectification error. The accelerometer bias is shown with the input vibration turned on and off at several different input levels. The output data was digitally filtered to remove the AC response so that only the bias rectification error due to the input vibration. Of course the filtering is not perfect and some random AC response is seen at the higher input levels. The bias also shows some instability attributed to the slip-plate vibration test head mounted and cabling sensitivity at high input levels. The well behaved response of the Litton SiAc™ silicon accelerometer as demonstrated in the rectification and frequency response testing permits hard mounting in systems and eliminates the need for isolators under most conditions.

The g capability for the accelerometer was successfully demonstrated to the 70 g design goal. Figures 12 and 13 show the results of scale factor linearity testing in low (20g) and high (70g) range conducted in a centrifuge. The control software for the range changing function was demonstrated during the testing process on a centrifuge.



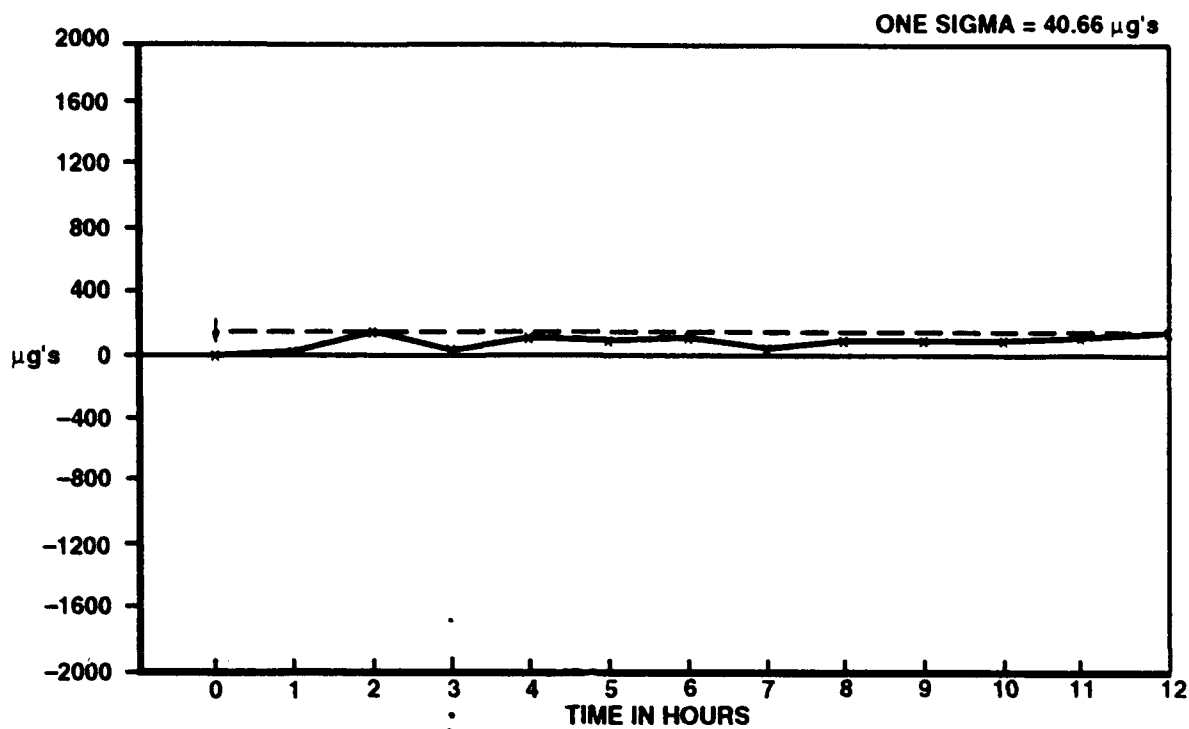


Figure 5. One-G Bias Stability

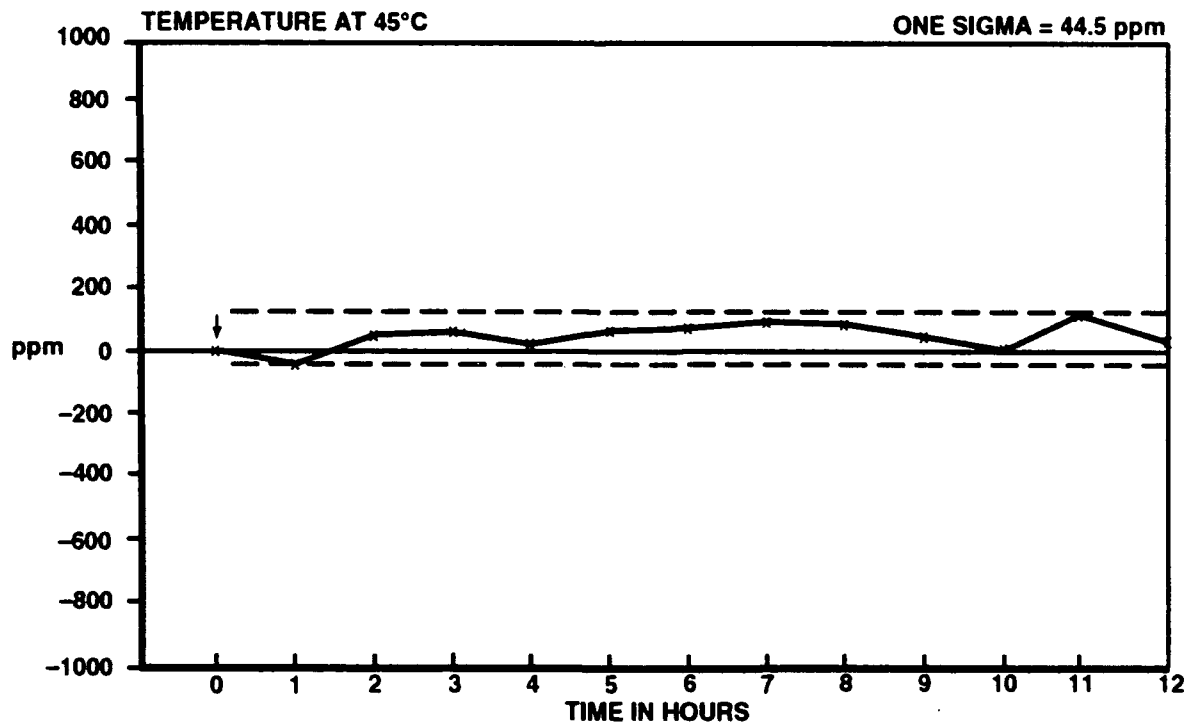


Figure 6. Scale Factor Stability

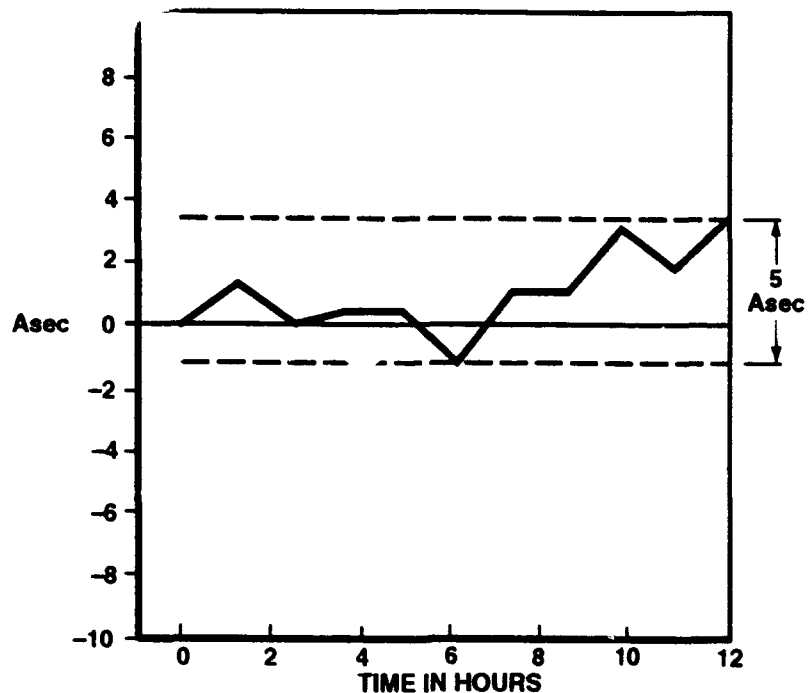


Figure 7. Axis Alignment Stability

DN RESID.

STD. = 31.6  
MAX = -55.2  
AT -25.0

UP RESID.

STD. = 31.1  
MAX = -58.7  
AT 23.0

ALL PTS RESID.

STD. = 50.5 ppm  
MAX = -119.8 ppm  
AT -25.0°C

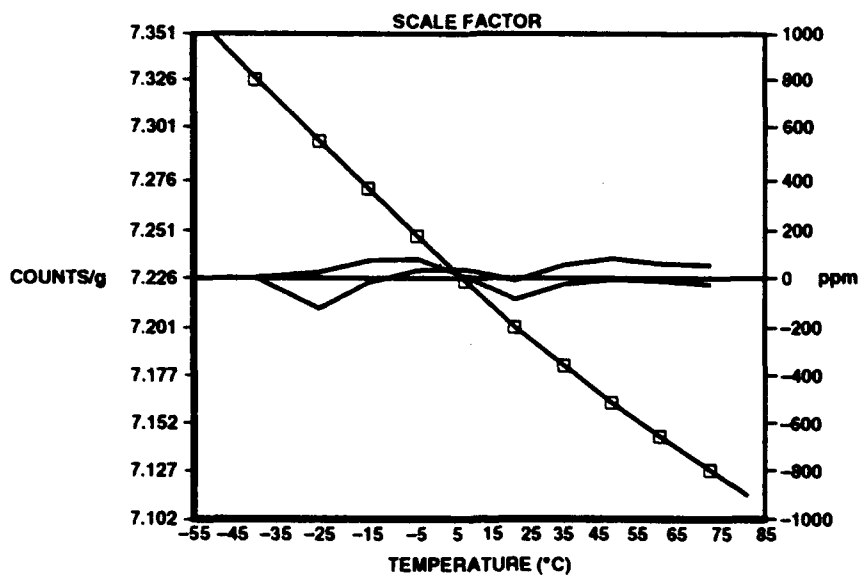


Figure 8. Thermal Model Scale Factor

DN RESID.

STD. = 15.1  
MAX = -31.6  
AT 23.0

UP RESID.

STD. = 46.4  
MAX = 90.5  
AT 35.0

ALL PTS RESID.

STD. = 94.4  $\mu\text{g/s}$   
MAX = -154.4  $\mu\text{g/s}$   
AT -1.0°C

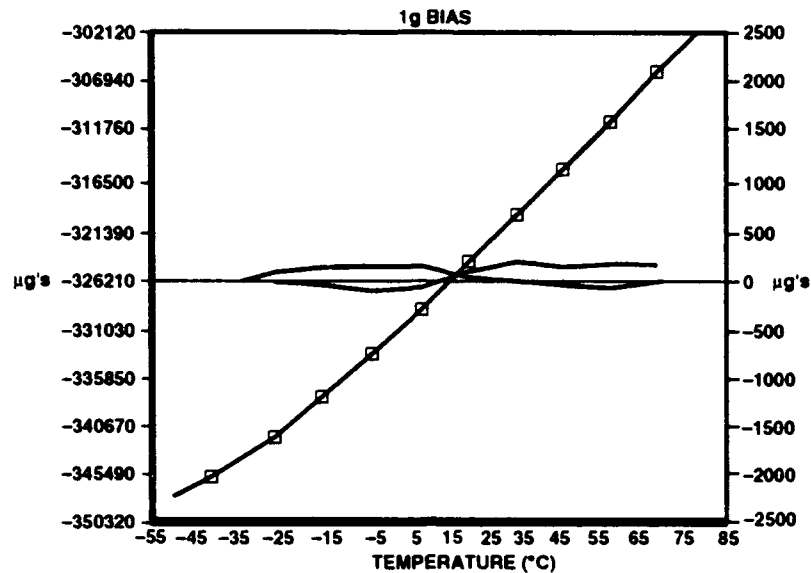
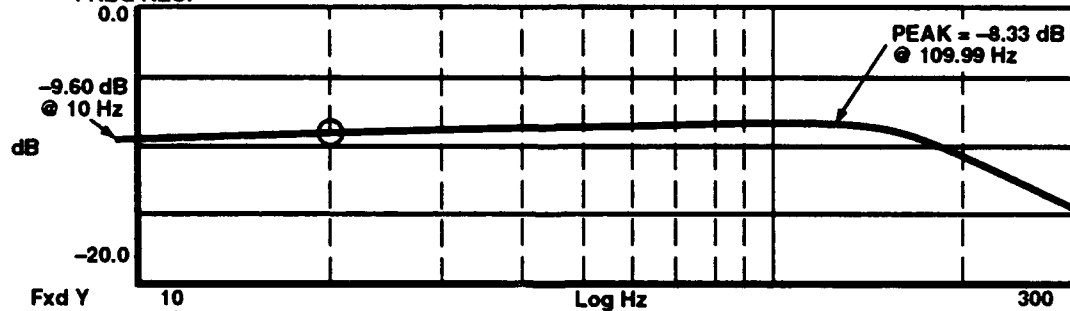


Figure 9. Thermal Model Bias

X = 19.997 Hz

Y<sub>a</sub> = -9.1813 dB

FREQ RESP



Fxd Y 10

Y<sub>b</sub> = 175.532 Deg

FREQ RESP

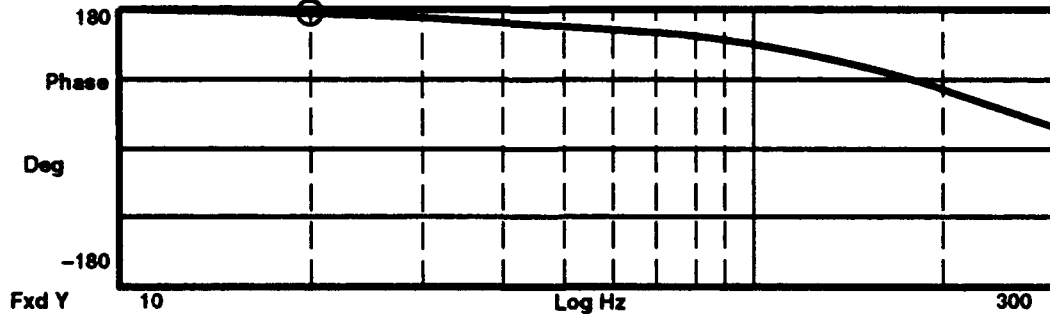


Figure 10. SiAc™ Silicon Accelerometer Bandwidth Frequency Response

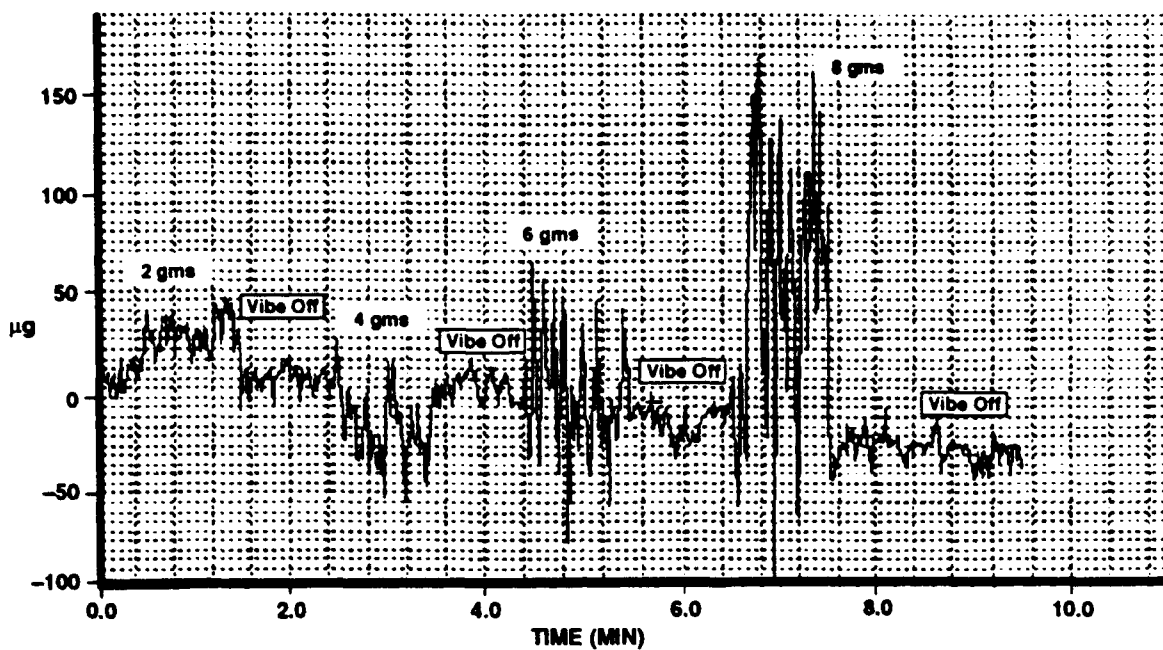


Figure 11. Vibration Rectification For Random G Inputs

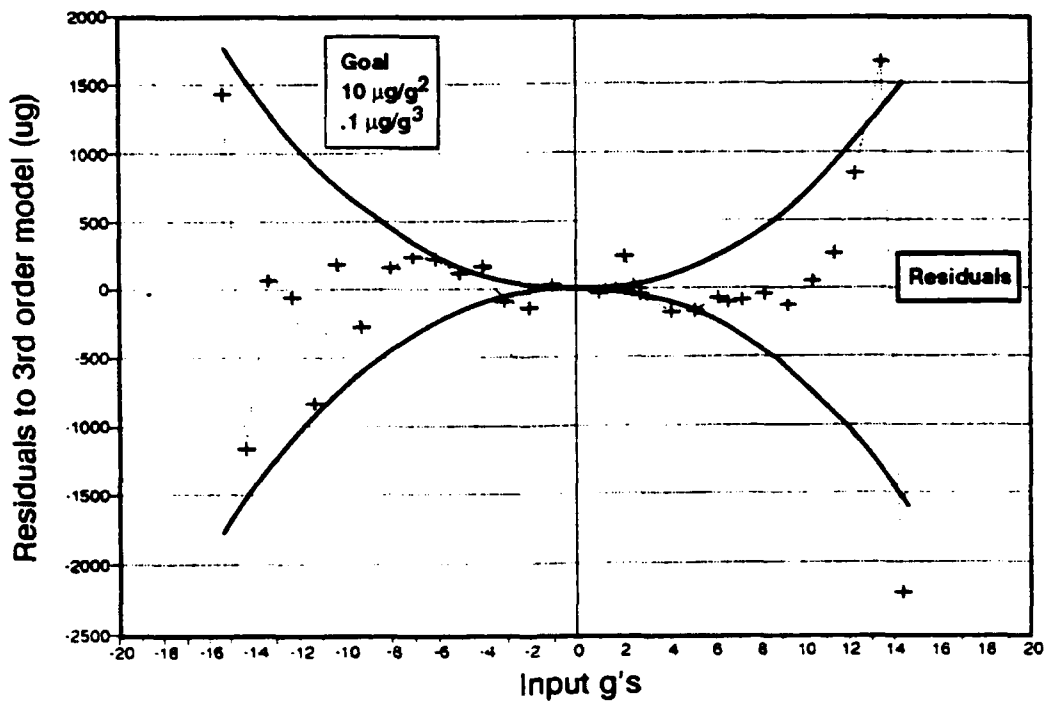


Figure 12. Silicon Accelerometer Scale Factor Linearity (Low Range)

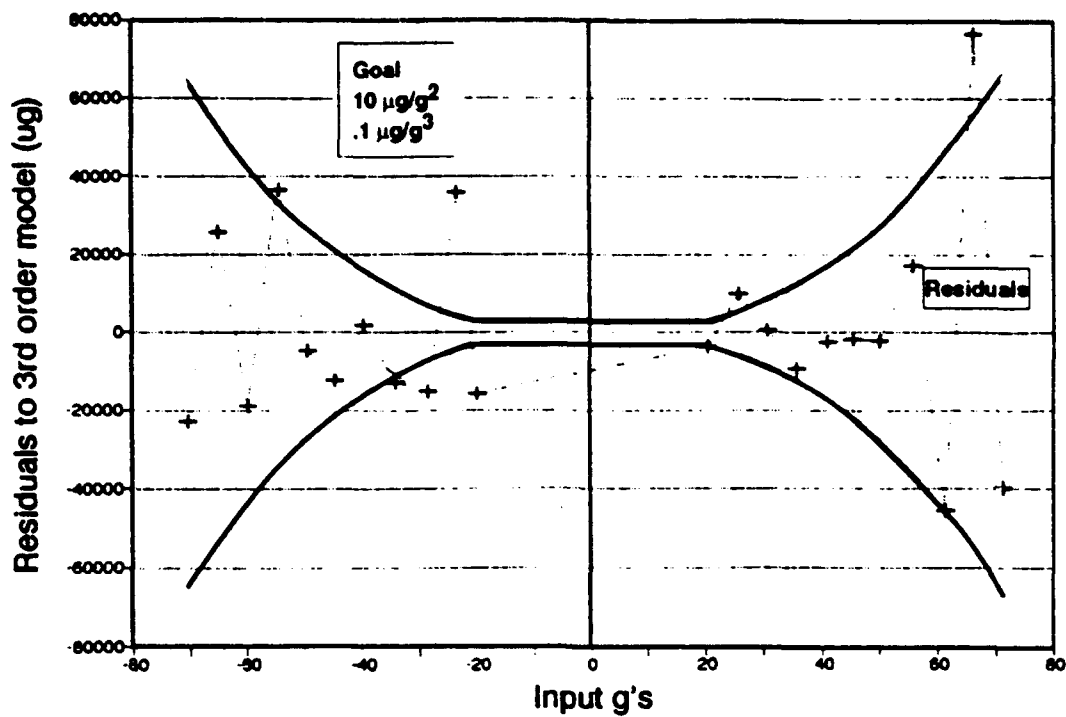


Figure 13. Silicon Accelerometer Scale Factor Linearity (High Range)

**Table 1 Inertial Grade SiAc™ Silicon Accelerometer Performance**

Parameter	Measured
Bias	
Stability (ug, 1 sigma)	40
Turn-on Repeatability (ug, 1 sigma)	28
Scale Factor	
Stability (ppm, 1 sigma)	44
Turn-on Repeatability (ppm, 1 sigma)	14
Modeled 2nd order linearity (ug/g <sup>2</sup> )	<10
Modeled 3rd order linearity (ug/g <sup>3</sup> )	<.1
Modeled linearity residuals over 20g low range (ppm, RMS)	64
Axis Alignment	
Stability (arc-sec, 1 sigma)	2
Temperature Sensitivity (-54 to 71 deg C)	
Bias (ug/deg C)	365
Modeled residuals (ug)	94
Scale Factor (ppm/deg C)	-257
Modeled residuals (ppm)	50
Bandwidth (phase lag at 20 Hz, deg)	4.5
Vibration Rectification (ug @ 2g)	25
(ug @ 8g)	75
Noise ( ug/root-Hz)	50
Quantization (ft/sec/cnt)	.00129
Range (g)	20
	80
Power Consumption (mW)	320

**THIS PAGE LEFT BLANK INTENTIONALLY**

## **The Microwave Resonator Accelerometer for Strategic System Application**

**A. Petrovich, R. Gels, J. Kutchmanich  
C. S. Draper Laboratory, Cambridge, MA 02139**

### **ABSTRACT**

The Microwave Resonator Accelerometer (MRA), presently under development for strategic system guidance applications, is being investigated through testing of a laboratory breadboard unit. Testing has focused on evaluation of static bias stability, bias stability under varying acceleration magnitude, and the requirements for the sensor readout electronics for high performance applications such as the strategic system thrust axis accelerometer.

Testing of a breadboard unit on a dividing head at 21 positions spaced equally in angle around  $360^\circ$  (tumble testing) showed the stability under conditions of varying acceleration and also the levels of cross axis response in the laboratory unit. Additional testing was performed from an initial orientation followed by  $180^\circ$  rotation and return to the initial orientation in order to more thoroughly characterize the bias repeatability. This testing along with static stability testing provided a basic characterization of the flexured mass subassembly which is central to strategic system accelerometer performance.

Stability of the electronics under changes in orientation was found to be critical to instrument bias repeatability and stability. Testing of the laboratory unit indicated the specific requirements on the electronics associated with a strategic thrust axis accelerometer.

### **INTRODUCTION**

Accelerometers currently used in ballistic missile inertial measurement units require fabrication and assembly of many high-precision components. Consequently, the devices are very expensive to manufacture and are costly to maintain. The objective of this effort is to develop an accelerometer with the capability of meeting strategic thrust axis performance requirements, but with a cost an order of magnitude lower and a Mean Time Between Failure (MTBF) in excess of 15 years.

The Microwave Resonator Accelerometer (MRA) has been identified as a possible alternative to the gyroscopically rebalanced pendulous gyro accelerometer currently used in high performance strategic missile guidance systems. The MRA is expected to fulfill the resolution, stability, dynamic range, and nuclear hardness requirements of high-performance inertial measurement units at a cost substantially less than that for



instruments currently in use. A down-sized version of the present breadboard MRA may also be considered for the strategic system cross axis accelerometer.

This paper presents a description of the MRA concept. The evaluation of the MRA sensor and electronics through a series of experiments on a laboratory breadboard unit is also described. Supporting the investigation of the MRA sensor and its application to a strategic system was an error compensation model described in the next section.

## **MRA CONCEPT**

The MRA sensor is based on the extremely high bias (frequency) stability provided by microwave cavity resonators and the high degree of dimensional stability typical of ceramic oxide materials. Because this device is considerably simpler and requires much fewer mechanisms, it is expected to show both a cost and reliability advantage over the accelerometer currently used in ballistic missile inertial guidance.

The MRA sensor consists of two microwave cavities separated by a flexure and proof mass assembly. A schematic representation of the MRA appears in Figure 1. The read out electronics are represented in the block diagram of Figure 2. Movable cavity endplates are mounted on a shaft which is supported by two flexible diaphragms. The proof mass consisting of the cavity endplates and connecting shaft are supported in such a manner that they can move in response to acceleration along the axis of the sensor cavities.

The position of this flexured proof mass assembly is determined by the magnitude of acceleration. Since the surfaces of the movable cavity end plates form the closure of the resonant sensor cavities, the position of the proof masses will, in turn, determine the resonant frequency of the two cavities. The frequency shifts for the two cavities occur with opposite sign when the proof mass is displaced along the sensor axis. This differential arrangement of the cavity sensors provides the capability of common-mode error subtraction. This feature can be used to significantly reduce bias shifts due to temperature variation, cross axis acceleration, and angular acceleration.

As shown in Figure 2, voltage controlled oscillators are locked in frequency to the resonant frequency of the resonant cavities with a phase locked loop. The acceleration is, therefore, represented as a change in the output frequencies from the oscillators locked to the cavity resonant frequency. The frequency-locking circuit and sensor cavities are constructed and packaged to minimize bias disturbances due to vibration, temperature variation, mechanical hysteresis, and radiation effects. For the strategic system accelerometer, the cavity resonant frequencies would be on the order of 10 to 25 GHz. The voltage controlled oscillators (VCO) shown in this figure provide the variable frequency portion of a synthesized signal which has a frequency in the resonant band of the sensor cavities. The VCO's, however, provide a frequency in a regime compatible with digital electronics (~ 50-250 MHz). The output signals from the VCO's representing the changes in the sensor cavity resonant frequencies are provided to a digital signal processor (DSP) where scale factors are applied, the differential response is calculated for the opposing cavities and any necessary corrections are applied. The frequency scale factor is on the order of 10 MHz/g for a cavity operating at 10 GHz.

The materials for the sensor cavities must have extremely low coefficient of expansion in order to minimize thermally induced bias shifts. The candidate materials chosen for the cavity have a zero coefficient crossover temperature below 50 °C. These

materials include titania modified silica (e.g. Corning ULE), Lithium Aluminum Silicate (e.g. Zerodur and Cervit), and Superinvar. As shown in Reference 1, all of these materials can develop through appropriate processing, an expansion coefficient which is zero at a temperature below 50 °C. Reference 1 also shows that in an interval of 0.1°C around the crossover temperature, the coefficient of expansion for ULE can be maintained to within  $1 \times 10^{-9} / ^\circ\text{C}$ . The dimensional stability achievable with temperature control of 0.1°C for this material is, therefore, 1 part in  $10^{10}$ .

The main requirement of the flexure is that it be capable of operating with a sufficiently low level of inversion transient, hysteresis, and anelasticity. A wide range of glass, ceramic, and crystalline materials may be used. Materials in these categories have been shown to have zero measurable hysteresis (to a  $10^{-8}$  strain sensitivity level) when loaded to stresses close to their fracture strength<sup>2</sup>. The first material selected for our investigation was Sapphire, a covalently bonded material of extremely high strength (up to 900,000 psi.<sup>3</sup>). Sapphire lacks the highly mobile defect configurations associated with impurities in quartz which is a potential contributor to inversion transients apparent in quartz resonator accelerometers. The high strength of Sapphire likewise reflects the stability of its covalently bonded crystalline structure. In order to benefit from Sapphire's high strength and resistance to anelastic response, the surfaces must be prepared properly to remove defects introduced during fabrication. Defects serve as sights for microcrack initiation which significantly reduce strength and provide a mechanism for anelastic and hysteretic response<sup>4</sup>. Chemical polishing<sup>5</sup> and flame polishing<sup>3</sup> are appropriate means of removing surface damage left by the Sapphire flexure fabrication process.

The use of the microwave sensor for which the wavelength is on the order of the proof mass size provides some advantage with respect to cross axis rejection. The use of a microwave resonator sensor rather than a piezoid for measuring proof mass response to acceleration provides advantages over quartz resonator accelerometers with regard to hardenability and design flexibility. Since no precision voltage reference is required to provide absolute accuracy of scale factor or bias, the MRA has an advantage over force rebalance accelerometers with regard to stability in a nuclear environment.

The flexure system consists of a flexing element of minimum anelasticity, a proof mass, and a damping system that relies on a gaseous squeeze-film effect. In a system accelerometer the damping characteristic can be tailored to the specific application.

## **MRA TESTING AND EVALUATION**

A laboratory breadboard system was constructed to evaluate components of the MRA. The breadboard unit included a dual cavity sensor in the configuration shown in Figure 1 and a set of phase locked electronics represented schematically in Figure 2. The breadboard sensor cavities and proof mass were fabricated from superinvar and plated with high conductivity silver. The flexures were fabricated from Sapphire. A series of tests were performed to establish the general function of the sensor and isolate the source of bias disturbances in the MRA system.

### **MRA Sensor Evaluation**

The performance requirements for the strategic accelerometer include a specification for bias stability, scale factor stability, dynamic range, error induced by shock and vibration, as well as nuclear hardness. There are additional requirements on size. The

emphasis in the present study was placed on bias stability, scale factor stability, and dynamic range. Specifically this program is focused on demonstrating adequate instrument accuracy and stability in a 1 g tumble test. Dynamic response characterization was not a part of this study.

Testing of the accelerometer subassembly (breadboard ) was performed on a dividing head that rotates the accelerometer to a series of precise orientations with respect to gravity. The tests performed included 13 and 21 positions with the initial position duplicated. These tests provide information regarding the scale factor, scale factor stability, cross-axis response, and the magnitude of bias disturbances; the degree of common mode error rejection is also provided. Before the tumble testing, stability tests were performed at a single orientation to provide a general characterization of bias stability. The dividing head tumble tests were performed with the device resident at each position for about 1 to 10 min with a precision of orientation of 1 arcsec and a repeatability of 0.25 arcsec. The purpose of tumble testing to date has been to verify the function of the flexured mass/ cavity sensor system and uncover any assembly problems or other shortcomings in the system. The resonant frequency variation for the two sensor cavities as a function of angle of orientation in the tumble test is shown in Figure 3.

In this development effort, two systems for reading sensor cavity response were used: swept frequency response and phase locking electronics. With the swept frequency electronics a constant amplitude signal from a synthesizer is stepped in frequency through the resonance of the cavity. The transmitted signal of the two port cavity as a function of frequency was measured and the resonant frequencies of the sensor cavities were calculated from these measured curves. Using a swept synthesized microwave source allows the evaluation of the cavity sensors independent of the frequency lock electronics with, however, a sacrifice in the bandwidth of the measurement. The phase locking electronics consists of a control loop that locks the frequency of a voltage-controlled oscillator to the resonant frequency of the cavity. A breadboard phase locked loop was constructed to perform this function.

In the experiments conducted to date with the phase locked electronics, the main limitation on resolution and stability appears to be related to the phase discriminator of the phase locked loop electronics. It is expected, however, that temperature control, appropriate design of the phase lock loop discriminator, and appropriate packaging of this component will provide an MRA breadboard that can be tumble tested with a bias stability of 1  $\mu$ g.

The tumble tests that were performed indicated appropriate accelerometer functionality as shown in Figure 3, with each cavity yielding a clear, symmetric cosinusoidal response. Both cavities were successfully phase locked to the voltage controlled oscillators. Static bias stability tests were run with the MRA outside of its temperature controlled enclosure and with a breadboard setup for the phase discriminator to allow phase adjustment in the phase discriminator reference loop. The bias variation generally increased with increasing periods of measurement indicative of disturbances with long (hours) characteristic cycles.

A compensation model was developed for the MRA that includes the corrections to sensor outputs due to coupling of cross axis acceleration, angular acceleration, flexure nonlinearities and temperature variation. The general expressions for the sensor output

corrected for cross axis acceleration, angular acceleration, and scale factor nonlinearity for each cavity sensor are as follows:

$$g_1 = B_1 + SF_{11} \nu_1 + SF_{12} \nu_1^2 + SF_{13} \nu_1^3 + K_{g11} g_{c1} + K_{g12} g_{c2} + C_{g11} g_{c1}^2 + C_{g12} g_{c2}^2 + C_{r11} \Theta_1^2 + C_{r12} \Theta_2^2 \quad (1)$$

and

$$g_2 = B_2 + SF_{21} \nu_2 + SF_{22} \nu_2^2 + SF_{23} \nu_2^3 + K_{g21} g_{c1} + K_{g22} g_{c2} + C_{g21} g_{c1}^2 + C_{g22} g_{c2}^2 + C_{r21} \Theta_1^2 + C_{r22} \Theta_2^2 \quad (2)$$

The accelerometer output is given by:

$$g = g_1 - g_2 \quad (3)$$

where,  $g_1, g_2$  are the corrected outputs of the two sensors,  $\nu_1, \nu_2$  are the frequencies from the two sensor cavities,  $g_{c1}, g_{c2}$  are the cross axis components of acceleration,  $\Theta_1, \Theta_2$  are the angular acceleration rates about the two axes orthogonal to the sense axis,  $C_{g11}, C_{g12}, C_{g21}, C_{g22}, K_{g11}, K_{g12}, K_{g21}, K_{g22}$  are the coefficients associated with the cross axis acceleration compensation, and  $C_{r11}, C_{r12}, C_{r21}, C_{r22}$  are the coefficients associated with the cross axis rotational acceleration compensation. The first scale factor coefficients,  $SF_{11}, SF_{21}$ , have the additional temperature dependence given by:

$$SF_{11} = SF_{110} + \sigma_{11} (T - T_0), \quad SF_{21} = SF_{210} + \sigma_{21} (T - T_0) \quad (4)$$

and the bias terms, similarly, have the temperature dependence:

$$B_1 = B_{01} + \beta_1 (T - T_0), \quad B_2 = B_{02} + \beta_2 (T - T_0) \quad (5)$$

The mechanisms giving rise to the terms in above expressions are as follows:

$$\begin{aligned} g_1 = & B_1 && : \text{Bias term} \\ & + SF_{11} \nu_1 && : \text{Linear scale factor term} \\ & + SF_{12} \nu_1^2 && : \text{Non linear scale factor} \\ & + SF_{13} \nu_1^3 && : \text{Non linear scale factor} \\ & + C_{g11} g_{c1}^2 && : \text{Cross axis acceleration coupling (from proof mass unbalance)} \\ & + C_{g12} g_{c2}^2 && : \text{Cross axis acceleration coupling (from proof mass unbalance)} \\ & + K_{g11} g_{c1} && : \text{Cross axis acceleration coupling (from cavity distortion)} \\ & + K_{g12} g_{c2} && : \text{Cross axis acceleration coupling (from cavity distortion)} \\ & + C_{r11} \Theta_1^2 && : \text{Cross axis angular acceleration (mostly from proof mass rotation)} \\ & + C_{r12} \Theta_2^2 && : \text{Cross axis angular acceleration (mostly from proof mass rotation).} \end{aligned} \quad (6)$$

Using mathematical perturbation methods on the solution of Helmholtz's equation<sup>6</sup>, the formulation for the evaluation of these correction terms for MRAs of the present

design was developed. For the breadboard unit the  $g^2$  cross terms are due primarily to flexure and proof mass unbalance and are less than  $100 \mu g/g^2$ . With improved balance and with common mode error subtraction these can be eliminated. For the breadboard unit under test an upper bound estimate for the linear cross axis coupling terms are on the order of  $240 \mu g/g$ . This can likewise be reduced by proper design. This cross axis term contributes to the axis misalignment and can, therefore, be eliminated by axis correction. The frequency shift for cross axis angular acceleration is less than  $1 \mu g/(\text{rad/sec}^2)$ . This factor is reduced by common mode error subtraction. The relationship between cavity resonant frequency and flexure deflection can be designed to be linear by modifying the cavity contour near the endplate. The axial non linear terms are due to flexure nonlinear response and irregularities in the fabricated cavity. The flexure nonlinearity is expected to provide the largest to the correction. The calculated nonlinear terms in the deflection versus acceleration relationship for the laboratory breadboard are  $3.5 \times 10^{-7} g/g^2$ ,  $-6 \times 10^{-6} g/g^3$ , and  $4.2 \times 10^{-9} g/g^4$ .

For the strategic system MRA several terms, therefore, may be eliminated by cavity design, common mode subtraction, and proof mass balance with the following compensation expression resulting:

$$g = B + SF_{11}\nu_1 + SF_{12}\nu_1^2 + SF_{13}\nu_1^3 - SF_{21}\nu_2 - SF_{22}\nu_2^2 - SF_{23}\nu_2^3 + C'_{r1}\theta_1^2 + C'_{r2}\theta_2^2 \quad (7)$$

### MRA Electronics Evaluation

Static bias stability on the order of  $2 \mu g$ 's for an interval of 20 minutes and  $8 \mu g$ 's for an interval of 10 hrs. was achieved. Large microwave probing signal amplitude variation that occurred during tumble testing resulted in a limitation on stability during tumble testing. The best experimental results for 5 consecutive tumble cycles including 0, 180, and 360 degrees showed a standard deviation of 220 micro g's.

A series of experiments were performed to isolate the source of the bias shifts that occur during tumble testing. These tests included the evacuation of the cavity to eliminate gas flow transients or gas thermal transients, testing with a signal frequency swept through resonance with output taken from the frequency discriminator circuit, testing with a signal frequency swept through resonance with output taken from a power meter measuring cavity transmitted power, and testing with the cavity sensor in a single fixed orientation and the 10 GHz supply cable varied in angular orientation. These tests showed that a significant contribution to bias variation, on the order of several hundred micro g's, resulted from changes in the orientation of the 10 GHz supply cable with its associated changes in probe signal amplitude. The magnitude of this bias shift resulting from supply cable orientation change varied in random fashion and was on the order of that for the unit in changing orientation from 0 to 180 to 360. degrees. Evacuation of the cavity had little influence on the bias variation.

The resonant frequency of each cavity is represented by a voltage controlled oscillator (VCO) which is locked in frequency to the cavity resonant frequency through a phase discriminator circuit and feedback amplifier (Figure 4). The phase discriminator is presently limiting the static stability and stability in tumble because of a spurious output that adds to the desired feedback signal representing phase of the cavity transmitted

signal. The dominant source of spurious signals in the lock electronics feedback loop is due to variation in the DC offset voltage provided by the phase discriminator mixer. The spurious DC voltage results from portions of the microwave signal input to the mixer reference and other signals arising from reflections in the phase discriminator circuit being coupled to the cavity signal mixer input. The spurious DC signals are indistinguishable from variations in the mixer output resulting from changes in the sensor cavity resonant frequencies.

This spurious DC voltage offset, caused primarily by rectification of the reference signal in the mixer, varies with the amplitude of the cavity probing signals (the 9.6 and 10.4 GHz signals supplied to the cavity sensors). These signals are expected to be of constant amplitude but can vary due to cable flexure or temperature variation. As shown in Figure 4, any change in this spurious DC voltage offset will result in a shift in the null frequency. Since the feedback circuit attempts to maintain the feedback signal at null, a change in the DC voltage offset will cause the VCO output frequency representing instrument bias to shift as well. These bias shifts can be reduced significantly by providing better control on signal amplitude and substituting a phase discriminator circuit which is substantially less sensitive to amplitude probe signal amplitude variation.

Several measures have been identified to eliminate the instrument bias variation associated with the spurious DC signal. The mixer used for phase comparison may be optimized to minimize the DC offset in the narrow band around sensor cavity resonant. The DC bias may also be significantly reduced by provided phase modulation of the cavity probing signal at a lower frequency and performing the phase detection at this lower frequency.

## CONCLUSION

A high performance accelerometer based on microwave cavity sensors is under development for application in strategic system inertial measurement units. The sensors appear to have generally appropriate response. Instrument bias stability in tumble testing, however, was limited by spurious DC signals in the phase lock feedback signal. Refinement of the phase locking electronics serving as a readout is expected to provide bias stability of 1  $\mu$ g. This will allow the evaluation of flexure material response to instrument levels of resolution.

## ACKNOWLEDGEMENT

The authors gratefully acknowledge the support of J. Barry (CSDL) for the structural design and analysis of the MRA sensor.

## REFERENCES

1. J. W. Berthold, S. F. Jacobs, and M. A. Norton, "Dimensional Stability of Fused Silica, Invar, and Several Ultra-low Thermal Expansion Materials" *Metrologia* 13, p.9-16, (1977).
2. J. W. Moberly, "Tensile Microstrain Properties of Telescope Mirror Materials," NASA report No. NASA CR-111948, Prepared by Stanford Research Institute, Menlo Park, California 94025 under Contract NAS19982, June, 1971.

3. F. P. Mallinder, and B. A. Proctor, "The Strength of Flame-polished Sapphire Crystals," *Phil. Mag.*, 13, 121, p.197, (1966).

4. B. M. Darinskii, N. V. Izmailov, V. A. Loginov, and N. P. Yaroslavl'tsev, "Anelastic relaxation in solids caused by surface damage," *Soviet Physics, Solid State*, 29 (12), December, 1987.

5. A. Reisman, M. Berkenblit, J. Cuomo, and S. A. Chan, "The Chemical Polishing of Sapphire and MgAl Spinel," *J. Electrochem. Soc.: Solid State Science*, Vol 118, No. 10, p. 1653.

6. P. M. Morse, H. Feshbach, *Methods of Theoretical Physics*, McGraw-Hill Book Company, New York, 1953.

:

Figure 1: Schematic Representation of the Microwave Resonator Accelerometer (MRA) Sensor.

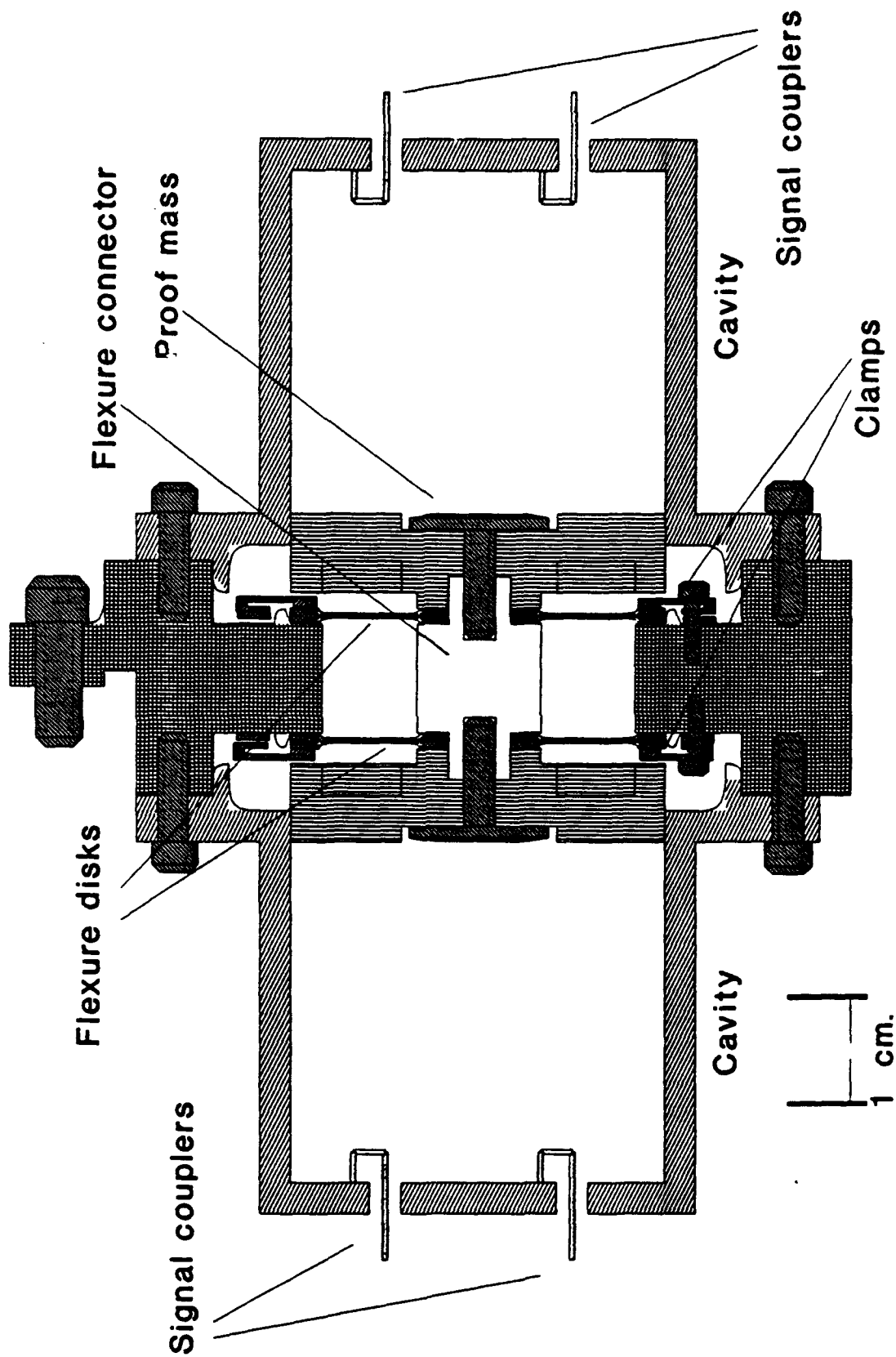
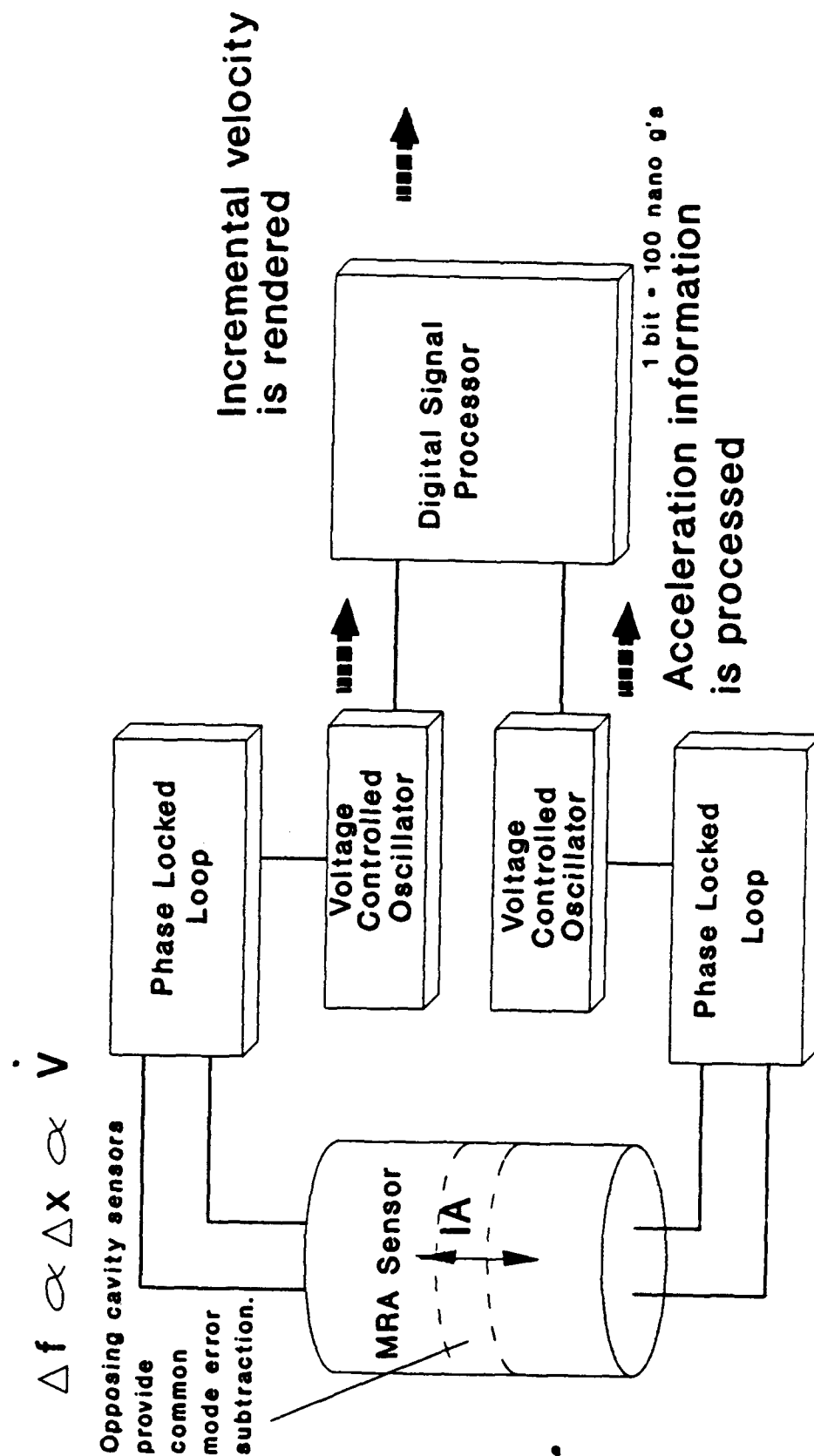




Figure 2: Schematic Representation of the MRA Readout Electronics.



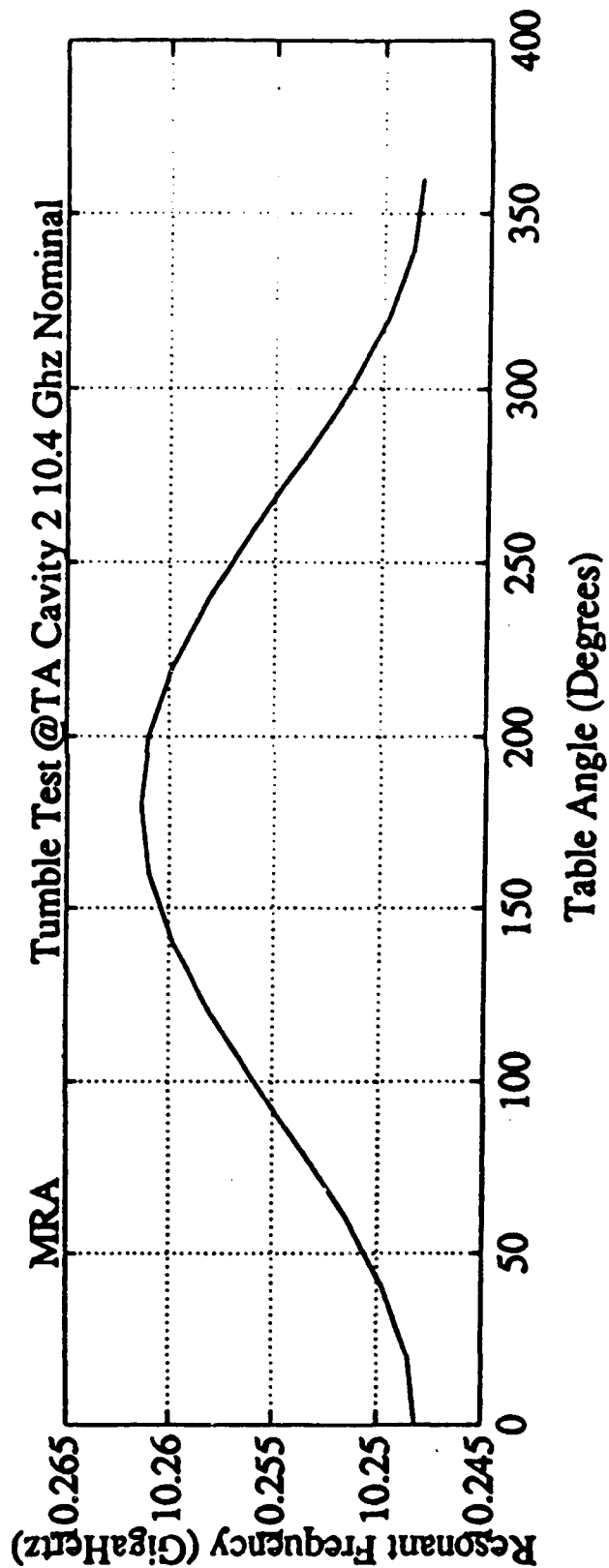
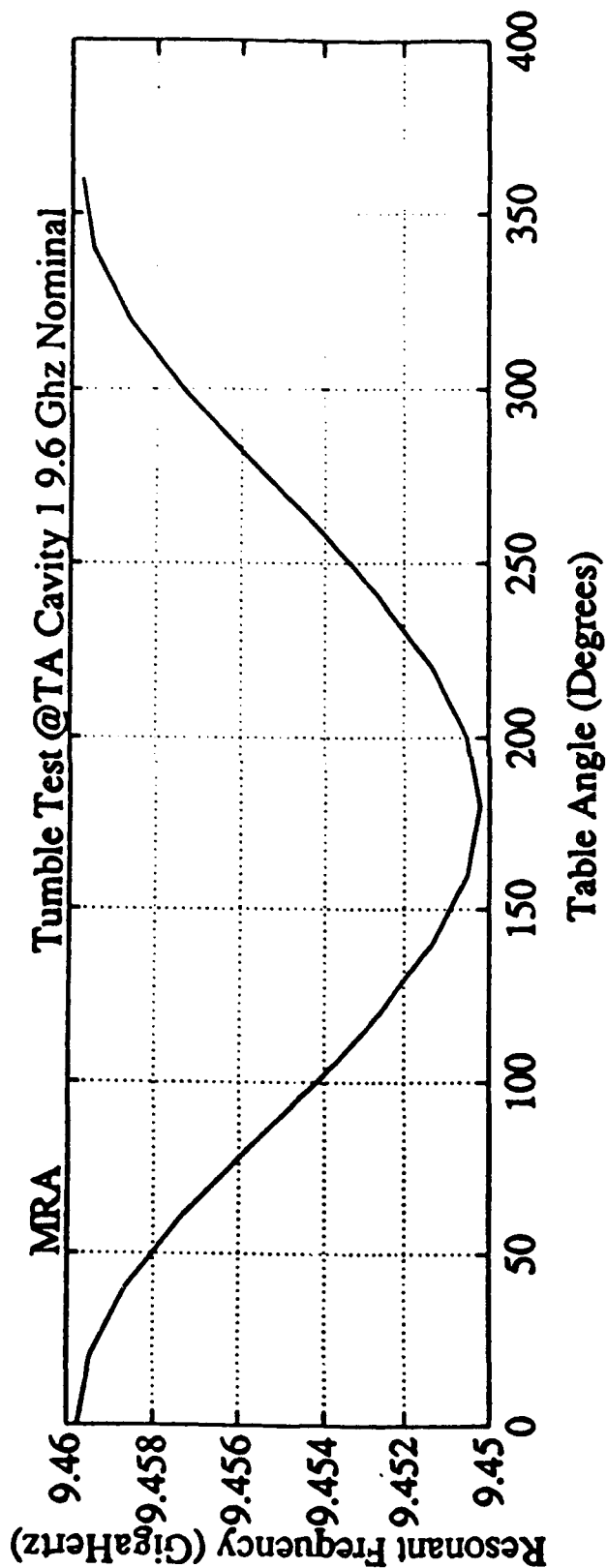


Figure 3: Cavity resonant frequency as a function of angle during a tumble test of the MRA.

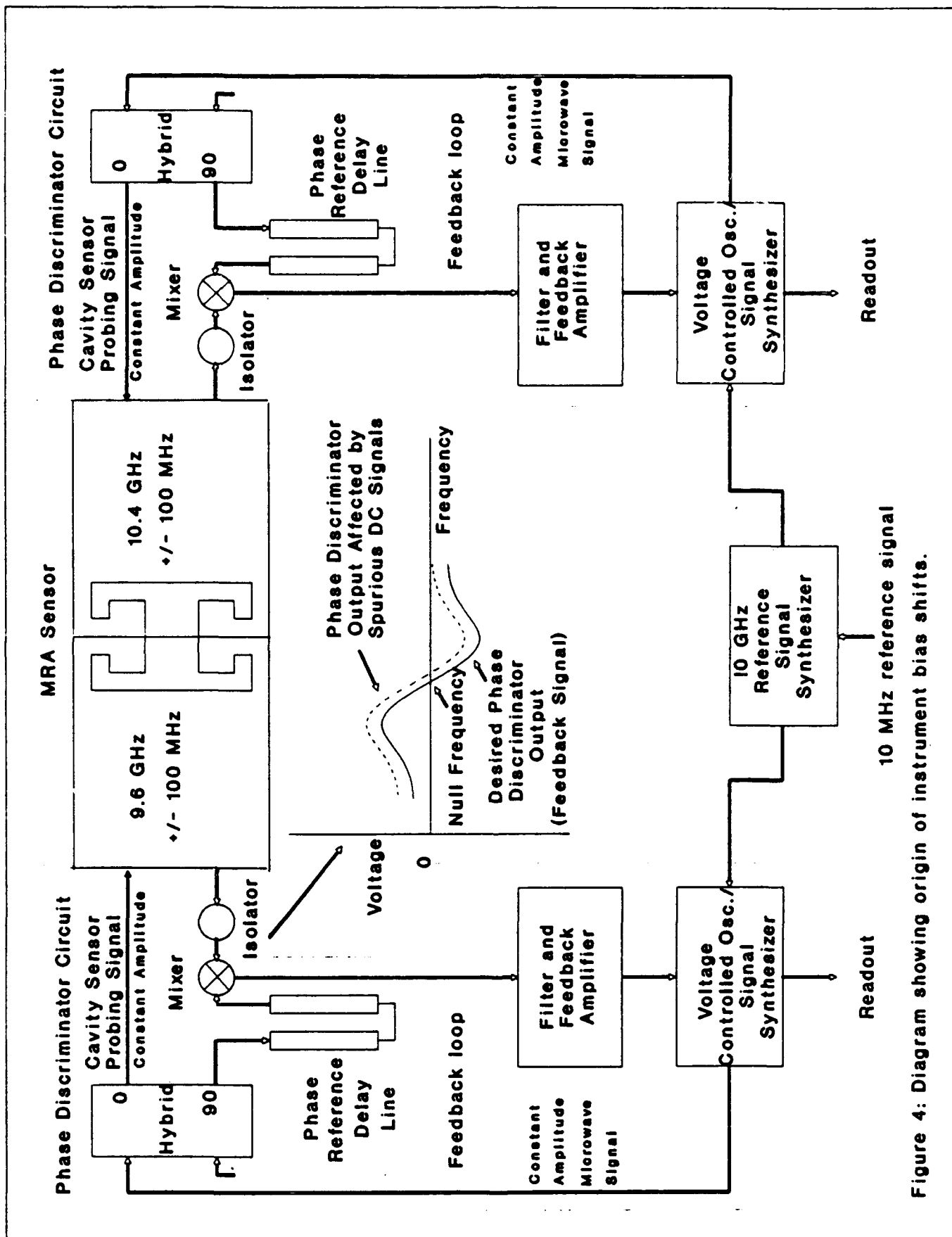


Figure 4: Diagram showing origin of instrument bias shifts.

**Results of Testing Linear Accelerometers on a  
Low Cost Centrifuge Using "IEEE STD 836-1991"**

**R. D. (Sam) Marquess  
Applied Motion Technology, Inc.  
Concord, California**

**Paper No. 93-52**

**Approved for Public Release; distribution is unlimited**

### **Abstract**

#### **Results of Testing Linear Accelerometers on a Low Cost Centrifuge using IEEE Std 836-1991**

**R. D. Marquess  
Applied Motion Technology, Inc.  
Concord, California**

Precision testing of linear accelerometers using a centrifuge and the associated data gathering equipment and means is usually a very expensive process. In general, the cost increases rapidly with improvements in precision. The Gyro and Accelerometer Panel (GAP) of the IEEE Aerospace and Electronics Systems Society developed over the course of ten plus years, IEEE Std 836-1991. This Standard is a guide to be used in the process of obtaining the various coefficients of a model equation that is typically used in precision applications to relate the output of an accelerometer to the acceleration input.

The testing that was performed incorporated most of the known error sources inherent with the process of operating a centrifuge. The intent was among other things, to prove the methods recommended or suggested by the Standard and to also investigate the effects of much larger error sources than would normally be associated with testing that would be considered "precision". For example, the centrifuge used had roller bearings with roughly an order of magnitude more radial runout than the lowest grade (ABEC 1) ball bearings allow. The velocity servo incorporated a phase locked loop with very good (10 ppb) average accuracy and stability, but the loop was closed around a vee-belt drive and during some of the tests, with an encoder that was a "reject" with a known error on the order of a hundred parts per million. An optical encoder with nominally 1 arc second accuracy was also used in the same loop and tests were run to compare the results with both types of encoder.

The accelerometers tested were loaned for the test program by Systron Donner and were not considered to be examples of "high performance" devices selected for this or any other specific purpose. They are "linear, force balance servo accelerometers" with analog outputs. The voltmeter used to obtain the data was a Fluke 895A that incorporates a center reading scale which allows the operator to get useful readings of the steady state output in the presence of periodic variations.

The term "low cost" is relative and as a point of comparison, in the case of the centrifuge, the target cost for "pieces" was \$2000. Most of the components were used and the optical encoder was only borrowed and therefore cannot be considered part of the actual cost. The program did go over budget and in reality, the parts cost was over \$2500. The labor and materials for the design, fabrication and assembly were obviously not included in the above figure.

The paper summarizes the results of the test program, which were surprisingly good. It describes the methods and means with which a user can separate the data that has a high probability of accuracy from that which is not legitimate for modelling.

# **RESULTS OF TESTING LINEAR ACCELEROMETERS ON A LOW COST CENTRIFUGE USING IEEE STD 836-1991**

## **1.0 INTRODUCTION**

The test program that produced the results presented herein was accomplished with Applied Motion Technology, Inc. R & D funds. The accelerometers were loaned to AMT from Systron Donner division of BEI and Sundstrand Data Control Inc. The optical encoder used was loaned to us for part of the testing by H S & S Machine Tool Builders of Santa Clara, Ca. They are a Heidenhain representative and the encoder was a Heidenhain Model ROD 260.

There are very few centrifuges that are considered "precision" that are also considered "low cost". A large part of the impetus for this program was to challenge the notion that only direct drive machines are capable of generating acceleration levels that are useful for much more than environmental purposes. The methods of data reduction along with the various recommendations contained in IEEE Std 836 will allow a centrifuge user the ability to obtain acceleration data with relatively high precision at very reasonable cost.

## **2.0 SYSTEM DESCRIPTION**

The centrifuge "Test Stand" began life as a Schaevitz Engineering type "B-6" and was manufactured in 1967. It was purchased from the government as salvage by an equipment dealer. AMT obtained it from the dealer and the price including shipping was \$1500. The shipping cost was twice the sale price of the centrifuge. The only thing of real significance here is that the machine has an arm that is nominally 6 feet long (end to end) and is fabricated from a structural steel "C Channel". An area of concern with any precision centrifuge is that of arm stretch. An analysis was made which indicated that the "Arm Stretch Coefficient" for this machine would be  $0.137 \mu\text{g}/\text{g}^2$ . This number is based on the nominal 29 inch radius to the center of the existing bolt pattern with 1 Lb. allotted for test fixture and accelerometer.

## 2.1 TEST STAND

The Test Stand was disassembled and cleaned up to allow evaluation of the useable pieces. In addition to the basic frame and circular enclosure, the spindle and slip rings were serviceable. The decision was made to use the existing roller bearings even though they are not a good choice for this application. All the major pieces were primed and painted. During subsequent testing, the existing steel top of the enclosure was replaced with one made from 1/2 inch plywood to allow the machine to also be used as a test bed for a GPS package.

### 2.1.1 MOTOR & MECHANICAL DRIVE

The existing motor and cog belt drive were not suitable and we replaced them with a used 5 HP @ 2500 rpm, 250 Volt DC Reliance Electric motor that we had previously reconditioned. A used Beckman 7.0 Volt/1000 rpm tachometer was mounted and coupled directly to the motor. We fabricated a new motor mount and purchased a set of sheaves and 3VX section vee-belts to produce a 2.24:1 drive ratio. The sheaves were turned true on the lathe and the belts were installed.

### 2.1.2 PULSE GENERATOR & ENCODER

We had one of our standard "600 toothed wheel" magnetic pulse generators that had been dropped and had a flat area that made it unusable. This reject wheel seemed to be a worst case velocity error generator and was therefor installed on the spindle. We also persuaded the local Heidenhain representative to loan us one of their incremental optical encoders (10,000 ppr). The encoder was coupled to the spindle with a ROCOM coupling which isolated, to some extent, the radial runout of the bearing adjacent to the magnetic pickup. The measured runout was 0.006 inches TIR. For comparison, the lowest precision grade ball bearing (ABEC 1) runout allowance for a bearing of the same nominal size is 0.0008 inches.



### 2.1.3 POWER AMPLIFIER

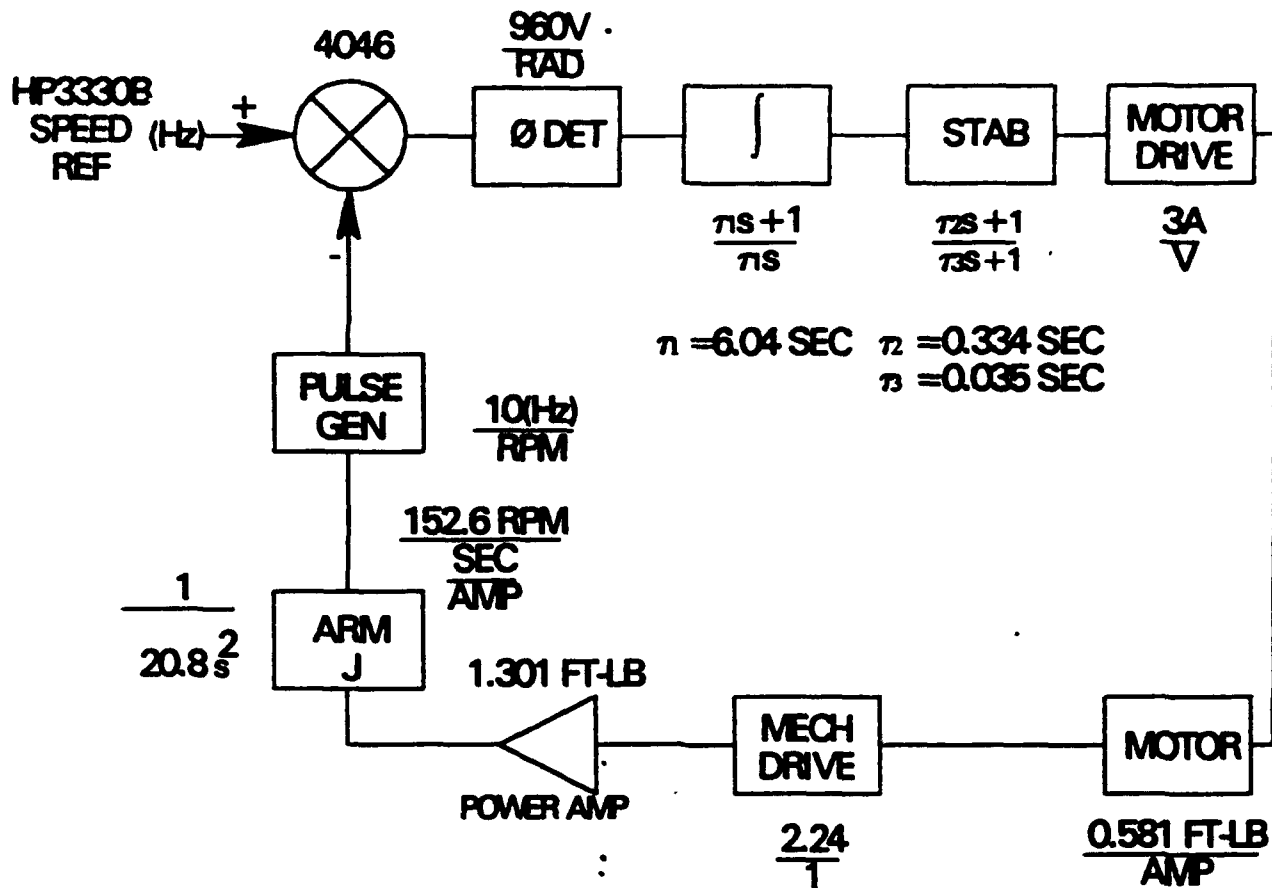
The power amplifier used is a pwm (25KHz) "Max 300 DC Servo Drive" from Electrocraft, which was recently acquired by Reliance Electric. The unit is capable of 1 KW plus continuous and we utilized the tachometer to compensate for an "automatic fold back" feature that was inconvenient for our use. The amplifier was designed for machine tool control and other applications where the response time is short. We essentially consider the amplifier as an Op Amp that would output up to 95 Volts and 12 Amps. With the drive ratio and the motor and amplifier, we were able to overcome the aerodynamic drag (7.6 Ft.Lb. @ 500 rpm) up to a relatively high g level. 492.76 rpm is 200 g at the nominal 29 inch radius. The time required to reach full speed from a dead stop was calculated to be 80 seconds and it was verified by test.

## 2.2 CONTROL RACK

The control rack contains the power supply for the field, the rate counter, the synthesizer and controlling computer, and the card cage with the servo board. There is also a panel with the various switches used to control the operation of the test stand. Since this test bed system is intended for in house use only, the usual interlocks and safety related hardware was not included.

### 2.2.1 SERVO SYSTEM

The servo is essentially the standard phase locked loop that we use in our all our systems. The speed or rate control reference is a Hewlett Packard Model 3330B synthesizer that is accurate to within 10 parts per billion. It is settable in 0.1 Hz steps which when used with the 600 pulse per rev pulse generator is equivalent to 0.01 rpm steps. The block diagram is as shown in Figure 1.



Servo System Block Diagram  
Figure 1

The existing structure that was used to support the motor mount was too compliant to allow a servo bandwidth compatible with the 10,000 pulse per rev output from the optical encoder. We used a digital 10:1 divider to solve the problem. With the 1000 ppr setup, we could switch back and forth between it and the 600 ppr generator without changing the servo compensation. The old HP 85 computer that we had laying around was used to handle the housekeeping chores of setting the proper frequency for the desired g level associated rates with the two encoders. The limiting factor as far as g capability is the power amplifier. The drive ratio was chosen such that we would run out of voltage (95 Volt max) with the Armature  $I^2R$  drop necessary to overcome aerodynamic drag (3.5 Volts) and the back emf (91.4 Volts) at 500 rpm.

As a means of evaluating the operation of the servo, with the once per revolution velocity perturbations due to the known errors in the 600 ppr generator, we measured the peak to peak output of the accelerometer at various g levels. We then purposefully loosened the drive belts. Up to the point of slippage and loss of phase lock, there was no difference in the peak to peak or average value of the output signal from the accelerometer. This seems to indicate that a properly designed servo will accommodate most inaccuracies that may be contained within the closed loop system.

The best we were able to do with the system was with the optical encoder. As a means of determining the "wow" of the system, George H. Neugebauer (who developed the data analysis technique used herein) had asked for someone to run a test with the sensitive axis of the accelerometer perpendicular to the centrifuge acceleration and in line with the tangential velocity vector. Several of these tests were performed with both encoders. We called this the "sideways" test and with the optical encoder, the result was about  $165 \mu g$  peak. With a 29 inch radius, this corresponds to  $0.0022 \text{ rad/sec}^2$  (peak). This "wow" amplitude was essentially constant from about 20 to 55 g. The following calculation was made with the assumption that the motion was sinusoidal:

$$\begin{aligned} \phi &= A \cdot \sin(\omega t) & \omega &= 27.06 & 55 \text{ g with a 29 inch radius} \\ \frac{d}{dt} \phi &= A \cdot \omega \cdot \cos(\omega t) \\ \frac{d}{dt} \frac{d}{dt} \phi &= -A \cdot \omega^2 \cdot \sin(\omega t) & \frac{d}{dt} \frac{d}{dt} \phi &= 0.0022 \\ A &= \frac{0.0022}{27.06^2} & A &= 0.000003 & \text{(radian) about 1 arc second (p-p)} \\ & & & & \text{position loop error} \end{aligned}$$

The magnitude of the velocity change is:

$$A \cdot \omega = 0.000081 \quad 81 \mu\text{rad/sec}$$

The same g levels (speeds) were run with the accelerometer mounted with the sensitive axis in line with the acceleration vector and the peak to peak reading of the output voltage was about  $100 \mu\text{volts}$ . This is equivalent to about  $820 \mu g$  (p-p).

The roughly 7 ppm acceleration output (peak) is in the right ballpark for the 3 ppm (peak) "wow" amplitude. The motion was not really sinusoidal, the wave form had a shape more like a half sine hump that occurred once per revolution.

Since AMT is a supplier of centrifuges with automatic dynamic balancing systems, we were very aware of the problems that imbalance can present when precision testing is involved. The test bed was balanced manually by trial and error until a dial indicator measuring the Test Stand motion showed less than 0.001 TIR at any speed within the test range.

### 3.0 TEST RESULTS

The data reduction method and a listing of the test data is presented first. The limiting factor in this program seems to be noise, or maybe signal to noise ratio. Resolution is definately a critical concern.

There are obvious things to watch for, as illustrated on the first examples. Those tests were actually not performed on our test bed centrifuge, but on a machine that we shipped to Kelly AFB two days after receiving the Systron Donner accelerometers. The data taken was the first test the technician had ever run on any accelerometer. He made a classic "typo" type error on the 55g data points.

The first part of the results contains the summary of the coefficients of the three accelerometers tested. The coefficients that are most sensitive to noise are the  $K_{0q}$  and  $K_3$  terms. With this test setup, the terms are of the same order or less than the standard deviation of the term. We feel that those terms are unreliable and should not be used. The main indicator of the quality of the test should be the magnitude of the residuals. In some cases, that assumption can lead to erroneous conclusions, but in general the author believes it is still the most reliable grading process.

The tests that follow are generally grouped as those done with the 600 tooth wheel, then the optical encoder, with the exception of the Sundstrand Q-Flex (accel #3). The optical encoder was no longer available at the time we received the accelerometer. The tests labled "load resistor doubled" were done to verify the improvement with increased resolution. The tests labled "small g step" were done with the voltmeter on the 1 Volt scale which allowed  $1\mu$ Volt resolution. This still is only on the order of  $10\mu$ g granularity. The two runs of both Accels #1 & #2 show extremely small residuals for a centrifuge test even though the input was limited to 8g.

The voltmeter used for all the data gathering is a Fluke 895A which is a differential Voltmeter with a center reading analog scale. While this may seem to be a "Dinosaur" it does allow the operator to resolve a steady state reading in the presence of a periodic variation.

George H. Neugebauer's iterative solution:

The following was done using "Mathcad 4.0" and is per Eq 5 on page 48 of IEEE STD 836-1991.

Centdata = Acc2\_Rm01

Collect Centrifuge and Accelerometer Data Here

Accel\_and\_Rm = Centdata<sub>0,0</sub>

Accelerometer = Centdata<sub>0,1</sub>

Radius = Centdata<sub>1,0</sub>

Date = Centdata<sub>1,1</sub>

HzMULT = Centdata<sub>2,0</sub>

SF = Centdata<sub>2,1</sub>

First Three Numerical Pairs Describe the Data Set

i = 0..rows(Centdata) - 4

DATAPAIR<sub>i,0</sub> = Centdata<sub>i+3,0</sub>

DATAPAIR<sub>i,1</sub> = Centdata<sub>i+3,1</sub>

SORTPAIR = csort(DATAPAIR, 1)

Hz<sub>i</sub> = SORTPAIR<sub>i,0</sub>

VDC<sub>i</sub> = SORTPAIR<sub>i,1</sub>

Extract and Sort Data to Centrifuge Input (Hertz) and Sensor Output (VDC) Data Pairs

$$a_i = (HzMULT \cdot Hz_i)^2 \cdot \left( \frac{Radius}{386.089} \right) \cdot \left( \frac{\pi}{30} \right)^2 \cdot (if(VDC_i < 0, -1, 1))$$

$$s_i = \frac{VDC_i}{SF}$$

Calculate Initial Centrifuge Input (g) and Sensor Output (g) Data Pairs

$$Nneg = \sum_i if(a_i < 0, 1, 0)$$

$$Npos = \sum_i if(a_i \geq 0, 1, 0)$$

Determine Number of Negative and Positive Inputs and Their Respective Ranges

in = 0..Npos - 1

ip = Npos..Npos + Nneg - 1

# Matrix Solution Per IEEE Standard 836

$$A(a) = \begin{bmatrix} \sum_i (a_i)^6 & \sum_{ip} (a_{ip})^5 - \sum_{in} (a_{in})^5 & \sum_i (a_i)^5 & \sum_{in} (a_{in})^4 & \sum_{ip} (a_{ip})^4 & \sum_{in} (a_{in})^3 & \sum_{ip} (a_{ip})^3 \\ \sum_{ip} (a_{ip})^5 - \sum_{in} (a_{in})^5 & \sum_i (a_i)^4 & \sum_{ip} (a_{ip})^4 - \sum_{in} (a_{in})^4 & \sum_{in} (a_{in})^3 & \sum_{ip} (a_{ip})^3 & \sum_{in} (a_{in})^2 & \sum_{ip} (a_{ip})^2 \\ \sum_i (a_i)^5 & \sum_{ip} (a_{ip})^4 - \sum_{in} (a_{in})^4 & \sum_i (a_i)^4 & \sum_{in} (a_{in})^3 & \sum_{ip} (a_{ip})^3 & \sum_{in} (a_{in})^2 & \sum_{ip} (a_{ip})^2 \\ \sum_{in} (a_{in})^4 & \sum_{in} (a_{in})^3 & \sum_{in} (a_{in})^3 & \sum_{in} (a_{in})^2 & 0 & \sum_{in} a_{in} & 0 \\ \sum_{ip} (a_{ip})^4 & \sum_{ip} (a_{ip})^3 & \sum_{ip} (a_{ip})^3 & 0 & \sum_{ip} (a_{ip})^2 & 0 & \sum_{ip} a_{ip} \\ \sum_{in} (a_{in})^3 & \sum_{in} (a_{in})^2 & \sum_{in} (a_{in})^2 & \sum_{in} a_{in} & 0 & Nneg & 0 \\ \sum_{ip} (a_{ip})^3 & \sum_{ip} (a_{ip})^2 & \sum_{ip} (a_{ip})^2 & 0 & \sum_{ip} a_{ip} & 0 & Npos \end{bmatrix}$$

$$B(a, s) = \begin{bmatrix} \sum_i [(s_i - a_i) \cdot (a_i)^3] \\ \sum_i [(s_i - a_i) \cdot |a_i| \cdot a_i] \\ \sum_i [(s_i - a_i) \cdot (a_i)^2] \\ \sum_{in} [(s_{in} - a_{in}) \cdot a_{in}] \\ \sum_{ip} [(s_{ip} - a_{ip}) \cdot a_{ip}] \\ \sum_{in} (s_{in} - a_{in}) \\ \sum_{ip} (s_{ip} - a_{ip}) \end{bmatrix}$$

$$[A][K] = [B]$$

or

$$[K] = [A]^{-1} [B] = \begin{bmatrix} K_3 \\ K_{0q} \\ K_2 \\ C_n \\ C_p \\ K_{0n} \\ K_{0p} \end{bmatrix}$$

# Inhouse Centrifuge Test

Accelerometer = 2

Date = 1.111292

Accel\_and\_Run = 2.01

$$T0(a,s) = (A(a))^{(-1)} \cdot B(a,s)$$

Iteration = 0

$$\begin{bmatrix} K_3 \\ K_{oq} \\ K_2 \\ C_n \\ C_p \\ K_{0n} \\ K_{0p} \end{bmatrix} = T0(a,s) \quad \begin{bmatrix} K_3 \\ K_{oq} \\ K_2 \\ C_n \\ C_p \\ K_{0n} \\ K_{0p} \end{bmatrix} = \begin{bmatrix} 2.727221 \cdot 10^{-7} \\ -1.57144 \cdot 10^{-5} \\ 8.687842 \cdot 10^{-6} \\ 0.001914 \\ 8.323726 \cdot 10^{-5} \\ 7.548155 \cdot 10^{-4} \\ 0.001365 \end{bmatrix}$$

Matrix  
Solution After  
First Iteration

$$a_m = (1 + C_n) \cdot a_m \quad a_p = (1 + C_p) \cdot a_p$$

$$T1(a,s) = (A(a))^{(-1)} \cdot B(a,s)$$

Iteration = 1

$$\begin{bmatrix} K_3 \\ K_{oq} \\ K_2 \\ C_n \\ C_p \\ K_{0n} \\ K_{0p} \end{bmatrix} = T1(a,s) \quad \begin{bmatrix} K_3 \\ K_{oq} \\ K_2 \\ C_n \\ C_p \\ K_{0n} \\ K_{0p} \end{bmatrix} = \begin{bmatrix} 2.711 \cdot 10^{-7} \\ -1.558847 \cdot 10^{-5} \\ 8.71456 \cdot 10^{-6} \\ -1.642972 \cdot 10^{-7} \\ -4.095763 \cdot 10^{-6} \\ 7.537512 \cdot 10^{-4} \\ 0.001391 \end{bmatrix}$$

Determine  
New Input  
Accelerations  
and Calculate  
Next  
Iteration(s)

$$a_m = (1 + C_n) \cdot a_m \quad a_p = (1 + C_p) \cdot a_p$$

$$T1(a,s) = (A(a))^{(-1)} \cdot B(a,s)$$

Iteration = 2

$$\begin{bmatrix} K_3 \\ K_{oq} \\ K_2 \\ C_n \\ C_p \\ K_{0n} \\ K_{0p} \end{bmatrix} = T1(a,s) \quad \begin{bmatrix} K_3 \\ K_{oq} \\ K_2 \\ C_n \\ C_p \\ K_{0n} \\ K_{0p} \end{bmatrix} = \begin{bmatrix} 2.711 \cdot 10^{-7} \\ -1.558834 \cdot 10^{-5} \\ 8.714692 \cdot 10^{-6} \\ -3.773149 \cdot 10^{-10} \\ -8.802838 \cdot 10^{-9} \\ 7.537487 \cdot 10^{-4} \\ 0.001391 \end{bmatrix}$$

$$Model_p = K_{0p} + a_p + K_2 \cdot \left[ \left( \frac{a_p}{s} \right)^2 \right] + K_{oq} \cdot \left[ \left( \frac{a_p}{s} \right)^2 \right] + K_3 \cdot \left[ \left( \frac{a_p}{s} \right)^3 \right]$$

$$Model_m = K_{0m} + a_m + K_2 \cdot \left[ \left( \frac{a_m}{s} \right)^2 \right] + K_{oq} \cdot \left[ \left( \frac{a_m}{s} \right)^2 \right] + K_3 \cdot \left[ \left( \frac{a_m}{s} \right)^3 \right]$$

$$Res_p = a_p - Model_p$$

$$Res_m = a_m - Model_m$$

Determine the Model  
and Residual for  
Each Input Level

The following seven pages are calculations of the Average Mean and Standard Deviation for a sample of the accelerometer non-linearity coefficients.

These coefficients are derived from applying the iterative matrix solution (described previously and in the IEEE Standard 836-1991) to accelerometer data produced using various test setups.

Each page is described as follows:

Accel and Run Numbers	Accelerometer	Centrifuge Configuration	Odd Quadratic
1.01, 1.02, 1.03, 1.04, 1.16, 1.17	#1	600 Tooth Wheel	Included Removed
1.05, 1.06, 1.07, 1.08, 1.09, 1.10	#1	Optical Encoder	Included Removed
2.01, 2.02, 2.03, 2.04, 2.16, 2.17	#2	600 Tooth Wheel	Included
2.05, 2.06, 2.07, 2.08, 2.09, 2.10	#2	Optical Encoder	Included
3.01, 3.02, 3.03, 3.04, 3.05	#3	600 Tooth Wheel	Included

$$\mu(\text{coeff}) = \text{mean}(\text{coeff})$$

$$\sigma(\text{coeff}) = \text{stdev}(\text{coeff}) \cdot \sqrt{\frac{\text{length}(\text{coeff})}{\text{length}(\text{coeff}) - 1}}$$

#### Average Mean Function

#### Standard Deviation Function

Note: MathCad's "stdev()" function is for a population.

The square root multiplier gives the standard deviation for a sample.



# Accelerometer #1 Non-linearity Coefficients (600 Tooth Wheel)

coeffdat = READPRN(c1tw)      i = 0..7      j = 0..5      dat<sub>i,j</sub> = coeffdat<sub>i+(j+0)·8</sub>

Acc\_Run<sub>j</sub> = dat<sub>0,j</sub>      K<sub>3j</sub> = dat<sub>1,j</sub>

K<sub>oqj</sub> = dat<sub>2,j</sub>

K<sub>2j</sub> = dat<sub>3,j</sub>

j	Acc_Run <sub>j</sub>	K <sub>3j</sub>	K <sub>oqj</sub>	K <sub>2j</sub>
0	1.01	-0.000000039	0.0000054	-0.0000049
1	1.02	0.000000082	-0.0000082	-0.0000040
2	1.03	0.000000024	-0.0000035	-0.0000034
3	1.04	-0.000000028	0.0000030	-0.0000039
4	1.16	-0.000000054	0.0000037	0.0000015
5	1.17	-0.000000027	0.0000030	-0.0000015

$$\mu(K_3) = -7.0 \cdot 10^{-9}$$

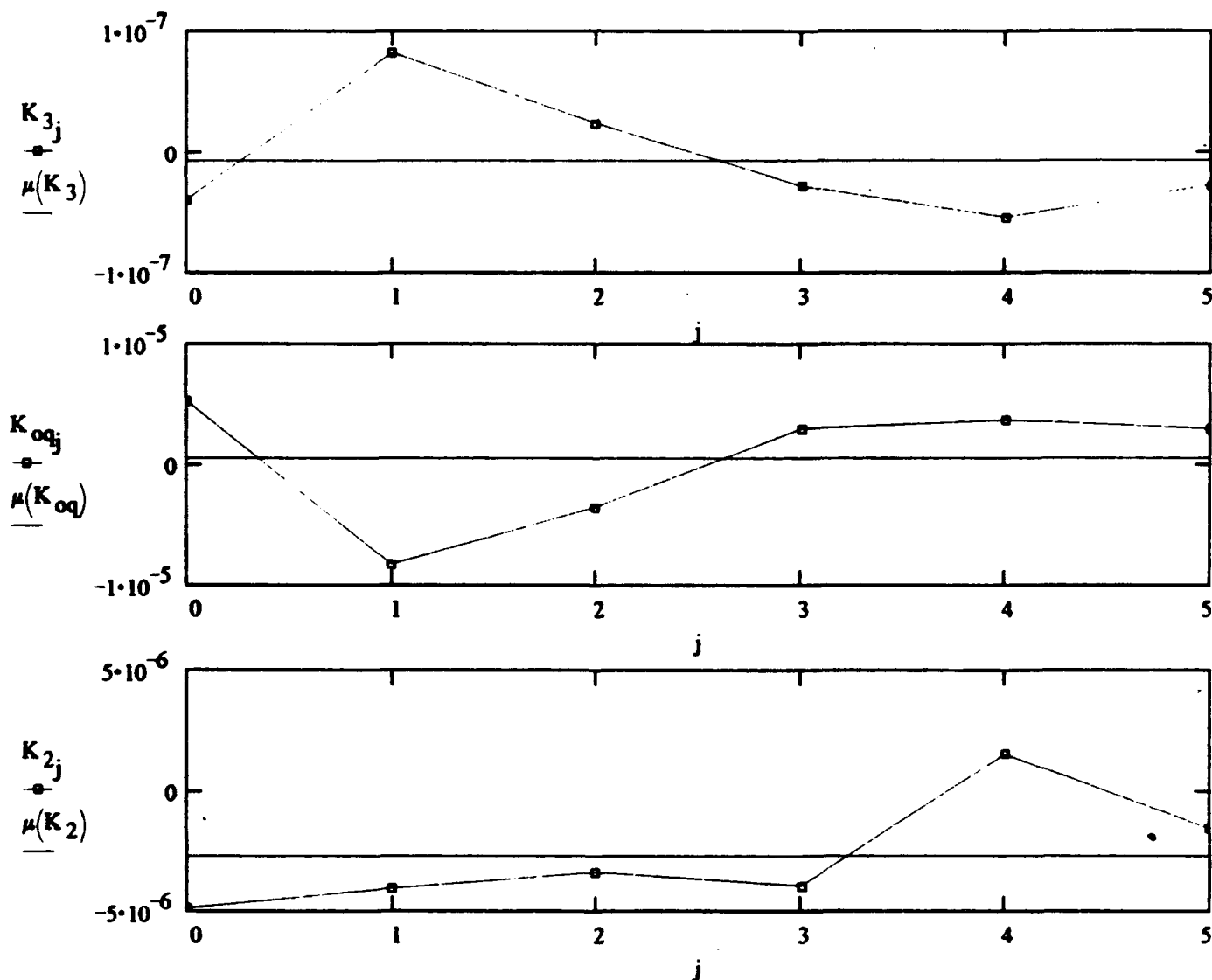
$$\mu(K_{oq}) = 5.6 \cdot 10^{-7}$$

$$\mu(K_2) = -2.7 \cdot 10^{-6}$$

$$\sigma(K_3) = 5.1 \cdot 10^{-8}$$

$$\sigma(K_{oq}) = 5.3 \cdot 10^{-6}$$

$$\sigma(K_2) = 2.3 \cdot 10^{-6}$$



## Accelerometer #1 Non-linearity Coefficients (600 Tooth Wheel

Odd-Quadratic Removed)

 $\text{coeffdat} = \text{READPRN}(\text{cltw}) \quad i = 0..6 \quad j = 0..5 \quad \text{dat}_{i,j} = \text{coeffdat}_{i+(j+6) \cdot 7+6}$ 
 $\text{Acc\_Run}_j = \text{dat}_{0,j} \quad K_{3,j} = \text{dat}_{1,j}$ 
 $K_{2,j} = \text{dat}_{2,j}$ 

j	Acc_Run <sub>j</sub>	K <sub>3,j</sub>
0	1.01	0.0000000201
1	1.02	0.0000000001
2	1.03	-0.0000000108
3	1.04	0.0000000024
4	1.16	0.0000000204
5	1.17	0.0000000028

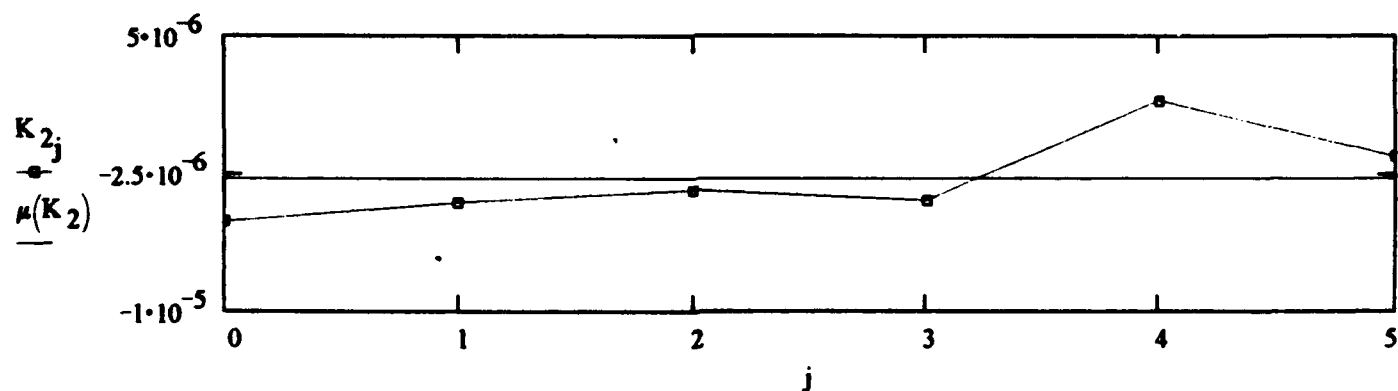
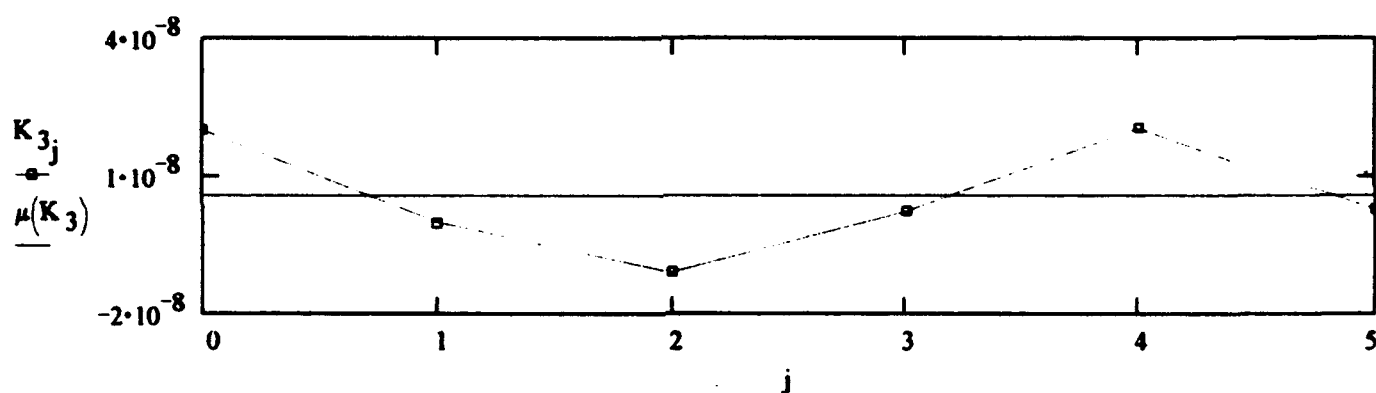
K <sub>2,j</sub>
-0.000005051
-0.000004043
-0.000003369
-0.000003939
0.000001513
0.000001534

$$\mu(K_3) = 5.8 \cdot 10^{-9}$$

$$\mu(K_2) = -2.7 \cdot 10^{-6}$$

$$\sigma(K_3) = 1.2 \cdot 10^{-8}$$

$$\sigma(K_2) = 2.4 \cdot 10^{-6}$$



# Accelerometer #1 Non-linearity Coefficients (Optical Encoder)

coeffdat = READPRN(cloe)      i = 0..7      j = 0..5      dat<sub>i,j</sub> = coeffdat<sub>i+(j+0)·8</sub>

Acc\_Run<sub>j</sub> = dat<sub>0,j</sub>      K<sub>3j</sub> = dat<sub>1,j</sub>

K<sub>oqj</sub> = dat<sub>2,j</sub>

K<sub>2j</sub> = dat<sub>3,j</sub>

j	Acc_Run <sub>j</sub>	K <sub>3j</sub>
0	1.05	-0.000000084
1	1.06	-0.000000156
2	1.07	-0.000000013
3	1.08	-0.000000029
4	1.09	-0.000000105
5	1.10	0.000000016

j	K <sub>oqj</sub>
0	0.0000082
1	0.0000102
2	0.0000010
3	0.0000031
4	0.0000118
5	0.0000020

j	K <sub>2j</sub>
0	-0.0000016
1	-0.0000014
2	-0.0000016
3	-0.0000014
4	-0.0000043
5	0.0000018

$$\mu(K_3) = -6.7 \cdot 10^{-8}$$

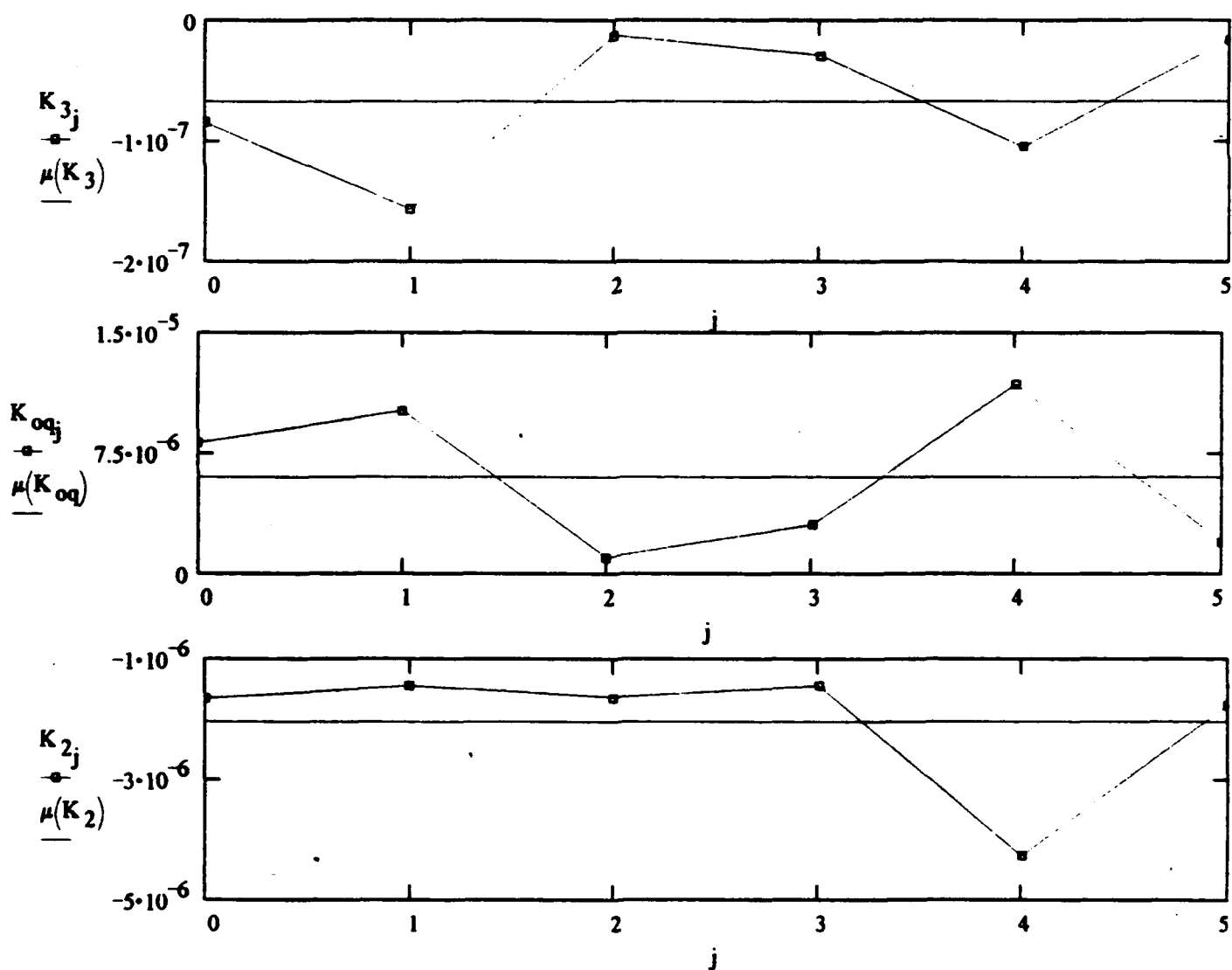
$$\mu(K_{oq}) = 6.0 \cdot 10^{-6}$$

$$\mu(K_2) = -2.0 \cdot 10^{-6}$$

$$\sigma(K_3) = 5.8 \cdot 10^{-8}$$

$$\sigma(K_{oq}) = 4.6 \cdot 10^{-6}$$

$$\sigma(K_2) = 1.1 \cdot 10^{-6}$$



# Accelerometer #1 Non-linearity Coefficients (Optical Encoder Odd-Quadratic Removed)

coeffdat = READPRN(cloe)      i = 0..6      j = 0..5      dat<sub>i,j</sub> = coeffdat<sub>i+(j+1)\*7+11</sub>

Acc\_Run<sub>j</sub> = dat<sub>0,j</sub>      K<sub>3j</sub> = dat<sub>1,j</sub>

K<sub>2j</sub> = dat<sub>2,j</sub>

j	Acc_Run <sub>j</sub>	K <sub>3j</sub>
0	1.05	-0.0000000022
1	1.06	-0.0000000543
2	1.07	-0.0000000025
3	1.08	0.0000000021
4	1.09	0.0000000247
5	1.10	0.0000000046

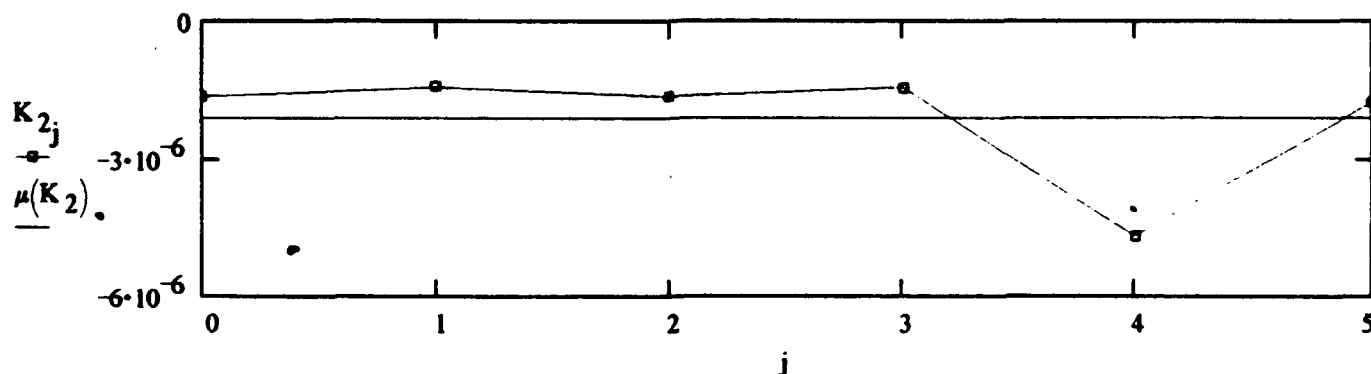
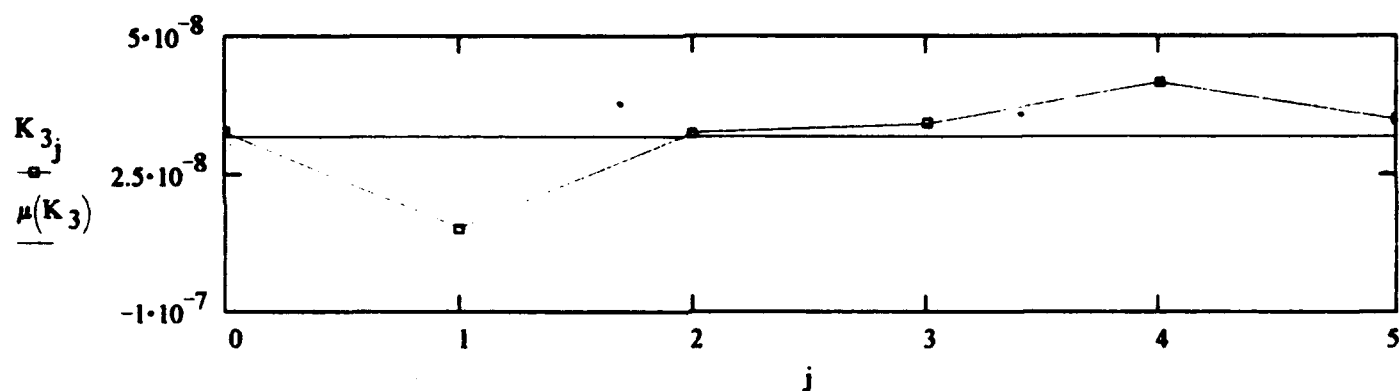
K <sub>2j</sub>
-0.000001640
-0.000001433
-0.000001633
-0.000001441
-0.000004676
-0.000001759

$$\mu(K_3) = -4.6 \cdot 10^{-9}$$

$$\mu(K_2) = -2.1 \cdot 10^{-6}$$

$$\sigma(K_3) = 2.6 \cdot 10^{-8}$$

$$\sigma(K_2) = 1.3 \cdot 10^{-6}$$



# Accelerometer #2 Non-linearity Coefficients (600 Tooth Wheel)

coeffdat = READPRN(c2tw)     $i = 0..7$      $j = 0..5$      $\text{dat}_{i,j} = \text{coeffdat}_{i+(j+0) \cdot 8}$

$\text{Acc\_Run}_j = \text{dat}_{0,j}$      $K_{3,j} = \text{dat}_{1,j}$

$K_{\text{oq},j} = \text{dat}_{2,j}$

$K_{2,j} = \text{dat}_{3,j}$

j	Acc_Run <sub>j</sub>	K <sub>3,j</sub>
0	2.01	0.000000271
1	2.02	0.000000272
2	2.03	0.000000335
3	2.04	0.000000295
4	2.16	0.000000067
5	2.17	0.000000158

j	K <sub>oq,j</sub>
0	-0.0000156
1	-0.0000201
2	-0.0000216
3	-0.0000170
4	0.0000016
5	-0.0000082

j	K <sub>2,j</sub>
0	0.0000087
1	0.0000022
2	0.0000025
3	0.0000006
4	-0.0000005
5	0.0000078

$$\mu(K_3) = 2.3 \cdot 10^{-7}$$

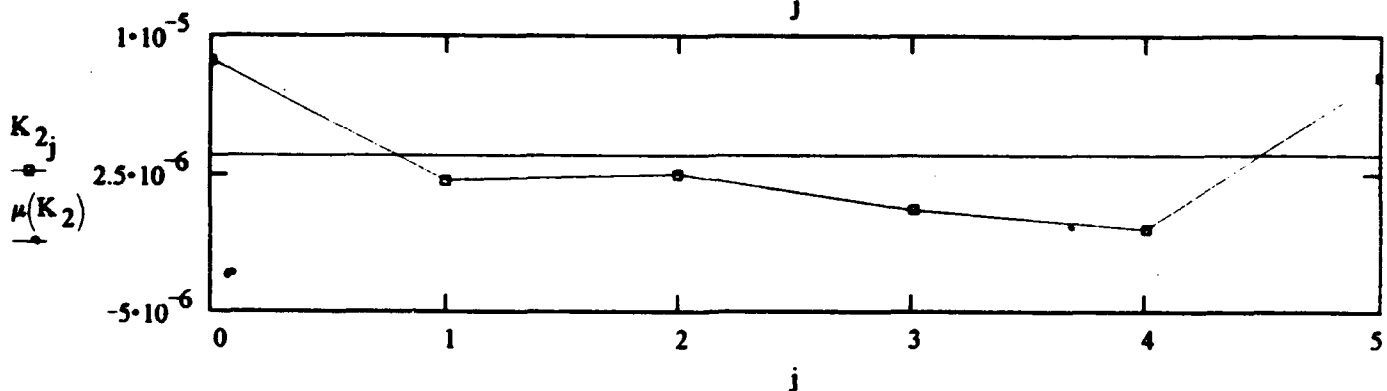
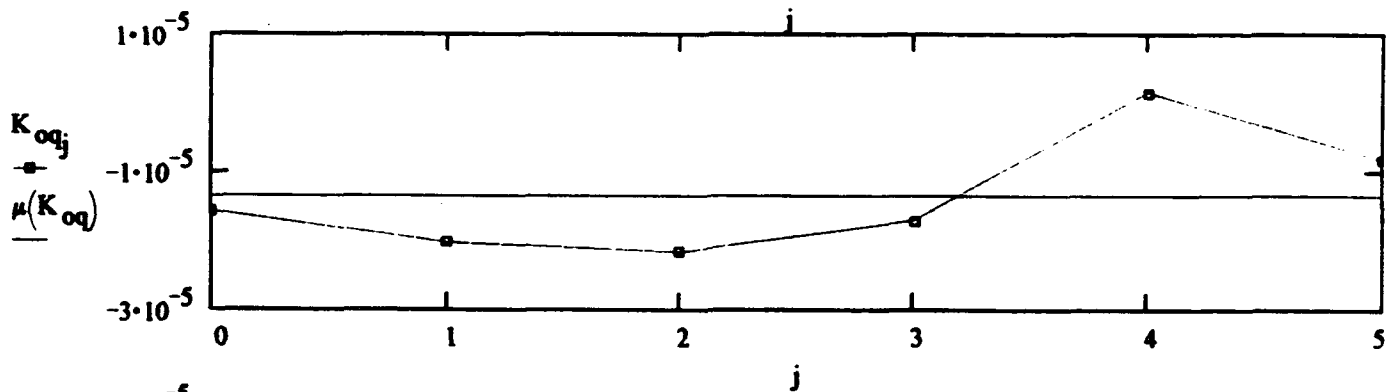
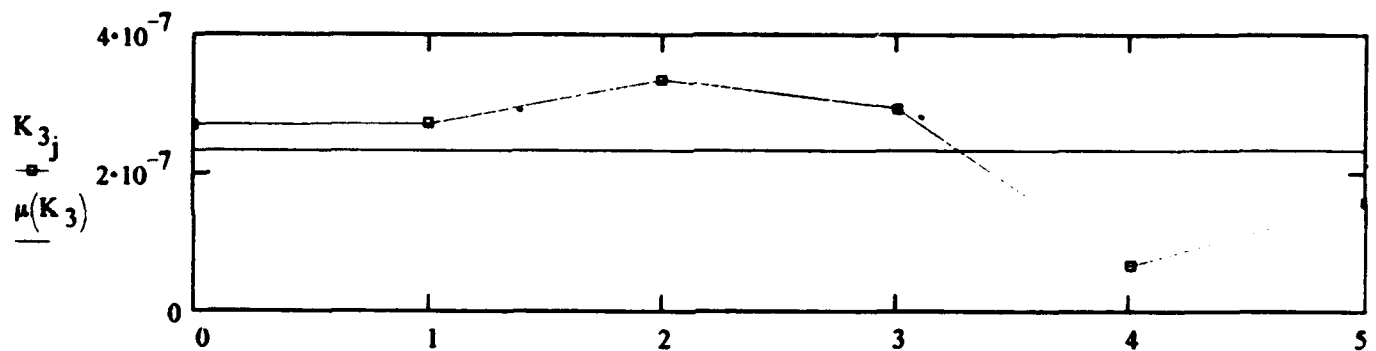
$$\mu(K_{\text{oq}}) = -1.3 \cdot 10^{-5}$$

$$\mu(K_2) = 3.5 \cdot 10^{-6}$$

$$\sigma(K_3) = 1.0 \cdot 10^{-7}$$

$$\sigma(K_{\text{oq}}) = 8.7 \cdot 10^{-6}$$

$$\sigma(K_2) = 3.8 \cdot 10^{-6}$$



# Accelerometer #2 Non-linearity Coefficients (Optical Encoder)

coeffdat = READPRN(c2oe)      i = 0..7      j = 0..5      dat<sub>i,j</sub> = coeffdat<sub>i+(j+0)·8</sub>

Acc\_Run<sub>j</sub> = dat<sub>0,j</sub>      K<sub>3j</sub> = dat<sub>1,j</sub>

K<sub>oqj</sub> = dat<sub>2,j</sub>

K<sub>2j</sub> = dat<sub>3,j</sub>

j	Acc_Run <sub>j</sub>	K <sub>3j</sub>
0	2.05	0.000000290
1	2.06	0.000000239
2	2.07	0.000000298
3	2.08	0.000000219
4	2.09	0.000000286
5	2.10	0.000000306

j	K <sub>oqj</sub>
0	-0.0000202
1	-0.0000150
2	-0.0000199
3	-0.0000136
4	-0.0000186
5	-0.0000217

j	K <sub>2j</sub>
0	0.0000055
1	0.0000080
2	0.0000067
3	0.0000086
4	0.0000069
5	0.0000056

$$\mu(K_3) = 2.7 \cdot 10^{-7}$$

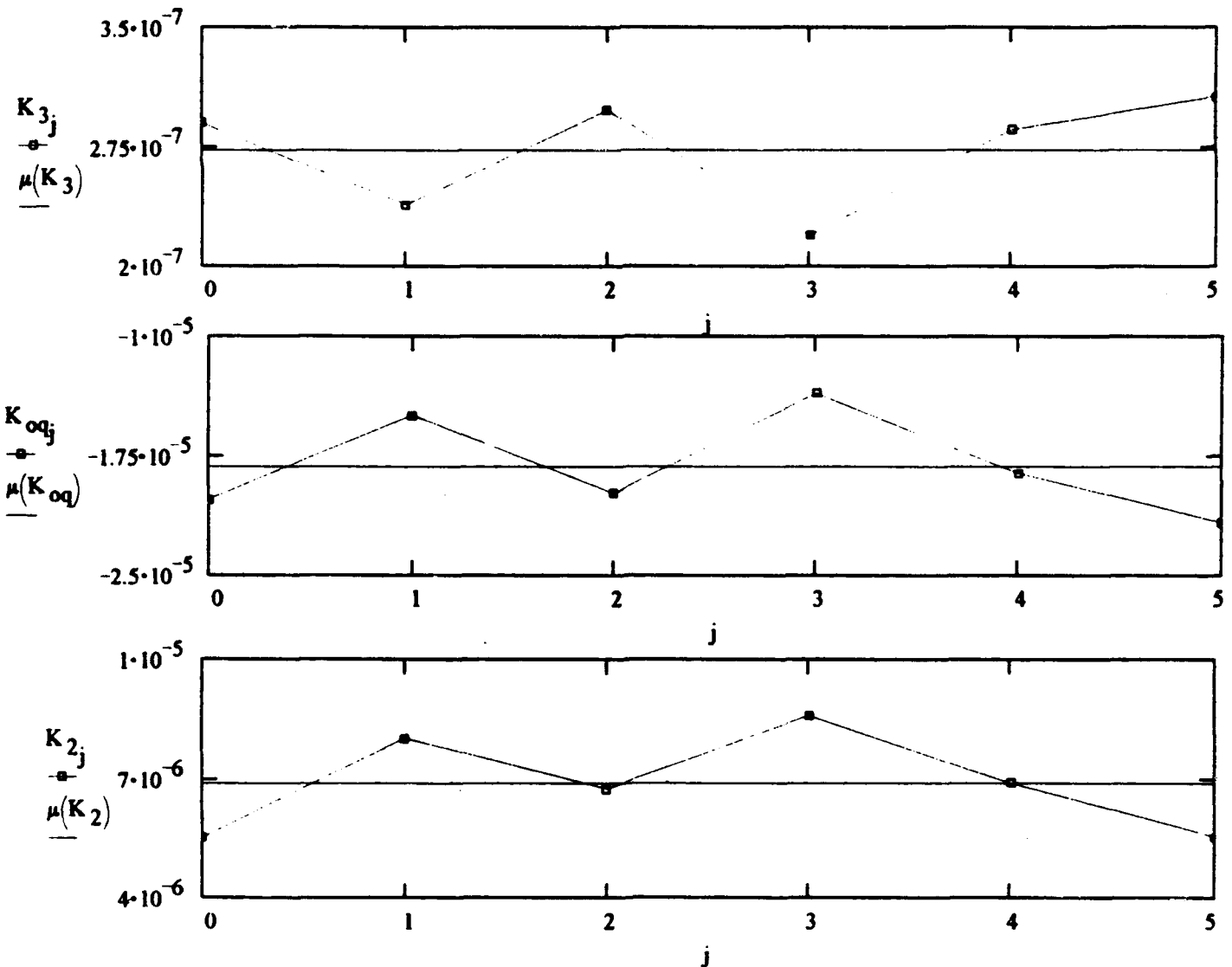
$$\mu(K_{oq}) = -1.8 \cdot 10^{-5}$$

$$\mu(K_2) = 6.9 \cdot 10^{-6}$$

$$\sigma(K_3) = 3.5 \cdot 10^{-8}$$

$$\sigma(K_{oq}) = 3.2 \cdot 10^{-6}$$

$$\sigma(K_2) = 1.2 \cdot 10^{-6}$$



# Accelerometer #3 Non-linearity Coefficients (600 Tooth Wheel)

coeffdat = READPRN(c3tw)      i = 0..7

j = 0..4

dat<sub>i,j</sub> = coeffdat<sub>i + (j + 0)·8</sub>

Acc\_Run<sub>j</sub> = dat<sub>0,j</sub>      a3K<sub>3j</sub> = dat<sub>1,j</sub>

a3K<sub>oqj</sub> = dat<sub>2,j</sub>

a3K<sub>2j</sub> = dat<sub>3,j</sub>

j	Acc_Run <sub>j</sub>	a3K <sub>3j</sub>	a3K <sub>oqj</sub>	a3K <sub>2j</sub>
0	3.01	0.000000099	0.0000004	-0.0000056
1	3.02	-0.000000015	0.0000052	-0.0000057
2	3.03	0.000000042	0.0000019	-0.0000057
3	3.04	-0.000000055	0.0000066	-0.0000057
4	3.05	0.000000317	-0.0000106	-0.0000054

$$\mu(a3K_3) = 7.8 \cdot 10^{-8}$$

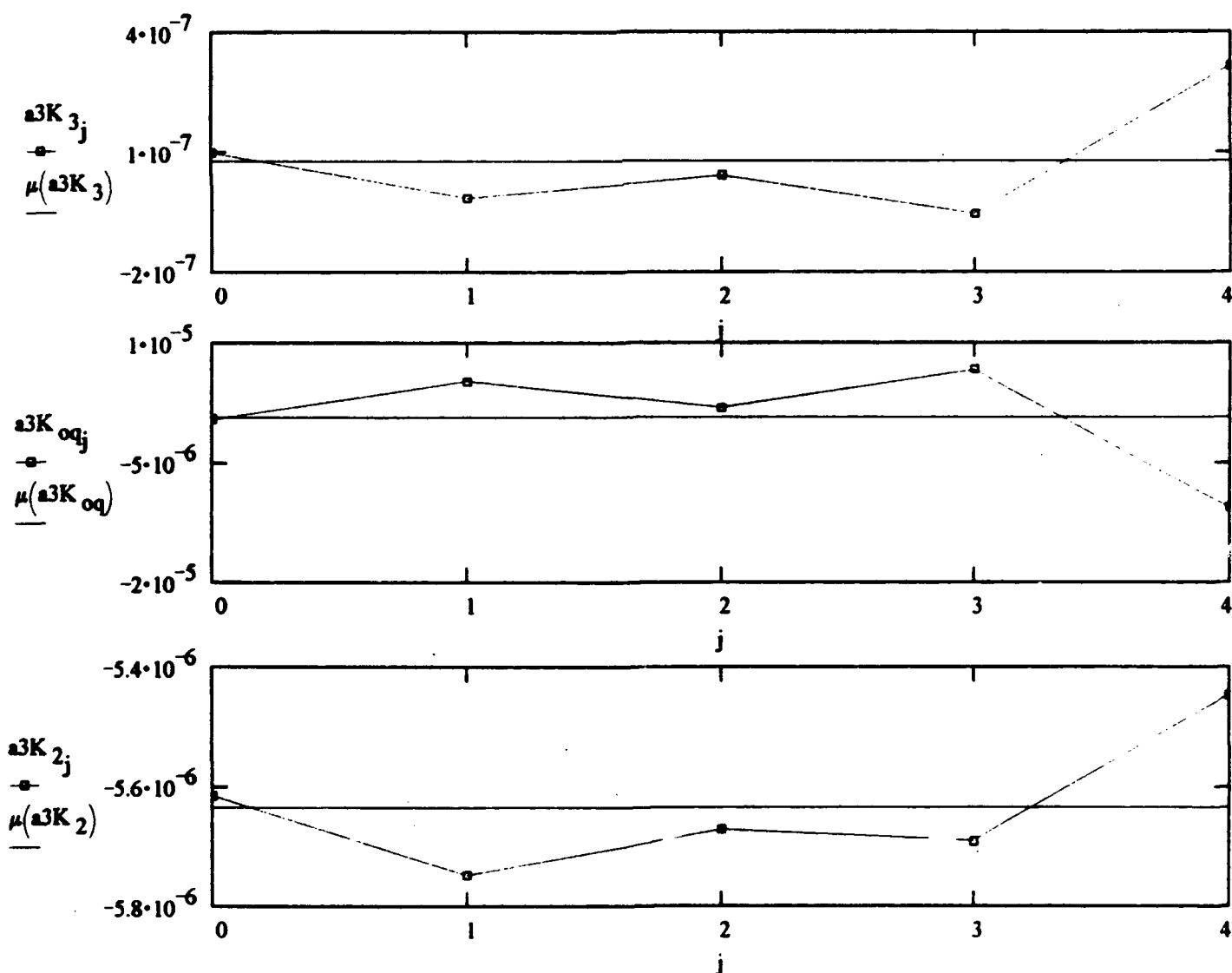
$$\mu(a3K_{oq}) = 7.0 \cdot 10^{-7}$$

$$\mu(a3K_2) = -5.6 \cdot 10^{-6}$$

$$\sigma(a3K_3) = 1.5 \cdot 10^{-7}$$

$$\sigma(a3K_{oq}) = 6.8 \cdot 10^{-6}$$

$$\sigma(a3K_2) = 1.2 \cdot 10^{-7}$$



Sideways  
→

Accel # 1

OPTICAL  
ENCODER

1/8/6

G	H <sub>z</sub>	DC V	≈ P-P $\mu$ V	RPM
5	1298.5	.00115	30	7791
30	3180.7	.00550	45	1.9085
55	4306.7	.01179	40	2.5840
20	2597	.00375	40	1.5582
45	3895.6	.00921	40	2.3374
10	1836.4	.00190	55	1.1018
35	3435.6	.00624	40	2.0613
60	4498.2	.01289	30	2.6990
25	2903.6	.00469	40	1.7422
50	4106.3	.01060	20	2.4638
15	2249.1	.00271	30	1.3495
40	3672.8	.00750	20	2.2037
5	1298.5	.00099	25	7791



# Kelly Centrifuge

(48 Inch Radius, 600 Tooth Wheel, 60 HP SCR Drive,

Accelerometer = 1

SF = 0.121225

Date = 1.100992

Random Sequence)

I	Raw Data Pair		Corrected	Accel	Residuals
	Hz	VDC	CF Input (g)	Output (g)	(g)
i			a <sub>i</sub>	s <sub>i</sub>	Res <sub>i</sub>
0	209.8	-7.28816	-60.241720	-60.120932	-0.018595
1	200.9	-6.67624	-55.239058	-55.073128	0.038918
2	191.5	-6.07200	-50.190780	-50.088678	-0.011730
3	181.7	-5.46639	-45.185204	-45.092926	-0.008134
4	171.3	-4.85857	-40.160686	-40.078944	-0.005182
5	160.2	-4.24915	-35.124602	-35.051763	-0.000890
6	148.3	-3.64130	-30.100152	-30.037534	0.001392
7	135.4	-3.03531	-25.091332	-25.038647	0.002928
8	121.1	-2.42796	-20.071262	-20.028583	0.003083
9	104.9	-1.82177	-15.060430	-15.028006	0.001304
10	85.6	-1.21309	-10.028453	-10.006929	-0.003100
11	85.6	1.21139	10.014701	9.992906	0.002727
12	104.9	1.81936	15.039778	15.008125	0.000133
13	121.1	2.42445	20.043739	19.999546	-0.003497
14	135.4	3.03076	25.056926	25.001114	-0.004050
15	148.3	3.63600	30.058877	29.993813	-0.000725
16	160.2	4.24285	35.076437	34.999794	0.001515
17	171.3	4.85100	40.105615	40.016498	0.003765
18	181.7	5.45800	45.123243	45.023716	0.008577
19	191.5	6.06256	50.121956	50.010806	0.012314
20	200.9	6.66567	55.163311	54.985935	-0.038564
21	209.8	7.27637	60.159113	60.023634	0.018065

K <sub>3</sub>	4.445279·10 <sup>-7</sup>
K <sub>oq</sub>	-6.199142·10 <sup>-5</sup>
K <sub>2</sub>	-2.052435·10 <sup>-6</sup>
C <sub>n</sub>	1.343211·10 <sup>-8</sup>
C <sub>p</sub>	-1.223863·10 <sup>-8</sup>
K <sub>on</sub>	1.904342·10 <sup>-2</sup>
K <sub>op</sub>	-1.854577·10 <sup>-2</sup>

Iteration = 2

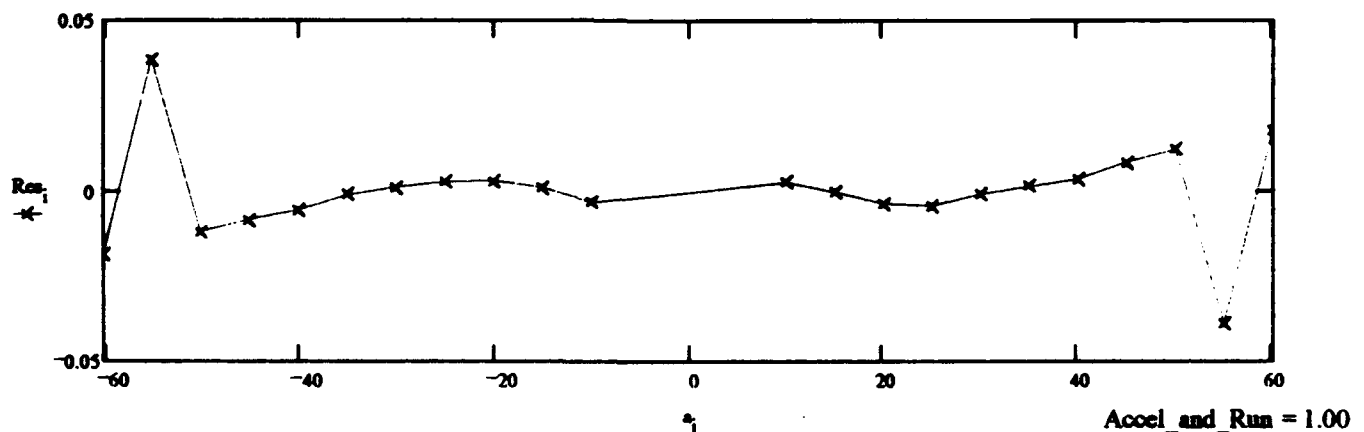
Sum Residuals (g)

$$\sum_i Res_i = -0.000010$$

Standard Deviation

$$\sigma_{Res} = \sqrt{\frac{\sum_i (Res_i)^2}{N_{pos} + N_{neg} - 7}}$$

$$(10^6) \cdot \sigma_{Res} = 16763 \mu g$$



## Kelly Centrifuge

(48 Inch Radius, 600 Tooth Wheel, 60 HP SCR Drive,

Accelerometer = 1

SF = 0.121225

Date = 1.100992

Random Sequence,  $\pm 55$  g Corrected)

I	Raw		Corrected	Accel	Residuals	Coefficients
	Data Pair		CF Input	Output		
i	Hz <sub>i</sub>	VDC <sub>i</sub>	a <sub>i</sub> (g)	s <sub>i</sub> (g)	Res <sub>i</sub> (g)	$\begin{bmatrix} K_3 \\ K_{oq} \\ K_2 \\ C_n \\ C_p \\ K_{On} \\ K_{Op} \end{bmatrix} = \begin{bmatrix} -5.518769 \cdot 10^{-8} \\ 5.908587 \cdot 10^{-6} \\ -2.091687 \cdot 10^{-6} \\ 1.150709 \cdot 10^{-10} \\ -2.773046 \cdot 10^{-10} \\ -7.630854 \cdot 10^{-4} \\ 1.192193 \cdot 10^{-3} \end{bmatrix}$
0	209.8	-7.28816	-60.103125	-60.120932	-0.000126	
1	200.8	-6.67624	-55.057121	-55.073128	-0.000203	
2	191.5	-6.07200	-50.075309	-50.088678	0.000526	
3	181.7	-5.46639	-45.081249	-45.092926	0.000288	
4	171.3	-4.85857	-40.068290	-40.078944	-0.000597	
5	160.2	-4.24915	-35.043793	-35.051763	0.000243	
6	148.3	-3.64130	-30.030903	-30.037534	-0.000147	
7	135.4	-3.03531	-25.033606	-25.038647	-0.000130	
8	121.1	-2.42796	-20.025085	-20.028583	0.000030	
9	104.9	-1.82177	-15.025781	-15.028006	0.000158	
10	85.6	-1.21309	-10.005381	-10.006929	-0.000040	
11	85.6	1.21139	9.991709	9.992906	-0.000321	
12	104.9	1.81936	15.005249	15.008125	0.001011	
13	121.1	2.42445	19.997722	19.999546	-0.000453	
14	135.4	3.03076	24.999399	25.001114	-0.001001	
15	148.3	3.63600	29.989867	29.993813	0.000810	
16	160.2	4.24285	34.995908	34.999794	0.000385	
17	171.3	4.85100	40.013539	40.016498	-0.000809	
18	181.7	5.45800	45.019648	45.023716	0.000176	
19	191.5	6.06256	50.006884	50.010806	0.000086	
20	200.8	6.66567	54.981889	54.985935	0.000489	
21	209.8	7.27637	60.020997	60.023634	-0.000373	

Iteration = 2

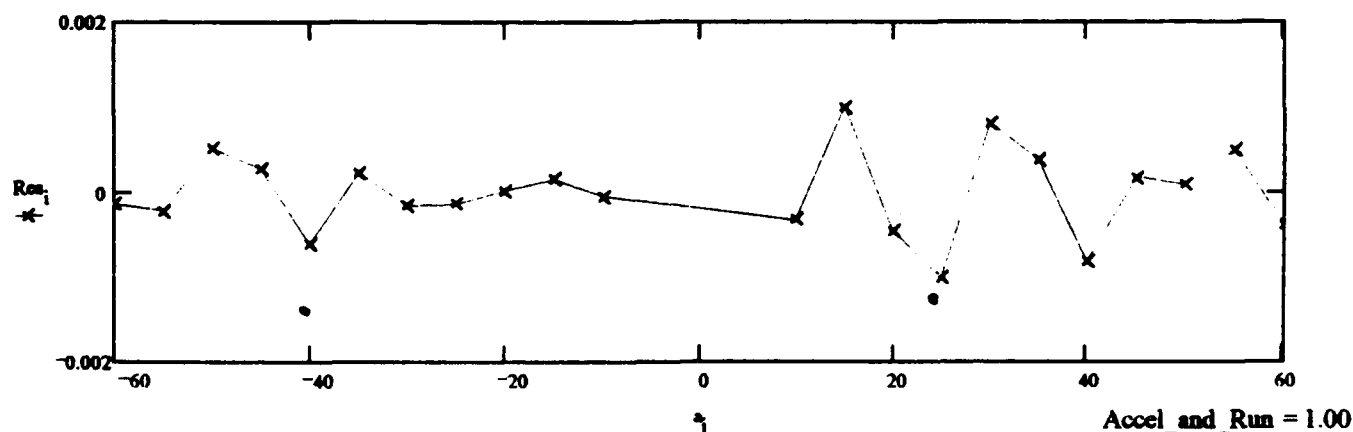
Sum Residuals (g)

$$\sum_i Res_i = -1.511341 \cdot 10^{-7}$$

Standard Deviation

$$\sigma_{Res} = \sqrt{\frac{\sum_i (Res_i)^2}{N_{pos} + N_{neg} - 7}}$$

$$(10^6) \cdot \sigma_{Res} = 583 \quad \mu g$$



**Kelly Centrifuge**

Accelerometer = 1

SF = 0.121225

Date = 1.100992

(48 Inch Radius, 600 Tooth Wheel, 60 HP SCR Drive,  
Random Sequence,  $\pm 55$  g Corrected)

$$\sigma_{Res} = 5.832591 \cdot 10^{-4}$$

Standard Deviation of Residuals

$$\mu = \frac{\max(|Res|)}{\sigma_{Res}}$$

$$\mu = 1.733311$$

Normalized Magnitude of  
Largest Residual

$$N = N_{neg} + N_{pos}$$

$$N = 22$$

Total Number of Readings

$$1.25 + \ln\left(\sqrt{\frac{N}{3}}\right)$$

$$\mu_c = 2.246215$$

Confidence Limit Check Value

$$K = \begin{bmatrix} K_3 \\ K_{oq} \\ K_2 \\ C_n \\ C_p \\ K_{0n} \\ K_{0p} \end{bmatrix}$$

$$i = 0 \dots \text{rows}(K) - 1$$

$$d = A(a)^{-1}$$

$$\sigma_{K_i} = \sigma_{Res} \cdot \sqrt{d_{i,i}}$$

$$\begin{bmatrix} \sigma K_3 \\ \sigma K_{oq} \\ \sigma K_2 \\ \sigma C_n \\ \sigma C_p \\ \sigma K_{0n} \\ \sigma K_{0p} \end{bmatrix} = \sigma_K$$

$$\begin{bmatrix} \sigma K_3 \\ \sigma K_{oq} \\ \sigma K_2 \\ \sigma C_n \\ \sigma C_p \\ \sigma K_{0n} \\ \sigma K_{0p} \end{bmatrix} = \begin{bmatrix} 4.179431 \cdot 10^{-8} \\ 4.427785 \cdot 10^{-6} \\ 5.621368 \cdot 10^{-7} \\ 1.468057 \cdot 10^{-4} \\ 1.464948 \cdot 10^{-4} \\ 0.001448 \\ 0.001445 \end{bmatrix}$$

Standard Deviations of  
Each Coefficient

$$f = N - \text{rows}(K)$$

$$f = 15$$

Number of Degrees of Freedom

$$t = 1.96 + \frac{2.392}{(f - 1.082)}$$

$$t = 2.131864$$

Student's t for P=95% Confidence

$$K_{2lower} = K_2 - \frac{t \cdot \sigma K_2}{\sqrt{N}}$$

$$K_2 = -2.092 \cdot 10^{-6}$$

$$K_{2upper} = K_2 + \frac{t \cdot \sigma K_2}{\sqrt{N}}$$

$$K_{2min} = \text{if}(|K_{2lower}| < |K_{2upper}|, K_{2lower}, K_{2upper})$$

$$K_{2max} = \text{if}(|K_{2lower}| < |K_{2upper}|, K_{2upper}, K_{2lower})$$

95% Confidence level K2 Lies Within the Range of:

$$K_{2min} = -1.836 \cdot 10^{-6} \leq K_2 \leq K_{2max} = -2.347 \cdot 10^{-6}$$

Accel\_and\_Run = 1.00

## Kelly Centrifuge

(48 Inch Radius, 600 Tooth Wheel, 60 HP SCR Drive,

Accelerometer = 2

SF = 0.122190

Date = 1.100992

Random Sequence,  $\pm 55$  g Corrected)

I	Raw		Corrected	Accel	Residuals	Coefficients
	Data Pair		CF Input	Output		
i	Hz <sub>i</sub>	VDC <sub>i</sub>	a <sub>i</sub> (g)	s <sub>i</sub> (g)	Res <sub>i</sub> (g)	
0	209.8	-7.34460	-60.249973	-60.107988	0.001209	$\begin{bmatrix} K_3 \\ K_{oq} \\ K_2 \\ C_n \\ C_p \\ K_{On} \\ K_{Op} \end{bmatrix} = \begin{bmatrix} 5.408179 \cdot 10^{-7} \\ -5.757095 \cdot 10^{-5} \\ 8.003096 \cdot 10^{-6} \\ 6.216675 \cdot 10^{-9} \\ -3.168607 \cdot 10^{-8} \\ 2.102149 \cdot 10^{-2} \\ -2.280836 \cdot 10^{-2} \end{bmatrix}$
1	200.8	-6.72783	-55.191640	-55.060398	0.001397	
2	191.5	-6.11961	-50.197657	-50.082740	-0.002932	
3	181.7	-5.50923	-45.191394	-45.087405	-0.001038	
4	171.3	-4.89684	-40.166188	-40.075620	-0.001200	
5	160.2	-4.28285	-35.129414	-35.050741	0.000175	
6	148.3	-3.67024	-30.104276	-30.037155	0.001427	
7	135.4	-3.05954	-25.094770	-25.039201	0.001799	
8	121.1	-2.44740	-20.074012	-20.029421	0.001519	
9	104.9	-1.83654	-15.062493	-15.030199	-0.001756	
10	85.6	-1.22231	-10.029826	-10.003355	-0.000601	$\begin{aligned} \text{Iteration} &= 2 \\ \text{Sum Residuals (g)} \\ \sum_i \text{Res}_i &= -0.000015 \\ \text{Standard Deviation} \\ \sigma_{\text{Res}} &= \sqrt{\frac{\sum_i (\text{Res}_i)^2}{N_{\text{pos}} + N_{\text{neg}} - 7}} \\ (10^6) \cdot \sigma_{\text{Res}} &= 2348 \mu\text{g} \end{aligned}$
11	85.6	1.22010	10.016093	9.985269	-0.003586	
12	104.9	1.83443	15.041868	15.012931	0.003245	
13	121.1	2.44500	20.046525	20.009821	0.001667	
14	135.4	3.05664	25.060408	25.015468	0.000487	
15	148.3	3.66700	30.063055	30.010639	0.000497	
16	160.2	4.27919	35.081312	35.020787	-0.000063	
17	171.3	4.89274	40.111188	40.042066	-0.001466	
18	181.7	5.50492	45.129514	45.052132	-0.003329	
19	191.5	6.11551	50.128921	50.049186	-0.000494	
20	200.8	6.72500	55.116067	55.037237	0.004005	
21	209.8	7.34143	60.167473	60.082044	-0.000976	

Iteration = 2

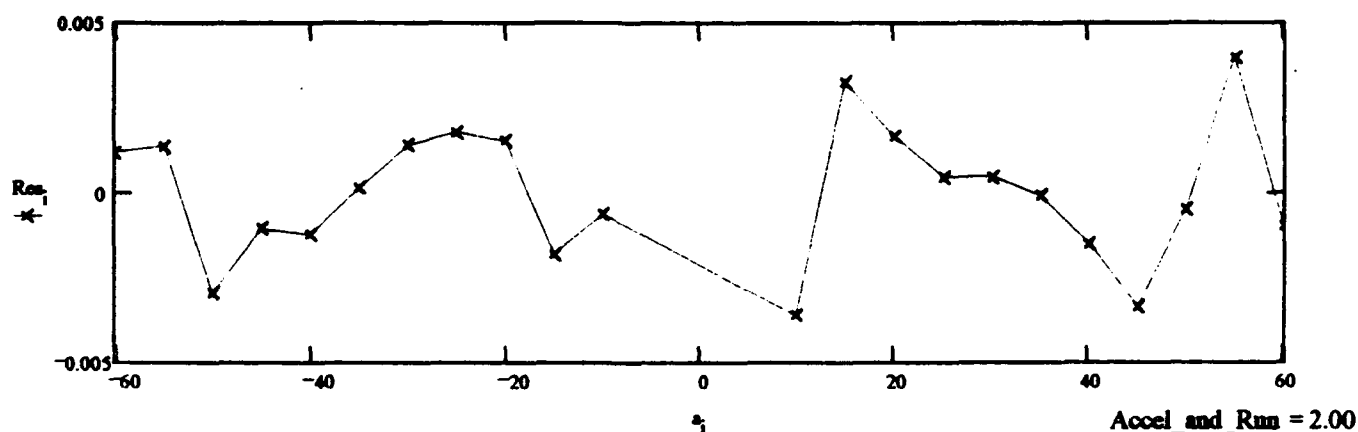
Sum Residuals (g)

$$\sum_i \text{Res}_i = -0.000015$$

Standard Deviation

$$\sigma_{\text{Res}} = \sqrt{\frac{\sum_i (\text{Res}_i)^2}{N_{\text{pos}} + N_{\text{neg}} - 7}}$$

$$(10^6) \cdot \sigma_{\text{Res}} = 2348 \mu\text{g}$$



**Kelly Centrifuge**

Accelerometer = 2

SF = 0.122190

Date = 1.100992

(48 Inch Radius, 600 Tooth Wheel, 60 HP SCR Drive,  
Random Sequence)

$$\sigma_{Res} = 0.002348$$

Standard Deviation of Residuals

$$\mu = \frac{\max(|Res|)}{\sigma_{Res}}$$

$$\mu = 1.705638$$

Normalized Magnitude of  
Largest Residual

$$N = N_{neg} + N_{pos}$$

$$N = 22$$

Total Number of Readings

$$\mu_c = 1.25 + \ln\left(\sqrt{\frac{N}{3}}\right)$$

$$\mu_c = 2.246215$$

Confidence Limit Check Value

$$K = \begin{bmatrix} K_3 \\ K_{oq} \\ K_2 \\ C_n \\ C_p \\ K_{0n} \\ K_{0p} \end{bmatrix}$$

$$i = 0 \dots \text{rows}(K) - 1$$

$$d = A(a)^{-1}$$

$$\sigma_{K_i} = \sigma_{Res} \sqrt{d_{i,i}}$$

$$\begin{bmatrix} \sigma K_3 \\ \sigma K_{oq} \\ \sigma K_2 \\ \sigma C_n \\ \sigma C_p \\ \sigma K_{0n} \\ \sigma K_{0p} \end{bmatrix} = \sigma_K$$

$$\begin{bmatrix} \sigma K_3 \\ \sigma K_{oq} \\ \sigma K_2 \\ \sigma C_n \\ \sigma C_p \\ \sigma K_{0n} \\ \sigma K_{0p} \end{bmatrix} =$$

$$\begin{bmatrix} 1.670402 \cdot 10^{-7} \\ 1.773984 \cdot 10^{-5} \\ 2.25219 \cdot 10^{-6} \\ 5.896118 \cdot 10^{-4} \\ 5.883607 \cdot 10^{-4} \\ 0.005831 \\ 0.005816 \end{bmatrix}$$

Standard Deviations of  
Each Coefficient

$$f = N - \text{rows}(K)$$

$$f = 15$$

Number of Degrees of Freedom

$$t = 1.96 + \frac{2.392}{(f - 1.082)}$$

$$t = 2.131864$$

Student's t for P=95% Confidence

$$K_{2lower} = K_2 - \frac{t \cdot \sigma K_2}{\sqrt{N}}$$

$$K_2 = 8.003 \cdot 10^{-6}$$

$$K_{2upper} = K_2 + \frac{t \cdot \sigma K_2}{\sqrt{N}}$$

$$K_{2min} = \text{if}(|K_{2lower}| < |K_{2upper}|, K_{2lower}, K_{2upper})$$

$$K_{2max} = \text{if}(|K_{2lower}| < |K_{2upper}|, K_{2upper}, K_{2lower})$$

95% Confidence level K2 Lies Within the Range of:

$$K_{2min} = 6.979 \cdot 10^{-6} \leq K_2 \leq K_{2max} = 9.027 \cdot 10^{-6}$$

Accel\_and\_Run = 2.00

# Inhouse Centrifuge (29 Inch Radius, 600 Tooth Wheel,

Accelerometer = 1

SF = 0.121225

Date = 1.121092

## Random Sequence)

i	Raw Data Pair		Corrected CF Input	Accel Output	Residuals
	Hz <sub>i</sub>	VDC <sub>i</sub>	(g) a <sub>i</sub>	(g) s <sub>i</sub>	(g) Res <sub>i</sub>
0	2698.9	-7.28501	-60.092032	-60.094947	0.000346
1	2584.0	-6.67790	-55.084362	-55.086822	-0.000331
2	2463.8	-6.07096	-50.078834	-50.080099	-0.000074
3	2337.3	-5.46351	-45.068409	-45.069169	-0.000332
4	2203.7	-4.85664	-40.063441	-40.063023	0.000242
5	2061.3	-4.24919	-35.053042	-35.052093	0.000306
6	1908.4	-3.64219	-30.045686	-30.044875	-0.000176
7	1742.2	-3.03535	-25.040288	-25.038977	0.000083
8	1558.2	-2.42805	-20.030404	-20.029284	-0.000266
9	1349.5	-1.82109	-15.024121	-15.022396	0.000249
10	1101.8	-1.21386	-10.014951	-10.013281	0.000152
11	779.1	-0.60689	-5.007601	-5.006269	-0.000198
12	779.1	0.60606	5.000463	4.999505	0.000552
13	1101.8	1.21200	10.000675	9.997938	-0.000734
14	1349.5	1.81830	15.002704	14.999381	-0.000520
15	1558.2	2.42425	20.001850	19.997938	-0.000021
16	1742.2	3.03059	25.004593	24.999711	0.000369
17	1908.4	3.63642	30.002856	29.997278	0.001284
18	2061.3	4.24223	35.003074	34.994679	0.000313
19	2203.7	4.84830	40.006331	39.994226	-0.001335
20	2337.3	5.45406	45.004164	44.991215	0.000080
21	2463.8	6.06023	50.007446	49.991586	-0.000391
22	2584.0	6.66591	55.005839	54.987915	0.000146
23	2698.9	7.27178	60.006371	59.985812	0.000257

### Coefficients

$$\begin{bmatrix} K_3 \\ K_{oq} \\ K_2 \\ C_n \\ C_p \\ K_{On} \\ K_{Op} \end{bmatrix} = \begin{bmatrix} 2.413069 \cdot 10^{-8} \\ -3.489943 \cdot 10^{-6} \\ -3.366504 \cdot 10^{-6} \\ 1.983485 \cdot 10^{-12} \\ -5.014595 \cdot 10^{-11} \\ 1.529855 \cdot 10^{-3} \\ -1.341429 \cdot 10^{-3} \end{bmatrix}$$

Iteration = 2

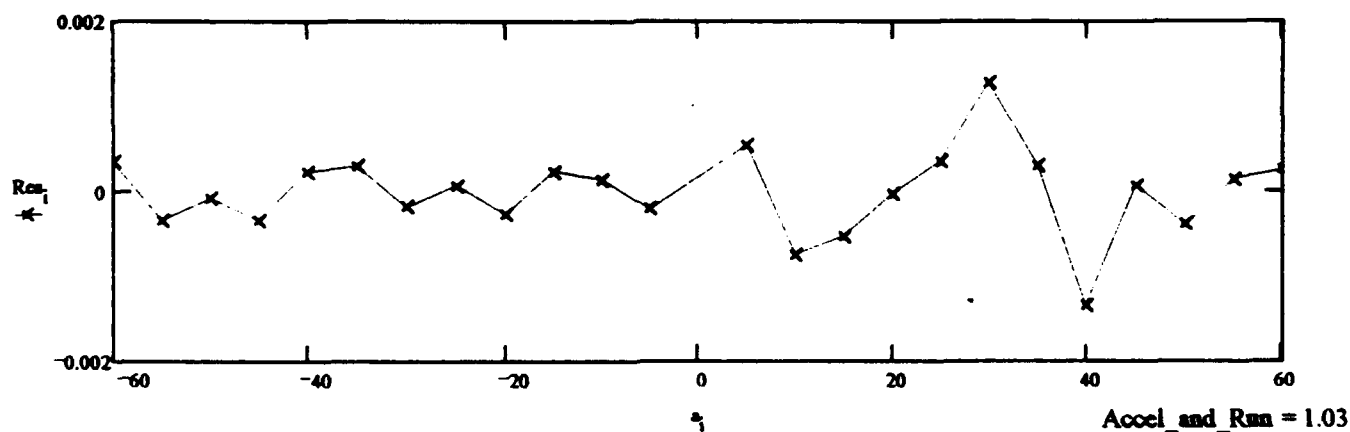
### Sum Residuals (g)

$$\sum_i Res_i = -2.033399 \cdot 10^{-8}$$

### Standard Deviation

$$\sigma_{Res} = \sqrt{\frac{\sum_i (Res_i)^2}{N_{pos} + N_{neg} - 7}}$$

$$(10^6) \cdot \sigma_{Res} = 582 \quad \mu g$$



# Inhouse Centrifuge (29 Inch Radius, 600 Tooth Wheel, Accelerometer = 1 SF = 0.121225 Date = 1.121092

## Random Sequence)

$$\sigma_{Res} = 5.818492 \cdot 10^{-4}$$

Standard Deviation of Residuals

$$\mu = \frac{\max(|Res|)}{\sigma_{Res}}$$

$$\mu = 2.294166$$

Normalized Magnitude of  
Largest Residual

$$N = N_{neg} + N_{pos}$$

$$N = 24$$

Total Number of Readings

$$\mu_c = 1.25 + \ln\left(\sqrt{\frac{N}{3}}\right)$$

$$\mu_c = 2.289721$$

Confidence Limit Check Value

$$K = \begin{bmatrix} K_3 \\ K_{oq} \\ K_2 \\ C_n \\ C_p \\ K_{0n} \\ K_{0p} \end{bmatrix}$$

$$i = 0 \dots \text{rows}(K) - 1$$

$$d = A(a)^{-1}$$

$$\sigma_{K_i} = \sigma_{Res} \sqrt{d_{i,i}}$$

$$\begin{bmatrix} \sigma K_3 \\ \sigma K_{oq} \\ \sigma K_2 \\ \sigma C_n \\ \sigma C_p \\ \sigma K_{0n} \\ \sigma K_{0p} \end{bmatrix} = \sigma_K$$

$$\begin{bmatrix} \sigma K_3 \\ \sigma K_{oq} \\ \sigma K_2 \\ \sigma C_n \\ \sigma C_p \\ \sigma K_{0n} \\ \sigma K_{0p} \end{bmatrix} = \begin{bmatrix} 3.05076 \cdot 10^{-8} \\ 3.010692 \cdot 10^{-6} \\ 4.497378 \cdot 10^{-7} \\ 9.120251 \cdot 10^{-5} \\ 9.102741 \cdot 10^{-5} \\ 7.969148 \cdot 10^{-4} \\ 7.954513 \cdot 10^{-4} \end{bmatrix}$$

Standard Deviations of  
Each Coefficient

$$f = N - \text{rows}(K)$$

$$f = 17$$

Number of Degrees of Freedom

$$t = 1.96 + \frac{2.392}{(f - 1.082)}$$

$$t = 2.11027$$

Student's t for P=95% Confidence

$$K_{2lower} = K_2 - \frac{t \cdot \sigma K_2}{\sqrt{N}}$$

$$K_2 = -3.367 \cdot 10^{-6}$$

$$K_{2upper} = K_2 + \frac{t \cdot \sigma K_2}{\sqrt{N}}$$

$$K_{2min} = \text{if}(|K_{2lower}| < |K_{2upper}|, K_{2lower}, K_{2upper})$$

$$K_{2max} = \text{if}(|K_{2lower}| < |K_{2upper}|, K_{2upper}, K_{2lower})$$

95% Confidence level K2 Lies Within the Range of:

$$K_{2min} = -3.173 \cdot 10^{-6} \leq K_2 \leq K_{2max} = -3.560 \cdot 10^{-6}$$

Accel\_and\_Run = 1.03

# Inhouse Centrifuge (29 Inch Radius, Optical Encoder, Arm Tapped, Random Sequence)

Accelerometer = 1

SF = 0.121225

Date = 1.011993

i	Raw Data Pair		Corrected CF Input	Accel Output	Residuals	Coefficients
	Hz <sub>i</sub>	VDC <sub>i</sub>	(g) a <sub>i</sub>	(g) s <sub>i</sub>	(g) Res <sub>i</sub>	
0	4498.2	-7.28437	-60.080662	-60.089668	-0.000064	$\begin{bmatrix} K_3 \\ K_{oq} \\ K_2 \\ C_n \\ C_p \\ K_{On} \\ K_{Op} \end{bmatrix} = \begin{bmatrix} -1.554591 \cdot 10^{-8} \\ 2.007596 \cdot 10^{-6} \\ -1.761198 \cdot 10^{-6} \\ 6.922166 \cdot 10^{-12} \\ -1.949004 \cdot 10^{-11} \\ 1.291327 \cdot 10^{-3} \\ 2.121037 \cdot 10^{-3} \end{bmatrix}$
1	4306.7	-6.67721	-55.073976	-55.081130	0.000389	
2	4106.3	-6.07027	-50.067804	-50.074407	-0.000398	
3	3895.6	-5.46317	-45.061527	-45.066364	0.000102	
4	3672.8	-4.85614	-40.054540	-40.058899	-0.000602	
5	3435.6	-4.24904	-35.047930	-35.050856	-0.000257	
6	3180.7	-3.64160	-30.040185	-30.040008	0.001865	
7	2903.6	-3.03492	-25.034030	-25.035430	-0.000573	
8	2597.0	-2.42773	-20.026317	-20.026645	-0.000232	
9	2249.1	-1.82082	-15.020166	-15.020169	-0.000497	
10	1836.4	-1.21379	-10.013635	-10.012704	0.000002	$\sum_i Res_i = -1.030145 \cdot 10^{-8}$
11	1298.5	-0.60674	-5.006579	-5.005114	0.000266	
12	1298.5	0.60614	4.997861	5.000124	0.000137	
13	1836.4	1.21204	9.996198	9.998268	-0.000060	
14	2249.1	1.81790	14.994011	14.996082	-0.000053	
15	2597.0	2.42370	19.991445	19.993401	-0.000139	
16	2903.6	3.02968	24.990437	24.992205	-0.000265	
17	3180.7	3.63554	29.987876	29.990019	0.000220	
18	3435.6	4.24154	34.986901	34.988987	0.000330	
19	3672.8	4.84735	39.984792	39.986389	0.000076	
20	3895.6	5.45321	44.983060	44.984203	-0.000062	$\sigma_{Res} = \sqrt{\frac{\sum_i (Res_i)^2}{N_{pos} + N_{neg} - 7}}$
21	4106.3	6.05896	49.980619	49.981110	-0.000305	
22	4306.7	6.66476	54.978074	54.978429	0.000072	
23	4498.2	7.27056	59.976043	59.975748	0.000052	

Iteration = 2

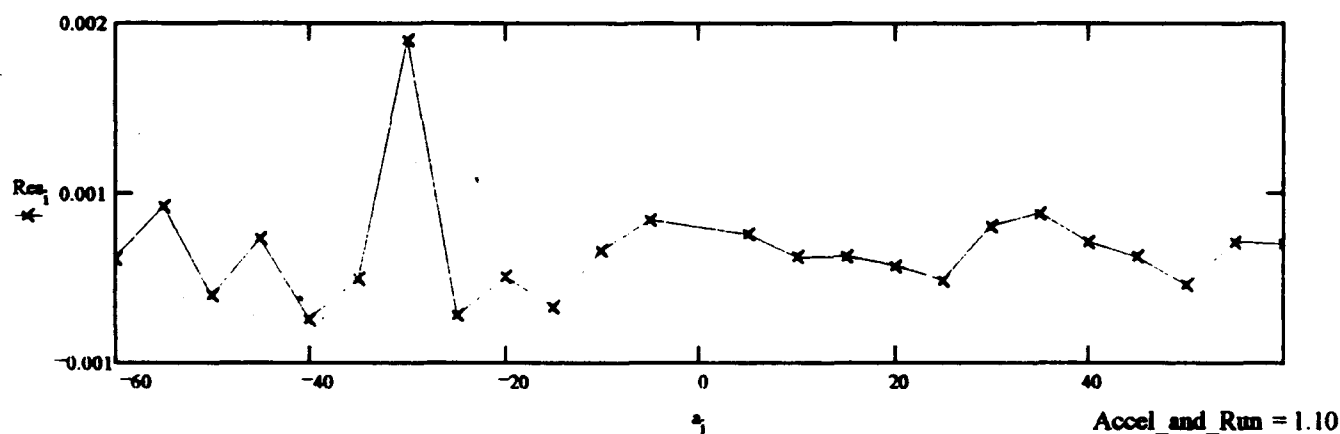
Sum Residuals (g)

$$\sum_i Res_i = -1.030145 \cdot 10^{-8}$$

Standard Deviation

$$\sigma_{Res} = \sqrt{\frac{\sum_i (Res_i)^2}{N_{pos} + N_{neg} - 7}}$$

$$(10^6) \cdot \sigma_{Res} = 559 \quad \mu g$$





# Inhouse Centrifuge (29 Inch Radius, Optical Encoder, Arm Tapped, Accelerometer = 1 SF = 0.121225 Date = 1.011993

Random Sequence)

$$\sigma_{Res} = 5.592166 \cdot 10^{-4}$$

Standard Deviation of Residuals

$$\mu = \frac{\max(|Res|)}{\sigma_{Res}}$$

$$\mu = 3.335666$$

Normalized Magnitude of  
Largest Residual

$$N = N_{neg} + N_{pos}$$

$$N = 24$$

Total Number of Readings

$$\mu_c = 1.25 + \ln\left(\sqrt{\frac{N}{3}}\right)$$

$$\mu_c = 2.289721$$

Confidence Limit Check Value

$$K = \begin{bmatrix} K_3 \\ K_{oq} \\ K_2 \\ C_n \\ C_p \\ K_{0n} \\ K_{0p} \end{bmatrix}$$

$$i = 0 \dots \text{rows}(K) - 1$$

$$d = A(a)^{-1}$$

$$\sigma_{K_i} = \sigma_{Res} \cdot \sqrt{d_{i,i}}$$

$$\begin{bmatrix} \sigma K_3 \\ \sigma K_{oq} \\ \sigma K_2 \\ \sigma C_n \\ \sigma C_p \\ \sigma K_{0n} \\ \sigma K_{0p} \end{bmatrix} = \sigma_K$$

$$\begin{bmatrix} \sigma K_3 \\ \sigma K_{oq} \\ \sigma K_2 \\ \sigma C_n \\ \sigma C_p \\ \sigma K_{0n} \\ \sigma K_{0p} \end{bmatrix} = \begin{bmatrix} 2.935087 \cdot 10^{-8} \\ 2.895548 \cdot 10^{-6} \\ 4.32554 \cdot 10^{-7} \\ 8.770381 \cdot 10^{-5} \\ 8.749813 \cdot 10^{-5} \\ 7.66076 \cdot 10^{-4} \\ 7.643575 \cdot 10^{-4} \end{bmatrix}$$

Standard Deviations of  
Each Coefficient

$$f = N - \text{rows}(K)$$

$$f = 17$$

Number of Degrees of Freedom

$$t = 1.96 + \frac{2.392}{(f - 1.082)}$$

$$t = 2.11027$$

Student's t for P=95% Confidence

$$K_{2lower} = K_2 - \frac{t \cdot \sigma K_2}{\sqrt{N}}$$

$$K_2 = -1.761 \cdot 10^{-6}$$

$$K_{2upper} = K_2 + \frac{t \cdot \sigma K_2}{\sqrt{N}}$$

$$K_{2min} = \text{if}(|K_{2lower}| < |K_{2upper}|, K_{2lower}, K_{2upper})$$

$$K_{2max} = \text{if}(|K_{2lower}| < |K_{2upper}|, K_{2upper}, K_{2lower})$$

95% Confidence level K2 Lies Within the Range of:

$$K_{2min} = -1.575 \cdot 10^{-6} \leq K_2 \leq K_{2max} = -1.948 \cdot 10^{-6}$$

$$\text{Accel\_and\_Run} = 1.10$$

# Inhouse Centrifuge (29 Inch Radius, Optical Encoder, Arm Tapped,

Accelerometer = 1

SF = 0.121225

Date = 1.012193

Ramping Up, Load Resistor Doubled to 1K)

Raw		Corrected		Accel	Residuals	Coefficients
I	Data Pair	CF Input	Output	Output		
		(g)	(g)	(g)	(g)	
i	Hz <sub>i</sub>	VDC <sub>i</sub>	a <sub>i</sub>	s <sub>i</sub>	Res <sub>i</sub>	
0	3180.7	-3.64265	-30.041662	-30.048670	0.000027	$\begin{bmatrix} K_3 \\ K_{oq} \\ K_2 \\ C_a \\ C_p \\ K_{on} \\ K_{op} \end{bmatrix} = \begin{bmatrix} 2.466396 \cdot 10^{-8} \\ -5.306060 \cdot 10^{-7} \\ -2.078453 \cdot 10^{-6} \\ 2.198387 \cdot 10^{-12} \\ -1.855800 \cdot 10^{-12} \\ -4.969627 \cdot 10^{-3} \\ -4.905020 \cdot 10^{-3} \end{bmatrix}$
1	3045.3	-3.33915	-27.538400	-27.545061	-0.000003	
2	2903.6	-3.03567	-25.035260	-25.041617	-0.000030	
3	2754.6	-2.73215	-22.531786	-22.537843	-0.000019	
4	2597.0	-2.42852	-20.027301	-20.033161	-0.000072	
5	2429.3	-2.12505	-17.524306	-17.529800	0.000084	
6	2249.1	-1.82157	-15.020904	-15.026356	-0.000050	
7	2053.1	-1.51799	-12.516956	-12.522087	0.000130	
8	1836.4	-1.21457	-10.014127	-10.019138	0.000139	
9	1590.4	-0.91115	-7.510888	-7.516181	-0.000226	
10	1298.5	-0.60757	-5.006825	-5.011928	-0.000091	$\begin{aligned} \text{Iteration} &= 2 \\ \text{Sum Residuals (g)} \\ \sum_i \text{Res}_i &= -7.910610 \cdot 10^{-10} \\ \text{Standard Deviation} \\ \sigma_{\text{Res}} &= \sqrt{\frac{\sum_i (\text{Res}_i)^2}{N_{\text{pos}} + N_{\text{neg}} - 7}} \\ (10^6) \cdot \sigma_{\text{Res}} &= 125 \quad \mu\text{g} \end{aligned}$
11	918.2	-0.30408	-2.503532	-2.508402	0.000110	
12	918.2	0.30237	2.499281	2.494279	-0.000081	
13	1298.5	0.60533	4.998324	4.993442	0.000085	
14	1590.4	0.90837	7.498134	7.493281	0.000188	
15	1836.4	1.21125	9.997123	9.991751	-0.000231	
16	2053.1	1.51415	12.495703	12.490410	-0.000028	
17	2249.1	1.81717	14.995399	14.990060	0.000070	
18	2429.3	2.12010	17.494550	17.488967	-0.000012	
19	2597.0	2.42299	19.993295	19.987544	-0.000001	
20	2754.6	2.72606	22.493528	22.487606	0.000023	
21	2903.6	3.02899	24.992751	24.986513	-0.000088	
22	3045.3	3.33192	27.491640	27.485420	0.000144	
23	3180.7	3.63481	29.990652	29.983997	-0.000068	

Iteration = 2

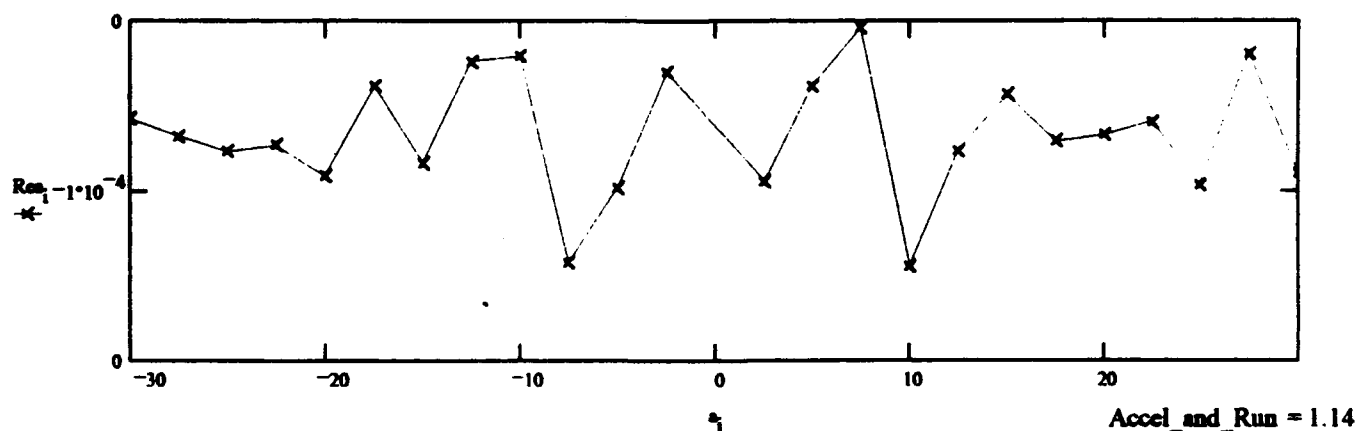
Sum Residuals (g)

$$\sum_i \text{Res}_i = -7.910610 \cdot 10^{-10}$$

Standard Deviation

$$\sigma_{\text{Res}} = \sqrt{\frac{\sum_i (\text{Res}_i)^2}{N_{\text{pos}} + N_{\text{neg}} - 7}}$$

$$(10^6) \cdot \sigma_{\text{Res}} = 125 \quad \mu\text{g}$$



**Inhouse Centrifuge (29 Inch Radius, Optical Encoder, Arm Tapped,  
Accelerometer = 1  
SF = 0.121225  
Date = 1.012193**

**Ramping Up, Load Resistor Doubled to 1K)**

$$\sigma_{Res} = 1.251617 \cdot 10^{-4}$$

**Standard Deviation of Residuals**

$$\mu = \frac{\max(|Res|)}{\sigma_{Res}}$$

$$\mu = 1.848399$$

**Normalized Magnitude of  
Largest Residual**

$$N = N_{neg} + N_{pos}$$

$$N = 24$$

**Total Number of Readings**

$$\mu_c = 1.25 + \ln\left(\sqrt{\frac{N}{3}}\right)$$

$$\mu_c = 2.289721$$

**Confidence Limit Check Value**

$$K = \begin{bmatrix} K_3 \\ K_{oq} \\ K_2 \\ C_n \\ C_p \\ K_{0n} \\ K_{0p} \end{bmatrix}$$

$$i = 0 \dots \text{rows}(K) - 1$$

$$d = A(a)^{-1}$$

$$\sigma_{K_i} = \sigma_{Res} \sqrt{d_{i,i}}$$

$$\begin{bmatrix} \sigma K_3 \\ \sigma K_{oq} \\ \sigma K_2 \\ \sigma C_n \\ \sigma C_p \\ \sigma K_{0n} \\ \sigma K_{0p} \end{bmatrix} = \sigma_K \begin{bmatrix} \sigma K_3 \\ \sigma K_{oq} \\ \sigma K_2 \\ \sigma C_n \\ \sigma C_p \\ \sigma K_{0n} \\ \sigma K_{0p} \end{bmatrix} = \begin{bmatrix} 5.254446 \cdot 10^{-8} \\ 2.591994 \cdot 10^{-6} \\ 3.871953 \cdot 10^{-7} \\ 3.925583 \cdot 10^{-5} \\ 3.916606 \cdot 10^{-5} \\ 1.714579 \cdot 10^{-4} \\ 1.710829 \cdot 10^{-4} \end{bmatrix}$$

**Standard Deviations of  
Each Coefficient**

$$f = N - \text{rows}(K)$$

$$f = 17$$

**Number of Degrees of Freedom**

$$t = 1.96 + \frac{2.392}{(f - 1.082)}$$

$$t = 2.11027$$

**Student's t for P=95% Confidence**

$$K_{2lower} = K_2 - \frac{t \cdot \sigma K_2}{\sqrt{N}}$$

$$K_2 = -2.078 \cdot 10^{-6}$$

$$K_{2upper} = K_2 + \frac{t \cdot \sigma K_2}{\sqrt{N}}$$

$$K_{2min} = \text{if}(|K_{2lower}| < |K_{2upper}|, K_{2lower}, K_{2upper})$$

$$K_{2max} = \text{if}(|K_{2lower}| < |K_{2upper}|, K_{2upper}, K_{2lower})$$

**95% Confidence level K2 Lies Within the Range of:**

$$K_{2min} = -1.912 \cdot 10^{-6} \leq K_2 \leq K_{2max} = -2.245 \cdot 10^{-6}$$

$$\text{Accel\_and\_Run} = 1.14$$

# Inhouse Centrifuge (29 Inch Radius, 600 Tooth Wheel,

Accelerometer = 1

SF = 0.242450

Date = 1.012293

Random Sequence, Load Resistor Doubled to 1K)

i	Raw Data Pair		Corrected CF Input	Accel Output	Residuals
	Hz <sub>i</sub>	VDC <sub>i</sub>	(g) <sub>i</sub>	(g) <sub>i</sub>	(g) <sub>i</sub>
0	1908.4	-7.27035	-29.985182	-29.987008	-0.000004
1	1827.1	-6.66415	-27.484795	-27.486698	-0.000062
2	1742.1	-6.05850	-24.986995	-24.988657	0.000170
3	1652.7	-5.45271	-22.488264	-22.490039	0.000025
4	1558.2	-4.84704	-19.990068	-19.991916	-0.000098
5	1457.5	-4.24086	-17.489806	-17.491689	-0.000196
6	1349.4	-3.63512	-14.991645	-14.993277	-0.000017
7	1231.8	-3.02912	-12.492469	-12.493793	0.000217
8	1101.8	-2.42358	-9.994784	-9.996205	0.000048
9	954.2	-1.81783	-7.496295	-7.497752	-0.000052
10	779.1	-1.21198	-4.997517	-4.998886	-0.000018
11	550.9	-0.60612	-2.498696	-2.500025	-0.000012
12	550.9	0.60671	2.503296	2.502392	0.000079
13	779.1	1.21372	5.006716	5.006063	0.000079
14	954.2	1.82070	7.510095	7.509590	0.000079
15	1101.8	2.42760	10.013182	10.012786	-0.000010
16	1231.8	3.03432	12.515465	12.515240	-0.000081
17	1349.4	3.64143	15.019241	15.019303	-0.000079
18	1457.5	4.24835	17.522001	17.522582	0.000122
19	1558.2	4.85570	20.026866	20.027635	-0.000038
20	1652.7	5.46260	22.529660	22.530831	-0.000009
21	1742.1	6.06967	25.032991	25.034729	0.000165
22	1827.1	6.67637	27.535389	27.537100	-0.000269
23	1908.4	7.28390	30.040379	30.042895	0.000120

## Coefficients

$$\begin{bmatrix} K_3 \\ K_{oq} \\ K_2 \\ C_n \\ C_p \\ K_{On} \\ K_{Op} \end{bmatrix} = \begin{bmatrix} -5.407114 \cdot 10^{-8} \\ 3.713493 \cdot 10^{-6} \\ 1.515939 \cdot 10^{-6} \\ -1.630669 \cdot 10^{-11} \\ 4.759453 \cdot 10^{-12} \\ -1.303741 \cdot 10^{-3} \\ -8.562025 \cdot 10^{-4} \end{bmatrix}$$

Iteration = 2

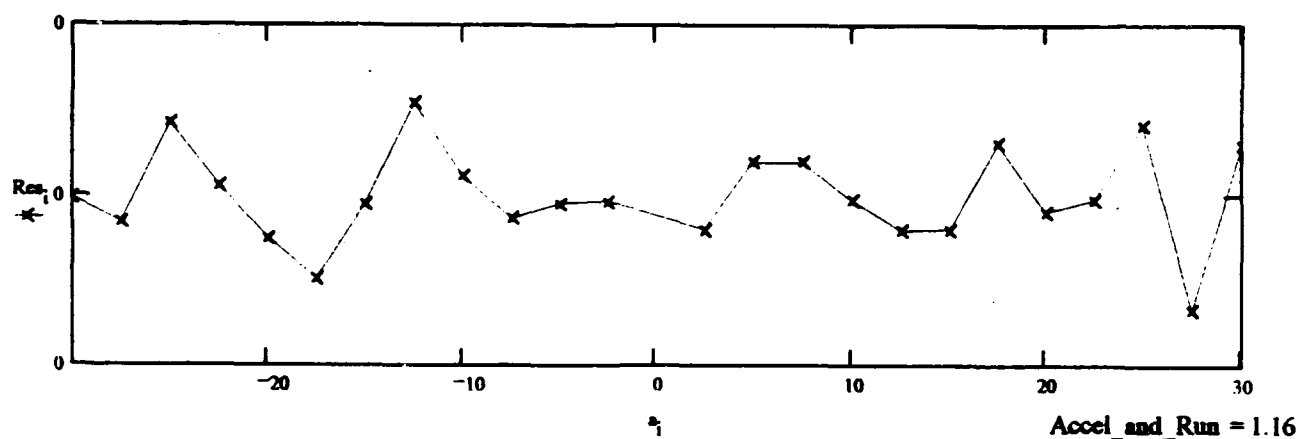
## Sum Residuals (g)

$$\sum_i Res_i = 4.107414 \cdot 10^{-9}$$

## Standard Deviation

$$\sigma_{Res} = \sqrt{\frac{\sum_i (Res_i)^2}{N_{pos} + N_{neg} - 7}}$$

$$(10^6) \cdot \sigma_{Res} = 132 \quad \mu g$$



# Inhouse Centrifuge (29 Inch Radius, 600 Tooth Wheel,

Accelerometer = 1

SF = 0.242450

Date = 1.012293

Random Sequence, Load Resistor Doubled to 1K)

$$\sigma_{Res} = 1.320007 \cdot 10^{-4}$$

Standard Deviation of Residuals

$$\mu = \frac{\max(|Res|)}{\sigma_{Res}}$$

$$\mu = 2.035499$$

Normalized Magnitude of  
Largest Residual

$$N = N_{neg} + N_{pos}$$

$$N = 24$$

Total Number of Readings

$$\mu_c = 1.25 + \ln\left(\sqrt{\frac{N}{3}}\right)$$

$$\mu_c = 2.289721$$

Confidence Limit Check Value

$$K = \begin{bmatrix} K_3 \\ K_{oq} \\ K_2 \\ C_n \\ C_p \\ K_{0n} \\ K_{0p} \end{bmatrix}$$

$$i = 0 \dots \text{rows}(K) - 1$$

$$d = A(a)^{-1}$$

$$\sigma_{K_i} = \sigma_{Res} \cdot \sqrt{d_{i,i}}$$

$$\begin{bmatrix} \sigma K_3 \\ \sigma K_{oq} \\ \sigma K_2 \\ \sigma C_n \\ \sigma C_p \\ \sigma K_{0n} \\ \sigma K_{0p} \end{bmatrix} = \sigma_K$$

$$\begin{bmatrix} \sigma K_3 \\ \sigma K_{oq} \\ \sigma K_2 \\ \sigma C_n \\ \sigma C_p \\ \sigma K_{0n} \\ \sigma K_{0p} \end{bmatrix}$$

$$\begin{bmatrix} 5.543125 \cdot 10^{-8} \\ 2.734068 \cdot 10^{-6} \\ 4.084619 \cdot 10^{-7} \\ 4.130474 \cdot 10^{-5} \\ 4.14072 \cdot 10^{-5} \\ 1.804088 \cdot 10^{-4} \\ 1.808369 \cdot 10^{-4} \end{bmatrix}$$

Standard Deviations of  
Each Coefficient

$$f = N - \text{rows}(K)$$

$$f = 17$$

Number of Degrees of Freedom

$$t = 1.96 + \frac{2.392}{(f - 1.082)}$$

$$t = 2.11027$$

Student's t for P=95% Confidence

$$K_{2lower} = K_2 - \frac{t \cdot \sigma K_2}{\sqrt{N}}$$

$$K_2 = 1.516 \cdot 10^{-6}$$

$$K_{2upper} = K_2 + \frac{t \cdot \sigma K_2}{\sqrt{N}}$$

$$K_{2min} = \text{if}(|K_{2lower}| < |K_{2upper}|, K_{2lower}, K_{2upper})$$

$$K_{2max} = \text{if}(|K_{2lower}| < |K_{2upper}|, K_{2upper}, K_{2lower})$$

95% Confidence level K2 Lies Within the Range of:

$$K_{2min} = 1.340 \cdot 10^{-6} \leq K_2 \leq K_{2max} = 1.692 \cdot 10^{-6}$$

Accel\_and\_Run = 1.16

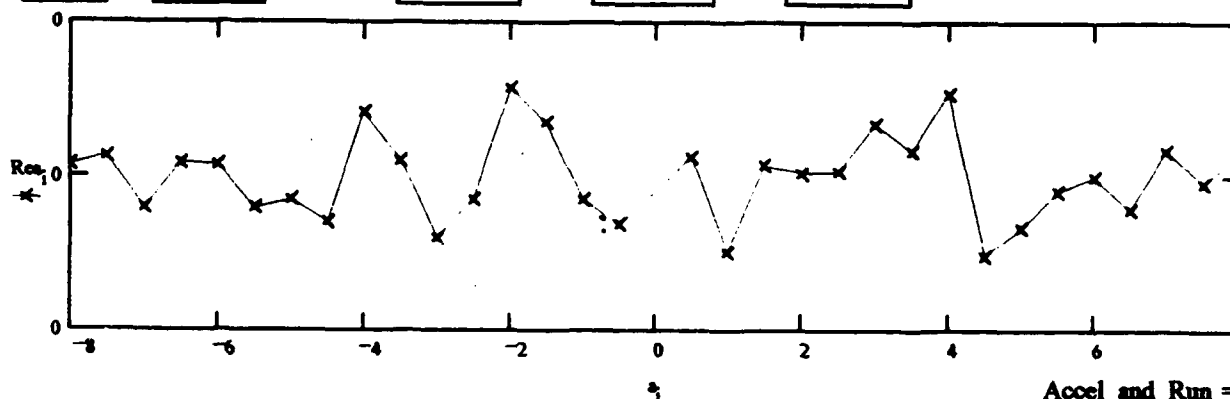
# Inhouse Centrifuge (29 Inch Radius, Optical Encoder, Arm Tapped, Small g-Step)

Accelerometer = 1

SF = 0.121225

Date = 1.012093

i	Raw Data Pair		Corrected CF Input (g)	Accel Output (g)	Residuals (g)	Coefficients
	Hz <sub>i</sub>	VDC <sub>i</sub>	a <sub>i</sub>	s <sub>i</sub>	Res <sub>i</sub>	
0	1642.5	-0.97176	-8.011508	-8.016160	0.000008	$\begin{bmatrix} K_3 \\ K_{oq} \\ K_2 \\ C_n \\ C_p \\ K_{On} \\ K_{Op} \end{bmatrix} = \begin{bmatrix} 8.496115 \cdot 10^{-7} \\ -7.099501 \cdot 10^{-6} \\ -2.445712 \cdot 10^{-6} \\ -2.164206 \cdot 10^{-12} \\ -2.401210 \cdot 10^{-11} \\ -4.521248 \cdot 10^{-3} \\ -4.418204 \cdot 10^{-3} \end{bmatrix}$
1	1590.4	-0.91112	-7.511320	-7.515925	0.000014	
2	1536.4	-0.85033	-7.009905	-7.014510	-0.000020	
3	1480.5	-0.78962	-6.509091	-6.513640	0.000009	
4	1422.5	-0.72900	-6.009081	-6.013611	0.000008	
5	1361.9	-0.66826	-5.508000	-5.512543	-0.000020	
6	1298.5	-0.60754	-5.007113	-5.011640	-0.000015	
7	1231.9	-0.54687	-4.506656	-4.511190	-0.000029	
8	1161.4	-0.48612	-4.005596	-4.010056	0.000042	
9	1086.4	-0.42543	-3.504960	-3.509449	0.000011	
10	1005.8	-0.36473	-3.004186	-3.008728	-0.000040	$\begin{aligned} \text{Iteration} &= 2 \\ \text{Sum Residuals (g)} \\ \sum_i \text{Res}_i &= -1.485061 \cdot 10^{-9} \end{aligned}$
11	918.2	-0.30406	-2.503676	-2.508196	-0.000014	
12	821.3	0.24337	2.003121	2.007573	0.000058	
13	711.2	-0.18263	-1.502059	-1.506537	0.000035	
14	580.7	-0.12194	-1.001399	-1.005931	-0.000015	
15	410.6	-0.06124	-0.500658	-0.505209	-0.000031	
16	410.6	0.06006	0.499816	0.495409	0.000013	
17	580.7	0.12065	0.999715	0.995240	-0.000048	
18	711.2	0.18124	1.499533	1.495104	0.000008	
19	821.3	0.24188	1.999753	1.995306	0.000003	
20	918.2	0.30246	2.499466	2.495005	0.000004	$\begin{aligned} \text{Standard Deviation} \\ \sigma_{\text{Res}} &= \sqrt{\frac{\sum_i (\text{Res}_i)^2}{N_{\text{pos}} + N_{\text{neg}} - 7}} \\ (10^6) \cdot \sigma_{\text{Res}} &= 31 \quad \mu\text{g} \end{aligned}$
21	1005.8	0.36303	2.999134	2.994688	0.000034	
22	1086.4	0.42363	3.499066	3.494584	0.000017	
23	1161.4	0.48422	3.998861	3.994399	0.000054	
24	1231.9	0.54485	4.499078	4.494494	-0.000051	
25	1298.5	0.60541	4.998694	4.994110	-0.000033	
26	1361.9	0.66603	5.498739	5.494164	-0.000010	
27	1422.5	0.72667	5.998977	5.994399	0.000000	
28	1480.5	0.78718	6.498146	6.493537	-0.000021	
29	1536.4	0.84779	6.998118	6.993541	0.000018	
30	1590.4	0.90847	7.498690	7.494090	-0.000004	
31	1642.5	0.96901	7.998037	7.993458	0.000016	



# Inhouse Centrifuge (29 Inch Radius, Optical Encoder, Arm Tapped, Small g Step)

Accelerometer = 1  
SF = 0.121225  
Date = 1.012093

$$\sigma_{Res} = 3.061997 \cdot 10^{-5}$$

Standard Deviation of Residuals

$$\mu = \frac{\max(|Res|)}{\sigma_{Res}}$$

$$\mu = 1.882044$$

Normalized Magnitude of Largest Residual

$$N = N_{neg} + N_{pos}$$

$$N = 32$$

Total Number of Readings

$$\mu_c = 1.25 + \ln\left(\sqrt{\frac{N}{3}}\right)$$

$$\mu_c = 2.433562$$

Confidence Limit Check Value

$$K = \begin{bmatrix} K_3 \\ K_{oq} \\ K_2 \\ C_n \\ C_p \\ K_{0n} \\ K_{0p} \end{bmatrix}$$

$$i = 0 \dots \text{rows}(K) - 1$$

$$d = A(a)^{-1}$$

$$\sigma_{K_i} = \sigma_{Res} \cdot \sqrt{d_{i,i}}$$

$$\begin{bmatrix} \sigma K_3 \\ \sigma K_{oq} \\ \sigma K_2 \\ \sigma C_n \\ \sigma C_p \\ \sigma K_{0n} \\ \sigma K_{0p} \end{bmatrix} = \sigma_K$$

$$\begin{bmatrix} \sigma K_3 \\ \sigma K_{oq} \\ \sigma K_2 \\ \sigma C_n \\ \sigma C_p \\ \sigma K_{0n} \\ \sigma K_{0p} \end{bmatrix} =$$

$$\begin{bmatrix} 5.740648 \cdot 10^{-7} \\ 7.412615 \cdot 10^{-6} \\ 1.144523 \cdot 10^{-6} \\ 2.935502 \cdot 10^{-5} \\ 2.929085 \cdot 10^{-5} \\ 3.352058 \cdot 10^{-5} \\ 3.345475 \cdot 10^{-5} \end{bmatrix}$$

Standard Deviations of Each Coefficient

$$f = N - \text{rows}(K)$$

$$f = 25$$

Number of Degrees of Freedom

$$t = 1.96 + \frac{2.392}{(f - 1.082)}$$

$$t = 2.060008$$

Student's t for P=95% Confidence

$$K_{2lower} = K_2 - \frac{t \cdot \sigma K_2}{\sqrt{N}}$$

$$K_2 = -2.446 \cdot 10^{-6}$$

$$K_{2upper} = K_2 + \frac{t \cdot \sigma K_2}{\sqrt{N}}$$

$$K_{2min} := \text{if}(|K_{2lower}| < |K_{2upper}|, K_{2lower}, K_{2upper})$$

$$K_{2max} := \text{if}(|K_{2lower}| < |K_{2upper}|, K_{2upper}, K_{2lower})$$

95% Confidence level K2 Lies Within the Range of:

$$K_{2min} = -2.029 \cdot 10^{-6} \leq K_2 \leq K_{2max} = -2.863 \cdot 10^{-6}$$

Accel\_and\_Run = 1.13

# Inhouse Centrifuge (29 Inch Radius, 600 Tooth Wheel, Random Sequence)

Accelerometer = 2

SF = 0.122190

Date = 1.111292

i	Raw Data Pair		Corrected CF Input (g)	Accel Output (g)	Residuals (g)
	Hz <sub>i</sub>	VDC <sub>i</sub>	a <sub>i</sub>	s <sub>i</sub>	Res <sub>i</sub>
0	2698.9	-7.34141	-60.113470	-60.081922	0.001863
1	2584.0	-6.72947	-55.104013	-55.073819	0.001006
2	2468.8	-6.14313	-50.300237	-50.275227	-0.002732
3	2337.3	-5.50593	-45.084487	-45.060398	-0.001220
4	2203.7	-4.89470	-40.077734	-40.058106	-0.002711
5	2061.3	-4.28245	-35.065547	-35.047467	-0.000868
6	1908.4	-3.67000	-30.056404	-30.035191	0.005866
7	1742.2	-3.05941	-25.049221	-25.038137	-0.000658
8	1558.2	-2.44734	-20.037550	-20.028971	0.000248
9	1349.5	-1.83577	-15.029481	-15.023897	0.000261
10	1101.8	-1.22379	-10.018524	-10.015468	0.000136
11	779.1	-0.61208	-5.009387	-5.009248	-0.001190
12	779.1	0.61087	5.000214	4.999345	0.002122
13	1101.8	1.22183	10.000178	9.999427	-0.001726
14	1349.5	1.83343	15.001958	15.004747	0.002029
15	1558.2	2.44449	20.000856	20.005647	0.003981
16	1742.2	3.05643	25.003350	25.013749	0.009068
17	1908.4	3.66509	30.001363	29.995008	-0.008881
18	2061.3	4.27677	35.001333	35.000982	-0.004946
19	2203.7	4.88925	40.004341	40.013504	0.001416
20	2337.3	5.49990	45.001925	45.011048	-0.003055
21	2468.8	6.13754	50.208124	50.229479	0.002979
22	2584.0	6.72430	55.003103	55.031508	0.002697
23	2698.9	7.33594	60.003386	60.037155	-0.001442

Coefficients	
K <sub>3</sub>	2.711000·10 <sup>-7</sup>
K <sub>oq</sub>	-1.558834·10 <sup>-5</sup>
K <sub>2</sub>	8.714692·10 <sup>-6</sup>
C <sub>n</sub>	-3.773149·10 <sup>-10</sup>
C <sub>p</sub>	-8.802838·10 <sup>-9</sup>
K <sub>0n</sub>	7.537487·10 <sup>-4</sup>
K <sub>0p</sub>	1.391381·10 <sup>-3</sup>

Iteration = 2

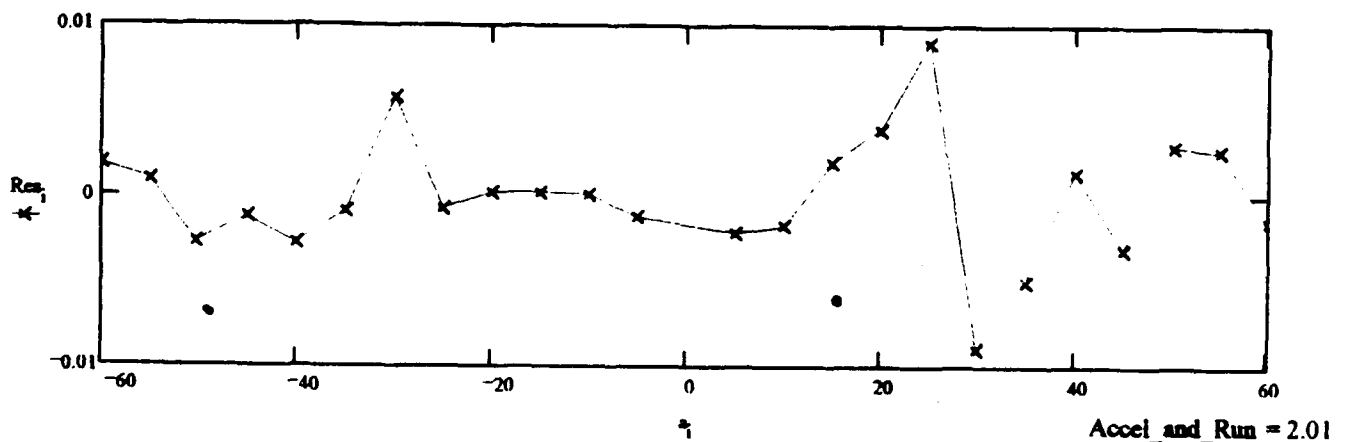
Sum Residuals (g)

$$\sum_i \text{Res}_i = -0.000003$$

Standard Deviation

$$\sigma_{\text{Res}} = \sqrt{\frac{\sum_i (\text{Res}_i)^2}{N_{\text{pos}} + N_{\text{neg}} - 7}}$$

$$(10^6) \cdot \sigma_{\text{Res}} = 4204 \mu\text{g}$$





# Inhouse Centrifuge (29 Inch Radius, 600 Tooth Wheel, Random Sequence)

Accelerometer = 2

SF = 0.122190

Date = 1.111292

$$\sigma_{Res} = 0.004204$$

Standard Deviation of Residuals

$$\mu = \frac{\max(|Res|)}{\sigma_{Res}}$$

$$\mu = 2.156753$$

Normalized Magnitude of  
Largest Residual

$$N = N_{neg} + N_{pos}$$

$$N = 24$$

Total Number of Readings

$$\mu_c = 1.25 + \ln\left(\sqrt{\frac{N}{3}}\right)$$

$$\mu_c = 2.289721$$

Confidence Limit Check Value

$$K = \begin{bmatrix} K_3 \\ K_{oq} \\ K_2 \\ C_n \\ C_p \\ K_{0n} \\ K_{0p} \end{bmatrix}$$

$$i = 0..rows(K) - 1$$

$$d = A(a)^{-1}$$

$$\sigma_{K_i} = \sigma_{Res} \cdot \sqrt{d_{i,i}}$$

$$\begin{bmatrix} \sigma K_3 \\ \sigma K_{oq} \\ \sigma K_2 \\ \sigma C_n \\ \sigma C_p \\ \sigma K_{0n} \\ \sigma K_{0p} \end{bmatrix} = \sigma_K \begin{bmatrix} \sigma K_3 \\ \sigma K_{oq} \\ \sigma K_2 \\ \sigma C_n \\ \sigma C_p \\ \sigma K_{0n} \\ \sigma K_{0p} \end{bmatrix} = \begin{bmatrix} 2.20724 \cdot 10^{-7} \\ 2.17779 \cdot 10^{-5} \\ 3.248407 \cdot 10^{-6} \\ 6.595957 \cdot 10^{-4} \\ 6.579684 \cdot 10^{-4} \\ 0.005762 \\ 0.005748 \end{bmatrix}$$

Standard Deviations of  
Each Coefficient

$$f = N - rows(K)$$

$$f = 17$$

Number of Degrees of Freedom

$$t = 1.96 + \frac{2.392}{(f - 1.082)}$$

$$t = 2.11027$$

Student's t for P=95% Confidence

$$K_{2lower} = K_2 - \frac{t \cdot \sigma K_2}{\sqrt{N}}$$

$$K_2 = 8.715 \cdot 10^{-6}$$

$$K_{2upper} = K_2 + \frac{t \cdot \sigma K_2}{\sqrt{N}}$$

$$K_{2min} = \text{if}(|K_{2lower}| < |K_{2upper}|, K_{2lower}, K_{2upper})$$

$$K_{2max} = \text{if}(|K_{2lower}| < |K_{2upper}|, K_{2upper}, K_{2lower})$$

95% Confidence level K2 Lies Within the Range of:

$$K_{2min} = 7.315 \cdot 10^{-6} \leq K_2 \leq K_{2max} = 1.011 \cdot 10^{-5}$$

Accel\_and\_Run = 2.01

# Inhouse Centrifuge (29 Inch Radius, Optical Encoder, Arm Tapped, Random Sequence)

Accelerometer = 2

SF = 0.122190

Date = 1.011993

Raw Data Pair			Corrected CF Input	Accel Output	Residuals	Coefficients	
			(g)	(g)	(g)		
i	Hz <sub>i</sub>	VDC <sub>i</sub>	a <sub>i</sub>	s <sub>i</sub>	Res <sub>i</sub>		
0	4498.2	-7.34194	-60.119020	-60.086259	-0.000786	K <sub>3</sub>	3.064189·10 <sup>-7</sup>
1	4306.7	-6.72911	-55.109137	-55.070873	0.005154		
2	4106.3	-6.11846	-50.099768	-50.073328	-0.005059		
3	3895.6	-5.50585	-45.090296	-45.059743	0.001609		
4	3672.8	-4.89486	-40.080112	-40.059416	-0.004980		
5	3435.6	-4.28240	-35.070306	-35.047058	0.001321		
6	3180.7	-3.67025	-30.059364	-30.037237	0.004200	K <sub>2</sub>	5.558001·10 <sup>-6</sup>
7	2903.6	-3.05944	-25.050012	-25.038383	-0.002280		
8	2597.0	-2.44712	-20.039103	-20.027171	0.001829		
9	2249.1	-1.83575	-15.029755	-15.023734	-0.000719		
10	1836.4	-1.22376	-10.020028	-10.015222	0.000754		
11	1298.5	-0.61199	-5.009776	-5.008552	-0.001046		
12	1298.5	0.61089	5.002064	4.999509	0.001050	C <sub>a</sub>	2.016224·10 <sup>-9</sup>
13	1836.4	1.22212	10.004604	10.001800	-0.000355		
14	2249.1	1.83325	15.006619	15.003274	0.000393		
15	2597.0	2.44432	20.008256	20.004256	0.001146		
16	2903.6	3.05596	25.011452	25.009903	0.004891		
17	3180.7	3.66583	30.013093	30.001064	-0.004637		
18	3435.6	4.27773	35.016322	35.008839	0.000288	C <sub>p</sub>	-7.057500·10 <sup>-9</sup>
19	3672.8	4.88891	40.018416	40.010721	0.000349		
20	3895.6	5.50010	45.020887	45.012685	-0.002314		
21	4106.3	6.11194	50.022649	50.019969	0.000487		
22	4306.7	6.72378	55.024306	55.027253	0.001898		
23	4498.2	7.33544	60.026477	60.033063	-0.000401		

K <sub>3</sub>	3.064189·10 <sup>-7</sup>
K <sub>oq</sub>	-2.169590·10 <sup>-5</sup>
K <sub>2</sub>	5.558001·10 <sup>-6</sup>
C <sub>a</sub>	2.016224·10 <sup>-9</sup>
C <sub>p</sub>	-7.057500·10 <sup>-9</sup>
K <sub>0a</sub>	1.623822·10 <sup>-3</sup>
K <sub>0p</sub>	-1.139730·10 <sup>-3</sup>

Iteration = 2

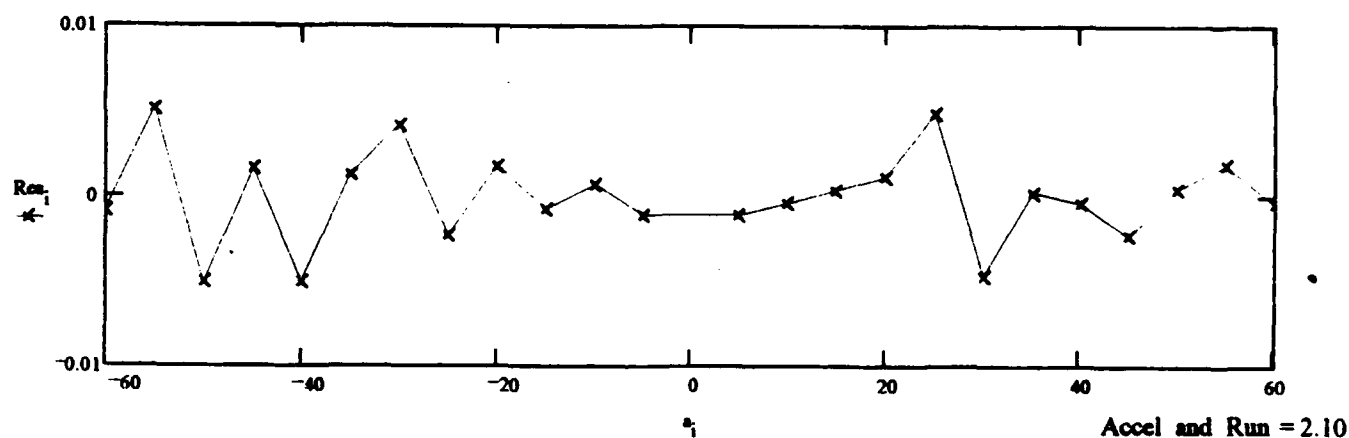
Sum Residuals (g)

$$\sum_i \text{Res}_i = -0.000004$$

Standard Deviation

$$\sigma_{\text{Res}} = \sqrt{\frac{\sum_i (\text{Res}_i)^2}{N_{\text{pos}} + N_{\text{neg}} - 7}}$$

$$(10^6) \cdot \sigma_{\text{Res}} = 3143 \mu\text{g}$$



# Inhouse Centrifuge (29 Inch Radius, Optical Encoder, Arm Tapped, Random Sequence)

Accelerometer = 2

SF = 0.122190

Date = 1.011993

$$\sigma_{Res} = 0.003143$$

Standard Deviation of Residuals

$$\mu = \frac{\max(|Res|)}{\sigma_{Res}}$$

$$\mu = 1.639767$$

Normalized Magnitude of  
Largest Residual

$$N = N_{neg} + N_{pos}$$

$$N = 24$$

Total Number of Readings

$$\mu_c = 1.25 + \ln\left(\sqrt{\frac{N}{3}}\right)$$

$$\mu_c = 2.289721$$

Confidence Limit Check Value

$$K = \begin{bmatrix} K_3 \\ K_{oq} \\ K_2 \\ C_n \\ C_p \\ K_{0n} \\ K_{0p} \end{bmatrix}$$

$$i = 0 \dots \text{rows}(K) - 1$$

$$d = A(a)^{-1}$$

$$\sigma_{K_i} = \sigma_{Res} \cdot \sqrt{d_{i,i}}$$

$$\begin{bmatrix} \sigma K_3 \\ \sigma K_{oq} \\ \sigma K_2 \\ \sigma C_n \\ \sigma C_p \\ \sigma K_{0n} \\ \sigma K_{0p} \end{bmatrix} = \sigma_K \begin{bmatrix} \sigma K_3 \\ \sigma K_{oq} \\ \sigma K_2 \\ \sigma C_n \\ \sigma C_p \\ \sigma K_{0n} \\ \sigma K_{0p} \end{bmatrix} = \begin{bmatrix} 1.645984 \cdot 10^{-7} \\ 1.625011 \cdot 10^{-5} \\ 2.427524 \cdot 10^{-6} \\ 4.924995 \cdot 10^{-4} \\ 4.914785 \cdot 10^{-4} \\ 0.004305 \\ 0.004297 \end{bmatrix}$$

Standard Deviations of  
Each Coefficient

$$f = N - \text{rows}(K)$$

$$f = 17$$

Number of Degrees of Freedom

$$t = 1.96 + \frac{2.392}{(f - 1.082)}$$

$$t = 2.11027$$

Student's t for P=95% Confidence

$$K_{2lower} = K_2 - \frac{t \cdot \sigma K_2}{\sqrt{N}}$$

$$K_2 = 5.558 \cdot 10^{-6}$$

$$K_{2upper} = K_2 + \frac{t \cdot \sigma K_2}{\sqrt{N}}$$

$$K_{2min} = \text{if}(|K_{2lower}| < |K_{2upper}|, K_{2lower}, K_{2upper})$$

$$K_{2max} = \text{if}(|K_{2lower}| < |K_{2upper}|, K_{2upper}, K_{2lower})$$

95% Confidence level K2 Lies Within the Range of:

$$K_{2min} = 4.512 \cdot 10^{-6} \leq K_2 \leq K_{2max} = 6.604 \cdot 10^{-6}$$

Accel\_and\_Run = 2.10

Inhouse Centrifuge (29 Inch Radius, Optical Encoder, Arm Tapped,  
 Accelerometer = 2  
 SF = 0.244380  
 Date = 1.012193  
 Random Sequence, Load Resistor Doubled to 1K)

I	Raw		Corrected	Accel	Residuals	Coefficients
	Data Pair		CF Input	Output		
i	Hz <sub>i</sub>	VDC <sub>i</sub>	a <sub>i</sub>	s <sub>i</sub>	Res <sub>i</sub>	
0	3180.7	-7.33995	-30.029731	-30.034986	0.000005	$\begin{bmatrix} K_3 \\ K_{oq} \\ K_2 \\ C_n \\ C_p \\ K_{on} \\ K_{op} \end{bmatrix} = \begin{bmatrix} -4.919976 \cdot 10^{-8} \\ 4.695870 \cdot 10^{-6} \\ -3.626272 \cdot 10^{-7} \\ 1.300305 \cdot 10^{-11} \\ 1.330763 \cdot 10^{-12} \\ -2.031482 \cdot 10^{-3} \\ -1.404905 \cdot 10^{-3} \end{bmatrix}$
1	3045.3	-6.72835	-27.527463	-27.532327	-0.000025	
2	2903.6	-6.11675	-25.025318	-25.029667	0.000079	
3	2754.6	-5.50510	-22.522838	-22.526803	0.000071	
4	2597.0	-4.89326	-20.019348	-20.023161	-0.000149	
5	2429.3	-4.28171	-17.517347	-17.520705	-0.000040	
6	2249.1	-3.67011	-15.014938	-15.018046	-0.000102	
7	2053.1	-3.05833	-12.511985	-12.514649	0.000063	
8	1836.4	-2.44686	-10.010150	-10.012521	0.000118	
9	1590.4	-1.83534	-7.507905	-7.510189	0.000012	
10	1298.5	-1.22359	-5.004837	-5.006915	0.000074	$\sum_i Res_i = -2.278687 \cdot 10^{-9}$
11	918.2	-0.61210	-2.502538	-2.504706	-0.000106	
12	918.2	0.61049	2.499463	2.498134	0.000050	
13	1298.5	1.22124	4.998688	4.997299	-0.000085	
14	1590.4	1.83224	7.498680	7.497504	0.000006	
15	1836.4	2.44300	9.997851	9.996726	-0.000103	
16	2053.1	3.05374	12.496612	12.495867	0.000079	
17	2249.1	3.66471	14.996490	14.995949	0.000056	
18	2429.3	4.27558	17.495823	17.495622	0.000140	
19	2597.0	4.88632	19.994750	19.994762	0.000078	
20	2754.6	5.49739	22.495164	22.495253	-0.000139	$\sigma_{Res} = \sqrt{\frac{\sum_i (Res_i)^2}{N_{pos} + N_{neg} - 7}}$
21	2903.6	6.10826	24.994569	24.994926	-0.000177	
22	3045.3	6.71909	27.493640	27.494435	-0.000053	
23	3180.7	7.32997	29.992834	29.994148	0.000149	

Iteration = 2

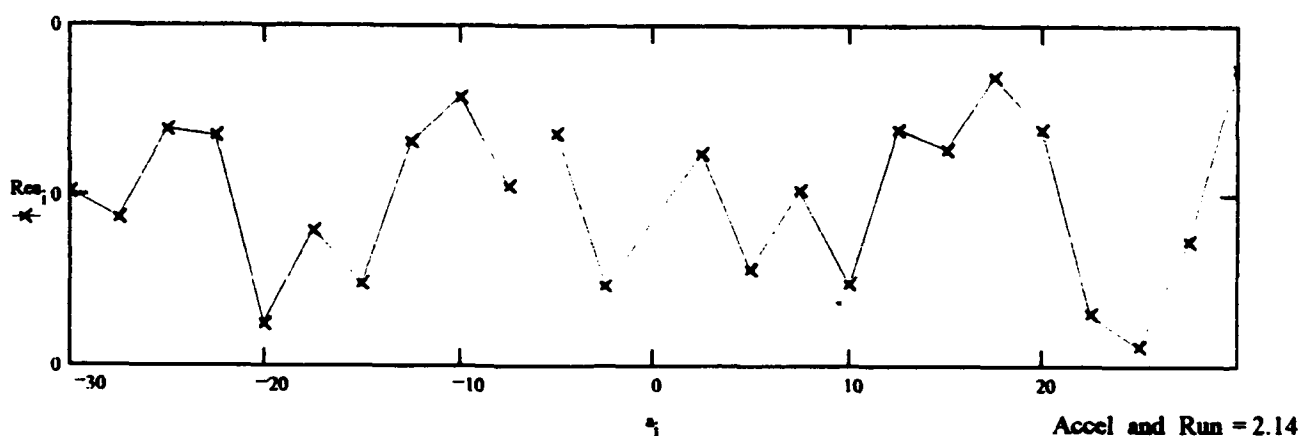
Sum Residuals (g)

$$\sum_i Res_i = -2.278687 \cdot 10^{-9}$$

Standard Deviation

$$\sigma_{Res} = \sqrt{\frac{\sum_i (Res_i)^2}{N_{pos} + N_{neg} - 7}}$$

$$(10^6) \cdot \sigma_{Res} = 112 \quad \mu g$$



**Inhouse Centrifuge (29 Inch Radius, Optical Encoder, Arm Tapped,  
Accelerometer = 2  
SF = 0.244380  
Date = 1.012193**

**Random Sequence, Load Resistor Doubled to 1K)**

$$\sigma_{Res} = 1.116841 \cdot 10^{-4}$$

**Standard Deviation of Residuals**

$$\mu = \frac{\max(|Res|)}{\sigma_{Res}}$$

$$\mu = 1.587066$$

**Normalized Magnitude of  
Largest Residual**

$$N = N_{neg} + N_{pos}$$

$$N = 24$$

**Total Number of Readings**

$$\mu_c = 1.25 + \ln\left(\sqrt{\frac{N}{3}}\right)$$

$$\mu_c = 2.289721$$

**Confidence Limit Check Value**

$$K = \begin{bmatrix} K_3 \\ K_{oq} \\ K_2 \\ C_n \\ C_p \\ K_{0n} \\ K_{0p} \end{bmatrix}$$

$$i = 0 \dots \text{rows}(K) - 1$$

$$d = A(a)^{-1}$$

$$\sigma_{K_i} = \sigma_{Res} \cdot \sqrt{d_{i,i}}$$

$$\sigma_K = \begin{bmatrix} \sigma K_3 \\ \sigma K_{oq} \\ \sigma K_2 \\ \sigma C_n \\ \sigma C_p \\ \sigma K_{0n} \\ \sigma K_{0p} \end{bmatrix} = \begin{bmatrix} \sigma K_3 \\ \sigma K_{oq} \\ \sigma K_2 \\ \sigma C_n \\ \sigma C_p \\ \sigma K_{0n} \\ \sigma K_{0p} \end{bmatrix} = \begin{bmatrix} 4.690934 \cdot 10^{-8} \\ 2.31364 \cdot 10^{-6} \\ 3.456104 \cdot 10^{-7} \\ 3.502335 \cdot 10^{-5} \\ 3.496539 \cdot 10^{-5} \\ 1.529488 \cdot 10^{-4} \\ 1.527066 \cdot 10^{-4} \end{bmatrix}$$

**Standard Deviations of  
Each Coefficient**

$$f = N - \text{rows}(K)$$

$$f = 17$$

**Number of Degrees of Freedom**

$$t = 1.96 + \frac{2.392}{(f - 1.082)}$$

$$t = 2.11027$$

**Student's t for P=95% Confidence**

$$K_{2lower} = K_2 - \frac{t \cdot \sigma K_2}{\sqrt{N}}$$

$$K_2 = -3.626 \cdot 10^{-7}$$

$$K_{2upper} = K_2 + \frac{t \cdot \sigma K_2}{\sqrt{N}}$$

$$K_{2min} = \text{if}(|K_{2lower}| < |K_{2upper}|, K_{2lower}, K_{2upper})$$

$$K_{2max} = \text{if}(|K_{2lower}| < |K_{2upper}|, K_{2upper}, K_{2lower})$$

**95% Confidence level K2 Lies Within the Range of:**

$$K_{2min} = -2.138 \cdot 10^{-7} \leq K_2 \leq K_{2max} = -5.115 \cdot 10^{-7}$$

**Accel\_and\_Run = 2.14**

Inhouse Centrifuge (29 Inch Radius, 600 Tooth Wheel,  
 Accelerometer = 2  
 SF = 0.244380  
 Date = 1.012293  
 Random Sequence, Load Resistor Doubled to 1K)

i	Raw Data Pair		Corrected CF Input (g)	Accel Output (g)	Residuals (g)
	Hz	VDC	$a_i$	$s_i$	$Res_i$
0	1908.4	-7.33983	-30.028231	-30.034495	0.000078
1	1827.1	-6.72775	-27.524255	-27.529872	0.000007
2	1742.1	-6.11632	-25.022869	-25.027907	-0.000037
3	1652.7	-5.50469	-22.520550	-22.525125	-0.000106
4	1558.2	-4.89319	-20.018767	-20.022874	-0.000089
5	1457.5	-4.28118	-17.514916	-17.518537	0.000023
6	1349.4	-3.66972	-15.013168	-15.016450	0.000059
7	1231.8	-3.05803	-12.510404	-12.513422	0.000083
8	1101.8	-2.44674	-10.009133	-10.012030	0.000021
9	954.2	-1.83525	-7.507058	-7.509821	0.000025
10	779.1	-1.22371	-5.004692	-5.007406	-0.000012
11	550.9	-0.61217	-2.502283	-2.504992	-0.000053
12	550.9	0.61020	2.499254	2.496931	0.000089
13	779.1	1.22104	4.998633	4.996481	0.000053
14	954.2	1.83186	7.497969	7.495949	0.000130
15	1101.8	2.44255	9.997016	9.994885	-0.000068
16	1231.8	3.05308	12.495258	12.493166	-0.000156
17	1349.4	3.66408	14.994992	14.993371	0.000142
18	1457.5	4.27476	17.493712	17.492266	0.000094
19	1558.2	4.88594	19.994532	19.993207	-0.000067
20	1652.7	5.49674	22.493285	22.492594	0.000220
21	1742.1	6.10750	24.992575	24.991816	-0.000263
22	1827.1	6.71817	27.490933	27.490670	-0.000260
23	1908.4	7.32962	29.991878	29.992716	0.000265

$K_3$	$6.688986 \cdot 10^{-8}$
$K_{oq}$	$1.609665 \cdot 10^{-6}$
$K_2$	$-4.863549 \cdot 10^{-7}$
$C_n$	$-5.596286 \cdot 10^{-12}$
$C_p$	$-2.680930 \cdot 10^{-11}$
$K_{0n}$	$-2.641644 \cdot 10^{-3}$
$K_{0p}$	$-2.241493 \cdot 10^{-3}$

Iteration = 2

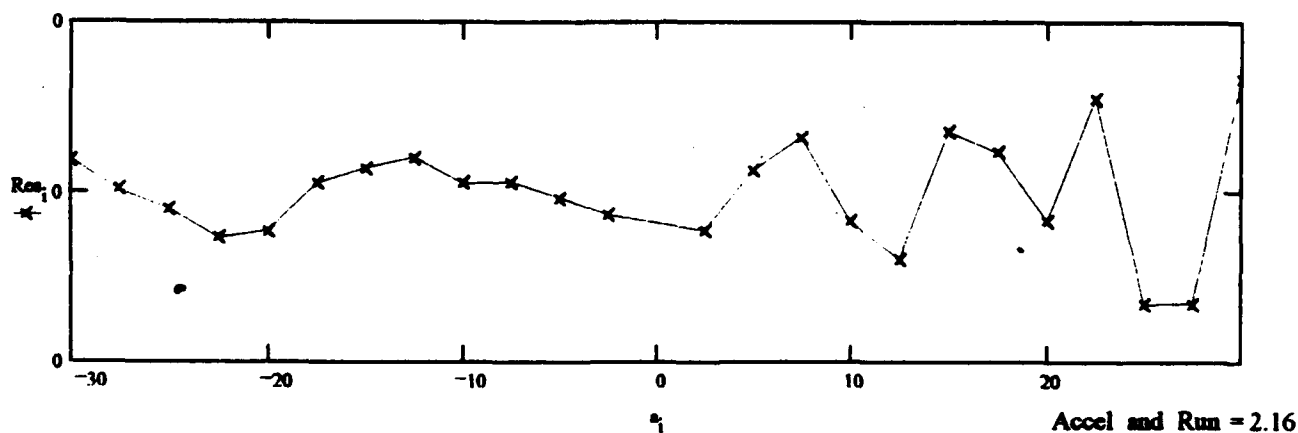
Sum Residuals (g)

$$\sum_i Res_i = -4.133943 \cdot 10^{-9}$$

Standard Deviation

$$\sigma_{Res} = \sqrt{\frac{\sum_i (Res_i)^2}{N_{pos} + N_{neg} - 7}}$$

$$(10^6) \cdot \sigma_{Res} = 151 \quad \mu g$$



Inhouse Centrifuge (29 Inch Radius, 600 Tooth Wheel,  
 Accelerometer = 2  
 SF = 0.244380  
 Date = 1.012293

Random Sequence, Load Resistor Doubled to 1K)

$$\sigma_{Res} = 1.509143 \cdot 10^{-4}$$

Standard Deviation of Residuals

$$\mu = \frac{\max(|Res|)}{\sigma_{Res}}$$

$$\mu = 1.756858$$

Normalized Magnitude of  
Largest Residual

$$N = N_{neg} + N_{pos}$$

$$N = 24$$

Total Number of Readings

$$\mu_c = 1.25 + \ln\left(\sqrt{\frac{N}{3}}\right)$$

$$\mu_c = 2.289721$$

Confidence Limit Check Value

$$K = \begin{bmatrix} K_3 \\ K_{oq} \\ K_2 \\ C_n \\ C_p \\ K_{0n} \\ K_{0p} \end{bmatrix}$$

$$i = 0 \dots \text{rows}(K) - 1$$

$$d = A(a)^{-1}$$

$$\sigma_{K_i} = \sigma_{Res} \sqrt{d_{i,i}}$$

$$\begin{bmatrix} \sigma K_3 \\ \sigma K_{oq} \\ \sigma K_2 \\ \sigma C_n \\ \sigma C_p \\ \sigma K_{0n} \\ \sigma K_{0p} \end{bmatrix} = \sigma_K$$

$$\begin{bmatrix} \sigma K_3 \\ \sigma K_{oq} \\ \sigma K_2 \\ \sigma C_n \\ \sigma C_p \\ \sigma K_{0n} \\ \sigma K_{0p} \end{bmatrix} =$$

$$\begin{bmatrix} 6.339116 \cdot 10^{-8} \\ 3.126394 \cdot 10^{-6} \\ 4.670668 \cdot 10^{-7} \\ 4.732459 \cdot 10^{-5} \\ 4.724743 \cdot 10^{-5} \\ 2.066645 \cdot 10^{-4} \\ 2.063422 \cdot 10^{-4} \end{bmatrix}$$

Standard Deviations of  
Each Coefficient

$$f = N - \text{rows}(K)$$

$$f = 17$$

Number of Degrees of Freedom

$$t = 1.96 + \frac{2.392}{(f - 1.082)}$$

$$t = 2.11027$$

Student's t for P=95% Confidence

$$K_{2lower} = K_2 - \frac{t \cdot \sigma K_2}{\sqrt{N}}$$

$$K_2 = -4.864 \cdot 10^{-7}$$

$$K_{2upper} = K_2 + \frac{t \cdot \sigma K_2}{\sqrt{N}}$$

$$K_{2min} = \text{if}(|K_{2lower}| < |K_{2upper}|, K_{2lower}, K_{2upper})$$

$$K_{2max} = \text{if}(|K_{2lower}| < |K_{2upper}|, K_{2upper}, K_{2lower})$$

95% Confidence level K2 Lies Within the Range of:

$$K_{2min} = -2.852 \cdot 10^{-7} \leq K_2 \leq K_{2max} = -6.875 \cdot 10^{-7}$$

Accel\_and\_Run = 2.16

Inhouse Centrifuge (29 Inch Radius, Optical Encoder, Arm Tapped,  
Accelerometer = 2  
SF = 0.122190  
Date = 1.012093  
Small g Step)

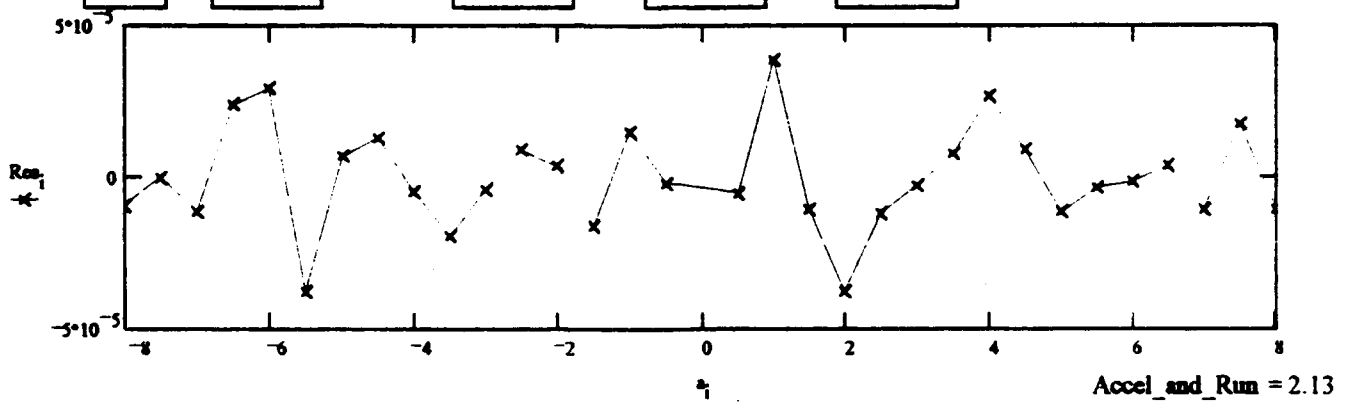
Raw Data Pair			Corrected CF Input	Accel Output	Residuals
			(g)	(g)	(g)
i	Hz <sub>i</sub>	VDC <sub>i</sub>	a <sub>i</sub>	s <sub>i</sub>	Res <sub>i</sub>
0	1642.5	-0.97873	-8.009056	-8.009903	-0.000009
1	1590.4	-0.91764	-7.509021	-7.509911	0.000000
2	1536.4	-0.85640	-7.007760	-7.008716	-0.000011
3	1480.5	-0.79522	-6.507099	-6.508078	0.000024
4	1422.5	-0.73415	-6.007242	-6.008274	0.000029
5	1361.9	-0.67296	-5.506315	-5.507472	-0.000037
6	1298.5	-0.61177	-5.005581	-5.006752	0.000007
7	1231.9	-0.55065	-4.505277	-4.506498	0.000013
8	1161.4	-0.48945	-4.004370	-4.005663	-0.000004
9	1086.4	-0.42831	-3.503887	-3.505246	-0.000019
10	1005.8	-0.36714	-3.003266	-3.004657	-0.000004
11	918.2	-0.30600	-2.502910	-2.504329	0.000009
12	821.3	0.24487	2.002508	2.003969	0.000004
13	711.2	-0.18366	-1.501599	-1.503110	-0.000016
14	580.7	-0.12251	-1.001093	-1.002594	0.000015
15	410.6	-0.06134	-0.500505	-0.502038	-0.000002
16	410.6	0.06087	0.499943	0.498183	-0.000005
17	580.7	0.12198	0.999967	0.998240	0.000039
18	711.2	0.18306	1.499912	1.498118	-0.000010
19	821.3	0.24419	2.000257	1.998412	-0.000037
20	918.2	0.30526	2.500096	2.498249	-0.000012
21	1005.8	0.36633	2.999891	2.998019	-0.000003
22	1086.4	0.42743	3.499949	3.498052	0.000008
23	1161.4	0.48851	3.999869	3.997954	0.000027
24	1231.9	0.54964	4.500213	4.498240	0.000009
25	1298.5	0.61070	4.999955	4.997921	-0.000011
26	1361.9	0.67181	5.500126	5.498060	-0.000003
27	1422.5	0.73294	6.000490	5.998388	-0.000001
28	1480.5	0.79395	6.499785	6.497651	0.000004
29	1536.4	0.85505	6.999883	6.997700	-0.000011
30	1590.4	0.91623	7.500581	7.498396	0.000018
31	1642.5	0.97725	8.000054	7.997815	-0.000011

Coefficients	
K <sub>3</sub>	1.132193·10 <sup>-6</sup>
K <sub>oq</sub>	-1.824557·10 <sup>-3</sup>
K <sub>2</sub>	1.714272·10 <sup>-6</sup>
C <sub>a</sub>	1.715596·10 <sup>-11</sup>
C <sub>p</sub>	-8.798545·10 <sup>-12</sup>
K <sub>0n</sub>	-1.535946·10 <sup>-3</sup>
K <sub>0p</sub>	-1.750371·10 <sup>-3</sup>

Iteration = 2

Sum Residuals (g)  
 $\sum_i Res_i = -1.706248 \cdot 10^{-9}$

Standard Deviation  
$$\sigma_{Res} = \sqrt{\frac{\sum_i (Res_i)^2}{N_{pos} + N_{neg} - 7}}$$
  
(10<sup>6</sup>)·σ<sub>Res</sub> = 19 μg





# Inhouse Centrifuge (29 Inch Radius, Optical Encoder, Arm Tapped, Small g Step)

Accelerometer = 2

SF = 0.122190

Date = 1.012093

$$\sigma_{Res} = 1.897102 \cdot 10^{-5}$$

Standard Deviation of Residuals

$$\mu = \frac{\max(|Res|)}{\sigma_{Res}}$$

$$\mu = 2.047662$$

Normalized Magnitude of Largest Residual

$$N = N_{neg} + N_{pos}$$

$$N = 32$$

Total Number of Readings

$$\mu_c = 1.25 + \ln\left(\sqrt{\frac{N}{3}}\right)$$

$$\mu_c = 2.433562$$

Confidence Limit Check Value

$$K = \begin{bmatrix} K_3 \\ K_{oq} \\ K_2 \\ C_n \\ C_p \\ K_{On} \\ K_{Op} \end{bmatrix}$$

$$i = 0 \dots \text{rows}(K) - 1$$

$$d = A(a)^{-1}$$

$$\sigma_{K_i} = \sigma_{Res} \sqrt{d_{i,i}}$$

$$\begin{bmatrix} \sigma K_3 \\ \sigma K_{oq} \\ \sigma K_2 \\ \sigma C_n \\ \sigma C_p \\ \sigma K_{On} \\ \sigma K_{Op} \end{bmatrix} = \sigma_K \begin{bmatrix} \sigma K_3 \\ \sigma K_{oq} \\ \sigma K_2 \\ \sigma C_n \\ \sigma C_p \\ \sigma K_{On} \\ \sigma K_{Op} \end{bmatrix} = \begin{bmatrix} 3.556997 \cdot 10^{-7} \\ 4.592848 \cdot 10^{-6} \\ 7.091359 \cdot 10^{-7} \\ 1.818123 \cdot 10^{-5} \\ 1.815466 \cdot 10^{-5} \\ 2.076137 \cdot 10^{-5} \\ 2.073411 \cdot 10^{-5} \end{bmatrix}$$

Standard Deviations of Each Coefficient

$$f = N - \text{rows}(K)$$

$$f = 25$$

Number of Degrees of Freedom

$$t = 1.96 + \frac{2.392}{(f - 1.082)}$$

$$t = 2.060008$$

Student's t for P=95% Confidence

$$K_{2lower} = K_2 - \frac{t \cdot \sigma K_2}{\sqrt{N}}$$

$$K_2 = 1.714 \cdot 10^{-6}$$

$$K_{2upper} = K_2 + \frac{t \cdot \sigma K_2}{\sqrt{N}}$$

$$K_{2min} = \text{if}(|K_{2lower}| < |K_{2upper}|, K_{2lower}, K_{2upper})$$

$$K_{2max} = \text{if}(|K_{2lower}| < |K_{2upper}|, K_{2upper}, K_{2lower})$$

95% Confidence level K2 Lies Within the Range of:

$$K_{2min} = 1.456 \cdot 10^{-6} \leq K_2 \leq 1.973 \cdot 10^{-6} = K_{2max}$$

Accel\_and\_Run = 2.13

## Inhouse Centrifuge (29 Inch Radius, 600 Tooth Wheel,

Accelerometer = 3

SF = 0.197702

Date = 1.051093

Random Sequence, 1K Load)

i	Raw Data Pair		Corrected CF Input	Accel Output	Residuals
	Hz	VDC	(g)	(g)	(g)
0	1908.4	-5.93365	-30.004572	-30.013176	-0.000018
1	1827.2	-5.43925	-27.505579	-27.512437	0.000249
2	1742.2	-4.94495	-25.006023	-25.012203	-0.000375
3	1652.8	-4.45025	-22.505529	-22.509946	0.000252
4	1558.2	-3.95540	-20.002994	-20.006930	-0.000243
5	1457.6	-3.46105	-17.503518	-17.506443	-0.000059
6	1349.5	-2.96660	-15.003563	-15.005450	0.000292
7	1231.9	-2.47214	-12.502577	-12.504407	-0.000205
8	1101.8	-1.97745	-10.001247	-10.002200	0.000238
9	954.2	-1.48320	-7.501143	-7.502219	-0.000206
10	779.1	-0.98875	-5.000749	-5.001227	0.000175
11	550.9	-0.49444	-2.500312	-2.500942	-0.000101
12	550.9	0.49449	2.500645	2.501195	0.000152
13	779.1	0.98879	5.001415	5.001429	-0.000297
14	954.2	1.48320	7.502142	7.502219	-0.000101
15	1101.8	1.97755	10.002579	10.002706	0.000120
16	1231.9	2.47215	12.504242	12.504457	0.000407
17	1349.5	2.96650	15.005562	15.004944	-0.000208
18	1457.6	3.46084	17.505850	17.505381	0.000167
19	1558.2	3.95490	20.005660	20.004401	-0.000396
20	1652.8	4.44975	22.508527	22.507416	-0.000031
21	1742.2	4.94427	25.009355	25.008763	0.000687
22	1827.2	5.43816	27.509244	27.506923	-0.000870
23	1908.4	5.93250	30.008569	30.007360	0.000374

## Coefficients

$K_3$	$9.911501 \cdot 10^{-8}$
$K_{0q}$	$4.050143 \cdot 10^{-7}$
$K_2$	$-5.614841 \cdot 10^{-6}$
$C_n$	$-3.346524 \cdot 10^{-9}$
$C_p$	$2.278424 \cdot 10^{-8}$
$K_{0n}$	$-4.902116 \cdot 10^{-4}$
$K_{0p}$	$4.289551 \cdot 10^{-4}$

Iteration = 1

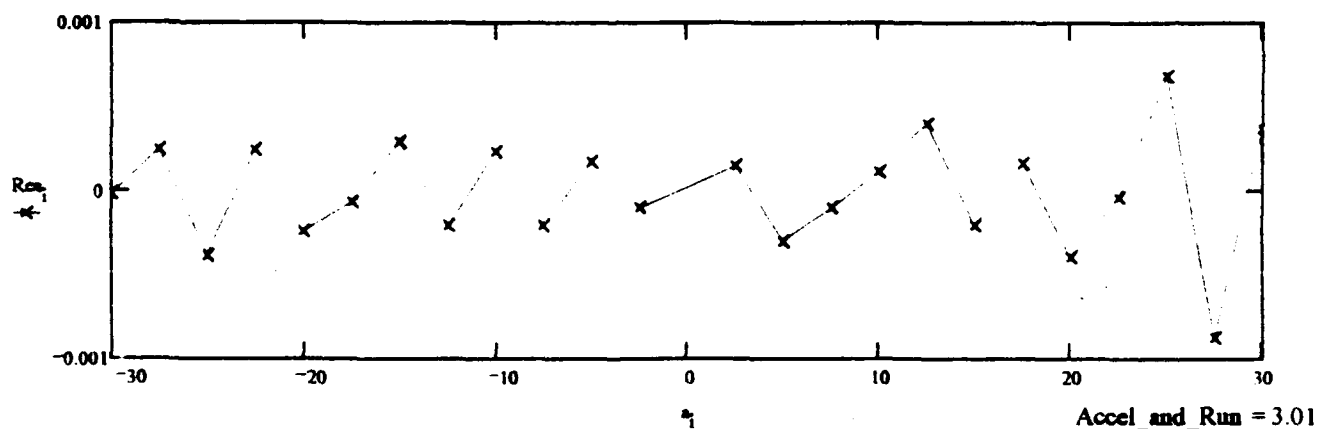
## Sum Residuals (g)

$$\sum_i Res_i = 0.000005$$

## Standard Deviation

$$\sigma_{Res} = \sqrt{\frac{\sum_i (Res_i)^2}{N_{pos} + N_{neg} - 7}}$$

$$(10^6) \cdot \sigma_{Res} = 383 \quad \mu g$$



# Inhouse Centrifuge (29 Inch Radius, 600 Tooth Wheel,

Accelerometer = 3

SF = 0.197702

Date = 1.051093

Random Sequence, 1K Load)

$$\sigma_{Res} = 3.832485 \cdot 10^{-4}$$

Standard Deviation of Residuals

$$\mu = \frac{\max(|Res|)}{\sigma_{Res}}$$

$$\mu = 2.269988$$

Normalized Magnitude of  
Largest Residual

$$N = N_{neg} + N_{pos}$$

$$N = 24$$

Total Number of Readings

$$\mu_c = 1.25 + \ln\left(\sqrt{\frac{N}{3}}\right)$$

$$\mu_c = 2.289721$$

Confidence Limit Check Value

$$K = \begin{bmatrix} K_3 \\ K_{oq} \\ K_2 \\ C_n \\ C_p \\ K_{0n} \\ K_{0p} \end{bmatrix}$$

$$i = 0 \dots \text{rows}(K) - 1$$

$$d = A(a)^{-1}$$

$$\sigma_{K_i} = \sigma_{Res} \sqrt{d_{i,i}}$$

$$\begin{bmatrix} \sigma K_3 \\ \sigma K_{oq} \\ \sigma K_2 \\ \sigma C_n \\ \sigma C_p \\ \sigma K_{0n} \\ \sigma K_{0p} \end{bmatrix} = \sigma_K$$

$$\begin{bmatrix} \sigma K_3 \\ \sigma K_{oq} \\ \sigma K_2 \\ \sigma C_n \\ \sigma C_p \\ \sigma K_{0n} \\ \sigma K_{0p} \end{bmatrix} = \begin{bmatrix} 1.610529 \cdot 10^{-7} \\ 7.942145 \cdot 10^{-6} \\ 1.18631 \cdot 10^{-6} \\ 1.200959 \cdot 10^{-4} \\ 1.201174 \cdot 10^{-4} \\ 5.243873 \cdot 10^{-4} \\ 5.244774 \cdot 10^{-4} \end{bmatrix}$$

Standard Deviations of  
Each Coefficient

$$f = N - \text{rows}(K)$$

$$f = 17$$

Number of Degrees of Freedom

$$t = 1.96 + \frac{2.392}{(f - 1.082)}$$

$$t = 2.11027$$

Student's t for P = 95% Confidence

$$K_{2lower} = K_2 - \frac{t \cdot \sigma K_2}{\sqrt{N}}$$

$$K_2 = -5.615 \cdot 10^{-6}$$

$$K_{2upper} = K_2 + \frac{t \cdot \sigma K_2}{\sqrt{N}}$$

$$K_{2min} = \text{if}(|K_{2lower}| < |K_{2upper}|, K_{2lower}, K_{2upper})$$

$$K_{2max} = \text{if}(|K_{2lower}| < |K_{2upper}|, K_{2upper}, K_{2lower})$$

95% Confidence level K2 Lies Within the Range of:

$$K_{2min} = -5.104 \cdot 10^{-6} \leq K_2 \leq K_{2max} = -6.126 \cdot 10^{-6}$$

Accel\_and\_Run = 3.01

Inhouse Centrifuge (29 Inch Radius, 600 Tooth Wheel,  
Accelerometer = 3  
SF = 0.197702  
Date = 1.051193  
Random Sequence, 1K Load)

i	Raw Data Pair		Corrected CF Input	Accel Output	Residuals
	Hz <sub>i</sub>	VDC <sub>i</sub>	(g)	(g)	(g)
0	1908.4	-5.93368	-30.003016	-30.013328	-0.000186
1	1827.2	-5.43922	-27.504152	-27.512285	0.000512
2	1742.2	-4.94499	-25.004727	-25.012405	-0.000393
3	1652.8	-4.45030	-22.504362	-22.510198	0.000211
4	1558.2	-3.95545	-20.001957	-20.007183	-0.000292
5	1457.6	-3.46110	-17.502610	-17.506696	-0.000139
6	1349.5	-2.96660	-15.002785	-15.005450	0.000421
7	1231.9	-2.47213	-12.501928	-12.504356	-0.000073
8	1101.8	-1.97750	-10.000728	-10.002453	0.000029
9	954.2	-1.48321	-7.500754	-7.502270	-0.000232
10	779.1	-0.98875	-5.000489	-5.001227	0.000209
11	550.9	-0.49445	-2.500182	-2.500993	-0.000068
12	550.9	0.49450	2.500492	2.501246	0.000101
13	779.1	0.98890	5.001109	5.001985	0.000034
14	954.2	1.48330	7.501684	7.502725	0.000221
15	1101.8	1.97755	10.001968	10.002706	-0.000050
16	1231.9	2.47213	12.503478	12.504356	0.000136
17	1349.5	2.96648	15.004644	15.004843	-0.000484
18	1457.6	3.46085	17.504779	17.505431	0.000043
19	1558.2	3.95505	20.004436	20.005159	0.000204
20	1652.8	4.44977	22.507151	22.507518	-0.000043
21	1742.2	4.94421	25.007826	25.008460	0.000352
22	1827.2	5.43822	27.507562	27.507227	-0.000468
23	1908.4	5.93240	30.006735	30.006854	0.000157

Coefficients	
$K_3$	$-1.464697 \cdot 10^{-8}$
$K_{oq}$	$5.191934 \cdot 10^{-6}$
$K_2$	$-5.747299 \cdot 10^{-6}$
$C_n$	$= 3.934141 \cdot 10^{-9}$
$C_p$	$3.416480 \cdot 10^{-10}$
$K_{0n}$	$-6.743202 \cdot 10^{-4}$
$K_{0p}$	$8.580259 \cdot 10^{-4}$

Iteration = 1

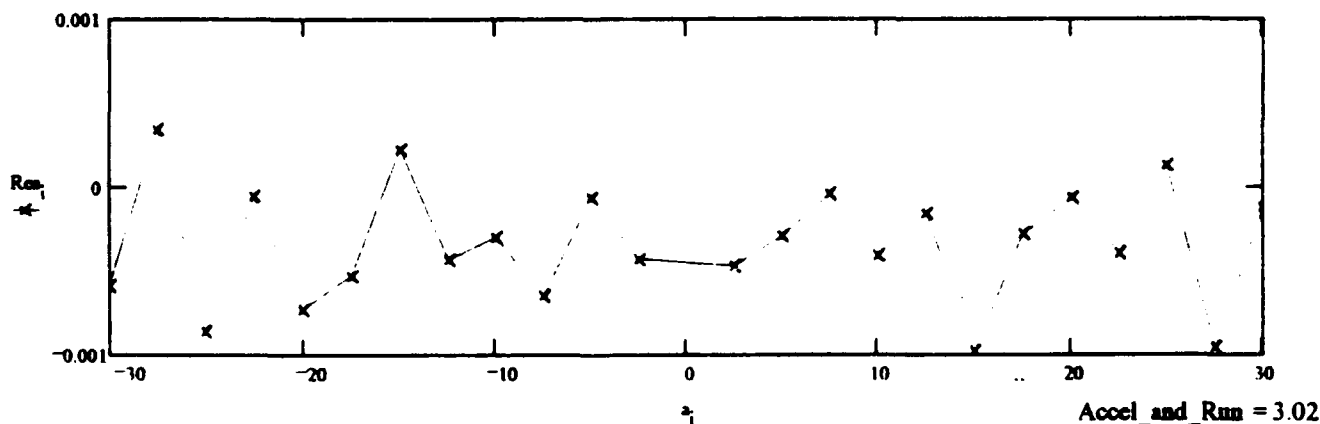
Sum Residuals (g)

$$\sum_i Res_i = -7.006273 \cdot 10^{-7}$$

Standard Deviation

$$\sigma_{Res} = \sqrt{\frac{\sum_i (Res_i)^2}{N_{pos} + N_{neg} - 7}}$$

$$(10^6) \cdot \sigma_{Res} = 308 \mu g$$



Inhouse Centrifuge (29 Inch Radius, 600 Tooth Wheel,  
Accelerometer = 3  
SF = 0.197702  
Date = 1.051193

Random Sequence, 1K Load)

$$\sigma_{Res} = 3.082477 \cdot 10^{-4}$$

Standard Deviation of Residuals

$$\mu = \frac{\max(|Res|)}{\sigma_{Res}}$$

$$\mu = 1.662378$$

Normalized Magnitude of  
Largest Residual

$$N = N_{neg} + N_{pos}$$

$$N = 24$$

Total Number of Readings

$$\mu_c = 1.25 + \ln\left(\sqrt{\frac{N}{3}}\right)$$

$$\mu_c = 2.289721$$

Confidence Limit Check Value

$$K = \begin{bmatrix} K_3 \\ K_{oq} \\ K_2 \\ C_n \\ C_p \\ K_{0n} \\ K_{0p} \end{bmatrix}$$

$$i = 0 \dots \text{rows}(K) - 1$$

$$d = A(a)^{-1}$$

$$\sigma_{K_i} = \sigma_{Res} \sqrt{d_{i,i}}$$

$$\begin{bmatrix} \sigma K_3 \\ \sigma K_{oq} \\ \sigma K_2 \\ \sigma C_n \\ \sigma C_p \\ \sigma K_{0n} \\ \sigma K_{0p} \end{bmatrix} = \sigma_K$$

$$\begin{bmatrix} \sigma K_3 \\ \sigma K_{oq} \\ \sigma K_2 \\ \sigma C_n \\ \sigma C_p \\ \sigma K_{0n} \\ \sigma K_{0p} \end{bmatrix} =$$

$$\begin{bmatrix} 1.295572 \cdot 10^{-7} \\ 6.388609 \cdot 10^{-6} \\ 9.542596 \cdot 10^{-7} \\ 9.659947 \cdot 10^{-5} \\ 9.66156 \cdot 10^{-3} \\ 4.217685 \cdot 10^{-4} \\ 4.218359 \cdot 10^{-4} \end{bmatrix}$$

Standard Deviations of  
Each Coefficient

$$f = N - \text{rows}(K)$$

$$f = 17$$

Number of Degrees of Freedom

$$t = 1.96 + \frac{2.392}{(f - 1.082)}$$

$$t = 2.11027$$

Student's t for P = 95% Confidence

$$K_{2lower} = K_2 - \frac{t \cdot \sigma K_2}{\sqrt{N}}$$

$$K_2 = -5.747 \cdot 10^{-6}$$

$$K_{2upper} = K_2 + \frac{t \cdot \sigma K_2}{\sqrt{N}}$$

$$K_{2min} = \text{if}(|K_{2lower}| < |K_{2upper}|, K_{2lower}, K_{2upper})$$

$$K_{2max} = \text{if}(|K_{2lower}| < |K_{2upper}|, K_{2upper}, K_{2lower})$$

95% Confidence level K2 Lies Within the Range of:

$$K_{2min} = -5.336 \cdot 10^{-6} \leq K_2 \leq K_{2max} = -6.158 \cdot 10^{-6}$$

$$\text{Accel\_and\_Run} = 3.02$$

Inhouse Centrifuge (29 Inch Radius, 600 Tooth Wheel,  
Accelerometer = 3  
SF = 0.197691  
Date = 1.051293  
Random Sequence, 1K Load)

i	Raw Data Pair		Corrected CF Input (g)	Accel Output (g)	Residuals (g)
	H <sub>r</sub>	VDC <sub>i</sub>	a <sub>i</sub>	s <sub>i</sub>	Res <sub>i</sub>
0	1908.4	-5.93326	-30.004419	-30.012798	-0.000104
1	1827.2	-5.43890	-27.505439	-27.512128	0.000244
2	1742.2	-4.94463	-25.005896	-25.011913	-0.000290
3	1652.8	-4.45000	-22.505414	-22.509877	0.000192
4	1558.2	-3.95514	-20.002892	-20.006677	-0.000074
5	1457.6	-3.46084	-17.503428	-17.506310	0.000012
6	1349.5	-2.96645	-15.003486	-15.005488	0.000197
7	1231.9	-2.47197	-12.502513	-12.504211	-0.000077
8	1101.8	-1.97738	-10.001196	-10.002377	-0.000024
9	954.2	-1.48310	-7.501105	-7.502112	-0.000203
10	779.1	-0.98870	-5.000723	-5.001239	0.000040
11	550.9	-0.49435	-2.500299	-2.500620	0.000090
12	550.9	0.49445	2.500539	2.501125	0.000076
13	779.1	0.98875	5.001203	5.001492	-0.000154
14	954.2	1.48315	7.501824	7.502365	0.000204
15	1101.8	1.97735	10.002155	10.002226	-0.000123
16	1231.9	2.47190	12.503712	12.503857	0.000126
17	1349.5	2.96623	15.004925	15.004376	-0.000366
18	1457.6	3.46053	17.505107	17.504742	0.000045
19	1558.2	3.95465	20.004811	20.004198	0.000044
20	1652.8	4.44940	22.507572	22.506841	0.000189
21	1742.2	4.94375	25.008294	25.007461	0.000362
22	1827.2	5.43770	27.508076	27.506057	-0.000541
23	1908.4	5.93185	30.007296	30.005665	0.000135

$$\begin{bmatrix} K_3 \\ K_{oq} \\ K_2 \\ C_n \\ C_p \\ K_{On} \\ K_{Op} \end{bmatrix} = \begin{bmatrix} 4.204958 \cdot 10^{-8} \\ 1.856203 \cdot 10^{-6} \\ -5.671462 \cdot 10^{-6} \\ -1.134494 \cdot 10^{-8} \\ -3.364741 \cdot 10^{-9} \\ -3.624894 \cdot 10^{-4} \\ 5.334978 \cdot 10^{-4} \end{bmatrix}$$

Iteration = 1

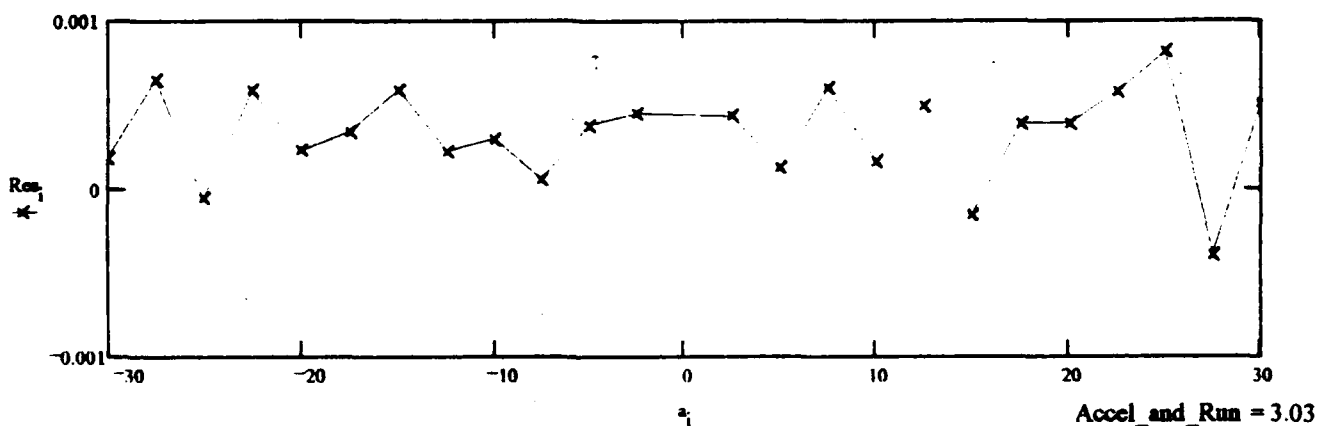
Sum Residuals (g)

$$\sum_i \text{Res}_i = 0.000002$$

Standard Deviation

$$\sigma_{\text{Res}} = \sqrt{\frac{\sum_i (\text{Res}_i)^2}{N_{\text{pos}} + N_{\text{neg}} - 7}}$$

$$(10^6) \cdot \sigma_{\text{Res}} = 244 \mu\text{g}$$



**Inhouse Centrifuge (29 Inch Radius, 600 Tooth Wheel,**  
**Accelerometer = 3**  
**SF = 0.197691**  
**Date = 1.051293**

**Random Sequence, 1K Load)**

$$\sigma_{Res} = 2.437692 \cdot 10^{-4}$$

**Standard Deviation of Residuals**

$$\mu = \frac{\max(|Res|)}{\sigma_{Res}}$$

$$\mu = 2.217688$$

**Normalized Magnitude of  
Largest Residual**

$$N = N_{neg} + N_{pos}$$

$$N = 24$$

**Total Number of Readings**

$$\mu_c = 1.25 + \ln\left(\sqrt{\frac{N}{3}}\right)$$

$$\mu_c = 2.289721$$

**Confidence Limit Check Value**

$$K = \begin{bmatrix} K_3 \\ K_{oq} \\ K_2 \\ C_n \\ C_p \\ K_{On} \\ K_{Op} \end{bmatrix}$$

$$i = 0 \dots \text{rows}(K) - 1$$

$$d = A(a)^{-1}$$

$$\sigma_{K_i} = \sigma_{Res} \sqrt{d_{i,i}}$$

$$\begin{bmatrix} \sigma K_3 \\ \sigma K_{oq} \\ \sigma K_2 \\ \sigma C_n \\ \sigma C_p \\ \sigma K_{On} \\ \sigma K_{Op} \end{bmatrix} = \sigma_K$$

$$\begin{bmatrix} \sigma K_3 \\ \sigma K_{oq} \\ \sigma K_2 \\ \sigma C_n \\ \sigma C_p \\ \sigma K_{On} \\ \sigma K_{Op} \end{bmatrix}$$

$$\begin{bmatrix} 1.024467 \cdot 10^{-7} \\ 5.051924 \cdot 10^{-6} \\ 7.546004 \cdot 10^{-7} \\ 7.639196 \cdot 10^{-5} \\ 7.640183 \cdot 10^{-5} \\ 3.3355 \cdot 10^{-4} \\ 3.335912 \cdot 10^{-4} \end{bmatrix}$$

**Standard Deviations of  
Each Coefficient**

$$f = N - \text{rows}(K)$$

$$f = 17$$

**Number of Degrees of Freedom**

$$t = 1.96 + \frac{2.392}{(f - 1.082)}$$

$$t = 2.11027$$

**Student's t for P = 95% Confidence**

$$K_{2lower} = K_2 - \frac{t \cdot \sigma K_2}{\sqrt{N}}$$

$$K_2 = -5.671 \cdot 10^{-6}$$

$$K_{2upper} = K_2 + \frac{t \cdot \sigma K_2}{\sqrt{N}}$$

$$K_{2min} = \text{if}(|K_{2lower}| < |K_{2upper}|, K_{2lower}, K_{2upper})$$

$$K_{2max} = \text{if}(|K_{2lower}| < |K_{2upper}|, K_{2upper}, K_{2lower})$$

**95% Confidence level K2 Lies Within the Range of:**

$$K_{2min} = -5.346 \cdot 10^{-6} \leq K_2 \leq K_{2max} = -5.997 \cdot 10^{-6}$$

**Accel\_and\_Run = 3.03**

Inhouse Centrifuge (29 Inch Radius, 600 Tooth Wheel,  
 Accelerometer = 3  
 SF = 0.222361  
 Date = 1.051393  
 Random Sequence, 2K Load, -32.5 to -40.0 g Removed)

Case = 1.051393

	Raw		Corrected	Accel	
I	Data Pair		CF Input	Output	Residuals
			(g)	(g)	(g)
i	Hz <sub>i</sub>	VDC <sub>i</sub>	a <sub>i</sub>	s <sub>i</sub>	Res <sub>i</sub>
0	1908.4	-6.67316	-29.999813	-30.010411	-0.000132
1	1827.2	-6.11714	-27.501216	-27.509888	0.000362
2	1742.2	-5.56125	-25.002057	-25.009950	-0.000194
3	1652.8	-5.00500	-22.501959	-22.508393	0.000032
4	1558.2	-4.44842	-19.999822	-20.005352	-0.000190
5	1457.6	-3.89245	-17.500741	-17.505054	0.000016
6	1349.5	-3.33644	-15.001183	-15.004576	0.000043
7	1231.9	-2.78025	-12.500594	-12.503289	-0.000030
8	1101.8	-2.22395	-9.999661	-10.001507	0.000178
9	954.2	-1.66805	-7.499953	-7.501523	-0.000054
10	779.1	-1.11205	-4.999955	-5.001091	0.000012
11	550.9	-0.55610	-2.499915	-2.500883	-0.000046
12	550.9	0.55620	2.500476	2.501332	0.000077
13	779.1	1.11225	5.001078	5.001990	-0.000033
14	954.2	1.66834	7.501636	7.502828	0.000233
15	1101.8	2.22425	10.001905	10.002856	-0.000018
16	1231.9	2.78050	12.503399	12.504413	0.000044
17	1349.5	3.33638	15.004549	15.005205	-0.000301
18	1457.6	3.89258	17.504669	17.505638	0.000043
19	1558.2	4.44842	20.004310	20.005352	0.000171
20	1652.8	5.00485	22.507009	22.507718	-0.000077
21	1742.2	5.56093	25.007668	25.008511	0.000175
22	1827.2	6.11663	27.507388	27.507595	-0.000302
23	1908.4	6.67240	30.006545	30.006993	0.000142

Coefficients	
K <sub>3</sub>	-5.473954·10 <sup>-8</sup>
K <sub>oq</sub>	6.641966·10 <sup>-6</sup>
K <sub>2</sub>	-5.689936·10 <sup>-6</sup>
C <sub>a</sub>	= 2.300882·10 <sup>-8</sup>
C <sub>p</sub>	-1.296738·10 <sup>-9</sup>
K <sub>0n</sub>	-8.452660·10 <sup>-4</sup>
K <sub>Op</sub>	9.279894·10 <sup>-4</sup>

Iteration = 1

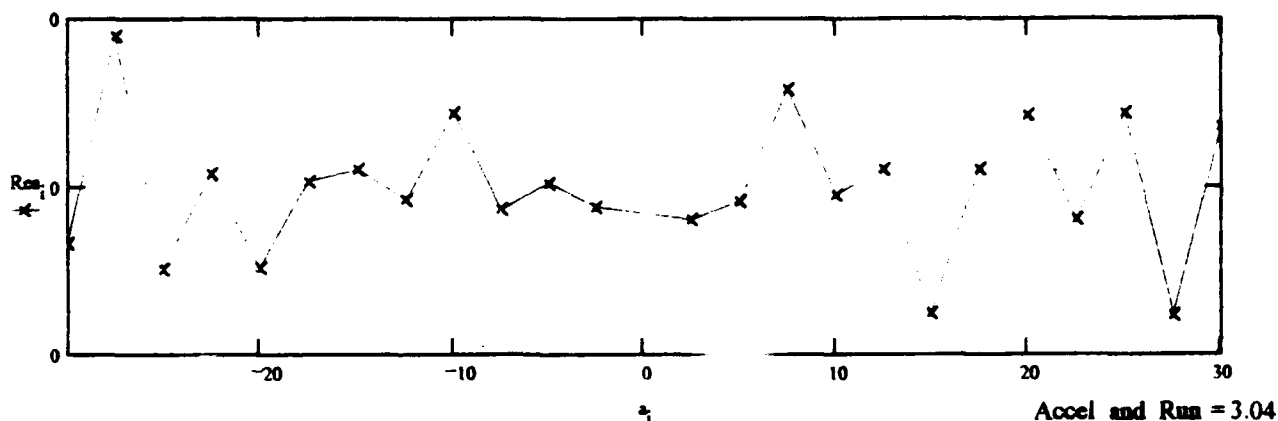
Sum Residuals (g)

$$\sum_i Res_i = -0.000005$$

Standard Deviation

$$\sigma_{Res} = \sqrt{\frac{\sum_i (Res_i)^2}{N_{pos} + N_{neg} - 7}}$$

$$(10^6) \cdot \sigma_{Res} = 187 \mu g$$





Inhouse Centrifuge (29 Inch Radius, 600 Tooth Wheel,  
 Accelerometer = 3  
 SF = 0.222361  
 Date = 1.051393  
 Random Sequence, 2K Load, -32.5 to -40.0 g Removed)

$$\sigma_{Res} = 1.872843 \cdot 10^{-4}$$

Standard Deviation of Residuals

$$\mu = \frac{\max(|Rcs|)}{\sigma_{Res}}$$

$$\mu = 1.930268$$

Normalized Magnitude of  
 Largest Residual

$$N = N_{neg} + N_{pos}$$

$$N = 24$$

Total Number of Readings

$$\mu_c = 1.25 + \ln\left(\sqrt{\frac{N}{3}}\right)$$

$$\mu_c = 2.289721$$

Confidence Limit Check Value

$$K = \begin{bmatrix} K_3 \\ K_{oq} \\ K_2 \\ C_n \\ C_p \\ K_{0n} \\ K_{0p} \end{bmatrix} \quad i = 0 \dots \text{rows}(K) - 1 \quad d = A(a)^{-1} \quad \sigma_{K_i} = \sigma_{Res} \cdot \sqrt{d_{i,i}}$$

$\sigma K_3$	$\sigma K_3$	$7.872934 \cdot 10^{-8}$
$\sigma K_{oq}$	$\sigma K_{oq}$	$3.882012 \cdot 10^{-6}$
$\sigma K_2$	$\sigma K_2$	$5.798521 \cdot 10^{-7}$
$\sigma C_n$	$\sigma C_n$	$5.869099 \cdot 10^{-5}$
$\sigma C_p$	$\sigma C_p$	$5.870873 \cdot 10^{-5}$
$\sigma K_{0n}$	$\sigma K_{0n}$	$2.562404 \cdot 10^{-4}$
$\sigma K_{0p}$	$\sigma K_{0p}$	$2.563145 \cdot 10^{-4}$

Standard Deviations of  
 Each Coefficient

$$f = N - \text{rows}(K)$$

$$f = 17$$

Number of Degrees of Freedom

$$t = 1.96 + \frac{2.392}{(f - 1.082)}$$

$$t = 2.11027$$

Student's t for P=95% Confidence

$$K_{2lower} = K_2 - \frac{t \cdot \sigma K_2}{\sqrt{N}}$$

$$K_2 = -5.690 \cdot 10^{-6}$$

$$K_{2upper} = K_2 + \frac{t \cdot \sigma K_2}{\sqrt{N}}$$

$$K_{2min} = \text{if}(|K_{2lower}| < |K_{2upper}|, K_{2lower}, K_{2upper})$$

$$K_{2max} = \text{if}(|K_{2lower}| < |K_{2upper}|, K_{2upper}, K_{2lower})$$

95% Confidence level K2 Lies Within the Range of:

$$K_{2min} = -5.440 \cdot 10^{-6} \leq K_2 \leq K_{2max} = -5.940 \cdot 10^{-6}$$

Accel\_and\_Run = 3.04

Inhouse Centrifuge (29 Inch Radius, 600 Tooth Wheel,  
Accelerometer = 3  
SF = 0.222361  
Date = 2.051393  
Random Sequence, 2K Load)

i	Raw Data Pair		Corrected CF Input	Accel Output	Residuals
	Hz <sub>i</sub>	VDC <sub>i</sub>	(g) a <sub>i</sub>	(g) s <sub>i</sub>	(g) Res <sub>i</sub>
0	1908.4	-6.67288	-30.005278	-30.009152	0.000038
1	1827.2	-6.11683	-27.506226	-27.508494	0.000422
2	1742.2	-5.56100	-25.006612	-25.008826	-0.000484
3	1652.8	-5.00474	-22.506059	-22.507224	-0.000163
4	1558.2	-4.44810	-20.003465	-20.003913	0.000029
5	1457.6	-3.89227	-17.503930	-17.504244	-0.000191
6	1349.5	-3.33622	-15.003916	-15.003587	0.000244
7	1231.9	-2.78012	-12.502871	-12.502704	-0.000014
8	1101.8	-2.22383	-10.001482	-10.000967	0.000323
9	954.2	-1.66800	-7.501320	-7.501299	-0.000129
10	779.1	-1.11196	-5.000866	-5.000686	0.000098
11	550.9	-0.55602	-2.500371	-2.500523	-0.000172
12	550.9	0.55606	2.500549	2.500703	0.000015
13	779.1	1.11200	5.001224	5.000866	-0.000230
14	954.2	1.66800	7.501855	7.501299	-0.000021
15	1101.8	2.22389	10.002197	10.001237	0.000095
16	1231.9	2.78000	12.503764	12.502164	0.000057
17	1349.5	3.33615	15.004988	15.003272	0.000595
18	1457.6	3.89184	17.505180	17.502310	0.000118
19	1558.2	4.44760	20.004894	20.001664	0.000426
20	1652.8	5.00339	22.507667	22.501152	-0.002225
21	1742.2	5.55992	25.008399	25.003969	0.000426
22	1827.2	6.11583	27.508191	27.503997	0.001130
23	1908.4	6.67115	30.007422	30.001372	-0.000381

K <sub>3</sub>	3.165048·10 <sup>-7</sup>
K <sub>oq</sub>	-1.060612·10 <sup>-5</sup>
K <sub>2</sub>	-5.446082·10 <sup>-6</sup>
C <sub>n</sub>	-6.081946·10 <sup>-9</sup>
C <sub>p</sub>	3.865849·10 <sup>-8</sup>
K <sub>0n</sub>	-7.111251·10 <sup>-6</sup>
K <sub>0p</sub>	2.335652·10 <sup>-4</sup>

Iteration = 1

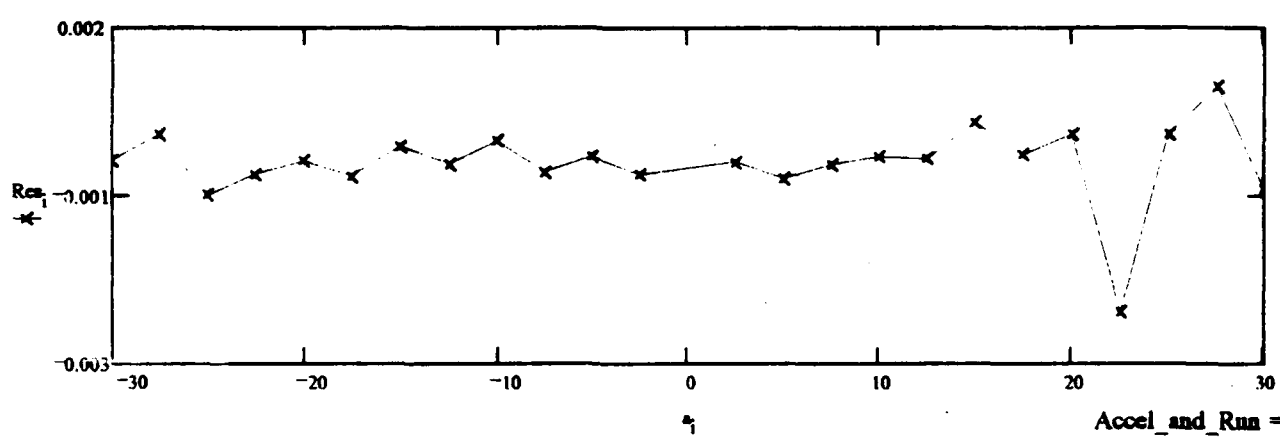
Sum Residuals (g)

$$\sum_i Res_i = 0.000009$$

Standard Deviation

$$\sigma_{Res} = \sqrt{\frac{\sum_i (Res_i)^2}{N_{pos} + N_{neg} - 7}}$$

$$(10^6) \cdot \sigma_{Res} = 680 \mu g$$



# Inhouse Centrifuge (29 Inch Radius, 600 Tooth Wheel,

Accelerometer = 3

SF = 0.222361

Date = 2.051393

Random Sequence, 2K Load)

$$\sigma_{Res} = 6.802586 \cdot 10^{-4}$$

Standard Deviation of Residuals

$$\mu = \frac{\max(|Res|)}{\sigma_{Res}}$$

$$\mu = 3.270233$$

Normalized Magnitude of  
Largest Residual

$$N = N_{neg} + N_{pos}$$

$$N = 24$$

Total Number of Readings

$$\mu_c = 1.25 + \ln\left(\sqrt{\frac{N}{3}}\right)$$

$$\mu_c = 2.289721$$

Confidence Limit Check Value

$$K = \begin{bmatrix} K_3 \\ K_{oq} \\ K_2 \\ C_n \\ C_p \\ K_{0n} \\ K_{0p} \end{bmatrix}$$

$$i = 0..rows(K) - 1$$

$$d = A(a)^{-1}$$

$$\sigma_{K_i} = \sigma_{Res} \cdot \sqrt{d_{i,i}}$$

$$\begin{bmatrix} \sigma K_3 \\ \sigma K_{oq} \\ \sigma K_2 \\ \sigma C_n \\ \sigma C_p \\ \sigma K_{0n} \\ \sigma K_{0p} \end{bmatrix} = \sigma_K = \begin{bmatrix} \sigma K_3 \\ \sigma K_{oq} \\ \sigma K_2 \\ \sigma C_n \\ \sigma C_p \\ \sigma K_{0n} \\ \sigma K_{0p} \end{bmatrix} = \begin{bmatrix} 2.85872 \cdot 10^{-7} \\ 1.409736 \cdot 10^{-5} \\ 2.105707 \cdot 10^{-6} \\ 2.131783 \cdot 10^{-4} \\ 2.131988 \cdot 10^{-4} \\ 9.308144 \cdot 10^{-4} \\ 9.309 \cdot 10^{-4} \end{bmatrix}$$

Standard Deviations of  
Each Coefficient

$$f = N - rows(K)$$

$$f = 17$$

Number of Degrees of Freedom

$$t = 1.96 + \frac{2.392}{(f - 1.082)}$$

$$t = 2.11027$$

Student's t for P = 95% Confidence

$$K_{2lower} = K_2 - \frac{t \cdot \sigma K_2}{\sqrt{N}}$$

$$K_2 = -5.446 \cdot 10^{-6}$$

$$K_{2upper} = K_2 + \frac{t \cdot \sigma K_2}{\sqrt{N}}$$

$$K_{2min} = \text{if}(|K_{2lower}| < |K_{2upper}|, K_{2lower}, K_{2upper})$$

$$K_{2max} = \text{if}(|K_{2lower}| < |K_{2upper}|, K_{2upper}, K_{2lower})$$

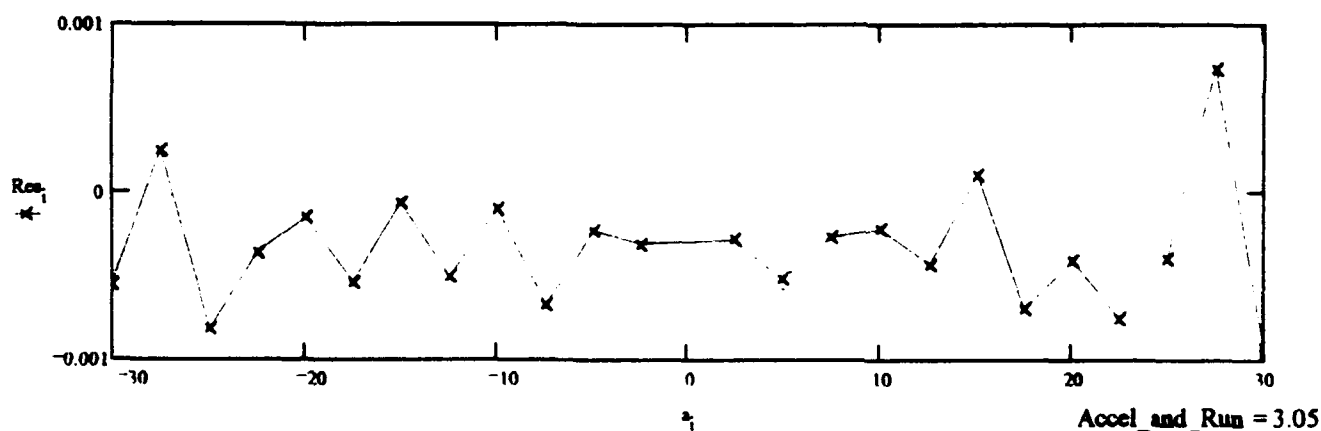
95% Confidence level K2 Lies Within the Range of:

$$K_{2min} = -4.539 \cdot 10^{-6} \leq K_2 \leq K_{2max} = -6.353 \cdot 10^{-6}$$

Accel\_and\_Run = 3.05

Inhouse Centrifuge (29 Inch Radius, 600 Tooth Wheel,  
 Accelerometer = 3  
 SF = 0.222361  
 Date = 2.051393  
 Random Sequence, 2K Load, 22.5 g Corrected)

i	Raw Data Pair		Corrected CF Input	Accel Output	Residuals	Coefficients
	Hz <sub>i</sub>	VDC <sub>i</sub>	(g)	(g)	(g)	
0	1908.4	-6.67288	-30.000300	-30.009152	-0.000156	$\begin{bmatrix} K_3 \\ K_{oq} \\ K_2 \\ C_n \\ C_p \\ K_{On} \\ K_{Op} \end{bmatrix} = \begin{bmatrix} 6.501588 \cdot 10^{-8} \\ 8.343724 \cdot 10^{-7} \\ -6.271763 \cdot 10^{-6} \\ -1.208650 \cdot 10^{-8} \\ 6.181111 \cdot 10^{-9} \\ -5.438267 \cdot 10^{-4} \\ 3.841042 \cdot 10^{-4} \end{bmatrix}$
1	1827.2	-6.11683	-27.501663	-27.508494	0.000440	
2	1742.2	-5.56100	-25.002464	-25.008826	-0.000360	
3	1652.8	-5.00474	-22.502325	-22.507224	-0.000016	
4	1558.2	-4.44810	-20.000147	-20.003913	0.000141	
5	1457.6	-3.89227	-17.501026	-17.504244	-0.000150	
6	1349.5	-3.33622	-15.001427	-15.003587	0.000203	
7	1231.9	-2.78012	-12.500797	-12.502704	-0.000126	
8	1101.8	-2.22383	-9.999823	-10.000967	0.000176	
9	954.2	-1.66800	-7.500075	-7.501299	-0.000252	
10	779.1	-1.11196	-5.000037	-5.000686	0.000081	Iteration = 1  Sum Residuals (g) $\sum_i Res_i = 0.000004$  Standard Deviation $\sigma_{Res} = \sqrt{\frac{\sum_i (Res_i)^2}{N_{pos} + N_{neg} - 7}}$  $(10^6) \cdot \sigma_{Res} = 317 \mu g$
11	550.9	-0.55602	-2.499956	-2.500523	0.000022	
12	550.9	0.55606	2.500311	2.500703	0.000041	
13	779.1	1.11200	5.000747	5.000866	-0.000137	
14	954.2	1.66800	7.501140	7.501299	0.000053	
15	1101.8	2.22389	10.001243	10.001237	0.000088	
16	1231.9	2.78000	12.502572	12.502164	-0.000069	
17	1349.5	3.33615	15.003557	15.003272	0.000335	
18	1457.6	3.89184	17.503511	17.502310	-0.000268	
19	1558.2	4.44760	20.002987	20.001664	-0.000052	
20	1652.8	5.00393	22.505521	22.503581	-0.000311	
21	1742.2	5.55992	25.006015	25.003969	-0.000047	
22	1827.2	6.11583	27.505569	27.503997	0.000804	
23	1908.4	6.67115	30.004561	30.001372	-0.000435	



**Inhouse Centrifuge (29 Inch Radius, 600 Tooth Wheel,**  
**Accelerometer = 3**  
**SF = 0.222361**  
**Date = 2.051393**

**Random Sequence, 2K Load, 22.5 g Corrected)**

$$\sigma_{Res} = 3.167830 \cdot 10^{-4}$$

**Standard Deviation of Residuals**

$$\mu = \frac{\max(|Res|)}{\sigma_{Res}}$$

$$\mu = 2.539226$$

**Normalized Magnitude of  
Largest Residual**

$$N = N_{neg} + N_{pos}$$

$$N = 24$$

**Total Number of Readings**

$$\mu_c = 1.25 + \ln\left(\sqrt{\frac{N}{3}}\right)$$

$$\mu_c = 2.289721$$

**Confidence Limit Check Value**

$$K = \begin{bmatrix} K_3 \\ K_{oq} \\ K_2 \\ C_n \\ C_p \\ K_{0n} \\ K_{0p} \end{bmatrix} \quad i = 0 \dots \text{rows}(K) - 1 \quad d = A(a)^{-1} \quad \sigma_{K_i} = \sigma_{Res} \sqrt{d_{i,i}}$$

$\sigma K_3$	$\sigma K_3$	$1.331771 \cdot 10^{-7}$
$\sigma K_{oq}$	$\sigma K_{oq}$	$6.566577 \cdot 10^{-6}$
$\sigma K_2$	$\sigma K_2$	$9.808426 \cdot 10^{-7}$
$\sigma C_n$	$\sigma C_n$	$9.928116 \cdot 10^{-5}$
$\sigma C_p$	$\sigma C_p$	$9.930015 \cdot 10^{-5}$
$\sigma K_{0n}$	$\sigma K_{0n}$	$4.334421 \cdot 10^{-4}$
$\sigma K_{0p}$	$\sigma K_{0p}$	$4.335215 \cdot 10^{-4}$

**Standard Deviations of  
Each Coefficient**

$$f = N - \text{rows}(K)$$

$$f = 17$$

**Number of Degrees of Freedom**

$$t = 1.96 + \frac{2.392}{(f - 1.082)}$$

$$t = 2.11027$$

**Student's t for P = 95% Confidence**

$$K_{2lower} = K_2 - \frac{t \cdot \sigma K_2}{\sqrt{N}}$$

$$K_2 = -6.272 \cdot 10^{-6}$$

$$K_{2upper} = K_2 + \frac{t \cdot \sigma K_2}{\sqrt{N}}$$

$$K_{2min} = \text{if}(|K_{2lower}| < |K_{2upper}|, K_{2lower}, K_{2upper})$$

$$K_{2max} = \text{if}(|K_{2lower}| < |K_{2upper}|, K_{2upper}, K_{2lower})$$

**95% Confidence level K2 Lies Within the Range of:**

$$K_{2min} = -5.849 \cdot 10^{-6} \leq K_2 \leq K_{2max} = -6.694 \cdot 10^{-6}$$

**Accel\_and\_Run = 3.05**

**SESSION VIII-A  
MEASUREMENT METHODS**

***CHAIRMAN***  
**SAM GEORGE**  
***TINKER AFB OK***

**THIS PAGE LEFT BLANK INTENTIONALLY**

## **16th Biennial Guidance Test Symposium**

### **Abstract**

#### **High Accuracy, Short Term Trajectory Measurement of an Airborne Vehicle for Control of Inverse Synthetic Aperture Radar Image Formation**

**Authors: John W. Sisak and Members of ERIM Staff**

Inverse Synthetic Aperture Radar (ISAR) techniques have been successfully used to measure the Radar Cross Section (RCS) of airborne vehicles. The very fine resolution available with ISAR can be valuable in the control of RCS during the design, development and maintenance stages of aircraft production. Motion compensation using inertial measurements on board the vehicle is used to focus the radar image during operations on an instrumented ISAR test range. This motion compensation approach for image focusing is independent of radar signal strength and scattering characteristics and thus has advantages over signal dependent focusing techniques, such as prominent point processing.

This paper presents a Motion Measurement Subsystem (MMSS) that records data from a strapdown inertial navigation unit installed on the aircraft during flight operations on the ISAR test range. The data is post-processed using high accuracy strapdown navigation software to calculate a fine motion trajectory over short time segments corresponding to radar aperture times. A Kalman filter is implemented using either a ground based laser tracker or differential GPS to provide a position measurement. GPS controlled rubidium clocks are used to synchronize the motion measurement with the radar signal. Preliminary flight test results are presented that show position measurement accuracy, and implications for use in other applications requiring high accuracy trajectory measurement are discussed.



## 1. INTRODUCTION

A traditional approach to high resolution imaging with Synthetic Aperture Radar (SAR) is to use a motion compensation (Mocomp) system to measure the wide-band motion of the antenna's phase center, relative to a fixed target, over a synthetic aperture integration interval. The motion data is used to correct the phase of the radar return and maintain a coherent phase history, required for producing the azimuth resolution in the image. Similarly, high resolution imaging with Inverse Synthetic Aperture Radar (ISAR) requires accurate knowledge of both the motion of the antenna phase center and motion of the target. For a ground based radar, the Mocomp system is installed on the target and measures the motion of the target relative to the static antenna phase center.

A high accuracy Mocomp system, termed the Motion Measurement Subsystem (MMSS), was developed for an ISAR application by the Environmental Research Institute of Michigan for the U.S. Air Force. This Mocomp system is employed as a subsystem in a Ground-to-Air Imaging Radar (GAIR) which is used for Radar Cross Section (RCS) measurement of airborne vehicles. The GAIR system was developed for the U.S. Air Force as part of the B-2 program and is described in Reference 1.

The GAIR program was initiated in 1988 with definition of the system requirements and the primary implementation approach. Development of the GAIR system (and MMSS subsystem) specifications began in the fall of 1989, with hardware and software development soon thereafter. GAIR system integration activities began late in 1991, with initial MMSS system flight testing performed from June through October 1992.

The primary system requirement is to measure, time tag, and record (in real time) relatively wide bandwidth, six-degree-of-freedom motion data for the host platform. This data is subsequently used in a non-real time navigation processor to reconstruct the platform's trajectory. The trajectory calculations are then used by an image processor to generate high quality geographic imagery (SAR) or high quality host platform imagery (ISAR).

The MMSS data collection hardware is mil-qualified, and conforms to B-2 Flight Justification Testing (FJT) requirements. The MMSS-to-host vehicle interface has been designed to allow a simple, cost-effective adaptation to other vehicles and their associated FJT requirements.

The MMSS system contains several key technology areas where significant design and development effort was emphasized. One of these areas is the Inertial Navigation System/Inertial Measurement Unit (INS/IMU). The INS/IMU was developed

by modifying the real time software of Honeywell's F15E navigator. The INS/IMU software retains the navigation function (long term position and attitude measurement) of the F15 system, as well as providing the SAR or ISAR Mocomp function (short term delta velocity and delta attitude measurement). A second key technology area was development of high accuracy navigation / mocomp processing algorithms employing Kalman filtering to reconstruct the host platform's trajectory. The successful completion of these two technical challenges is attributable to the team effort of ERIM, Honeywell Military Avionics Division, and Strapdown Associates (SAI).

## 2. SYSTEM DESCRIPTION

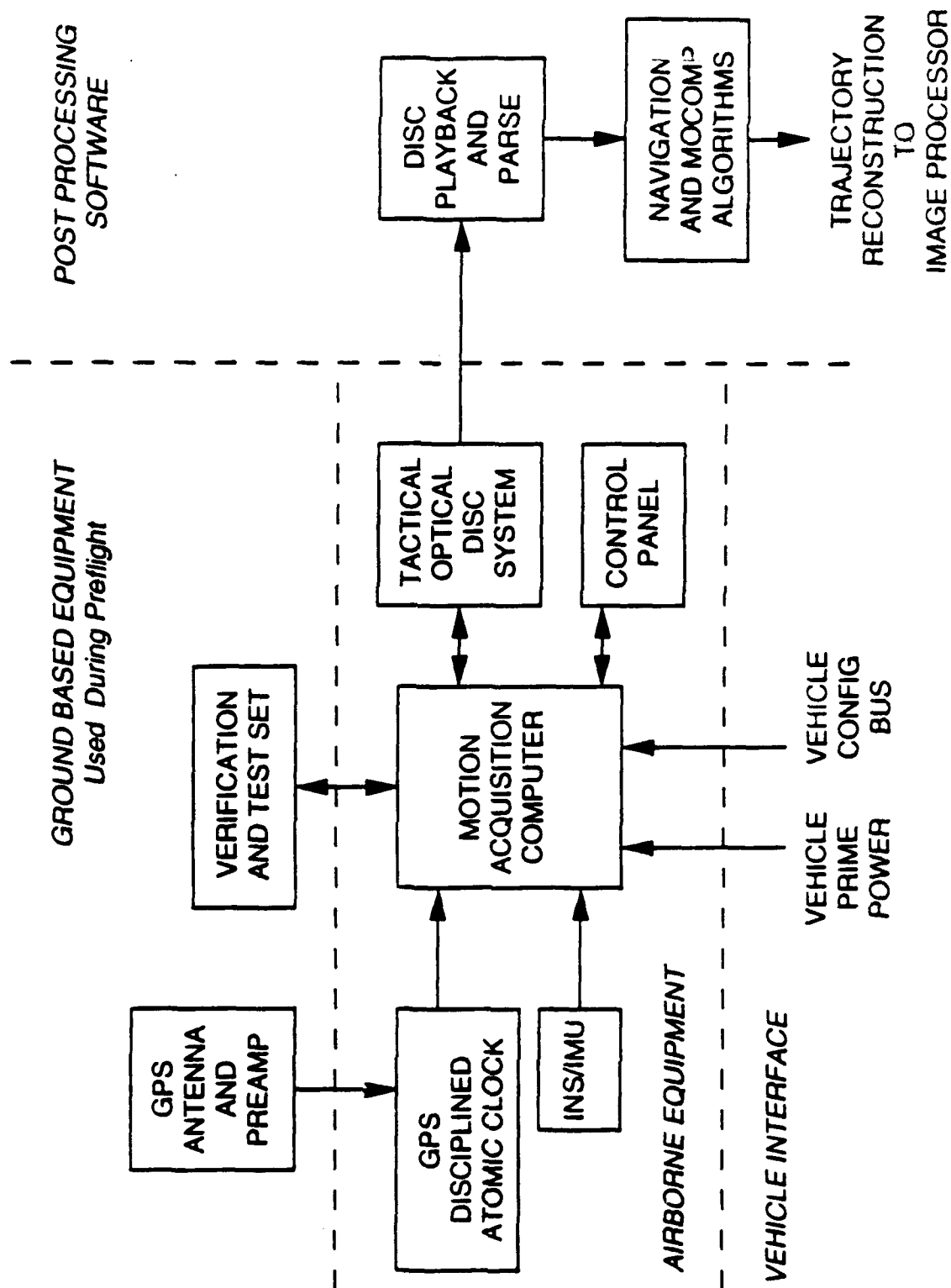
The MMSS system consists of three areas, the airborne equipment, the ground based equipment and the navigation mocomp processing software. Figure 1 shows the functional relationships of these areas.

The airborne equipment interfaces to the host vehicle's prime power and also, optionally, to a standard 1553 bus for the purpose of recording vehicle configuration data such as control surface position, door or hatch status, etc. The INS/IMU outputs the motion data to the Motion Acquisition Computer (MAC). The GPS disciplined time reference contains a rubidium atomic clock, which is synchronized to UTC time prior to flight, and provides the time tagging for the motion measurement. The MAC formats the INS/IMU data, the time tag and any vehicle configuration data. The data is then recorded on the non-volatile storage media of the Tactical Optical Disk System (TODS). A control panel (CP) provides on/off recording capability and status to the pilot. Data can be recorded continuously for up to three hours.

The ground based equipment consists of a computer work station, called the Verification & Test Set (VTS) installed in an environmentally controlled cart. The VTS is used to perform pre-flight checks of the airborne equipment and also to configure the equipment for a specific mission. A GPS antenna and pre-amp is included for the purpose of disciplining the rubidium atomic clock prior to flight. At the completion of pre flight tests, the VTS and the GPS antenna are disconnected and the system is autonomous and awaits the pilots record command.

During post flight operations, the TODS disc is removed from the TODS and is post-processed at a convenient location using the high accuracy Navigation and Mocomp algorithm. In the Navigation and Mocomp algorithm the IMU data is combined in a Kalman filter with a recorded time-tagged position measurement derived from range-angle-angle measurements of a ground based tracker. During the initial flight testing of the MMSS the range-angle-angle measurement was replaced by a differential GPS(DGPS) trajectory measurement which was available on the ERIM test target aircraft.

**Figure 1 : MMSS Functional Flow Diagram**



Following is a brief description of each element of the system.

#### **INERTIAL NAVIGATION SYSTEM/INERTIAL MEASUREMENT UNIT**

The INS/IMU hardware is an "off-the-shelf" Honeywell H-770 Laser Inertial Navigation System (LINS) designed for the high performance F15 aircraft. The H-770 is a full mil-spec system, and is procured as a production-tested LINS. The LINS is configured to the ERIM INS/IMU specification by software modification only. This is achieved by replacing programmable read only memory firmware on the H-770's two processor boards.

The H-770 was selected for the ERIM INS/IMU function because it is a mature production product, has excellent navigation performance, employs state-of-the-art inertial sensors, and has a software/hardware architecture adaptable to simultaneously providing the Mocomp function. Specifically, this architecture allows access to the raw sensor outputs of delta angle and delta velocity and the raw inertial sensor calibration coefficients. The standard H-770 real-time navigation outputs are not affected and are recorded for possible use as quick-look check for data validity. The standard H-770 navigation outputs are referred to as the INS function of the MMSS. The custom sensor outputs of delta angle, delta velocity and sensor calibration coefficients are referred to as the IMU function. Table 1 highlights some of the navigation and Mocomp performance characteristics for the INS/IMU.

The inertial sensor assembly contains three Honeywell GG1342 ring laser gyroscopes, and three Sundstrand QA-2000 quartz-flexure accelerometers. The A/D converted data is compensated in the H-770 Inertial Processor, and sent to the H-770 Navigation Processor for developing the F15 real-time navigation solution. The modified software in the Inertial and Navigation processors allows the real time navigation solution, A/D sensor data, and data compensation factors to be output to the MMSS through a dual redundant MIL-STD-1553B interface.

#### **GPS DISCIPLINED ATOMIC TIME REFERENCE**

The function of the GPS disciplined time reference is to provide accurate time tagging of the IMU data. The time reference receiver is a Datum model 9290 - 5730 GPS Time/Frequency Monitor. This element consists of a basic Datum production unit, to which ERIM specified modifications have been added.

The receiver connects to an external GPS antenna, which can be remotely located up to 100 feet. The GPS sync signals are used to discipline a 10.0 MHz EFRATOM FRS-N low noise Rubidium atomic clock. If the GPS antenna/ preamp/

**Table 1. INS / IMU Performance Characteristics**

---

**Navigation Performance**

Parameter update rate	50	Hz
Position accuracy (horizontal)	0.8	NMI/HR (CEP)
Roll, pitch accuracy	.033	deg (RMS)
Heading accuracy	0.05	deg (RMS)
Velocity error (horizontal)	2.5 ft	ft/sec (RMS)

---

**Mocomp Performance**

Sensor sampling rate	1200	Hz
Gyro:		
Path length	4.2	inches
Resolution	2	arc/sec
Bias error drift	0.01	deg/hour
Scale factor error	5	PPM
Random walk	0.0022	deg/root-hour
Bandwidth	essentially infinite	
Accelerometer:		
Resolution	.0058	ft/s
Bias residual	40	$\mu$ g
Scale factor residual	100	ppm
Bandwidth	1	KHz

---

**Partial list of aux data**

Quaternion  
 Sensor calibration coefficients  
 Sensor misalignment matrices  
 Laser gyro monitor data

cable assembly is disconnected from the receiver time reference monitor (or if the last valid UTC time is saved, and the offset time interval is derived by integrating the atomic clock frequency output), the autonomous time transfer precision of this system is better than 48 microseconds, referenced to UTC, for periods up to 48 hours.

The receiver is designed to be remotely located from the MMSS during a 3 to 4 hour GPS signal acquisition/Rubidium disciplining period. An internal battery pack allows the receiver to be disconnected from the antenna/preamp and AC power, and transported to the MMSS within a half hour without loss of time transfer information.

An identical time reference unit is employed in the GAIR ground based radar system to time tag each radar pulse and each measurement of the ground-based laser tracker.

#### **MOTION ACQUISITION COMPUTER**

The function of the MAC is to acquire and format time-stamped data. The MAC housing is a Radstone 1 ATR long conduction cooled chassis, containing a MIL-STD-VME bus backplane and associated computer subsystem. The majority of the internal components are procured from Radstone as "off-the-shelf" military grade hardware, tested to MIL-STD-810E. The exception is the ERIM designed and fabricated military grade board which interfaces to the GPS Atomic Time Reference.

The MAC CPU communicates to the INS/IMU through the dual redundant 1553 B Multiplex Bus Interface board. A similar board allows optional communication between the MAC CPU and the host vehicles avionics data bus. The Time Stamp and Control board is tasked with interfacing to the IMU sync clocks (related to inertial sensor A/D sampling) and the GPS Atomic Time Reference. This board provides the time stamps for the IMU and avionics data. Finally, a small computer systems interface board is used to transfer all MMSS data from the MAC to the high density mass storage (TODS). The maximum continuous data transfer rate is 614 Kbytes/second.

#### **TODS**

The function of the TODS is to provide a non-volatile storage media. The hardware is an "off-the-shelf" Sundstrand Tactical Optical Disc System, which has been successfully flown on a high performance F16 aircraft. The system provides 300 Mbytes of random access storage on a rugged erasable disc cartridge. The optical and mechanical components are designed for use in severe operating environments. The disc cartridge and optical/mechanical components are hermetically sealed. The disc is spun by means of a rotating permanent magnet. Read/write is accomplished through laser diodes and magneto-optical methods.

## **POWER UNIT AND CONTROL PANEL**

The power unit (PU) hardware element is the sole power interface between the host vehicle and the airborne MMSS hardware. The PU inputs 115 VAC, 400 Hz, 3 phase aircraft prime power. This AC power is distributed to other hardware elements via individual circuit breakers. The PU also generates regulated 28 VDC and 5 VDC.

The control panel is the sole interface between the MMSS and the pilot. Emergency power down control, data record control, and a simple status/error code display comprise the interface.

## **GROUND BASED HARDWARE ELEMENTS**

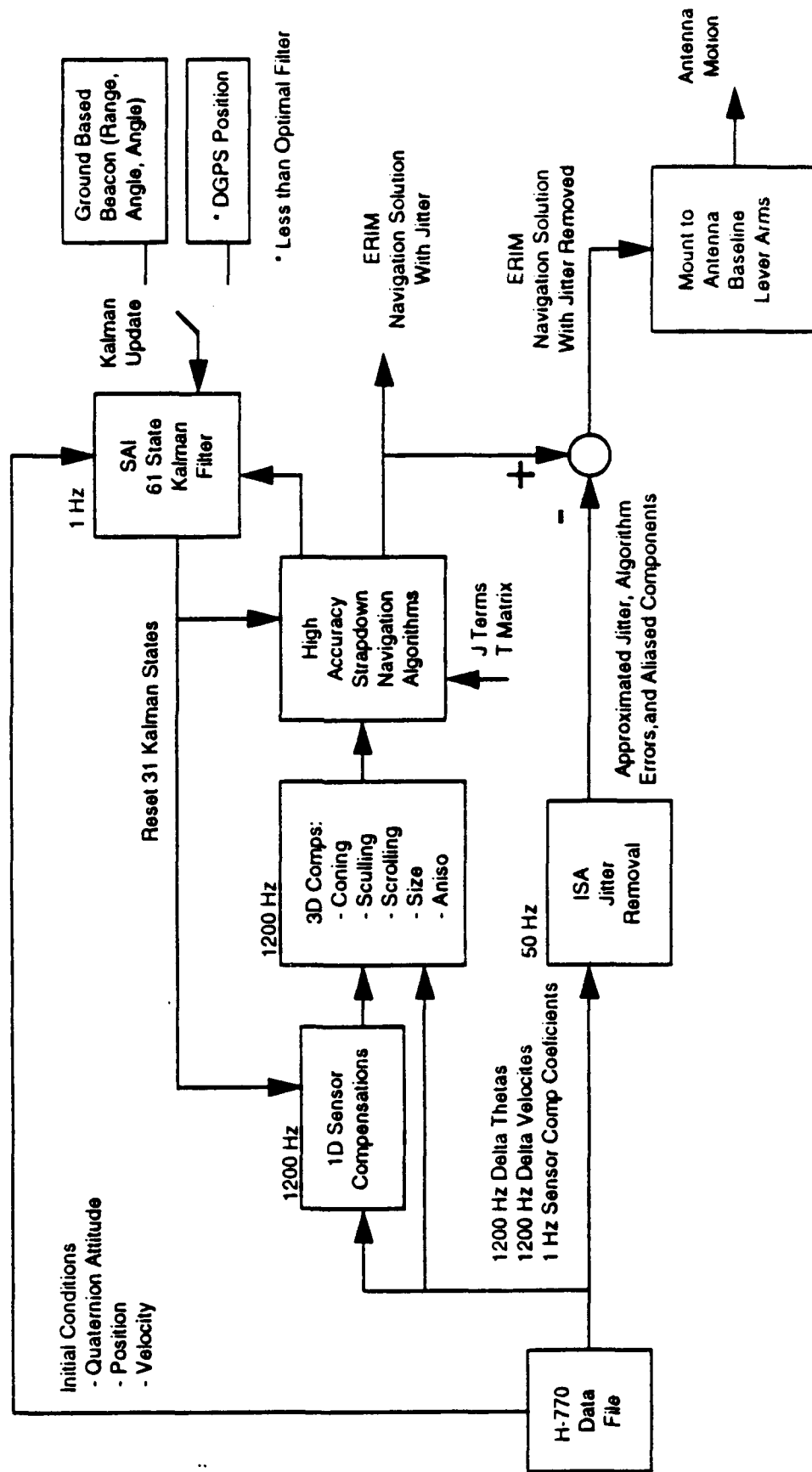
MMSS test and verification is provided by Sun SPARC Station 2GS, termed the Verification Test Set (VTS). The VTS is installed in a ground test cart which can be rolled up to the host aircraft during preflights. The VTS is hooked up to the MMSS airborne equipment and is used to perform IMU alignment and other hardware tests. Sufficient power distribution and space is available within the cart to store and test the entire airborne portion of the MMSS. This allows an autonomous, environmentally controlled, "portable workbench" for checking the MMSS in locations remote from the aircraft or laboratory.

## **NAVIGATION AND MOCOMP SOFTWARE**

The airborne MMSS hardware measures the host vehicle motion and stores the motion data in real time. The Navigation and Mocomp software is used in post-processing of the data in order to reconstruct the trajectory of the vehicle for use in the SAR image formation processor. The Navigation and Mocomp software is an expanded and enhanced version of the Strapdown Associates RLG INS Strapdown Kalman Filter Navigator. ERIM specified enhancements, developed by SAI, maximize the fidelity of the position and attitude of a point on the vehicle called the motion compensation point. The motion compensation point for a SAR application is usually the phase center of the SAR antenna. For this ISAR application the motion compensation point can be selected to be any point on the vehicle. The attitude and acceleration measured by the IMU and the lever arm from the IMU sensor triad to the motion compensation point are used to solve for a phase correction which is applied to each recorded radar pulse return. This phase correction controls image focusing and registration. A block diagram of the navigation and mocomp algorithm is given in Figure 2.

**Figure 2 : Navigation and Motion Compensation Block Diagram**

*Post Processing Software*





The delta attitude and delta velocity data is recorded at a rate of 1200 Hz. The navigation motion compensation algorithm processes the IMU data at two rates. The mainline navigation solution is propagated at an equivalent 50 Hz rate. That is, the delta angle and delta velocity data is first summed to an equivalent 50 Hz rate before being integrated in the navigation algorithm. The integration routines, which are trapezoidal integration algorithms, provide a first order approximation to each integration. This solution is exact if the angular rates and linear accelerations are constant over the 50 Hz cycle. For non-constant rates and accelerations a higher rate calculation is necessary to provide a high accuracy estimate of the antenna trajectory. Thus the 1200 Hz delta angle and delta velocity data is used in high rate algorithms for coning, sculling, scrolling and jitter removal. Each routine calculates a correction term from the 1200 Hz data to be applied to the navigation solution at each 50 Hz time epoch. This correction is exact if the angular rates and accelerations are constant over the 1200 Hz.

Coning and sculling corrections are well known in the navigation community. They are corrections applied to the attitude and velocity integrations to account for the effects of the discrete integration of signals with high frequency content by medium rate navigation algorithms. The scrolling algorithm is a similar correction which is applied to the position integration. The development of the scrolling algorithm is described in an ERIM report prepared by SAI, Reference 2. While insignificant for navigation, the high rate scrolling correction to the position integration can become significant for SAR image focusing at x-band frequencies where the wavelength is 30 mm or .1 foot.

The jitter algorithm is another high rate algorithm for increased accuracy of trajectory measurement. The jitter algorithm is a filter which is designed to compensate for two effects. The first effect is the reaction of the Inertial Sensor Assembly (ISA) block to gyro dither. The gyros are dithered at frequencies between 300-450 Hz. This angular dither causes a reaction torque on the ISA which is sensed by the accelerometers. These dither frequencies can alias into a low frequency in a 50 Hz navigation algorithm. This real motion of the accelerometer is visible in spectral analysis of 50 Hz data without dither removal. Since the antenna does not feel the dither vibration, this effect can cause a pair of raised sidelobes around each target in the imagery. The jitter removal algorithm has shown a 10 dB reduction of these dither reaction frequencies. The second effect which the jitter filter is designed to compensate is broadband vibrations of the IMU which are uncorrelated with the vibration of the antenna or aircraft body. If left unfiltered this uncorrelated vibration will contribute to the background noise in the imagery by raising the Integrated Sidelobe Ratio of the impulse response.

The recorded output of the INS/IMU includes the sensor calibration coefficients which are generated by Honeywell algorithms in the H-770 firmware. These sensor calibration coefficients for bias, scale factor, misalignment etc. are applied at a 1 Hz rate in the Navigation Mocomp algorithm. Residual sensor calibration errors, in addition to navigation errors, are then estimated by the Kalman filter.

The Kalman filter is a 61 state filter developed by SAI for this ISAR application. The measurement of the Kalman filter is provided by a ground-based beacon or tracker system that provides a range-angle-angle measurement relative to a position located very near the ground-based radar antenna. The position derived from the range-angle-angle measurement is differenced with the IMU position. The differenced position is the input to the Kalman filter which then generates estimates of position, velocity and attitude error and residual sensor calibration errors. The error state vector for the Kalman filter is presented in Table 2. The range-angle-angle measurements are recorded and time tagged separately on the ground and are time aligned with the IMU data as part of the Navigation Mocomp algorithm.

### 3. BASIC REQUIREMENTS

Basic motion compensation requirements are usually derived from image quality requirements that establish allowable phase error requirements over a synthetic aperture. Phase errors are divided into three categories of frequency relative to aperture time. The first is quadratic phase error. Examples of quadratic error include along-radar-line-of-sight acceleration bias or platform tilt error coupled with the gravity vector, and across-line-of-sight velocity error. The second category is quadratic-to-single-cycle or low frequency error. This category includes gyro drift error which generates a cubic phase error. The third category is high frequency error which includes sinusoidal or wideband errors with frequency content greater than one cycle per aperture. Figure 3 shows examples of the effects of phase errors on the impulse response of a point target in a SAR image.

Figure 3A is the impulse response with 35dB Taylor weighting and no errors. The effects of quadratic error are shown in Figure 3B. Quadratic error broadens the mainlobe of the impulse response, therefore degrading image resolution. A  $60^\circ$  quadratic phase error requirement controls the increase in mainlobe width to 20%. Figure 3C shows the effect of a  $22.5^\circ$  cubic requirements on the impulse response. High frequency phase errors have a peak requirement of  $3^\circ$ . Figure 3D shows the effects of a three cycle per aperture phase error with a peak amplitude of  $3^\circ$  and Figure 3E shows a wideband random phase error with a standard deviation of  $3^\circ$ .

As an example, allowable acceleration error along the radar line-of-sight is given by:

**Table 2. Navigation Mode Kalman Filter Error States**

Error State	Model Type: N=Nav Error C = Random CNST M=1st Order MRKV	Description
1,2,3	N	X,Y,Z Attitude error
4,5,6	N	X,Y,Z Velocity error
7,8,9	N	X,Y,Z Position error
10	M	Barometric altimeter bias error
11,12,13	CX,Y,Z	Fixed gyro bias error
14,15,16	CX,Y,Z	Fixed accel bias error
17,18,19	CXY,YZ,ZX	Fixed gyro orthogonality error
20,21,22	CX,Y,Z	Fixed gyro scale factor error
23,24,25	CX,XY,XZ	Accel fixed scale factor error, misalign into Y, misalign into Z
26,27,28	CY,YX,YZ	Accel fixed misalign into X, scale factor error, misalign into Z
29,30,31	CZ,ZX,ZY	Accel fixed misalign into X, misalign into Y, scale factor error
32,33,34	MX,Y,Z	Random gyro bias error
35,36,37	MX,Y,Z	Random accel bias error
38,39,40	MX,Y,Z	Random gyro orthogonality error
41,42,43	MX,Y,Z	Random gyro scale factor error
44,45,46	MX,XY,XZ	Accel random scale factor error, misalign into Y, misalign into Z
47,48,49	MY,YX,YZ	Accel random misalign into X, scale factor error, misalign into Z
50,51,52	MZ,ZX,ZY	Accel random misalign into X, misalign into Y, scale factor error
53,54,55	CX,Y,Z	Fixed lever arm uncertainty
56,57,58	MX,Y,Z	Random lever arm uncertainty
59	M	Beacon random range measurement scale factor error
60,61	M	Beacon random elevation, azimuth angle measurement error

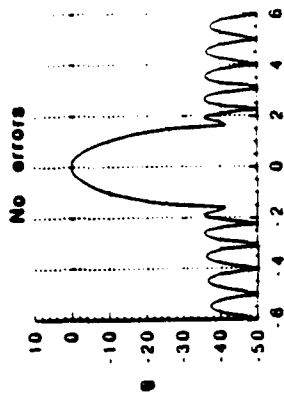


Figure 3A. Ideal Point Target Response

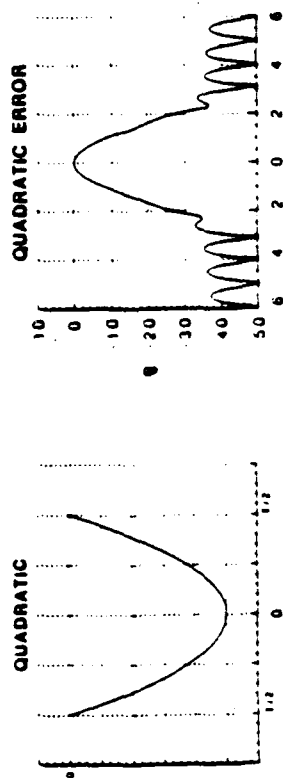


Figure 3B. 60° Quadratic Phase Error Effect on Point Target

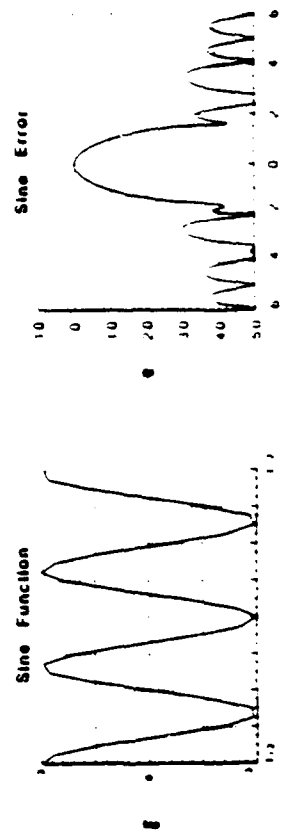


Figure 3C. Sinusoidal Phase Error Effect on Point Target

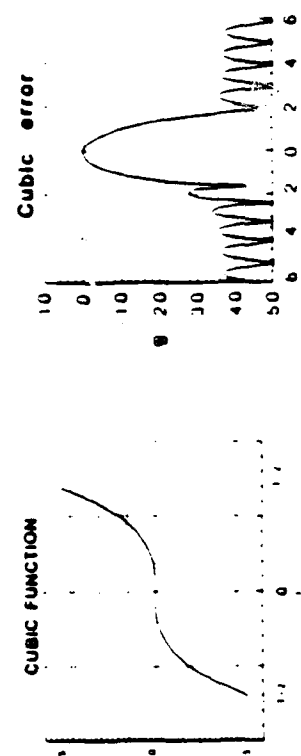


Figure 3D. 225° Cubic Phase Error Effect on Point Target

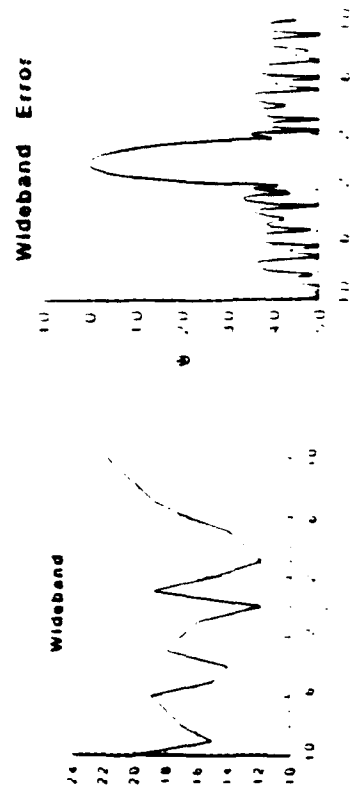


Figure 3E. Wideband Phase Error Effect on Point Target

$$\frac{2(360^\circ)}{\lambda} \cdot \frac{1}{2} a \left(\frac{T}{2}\right)^2 \leq 60^\circ$$

where

$\lambda$  = radar wavelength = 30 mm

$a = a_b$  = accelerometer bias

$= g\theta$  = acceleration error due to tilt error  $\theta$

For a 5 second aperture the total allowable acceleration error is  $82\mu g$  or  $82 \mu rad$ . These reduce to  $20\mu g$  and  $20\mu rad$  for a 10 second aperture.

#### 4. LABORATORY TEST AND ANALYSIS

Two INS/IMU units were acquired for the program and underwent laboratory testing in the ERIM Motion Testing Laboratory. This testing facility includes a three-degree-of-freedom CARCO S460-ND flight motion simulator and an Anorad Precision Linear Translation Table. The CARCO flight motion simulator provides the capability of applying 3-axis simultaneous rotational motion to the INS/IMU under test. The precision linear table provides a single axis linear translation capability which was used to measure accelerometer sensitivity to fractional wavelength translations. Computer controlled motion inputs are applied to the INS/IMU under test on either test device and the resulting gyro and accelerometer outputs are read into a SUN workstation at 1200 Hz for either real time processing or recorded for post processing.

The CARCO flight motion simulator provides measurement capabilities for system navigation performance and individual sensor error coefficients that are similar to capabilities in the inertial navigation community. The test and analysis software used to perform these measurements is the Ring Laser Gyro Sensor Assembly Test (RLGSAT) program developed by Strapdown Associates. A list of the tests performed and measurements made by RLGSAT is presented in Table 3.

Each INS/IMU unit was put through the series of RLGSAT tests. The 1200 Hz delta angle and delta velocity data were acquired along with the unit's sensor calibration coefficients which were applied to the sensor data by the RLGSAT software. The RLGSAT routines then measured the residual sensor errors. Typical results are shown in Table 4. These results are consistent with approximately a factor of 2 improvement of the INS/IMU performance specifications given in Table 1. These results are also consistent with the standard performance acceptance tests performed

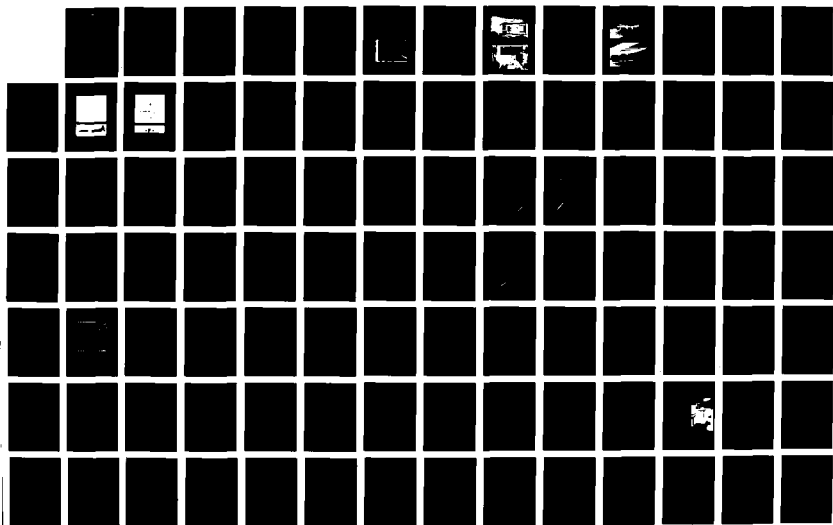
**Table 3. RLGSAT Capabilities**

<b>Test</b>	<b>Measurements</b>
Navigation Performance	System velocity & position errors over 1/2 Schuler cycle
Repeated Alignment	Gyro random walk
Schuler Pump	Gyro bias, composite accelerometer errors
21 - Rotation Sequence	Gyro scale factor, misalignment accelerometer bias, scale factor, misalignment scale factor unbalance. Sensor assembly misalignment
12 Hour Gyro Bias Drift	Vertical & north gyro bias
Spin Oscillation	Size - effect and amiso inertia

AD-A283 898

BIENNIAL GUIDANCE TEST SYMPOSIUM (16TH) HELD IN  
HOLLOMAN AIR FORCE BASE NEW MEXICO ON OCTOBER 5-7 1993  
VOLUME 1(U) AIR FORCE DEVELOPMENT TEST CENTER EGLIN AFB  
FL OCT 93 AFDTC-TR-93-06-VOL-1 XC-46TG

NL



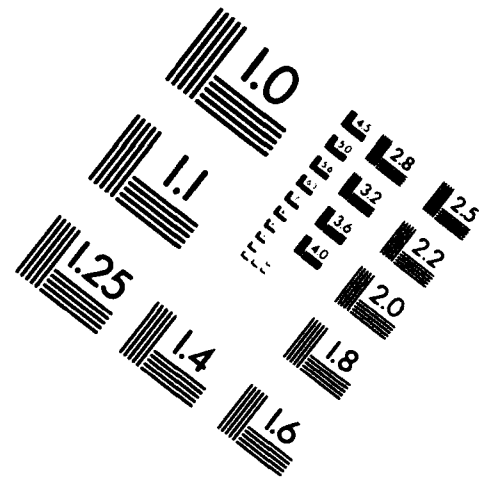
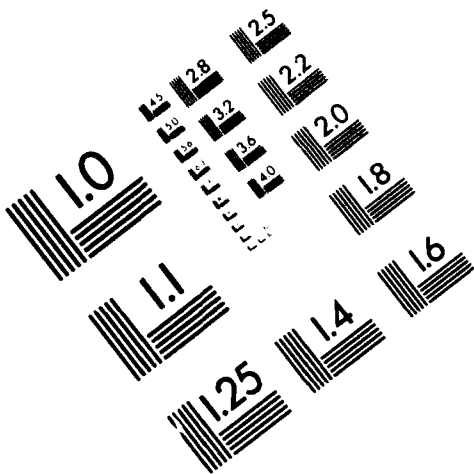


**AIM**

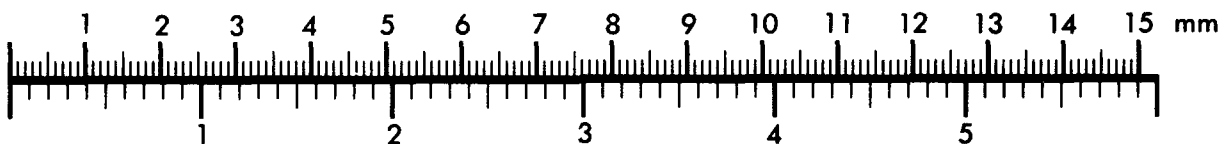
**Association for Information and Image Management**

1100 Wayne Avenue, Suite 1100  
Silver Spring, Maryland 20910

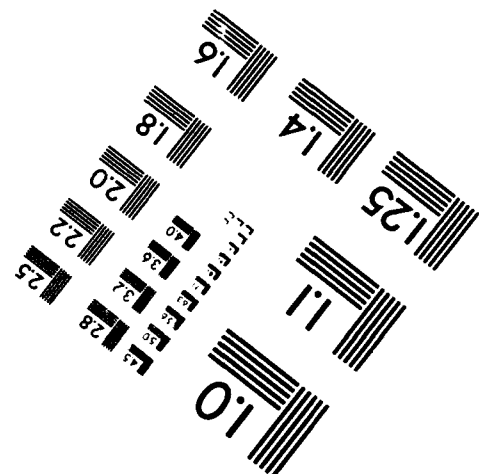
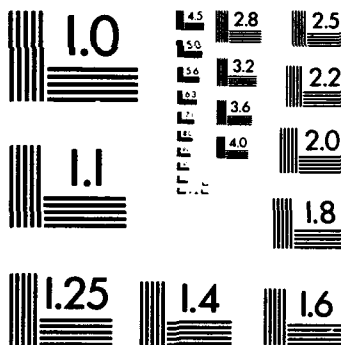
301/587-8202



**Centimeter**



**Inches**



MANUFACTURED TO AIM STANDARDS  
BY APPLIED IMAGE, INC.

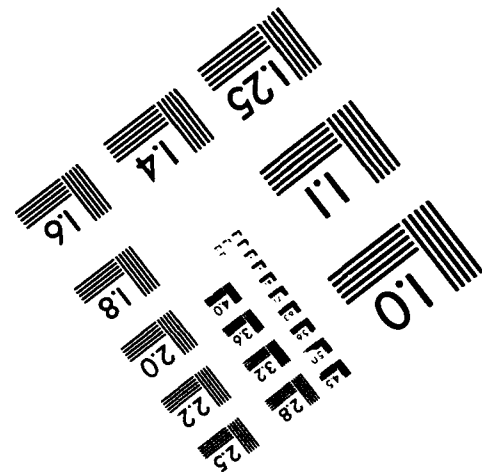




**Table 4. Typical Results of IMU Residual Sensor Error Measurements**

	<u>Typical</u>	<u>Spec</u>
Gyro Bias (deg/hr)	<.0045	.007
Gyro Random Walk (deg/hr <sup>1/2</sup> )	<.001	.0022
Gyro Scale Factor (ppm)	<3	5
Gyro Misalignment (μrad)	<6	30
Accelerometer Bias (μg)	<20	40
Accelerometer Scale Factor (ppm)	<42	100
Accelerometer Asymetry (ppm)	<26	100
Accelerometer Misalignment	<15	30

by Honeywell prior to delivery which showed navigation performance approaching the 1/3 nautical mile per hour class. Of particular interest to ISAR image formation were the residual accelerometer bias and scale factor, and the gyro random walk coefficients.

Navigation performance tests were also conducted using the Navigation Mocomp software algorithm. The INS/IMU units were again installed on the CARCO flight motion simulator. The internal H-770 ground alignment was completed and the INS and IMU outputs were recorded for the length of the test. The H-770 INS output of position velocity and quaternion was used to initialize the Navigation Mocomp Software in the SUN workstation and the 1200 Hz delta attitude and delta velocity output and the 1 Hz sensor calibration coefficients were used to propagate the navigation solution. The position of the CARCO flight motion simulator was used as the beacon/ground tracker input to the Kalman filter. The covariance parameters of the measurement in the Kalman filter were set to 1 meter. The Kalman filter used a position update at a 1 second rate for four minutes, then the position update was inhibited and the INS/IMU was rotated 180°. Figure 4 shows an example of the velocity output of the Navigation Mocomp algorithm. The x-axis velocity reaches a peak of approximately -.6 ft/s and the y-axis velocity reaches a peak of about -.9 ft/s which is consistent with the RLGSAT measurements and the Honeywell acceptance test measurements. The x-axis velocity appears to be a sine wave oscillation which implies the error is mostly due to gyro drift. The y-axis velocity appears to be mostly a cosine wave which implies the error is mostly due to accelerometer bias or residual tilt error.

The Navigation Mocomp algorithm was essentially designed to be an airborne transfer alignment. The data used in the Figure 4 plots was reprocessed and the position update was continued through the 180° rotation. Figure 5 shows that the Schuler oscillation of velocity have been reduced indicating that the filter is performing as designed, i.e., it can begin to separate the error states after some kind of maneuver. The sine wave oscillation of x velocity has been reduced to a peak of approximately -.4 ft/s and the y-axis velocity cosine wave is reduced to an apparent random walk response. By analysis as outlined in Reference 3, this laboratory test controls the gyro bias to less than .002°/hr and the attitude error to less than 10μrad and the accelerometer bias to less than 10μg.

The RLGSAT tests and the navigation performance test indicate that low frequency imaging errors are controlled by the quality of the sensors themselves or by estimating residual sensor errors such as acceleration bias or initial attitude error. High frequency image errors are created by random IMU errors such as gyro random walk or quantization error. Figure 6 shows an example of the output of a laboratory test that measures the noise floor of the IMU as a motion sensor. For this test, the IMU

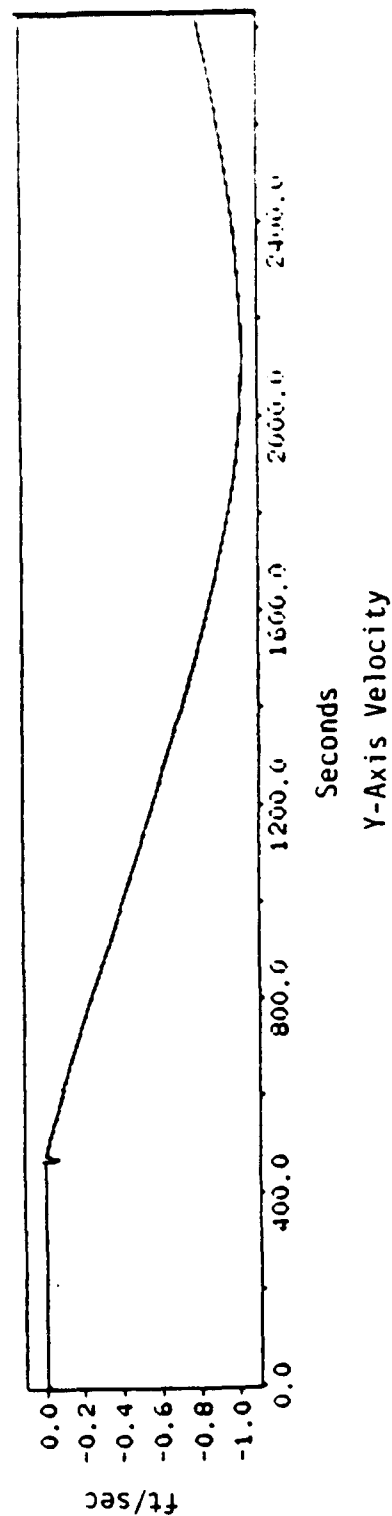
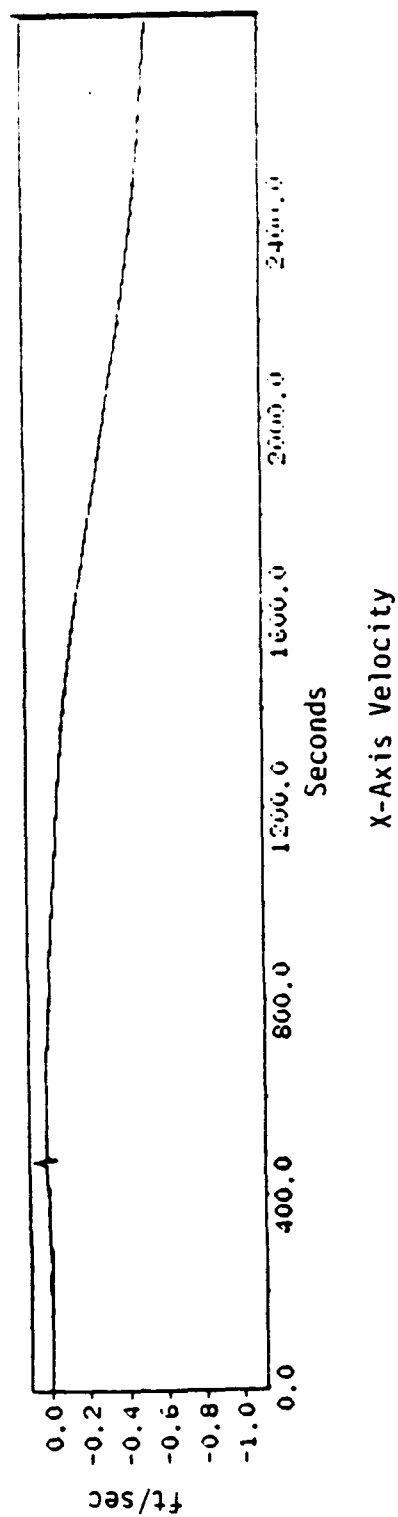


Figure 4. Navigation Performance Test, Updates Inhibited  
Before 180° Rotation

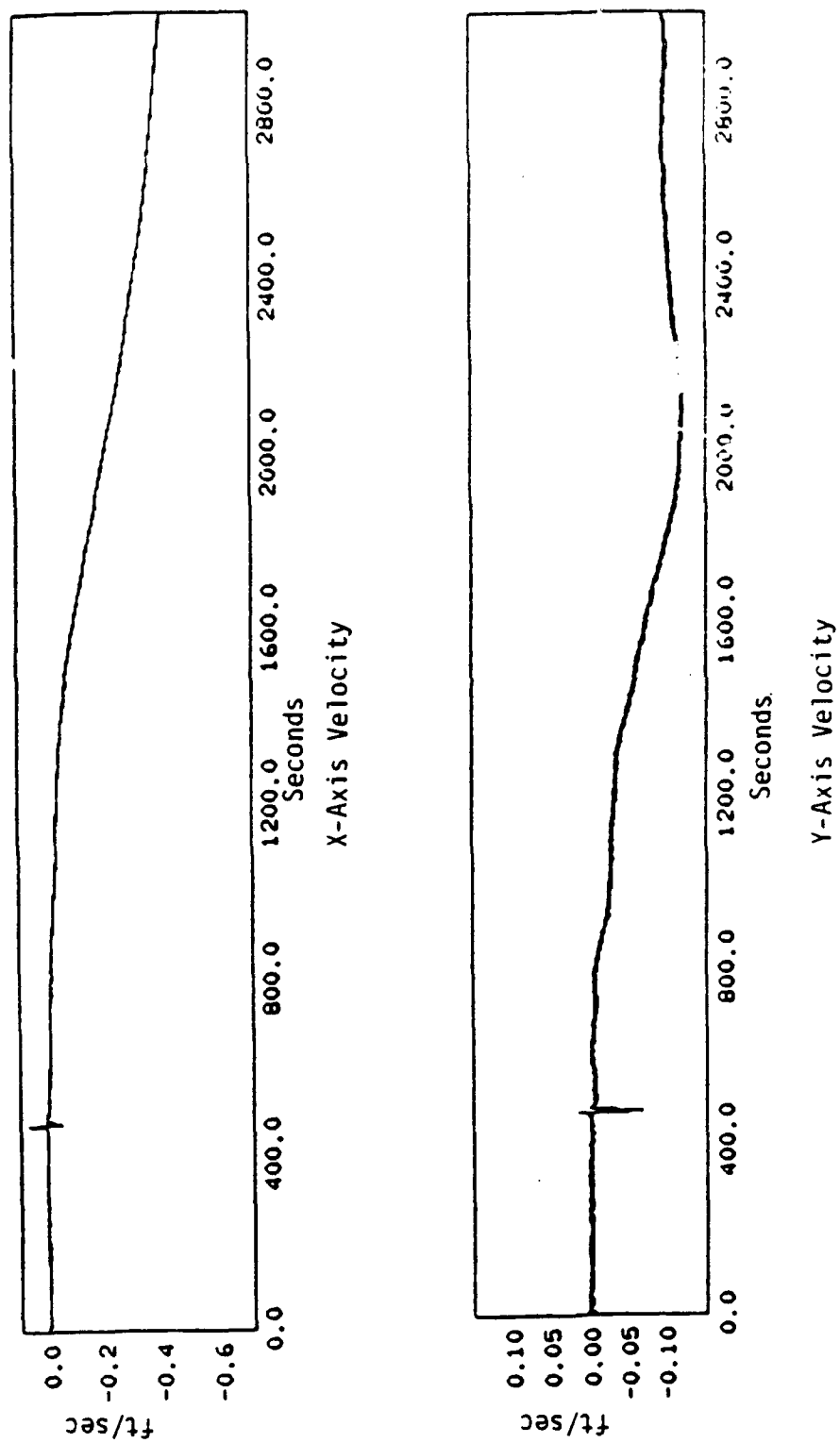


Figure 5. Navigation Performance Test, Updates Inhibited after 180° Rotation

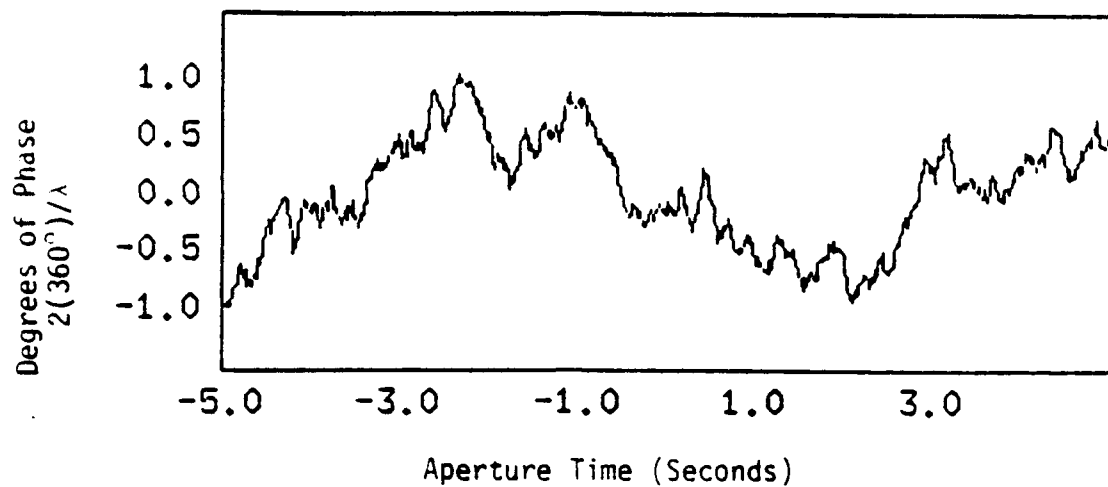


Figure 6. Position Noise of IMU Output  
(Note:  $1^\circ$  of two-way radar phase = .04mm)

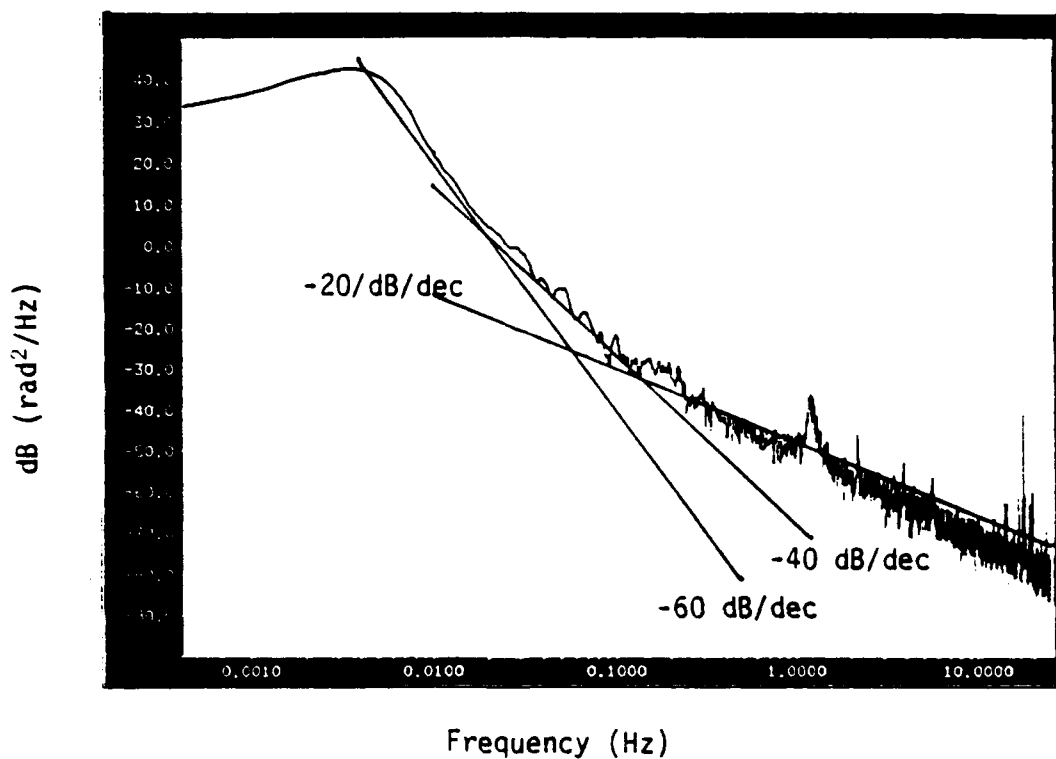


Figure 7. PSD of Position Noise of IMU Output

is stationary. The data is a 10 second segment of position output of the Navigation Mocomp software where the position variable of the vertical axis has been converted to two-way degrees of radar phase. A quadratic polynomial has been removed from the data to eliminate the effects of acceleration bias. The residual error is less than  $1^\circ$  RMS which compares favorably with the requirement of  $3^\circ$  RMS for high frequency phase error; where high frequency is greater than 1 cycle per aperture.

Figure 7 is a power spectral density (PSD) representation of the IMU noise floor. The PSD is proportional to the PSD of position error. Asymptotes of -60 dB/decade, -40 dB/decade and -20 dB/decade have been added for reference. Gyro random walk is white noise that is integrated 3 times into position. Gyro random walk should have a PSD proportional to -60 dB/decade. The data appears to match this slope between .01 Hz and .02 Hz. A -40 dB/decade PSD would indicate accelerometer noise which is integrated twice into position error. For frequencies greater than .1 Hz the data shows a better fit to a -20 dB/decade PSD. This indicates that for aperture of 10 seconds or less the noise floor of the IMU is dominated by velocity quantization noise. Gyro random walk noise dominates at lower frequencies down to approximately .01 Hz, or 100 sec time frames. By calculation, using the basic IMU specifications, the gyro bias error will dominate the gyro random walk error for time frames greater than approximately 100 seconds. For apertures of less than 10 seconds the energy in the random walk error is concentrated in low frequencies that can be approximated as quadratic or cubic errors. Based on the random walk measurements the random walk contribution to cubic error has an estimated RMS value of  $1^\circ$  cubic phase error and the contribution to quadratic error has an estimated value of  $5^\circ$ .

## 5. FLIGHT TEST RESULTS

Integration of the GAIR system began ahead of schedule in late 1991. The GAIR radar subsystem was installed in a field west of Ann Arbor, MI, in early spring of 1992. The MMSS system was installed in an ERIM CV580 aircraft used for SAR development and research. Figure 8 is a photograph of the H-770 IMU installed in the ERIM CV580. Figure 9 shows the remaining MMSS airborne hardware installation. The ground-based laser tracker subsystem, which was to provide the radar antenna pointing function and also the position measurement to the Navigator and Mocomp software, Kalman filter was not yet released to integration. Instead, the radar antenna pointing function was provided by a video camera tracking system and the position measurement for the Kalman filter was replaced by Differential GPS (DGPS).

The CV580 aircraft instrumentation included a Trimble GPS receiver. A second Trimble GPS receiver was placed on a surveyed point near the ground based radar antenna. Trimble post-processing software was used to provide a differential GPS

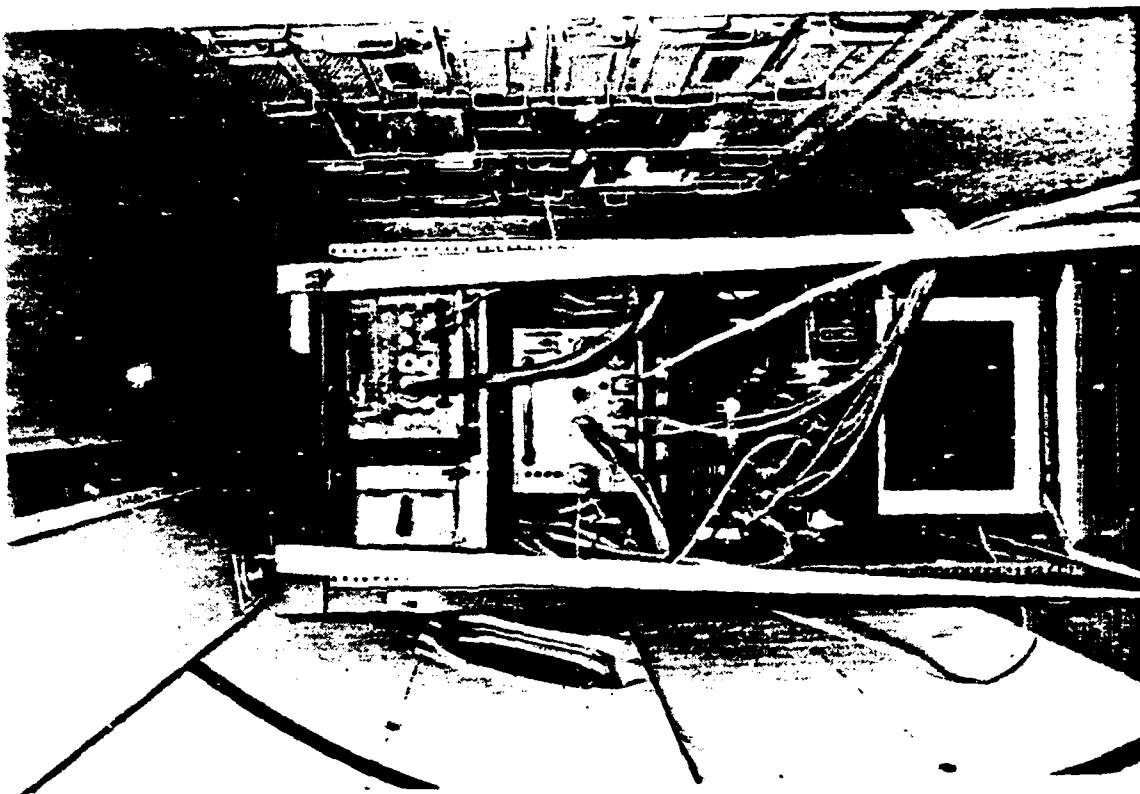


Figure 9. MMSS Airborne Hardware Installation

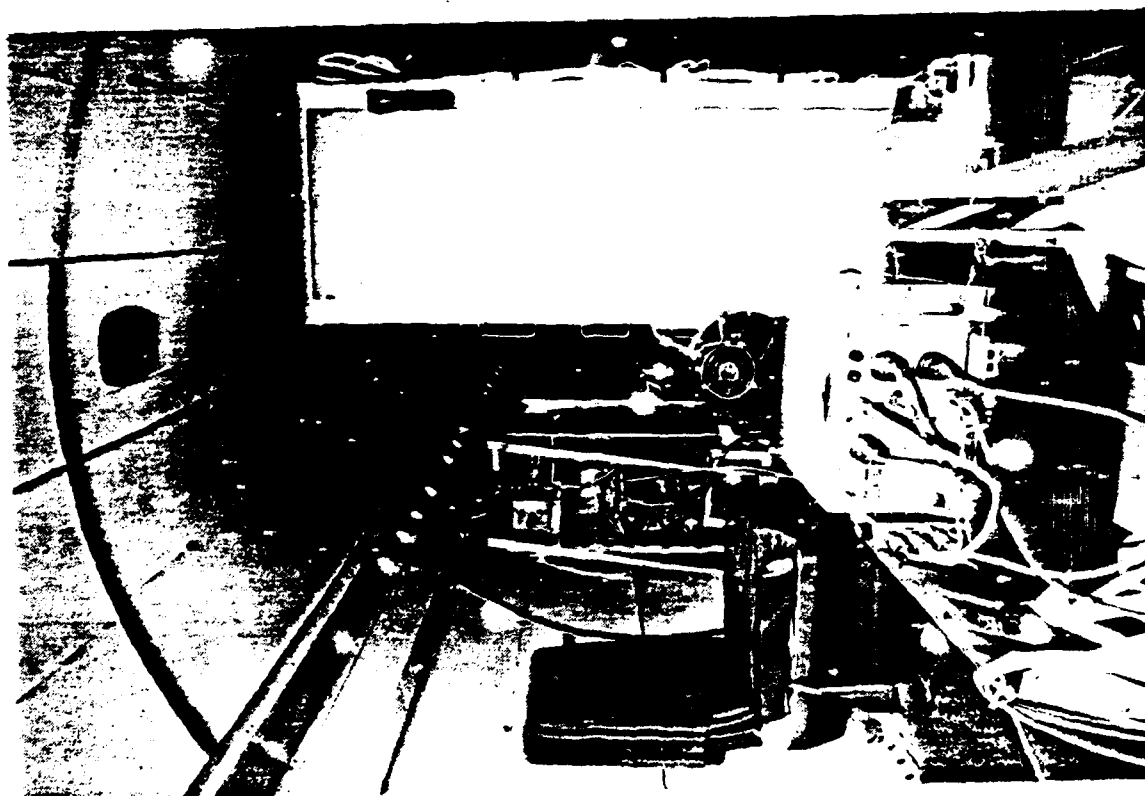


Figure 8. H-770 INS/IMU Installation in ERM CV580

trajectory using code pseudo-range measurements that was used as the position input to the Kalman filter of the Navigation and Mocomp software. The noise of the GPS code-differential measurement was estimated to be 3 meters for the horizontal dimensions and 5 meters for the vertical dimension. At the suggestion of SAI, covariance parameters associated with the ground based tracker error states and the measurement noise variance were altered to allow the substitution of the GPS trajectory for the expected ground-based tracker range-angle-angle measurement.

The ERIM CV580, shown in Figure 10, was used as the target to be imaged. The standard CV580 instrumentation includes a SAR antenna that is steerable in azimuth and elevation. The antenna was replaced with a large corner reflector and the CV580 SAR control system was used to point the corner reflector at the ground radar site during the imaging passes. The corner reflector is shown in Figure 11. The corner reflector provides a point target with a cross section that is approximately 8dB larger than the total cross-section of the CV580. Initial flight testing using the MMSS system was conducted from June through October of 1992.

Imagery for several passes using the collected motion data and the Navigation Mocomp software was processed and analyzed. Analysis of radar system performance is performed by comparing the phase and amplitude response of a large point target, in this case, the corner reflector mounted in the belly radome of the aircraft, to the response of a perfect point target. It is possible to use the radar as a highly accurate, one dimensional measurement of IMU performance because of the very high signal-to-noise ratio provided by the corner reflector. By tracking the phase of the peak signal, the strong corner reflector, it is possible to achieve millimeter range accuracy. The location of the corner reflector was selected to be the motion compensation point in the navigation and mocomp software. Thus with no errors, the range calculated by the navigation and mocomp software would be identical to the range measured by the radar.

The absolute position requirement is determined by the registration requirement of the GAIR system and is assigned to the ground-based laser tracker. In the operational design of the GAIR system the range gate of the radar is set by the ground-based laser tracker which measures the range to an optical reflector with a range accuracy of  $\pm 1.5$  meters. In these preliminary flight tests, the range gate is set by an early/late filter on the radar signal return of the corner reflector. The position error is established by the calculated position of the motion compensation point and the measured position of the corner reflector in the image. The average radial position error was 6 meters and is attributed primarily to the implementation of the code pseudo-range DGPS measurement as a temporary position measurement during the early part of the system integration and to a residual velocity error component in the Kalman filter



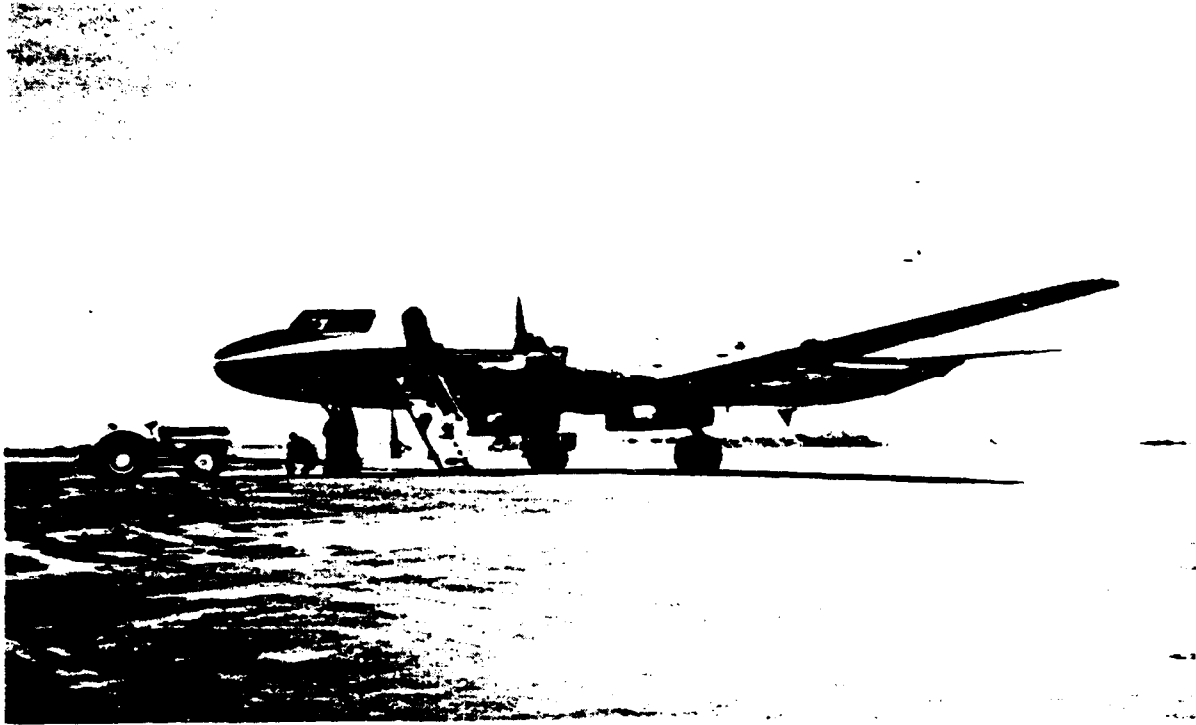


**Figure 10. ERIM CV580**

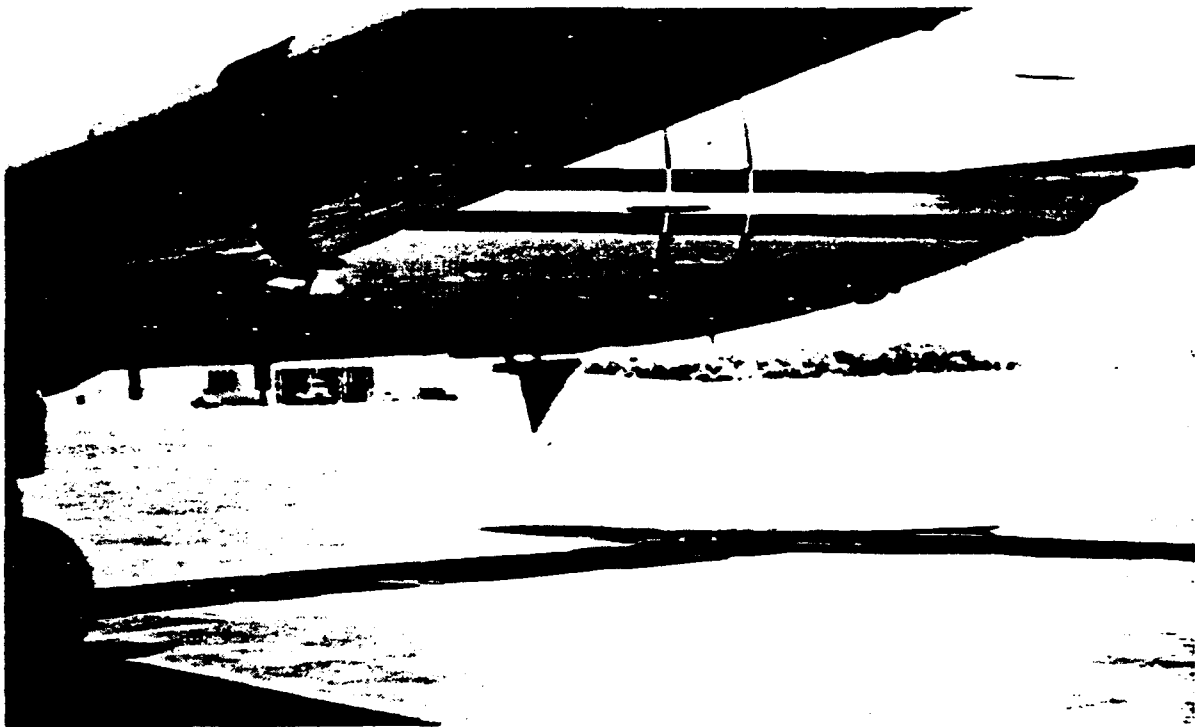


**Figure 11. Corner Reflector Used as Point Target on ERIM CV580**

along the radar line-of-sight. The filter times varied from 30 seconds to 4 minutes using the DGPS position measurement at a 1 Hz rate.

The next series of figures show a typical comparison of the range calculated by the x, y, z components of the position output of the navigation and mocomp software versus the range calculated by tracking the phase of the corner reflector return. Figure 12 shows the range calculated from the motion data. The aircraft was flying a nominally straight and level pass past the radar antenna at an approximate range of 6250 m. The aperture length is 5 seconds and it occurred just prior to the aircraft passing abeam of the radar site. The change in range due to the aircraft motion is 28 meters over the 5 second aperture. A second order curve fit to the difference of the range calculated by motion measurement minus the radar range shows a range rate error of .008 m/s and a range acceleration error of 100 $\mu$ g.

The range rate error can be attributed to residual velocity error in the Kalman filter. An along radar line-of-sight velocity error creates a linear phase error in the radar signal which creates a position shift in the image in the cross-line-of-sight direction. In this example the .008 m/s error creates a shift of .5m which is included in the absolute position error. The 100  $\mu$ g range acceleration error is equivalent to a 72° quadratic phase error over the aperture which causes a slight defocusing of the image. There are three major components to this error. The first is an acceleration error along the radar line-of-sight due to accelerometer bias or residual tilt error. The second is an across-line-of-sight velocity error. The third component is a height-of-focus effect due to a nearly quadratic roll of the aircraft of a couple of tenths of a degree over the 5 second aperture. This roll, multiplied by the range to the radar antenna, creates a relative trajectory of the antenna to the aircraft body frame which is similar to a pop-up maneuver of a fighter aircraft using a standard SAR. A target located above or below the focus plane of the image has a quadratic phase error that is proportional to the height above or below that focus plane. The focus plane is calculated to pass through the motion compensation point and is parallel to the waterline plane of the aircraft. Any vertical position error will place the focus plane above or below the real location of the corner reflector. The geometry of this pass and the roll motion would generate 50° of quadratic error per foot of vertical error. The effects of this height-of-focus error can be seen by changing the focus plane in the image processor but the height-of-focus error cannot be separated from the first two error components mentioned above.

The above errors are low frequency image errors and are controlled primarily by the Kalman filter. Refinement of the Kalman filter performance has been deferred until integration of the ground-based laser tracker into the GAIR system or until implementation of a specific GPS measurement model in the Kalman Filter.

Figure 12: Point Target Range Using Imu Data

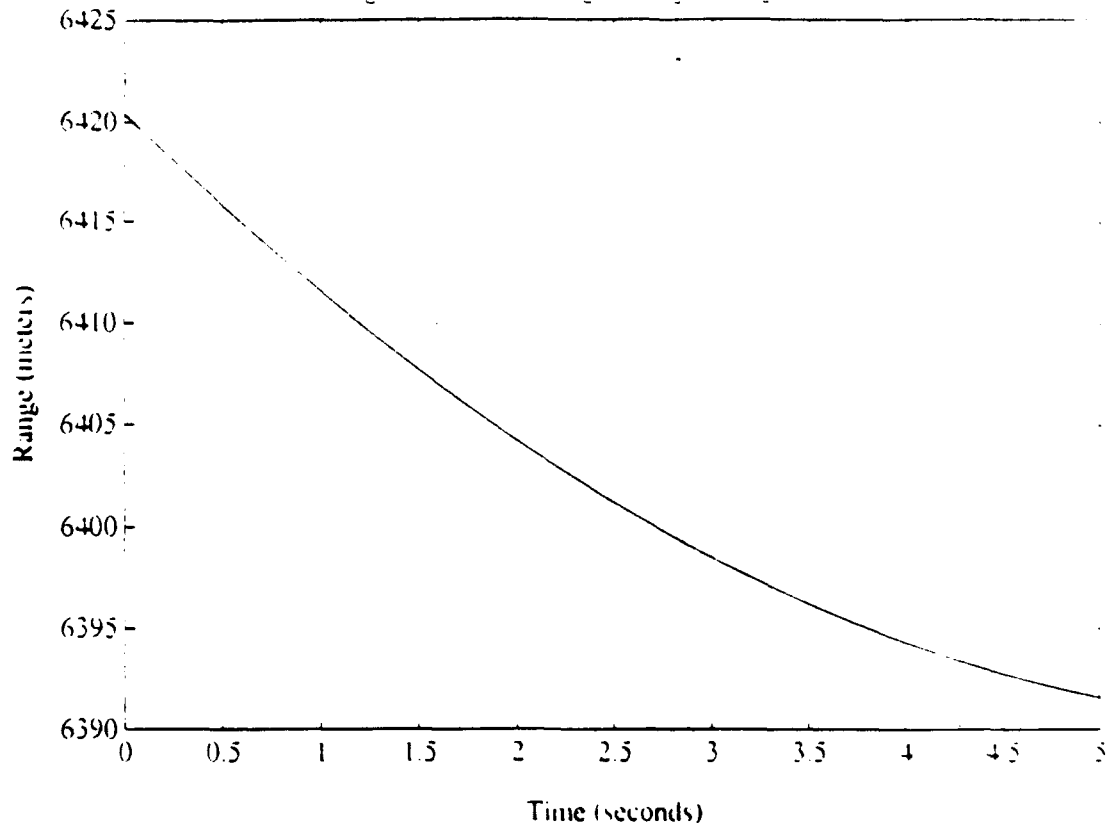
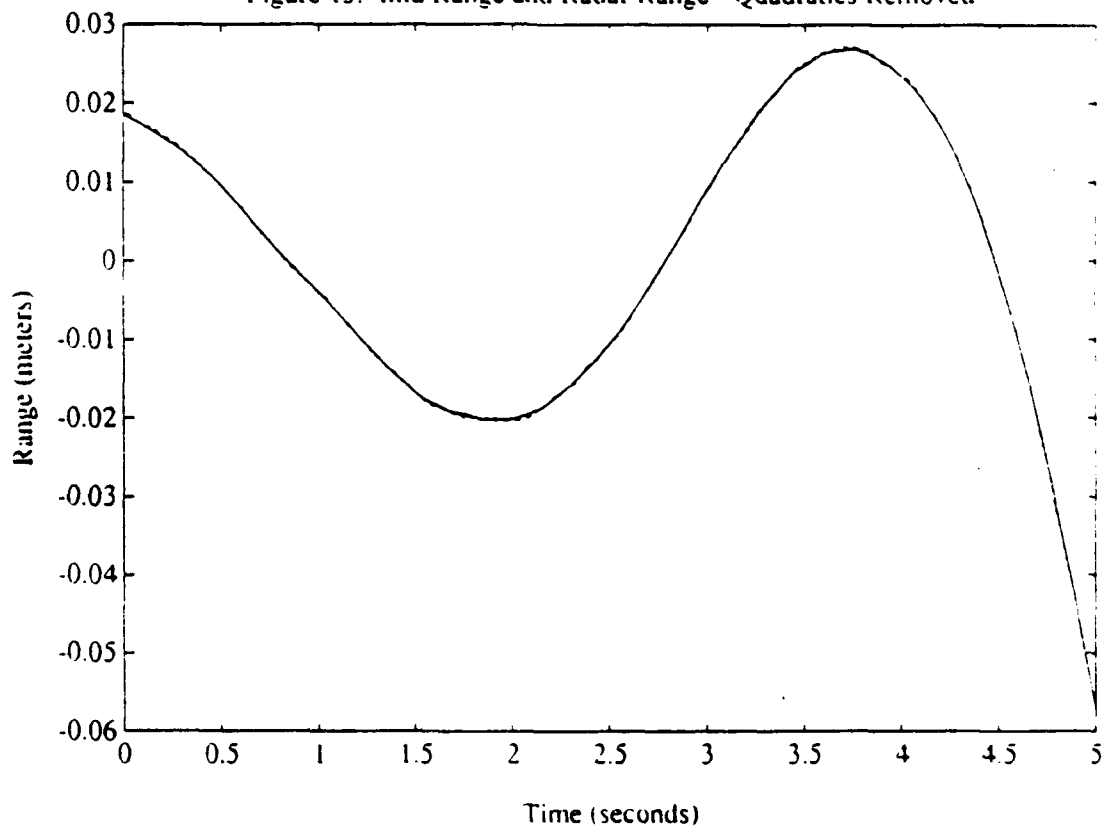


Figure 13: Imu Range and Radar Range - Quadratics Removed



To observe high frequency errors, the linear and quadratic components of each set of range data, the range calculated by motion measurement and the radar range, are removed with best-fit second order polynomials. Plots of both sets of residual range data are presented in Figure 13. The vertical scale is in meters and the two sets of data overlay each other very well. This plot shows that the high frequency motion of the aircraft is about 1 cycle over a 5 second aperture and the peak motion of +20 to -40 millimeters or  $2160^\circ$  of phase. This is the motion that must be reduced to  $15^\circ$  in the quadratic to single cycle region or to  $3^\circ$  in the frequency region greater than 1 cycle per aperture.

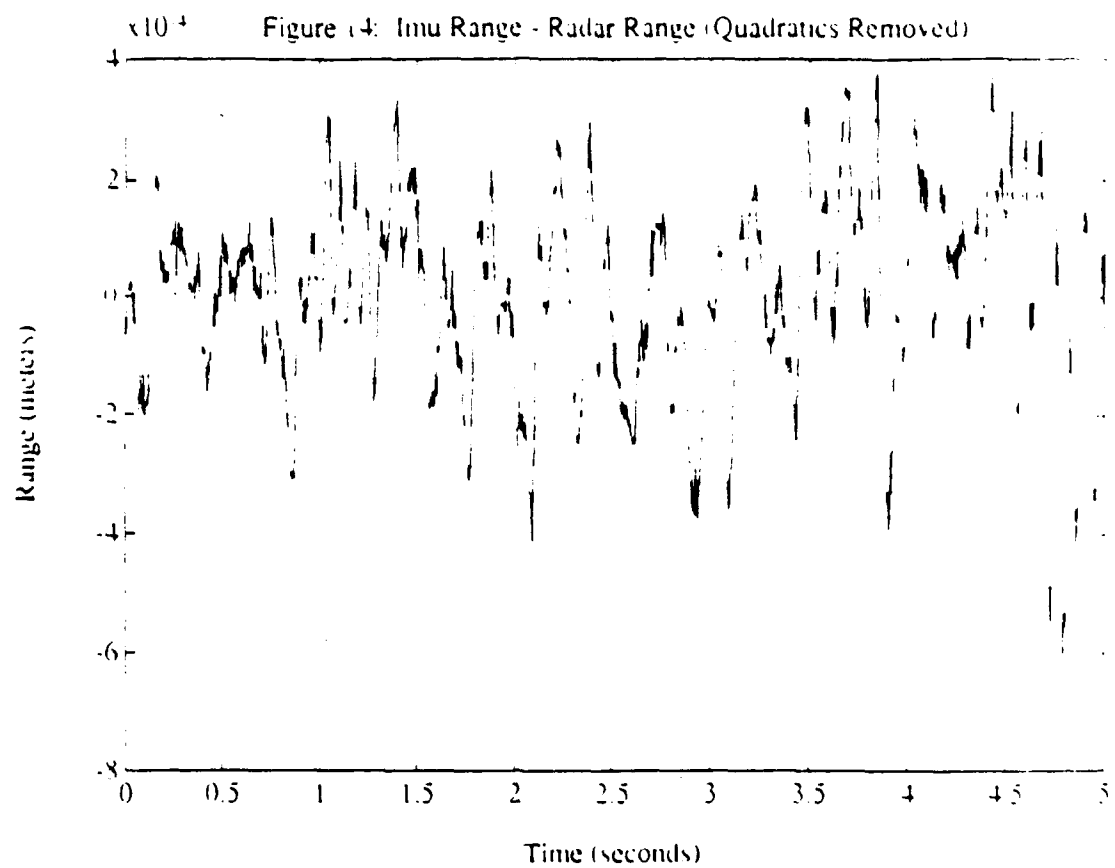
Figure 14 shows the difference of the residual range calculated from motion and the residual radar range. Note the vertical scale is in meters  $\times 10^{-4}$ . The nearly single cycle residual motion appears to be nearly cancelled. The high frequency motion has an RMS value of approximately .2 mm or  $5^\circ$  of two-way radar phase. This difference plot represents total system wideband noise. The components of this noise are the random walk noise and velocity quantization noise discussed previously, the vibration of the corner reflector that is uncorrelated with the inertial sensor assembly and pulse-to-pulse starting phase noise of the radar signal chain.

The radar image of the ERIM CV580 is shown in Figure 15. The radar illumination is from the bottom of the figure. The radar is viewing the bottom of the aircraft. The shape of the wings, fuselage and engine nacelles are easily seen. The corner reflector is the large return halfway between the wing root and the tail. Figure 16 is a near head-on view of the CV580. Note that the leading edge of one wing is caught perpendicular to the line of sight of the radar causing a signal flash from a line target. Such a signal could cause problems with prominent point processing techniques but because the motion measurement technique is signal independent, the image can be properly focused.

## 6. SUMMARY

The preliminary results show that the aircraft trajectory can be accurately reconstructed using inertial sensors. Although the height-of-focus effect due to the aircraft attitude change during the aperture cannot be separated from the error effects, the form of the height-of-focus error is analytically determined from the attitude. In the example presented the aircraft attitude change that generates the height-of-focus is a nearly quadratic-in-time roll. The example of results presented show that the IMU sensors accurately follow the aircraft motion in the quadratic to single cycle and in the wideband frequency range.

Future work will include efforts to separate height-of-focus effects from quadratic errors generated from sensor errors. This involves refining the accuracy of the



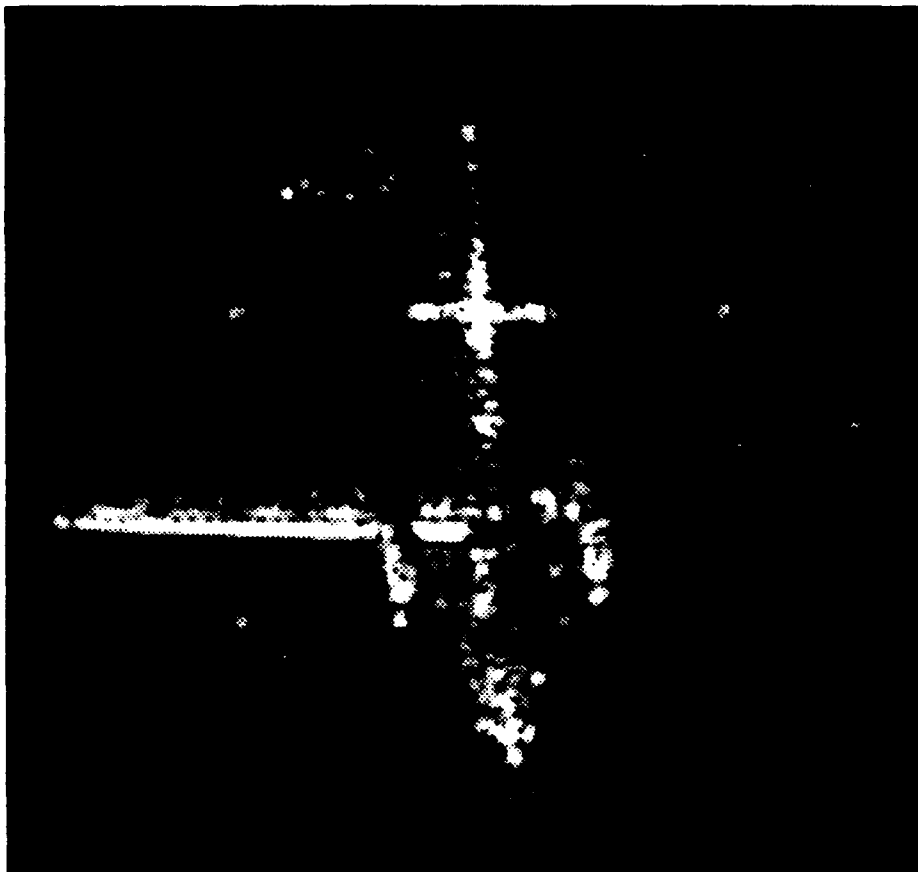


ISAR Radar Image

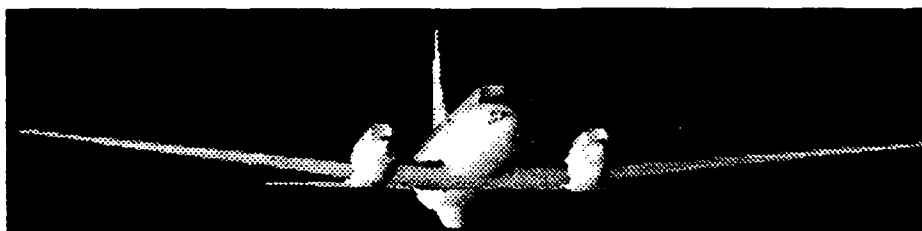


Target Viewing Aspect

Figure 15. Near Broadside Radar Image of CV580



ISAR Radar Image



Target Viewing Aspect

Figure 16. Near Head-on Radar Image of CV580

estimate of the vertical distance of the motion compensation point above the radar antenna. Note that the height-of-focus error is a geometric error of the SAR image process. If the position, velocity and attitude of the corner reflector are measured perfectly, the corner reflector will focus but points above or below the image plane will have the height-of-focus error. Efforts to refine altitude accuracy involve integration of the ground based laser tracker and inclusion of code and carrier phase differential GPS for position measurements. Other efforts will extend the motion compensation analysis to trajectory segments that include deliberate aircraft maneuvers.

## 7. OTHER APPLICATIONS

ERIM has a conceptual design for repackaging and downsizing the airborne equipment of the MMSS. This design includes installation in a standard pod where the only interface requirement would be prime power. The system can be configured for autonomous operation where no pilot interface is desired or for drone applications. The system can then be used for any application requiring high accuracy reconstruction of a vehicle trajectory.

The existing system will be integrated in the existing airborne SAR laboratory on the ERIM CV580 which was used as the test target. The preliminary test results offer encouragement that motion compensation of standard SAR imagery will be substantially improved. The integration into the standard SAR system offers one advantage to MMSS system testing, in that the height of focus effect of ISAR can be eliminated.

The existing system will be integrated into an interferometric SAR (IFSARE) system which will be used to provide terrain elevation information in addition to standard SAR stripmap output products. A principle requirement of this interferometric SAR is absolute attitude accuracy of IFSARE antennas relative to the terrain. This attitude accuracy is composed of absolute aircraft roll accuracy of less than  $40\mu\text{rad}$  and absolute three-dimensional position accuracy of less than 1 meter. Laboratory testing indicates that the roll accuracy can be easily provided by the MMSS, absolute position accuracy will be provided by designing and integrating code and carrier phase DGPS measurement model into the Kalman filter of the navigation and motion compensation software.

Development of the MMSS and the laboratory facilities has provided ERIM with the capability and experience needed for the development, testing and analysis of new algorithms for motion compensation and trajectory reconstruction, and also for testing and analysis of new inertial sensors and new motion sensor error models.



## **ACKNOWLEDGEMENT**

The author wishes to thank the officers and civilian employees of the B2 SPO, for their sponsorship, support and technical interest in the MMSS and GAIR system. Also the cooperation and professionalism provided by Honeywell Military Avionics Division and Strapdown Associates, Inc. is greatly appreciated.

The author also wishes to thank the ERIM employees who formed the MMSS development team for their engineering abilities and dedication in support of the MMSS development and the production of this paper.

## **BIOGRAPHY**

J. Sisak received a BSEE from Michigan State University in 1972 and MSE from the University of Michigan in 1984. He has been employed at ERIM since 1979. He has recently been the system engineer assigned to motion compensation analysis and the MMSS development team.

## **LIST OF FIGURES**

1. **MMSS Functional Flow Diagram**
2. **Navigation and Motion Compensation Block Diagram**
3. **Example of the Effects of Phase Error on Point Target Response**
4. **Navigation Performance Test, Updates Inhibited Before 180° Rotation**
5. **Navigation Performance Test, Updates Inhibited After 180° Rotation**
6. **Position Noise of IMU Output**
7. **PSD of Position Noise of IMU Output**
8. **H-770 INS/IMU Installation in ERIM CV580**
9. **MMSS Airborne Hardware Installation**
10. **ERIM CV580**
11. **Corner Reflector Used as Point Target on ERIM CV580**
12. **Point Target Range Using IMU Data**
13. **IMU Range and Radar Range - Quadratics Removed**
14. **Difference of IMU Range - Radar Range - Quadratics**
15. **Near Broadside Radar Image of CV580**
16. **Near Head-on Radar Image of CV580**

## **LIST OF TABLES**

1. **INS/IMU Performance Characteristics**
2. **Navigation Mode Kalman Filter Error States**
3. **RLGSAT Capabilities**
4. **Typical Results of IMU Residual Sensor Error Measurement**

## LIST OF ACRONYMS

AD	Analog to Digital Conversion
CP	Control Panel
DGPS	Differential GPS
ERIM	Environmental Research Institute of Michigan
FJT	Flight Justification Testing
GAIR	Ground-to-Air Imaging Radar
GPS	Global Positioning System
IFSARE	Interferometric SAR
IMU	Inertial Measurement Unit
INS	Inertial Navigation System
ISA	Inertial Sensor Assembly
ISAR	Inverse Synthetic Aperture Radar
LINS	Laser Inertial Navigation System
MAC	Motion Acquisition Computer
MMSS	Motion Measurement Subsystem
Mocomp	Motion Compensation
PSD	Power Spectral Density
PU	Power Unit
RLG	Ring Laser Gyro
RLGSAT	Ring Laser Gyro Sensor Assembly Test
SAI	Strapdown Associates, Inc.
SAR	Synthetic Aperture Radar
TODS	Tactical Optical Disk System
UTC	Coordinated Universal Time
VTs	Verification and Test Set

## REFERENCES

1. A High Performance Inverse Synthetic Aperture Radar System for Imaging Low Observable Airborne Targets, S.L. Crippen, W.D. Gallaway, P.R. Lumley, E.L. Johansen, H.W. Klimach, S.J. Shackman, J.P. Steinbacher, J.W. Wilhelm and D.D. Young. Environmental Research Institute of Michigan, Proceedings of the 39th Annual Tri-Service Radar Symposium, 22-24 June 1993.
2. MIS Inertial Algorithm Analytical Definition Report, ERIM 89-66-2, 28 May 1992, Prepared by Strapdown Associates, Inc.
3. Introduction to Strapdown Inertial Navigation System, P.G. Savage, Strapdown Associates, Inc.

**THIS PAGE LEFT BLANK INTENTIONALLY**

# **RLG Bias or Random Walk ?**

**M. M. Tehrani**

**Litton Guidance and Control Systems, Woodland Hills, CA 91367**

## **Abstract**

Does a particular random process contribute to the bias or the random walk of a ring laser gyro (RLG) ? This paper discusses the issue by using the randomized RLG phase equation and presents a fundamental relationship between the statistics of the gyro output and the characteristics of the input noise. It is shown that if the correlation times of the underlying random processes are long compared to the sample time the gyro output exhibits a random bias. In the opposite case, the random processes contribute to the gyro random walk. The RLG error coefficients for both cases are derived, and the example of secondary dither discussed.

## **Introduction**

Random walk and random bias are the two error terms frequently mentioned in the RLG data analysis. The output noise is customarily divided into random walk and random bias according to the noise frequency. Thus, the high frequency noise is loosely associated with random walk and the low frequency noise with the random bias. This classification may be misleading in the case of RLG whose output is the integral of the (beat) frequency. The significance of the issue is in the fact that the instrument random walk and bias propagate differently in time and contribute to different kinds of errors in the system. Therefore, it is important to understand under what conditions a particular noise at the gyro output is truly a random walk or a random bias.

During the test or the actual operation, the RLG is subjected to a number of random inputs either by design (as in the case of randomized dither) or from the environment. Each random input is characterized by its set of correlation functions. The RLG accepts a portion of the input noise spectrum that falls within its bandwidth. The coupled noise affects the gyro beat frequency which is integrated over the sample time. In the followings we apply the random function theory to the process just described and establish a mathematical foundation for the RLG output noise classification.

## Analysis and Discussion

Consider a RLG which, in addition to the input rate  $\Omega$ , is under the influence of a number of random inputs. The phase equation of such a gyro can be written as:

$$\dot{\Phi}(t) = \Omega + \sum_{i=1}^k \xi_i(t) \quad (1)$$

where  $\dot{\Phi}(t)$  is the gyro beat frequency and  $\xi_i(t)$  is a random function representing the  $i^{th}$  random input affecting the gyro. For simplicity, we have set the gyro scale factor equal to 1. We have also assumed that the gyro is operating far above the lock-in threshold so that the nonlinearities due to the lock-in term can be ignored.

As a rate integrating device, the gyro output (counts) is the integral of the beat frequency:

$$n = \int_0^T \dot{\Phi}(t) dt \quad (2)$$

where  $n$  is a random variable representing the gyro counts within the sample time  $T$ . The average count per sample time is given by:

$$\langle n \rangle = \int_0^T \langle \dot{\Phi}(t) \rangle dt \quad (3)$$

The brackets in (3) represent the ensemble average of the respective random process. Substitution of (1) in (3) yields:

$$\langle n \rangle = \Omega T + \sum_{i=1}^k \int_0^T \langle \xi_i(t) \rangle dt \quad (4)$$

where we have assumed that the (deterministic) input rate  $\Omega$  is constant over the sample time. It is seen from (4) that if all error terms are zero mean random processes (implying rapid fluctuations with zero average over the sample time) they will not affect the mean gyro output. However, *all* random inputs affect the gyro output variance, as discussed below.

### RLG Output Variance

The variance of gyro counts is defined as:

$$\sigma_n^2 = \langle n^2 \rangle - \langle n \rangle^2 \quad (5)$$

From (2) we obtain:

$$\langle n^2 \rangle = \int_0^T dt \int_0^T dt' \langle \dot{\Phi}(t) \dot{\Phi}(t') \rangle \quad (6)$$

If we now use (1), (4), and (6) in (5) and simplify the result we get:

$$\sigma_n^2 = \sum_{i,j=1}^k \int_0^T dt \int_0^T dt' R_{ij}(t, t') \quad (7)$$

where  $R_{ij}(t, t') = \langle \xi_i(t) \xi_j(t') \rangle - \langle \xi_i(t) \rangle \langle \xi_j(t') \rangle$  is the two-time correlation function between the  $i^{th}$  and the  $j^{th}$  random processes.

Equation (7) is the general formula applicable to all random processes operating on the gyro. To proceed further, we assume that each  $\xi_i(t)$  represents a process that is stationary<sup>(1)</sup> in time. This means that the two-time correlation functions in (7) are independent of the time origin and are functions of time difference only, i.e.,

$$R_{ij}(t, t') = R_{ij}(t - t') \quad (8)$$

With this assumption the variance equation (7) reads as :

$$\sigma_n^2 = \sum_{i,j=1}^k \int_0^T dt \int_0^T dt' R_{ij}(t - t') \quad (9)$$

Since the integrand in (9) is a function of the difference of the two variables it can be shown that the double integral reduces to a single integral. This simplifies (9) to:

$$\sigma_n^2 = 2 \sum_{i,j=1}^k \int_0^T (T - \tau) R_{ij}(\tau) d\tau \quad (10)$$

We now consider the case of  $k$  uncorrelated random processes operating on the gyro and each having an exponentially decaying correlation function represented by:

$$R_{ij}(\tau) = \delta_{ij} N_i^2 \exp\left(\frac{-|\tau|}{\tau_i}\right) \quad (11)$$

where  $N_i$  and  $\tau_i$  are the amplitude and the correlation time of the  $i^{th}$  random process, respectively.  $\delta_{ij}$  is the Kronecker symbol defined as:

$$\delta_{ij} = 1 \text{ for } i = j, \quad \delta_{ij} = 0 \text{ for } i \neq j$$



Equation (11) describes a Markov process with the correlation time of  $\tau_i$ . The white noise is a special case of (11) as the correlation time approaches zero. The power spectral density (PSD) of the process is obtained by taking the Fourier transform of (11):

$$S_{ij}(f) = \int_{-\infty}^{\infty} R_{ij}(\tau) \exp(-2\pi i f \tau) d\tau = \delta_{ij} N_i^2 \int_{-\infty}^{\infty} \exp\left(\frac{-|\tau|}{\tau_i}\right) \exp(-2\pi i f \tau) d\tau \quad (12)$$

Carry out the integral gives the (double sided) PSD as:

$$S_{ij}(f) = \delta_{ij} \frac{2N_i^2 \tau_i}{1 + (2\pi f \tau_i)^2} \quad (13)$$

which describes a family of uncorrelated random processes with Lorentzian PSD's and noise equivalent bandwidths of  $(2\tau_i)^{-1}$ . The white noise is a special case of (13) with the bandwidth approaching infinity.

To determine the output variance of a gyro that is under the noise inputs characterized by the correlation functions (11), we substitute (11) in (10) and perform the integration. We obtain:

$$\sigma_n^2 = 2 \sum_{i=1}^k (N_i \tau_i)^2 \left[ \frac{T}{\tau_i} - 1 + \exp\left(\frac{-T}{\tau_i}\right) \right] \quad (14)$$

The gyro rate output error is the noise standard deviation per sample time:

$$\frac{\sigma_n}{T} = \sqrt{2} \left\{ \sum_{i=1}^k N_i^2 \left[ \frac{\tau_i}{T} - \left(\frac{\tau_i}{T}\right)^2 + \left(\frac{\tau_i}{T}\right)^2 \exp\left(\frac{-T}{\tau_i}\right) \right] \right\}^{\frac{1}{2}} \quad (15)$$

Equation (15) is the key result of this analysis. Figure 1 shows the log-log plot of the gyro rate error in units of noise amplitude versus the ratio of the sample time to the correlation time. As seen, for sample times much shorter than one correlation time the gyro rate output exhibits a bias error with an amplitude equal to the input noise amplitude. On the other hand, for sample times much longer than the correlation time the plot shows the slope of  $-1/2$  which is the characteristic of a random walk. Thus, random walk and random bias are simply the two limits of the same process. And, the gyro rate output follows a smooth transition between the two as the sample time is increased with respect the correlation time

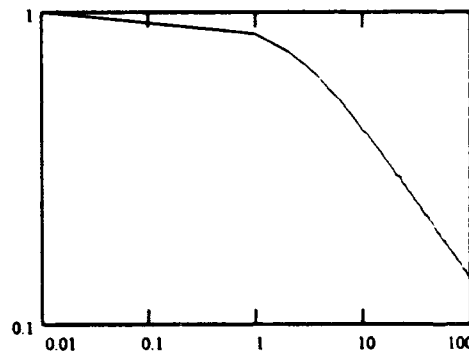


Fig. 1. Rate output error (in units of noise amplitude) vs sample time (in units of correlation time)

of the underlying random process. We demonstrate this further by discussing the limits of equation (15) below.

### **Random Walk**

For random processes whose correlation times are short compared to the sample time ( $T \gg \tau_i$  for all  $i$ 's) only the first term in the square bracket of (15) survives and we obtain:

$$\frac{\sigma_n}{T} = \frac{\sqrt{2 \sum_{i=1}^k N_i^2 \tau_i}}{\sqrt{T}} \quad (16)$$

which shows that the gyro rate output exhibits a random walk whose coefficient is determined by the RSS of noise amplitudes multiplied by the square root of the corresponding correlation times.

We now apply equation (16) to the case of RLG secondary dither. The latter is a noise intentionally added to the gyro sinusoidal dither to impede the build up of errors during the zero rate crossings. However, because of the finite mechanical  $Q$  of the RLG structure, only a limited range of the added noise frequencies can be effectively coupled to the gyro. The noise equivalent bandwidth of the gyro is  $\frac{\pi f_d}{2Q}$ , where  $f_d$  is the dither frequency. This same bandwidth, from (13), is also equal to  $(2\tau)^{-1}$  where  $\tau$  is the correlation time of the secondary dither as experienced by the gyro. Thus, we have:

$$\tau = \frac{Q}{\pi f_d} \quad (17)$$

whose substitution in (16) with only one noise term present yields:

$$\sigma_{rw} = N \sqrt{\frac{2Q}{\pi f_d T}} \quad (18)$$

For example, for a RLG with  $Q = 200$  and  $f_d = 400$  the secondary dither correlation time is about 0.16 second. Thus, for sample times of one second or longer the effect of secondary dither is a random walk at the gyro output. Conversely, for sample times much shorter than 0.16 second the gyro exhibits a random bias, as shown below.

### **Random Bias**

If correlation times of the random processes are long compared the sample time ( $T \ll \tau_i$  for all  $i$ 's) one can expand the exponential in the square bracket of (15). Keeping terms up to the third order in the expansion, one obtains:

$$\frac{\sigma_n}{T} = \sqrt{\sum_{i=1}^k N_i^2} \quad (19)$$

which is indicative of a random bias whose magnitude is the RSS of all applicable noise amplitudes. In our previous example, (19) indicates that *all* noise terms appear as a random bias at the gyro output if the sample time is much less than 0.16 second.

For the more general case where both long and short correlation time random processes are present the total gyro output error can taken to be the RSS of (16) and (19):

$$\frac{\sigma_n}{T_{total}} = \sqrt{\sum_{i=1}^l N_i^2 + \frac{2}{T} \sum_{i=1}^s M_i^2 \tau_i} \quad (20)$$

where  $l$  is the number of long correlation time random inputs with amplitudes  $N_i (i = 1, 2, \dots, l)$ .  $s$  and  $M_i$  are the corresponding quantities for the short correlation time random inputs.

## Conclusion

RLG bias or random walk? It is evident from the above analysis that the answer lies in the relationship between the sample time and the noise correlation time. To determine how a particular input noise affects the gyro output one first has to obtain an estimate of the noise correlation time ( $\tau$ ) and compare it to the sample time ( $T$ ). As shown here, if  $\frac{T}{\tau} \gg 1$  the input noise *always* causes a random walk at the RLG output. And, in the opposite limit the input noise *always* appears as a random bias. A key step here is the estimation of noise correlation time. Sometimes a measurement of the two-time correlation function (whose decay rate is the correlation time, see Eq. 11) of the input noise is not possible. Also, because of the system bandwidth, the noise experienced by the RLG could be different than the one intended, as is the case for randomized dither. In such cases one has to estimate the correlation time from the physics of the instrument, as was done here for the randomized dither.

## References:

- (1) See, for example, Papoulis, A., Probability, Random Variables, and Stochastic Processes, Third Edition, McGraw-Hill, Inc. (1991)

## Methods for Improved Estimation and System Integration for Time-Space-Position Information

James Chaffee  
Arrowsmith Technologies, Inc.  
1301 W 25th St, Ste 300  
Austin, TX 78705

Jonathan Abel  
Abel Innovations  
184 Tennyson Ave  
Palo Alto, CA 94301

Barbara McQuiston  
Sytronics, Inc.  
1656 Mardon Dr  
Dayton, OH 45432

### Introduction

In earlier work, two of the authors presented a two stage approach for integrating GPS with other sensors [1,2]. The basis for the method is prelinearization of the measurements by solving the pseudorange equations with a point estimator of position and bias. In the case of four pseudoranges, a simple exact solution that does not involve iteration is available [3,4]. It is in the over-determined case that the point estimator requires special attention.

This paper will first outline the two-stage approach to GPS emphasizing GPS/INS integration. Then the problem of statistical point estimation of position and bias for over-determined pseudorange equations is discussed. Of particular interest are methods which provide resistance to such problems as large outliers, time-correlated measurements, or very poor geometry. Finally, three different solution methods are compared with a Monte Carlo simulation.

### Two Stage Estimation

The two stage approach is illustrated in Figure 1 below. The essential requirement is that the position-bias

estimator be a sufficient or nearly sufficient statistic. This means that the estimate contains all the information which was in the original pseudorange data regarding position and bias. This property, together with the fact that the estimates are as serially independent as the original data, allows the estimates to be used as a data source. In essence, a data compression from pseudorange space to position-bias space has been performed. For more on this, see [1,2].

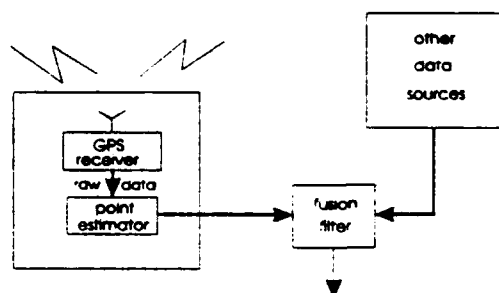


FIGURE 1 Two-Stage Estimation

As discussed in [1,2], it is not necessary for there to be extra data to integrate with GPS in order to render the method effective. There are three primary strengths to this method. These can be easily seen without considering the integration problem.

First, the position point estimator is not a sub-optimal estimator obtained by linearization as in the case of an extended or linearized Kalman-type filter. Instead,

the point estimator can be chosen to be a sufficient or nearly sufficient estimate of position and bias. In the exactly determined four satellite case, the solution is exact. This means it identically satisfies the pseudorange equations and so can be inverted to provide the pseudorange equations. In the over-determined case, there are a number of criteria which can be applied to the error for obtaining the most suitable estimator.

A second advantage is that the spatial and temporal aspects of the filtering task are decoupled. Thus, instead of simultaneously solving the pseudorange equations, estimating the dynamical behavior of the user and smoothing the result, the filter only estimates the dynamics and smooths the results. In the GPS case, the data coming out of the point estimator is position and bias. These measurements are linear in the state, avoiding linearized or extended sub-optimal Kalman-like filters, at least in the measurement updates.

The third advantage is related to the second. The filter does not need to build up the correlations between position and bias which are necessary to obtain an approximate solution by linearization. Such solutions can be sensitive to the pseudo-diagonalization of the covariance matrix which results from the common mistake of adding diagonal process noise covariance matrices during the filter time update, often in a misguided attempt to use process noise to overcome mismodeled measurement equations or dynamics. The use of a position point estimate provides an accurate solution and also allows more realistic process noise values to be used in the filter.

Because the position and bias are estimated externally, they can be passed to the filter with an estimate of the

measurement noise covariance matrix such as a weighted GDOP matrix. This avoids transients incurred while the filter builds up the required covariance to solve the linearized pseudorange equations. In the two-stage approach it is a simple matter to use the first position-bias estimate as initial condition. This creates a more robust filter, less subject to transients when initially operating and when GPS data is lost.

### **Advantages for GPS/INS Integration**

The advantages are even more pronounced when integrating GPS with an inertial sensor. The integrating filter can act as a navigation processor if raw sensed data is available, doing away with the need for an external navigation computer. In this case, the combined GPS receiver and inertial sensor becomes an inertial navigation system aided by GPS when pseudoranges are available. If either the inertial system or the GPS receiver is lost, the system functions in a stand alone mode without any need to switch to a different filter.

The system can be considered universal in that integration with a variety of inertial systems is simplified. For example, with the same design it is possible to integrate GPS with inertial systems that provide position and velocity instead of raw sensed inertial data. These advantages are because the sequence of point estimates from the GPS receiver are as serially independent as the raw data used to form them. Furthermore, because of sufficiency they retain the same information as the raw data used to form them.

In the remainder of this paper, the focus will be point estimates of position and bias from over-determined systems

of pseudorange equations. The concern is finding methods which provide different statistical qualities for different applications. For example, a point estimation method which is robust to serial correlation would be of great interest when selective availability is a problem.

### Point Estimation

Point estimation means the computation of a position and bias from pseudoranges collected at a single time. This requires a multichannel receiver. The estimation process is a static multivariate statistics problem and is analyzed in that light. The sample space is the set of all vectors of noisy pseudoranges for a satellite configuration at a fixed time. The noise statistics determines the distribution on the sample space.

Given a vector of pseudoranges  $\rho$  and a function  $f: \mathfrak{R}^m \rightarrow \mathfrak{R}^4$ , with  $f(\rho) = \hat{\theta}$

where  $\hat{\theta} = \begin{bmatrix} \hat{u} \\ \hat{b} \end{bmatrix}$  is an estimate of the true position and bias  $\theta$ , the estimation problem can be formulated in several ways, all aimed at producing errors which are small in some sense. The notion of error can also be approached in different ways. One approach is to consider the *estimation error*  $\theta - \hat{\theta}$ . Many statistical methods attempt to minimize the expectation of some function of this error. For example, least squares attempts to minimize the  $L_2$  norm of this error, namely

$E\left((\theta - \hat{\theta})'(\theta - \hat{\theta})\right)$ . Minimization of the sum of the absolute deviation of the

components of the error vector may provide different characteristics than maximizing the absolute deviation of the error vector components. Each of these estimation techniques has advantages and disadvantages. For example, minimization of the sum of the absolute deviation of the components of the error vector provides an estimator which is less effected by outliers than is minimization of the sum of the squared errors.

Quite frequently the estimator is required to be unbiased, that is,

$E(\theta - \hat{\theta}) = 0$ . Another criterion is that the estimator be a sufficient statistic. For our application in two stage estimation this is an important criterion. In essence, this means that the estimator  $\hat{\theta} = f(\rho)$  uses all the information in the sample of pseudoranges about the position and bias. This is easily understood when there are only four pseudoranges, since then the solution is exact and can be inverted back to the original pseudoranges. If the estimate of position and bias is to be used as a data source in two-stage estimation, the estimator should be as serially uncorrelated as the original data and lose no information. In practice, some information will be lost, but the estimator should be "nearly sufficient" [5]. The real point is that the estimator should make at least as much use of the information in the data as the linearized solution produced by a linearized or extended filter. Sufficiency is related to minimum variance estimation in that a sufficient statistic provides a minimum variance estimator and will therefore provide an estimator which reaches the Cramer-Rao lower bound on estimator variance when it can be reached [6].

Besides the estimation error, the pseudorange error  $\rho - \hat{\rho}$  can also be considered. In this case,  $\hat{\rho}$  refers to the vector of pseudoranges obtained by computing  $\hat{\rho}_i = \|S_i - \hat{u}\| + \hat{b}$ , where  $S_i$  refers to the  $i^{\text{th}}$  satellite position. In this case,  $\rho$  may have two meanings. It may refer to the "true" pseudoranges produced by  $\theta$  or it may refer to the noisy pseudoranges actually measured. In the latter case, with four pseudoranges the pseudorange error would be zero while the estimation error would not be zero.

It is not clear that minimizing the true pseudorange error would be equivalent to minimizing the estimation error. For example,

$$E((\theta - \hat{\theta})'(\theta - \hat{\theta})) = E(\|u - \hat{u}\|^2) + E((b - \hat{b})^2)$$

while

$$E((\rho_i - \hat{\rho}_i)^2) =$$

$$E((r_i - \hat{r}_i)^2) + E((b - \hat{b})^2) + 2E((b - \hat{b})(r_i - \hat{r}_i)),$$

where  $r_i$  refers to the range. Noteworthy is that  $|r_i - \hat{r}_i| \leq \|u - \hat{u}\|$ . The covariance between range error and bias error is a function of geometry. One basic problem is relating these two errors so that statistics based on one error source can be related to statistics based on the other.

A third way to view this estimation problem is more deeply embedded in the pseudorange space than in the position-bias space. Given five or more pseudoranges, instead of determining a function from pseudorange to position and bias, determine a function which operates on the pseudoranges to provide a set of four pseudoranges. These

pseudoranges could then be mapped directly to position and bias, providing a statistic. Though this may sound like a round about method, it may be that it is easier to compress the pseudoranges into a smaller set, still containing the same information about position and bias and possibly superior in some statistical sense. In fact, a similar approach is routine in GPS estimation when users discard all but the four pseudoranges providing the best GDOP. This amounts to simply discarding information. The proposed sufficient estimator would retain this information.

The process can be illustrated in the diagram below:

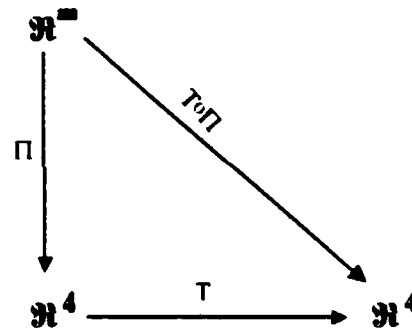


Figure 2: Estimation in the Pseudorange Domain

The map  $T \circ \Pi$  is the estimator of position, but  $T$  is simply the exact solution for four pseudoranges. (Note that  $T$  may produce two solutions and so is not necessarily a function [4].) The map  $\Pi$  determines a set of four pseudoranges from  $m$  pseudoranges. This should be done in such a way that no information is lost (sufficiency) and certain properties, such as robustness to outliers or to serial correlation's, are insured. Keeping only the four with the highest GDOP does not provide a sufficient statistic. This will be illustrated at the end of the final section.

There are several standard methods for estimating nonlinear structural relationships, with nonlinear least squares and maximum likelihood the two most commonly used. The former is not robust to outliers and is difficult to formulate. Both methods are parametric, depending on some known density of errors being given.

The MLE has certain large sample properties, such as consistency, under very general conditions [6]. However, in cases where the structural relationship implies a transformation relying on the parameter being estimated, such as the position or bias, the general likelihood equation  $\text{lik}(\theta|\mathbf{d}) = d \Pr(\mathbf{d}|\theta) = p(\mathbf{d}|\theta)d\mathbf{d}$  must include the differential element  $d\mathbf{d}$  [7]. Moreover, small sample properties for the MLE may not be good [8]. With GPS point estimates it is not so much the size of the sample as the information in the sample. However, increasing the number of satellites provides a larger sample and thus more information for a fixed geometry.

In general, statements about large samples can be reformulated in terms of statements about large information content for fixed variance. However, with GPS, the information content is limited by geometry. If one were to estimate a position from satellites on a sphere about the user, with unlimited, unobstructed visibility, the information content would go to infinity as the number of satellites went to infinity. Estimating the position components, which must be separated from the bias, would be trivial if satellites were placed exactly opposite one another in each of at least three orthogonal directions. If the satellites are restricted to a hemisphere, as is actually the case, this would not be

possible and the bias could only be asymptotically decoupled from one of the position components. This illustrates the fact that GPS point estimates have limited information available, even if the sample size is made very large. For this reason, the statistical theory of GPS point estimates of position and bias must be a small sample theory. This is also true for solutions obtained from Kalman-like filters, since the number of points in the time series of pseudoranges is not really relevant.

It should be noted that there are MLE estimators for dependent data [6]. Any point estimator which is robust to serial correlation would be of help in the presence of SA. This is true even when differential corrections are available since these corrections are often correlated by the filtering process that is used to form them.

The authors have introduced an approximate closed form maximum likelihood point estimator of position and bias in earlier papers [9,10] and will compare it to two other point estimators in this paper. The other two estimators are what we call Bancroft's algorithm for the over determined case [3,4] and iterative least squares. Bancroft's algorithm provides an exact closed form solution in the exactly determined case. However, in the over determined case its norm optimization properties have not been determined. (It is noteworthy that the statistics of exact solutions to the pseudorange equations remains an open item.) Nonetheless, the first author has used it quite successfully with real data in the over determined case.

Iterative least squares essentially minimizes the pseudorange error for fixed data. This is done for each data set, providing a local function. It should



minimize, at least locally, the expectation of the least squares norm with respect to the noise density for a fixed constellation. For the case of Gaussian measurement errors, the iteration will provide an MLE estimate.

This section has been a brief review of existing and potential methods for obtaining point estimates with consideration of special needs such as robustness. In the next section, a comparison of three of these methods is presented.

### A Comparison

In this section iterative least squares, a maximum likelihood approximation (based on an equation error as described in [9,10]) and Bancroft's method [3,4] are compared. Of 19 satellites, seven were above the horizon, though three were below ten degrees and two were really too low for use in most applications. The azimuths and elevations to a user near San Antonio are given in the list below, with azimuth listed first.

-126	2
-45	8
-73	36
67	25
126	38
130	3
7	87

All seven were used in case 1; satellites two through seven were used in case two; and satellites two through five and seven were used in case three.

The random errors added to the pseudoranges were white zero mean

Gaussian with standard deviation of 100 meters. As noted earlier, in this case iterative least squares is the maximum likelihood estimator. There were 10,000 samples taken with the satellite geometry fixed as noted earlier. All results are presented in local level coordinates about the true position. The initial iterative least squares estimate was the center of the earth with a perfect bias estimate. It took seven iterations to converge. For the remaining estimates, which started at the previous estimate, it took four iterations to converge. One case took three only iterations.

In order to compare these three methods, it is important to hold the satellite geometry fixed. The random errors will effect the pseudorange measurements, providing a density dependent on a fixed geometry. There is no random error on the satellite positions.

The three GDOPS were

57.9099	.3372	-.2206	-.1976
.3372	85.6924	-.2821	-.2863
-.2206	-.2821	120.5820	.7992
-.1976	-.2863	.7992	63.2400

80.8427	.6496	.1188	.2748
.6496	116.2610	.0643	.2050
.1188	.0643	130.3492	.8250
.2748	.2050	.8250	76.4345

81.6570	.5302	.1835	.2633
.5302	176.1767	.6138	.7095
.1835	.6138	208.9979	.9355
.2633	.7095	.9355	144.7711

These matrices have standard deviations on the diagonal and correlations off diagonal.

Below are listed the means of the three sets of error with their sample covariance matrices in the same form as for the GDOP. The sample covariances are about the actual error rather than the mean error. Of particular interest is the fact that Bancroft's method and the MLE estimates are much closer in their errors than to the errors in iterative least squares. Preliminary work by Abel seems to suggest that this will be true for certain information cases. In essence, Abel's work suggests that Bancroft's method may be an approximation to the approximate MLE estimator, particularly in those directions which have higher information content.

All three methods are remarkably close to the GDOP. This indicates that the estimators may all be nearly sufficient [1].

For the three cases, the mean errors for the iterative least squares are

$$\begin{bmatrix} -.0878 \\ -.2171 \\ -.8541 \\ -.0869 \end{bmatrix}, \begin{bmatrix} .2532 \\ .2579 \\ -.5547 \\ .1752 \end{bmatrix} \text{ and } \begin{bmatrix} .2992 \\ .7875 \\ .0989 \\ .6638 \end{bmatrix}$$

For the approximate MLE, the errors

$$\text{are } \begin{bmatrix} -.0990 \\ -.2836 \\ -.7427 \\ -.0381 \end{bmatrix}, \begin{bmatrix} .2762 \\ .2241 \\ -.6081 \\ -.1489 \end{bmatrix} \text{ and } \begin{bmatrix} .3228 \\ .8190 \\ .1568 \\ .7016 \end{bmatrix}$$

For Bancroft's method, the errors are

$$\begin{bmatrix} -.0975 \\ -.2795 \\ -.8206 \\ -.0699 \end{bmatrix}, \begin{bmatrix} .2758 \\ .2210 \\ -.5364 \\ .1826 \end{bmatrix}, \text{ and } \begin{bmatrix} .3226 \\ .8169 \\ .2150 \\ .7331 \end{bmatrix}$$

The sample covariance matrices are presented with standard deviations on the diagonal and correlations off the diagonal. For iterative least squares they are as follows:

$$\begin{bmatrix} 56.7344 & .3353 & -.2160 & -.1839 \\ .3353 & 86.2989 & -.2790 & -.2808 \\ -.2160 & -.2790 & 120.6736 & .8063 \\ -.1839 & -.2808 & .8063 & 63.4514 \end{bmatrix}$$

$$\begin{bmatrix} 79.2216 & .6431 & .1132 & .2742 \\ .6431 & 115.4382 & .0507 & .1903 \\ .1132 & .0507 & 120.6736 & .8286 \\ .2742 & .1903 & .8286 & 75.9983 \end{bmatrix}$$

$$\begin{bmatrix} 80.0628 & .5267 & .1829 & .2660 \\ .5267 & 175.9115 & .6102 & .7069 \\ .1829 & .6102 & 207.8643 & .9365 \\ .2660 & .7069 & .9365 & 144.0565 \end{bmatrix}$$

For the approximate MLE method they are

$$\begin{bmatrix} 57.1708 & .3348 & -.2270 & -.1930 \\ .3348 & 86.6009 & -.2842 & -.2856 \\ -.2270 & -.2842 & 122.5139 & .8103 \\ -.1930 & -.2856 & .8103 & 64.0456 \end{bmatrix}$$

79.3401	.6405	.1117	.2723
.6405	115.6060	.0570	.1946
.1117	.0570	130.8228	.8306
.2723	.1946	.8306	76.4194

80.2107	.5277	.1856	.2683
.5277	176.0497	.6110	.7075
.1856	.6110	208.1743	.9367
.2683	.7075	.9367	144.2498

For Bancroft's method they are

57.1498	.3341	-.2178	-.1854
.3341	86.5629	-.2795	-.2817
-.2178	-.2795	121.5972	.8083
-.1854	-.2817	.8083	63.7376

79.3366	.6403	.1163	.2757
.6403	115.6124	.0549	.1927
.1163	.0549	131.0667	.8312
.2757	.1927	.8312	76.5243

80.2078	.5276	.1879	.2699
.5276	176.0328	.6103	.7069
.1879	.6103	209.0503	.9370
.2699	.7069	.9370	144.2498

Cursory examination of these matrices reveals that all three methods are close in their estimates. For the most part, iterative least squares seems to have a slight advantage in the horizontal while the other two methods seem to have a slight edge in the estimation of zenith and bias. What is not revealed in these arrays is that Bancroft's method and the MLE are closer to one another than to the iterative least squares. As an example, consider the two plots below. One is of

latitude error in Bancroft versus the same error in the MLE. The other is of the least squares versus the MLE. These use the case 1 data, with all seven satellites.

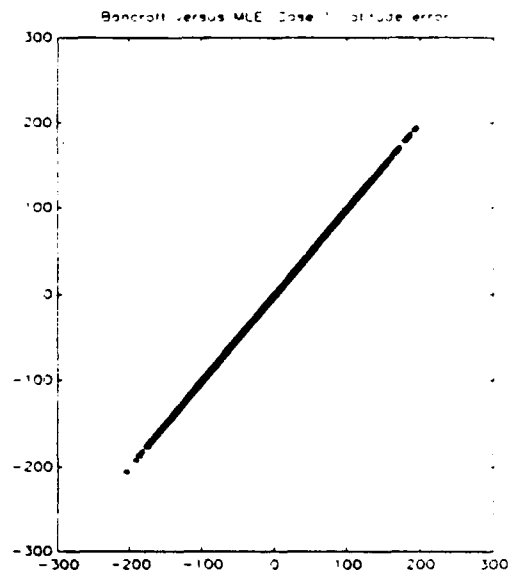


Figure 3

Compare this with the next figure. The basic point is that the MLE errors are far less correlated with the least squares errors than with the errors from Bancroft's method. However, this is only partly true as is seen in figures 5 and 6.

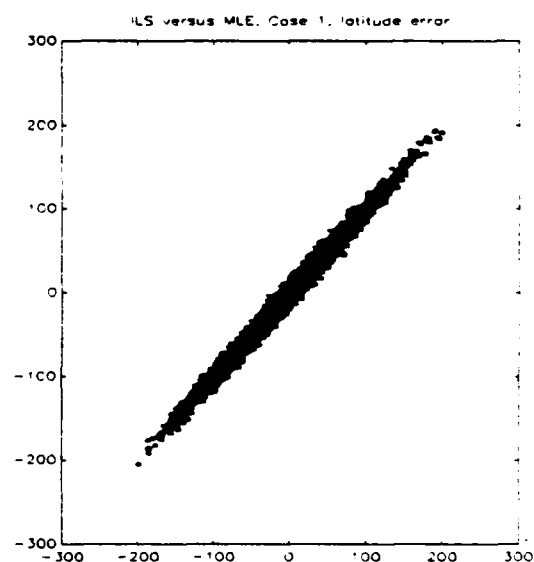


Figure 4

The longitude errors are very similar to the latitude errors and are not shown. As figures 5 and 6 illustrate, the correlations are not so strong for the bias (and zenith) errors.

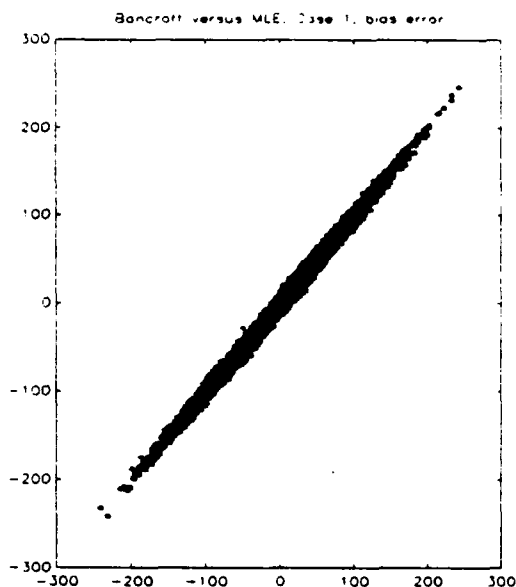


Figure 5

In cases 2 and 3 similar results were noted, except that the MLE and Bancroft's methods were not quite so closely related. They were still closer in

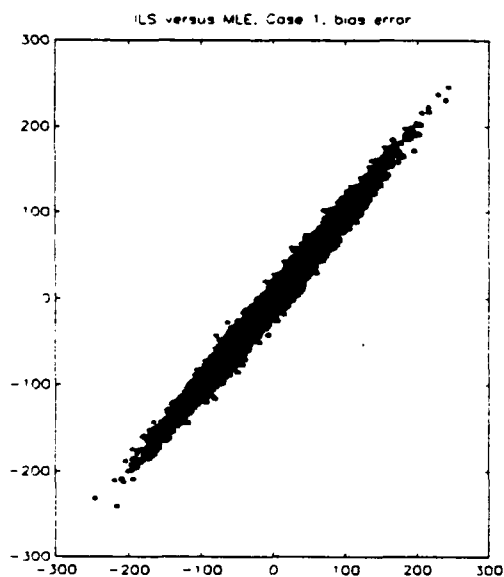


Figure 5

horizontal errors than in bias and zenith.

To consider the case of a large amount of information, something at least near the idea of a large sample, a "glass earth" solution using all nineteen satellites was computed. The results of this run are presented below.

For iterative least squares, MLE and Bancroft's method the mean errors were

$$\begin{bmatrix} -.5070 \\ -.0764 \\ -.1490 \\ .1626 \end{bmatrix}, \begin{bmatrix} -.4713 \\ .0251 \\ -.0934 \\ .1442 \end{bmatrix} \text{ and } \begin{bmatrix} -.4732 \\ .0255 \\ -.0327 \\ .1251 \end{bmatrix}$$

The covariances were

$$\begin{bmatrix} 40.4204 & .0582 & -.0473 & .0399 \\ .0582 & 41.5416 & -.0944 & -.0736 \\ -.0473 & -.0944 & 41.1022 & -.3464 \\ .0399 & -.0736 & -.3464 & 24.7555 \end{bmatrix}$$

$$\begin{bmatrix} 41.6992 & .0462 & -.0823 & .0614 \\ .0462 & 42.0963 & -.0944 & -.0736 \\ -.0823 & -.0944 & 41.1022 & -.3464 \\ .0614 & -.0736 & -.3464 & 24.7555 \end{bmatrix}$$

$$\begin{bmatrix} 41.6445 & .0471 & -.0425 & .0425 \\ .0471 & 42.0925 & -.0925 & -.0737 \\ -.0425 & -.0925 & 42.5835 & -.3688 \\ .0425 & -.0737 & -.3688 & 25.0272 \end{bmatrix}$$

with a GDOP of

$$\begin{bmatrix} 40.1910 & .0585 & -.0493 & .0295 \\ .0585 & 41.5770 & -.0969 & -.0823 \\ -.0493 & -.0969 & 41.2102 & -.3482 \\ .0295 & -.0823 & -.3482 & 24.6574 \end{bmatrix}$$

Note that in this case iterative least squares performed better than either of the other estimators, coming much closer to the GDOP. Moreover, the large standard deviation of zenith in the approximate MLE estimator is curious. Unfortunately, there was not enough time to examine the data more closely. However, Bancroft's method was still closer to the closed form MLE than to the iterative least squares. This was particularly true in the horizontal errors, which showed the same high correlations as on scatter plots from earlier runs. As before, there was a greater difference in the bias error but in this case the zenith errors were almost totally uncorrelated, as is indicated by the numbers.

Of note is that there were no intentional outliers in this data. It would be useful to model data with outliers as is discussed in [11] to determine which, if any, of the above methods are resistant.

One other test would be to produce data as above, but preceded by SA correlated data. This would determine robustness with respect to SA.

Finally, compare the GDOP of the "best four" satellites. The sum of squares of the diagonals is minimized with satellites 7, 6, 2 and 1. Note that this set contains the lowest three satellites. The GDOP is

$$\begin{bmatrix} 91.6845 & .4914 & -.2996 & -.4699 \\ .4914 & 109.7344 & -.3823 & -.4897 \\ -.2996 & -.3823 & 136.1183 & .6834 \\ -.4699 & -.4897 & .6834 & 75.7597 \end{bmatrix}$$

Given the results of the simulation, it is apparent that choosing the best four does not beat estimates based on all in view. If the best four are chosen from those left

when the two lowest are dropped, the resulting GDOP is

$$\begin{bmatrix} 110.5549 & .5577 & .1194 & .3416 \\ .5577 & 182.1498 & .5843 & .7259 \\ .1194 & .7259 & 209.1290 & .9028 \\ .3416 & .7259 & .9028 & 148.6148 \end{bmatrix}$$

This is clearly not competitive with using all five. The extra information sharpens the estimate.

## Conclusion

This paper has stressed point estimation of GPS position-bias solutions. The sample is a fixed set of pseudoranges at a fixed time and it is argued that because of this it is necessary to develop a small sample theory of GPS point estimates. A first step would be to determine the statistical properties of the exact solution.

A comparison of three solution methods based on simulated uncorrelated Gaussian errors has been presented. It is noted that in the case of only a few satellites, all the methods were comparable in accuracy, achieving the GDOP. This indicates to the authors that the three methods are nearly sufficient in the case presented. However, in the case of a "glass earth" solution with 19 satellites, iterative least squares seemed to use the larger amount of available information more efficiently.

Future work should stress robustness properties, particularly with respect with large deviations, non-normality, and time correlated data. It would be instructive to test these algorithms with t-distributed errors.

## Bibliography

1. Sufficiency, Data Reduction and Sensor Fusion for GPS, ION Nat. Tech. Mtg., Jan 27-29, 1992, San Diego.
2. The GPS Filtering Problem, IEEE PLANS 92, Mar 23-27, 1992, Monterey, CA.
3. Steven Bancroft, An Algebraic Solution of the GPS Equations, IEEE Trans. Aerosp. Elec. Systems, Vol AES-21, 56-59, Jan, 1985.
4. J. Chaffee and J. Abel, Bifurcation of the Pseudorange Equations, ION Nat. Tech. Mtg., Jan 20-23, 1993, San Francisco.
5. L. Le Cam, *Asymptotic Methods in Statistical Decision Theory*, Springer-Verlag, 1986.
6. Alan Stuart and J. Keith Ord, *Kendall's Advanced Theory of Statistics, Volume 2, Fifth Edition*, Oxford University Press, 1991
7. Nico J. D. Nagelkerke, *Maximum Likelihood Estimation of Functional Relationships*, Springer-Verlag, 1992.
8. V. K. Rohatgi, *An Introduction to Probability Theory and Mathematical Statistics*, John Wiley and Sons, 1976.
9. J Chaffee, J. Abel and B. McQuiston, GPS Positioning, Filtering, and Integration, NAECON 93, May 24-27, 1993, Dayton.
10. J. Abel and J. Chaffee, Direct GPS Solutions, ION 49th Annual Meeting, Boston, June 21-23, 1993.
11. Peter J. Huber, *Robust Statistical Procedures*, SIAM, 1977.

**THIS PAGE LEFT BLANK INTENTIONALLY**

**CSDL - P - 3304**

**An Adaptive Kalman Filter to Improve  
Micromechanical Inertial Instrument Performance**

**by**

**Jonathan Kossuth  
Charles Kochakian**

**May 1993**

**C.S. Draper Laboratory  
555 Technology Square  
Cambridge, MA 02139**

**Approved for Public Release; distribution is unlimited**



## Abstract

As newer inertial technologies in inertial instruments emerge, the need for improved data filters is growing because both unmodeled errors and unknown factors may exist in the instrument data. Two online adaptive Kalman filters have been developed for analysis of these inertial instruments. These adaptive Kalman filters use the innovation sequence of the Kalman filter, which is the difference between an actual measurement and the estimate of that measurement based on the state vector at that time, in order to determine the optimal filter parameters. In an optimal filter, the innovation sequence is a Gaussian white noise process. However, if the innovation sequence is not a Gaussian process, then improvements in either the parameter matrices or state vector are necessary to optimize the filter. An optimality test using autocorrelation methods has been successfully implemented and verified for use with these adaptive Kalman filters. By examining the innovation sequence, the adaptive Kalman filters can extract all of the information that is necessary for improving the filter performance. Performance of the filters is improved by determining the proper system model, by estimating any unknown parameters in the system matrices or by identifying any periodic noise in the signal. A fault tolerant algorithm is included in one of the adaptive Kalman filters.

The adaptive Kalman filters use several techniques to exploit the information stored in the innovation sequence. Maximum likelihood techniques are used to estimate the parameters of the filter matrices by choosing those parameter values that maximize the likelihood function of the parameters. Correlation methods are used to determine the proper system model by comparing the innovation sequence to a known signal. Power spectral density analysis is used to identify periodic signals by examining the PSD of the innovation sequence. Simulations have been run successfully to verify the filter performance for a number of cases. In each of these simulations, the adaptive Kalman filters were able to modify the filter matrices online to achieve optimality.

These adaptive Kalman filters have been applied for both raw data reduction and reduced data analysis to data from various micromechanical gyroscope tests, including a stationary drift test and a commanded rate test. For raw data reduction, the maximum likelihood estimator has been combined with the PSD analysis in order to minimize the noise associated with data decimation. By determining accurately the value of the measurement noise and by identifying any periodic noise, the reduced data is more accurate than with conventional data reduction methods. For reduced data analysis, all three adaptive concepts have been combined into one filter. With this adaptive filter, any unmodeled terms will be identified and, with an accurate estimate of the measurement noise and other unknown matrix parameters, the final estimate of the state vector will be more accurate than that of a traditional Kalman filter. By applying these adaptive Kalman filters to micromechanical gyroscope data, reductions of up to 50 percent in the RMS of the innovation sequence have been achieved and a pressure sensitivity in the micromechanical gyroscope has been identified.

## 1.0 Introduction

As newer inertial instrument technologies emerge, better data processing is needed for characterizing these instruments. These newer instruments are more sophisticated and their behavior challenges traditional data processing techniques, which have commonly included a triangular filter for reducing raw data and a Kalman filter for analyzing this reduced data. These filters, however, can result in a less-than-optimum indication of instrument quality because neither unmodeled error sources in the original signal nor unknown factors in the instrument performance are accounted for in either aspect of the data processing. Adaptive Kalman filters give flexibility to data analysis by seeking out the system model that optimizes both filter performance and instrument characterization.

By accounting for unmodeled terms and errors, the results from both data decimation and data analysis will be improved. Adaptive filters are necessary to compensate for limitations in the Kalman filter. A Kalman filter only analyzes the data with respect to a given state vector and given parameter values. If this description of the system is not adequate, then errors in the state vector estimates will result because the filter cannot improve the state model on its own. These limitations of the Kalman filter are the driving forces in developing adaptive filters that are capable of compensating for unknown errors.

Maximum likelihood estimation, correlation methods and power spectral density analysis are used for parameter estimation, system identification and periodic noise location. These three concepts are successfully incorporated into two separate adaptive Kalman filters: one for data decimation and one for data analysis. These two filters are then used for data analysis of various micromechanical gyroscopes in several tests.

## 1.1 Kalman Filter Theory

A linear system can be expressed by the following stochastic difference equation

$$\mathbf{x}(t_{i+1}) = \Phi(t_{i+1}, t_i) \mathbf{x}(t_i) + \mathbf{B}(t_i) \mathbf{u}(t_i) + \mathbf{G}(t_i) \mathbf{w}(t_i) \quad (1)$$

with available discrete-time measurements modeled by the linear relation

$$\mathbf{z}(t_i) = \mathbf{H}(t_i) \mathbf{x}(t_i) + \mathbf{v}(t_i) \quad (2)$$

where

$\mathbf{x}$  = state vector =  $n \times 1$  vector

$\Phi$  = state transition matrix between times  $t_{i+1}$ ,  $t_i$  =  $n \times n$  matrix

$\mathbf{u}$  = deterministic input vector =  $r \times 1$  vector

$\mathbf{B}$  = deterministic input matrix =  $n \times r$  matrix

$\mathbf{G}$  = system plant noise input matrix =  $n \times q$  matrix

$\mathbf{z}$  = the measurement vector =  $m \times 1$  vector

$\mathbf{H}$  = observability matrix =  $m \times n$  matrix

and,  $\mathbf{w}$  and  $\mathbf{v}$  are independent, zero mean, white Gaussian noise processes with covariances  $\mathbf{Q}(t_i)$  and  $\mathbf{R}(t_i)$ , respectively.

The measurements,  $\mathbf{z}$ , are processed to produce the state estimates,  $\hat{\mathbf{x}}$ . The *state transition equations* are

$$\hat{\mathbf{x}}(t_i^-) = \Phi(t_i, t_{i-1}) \hat{\mathbf{x}}(t_{i-1}^+) + \mathbf{B}(t_{i-1}) \mathbf{u}(t_{i-1}) \quad (3)$$

$$\mathbf{P}(t_i^-) = \Phi(t_i, t_{i-1}) \mathbf{P}(t_{i-1}^+) \Phi(t_i, t_{i-1})^T + \mathbf{G}(t_{i-1}) \mathbf{Q}(t_{i-1}) \mathbf{G}(t_{i-1})^T \quad (4)$$

$$\mathbf{K}(t_i) = [\mathbf{P}(t_i^-) \mathbf{H}(t_i)^T] \mathbf{S}(t_i)^{-1} \quad (5)$$

$$S(t_i) = H(t_i)P(t_i^-)H(t_i)^T + R(t_i) \quad (6)$$

The *measurement incorporation equations* introduce the new measurement into the state vector estimates:

$$r_i = z_i - H(t_i)\hat{x}(t_i^-) \quad (7)$$

$$\hat{x}(t_i^+) = \hat{x}(t_i^-) + K(t_i)r(t_i) \quad (8)$$

$$P(t_i^+) = [I - K(t_i)H(t_i)]P(t_i^-) \quad (9)$$

where,

$\hat{x}$  = the estimate of  $x$  based upon the most recent measurement

$r$  = innovation sequence

$S$  = covariance of innovation sequence

$K$  = the Kalman gain matrix =  $n \times m$  matrix.

The (+) and (-) superscripts on  $t_i$  indicate whether the value at a particular  $t_i$  is immediately before or immediately after the measurement incorporation at time  $t_i$ .

### 1.1.1 The Innovation Property of an Optimal Filter

In an optimal Kalman filter, the innovation sequence  $r$  is a Gaussian white noise sequence with covariance  $S$  [7, 8]. The autocorrelation sequence of white noise, because it is an impulse at the zeroth lag term, will be used to implement a white noise test for the adaptive Kalman filter. By implementing a white noise test, state vector modification can be limited to only situations in which the present state vector does not optimize the filter. After calculating a biased estimate of autocorrelation function, confidence limits for this process can be established based on the standard deviation of the measurement of autocorrelation, which is the inverse of the square root of the length of the innovation sequence [7]. If the autocorrelation of the innovation sequence remains within these confidence limits, then no state vector modification is necessary.

## 1.2 Maximum Likelihood Estimator

In order to obtain the optimal state vector estimate, an accurate description of the parameter matrices  $\Phi$ ,  $B$ ,  $G$ ,  $Q$ , and  $R$  is necessary. With a maximum likelihood estimator, the true values of the parameters can be estimated both efficiently and in real time by minimizing a likelihood function with respect to the unknown parameters. The maximum likelihood estimator will have a unique solution equal to the efficient estimate, if such an estimate exists, and that estimate will be consistent. This solution is both asymptotically Gaussian and asymptotically efficient. Also, given a single sufficient statistic for the estimated variable, the maximum likelihood estimate will be sufficient, and it will also be at least asymptotically efficient and unbiased [6]. The maximum likelihood estimator provides the optimal state estimates and covariances, as well as the optimal parameter estimates and covariances. It is assumed that the parameters are *essentially constant over a given interval of  $N$  sample periods*, where  $N$  is arbitrary.

The maximum likelihood estimator flowchart is presented in Figure 1; the derivation of this maximum likelihood estimator is presented in Appendix A. At every  $N$  points, parameter estimates can be based on the previous  $N$  data points ( $t_N, t_{2N}, t_{3N}, \dots$ ). During each estimation interval, the derivatives of the Kalman filter matrices are computed, and the parameter estimates are updated at the end of the interval. These new parameter estimates are then used to update the system matrices that are dependent upon the parameters. The  $J$  matrix and score vector in Figure 1 are discussed in Appendix A.

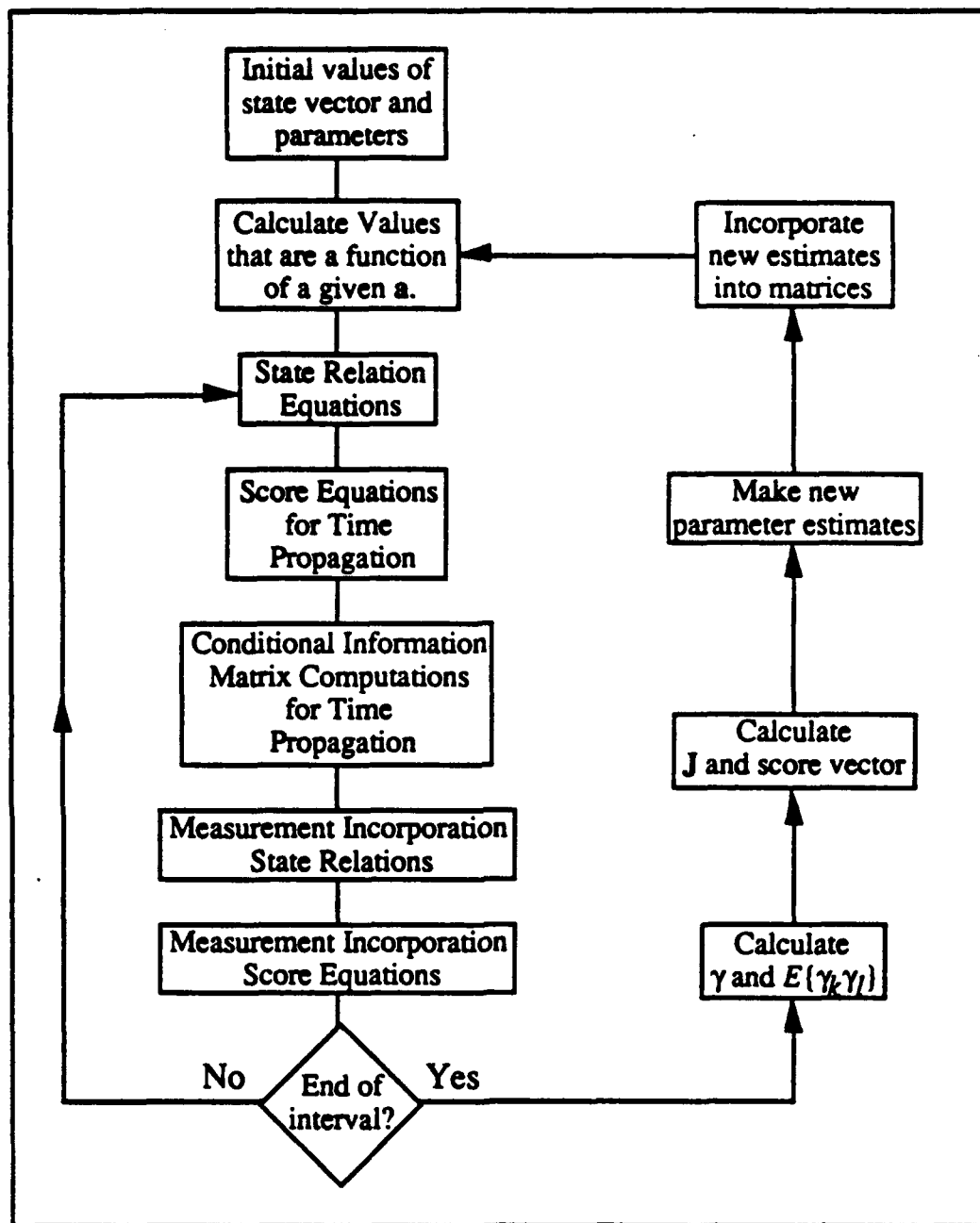


Figure 1. Flowchart of Maximum Likelihood Estimator

### 1.2.1 Verification of Maximum Likelihood Estimator

In order to verify the code, as well as the theory, for the maximum likelihood estimator, several runs were made with simulated data. The test cases include unknown measurement noise standard deviation, unknown process noise standard deviation, and unknown measurement and process noises.

The results of these test cases are presented in Table 1. In all three tests, the maximum likelihood estimate was able to converge to the actual values of the parameters. Test 3 demonstrates that this maximum likelihood estimator can estimate both process and measurement noise accurately.

**Table 1. Results of Maximum Likelihood Estimator Verification**

Test Number	Parameters	Initial Guess	Actual Value	Estimate
1	Measurement Noise	1.0000	0.09935	$0.09700 \pm 0.00451$
2	Process Noise	0.0100	0.09902	$0.09028 \pm 0.01916$
3	Measurement Noise	1.0000	0.10036	$0.09835 \pm 0.00461$
	Process Noise	0.0100	0.09922	$0.07038 \pm 0.01832$

### 1.3 Model Adaptive Filter Using Correlation Methods

Often, when processing data, the system model which describes the behavior of the instrument has not been completely described. In order to test the completeness of a given system model, a term can be added to the system model, and the measurements can then be processed using this enhanced model. However, the results from this procedure may be misleading. When terms are added to a state vector, the Kalman filter estimates a value for the term, regardless of the truth of the state vector. As a result, terms that do not actually exist may appear to be present because of the given state vector. However, by exploiting the information in the nonoptimal innovation sequence using correlation methods, the existence of unmodeled terms can be determined, and the innovation sequence can be reduced to a white noise process.

#### 1.3.1 Derivation of Model Adaptive Filter

Suppose that a random process  $P(t)$ , such as temperature, pressure, rate, etc. is known completely throughout the measurement interval [5]. If another random signal,  $S(t)$ , such as the innovation sequence, is an unknown linear function of this random process, then

$$S(t) = kP(t - T) + N(t) \quad (10)$$

where  $k$  is an unknown constant,  $T$  is a time delay, and  $N(t)$  is a white noise process. It can be shown that, if  $N(t)$  is a zero mean noise process not independent of  $P(t)$ , then the stationary crosscorrelation function between the signal and the random process is [5]

$$\varphi_{SP}(\tau) = k\varphi_{PP}(\tau - T) + \varphi_{NP}(\tau) \quad (11)$$

The crosscorrelation function between  $P(t)$  and  $S(t)$  is directly proportional to the autocorrelation function of  $P(t)$ , which is known. Therefore, by taking the crosscorrelation between  $S(t)$  and  $P(t)$  and the autocorrelation of  $P(t)$ , a relationship between the signal  $S(t)$  and  $P(t)$ , if it exists, can be found.

##### 1.3.1.1 Implementation of Model Adaptive Filter

If the innovation sequence is colored noise, then the model adaptive filter implements the following procedure to identify possible unmodeled terms. First, the necessary autocorrelation and crosscorrelation functions are determined. The delay, if it exists, can be calculated by determining the time difference between the maxima of the crosscorrelation and autocorrelation. Next, the value of the scaling  $k$  must be calculated by removing the delay, and expressing the sum of the square of the errors of the best estimate of  $k$  as

$$\varepsilon = \sum_{j=1}^N \left( \varphi_{SP}(\tau_j) - k\varphi_{PP}(\tau_j) \right)^2 \quad (12)$$

The value of  $k$  that minimizes this value of  $\epsilon$  is

$$k = \frac{\sum_{j=1}^N \varphi_{PP}(\tau_j) \varphi_{SP}(\tau_j)}{\sum_{j=1}^N (\varphi_{PP}(\tau_j))^2} \quad (13)$$

The signal  $S$  is the innovation sequence, and the process  $P$  is the unmodeled variable. To determine whether the process  $P$  should be included in the system model,  $P$  is multiplied by the best estimate of  $k$ , and this product is subtracted from the innovation sequence for all past time, resulting in a difference sequence. This difference sequence represents the innovation sequence if the additional term has been included in the original system model. The RMS of this difference sequence is then compared with the RMS of the innovation sequence over the same time interval. If the addition of this term improves the RMS by at least five percent, then the term is included in the system model. Otherwise, the term is not added. Simulations have shown that by using the maximum likelihood technique to determine the scaling factor  $k$ , only significant terms are identified and added to the model [5].

## 1.4 Power Spectral Density Analysis

Besides the unmodeled effects discussed in Section 1.3, periodic noise signals may exist in instrument outputs. A periodic noise signal may be due to a malfunction in the instrument hardware. For example, in the micromechanical gyroscope, the inertial element is vibrated at its natural frequency. Later, this sinusoidal signal is demodulated to obtain a DC signal (see Figure 4). If there is a discrepancy between the demodulation frequency and the vibration frequency, then a periodic noise signal will result. This periodic noise signal, if it is not removed by the baseband filter, will exist in the gyroscope output. Fortunately, modeling a periodic noise signal is easily accomplished with a combination of sine and cosine terms. The identification of periodic noise can be accomplished using power spectral density methods.

### 1.4.1 Power Spectral Density Theory

The power spectral density function (PSD) of a stationary random process determines the frequency content of that process. By expressing the power spectral density function in terms of the Fourier transform of a crosscorrelation function, it can be shown that, for a finite data set, an approximation to the power spectral density is:

$$\tilde{\Phi}_{XX}(\omega) = \frac{1}{T} |F\{X_T(t)\}|^2 \quad (14)$$

For discrete data, the Fast Fourier Transform (FFT) can be used to generate a PSD of the innovation sequence using Equation 14 [2].

### 1.4.2 Filter Design

To implement the periodic noise identification filter using PSD methods, the following procedure is used. If the innovation sequence over a given estimation interval does not test as white noise, then the Power Spectral Density of the innovation sequence is constructed using Equation 14 and the FFT. The frequency of the maximum power is identified and recorded. The filter then proceeds to the next segment of the innovation sequence. If this segment tests as non-white noise, then the PSD is again constructed. If the frequency of maximum power for this PSD is within a given tolerance of the

previously identified frequency, then a sine and cosine term at that frequency are added to the filter. This two step procedure ensures that the innovation sequence is colored due to periodic noise, not for another reason, such as a poor system model or a bad data point. Also, the next frequency must be identified again in one of the next two estimation intervals of the first frequency in order to be added.

## **1.5 Adaptive Data Analysis Filter Development**

In this section, two adaptive filters are created: one for raw data reduction and one for reduced data analysis. These filters can determine a proper system model through estimation of noise processes, identification of periodic noise and enhancement of the state vector. By implementing these two adaptive filters, micromechanical inertial instrument performance can be improved. Figure 2 is a flowchart of the reduced data analysis adaptive filter. For the raw data reduction adaptive filter, the steps within the dashed box are not implemented.

### **1.5.1 Raw Data Reduction Adaptive Filter**

In data decimation, the purpose is to provide estimates of the mean of a segment of data over a given interval. Therefore, the raw data reduction adaptive filter must "re-estimate" the mean over each interval. This requires that, after the estimate of the mean is recorded, the values of the state vector and its covariance are reset to their initial values and allowed to converge again over the next estimation interval. The raw data reduction filter combines the maximum likelihood estimation with the PSD analysis in order to provide an accurate estimate of the mean over an estimation interval and to remove periodic noise signals. However, the noise and frequency estimates will be allowed to converge over the entire data set. This is permissible because it is assumed that the noise sources are nearly constant throughout the data acquisition.

When comparing this adaptive filter with a triangular filter, equal bandwidths are used. By comparing equal bandwidths, each filter makes estimates based on the same number of data points, and an accurate picture of the behavior of each filter can be drawn. For equal bandwidth, the full size of the triangular filter must be equal to the estimation interval of the raw data reduction adaptive filter.

### **1.5.2 Reduced Data Analysis Adaptive Filter**

Once the data has been prepared for analysis, e.g. data decimation, instrument performance must be characterized according to a system model. Because of the rigid system model in the Kalman filter, this method cannot account for an inaccurate description of the noise, unmodeled system behavior, and unknown periodic noise. By combining the three adaptive filter concepts discussed in Section 1.2 through Section 1.4, a more powerful adaptive Kalman filter has been developed; the flowchart in Figure 2 is a representation of this adaptive filter. All three concepts, as well as a fault tolerant algorithm, are included so that, if the raw data reduction adaptive filter is not needed, then the reduced data analysis adaptive filter can determine independently the system parameters as well as identify periodic noise.

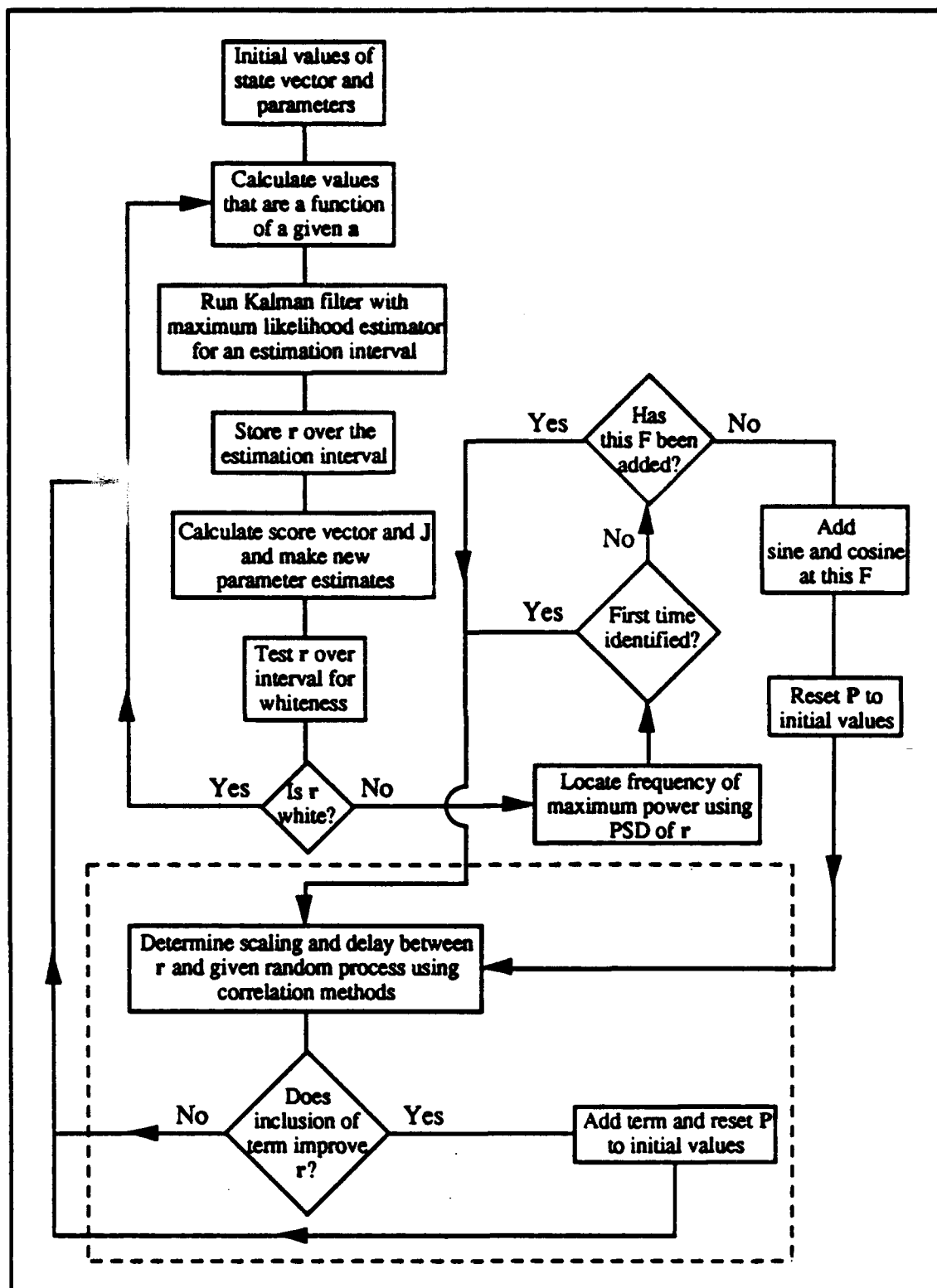


Figure 2. Flowchart of Adaptive Kalman Filter



### 1.5.2.1 Fault Tolerant Algorithm

A fault tolerant algorithm can detect unexpected jumps in the gyro output by examining the innovation sequence. The variable  $\epsilon$  is defined as [5]

$$\epsilon = \sum_{j=1}^N \mathbf{r}_j^T \mathbf{S}_j^{-1} \mathbf{r}_j \quad (36)$$

where  $N$  is the length of the estimation interval,  $\mathbf{r}$  is the innovation sequence and  $\mathbf{S}$  is the covariance of the innovation sequence. The variable  $\epsilon$  is a chi-squared distribution random variable with  $mN$  degrees of freedom, where  $m$  is the dimension of the innovation vector  $\mathbf{r}$ . For each estimation interval, the variable  $\epsilon$  is computed, and the mean, which is equal to the degrees of freedom, is subtracted from the value. This value is then compared to a confidence limit that depends on the standard deviation, which is the square root of the product  $2mN$ . If the value of  $\epsilon$  exceeds this confidence limit, then the state vector covariance matrix is reset to its initial values, and the state vector estimate is able to converge to a new estimate.

## 1.6 Micromechanical Gyroscopes

The basic vibratory micromechanical gyroscope is fabricated from a single silicon block, with gold electroplate as an inertial element, as shown in Figure 3. Two torsional flexures connect the outer gimbal to the case. Similarly, two flexures connect the inner gimbal to the outer gimbal. These two orthogonal sets of flexures are weak in torsion, but stiff in all other directions [3, 4]. Torquing electrodes embedded in the chip vibrate the outer gimbal, creating an oscillatory angular momentum vector,  $\mathbf{H}$ , about the Vibratory Driven Axis shown in Figure 3. In order to achieve maximum resolution, the outer gimbal is vibrated at the resonant frequency of the inner gimbal. If there is an angular rate about the input axis, the inner gimbal will oscillate about its flexures at a magnitude proportional to the angular rate about the input axis. Readout electrodes, mounted above the inner gimbal, detect a change in capacitance as the inner gimbal oscillates. By sensing this change in capacitance, the angular rate about the input axis can be determined [3, 4]. Closed loop operation is achieved by torquing the inner gimbal back to a null position.

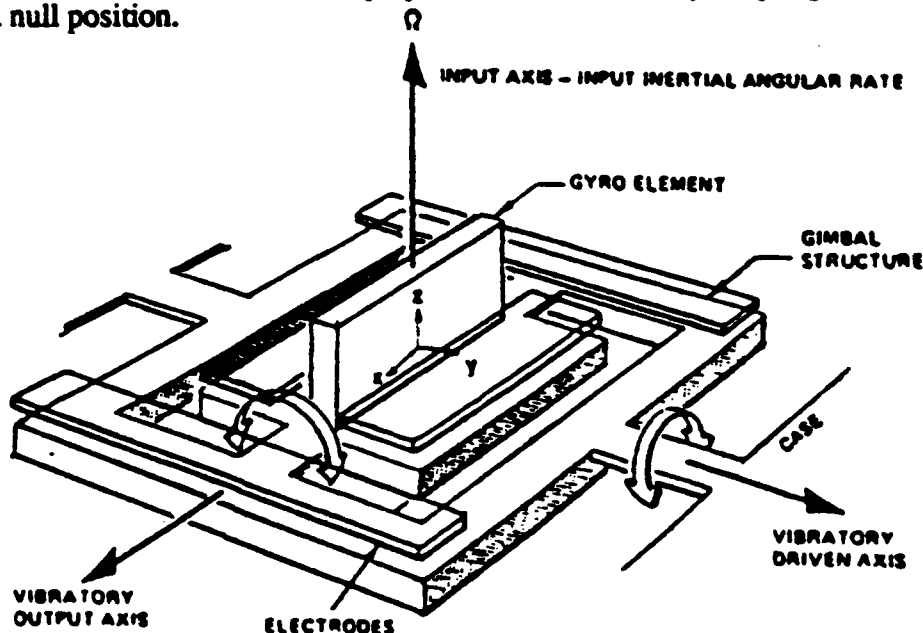


Figure 3. Vibratory Micromechanical Gyroscope

Open loop operation of a typical micromechanical gyroscope is shown in Figure 4. The inertial element is driven at its natural frequency and a 100 kHz carrier signal is applied to the output axis. Motion from mass imbalance or rate input causes a modulation of this 100 kHz signal at the resonant frequency of the gyro element. If the resonant frequency of the element is 30 kHz, then the modulated frequencies are 70 kHz and 130 kHz. These carrier signals then pass through the preamp, postamp and various filters. At the carrier demodulation, the 100 kHz signal is removed, and the resulting frequency components are 30 kHz, 170 kHz and 230 kHz. The low pass filter removes the 170 kHz and 230 kHz signals. The remaining 30 kHz signal is then demodulated at the natural frequency, resulting in a D.C. signal and a 60 kHz signal. Next, a low pass filter allows only the D.C. signal to pass. This D.C. signal is the rate sensed by the gyroscope. For closed loop operation, this signal would be remodulated and applied to rebalance the capacitor plates.

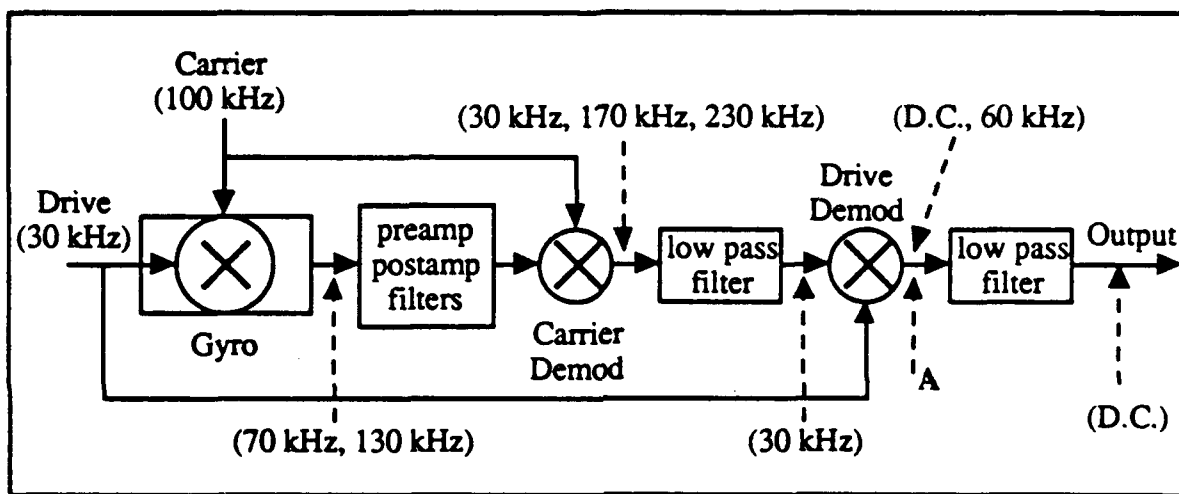


Figure 4. Schematic of Micromechanical Gyroscope Operation

### 1.6.1 Noise Sources

Three major sources of error in the micromechanical gyroscopes are conversion factor stability, the minute size of the instrument and bandwidth. One major source of error is the stability of the conversion factor that converts the gyro output from volts to deg/hr. Presently, the conversion factor is so large (~1,000,000 deg/hr/volt) that the output voltage reading must be accurate to  $\mu$ volts in order to achieve an accuracy of less than 10 deg/hr. Because of the minute size of this instrument, Brownian motion and damping are forces that significantly limit gyroscope performance [1, 9]. A method of isolating the gyroscope in a vacuum is needed in order to reduce the impact of these effects. The data analysis adaptive filter can adjust for noise sources such as Brownian motion and pressure sensitivity. Thermal variations have a very small effect on these instruments. Bandwidth is an important component of the gyroscope performance [1, 9]. The readout noise is proportional to the bandwidth, and the mechanical noise of the instrument is proportional to the square root of the bandwidth. In order to improve instrument performance, the noise due to bandwidth must be reduced.

### 1.6.2 Inverted Gyroscope

The inverted gyroscope design is an attempt to improve the vibratory gyroscope performance. This design is very similar to the basic vibratory gyroscope, but the method of operation is different. In this gyroscope, the inner gimbal is vibrated at the natural frequency of the outer gimbal. When an inertial rate is applied about the input axis of the

gyro, the outer gimbal will oscillate with a magnitude proportional to the input rate. Because the outer gimbal oscillates to generate output, the oscillations are relative to a fixed case, providing a more stable and more accurate output than the vibratory gyroscope. The conversion factor of the inverted gyro is four times less than that of the original micromechanical gyroscope (360,000 deg/hr/volt vs. 1,200,000 deg/hr/volt). The inverted gyroscope design is affected by the same noise sources as the original design.

## 2.0 Micromechanical Gyroscope Data Analysis

Data from different micromechanical inertial instruments and from various test procedures were analyzed to demonstrate that both of the adaptive filters improve the estimates of instrument performance. These analyses were compared with those of the traditional triangular and Kalman filters. Data was collected from both the original micromechanical design and from the inverted gyro design. The tests that were conducted include stationary drift tests, commanded rate tests and pressure variation tests; sampling rates ranged from 1 Hz to 1500 Hz in these tests.

### 2.1 Stationary Drift Test with Original Gyro Design

Data was collected at 3 Hz for 16 hours in a stationary drift test with LA perpendicular to the earth's axis using the original vibratory gyroscope design. The gyro output was analyzed using both the raw data reduction and reduced data analysis adaptive filters.

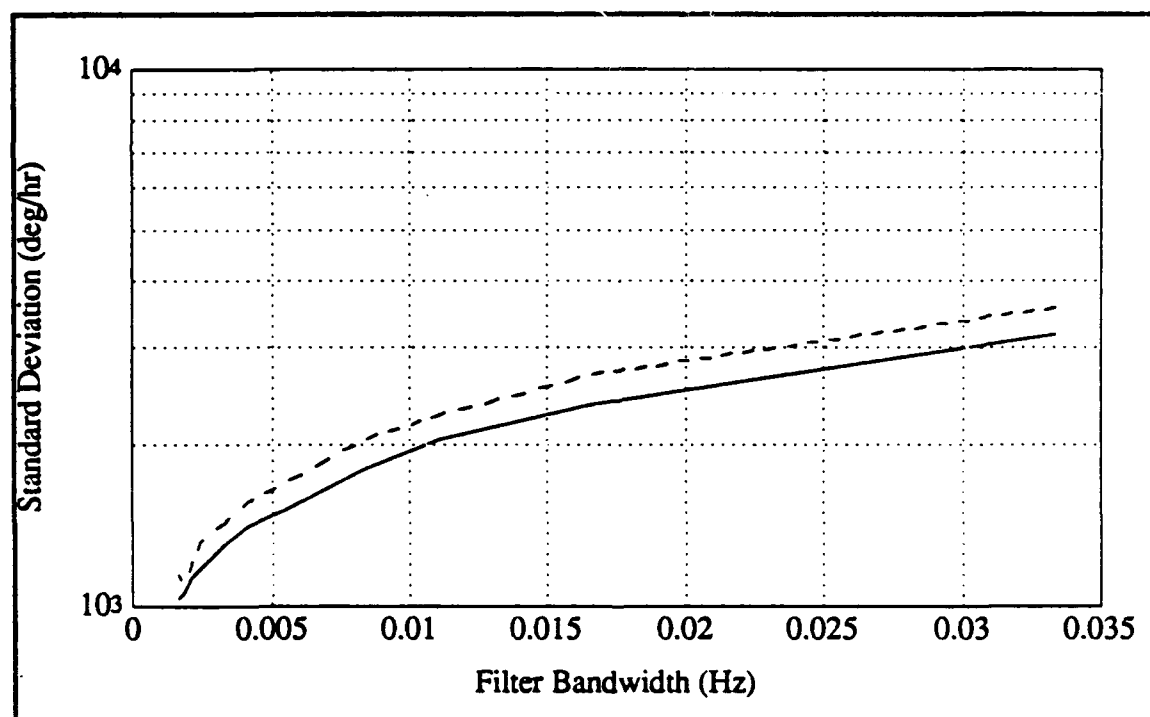


Figure 5. Standard Deviation vs. Bandwidth for Stationary Drift Test

#### 2.1.1 Raw Data Reduction of 3 Hz Stationary Drift Test

The gyro output was decimated at bandwidths ranging from 0.002 Hz to 0.033 Hz, using both the raw data reduction adaptive filter and the triangular filter. Figure 5 presents a comparison of the standard deviations of the decimated data versus bandwidth (in deg/hr, using a conversion factor of 1,238,870 deg/hr/volt). The dashed line represents the triangular filter standard deviations, and the solid line represents the raw data reduction adaptive filter standard deviations. The data reduction adaptive filter

performed, on average, 10 percent better than the triangular filter. The greatest improvement was 403 deg/hr at a bandwidth of 0.033 Hz. A FSD of the gyro output verified the adaptive filter conclusion that no periodic noise exists in this data.

### 2.1.2 Reduced Data Analysis of 3 Hz Stationary Drift Test

After the data decimation analysis, the gyro output was analyzed using the reduced data analysis adaptive filter with an estimation interval of 1000 points. Because this is a stationary drift test, the bias term cannot be distinguished from the rate dependent terms. Therefore, only the bias and the measurement noise standard deviation were estimated using the adaptive Kalman filter; a random walk parameter was included in a second analysis of this data. This data was then analyzed using a Kalman filter with a given measurement noise standard deviation of 123,887 deg/hr. The second analysis with the adaptive filter concluded that no random walk existed, because the random walk estimate was  $451 \pm 726$  deg/hr/ $\sqrt{\text{sec}}$ , and the other estimates were near those of the first adaptive filter analysis. In Table 2, the results from the first adaptive filter and the Kalman filter are compared. This data has been converted to deg/hr using a conversion factor of 1,238,870 deg/hr/volt. The adaptive filter improved the standard deviation of the estimate of the mean by 84 percent over the traditional Kalman filter.

**Table 2. Data Analysis on Stationary Drift Data**

Term (deg/hr)	Traditional Kalman Filter		Adaptive Kalman Filter	
	Initial	Final	Initial	Final
Bias	0.0000	-449,093 $\pm$ 303	0.0000	-449,164 $\pm$ 48
$\sigma_{\text{measurement}}$	123,887		1,238,870	19,377 $\pm$ 438
Innov. Seq. RMS	—	19,452	—	19,447

## 2.2 Stationary Drift Test with Inverted Design

For the second test, the raw data reduction filter identified and modeled periodic noise. By sampling at a higher rate, a distributed high frequency noise signal can be identified more easily, and the instrument will have a higher operating bandwidth [5]. A triangular filter cannot account for periodic noise, and its performance will degrade as the bandwidth increases. However, for an adaptive filter, performance does not deteriorate for increased bandwidth because the periodic noise can be removed from the original signal. To obtain data with periodic noise, samples were taken at 1500 Hz from point A in Figure 4. Since the data is taken after the drive frequency demodulation, but before the baseband filter, a high frequency noise signal equal to twice the drive frequency of the inertial element of the gyroscope is present in the data. For this inverted gyroscope, the drive frequency is 2500 Hz, resulting in a high frequency signal at 5000 Hz. The sampling rate was 1500 Hz, which aliases the 5000 Hz signal to a 500 Hz signal. This stationary drift test was conducted for 6 seconds and was analyzed using both the raw data reduction adaptive filter and triangular filter.

### 2.2.1 Raw Data Reduction of 1500 Hz Stationary Drift Test

The data was decimated using both the raw data reduction adaptive filter and the triangular filter at various bandwidths. Figure 6 is a plot of the log of the standard deviations in deg/hr for both filters as a function of bandwidth. The solid line represents the adaptive filter; the dashed line represents the triangular filter. As the bandwidth increases, the adaptive filter has a lower standard deviation that achieves a 51.38 percent improvement at 10.71 Hz bandwidth, which, using a conversion factor of 360,000 deg/hr/volt, gives an improvement of about 3620 deg/hr. Larger bandwidths are not

possible with the adaptive filter because there are too few data points in an estimation interval (less than 70 points), and the filter cannot converge to the true estimate of the mean in such a short interval. However, if the sampling rate were increased further, then the bandwidth of the instrument would likewise increase.

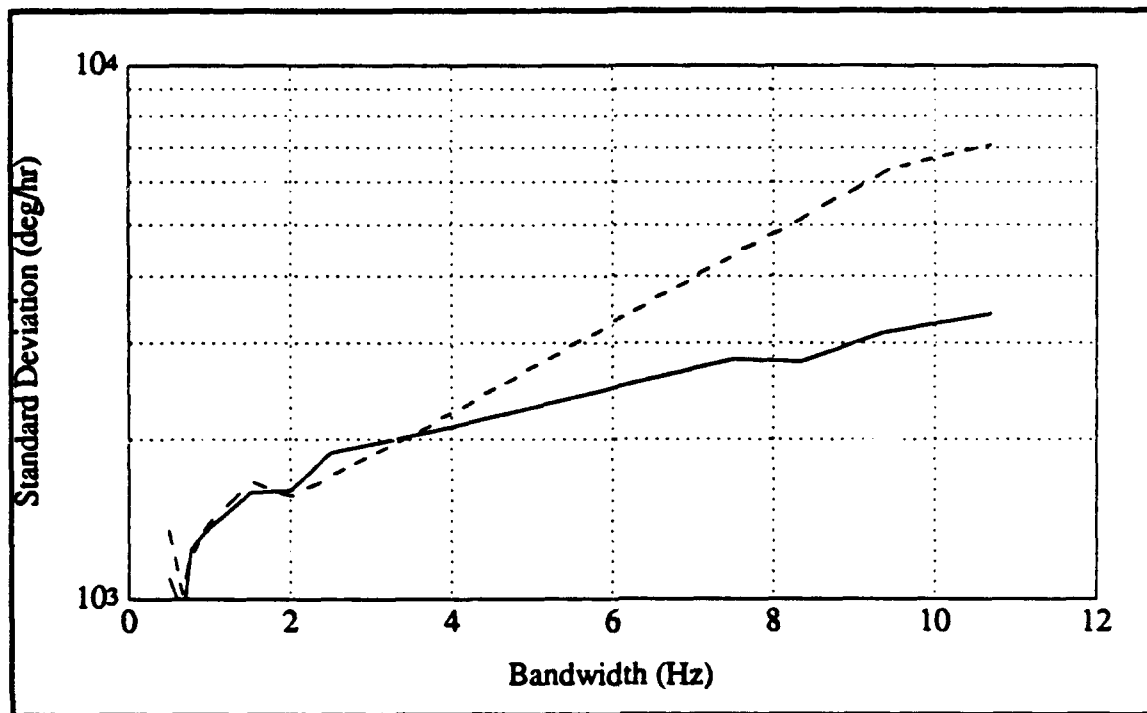


Figure 6. Standard Deviation vs. Bandwidth for Inverted Gyro Drift Test

### 2.2.2 Reduced Data Analysis of 1500 Hz Stationary Drift Test

The data set was analyzed using two state vector estimators: the reduced data analysis adaptive filter and the Kalman filter. Because this was a stationary drift test, only the bias of the data could be estimated. Two tests were run using the reduced data analysis adaptive filter with an estimation interval of 100 points: one estimating measurement noise  $\sigma$ , and one estimating both the noise  $\sigma$  and the random walk parameter. In these two tests, frequency components were removed at multiple frequencies. The reason for the wide range of frequency components most likely has to do with frequency beating that results from the inability of the filter to identify a frequency component exactly. For the second test, the estimate of the random walk parameter was  $11,628 \pm 20,988$  deg/hr/ $\sqrt{\text{sec}}$ , suggesting that random walk does not exist in this data. Because the remaining estimates from this test were similar to those in the first test, the results from the second test are not presented. In the third test, a Kalman filter was used, with a given measurement noise standard deviation of 36,000 deg/hr. Table 3 presents the results from the first adaptive filter and the Kalman filter analyses. This table shows that the traditional Kalman filter performs non-optimally when unmodeled noises, such as periodic noise, exist in the signal. If a periodic signal is not identified and removed during raw data reduction, then the Kalman filter will give non-optimal results. The RMS of the innovation sequence for the Kalman filter is almost twice as large as that for the adaptive Kalman filter.

**Table 3. Results for Stationary Drift Test for Inverted Design**

Parameter (deg/hr)	Traditional Kalman Filter		Adaptive Kalman Filter	
	Initial Value	Final Estimate	Initial Value	Final Estimate
Bias	0.0000	36,432 $\pm$ 396	0.0000	37,404 $\pm$ 1008
$\sigma_{\text{measurement}}$	36,000		360,000	26,388 $\pm$ 1836
Freq. ID (Hz)	Not Estimated		15.93, 478.6, 494.8, 510.3, 526.6	
Innov. RMS	—	53,496	—	31,428

### 2.3 Scale Factor Test with Inverted Gyroscope Design

The inverted gyroscope design was used for the third test. Data was collected at 1 Hz over 95 minutes for a commanded rate test, with a commanded rate profile of 100 deg/sec to -100 deg/sec in 10 deg/sec increments with a 0 deg/sec rate between each nonzero rate. During data acquisition, the bias term of the gyroscope jumped dramatically and unexpectedly (around 1.5 volts) near 3900 seconds. This unexpected shift in bias encouraged the development of the fault tolerant algorithm that was discussed in Section 1.5. This data set was used to successfully demonstrate that the fault tolerant algorithm is capable of detecting and accounting for radical jumps in the system behavior.

#### 2.3.1 Reduced Data Analysis of Commanded Rate Test

When this data was analyzed using the reduced data analysis filter, the fault tolerant algorithm shifted the bias estimate at 3900 seconds, as expected. Figures 7 and 8 show the bias estimate versus time for both the Kalman and adaptive filters. In Figure 7, the Kalman filter is unable to adjust for the shift in the bias estimate at 3900 seconds. However, in Figure 8, the adaptive filter quickly adjusts to the bias shift. This rapid adjustment of the bias estimates affects the innovation sequence, as shown in Figures 9 and 10. In Figure 9, the innovation sequence reflects the poor bias estimate because the traditional Kalman filter is unable to account for the jump in the bias term. Figure 10 shows the innovation sequence versus time for the reduced data analysis adaptive filter. While the innovation sequence of the Kalman filter is erratic after the bias jump, as the filter slowly converges to a new bias estimate, the adaptive filter innovation sequence correctly quickly because the fault tolerant algorithm rapidly adjusted the bias estimate with a step change. A comparison between the reduced data analysis adaptive filter and Kalman filter is shown in Table 4. All of the results in this table are given in volts. No attempt is made to convert the voltage output into deg/hr because of the noise in the test and the large bias shift. The adaptive filter reduces the innovation sequence RMS to one fourth the value of the Kalman filter innovation sequence RMS.

**Table 4. Results for Commanded Rate Test**

Parameter (Volts)	Traditional Kalman Filter		Adaptive Kalman Filter	
	Initial Value	Final Estimate	Initial Value	Final Estimate
Bias	0.0000	-0.9340 $\pm$ 1.3e-3	0.0000	-1.9412 $\pm$ 7.3e-3
Scale Factor	0.0000	0.0124 $\pm$ 3.1e-5	0.0000	6.23e-3 $\pm$ 1.7e-4
$\sigma_{\text{measurement}}$	0.1000		1.0000	0.0656 $\pm$ 0.0052
Innov. RMS	—	0.6246	—	0.1553

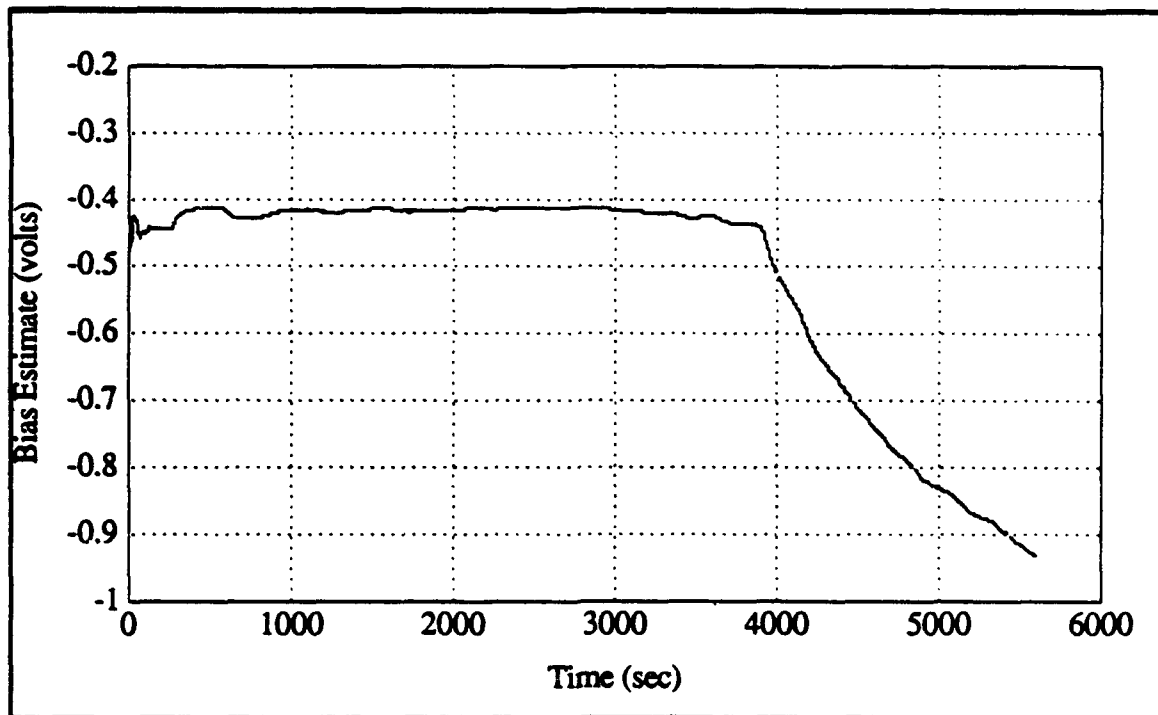


**Figure 7. Bias Estimate of Kalman Filter in Commanded Rate Test**

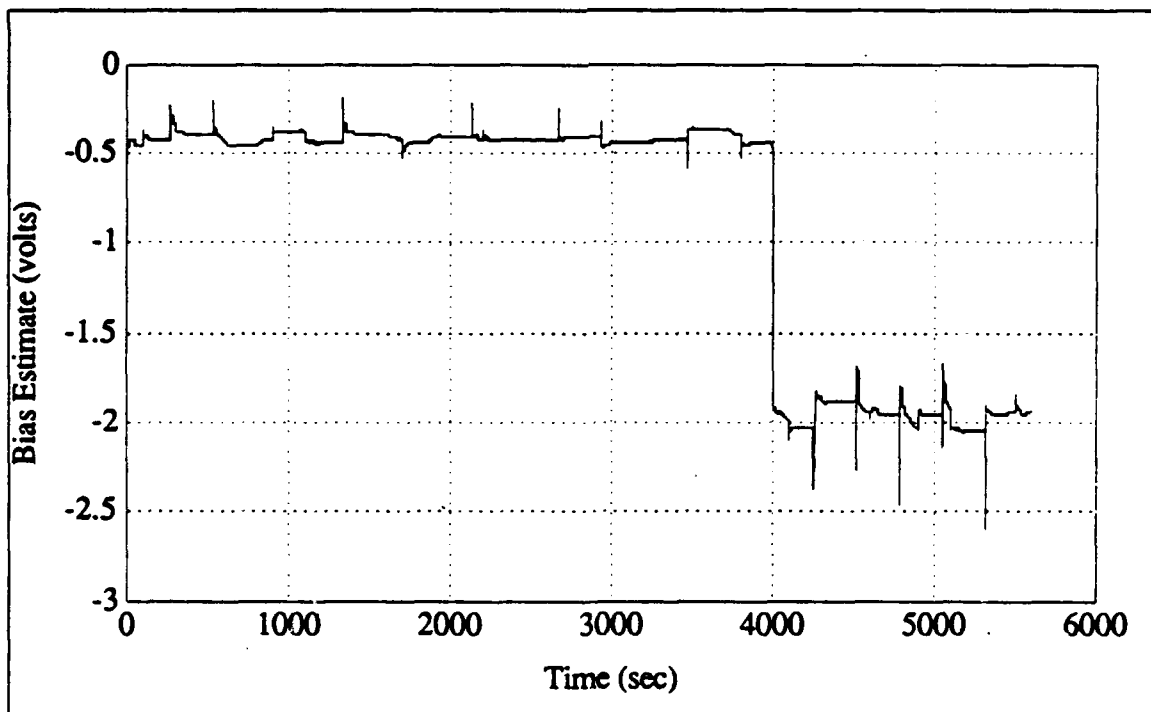


**Figure 8. Bias Estimate of Adaptive Filter in Commanded Rate Test**

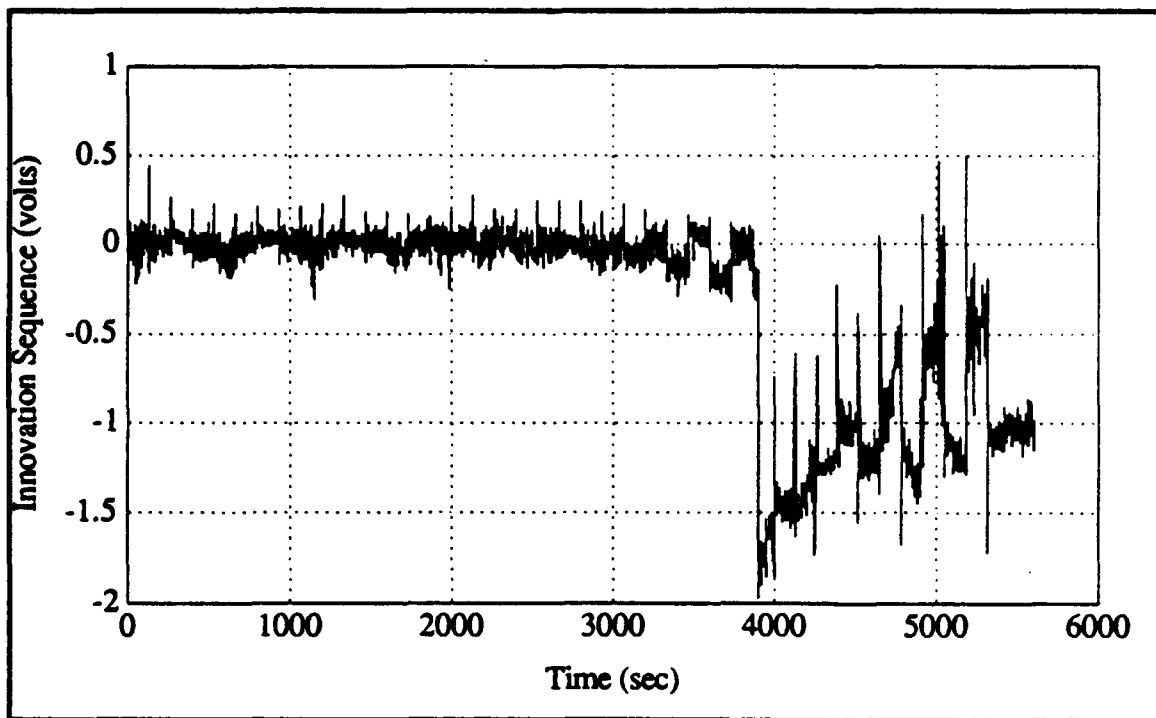


**Figure 9. Kalman Filter Innovation Sequence for Commanded Rate Test**

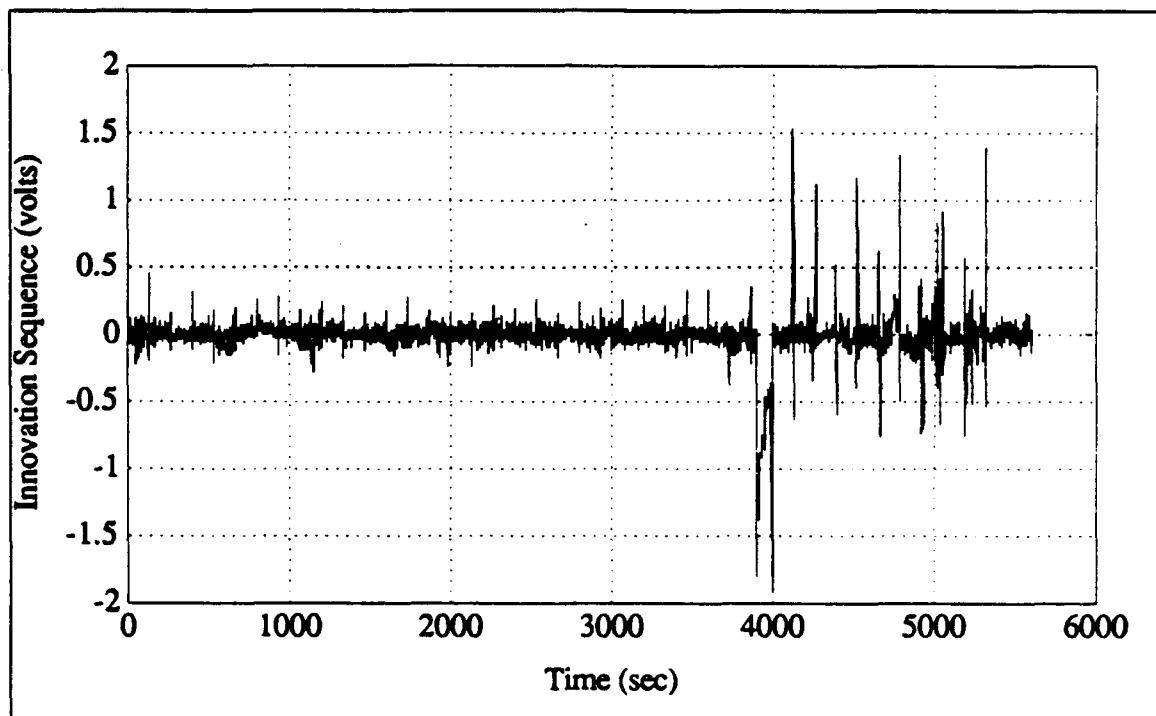


**Figure 10. Adaptive Filter Innovation Sequence for Commanded Rate Test**



## 2.4 Pressure Variation Test for Inverted Design

For the final test, the pressure around the gyroscope was varied. The test itself involved commanded rates at 100 deg/sec, 90 deg/sec and 80 deg/sec with 0 deg/sec rates between each of the nonzero commanded rates. The pressure was allowed to vary through a leak in the setup. Data was taken at 1 Hz for 12.5 minutes.

Because of the current setup of the gyroscope, however, pressure readings near the gyroscope cannot be taken accurately; the pressure is on the order of millitorr, much smaller than the pressure reading accuracy. Therefore, the pressure variation was modeled as linearly dependent on time. The slope for this approximation is unknown because of the limits of the measuring instruments. With this linear model, time was used to test whether an additional pressure-dependent term could be added to the system model. The gyro output was analyzed using both the reduced data analysis adaptive filter and the traditional Kalman filter. Using an estimation interval of 100 points, the reduced data analysis adaptive filter successfully identified both the measurement noise and the time/pressure dependence of the instrument, and adjusted the system model accordingly.

The results from these two test runs are compared in Table 5, using a conversion factor of 360,000 deg/hr/volt. As Table 5 shows, the bias estimate for the Kalman filter is very poor, and the Kalman filter innovation sequence RMS is almost twice as large as that of the reduced data analysis adaptive filter. The adaptive filter added the pressure sensitivity/trend term at the end of the first estimation interval, when the inclusion of the term improved the RMS of the innovation sequence by 60.2 percent. Although the pressure contributes significantly to the performance of the gyroscope, the final design of the gyroscope will be sealed in a vacuum, and therefore unaffected by variations in pressure. Figure 11 shows the innovation sequence before (dashed line) and after (solid line) the pressure sensitivity term was added to the model. Inclusion of the pressure sensitivity improved the RMS of the innovation sequence by 60 percent.

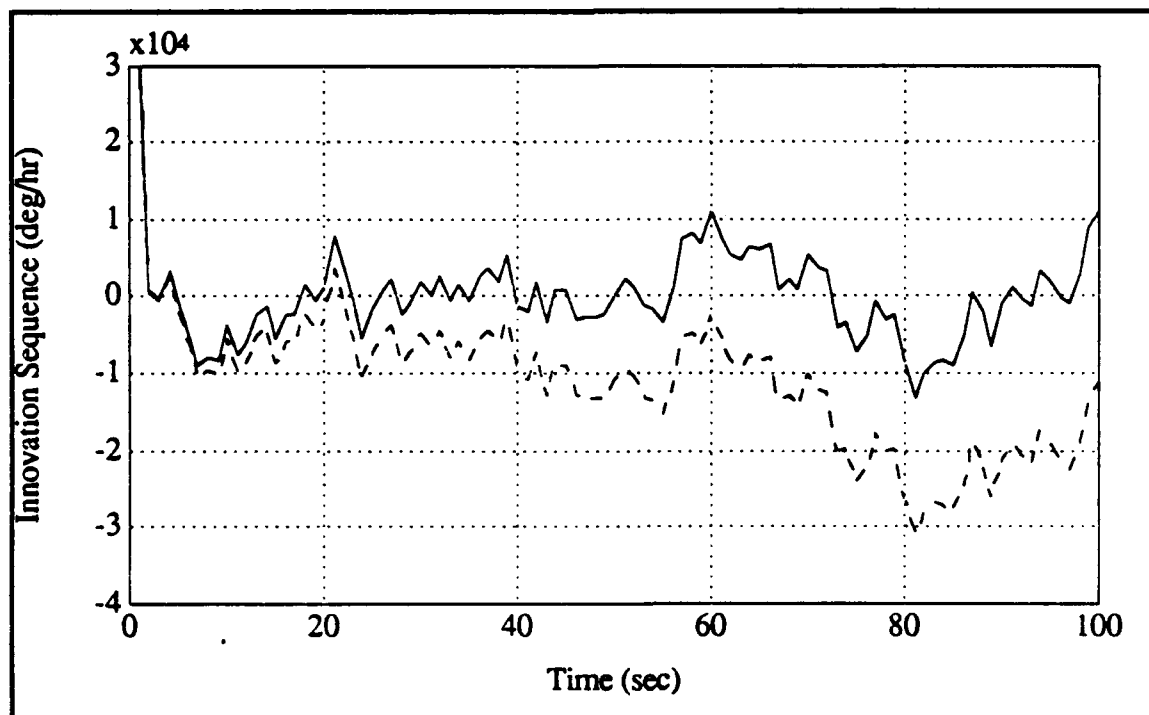


Figure 11. Modified Innovation Sequence for Pressure Variation

**Table 5. Results for Pressure Variation Test on Inverted Gyro**

Parameter (deg/hr)	Traditional Kalman Filter		Adaptive Kalman Filter	
	Initial Value	Final Estimate	Initial Value	Final Estimate
Bias	0.0000	-89,450 ± 18900	0.0000	42,118 ± 9166
Scale Factor	0.0000	3174 ± 30	0.0000	3431 ± 60
Press. (°/hr/s)	Not Modeled	Not Modeled	Not Modeled	-405 ± 17
$\sigma_{\text{measurement}}$	36,000		360,000	55,388 ± 1783
Innov. RMS	—	92,469	—	52,145

### 3.0 Conclusions

A maximum likelihood estimator has been developed for parameter estimation. This estimator is capable of accurate estimates of both  $Q$  and  $R$ , as well as estimating time varying parameters. A state vector determination filter has been developed using correlation methods. This filter is effective in online location and inclusion in the state vector of previously unmodeled terms. Trend, pressure and acceleration dependent terms can be identified and included in the state vector. Power spectral density analysis is used for periodic noise identification. This filter has successfully identified unmodeled frequency components in both simulated and real data.

These three concepts have been combined into two adaptive filters; one for raw data reduction, the other for reduced data analysis. Characterization of micromechanical inertial instruments can be improved using these adaptive filters. For raw data reduction, improvements from 10 to 50 percent over the triangular filter have been achieved in real micromechanical gyroscope output. The reduced data analysis filter is quite effective in identifying unmodeled terms. This adaptive filter has identified a pressure sensitivity for the micromechanical gyroscope. This filter has also accurately estimated the initially unknown measurement noise standard deviation of various instruments. Because of their versatility and performance accuracy, both of these filters should be considered for use in future data analysis.

These filters can be implemented online for sampling rates on the order of 50 Hz. Real time processing with these filters at higher sampling rates is possible by using parallel processors. With three processors, one filter could solve the Kalman filter and maximum likelihood estimator equations to generate the state vector and parameter estimates, as well as the innovation sequence, another filter could determine the PSD of this innovation sequence, and the third processor could test additional terms for inclusion in the system model. With parallel processing, the filter outputs would not be delayed by either the PSD or correlation methods; real time output would be generated, and the model could be adapted as the secondary processors determined a new system model.

## Appendix A

### Derivation of a Maximum Likelihood Estimator

#### A.1 Maximum Likelihood Estimator Theory

For a given likelihood function  $L[\theta(t_i), \mathcal{E}_i]$ , where  $\theta(t_i)$  is the  $p$  length vector of variables (unknown parameters) and  $\mathcal{E}_i$  is the set of realized values of the measurements to be used as data, the objective of the maximum likelihood estimator is to find a value of  $\theta^*(t_i)$  that maximizes  $L[\theta(t_i), \mathcal{E}_i]$  as a function of  $\theta(t_i)$ . This value can be estimated with the likelihood function [6]

$$L = \ln f_{\mathbf{x}(t_i), \mathbf{Z}_N(t_i) | \mathbf{Z}(t_{i-N}), \mathbf{a}}(\xi, \mathcal{E}_{i, i-N+1} | \mathcal{E}_{i-N}, \alpha) \quad (\text{A-1})$$

where

$\mathbf{x}(t_i)$  = state vector at time  $t_i$

$\mathbf{a}$  = the parameter vector

$\alpha$  = best estimate of parameter vector

$\xi$  = best estimate of state vector

$\mathbf{Z}(t_i)$  = measurement history  $z(t_1), z(t_2), z(t_3), \dots, z(t_i)$

$\mathbf{Z}_N(t_i)$  = most recent  $N$  measurements  $z(t_{i-N+1}), z(t_{i-N+2}), z(t_{i-N+3}), \dots, z(t_i)$

$\mathbf{Z}(t_{i-N})$  = measurement history  $z(t_1), z(t_2), z(t_3), \dots, z(t_{i-N})$

This likelihood function exploits all *a priori* information and yields an effective and computationally feasible fixed-length memory parameter estimator [6].

By applying Bayes' rule to Equation A-1 and then expressing the probability densities as normal distributions, a solution for both the state and parameter vector can be derived. Substituting each of these probability densities into the likelihood function and then differentiating with respect to both  $\alpha$  and  $\xi$  yields the following results. First, the best estimate of the state vector  $\xi$  is that which is provided by the Kalman filter itself,  $\hat{\mathbf{x}}$ . The best estimate of  $\alpha$  that maximizes the likelihood of  $L$  requires an iterative procedure to find the optimal parameter vector,  $\mathbf{a}^*(t_i)$ .

#### A.2 Derivation of the Maximum Likelihood Estimator

It can be shown that, for the likelihood function defined in Equation A-1, the solution for the best estimates of the parameter vector solves the equation [5, 6]

$$\hat{\mathbf{a}}^*(t_i) = \hat{\mathbf{a}}_*(t_i) + \mathbf{J}[t_i, \hat{\mathbf{x}}_*(t_i), \hat{\mathbf{a}}_*(t_i)]^{-1} \left\{ \frac{\partial L[\hat{\mathbf{x}}_*(t_i), \hat{\mathbf{a}}_*(t_i), \mathbf{Z}_i]}{\partial \mathbf{a}} \right\}^T \quad (\text{A-2})$$

where  $\hat{\mathbf{a}}^*(t_i)$  is the new estimate of the parameters at  $t_i$  and  $\hat{\mathbf{a}}_*(t_i)$  is the previous estimate of the parameters. The covariance matrix of these estimates is provided by the  $\mathbf{J}$  matrix defined below [6]. The first derivative matrix in Equation A-2 is called the *score vector*,

which can be broken down into the sum of the  $N$  most recent *single measurement scores*,  $s_k^1[Z_j, \hat{a}_*(t_i)]$ , and a final term  $\gamma[Z_i, \hat{a}_*(t_i)]$ :

$$\frac{\partial L}{\partial a_k}[\hat{x}_*(t_i), \hat{a}_*(t_i), Z_i] = \gamma_k[Z_i, \hat{a}_*(t_i)] + \sum_{j=i-N+1}^i s_k^1[Z_j, \hat{a}_*(t_i)] \quad (A-3)$$

where

$$s_k^1[Z_j, a] = \frac{\partial \hat{x}(t_j^-)^T}{\partial a_k} H(t_j)^T S(t_j)^{-1} r_j - \frac{1}{2} \text{tr} \left\{ [S(t_j)^{-1} - S(t_j)^{-1} r_j r_j^T S(t_j)^{-1}] \frac{\partial S(t_j)}{\partial a_k} \right\} \quad (A-4a)$$

and

$$\gamma_k[Z_i, a] = -\frac{1}{2} \text{tr} \left\{ P(t_i^+)^{-1} \frac{\partial P(t_i^+)}{\partial a_k} \right\} \quad (A-4b)$$

For computational efficiency,  $J$  is an approximation to the second derivative Hessian matrix. This approximation states that the second derivative matrix, the Hessian, for a particular realization of  $Z_i$  can be adequately represented by its ensemble average over all possible measurement time histories.  $J$  is defined as

$$J[t_i, \hat{\theta}_*(t_i)] \equiv E \left\{ \frac{\partial L[\theta, Z(t_i)]^T}{\partial \theta} \frac{\partial L[\theta, Z(t_i)]}{\partial \theta} \middle| \theta = \hat{\theta}_*(t_i) \right\} \quad (A-5)$$

and it is called the *conditional information matrix*, which can similarly be expressed in terms of a sum over the  $N$  most recent terms and a final term, if the parameter value is allowed to assume a true, but unknown value,  $a_t$ .

$$J_{kl}[t_i, \hat{x}_*(t_i^+), a_t] = E \{ \gamma_k[Z(t_i), a] \gamma_l[Z(t_i), a] | a = a_t \} + \sum_{j=i-N+1}^i E \{ s_k^1[Z(t_j), a] s_l^1[Z(t_j), a] | a = a_t \} \quad (A-6)$$

For computational efficiency, the approximation is made that:

$$E \left\{ \frac{\partial \hat{x}(t_j^-)}{\partial a_k} \frac{\partial \hat{x}(t_j^-)^T}{\partial a_l} \middle| a = \hat{a}_*(t_i) \right\} \equiv \frac{\partial \hat{x}(t_j^-)}{\partial a_k} \frac{\partial \hat{x}(t_j^-)^T}{\partial a_l} \quad (A-7)$$

This approximation greatly simplifies the required calculations [6].  $E\{s_k s_l\}$  can then be approximated by

$$E\{s_k^1[Z(t_j), \mathbf{a}] s_l^1[Z(t_j), \mathbf{a}] \big|_{\mathbf{a}=\hat{\mathbf{a}}_k(t_i)}\} \cong \frac{1}{2} \text{tr} \left[ \mathbf{S}(t_j)^{-1} \frac{\partial \mathbf{S}(t_j)}{\partial a_k} \mathbf{S}(t_j)^{-1} \frac{\partial \mathbf{S}(t_j)}{\partial a_l} \right] + \frac{\partial \hat{\mathbf{x}}(t_j^-)^T}{\partial a_k} \mathbf{H}(t_j)^T \mathbf{S}(t_j)^{-1} \mathbf{H}(t_j) \frac{\partial \hat{\mathbf{x}}(t_j^-)}{\partial a_l} \quad (\text{A-8})$$

And  $E\{\gamma_k \gamma_l\}$  can approximated by

$$E\{\gamma_k[Z(t_i), \mathbf{a}] \gamma_l[Z(t_i), \mathbf{a}] \big|_{\mathbf{a}=\hat{\mathbf{a}}_k(t_i)}\} \cong \frac{1}{2} \text{tr} \left[ \mathbf{P}(t_i^+)^{-1} \frac{\partial \mathbf{P}(t_i^+)}{\partial a_k} \mathbf{P}(t_i^+)^{-1} \frac{\partial \mathbf{P}(t_i^+)}{\partial a_l} \right] + \frac{\partial \hat{\mathbf{x}}(t_i^+)^T}{\partial a_l} \mathbf{P}(t_i^+)^{-1} \frac{\partial \hat{\mathbf{x}}(t_i^+)}{\partial a_k} \quad (\text{A-9})$$

### A.3 Implementation of Maximum Likelihood Kalman Filter

At a sample time  $t_i$ , the quantities at time  $t_{i-N}$  are unchangeable. Therefore, the initial conditions of the  $N$ -step recursion for parameter estimation are the values of the state vector estimate and its covariance previously computed at  $t_{i-N}$ ; the derivatives of these two matrices with respect to the parameters are equal to zero at  $t_{i-N}$  [6]. To solve for the parameter estimates, each of the components in both the score vector and conditional information matrix must be calculated. These components depend on the derivative of the state vector, the derivative of its covariance, and the derivative of the innovation sequence covariance  $\mathbf{S}$  with respect to the parameter vector. In order to determine this dependence, the derivatives of the Kalman filter equations are taken with respect to the parameter vector  $\mathbf{a}$ , using given derivatives of the parameter matrices with respect to  $\mathbf{a}$ . The Kalman filter is implemented as discussed above, but between each of the updates of the state vector, the derivatives of these vectors are also calculated. Also, the system matrices must be recomputed for each new estimate of  $\mathbf{a}$ .

First, the *state transition equations* (Equations 3-6) are processed using the most recent parameter estimate  $\hat{\mathbf{a}}^*(t_i)$  and recomputing  $\Phi$ ,  $\mathbf{B}$ ,  $\mathbf{Q}$ ,  $\mathbf{G}$  and  $\mathbf{R}$  as required. Next, the *score equations* for the time propagation given by the  $p$  set of "sensitivity system" equations are evaluated. The state vector estimate derivative is updated using

$$\frac{\partial \hat{\mathbf{x}}(t_j^-)}{\partial a_k} = \Phi(t_j, t_{j-1}) \frac{\partial \hat{\mathbf{x}}(t_{j-1}^+)}{\partial a_k} + \frac{\partial \Phi(t_j, t_{j-1})}{\partial a_k} \hat{\mathbf{x}}(t_{j-1}^+) + \frac{\partial \mathbf{B}(t_{j-1})}{\partial a_k} \mathbf{u}(t_{j-1}) \quad (\text{A-10})$$

Next, the derivative of the covariance matrix  $P$  is updated using:

$$\begin{aligned} \frac{\partial P(t_j^-)}{\partial a_k} &= \Phi(t_j, t_{j-1}) \frac{\partial P(t_{j-1}^+)}{\partial a_k} \Phi(t_j, t_{j-1})^T \\ &+ \frac{\partial \Phi(t_j, t_{j-1})}{\partial a_k} P(t_{j-1}^+) \Phi(t_j, t_{j-1})^T + \Phi(t_j, t_{j-1}) P(t_{j-1}^+) \frac{\partial \Phi(t_j, t_{j-1})^T}{\partial a_k} \\ &+ G(t_{j-1}) \frac{\partial Q(t_{j-1})}{\partial a_k} G(t_{j-1})^T + \frac{\partial G(t_{j-1})}{\partial a_k} Q(t_{j-1}) G(t_{j-1})^T \\ &+ G(t_{j-1}) Q(t_{j-1}) \frac{\partial G(t_{j-1})^T}{\partial a_k} \end{aligned} \quad (A-11)$$

For the innovation sequence covariance matrix,  $S$ , the derivative update equation is:

$$\frac{\partial S(t_j)}{\partial a_k} = H(t_j^-) \frac{\partial P(t_j^-)}{\partial a_k} H(t_j^-)^T + \frac{\partial R(t_j)}{\partial a_k} \quad (A-12)$$

Also needed is the *conditional information matrix computation for forward time propagation*, Equation A-8, which updates  $E\{s_k s_l\}$ . Next, the *measurement incorporation equations* (Equations 7-9) at time  $t_j$  are processed. The *measurement update score equations* are then processed using these definitions:

$$D(t_j) = I - K(t_j) H(t_j) \quad (A-13)$$

$$\mathbf{n}_j = S(t_j)^{-1} \mathbf{r}_j \quad (A-14)$$

$$C(t_j) = S(t_j)^{-1} - \mathbf{n}_j \mathbf{n}_j^T \quad (A-15)$$

For  $k = 1, 2, \dots, p$ , the *measurement update score equations* are

$$s_k^1[Z_j, \hat{\mathbf{a}}_*(t_i)] = \frac{\partial \hat{\mathbf{x}}(t_j^-)^T}{\partial a_k} [H(t_j)^T \mathbf{n}_j] - \frac{1}{2} \text{tr} \left\{ C(t_j) \frac{\partial S(t_j)}{\partial a_k} \right\} \quad (A-16)$$

$$\frac{\partial \hat{\mathbf{x}}(t_j^+)}{\partial a_k} = D(t_j) \left\{ \frac{\partial \hat{\mathbf{x}}(t_j^-)}{\partial a_k} + \frac{\partial P(t_j^-)}{\partial a_k} [H(t_j)^T \mathbf{n}_j] \right\} \quad (A-17)$$

$$\frac{\partial P(t_j^+)}{\partial a_k} = D(t_j) \frac{\partial P(t_j^-)}{\partial a_k} D(t_j)^T + K(t_j) \frac{\partial R(t_j)}{\partial a_k} K(t_j)^T \quad (A-18)$$

At the end of processing  $N$  points, the score vector and conditional information matrix are computed. First,  $\gamma$  is calculated using Equation A-4b and  $E\{\gamma_k \gamma_l\}$  is calculated using Equation A-9. Using Equation A-6 and Equation A-3, both  $J$  and the score vector can be calculated. A new parameter estimate is then made using Equation A-2. This process continues for every estimation interval  $N$ , until all of the data is processed.

## References

- [1] Boxenhorn, B. and J. Connally. "Micromechanical Gyro Noise Analysis." CSDL Memo EAC-90-396. November 12, 1990.
- [2] Brown, Robert Grover and Patrick Y.C. Hwang. *Introduction to Random Signals and Applied Kalman Filtering*. New York: John Wiley & Sons, Inc., 1992.
- [3] Greiff, P. and B. Boxenhorn, *et al.* "Silicon Monolithic Micromechanical Gyroscope." C.S. Draper Laboratory Memo, 1991.
- [4] Greiff, P. and B. Boxenhorn. "A Vibratory Micromechanical Gyroscope." C.S. Draper Laboratory Memo, 1988.
- [5] Kossuth, Jonathan A. *The Adaptive Kalman Filter and Micromechanical Inertial Instrument Performance*. CSDL-T-1171. C. S. Draper Laboratory, Cambridge, MA. May 1993.
- [6] Maybeck, Peter S. *Stochastic Models, Estimation and Control Volume 2*. New York, Academic Press, 1982.
- [7] Mehra, Raman K. "On the Identification of Variances and Adaptive Kalman Filtering." *IEEE Transactions on Automatic Control*. Vol. AC-15, No. 2, April 1970. pp. 175-184.
- [8] Mehra, Raman K. "On-line Identification of Linear Dynamic Systems with Applications to Kalman Filtering." *IEEE Transactions on Automatic Control*. Vol. AC-16, No. 1, February 1971. pp. 12-21.
- [9] Petranic, T. and C. Pu. "μGyro Noise Analysis". CSDL Memo TDP:μGyro-90-01. 2 January 1990.

**SESSION VIII-B  
TEST FACILITIES**

***CHAIRMAN***  
**DR. RICHARD GREENSPAN**  
***DRAPER LABORATORY***



**THIS PAGE LEFT BLANK INTENTIONALLY**

# **Improved Synchronization Capabilities of the Little Mountain Pulserad 958 Gamma Simulator**

**S. S. Spring and R. D. May**  
Rockwell International, Ogden, Utah 84404

**B. H. Bernstein**  
Bernstein Design Services, Livermore, California 94550

## **I. Abstract**

The experimental synchronization capabilities of the Little Mountain Flash X-ray simulator have been improved from  $> 50$  to 20 nsec jitter following modifications to the trigger circuit of the Marx generator. Previous utilization of the Little Mountain simulator for Minuteman and Peacekeeper guidance system hardness testing did not require stringent jitter requirements. Subsequent tests indicated the need to provide more precise timing of the radiation event, such as those experienced on the Small Missile processor which was designed to operate through the radiation environment without circumvention. The improved synchronization capabilities are presented herein, in addition to schemes that illustrate interface between simulator and devices which require precise timing of the radiation event.

## **II. Introduction**

The Pulserad 958 Large Flash X-ray (LFXR) system is a 6 MeV pulsed X-ray source capable of producing photons in the gamma or high energy X-ray portion of the electromagnetic spectrum with a nominal pulse width of 50 nsec. The primary use of the system is to study the transient response of electronic components and systems to intense bursts of radiation. In some circumstances, it is desirable to synchronize the onset of radiation with

particular electrical events occurring within the device under test. While the LFXR can be synchronously triggered to produce X-rays, the uncertainty (jitter) of the time delay between the triggering signal and the X-ray burst is in many cases too great. The increasing speed of electronic circuitry demands more precise timing of the radiation than permitted by the original specifications for the Pulserad 958.

The goal was to decrease the Pulserad 958 jitter characteristic to 20 nsec or less to ensure consistent upset threshold data during testing of "operate through" electronic systems of subsystems<sup>1</sup>. Other electronic circuitry tests that require precise timing would also benefit from jitter improvement.

The Data Acquisition System (DAS) was set up to independently monitor the system components that contribute significantly to the jitter. After analysis of the initial results, the Marx generator was identified as the major source. A modification to the Marx trigger was designed and following implementation, the jitter goal was realized<sup>2</sup>. This enhanced capability enables the LFXR to perform tests that require precise synchronization timing of the X-ray environment for verification of operation at micro-processor speeds. Triggering scheme examples that interface the LFXR with test devices are presented.

### III. Experimental Details

There are three principle sources of jitter within the LFXR, the TG-70 trigger amplifier, the Marx generator, and the Blumlein switch (main switch). A KN6B Krytron switch tube and an output spark gap contribute to the TG-70 jitter which is normally less than 4 nsec. Consequently, the remaining two sources of jitter were addressed.

The 958 Pulserad Marx generator has 58 spark gap switches, all of which must close before charge can be transferred to the Blumlein. The time required to close all the switches is termed the erection time. The first four switches are externally triggered by the TG-70 and the remainder are triggered by voltage transients created by firing the first four. Experience has shown that the first 25% of the spark gaps in a Marx generator account for one-half of the erection time and contribute about 90% of its jitter. In general, erection delay shortens and jitter decreases when the spark gaps are operated close to their self firing voltage, but the incidence of prefire increases markedly. As originally configured, the Marx could achieve 50 nsec jitter with acceptably low probability of prefire in a narrow operating range. Small changes in spark gap pressure or charge voltage resulted in jitter as large as several microseconds, or frequent prefires.

The second major source of jitter, the Blumlein switch, is self-closing and therefore subject to statistical variations of its breakdown strength from shot-to-shot. Since voltage is applied to the switch over a period of several hundred nanoseconds, rather than in a step function, breakdown voltage variations translate directly to time variations. In fact, the breakdown process also depends on the spacing of electrodes, the shape of the applied voltage waveform,

as well as the area of the electrodes that is subject to electrical stress. Experimental evidence indicates<sup>3</sup> that the breakdown field,  $F$ , fits the following relationship:

$$F = k t^{-1/3} d^{1/6}$$

Where:  $k$  = constant  
 $d$  = electrode spacing  
 $t$  = the effective time of voltage application

The pulse shape is taken into account by adjusting  $t$  to an effective value which is equal to the time that voltage is greater than 63% of the final breakdown value.

The concept of effective time has a great deal of significance on the performance of the LFXR since the voltage across the switch increases with approximately  $1 - \cos \omega t$  dependence. If the breakdown potential is reached  $\pi/2$  (half way to the peak) the effective time is significantly less than when switching occurs at the peak of the waveform. Based upon the field breakdown relationship, a particular switch spacing will breakdown at a higher voltage if the rate of voltage rise is increased. In practical terms, if the Marx charging voltage is increased, the Blumlein switch closure voltage will also increase even if its spacing is not changed.

These discussions indicate that the time periods (delay) required for the Marx to erect and the Blumlein switch to close are dependent upon their settings. Further, the Blumlein switch delay is also dependent on the voltage being applied by the Marx. These dependencies must be taken into account when trying to predict the overall delay between simulator trigger time,  $t_0$ , and radiation output.

Because of the inter-dependence between

Marx and Blumlein switch performance, and overall system jitter, it is necessary to independently measure the performance of each one. The monitor output of the PT-55 in the TG-70 trigger amplifier was chosen as the start point for measuring the Marx erection delay. The end point for Marx measurements is either the start of pulse charge or the start of the prepulse signal (a component of the tube voltage signal), plus an offset constant resulting from the propagation delay between the pulse charge and tube voltage monitors. The prepulse signal was chosen for monitoring the end of Marx erection due to less noise and ease of interpretation. A time interval counter with sub-nanosecond resolution was used to measure Marx erection delay.

The delay of the Blumlein switch was also measured using the prepulse signal. The delay interval of the switch is defined as beginning with the start of prepulse and ending with the arrival of the main output pulse, as indicated on the tube voltage waveform. The waveform was acquired and the interval measure determined utilizing the facility Data Acquisition System (DAS) capabilities<sup>4</sup>. Examples of the pulse charge monitor and the prepulse signals are provided in Figures 1 and 2.

#### IV. Results and Marx Generator Modification

Initial testing determined the Marx jitter values, ranging from 71 to more than 3000 nsec as Marx switch gap pressure was increased, to be inconsistent with the goal of 20 nsec overall system jitter. A decision was made to modify the Marx trigger circuitry with the intention of reducing jitter and, at the same time allowing operation at higher pressure. The modifications were designed to increase the strength of the trigger signals coupled to the first 11 spark

gaps through decreasing the impedances of their trigger circuits. Figure 3 illustrates the changes that were made.

The results achieved by the modifications were quite dramatic as can be seen in Figure 4. The jitter improved to less than 9 nsec at 38 psig. At 46 psig, well above the normal operating point, the jitter was less than 35 nsec. The Marx jitter results for all tests performed after modifications are plotted in Figure 5.

The Blumlein switch jitter was determined to range between 16 and 18 nsec. This is as good as can be expected with a self closing switch that operates at several megavolts. The dependence of the Blumlein switch delay on the Marx charging voltage is depicted in Figure 6.

The expected overall system jitter has been improved to 20 nsec when combining the Marx generator jitter, now less than 10 nsec, in quadrature with the Blumlein switch jitter of 17 nsec and the TG-70 jitter of 4 nsec. This result is just at the upper end of the established goal.

#### V. Synchronization Applications

Schemes for interfacing the LFXR simulator to devices which require precise radiation event timing have been developed and previously utilized. The results of previous testing sometimes had limited success due to the unacceptably high pulser jitter. Test synchronization success is a function of the length of time that the device function to be tested is active (denoted as the event window) and the uncertainty, or jitter, of the time delay between the triggering signal and the radiation event. Examples of previous Little Mountain test activities are described in the following paragraphs.

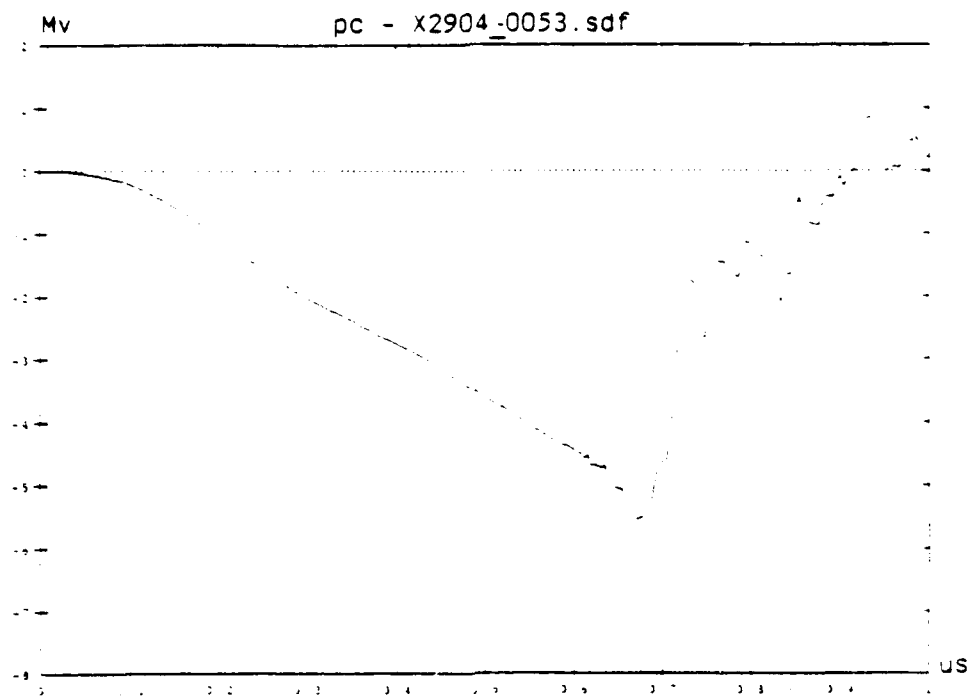


Figure 1 Pulse Charge Monitor Signal

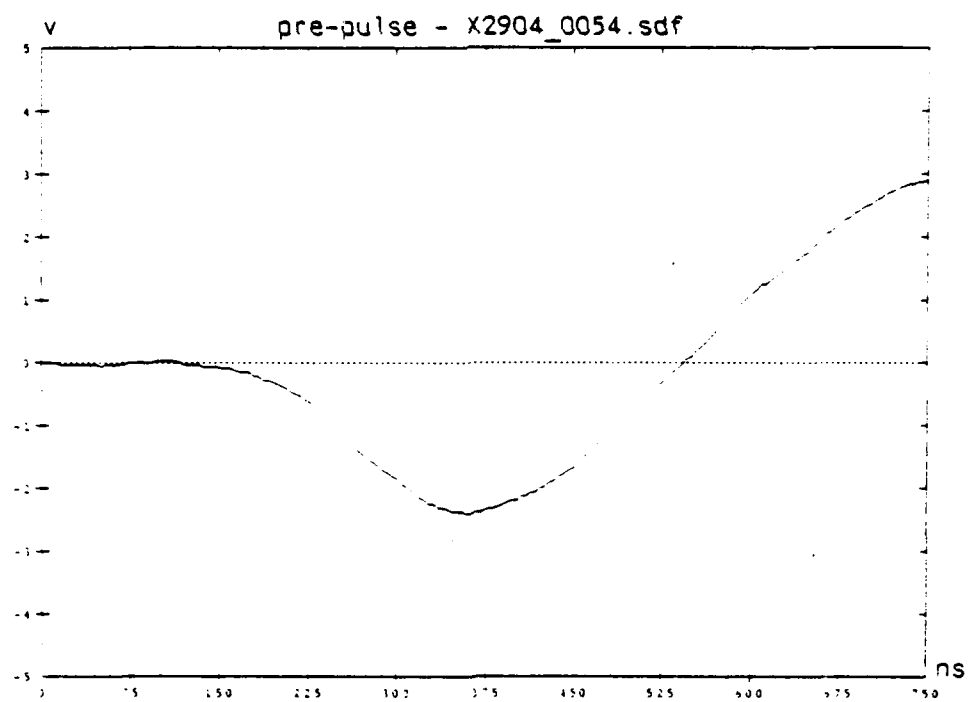


Figure 2 Prepulse Signal

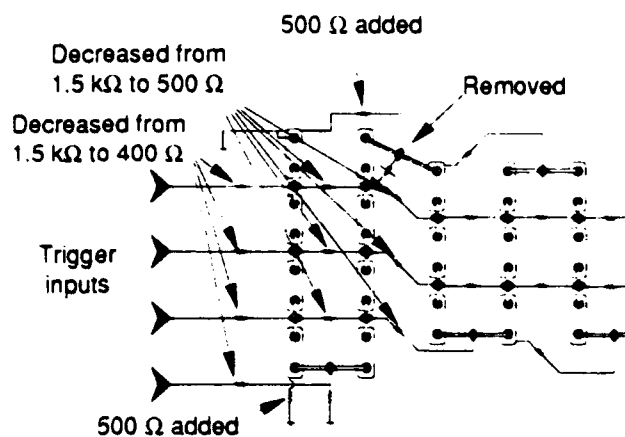


Figure 3 Marx Generator Trigger Circuit Modifications

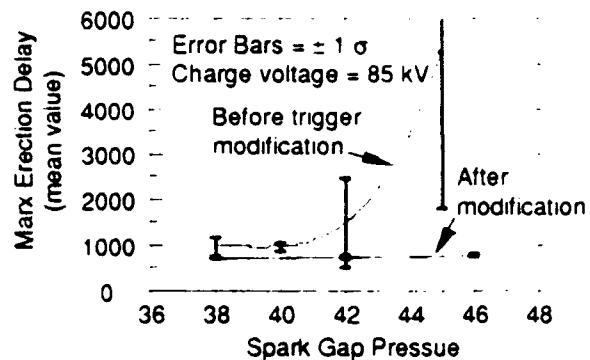


Figure 4 Reduction of Erection Delay and Jitter

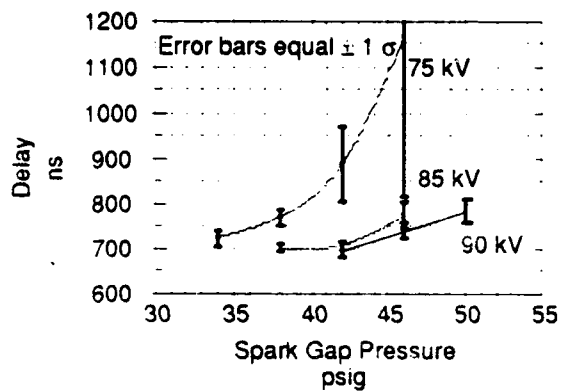


Figure 5 Pulserad 958 Marx Erection Delay

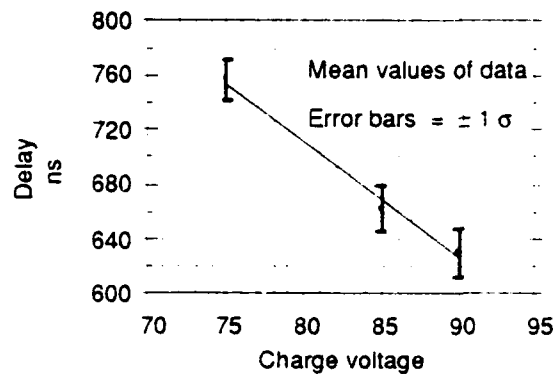


Figure 6 Main Switch Delay Dependency

### a. Peacekeeper Testing

Peacekeeper system and subsystem synchronization testing<sup>5,6</sup> conducted at Little Mountain has been very successful since the most stringent event window is 300 nsec, with the maximum event window lasting 29 msec.

A number of Peacekeeper system functions that require synchronization are tested. The basic scheme for accomplishing and verifying synchronization testing is illustrated in Figure 7. Due to software/hardware timing constraints, variations to this scheme are required to test certain system functions. Selected Peacekeeper system functions are synchronized with the radiation event by utilizing trigger delay to the FXR, along with event flags which are issued at predetermined time intervals prior to the execution of the system function to be tested.

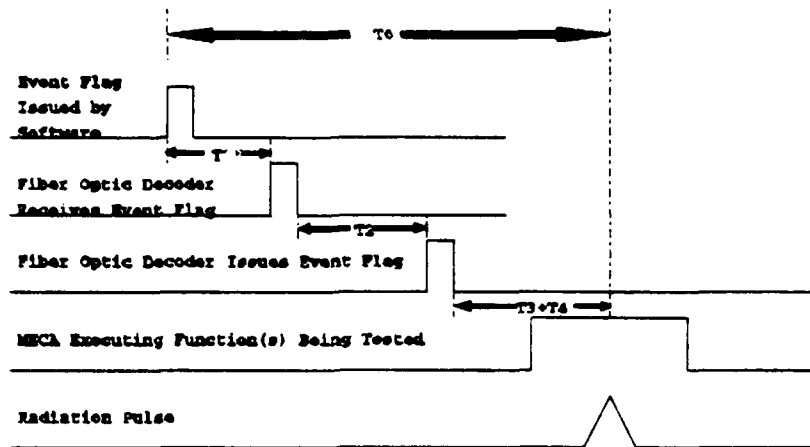
The timing sequence in Figure 7a depicts typical events and time delays in the Peacekeeper setup. The block diagram in Figure 7b illustrates the basic hardware interconnect used for triggering of the test exposure; it also indicates where, in the hardware setup, the delays ( $T_1$  through  $T_4$ ) originate. The time interval  $T_0$  between the event flag to the midpoint of system function execution will vary from one test sequence to the next. This variation and the delay from the receipt of the simulator trigger pulse at the FXR control panel to the radiation event  $T_4$  are compensated for by the time delay  $T_2$  which is preset into the countdown timer in the Fiber Optic Decoder (FOD).  $T_0$  also includes the constant system delays (cable, logic and electronic delays) which have been denoted as  $T_1$  and  $T_3$ .  $T_4$ , the sum of FXR system delays, consists primarily of the time from FXR console

output to TG-70 trigger initiation, the Marx erection delay and the Blumlein switch delay. From Section II Figures 5 and 6, it was determined that the Marx erection and Blumlein switch delays are a function of FXR setup parameters, primarily charge voltage and spark gap pressure. For proper test synchronization  $T_0 = \Sigma (T_1, T_2, T_3, T_4)$ . For each test exposure, the FXR Marx generator charging is coordinated with facility personnel so that the FXR is brought to full charge 3 to 4 seconds before the FOD issues the FXR trigger pulse.

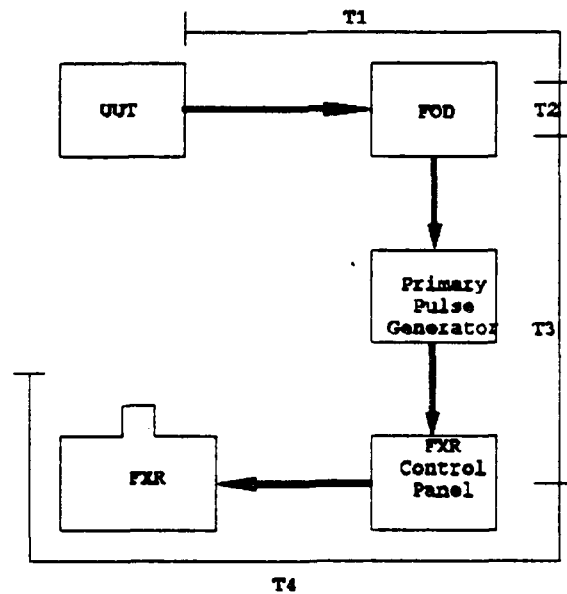
### b. Small ICBM Testing

Nuclear radiation synchronization testing performed on the SICBM Electronic Computer Assembly (ECA) Central Processing Unit (CPU) module during the development program<sup>7</sup>, utilized a scheme comparable to that used for Peacekeeper testing. The primary difference between these two tests are the level of assembly (module versus subsystem/system), and radiation dose rate levels for upset threshold testing (higher "operate through" levels versus circumvention protected upset threshold levels). Another difference, which is a compelling reason for the jitter improvement, is that the minimum event window is 20 nsec.

The purpose of the SICBM prompt pulse ionization testing was to assess upset threshold level survivability tolerance of the CPU module to the radiation requirements. The CPU module test was also a test of the CPU firmware, thus the Unit Under Test (UUT) was exposed to pulses during various routines and at time intervals within its operations. The triggering scheme for synchronization testing is illustrated in Figure 8. In contrast to Peacekeeper triggering which is initiated by a system



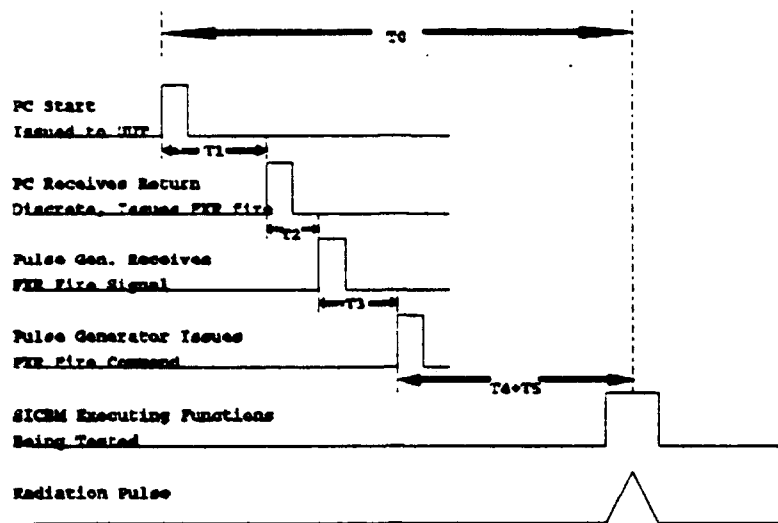
a) Timing Sequence



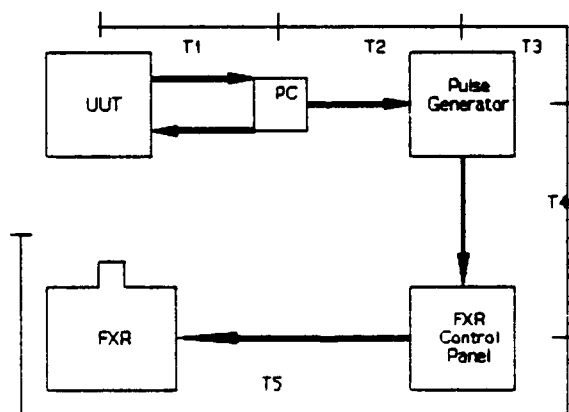
b) Hardware Interconnect

Figure 7 Peacekeeper Synchronization Testing Scheme.





a) Timing Sequence



b) Hardware Interconnect

Figure 8 SICBM Synchronization Testing Scheme.

issued function event flag, the SICBM trigger sequence is initiated by either user control (via PC) or facility control, with an optional preprogrammed delay up to several milliseconds. The triggering sequence shown is initiated by user control.

Generally, a PC signal is sent to the UUT to initiate CPU module processing, at which time a discrete is returned to the PC indicating that processing has begun. Once the signal is received by the PC, a FXR fire command is issued to the FXR through a preprogrammed delay. The preprogrammed delay is adjusted to compensate for the varying time of the function to be tested and the FXR delay which is a function of the FXR setup parameters. This preprogrammed delay is accomplished using the digital delay generator in the FXR control panel or a pulse generator connected between the PC and FXR trigger. Examples of CPU functions to be tested are read cycles, write cycles,

read/write time segments, multiply and divide.

### c. SRAM Testing

Testing performed on Static Random Access Memory (SRAM) modules<sup>8</sup> illustrates the third synchronization method which has been utilized. Similar to SICBM testing, an objective of these tests is to accomplish dynamic upset testing while the Device Under Test (DUT) is operating in both the read and write modes. The event windows are also comparable to those during SICBM testing. In this case triggering is initiated by facility control using the preprogrammed delay provided by the digital delay generator in the FXR control panel. A Mosaid MS2200 memory tester is used to provide all the signals required for exercising the DUT and detecting data upsets. The triggering scheme is illustrated in Figure 9.

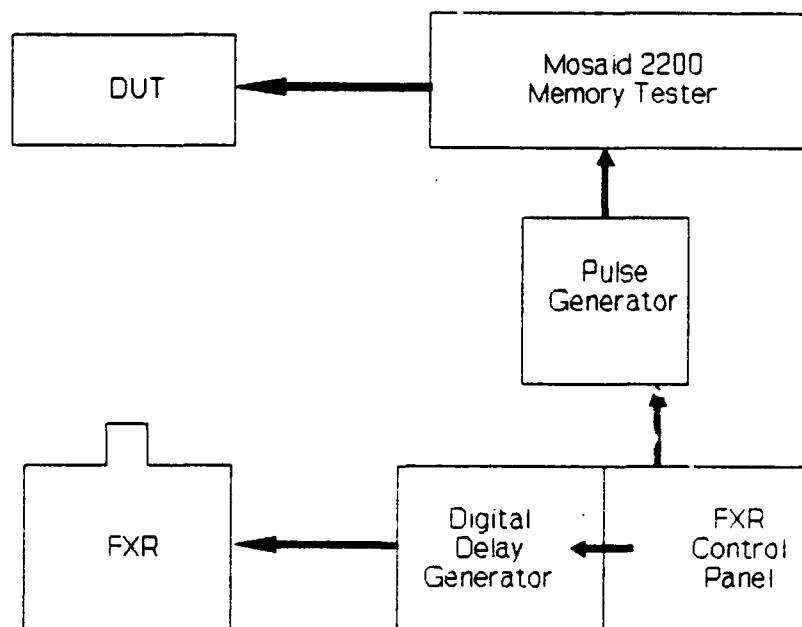


Figure 9 SRAM Synchronization Testing Scheme.

## VI. Little Mountain Test Facility

The Pulserad 958 gamma simulator, is an element of the Survivability and Vulnerability Integration Center (S&VIC) facility, which is a secure, TEMPEST approved test facility located fifteen miles west of Ogden, Utah. The facility is owned by the Air Force and Operated in conjunction with a number of defense contractors.

The S&VIC consists of test laboratories for simulating basically six environments; 1) Nuclear Radiation, provided by the Pulserad 958 FXR simulator, a smaller Pulserad 216AH FXR simulator, and a linear accelerator, 2) Airblast, provided by a Blast Load Generator, 3) Shock and Vibration, provided by various dynamic shakers, accelerators, and impulse testers, 4) In-flight Shock and Vibration profiles, provided by the vibration facility, 5) Electromagnetic Pulse (EMP) provided by electrical pulser of various waveforms and energy capabilities, and 6) Electromagnetic Interference and Compatibility (EMI/EMC) testing, provided by EMI generators and instrumentation equipment.

Qualified facility personnel are available to assist users with test planning to implement their synchronization testing requirements, making Little Mountain a convenient facility to accomplish this type of testing.

## VII. Conclusions

The results indicate a Pulserad 958 gamma simulator Marx generator jitter improvement to less than 10 nsec. The largest component is now the Blumlein switch jitter which has been shown to be 17 nsec. Coupled with the TG-70 jitter of 4 nsec, the overall system jitter is expected to be 20 nsec, allowing the required timing precision

of the radiation event for improved upset threshold testing.

Three differing FXR triggering schemes were illustrated to take advantage of the jitter improvement, they included; a) trigger sequence initiation under system control, utilizing system issued event flags, b) trigger sequence initiated by user control through a Personal Computer and c) triggering which is initiated by facility control. In all cases, a preprogrammed delay is utilized to synchronize the radiation event with the execution of the function to be tested, which is known to occur at a precise time interval following trigger initiation.

## VIII. Acknowledgements

The authors would like to thank the S&VIC Facility Manager, Mike Shafer and the Rockwell Manager, Jay Donaldson for the contractual support for the jitter improvement task, and the Rockwell 958 FXR facility personnel for their test support. Support of Barry Kolesar, Scot Southwick, Charles Rigal and Marva Morton for inputs to and review is also gratefully acknowledged.

## IX. List of References

1. R. F. Meideman, Hardness Assurance/ Hardness Surveillance Radiation Testing for Small Missile ECA at S&VTC, TRW IOC F543.RFW.91-004, June 1991.
2. B. H. Bernstein, Large Flash X-Ray Jitter Reduction Study Test Report, Bernstein Design Services, June 1992.
3. C. E. Baum, Dielectric Strength Notes, AFWL Report PEP 5-1, Air Force Weapons Laboratory, Albuquerque, NM, 1975

4. **Survivability and Vulnerability Test Center (S&VTC) facility brochure, Hill Air Force Base, Utah 84056-5609.**
5. **C89-676.2/601, Peacekeeper MGCS Hardness Surveillance Test Plan, Little Mountain FXR, Test Requirements, revised February 1993.**
6. **C89-642.3/601, Peacekeeper MECA Hardness Surveillance Test Plan, Little Mountain FXR, Test Requirements, revised February 1993.**
7. **Small ICBM Test Plan for Central Processing Unit circuitry, Rockwell International, 1989.**
8. **Flash X-ray Dose Rate Test Plan for CMOS/SOS SRAMs, Harry Diamond Labs, 1990.**

**THIS PAGE LEFT BLANK INTENTIONALLY**

# **NAVIGATION/SURVEY TEST VAN**

**Brian E. Fly**

**Blake F. Lenett**

**Honeywell Military Avionics  
Guidance and Navigation Organization  
Florida Operations**

***Approved for Public Release; distribution is unlimited.***

## **Abstract**

This paper describes the features and capabilities of the Honeywell Navigation/Survey Test Van and how it is being used to evaluate the system performance and software operation of various Honeywell Inertial Guidance Units.

## **Introduction**

While the majority of system development and evaluation is still performed in various in-plant laboratories and test areas, a growing amount of testing is migrating to the survey vehicle. Through dynamic testing, the system performance can be more accurately verified prior to the first field integration at the customer facility, thus allowing for a cleaner integration, less cost, and considerably fewer surprises. For more than 10 years, Honeywell's Guidance and Navigation Operation (GNO) has used various types of vehicles to evaluate the performance of our products (primarily, land navigation applications). As the maturity and diversity of our product line increased, and more stringent requirements were placed on the products, it became apparent that a larger, more capable test bed was required. To fill this need, the new Navigation/Survey Test Van recently entered service at GNO and has since made a significant impact in the quality of products which are delivered. The vehicle's enhanced capabilities allow for a more in depth, realistic evaluation of system performance and software operation.

The new test vehicle is a replacement for a 1985 Suburban truck which had reached the end of its economical life. The original reason to have a vehicle dedicated to survey/navigation applications was for testing of the Modular Azimuth Positioning System (MAPS) Dynamic Reference Unit (DRU) under dynamic conditions. Over the last 7 years and thousands of miles, many people have spent uncounted hours driving area highways developing and refining the MAPS software. This work paid off with the award of MAPS Production contracts from the U.S. Army as well as the British, Finnish, and the Swedish Armies. MAPS DRU testing is still the primary program using the van, however, the scope of the van has evolved so that almost every inertial navigation program currently under development is using this resource.

During the initial stages of the MAPS DRU program, survey courses were laid out with known position points using U.S. National Geodetic Survey Control Points. Each survey control point (SCP) and azimuth reference (if available) is used to determine the errors (horizontal and vertical position and azimuth accuracy) of the UUT. To meet the needs of the flight navigation units, some of these courses were modified to give a more accurate testing scenario by allowing for straight line travel (where possible). Although the van obviously can't fly, simulated taxi speeds and take-off conditions are possible. Some of the most commonly used survey courses are shown in Figure 1.

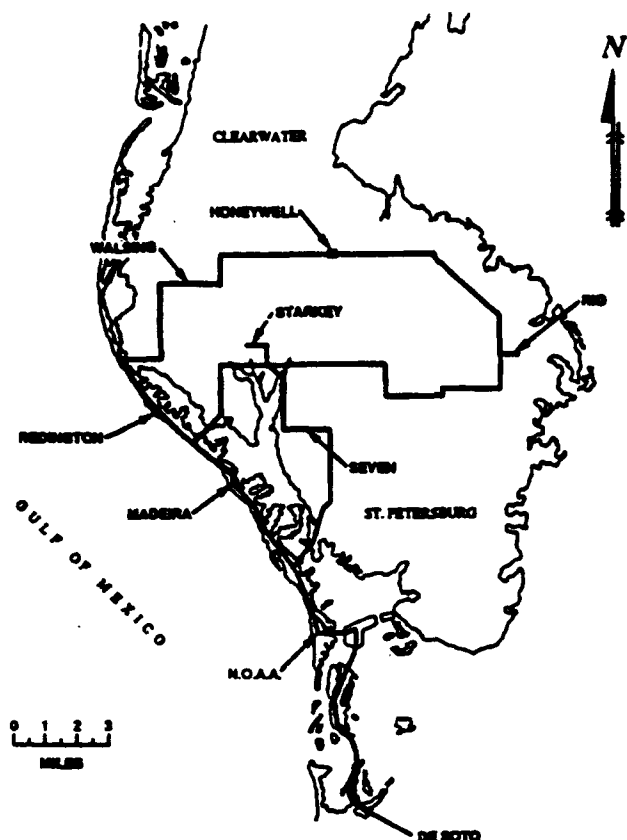


**Figure 1. Typical Survey Course Map**

### Capabilities

The new vehicle is a Dodge MaxiVan (equipped with heavy duty package) which Honeywell bought and then modified in a local van conversion shop under a capital appropriation. Lessons learned from previous test vehicles were incorporated into the layout and functionality of the new vehicle. Also, ideas for improved capabilities were widely solicited, and then utilized during the outfitting of the van. The final wiring and setup required for present programs

and anticipated future programs was completed in-house. Figure 2 shows the interior of the test vehicle with a MAPS unit installed for test.



**Figure 2. Interior of Navigation/Survey Test Van**

Some of the key capabilities of the new van are:

*Unit Under Test (UUT) Power:* Power is available for up to two UUTs with any combination of the following: 24 VDC 80 Amp, 120 VAC 400 Hz 15 Amp, 26



VAC 400 Hz 10 Amp. A 100 Amp auxiliary alternator supplies power to static inverters and a distribution panel then routes power out in a very clear and understandable manner. For extended stationary operation, the van has an external power interface capability (120 VAC 60 Hz), which maintains all of the above power outputs without running the vehicle's engine. In addition, change over from internal to external power (and vice versa) can be performed without effecting UUT operation. Also available is a 120 VAC 60 Hz power strip for test sets/computers and/or other ancillary gear such as printers, recorders, and cooling fans.

*Global Positioning System (GPS):* Provisions were made for mounting GPS antennas inside the van. The roof of the vehicle is fiberglass which does not block the GPS signal. We currently use both military and commercial band antennas/receivers with excellent results.

*Communications:* History has proven again and again that quick communication can be a big cost saver. For the new van, a cellular phone was installed which allows for updates and changes to be made "on the fly" to any testing in progress. Problems and proposed solutions are now relayed in "real time" by the operator to and from systems and software engineering.

*Improved space and work area:* The new van is a stretch model with a high top added allowing for a 6' tall person to stand erect. Also, there is a built-in desk/work surface for writing and data collection. Slots in the desk top allow for mounting and securing of portable PCs

which are used as test sets and for data collection. Storage areas have been built in to allow for stowing of survey instruments, tripods, tool boxes, and miscellaneous equipment. Seating allows for 4 people to work in the van simultaneously and the rear two seats rotate/move forward to allow for access to the work surface or for working on the UUT. In addition, the area surrounding the UUT mounting surfaces has been greatly expanded which allows for easier access for troubleshooting and repair/removal.

*UUT Mounting:* There are two 24" by 24" aluminum plates available for UUT mounting. Each plate is machined to adapt to any program application required. Testing can support two entirely different applications at once.

## Applications

*Flight Systems:* As stated earlier, while the developmental labs at Honeywell provide a suitable environment for performing static navigation testing, the navigation/survey test vehicle accommodates more realistic mobile testing. This mobile environment is one step closer to the actual flight environment of an Inertial Navigation Unit. Therefore, valuable test data is made available during van testing that may not be manifested in the static environment. This mobile test environment has been utilized to test many of Honeywell's medium and high accuracy aircraft navigation systems.

In a series of tests, the H-770 F-15 Inertial Navigation Unit (INU) was installed in the van to evaluate two

methods of improving system alignment. The INU's Navigation Alignment Refining Feature (NARF) and Interrupted Alignment (IA) function were tested to verify proper operation and demonstrate improvement in system performance. The results of these tests indicated that both NARF and IA provided enhanced system performance beyond the requirements of the U.S. Air Force specification.

To evaluate INU performance improvement with NARF and IA, three ensembles of van runs were performed using the test cases shown in Table I.

**Table I - NARF and IA Test Cases**

Test Case	Initial Heading (degrees)	Taxi Time (min)	Second Heading (degrees)	Delta Heading (degrees)
1 South	0 +/-5	1	90 +/-5	90
2 North	45 +/-5	1	135 +/-5	90
3 West	90 +/-5	2	180 +/-5	90
4 East	135 +/-5	2	315 +/-5	180
5 South	180 +/-5	4	0 +/-5	180
6 North	225 +/-5	4	45 +/-5	180
7 West	270 +/-5	8	345 +/-5	75
8 East	315 +/-5	8	30 +/-5	75

Data from the NARF and IA ensembles was used to evaluate the INU's ability to compensate for known errors and determine how well the Kalman Filter feedback loop worked. Prior to each ensemble, inertial sensor errors were intentionally inserted into the INU software.

The first ensemble consisted of four van runs, each following a 4 minute (GC) gyrocompass alignment with NARF disabled. Data from this ensemble (shown in Table II) was used as the baseline for evaluating the performance improvement provided by the NARF and

IA runs. Also, this ensemble would insure that measured velocity errors agreed with expected errors for the inserted sensor error magnitudes.

**Table II- System Baseline Runs**

<i>Baseline Van Runs</i>		
VAN RUN	RER	CEP
	(nmph)	(nmph)
BASE-S	2.48	2.06
BASE-N	2.24	1.96
BASE-W	1.65	1.37
BASE-E	1.97	1.51

Inertial Sensor errors inserted for Baseline

The second ensemble consisted of eight van runs, each following a 4 minute GC alignment, a taxi maneuver, and then a 10 minute NARF alignment while in the Align Hold condition (vehicle remains stationary after a taxi maneuver). Results are shown in Table III.

The third ensemble consisted of eight van runs, each following a 4 minute GC alignment, a taxi maneuver, and then a 10 minute IA alignment with NARF disabled. Delta position and residual velocity data was recorded at 21 and 42 minutes into each run. The total Nav time for each van run was approximately 42 minutes.

**Table III- NARF Runs**

<i>NARF in Align Hold Van Runs</i>		
VAN RUN	RER	CEP
	(nmph)	(nmph)
NARF1-S	0.65	0.54
NARF2-N	0.41	0.45
NARF3-W	0.22	0.38
NARF4-E	0.42	0.37
NARF5-S	0.49	0.38
NARF6-N	0.22	0.35
NARF7-W	0.14	0.33
NARF8-E	0.26	0.32

**Table IV- Interrupted Align Runs**

<i>Interrupted Align Van Runs</i>		
VAN RUN	RER	CEP
	(nmph)	(nmph)
INTA1-S	0.29	0.24
INTA2-N	0.46	0.32
INTA3-W	0.08	0.26
INTA4-E	0.23	0.25
INTA5-S	0.29	0.24
INTA6-N	0.05	0.22
INTA7-W	0.12	0.21
INTA8-E	0.05	0.2

Tables II, III, and IV compare the Radial Error Rates (RER) and Circular Error Probabilities (CEP) for each van run performed in the three ensembles. The combined results of the NARF and IA ensembles show a 10 to 1 order of improvement in system performance over the Baseline GC runs. This improvement can be correlated to the Kalman Filter's computation of accelerometer and gyro bias corrections during the extended time in alignment at a different heading. This change in heading allows the Kalman Filter to make additional observations of inertial sensor errors.

It was determined that the Navigation Alignment Refining Feature and the Interrupted Alignment function operated superbly in the upgraded F-15 flight software. The van testing verified that INU system performance was improved significantly with NARF or IA alignments even in the presence of inserted inertial errors. As a result of the van testing, there is evidence that NARF and IA successfully compensate for inertial errors and provide improved INU system performance. This capability will be a

major benefit to the overall Flight INU system performance verification task.

*Land Nav Systems:* Although the Survey van is utilized on an increasing scale by the aircraft INU programs, the primary user of the vehicle is the Land Nav product line. Recently completed Acceptance Testing results for the Swedish Army MAPS Dynamic Reference Unit (DRU) are shown in Table V. The survey van was utilized to simulate conditions on 4 separate applications for the Swedish Army POS-2 effort: 1) Survey Vehicle (Tgb-11); Self-Propelled Howitzer (Bkan-1); Towed Howitzer (FH-77B); and a Forward Observer Vehicle (Epbv-3022). Extensive system checkout in the van allowed for an error free integration in Sweden.

**Table V POS-2 Acceptance Test Results**

Applic- ation	RMS Easting (meter)	RMS Northing (meter)	RMS Alt (meter)	RMS Azimuth (mils)
Tgb-11	4.17	2.47	2.21	0.446
Bkan-1	2.31	2.69	0.816	0.475
FH- 77B	8.199	4.057	2.166	0.525
Epbv- 3022	5.17	4.39	2.27	0.509

Distance Traveled = 118.7 km for each test run

With the enhanced capabilities of the survey vehicle, the software verification task has expanded to more thoroughly test the Land Nav software operation. Results of the latest certification of the standard MAPS software are shown in Table VI. By using the survey van to "shake-out" the software, many problems that were not noted in the lab were discovered and corrected prior to delivery to the customers.

**Table VI MAPS Operational Software Test**

<b>Run Type</b>	<b>CEP (meter)</b>	<b>PE ALT (meter)</b>	<b>PE AZ (mils)</b>	<b>DIST TRAVEL (km)</b>
Odo-Aided	18.54	5.14	N/A	163.41
10 Min ZUPT	2.08	0.95	N/A	57.64
Survey Mission	8.17	0.754	0.452	144.2

The survey vehicle is currently being used to conduct the software verification of the MAPS Hybrid system which is a mating of the existing DRU with the PLGR (Precision Lightweight GPS Receiver). In addition, the Honeywell Marine Inertial Navigation System (MINS) is undergoing final checkout and debug prior to delivery to the customer.

### **Summary**

As the nature of GNO's business has evolved, so has the survey van's capabilities. This trend is expected to continue with more extensive use of the van as a primary test bed. Additions such as a differential GPS system, or a SNU 84-1/E Enhanced INU with compatible GPS receiver as a continuous reference system, will provide very accurate position determination while moving. With this improvement, the test van will not be limited to National Geodetic survey points.

**THIS PAGE LEFT BLANK INTENTIONALLY**

# **Configurable Data Acquisition Test Software**

**PC based MIL-STD-1553B Multiplexed Data Bus test software**

David R. Hollingsworth  
Honeywell Inc., MAVD/GNO  
11601 Roosevelt Blvd.  
St. Petersburg, FL

October, 1993

**TITLE:****Configurable Data Acquisition Test Software  
PC based MIL-STD-1553B Multiplexed Data Bus test software****ABSTRACT:**

The Configurable Data Acquisition Test Software (CDATS) provides a set of programs for the data display and control of a MIL-STD-1553 Multiplex Data Bus, which can be easily configured for any set of 1553 messages. The software operates in an 80286 or above PC with an ILC Data Device Corp. 1553 interface board (BUS-65517). The use of text control files allows configuration of data bus message structures without impact to the executable files. This feature permits the introduction of differing message structures in a convenient and timely manner for engineering verification and production testing of 1553 devices.

**INTRODUCTION:**

The CDATS software provides several desirable features for general purpose 1553 test software. These features include: timely adaptation to new or different messages and formats; the display of data bus traffic in formats other than hexadecimal, with the ability to include scaling to produce displays of data more easily understood (i.e. 27°52'43" vs. 13D32570); and the ability to record large amounts of 1553 data bus traffic for post test analysis or playback.

The CDATS programs :

- operate in the bus controller, remote terminal, and/or bus monitor modes;
- display the data in hexadecimal format and in its most useful format (e.g., binary, integer, floating-point, ASCII, degrees-minutes-seconds);
- record all or selected messages on the data bus at full rate, at timed intervals, or on specific events;
- provide a real-time rescalable graphical plot display of up to four parameters;
- allow the operator to obtain a hard copy printout or generate a graphics file of the plot display;
- are configured from text files created by an ASCII text editor or an editor with ASCII output;
- allow definition of function keys to enable setting and resetting of bits in transmitted data words;
- provide indicators of selected data bits that are set or reset;
- are controlled by keyboard input and text command file input;
- inject asynchronous messages and transmit mode codes;
- display successful and unsuccessful message counters and last unsuccessful message error;
- playback, plot, and extract (for spreadsheet use) recorded data.

## **HISTORY:**

Early applications of the ILC Data Device Corp. BUS-65517 1553 Data Bus Interface Card began in 1988 with the investigation and development of a low cost bus analyzer. This effort led to the development of a low cost data collection system and high speed recording of 200 Hz 1553 data. This test software functioned as a Bus Controller with a frame consisting of 4 (four) 23 word messages at 200 Hz and 2 (two) 17 word messages at 50 Hz. The next application specific version with configurable options was developed during Cobra Ball program testing. This was a Remote Terminal Simulator and Recorder only. Although the Cobra Ball Integrated Test Software allowed completion of testing in a timely and economical manor, it also verified further development was warranted.

After internally funded development of a generic Bus Controller with unique functions associated with Global Positioning System testing in an Integrated INS/GPS, CDATS began to emerge as a generic application with fully configurable options. Recent enhancements have included emulation of both a Generalized CDU and a Unique CDU interface to facilitate operator entry and the inclusion of a command file processor to aid in automation. During F-16 Operational Flight Program (OFP) demonstration tests, a series of 47 command files performed about 17 hours of automated testing without operator intervention and provided printed documentation of the results of all tests. CDATS' most recent application involved the control of two separate data buses. Attitude and attitude rate data retrieved from an Enhanced INU on one bus was used to project the attitudes forward or backward in time before being retransmitted on the second bus for utilization by a second device. Though not generic in nature, this application lays the ground work for CDATS' use as a mission computer simulator.

CDATS has been used extensively in dynamic testing in the Honeywell Survey Van with virtually all aircraft navigation units produced at MAVD/GNO including H-423 (F3, F16, and Enhanced), H-770 (F15), H764 (C2, and G models), as well as special derivatives of these units. It is the ability to easily adapt to special applications that makes this software valuable as a strong engineering tool. This software has also seen use in portable PC based testers in actual aircraft flights aboard a C-141, an OH-58D, and an AH-1W, with an Enhanced INU on the C-141 and Integrated INS/GPS systems on the two helicopters. Integration of an Enhanced INU/MAGR combination was accomplished through the use of this software package and it is utilized extensively in the lab as control, display, and recording software.

## **REAL TIME PROGRAMS:**

The CDATS bus controller (1553-BC) is the most versatile of the three real time programs. It contains the capability to operate as multiple remote terminals and monitor bus traffic while acting as the bus controller. The remote terminal (1553-RT) program is capable of providing multiple remote terminals, either actual or emulated, and functioning as a bus monitor. The monitor software (1553-MN) is able to monitor any active bus. It is completely passive and is a valuable tool as an independent verification of traffic present on the bus. The monitor software is particularly useful during initial integration of hot mockups, other test sets, and aircraft installations.

The following features are common to all three real time programs and the playback program:

:



### Message display page:

Shows individual messages by terminal address, subaddress, word count, and mode (receive/transmit) with successful and unsuccessful message counters and last unsuccessful message error. Message data is displayed at a user defined interval ranging from a minimum of 0.25 seconds (4 Hz refresh) to a maximum of 65535 seconds. Intervals of about 1 second (1 Hz refresh) seem to offer the best compromise between speed and readability. Up to sixteen lines of data are shown per screen with the ability to toggle to a second page for the remaining data if necessary.

### Snapshot page:

Allows collection of up to sixteen data items from the bus to be displayed one per line in groupings defined by the user. The refresh rates for this screen are the same as those for the message display page. This page is useful for displaying similar data from different messages or to observe both input parameters and resulting output without swapping from one message display page to the other. Items in the snapshot list can be added or deleted in real time as well as defined in the setup file prior to program execution.

### Tabular page:

Five preselected data items are displayed at a user defined rate in a scrolling display of the last sixteen samples in columnar format. As the display scrolls, changes in the values being displayed are easily detected by the user. Since all displayed items are sampled simultaneously, a rough approximation of time of response from input to output can be observed. Tabular data items can be defined in the setup file or changed during operation.

### Plot page:

The plot display, a graphics display page, allows the user to plot up to four parameters on a rescalable grid. The X axis of the plot is usually time based. Internal time, time in nav, or time in align are common choices, however the X axis can be driven by any parameter on the data bus. For example, when driven by longitude with the Y axis driven by latitude a two dimensional ground track is plotted. The parameter description for any of the four possible plot parameters ( Y values ) contains provisions for offset and multiplier factors to be applied to that parameter. This gives the capability to plot values of different magnitude on the same screen without sacrificing resolution. Minimum and maximum values for the major axis and offset and multiplier values for all parameters can be changed in real time with the plot updated to reflect the new values. The plot can be toggled between a point type trace and a line draw mode with the traces in different colors on a color display. Optional trace numbering is available to aid viewing on a monochrome display. Labels can be inserted in the plot display by the user during operation. The data items associated with plot parameters (X or Y) must be specified in the setup file and cannot be changed while running. While all display pages can be printed, the plot page can also be directed to an HPGL format disk file to be plotted later.

:

### **Statistics page:**

Statistical calculations are performed on a user definable size sample of selected data items and the results are displayed on the screen. The sample start is operator controlled and continues until the appropriate number of samples has been taken at which time minimum, maximum, mean, standard deviation, and RMS calculations are performed on the data set. Up to sixteen parameters may be specified for this statistical analysis.

### **Function keys and indicators:**

Twelve function key assignment options are available to the user. The twelve function key combinations <ALT>, <SHIFT>, or <CTRL> + <F1>-<F4> are defined in the setup file as either action keys (output), indicators (input), or both. When operating the monitor or playback software, action type function key assignments are ignored (monitor can not update message data). A common definition for a SNU 84-1 application is <ALT> + <F4> to set D01 word 1 to 0800h to command Gyro Compass Alignment (GC Align) and indicate GC Align by highlighting (in inverse video) the selection on the screen based on the bit pattern in the response message I09 word 1 that indicates the INU has transitioned to the GC Align mode. The indication can be defined to trigger on setting the desired bit pattern or value in a data item or on detection of a particular bit pattern in an output word. Bits are defined as 0, 1, or X for 'Don't Care' in determining indications or defining action. Function keys and indicators appear on all display pages except the plot page, however they are active while displaying the plot page.

### **Command line:**

Transmitted data can be updated from the command prompt present on all CDATS display pages. The new data is transmitted on the next occurrence of the message. Complete values in hex or in units of a particular parameter may be entered, or individual bits of a parameter can be set or reset. Message data entered on the command line in playback or monitor has no effect. A message display page is brought up by typing the message name on the command line. Command file execution and insertion of asynchronous messages are also available from the command line.

### **Command file processor:**

Available to the user is a robust command file processor that reads an ASCII text file to control operation of the test software. Virtually any command or action that can be performed from the keyboard can be duplicated using the command file processor. Also contained in the processor language are many assembly language type operators such as logical, conditional, looping, jumping, input, and output operations. Once a sequence of operations is defined they can be used to provide repeatability to test scenarios. Command files can call other command files to form increasingly complex or long duration tests. This capability was well demonstrated during F-16 OFP testing with many tests performed repeatedly during initial OFP development and then concatenated to form the basis for a seventeen hour unassisted demonstration and validation test.

## **Data record:**

In the past, collection of data bus traffic in sufficient quantities to provide enough information for analysis was difficult at best. With the ability to record all data bus activity or selectable subsets, data collection for system analysis is now limited only by available hard disk storage space. Data rates exceeding one megabyte per minute have been recorded for post test processing. This extended window into the operation and interaction in INS testing have provided insights to events not trapped using conventional methods. A subset of data can be obtained by selecting timed sampling or specific event triggers based on data contained in the data stream. Specific event triggers can override timed sampling to provide higher recording rates immediately following the event of interest.

## **Summary data printout:**

An end of test printout option is supported in all real time programs and in the post test playback software. This printout contains a print of the plot display and optionally a summary of velocity data at the 0, 21, and 42 minute points, and terminal data with RMS and peak-to-peak values. Also reported are Radial Position Error (RPE), Radial Position Error Rate (RPER), time in alignment, time in navigate, heading information at transition to nav and terminal, and gyro block temperature.

## **POST TEST PROGRAMS:**

### **Playback:**

The playback software reads a saved data file to provide the ability to review recorded data bus traffic. All displays and outputs available from the real time programs are provided. Message data can be single stepped forward or backward during playback. Pause and run (continuous read and display) functions are available to stop or "fast forward" the data playback. Function key indicators operate as they did during collection of the saved data, however action produced by the function keys is suppressed during playback (pressing <ALT>+<F4> for GC Align during playback will not change the saved data or be acknowledged on screen). Different plot parameters can be specified in a setup file or all setup information (stored in data file) used during the real time recording can be used.

### **Plot only:**

To increase efficiency during post test analysis, the plot only software is useful when the only output needed is the data plot. This software acts on a saved data file to produce a plot of the user defined plot parameters. Either the plot parameters specified during data collection or new parameters defined in a setup file can be plotted. All user alterable plot parameters are available (i.e. scaling, X and Y axis ranges). Any data contained in the save file is available to be plotted.

### **Extract**

The extract program is used to produce a comma separated value (CSV) output file suitable for import into most commercial spreadsheet programs. Extraction of up to 36 data items can be specified during program execution. The interval between extracted data points can be specified, from all available points to a subset based on the number of samples ( i.e. every tenth data point). Also a minimum and maximum value to be extracted can be used to determine the beginning and end point of the extraction.

Output data is formatted according to information used at the time the data was collected (hex, binary, real, etc.).

## **SUPPORT FILES:**

### **Parameters file:**

This file is used to describe the message structure to be used for the test and consists of two parts. First all messages are defined with a message name, terminal address, subaddress, word count, receive/transmit, frame rate, and optional text note. If the RT is the receiver in an RT-to-RT transfer, the terminal address and subaddress of the transmitting RT is also specified. Secondly, each message is broken down by word to define the number of words for each parameter, the parameter name, units, scale factor, and initial value.

### **Setup file:**

The setup file is used to define text and plot display parameters, data record and statistical analysis parameters, post-test report options, function key definitions and indicator selections. A unit-under-test definition for certain predefined systems is available and allows access to features unique to particular interfaces. Included currently are definitions to select from Generalized (F3) or Unique CDU (F-16 & F3) interface simulation, support for GPS unique functions (INS/GPS), and rudimentary discrete control (F-15 & F-16).

### **Frame file:**

For operation as a bus controller, a frame file is used to configure the parameters for data bus operation. Minor frame time, minor and major frame breaks, mode commands, injectable messages and actual bus command sequence are specified here.

### **Help file:**

A user maintainable help file is used to assist the user during program execution. The basic help file provided with the CDATS software is an ASCII text file that is read in at startup and can be displayed during operation. This file can be modified to reflect any function key definitions created by the user or other useful information.

### **Save data file:**

The save data file is created during initialization with a header containing copies of both parameter file and setup file information in ASCII text format to identify the recorded data. Data bus traffic is then recorded in binary format for use in any of the post processing programs.

:

## DEVELOPMENT DIRECTIONS:

The planned migration to operation in the protected mode available in the 80386/80486/Pentium series of processors would allow addition of automatic table and temperature control, increased UUT unique functionality as well as increase the capacity of the data plot buffers. Though real mode operation is effective for current use, the application as a basic mission computer simulator has demonstrated that increased throughput available from protected mode operation would allow further growth and provide valuable experience in possible migration from the PC platforms to a VME/VXI environment. The CDATS baseline software for the bus controller was used as the basis for the Honeywell Portable Ruggedized Intermediate-level Diagnostic Equipment (PRIDE). This same baseline has recently been modified by removing the 1553 interface and replacing it with an IEEE-488 interface to meet the need for test software with a different interface. With increasing demand for various communication protocols and tightening budgets, reusable, adaptable code becomes a valuable asset.

### Feature Summary

	1553-BC	1553-RT	1553-MN	PLAYBACK	PLOT ONLY	EXTRACT
BUS CONTROLLER	●					
REMOTE TERMINAL	●	●				
BUS MONITOR	●	●	●			
DATA DISPLAY	●	●	●	●		
RECORD	●	●	●			
PLOT	●	●	●	●	●	
PRINTOUTS	●	●	●	●	●	
FUNCTION KEY(ACTION)	●	●				
FUNCTION KEY(INDICATOR)	●	●	●	●		
COMMAND FILE	●	●	●			
INJECT MESSAGE	●					
MODE CODE	●					
MESSAGE COUNTER	●	●	●	●		
SPREADSHEET FILE				●		●

# Sample message display page

successful messages = 3197

unsuccessful msgs = 0

msg: 101 tadr:16 sadr:16 words:32 mode:bc\_R

01	IMU_MODE	1420	0001 0100 0010 0000	STATUS
02	TIMETAG	73F9	+1900096.	
03	X_VEL	0000003F	+0.0002403259	FPS
05	Y_VEL	FFFFFFC5	-0.003154755	FPS
07	Z_VEL	00000025	+0.0001411438	FPS
09	AZIMUTH	FFF3	-0.000	-001 08'33" °RADS
10	ROLL	FF08	-0.001129150	-000 12'12" °RADS
11	PITCH	FE07	-0.01541138	-002 46'27" °RADS
12	TRUEHDG	C000	-0.4932556	-088 47'10" °RADS
13	MAG_HDG	C308	-0.4762268	-085 43'15" °RADS
14	X_ACCEL	0000	+0.0000000	FPS2
15	Y_ACCEL	0001	+0.03125000	FPS2
16	Z_ACCEL	0402	+32.06250	FPS2
17	CNEXX	01438B27	+0.01975898	-----
19	CNEXY	C7712441	-0.8837194	-----
21	CNEXZ	10ED27FC	+0.4675999	-----

## COMMAND:

AF1:OFF	AF2:STANDBY	AF3:SH_ALIGN	AF4:EGC_ALIGN
SF1:NAVIGATE	SF2:ATTITUDE	SF3:TEST	SF4:EIA_ALIGN
CF1:NAV_READY	CF2:DATA_RDY	CF3:DRDY_ACK	CF4:ILLEGAL_CMD
F5:PLOT	F6:SNAPSHOT	F7:TABULAR	F8:MESSAGE
			F10:HELP

**THIS PAGE LEFT BLANK INTENTIONALLY**

## **Advanced Magnetic Azimuth Detector (AMAD) Development**

**Michael A. Friday, Navigation Engineer  
USAF, Oklahoma City Air Logistics Center**

**John N. Hericks, Electrical Engineer  
Honeywell, Military Avionics Division, Minneapolis MN**

**Heather Jewett  
Lear Astronics Corp, Santa Monica CA**

**Gordon F. Rouse, Electrical Engineer  
Honeywell, Systems & Research Center, Minneapolis MN**

**Approved for Public Release; distribution is unlimited**

### **ABSTRACT**

The Magnetic Azimuth Detector (MAD) is the reference sensor for compass and attitude heading reference systems. This paper will describe the efforts to develop a new generation of strapdown MADs. Specific topics to be addressed include: reliability & performance increases, technical approaches, specification & interface control document, cost targets, test results, development plan & schedule. The AMADs are not targeted for retrofit programs but rather for new developments.

This MAD replacement program has been under consideration for some time. Recent advances in sensor and microprocessor technology now make strapdown MADs feasible. This project is being realized by the the Commodities Manager at the Oklahoma Air Logistics Center.

### **INTRODUCTION**

Navigation charts reference magnetic north rather than true north. True north, as measured by an inertial navigation unit, reflects the earth's spin axis intercept with the earth's sphere whereas magnetic north is the intercept with the earth's magnetic field. Magnetic north and true north do not coincide and magnetic north tends to drift with time. Local variation in the magnetic field also distorts magnetic heading. The initial high cost of inertial navigation equipment is why we still utilize magnetic heading for navigation. As satellite navigation becomes less expensive and accepted universally, this may change the way we navigate from place to place.

Early compasses (whisky-type) used a bar magnet floated in a liquid coupled to a indicator card. These devices are very prone to errors (turning, acceleration, etc). This progressed to using the whiskey compass to manually set the directional gyro (DG). The next step in the evolution was the slaved compass system. In this system the DG is electrically slaved to the remote compass transmitter or MAD. The MAD being the magnetic north-sensing device.



The design of current Magnetic Azimuth Detectors are all basically the same variation mainly of case material (metal or plastic), with size (standard or ML-1), calibration limits and pre-indexing. These devices were built by only a few manufacturers, only one remains Honeywell (Sperry) at Durham N.C. A MAD is a hermetically-sealed unit filled with a damping fluid which suspends four coils (Flux-valve) by way of a pendulous mass. The purpose of the gimbal structure is to keep the sensing elements level, because only the horizontal component of the magnetic field is useful for navigation. The output of this device is a modulated 800 Hz signal.

These MADs require precision machined parts that are non-magnetic. The depot facilities are also built with as little magnetic material as possible. Helmholtz cages that permit varying magnetic fields are required to calibrate these devices at the depot. The technicians require years of experience to master the overall process. Once a MAD is installed in an aircraft, a lengthy process of removing one-cycle, two-cycle and index errors is required, typically called a "compass swing". These compass swings require physical rotation of the aircraft through 360 degrees of heading or a compass calibrator device (MC-1/M or MC-2000) which simulates this rotation by applying DC signals into a MAD creating the desired headings.

### PROBLEMS

From the above brief discussion it can be seen that these devices are labor intensive. MADs typically have a Mean Time Between Depot Demand (MTBD) of 1500 hours depending upon aircraft application. The failure modes are generally: coil failure or stiction of gimbals. When stiction occurs the MAD indicates the vertical component of the magnetic field which is totally useless and invalid for heading.

The gimbal structure of a MAD only permits accurate data within 20 degrees of vertical, after which the compass or AHRS decouples from the MAD and is operating in free gyro drift. This occurrence also applies during aircraft acceleration.

MADs tend to be non-linear, as the MAD is rotated it will reflect a different error at different quadrants. In applications that require a high linearity, the yield at depot for these MADs is typically 25%.

### SOLUTION

The concept for the Advanced Magnetic Azimuth Detector, or AMAD, is a strapdown device with a digital output (RS-485 or 422). The AMAD is intended for use with only the new compasses (Bendix UCR) and AHRSs (Smith's Industry C/AHRS & Honeywell's GSSR) systems. An AMAD tightly coupled to these systems can achieve more consistent and accurate magnetic heading in the high dynamics of modern day aircraft. Further compass calibration can be performed continuously as a background task eliminating the time consuming compass swing procedures.

The AMAD conforms to the basic dimension of current MADs and operate with 28 VDC or 26 VAC inputs. This new approach expands the operational envelope to provide increased accuracy and performance. The typical heading accuracy for most MADs is 0.4 degrees under ideal conditions. In service, system accuracy are on the order of 1.0 degrees. With the AMAD it is anticipated to meet a system accuracy of 0.5 degrees. Since the device is strapdown, it is not limited to 20 degrees of bank, so useful data will be available almost to vertical. The AMAD also can provide attitude, temperature, field strength and acceleration. Extensive Built-In-Test (BITE) is also inherent in the device. The

AMAD has a reliability goal of 25,000 hours MTBD. Production unit cost of \$3.5k in large quantities is anticipated, which makes the device potentially throw-away.

Currently, two vendors approaches are being pursued by the Air Force. Other contractors have also shown an interest in AMAD development. Honeywell has pursued a permalloy sensor and Lear Astronics approach utilizes a convention toroid. Proof-of-concept demonstration units have been built and tested at the Avionics Reliability Center (Tinker AFB, OK) and MAD Depot facilities (Hill AFB, UT).

### HONEYWELL PERMALLOY APPROACH

The challenge of coming up with a design within the constraints of building a demonstration unit that would fit within the existing MAD volume was quite a feat (see Figure 1). The demonstration unit worked quite well, at about 2 degrees of heading accuracy.

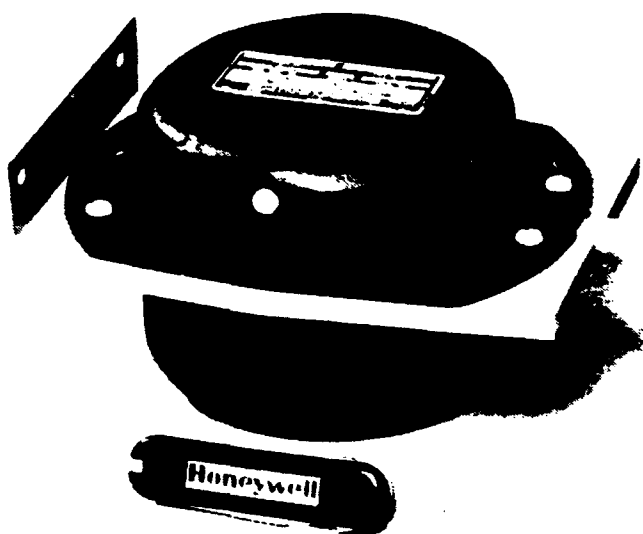


Figure 1 - Honeywell Permalloy MAD proof-of concept model

The unit contained three single-axis magnetically closed-loop permalloy magnetometers, two electrolytic tilt sensors, a microprocessor for converting the sensor signals into magnetic heading, support electronics and power supplies. The tilt sensors provide the vertical reference and allow the unit to work over a  $\pm 60$  degree elevation range, which is quite an improvement over the current 20 degree on existing MADs.

The magnetometer sensor is based on the change of resistance in permalloy (NiFe) with the applied magnetic field, a phenomenon known as magnetoresistance <sup>1,2</sup>. The permalloy is deposited onto a silicon wafer using similar steps that are used in low-cost integrated circuit processing. The transducer design used consists of four barberpole-biased magnetoresistors that are connected as a Wheatstone bridge to minimize the temperature sensitivity (see Figure 2). The magnetoresistive transducer is

operated magnetically closed-loop. In this mode the transducer is operated as a null detector since the sensed field is nearly proportional to the current through the feedback coil.

Future planned improvements include a smaller, lower-cost tilt sensor and the addition of an ASIC which greatly reduces electronics volume and cost. A technique to remove temperature-induced bias in the magnetometers is slated for use in future units since it virtually eliminates the need for magnetometer bias compensation. This technique uses a coil to periodically switch the magnetization of the transducer film. The result is the magnetically-induced signal and temperature-induced signals are separated such that the temperature-induced bias is removed.

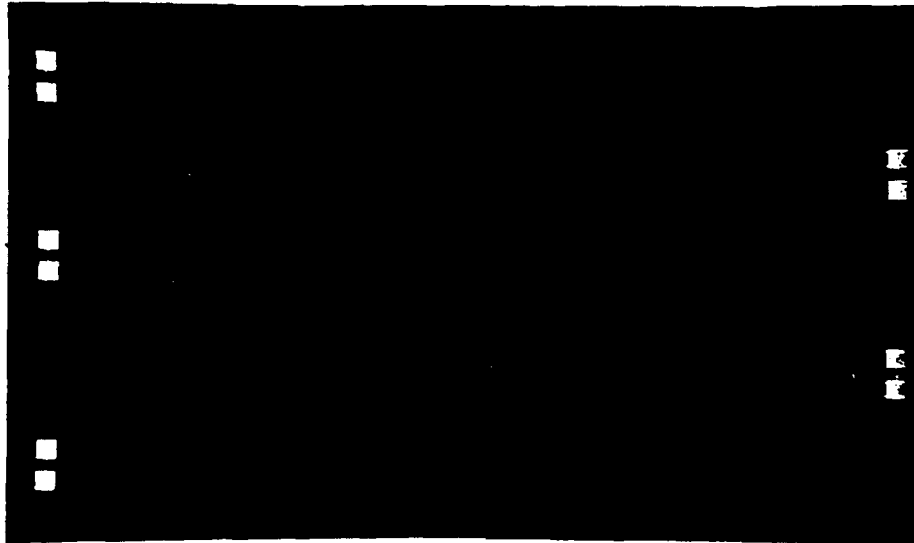


Figure 2 - Honeywell Permalloy magnetic-sensing transducer

#### LEAR ASTRONICS ACCELEROMETER-AIDED APPROACH

The Accelerometer-Aided Magnetic Azimuth Detector (AAMAD) is a solid-state design developed by Lear Astronics Corporation as an inexpensive and accurate line replaceable unit for the present gimbaled-type MADs (see Figure 3). The new device senses the earth's magnetic field, compensates for field anomalies and computes accurate heading with respect to the earth's magnetic poles.

The AAMAD uses a three-axis flux-gate magnetometer to sense the earth's magnetic field. The third axis allows this design to compensate for the earth's vertical magnetic field. The magnetometer uses toroidal cores in a closed-loop configuration for its sensing elements.

This MAD uses three accelerometers to measure the attitude of the magnetometer with respect to the gravity vector. Attitude information coupled with the three-axis magnetic field strength enables it to decouple the vertical and horizontal components of the earth's magnetic field. From the horizontal field strength the magnetic heading is computed.



**Figure 3 - Lear Astronics Accelerometer-Aided MAD proof-of concept model**

The AAMAD processor samples and averages the accelerometer and magnetometer outputs. Calibration parameters calculated and stored during factory level calibration procedures are used to compensate the sensor readings for scale factor and bias errors. The attitude of the vehicle is then calculated using the accelerometer readings. Finally, the magnetic field vector is rotated to the local level frame using previously computed attitude and magnetic heading is computed.

The unit can be used as a stand-alone magnetic heading reference or in conjunction with an AHRS system as a slaved magnetic heading reference. In stand-alone mode, the calculated heading is valid only during static flight conditions when the gravity vector is the only acceleration present. When used in conjunction with an AHRS system, heading is valid in all flight conditions.

During the next phase of development, the AAMAD will be repackaged in order to meet the height requirement for existing flux-valves. The design will be also modified to meet applicable environmental requirements. Composite materials for the chassis will also be investigated for a lighter, lower-cost alternative to traditional materials. Finally, work will continue to verify and improve the method for both attitude and magnetic calibration.

### **PRELIMINARY TEST RESULTS**

In early April 1993 the proof-of-concept prototypes were tested at the Hill AFB (Ogden Utah). This facility is built exclusively for the test and overhaul of MADs (see Figure 4). The test equipment include Helmholtz cages which feature reference bearings, varying of field intensities, heading positioning from 0 to 345 degrees at 15 degree steps, and tilt capability.



Figure 4 - Test Facility for MADs at Hill AFB (Ogden Utah)

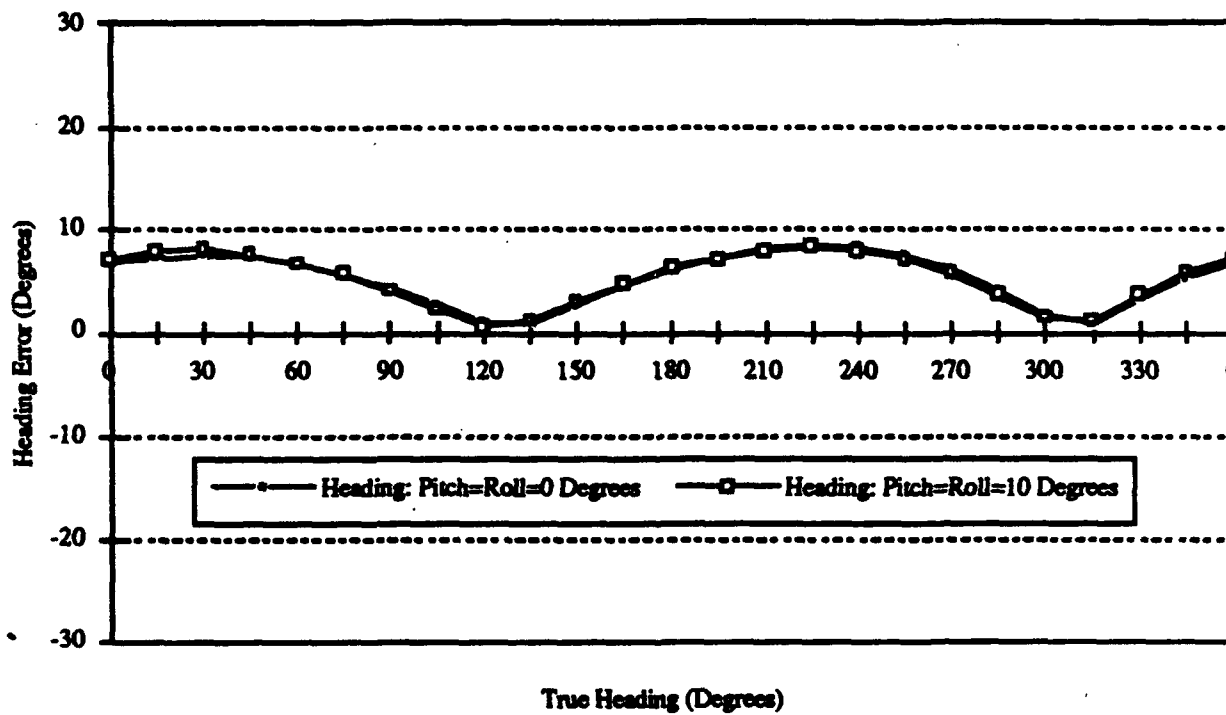


Figure 5 - Uncalibrated AAMAD heading error for pitch=roll=0 and pitch=roll=10 degrees

Overall heading error for Honeywell was 2.4 degrees and 5.2 degrees for Lear Astronics in the level plane. Attitude computational error was 0.5 degrees for Honeywell and 3.0 degrees for Lear Astronics varying over a 30 degree roll and pitch range. The heading error associated with 10 degree tilts was 2.3 degrees for Honeywell and 0.4 degrees for Lear Astronics.

Both Honeywell and Lear Astronics show a sensitivity to field strength. The Honeywell unit appeared to have a coupling effect between axes. Both would have benefited from a better calibration technique, as residual-bias error became significant at low-field intensities.

Repeatability was excellent for both Honeywell and Lear Astronics. This is most encouraging since most of the errors identified above should be correctable by better calibration techniques. Long-term stability needs to be evaluated to insure that calibration and characterization do not change. No temperature tests were performed at this time but will be accomplished in the next phase.

### FUTURE ACTIVITIES

The Air Force is committed to fielding the AMAD for use with the new compasses and AHRS systems. A draft government military specification (see Appendix A) and an Interface Control Document (ICD) (see Appendix B) have been written stating the operational and functional requirements for the AMAD. It is the government's intent to maintain two qualified sources for the new sensor. This will prevent support problems of the past and provide competition.

It is anticipated that Honeywell and Lear Astronics will have units for qualification in 1995. Both vendor units will be functionally interchangeable and meet all the minimum requirements of the ICD and military specification. Integration units for use with development programs are scheduled to be available in late 1994. Software and interface provisions for the AMAD have been incorporated on several programs so that qualification of AMADs will progress as envisioned.

### SUMMARY

The Air Force is pleased with the preliminary results of the AMAD proof-of-concept demonstration. As a result of testing accomplished at Hill AFB both vendors know what areas require attention. Design changes have been discussed to reduce package size and reduce the cost for production. It is planned to have an integration unit available in 1994 for compass and AHRS development programs.

The performance goal of 0.4 degrees heading accuracy seems achievable. It remains to be seen whether these new devices will be able to operate at high-temperatures. The high reliability AMAD, integrated into a new compass/attitude system will result in better system performance, limited on-aircraft maintenance, and significant logistic cost savings.

### REFERENCES

1. Pant, B.P., and Krahn, D.R., "High sensitivity magnetoresistive transducers", Presented at the *35th Annual Conference on Magnetism and Magnetic Materials*, Oct. 29 - Nov. 1 1990, San Diego CA.
2. Lenz, J.E., et. al., "A High-Sensitivity Magnetoresistive Sensor", Presented at the *IEEE Solid-State Sensors and Actuators Workshop*, Hilton Head SC, June 1990.

## **AUTHOR BIOGRAPHIES**

### **Michael A. Friday**

Mr. Friday is a Navigation System Engineer for The Air Force Material Command at Oklahoma City OK.

Mr. Friday received his BS in Electrical Engineering from the University of Miami in 1979.

Mr. Friday has been employed with the United States Air Force, Tinker AFB Oklahoma since 1984. He is technically responsible for Compasses, Attitude Heading Reference Systems, Magnetic Azimuth Detectors, and Compass Calibrator System. Engineering developments under his direction include: the MC-2000 Compass Calibrator, Universal Compass Amplifier Replacement, B-1B Gyro Stabilization System Replacement, Magnetic Azimuth Detector Support Facility Modernization, Advanced Magnetic Azimuth Detector and Avionics Reliability Center.

### **John N. Hericks**

John N. Hericks received his B.S. degree in Electrical Engineering from South Dakota School of Mines and Technology, Rapid City SD, in 1981.

Joining Honeywell Incorporated in Minneapolis, MN upon graduation, he worked in the development and evaluation of Ring Laser Gyro guidance and navigation systems for military aircraft. The majority of his work at Honeywell has been as a lead engineer in the development of Military Electronic Warfare test equipment. His most recent work has been in the development of a permalloy based MAD and a magnetic helmet positioning System.

### **Heather Jewett**

Ms. Jewett is an Electrical Engineer at Lear Astronics in Santa Monica CA. Ms. Jewett received her BS in Electrical Engineering from Gonzaga University in Spokane WA in 1991.

Ms. Jewett started at Lear Astronics in 1991 with responsibility for systems engineering on the Accelerometer Aided Magnetic Azimuth Detector. Other programs include the systems engineering for the Side Arm Controller and MAD for the Comanche helicopter.

### **Gordon F. Rouse**

Mr. Rouse is a Research Engineer with the Honeywell Systems and Research Center. Mr. Rouse received his BS in Electrical Engineering from Michigan State University in 1978 and Masters in Electrical Engineering from the University of Minnesota in 1985.

At SRC since 1984, Gordon has worked on electronics design for ring laser gyroscopes and research for resonator and interferometric fiber optic gyroscopes. Presently co-principal investigator for Honeywell SRC's permalloy magnetometer development programs, he has been developing low-noise, low-power electronics, and magnetic measurement techniques for applications such as magnetic anomaly detection, compassing, and position tracking.

## APPENDIX A

### ADVANCED MAGNETIC AZIMUTH DETECTOR (AMAD) DRAFT MILITARY SPECIFICATION

MIL-D-XXXX (USAF)  
03 May 1993  
MILITARY SPECIFICATION  
Detector, Magnetic Azimuth (Digital)

#### 1.0 SCOPE AND CLASSIFICATION

1.1 Scope. The Advanced Magnetic Azimuth Detectors (AMAD) covered by this specification are used as the direction sensing component of a Magnetic Compass System or Attitude Heading Reference System (AHRS). This specification covers the requirements for the new solid state or strapdown detector with a totally digital interface in lieu of the conventional 3 wire analog.

1.2 Classification. This specification covers the following items:

P/N LG1254AA	Honeywell Permalloy Magnetic Azimuth Detector
P/N XXXXXXXX	Lear Astronics Accelerometer Aided Magnetic Azimuth Detector

#### 2.0 APPLICABLE DOCUMENTS

2.1 The following documents of the issue in effect form a part of this specification to the extent specified herein.

##### SPECIFICATION

MIL-P-116	Preservation, Methods of
DOD-D-1000	Drawing, Engineering and Associated List
MIL-C-5541	Chemical Films for Aluminum Alloys
MIL-S-6872	Soldering Process, General Specification
MIL-A-8625	Anodic Coatings, for Aluminum and Alloys
MIL-D-26503A	Detector, Magnetic Azimuth, and Compensator
MIL-STD-130	Identification Marking of US Military Property
MIL-STD-143	Specification and Standards, Order of Precedence for the Selection of
MIL-STD-781	Reliability Tests Exponential Distribution
MIL-STD-785	Reliability Program for System and Equipment Development and Production
MIL-STD-810	Environmental Test Methods
MIL-STD-831	Test Reports, Preparation

#### 3.0 REQUIREMENTS

3.1 Qualification Requirements. This specification makes provision for qualification requirements.



**3.2 Data.** Unless otherwise specified in the contract, no data (other than Qualification Test Reports) are required by this specification or any of the documents herein.

**3.3 Components.**

**3.4 Materials.**

**3.4.1 Metals.** Metals shall be corrosion resistant or shall be suitably protected to resist corrosion during normal service life. Materials contained within heretically sealed enclosures are considered to be suitably protected from corrosion. Requirements specified for fungicidal and corrosion-protective treatment, for anodizing the aluminum alloy parts, and for cadmium plating of steel parts, are not applicable for parts within hermetically sealed instruments.

**3.4.2 Nonmagnetic materials.** Nonmagnetic materials shall be used for all parts of the detector except where magnetic materials are essential.

**3.4.3 Fungus-proof materials.** Materials that are nutrients for fungi shall not be used where it is practical to avoid them. Where used and not hermetically sealed, they shall be treated with fungicidal agent acceptable to the procuring activity. However, if they are used in the hermetically sealed enclosure, fungicidal treatment will not be necessary.

**3.4.4 Protective treatment.** When materials are used in the construction of the AMAD that are subject to corrosion in salt air or other atmospheric conditions likely to occur during service usage, they shall be protected against such corrosion in a manner that will in no way prevent compliance with the performance requirements of this specification. The use of any protective coatings that will crack, chip, or scale with age or extremes of atmospheric conditions shall be avoided.

**3.4.5 Specifications and standards.** Specifications and standards for all materials, parts, and government certification and approval of processes and equipment, which are not specifically designated herein and which are necessary for the execution of this specification, shall be selected in accordance with MIL-STD-143, except as provided in the following paragraphs.

**3.4.5.1 Standard parts.** Military Standard (MS) parts shall be used wherever they are suitable for the purpose, and shall be identified by their part numbers. Commercial utility parts such as screws, bolts, nuts may be used, provided they develop suitable properties and are replaceable by the MS parts without alteration, and provided the corresponding MS part numbers are referenced on the drawings and in the parts list. In applications for which no suitable corresponding MS part is in effect commercial parts may be used provided they conform to this specification.

**3.5 Design.** This AMAD shall be of solid-state design with digital interface for use with the new generation of totally digital navigation systems.

**3.5.1 Physical Dimensions.** The AMAD shall conform to the dimensions.

**3.5.2 Connector.** The AMAD shall interface with the external world via a connector of type MS27505T 11 C35S. Pin assignment shall be IAW of the ICD.

**3.5.3 Power Requirements.** The AMAD shall operate with either 23.5 VAC at 400 HZ or 28VDC. Maximum power consumption shall not exceed 250mA.

**3.5.4 Signal Interface.** The AMAD shall be capable of communicating via RS-485 or RS-422. Word and message protocol are contained in attached Interface Control Documents (ICD).

**3.5.4.1 RS-485 operations.** The MAD shall support both an EIA RS-485 and an EIA RS-422 interface operating in a half-duplex configuration. The default mode of operation shall be RS-485 unless the interfacing item commands the MAD otherwise. All interconnecting items which only allow for less than six signals from the MAD shall operate in RS-485 mode.

**3.5.4.2 RS-422 operations.** See 3.5.4.1

**3.5.5 Performance Requirements.**

**3.5.5.1 Heading Accuracy.** The AMAD shall provide compensated heading information accurate to 0.25 degrees at all heading.

**3.5.5.1 Attitude.** The AMAD shall be capable of providing accurate heading information at up to 60 degrees roll and/or pitch (non- accelerating).

**3.5.5.2 Tilts.** The AMAD shall be capable of providing X and Y tilts accurate to 1% of measurement angle.

**3.5.5.3 Temperature.** The AMAD shall provide unit core temperature measurements accurate to 1 degree Celsius.

**3.5.5.4 Headings.** The AMAD shall provide the following heading outputs: composite heading (0 - 359.99 degrees) and sine & cosine heading.

**3.5.6 Protection.** The AMAD shall be protected to insure that sand, dust, humidity, fluids and fungus producing conditions in service life will not interfere with the proper operation of the AMAD.

**3.5.7 Service life.** The equipment shall have a service life of not less than 50,000 hours or ten years. Service life is defined as the period of time the Mean Time Between Failure (MTBF) remains constant.

**3.5.8 Reliability.** Failure shall be defined as any condition of the equipment in which fully operational service is not possible within the performance requirements specified herein. The minimum acceptable MTBF, as defined in MIL-STD-781, shall be 25,000 hours.

**3.5.9 Weight.** The weight of the AMAD shall not exceed 2.0 pounds.

**3.5.10 Interchangability.** All AMADS shall be interchangeable and require no readjustments or realignments. They shall be software configurable per IAW 3.5.4.

**3.5.11 Soldering.** Soldering shall be IAW MIL-S-6872.

**3.5.12 Finish.** Metal surfaces shall be protected IAW MIL-A-8625 or MIL-C-5541 as applicable.

**3.5.13 Identification.** The AMAD and subassemblies shall be marked for identification IAW MIL-STD-130.

**3.5.14 Built in test.** The AMAD shall be capable of self diagnose of heading validity. A status word shall provide a GO/NO GO indication.

## 4.0 QUALITY ASSURANCE PROVISIONS

4.1 Responsibility for inspection. Unless otherwise specified, the supplier is responsible for the performance of all inspection requirements as specified herein. The government reserves the right to perform any of the inspections set forth in this specification where such inspection are deemed necessary to assure supplies and services conform to prescribed requirements.

4.2 Test samples. The contractor shall conduct tests on at least seven sample AMADs to determine that the design of the AMAD meets the requirements specified herein.

4.3 Test report. The contractor shall furnish a test report IAW MIL-STD-831 giving the results of the tests specified herein.

### 4.4 Testing.

4.4.1 Examination. Each AMAD shall be inspected to determine conformance to dimensions and materials.

4.4.2. Scale error. The AMAD shall be mounted on a turntable in a normal position with a standard field strength of 0.18 oersted horizontal and 0.54 oersted vertical ( $\pm 0.02$  oersteds). The AMAD shall be rotated at 30 degree increments through 360 degrees. At each heading record the difference between the turntable heading and the composite heading of the AMAD. The difference shall not exceed  $\pm 0.4$  degree after index error is removed.

4.4.3 Tilt error pitch. The AMAD shall be tilted 15 degrees in pitch (fore end up). Scale error test (4.4.2) shall be repeated with the exception of mounting arrangement. Record the test results.

4.4.4 Tilt error roll. The AMAD shall be tilted 15 degrees in roll (port side low). Scale error test (4.4.2) shall be repeated with the exception of mounting arrangement. Record the test results.

4.4.5 Tilt error combined. The AMAD shall be tilted 45 degrees in pitch and roll. Scale error test (4.4.2) shall be repeated with the exception of mounting arrangement. Record the test results.

4.4.6 Level field test. The AMAD shall be mounted on a turntable in the normal position with a horizontal field strength of  $0.18 \pm 0.02$  oersteds and a vertical field less than 0.02 oersteds. The AMAD shall be rotated at 45 degree increments through 360 degrees. At each heading record the difference between the turntable heading and the composite heading of the AMAD. The difference shall not exceed  $\pm 0.3$  degrees after index error is removed.

4.4.7 Weak field test. The AMAD shall be mounted on a turntable in the normal position with a horizontal field strength of  $0.08 \pm 0.01$  oersteds and a vertical field of  $0.54 \pm 0.02$  oersteds. The AMAD shall be rotated at 30 degree increments through 360 degrees. At each heading record the difference between the turntable heading and the composite heading of the AMAD. The difference shall not exceed  $\pm 0.5$  degrees after index error is removed.

4.4.8 Low temperature. The AMAD shall be subjected to a temperature of -73 degrees C for three hours operating. Then removed from chamber and immediately perform scale error test (4.4.2). Document test results.

4.9 High temperature. The AMAD shall be subjected to a temperature of 142 degrees C for three hours operating. Then removed from chamber and immediately perform scale error test (4.4.2). Document test results.

4.10 Vibration test. The AMAD shall be vibrated IAW MIL-STD-810E, Method 514.4, Table 14.4-III, Figure 514.4-8. Following vibration, while operating, the AMAD shall be subjected to test 4.4.2 thru 4.4.7.

4.11 Acceleration test. The AMAD shall be acceleration IAW MIL-STD-810E, Method 513.4, Table 13.4-I. Following vibration, while operating, the AMAD shall be subjected to test 4.4.2 thru 4.4.7.

4.12 Shock test. The AMAD shall be shock IAW MIL-STD-810E, Method 516.4, Procedure 1, Figure 516.4-1. Following vibration, while operating, the AMAD shall be subjected to test 4.4.2 thru 4.4.7.

4.13 Voltage-frequency variation. The AMAD shall be set up as specified in the scale error test (4.4.2). The supply voltage shall be varied by +/-20% for both 400VAC and DC operations. With no effect on the AMAD's performance.

4.14 Reliability demonstration. The reliability of the item shall be tested IAW Test Plan IV of MIL-STD-781. Test conditions include: operating at temperature of 40 degrees C, an altitude of 0 to 5000 feet, a relative humidity of 80 to 90%, nominal voltages and vibration of 100 - 2000 HZ at 0.015 - 0.030 inch on a duty cycle of 25%. No BITE shall occur during this demonstration.

4.15 Salt fog. The AMAD shall be subjected to salt fog test of MIL-STD-810, method 509.1, procedure I. Following this test, the AMAD shall be subjected to test 4.4.2 - 4.4.7.

## 5.0 PREPARATION FOR DELIVERY

## **APPENDIX B**

### **INTERFACE CONTROL DOCUMENT (ICD) FOR THE ADVANCED MAGNETIC AZIMUTH DETECTOR (AMAD)**

**Prepared by:  
Lear Astronics Corp.  
3400 Airport Avenue, Santa Monica, CA 90406-0442**

**ICD 488876-01 April 16, 1993  
Rev. -**

---

**Prepared By**

**Date**

**Appendix B-1**

## TABLE OF CONTENTS

1.	Introduction	1
1.1.	Electrical Interface	1
1.1.1.	Power Interface	1
1.1.1.1.	Power Consumption	1
1.1.2.	Serial Interface	1
1.1.3.	External Connector	1
1.2.	Serial Interface	3
1.2.1.	Protocol	3
1.2.2.	Data Rate	3
1.2.3.	Baud Rate	3
1.2.4.	Data Format	3
1.2.5.	Order of Transmission	3
1.2.6.	Message Length	3
1.2.7.	Encoding Format	3
1.2.8.	Byte Intervals	3
1.2.9.	Data Throughput	3
1.2.10.	Electrical Characteristics	3
1.3.	Software Interface	4
1.3.1.	Message Definition	4
1.3.1.1.	Message structure	4
1.3.1.2.	Message Header Definition	5
1.3.1.3.	Checksum	6
1.3.2.	Controller to MAD Communications	6
1.3.3.	Error Handling	6
1.3.4.	Initialization	6
1.3.4.1.	Test Mode	6
1.3.4.2.	Normal Mode	6
1.3.4.3.	BIT Mode	7
1.3.4.4.	Start-up Mode	7
1.4.	Message Definitions	7
1.4.1.	Initialization Message	7
1.4.2.	Initiated BIT Message	8
1.4.3.	Magnetic Field Strength Message Definitions	9
1.4.3.1.	Bx Comp Message	9
1.4.3.2.	By Comp Message	10
1.4.3.3.	Bz Comp Message	10
1.4.4.	Tilt Message Definitions	11
1.4.4.1.	Tilt x Message	11
1.4.4.2.	Tilt Y Message	11
1.4.5.	Temperature Message	12
1.4.6.	Heading Message	13
1.4.7.	Sine Cosine Message	14
1.4.7.1.	Sine Message	14
1.4.7.2.	Cosine Message	14
1.4.8.	Accelerometer Data Messages	15
1.4.8.1.	Ax Message	15
1.4.8.2.	Ay Message	16
1.4.8.3.	Az Message	16
1.4.9.	Raw Magnetic Field Strength Message Definitions	17

1.4.9.1.	Bx Message	17
1.4.9.2.	By Message	18
1.4.9.3.	Bz Message	18

## LIST OF TABLES

Table 1	Connector Definition	1
Table 2	Adapter Cable Connector Pin Definition	2
Table 3	MAD Data Format	3
Table 4	Message Structure Definition	5
Table 5	Message Field Definitions	5
Table 6	Message Byte Definitions	5
Table 7	Message Error Conditions	6
Table 8	Initialization Message Format	7
Table 9	Initialization Message Field Definitions	7
Table 10	Initiated BIT Response Message Format	8
Table 11	Initiated BIT Message Field Definitions	8
Table 12	Magnetic Field B(x,y,z) Data Definition	9
Table 13	Bx Comp Message Format	9
Table 14	Bx Comp Message Field Definitions	9
Table 15	By Comp Message Format	10
Table 16	By Comp Message Field Definitions	10
Table 17	Bz Comp Message Format	10
Table 18	Bz Comp Message Field Definitions	10
Table 19	Tilt T(x,y) Data Definition	11
Table 20	Tilt X Message Format	11
Table 21	Tilt X Message Field Definitions	11
Table 22	Tilt Y Message Format	11
Table 23	Tilt Y Message Field Definitions	11
Table 24	Temperature Data Definition	12
Table 25	Temperature Message Format	12
Table 26	Temperature Message Field Definitions	12
Table 27	Heading Data Definition	13
Table 28	Heading Message Format	13
Table 29	Heading Message Field Definitions	13
Table 30	Sine-Cosine Data Definition	14
Table 31	Sine Message Format	14
Table 32	Sine Message Field Definitions	14
Table 33	Cosine Message Format	14
Table 34	Cosine Message Field Definitions	14
Table 35	Acceleration A(x,y,z) Data Definition	15
Table 36	Ax Message Format	15
Table 37	Ax Message Field Definitions	15
Table 38	Ay Message Format	16
Table 39	Ay Message Field Definitions	16
Table 40	Az Message Format	16
Table 41	Az Message Field Definitions	16
Table 42	Magnetic Field B(x,y,z) Data Definition	17
Table 43	Bx Message Format	17

Table 44	Bx Message Field Definitions	17
Table 45	By Message Format	18
Table 46	By Message Field Definitions	18
Table 47	Bz Message Format	18
Table 48	Bz Message Field Definitions	18

## 1. Introduction

This document defines the interface for the Magnetic Azimuth Detector (MAD) to systems which require a MAD.

### 1.1. Electrical Interface

#### 1.1.1. Power Interface

The MAD shall operate on both 28 Vdc and 23.5 Vac 400Hz aircraft power in accordance with MIL-STD-704(TBD).

##### 1.1.1.1. Power Consumption

The MAD shall not draw more than 0.5A maximum current on the 23.5 Vac supply. The nominal drawn current shall be 0.25A.

#### 1.1.2. Serial Interface

The MAD shall support both an EIA RS-485 and an EIA RS-422 interface operating in a half duplex configuration. The default mode of operation shall be RS-485 unless the interfacing item commands the MAD otherwise. All interconnecting items which only allow for less than 6 signals from the MAD shall operate in RS-485 mode.

#### 1.1.3. External Connector

The MAD shall have a connector which mates with a MS27505T 11 C35S or its equivalent (typically a MS27467T 11 B35P). A cable adapter shall be defined for each interfacing unit. This cable shall mate with a common connector on the MAD end as shown in Table 1, and shall mate with the existing aircraft connectors on the interfacing unit end. Most of the aircraft connectors are undefined at this time. For the aircraft units which conform with the Magnetic Azimuth Detector specification MIL-D-26503A, the aircraft connector pinout shall be as defined in Table 2.



**Table 1 - MAD Connector Pin Definition**

Pin Number	Signal Name	Notes
1	23.5 Volts 400 Hz	
2	Power Return	
3	(Spare) User Defined	
4	Reserved	Chassis Grounds
5	(Spare) User Defined	
6	Reserved	Shield Command
7	(Spare) User Defined	
8	TX_422 LO	
9	(Spare) User Defined	+28Vdc HI ?
10	(Spare) User Defined	+28Vdc LO ?
11	TX_422 LO	
12	RX_422_TX_RX_485_HI	
13	RX_422_TX_RX_485_LO	

**Table 2 - Adapter Cable Connector Pin Definition for MIL-C-5015, Canon CA3106E-14S-6P**

Pin Number	Signal Name	Notes
A	TX_422_HI	
B	TX_422_LO	
C	422_TX_485_RX_TX	
D	23_5_VAC_HI	:
E	23_5_VAC_LO	
F	422_TX_485_RX_TX	

## 1.2. Serial Interface

### 1.2.1. Protocol

The interface shall be EIA Standard RS-485 or RS-422 operating in a half-duplex configuration. Data can flow in both directions, but only one direction at a time. The RS-485 configuration supports a multi-drop line.

### 1.2.2. Data Rate

The data rate is limited by the baud rate. The data shall be updated at a minimum rate of 3 Hz.

### 1.2.3. Baud Rate

The baud rate shall be 1200 bits/second.

### 1.2.4. Data Format

The format of the serial data shall be as shown in Table 3:

**Table 3 - MAD Data Format**

Parameter	Definition
Start	1 bit
Data	8 bits
Parity	odd
Stop	1 bit

**1.2.5. Order of Transmission**

**Least Significant Byte First**

**Least Significant Bit First**

**1.2.6. Message Length**

**All messages are 5 bytes long.**

**1.2.7. Encoding Format**

**Data to be transmitted shall be encoded into the Non-Return to Zero (NRZ) format.**

**1.2.8. Byte Intervals**

**All communication on the asynchronous link, i.e., each character, uses a start and stop bit for byte framing. Data bytes transmitted as part of a message shall have a maximum byte gap time of 1.67 milliseconds which corresponds to 2 bit times, and a minimum gap time of one baud clock cycle (16 x 1200) or 208.4 microseconds.**

**1.2.9. Data Throughput**

**The serial bus shall support a minimum of 5.0 messages per second including gap time, response time, and data transfer time for 5 byte messages having a 5 byte acknowledgement response. The serial bus shall perform with less than 1.0% message rejection.**

**1.2.10. Electrical Characteristics**

**The electrical characteristics of the peripheral serial bus shall include filtering, termination, and series impedance.**

**1.3. Software Interface**

**1.3.1. Message Definition**

**Information is transferred as a message, where a message is defined as a sequential combination of bytes with a defined format. Messages shall be a fixed length having exactly 5 bytes. A normal communication sequence shall consist of one controller generated command/data message and one terminal generated acknowledgement message, each being 5 bytes in length, and separated by a maximum of 17.5 milliseconds (21 bit times).**

**Message communication is between nodes. One node, called the "controller," initiates activity on the link. The controller initiates message activity with one tributary terminal.**

**Two types of messages are used in the serial bus protocol: Command/Data, and Acknowledgement. Command/Data messages are controller output messages which include both command and data bytes. Acknowledgement messages are terminal output messages which provide positive or negative acknowledgement to the controller, and include the controller requested data.**

### 1.3.1.1. Message structure

All messages passed on the serial bus shall have a two byte header (initiator byte, message byte) as defined in section Message gap times, specified for maximum duration ,shall ensure proper message synchronization between terminals and the controller. The data in the messages are sent in byte form although some of the data consist of 16 bit words. All sixteen bit data consist of one sign bit and 15 data bits. The data shall be sent Least Significant Byte First and Least Significant Bit First. Each message is terminated by a single byte checksum as defined in section

### 1.3.1.2. Message Header Definition

Each message to and from the MAD is initiated by an identifier byte and a message ID byte. The format for each message are defined in Table 4 . Because the MAD operates in a half-duplex configuration, one of the two interfacing items must control communications on the bus. The MAD is the terminal and the interfacing item is the controller, therefore the interfacing item shall control the communications on the bus. An exception exists to this definition when the MAD is in test mode. In test mode, the MAD will periodically send data without the controller initiating the communication. This is described in the initialization section. The identifier byte is considered the first byte of each message. The message field definitions are listed in Table 5. The message identifiers are listed in Table 6.

Table 4 - Message Structure Definition

Byte	Byte Name	Bit 7	Bit 6	Bit 5	Bit 4	Bit 3	Bit 2	Bit 1	Bit 0
1	Identifier	A/N	ID1	ID0	Status	X	X	X	X
2	Message	X	X	M5	M4	M3	M2	M1	M0
3	Data	D7	D6	D5	D4	D3	D2	D1	D0
4	Data	D15	D14	D13	D12	D11	D10	D9	D8
5	Checksum	CS7	CS6	CS5	CS4	CS3	CS2	CS1	CS0

Table 5 - Message Field Definitions

Field	Definition
A/N	Acknowledge/Negative Acknowledge
ID0 - ID1	Receiver Identifier (0, 1 =Reserved, 2 = IRU(Controller), 3 = MAD)
Status	Pass/Fail status of Controller
M0 - M5	Message Code (see Table 6 for codes)
D0 - D15	Data
Checksum	XOR additive checksum of the first four bytes

**Table 6 - Message Byte Definitions**

Message	M5	M4	M3	M2	M1	M0
Initialization	X	X	0	0	0	0
Sin	X	X	0	0	0	1
Cos	X	X	0	0	1	0
Heading	X	X	0	0	1	1
Initiate BIT	X	X	0	1	0	0
Bx - Comp	X	X	0	1	0	1
By - Comp	X	X	0	1	1	0
Bz - Comp	X	X	0	1	1	1
Tiltx	X	X	1	0	0	0
Tilty	X	X	1	0	0	1
Temperature	X	X	1	0	1	0
Ax	X	X	1	0	1	1
Ay	X	X	1	1	0	0
Az	X	X	1	1	0	1
Bx	X	X	1	1	1	0
By	X	X	1	1	1	1
Bz	X	1	0	0	0	0

#### 1.3.1.3. Checksum

Each message is terminated by a 1-byte checksum. The checksum is computed on the data as the XOR additive checksum of the first four bytes of the message. The checksum test passes when the computed checksum equals the checksum byte.

#### 1.3.2. Controller to MAD Communications

When the MAD receives a message from the controller, the MAD shall decipher the ID bits in the Identifier byte to determine whether the message is meant for the MAD. (i.e. if the ID is for another LRU on the RS-485 line, the MAD shall ignore the data). Each message from the controller requires a response from the MAD. If the message is a command message, the MAD will respond with the same message ID verifying that the command was received. If the message is a request for data message, the MAD will respond with the requested data. The message ID for the transmitted data shall be the same as the message ID for the received data.

#### 1.3.3. Error Handling

If the MAD receives an erroneous message, it ignores the message and does not respond. Errors in the messages which would cause the MAD to ignore the data from the controller are listed in Table 7. The MAD does not send the negative acknowledge message. If a valid message is received from the controller but the message ID is undefined, the MAD will not respond to the message.

**Table 7 - Message Error Conditions**

Byte Level Errors:	Framing, Data Noise, Overrun, Parity
Message Level Errors:	Message length, Message checksum, response time

#### 1.3.4. Initialization

Upon power-up, the MAD requires the initialization message within 10 seconds. Initialization sets the protocol and mode of operation of the MAD. The protocol may be set to either RS485 or RS422 and the mode may be set to Test, Normal, BIT, or Start-up. If the MAD does not receive an initialization message within 10 seconds from power-up it will automatically default to test mode where it sends all of the messages at a rate of TBD Hz in an RS-422 configuration.

##### 1.3.4.1. Test Mode

Once the MAD enters test mode, it cannot receive any communications from the controller and must cycle power for a reinitialization. Test mode may also be commanded. In test mode, the MAD reads raw magnetic field data, tilt, and temperature and computes compensated magnetic field data along with magnetic heading. All of these data are formatted into messages and are sent at a periodic rate. The messages are sent sequentially according to their message ID. The MAD may be reinitialized to another mode at any time using the Initialization Message.

##### 1.3.4.2. Normal Mode

If the MAD is initialized into normal mode, the controller must send a message to the MAD every time it wants the MAD to send it a message. In this mode the MAD reads raw magnetic field data, tilt, and temperature and computes compensated magnetic field data along with magnetic heading. All of this data is available to the controller via the messages defined in section . The MAD will respond to all communications from the controller in this mode.

##### 1.3.4.3. BIT Mode

If the MAD is initialized into BIT mode, the MAD performs the built in test functions and provides the results to the controller when complete. When the MAD has completed the tests, it defaults to Normal Mode.

##### 1.3.4.4. Start-up Mode

If the MAD is initialized to Start-up mode, the MAD performs hardware and software initialization as well as built in test functions. This mode is used to attempt to reinitialize the MAD if a failure is detected during BIT. When the MAD has completed start-up, it defaults to Normal Mode.

### 1.4 Message Definitions

#### 1.4.1 Initialization Message

The initialization message contains the data defined in Table 8 and Table 9. The controller shall transmit the initialization message at a rate of 3 Hz until the MAD transmits the response message. The MAD responds with the same data to verify the correct mode was set.

Table 8 - Initialization Message Format

Byte	Byte Name	Bit 7	Bit 6	Bit 5	Bit 4	Bit 3	Bit 2	Bit 1	Bit 0
1	Identifier	A/N	ID1	ID0	Status	X	X	X	X
2	Message	X	M5	M4	M4	M3	M2	M1	M0
3	Data	SERIAL	X	X	X	X	X	MODE	MODE
4	Data	X	X	X	X	X	X	X	X
5	Checksum	CS7	CS6	CS5	CS4	CS3	CS2	CS1	CS0

**Table 9 - Initialization Message Field Definitions**

Field	Definition
A/N	Acknowledge/Negative Acknowledge
ID0 - ID1	Receiver Identifier (0, 1 =Reserved, 2 = IRU(Controller), 3 = MAD)
Status	Pass/Fail status of Controller
Message	\$00
SERIAL	0 = RS422 1 = RS485
MODE	00 = Test Mode 01 = Normal Mode 10 = BIT Mode 11 = Start-up Mode
Checksum	XOR additive checksum of the first four bytes

#### 1.4.2 Initiated BIT Message

The status message contains the results of the built in test as defined in Table 10 , Table 11. If all of the tests pass, the data shall be all zeros. If BIT or Start-up Mode have not been commanded, this message contains the results of the previously stored test results.

**Table 10 - Initiated BIT Response Message Format**

Byte	Byte Name	Bit 7	Bit 6	Bit 5	Bit 4	Bit 3	Bit 2	Bit 1	Bit 0
1	Identifier	A/N	ID1	ID0	Status	X	X	X	X
2	Message	X	X	M5	M4	M3	M2	M1	M0
3	Data	UART	PROC	MAG	TILT	A/D	X	X	X
4	Data	X	X	X	X	X	X	X	X
5	Checksum	CS7	CS6	CS5	CS4	CS3	CS2	CS1	CS0

**Table 11 - Initiated BIT Message Field Definitions**

Field	Definition
A/N	Acknowledge/Negative Acknowledge
ID0 - ID1	Responder Identifier (0, 1 =Reserved, 2 = IRU (Controller), 3 = MAD)
Status	Pass/Fail status of MAD
Message	\$04
UART	1 = UART Failure
PROC	1 = Processor Failure
MAG	1 = Magnetic Sensor Failure
TILT	1 = Tilt sensor Failure
A/D	1 = A/D Failure
Checksum	XOR additive checksum of the first four bytes

#### 1.4.3 Magnetic Field Strength Message Definitions

The MAD measures the local magnetic field strength in three vectors: x, y, and z. The data has the format shown in Table 12.

**Table 12 - Magnetic Field B(x,y,z) Data Definition**

Name	Units	Range	Resolution
BX0 - BX15	Oersted	+/-2	1LSB = $6.0 \times 10^{-5}$
BY0 - BY15	Oersted	+/- 2	1LSB = $6.0 \times 10^{-5}$
BZ0 - BZ15	Oersted	+/-2	1LSB = $6.0 \times 10^{-5}$

#### 1.4.3.1. Bx Comp Message

The Bx Comp Message contains the x axis magnetic field strength, compensated for internal errors but not corrected for attitude errors. See Table 13 and Table 14.

**Table 13 - Bx Comp Message Format**

Byte	Byte Name	Bit 7	Bit 6	Bit 5	Bit 4	Bit 3	Bit 2	Bit 1	Bit 0
1	Identifier	A/N	ID1	ID0	Status	X	X	X	X
2	Message	X	X	M5	M4	M3	M2	M1	M0
3	Data	BXC7	BXC6	BXC5	BXC4	BXC3	BXC2	BXC1	BXC0
4	Data	BXC15	BXC14	BXC13	BXC12	BXC11	BXC10	BXC9	BXC8
5	Checksum	CS7	CS6	CS5	CS4	CS3	CS2	CS1	CS0

**Table 14 - Bx Comp Message Field Definitions**

Field	Definition
A/N	Acknowledge/Negative Acknowledge
ID0 - ID1	Responder Identifier (0 = CI, 1 = FDMU, 2 = IRU, 3 = MAD)
Status	Pass/Fail status of MAD
Message	\$05
BXC0- BXC15	Compensated X-Axis Magnetic Measurement
Checksum	XOR additive checksum of the first four bytes

#### 1.4.3.2 By Comp Message

The By Comp Message contains the y axis magnetic field strength, compensated for internal errors but not corrected for attitude errors. See Table 15 and Table 16.

**Table 15 - By Comp Message Format**

Byte	Byte Name	Bit 7	Bit 6	Bit 5	Bit 4	Bit 3	Bit 2	Bit 1	Bit 0
1	Identifier	A/N	ID1	ID0	Status	X	X	X	X
2	Message	X	X	M5	M4	M3	M2	M1	M0
3	Data	BYC7	BYC6	BYC5	BYC4	BYC3	BYC2	BYC1	BYC0
4	Data	BYC15	BYC14	BYC13	BYC12	BYC11	BYC10	BYC9	BYC8
5	Checksum	CS7	CS6	CS5	CS4	CS3	CS2	CS1	CS0

**Table 16 - By Comp Message Field Definitions**

<b>Field</b>	<b>Definition</b>
A/N	Acknowledge/Negative Acknowledge
ID0 - ID1	Responder Identifier (0 = CI, 1 = FDMU, 2 = IRU, 3 = MAD)
Status	Pass/Fail status of MAD
Message	\$06
BYC0- BYC15	Compensated Y-Axis Magnetic Measurement
Checksum	XOR additive checksum of the first four bytes

#### 1.4.3.3 Bz Comp Message

The Bz Comp Message contains the z axis magnetic field strength, compensated for internal errors but not corrected for attitude errors. See Table 17 and Table 18.

**Table 17 - Bz Comp Message Format**

Byte	Byte Name	Bit 7	Bit 6	Bit 5	Bit 4	Bit 3	Bit 2	Bit 1	Bit 0
1	Identifier	A/N	ID1	ID0	Status	X	X	X	X
2	Message	X	X	M5	M4	M3	M2	M1	M0
3	Data	BZC7	BZC6	BZC5	BZC4	BZC3	BZC2	BZC1	BZC0
4	Data	BZC15	BZC14	BZC13	BZC12	BZC11	BZC10	BZC9	BZC8
5	Checksum	CS7	CS6	CS5	CS4	CS3	CS2	CS1	CS0

:

**Table 18 - Bz Comp Message Field Definitions**

<b>Field</b>	<b>Definition</b>
A/N	Acknowledge/Negative Acknowledge
ID0 - ID1	Responder Identifier (0 = CI, 1 = FDMU, 2 = IRU, 3 = MAD)
Status	Pass/Fail status of MAD
Message	\$07
BZC0- BZC15	Compensated Z-Axis Magnetic Measurement
Checksum	XOR additive checksum of the first four bytes

#### 1.4.4 Tilt Message Definitions

The MAD measures the local attitude in two angles x-axis tilt and y-axis tilt. The data has the format shown in Table 19.

**Table 19 - Tilt T(x,y) Data Definition**

Name	Units	Range	Resolution
TX0 - TX15	Degrees	+/-180	1LSB = $5.5 \times 10^{-3}$
TY0 - TY15	Degrees	+/- 180	1LSB = $5.5 \times 10^{-3}$



#### 1.4.4.1. Tilt X Message

The TiltX message contains the x-axis tilt compensated for internal errors. The message is defined in Table 20 and Table 21.

Table 20 - Tilt X Message Format

Byte	Byte Name	Bit 7	Bit 6	Bit 5	Bit 4	Bit 3	Bit 2	Bit 1	Bit 0
1	Identifier	A/N	ID1	ID0	Status	X	X	X	X
2	Message	X	X	M5	M4	M3	M2	M1	M0
3	Data	TX7	TX6	TX5	TX4	TX3	TX2	TX1	TX0
4	Data	TX15	TX14	TX13	TX12	TX11	TX10	TX9	TX8
5	Checksum	CS7	CS6	CS5	CS4	CS3	CS2	CS1	CS0

Table 21 - Tilt X Message Field Definitions

Field	Definition
A/N	Acknowledge/Negative Acknowledge
ID0 - ID1	Responder Identifier (0 = CI, 1 = FDMU, 2 = IRU, 3 = MAD)
Status	Pass/Fail status of MAD
Message	\$08
TX0- TX15	X-Axis Tilt
Checksum	XOR additive checksum of the first four bytes

#### 1.4.4.2 Tilt Y Message

The TiltY message contains the Y-axis tilt compensated for internal errors. The message is defined in Table 22 and Table 23.

Table 22 - Tilt Y Message Format

Byte	Byte Name	Bit 7	Bit 6	Bit 5	Bit 4	Bit 3	Bit 2	Bit 1	Bit 0
1	Identifier	A/N	ID1	ID0	Status	X	X	X	X
2	Message	X	X	M5	M4	M3	M2	M1	M0
3	Data	TY7	TY6	TY5	TY4	TY3	TY2	TY1	TY0
4	Data	TY15	TY14	TY13	TY12	TY11	TY10	TY9	TY8
5	Checksum	CS7	CS6	CS5	CS4	CS3	CS2	CS1	CS0

Table 23 - Tilt Y Message Field Definitions

Field	Definition
A/N	Acknowledge/Negative Acknowledge
ID0 - ID1	Responder Identifier (0 = CI, 1 = FDMU, 2 = IRU, 3 = MAD)
Status	Pass/Fail status of MAD
Message	\$09
TY0- TY15	Y-Axis Tilt
Checksum	XOR additive checksum of the first four bytes

#### 1.4.5 Temperature Message

The Temperature message contains the ambient box temperature. The temperature data format is defined in Table 24. The message is defined in Table 25 and Table 26.

Table 24 - Temperature Data Definition

Name	Units	Range	Resolution
TP0 - TP15	Degrees C	- 55 to +70	1LSB = TBD

Table 25 - Temperature Message Format

Byte	Byte Name	Bit 7	Bit 6	Bit 5	Bit 4	Bit 3	Bit 2	Bit 1	Bit 0
1	Identifier	A/N	ID1	ID0	Status	X	X	X	X
2	Message	X	X	M5	M4	M3	M2	M1	M0
3	Data	TP7	TP6	TP5	TP4	TP3	TP2	TP1	TP0
4	Data	TP15	TP14	TP13	TP12	TP11	TP10	TP9	TP8
5	Checksum	CS7	CS6	CS5	CS4	CS3	CS2	CS1	CS0

Table 26 - Temperature Message Field Definitions

Field	Definition
A/N	Acknowledge/Negative Acknowledge
ID0 - ID1	Responder Identifier (0 = CI, 1 = FDMU, 2 = IRU, 3 = MAD)
Status	Pass/Fail status of MAD
Message	\$0B
TP0- TP15	Temperature
Checksum	XOR additive checksum of the first four bytes

#### 1.4.6. Heading Message

The Heading message contains the magnetic heading corrected for internal errors and external alignment. The data format is defined in Table 27. The message is defined in Table 28 and Table 29.

Table 27 - Heading Data Definition

Name	Units	Range	Resolution
HD0 - HD15	Degrees	+/- 180	1LSB = $5.5 \times 10^{-3}$

Table 28 - Heading Message Format

Byte	Byte Name	Bit 7	Bit 6	Bit 5	Bit 4	Bit 3	Bit 2	Bit 1	Bit 0
1	Identifier	A/N	ID1	ID0	Status	X	X	X	X
2	Message	X	X	M5	M4	M3	M2	M1	M0
3	Data	HD7	HD6	HD5	HD4	HD3	HD2	HD1	HD0
4	Data	HD15	HD14	HD13	HD12	HD11	HD10	HD9	HD8
5	Checksum	CS7	CS6	CS5	CS4	CS3	CS2	CS1	CS0

**Table 29 - Heading Message Field Definitions**

Field	Definition
A/N	Acknowledge/Negative Acknowledge
ID0 - ID1	Responder Identifier (0 = CI, 1 = FDMU, 2 = IRU, 3 = MAD)
Status	Pass/Fail status of MAD
Message	\$03
HD0- HD15	Heading angle
Checksum	XOR additive checksum of the first four bytes

#### 1.4.7. Sine-Cosine Message

The sine-cosine data is the normalized x and y components of the heading angle. The data is defined in Table 30.

**Table 30 - Sine-Cosine Data Definition**

Name	Units	Range	Resolution
sin0 - sin15	Normalized	+/-1	1LSB = $3.05 \times 10^{-5}$
cos0 - cos15	Normalized	+/-1	1LSB = $3.05 \times 10^{-5}$

#### 1.4.7.1. Sine Message

The Sine message contains the sine of the heading angle compensated for internal errors and attitude. The message is defined in Table 31 and Table 32.

**Table 31 - Sine Message Format**

Byte	Byte Name	Bit 7	Bit 6	Bit 5	Bit 4	Bit 3	Bit 2	Bit 1	Bit 0
1	Identifier	A/N	ID1	ID0	Status	X	X	X	X
2	Message	X	X	M5	M4	M3	M2	M1	M0
3	Data	SIN7	SIN6	SIN5	SIN4	SIN3	SIN2	SIN1	SIN0
4	Data	SIN15	SIN14	SIN13	SIN12	SIN11	SIN10	SIN9	SIN8
5	Checksum	CS7	CS6	CS5	CS4	CS3	CS2	CS1	CS0

**Table 32 - Sine Message Field Definitions**

Field	Definition
A/N	Acknowledge/Negative Acknowledge
ID0 - ID1	Responder Identifier (0 = CI, 1 = FDMU, 2 = IRU, 3 = MAD)
Status	Pass/Fail status of MAD
Message	\$01
SIN0- SIN15	Sine of Heading angle
Checksum	XOR additive checksum of the first four bytes

#### 1.4.7.2 Cosine Message

The Cosine message contains the cosine of the heading angle compensated for internal errors and attitude. The message is defined in Table 33 and Table 34.

Table 33 - Cosine Message Format

Byte	Byte Name	Bit 7	Bit 6	Bit 5	Bit 4	Bit 3	Bit 2	Bit 1	Bit 0
1	Identifier	A/N	ID1	ID0	Status	X	X	X	X
2	Message	X	X	M5	M4	M3	M2	M1	M0
3	Data	COS7	COS6	COS5	COS4	COS3	COS2	COS1	COS0
4	Data	COS15	COS14	COS13	COS12	COS11	COS10	COS9	COS8
5	Checksum	CS7	CS6	CS5	CS4	CS3	CS2	CS1	CS0

Table 34 - Cosine Message Field Definitions

Field	Definition
A/N	Acknowledge/Negative Acknowledge
ID0 - ID1	Responder Identifier (0 = CI, 1 = FDMU, 2 = IRU, 3 = MAD)
Status	Pass/Fail status of MAD
Message	\$02
COS0 - COS15	Cosine of heading angle
Checksum	XOR additive checksum of the first four bytes

#### 1.4.8 Accelerometer Data Messages

The MAD measures the local accelerations in three vectors: x, y, and z. The data has the format shown in Table 35.

Table 35 - Acceleration A(x,y,z) Data Definition

Name	Units	Range	Resolution
AX0 - AX15	g	+/- 1	1LSB = $3.05 \times 10^{-5}$
AY0 - AY15	g	+/- 1	1LSB = $3.05 \times 10^{-5}$
AZ0 - AZ15	g	+/- 1	1LSB = $3.05 \times 10^{-5}$

##### 1.4.8.1. Ax Message

The Ax Message contains the x axis acceleration, compensated for internal errors. See Table 36 and Table 37.

Table 36 - Ax Message Format

Byte	Byte Name	Bit 7	Bit 6	Bit 5	Bit 4	Bit 3	Bit 2	Bit 1	Bit 0
1	Identifier	A/N	ID1	ID0	Status	X	X	X	X
2	Message	X	X	M5	M4	M3	M2	M1	M0
3	Data	AX7	AX6	AX5	AX4	AX3	AX2	AX1	AX0
4	Data	AX15	AX14	AX13	AX12	AX11	AX10	AX9	AX8
5	Checksum	CS7	CS6	CS5	CS4	CS3	CS2	CS1	CS0

**Table 37 - Ax Message Field Definitions**

Field	Definition
A/N	Acknowledge/Negative Acknowledge
ID0 - ID1	Responder Identifier (0 = CI, 1 = FDMU, 2 = IRU, 3 = MAD)
Status	Pass/Fail status of MAD
Message	\$0C
AX0- AX15	X-Axis Accelerometer Measurement
Checksum	XOR additive checksum of the first four bytes

#### 1.4.8.2. Ay Message

The Ay Message contains the y axis acceleration, compensated for internal errors. See Table 38 and Table 39.

**Table 38 - Ay Message Format**

Byte	Byte Name	Bit 7	Bit 6	Bit 5	Bit 4	Bit 3	Bit 2	Bit 1	Bit 0
1	Identifier	A/N	ID1	ID0	Status	X	X	X	X
2	Message	X	X	M5	M4	M3	M2	M1	M0
3	Data	AY7	AY6	AY5	AY4	AY3	AY2	AY1	AY0
4	Data	AY15	AY14	AY13	AY12	AY11	AY10	AY9	AY8
5	Checksum	CS7	CS6	CS5	CS4	CS3	CS2	CS1	CS0

**Table 39 - Ay Message Field Definitions**

Field	Definition
A/N	Acknowledge/Negative Acknowledge
ID0 - ID1	Responder Identifier (0 = CI, 1 = FDMU, 2 = IRU, 3 = MAD)
Status	Pass/Fail status of MAD
Message	\$0D
AY0- AY15	Y-Axis Acceleration Measurement
Checksum	XOR additive checksum of the first four bytes

#### 1.4.8.3. Az Message

The Az Message contains the z axis acceleration, compensated for internal errors. See Table 40 and Table 41.

**Table 40 - Az Message Format**

Byte	Byte Name	Bit 7	Bit 6	Bit 5	Bit 4	Bit 3	Bit 2	Bit 1	Bit 0
1	Identifier	A/N	ID1	ID0	Status	X	X	X	X
2	Message	X	X	M5	M4	M3	M2	M1	M0
3	Data	AZ7	AZ6	AZ5	AZ4	AZ3	AZ2	AZ1	AZ0
4	Data	AZ15	AZ14	AZ13	AZ12	AZ11	AZ10	AZ9	AZ8
5	Checksum	CS7	CS6	CS5	CS4	CS3	CS2	CS1	CS0

**Table 41 - Az Message Field Definitions**

Field	Definition
A/N	Acknowledge/Negative Acknowledge
ID0 - ID1	Responder Identifier (0 = CI, 1 = FDMU, 2 = IRU, 3 = MAD)
Status	Pass/Fail status of MAD
Message	\$0E
AZ0- AZ15	Z-Axis Acceleration Measurement
Checksum	XOR additive checksum of the first four bytes

#### 1.4.9. Raw Magnetic Field Strength Message Definitions

The MAD measures the local magnetic field strength in three vectors: x, y, and z. The data has the format shown in Table 42.

**Table 42 - Magnetic Field B(x,y,z) Data Definition**

Name	Units	Range	Resolution
BX0 - BX15	Oersted	+/-2	1LSB = $6.0 \times 10^{-5}$
BY0 - BY15	Oersted	+/- 2	1LSB = $6.0 \times 10^{-5}$
BZ0 - BZ15	Oersted	+/-2	1LSB = $6.0 \times 10^{-5}$

#### 1.4.9.1 Bx Message

The Bx Message contains the raw (uncompensated) x axis magnetic field strength. See Table 43 and Table 44.

**Table 43 - Bx Message Format**

Byte	Byte Name	Bit 7	Bit 6	Bit 5	Bit 4	Bit 3	Bit 2	Bit 1	Bit 0
1	Identifier	A/N	ID1	ID0	Status	X	X	X	X
2	Message	X	X	M5	M4	M3	M2	M1	M0
3	Data	BX7	BX6	BX5	BX4	BX3	BX2	BX1	BX0
4	Data	BX15	BX14	BX13	BX12	BX11	BX10	BX9	BX8
5	Checksum	CS7	CS6	CS5	CS4	CS3	CS2	CS1	CS0

**Table 44 - Bx Message Field Definitions**

Field	Definition
A/N	Acknowledge/Negative Acknowledge
ID0 - ID1	Responder Identifier (0 = CI, 1 = FDMU, 2 = IRU, 3 = MAD)
Status	Pass/Fail status of MAD
Message	\$0E
BX0- BX15	X-Axis Magnetic Field Measurement
Checksum	XOR additive checksum of the first four bytes

#### 1.4.9.2 By Message

The By Message contains the raw (uncompensated) y axis magnetic field strength. See Table 45 and Table 46.

Table 45 - By Message Format

Byte	Byte Name	Bit 7	Bit 6	Bit 5	Bit 4	Bit 3	Bit 2	Bit 1	Bit 0
1	Identifier	A/N	ID1	ID0	Status	X	X	X	X
2	Message	X	X	M5	M4	M3	M2	M1	M0
3	Data	BY7	BY6	BY5	BY4	BY3	BY2	BY1	BY0
4	Data	BY15	BY14	BY13	BY12	BY11	BY10	BY9	BY8
5	Checksum	CS7	CS6	CS5	CS4	CS3	CS2	CS1	CS0

Table 46 - By Message Field Definitions

Field	Definition
A/N	Acknowledge/Negative Acknowledge
ID0 - ID1	Responder Identifier (0 = CI, 1 = FDMU, 2 = IRU, 3 = MAD)
Status	Pass/Fail status of MAD
Message	\$0F
BY0- BY15	Y-Axis Magnetic Field Measurement
Checksum	XOR additive checksum of the first four bytes

#### 1.4.9.3 Bz Message

The Bz Message contains the raw (uncompensated) z axis magnetic field strength. See Table 47 and Table 48.

Table 47 - Bz Message Format

Byte	Byte Name	Bit 7	Bit 6	Bit 5	Bit 4	Bit 3	Bit 2	Bit 1	Bit 0
1	Identifier	A/N	ID1	ID0	Status	X	X	X	X
2	Message	X	X	M5	M4	M3	M2	M1	M0
3	Data	BZ7	BZ6	BZ5	BZ4	BZ3	BZ2	BZ1	BZ0
4	Data	BZ15	BZ14	BZ13	BZ12	BZ11	BZ10	BZ9	BZ8
5	Checksum	CS7	CS6	CS5	CS4	CS3	CS2	CS1	CS0

Table 48 - Bz Message Field Definitions

Field	Definition
A/N	Acknowledge/Negative Acknowledge
ID0 - ID1	Responder Identifier (0 = CI, 1 = FDMU, 2 = IRU, 3 = MAD)
Status	Pass/Fail status of MAD
Message	\$10
BZ0- BZ15	Z-Axis Magnetic Field Measurement
Checksum	XOR additive checksum of the first four bytes

**SESSION IX-A**  
**NAVIGATION SYSTEMS**

***CHAIRMAN***  
**ROBERT McADORY**  
***DAYTON OH***



**THIS PAGE LEFT BLANK INTENTIONALLY**

# **B-1B GSS Replacement Program**

**Michael A. Friday  
Avionics Reliability Center  
Oklahoma City Air Logistics Center**

**Charles T. Bye and Daniel J. Murphy  
Honeywell Inc.  
Military Avionics Division  
St. Louis Park, Minnesota**

**Approved for public release; distribution unlimited.**

## **ABSTRACT**

The Gyro Stabilization Subsystem (GSS) is the attitude heading reference systems (AHRS) for the B-1B aircraft. It provides the aircraft's instruments and navigation complex with heading, pitch, roll, and angular rate information. The B-1B GSS was designed in the 1970's with Transistor-Transistor Logic (TTL) technology, which has become difficult to support due to component obsolescence. OCALC/LII, the commodity managers, initiated a program to study approaches for a GSS Replacement Program. The objectives of this program were to increase supportability, reliability, and performance without impacting the aircraft. A design based upon Honeywell's Integrated Flight Management Unit (IFMU) was selected to achieve the objectives of the GSS Replacement Program. This approach features state-of-the-art electronics, small ring laser gyroscopes, and Ada® software. Additionally, a permalloy-based magnetometer is being evaluated to improve the performance and reliability of the magnetic azimuth detector.

This paper provides an overview of problems with the existing GSS, a description of the new approach for the Electronic Control Amplifier and the Gyroscope Reference Unit, a summary of the advantages of the new approach, a GSS Replacement Program status update, and a review of recent test results.

## **INTRODUCTION**

The B-1B GSS (Figure 1) consists of four line replaceable units (LRUs), including a Compass Control Unit (CCU), an Electronic Control Amplifier (ECA), a Gyroscope Reference Unit (GRU), and a Magnetic Azimuth Detector (MAD). The primary function of the B-1B GSS is to provide heading, pitch, and roll information to cockpit instruments and navigation subsystems.

Parts obsolescence and performance problems drove the Gyro Stabilization System Replacement. The Air Force approach took advantage of an off-the-shelf product to reduce development cost. Since only 97 B-1B aircraft exist, a development program would have been difficult to amortize over this small population quantity. A common or standard solution was considered, but was determined to be unfeasible due to unique characteristic of the B-1B.

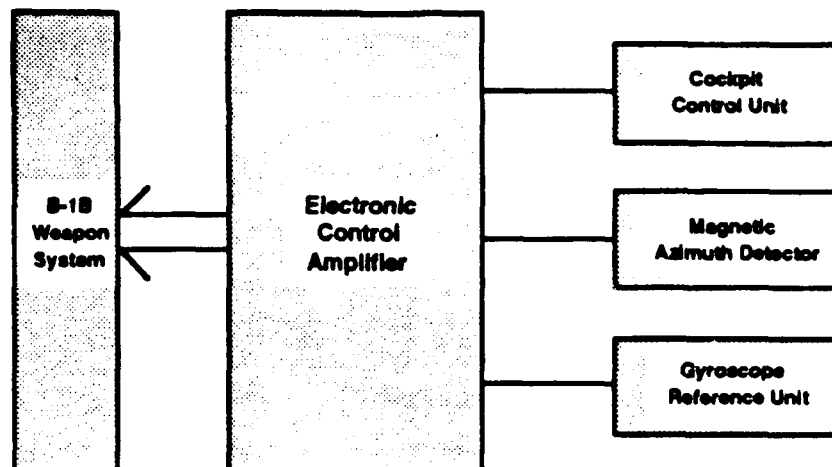


**Figure 1. B-1B Gyro Stabilization Subsystem Block Diagram**

Several contractors approaches were evaluated. Honeywell was selected for reduced program risk, cost savings, and the Integrated Flight Management Unit (IFMU) program<sup>1</sup>. Program risk was our major concern since the government's design documentation had several gaps. The Minneapolis GSS Replacement team included members from the original GSS development program. This insured continuity that all the requirements for the GSS would be implemented. Honeywell had invested in the development of the IFMU program which combines navigation, flight control, mission computer, and air data modules in a mix or match system. This off-the-shelf product was ideal for our GSS Replacement and represented significant cost savings.

The GSS ECA is the processing and signal distribution portion of the AHRS. The current ECA contained 1970s TTL logic with obsolete bit slice processors, memory chips, and system electronics. A known software deficiency existed but insufficient memory within the current design prevented correction. Due to the system age and technology, the ECA exhibited a reliability of 415 hours Mean-Time-Between-Depot Demand (MTBD). The replacement program solves these ECA problems by a repackaging of IFMU core modules (Figure 2).

The GRU is a typical two gyro gimbaled platform that has a MTBD of only 256 hours. Typical failure modes are bearing wear out. The GRU MTBD is the driving factor for the entire system in terms of reliability. This project solves the problems identified above by a repackaging of Honeywell's HG1500AC01 IMU.

The Magnetic Azimuth Detector (MAD) was also addressed. The MAD is the azimuth or north reference for the AHRS system. Unlike an inertial navigation system that gyro compasses, an AHRS requires an external reference. The MAD is a driver in reliability at 1984 hours MTBD. Honeywell System Research Center (SRC) has been working on a silicone wafer magnetometer sensor (permalloy) technology which looks promising. This silicone sensor is the basis for a solid state MAD built as part of the project.

The remaining LRU is the Compass Control Unit (CCU). This is a passive device and does not offer opportunity for significant benefit from improvement. Therefore, no action was taken on this assembly.

The ground rule for this program was a form-fit-functional replacement for the current system with no system impact on the B-1B aircraft. This meant the GSS replacement must interface using the existing aircraft wiring, utilize the 230 VAC power source, interface with the B-1B computer complex, and perform navigation functions equivalent to current GSS specifications.

Testing was accomplished at Honeywell's Minneapolis and Albuquerque facilities and at Air Force facilities. The results exceeded specifications in all areas. Testing validated that the GSS Replacement concept as defined was feasible.

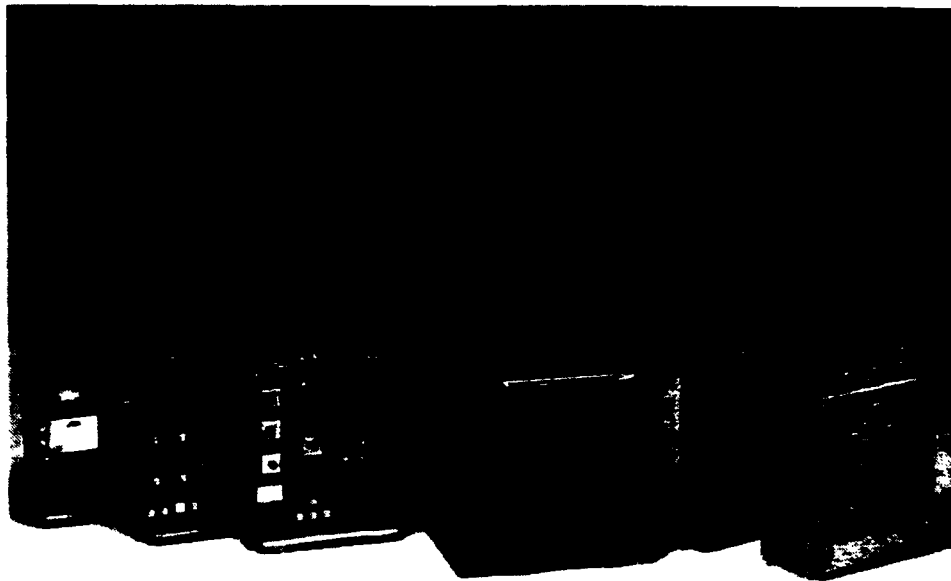


**Figure 2. BG1232 Integrated Flight Management Unit**

### **SYSTEM DESCRIPTION**

The objective of the GSS Replacement program was to improve reliability, maintainability, performance, and supportability without affecting B-1B aircraft interfaces. This pilot program addressed the ECA (limited), GRU, and MAD. The ECA is the interface with the B-1B weapon systems, taking angular data from the GRU, magnetic heading from the MAD, and mode commands from the CCU. The ECA compensates the MAD signal for appropriate one cycle, two cycle, and index errors. The ECA outputs the digital and analog information to flight instruments, flight control systems, Central Integrated Test System (CITS), and navigation complex.

An existing ECA was modified to remove the current processor and memory modules (Figure 3). These cards caused the Air Force the most concern. Features inherent to the IFMU architecture resulted in the MIL-STD-1553 and air data interface card also to be consolidated. A custom interface card was built to interface new electronics and the remaining cards.

The modified ECA's main processor uses an Intel 80960MC™ operating at 7.5 MHz with 20 MHz burst rates. The ECA's Operational Flight Program (OFP) is written in standard Ada. The main processor board also contains RS-422 interfaces to communicate with the PMAD, GRU, and test port. All the systems outputs are available on the test port connector making OFP changes or ECA testing simple. The module contains 1 MByte of EEPROM program memory. In addition, 0.5 MByte of static RAM and 2.0 KByte of non-volatile RAM are provided on the module. Memory limitations in the existing GSS impeded effectiveness of the B-1B weapon system. The increased memory provided by the system processor/interface module allowed correction of the known deficiencies in the GSS software which improves the B-1B weapon system performance.

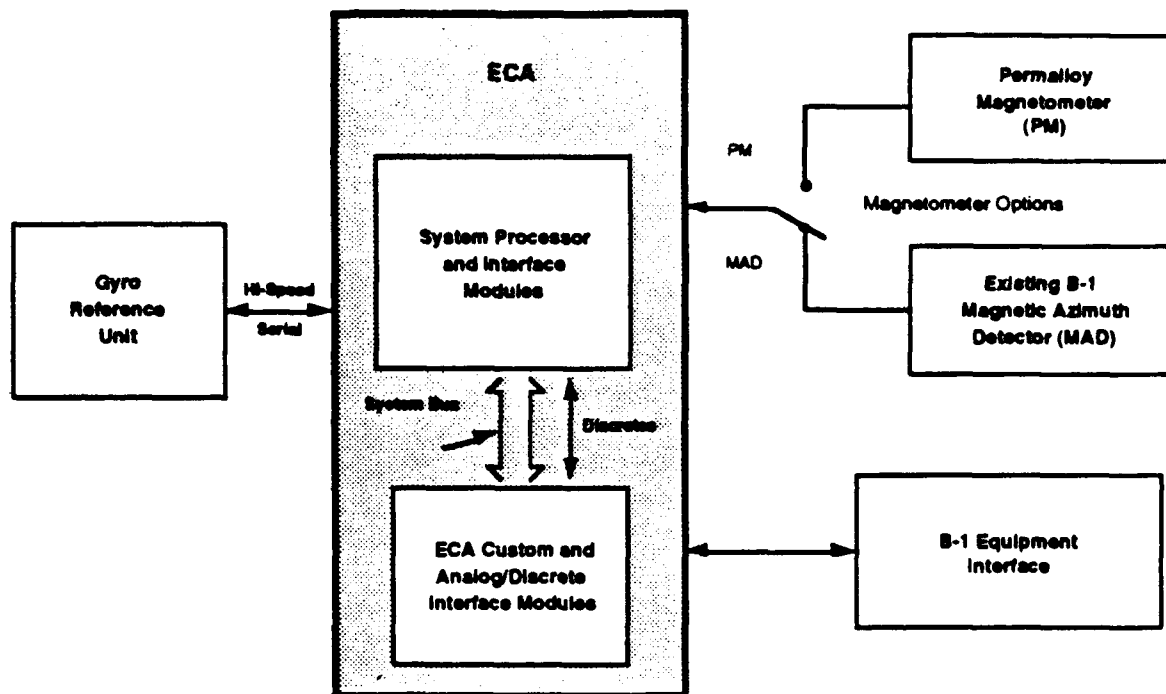


**Figure 3. Upgraded B-1 Gyro Stabilization System**

The IFMU system software architecture (Figure 4) provided unique advantages that provided benefits for the GSS Replacement Program. The system is designed so that it can be tailored by the user to meet application requirements. The system software is based upon a Honeywell software architecture called the Embedded Computer Toolbox and Operating System (ECTOS™). All system software is embedded in the system processor/interface module. ECTOS provides multirate tasking, an interface to control the mode of operation of the navigation/Kalman filter, and interface drivers. Application code is then written to perform the functions required by the B-1B GSS system specification. The application code calls the ECTOS function to perform its tasks. The application code is approximately 10% of the total OFP. Modes used for the GSS Replacement program are as follows:

- Standby
- Attitude Heading Reference System.

Other modes available in ECTOS that can be used by the production GSS are:

- INS-Aided Navigation
- GPS-Aided Navigation
- Gyro Compass Alignment.

All of the software used on the project was programmed in Ada and was easily adapted for use on this project.

The prototype ECA was designed to interface with either the existing MAD or the digital AMAD. At production, a decision will be made whether to maintain both MAD interfaces based upon the maturity of the AMAD development at that time.

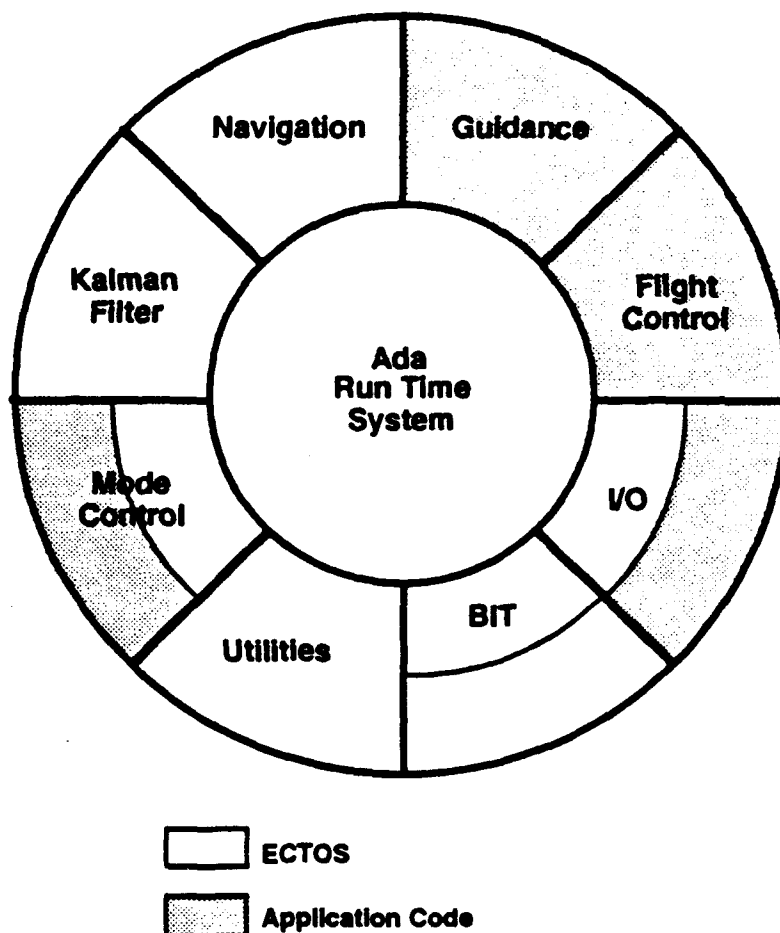


**Figure 4. IFMU Modular System Software**

HG1500AC01<sup>2</sup> GRU contains three Honeywell low cost miniature GG1308 ring laser gyros (RLG), three Sunstrand Data Control RBA-500 accelerometers, and all the support electronics required for gyro control, accelerometer control, compensation algorithms, and ECA interface. The GG1308's are specified to be at least 1.0 deg/hr. The RBA-500's are digital pulsed output of 1

milligrams accuracy. The GRU outputs compensated delta velocities and delta angles over a RS-422 Synchronous Data Link Control (SDLC) interface. One of the concerns was whether a high speed digital signal would communicate over the existing aircraft's wiring. During aircraft testing at Grand Forks this did not pose a problem. This GRU requires only 21 watts at  $\pm 15\text{Vdc}$  and 5 Vdc provided by the ECA.

In addition to design of ECA and GRU, the GSS Replacement program evaluated an Advanced Magnetic Azimuth Detector (AMAD) concept<sup>3</sup>. Honeywell provided a brassboard Permalloy MAD as part of this concept task. The PMAD is meant to be a direct replacement for the DT-309 MAD with the exception of a digital interface. The PMAD contains: a permalloy three-axis magnetometer, a two-axis tilt sensor, and processor and control electronics. The PMAD operates on 26 VAC and communicates via RS-422 UART digital interface. With the processing capability of this new sensor, characterization and modeling should provide more consistent magnetic headings. This will be even more apparent in the GSS compass mode of operation which typically provide poor heading information.

### RECENT TEST RESULTS

The brassboard GSS replacement (Figure 5) was tested by the Avionics Reliability Center (ARC) during the summer of 1992. The ARC is the Commodities Manager's test facility at Tinker AFB for inertial and flight control systems. The test ensured that the replacement system met the static performance and interchangeability requirements with the existing system. Static testing included attitude and heading accuracy including free gyro drift performance. The gyro drift tests were consistently well under 0.5 degrees per hour. Errors associated with attitude accuracy test were nil.

After the successful laboratory demonstration, it was determined that on-aircraft testing would be appropriate. Scheduling posed the biggest challenge for this task, but in May of 1993 the replacement prototype was taken to Grand Forks AFB ND. Aircraft integration tests were performed for two days. The B-1B is highly integrated and all subsystems are continuously monitored by the CITS for valid operation. A soft bit error caused several status bits to be annunciated. An OFP change easily corrected the BIT error. All heading and attitude information was correctly displayed on appropriate displays.

A taxi test was then accomplished on the ramp area at Grand Forks. Since this was not a planned activity, only 45 minutes of operation was permitted. With the reduced drift of the new GRU, the variability in the latitude pots in the CCU reference voltage was noticed. Under laboratory conditions this can be set exactly by monitoring test ports of the ECA. Once in the aircraft, actual system performance revealed this situation. Several solutions to improve the accuracy of the latitude pots are being studied.

Recent test results validated that the system achieved the goals established at the beginning of the program (See Table 1). Flight demonstration is anticipated in the fall of 1993. The Central Inertial Guidance Test Facility (CIGTIF) organization at Holloman AFB NM is scheduling support for this activity.

:

## SUMMARY AND CONCLUSIONS

The problem of parts obsolescence is not unique to this program but rather a DOD-wide issue. In order to support the B-1B into the next decade, a replacement GSS is the only viable solution. Planning and budgetary processes are underway at OCALC to obtain the required funding.

Our approach of utilizing off-the-shelf designs to reduce program cost, leadtimes, and produce a good return on the life cycle cost are likely to be the programs to be funded. Beside the parts obsolescence issues, this initiative reduces depot support requirements, reduces on-aircraft maintenance and calibration, and increase reliability and system performance.

This initiative projects a side benefit of a 27.2 times improvement in system reliability (MTBD from 147 to 4000). Between repair cost and associated field man-hours for remove/replace, an estimated payback for a GSS replacement program is less than 8 years. When other indirect costs are considered, this payback schedule is even further reduced.

Operational units will realize a system that exceeds current specifications and is likely to exhibit a system failure on the average of once every 8 years. Support equipment for compass swings will also be eliminated since this operation can be performed continuously as a background task.

We are pleased with the results of the GSS replacement program to date. All projects goals were exceeded in each area. This phase was never meant to provide a production design, but rather demonstrate an approach. There are various options available to the Air Force for the production design. Future funding will determine the extent of possible performance enhancements.

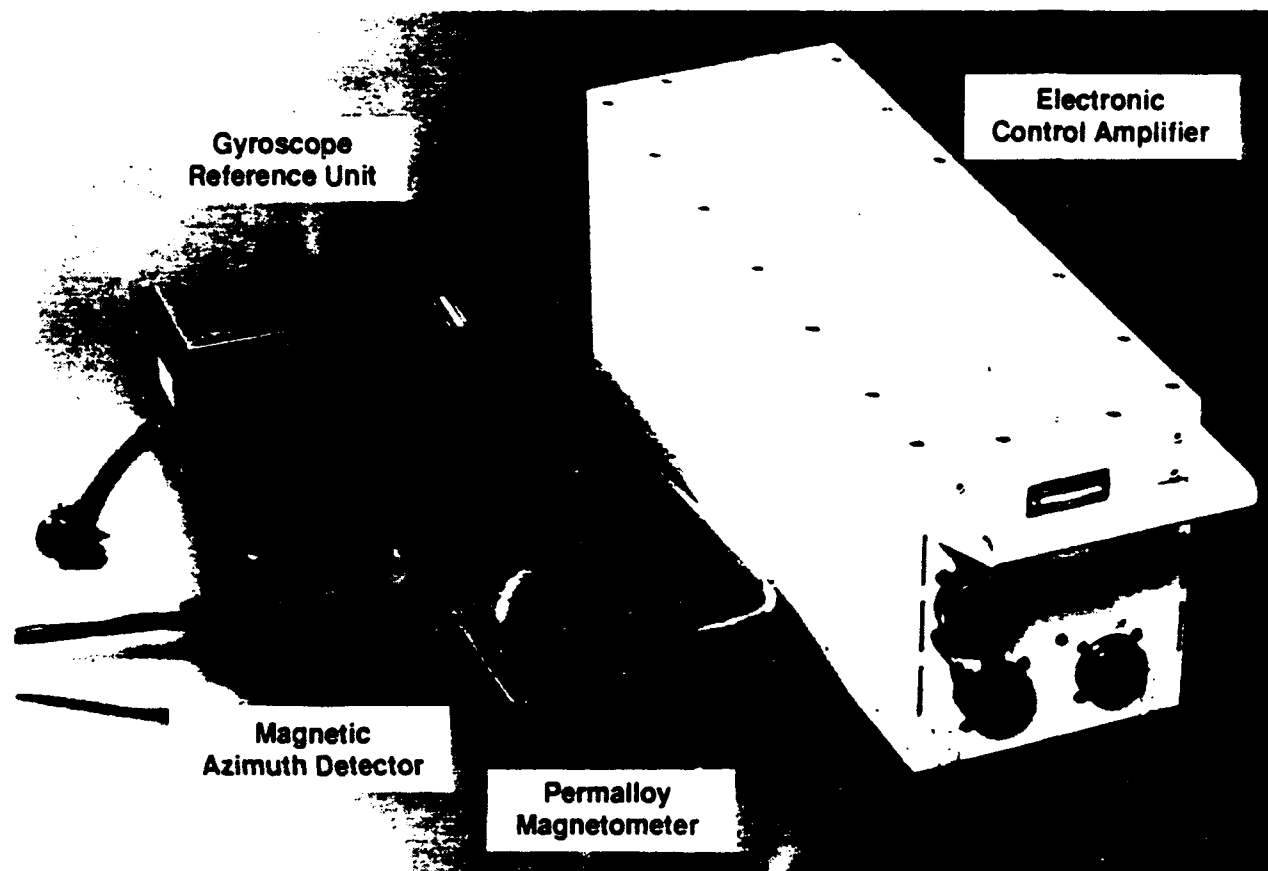


**Figure 5. Brassboard Prototype Replacement System**



**Table 1. Performance Comparison**

<b>Parameter</b>	<b>Requirement</b>	<b>RLG GSS Goals</b>
<b>Angular Rate</b> Pitch Roll Yaw	69 deg/sec 287 deg/sec 201 deg/sec	470 deg/sec 470 deg/sec 470 deg/sec
<b>Angular Acceleration</b> Pitch Roll Yaw	210 deg/sec/sec 1032 deg/sec/sec 201 deg/sec/sec	1500 deg/sec/sec 1500 deg/sec/sec 1500 deg/sec/sec
<b>Heading Requirements</b> Stored Heading (static) Slaved Mode (static) Compass Mode (static) Slaved Mode (dynamic) Gyro Drift	0.1 deg of stored value in 35 sec 0.5 deg of MAD within 1 min 0.5 deg of MAD within 1 min 1.5 deg of MAD 1 deg/hour (no aiding)	0.1 deg of stored value in 10 sec 0.5 deg of MAD within 10 sec 0.5 deg of MAD within 10 sec 1.5 deg of MAD 1 deg/hour
<b>Vertical Accuracy</b> Static Static Dynamic	1 deg within 35 sec 0.25 deg within 3 min 1 deg	1 deg within 10 sec 0.25 deg within 20 sec 1 deg

### REFERENCES

1. **Honeywell Inc.** 1992. *Integrated Flight Management Unit User's Manual*. Honeywell Inc., Minneapolis MN.
2. **M.G. Secord, J.G. Messier, L.O. Theilman.** 1991. Honeywell's GG1308 Ring Laser Gyro Inertial Measurement Systems - Test Results. *Proceedings, CIGTIF's Fifteenth Biennial Guidance Test Symposium*. 46th Test Group/GD, Holloman AFB, NM.
3. **M.A. Friday, J.N. Hericks, G.F. Rouse, H. Jewett.** 1993. Advanced Magnetic Azimuth Detector (AMAD) Development. *Proceedings, CIGTIF's Sixteenth Biennial Guidance Test Symposium*. 46th Test Group/GD, Holloman AFB, NM.

## **AUTHOR BIOGRAPHIES**

### **Michael A. Friday**

Mr. Friday is a Navigation System Engineer for the Air Force Material Command at Oklahoma City, OK.

Mr. Friday received his BS in Electrical Engineering from the University of Miami in 1979.

Mr. Friday has been employed with the United States Air Force, Tinker AFB Oklahoma since 1984. He is technically responsible for Compasses, Attitude Heading Reference Systems, Magnetic Azimuth Detectors, and Compass Calibrator Systems. Engineering developments under his direction include: the MC-2000 Compass Calibrator, Universal Compass Amplifier Replacement, B-1B Gyro Stabilization System Replacement, Magnetic Azimuth Detector Support Facility Modernization, Advanced Magnetic Azimuth Detector, and Avionics reliability Center.

### **Charles T. Bye**

Mr. Bye is a Senior Staff Engineer for Honeywell Inc. Military Avionics Division in St. Louis Park, MN.

Mr. Bye received his MS in Electrical Engineering from the University of Colorado, Boulder, CO in 1984.

Mr. Bye is a systems engineer with expertise in developing modular hardware and software systems. He is the technical director for the Integrated Flight Management Unit development effort at Honeywell. He is technically responsible for the B-1B Gyro Stabilization System Replacement program.

### **Daniel J. Murphy**

Mr. Murphy is a Principal Marketing Representative for Honeywell Inc. Military Avionics Division in St. Louis Park, MN.

Mr. Murphy received his BS in Natural Science from St. John's University in Collegeville, MN in 1980.

With Honeywell since 1980, Mr. Murphy started his career as a production coordinator for inertial components used on the Trident Missile, F-14 Fighter, and M-60 Tank. His career progressed through positions in Contracts Management and Marketing until he reached his current position. Mr. Murphy is responsible for marketing the Integrated Flight Management Unit for applications on fixed wing aircraft, missiles, and precision guided munitions.

**THIS PAGE LEFT BLANK INTENTIONALLY**

# **CIGTF VERIFICATION TESTING OF THE SNU 84-1/E**

## **THE USAF ENHANCED ACCURACY STANDARD NAVIGATION UNIT**

**June 1993**

by

**Mark Petersen  
F<sup>3</sup> Enhanced Systems Engineer  
Honeywell Military Avionics  
St. Petersburg, Florida**

**B. T. Stiles  
Technical Director  
F<sup>3</sup> Enhanced INU  
Honeywell Military Avionics  
St. Petersburg, Florida**

**Larry Boykin  
Program Test Manager  
CIGTF Guidance Test Division  
Holloman AFB, New Mexico**

## **TITLE**

**CIGTF VERIFICATION TESTING OF THE SNU 84-1/E. THE USAF ENHANCED ACCURACY STANDARD NAVIGATION UNIT.**

## **ABSTRACT**

The USAF SNU 84-1/E Enhanced Accuracy Inertial Navigation Unit represents a significant step in the evolution of ring laser gyro (RLG) based precision navigation. The Enhanced INU, developed from refinements to a continually improving product line, employs the same hardware configuration as the Honeywell H-423 SNU 84-1 Standard Navigation Unit currently in production. The SNU 84-1/E performance level is achieved through specific enhancements to the INU flight software and system level calibration process. In addition to improved free inertial navigation performance, the Enhanced INU is fully integrated with the Rockwell-Collins Miniaturized Airborne GPS Receiver (MAGR).

Under the current F-117A avionics upgrade program, the SNU 84-1/E will replace the Standard Precision Navigator (SPN GEANS) as the primary navigation system. The Enhanced INU will provide RLG based fast reaction, improved reliability, and autonomous high accuracy navigation performance.

## **INTRODUCTION**

This paper covers the Enhanced INU system requirements, system description and the performance results achieved during the SNU 84-1/E Verification Test Series recently conducted at the Central Inertial Guidance Test Facility (CIGTF). Testing of the Enhanced INU was completed in March of 1993, totaling over five months of detailed laboratory and flight tests. With the support of a dedicated test management/test team initiative, all project requirements were satisfied on schedule. In terms of system performance, the Enhanced INU surpassed all specified requirements, most noteworthy being free inertial flight performance in the 0.1 NMPH CEP class.

## **ENHANCED INU SYSTEM REQUIREMENTS**

### **Free Inertial Performance**

Over the last ten years, the RLG based H-423 INU has matured sufficiently such that the system performance capabilities are significantly better than the 0.8 NMPH medium accuracy requirement. Therefore, the Enhanced INU system is based on the H-423 SNU 84-1 system configuration, with flight software and system level calibration enhancements being the only modifications. Table 1 is a comparison of the key SNU 84-1 and SNU 84-1/E free inertial performance requirements.

**Table 1 Free Inertial Performance Requirements**

REQUIREMENTS	SNU 84-1		SNU 84-1/E	
	GC	EIA	GC	EIA
Align time (Minimum)	8 min.	8/4 min.	9 min.	9/6 min.
Position Accuracy (NMPH CEP) CEP = 50% Circular Error Probable	0.8 <sup>1</sup>	0.5 <sup>1</sup>	0.3 <sup>2</sup> 0.6 <sup>3</sup>	0.22 <sup>2</sup> 0.44 <sup>3</sup>
Velocity Accuracy (FPS RMS) X and Y Velocity	2.5	2.0	1.5	1.5
Static Attitude (Roll,Pitch,Azimuth) Digital (DEG RMS)	0.05	0.05	0.033	0.033
True Heading (DEG RMS)	0.10	0.10	0.05	0.05
EIA - Initial GC alignment, taxi to new heading >70 degree delta, perform secondary alignment.				

- 1 Specified for flight times up to one hour.
- 2 Specified for flight times from two to six hours.
- 3 Specified at one hour.

As this table shows, the Gyro Compass (GC) and Enhanced Interrupted Alignment (EIA) navigation performance requirements for the Enhanced INU represent a two and one half times improvement over that of the SNU 84-1 system. As such, the SNU 84-1/E free inertial performance specification is more closely aligned to that of the SNU 84-3 Standard Precision Accuracy INU, somewhat remarkable when the much shorter alignment times of the Enhanced INU are considered.

### **MAGR GPS Aided Performance**

In addition to the increased free inertial performance requirements, the Enhanced INU is also fully integrated with the Rockwell-Collins MAGR (ICD-GPS-059). Honeywell was given the responsibility of performing the Enhanced INU/MAGR integration, which has subsequently undergone successful laboratory and dynamic testing at both Naval Research and Development (NRAD) and CIGTF.

The INU Kalman filter is required to accept and process GPS position and velocity updates, for both aided navigation performance and In-Flight-Alignment, when valid GPS data is available, (as determined by the GPS). The Enhanced INU/MAGR integration affords further improved free inertial navigation performance, through the trimming of error states by the INU Kalman filter, during periods of GPS aided navigation. Due to the dependency on the GPS supplied position and velocity updates, the SNU 84-1/E INU specification currently does not stipulate a GPS aided or post aiding performance requirement.

## **ENHANCED INU SYSTEM DESCRIPTION**

To achieve the required degree of precision in free inertial performance, the Enhanced INU uses four key means of improvement, (1) a precise system level calibration process developed to achieve the requirements of the Enhanced INU system error budget, (2) optimized Kalman filter sensor error estimation in the GC, EIA and the Navigation Alignment Refinement Function (NARF) modes, (3) more precise dynamic error compensation and (4) the capability to compensate for local gravity deflections.

### **(1) System Level Calibration**

As part of the Enhanced INU development process, a system level error budget was established through the use of suboptimal covariance performance analysis. This analysis provides a statistical estimation of navigation performance based on modeled inertial error sources processed through various flight trajectory profiles. The SNU 84-1/E error budget, shown in Table 2, is based on the requirements for precision navigation and Honeywell's assessment of performance capabilities demonstrated at the component and system level. Gyro performance is a critical element in achieving the navigation accuracy required for the SNU 84-1/E system. In the covariance performance analysis, the RLG performance criteria is baselined to the average Honeywell GG1342 Military Grade RLG performance. The gyro and accel bias error terms were modeled as a fixed bias plus a Gauss-Markov bias with a two hour time constant. With the exception of the gyro random walk and accel random noise errors, all remaining error sources were modeled as random constants.

**Table 2 SNU 84-1/E Error Budget**

Sensor Parameters	Units	One Sigma Values
<b>Gyro</b>		
Random walk (level axis)	deg/root hour	0.0006
Random walk (vertical axis)	deg/root hour	0.0013
Bias (level axis)	deg/hour	0.0025
Bias (vertical axis)	deg/hour	0.0025
Temperature Transient Bias	deg/hour (two hour time constant)	0.001
Scale Factor	ppm	2.0
Nonorthogonality	$\mu$ radians	3.75
Triad Misalignment	$\mu$ radians	3.75
<b>Accelerometer</b>		
Bias (level axis)	$\mu$ g's	15.0
Bias (vertical axis)	$\mu$ g's	30.0
Temperature Transient Bias	$\mu$ g's (two hour time constant)	10.0
Scale Factor	ppm	100
Nonorthogonality	$\mu$ radians	10.0
Scale Factor Asymmetry	ppm	20.0
Random Error	ft/sec (1 sigma at one hour)	0.0025

As compared to the medium accuracy INU error budget, the Enhanced INU error budget requires an approximate two-fold increase in measurement/calibration accuracy. To achieve this level of precision, the following refinements were implemented to the automated calibration process.

- (a) To provide increased error measurement accuracy, test equipment modifications were made to allow external/interactive control of the Enhanced INU Kalman filter and internal calibration software during specific production calibration tests.
- (b) The accuracy in the measurement and correction of system level calibration parameters was improved through the development of a new rotational "tumble" test sequence. The rotational maneuvers, (used to excite and decouple bias, scale factor and misalignment errors), were restructured and an additional six maneuvers were developed. The revised test sequence provides an overall factor of two improvement in parameter measurement accuracy as well as redundancy in all measurements within each test sequence.
- (c) Previously, INU system level calibration utilized gyro sensor level temperature bias compensation only. In the enhanced calibration process, system level gyro bias measurements are made over the full military temperature range and compensated by means of a second order least squares fit.

The following figures represent approximately 250 system level gyro bias residual measurements collected on five separate systems in the enhanced calibration process. Figure 1 compares the bias performance over temperature to the 0.0025 degree/hour one sigma bias requirement. Figure 2 is a histogram of the bias performance along with the error budget and measured data distribution curves.

**Figure 1 Gyro Bias Residuals**

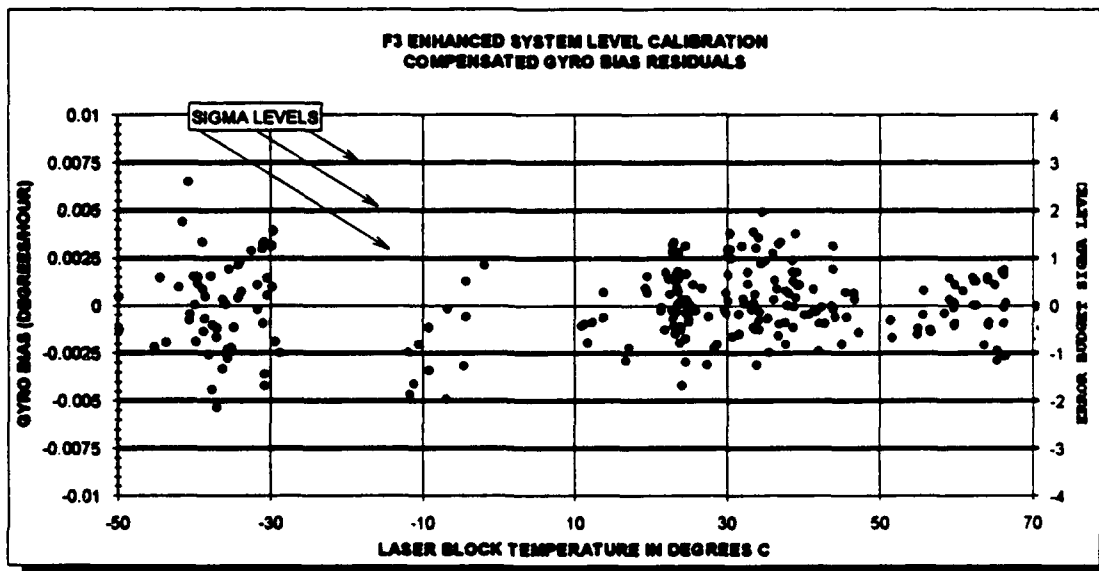
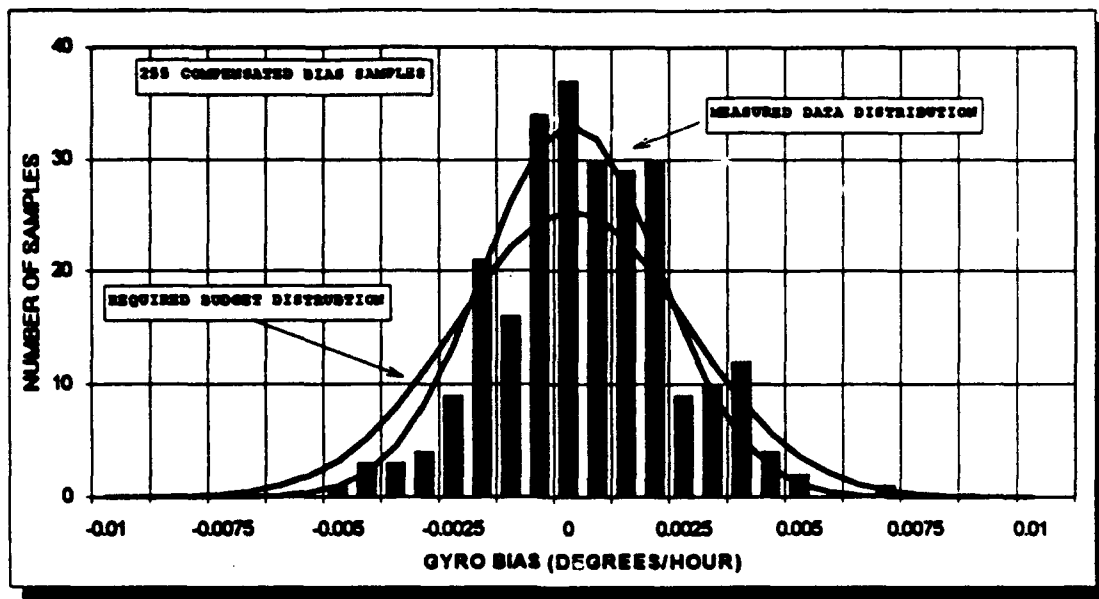




**Figure 2 Budgeted Gyro Bias Distribution**



## **(2) Kalman Filter Sensor Error Estimation**

The Enhanced INU alignment and navigation aiding functions are processed by a 14 state, two partition Kalman filter. The first partition consists of 8 states, 2 position, 2 velocity and either 3 or 4 alignment angle states dependent on the type and status of the alignment. The second partition is a 6 state inertial sensor trimming section consisting of 3 gyro bias and 3 accelerometer bias states. Sensor trimming is accomplished by means of filter estimation of residual errors as compared to an established reference, with the reference being developed from external inputs or from the sensors undergoing correction. In both cases, the degree of performance enhancement is dependent on the visibility and separation of the contributing sensor errors as well as the characterization of the error sources, in terms of noise and stability, within the filter design. In addition to forming sensor corrections during periods of GPS aided navigation, the Enhanced INU Kalman filter implementation provides the capability to enhance the functional operation of the various ground alignment modes, as described below.

- (a) In the case of a single position GC alignment, no separation of inertial sensor errors occurs, so that the only reference available to the filter is the calculated component of local Earth's rate, (derived from the initialized position). During the alignment process, the filter can estimate residual composite angular rate errors about the north/south axis and apply corrections to the appropriate gyro bias compensation terms, with the only restriction being the 9 minute period of observation during the alignment.
- (b) To gain additional performance enhancement, the two position EIA technique can be employed. The EIA requires two separate alignments to be performed with a minimum heading difference of 70 degrees. During the initial 9 minute GC alignment, residual

accelerometer bias and composite angular rate errors about the east/west axis are not observable and are included in the navigation frame level and azimuth estimates respectively. Following the heading rotation, the 6 minute EIA estimates corrections to the navigation frame based on the reoriented inertial sensors. The result is a decoupling of accelerometer bias and composite angular rate errors relative to the navigation frame, providing direct residual error observations to the Kalman filter. The filter then refines the navigation frame by estimating and applying corrections to the appropriate inertial sensor compensation terms, with the compensation remaining active for the duration of the mission.

- (c) In addition to the GC and EIA sensor trimming capabilities, the Enhanced INU also provides sensor error correction by means of the Navigation Alignment Refinement Feature (NARF). Similar to the automatic interrupted alignment capability, in which the INU detects aircraft motion to automatically suspend and resume the alignment, the NARF mode gives the INU authority to automatically resume alignment from the navigation mode. As such, NARF can take advantage of extended ground operation and maneuvering time, providing increased sensor error visibility and separation for further trimming by the INU Kalman filter. Providing that similar decoupling maneuvers and stationary periods occur, NARF is required to provide the EIA level of free inertial performance (0.22 NMPH).
- (d) The trimming capabilities described above are designed to accommodate subtle residual errors in the inertial sensor calibration. As a method to fully utilize the Kalman filter derived sensor corrections, the SNU 84-1/E saves fixed percentages of the corrections in INU non-volatile memory, (providing specific criteria is met). Subsequent INU operation applies the saved corrections in addition to further filter trimming. As a result, performance enhancements developed from previous correction tendencies are available, regardless of the current alignment type. The significant benefit of this technique is the additional refinement of the GC alignment free inertial performance.

Considerable flexibility is supported by the various ground alignment options available. The GC full performance alignment is complete in 9 minutes, giving the pilot the option to continue with the mission (0.3 NMPH) or perform the secondary EIA (0.22 NMPH). The NARF mode is active by default, providing additional sensor trimming up to the 80 knot lock-out speed. With sufficient GPS coverage, the NARF and EIA modes are automatically disabled while MAGR provided position and velocity updates are accepted and used to form the sensor error estimates, again providing improved free inertial performance in the event that GPS data becomes unavailable.

### **(3) 2400HZ Inertial Processor**

In the H-423 INU system design, the inertial data processor operating speed is configured by means of the INU flight software. The system architecture is designed to accommodate 1200hz or 2400hz inertial processor operation, as requested by the INU flight software during system

power-up. The Enhanced INU flight software implements the 2400hz option to provide improved accuracy in the compensation of dynamic error sources, (e.g. coning, sculling and size effect).

#### **(4) Gravity Deflection Compensation**

As required by the SNU-84-1/E specification, the Enhanced INU provides the capability to compensate for local gravity deflections. During the INU alignment/leveling process, local gravity deflections are observed as an error in the INU local level estimate, degrading the inertial performance as the aircraft exits the area. In the Enhanced INU, the operator entered corrections (via the 1553 data bus) are included in the INU local level estimate and gradually removed as a function of distance from the alignment position.

### **CIGTF VERIFICATION TESTING**

The SNU 84-1/E Enhanced Accuracy Inertial Navigation Unit test project was sponsored by the Aeronautical Systems Center, Wright-Patterson AFB, Ohio, and the 46th Test Group, Guidance Test Division at CIGTF. The primary goal of the test project was to verify that the Enhanced INU satisfied performance and accuracy requirements in accordance with the *Specification for USAF Standard Form, Fit, and Function (F<sup>3</sup>) Enhanced Accuracy Inertial Navigation Unit, ASC, SNU 84-1/E, Rev B*.

The test project began in October of 1992 with the delivery of three government furnished Enhanced INUs to CIGTF. Following the initial performance and functional tests, the test items entered a dual path test flow. One system was assigned to the laboratory and environmental performance tests, another system delivered to the Aircraft Test Group for integration into the aircraft test pallet, and the third system reserved as a dedicated spare. The project test plan included:

- (1) Laboratory functional tests, including calibration accuracy, gyro compass (GC) alignment navigation performance over the full military temperature range and Enhanced Interrupted Alignment (EIA) navigation performance.
- (2) Laboratory INU/GPS integration verification tests.
- (3) EIA and GC alignment free inertial flight navigation performance for both two hour and six hour missions.
- (4) Flight navigation performance during periods of GPS aiding.
- (5) Free inertial flight navigation performance following periods of GPS aiding.
- (6) Specialized testing unique to the F-117A application.

## Laboratory Testing

Laboratory testing of the Enhanced INU free inertial performance was comprised of both GC alignment and EIA navigation tests. To verify compliance to the GC alignment 0.3 NMPH CEP requirement, twenty 120 minute GC tests were conducted over the full military temperature range, (-40F, +70F and +160F). Verification of the EIA 0.22 NMPH CEP requirement was also performed, with twelve 120 minute tests conducted, six each at 71 and 180 degree rotation angles. Results from this testing, shown in Tables 3 and 4 and Figure 3, indicated system performance comfortably meeting the requirement.

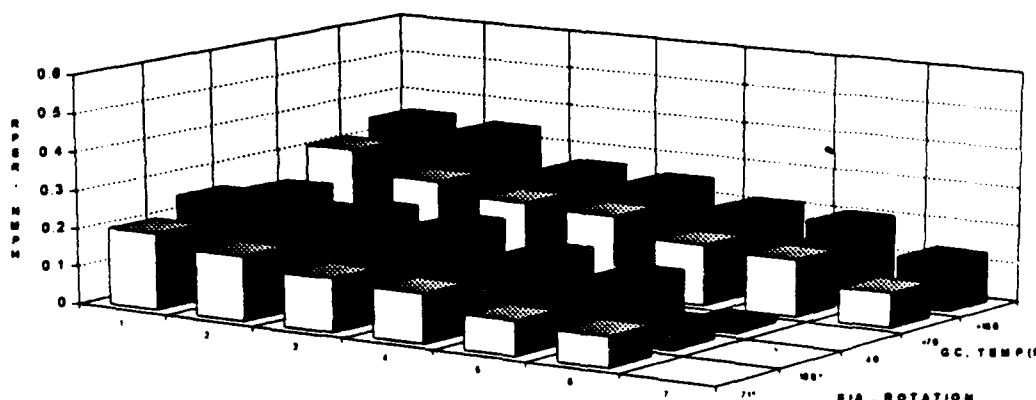
**Table 3 Gyrocompass Alignment (GC) Test Results**

Nav Time	Spec	Radial Position Error Rate 50th % CEP (NMPH)			RMS Velocity Error Feet/Second					
(Minutes)		-40F	+70F	+160F	-40F		+70F		+160F	
					Vn	Ve	Vn	Ve	Vn	Ve
60	0.6	.12	.09	.22	.30	.16	.38	.33	.53	.32
120	0.3	.13	.21	.24	.31	.17	.43	.29	.51	.34

**Table 4 EIA Test Results**

Nav Time	Spec	Radial Position Error Rate 50th % CEP (NMPH)		RMS Velocity Error Feet/Second			
(Minutes)		71 Deg	180 Deg	71 Deg		180 Deg	
				Vn	Ve	Vn	Ve
60	0.44	.06	.08	.25	.22	.38	.26
120	0.22	.12	.15	.26	.25	.38	.26

**Figure 3 GC and EIA Performance Test Results (120 minutes)**



Note: Data sorted by performance

## **INU/GPS Integration Testing**

The Enhanced INU/MAGR integration was successfully verified using the CIGTF GPS simulator laboratory capabilities. The purpose of the testing was to verify that the Enhanced INU/MAGR interface functioned correctly and that the INU correctly processed GPS updates in accordance with the SNU 84-1/E specification.

Specific items verified were: (1) While a minimum of four satellites are in state five tracking, the Enhanced INU Kalman filter alternately processed GPS position and velocity corrections at an eight second update rate. (2) During periods of state three tracking, the INU processed only position updates at a reduced sixty second rate. (3) When less than four satellites are available, all GPS updates were rejected. (4) The Enhanced INU instrumentation messages correctly reported the simulated changes.

## **Flight Testing**

### **General Test Description**

A total of eighteen flight tests were conducted to evaluate the Enhanced INU free inertial and GPS aided navigation performance. Twelve of the flights were dedicated free inertial tests, sequentially mixing six GC and six EIA alignment types, with one EIA and one GC alignment flight extended to six hours. The remaining six flights were separated into two groups, an initial GPS aided period and a subsequent period of free inertial navigation, (GPS disabled by software command). Due to the difficulty in providing identical ground maneuvering operations from test to test (required for a statistical comparison) the NARF mode was manually disabled for all flight tests. The resulting data was categorized into four ensembles of six tests each, GC free inertial, EIA free inertial, full GPS aided and free inertial performance following GPS aiding.

During the flight test series, test item data was recorded by two independent instrumentation systems. The official CIGTF performance verification data was extracted directly from the MAGR RS-422 data bus, receiving INU data at all times, and then time correlated with the certified position/velocity reference system, (CIRIS). In addition, Honeywell supplied test equipment, consisting of an airworthy PC and the Configurable Data Acquisition Test Software (CDATS), performed 1553 bus controller functions, provided system mode control, initialization, data display and high speed 1553 data bus recording.

### **Flight Profiles**

The Enhanced INU flight test series used three flight profiles to evaluate the free inertial and GPS aided performance. Two free inertial profiles were developed to provide a minimum of two and six hour mission durations. These flights consisted of an approximate 2½ hour outbound and return to base loop for the two hour missions, with the six hour flight profile including an additional 3½ hour loop. The GPS aiding/free inertial flight profile consisted of a GC alignment

followed by approximately 75 minutes of GPS aided navigation through a series of maneuvers, after which GPS aiding was disabled for the remainder of the flight (approximately 140 minutes). Figures 4 and 5 represent recorded aircraft position data for the six hour free inertial and GPS aided flight profiles.

**Figure 4 Six Hour Free Inertial Profile**

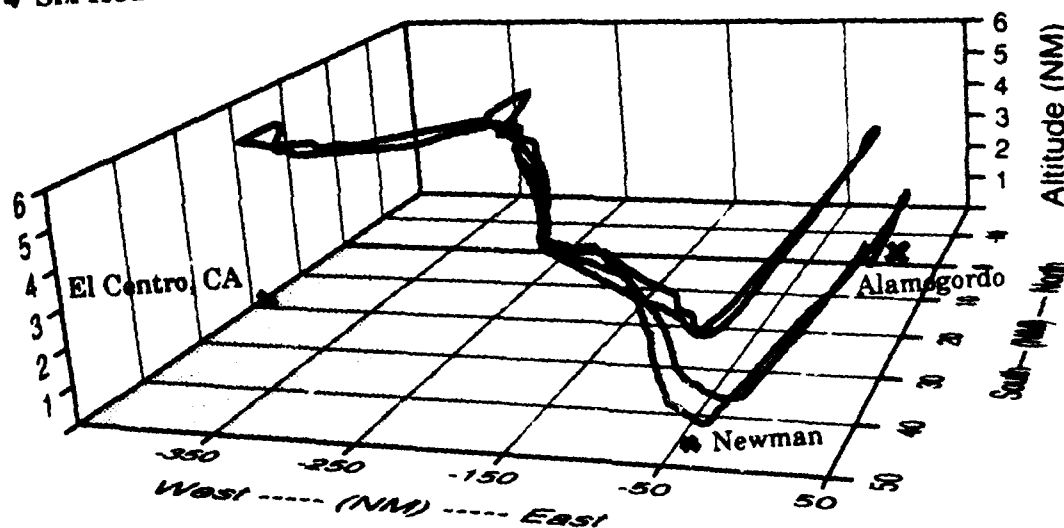
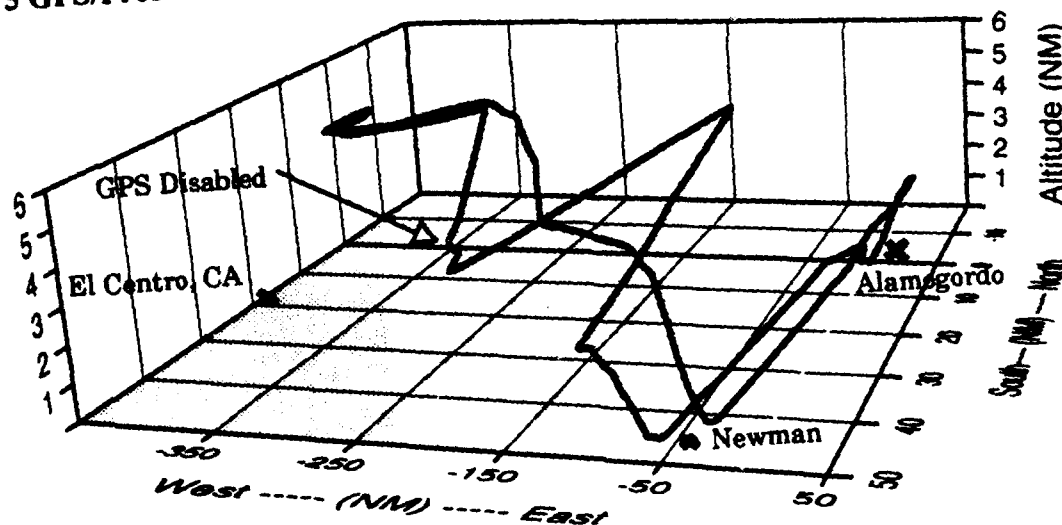


**Figure 5 GPS/Free Inertial Profile**



### Free Inertial Flight Performance

The free inertial flight performance summary is shown in Tables 5 and 6, Figures 6 and 7. Figure 6 shows the position error rate, on an hourly basis, for the two six hour flight tests. Since only two tests were conducted, insufficient data was available for a CEP calculation (minimum of six tests required). Figure 7, showing flight performance in a "bull's eye" format, where the outer circle represents the SNU 84-1/E CEP performance requirement for the specific alignment type and test duration. The actual test ensemble CEP performance is represented by an inner circle, shown with the individual test results.

**Table 5 EIA and GC Alignment Free Inertial Flight Performance**

Nav Time	Spec		Radial Position Error Rate 50th % CEP (NMPH)		RMS Velocity Error Feet/Second			
(Minutes)	GC	EIA	GC	EIA	GC		EIA	
					Vn	Ve	Vn	Ve
60	0.6	0.44	.12	.07	.31	.21	.15	.25
120	0.3	0.22	.09	.08	.38	.53	.27	.48
150	0.3	0.22	.09	.09	.45	.59	.32	.53

**Table 6 Six Hour Free Inertial Flight Performance**

Nav Time	Spec		Radial Position Error Rate (NMPH)		RMS Velocity Error Feet/Second			
(Minutes)	GC	EIA	GC	EIA	GC		EIA	
					Vn	Ve	Vn	Ve
60	0.6	0.44	.22	.06	.40	.17	.08	.13
120	0.3	0.22	.14	.05	.34	.61	.29	.43
180	0.3	0.22	.15	.08	.42	.91	.38	.50
240	0.3	0.22	.09	.06	.47	1.03	.42	.49
300	0.3	0.22	.07	.06	.60	1.03	.46	.46
356/360	0.3	0.22	.06	.06	.72	.97	.48	.48
387	0.3	0.22	n/a	.05	n/a	n/a	.47	.49

**Figure 6 Free Inertial Flight Performance 6 Hour**

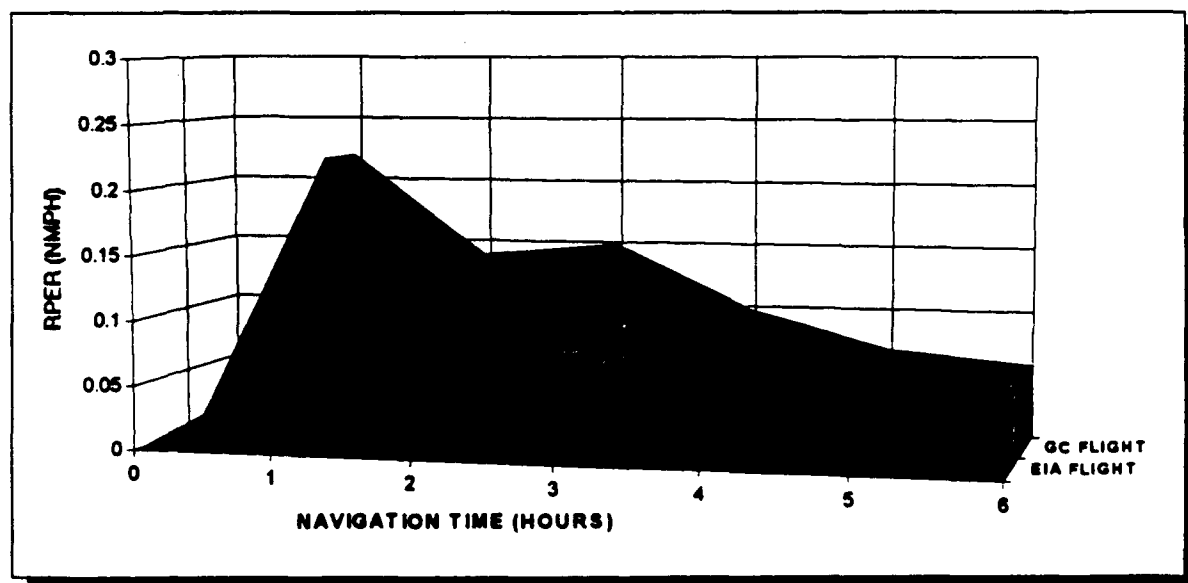
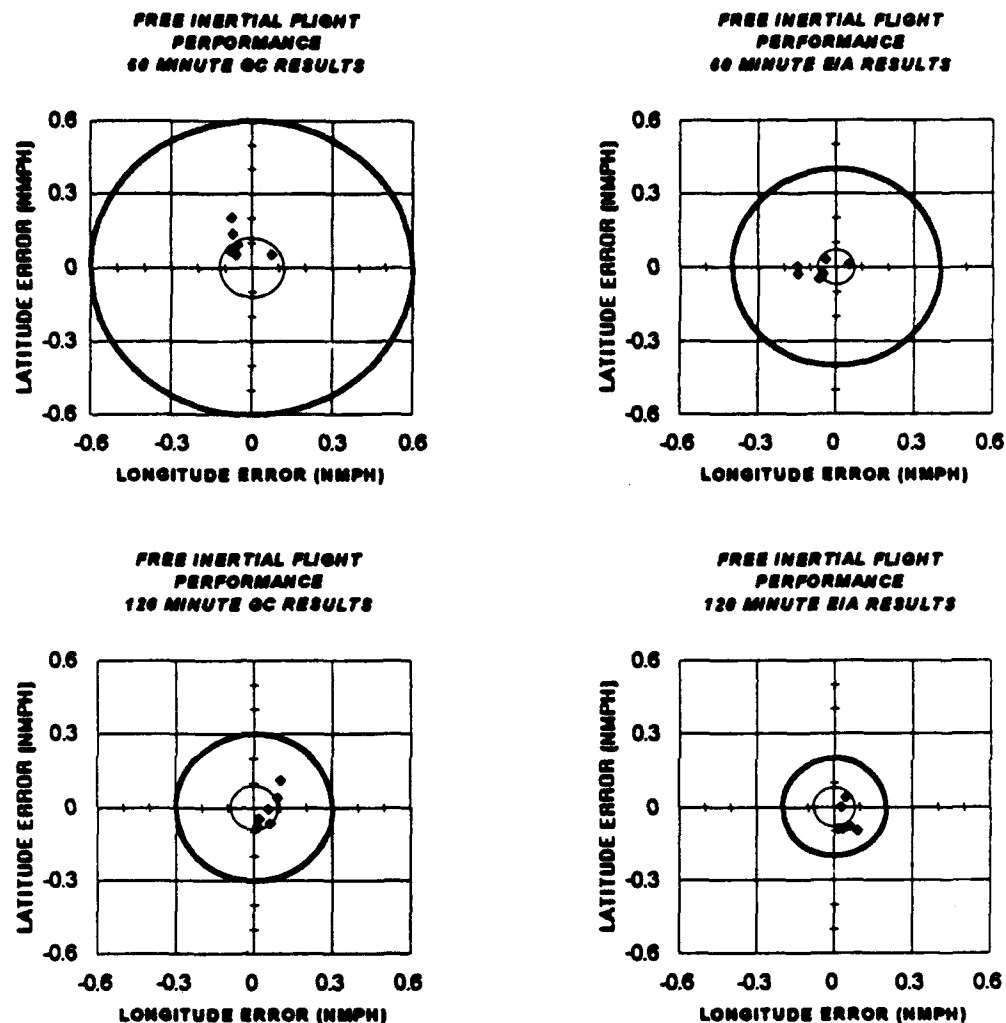


**Figure 7 Flight Test Performance**

(NOTE: darker circle is CEP spec and lighter circle is CEP for ensemble of tests)



### GPS Aided/Free Inertial Performance

In the analysis of the GPS aided performance, the initial aided period was extracted from each of the six GPS aided/free inertial flight tests. This data was then combined, providing a composite GPS aided performance assessment for the six flights, (shown in Table 7). As can be seen, the Enhanced INU/MAGR combination demonstrated exceptional performance, competing with the accuracy of the position/velocity reference system.

**Table 7 GPS Aided Performance**

Parameter	Mean	Standard Deviation
Latitude Error (FT)	3.0	18.9
Longitude Error (FT)	8.9	13.4
Vn Error (FPS)	-0.04	0.17
Ve Error (FPS)	+0.01	0.11

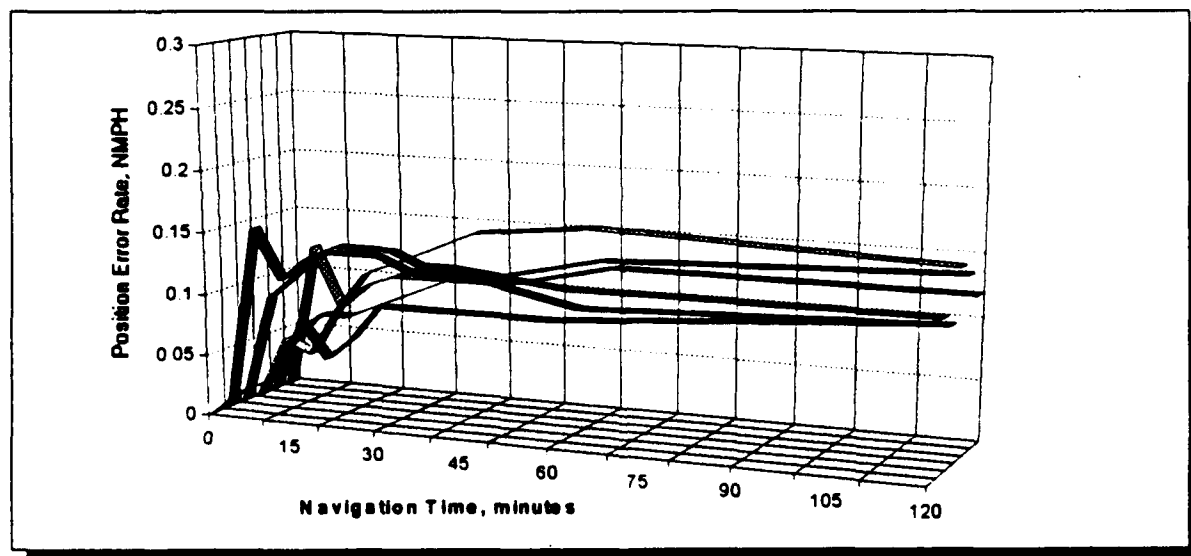


During GPS aided navigation, the INU Kalman filter sensor and misalignment corrections are derived entirely from the GPS position/velocity updates. These corrections are developed and applied on a individual mission basis, remaining active for the duration of the flight. In the six GPS aided/free inertial flight tests, the extracted free inertial periods were combined to provide a statistical CEP performance ensemble. Performance was equivalent to the GC and EIA test results, indicating that a comparable level of filter error corrections were derived during each mission. Table 7 summarizes the CEP free inertial performance data, including the position error based on the CEP error growth rate. Individual test results are shown in Figure 8. Note that in the early stages of navigation, the estimated error growth rate is extremely dependent on the accuracy of the reference system.

**Table 8 Free Inertial Performance following GPS Aiding**

Nav Time (Minutes)	Radial Position Error Rate 50th % CEP (NMPH)	Position Error Feet	RMS Velocity Error Feet/Second	
			Vn	Ve
5	.06	30	.04	.08
10	.07	71	.06	.17
15	.09	137	.06	.21
20	.10	203	.07	.21
25	.11	278	.07	.21
30	.11	334	.08	.20
35	.11	390	.10	.20
40	.11	445	.14	.20
60	.12	729	.36	.34
120	.12	1458	.48	.69

**Figure 8 Free Inertial Performance following GPS Aiding**



## **CONCLUSIONS**

Through a comprehensive test program conducted by the CIGTF, the USAF has verified that all objectives of the SNU 84-1/E Enhanced Accuracy INU have been achieved. Free inertial performance in the 0.1 NMPH class was verified with the 15 minute enhanced interrupted alignment, the 9 minute gyro compass alignment and following an appropriate period of GPS aiding. The GPS aided performance demonstrated the advantages of a GPS integrated with a high precision INU. In addition, the Enhanced INU offers these advantages with no hardware design changes from the H-423 SNU 84-1 Standard INU. As such, no new Government inventory items are required, inclusive of depot maintenance test equipment.

The Enhanced INU combines the advantages of GPS aided navigation with the autonomy of a high precision free inertial navigation system. With the low life cycle costs and high reliability associated with RLG strapdown technology, the Enhanced INU offers a cost-effective alternative for all precision inertial navigation system applications.

## **References:**

ASD AFSC, WPAFB, OH  
SNU 84-1/E, Rev B,  
31 Jan 1992

Specification for USAF Standard Form, Fit and  
Function (F<sup>3</sup>) Enhanced Medium Accuracy Inertial  
Navigation Unit

ASCC AIR STD 53/16A  
6 Apr 1988

The Specification for Evaluation of the Accuracy of  
Hybrid Navigation Systems

AFDTC-TR-93-  
June 1993

Performance Evaluation Testing of the Enhanced SNU 84-1/E  
Guidance Test Division , 46th Test Group, HAFB

GPS-93-YB-005  
20 January 1993

F-117A/GPS Anti-Jam Performance Test Report  
Naval Command, Control, and Ocean Surveillance Center  
Research and Development Division

**THIS PAGE LEFT BLANK INTENTIONALLY**

## AIR ALIGNMENT FOR THE BASE INERTIAL NAVIGATION SYSTEM - LINS 300

R. H. W. REILLY

BRITISH AEROSPACE (SYSTEMS & EQUIPMENT) LTD.

PLYMOUTH, ENGLAND, PL6 6DE.

### ABSTRACT

British Aerospace Systems and Equipment (BASE) are providers of a SNU 84-1 type INS for various aircraft platforms. These include: MERLIN, the Naval variant of the Anglo-Italian EH101 helicopter, for the UK Royal Navy; NSA, the naval variant of EH101 for the Canadian government; HAWK, a light attack fighter selling to various air forces around the world, and F5 updates.

The Merlin application, in particular, includes an integral Air Align mode, allowing full alignment of the INS in flight, using velocity reference gyro-compassing. The velocity reference is provided by Doppler radar. This variant of the INS has been the subject of extensive flight testing in EH101, and has demonstrated full alignment over land and sea.

The Air Align mode features a Doppler/INS Kalman filter used in feed-back configuration. This configuration was chosen, because of the paramount need to align in flight.

Various mode sequences are available, the usual sequence involving take-off from the deck of a frigate. The alignment process is independent of the ship's system, using an On-Deck Level mode to level the platform frame approximately, followed by Coarse Alignment of heading from the AHRS in flight, and finally full alignment in Air Align mode.

An alternative sequence begins with Attitude mode in flight, to level the platform frame approximately, followed by Coarse Alignment of heading from the AHRS, and full alignment by Air Align mode. For land based operation a full Gyro-Compass align or a Stored Heading align followed by free Nav mode may be used. An alternative is the use of a short 1 minute GC align, followed by Air Align mode, for a quick take-off.

These modes have been successfully tested in the adverse vibration environment of a helicopter. This includes GC align on the ground, with the rotor turning. Some details of filter development and trials results are given.

More recently a GPS/INS filter has been developed and subjected to flight trials in the UK Royal Air Force 'ARIES' Comet flights. This is also implemented in a feed-back configuration, and enables full in-flight alignment to occur. There are two specific applications for this type of filter on the EH101 helicopter, and other future applications are under review for a variety of platforms.

The alignment mechanisms for the GPS/INS filter are velocity reference gyro-compassing, as for the Doppler/INS filter, but also transfer alignment. This is possible because the GPS receiver provides a reference velocity in NED frame, whereas the Doppler provides a reference velocity in body frame. The latter mechanism, transfer alignment, allows faster alignment. Details are given of the development and flight trials of this filter.

The GPS/INS filter provides an alternative Air Align sub-mode to the Doppler/INS filter. These sub-modes are seen as complementary. Normally the GPS source allows a rapid and accurate alignment (at least as good as a full ground based GC align), with closely bounded errors, but in its absence the Doppler allows autonomous operation, with larger errors.

### 1. INTRODUCTION

British Aerospace (Systems & Equipment) Ltd, BASE, has developed a SNU 84-1 laser gyro INS, generically known as LINS 300. There are several variants of this, customised to different user requirements. These include a baseline version, standard fit on the HAWK 100 and 200, and a modified version with an ARINC 429 interface,

for the Westlands/Agusta EH101 helicopter. The SNU-84 Air Align mode normally features an interface to accept corrections generated by a Kalman filter external to the INS, but customer requirements are increasingly mandating the provision of an internal filter, and this has been provided in the LINS 300 series.

BASE has developed filters to provide in-air alignment of the INS, using GPS and/or Doppler radar as an alignment reference. The immediate application of these filters lies in the various EH101 helicopter variants. However other applications are emerging.

Figure 1 is an outline of the relevant parts of the Doppler/INS system flown on EH101, and the GPS/INS system flown on the ARIES flights.

EH101 is a joint Anglo-Italian helicopter project, under development by Westland Helicopters Ltd, and Agusta. Merlin is a naval variant of this, for the UK Royal Navy. The requirement for an Inertial Reference Unit (IRU) is met by LINS 300. Merlin calls for Doppler radar aiding of the IRU, and a Racal 91E Doppler radar is fitted to Merlin. This provides a reference velocity to the IRU. Corrections to the reference velocity are made in the Aircraft Management Computer (AMC), to minimise errors due to wind and bulk water motion effects, and manoeuvre effects. ARINC 429 interfaces are used for communications.

The Merlin helicopter has a main role in anti-submarine warfare (ASW), but has other roles including search and rescue. In the ASW role the helicopter will operate from the deck of a frigate, and will operate primarily over sea. Other roles may involve land based operation.

The GPS/INS system flown on ARIES features a Canadian Marconi Control and Display Unit (CDU), and a Cossor 2515 GPS receiver, together with a LINS 300. A 1553 bus was used for communications.

The ARIES flights are a major element of the UK RAF Aerosystems coarse, and comprise several long range flight trials on which state of the art navigation equipments undergo a detailed evaluation.

This paper addresses the design and development of the Air Align mode of the LINS 300. This mode incorporates Kalman filters, which use the Doppler radar or GPS reference velocity to perform air alignment of LINS. Reference 1 gives details of the LINS specification for EH101, developed to meet the requirements of reference 2.

## 2. MERLIN DOPPLER-REFERENCED ALIGNMENT

The sequence of modes is shown in figure 2. This sequence applies in a reversionary situation where GPS data is not available to the requisite accuracy.

On-deck levelling mode is used to perform the initial levelling of the IRU platform frame while the aircraft is still on the deck of the ship. At this stage azimuth is arbitrary, and no velocity calculations occur.

Following take-off, the system switches automatically to air-align mode. Doppler reference velocity is available, but the lack of initial heading prevents navigation calculation beginning in the IRU.

The Attitude and Heading Reference System (AHRS) is used to provide initial heading to the IRU.

This initiates the navigation calculations, and the availability of IRU velocity and Doppler velocity enables operation of the Kalman filter, which performs fine alignment of the IRU.

The Doppler/INS filter first corrects velocities, then tilts, and finally azimuth. This then enables the mission to proceed.

Alternative mode sequences include;

STANDBY - GC ALIGN - NAV

STANDBY - SH ALIGN - NAV

These apply to land based missions only, i.e., taking off from land.

Other mode sequences are possible, although not part of the MERLIN requirements;

STANDBY - SHORT GC ALIGN - AIR ALIGN

This allows a quick take-off with completion of alignment in the air.

STANDBY - ATTITUDE MODE - AIR ALIGN

This enables restart in flight. This would normally use the AHRS as a source of coarse azimuth, however an alternative is the use of a manually entered heading, accurate to a few degrees.

Other mode sequences may occur in special cases. For example, in operations over the land-sea boundary the Doppler reference velocity is subject to errors due to tidal current effects, and a temporary switch to NAV mode is desirable.

All the above modes have been implemented, and tested in flight.

### 3. GPS REFERENCED ALIGNMENT

The following mode sequences have been defined;

- For on-deck initialisation;

ON-DECK LEVEL, COARSE AZIMUTH ALIGN, AIR ALIGN.

- For in-air initialisation;

ATTITUDE MODE, COARSE AZIMUTH ALIGN, AIR ALIGN.

On-Deck Level (ODL) and attitude mode are common to the Doppler approach. They provide the basic coarse levelling of the platform frame. Coarse azimuth mode is introduced to set up heading in the absence of an external approximate heading reference. This mode will make use of GPS reference data to pull-in heading to within a few degrees, and may also be used to refine horizontal tilt errors. Finally air align mode is used to complete alignment of the system.

ODL and attitude mode have been implemented and demonstrated in flight. Air align using GPS has been implemented and demonstrated in flight.

Separate filters have been developed for Doppler/INS alignment and GPS/INS alignment. This approach allows advantage to be taken of the merits of each configuration. Furthermore the two references differ so much in the magnitude of errors and noise that little advantage is gained in trying to use both sources simultaneously in a combined filter.

### 4. ERROR MODELS

The starting point for the design of a filter is the development of error models. These define the generation and interaction of errors in a system, or give a behavioural description of the errors in the output of a system.

#### 4.1 INS ERROR MODEL

Error models for an INS may take different forms. Reference 4 gives details of the main division, which is between  $\phi$  and  $\psi$  error models. The BASE GPS and Doppler applications use a  $\phi$  type error model. The next choice is between the different frames of reference, e.g. North, East, Down (NED) and wander azimuth. In this case NED was chosen. A further choice was between the form of representation of position error; spherical

polar coordinates (latitude, longitude, height) or Cartesian coordinates (north position, east position, height, all with dimensions of length). The former was chosen.

An error model for the laser gyro INS was developed by BASE, of the type outlined above; reference 5. This takes the form

$$\dot{\mathbf{x}} = \mathbf{F}\mathbf{x} + \mathbf{B}\mathbf{u} + \mathbf{w} \quad (1)$$

The INS is a strap-down system, and its instrument errors are embodied in the forcing function term  $\mathbf{B}\mathbf{u}$  in equation (1). Instrument errors  $\mathbf{u}$  and system noise  $\mathbf{w}$  are defined in reference 6. The matrix  $\mathbf{B}$  is partitioned into submatrices, some of which are direction cosine matrices transforming errors from body frame to NED frame. Equation (1) can be rewritten in the form given below,

$$\dot{\mathbf{x}}' = \mathbf{F}'\mathbf{x}' + \mathbf{w}'$$

where the state vector  $\mathbf{x}'$  is an extended form of  $\mathbf{x}$  in equation (1), with gyro scale factor, misalignment, bias, accelerometer scale factor, misalignment, bias, and gravity model tilt errors added. The sub-matrices of the matrix  $\mathbf{B}$  now appear in  $\mathbf{F}'$ .

The core of the error model is;

$$\dot{\mathbf{x}} = \mathbf{F}\mathbf{x} + \mathbf{w}$$

The INS vertical channel is inherently unstable, and is stabilised by using baro-inertial mixing. In a cruise-type vehicle the vertical channel is virtually decoupled from the horizontal channels, hence height error and height rate error can be ignored, when modelling errors in the horizontal channels. Thus the core of the  $\mathbf{x}$  vector can be reduced to 7 elements, and the core of the  $\mathbf{F}$  matrix to  $7 \times 7$ .

The vector

$$\mathbf{x} \triangleq \{\phi_n, \phi_e, \phi_d, \delta L, \delta l, \delta V_n, \delta V_e\}$$

has elements for attitude error, latitude and longitude error and north and east velocity errors.

The  $\mathbf{F}$  matrix may be partitioned into sub-matrices. One sub-matrix forms a cross-product of frame rate with attitude error, contributing to rate of change of attitude error. Another sub-matrix forms a cross-product of specific force with attitude error, contributing to the rate of change of velocity error.

#### 4.2 DOPPLER RADAR ERROR MODEL

The Racal 91E Doppler radar is a strap-down type. It measures aircraft velocity in aircraft body axes. Racal provided a detailed residual error model. Table 2 gives a break-down of these errors. The nature of the errors is scale factors, misalignments and biases in body axes, and biases in geographic axes, due to wind and bulk sea motion. The various errors are combined by root-sum-squaring (RSS) the different error sources. Reference 3 gives details of the Doppler Radar error model.

Fixed errors are the constant or slowly changing component of errors, in Doppler axes. Manoeuvre induced errors depend on the inclination and bank angles of the aircraft, and are also in Doppler axes.

Over sea, wind causes errors by disturbing the sea surface. These errors are also in Doppler axes. Wind also causes capillary wave motion (CWM) over the sea. This appears as a bias in geographic axes.

Bulk water motion (BWM) due to tidal or sea currents, is the final error considered. This is also a bias in geographic axes.

The wind and current errors are bias-like, but subject to variation in time and space. These could be modelled as Markov processes. However, due to widely varying conditions, the time constants would vary.

Over land the errors are fixed errors, manoeuvre induced errors, and errors due to the nature of the terrain. All are in Doppler axes.

The RSS of the above errors gives 3 scale factor, 6 misalignment and 3 bias errors in body axes, a total of 12 parameters. In addition the over-sea case has additional parameters for the various Markov processes.

Harmonisation errors exist between the Doppler radar antennae axes and the INS Inertial Measurement Unit (IMU) axes. These errors are not distinguishable from the Doppler misalignment errors. The azimuth harmonisation error is particularly important, since during acceleration it causes velocity divergence between the INS and Doppler.

#### 4.3 GPS ERROR MODEL

The GPS receiver used was a Cossor 2515, operating in PPS mode. Cossor provided a preliminary form of the error model for the design of the GPS/INS filter. This amounted to white noise on the velocity data, when 4 SVs STATE 5, FOM = 1,2,3 was achieved. Some small velocity biases were seen in static laboratory tests under these conditions, but these were not significant in the context of the design requirement.

Position error can be modelled as a time varying bias, or Markov process, with additional white noise. This white noise is equivalent to a rate of change of position error that is an order of magnitude more significant than the velocity noise.

#### 4.4 SYSTEM ERROR MODEL

This is based on an amalgam of the INS error model, the Doppler error model, and the observation model, in the case of the Doppler/INS filter. Different options exist here, and the equations can be recast to give a low dynamic form for the Doppler/INS application. This form of the model, used in with a pre-filter, enabled use of a relatively long filter period, without sacrificing accuracy in dynamic conditions.

The GPS/INS system error model was based on the GPS error model, the INS error model, and the observation error model. These were combined into a suitable form for the GPS/INS filter.

#### 4.5 GPS/INS ALIGNMENT MECHANISMS

The GPS/INS filter has two alignment mechanisms that are naturally inherent in its structure. These are velocity reference gyro-compassing and transfer alignment. The following explanation should be read in the context of the form of INS error model described above. With other forms of error model, the apparent mechanisms differ, though they are equivalent in overall effect.

Velocity reference gyro-compassing, with a GPS reference source, has a mechanism that depends mainly on the horizontal vector component of Earth rate. An additional contribution arises from profile (or transport) rate. This is the rate at which the INS platform frame is rotated, to keep it level as it moves over the Earth's surface.

The Earth rate and profile rate vectors add to give the platform frame rate vector. In the error model this gives a cross-product with azimuth error, contributing to the rate of change of tilt errors. These in turn give rise to velocity errors, which is how azimuth error is observed by this mechanism.

The relative importance of earth rate and profile rate varies with latitude and velocity.



At high latitudes the Earth rate contribution diminishes, leaving profile rate as the major contribution, in the case of the GPS/INS filter. With the aircraft travelling at typical helicopter speeds, profile rate is equal in magnitude to the horizontal component of Earth rate at high latitudes. If the aircraft is flying east, the rate vectors are additive, but if it is flying west vector cancellation occurs, and there is no gyro-compassing effect. Flying north/south gives intermediate effects.

The second way of observing azimuth error is via a cross-product of attitude error and specific force. This mechanism is not a function of latitude, but depends on the aircraft performing manoeuvres. This gives rise directly to a contribution to rate of change of velocity error, which is observed by comparison with GPS velocity. This is velocity reference transfer alignment.

In the absence of a velocity reference, a position reference is an alternative means of observing azimuth error. In this case the velocity error generated by the above mechanisms integrates up to give position error, so enabling alignment. The dependence on latitude is still present for gyro-compassing, whereas transfer alignment depends on aircraft acceleration.

The above descriptions cover the 'signal' content in any observation. There is also 'noise' present, as described in the above error models. Alignment times are a function of the noise level, which differs for velocity reference and position reference observations.

With a GPS/INS filter, aircraft manoeuvres are helpful in achieving alignment.

#### 4.6 DOPPLER/INS ALIGNMENT MECHANISM

With a Doppler reference velocity the profile rate is cancelled out, and the velocity reference gyro-compassing mechanism depends on the cross-product of azimuth error and the horizontal component of earth rate, in the Doppler/INS filter. The cancellation of profile rate occurs because soon after alignment begins, the INS velocity error becomes highly correlated with azimuth error in the NED frame.

Transfer alignment, as defined for the GPS/INS filter, does not occur with a Doppler reference. The INS error model features a cross-product of specific force and azimuth error, whereas the Doppler error model, in NED frame, features a cross-product of acceleration and azimuth error. The resulting velocity divergence is not a function of specific force, due to cancellation, and aircraft acceleration does not enable observation of azimuth error.

This cancellation arises because the Doppler velocity is converted from body frame to NED frame by the INS Euler angles.

The preferred form of flight for alignment with a Doppler/INS filter is straight and level.

#### 5. FILTER EQUATIONS

These are given in standard form in reference 7. A feedback configuration is chosen for both the Doppler/INS filter and the GPS/INS filter, as opposed to a feed-forward configuration. This is necessary early in flight, due to large initial errors. This leads to simplification, since the INS holds the state vector. Filter state vector updates take the form of corrections applied to the INS. This correction process needs to be carefully considered.

The choice of H matrix in the observation model

$$y = Hx + v$$

determines the form of  $P_0$ , the initial value of the system covariance matrix  $P$ . In the case of the Doppler/INS filter, for example, correlation of velocity and azimuth error would be reflected in  $H$ , and also in the velocity initialisation of the INS, which occurs in flight. The latter is reflected in  $P_0$ .

It emerges that the four concepts of the INS error model, the observation model, the correction process and the

initialisation process are all closely linked together.

Choice of filter states is influenced by various factors, including the nature and magnitude of instrument errors, and the nature of the mission.

For example 180° turns lead to disturbances, due to accelerometer biases being fixed in body axes in a strapdown INS. The filter will model these at one of three levels of complexity. Accelerometer biases could be modelled in both the state vector and the covariance matrix of the standard filter equations; it could be modelled in the covariance matrix only, as in the Schmidt-Kalman filter, reference 8. Finally, the simplest method is to use the system noise covariance matrix  $Q$ . This boosts the  $P$  matrix after a turn, causing the filter to correct the INS alignment.

## 6. PRE-FILTERING

### 6.1 DOPPLER/INS PRE-FILTERING

Doppler data is available at close to 10 Hz from the Racal 91E, and if valid, should all be used, to minimise noise effects. However, running the filter at 10 Hz would impose an unnecessarily high load on the processor. Different approaches to pre-filtering were considered, and the simplest was chosen. The differences between the INS and Doppler velocity were averaged over 16 s. This average difference was passed to the filter.

This averaging process can be modelled in the filter using an observation matrix

$$H^* = f(H, \Phi)$$

See reference 9. This could be calculated using the transition matrix  $\Phi$  for all 160 samples, but in practice a simplified form is used.

### 6.2 GPS/INS PRE-FILTERING

GPS data is available at 1 Hz from the Cossor receiver. As for the Doppler case, all data is used if valid. A similar form of pre-filter is employed, and a suitably calculated  $H$  matrix is passed to the filter. This approach leads to a reduced processor loading, without compromising performance during manoeuvres. The effect is equivalent to a series of updates at the 1 Hz data rate of the GPS receiver. An additional advantage of the use of a pre-filter is that it allows a form of batch processing. Advantage may be taken of this to help reject bad data.

## 7. ANCILLARY ALGORITHMS

These include reasonability checks, to exclude spikes from the Doppler/GPS data; a validity check to determine Doppler/GPS status (up or down). When down, the state covariance matrix  $P$  is propagated with no updates. Lever arm corrections allow for turns of the aircraft; the INS and Doppler antennae are separated by a few feet, the IMU and GPS antennae by rather more. Data synchronisation between the INS and GPS is performed by a Synchronise Mode Command transmitted over the 1553 bus. Finally control logic links the various algorithms.

## 8. IMPLEMENTATION ALGORITHMS

The filter equations were translated into the U-D form of reference 10.

## 9. SOFTWARE TESTING

A variety of tests were applied to the software during integration. These tests culminated in lab tests, with simulated Doppler data for the Doppler/INS filter, and trials on a moving platform, for the GPS/INS filter. The latter were particularly useful, to gain confidence for the first flight trials.

## 10. FLIGHT TRIALS RESULTS

### 10.1 DOPPLER/INS FILTER

Extensive flight trials have been performed, initially over land, and later over sea. The latter presents special difficulties due to the environmental errors that Doppler radar is subject to. Disturbances seen on the Doppler

reference include low frequency effects, due to variations in wind and bulk water motion, and also some evidence of oscillatory behaviour. Figure 3 shows results from a typical flight over sea. This was performed over in-shore waters, and was subject to wind induced, and bulk sea motion errors. Turns of up to 180° degrees were performed.

## 10.2 GPS/INS FILTER

A series of flight trials have been performed. These include alignment on the ground using the air align mode, alignment commencing on the ground and completed in air, and full in-flight restarts of the INS, using attitude mode as a precursor. Trials have been conducted over a range of latitudes, from 35 degrees north to 65 degrees north.

The mode sequences were as follows;

- Full GC align (on ground) followed by air align mode.
- Short (1 minute) GC align mode (on ground) followed by air align.
- Attitude mode (in flight) followed by air align.

Table 1 summarises results logged. Generally FOM was variable, and the velocity errors as well as position errors varied. Tilt errors were a fraction of accelerometer biases. Heading errors were approximate estimates, but were of the order expected. Times to align were variable, depending on the GPS accuracy at the time. Aircraft manoeuvres did not occur, in general, during the alignment phases, but buffeting, which would have aided alignment, was seen to have a beneficial effect in one case.

The conclusions from these flights of the GPS/INS filter are that the system is aligning very accurately in flight. Flight tests are continuing at the time of writing (May 1993) with the A&AEE Boscombe Down Comet aircraft, with the GPS/LINS system on board, on an intensive period of flight testing in the USA.

## 11. CONCLUSIONS

BASE have demonstrated operation of LINS 300 with both Doppler/INS and GPS/INS filters in flight, including in-flight restarts. The former has involved extensive flight trials, and is embodied in production LINS units. The latter is still undergoing flight trials, but has shown excellent performance. This performance provides a firm basis for future production orders.

## 12. FUTURE DEVELOPMENTS

Future developments include a LINS 300 interfaced with a GPS receiver, a Doppler radar, and BASE's TERPROM™. The latter is a terrain reference navigation system, already in the USAF F-16 inventory.

With this configuration the Doppler provides an autonomous alignment reference over land and sea, the GPS provides a non-autonomous but highly accurate alignment reference over land and sea, and terrain reference navigation provides a covert, highly accurate reference, with the added benefit of ground collision avoidance, and terrain following over digitally mapped land. Thus the three air alignment sub-modes are complementary.

## 13. ACKNOWLEDGEMENTS

BASE would like to thank the MoD EH101 project office for its sponsorship, Westland Helicopters Ltd, Racal Avionics, Cossor and the Canadian Marconi Company for their help in the development of these systems, and Westlands and A&AEE Boscombe Down for flight trials and data processing.

## REFERENCES

1. Product Specification for the EH101 Inertial Reference Unit. PS294504-0100. BASE, Plymouth.
2. Requirement Specification for the Inertial Reference Unit for the EH101 helicopter. EB34E024W. Westland Helicopters Ltd, Yeovil, & Agusta, Italy.
3. Velocity Errors and Correction Methods for the EH101 Doppler 91E. AO22SY/DVE-001. Racal Avionics Ltd.
4. A Comparison of two Approaches to Pure-Inertial and Doppler-Inertial Error Analysis. D.O.Benson. IEE Transactions on Aerospace and Electronic Systems vol AES-11 No 4. July 1975.
5. The General Error Model for a Strap-down Inertial Navigation System. TN3586. BASE, Plymouth.
6. LINS 300 Error Budgets. TN3179. BASE, Plymouth.
7. Stochastic Models, Estimation, and Control. P.S.Maybeck. Academic Press.
8. Stochastic Processes and Filtering Theory. A.H.Jazwinski. Academic press.
9. Application of Kalman Filtering to the C-5 Guidance and Control System. Agardograph 139. 1970.
10. Factorization Methods for Discrete Sequential Estimation. G.J.Bierman. Academic Press.

**TABLE 1 SUMMARY OF ARIES GPS/INS FLIGHT RESULTS**

VELOCITY ERRORS AFTER ALIGNING [Ft/s]	FOM	TILT ERRORS [micro rads]	HEADING ERROR [degrees]
0.25, -0.42	2	***	***
0.16, 0.11 -0.03, 0.10	> 3 1	12, 13	0.04
0.45, 1.02	***	***	< 0.05
0.62, -0.80	***	6, 20	***
-0.09, 0.00	***	***	***
ALIGN TIME [minutes]			
11	FOMs of 2 and 3 occurring. FOMs of 1 and 2. FOM of 1. FOM of 1, and > 3 briefly. FOM *** FOM > 3 at times.		
9			
6			
8			
8			
12			

\*\*\* Denotes data awaiting trials analysis.

**TABLE 2 DOPPLER ERRORS**

**LAND**

FIXED            SF, BIAS, MIS  
MANOEUVRE       SF  
SURFACE           SF

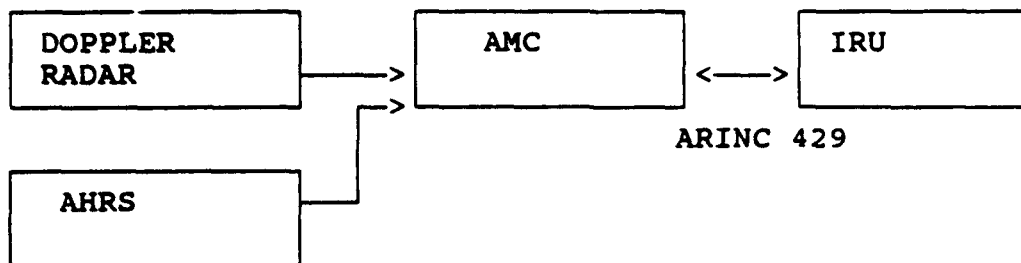
**SEA**

FIXED            SF, BIAS, MIS  
MANOEUVRE       SF  
SURFACE           SF  
BWM               MARKOV  
CWM               MARKOV

SF       denotes Scale Factor errors.  
MIS      denotes Misalignment errors.

**FIGURE 1 NAV SYSTEM OVERVIEW**

**DOPPLER/INS FILTER**



**GPS/INS FILTER**

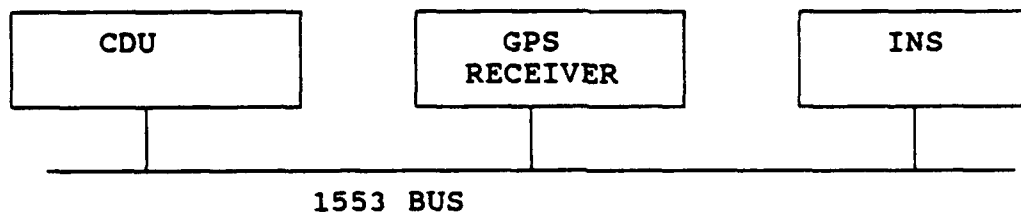
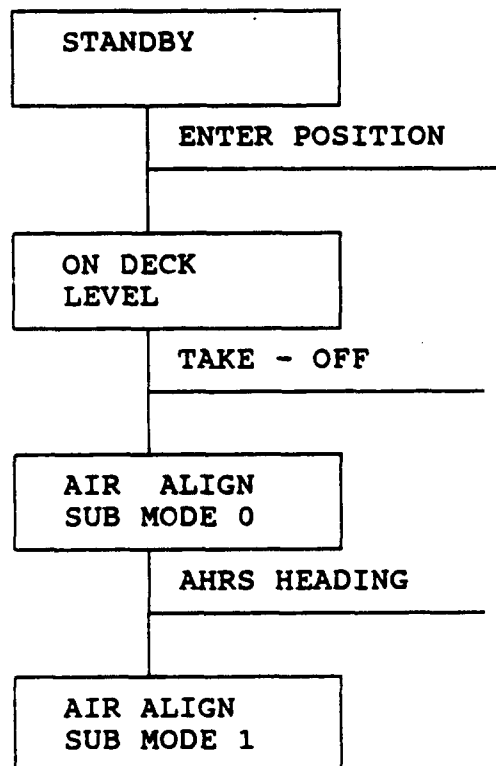


**FIGURE 2 TYPICAL MODE SEQUENCES**

**DOPPLER/INS FILTER**



**GPS/INS FILTER**

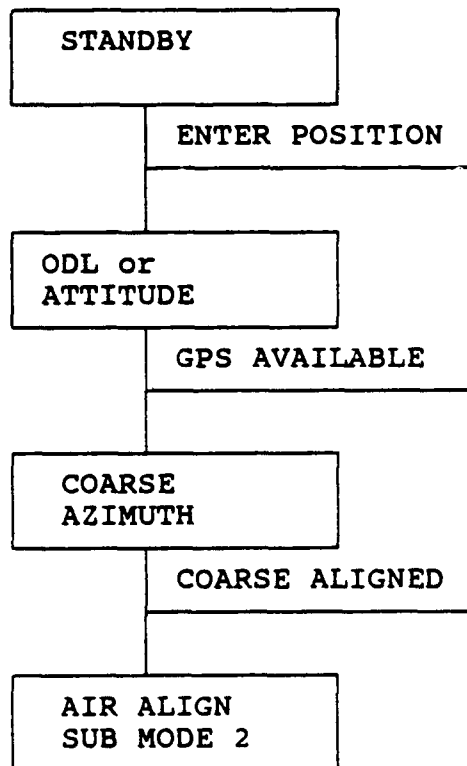
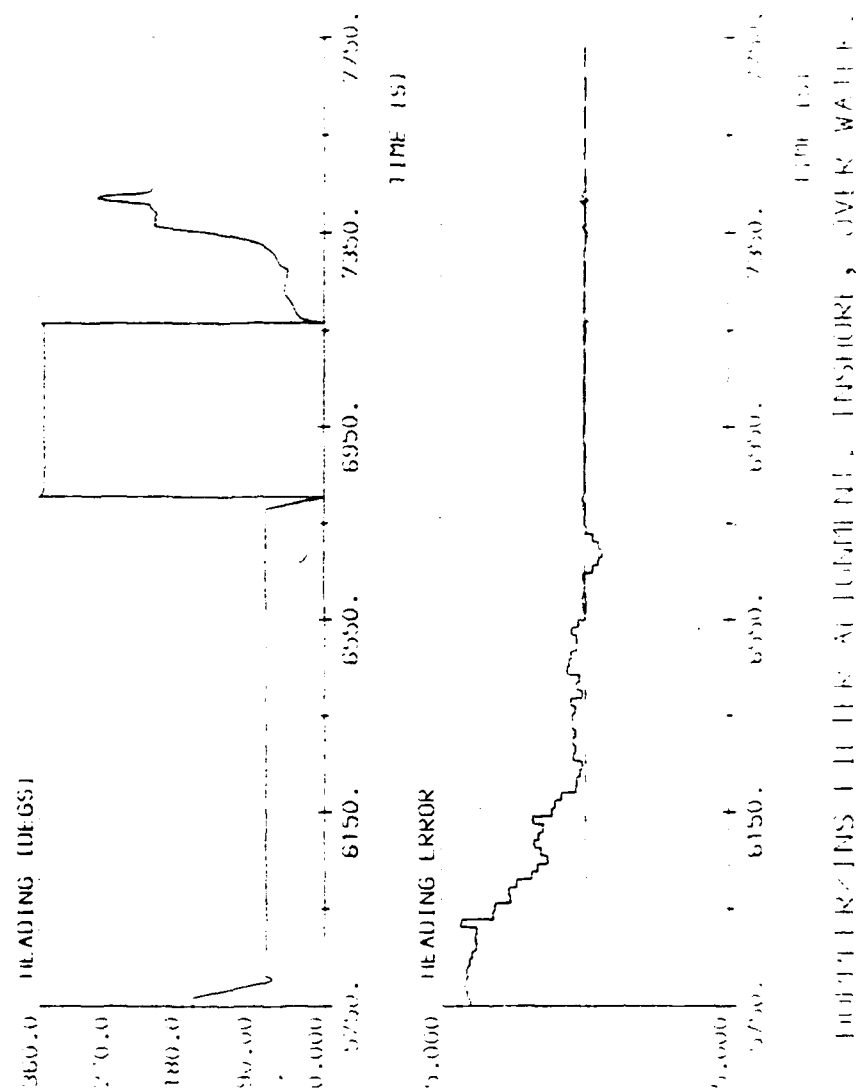


**FIGURE 3 DOPPLER/INS TRIALS RESULTS**



**SESSION IX-B**

**GPS TESTING**

***CHAIRMAN***

**Maj JOSEPH T. SANFORD**

***LOS ANGELES AFB CA***



**THIS PAGE LEFT BLANK INTENTIONALLY**

# **Test and Evaluation Status of the Honeywell H-764G Embedded GPS/INS at CIGTF**

By

Joseph J Elchynski  
Systems Engineer, Navigation Products Engineering  
Honeywell Military Avionics Division  
11601 Roosevelt Blvd.  
St. Petersburg, FL. 33716-2202  
Phone (813) 579-6230

and

Dave Syse  
Test Analyst, 6585th Test Group  
Central Inertial Guidance Test Facility  
Holloman Air force Base, New Mexico

Approved for Public Release; distribution is unlimited.

## **BIOGRAPHIES**

Joseph J. Elchynski is a systems design engineer at the Guidance and Navigation operations of Honeywell's Military Avionics Division in St. Petersburg, Florida. He has eight years experience in navigation systems integration and development along with field support testing at various sites around the world. Mr. Elchynski holds a B.S. in Electrical Engineering Technology from Old Dominion University (1985).

Dave Syse is an Analyst at the Central Inertial Guidance Test Facility (CIGTF). He has approximately two years experience in navigation systems analysis. Mr. Syse has Bachelors degrees in Math, Physics, and Civil Engineering.

## **ABSTRACT**

In 1991 Honeywell's Military Avionics Division began producing the H-764G, the first truly Embedded Global Positioning System Inertial Navigation System (EGI). This system contains the features deemed necessary for most military applications today including: a standard 7x7x11 inch modular design that includes a 1553B bus and a spare expansion slot for program-specific requirements, an authorized six-channel L1/L2 P-Code Embedded Global Positioning System (GPS) Receiver (EGR) with 16 meter Spherical Error Probable (SEP) position accuracy that is unclassified when keyed, inertial sensors that provide 1 nmi/hr Circular Error Probable (CEP) free inertial performance unaided, and a Upper-Diagonal (UD) Kalman filter that integrates the inertial sensor data with the GPS raw pseudo range and delta range measurements to produce a robust hybrid navigation solution. In early 1992, H-764Gs were delivered to various military avionics-related organizations for independent evaluation and test. The Central Inertial Guidance Test Facility (CIGTF) at Holloman Air Force Base, New Mexico, hosted two very significant test programs on the H-764G. The first test program was conducted for a H-764G customer with the primary objective being functional and performance verification testing. The second test program was conducted for the Department of Defense (DoD) for concept demonstration of current EGI systems.

This paper concentrates primarily on the test and evaluation aspects of the two CIGTF EGI test programs completed on the H-764G in 1992. More specifically, a brief system overview and modes of operation description are included, followed by details and results on some of the CIGTF EGI test cases performed. In addition, upcoming future enhancements are discussed.

## **INTRODUCTION**

The H-764G Honeywell EGI system is the result of a multi-year Internal Research and Development (IR&D) program that combined the technologies created on a variety of related IR&D projects. The three most significant technologies that made the EGI system a reality were the advancements made in Ring Laser Gyro (RLG) strapdown INS, GPS receiver design, and the Upper-Diagonal (UD) Kalman filtering technique. Honeywell successfully miniaturized the 1 nmi/hr class INS by more than a factor of two through the development of a state-of-the-art GG1320 RLG that is less than one-quarter the size and weight of its predecessor with comparable performance. Reduction of the INS circuit card assemblies was achieved through the incorporation of Large Scale Integrated Circuits (LSICs) and gate arrays. GPS improvements

also included miniaturization of circuitry using LSICs along with improved GPS signal processing techniques. The EGR processes the satellite signals digitally prior to any code removal and under processor control. The UD Kalman filter technique using Bierman's UDU<sup>T</sup> factorization ensures numerical stability and improved efficiency of computation time. This allows for a robust core GPS/INS Kalman filter mechanization with room for additional application-specific filter states. GPS/INS integration studies proved that a synergism existed between both systems when GPS measurements (pseudo range, delta range) and inertial sensor measurements are processed in a tightly integrated centralized navigation filter. The resulting integrated navigation solution is more accurate than either the GPS or INS stand-alone navigation solutions and can be used to enhance GPS tracking.

The Honeywell H-764G EGI system, currently in low-rate initial production with full block II production in 1994, has been delivered to several government agencies. This current availability of flight worthy EGI systems subsequently led to DoD sponsored test programs at several government test facilities. Because of CIGTF's diverse resources, capabilities, and background in testing navigation systems, its facility tested EGI systems and consequently the H-764G on two separate occasions. The first test program was a functional and performance verification test program for an H-764G customer. The second was an Air Force sponsored test for EGI concept demonstration to verify that existing EGI systems can meet the DoD's current and future requirements for "complementary aiding" small integrated navigation systems. The CIGTF testing included a broad spectrum of test scenarios using the lab, van, and flight test capability. This paper contains CIGTF flight test results from both test programs that represent typical EGI performance.

### **H-764G SYSTEM OVERVIEW**

The H-764G EGI systems delivered to CIGTF were built on the Honeywell production line in 1992. The H-764G is designed around a small (7x7x11 inches), light weight (22 pounds), low power (55 watts), medium accuracy (1 nmi/hr) RLG navigator and six channel P-code EGR. Figure 1 is a photograph of a H-764G that accurately represents the EGI systems tested at CIGTF with the baseline system characteristics listed below:

<u>POSITION ACCURACY</u>	
Pure inertial(CEP)	<1.0 nmi/hr
GPS/INS (CEP)	<10 m
<u>VELOCITY ACCURACY</u>	
Pure inertial(RMS)	<1.0 m/s
GPS/INS (RMS)	<0.03 m/s
<u>ALIGNMENT TIME</u>	
Gyro Compass	4 minutes
Stored Heading	30 seconds
In-Air-align	<8 minutes

### OPERATING RANGES

Angular Rate	>600 deg/sec
Angular Acceleration	>2,000 deg/sec/sec
Acceleration	20 g's (all axis)

The H-764G contains an Inertial Sensor Assembly (ISA) equipped with three Honeywell GG1320 RLGs, three Sundstrand QA2000 accelerometers and associated sensor electronics. The ISA provides the autonomous inertial measurements (angular rates and linear accelerations) to the EGI navigation processing.

The EGR contained within the H-764G is a six-channel L1 and L2, fast acquisition, authorized P(Y) code receiver using a DoD approved Precise Positioning Service Security Module (PPS-SM). It is a GPS satellite sensor that measures pseudo-range and delta range for use in the integrated hybrid navigation solution and is also an independent navigation subsystem that derives a "GPS only" Position Velocity and Time solution (PVT) to provide fault isolation/tolerance between the EGR and EGI.

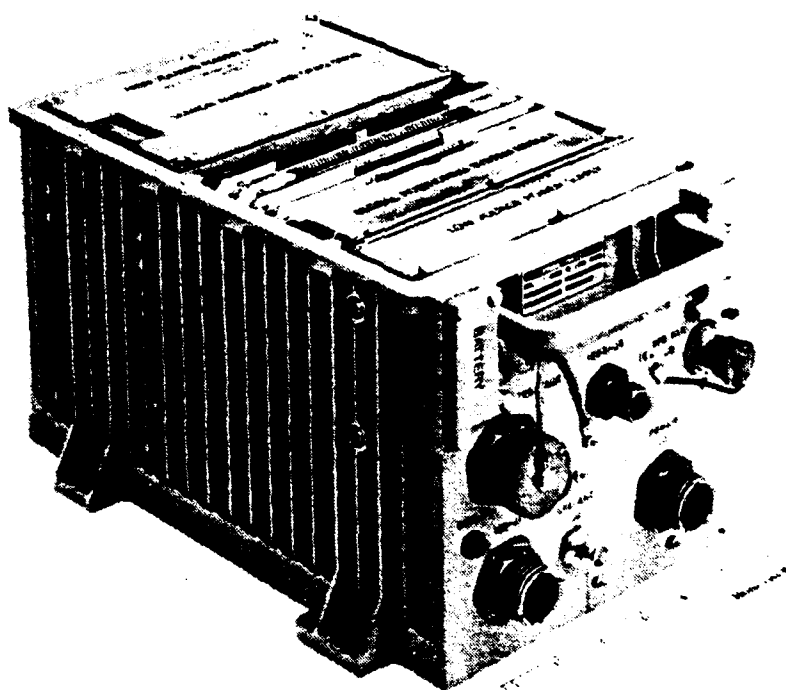


Figure 1. The Honeywell H-764G

The remaining subassemblies are the Navigation/Inertial Processor (NIP), the Low Voltage Power Supply (LVPS) and the 1553B Input/Output (I/O) interface.

The H-764G system mechanization is a tightly coupled EGI configuration. The EGI three-dimensional UD Kalman filter is capable of processing up to six pseudo range and delta range observations from the EGR. It also processes zero velocity, altimeter and waypoint observations when available. When the EGI is processing four or more pseudo range and/or delta range measurements, the EGI operational status is defined as "full GPS/INS navigation." In this state of operation the EGI velocity accuracy is better than stand-alone GPS, and the position accuracy is equivalent. The EGR can also accept the precise EGI navigation solution and use it to aid the GPS tracking loops, which is defined as "EGI aided receiver tracking" mode. In this mode the EGR tracking function provides a higher jamming immunity and a faster reacquisition capability to the EGI. The block diagram in Figure 2 illustrates the baseline EGI architecture along with the external interfaces.

The H-764G external interfaces support all necessary GPS and Inertial Navigation System (INS) functions. The EGI 1553B was the primary interface to the CIGTF test instrumentation data collection system for both EGI and EGR evaluation. A KYK-13 interface was available for easy key loading in an unclassified environment. The EGI contains an RF interface that was connected to the CIGTF Radio Frequency (RF) antenna subsystem. A dedicated EGR RS-422 test port was also available for independent EGR test.

The primary operating modes of the H-764G are initialization, inertial align and navigation. The primary tasks performed in the initialization mode are startup Built-In-Test (BIT) routines and user input of present conditions. Because the EGR used in the H-764G contains a fast search implementation that allows cold search-the-sky acquisition, initialization with initial coordinates and time is optional (except for low signal environments). Once the EGR is tracking four satellites and is navigating, an inertial align is initiated using GPS position. If initial coordinates are entered the align is accomplished in conjunction with GPS normal acquisition, thus shortening the total time required to enter navigation mode.

## H-764G EMBEDDED GPS/INS BLOCK DIAGRAM

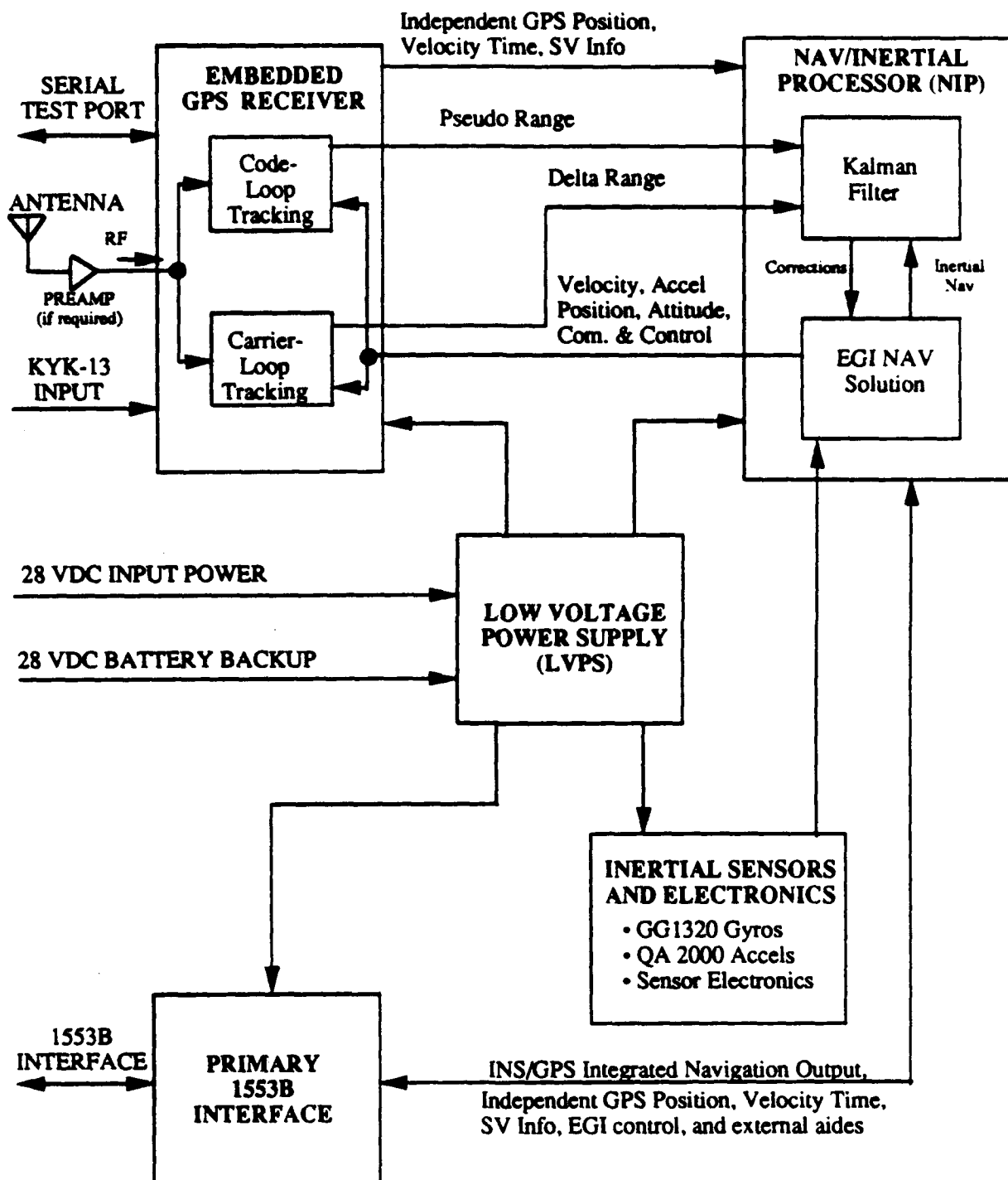


Figure 2

The primary purpose of inertial align is to determine attitude and reduce initial velocity errors to allow system performance within the required accuracy. The H-764G contains the following inertial alignment types: normal ground, stored heading, in-flight, and fast GPS-aided hybrid align. The normal ground align is a gyrocompass align using standard strapdown INS techniques and is the default align type. The typical ground alignment time is 4 minutes to achieve less than 1 nmi/hr CEP navigation performance. The stored heading align uses "stored heading" from the previous orderly shutdown to accomplish a fast 30 second alignment before transition into navigation. The In-Flight-Align (IFA) mode is available when an alignment is required while in motion. In this mode, attitude and velocity errors are estimated in the Kalman filter using the GPS measurements. IFA duration varies with vehicle trajectory but typically requires less than 8 minutes of "full GPS coverage" to achieve required performance levels. The fast GPS-aided hybrid align is a combination of ground alignment and GPS-aided IFA. In this type of align the H-764G is allowed to engage full GPS tracking and complete coarse ground align (typically 30 seconds) while the vehicle is stationary to receive an initial EGI GPS position fix, coarse attitude, and heading estimations. Then the pilot may set the "in-motion" flag, which switches the alignment to IFA, and start the mission. The Kalman filter will then use the GPS measurements to complete the inertial align while the aircraft is "in-motion" (taxing or in-flight). What typically occurs is that the combination of heading changes (typical of runway taxis) and GPS aiding results in rapid heading convergence and subsequent full navigation performance, before the pilot takes off. When full GPS coverage is available this type of align is ideal for rapid deployment scenarios. If GPS coverage is not available the stored heading option is always available.

The navigation performance of the H-764G varies depending on the availability and quality of observations at any given time because of external conditions such as satellite geometry, antenna shading, jamming, and high dynamics. The navigation performance of the H-764G is enhanced by GPS even when tracking fewer than 4 satellites and bounded by the inertial drift rate when no satellites are available. In many scenarios the tightly coupled H-764G performance is superior to both the stand-alone GPS or INS under the same set of external conditions. The H-764G CIGTF flight test results herein disclose some of the external conditions where the performance of a tightly coupled EGI stands out over the performance of its stand-alone GPS and INS counterparts.

#### **CIGTF EGI FLIGHT TEST CAPABILITIES OVERVIEW**

The core CIGTF test support equipment for EGI flight testing comprised two reference systems and an EGI test/instrumentation system. Equipment was organized on convenient removable racks so test support equipment could be checked with the H-764G in a lab and van environment to establish the adequacy of test procedures and functional operation of the EGI as a precursor to flight testing. A C-12 and C-141 cargo aircraft served as test beds for the flight tests.

The two reference systems used for Time Space and Position Information (TSPI) were the Completely Integrated Reference Instrumentation System (CIRIS) and Differential GPS. The CIRIS hardware includes a government furnished inertial navigator aided by barometric altitude from an air data computer, and a precision Cubic CR-100 interrogator radio range/range-rate system that uses transponders located on the ground at surveyed locations to provide coverage



along predetermined flight paths. The CIRIS accuracy is principally dependent on the range/range-rate measurements obtained from the interrogator. A set of eight transponders nearest the current aircraft location is used to provide data in a time-phase triangulation scheme. CIRIS degradation can occur when flight paths leave areas of radio range coverage and during antenna shading that can occur during take off and landing. The Differential GPS reference system generates TSPI data using the Holloman Satellite Reference Station (SRS) and a government furnished GPS receiver set aboard the test bed. The SRS and GPS receiver data are processed post-test to remove errors introduced by the space and control segments of the GPS. The differential GPS accuracy is dependent on the Geometric Dilution Of Precession (GDOP) and on the accuracy of the fitted ionospheric and observed range errors. The optimum (1 sigma) accuracy of CIRIS and typical accuracy of differential GPS is shown in Table 1.

Table 1. Reference System Accuracy

	Position (3 axis 1 $\sigma$ ft)	Altitude (feet)	Velocity (3 axis 1 $\sigma$ ft/s)	Attitude (arc min)
<b>CIRIS (optimum)</b>	13	40	0.1	6.0
<b>D-GPS (typical)</b>	6	6	0.3	Not available

The EGI test/instrumentation system was the primary interface to the H-764G for EGI control, display and data record. It consisted of a flight worthy computer with a removable hard drive and 1553B interface card. The CIGTF test and instrumentation group designed the unique software for the EGI test/instrumentation system to communicate with the H-764G and execute the required test functions.

Flight data from both the reference systems and the EGI were loaded and then processed on a mainframe for post-flight analysis. Comparison plots were generated using the accurate "UTC time of solutions" for EGI to reference system time tagging. An independent government furnished GPS receiver was also included and used as a control item for comparative results.

#### **H-764G CIGTF FLIGHT TEST RESULTS**

Between the two H-764G CIGTF test programs an extensive amount of flight tests was conducted under a wide variety of conditions. H-764G flight tests performed at CIGTF included: full GPS coverage EGI, independent EGR, limited coverage EGI, EGI/ independent EGR satellite signal reacquisition, Pure inertial, GPS aided IFA, and EGI/ independent EGR maneuver jamming. The testing completed at CIGTF on the H-764G was very encouraging and disclosed the benefits and current need for integrated systems like the H-764G EGI in the military fleet. The overall performance demonstrated that it could function as a navigator accomplishing the requirements of both types of systems with the added bonuses associated with complementary aiding. Highlights from some the CIGTF H-764G flight test results are described as follows:

### Full GPS Coverage EGI Flight Conducted on February 2, 1993

**Test Procedures.** The test began on the ground over a surveyed benchmark. Following a GPS-aided gyrocompass alignment, the C-141 aircraft departed the benchmark with the H-764G in full GPS coverage EGI navigation. The flight test results shown herein were from about one hour of the flight when the aircraft was flying level with a ground speed of approximately 250 m/s. The aircraft heading is shown in Figure 3. The reference system used was CIRIS.

**Test Results.** The GPS PDOP and EGI 3-D position error are shown in Figure 4. The position errors are consistent with typical GPS position performance as expected. The velocity errors are shown in Figure 5. The results illustrate some of the difficulties associated with testing accurate EGI systems. Portions of the errors shown in the position and particularly the velocity error plots are probably attributed to time tagging, lever arm and reference system errors and are not real, which makes analysis difficult. Some of the EGI north velocity errors appear to be correlated with the CIRIS heading. The EGI velocity errors appear to be less than stand-alone GPS velocity errors; however, due to the magnitude of the CIRIS velocity sigmas, also shown in Figure 5, it is impossible to discern any definitive conclusions.

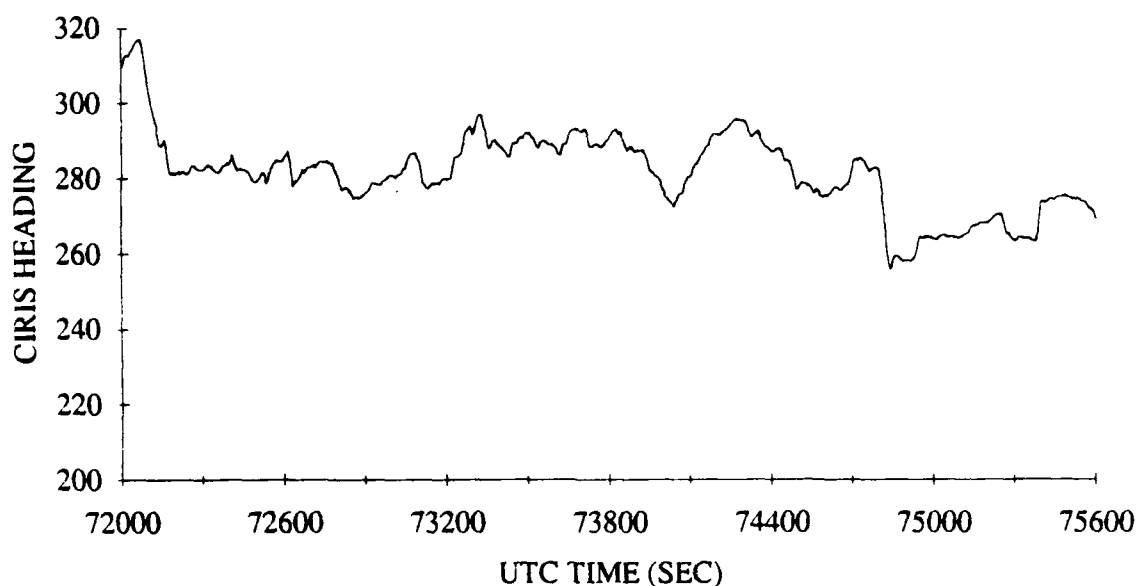


Figure 3 CIRIS Heading for Full GPS Coverage Flight

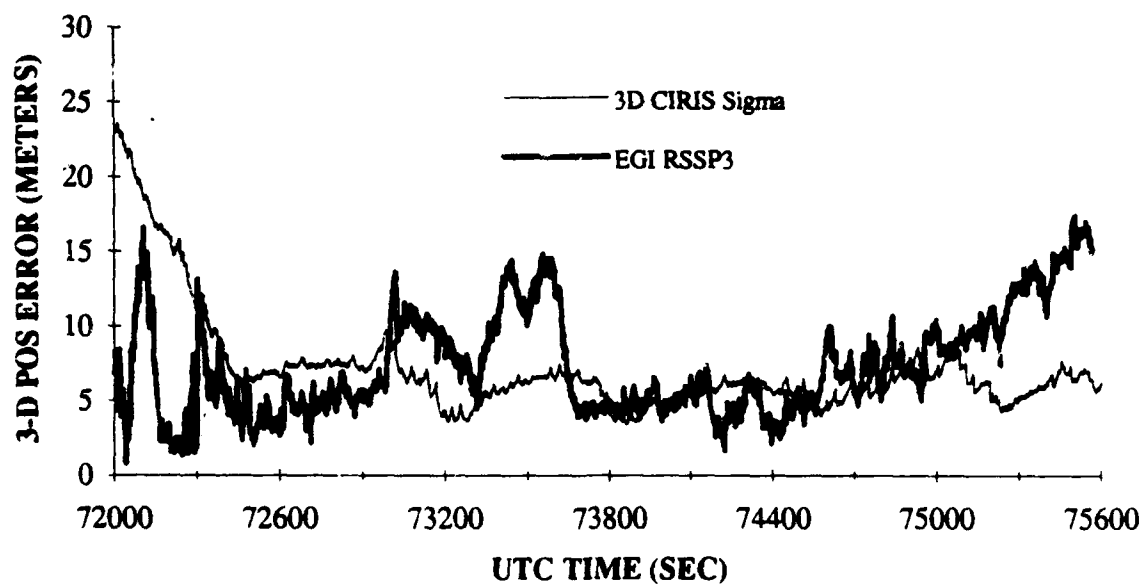
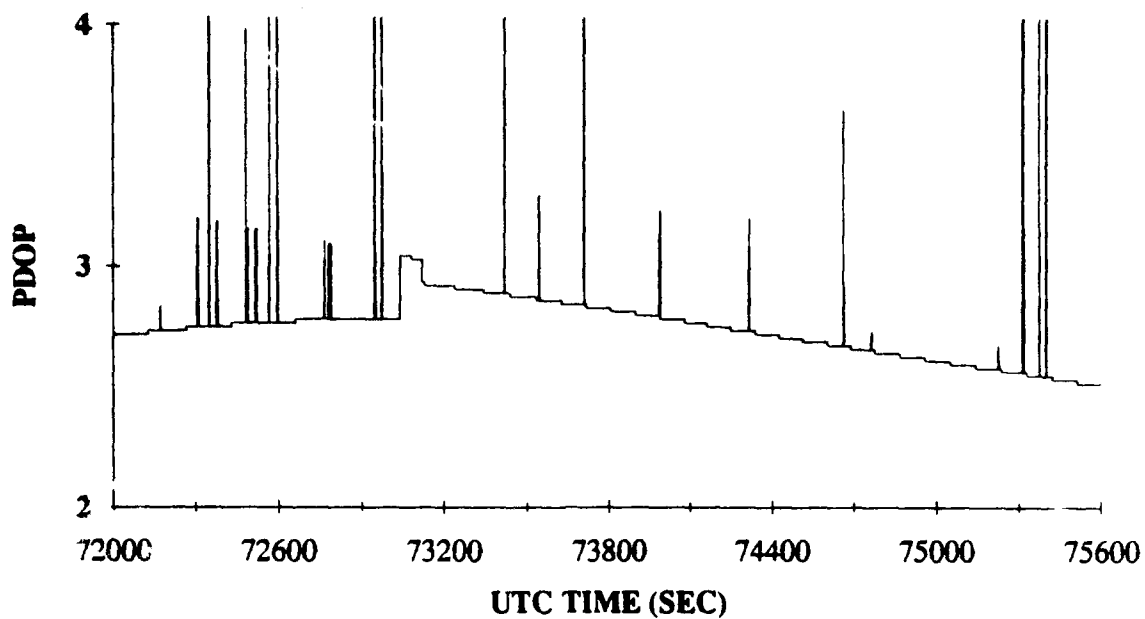


Figure 4. H-764G PDOP and 3-D Position Error for Full GPS EGI Flight

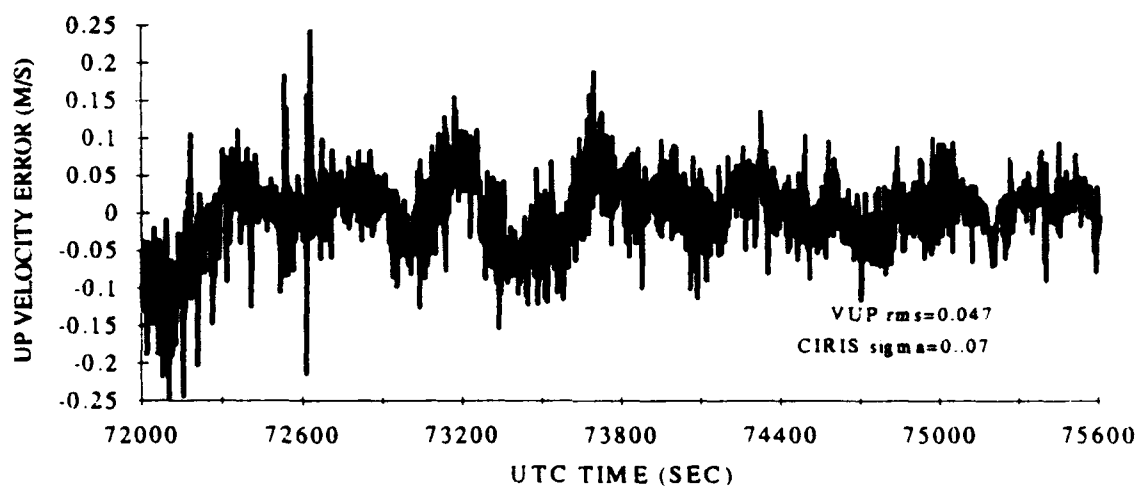
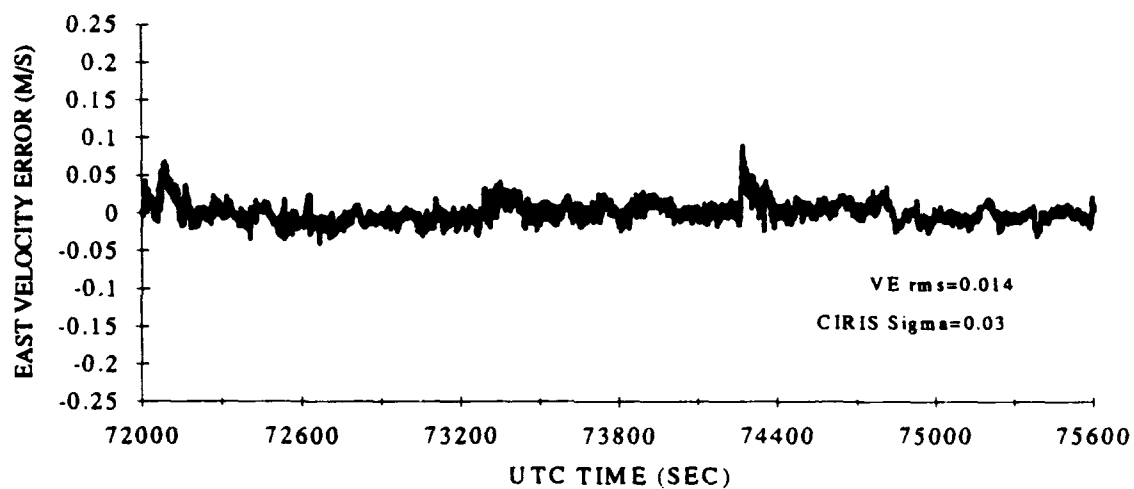
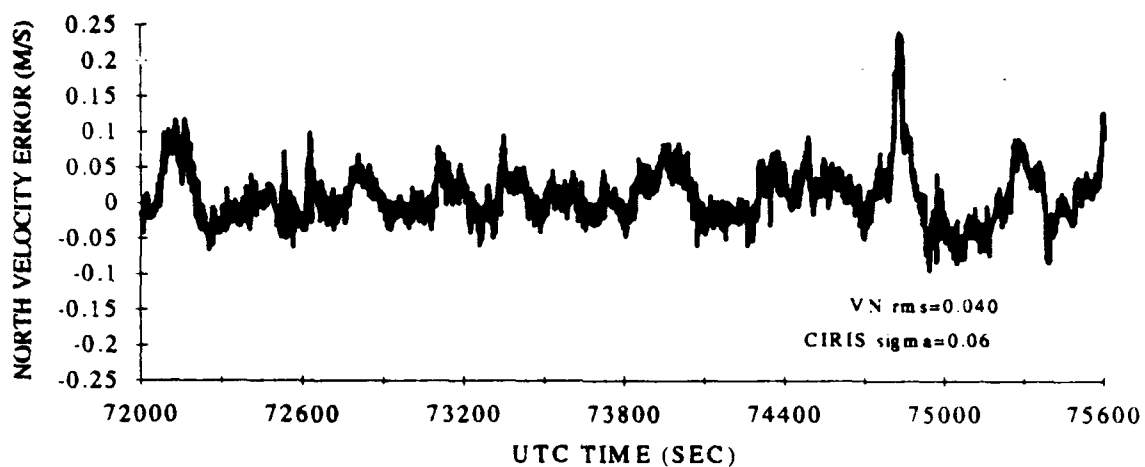


Figure 5. H-764G Velocity Errors For Full GPS EGI Flight

### Free Inertial Flights Conducted January 15 through 29, 1993

**Test Procedures.** Free inertial flight tests began on the ground over a surveyed benchmark. Following a gyrocompass alignment at a true heading of approximately 0 degrees, the C-141 aircraft departed the benchmark with the H-764G in free inertial navigation. At approximately 30 minutes into navigation the aircraft reached a cruising altitude of approximately 30,000 feet and flew in a westerly direction for the remainder of the test. The H-764G was altimeter-aided for the duration of the flight. CIRIS was the primary reference system used.

**Test Results.** Table 2 contains the composite position and velocity performance from the six flights. The results are consistent with the less than 1 nmi/hr navigator design requirements of the H-764G. The RSS data generated from these flights were used to calculate the 50th percentile of radial position errors as defined in AIR STD 53/16A. The growth rates were then generated by fitting a straight line, zero intercept model to the errors.

Table 2. H-764G Composite Position Error Growth (CEP) and Horizontal RMS Velocity Error from six Free Inertial Flights

TIME (MINUTES)	R(50) RADIAL ERROR GROWTH (NM/HR)	COMPOSITE RMS EAST VEL. ERROR (F/S)	COMPOSITE RMS NORTH VEL. ERROR (F/S)
42	0.68	1.05	1.61
60	0.74	1.54	1.77

### GPS Aided In-Flight-Align Conducted on December 3, 1992

**Test Procedures.** This IFA test was conducted in the C-141 at an altitude of approximately 30,000 feet under straight and level flight conditions at a ground speed of approximately 100 m/s. All power was removed from the H-764G and the GPS antenna was connected. The H-764G was then turned on with absolutely no initial condition except for an input discrete that indicated in-motion conditions. Shortly after turn-on the H-764G EGR completed a cold search-the-sky acquisition and then the IFA sequence began. The H-764G was allowed GPS coverage for approximately 12 minutes from turn-on. Then the GPS antenna was removed at UTC time of 70,800 seconds to initiate free inertial navigation along with altimeter-aiding for the duration of the flight. The reference system used was CIRIS.

**Test Results.** Figure 6 shows the radial position error plot of the free inertial portion after the IFA was completed. The excellent free inertial performance demonstrates the H-764G's unique capability to internally self-initialize and navigate complete with accurate attitude outputs without any external aiding inputs from other onboard avionics.

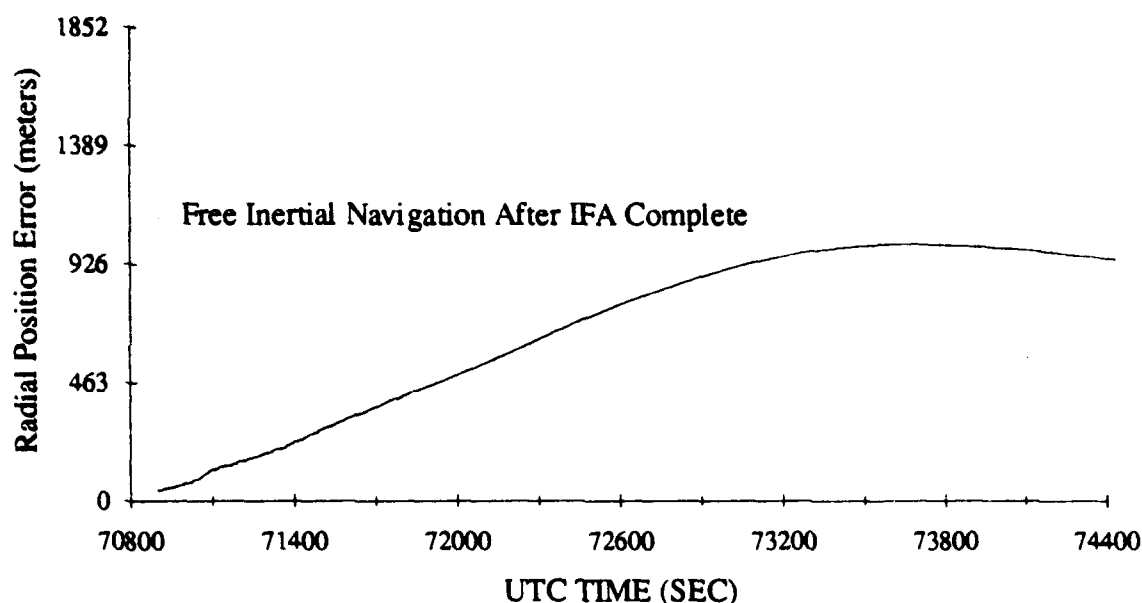


Figure 6. H-764G IFA Flight Test, Free Inertial Position Error Growth After IFA & Antenna Disconnect

#### Limited GPS Coverage EGI Flight Test Conducted on August 8, 1992

**Test Procedures.** This Limited GPS coverage test was conducted on the C-12 flying in a Racetrack profile. The H-764G's GPS coverage was deliberately limited to fewer than four satellites throughout the test to determine the performance of the tightly integrated EGI when operating with an under-determined GPS solution. The reference system used was CIRIS. The H-764G was altimeter aided. The detailed test procedures are as follows:

- Align at the surveyed benchmark with full GPS coverage
- Command the H-764G to manually track only three satellites then depart the surveyed benchmark and proceed along the flight profile
- After 70 to 75 minutes of three satellite navigation is completed, revert to full coverage for approximately eight minutes
- Command the H-764G to manually track only one satellite and continue navigating for another 70 to 75 minutes
- After completion of one satellite navigation, revert to full GPS coverage again for eight minutes
- Command the H-764G to manually track two satellites for the remainder of the run.

The maneuvering aspects of the flight are gleaned from the CIRIS roll and pitch plot shown in Figure 7. The average groundspeed during the flight was approximately 100 m/s.

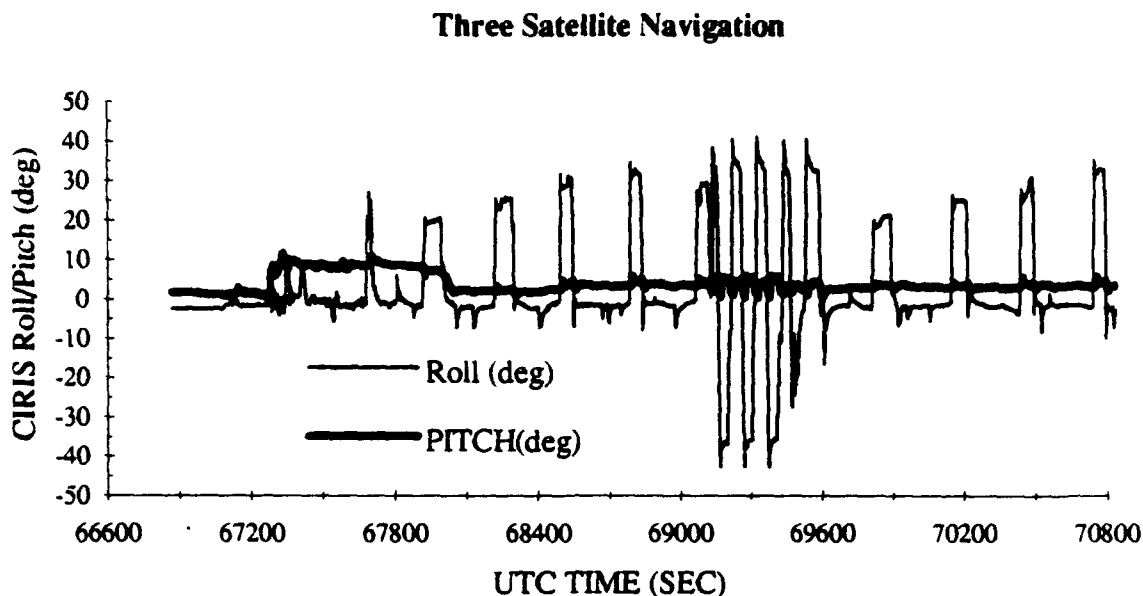


Figure 7. CIRIS Roll/Pitch for Limited GPS Coverage EGI Flight Test

**Test Results.** The Horizontal EGI RPE results along with the number of valid satellite vehicles in the solution (SVs Valid) of the H-764G limited GPS coverage flight tests are shown in figure 8.

The three satellite coverage portion produced a position solution that was bounded by the three tracking satellites. The blank spot shown in the RPE plot from UTC time 67150 to 67800 is due to degraded CIRIS reference data that is typical during take off and landing. The 200 meter error seen shortly after aircraft ascent may have been induced by the altitude change and/or altimeter error. It was later discovered that there was a three second lag in the altitude data input to the H-764G. Throughout the course of the three satellite coverage the EGI navigation filter was able to eventually estimate out most of this error. The occasional satellite coverage dropdowns were probably due to wing tip shading during the maneuvers.

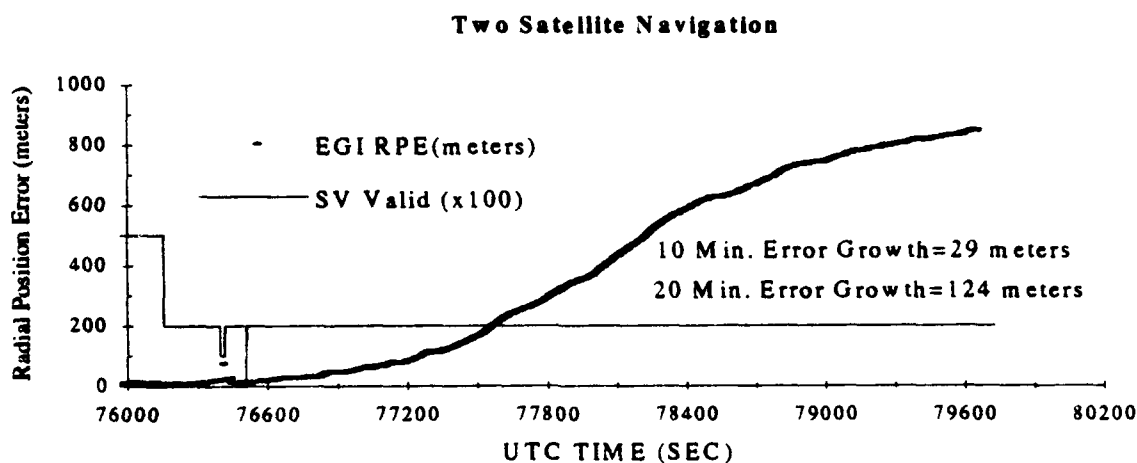
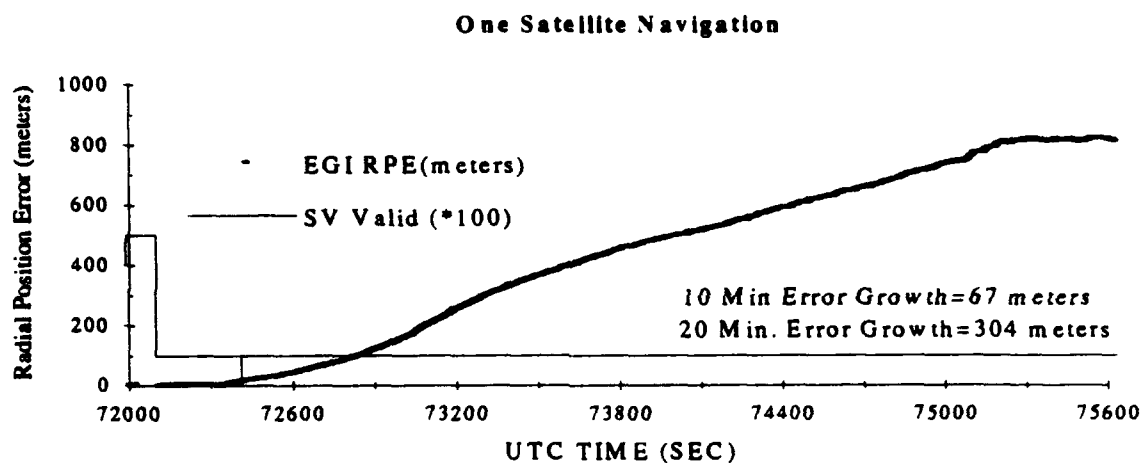
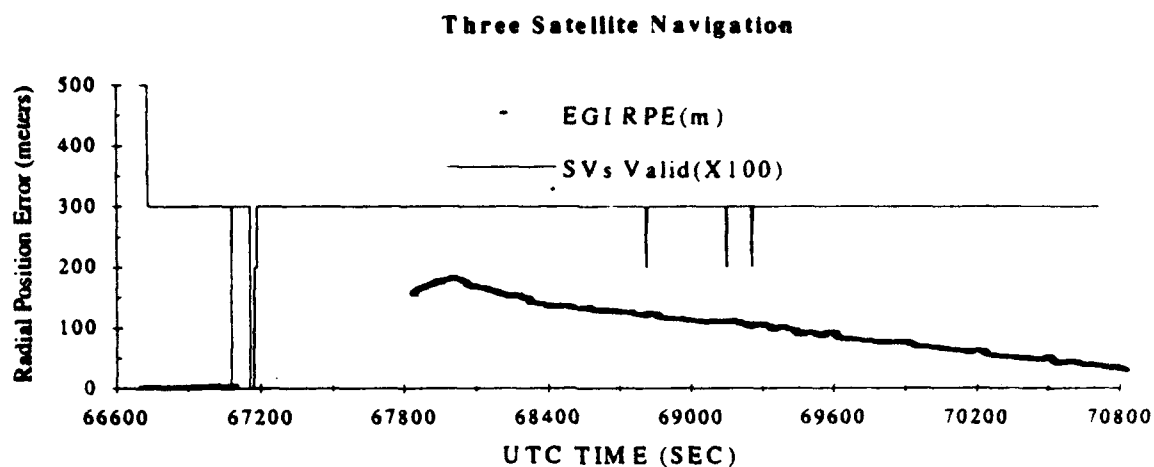


Figure 8. H-764G Horizontal Position Error and Number of Satellites Tracked for Limited GPS coverage EGI Flight Test



One satellite coverage EGI horizontal position performance relative to EGI free inertial performance is negligible especially when tracking a high elevation satellite. The one satellite horizontal performance of this test produced an error growth that mimicked a good free inertial test.

Two satellite coverage horizontal performance is typically better than EGI free inertial performance. The two satellite horizontal performance of this test produced an error growth that was exceptional during the first 30 minutes of the test. Two satellite coverage horizontal error growth rates are driven predominately by the relative two satellite geometry and the unmodelable GPS clock drift and can vary widely.

The overall results of the H-764G Limited coverage flight tests demonstrated that a tightly integrated EGI provides a navigation solution that is significantly better than free inertial performance when tracking as few as two satellites. This enhancement is only achievable in a tightly coupled EGI and is very useful for applications that demand superior navigation performance in harsh GPS coverage environments such as signal jamming, high dynamics, and shading.

### **EGI Aided Receiver Tracking Reacquisition Tests**

**Test Procedures.** The tests began on the ground over a surveyed benchmark. Following a gyrocompass alignment, the C-141 aircraft departed the benchmark at CIGTF with the H-764G in full GPS coverage EGI navigation and climbed to a cruising altitude of 30,000 feet. After a pre-determined period of full GPS coverage, GPS coverage was denied for a five minute interval. After 15 minutes of flight with full GPS tracking regained, GPS coverage was denied again for a 10 minute interval. The GPS outages were scheduled such that the aircraft maintained the same heading or made a 180 degree heading change during the outage. Reacquisition times were measured from the time the GPS antenna was reconnected to the time four satellites tracked was indicated.

**Test Results.** The results of the H-764G EGI-aided receiver tracking reacquisition tests are summarized in Table 3. The excellent reacquisition results are superior compared to the typical stand-alone receiver because of the "EGI aided receiver tracking" mechanization. This allows the EGR to accomplish an EGI aided Direct P-code reacquisition with a small search window rather than the slower C/A code reacquisition. Receiver aiding also desensitizes the variability in reacquisition performance due to vehicle trajectory/dynamics and allows for reacquisition in significantly higher jamming fields.

Table 3. H-764G EGI-Aided Receiver Tracking Reacquisition Results

Date	TIME TO REACQUIRE FOUR SATELLITES (SEC)			
	5 Minute GPS Signal Denial		10 Minute GPS Signal Denial	
	Straight	180° Turn	Straight	180° Turn
11 Nov 92	4	8	4	4
16 Nov 92	3	30 3	9	8
14 Dec 92	2 3	No Test	8 3	No Test
15 Dec 92	3 2	No Test	5 2	No Test
11-Feb-93	3	No Test	6 (20 min outage)	4
Average	2.9	13.7	5.1	5.3
Standard Deviation	0.7	14.4	2.4	2.3

### FUTURE ENHANCEMENTS

The EGI test program conducted at CIGTF played a key roll in definition of some of the enhancements planned for both the H-764G product line and the CIGTF EGI test capabilities. The enhancements described below will improve the robustness of the H-764G to the user community as well as the effectiveness of the CIGTF EGI test capabilities.

#### H-764G Enhancements.

The real-time GPS observation error detection algorithms in the H-764G will be upgraded to include a Reliability Autonomous Integrity Monitoring (RAIM) scheme. This algorithm will be capable of autonomously detecting the presence of a bad GPS measurement when processing five or more satellite measurements and prevent bad GPS from corrupting the EGI solution. If six or more independent satellite measurements are available, RAIM can also identify which satellite measurement is bad. During some of the flight tests at CIGTF a satellite was producing large range errors. The measurements from this satellite were processed by the H-764G and slightly degraded the EGI performance. This could have been avoided with RAIM. Additionally, logic will be added that uses RAIM to provide smart protection and recovery schemes from bad external inputs such as initial position entry and bad altimeter data. If the user enters the wrong initial position to initiate a gyro compass ground align the EGI can automatically recover once RAIM checked GPS measurements are available. If the altimeter is producing bad altitude data the RAIM equipped EGI can protect against bad altimeter inputs and notify the user that it has failed.

The use of external altimeter data to aid the EGI navigation solution is incorporated in the design. During good GPS coverage, some of the error characteristics of the altimeter data is calibrated by the EGI filter and the altitude estimate of the EGI is predominately that of GPS. When GPS

coverage is poor, the EGI will produce an altitude estimate based on a more accurate calibrated altimeter. Further enhancements in the calibration and use of altimeter data will be added. An additional Kalman filter error state is being incorporated to better measure the altimeter error.

A hover hold mode for helicopters has recently been incorporated into the H-764G baseline design and is currently under test. This mode helps the helicopter pilot to stay hovering in a fixed location or it can be used by the pilot to mark a location, leave that location for a short period of time, and return to the same place. Preliminary results are exceeding the performance design goal of no more than 1 meter drift (per axis) in 3 minutes. The H-764G achieves this high level of relative accuracy by using a technique that involves accumulating GPS delta range measurements when the hover mode is commanded.

The most significant enhancement to the H-764G product line is the introduction of the Block II production systems available in early 1994. The Block II H-764G EGI is a highly modular, Open System Architecture (OSA) upgrade consisting of a sub-nmi/hr-class INS with five application-specific expansion slots, one of which contains the embedded, tightly coupled Global Positioning System (GPS) receiver. The H-764G Block II OSA standard backplane features the System Processor (SP) a 32-bit processor with 1553B and quad serial data bus interfaces on a single card, and a Power Supply (PS). The H764G Block II expansion slots include provisions for a wide assortment of add-on EGI options such as: synchros, Digital Map, ARINC 429, F-15 Radar/H009, IEEE-488, 400 hz 115 VAC Power Converter, and embedded GPS-DAC (Digital to Analog Converter).

Additional H-764G Block II enhancements include:

- DoD standard 1553B message structures (SNU84-1, ICD-059 & ICD-GPS-104)
- 7"x7"x11" chassis size (down to 7.0"x7.0"x7.5" for INS-only).
- An i960 32-bit, 10 MIP, 2/4 megabyte processor
- Highly Modular Ada software
- At-sea align, odometer aiding, Doppler aiding, etc.
- Triple nav solutions (INS, GPS & blended INS/GPS)

#### **CIGTF EGI Test Capability Enhancements.**

New reference systems are being developed at CIGTF to meet the demands of the more sophisticated integrated navigation systems such as the EGI. The CIGTF High Accuracy Post Processing System (CHAPS) is currently under development. The CHAPS system is based on post processing of flight data from ground based transponders, a differential-GPS and INS on board the host vehicle. CHAPS performance goals are less than 1 Meter CEP position error and less than .01 m/s horizontal velocity error.

Enhancements in the data acquisition systems and record capabilities are also being made. A more sophisticated time tagging scheme is being designed to reduce reference system to system under test time tag errors. To provide better time tagging of data, each message will have its own time tag and the data recording itself will be synchronized more closely to the reference UTC time. A

Versa Module Eurocard (VME) based multitasking 68030 computer running the OS-9 operating system and programmed in ADA is under test for control display and data collection.

#### **REFERENCES**

Department Of Defense Honeywell Embedded GPS Receiver/INS Concept Demonstration Final Report, Prepared by Guidance Test Division 46th Test Group Holloman AFB, New Mexico, June 1993.

**THIS PAGE LEFT BLANK INTENTIONALLY**

# NEURAL NET-DIRECTED COMPLEMENTARY FILTERS AND APPLICATIONS TO GPS DATA AND ACOUSTIC SIGNAL ENHANCEMENT

Bal N. Agamata

Naval Command Control & Ocean Surveillance Center (NCCOSC), NISE West  
San Diego, California

## BIOGRAPHY

Bal N. Agamata is an Electronics Engineer with the Communications Division, NCCOSC In-Service Engineering (NISE) West. He provides technical support to the West Coast Telecommunication Realignment Projects Systems, Joint Operational Tactical System (JOTS), Navigation Sensor System Interface (NAVSSI). Previously, he was a GPS systems engineer and design and test engineer for the Naval Weapons Center (NWC) Integrated Range Communication System (IRCS) in China Lake.

He was a member of the Technical Staff, Guidance, Navigation & Controls, both with the Space Divisions of Rockwell International and General Dynamics. At General Dynamics, he was autopilot systems engineer for the all-digital flight control and strapdown guidance system for the Airforce OV-1 2nd stage solid propulsion rocket and satellite. He was lead design engineer for the automatic launch control and checkout equipment for the Atlas ICBM Autopilot. He supported R&D and proposal efforts related to guidance and flight control systems. At Rockwell, he performed controls and aerodynamic analyses for the Space Shuttle during the landing mode.

He holds a BSEE from FEATI Tech, Manila, a MSEE from USC. He pursued further graduate studies in communications, radar and electronics at UCSD and UCLA. He has certificates in Guidance and Controls, Satellite Communications and Signal Intelligence from the Naval Post Graduate School and UCLA.

## ABSTRACT

The design of neural net-directed complementary filters for data enhancement is presented as an initial exploratory or conceptual development effort. The baseline system consists of two sets of multi-stage error detection and smoothing recursive filters and a neural net. The neural net, which is either a counterpropagation network (CPN) or backpropagation network (BPN), performs on-line classification of errors and filter weight vector adjustment.

Sample applications consider two apparently diversified data: acoustic and GPS navigation data. Acoustic signal enhancement suggests a method of detecting broadband and noiselike signals, and distortions due to environmental effects, internal degradations or impending failures. GPS data enhancement is emphasized where all types of dominant errors are considered, including selective availability (SA) effects. The complementary filters fall in a new class of curve-fit polynomial filters, requiring no assumption on the correlation properties of signal and errors.

## INTRODUCTION

### Background

The complementary filters evolved from a system called Adaptive Recursive Multi-Sensor System, ARMSS, [1]. The upgraded version, shown in Figure 1, incorporates, among others, complementary filters designed

to reduce the effects of unknown stationary and non-stationary errors.

ARMSS is an exploratory development design, a proof-of-principle effort. ARMSS requires no modification to the existing sensor suite. It is a new approach to multi-sensor integration. It suggests an alternative to the Navy's original Navigation Similar Source Integrator (NAVSSI) [2], the Army's Adaptive Tactical Navigation (ATN) [3], and the Airforce's Performance Enhanced Navigation using Neural Network Technology (PENANT) [4].

The primary objective of NAVSSI is to provide a composite best estimate of the navigation sensors. A development option plan (DOP) specified cascaded and/or series Kalman filters, assumed to be non-developmental items (NDI's). Reflecting the current design effort [5], which calls for pre-planned product improvement (P3I), and the initial January 1993 installation, NAVSSI was changed to mean, for the present, "Navigation Sensor System Interface."

The Army's ATN is for a tactical aircraft with a sensor suite that includes, among others, GPS, Inertial Navigation Unit, Baro/Radar Altimeter and a Terrain Reference Navigation System [2]. The objectives of ATN are more stringent than NAVSSI's. And, unlike NAVSSI, the adaptive algorithm is not assumed to be NDI. ATN is to be pursued in two phases: Phase 1 Algorithm development and demonstration through computer simulation, and Phase 2 Functional prototype, at the option of the government, with ATN algorithm implemented in a mission computer. Additionally, it will be installed in an Army helicopter for flight test. The author is not aware of the current status of ATN.

The Airforce PENANT is under exploratory development and is supported by the small business innovation research (SBIR) program [4]. It is similar to ATN in a Phase 1 effort only. PENANT uses "advanced statistical methods with a neural network. It uses a Net Information Approach (NIA), a variation of Kalman filtering that partitions information from the navigation sensors into several local solutions. PENANT represents a new approach to fault detection, identification and

reconfiguration (FDIR) for integrated multi-sensor aircraft navigation systems." Like ATN, PENANT assumes no NDI algorithm. It recognized the difficulties of applying conventional approach.

ARMSS neural net-directed complementary filters use new adaptive recursive filters specially configured for error detection and data enhancement. The design also represents a new approach to pre-filtering prior to data fusion as depicted in Figure 1. The data source or sensor is unmodified. Based on the initial analysis and simulation results, the filter configuration is presented as an alternative for a Phase 1 study. A general application is the focus of this paper.

### Complementary Filters Baseline

Figure 2 is a functional baseline diagram. The input raw data,  $z$ , consists of the true signal,  $s$ , and any combination of additive errors,  $e$ , assumed with unknown correlation properties. The complementary filters perform tasks of error detection, estimation, correction and classification, followed by data enhancement.

### Application to GPS and Acoustic Data

Figures 3 and 4 show simplified block diagrams applying complementary filtering for GPS and acoustic instrumentation (sensor) data.  $G(z)$  and  $E(z)$  denote data enhancement and error detection filters, respectively.  $H(z)$ , a roving high-pass (HP) or band-rejection (BR) filter in the error detection loop, is designed to reject the true signal. The complementary filters may be also applied to seismic, sonar, biological, and communication baseband signals.

### Acoustic Signal Enhancement

Figure 5 is an for acoustic signal, with time-varying amplitude and frequency. The error detection filters  $E1$  and  $E2$ , and data enhancement filters,  $G1$  and  $G2$ , are not coupled. The additive errors in the data enhancement loop are decoupled (low-pass filtering effect) by a proper choice of sampling frequency. The filter sets have similar structure. The error estimate,  $ee$ , and enhanced data,  $a$ , will have similar transfer

functions.  $a_e$  and  $e_{av}$  are differential errors.  $e_{av}$  contains both error terms and smoothed true data. Error correction is an integral function of the data enhancement filters. The  $U(.)$ 's are filter weight vectors.

### GPS Data Enhancement

GPS, as will be for other navigation sensors, is treated as a special case. Figure 6 depicts two coupled sets (position and velocity) of error detection and data enhancement filters. There would be six sets for the complete system, i.e., for north, east and downward position and velocity vector components. The error filters are E11, E12, E21, and E22, and enhancement filters are G11, G22, G21, and G22. The roving HP filters are Hv and Hp. The  $U(.)$ 's are filter weight vectors.

The dominant velocity errors are assumed to have high frequency contents relative to the true velocity. Position errors are both in-band and out-of-band. The input data to the HP filters,  $e_{vc}$  and  $e_{pc}$ , have error and smoothed data. Both position and velocity error estimates,  $ee_p$  and  $ee_v$ , are fed directly to the enhancement filters. Additional error correction are provided by  $ec_p$  and  $ec_v$ . The enhanced velocity,  $v$ , and position  $p$ , are the weighted sum of the output data from the two stages, G21 and G22, and G21 and G22, respectively.

The initial position error estimate  $e_{pv}$ , an input to the position error filters, is the difference between the velocity dead-reckoning (VDR) position (integral of enhanced velocity), treated as a reference trajectory, and raw position data. A VDR mode is determined by the CPN.

### Neural Net Applications

A standard CPN or BPN is used depending on the application. For the future and final analysis or design a variant of these networks may be configured. In this paper, only a baseline is presented. CPN is for GPS and BPN is for acoustic or high frequency signals. Both classify unknown errors, sampling frequencies and determine high-pass filter 3 dB cut-offs. The associated feature vector processor or extractor derives on-line the filter weight vectors. Figure 7 is a training

or learning diagrams for the recursive filters. The filters are trained off-line using a BPN-type algorithm. Figure 8 is a training and error analysis diagram for a single stage filter. Three identical filters are required to verify the error characteristics.

### FILTER DESIGN

Filter derivation, a lengthy process, is omitted. Only salient characteristics and features are presented. There are two types of filters used: an adaptive recursive filter and roving HP or BR filters.

#### Single Stage Filter Background

Figure 9 is the basic single stage filter which was discussed in some detail in [1]. Its development is traceable in polynomial generators in analog computers, and their discrete or digital equivalent, in particular the Porter-Stoneman polynomial curve-fit data extrapolators. For  $q$ -degree polynomials,  $q = 1, 2, 3$ , there are  $q + 1$  data points. These type of extrapolators or filters are extremely noise-sensitive. For  $q = 3$ , the noise variance reduction factor ( $V_{rf}$ ), the ratio of output over input noise variances, equals 69. Variance is taken as the time-averaged mean-squared error. To remove the undesirable  $V_{rf}$  feature, a filter with  $V_{rf} \ll 1$  was developed. The components are as noted. After some lengthy algebraic manipulations, the resultant transfer function is

$$(1) G(z) = N(z)/[1 + D(z)]$$

where

$$(2) N(z) = N_0 + N_1 z^{-1} + \dots + N_L z^{-L}$$

$$(3) D(z) = D_1 z^{-1} + \dots + D_{L+1} z^{-(L+1)}$$

and  $N(.)$ 's and  $D(.)$ 's are adaptive coefficients,  $L = N + q + 1$ ,  $q = 3$ ,  $N > 9$ .  $N$  is the length of  $K(z)$ , a non-recursive absolutely stable input error filter with  $V_n < 1$ . The scalar output with time index  $n$  is

$$(4) y_n = U_n^T Z_n$$

where the weight and sampled sequence vectors are



$$(5) U_n = [N_{0n}, N_{1n}, \dots, N_{Ln}, D_{1n}, D_{2n}, \dots, D_{(L+1)n}]^T$$

$$(6) Z_n = [x_n, x_{n+1}, \dots, x_{nL}, (y_{n+1}, y_{n+2}, \dots, y_{n(L+1)})]^T$$

The components of  $U_n$ ,  $N(.)$ 's and  $D(.)$ 's, are denoted as  $N_i$ 's and  $D_i$ 's in Figure 9. The CPN computes on-line the weight vector  $U_n$ . Unique to this filter, is the initial off-line training which uses a BPN type learning algorithm. With all due credit to Porter-Stoneman and others, equations (1) and (4) are neither mathematically nor performance-wise equivalent to the classical data extrapolators.

### Multi-Stage Error Detection Filters

In [1] it was shown that two ( $q=3$ ) filters in Figure 9, in pairs of  $\{G1, G2\}$ ,  $\{E1, E2\}$ ,  $\{E11, E12\}$ , and  $\{E21, E22\}$ , as indicated in Figures 5 and 6, are capable of tracking noise-like, random walk and Brownian type signals, and non-linear functions whose frequency contents extend well beyond the acoustic range. This configuration of paired filters is used for error detection and for data enhancement for highly dynamic signals. The complete error equation is quite complex. However, in terms of paired filter outputs,

$$e_1 = a_1, e_{s1}, e_{p1}, e_{v1}$$

$$e_2 = a_2, e_{s2}, e_{p2}, e_{v2}$$

the error estimate is

$$(7) ee = a, ea, ep, ev$$

$$= e_1 - w_d(e_2 - e_1)$$

$$= e_1 - w_d(eo_2 - eo_1)$$

where  $w_d = w_{ad}, w_{sd}, w_{vd}, w_{pd}$ , and  $eo_1$  and  $eo_2$  are inaccessible output errors of stage 1 and stage 2, respectively. Ideally

$$(8) w_d = (eo_1/eo_2 - 1)^{-1}$$

An approximation (8) is

$$(9) w_d = w_{do} + k_{wd}(V[e] - V[e_s])$$

$w_{do}$  and  $k_{wd}$  are constant coefficients. The error in the estimate is

$$(10) de = e - e_s$$

It is desired to minimize the variance,  $V[de]$ , in selecting  $w_{do}$  and  $k_{wd}$ .

### GPS Multi-Stage Data Enhancement Filters

The coupled and paired ( $q=2$ ) filters,  $\{G11, G12\}$  and  $\{G21, G22\}$ , are used for very low frequency type signals, i.e. GPS data. The enhanced data, position or velocity, is denoted  $y = p, v$ . The paired filter outputs are

$$y_1 = p_1, v_1, \quad y_2 = p_2, v_2$$

The enhanced data, position or velocity is

$$(11) y = p, v = w_{y1} y_1 + w_{y2} y_2$$

$$(12) w_{y1} = w_{p1}, w_{v1} \\ = V[ey_2]/(V[ey_1] + V[ey_2])$$

$$(13) w_{y2} = w_{p2}, w_{v2} \\ = V[ey_1]/(V[ey_1] + V[ey_2])$$

$ey_1 = x - y_1$  and  $ey_2 = x - y_2$ , and  $V[.]$  is the variance. The first stage filter input variable is

$$(14) x = z - e_s - e_{cy}$$

and the error correction signal is

$$(15) e_{cy} = w_{ec} (y_1 - z - e_s)^{\wedge}$$

$(..)^{\wedge}$  denotes the quantity delayed by a sampling interval.  $w_{ec}$  is a feedback gain.

### GPS Velocity Dead-Reckoning (VDR) Position

The VDR position,  $p_v$ , integral of enhanced velocity,  $v$ , is taken as a reference trajectory. A reference trajectory ensures that both in-band and out-of-band errors are input to the error detection filters. The initial position error estimate is

$$(16) e_{pv} = z - p_v = e - e_{vdr}$$

where the unknown  $e_{vdr}$  is an extremely low frequency error in the integrated enhanced velocity.

### Prototype Low-Pass for Roving High-Pass or Band-Rejection Filters

A normalized low-pass (LP) Butterworth or Chebyshev filter whose pole locations were obtained by Weinburg is taken as a prototype (6). Utilizing a 5th order LP, with normalized 1 rad/sec 3 dB cut-off, as the nominal prototype gives

$$(17) H(p) = a_0/[b_0 + b_1 p + \dots + b_5 p^5]$$

where  $p$  is the Laplace variable, and

$$a_0 = a_{0N} w_r^6, \quad b_0 = a_{1N} w_r^5$$

$$b_1 = b_{1N} w_r^4, \quad b_2 = b_{2N} w_r^3$$

$$b_3 = b_{3N} w_r^2, \quad b_4 = b_{4N} w_r, \quad b_5 = 1$$

$a(.)_N$ 's and  $b(.)_N$ 's are the coefficients of the normalized LP filter.  $w_r$  is the reference or "fictitious" LP filter 3 dB cut-off. The LP filter is transformed to a HP or BR analog filter by

$$p = w_b^2 s/[s^2 + w_b^2], \text{ for BR, } w_r = 6.28 (f_b^2/B)$$

$$p = w_r w_n/s, \text{ for HP, } w_r = 1$$

where  $s$  is the Laplace variables for the BR or HP filters.  $f_b$  or  $w_b$  is the BR center frequency.  $B$  is the 3 dB rejection band.  $w_n$  is the HP 3 dB cut-off frequency. The HP and BR filters will be 5th and 10th order, respective;y.

### Roving High-Pass or Band-Rejection Filters

The transformation of the HP and BR filters to their digital equivalent is a lengthy process and is not discussed. Since the filters are recursive, the error estimate with time index  $n$  is

$$(18) ee_n = ee_n, ee_p, ee_s, \\ = U_n^T Ze_n$$

The bilinear transformation weight vector, with components  $a(.)$  and  $b(.)$ , is

$$(19) U_n = U_{v_n}, U_{p_n}, U_{a_n} \\ = (a_0, a_1, a_2, \dots, a_L, b_1, b_2, \dots, b_L)^T$$

with  $ec = e_{vc}, e_{pc}, e_{ac}$ ,

$$(20) Ze_n = [ec_n, ec_{n-1}, \dots, ec_{n-L}, \\ -(ee_{n-1}, ee_{n-2}, \dots, e^*_{n-L})]^T$$

It is noted that  $H(z)$  follows the error detection filters since the input data is smoothed or filtered and, primarily to avoid restriction on sampling frequencies and distortions due to input white noise.

### FILTER COEFFICIENT ADJUSTMENT

Conventional or standard analysis procedures do not apply in the determination of the filter time-varying coefficients, more so when the correlation properties of the additive noise and errors are unknown. An heuristic method is an alternative which neural nets offer. The BPN and CPN type algorithms used here are uniquely applied for this particular design.

#### Single Stage Filter Coefficients

With reference to Figure 9, the system weight vector is defined as

$$(21) W = (w_0, w_1, w_2, w_3)^T$$

with initial conditions

$$(22) W_0 = (w_{00}, w_{01}, w_{02}, w_{03})^T$$

With  $K(z) = 1$ , initial stability requires that:

1.  $W_0$  is a bilinear transformation weight vector, given the maximum values of the staleness factors  $B1, B2, B3$ .

$$2. -1 < B_e < 0, \quad 0 < B_N < 2$$

The components of  $W$  are related by

$$(23) w_i = w_0 c_i M_i, \quad i = 0, 1, 2, 3$$

$$(24) M_i = c_4 T + M_s + M_b [1 - c_6$$

$$\log(S_{xy} + 1), \quad i = 0, 1, 2, 3$$

$$(25) M_s = c_9 |y| \quad \text{for small signals}$$

$$= c_9 \log(c_9 |y| + 1) \quad \text{for GPS}$$

$$(26) M_b = c_7 |dy| \quad \text{for small signals}$$

$$= c_{10} \log(c_{11} |dy| + 1) \quad \text{for GPS}$$

$$(27) S_x = (V[e_{xy}]1/2, e_{xy} = y - x$$

and for the staleness factors,

$$(28) B_i = B_{i\max} - dB_i, i = 1,2,3, j = 12,13,14$$

$$(29) dB_i = c_i S_x = c_i \log(S_x k_x + 1)$$

T is the sampling interval.  $|y|$  and  $|dy|$  are the absolute value of y (or approximate reference model) and its approximate derivative (or enhanced velocity data for GPS), respectively. The  $c_j$ 's, are constant coefficients of a weight vector C discussed below.

#### Constant Coefficient Vector C

A constant coefficient vector, with components,  $c_i$ 's, is specified as

$$(30) C = (c_1, \dots, c_j, \dots, c_{16}, c_{18}, c_{17})^T$$

$c_{15} = w_{da}$ ,  $c_{16} = k_{wd}$  and  $c_{17} = w_{ac}$  of equations (8) and (15), respectively. There are no conventional or standard methods to derive optimum value of the  $c_i$ 's for which there is a minimum output error in the least-mean-square-error sense.

#### Single Stage Filter

##### Off-line BPN Learning Algorithm

The learning approach is similar to [7] in which the filter or multi-stage filter is regarded as dynamic neural units or controller in a nonlinear system. While the procedures are different, the objective is also to minimize the mean-square-error. Standard BPN algorithms are based on gradient techniques in which the components of the weight vector U are directly processed.

With reference to Figure 7, it is desired to derive off-line all the components of the vector C,  $c_i$ 's, and all other system coefficients, using a BPN learning type of algorithm. As previously stated, the CPN feature vector extractor computes the weight vector  $U_n$  of equation (5), using the learned C vector. To train a single stage filter and verify its

performance and error characteristics, three filters, G1, G2, and G3, as shown in Figure 8, are used. These filters have identical weight vectors  $U_n$  with respect to G1. The desired signal, s, and the estimate,  $y_1$ , is differenced to obtain an output error equation

$$(31) e_o = y_1 - s = e_{xy} + e_n + e_{nc}$$

where  $e_{xy}$  is a signal and frequency dependent error,  $e_n$  is the output noise and  $e_{nc}$  is the correlated error.

A variant of the BPN delta rule learning law [8] is to be used. Every component,  $c_i$ , of vector C (30) is learned with full signal dynamics range under noiseless and maximum white noise conditions. The desired component is

$$(32) c_i = c_{0i}(1 + dc_i)$$

where  $c_{0i}$  is the initial value, and  $dc_i$  is the desired fractional correction.  $c_i$  and  $dc_i$ ,  $j = 1,2,\dots,17$ , are learned as illustrated in Figure 10. Each increment of delta  $c_i$  is

$$(33) c_{j\min} = c_{0j}/2^K, K = , > 3$$

$$(34) c_{j\max} = c_{0j}(2 - 1/2^K)$$

$K = 3$  is sufficient for this particular design. Repeated computer simulation "Runs" are made to learn the value of  $c_i$  which corresponds to a minimum value of  $V[e_o]n$ ,  $n = 1,2,3,\dots,8_u$ , and  $2,3,\dots,8_i$ . Three runs are required to start the selection. For  $k=3$ , a minimum of 3 Runs and maximum of 7 Runs are required. The learning algorithm is

$$(35) \begin{aligned} &1. \text{ Run } 1_u, 5_i \text{ \& } 5_u \\ &\quad \text{Select } 1_u, \text{ if } V[e_o]5_i = V[e_o]5_u \end{aligned}$$

$$\begin{aligned} &11. \text{ Run } 3_u \text{ \& } 7_u, \text{ if } V[e_o]5_u < V[e_o]5_i \\ &\quad \text{Select } 5_u, \text{ if } V[e_o]3_u = V[e_o]7_u \end{aligned}$$

$$\begin{aligned} &12. \text{ Run } 6_u \text{ \& } 8_u, \text{ if } V[e_o]7_u < V[e_o]3_u \\ &\quad \text{Select } 6_u, \text{ if } V[e_o]6_u < V[e_o]8_u \\ &\quad \text{Select } 7_u, \text{ if } V[e_o]6_u = V[e_o]8_u \\ &\quad \text{Select } 8_u, \text{ if } V[e_o]8_u < V[e_o]6_u \end{aligned}$$

$$\begin{aligned} &13. \text{ Run } 2_u \text{ \& } 4_u, \text{ if } V[e_o]3_u < V[e_o]7_u \\ &\quad \text{Select } 2_u, \text{ if } V[e_o]2_u < V[e_o]4_u \\ &\quad \text{Select } 3_u, \text{ if } V[e_o]2_u = V[e_o]4_u \\ &\quad \text{Select } 4_u, \text{ if } V[e_o]4_u < V[e_o]2_u \end{aligned}$$

21. Run 3, & 7, if  $V[e_o]5_i < V[e_o]5_o$   
Select 5, if  $V[e_o]3_i = V[e_o]7_i$
22. Run 6, & 8, if  $V[e_o]7_i < V[e_o]3_i$   
Select 6, if  $V[e_o]6_i < V[e_o]8_i$   
Select 7, if  $V[e_o]6_i = V[e_o]8_i$   
Select 8, if  $V[e_o]8_i < V[e_o]6_i$
23. Run 2, & 4, if  $V[e_o]3_i < V[e_o]7_i$   
Select 2, if  $V[e_o]2_i < V[e_o]4_i$   
Select 3, if  $V[e_o]2_i = V[e_o]4_i$   
Select 4, if  $V[e_o]4_i < V[e_o]2_i$

The equality or inequality is evaluated with a predetermined variance threshold. The system can perform efficiently within at least 25 % variation of the coefficients.

#### BPN Learning Algorithm for Two-Stage Filters {G1,G2}, {E1,E2}, {E11,E12}, {E21,E22}

$W_{de}$  and  $k_{wd}$  are learned using a similar procedure as in deriving  $c_i$ . It will be necessary also to repeat the vector C selection process on both stages to obtain a desired minimum  $V[de]$ , although not all  $c_i$ 's may be considered. In general the C vectors for both stages will not have identical coefficient values.

#### BPN Learning Algorithm for Two-Stage Filters {G11,G12}, {G21,G22}

The coefficient to be learned is

$$(36) \quad w_{ec} = w_{eco} + dw_{ec}$$

$W_{eco}$  is an initial value, and  $dw_{ec}$  is the desired change selected, similarly as  $c_i$ , for a minimum variance  $V[e_o]$ . It will be also required to repeat the learning process for the C vectors for both stages. There is no training required for (9).

#### COUNTER-PROPAGATION NETWORK, CPN

The CPN, devised by R. Hecht-Nielsen [8], combines Kohonen and Grossberg layers. For the sake of emphasis, the training and learning laws will be repeated. In addition to filter weight computations, the CPN provides the following on-line tasks:

1. Error Classification
2. High-pass filter 3 dB cutoff

#### 3. VDR Enable

#### 4. EPR data (Figure 1)

#### GPS Feature Vectors

There is a specific feature vector for error classification, VDR mode enable, or high-pass filter coefficients. The feature vector components are the variances  $V[...]$ 's and their derivative as  $d[...]$ 's. For GPS velocity error classification

$$(37) \quad F_v = (f_{v1}, f_{v2}, f_{v3})^T$$

$$f_{v1} = V[e_v], f_{v2} = V[ee_v], f_{v3} = df_{v2}$$

and position error classification

$$(38) \quad F_p = (f_{p1}, f_{p2}, f_{p3}, f_{p4}, f_{p5})^T$$

$$f_{p1} = V[e_{pv}], f_{p2} = df_{p1}$$

$$f_{p3} = V[(e_{p1} - e_{pv})], f_{p4} = [oe_p]$$

$$f_{p5} = df_{p4}$$

For VDR mode enable, the feature vector is

$$(39) \quad F_{pv} = (f_{pv1}, f_{pv2}, f_{pv3})^T$$

$$f_{pv1} = V[e_{pv}], f_{pv2} = df_{pv1}$$

$$f_{pv3} = V[e_{p1} - e_{pv}]$$

The position and velocity high-pass filters 3 dB cut-off frequencies will be pre-set.

#### GPS CPN

A forward-only CPN, shown in Figure 11, is a standard configuration [8]. There are 3 layers: Input and fan-out Layer 1 with  $n$  input units; Kohonen Layer 2 with  $N$  processing elements; and Grossberg Layer 3 with  $m$  processing elements. The normalized input feature vector is denoted by

$$(40) \quad X = (F_{Nv}, F_{Np}, F_{Npv}, F_{Nh})_{normalized} \\ = (x_1, x_2, \dots, x_n)^T$$

The correct output signal or training vector is

$$(41) \quad Y = (y_1, y_2, \dots, y_m)^T = f(X)$$

The output of the Kohonen layer is

$$(42) Z = (z_1, z_2, \dots, z_N)^T$$

The output of the Grossberg layer which approximates Y is

$$(43) Y' = (y'_1, y'_2, \dots, y'_m)^T$$

#### Training and Learning Laws

The Kohonen processing element [8] calculates the Euclidean distance

$$(44) D(W_i, X) = |W_i - X|$$

where the connection weight vector is

$$W_i = (w_{i1}, w_{i2}, \dots, w_{in})^T$$

The output of each Layer 2 element, if i is the smallest integer for all j, is

$$(45) z_i = 1, \quad D(W_i^{OLD}, X) =, < D(W_j^{OLD}, X) \\ = 0, \quad \text{otherwise}$$

The winning processing element, with minimum distance, has output set to 1 and all others have outputs set to 0. Kohonen learning law for weight adjustment for the winning processing element is

$$(46) W_i^{new} = W_i^{old} + a(X - W_i^{old}) z_i \\ = (1 - a)W_i^{old} + aX$$

and  $W_i^{new} = W_i^{old}$  for the losers. The learning rate is  $0 < a < 1$ .

The layer 3 processing elements are governed by Grossberg's learning law [8]. The response,  $y'_i$ , or the weight of processing element j, is associated with the winning layer 2 processing element ( $z_i = 1$ ), has a transfer function

$$(47) y'_i = \sum_{i=1}^N u_{ji}^{old} z_i$$

and the weight is updated by

$$(48) u_{ji}^{new} = u_{ji}^{old} + a(y_i - u_{ji}^{old}) z_i$$

where the weight vector for jth processing

element is

$$(49) U_j = (u_{j1}, u_{j2}, \dots, u_{jn})^T$$

After the learning process, the  $W_i$  and  $U_j$  weight vectors will be selected and "frozen". A CPN that is risk-free and fail-safe is required. The CPN classifications must be constrained to ensure system stability.

#### BACKPROPAGATION NETWORK, BPN

A BPN is considered for acoustic data. The BBN decides the following:

1. Sampling frequencies
2. Error classification
3. BR or HP filter 3 dB cut-off
4. Frequency of signal and errors

#### BPN Feature Vector Processor

The true signal frequency is assumed to be time varying and has the largest valued amplitude. The BPN feature vector extractor also computes the filter weight vector, U. The feature vectors are the power spectrum of the raw data, x, smoothed composite data and

error,  $e_{AC}$ , and error estimate,  $e_{EA}$ .

$$(50) F_x = (f_{x1}, f_{x2}, \dots, f_{xr})^T$$

$$(51) F_{ee} = (f_{ee1}, f_{ee2}, \dots, f_{eer})^T$$

$$(52) F_{sec} = (f_{sec1}, f_{sec2}, \dots, f_{seer})^T$$

where the subscript of F denotes the signal. The  $f(.)$  component is the power spectrum in the frequency band of  $f(.)$ . r, s, t are number of frequency bands and are not necessarily equal.

#### Normalization Procedure

The largest valued component of  $F_x$ ,  $z_x$ , determines the low-pass prototype filter with 3 dB cut-off,  $w_i$  (17). All components of  $F_{ee}$  and  $F_{sec}$  are normalized by dividing them all by  $z_x$ . The normalized component is  $z_i$ . The normalized feature vector is converted to a binary pattern vector. The pth input pattern

vector, for  $p = 1, 2, \dots, M$ , is

$$(53) X_p = (x_{p1}, \dots, x_{p1}, \dots, x_{pm})^T, \quad m = s, t$$

where

$$(54) x_{pj} = 1, \quad z_j/z_i - t_j > 0, \quad j = 1, 2, \dots, m \\ = 0, \quad \text{otherwise}$$

### BPN

A feedforward or forward-only BPN by Rumelhart, Hinton and Williams [8,9,10] is chosen. Again for emphasis, the learning algorithm is repeated. Similar to the CPN, the BPN consists of input and output layers. The number of input nodes,  $r, s, t$ , equals to the number of components of the pattern vector,  $X_p$ . The number of output nodes equals to  $K$ , the number of error classes to be classified. The mid layers, called hidden layers, can be one or more layers of  $N$  number of neurons or processing elements. For this application, one hidden layer is specified for a start. The output of the  $i$ th neuron is

$$(55) y_i = \text{sig} \left( \sum_{j=1}^m w_{ij} x_{pj} + T_i \right), \quad i = 1, 2, \dots, m$$

$T_i$  is a threshold.  $\text{sig}$  denotes the sigmoidal function, a rounded unity step function

$$(56) \text{sig}(y) = 1/[1 + e^{-y}]$$

The error or cost function is

$$(57) E = 1/2 \sum_{p=1}^M E_p$$

$$(58) E_p = \sum_{i=1}^m (t_{pi} - o_{pi})^2$$

$M$  is total number of pattern vectors.  $E_p$  is the error on pattern vector,  $X_p$ .  $t_{pi}$  the desired output for the  $i$ th output unit, and  $o_{pi}$  is the actual output. For the  $k$ th iteration the BPN learning algorithm updates the weights according to

$$(59) w_{ij} = w_{ij(0)} + dw_{ij}^{(k)}$$

$$(60) dw_{ij}^{(k)} = -a (Gr E_p)_{ij}^{(k)} + b dw_{ij}^{(k-1)}$$

$-1 < w_{ij(0)} < 1$  is the randomly selected initial weight.  $(Gr E_p)$  is gradient  $E_p$ .  $0 < a < 1$  and  $b$  are the learning rate and momentum term,

respectively.

## SAMPLING FREQUENCIES

### GPS Filters Sampling Frequencies

The input sampling frequency,  $fs_1$ , for the 1st stage filters, E11, G11, E21 and G21 (Figure 6), depends on the instrumentation port data update rate.  $fs_1 =, > 4$  Hz is desired, although 1 Hz may be adequate. The 2nd stage filters, G12, E12, E22, and G22, sampling frequencies are

$$(61) fs_2 = 2^n fs_1, \quad n = 0, 1, 2, \dots$$

The sampling interval,  $T = 1/fs_2$ , is specified or selected during the learning phase for the vector  $C$  (30). In general,  $n = 0$  or 1.

There will no constraints on the sampling frequency,  $fs_n$ , for the roving high-pass filter. In general the 3 dB cut-off frequency is predictable and can be preset. However, with highly dynamic platforms, a roving high-pass filter is desired.

### Acoustic Signal Sampling Frequencies

When the true signal,  $s$ , has time-varying amplitude and frequency, a multi-rate sampler is required. A more practical alternative is to sample the raw data,  $x$ , with a constant and high sampling frequency,  $fs_{max}$ . The sampled data is stored in a zero-order-hold, and then sampled at the desired sampling rate by the complementary filters. If  $f_{emax}$  is the expected highest frequency of the additive errors in  $x$ , a constant input sampling frequency is specified as

$$(62) fs_{max} = 2 M f_{emax}$$

where  $M = L + 1$  is the order the filter (5).

If  $f_{s1}$  (51) is the frequency band which  $s$  belongs and the mid-frequency is  $f_{mx1}$ , the sampling frequency for G1 is

$$(63) f_{s11} = 2 M f_{mx1}$$

which is valid for signal frequencies  $\pm 0.5 f_{mx1}$ . The sampling frequency for G2 is

$$(64) f_{s2i} = 2^n f_{s1i}, n = 0, 1, 2, \dots$$

Similarly the error detection filters, E1 and E2, may have identical sampling frequency

$$(65) f_{sm} = 2 M f_m = 2^n f_{s1i}, n > 2$$

$f_m$  is the expected highest frequency of the input error.

## COMPUTER SIMULATION TEST BED

### PC Continuous System Modelling Program (CSMP)

A PC version of CSMP has been used for simulation. The simulation has been partitioned to "Error Detection" and "Data Enhancement." This was necessary to verify the subsystem characteristics. Total coupled simulation with neural nets was not performed.

### Advanced Continuous Simulation Language (ACSL)

For future development, if funded, ACSL will be utilized. ACSL is capable of simulating ARMSS in its entirety as indicated in Figure 1. ACSL can also provide real-time data for neural net processing. A commercial neural net SW would be used.

## COMPUTER SIMULATION & ANALYSIS

### GPS Simulations

Any combination of errors as noted in Figure 2 were simulated. SA errors, with profiles from [11], and random spikes were also simulated by non-linear function generators. In the simulation, one arsec equals 31.0 meters. The following figures give some initial simulation results:

#### Figure 12 True Vehicle Dynamics

A accelerating vehicle is in a near circular trajectory, with peak velocity of 100 m/sec.

#### Figure 13:

- (a) Velocity Errors & Error Detection
- (b) Velocity Errors, Errors in Estimates, & RMS, m/sec

- (c) East Velocity Input, Enhancement & RMS Errors, m/sec
- (d) VDR Errors

Error detection shows actual errors and error estimate apparently coincident. Error in the estimate is less than 10%. The VDR errors represent a worst case values which assume that the errors in the velocity enhancement is the same as the error in the estimate. Enhanced velocity errors are less than 0.1 m/sec.

#### Figure 14:

- (a) Input, Output Position Errors & variances, mtrs<sup>2</sup>
- (b) Input & Output SA Errors, arcsec
- (c) Latitude & Longitude Errors with Markov Errors, arcsec

The position data enhancement loop used output error estimates from an ideal HP filter. A controlled (time-constant set) low-pass filter also provides equivalent errors in the error estimates. Position errors are less than 15 meters. As in the velocity loop, the error detection filters are extremely accurate, and the data would be similar to Figure 13 (c).

### Acoustic or High Frequency Signal Simulations

Amplitude is normalized to unity and the frequency range is 0 - 4 kHz. Sampling frequencies vary according to (63), (64) and (65). As a special note, all E(.)'s and G(.)'s are 3rd degree (q=3) polynomial filters. The C vector is learned at mid-frequency, say 2 KHz. The components of C will generally be maintained constant, except for the sampling frequency, or sampling interval, T, and the coefficient  $c_4$  in (24). Of course, the weight vector  $U_n$  (5) is always time-varying with signal frequency and amplitude. These filters can track signals and errors in the MHz ranges, limited only by the realizable input/output (I/O) sampling rates. The following figures also give some initial simulation results:

#### Figure 15:

- (a) 0.25 Hz Signal + Errors & Enhancement
- (b) 4 KHz Signal + Errors & Enhancement
- (c) 4 KHz signal + Errors, Enhancement Details

For high frequency signal, as should be

expected, there are significant time and group delays. This is one reason why direct error correction is not performed. It is not required however, since the data enhancement filter behaves like a band-pass filter. There is some amplitude distortion due to relatively large additive errors. For a well defined frequency and smoothed signal, the output of the 2nd stage filter may be used as indicated in Figure (15).

## FUTURE DEVELOPMENT

### Real-Time SW and Test.

A C language coding and quick-look test and evaluation of the GPS complementary filters may be performed by the staff of the NISE West GPS Test Facility in Imperial Beach California. A "live" GPS receiver will be used. Testing will utilize the GPS Movable Antenna Platform (MAP) and STeL-CAST GPS Tester (GPST). The MAP uses actual GPS satellites, while the GPST uses the STeL satellite signal generators. GPS errors, which is mostly jamming effected, will be induced via RF or IF. SA and other errors will be simulated in the future.

### Complete Simulation Test Bed & Analysis

The complementary filter design represents an initial exploratory development, a proof-of-principal effort. If funded, it would be a Phase 1 "Analysis and Simulation" only. A follow-on will be a Phase 2 "SW Coding and Prototype Design and Test." The neural nets will be incorporated into the SW.

ARMSS, of course, would be a major development effort, comparable to PENANT. A Phase 1 effort is a desired goal. ARMSS design assumes an existing sensor suite that will not be modified. It is an autonomous system. Its performance and accuracy can be verified in a dedicated simulation test bed. If ARMSS performs as expected, one application would be for self-correcting multi-sensor Integrated Guidance, Navigation & Control (GN&C) systems.

## ACKNOWLEDGMENT

This paper, in part the result of proposal efforts, is largely the product of private studies by the author. For their review and support, thanks are due to Ben Balanag of Code 00B7, Joe Osa, Craig Stroing and Jaime Radulovich of Code 3131 GPS Imperial Beach Test Facility, Therese Tanksley of Code 324 NTCSA, Bill La Fond and John Mayr of NCCOSC NRaD Code 78 Analysis & Simulation Division, and Stan Maki of the Space Division of GD.

## REFERENCES

- [1] B. N. Agamata, "Adaptive Recursive Multi-Sensor System (ARMSS) with Error Pattern Recognition," ION-GPS 5th International Meeting, September 1992.
- [2] Office of the Chief of Naval Operations (CNO), "Tentative Operational Requirements (TOR) for NAVSSI," October 1987.
- [3] Solicitation No. DAABO791RP267, "Statement of Work for Development of Adaptive Tactical Navigation (ATN)," US Army CECOM, Fort Monmouth, NJ, August 1991.
- [4] B. Griffiths, A. Orlando & S. Berning, "Performance Enhanced Navigation Using Neural Net Technology", ION-GPS National Meeting, January, 1993.
- [5] K. J. Cowley, "Navigation Sensor System Interface (NAVSSI)," ION National Meeting, January 1992.
- [6] W. Stanley, C. Dougherty, & Ray Dougherty, "Digital Signal Processing," Reston Publishing Co., 1984
- [7] M. Gupta & D. Rao, "Dynamic Neural Units in the Control of Linear and Nonlinear Systems," International Joint Conference on Neural Networks, 1992.
- [8] R. Hecht-Nielsen, "Neurocomputing" Addison-Wesley Publishing Co., 1989
- [9] J. McClelland & D. Rumelhart, "Explorations in Parallel Distributed Processing," MIT Press, 1988.
- [10] L. Alfred, "Supervised Learning Techniques for Backpropagation Networks," International Joint Conference on Neural Networks, 1990.
- [11] S. Y. Braasch, "Realtime Identification and Mitigation of GPS SA Errors Using LORAN C," ION-GPS 5th International Meeting, September 1992.



## SYSTEM LEGEND

$a$  = recursive filter constant, also enhanced acoustic signal and CPN learning rate  
 $ad$  = differential acoustic output  
 $a_1, a_2$  = 1st, 2nd stage filter output  
 $ARMSS$  = Adaptive Recursive Multi-Sensor System  
 $ATN$  = Adaptive Tactical Navigation  
 $b$  = BPN momentum term  
 $BPN$  = Back-Propagation Network  
 $BR$  = Band-Rejection  
 $B_s, B_n, B_1, B_2, B_3$  = filter staleness factors  
 $C$  = constant coefficient vector  
 $CPN$  = Counter Propagation Network  
 $C_e, C_{ae}, C_{pe}, C_{ve}$  = CPN classified errors  
 $C(.)$  = Complementary filters  
 $E(.)$  = error detection complementary filters  
 $EPR$  = Error Pattern Recognition  
 $e$  = unknown additive error (or any combination of errors)  
 $ee$  = estimate of  $e$   
 $ee_a, ee_p, ee_v$  = estimate of acoustic, position, velocity input errors  
 $e_c, e_{cp}, e_{cv}$  = position, velocity data error correction  
 $e_{a1}, e_{p1}, e_{v1}$  = 1st stage outputs of error detection filters  
 $e_{a2}, e_{p2}, e_{v2}$  = 2nd stage outputs of error detection filters  
 $e_{ad}, e_{pd}, e_{vd}$  = acoustic, position, velocity error differentials  
 $ee_v, ee_p, ee_a$  = velocity, position, acoustic data error estimate  
 $ee_n, ee_a, ee_p, ee_v$  = high-pass filter output  
 $e_1, e_2$  = error detection filters output  
 $e_{o1}, e_{o2}$  = inaccessible error detection filters output errors  
 $E, E_p$  = error or cost function  
 $E(z)$  = pulse transfer function  
 $de$  = error in the estimate of  $e, ee$   
 $D(.)$  = Data Fusion  
 $D(W, X)$  = Euclidean distance  
 $fe, fe_{max}$  = additive error frequency  
 $fs(.)$  = sampling frequency  
 $F(.)$  = CPN or BPN feature vector  
 $G(.)$  = enhancement complementary filters  
 $G(z)$  = pulse transfer function  
 $(Gr Ep)$  = gradient of  $E_p$   
 $Ha, Hp, Hv$  = High-pass filters  
 $HP$  = High-Pass

$H(z)$  = pulse transfer function  
 $NAVSSI$  = Navigation Similar Source Integrator, also Navigation Sensor System Interface  
 $M$  = order of recursive filter, also CPN number of pattern vectors  
 $o_n$  = BPN actual output  
 $p$  = enhanced position data, also Laplace variable for HP and BR filter  
 $p_1, p_2, p$  = 1st, 2nd stage outputs and enhanced position  
 $p_v$  = velocity dead-reckoning data  
 $PENANT$  = Performance Enhanced Navigation using Neural Network Technology  
 $q$  = polynomial degree  
 $s$  = true signal, also Laplace variable for prototype low-pass filter  
 $SA$  = selective availability  
 $S(.)$  = sensor  
 $sig(y)$  = sigmoidal function  
 $t_i$  = BPN desired output  
 $T$  = sampling interval, also transpose  
 $T_i$  = neural net processing element threshold  
 $u$  = GPS raw velocity data  
 $U, U(.)$  = filter weight vector set  
 $U_i$  = BPN connection weight vector  
 $v_1, v_2, v$  = 1st, 2nd stage outputs and enhanced velocity (m/sec)  
 $VDR$  = velocity dead reckoning  
 $V[.]$  = variance estimate  
 $W_i$  = recursive filter input error gain, also CPN connection weight vector  
 $W$  = recursive filter system weight vector  
 $W_o$  = filter initial system weight vector  
 $w_d, w_{ad}, w_{pd}, w_{vd}, w_{pd}$  = error gain  
 $w_{y1}, w_{y2}, w_{v1}, w_{v2}, w_{p1}, w_{p2}$  = summing gain  
 $w_r$  = reference HP filter 3 dB cut-off  
 $w_b$  = BR filter center frequency  
 $w_n$  = HP filter 3 dB cut-off  
 $x$  = input to data enhancement filters  
 $X$  = normalized feature vector  
 $X_p$  = pattern vector  
 $y, y_n$  = enhanced data  
 $Y$  = CPN training vector  
 $y'$  = CPN output vector  
 $z$  = GPS raw position data  
 $Z$  = CPN mid layer output vector  
 $Z_n, Z_e$  = sampled sequence vector

Neural Net-Directed  
Complementary Filters  
(This Paper)

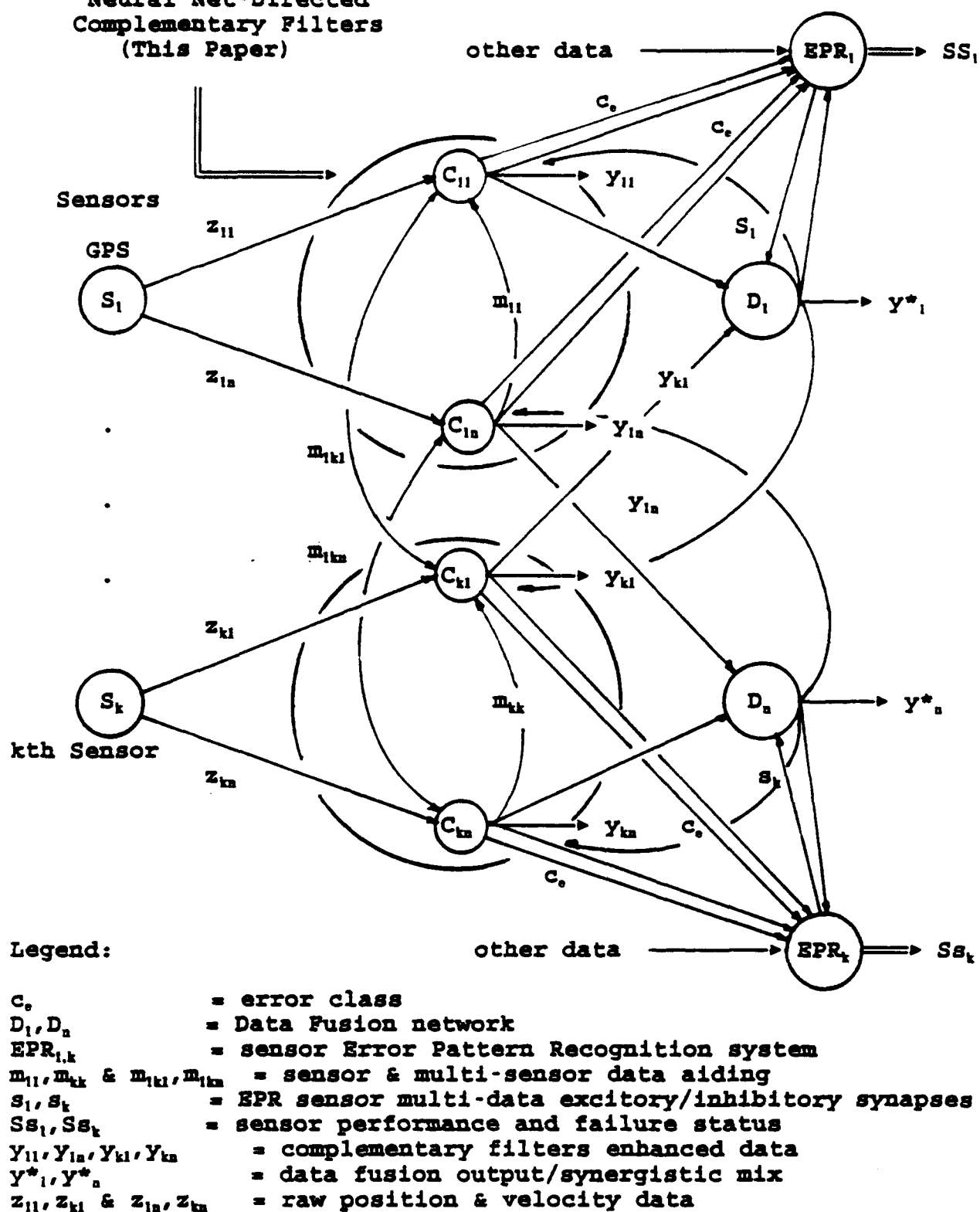


Figure 1 Adaptive Recursive Multi-Sensor System (ARMSS)

### Error (Generators) Classes

White Noise	Random Pulse	Brownian Motion	Non-linear Function	Markov Errors	Others
-------------	--------------	-----------------	---------------------	---------------	--------

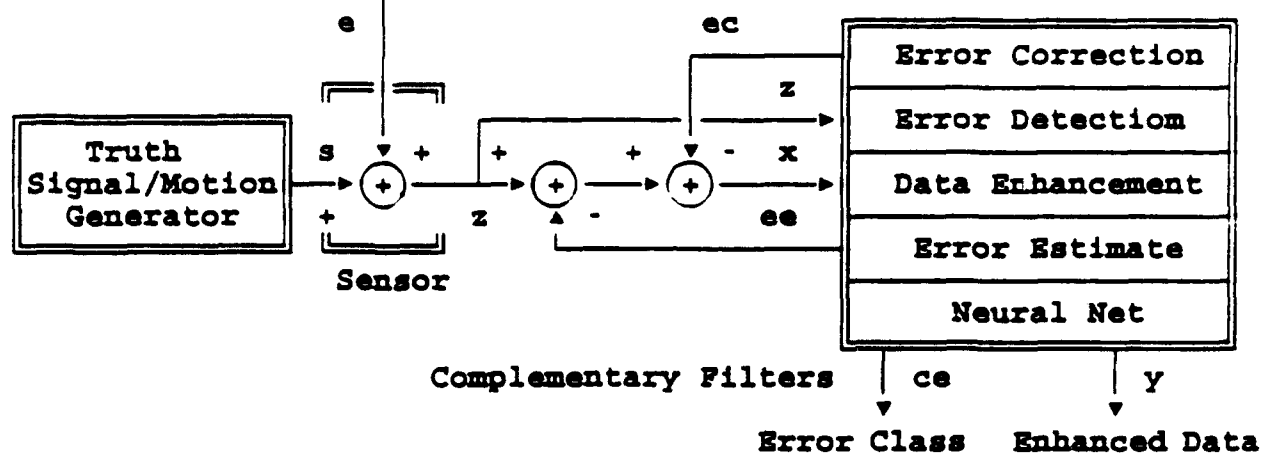


Figure 2 Interface of Neural Net - Directed Complementary Filters

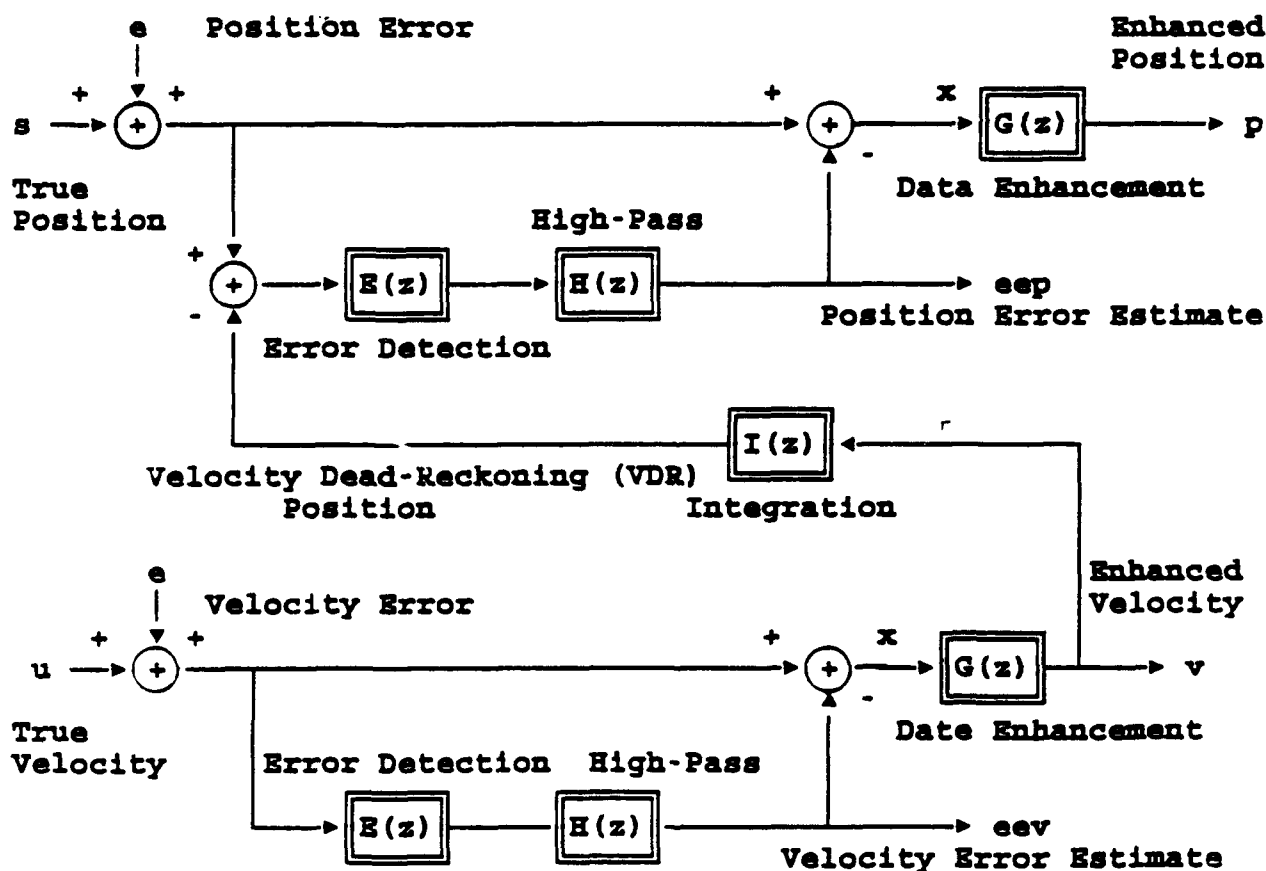


Figure 3 GPS Complementary Filters General Diagram

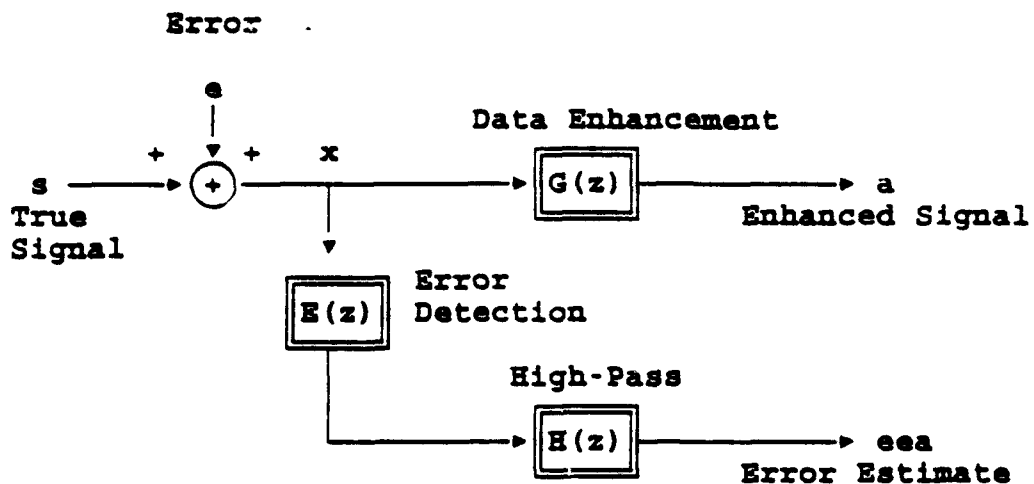


Figure 4 Acoustic Complementary Filters General Diagram

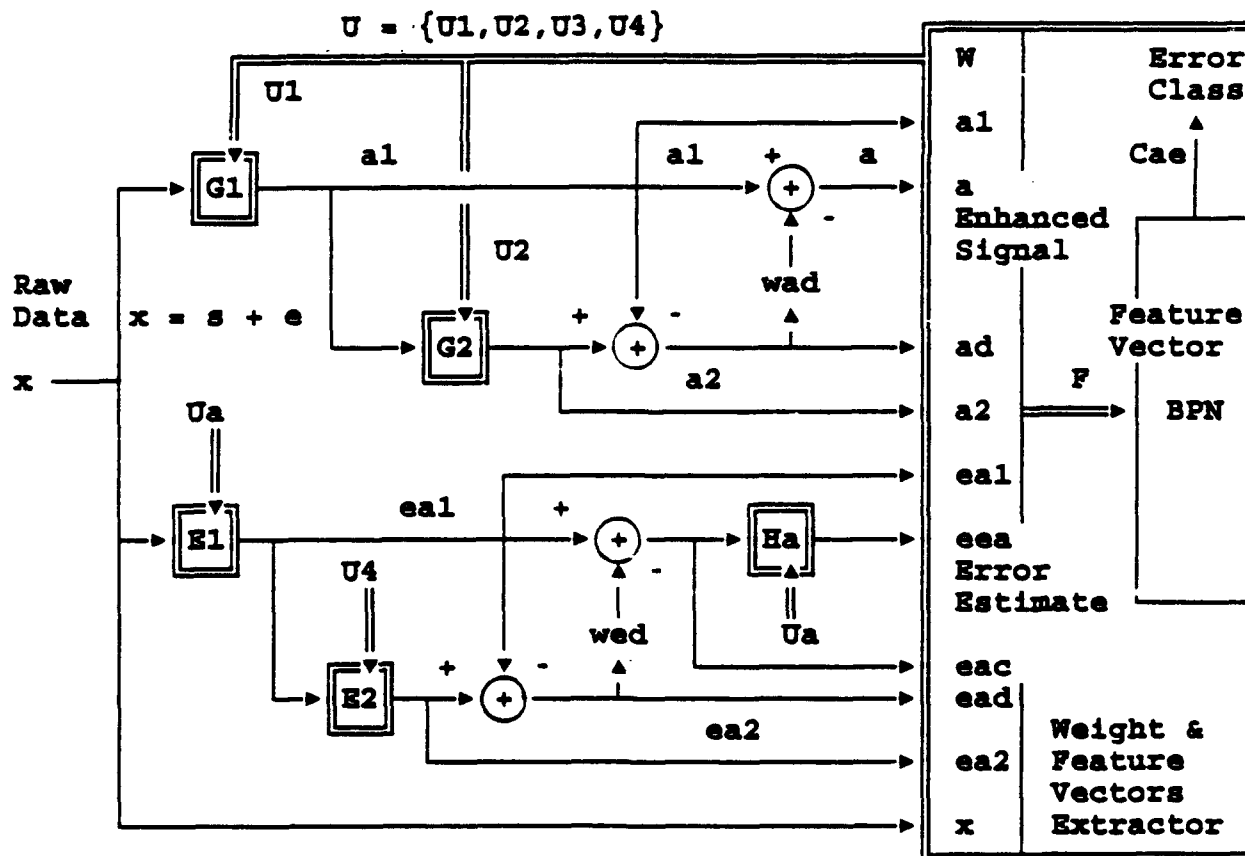


Figure 5 Acoustic Signal Complementary Filters & Neural Net

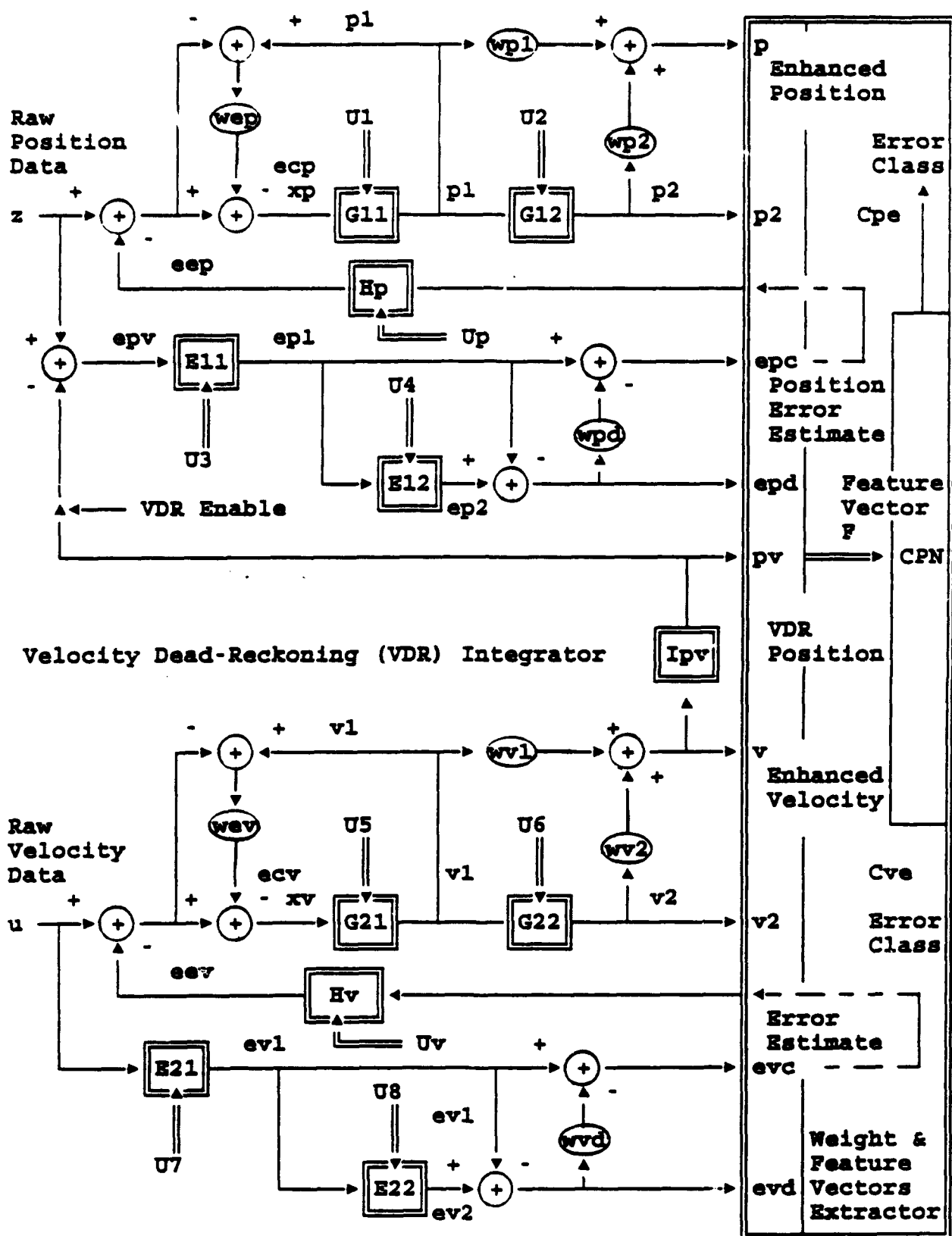


Figure 6 Gps Complementary Filters & Neural Net

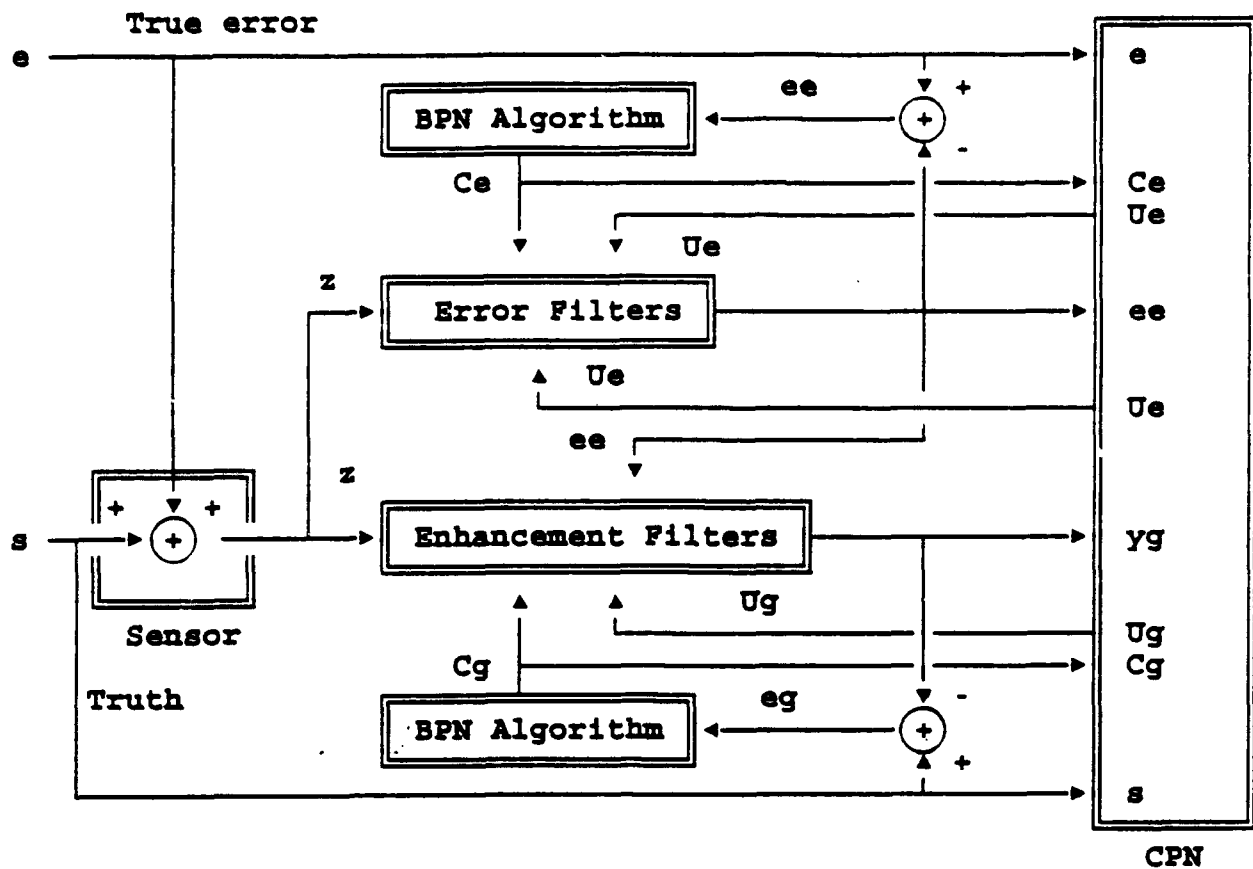


Figure 7 Neural Net & Filter Simulation Training Diagram

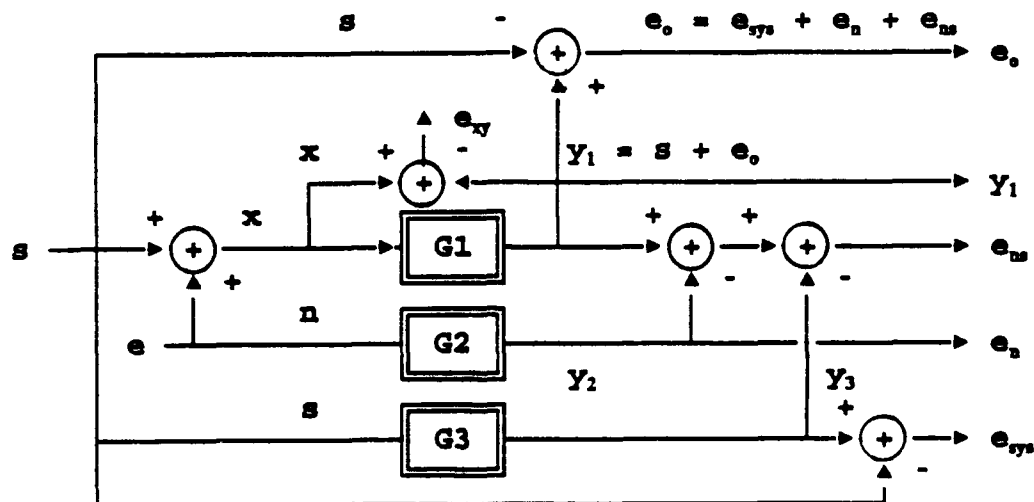
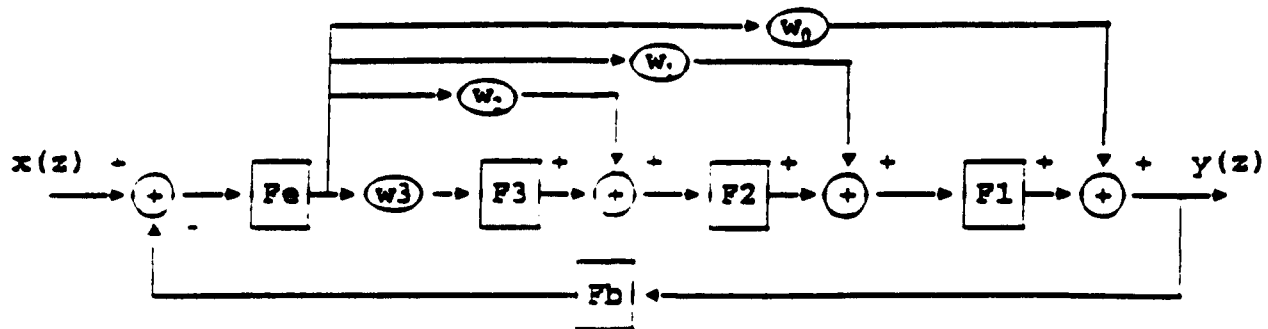


Figure 8 A Single Stage Filter Error Analysis & Training Diagram



$$F1(z) = (1 + B_N z^{-1}) / (1 - B_1 z^{-1}), \quad F2(z) = (1 + z^{-1}) / (1 - B_2 z^{-1})$$

$$F3(z) = [1 + (5 - B_3) z^{-1} + B_3^2 z^{-2}] / (1 - B_3^2 z^{-2}), \quad Fb(z) = z^{-1}$$

$$Ke(z) = W_1 [K(z) / (1 - B_1 z^{-1})], \quad K(z) = \sum_{j=0}^{N-1} A_j z^{-j}, \quad W_1 = 1/aT, \quad 0 < a < 1$$

$$G(z) = N(z) / [1 + D(z)], \quad N(z) = \sum_{j=0}^L N_j z^{-j}, \quad D(z) = \sum_{j=0}^{L+1} D_j z^{-j}, \quad L=N+q$$

$$N_j = n_0 A_j + n_1 A_{j+1} + n_2 A_{j+2} + n_3 A_{j+3} + n_4 A_{j+4}$$

$$n_0 = w_0 + w_1 + w_2 + w_3$$

$$n_1 = -(B_1 + B_2) w_0 + (B_N - B_2) w_1 + (1 + B_N) w_2 + (6 - B_3 + B_N) w_3$$

$$n_2 = [B_1 B_2 - B_3^2] w_0 + (B_N B_2 - B_3^2) w_1 + (B_N - B_3^2) w_2 + [5 + B_N(6 - B_3)] w_3$$

$$n_3 = [(B_1 + B_2) B_3^2] w_0 + (B_2 - B_N) B_3^2 w_1 - (1 + B_N) B_3^2 w_2 + (5 B_N + B_3) w_3$$

$$n_4 = B_1 B_2 B_3^2 w_0 + B_N B_2 B_3^2 w_1 - B_N B_3^2 w_2 + B_N B_3 w_3$$

$$D_j = N_{j+1} + d_j, \quad D_j, \quad j = 1, 2, \dots, L+1, \quad \text{and} \quad d_j, \quad j = 0, 1, 2, 3, 4, 5$$

$$d_0 = 1, \quad d_1 = -(B_1 + B_2 + B_3)$$

$$d_2 = B_1 B_2 - B_3^2 + B_3(B_1 + B_2)$$

$$d_3 = (B_1 + B_2) B_3^2 - B_3(B_1 B_2 - B_3^2)$$

$$d_4 = -[B_1 B_2 - B_3(B_1 + B_2)] B_3^2$$

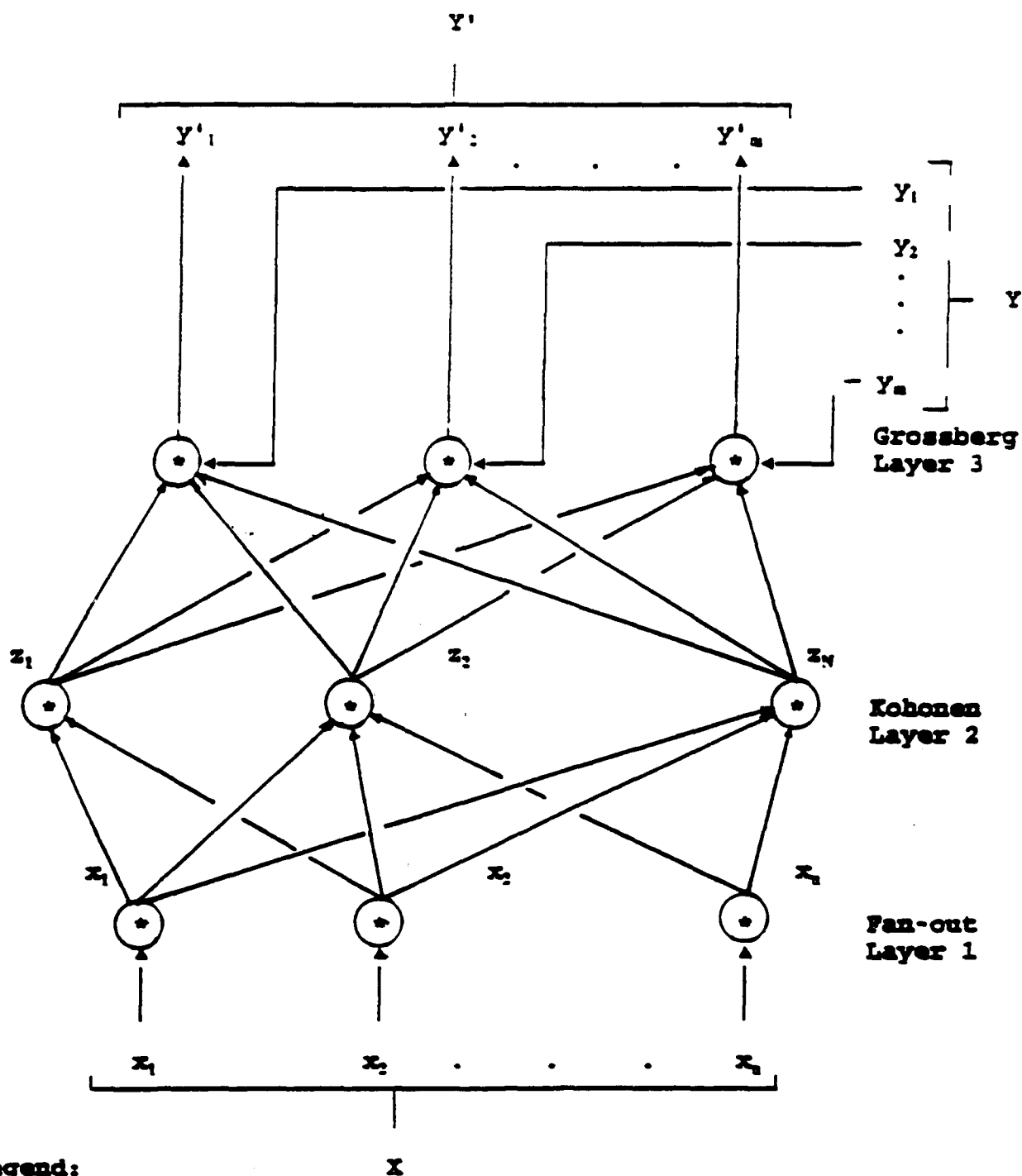
$$d_5 = B_1 B_2 B_3^2$$

Figure 9 Single Stage Error or Data Adaptive Recursive Filter

Designation	$c_j$	Coefficient Value > 0
$2_u^a$	—	$co_j(1 + 1/2 + 1/4 + \dots + 1/2^k + \dots + 1/2^K)$
$8_u$	—	$co_j(1 + 1/2 + 1/4 + 1/8)$
$7_u$	—	$co_j(1 + 1/2 + 1/4)$
$6_u$	—	$co_j(1 + 1/2 + 1/4 - 1/8)$
$5_u$	==	$co_j(1 + 1/2)$
$4_u$	—	$co_j(1 + 1/2 - 1/4 + 1/8)$
$3_u$	—	$co_j(1 + 1/2 - 1/4)$
$2_u$	—	$co_j(1 + 1/2 - 1/4 - 1/8)$
$1_o$	==	$co_j$
$2_i$	—	$co_j(1 - 1/2 + 1/4 + 1/8)$
$3_i$	—	$co_j(1 - 1/2 + 1/4)$
$4_i$	—	$co_j(1 - 1/2 + 1/4 - 1/8)$
$5_i$	==	$co_j(1 - 1/2)$
$6_i$	—	$co_j(1 - 1/2 - 1/4 + 1/8)$
$7_i$	—	$co_j(1 - 1/2 - 1/4)$
$8_i$	—	$co_j(1 - 1/2 - 1/4 - 1/8)$
$2_i^a$	—	$co_j(1 - 1/2 - 1/4 - \dots - 1/2^k - \dots - 1/2^K)$
	—	0

Figure 10 Coefficient  $c_j$  Weight Space





Legend:

$X$  = feature vector  
 $Y$  = training Vector  
 $Y'$  = Output vector

Figure 11 Forward-only CPN

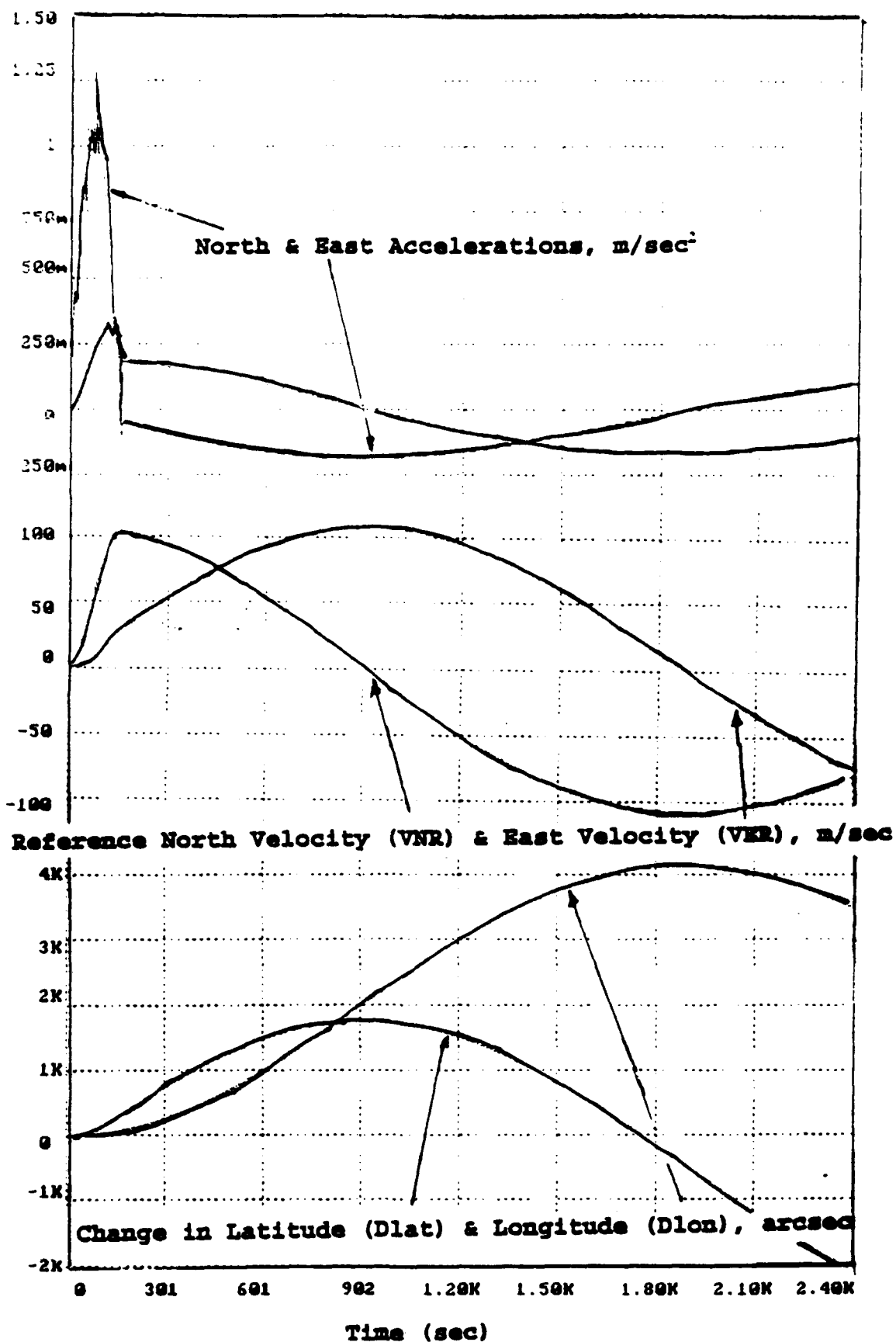


Figure 12 True Vehicle Dynamics

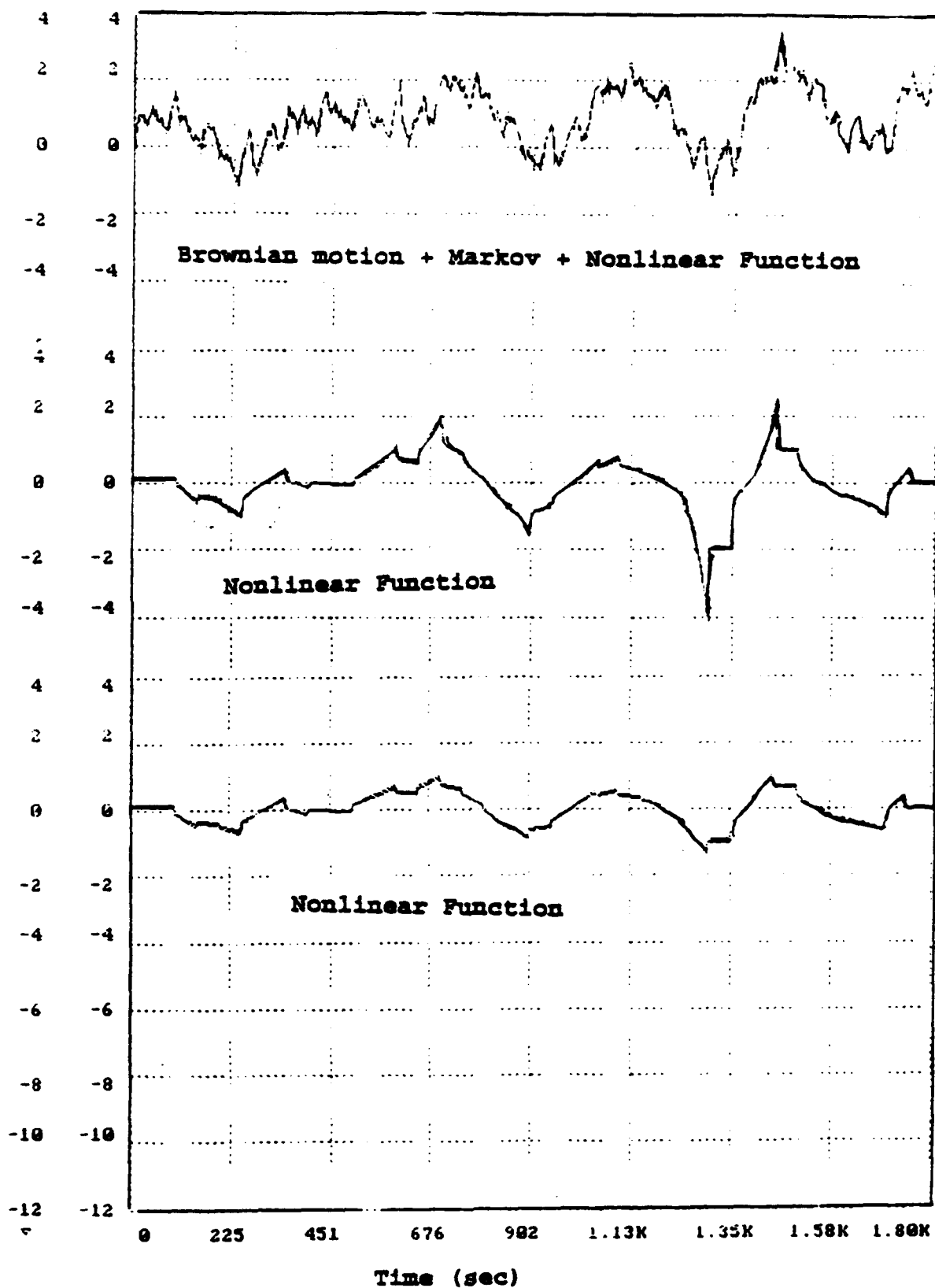


Figure 13 (a) Velocity Errors & Error Detection

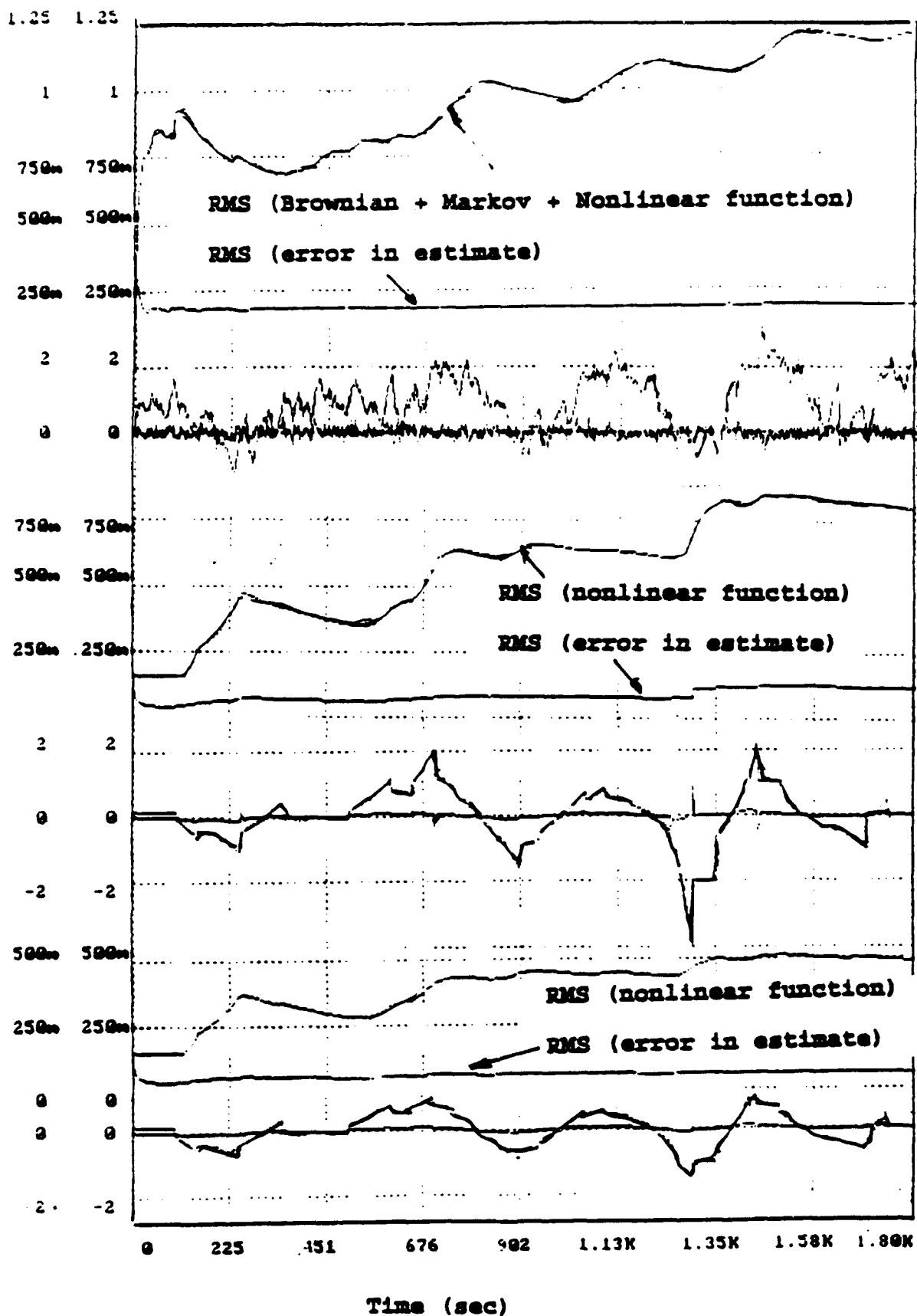


Figure 13 (b) Velocity Errors, Errors in Estimate, & RMS, m/sec

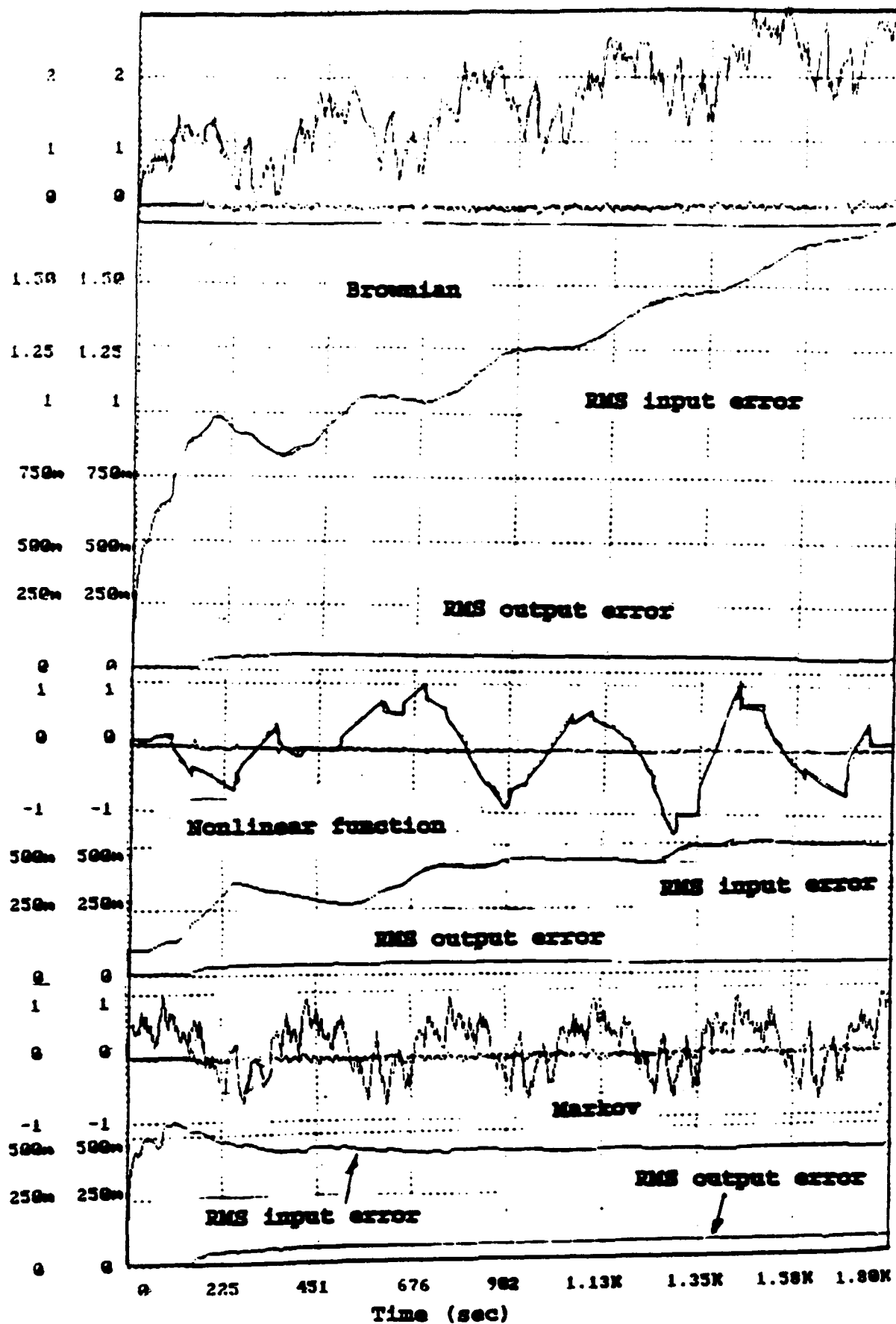


Figure 13 (c) East Velocity, Enhancement & RMS Errors, m/sec

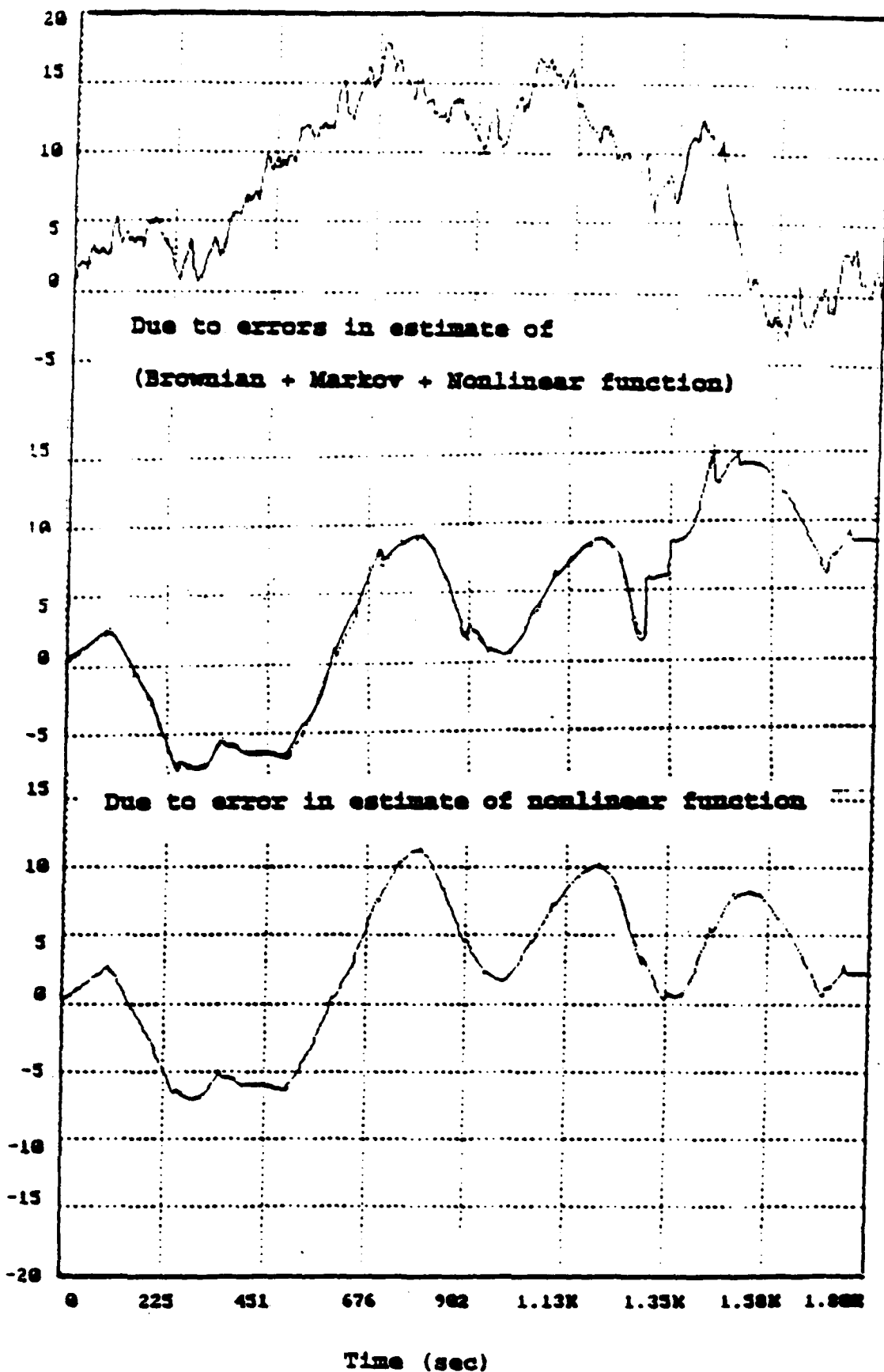


Figure 13 (d) Velocity Dead Reckoning Errors, mtrs

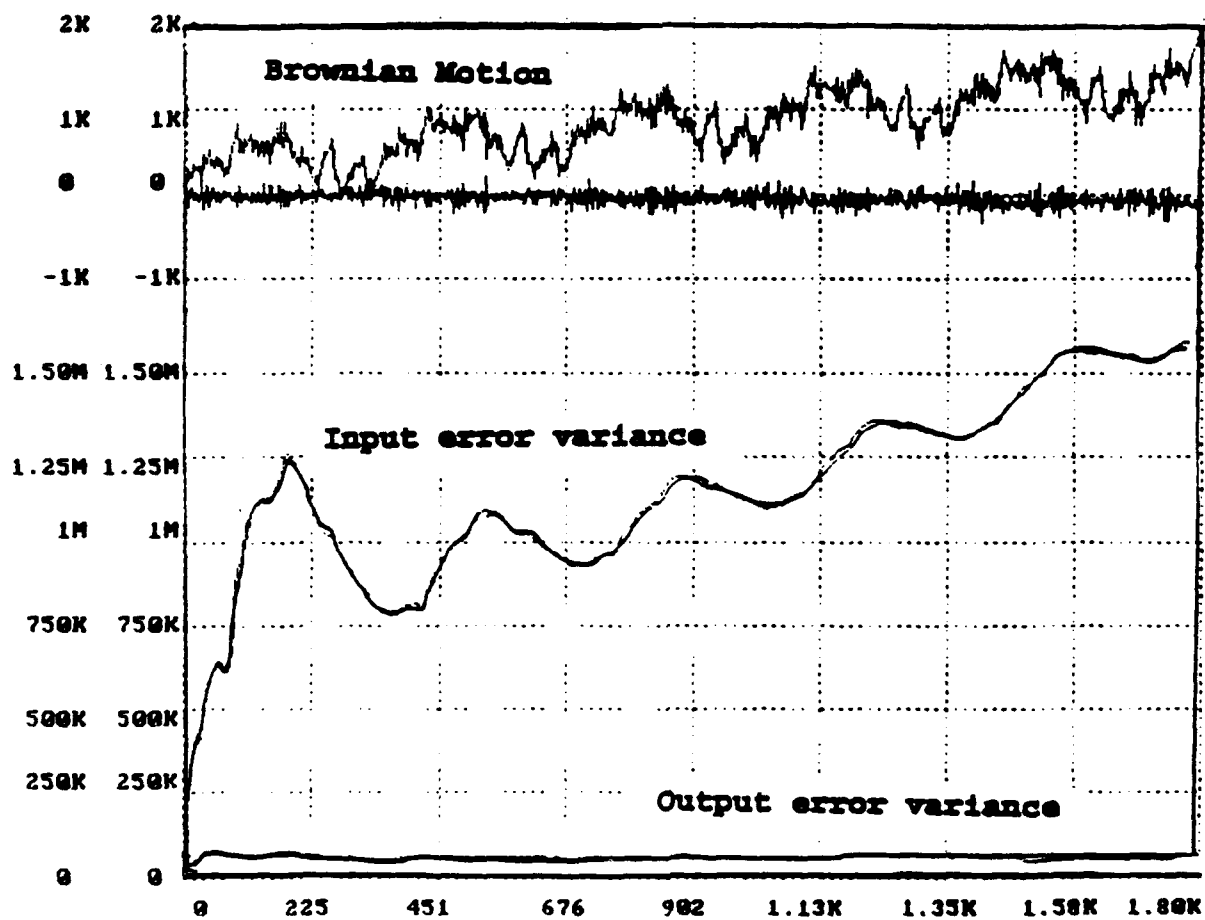
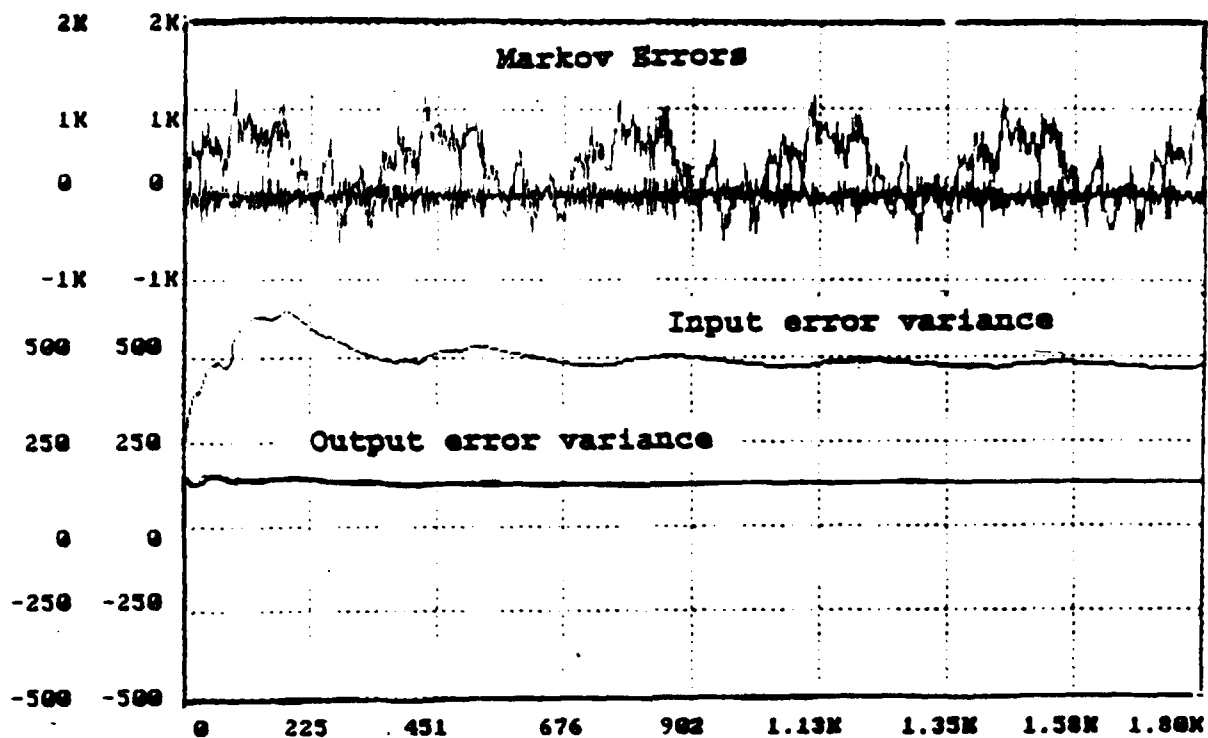
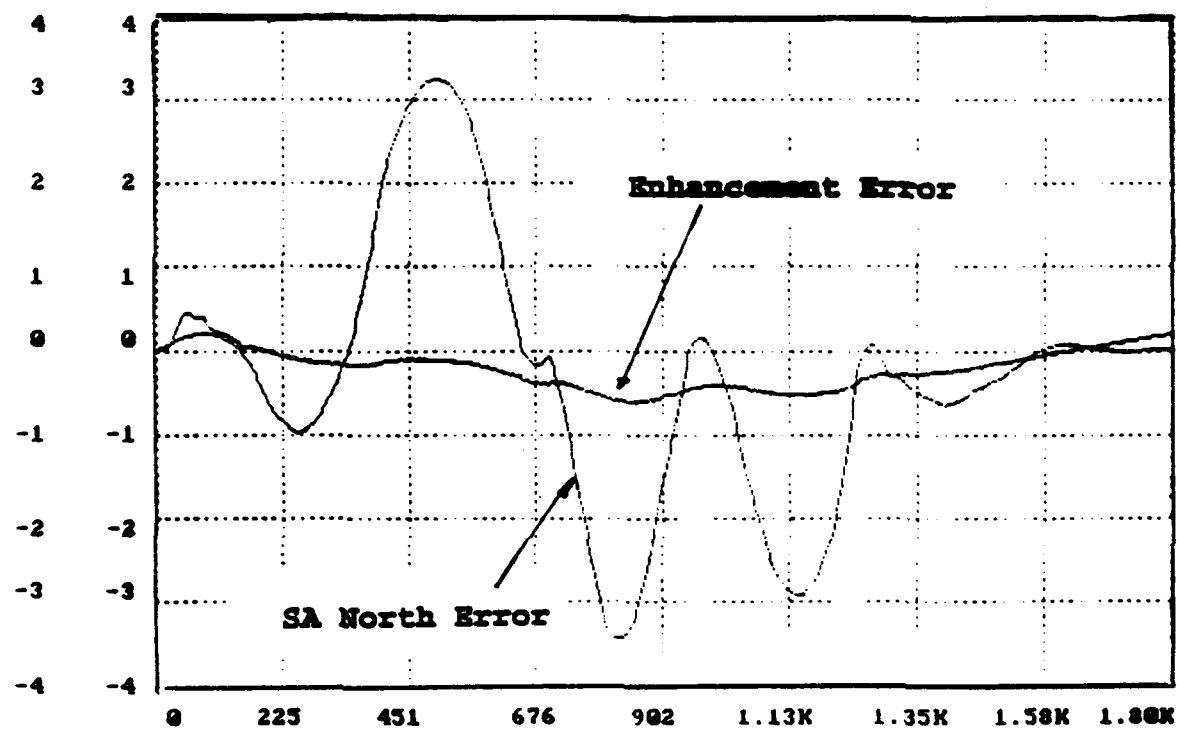
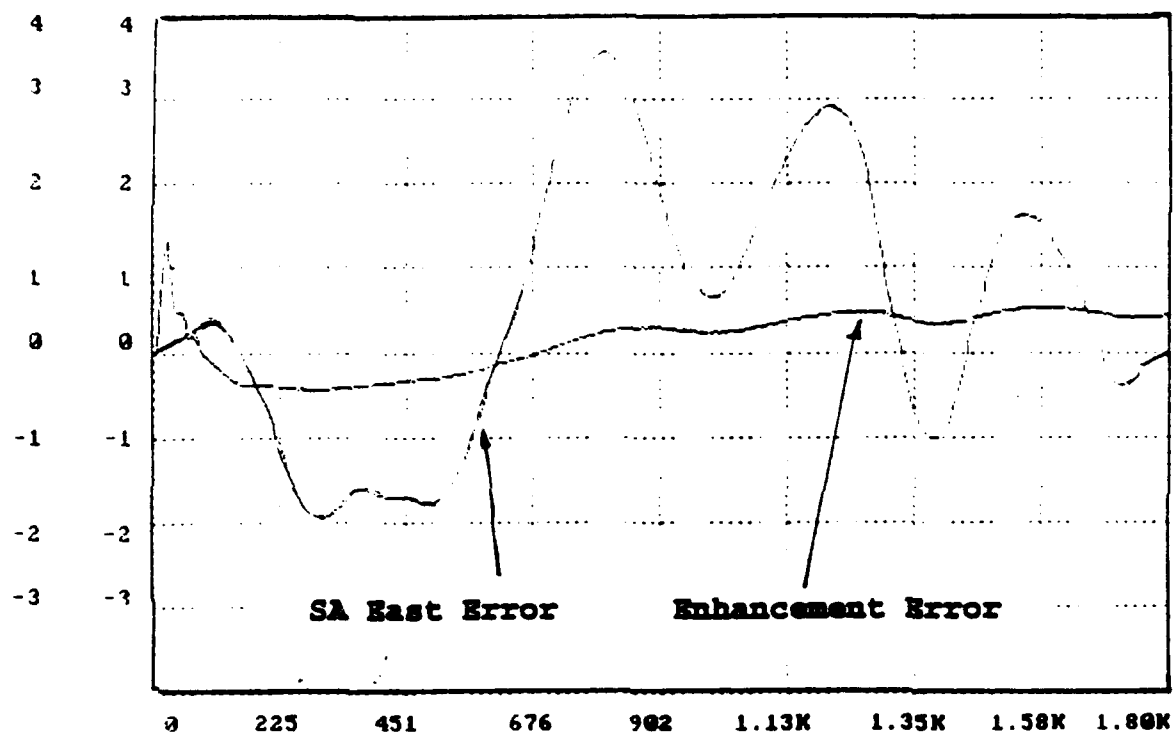


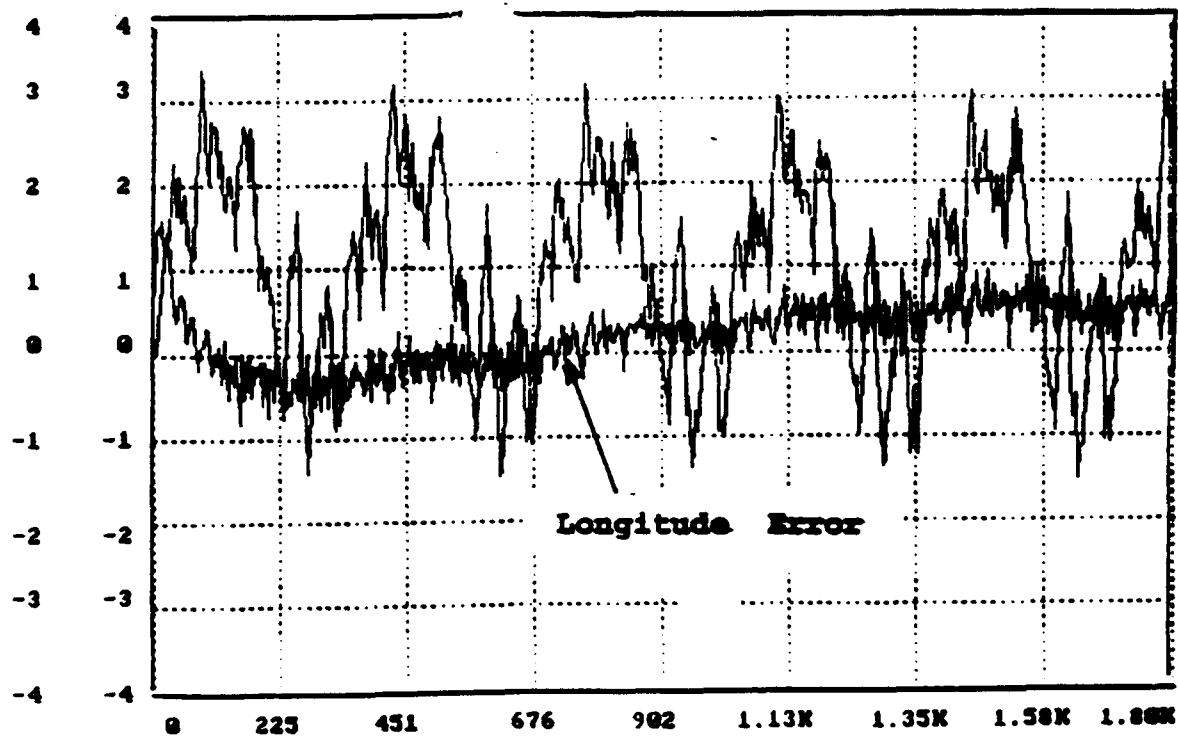
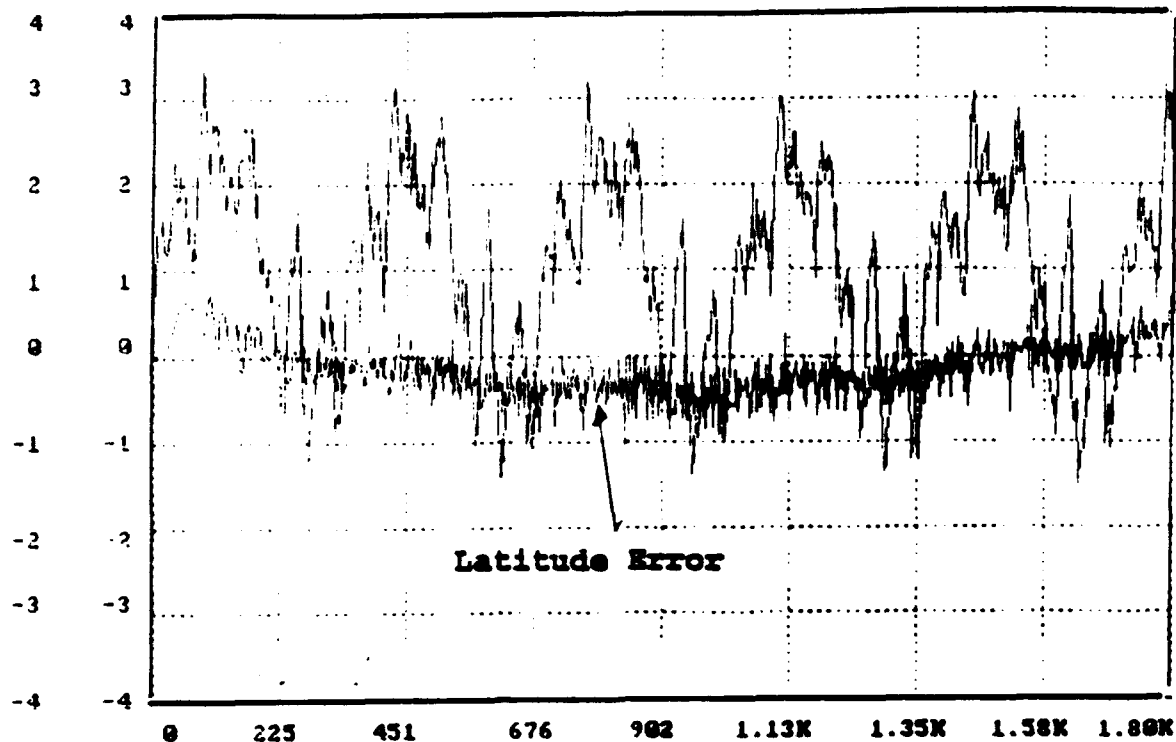
Figure 14 (a) Input, Output Position Errors, & Variances, mtrs<sup>2</sup>



Time (sec)

Figure 14 (b) Input & Output SA Errors, arcsec





Time (sec)

Figure 14 (c) Latitude, Longitude Errors With Markov Errors, arsec

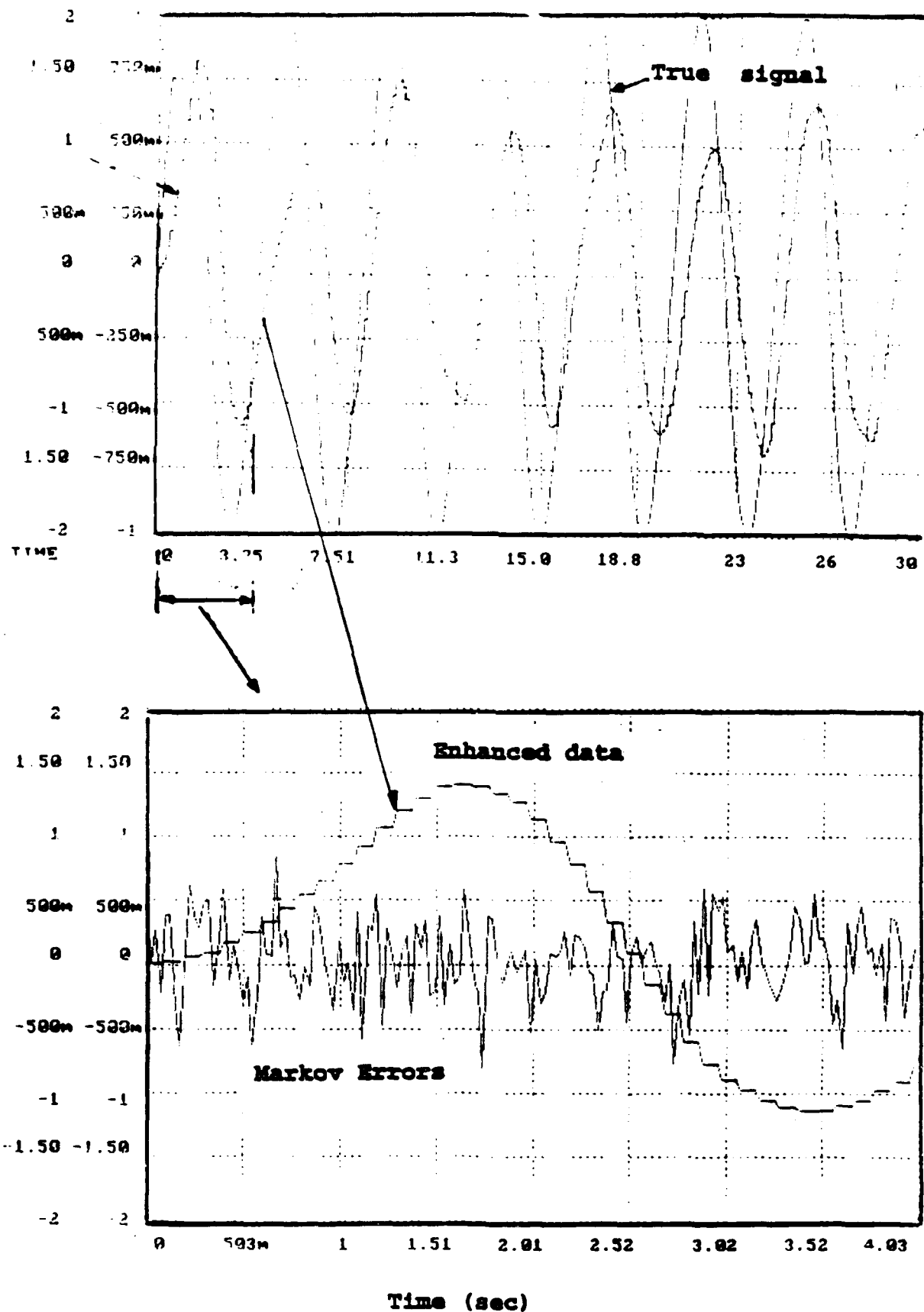


Figure 15 (a) 0.25 Hz Signal + Errors & Enhancement

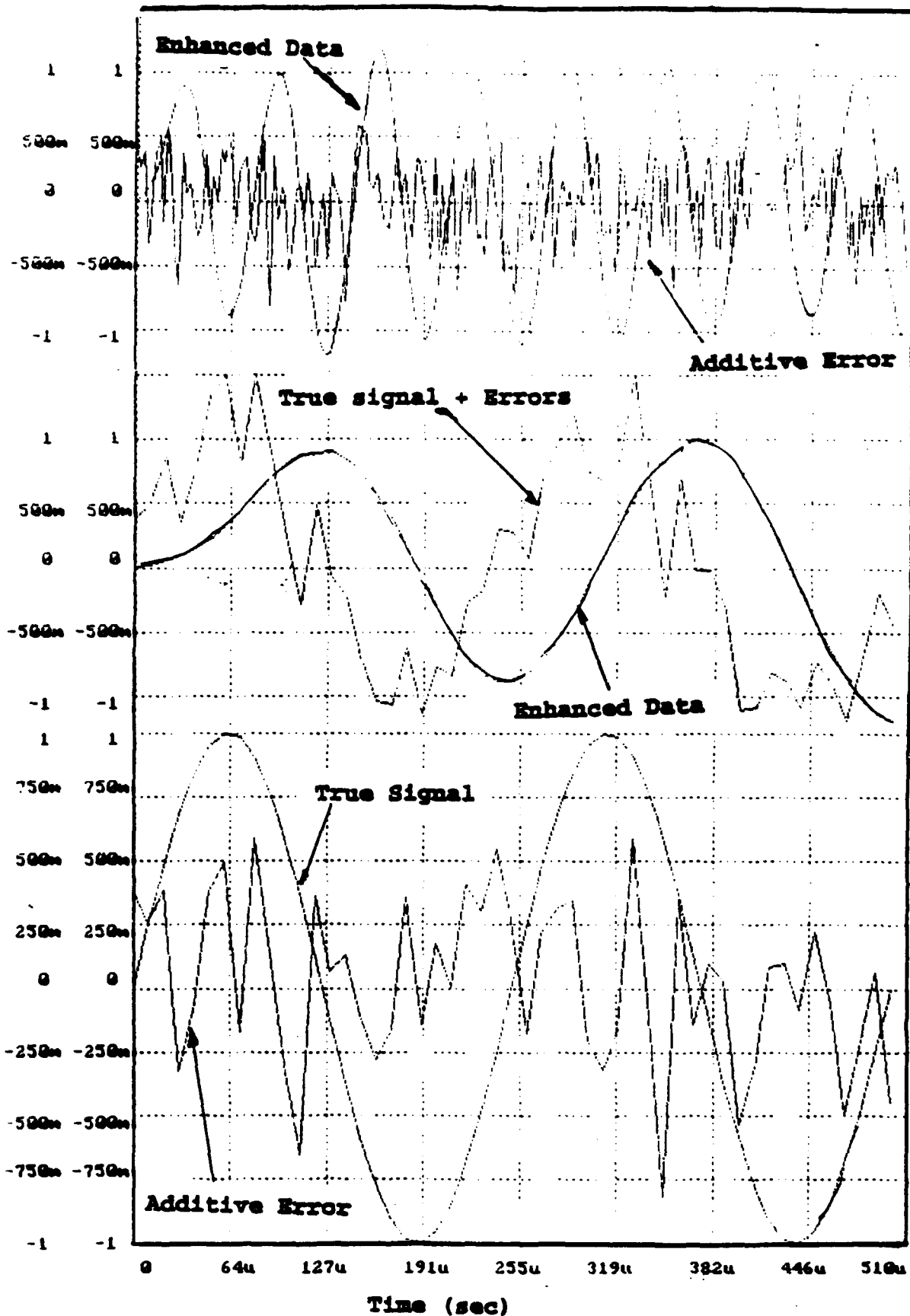
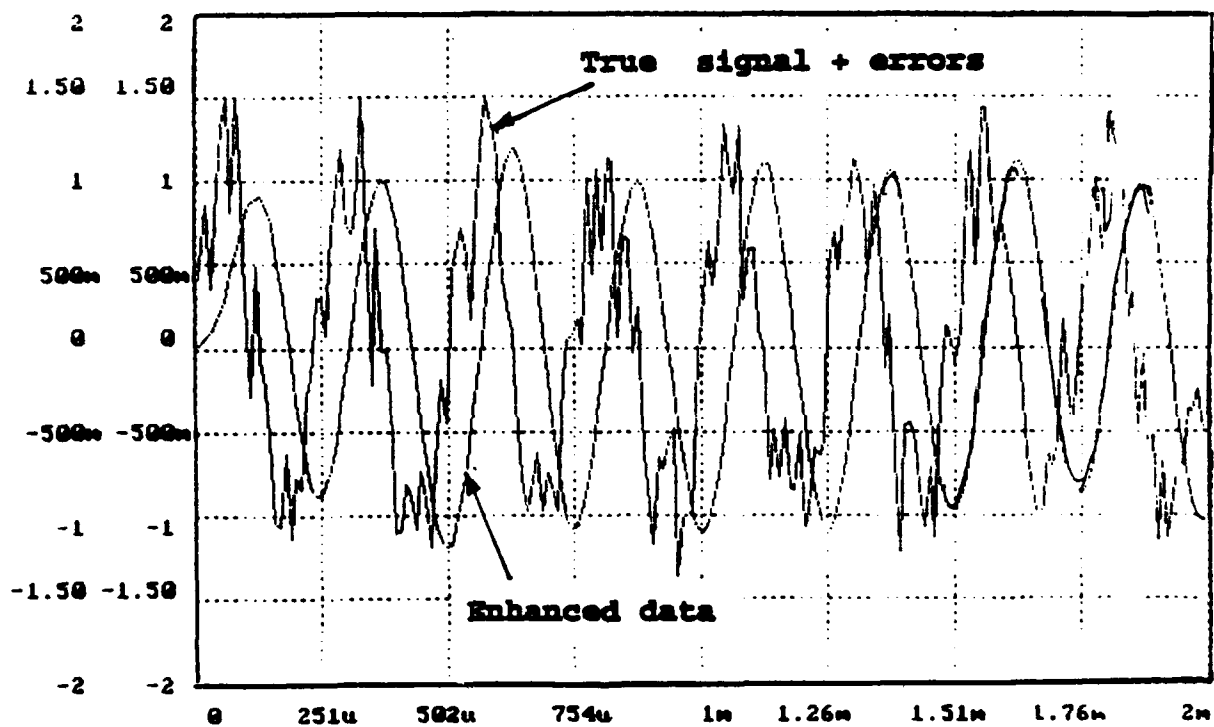
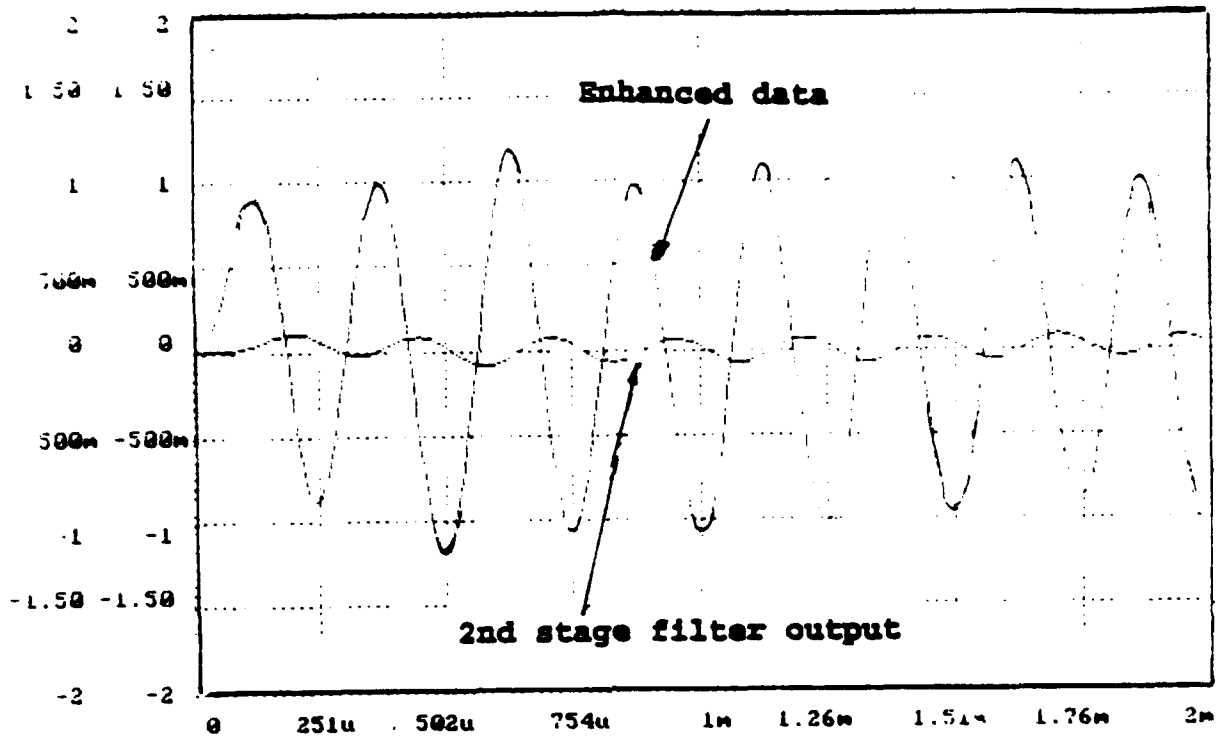


Figure 15 (b) 4 KHz Signal + Errors & Enhancement



Time (sec)

Figure 15 (c) 4 KHz Signal + Errors & Enhancement

**THIS PAGE LEFT BLANK INTENTIONALLY**

# **TEST RESULTS OF A GPS TRANSLATOR POST-TEST PROCESSING SYSTEM**

by

David E. Reed and Peter Brown

NAVSYS Corporation  
14960 Woodcarver Road  
Colorado Springs, CO 80921  
(719) 481-4877  
Fax (719) 481-4908

Presented at 16th Biennial Guidance Test Symposium, Holloman AFB, NM, October 1993

. Approved for Public Release; distribution is unlimited.

## ABSTRACT

GPS translators are currently used on US Ranges for instrumenting tests of high dynamic vehicles such as ballistic missiles. This has previously involved the use of an expensive and complicated ground processing system to track translator signals. A translator processing system (TPS) must be designed to track the translated GPS signals through very high dynamics and under low signal-to-noise conditions. Because of the nature of the missile antennas, both RHCP and LHCP signals must also be combined and tracked to obtain the best performance. Much of the expense involved with the ground based TPS equipment can be avoided if real-time data is not required.

NAVSYS Corporation has built and tested a custom translator post-test processing system (PTPS) workstation consisting of a predetection data recorder (PDR) and DSP computer cards which enable the PTPS workstation to process data in near real-time. The PTPS software allows the recorded signals to be optimally combined and tracked, even through high dynamic maneuvers. The software is also designed to allow the complete trajectory to be reconstructed through multiple passes, hence recovering data that would be lost in initial signal acquisition in a real-time system. External aiding data (from sources such as inertial or radar) can be optionally used to aid the tracking loops.

In this paper, the design of the PTPS hardware and software is described and ballistic missile translator (BMT) test results are shown to demonstrate the system performance.

## INTRODUCTION

GPS translator tracking systems have been developed by the US Navy and by the tri-service Range Applications Joint Program Office (RAJPO). These are designed to provide real-time Time Space Position Information (TSPI) data for high dynamic flight test and tracking applications.

The GPS translator concept is illustrated in Figure 1. The translator installed on-board the missile converts the received L-band GPS signals to S-band and rebroadcasts them to a ground-based translator processing system (TPS) where the location of the vehicle is determined. The RAJPO ballistic missile translator (BMT) signal spectrum is illustrated in Figure 2. To limit the S-band signal bandwidth, only the C/A code GPS signals are translated and broadcast to the TPS.

For many of the potential applications for GPS translators, the size and cost of the translator processing system currently in use in the United States is prohibitive. NAVSYS has developed a smaller, low cost translator post-test processing system (PTPS) suitable for use in these applications.

The reduction in size and cost of the system was achieved through the use of off-the-shelf components where possible. The PTPS is a "software" receiver which tracks signals from digital data recorded by a predetection data recorder (PDR).

The purpose of the PDR and PTPS is to record signals from a GPS BMT and analyze this data post-test to derive a precise trajectory for the vehicle. The PDR and PTPS adopt a fully digital architecture for recording and processing the GPS data. The translated GPS signals are sampled and stored as digital data on a high speed commercial tape recorder. The recorded digital data is processed post-test using high speed digital signal processor (DSP) cards installed in an IBM PC-compatible host computer. These DSP cards emulate the functions performed by the hardware in a GPS receiver and provide highly precise code phase and carrier phase/frequency measurements to the host computer for analysis.

This "software" receiver has a number of advantages for post-processing raw GPS data. By replaying the data through the DSP cards sequentially, it is possible to reconstruct the measurements from all satellites in view. The software receiver architecture also provides a convenient medium for developing custom high performance tracking loops. The software receiver architecture also allows integration of other sources of aiding data into the post-processed solution. The performance of the code and carrier tracking loops can be significantly improved by using aiding data from previous analyses or from other sensor data collected during the test (e.g. inertial or radar).

The software receiver architecture also allows control over the types of measurements provided to the host computer. Conventional GPS receivers provide code phase and carrier phase/frequency measurements for

computation of the position and velocity solutions. High accuracy trajectories can be generated post-test using contiguous carrier phase measurements provided by the DSP cards. These allow a kinematic GPS solution to be generated for the vehicle trajectory which is accurate to within 10 cm.

The PDR and PTPS is designed to be used on test and training ranges to derive TSPI data on participating vehicles. These include high dynamic vehicles such as ballistic and air-to-air missiles. The preamplifier/downconverter (P/DC) subsystem can also be used as a stand-alone system, integrated with a GPS receiver to provide a static test capability for GPS translators.

### SYSTEM DESCRIPTION

The functional system level diagram of the PDR and PTPS illustrated in Figure 3 conveys the functions to be accomplished, interfaces to be accommodated, and the overall architecture of the PDR and PTPS. The system includes the following functional components:

- Preamplifier/Downconverter (P/DC)
- Predetection GPS Receiver (PGR)
- Predetection Data Interface (PDI)
- Timing Reference
- VLDS Data Recorder(s)
- PC Host Computer
- Digital Signal Processing (DSP) card(s).

### VEHICLE DYNAMICS

The PDR and PTPS are capable of recording and processing the translator signals from a vehicle experiencing 50g-50g/s dynamics and 6,000 m/s velocity. In addition to the dynamics (Doppler shift) of the vehicle, the PTPS is capable of tracking the Doppler inserted by a translator clock offset of up to  $\pm 10$  ppm (24 kHz). The worst case Doppler that can be experienced on the S-band signal is  $\pm 72$  kHz. The maximum Doppler on the L-band link is 20 kHz. Thus, the PTPS is designed to track over  $\pm 92$  kHz of total frequency offset.

### PREAMPLIFIER/DOWNCONVERTER

The preamplifier/downconverter (P/DC) is illustrated in Figure 4. The following functions are performed by the P/DC.

#### Signal Polarization

The S-band signals originate from GPS translators aboard remote vehicles. Two S-band channels are required to receive both RHCP (right hand circular polarization) and LHCP (left hand circular polarization) translated S-band GPS signals. This facilitates the use of small, linearly polarized wrap-around antennas on the test vehicle and mitigates the effect of polarization changes due to Faraday rotation on very high velocity vehicles.

The RHCP and LHCP signals received by the S-band range antennas are processed by dual P/DCs. This allows both RHCP and LHCP signals to be recorded for post-test analysis.

#### S-Band Downconversion

The P/DC filters the S-band signals, adjusts the received signal level using an automatic gain control (AGC) loop, and mixes them to an IF where the signal is filtered to reduce the signal noise. The IF signal is mixed to L-band and provided as an output from the P/DC for direct input either to the predetection GPS receiver (PGR) for sampling or to a conventional GPS receiver. This provides the option of recording the signals for post-test analysis or tracking the signals in real-time for static test applications.

The received translator pilot carrier (PC) signal is also mixed to an IF and provided for sampling and recording. The PC signal is also sampled and provided to the P/DC controller (PDCC) card embedded in the host computer for use in AGC and PC frequency tracking.

The PDCC can track the PC frequency in either an open or closed loop mode. The open loop mode is used when the P/DC is operated using the 10 MHz external oscillator. The frequency of the PC is estimated in the PDCC using a software implementation of a frequency locked loop (FLL), and provided along with the AGC status data for logging on the data recorder direct channel. The closed loop frequency tracking mode is used when the P/DC is operating from the internal VCXO. In this mode, the PDCC operates an FLL that adjusts the VCXO control voltage by addressing a D/A converter in the P/DC which drives the PC frequency offset to zero.



## PREDETECTION GPS RECEIVER

The predetection GPS receiver (PGR) is used to sample the L-band GPS signals for recording and post-test analysis. The PGR can be operated interfaced with an L-band antenna and preamplifier, or connected to the L-band output of the P/DC. The PTPS system consists of two PGRs for LHCP and RHCP signals, and a third PGR as a static reference.

The L-band signal input is mixed to an IF frequency, filtered to prevent aliasing, and then hardlimited. Both In-phase (I) and Quadrature (Q) signals are generated at a convenient IF near base-band. The I and Q signals are lowpass filtered to 1 MHz to reduce the signal noise and prevent aliasing. The signals are then hardlimited and provided to the PDI, where they are sampled at 2 MHz to provide a 1-bit I and Q digital output to the data recorder. This provides a total of 4 Mbits/sec of predetection data to be recorded for post-processing. A block diagram of the PGR is shown in Figure 5.

## OPERATOR INTERFACE

After initial start-up, the operator can control the system by typing commands from a keyboard. These must be entered with the appropriate keyword, and any values or qualifiers are specified after the keyword. Parameters entered from the keyboard during processing do not interrupt an active module, but are enacted at the next execution of the module.

The software displays the status screen shown in Figure 6. This screen is refreshed at a 1-Hz rate. The PTPS can also operate without either a keyboard or a monitor connected to the PC card. PTPS operation can also be controlled through the RS-232 serial interface from the SUN. ASCII characters sent across this interface are interpreted in the same manner as command line inputs typed from the PC keyboard. The SUN operator can view the status and message displays using the SUN's X-Windows software.

## TRACKING LOOPS

On receipt of a tracking command, the system initializes the software that performs code correlation and complex multiply on the 2 MHz raw digital data provided by the PDR. The appropriate data outputs are selected and the correct C/A code table is downloaded for the satellite to be tracked. The TRACK software module then processes the I/Q accumulated data at a

1-kHz interrupt to acquire and track the GPS signals. The code and carrier tracking loops are controlled through phase and frequency corrections. The TRACK program also logs the PTPS raw data or reads prior data files to remove the 50 bps data from the GPS signals. TRACK can also use dynamic aiding to enhance the tracking loop performance.

The TRACK program can operate in States 1 through 7. The starting and ending states are defined as inputs to the TRACK software. The mode control between the states is illustrated in Figure 7.

## CODE-TRACK

The TRACK software activates a first-order delay locked loop (DLL) with the nominal bandwidth specified by the user. The DLL can be rate-aided in each state by the carrier loop and the PC aiding data, as shown in Figure 8. Rate aiding from the PC corrects the separation between carrier and code Doppler caused by the translator. This code loop aiding is independent of S-band Doppler.

## REAL-TIME AIDING

During operation in all states, aiding data is read from common memory. This data consists of carrier frequency, code phase and rate, and/or navigation data and transition time. The carrier frequency used for tracking, DLL aiding, and writing to the PTPS file is the sum of the carrier aiding frequency plus the tracking loop frequency. The aiding code phase is also added to the DLL phase for use in tracking and for PTPS file output during acquisition only. The code rate is added to the DLL error term and carrier aiding in the code phase update during tracking.

When using PC frequency for code rate aiding, the software calculates the code rate correction frequency through the following equation

$$\dot{T}_{corr} = \frac{f_{PC}(f_S - f_L)}{(f_S - 1.92\text{MHz})1540}$$

where  $f_{PC}$  is the measured PC frequency in Hz,  $f_S$  is the nominal S-band GPS center frequency, and  $f_L$  is L1.

The PC frequency may be used in one of two ways for aiding the carrier frequency. In the clock mode (default), the PC frequency is used to remove translator offset from the carrier by adding

$$f_{\text{corr}} = \frac{f_{\text{PC}}(f_s - f_L)}{(f_s - 1.92 \text{ MHz})}$$

to the carrier loop frequency. In the Doppler mode, the PC aiding removes S-band Doppler by using

$$f_{\text{corr}} = \frac{f_{\text{PC}}(f_s)}{(f_s - 1.92 \text{ MHz})}$$

## SIMULATION

Simulation software is used to validate the performance of the high speed digital signal processing algorithms and the code and carrier tracking loops. This simulation tool generates simulated code phase and carrier phase/frequency measurements for a simulated vehicle trajectory. The simulation also provides a file of raw predetection data in the format generated by the PDR. This simulated predetection data is used to test and integrate different components of the PTPS software. The simulation software also tests the interfaces between the customer-furnished navigation and high dynamic signal tracking software.

The simulation has two main components: the dynamics simulation, and the translator, P/DC, and PGR sampler simulation. The dynamics simulation generates linear velocity profiles for testing tracking loop thresholds and PR/DR offset for testing pilot carrier aiding. The translator-P/DC-PGR simulation includes receiver filtering and sampling.

### Dynamics Simulation

First the dynamics simulation reads the input file with dynamics parameters and writes the dynamics file header. Then the program loops through the full simulation time, generating the carrier and code rates and C/N0 for each of the five SVs in the reference and translator channels and the pilot carrier channels. The dynamics simulation implements jerk pulse dynamics and sinusoidal dynamics for L-band and S-band Doppler. The reference channel and translator channels have the same L-band dynamics. The S-band dynamics are applied to the translator signals including the pilot carrier. The dynamics simulation writes the dynamics file. The jerk pulse dynamic profile used in making the PTPS simulation data is shown in Figure 9.

The translator signal is modeled with fading between the two polarizations. The fade profile is shown in Figure 10. This fade profile is the same for PC and

translator signals. The offset in C/N0 between PC and translator is controlled by the max and min values for C/N0.

This fading model simulates vehicle rotation, dynamics, and other propagation anomalies.

### Sampler Simulation

The sampler simulation generates simulated signal samples for the three GPS channels: the reference channel, the RHCP and LHCP translator channels, and the RHCP and LHCP pilot carrier channels. The carrier and code rates and C/N0s for each signal are taken from the dynamics file and signal samples are generated, including five GPS signals plus noise in the GPS channels and carrier signal samples plus noise in the PC channels. The signals are then filtered, sampled, and quantized to give the PDRCTRL bytes as they are recorded by the PDRCTRL.

The sampler simulation of the GPS channels is processed according to the PGR simulation model shown in Figure 11. The input for this simulation is the output of the dynamics simulation. The simulation has three GPS channels, reference, RHCP, and LHCP. The reference channel has a single PGR which simulates GPS signals with reference dynamics plus white Gaussian noise. The signal is simulated as I and Q lowpass signals. Both I and Q signal paths have first-order highpass filters followed by fifth-order lowpass filters, nominally 0.1 dB ripple Chebyshev with a 900 kHz 3 dB cutoff frequency. The I and Q signals are quantized to one bit and sampled at 2 Ms/s.

The translator channels are identical to the reference channels, except that translator signal dynamics and C/N0s are used. The translator channels use the same noise samples, simulating the fact that the dominant noise for both RHCP and LHCP channels originates from the translator L-band receiver. The signal paths including filters and quantizers are different, allowing for different C/N0 in RHCP and LHCP channels. The C/N0 for each SV is computed as

$$\begin{aligned} C/N0_{\text{dB}}(SV\#n) = & C/N0_{\text{dB}}(\text{L-band for } SV\#n) \\ & - 10 \log_{10} \left[ 1 + \frac{BW = 2 \times 10^6}{C/N0\_S} \right] \end{aligned}$$

where  $C/N0\_S = 10^{[C/N0_{\text{dB}}(\text{translator RHCP or LHCP})/10]}$ .

The sampler simulation of the PC channels is a simplified version of the PGR simulation. The

simulation generates samples of a single carrier plus white Gaussian noise for each RHCP and LHCP channel. Each channel is simulated with I and Q signals. The I and Q signals are filtered with second-order lowpass filters with nominal bandwidth of 100 kHz. The PC signal samples are generated from I and Q and quantized to 5 bits at a sample rate of 400 ks/s. The sample bits are shifted in serial on single bits of the 2 Ms/s bytes.

## SIMULATION TEST RESULTS

The simulation system was used to produce test data in the form recorded by the PDR. This simulated data was tracked by the PTPS to demonstrate the accuracy of the tracking loops under high dynamics and with weak signals.

Figure 12 shows the SNR and state for the PTPS loops tracking a simulated GPS signal with 40 dB-Hz C/N0 and 10g-10g/s dynamics. The loops acquire rapidly and track with a PLL. In this case, a NAV-data aiding file removes data modulation and the half-cycle phase ambiguity to simulate the case where reference receiver data aids the translator tracking. The code phase and carrier phase errors are shown in Figure 13 and Figure 14, respectively.

Figure 15 shows the loop state and C/N0 for a simulated signal with 10g-10g/s dynamics near the AFC tracking threshold. Notice that the C/N0 is about 21 dB-Hz. The frequency tracking error for this track is shown in Figure 16. Thus, the system has demonstrated excellent weak signal tracking, even under high dynamics.

Figure 17 shows C/N0 for pilot carrier tracking with 50g-50g/s dynamics and a two-second fading period. The AFC frequency error for this track is shown in Figure 18. Notice that the second-order AFC has frequency error during periods of jerk which depend on the dynamics and loop bandwidth. This loop bandwidth may be varied by user input, and other loop implementations are possible with only minor software changes.

Figure 19 shows C/N0 for a simulated translator GPS signal. The signal has 50g-50g/s S-band dynamics and 10g-10g/s L-band dynamics. Here, the S-band dynamics are largely removed by aiding from the pilot carrier Doppler. The residual L-band dynamics are tracked by the PLL. This translator signal is tracked

on both polarization channels and the tracking data from the stronger channel is used. Figure 20 shows the strongest signal PR error of 3.8 m and Figure 21 shows the strongest signal DR error of 0.7 cm.

The simulation tests demonstrate that the PTPS is capable of tracking high dynamics and providing very flexible performance. The simulation tracking has verified the tracking performance, acquisition, and SNR thresholds of the PTPS.

## BMT TEST RESULTS

The PDR and PTPS were tested using a BMT in a static laboratory setup to demonstrate the compatibility of the system with standard equipment. The test setup is shown in Figure 22. An antenna/preamp feeds the test equipment through a coaxial cable. The amplified L-band signal is split between the PDR reference receiver, the BMT input, and a Novatel commercial receiver. The BMT output is padded and split between the inputs of the LHCP and RHCP S-band PDC inputs. Thus, all receivers see the same signal through different electronics.

The data was recorded with the PDR and signals were tracked with the PTPS. Tracking results were compared between LHCP and RHCP translator channels and double difference measurements were made between translator data and Novatel data. These results demonstrate that the PDR and PTPS correctly process the translator signals with good precision for navigation.

Figure 23 and Figure 24 show signal strengths (C/N0) vs test time for satellite signals on the reference and translator channels. Notice that the translator adds noise producing C/N0 levels about 1 dB lower than the reference channel. Figure 25 and Figure 26 show LHCP-RHCP PR and DR, respectively, for satellite #21. The variation between channels is about 0.5 m in PR and 1 mm in DR.

Double difference measurements were made between different satellites and between the PTPS BMT channels and the Novatel. Results for satellites #3 and #21 for PR and DR are shown in Figure 27 and Figure 28, respectively. The resulting PR error is 0.65 m and the DR error is 0.8 mm. These may be optimistic, since the PTPS DLL bandwidth may be larger than that used for the Novatel. Assuming zero error in the Novatel, the PR error would be 0.92 m.

Thus, the PTPS has tracked BMT translator signals, including translated GPS signals and the pilot carrier. The pilot carrier was tracked and used to aid the tracking of the translated GPS signals. Double difference measurements show that the tracking loops correctly compensate for the translator offset and give PR and DR data sufficient for high accuracy navigation.

## CONCLUSIONS

The PDR and PTPS provide excellent performance and flexibility for a fraction of the cost of standard TPS equipment. The system has been proven with live data in static tests and in high dynamic scenarios with simulated data. The system is scheduled for live flight trials in 1993. Furthermore, the system has been tested with a standard BMT demonstrating its compatibility and accuracy. The software receiver architecture gives unparalleled flexibility for making maximal use of test data by allowing adaptive processing with multiple passes through the difficult or interesting moments.

## REFERENCES

- [1] J.B. McConnell, R.H. Greenberg, R.B. Pickett, P.C. Wildhagen, A.K. Brown, "Advances in GPS Translator Technology," ION Satellite Division Conference Proceedings, September 1989.
- [2] "Miniaturized GPS Translator and Translator Processing System Development, Phase II Final Report," NAVSYS Document TPS-91-05, August 1991.
- [3] A. Brown, W. Sward, P. Brown, "Test Results of the Advanced Translator Processing System," AGARD Conference Proceedings and Symposium on Radio Location Techniques, London, May 1992.

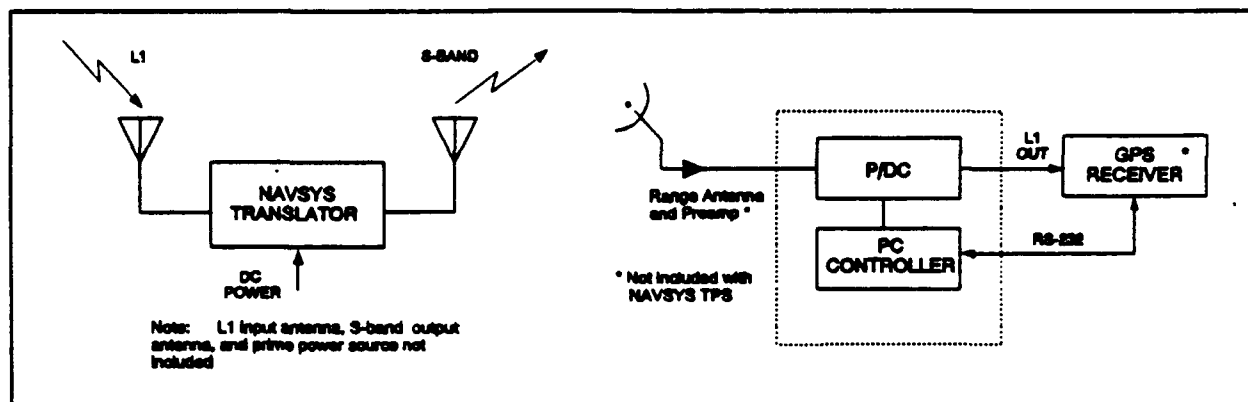


Figure 1 GPS Translator and Advanced Translator Processing System

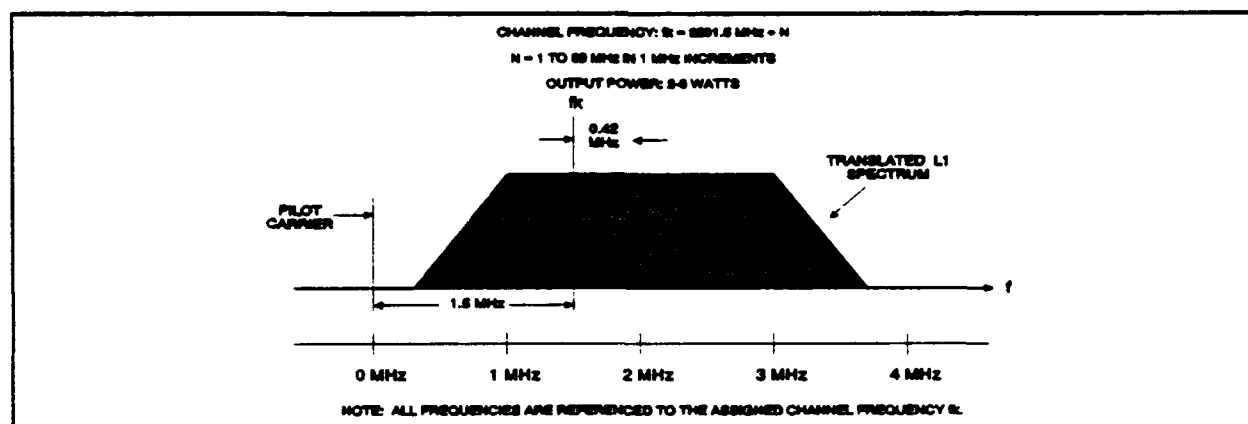


Figure 2 BMT Translator Signal Spectrum

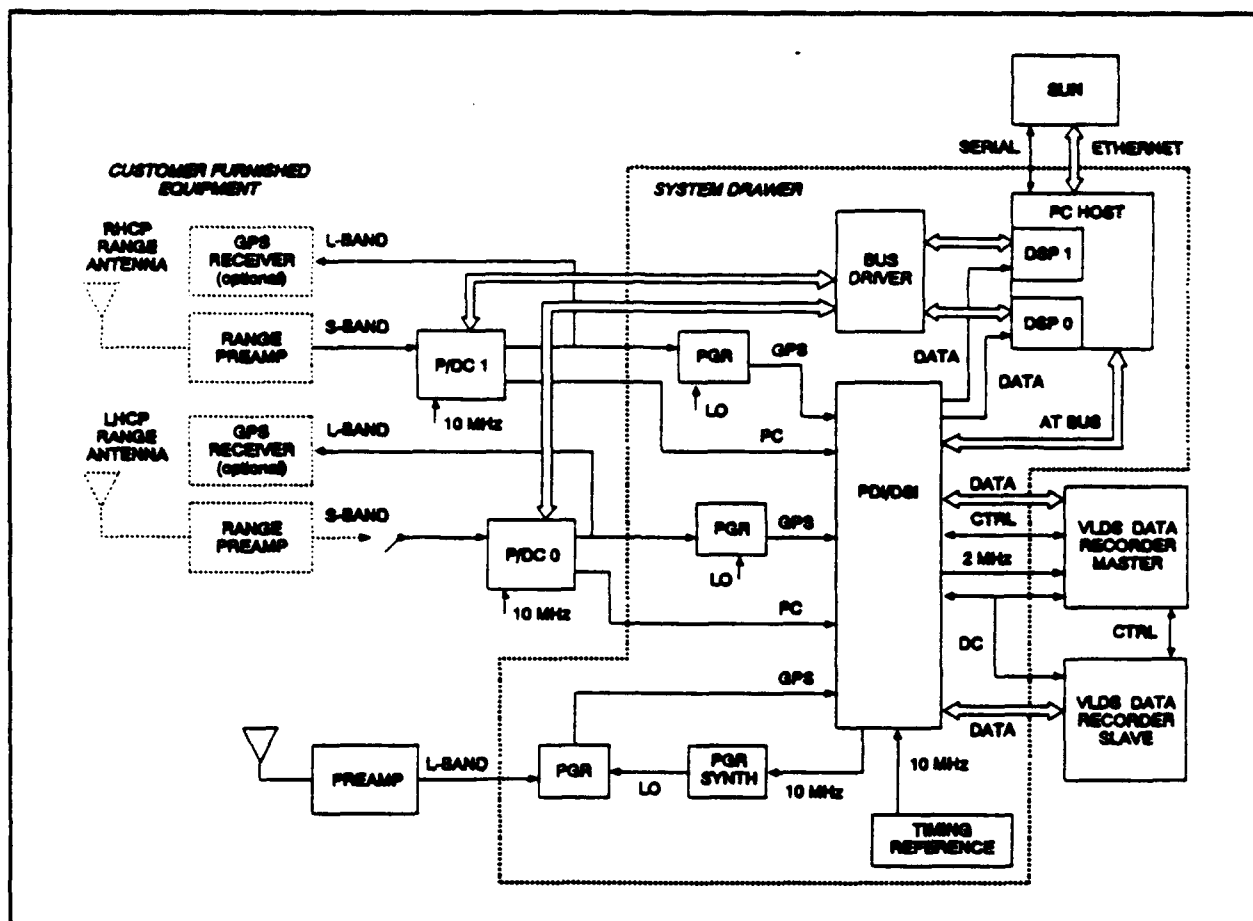


Figure 3 PDR and PTPS Functional Block Diagram

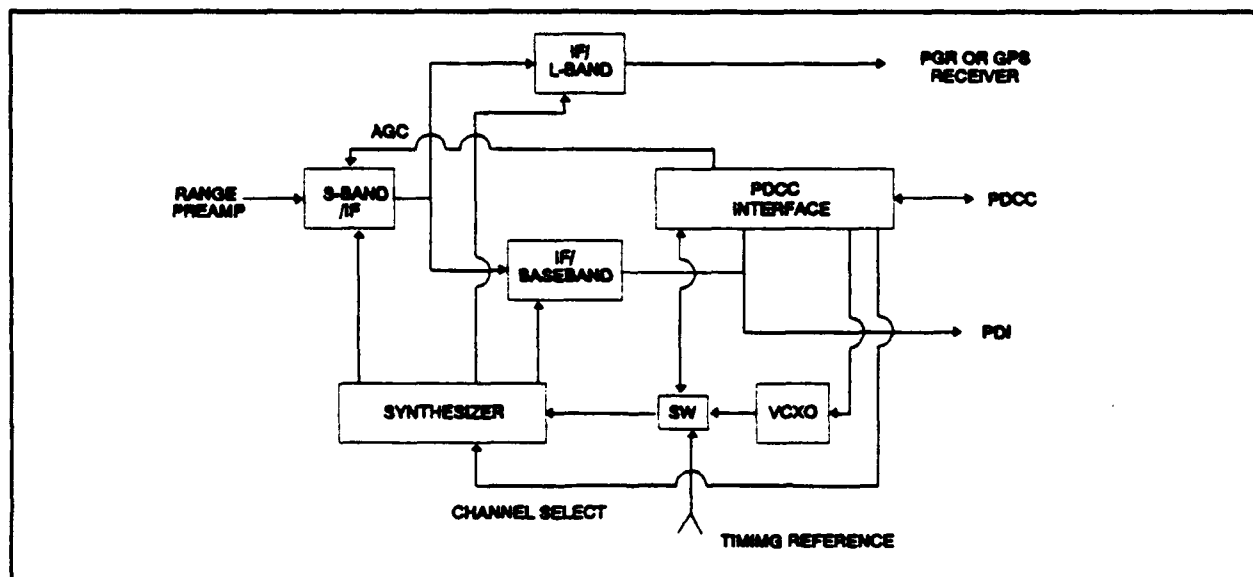


Figure 4 P/DC Functional Block Diagram

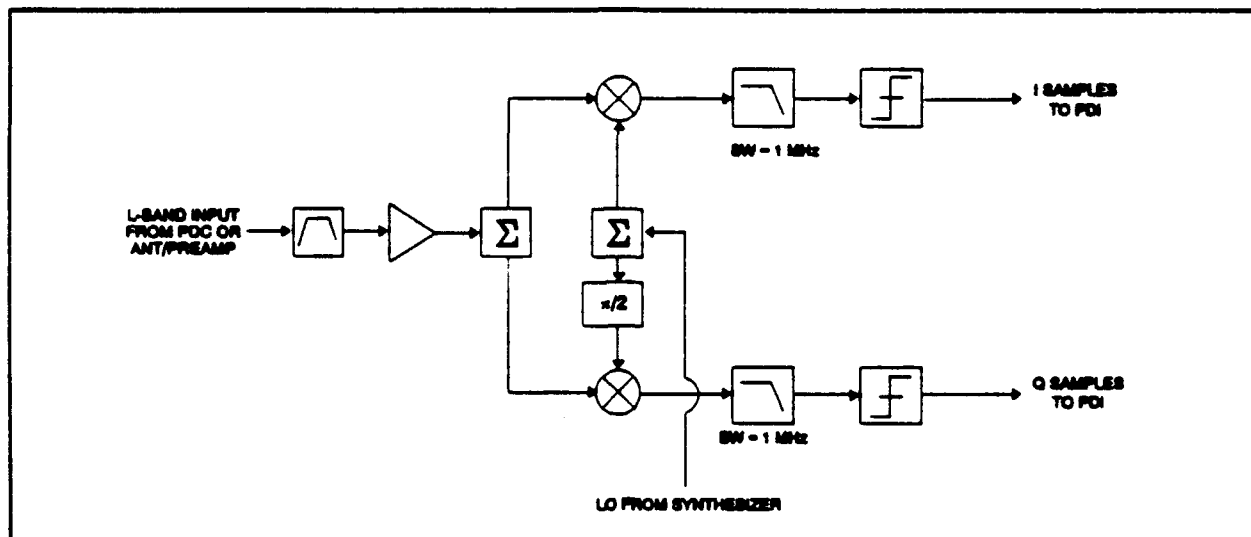


Figure 5 PGR Block Diagram

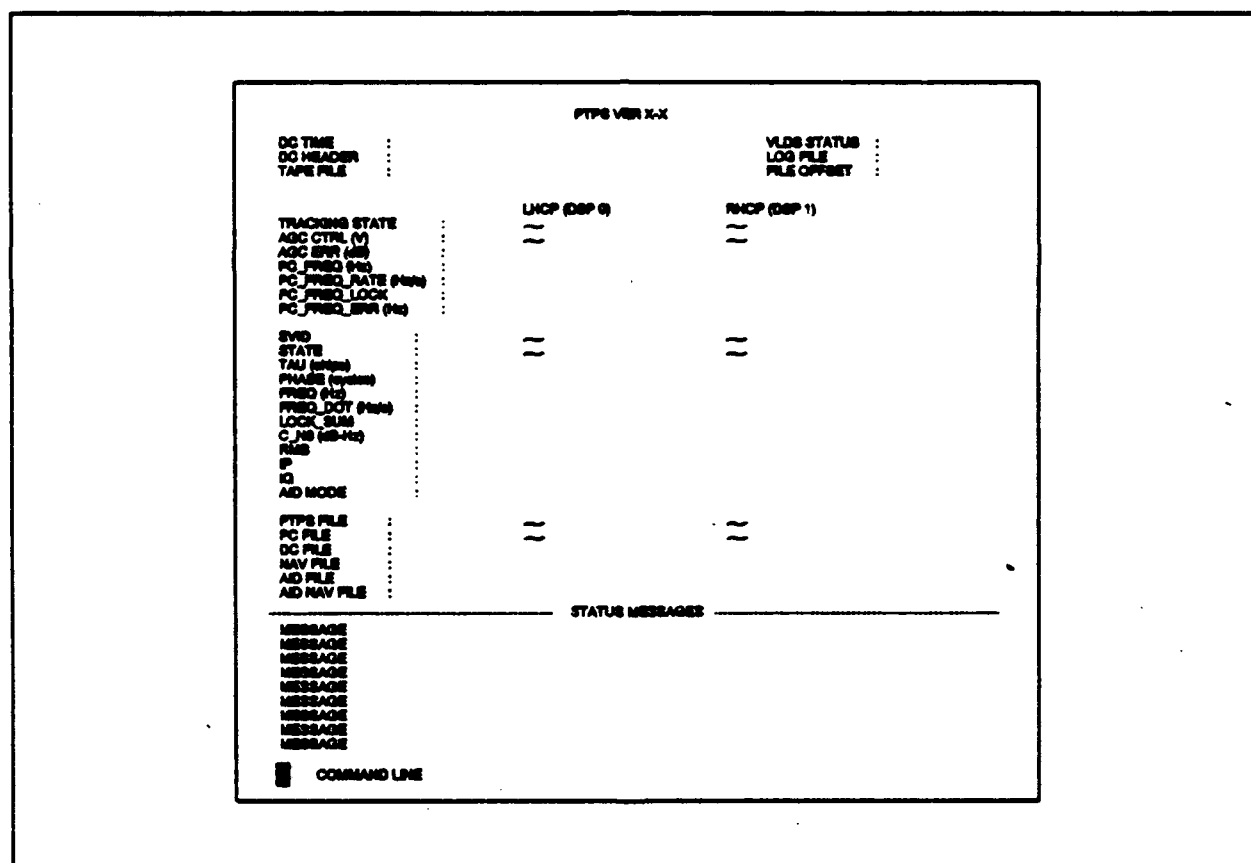
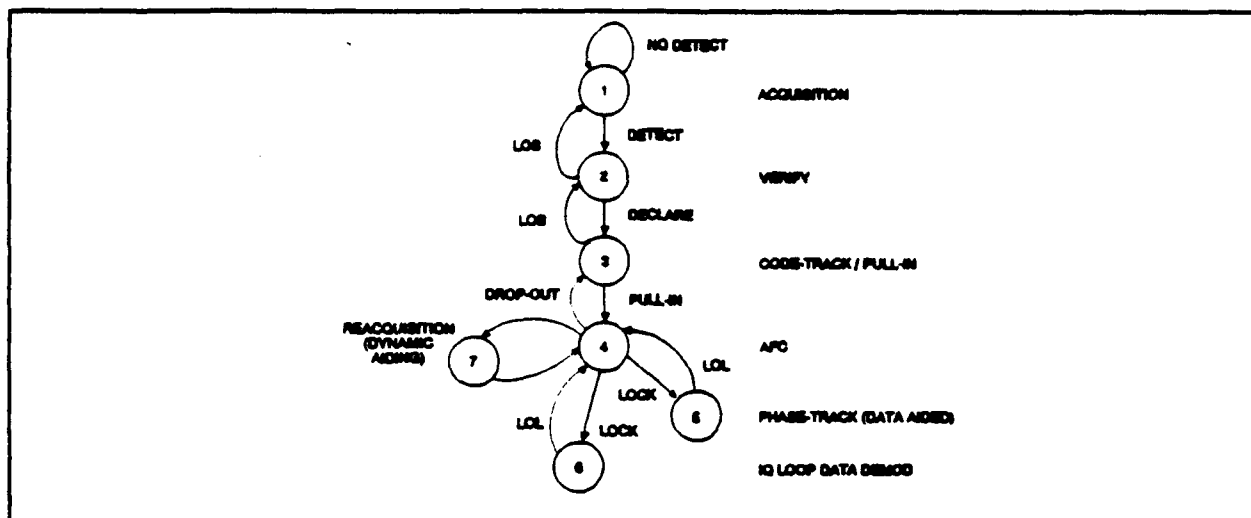
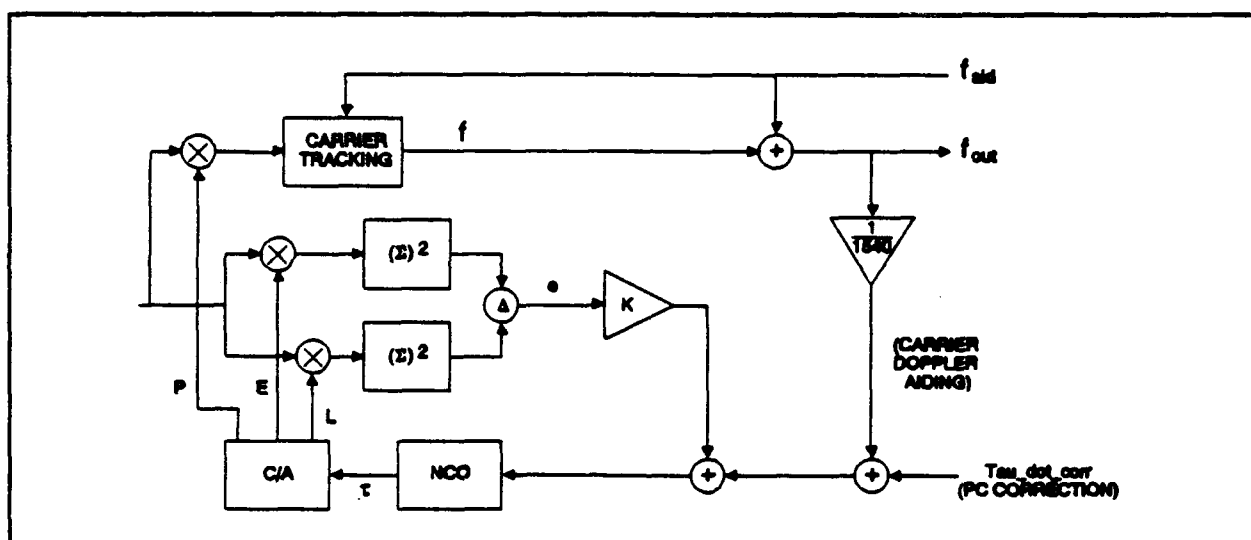


Figure 6 PTPS Display Screen



### Figure 7 TRACK Software States



### Figure 8 Tracking Loop Rate Aiding

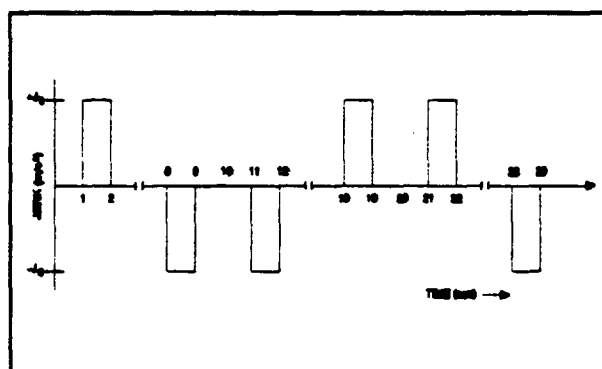


### Figure 9 Jerk Pulse Profile

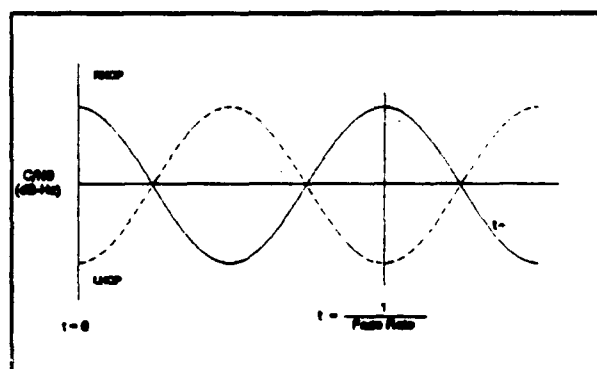


### Figure 10 Fade Profile

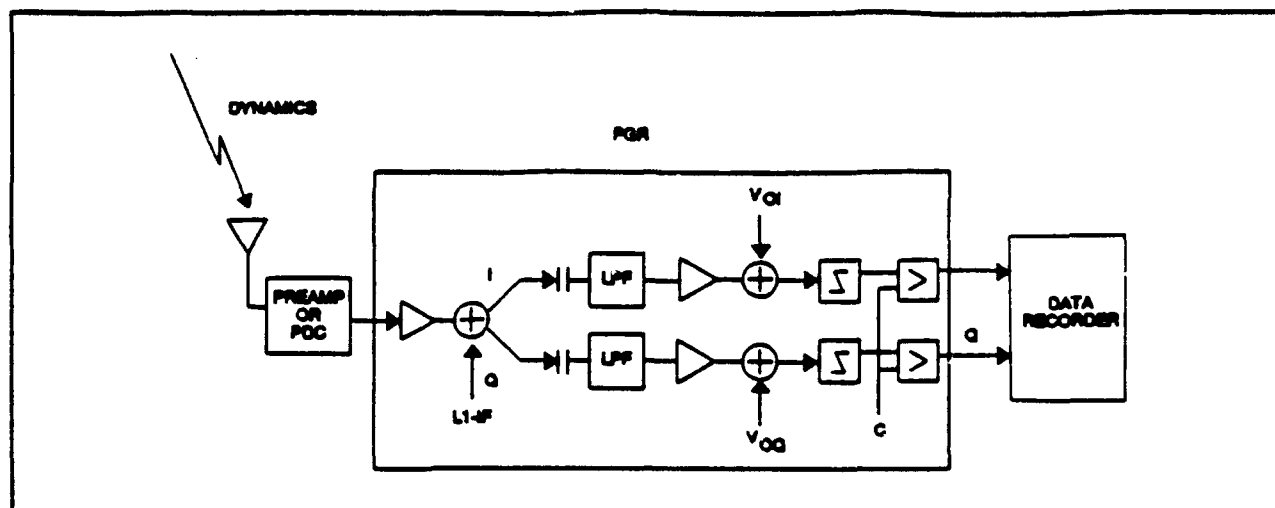


Figure 11 PGR Receiver Simulation

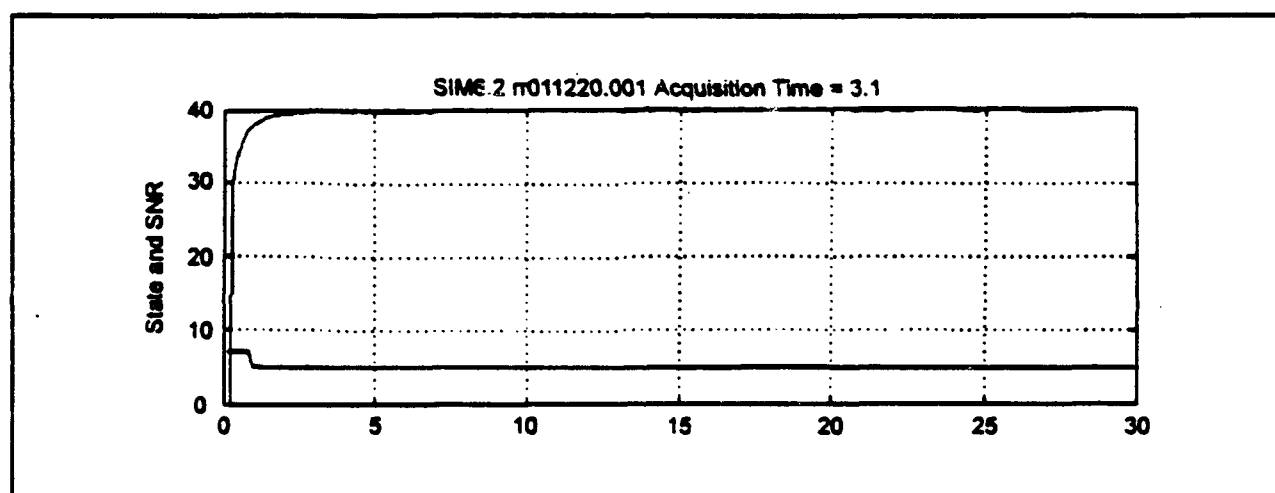


Figure 12 Simulated High Dynamic Signal Tracking

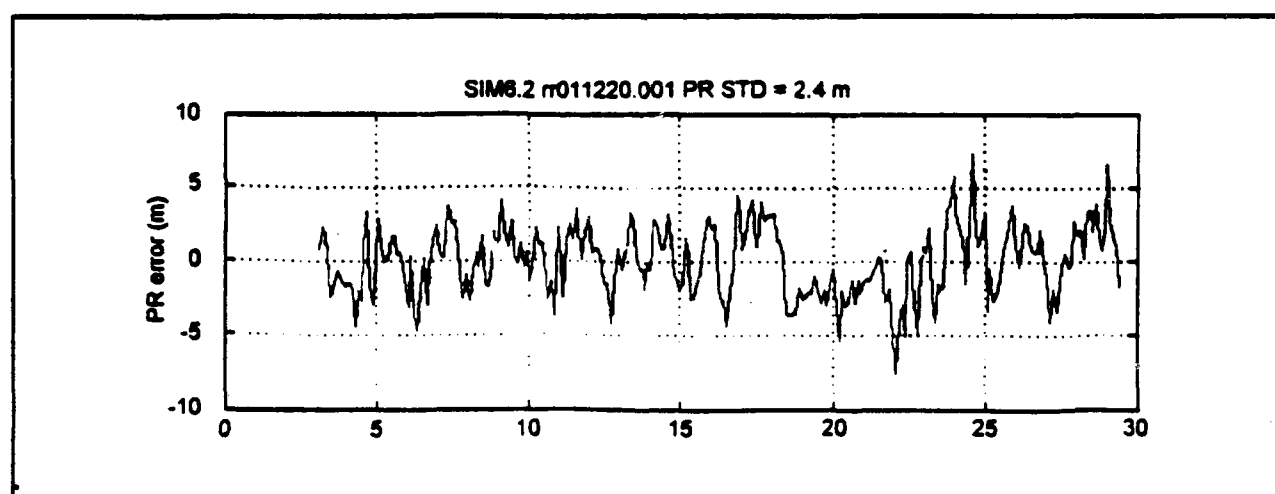


Figure 13 Simulated 10g-10g/s Tracking PR Error



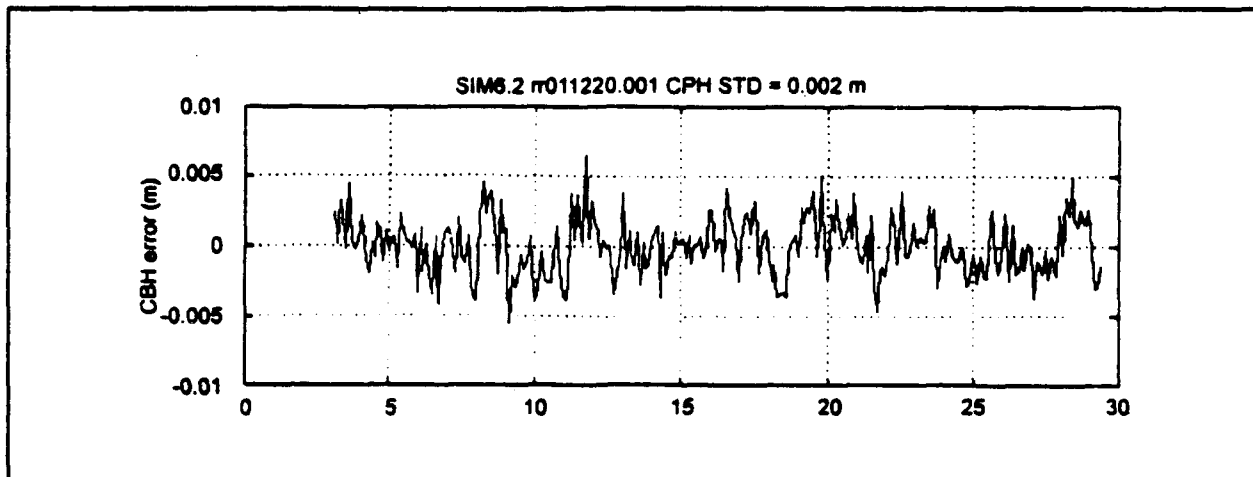


Figure 14 Simulated 10g-10g/s Tracking Carrier Phase Error

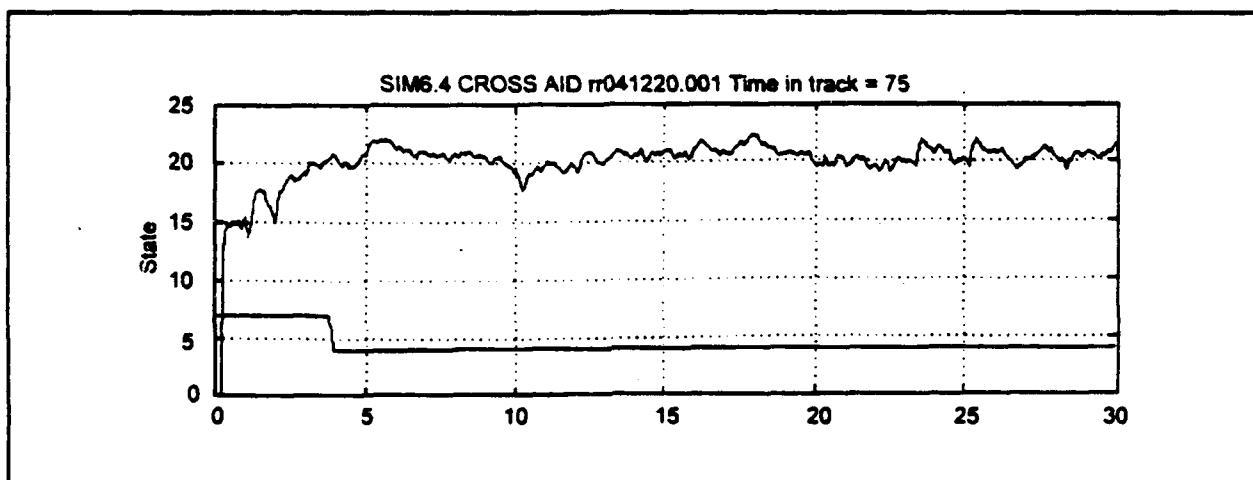


Figure 15 Simulated 10g-10g/s Track at AFC Threshold SNR Error

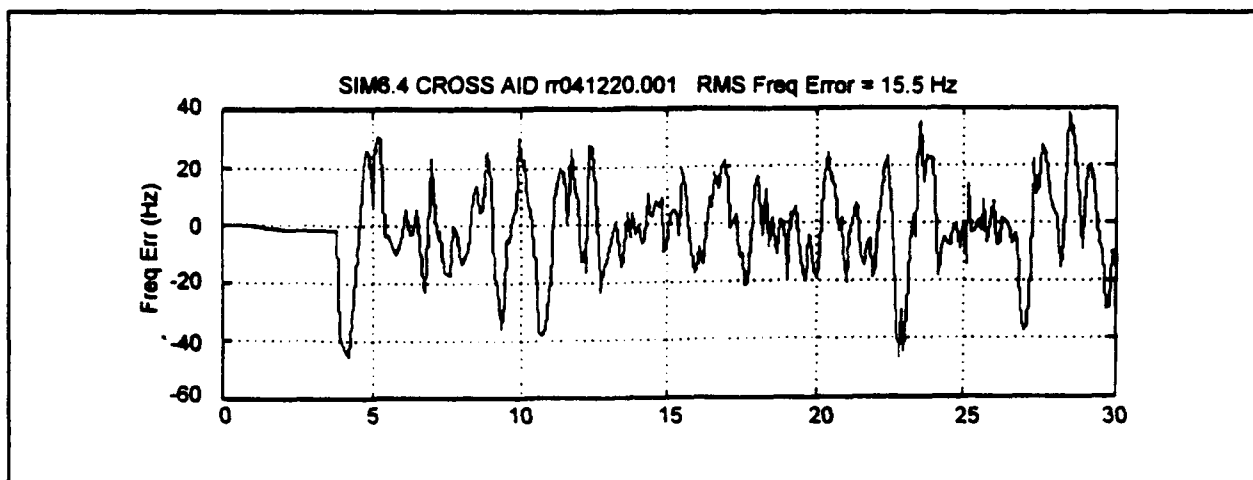


Figure 16 Simulated 10g-10g/s Track at AFC Threshold Frequency Error

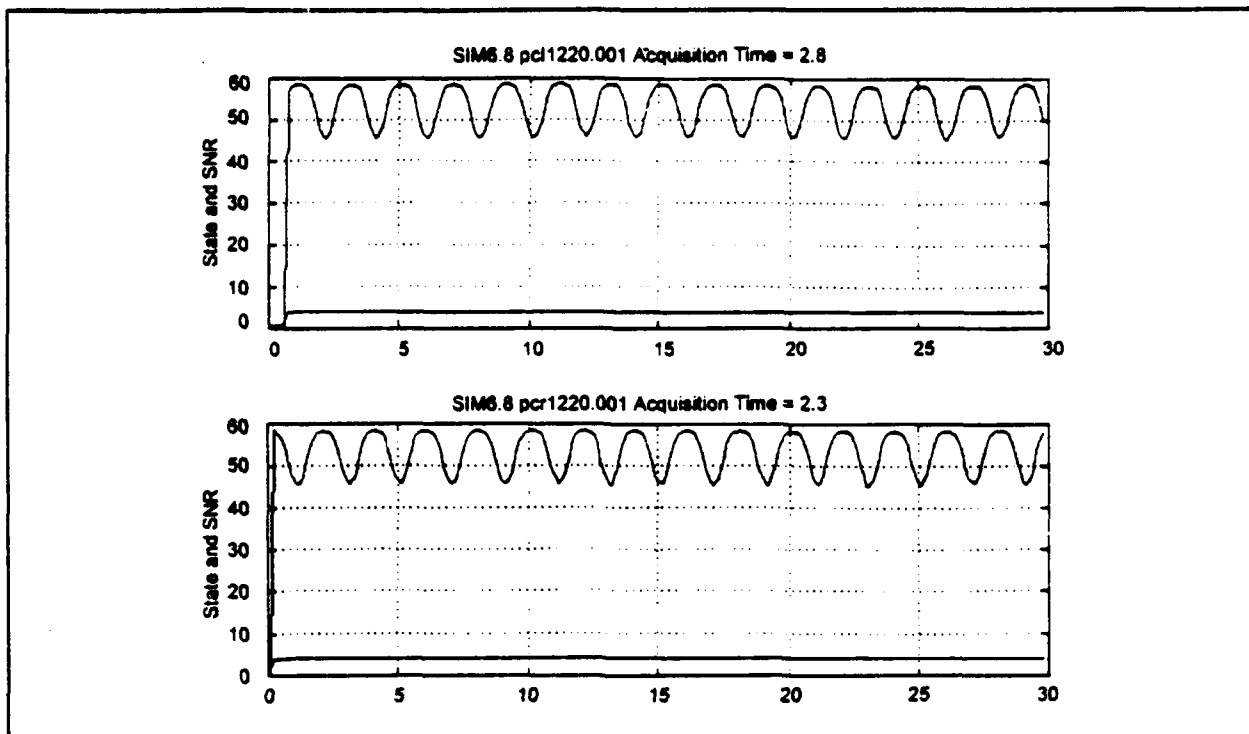


Figure 17 LHCP and RHCP Pilot Carrier Track SNR

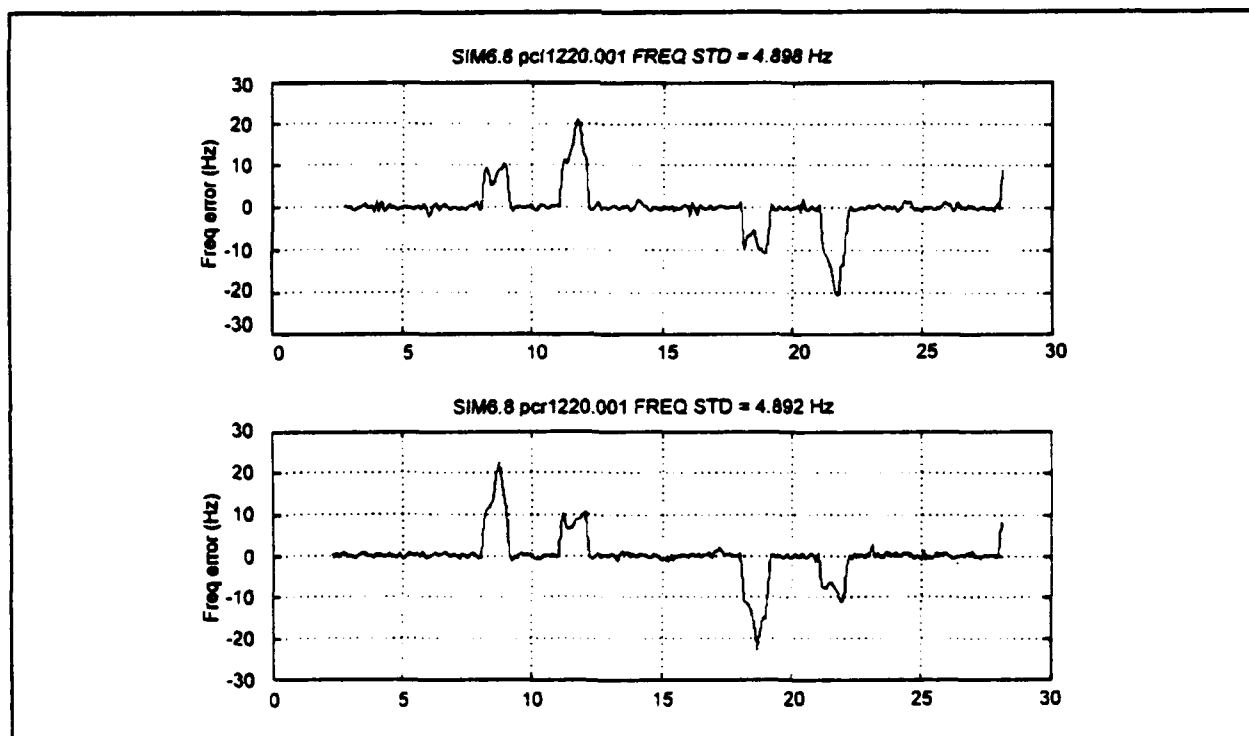


Figure 18 LHCP and RHCP Pilot Carrier AFC Error, 50g-50g/s

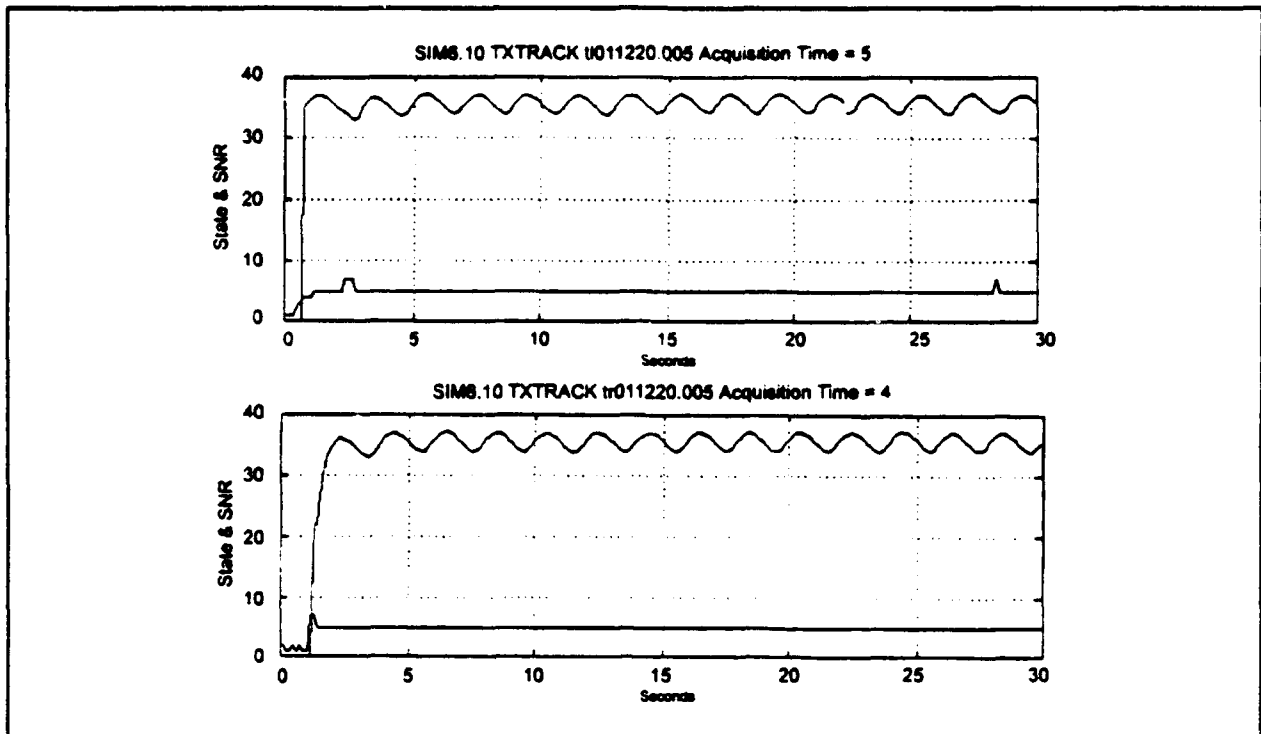


Figure 19 LHCP and RHCP Translated GPS Track SNR

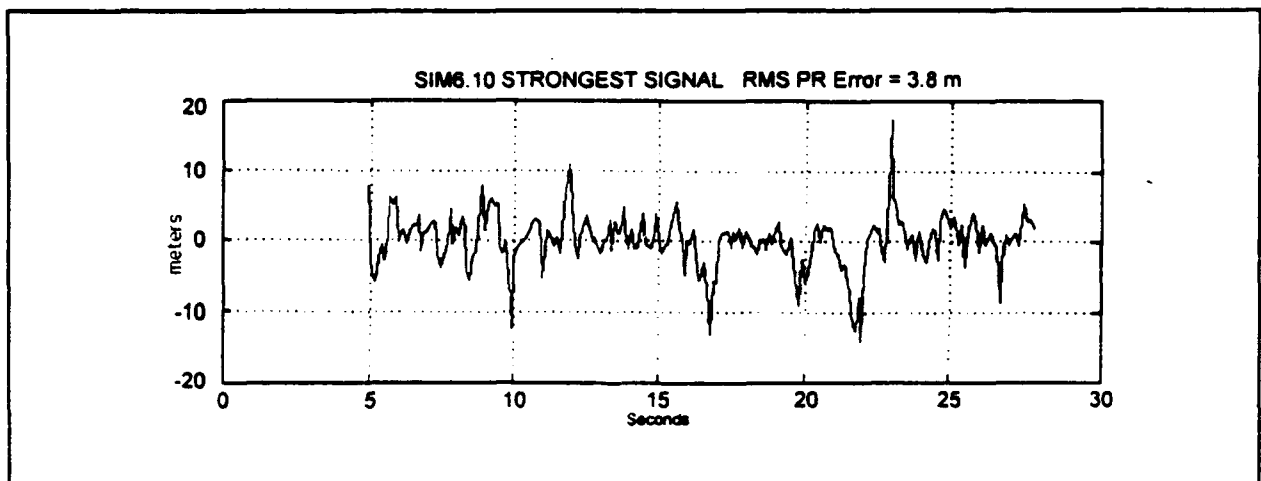


Figure 20 Strongest Polarization PR Error

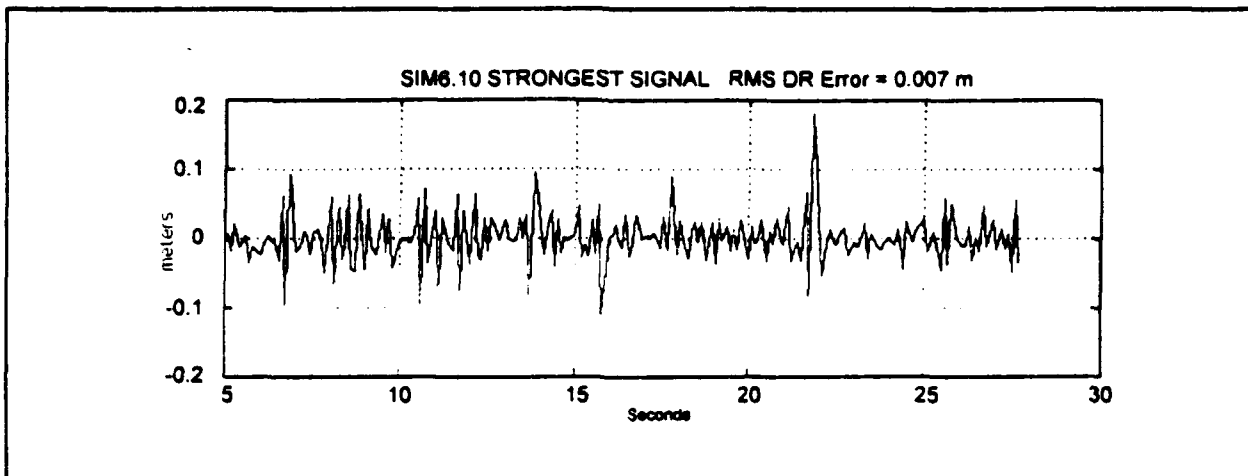


Figure 21 Strongest Polarization DR Error

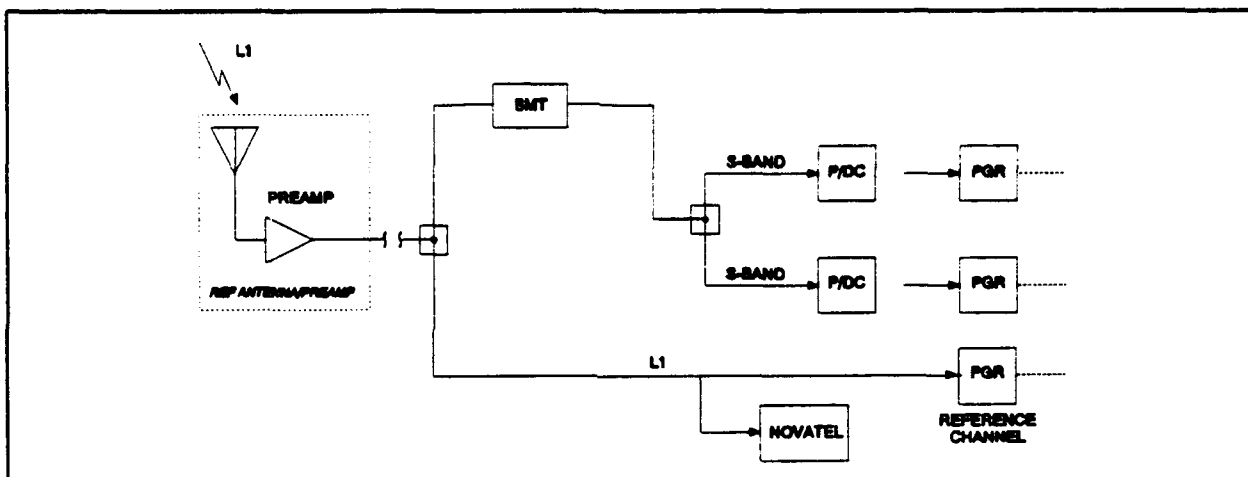


Figure 22 BMT Test Setup

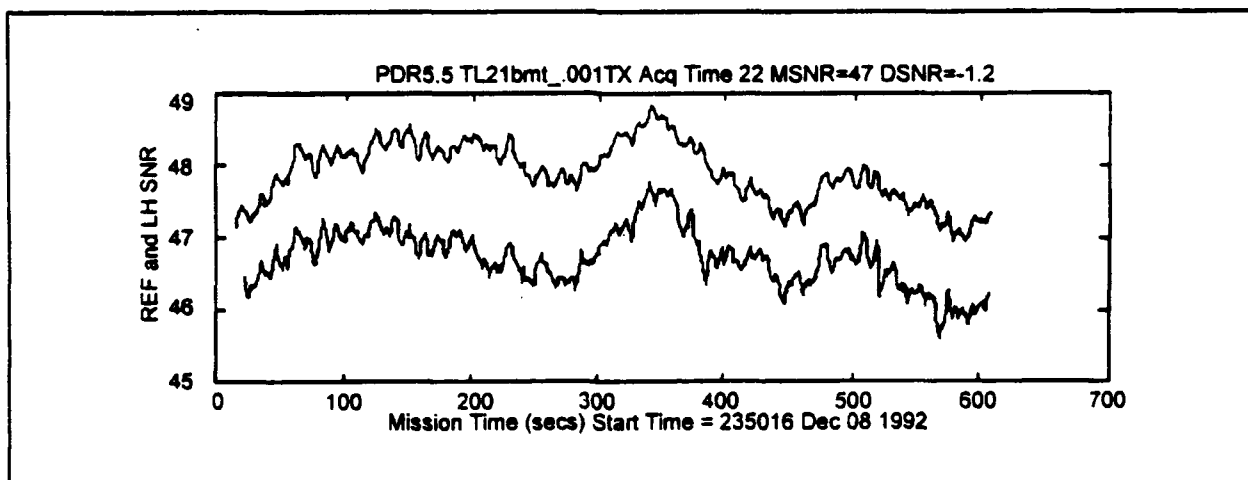


Figure 23 LHCP Channel BMT SNR, SV #21

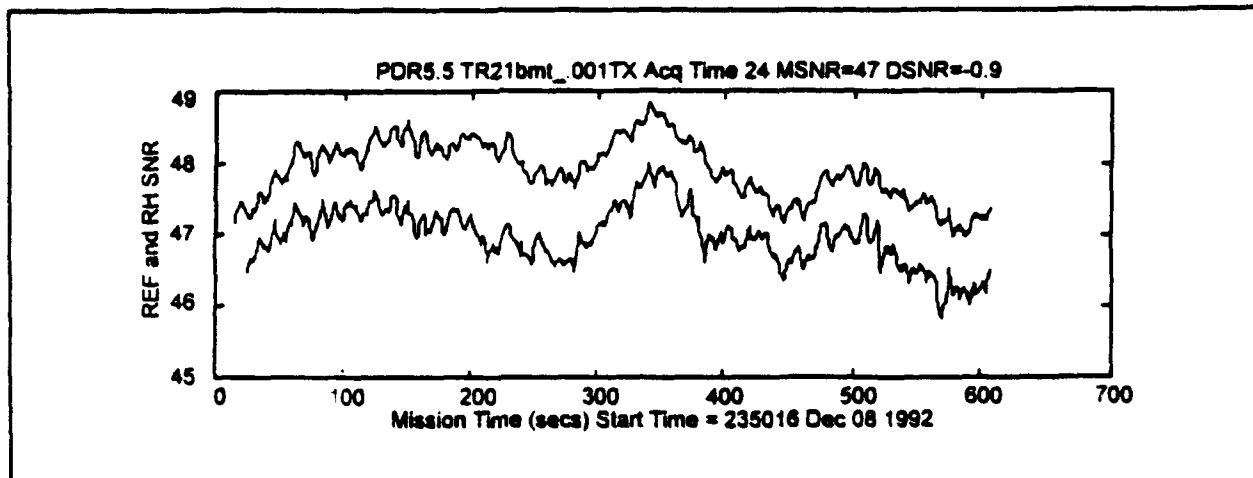


Figure 24 RHCP Channel BMT SNR, SV #21

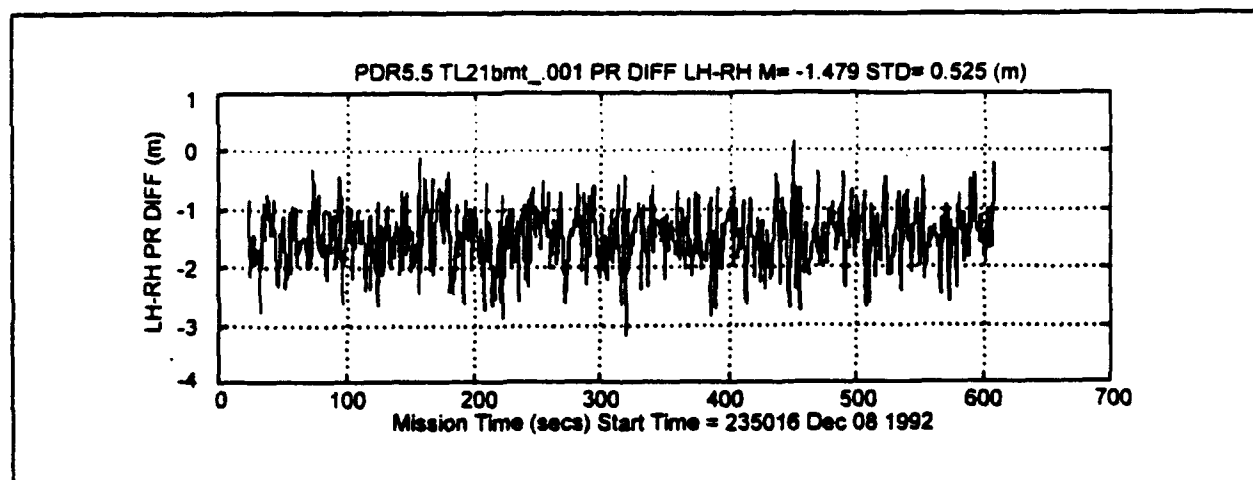


Figure 25 LHCP and RHCP Channel BMT PR Difference

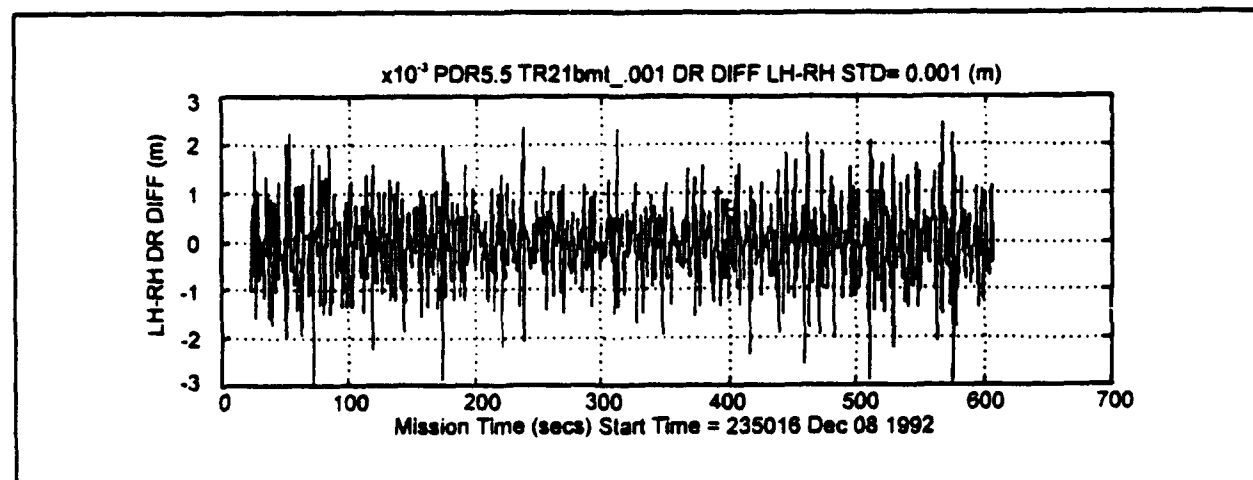


Figure 26 LHCP and RHCP Channel BMT DR Difference

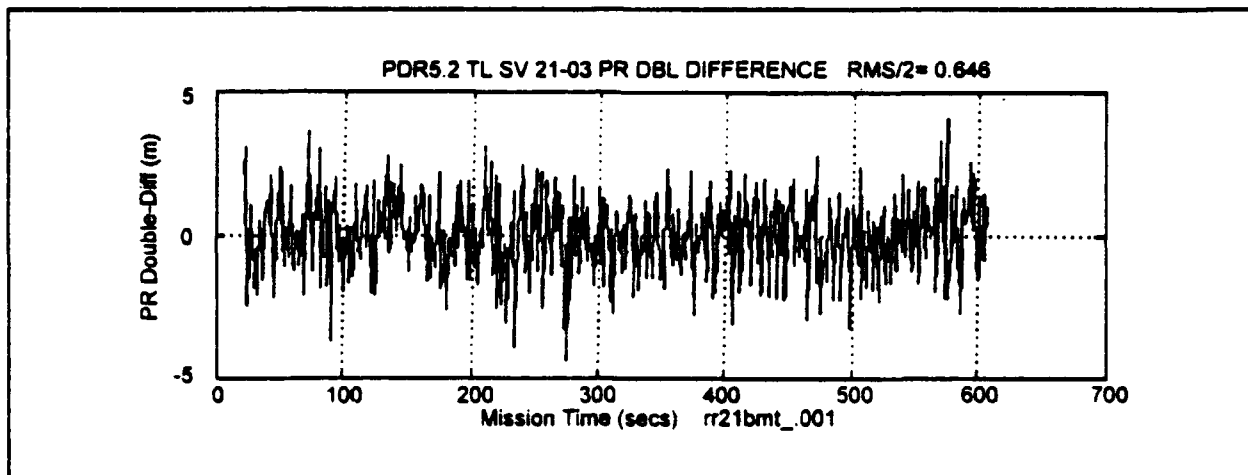


Figure 27 BMT PTPS-Novatel Double Difference PR

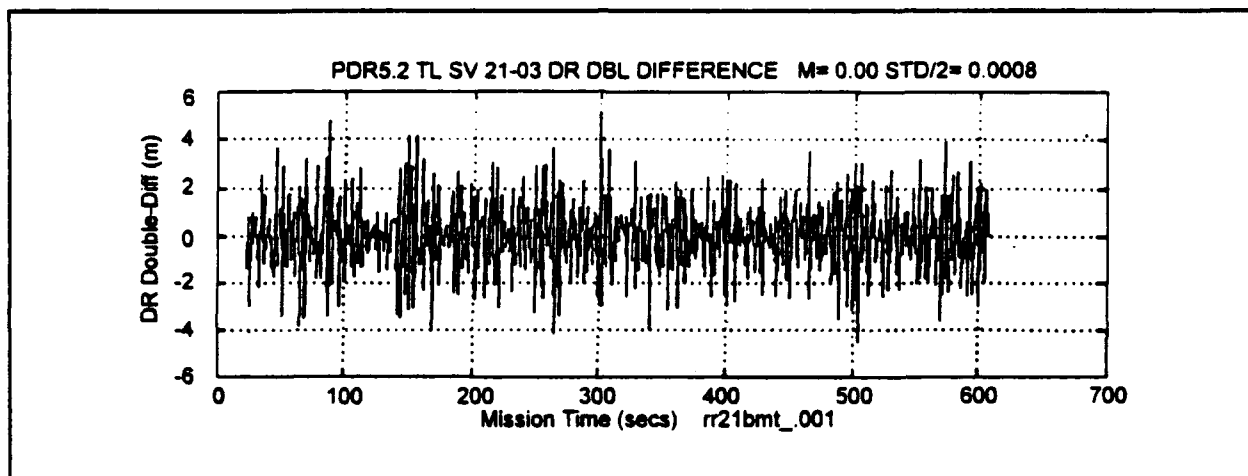


Figure 28 BMT PTPS-Novatel Double Difference DR

**THIS PAGE LEFT BLANK INTENTIONALLY**

**AFDTC-TR-93-06**

**VOLUME I**

**STANDBY PAPER**



**THIS PAGE LEFT BLANK INTENTIONALLY**

**HIGH ACCURACY PERFORMANCE CAPABILITIES  
OF THE  
MILITARY STANDARD RING LASER GYRO INERTIAL  
NAVIGATION UNIT**

Prepared by

George Gllster

Litton Systems, Inc.  
Guidance and Control Systems Division  
5500 Canoga Avenue  
Woodland Hills, California 91367-6698

(Approved for Public Release; Distribution is Unlimited)

**ABSTRACT**

The Medium Accuracy Standard Ring Laser Gyro (RLG) Inertial Navigation Unit (INU) exemplified by Litton's LN-93 system has benefitted from continual improvements during the production process such that the present navigational accuracy and reliability are better by a factor of two or more over the original requirements as defined by SNU 84-1. Performance enhancements are now available which further improve navigation performance to the high-accuracy category while maintaining the reliability of the production system. Two enhancement mechanizations are described - one that requires software-only changes to improve inertial performance, and one that employs a self-contained (embedded) GPS to augment the inertial performance. These enhancements may be applied in combination to provide uniquely effective immunity to GPS spoofing countermeasures. These enhancements retain the present standard RLG INU form factor, mounting, and electrical interface, and are therefore particularly advantageous for retrofit application. Potential retrofit applications with various aircraft avionics architectures are discussed.

**INTRODUCTION**

Standard (STD) Ring Laser Gyro (RLG) Inertial Navigation Units (INU) designed in conformance with the military specification SNU 84-1 have been in production for more than seven years. Litton's LN-93 STD RLG INU (Figure 1),

designed and built-in conformance with SNU 84-1, has been produced in quantity of more than 1,800 units for US and foreign military application. Its US military deployment has been covered by a five-year reliability-improvement-warranty (RIW). The flexibility for change and the incentives provided by the RIW combined with the normally occurring production process improvements have resulted in recent operational accuracy and reliability much better than required by specification. Figure 2 shows the navigational performance distribution reported for the Springfield, IL Air National Guard for over 4,000 sorties. This data represents terminal position error recorded post-flight for maintenance purposes. The data median or CEP value is 0.255 nmi/hr - more than three times as good as the 0.8 nmi/hr required by specification.

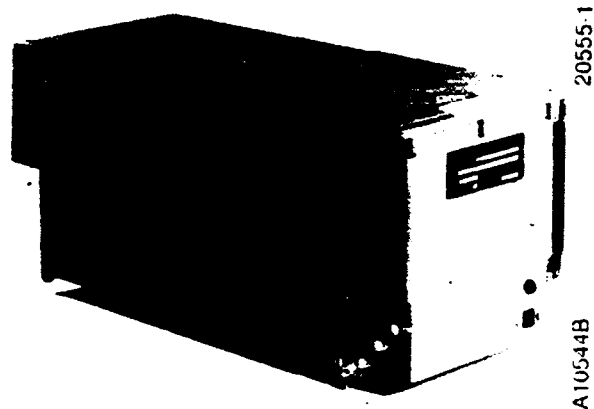


**Figure 1. LN-93 STD RLG INU  
(CN-1656/ASN and CN-1647/ASN)**

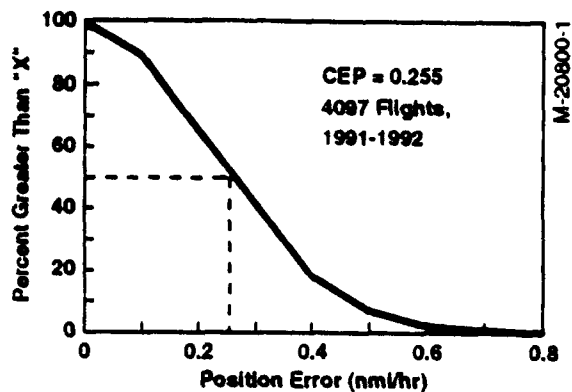


**Figure 2. LN-93 Operational Navigation Accuracy**

The contractual reliability requirements for the LN-93 under the RIW program and with the INU used on fighter aircraft is shown in Figure 3 with the comparison curve of the actual measured reliability. As can be seen, the mean-time-before-failure (MTBF) after only seven measurement periods (3.5 years) was 3,720 hours – more than twice the requirement at that time and much better than required at the end of the RIW period (5 years).

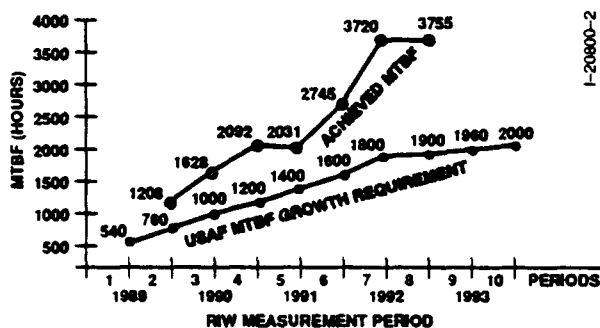


**Figure 3. Reliability Mean-Time-Before-Failure for LN-93 under Reliability Improvement Warranty (RIW) Program**

These system attributes make the LN-93 a superb, medium accuracy inertial navigation system (INS); but, system modifications are available to transform the LN-93 into a high-accuracy navigator. These modifications take two forms: (1) software and procedure changes (no hardware modifications) which enhance the system free-inertial navigation performance and, (2) embedding a GPS receiver within the LN-93

to provide optimum GPS aiding to the INS. These two forms of improvement were separately developed, as the LN-93E and LN-93G respectively, but may be applied in combination to provide a broad spectrum of STD RLG INU performance enhancement.

### LN-93E ENHANCED PURE INERTIAL

The LN-93E was developed as an enhanced inertial system capable of providing pure inertial navigation to an accuracy of better than 0.2 nmi/hr CEP when initialized by a ground alignment. It is a candidate for both the F-117 and for standard precision accuracy applications conforming to SNU 84-3. The LN-93E requires no hardware change from the STD RLG INU configuration, but achieves the improved navigational performance by solely software and procedural changes.

The previously described improvements provide a performance basis which requires only modest additional changes to achieve high accuracy. The LN-93E incorporates changes in the following areas:

- Expanded system calibration with corresponding expanded in-flight instrument compensation
- Improved ground alignment software
- Compensation for gravity deflection at the align location.

### System Calibration

System calibration performed in the factory or depot is expanded to include a second calibration with a lower temperature rate of change. The results of these two system calibrations are compared and tested for limits. This additional calibration data, combined with corresponding expansion to the Operational Flight Program (OFP), provides a more precise thermal compensation for the inertial sensors and, therefore, improved system performance.

### Alignment Software Improvements

Best performance is achieved for the LN-93E with a two-position ground alignment termed enhanced interrupted alignment (EIA). This

alignment begins with an initial gyrocompass align period of typically nine minutes and is then interrupted while the aircraft is taxied to a new heading and stopped. The gyrocompass align then continues for typically another six minutes. The heading change during the taxi period should preferably be 70° or more for best accuracy. But, the system is mechanized to automatically detect when the aircraft is in motion or stopped and it will then automatically make best use of whatever heading changes and align durations are provided. Six additional states were added to the OFP Kalman filter to enhance ground alignment performance. These added states are particularly effective for a two-position (EIA) alignment.

### Gravity Deflection Compensation

Deflection of the vertical represents deviation of the actual geoid from a mathematical ellipsoidal model of the earth (WGS-84) employed for navigation. These deflections adversely affect navigation performance by introducing acceleration measurement errors into the inertial solution. The navigation solution is affected differently depending on whether the deflection effects are introduced at the ground align point or during free flight. The navigation errors induced by gravity deflection are independent of the quality of the inertial system and therefore, if uncompensated, produce a limit to the achievable high accuracy.

Figure 4 shows the effects of a typical gravity deflection at the initial alignment point and also that induced by gravity deflection during free-inertial flight. Compensation for align point gravity deflection (expressed as N-S and E-W deflection in arcseconds) is included in the LN-93E. Compensation for the gravity deflection during free flight could be included but was not selected because of the large quantity of possibly classified data which must be stored.

Gravity deflection at the ground alignment location produces an initial tilt error which, after takeoff, propagates as an equivalent accelerometer bias change as the deflection changes when the vehicle moves from the initial point. Compensation for this error is particularly effective for locations

such as Holloman-CIGTF where the gravity deflection error is almost twice the 5 arc second rms per axis value which represents worldwide conditions.

These software and procedural changes were added to two LN-93 systems to convert them to the LN-93E configuration for laboratory and flight test evaluation at CIGTF. The CIGTF test results showed the LN-93E to fully meet all qualification requirements for application to the F-117 aircraft. Performance was also evaluated for 6-hour missions representative of transport or bomber aircraft. This data is summarized in Table 1 and shows navigation performance of 0.15 nmi/hr for both single-position and two-position alignments.

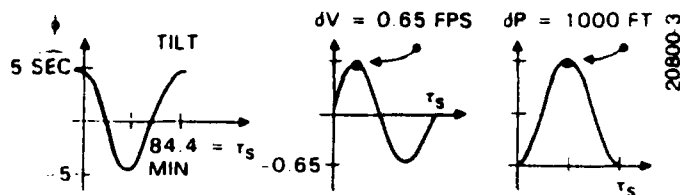
**Table 1. CIGTF Test Results for 6-Hour Flights with LN-93E**

Flight (6-Hr Flights)	Date	Alignment	Perfor- mance (nmi/hr)
1	23 July 91	EIA	0.151
2	26 July 91	EIA	0.156
3	09 July 91	GC	0.202
4	11 July 91	GC	0.106
Average = 0.154			
EIA - Enhanced Interrupted Alignment			
GC - Gyrocompass			

### LN-93G GPS EMBEDDED INERTIAL SYSTEM

Another STD RLG INU performance enhanced configuration uses a self-contained (embedded) GPS receiver to provide individual satellite line-of-sight (LOS) data for optimum GPS/inertial integration. This LOS data is in the form of pseudo range/delta range (PR/DR) values for each satellite which provides both optimum accuracy with four satellites and very little performance degradation with fewer than four satellites. This system variant of the LN-93 is designated LN-93G and can electrically and mechanically replace the present LN-93 or any other unit which meets the requirements of specifications ENAC 77-1 or SNU 84-1.

- **GROUND ALIGN POINT GRAVITY ERROR**  
**INITIAL ALIGNMENT ERRORS**  
**TILT – LOCAL DEFLECTIONS –**  
 $(\eta, \xi) \sim 5 \text{ SEC}$   
**AZIMUTH –  $\eta \cdot \tan(\phi)$**



- **IN-FLIGHT GRAVITY NOISE INDUCES ERROR**  
**DEFLECTION ERROR:**  
 – 5 SEC RMS PER AXIS  
 – CORRELATION DISTANCE 20 N M  
**ASSUMED SPEED – 300 KT**  
**(500 FPS)**  
**ASSUMED ALTITUDE = 0 FT**

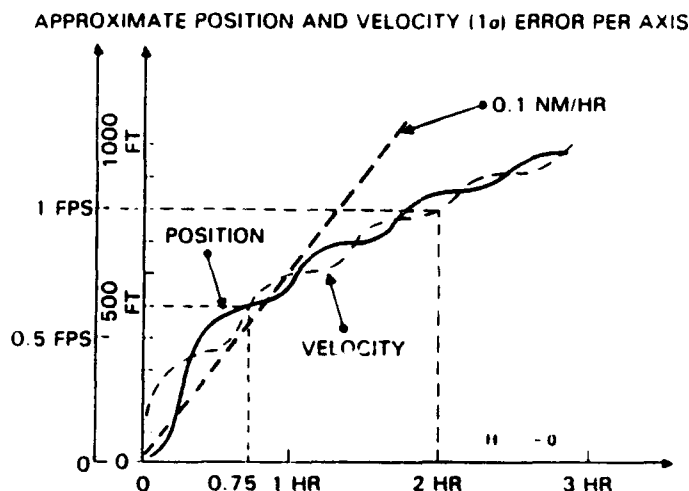


**Figure 4. Navigational Errors due to Gravity Disturbance Propagate from Two Effects**

#### **STD RLG INU Modification for Embedded GPS**

Major portions of the present production LN-93 STD RLG INU are common with the embedded LN-93G. Hardware changes are required only to:

- Consolidate present input/output (I/O) functions by use of newer electronic technology to make room for the added one board GPS receiver and an auxiliary system processor board.
- Revise the low voltage power supply design to provide power to the GPS.
- Revise the chassis for added GPS connectors and a support battery for GPS functions (cold key loading, RAM support, and low-power time source).

The extent of modifications to the present production system is summarized in Table 2. The large percent of common assets makes retrofit to existing LN-93 units practical. Figure 5 shows the locations of the LN-93G internal elements.

**Table 2. Application of LN-93 Modules for LN-93G**

<b>Retained</b>	
	Inertial Sensor Assembly
	Inertial Data/Gyro Dither
	A/D Converter
	Sensor Data Correction Processor
	Navigation Processor
	Range Buffer
	Synchro Buffer
	High Voltage Power Supply
<b>Changed (modified design substituted)</b>	
	DC Power Supply
	Chassis
	Master Interconnect
	AC Power Supply
<b>Deleted</b>	
	AMUX No. 1
	AMUX No. 2
	Power Supply Sequencer
<b>Added</b>	
	GPS Receiver
	System Processor (with dual AMUX)

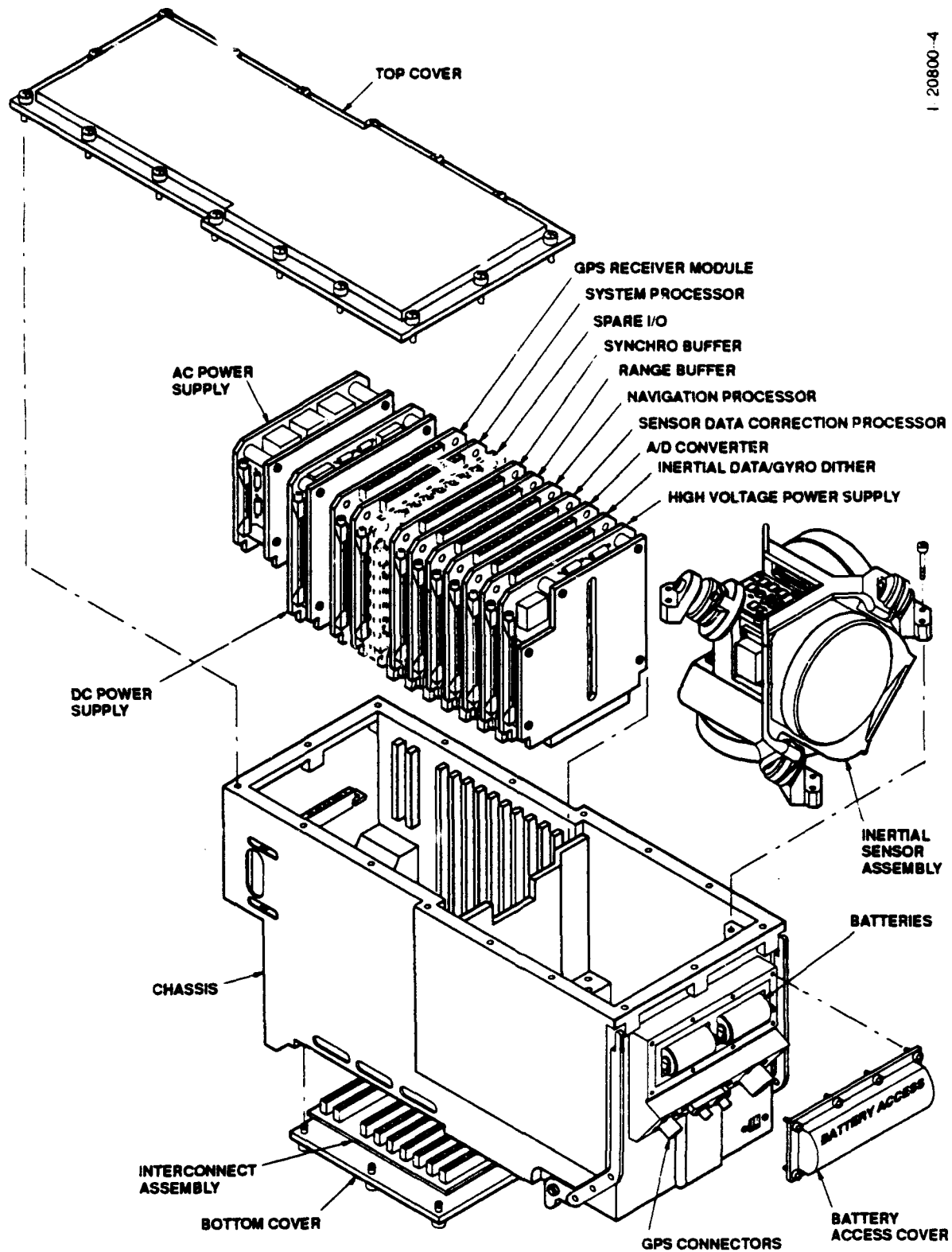


Figure 5. Exploded View of the LN-93G

### GPS Module

The GPS receiver is a Rockwell Collins single-board module which has performance characteristics equal to or better than the MAGR receiver. Table 3 summarizes the receiver characteristics. Either of two single-board GPS receivers may be employed in the system. One provides compatibility with IF input from L<sub>1</sub> and L<sub>2</sub> and the other for RF input.

**Table 3. GPS Module Characteristics**

Size:	Single board
Power:	IF Input - 11 watts (includes AE-4 antenna preamp) RF Input - 8.5 watts
Channels:	5 + noise sensing
Correlators per Channel:	10
J/S, State 5:	41 dB
J/S, State 3:	65 dB
Tracking:	CA, P(Y)
Input:	IF or RF, L <sub>1</sub> and L <sub>2</sub>
Crypto Load:	KYK-13 Interface Lithium battery support Cold load and cold zeroize capable
Module Memory:	Nonvolatile, loadable via RS-422 data bus
Data Output:	Pseudo Range and Delta Range for each tracked channel PVT for ensemble of tracked satellites (12 state Kalman filter) Have Quick precision time interface

### System Processor Module

The added System Processor module provides generous auxiliary computation capacity to the system by adding an Intel 80960MC 32-bit processor to the system. This single-board module also includes two independent, dual, MIL-STD-1553 buses which replace two present LN-93 boards by the application of ASIC technology. Note that overall, three boards are

deleted and only two boards added. There is therefore, a spare board slot for growth.

The LN-93G is designed to directly replace an LN-93 STD RLG INU. It has the same form-factor with the exception of front panel projections for GPS functions. It installs in the same mount and has essentially the same weight, power dissipation, cooling air pressure drop, environmental immunity and I/O functions.

### LN-93/LN-93G Mechanization

The LN-93G employs a unique system mechanization which allows the system to be utilized in aircraft with a wide variety of avionics architectures, including direct replacement of the LN-93. The present production LN-93 conforms to the requirements of the STD RLG INU specification SNU 84-1 which stipulates that the system will not have a self-contained airborne alignment filter, but instead, be capable of accepting externally computed correction vectors for position, velocity, attitude, and instrument biases. In conformance with this, the LN-93 contains three MIL-STD-1750A processors partitioning the computational tasks as shown in Figure 6. The LN-93G configuration adds a fourth high-capacity processor which contains the GPS/INS integration Kalman filter. This additional processor, called the System Processor, performs, internally to the INU, the same integrating function otherwise commonly performed by an external mission computer. As shown in Figure 7, the present LN-93 software functions remain unchanged, and a Kalman filter in the added system processor provides correction vectors derived from GPS and air data using the same message form (F02) as presently externally supplied.

The added system processor also performs a separate pure inertial navigation solution in parallel with the integrated (aided) solution. Careful attention has been paid to the software partitioning to assure that this pure inertial computation is not "contaminated" by aiding data. Updated instrument calibration coefficients (for bias, scale factor, thermal effects, etc.), are applied by the integrating Kalman filter to the aided solution, but the pure inertial solution uses

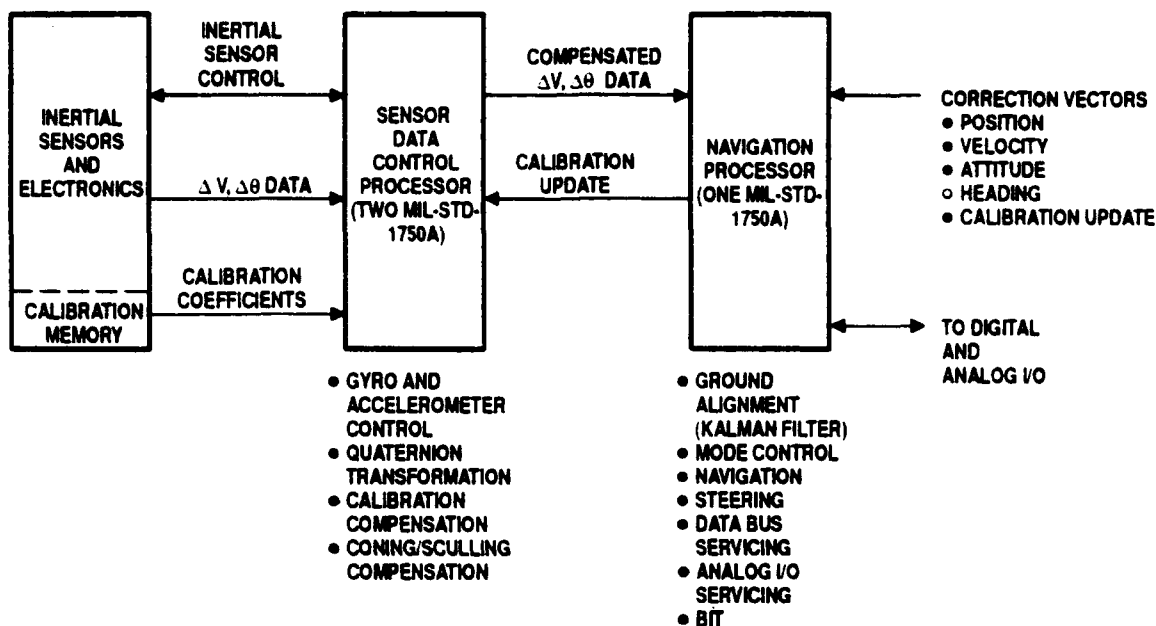


**Figure 6. LN-93 STD RLG INU Software Partitioning**

instrument compensations only from the system calibration memory which contains long-term instrument calibration coefficients. Just before shutdown, the EEPROM system calibration memory is selectively and carefully updated using only a small percent of the computed calibration update values to allow long-term calibration enhancement. A third, independent navigational output is obtained directly from the embedded GPS receiver and provided GPS-only navigation data which may be used as a back-up navigation data source or for external GPS/inertial integration.

Thus, in summary, the simultaneously available data bus outputs are:

- a. Aided inertial navigation solution where the aiding reference is GPS pseudo-range/delta-range (PR/DR) data with an optimum (tightly coupled) Kalman filter.
- b. Pure inertial navigation solution propagated from the ground alignment point.
- c. GPS position-velocity-time (PVT) data supplied directly from the GPS receiver and derived from the ensemble of tracked satellites. Mode selection allows the GPS receiver to be

mode controlled and aided either internally to the LN-93G or from external sources.

The versatility of the LN-93G allows it to be directly applied to various aircraft architectures as shown in Figure 8. The preferred aircraft integration is as shown in Figure 8(a) which uses the optimum INS/GPS navigation data derived from the internal Kalman filter using GPS PR/DR data. With this mechanization the independent pure inertial data and the independent GPS-only PVT data may be used for backup navigation and/or validity verification purposes.

Figure 8(b) shows an application where it is desired to have the integration Kalman filter external to the INU (e.g., in a mission computer), but the LN-93G is used to allow convenient installation of the GPS receiver in the aircraft. Since the receiver is located within the confines of the STD RLG INU, installation efforts are limited to the antenna and wiring. With this implementation, the LN-93G allows the GPS aiding and mode control to be supplied by the external customer. Again, the independent pure inertial solution may be used for backup navigation and/or validity verification.



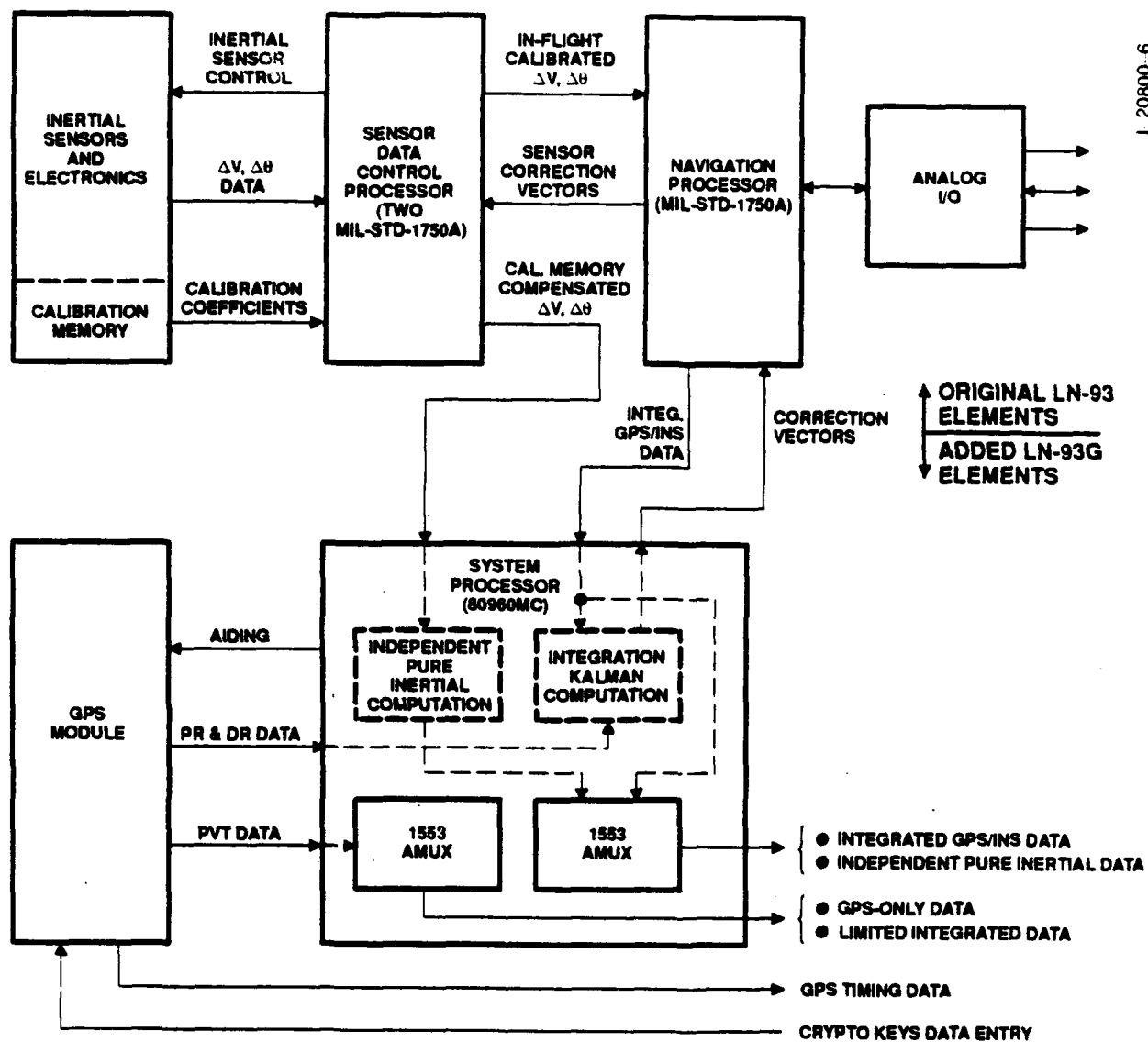
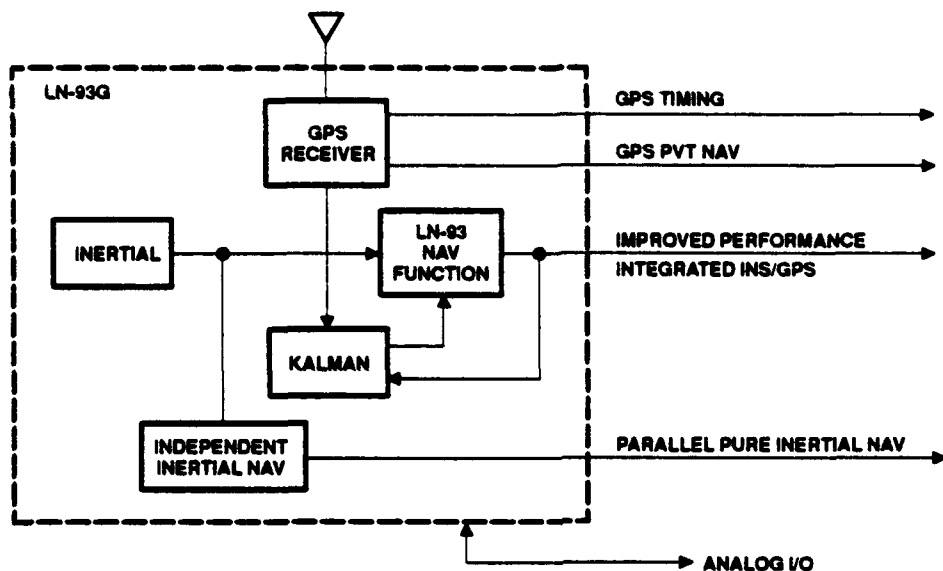
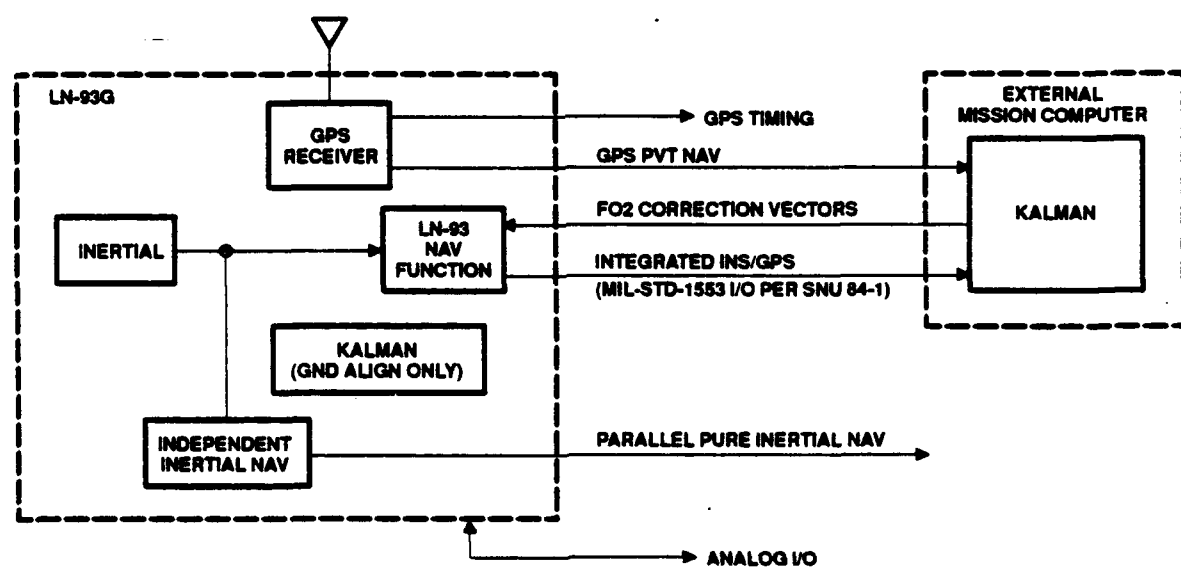


Figure 7. LN-93G Mechanization Retains the Present LN-93 Functions

I 20800-7



a. INTERNALLY INTEGRATED INS/GPS



b. EXTERNALLY INTEGRATED INS/GPS

Figure 8. LN-93G Compatible Aircraft Integrations

Since the various forms of available digital navigation data are communicated on MIL-STD-1553B buses and with standard message structure (e.g., GPS-only data is per ICD GPS-059 and INS/GPS data is per SNU 84-1), the GPS embedded INU I/O may be selectively applied in any manner best suiting the aircraft avionics requirements. The full complement of LN-93 analog I/O is retained in the LN-93G and GPS analog I/O functions, such as Have Quick time reference, are also available.

The specified navigation performance for the LN-93G (without the enhancement developed in the LN-93E) is shown in Table 4. As with the present production LN-93, the actual field performance is expected to be considerably better than the specified values. The velocity accuracy for the integrated mode when GPS PR/DR data is used, for example, has been shown by both simulation and test to be improved by a factor of five to less than 0.02 m/sec per axis.

**Table 4. LN-93G Specified Navigation Performance**

Function	Mode	Position	Velocity (per axis)	Time Accuracy
Inertial Only	GC Align	0.8 nmi/hr CEP	2.5 fps	
	SH Align	0.8 nmi/hr CEP	5.0 fps	
GPS/INS	Aided	16 meters (SEP)	0.1 m/sec	< 100 nanoseconds
	Aided INS, after loss of GPS	0.3 nmi/hr	1.0 ft/sec	
	In-flight align	16 meters (SEP)	0.1 m/sec	
GPS	GPS only	16 meters (SEP)	0.1 m/sec	< 100 nano-second
Note: GC - Gyrocompass SH - Stored Heading				

## COMBINED PURE INERTIAL ENHANCEMENT WITH GPS EMBEDDING

The unique parallel pure inertial navigation computation of the LN-93G makes the simultaneous incorporation of the high accuracy techniques developed on the LN-93E a feasible and interesting alternative. This parallel computation assures that the enhanced pure inertial performance will not be perturbed by GPS data, and it can therefore be used as a high-accuracy, reliable, independent reference for evaluating the validity of the integrated INS/GPS data. With the world situation today, it is generally acknowledged that GPS referenced data is more accurate than enhanced pure inertial data. However, as GPS electronic countermeasures become more sophisticated and widespread, it is likely that this dual computation mechanization will become increasingly important to mission success.

## SUMMARY

Two modification approaches have been developed for the widely deployed LN-93 STD RLG INU which increase the system accuracy to the high-accuracy category while maintaining the present installation footprint and electrical interface. These modifications may be applied individually or jointly and may be incorporated by INU retrofit.

## REFERENCES

R.F. Cox, T.T. Rockey "Litton's LN-93G: The Production Embedded GPS/Inertial System ION January 1993.

J.S. Lipman, "Tradeoffs in the Implementation of Integrated Inertial Systems," ION, September 1992.

Guidance Test Division (CIGTF) "Standard INU Enhanced Accuracy Test Data Package, Litton LN-93," AFDTC-DP-91-05, September 1991.

**ATTENDANCE LIST**

**THIS PAGE LEFT BLANK INTENTIONALLY**

# ATTENDANCE LIST SIXTEENTH BIENNIAL GUIDANCE TEST SYMPOSIUM 4 - 7 October 1993

NAME	COMPANY	STREET	CITY	STATE	ZIP CODE
ABBY DARWIN G MR	INTERMETRICS INC AEROSPACE SYSTEMS	PO BOX 1117	HOLLOMAN AFB	NM	88330-1117
ACKER ROBERT H MR	KEARFOTT GUIDANCE & NAVIGATION CORP	150 TOWNA ROAD	WAYNE	NJ	07470
ADAM WALLACE B MR	DYNACORP RADAR SERVICES DIVISION	1812 ARIZONA AVENUE	ALAMOGORDO	NM	88310
ADAMS GARY MR	HONEYWELL SYSTEMS & RESEARCH CENTER	PO BOX 21111 M/S 127D2	PHOENIX	AZ	85036-1111
ADOLPH CHARLES E MR	OUSD(A)/DT&E	PENTAGON ROOM 3E1060	WASHINGTON	DC	20301-3110
AGAMATA BAL N MR	NCOSC NISE WEST CODE 212BA	PO BOX 85137	SAN DIEGO	CA	92186-5137
AGOPOVICH JOHN W MR	C S DRAPER LABORATORY INC	555 TECHNOLOGY SQ MS 42	CAMBRIDGE	MA	02139-3563
AIRTH WALTER E MR	MAGNAVOX ADVANCED PRODUCTS	2828 MARIPOSA STREET	TORRANCE	CA	90503
ALEXANDER RICHARD B MR	46TH GUIDANCE TEST SQUADRON/GDX	1844 VANDERGRIFT ROAD	HOLLOMAN AFB	NM	88330-7850
ANDERMAN ALFRED MR	ROCKWELL SPACE SYSTEMS DIVISION	12214 LAKEWOOD BLVD	DOWNEY	CA	90241
ANDERSON GERALD M MR	AGMC/MAE	813 IRVINGWOOD DR W	NEWARK AFB	OH	43057
ANTICOLE ROBERT MR	CONTRAVES USA INC	815 EPSILON DRIVE	PITTSBURGH	PA	15238
ARAJA VISI MR	ASC/VFES	2100 MONAHAN WAY STE 1	WRIGHT-PATTERSON	OH	45433-7015
ARAUJO PETER DE MR	46TH GUIDANCE TEST SQUADRON/GDMR	1844 VANDERGRIFT ROAD	HOLLOMAN AFB	NM	88330-7850
ARMSTRONG WOODIE MR	46TH GUIDANCE TEST SQUADRON/GDMI	1844 VANDERGRIFT ROAD	HOLLOMAN AFB	NM	88330-7850
ARONOWITZ FREDERICK DR	ROCKWELL INTERNATIONAL	3370 MIRALOMA MC 031-FB02	HOLLOMAN AFB	CA	92803
BABIN RICHARD G MR	46TH TEST GROUP/GDMR	1844 VANDERGRIFT ROAD	HOLLOMAN AFB	NM	88330-7850
BABU B A KUMAR MR	DEL NORTE TECHNOLOGY	1100 PAMELA DRIVE	EULESS	TX	76040
BACA LARRY J MR	46TH TEST GROUP/TKPA	1531 TEST TRACK RD	HOLLOMAN AFB	NM	88330-7847
BAGLEY DANIEL T CAPT	46TH GUIDANCE TEST SQUADRON/GDTN	1844 VANDERGRIFT ROAD	HOLLOMAN AFB	NM	88330-7850
BALDASTI WALTER J MR	LITTON GUIDANCE & CONTROL	5500 CANOGA AVENUE MS 73	WOODLAND HILLS	CA	91367-6898
BANKO DAVID E CAPT	46TH GUIDANCE TEST SQUADRON/GDTN	1844 VANDERGRIFT ROAD	HOLLOMAN AFB	NM	88330-7850
BARANOWSKI DAVID J TSOT	46TH GUIDANCE TEST SQUADRON/GDMG	1844 VANDERGRIFT ROAD	HOLLOMAN AFB	NM	88330-7850
BARKER CLEON MR	46TH GUIDANCE TEST SQ/GDXP	1844 VANDERGRIFT ROAD	HOLLOMAN AFB	NM	88330-7850
BARTONE CHRIS MR	NAMC	SYOYCN	PATUXENT RIVER	MD	20670
BASKETT JOHN R MR	DELCO ELECTRONICS CORP	8767 HOLLISTER AVENUE	GOLETA	CA	93117
BASQUE RICHARD A MR	DYNAMICS RESEARCH CORP	60 FRONTAGE ROAD	ANDOVER	MA	01810
BEALE ROBERT E COL (RET)	46TH GUIDANCE TEST SQUADRON/GDT	1809 MONTE LARGO DRIVE NE	ALBUQUERQUE	NM	87112
BEATY CHRISTINA M MS	46TH TEST GROUP/RX	1844 VANDERGRIFT ROAD	HOLLOMAN AFB	NM	88330-7850
BELL JACKIE W MR	46TH TEST GROUP/RX	1844 VANDERGRIFT ROAD	HOLLOMAN AFB	NM	88330-
BENNETT SID MR	ANDREW CORPORATION	10500 W 153 STREET	ORLAND PARK	IL	60462
BERARDUCCI MICHAEL P MR	WL/AAAI-3	2185 AVIONICS CIRCLE	WRIGHT PATTERSON	OH	45433-7301
BERNSTEIN BERNARD MR	BERNSTEIN DESIGN SERVICES	1330 HUDSON WAY	LIVERMORE	CA	94550
BEYERS RONALD J CAPT	OLAT ESC, JTF/ENR	PO BOX 9650 MS E08-221	MELBOURNE	FL	32902-9650
BICKETT JOHN ETCs	MOTU 5 BOX 368109	2550 VESTA STREET	SAN DIEGO	CA	92136-5285
BLIZZARD C ROBERT MR	HONEYWELL INC/SPACE & STRATEGIC SYS	1027 GROVEWOOD COURT	CLEARWATER	FL	34624-4824
BLOUIN ERIC LT	46TH GUIDANCE TEST SQUADRON/GDMI	1844 VANDERGRIFT RD	HOLLOMAN AFB	NM	88330-7850
BONGIOVANNI STEPHEN A MR	HONEYWELL SASSO M/S 228-1	13350 US HWY 19 N	CLEARWATER	FL	34624-7290
BOYKIN LARRY W MR	46TH TEST GROUP/GDTN	1844 VANDERGRIFT ROAD	HOLLOMAN AFB	NM	88330-7850
BREWER JAMES MR	46TH TEST GROUP/GDSG	1844 VANDERGRIFT ROAD	HOLLOMAN AFB	NM	88330-7850
BROOKS WENDELL MR	SWEDISH AIR FORCE/FMV	AIR MATERIEL DEPT S-115 88	STOCKHOLM	SWEDEN	
BROUGHTON COLLIN MR	DEL NORTE TECHNOLOGY INC	1100 PAMELA DRIVE	EULESS	TX	76040
BROWN PETER MR	46TH GUIDANCE TEST SQ/GDMR	1844 VANDERGRIFT RD	HOLLOMAN AFB	NM	88330-7850
BROWN ROBERT J MR	NAVSYCS CORPORATION	14960 WOODCARVER ROAD	COLORADO SPRING	CO	80921
BROWNE JOSEPH F MR	SYSTRON DONNER COMPANY	2700 SYSTRON DRIVE	CONCORD	CA	94518
BURKLE MICHAEL MR	NAVAL AIR WARFARE CENTER ad	CODE SA418	PATUXENT RIVER	MD	20670-5304
BYE CHARLES T MR	ROCKWELL-COLLINS	350 COLLINS RD NE	CEDAR RAPIDS	IA	52402
BYERS THOMAS E MR	HONEYWELL MILITARY AVIONICS DIVISIO	1825 ZARTHAN AVENUE	ST LOUIS PARK	NM	55416
CADWALLADER CURT B MR	46TH GUIDANCE TEST SQUADRON/GDMI	1844 VANDERGRIFT ROAD	HOLLOMAN AFB	NM	88330-7850
CALICCHIA LUIGI MR	46TH GUIDANCE TEST SQUADRON/GDMG	1844 VANDERGRIFT ROAD	HOLLOMAN AFB	NM	88330-7850
CANAVAN EDGAR R MR	TRW AT PHILLIPS LABORATORY	1126 SANTA ANA AVE	ALBUQUERQUE	NM	87123
CARON DENNIS LT	UNIVERSITY OF MARYLAND	DEPT OF PHYSICS & CSRSCH	COLLEGE PARK	MD	20742
CARTER JOHN M MR	46TH TEST GROUP/GDMT	1844 VANDERGRIFT ROAD	HOLLOMAN AFB	NM	88330-7850
CASTLEMAN BRUCE W MR	CARCO ELECTRONICS	195 CONSTITUTION DRIVE	MENLO PARK	CA	94025
CHASKO ANDREW J MR	HONEYWELL INC	13350 US HIGHWAY 19 N	CLEARWATER	FL	34624-7290
CHIEN TZE THONG MR	INTERMETRICS INC	PO BOX 310	HIGH ROLLS/MOUN	NM	88325
	C S DRAPER LABORATORY INC	555 TECHNOLOGY SQUARE	CAMBRIDGE	MA	02139 3563

NAME	COMPANY	STREET	CITY	STATE	ZIP CODE
CHRISTIANSEN ROBERT G MR	ROCKWELL INTL MC GE14	3370 MIRALOMA AVENUE	ANAHEIM	CA	92803
CLYETT KATHY MS	ASC/SMAA	1895 FIFTH ST BLDG 96	WRIGHT PATTERSON	OH	45433-7200
CLUPNY ALLEN B TSQT	46TH GUIDANCE TEST SQUADRON/GDX	1644 VANDERGRIFF ROAD	HOLLOMAN AFB	NM	88330-7850
COCOLLI J DAVID MR	C S DRAPER LABORATORY INC	555 TECHNOLOGY SQ MS 61	CAMBRIDGE	MA	02139-3563
COMALLIE LEO B MR	46TH GUIDANCE TEST SQUADRON/GDMI	1644 VANDERGRIFF ROAD	HOLLOMAN AFB	NM	88330-7850
CONANT JAMES MR	INTERMETRICS INC	1644 VANDERGRIFF ROAD	HOLLOMAN AFB	NM	88330-7850
CONNORS MARK LT	46TH GUIDANCE TEST SQUADRON/GDSG	1644 VANDERGRIFF ROAD	HOLLOMAN AFB	NM	88330-7850
COSENTINO BARBARA A MRS	46TH TEST GROUP/GDTN	1644 VANDERGRIFF ROAD	HOLLOMAN AFB	NM	88330-7850
COUCH MARTIN MR	BRITISH AEROSPACE SYS & EQUIP LTD	CLITTAFOOD ROAD	PLYMOUTH DEVON	ENGLAND	88330-7850
COUGHLIN PATRICK MR	DYNACORP	PO DRAWER R	HOLLOMAN AFB	NM	88330
CRANSTON STEWART E BRIG GEN	AFDTC/CC	101 W D AVE STE 117	EGLIN AFB	FL	32542-5495
CRAVETS ARTHUR O MR	SCIENCE APPLICATIONS INTL CORP (SAI	10770 WATERIDGE CIRCLE W	SAN DIEGO	CA	92121
CRIGGER WILLIAM H MR	AGMC/MAEL(2)	813 IRVINGWICK DR W	NEWARK AFB	OH	43057-0005
CROUCH DAN S MR	46TH GUIDANCE TEST SQUADRON/GDTI	1644 VANDERGRIFF ROAD	HOLLOMAN AFB	NM	88330-7850
CUMMINGS MICHAEL J MR	INTERMETRICS INC	PO BOX 1117	HOLLOMAN AFB	NM	88330-1117
DAVIS RICHARD G DR	HQ USAF/HQ	170 LUNE AVE STE 400	BOLLING AFB	DC	20332-5113
DE BRABANDER EDWARD T MR	NAWC AIRCRAFT DIVISION	CODE FW 42	PATUXENT RIVER	MD	20670-5304
DE DOES DIRK DR	INTERMETRICS INC	5312 BOLSA AVE	HUNTINGTON BEAC CA	CA	92649-1090
DE MORE LOUIS A DR	WL/MWG	101 W EGLIN BLVD STE 268	EGLIN AFB	FL	32542-6810
DE TORRES DON MR	CONTRAVES USA INC	610 EPSILON DRIVE	PITTSBURGH	PA	15238-2880
DEGRANDCOURT ROBERT F MR	INTERMETRICS INC	1644 VANDERGRIFF ROAD	HOLLOMAN AFB	NM	88330-7850
DEL ROSARIO MARK MR	ROCKWELL INTL SUITE 1200	1745 JEFFERSON DAVIS HWY	ARLINGTON	VA	22202
DENHARD WILLIAM G MR	46TH GUIDANCE TEST SQUADRON/GDTN	1644 VANDERGRIFF ROAD	HOLLOMAN AFB	NM	88330-7850
DENNIS JAMES CAPT	JOINT SERVICES DATA EXCHANGE GROUP	25 SPRINGVALE ROAD	READING	MA	01867
DERRICK BRIAN M MR	HQ ACC/DRPS	204 DODD BLVD STE 226	LANGLEY AFB	VA	23665-2777
DESFOSSÉ DONALD P MR	SUNDSTRAND DATA CONTROL INC	15001 NE 36 STREET	REDMOND	WA	98073
DIAZ JOSE LUIS MR	THE MITRE CORP	202 BURLINGTON RD MS ON-15	BEDFORD	MA	01730
DICKER MICHAEL P LTC	46TH GUIDANCE TEST SQUADRON/GDTN	1644 VANDERGRIFF ROAD	HOLLOMAN AFB	NM	88330-7850
DOLBEY STEPHEN C MR	46TH TEST GROUP/GD	1644 VANDERGRIFF ROAD	HOLLOMAN AFB	NM	88330-7850
DOYLE THOMAS MR	ANALEX CORPORATION	7801 SOUTHPARK PLAZA #210	LITTLETON	CO	80120
DUFF KEITH MR	WAYFLOWER COMMUNICATIONS	80 MAIN STREET	READING	MA	01867
DURIEUX PATRICK MR	APPLIED RESEARCH LABORATORIES AT UT	10000 BURNET RD	AUSTIN	TX	78758
DUTOT P MR	SAGEM	CENTRE D'ERAGNY	95612 CERGY PON FRANCE	FRANCE	
EFAM ROBERT MR	LRBA/France	27207	VERNON CEDEX	FRANCE	
EIDSAUNE DAVE LTC	DELCO SYSTEMS OPERATIONS	6767 HOLLISTER AVE MS E207	GOLETA	CA	93117
EL SHERIEF HOSSNY DR	SMC/CZUI	2435 VELA WAY STE 1613	LOS ANGELES AFB CA	CA	90245-5500
ELCHYNSKI JOSEPH J MR	TRW BALLISTIC MISSILES DIVISION	PO BOX 1310 SB2/1051	SAN BERNARDINO	CA	92402-1310
ELDER JAMES F MR	HONEYWELL MILITARY AVIONICS DIVISIO	11801 ROOSEVELT BLVD 524M	ST PETERSBURG	FL	33716-2202
ELLIOTT PATRICK MR	HONEYWELL INC	1001 HAMLIN PLACE	REDLANDS	CA	92373-5088
ELWELL JOHN MR	MADEP NORTH ISLAND	PO BOX 357058	SAN DIEGO	CA	92135-7058
EMERLE REBECCA MS	C S DRAPER LABORATORY INC	555 TECHNOLOGY SQ MS 79	CAMBRIDGE	MA	02139-3563
ERICKSON GEORGE W MR	APPLIED RESEARCH LABORATORIES AT UT	10000 BURNET RD	AUSTIN	TX	78758
EVANS CHARLES MR	SPERRY MARINE INC	1070 SEMINOLE TRAIL	CHARLOTTESVILLE VA	VA	22906
FARMER ROY H MR	APPLIED TECHNOLOGY ASSOCIATES	7320 N MAIN	LAS CRUCES	NM	88011
FAY CHARLES L MR	DELCO ELECTRONICS CORP MS P104	6767 HOLLISTER AVENUE	GOLETA	CA	93117
FEDER EARL I MR	NORTHERN TELECOM EUROPE LTD	475 N MARTINGALE ROAD	SCHAUMBURG	IL	60173
FENRLE THOMAS L MR	US ARMY AVIONICS	AVRADA/SAVA-A	FORT MONMOUTH	NJ	07703
FEIST JON MR	OC-ALC/LAKR	3001 STAFF DR STE 2AH110	TINKER AFB	OK	73145-3022
FERNANDEZ RONALD MR	46TH GUIDANCE TEST SQUADRON/GDS	1644 VANDERGRIFF ROAD	HOLLOMAN AFB	NM	88330-7850
FILIATREAU THOMAS R MR	C S DRAPER LABORATORY INC	555 TECHNOLOGY SQ MS 86	CAMBRIDGE	MA	02139-3563
FINNEN SCOTT A MR	46TH GUIDANCE TEST SQUADRON/GDMT	1644 VANDERGRIFF ROAD	HOLLOMAN AFB	NM	88330-7850
FISCHER CURTIS H MR	NCCOSC NRad	PO BOX 5152 CODE 322	WARMINSTER	PA	18974-0591
FITZGERALD WARREN J DR	46TH GUIDANCE TEST SQUADRON/GDTN	1644 VANDERGRIFF ROAD	HOLLOMAN AFB	NM	88330-7850
FITZPATRICK WILLIAM J DR	C S DRAPER LABORATORY INC	555 TECHNOLOGY SQ MS 48	CAMBRIDGE	MA	02139-3563
FLORES MATT MR	LOGICON INC	PO BOX 471	SAN PEDRO	CA	90733-0471
FLY BRIAN E MR	46TH GUIDANCE TEST SQUADRON/GDSG	1644 VANDERGRIFF ROAD	HOLLOMAN AFB	NM	88330-7850
	HONEYWELL MIL-AV/GHO	11601 ROOSEVELT BLVD	ST PETERSBURG	FL	33716-2202

NAME	COMPANY	STREET	CITY	STATE	ZIP CODE
FOSTER DALE C	46TH TEST GROUP/GDTN	1644 VANDERGRIFT ROAD	HOLLOMAN AFB	NM	88330-7850
FRIDAY MICHAEL A MR	OC-ALC/LIIRN	3001 STAFF DR STE 1AE196	TINKER AFB	OK	73145-3029
FULLINGTON GARY MAJ	SAC/CZF	2435 VELA WAY STE 1613	LOS ANGELES AFB CA	CA	90245-5500
FURMAN DENNIS LT COL	46TH TEST GROUP/CV	871 DE ZONIA ROAD	HOLLOMAN AFB	NM	88330-7715
GALLOS JORGE MR	MAYFLOWER COMMUNICATIONS	80 MAIN STREET	READING	MA	01867
GALLIANETTI JOSEPH SRA	46TH GUIDANCE TEST SQUADRON/GDMG	1644 VANDERGRIFT ROAD	HOLLOMAN AFB	NM	88330-7850
GALLOWAY JOHN MR	ASC/SMEA	1895 FIFTH ST BLDG 96	WRIGHT PATTERSON OH	OH	45433-7200
GARCIA BILL MR	STEW'S-ID-SG	1644 VANDERGRIFT ROAD	WANDS MISSILE	NM	88002
GARCIA FRANK H MR	46TH TEST GROUP/GDSG	555 TECHNOLOGY SQ MS 1C	HOLLOMAN AFB	NM	88330-7850
GAUTHIER ROBERT J MR	C S DRAPER LABORATORY INC	4115 HEBBLE CR RD STE 26	CAMBRIDGE	MA	02139-3563
GAYHEART DOUG MR	HQ FASTC/TAEQ	1644 VANDERGRIFT ROAD	WRIGHT PATTERSON OH	OH	45433-5630
GAYLOR DAVE MR	INTERMETRICS INC	3001 STAFF DR STE 1AE196	HOLLOMAN AFB	NM	88330-7850
GEORGE SAMUEL K MR	OC-ALC/LIIRN	5450 KATELLA AVE STE 103	TINKER AFB	OK	73145-3029
GIBSON RICHARD T MR	CAST, INC.	13350 US HWY 19 N	LOS ALAMITOS	CA	90720
GILLESPIE G H MR	HONEYWELL INC	1844 VANDERGRIFT ROAD	CLEARWATER	FL	34624-7290
GLASCOE WILLIAM O CAPT	46TH GUIDANCE TEST SQUADRON/GDTN	2301 W 120 ST	HOLLOMAN AFB	NM	88330-7850
GRUISE JAMES R MR	NORTHROP CORP ESD HS	150 TOWNA RD MS 12840	HAWTHORNE	CA	90251-5032
GOETZ WALTER MR	KEARFOTT GUIDANCE & NAVIGATION CORP	100 PLASTICS AVE	WAYNE	NJ	07474-0946
GOGOSHA OREST R MR	MARTIN MARIETTA CORP	1644 VANDERGRIFT ROAD	PITTSFIELD	MA	01201
GONZALES GLORIA MS	46TH GUIDANCE TEST SQUADRON/CA	1011 LOCKHEED WAY #7217 86	HOLLOMAN AFB	NM	88330-7850
GONZALES STEVE MR	STEW'S-ID-SG	1011 LOCKHEED WAY #7217 86	ALMADALE	CA	93599-0250
GOODALL DAVID MR	LOCKHEED (LADC) PLANT 86	1644 VANDERGRIFT ROAD	ARNOLD AFB	TN	37389-1303
GRAVISS LAWRENCE P COL	AEDC/CC	555 TECHNOLOGY SQUARE	HOLLOMAN AFB	NM	88330-7850
GREEN JOHN J TSGT	46TH TEST GROUP/GDSG	1644 VANDERGRIFT ROAD	CAMBRIDGE	MA	02139-3563
GREENSPAN RICHARD MR	C S DRAPER LABORATORY INC	11601 ROOSEVELT BLVD 838M	HOLLOMAN AFB	NM	88330-7850
GREY FLORENA MS	46TH GUIDANCE TEST SQUADRON/GDMI	300 BREAKAWAY ROAD	ST PETERSBURG	FL	33716-2202
GRIEBLER JERRY MR	HONEYWELL MILITARY AVIONICS DIVISIO	3370 MIRALOMA AVE MC F835	CEDAR PARK	TX	78613
GRIFFIN CARROLL R MR	GRIFFIN AND SON	AVENUE DU GROS CHENE	ANAHEIM	CA	92803
GRIMALDI GERALD MR	ROCKWELL INTERNATIONAL	555 TECHNOLOGY SQUARE	CAMBRIDGE	MA	02139-3563
GUDON JEAN YVES MR	C S DRAPER LABORATORY INC	58183 LINKOPING	STOCKHOLM	SWEDEN	20332-5113
HAAYISTO JOHN R DR	A/C SYSTEMS DIVISION FFV AEROTECH A	170 LUKE AVE STE 400	BOLLING AFB	DC	20332-5113
HAGSTEDT ANDERS MR	HQ USAF/HQ	102 W D AVE STE 300	EGLIN AFB	GL	32542-6808
HALLON RICHARD P DR	ASC OL/YOG	555 TECHNOLOGY SQ MS 86	CAMBRIDGE	MA	02139-3563
HANCOCK THOMAS P MR	C S DRAPER LABORATORY INC	448 EUCALYPTUS DRIVE	REDLANDS	CA	92373
HAND JAMES MR	LITTON GUIDANCE & CONTROL	961 DEZONIA ROAD	WSMR	NM	88330-7717
HANDZEL JAMES R MR	STEW'S-ID-SG	100 PLASTICS AVE RM 27571	HOLLOMAN AFB	NM	01201
HARDING GILBERT MR	46TH TEST GROUP/SP	DEPT 9722	PITTSFIELD	MA	01201
HARVEY RICK MSGT	MARTIN MARIETTA	PO BOX 17 CD2501	ALBUQUERQUE	NM	87185-5800
HAUGE LEE J MR	SANDIA NATIONAL LABORATORIES	1644 VANDERGRIFT ROAD	THE HAGUE	NETHERL	88330-7850
HEAD ROGER C COL (RET)	SHAPE TECHNICAL CENTER (NATO)	1844 VANDERGRIFT ROAD	HOLLOMAN AFB	NM	88330-7850
HEGELS HERMANN F MR	46TH TEST GROUP/GDSQ	101 W EGLIN BLVD STE 331	EGLIN AFB	FL	32542-6810
HENDERSON FRANK MR	46TH GUIDANCE TEST SQUADRON/GDS	PO BOX 4000	MEDICINE HAT AL CANADA	T1A 8K6	45433-7015
HERNANDEZ LYNDIA MS	WRIGHT LABORATORY	2100 THIRD ST STE 1	WRIGHT PATTERSON OH	OH	45433-7015
HERRERA THEODORE D CAPT	DEFENCE RESEARCH EST SUFFIELD	1644 VANDERGRIFT ROAD	HOLLOMAN AFB	NM	88330-7850
HERRING ROBERT W MR	ASC/VFEA BLDG 56	1644 VANDERGRIFT ROAD	HOLLOMAN AFB	NM	88330-7850
HICKS SUE MS	46TH TEST GROUP/GDMR	4531 Q PLACE NW	WASHINGTON	DC	20007
HIGHT DALAYR W CAPT	46TH TEST GROUP/GDSD	11601 ROOSEVELT BLVD	HOLLOMAN AFB	NM	88330-7715
HIRNING JAMES L MR	CONSULTANT	14732 MANSA DRIVE	ST PETERSBURG	FL	33716-2202
HIRSHON SIDNEY MR	46TH TEST GROUP/CA	2185 AVIONICS CR BLDG 635	LA MIRADA	CA	90638
HOLLAND KEN R MR	HONEYWELL INC MAYD/GMO MS 838-M	1644 VANDERGRIFT ROAD	WRIGHT PATTERSON OH	OH	45433-7301
HOLLINGWORTH DAVID R MR	ROCKWELL INTERNATIONAL	3320 CANDELARIA ROAD	HOLLOMAN AFB	NM	88330-7850
HOLMES DONALD W MR	WL/AAAI-3	2435 VELA WAY STE 1613	ALBUQUERQUE	NM	87107-1909
HOLSAPPLE BOYD E MR	46TH TEST GROUP/GDXP	2185 AVIONICS CR BLDG 635	LCS ANGELES AFB CA	CA	90245-5500
HOOVER MICHAEL D DR	HONEYWELL INC	2185 AVIONICS CR BLDG 635	WRIGHT PATTERSON OH	OH	45433-7301
HORN RANDY MR	SAC/CZF				
HOULE SARAH 2LT	WL/AAAI				
HONE PETER G MR					



NAME	COMPANY	STREET	CITY	STATE	ZIP CODE
HUGHES HAROLD S MR	ROCKWELL INTERNATIONAL/AESD	3370 MIRALOMA MS 031CA31	ANAHEIM	CA	92803
HUNT COY MR	46TH TEST GROUP/GDTN	1644 VANDERGRIFT ROAD	HOLLOMAN AFB	NM	88330-7850
HUO MITO MR	INTERMETRICS INC	1644 VANDERGRIFT ROAD	HOLLOMAN AFB	NM	88330-7850
HURTIG PER-JOHAN MR	SWEDISH AIR FORCE/FMV	AIR MATERIEL DEPT S 115 88	STOCKHOLM	SWEDEN	
HUTCHISON BILL MR	TEXAS INSTRUMENTS	PO BOX 405 W/S 3482	LEWISVILLE	TX	75067
HYMAS CARL E LTC (RET)	TRW - OGDEN	6031 GUM LANE	HILL AFB	UT	84056-5826
INGOLD NORMAN L MR	46TH GUIDANCE TEST SQUADRON/CA	1644 VANDERGRIFT ROAD	HOLLOMAN AFB	NM	88330-7850
ISRAEL HOWARD MR	TRW DEFENSE SYSTEMS GROUP	PO BOX 1310 520/125	SAN BERNARDINO	CA	92402-1310
JACOB RONALD MR	46TH TEST WING/CA	101 W D AVE STE 22	EGLIN AFB	FL	32542-5492
JAEKKE MARTIN DR	HQ USAF/HQ	1716 MONTE VISTA CT	ALAMOGORDO	NM	88310
JAMIESON PERRY D DR	HQSC NRAd CODE 311	170 LUKE AVE STE 400	BOLLING AFB	DC	20332-5113
JANKOVITZ JACK MR	SUNDSTRAND DATA CONTROL INC	STREET & JACKSONVILLE RD	WARMINGSTER	PA	18974-0591
JENSEN DAVID P MR	LEAR ASTROINCS CORP	15001 NE 36 STREET	REDMOND	WA	98073-9701
JEWETT HEATHER MS	C S DRAPER LABORATORY INC	3400 AIRPORT AVE	SANTA MONICA	CA	90405
JOHNSON JOHN G MR	46TH GUIDANCE TEST SQUADRON/GDMG	555 TECHNOLOGY SQUARE	CAMBRIDGE	MA	02139-3563
JOINER TIM SSGT	WL/MMAG	1644 VANDERGRIFT ROAD	HOLLOMAN AFB	NM	88330-7850
JOLLEY VINCE LT	46TH TEST GROUP/PR	101 W EGLIN BLVD STE 331	HOLLOMAN AFB	NM	88330-7714
JOLLIFFE JAMES A CAPT	C S DRAPER LABORATORY INC	872 DE ZONTA ROAD	CAMBRIDGE	MA	02139-3563
KATISER KENNETH W DR	46TH GUIDANCE TEST SQUADRON/GDMR	555 TECHNOLOGY SQ MS 2A	HOLLOMAN AFB	NM	88330-7850
KANTOROWICZ RICHARD MR	ASC/ENAEH	1644 VANDERGRIFT ROAD	WRIGHT PATTERSON	OH	45424-1619
KEEN DAN MR	46TH TEST GROUP/GDS	NAVIGATION BRANCH	HOLLOMAN AFB	NM	88330-7850
KELHER ROBERT MR	C S DRAPER LABORATORY	1644 VANDERGRIFT ROAD	ACTON	MA	
KELLEHER WILLIAM DR	46TH GUIDANCE TEST SQUADRON/GDTI	3 BETSY ROSS CIRCLE	HOLLOMAN AFB	NM	88330-7850
KING KERRY LT	GMM CONSULTING SERVICE	1644 VANDERGRIFT ROAD	N SYRACUSE	NY	13212-1901
KIRKPATRICK GEORGE M MR	STEWIS-10-SG	202 DAVID DRIVE	WSNR	NM	
KITCHENS DON R MR	PL/VT-B	3550 ABERDEEN AVE SE	KIRTLAND AFB	NM	87117-5776
KLEIFGES KELLY 1LT	TRW DEFENSE SYSTEMS GROUP	38506 CLEAR WATER DRIVE	YUCAIPA	CA	92399
KNIGHT DAVID S MR	KNIGHT SYSTEMS	973 12TH STREET STE 3	SAN PEDRO	CA	90731-3974
KNIGHT DONALD T MR	LITTON GUIDANCE & CONTROL	5500 CANOGA AVENUE MS 73	WOODLAND HILLS	CA	91367-6698
KONIK EDWARD H MR	C S DRAPER LABORATORY INC	555 TECHNOLOGY SQUARE	CAMBRIDGE	MA	617-258-36
KOSSUTH JONATHAN MR	SYSTEC	2107 DEWEY LANE	ALAMOGORDO	NM	88310
KUHN FERDINAND F DR	46TH TEST GROUP/GDSG	1644 VANDERGRIFT ROAD	HOLLOMAN AFB	NM	88330-7850
LAWRENCE ROBERT MR	NORTHROP CORP ESD HS	2301 W 120 STREET	HAWTHORNE	CA	90251-5032
LEVINE SEYMOUR MR	APPLIED TECHNOLOGY ASSOCIATES INC	2450 MISSION	SAN MARINO	CA	91108
LEVY ROBERT E MR	AEROSPACE CORPORATION	PO BOX 9045	ALBUQUERQUE	NM	87119
LEWIS ALAN MR	HONEYWELL INC	914 S FLORIDA	ALAMOGORDO	NM	88310
LITTEER ROBERT D MR	46TH GUIDANCE TEST SQUADRON/GDMG	13350 US HIGHWAY 19 N	CLEARWATER	FL	34624-7290
LLOYD MICHAEL T MR	STEWIS-10-SG	1644 VANDERGRIFT RD	HOLLOMAN AFB	NM	88330-7850
LOCHER JASON A A1C	LEAR ASTROINCS CORP	3400 AIRPORT AVENUE	WSNR	NM	
LOCKYEAR BOB MR	HQSC NRAd	PO BOX 5152 CODE 309	SANTA MONICA	CA	90405
LOOSE JOHN R MR	THE AEROSPACE CORPORATION	PO BOX 9045	WARMINGSTER	PA	18974-0591
LOWENSTEIN GEORGE MR	46TH TEST GROUP/CC COMMANDER	871 DeZONTA ROAD	ALBUQUERQUE	NM	87119-9045
LUKE ROBERT MR	APPLIED MOTION TECHNOLOGY INC	2336-B STANWELL CIRCLE	HOLLOMAN AFB	NM	88330-7715
LYDAY CARL V COL	INTERMETRICS	1644 VANDERGRIFT ROAD	CONCORD	CA	94520
MARQUESS R D SAM MR	ROCKWELL INTERNATIONAL	350 COLLINS RD NE	HOLLOMAN AFB	NM	88330-7850
MARTIN KYMBERLY MS	ROCKWELL INTL LITTLE MT TEST FACIL	12000 W 12TH STREET	CEDAR RAPIDS	IA	52402
MASKO CHARLES MR	MAYCO INC	11910 CENTRAL SE	OGDEN	UT	84404
MAY RICK D MR	GEC-MARCONI ELECTRONIC SYSTEMS CORP	235 ELM HILL DRIVE	ALBUQUERQUE	NM	87123
MAYES RICHARD A MR	APPLIED PHYSICS LAB-JOHN HOPKINS UN	JOHNS HOPKINS ROAD	DAYTON	OH	45415-2941
MC ADORY ROBERT W MR	INTERMETRICS, INC	1720 ROUTE 34	LAUREL	MD	20723-6099
MC DONALD JERRY MR	46TH TEST GROUP/GDT	1644 VANDERGRIFT ROAD	WALL	NJ	07719
MC GOWAN JOE MR	SYTRONICS INC	1656 MARDON DRIVE	HOLLOMAN AFB	NM	88330-7850
MC GUIRE JERRY MAJ	46TH GUIDANCE TEST SQUADRON/IM	13350 US HWY 19 N MS 840-3	DAYTON	OH	45432
MC QUISTON BARBARA K MS	HONEYWELL INC	872 DE ZONTA ROAD	HOLLOMAN AFB	NM	88330-7714
MEANS JOY MS	46TH TEST GROUP/PR				
MILLER CLYDE MR					
MILLER JAMES C CAPT					

NAME	COMPANY	STREET	CITY	STATE	ZIP CODE
MILLER MIKEL M CAPT	ASC/YFMA	2130 FIFTH STREET	WRIGHT-PATTERSON	OH	45433-7003
MILLER THEODORE E MR	46TH TEST GROUP/TKPM		HOLLOMAN AFB	NM	88330
MITCHELL BRIAN MR	COMMAND & CONTROL SYS INTEG DIR (C2	AMSEL-RD-C2-TS BLDG 2525	FORT MONMOUTH	NJ	07703-5603
MOFFITT CONNIE MS	46TH GUIDANCE TEST SQUADRON/GDX	1644 VANDERGRIFT ROAD	HOLLOMAN AFB	NM	88330-7850
MOLNAR LAWRENCE B MR	C S DRAPER LABORATORY INC	808 E MILL ST RM 108	SAN BERNARDINO	CA	92408
MONTANO NORMAN C MR	U.S. ARMY, SANDIA LAB	PO BOX 1500	HUNTSVILLE	AL	35807
MOORE JOHN B MR	NAVAL UNDERWATER WARFARE CENTER	116 LAKEVIEW PKWY	SUFFOLK	VA	23435-2099
MORGAN MARJORIE MS	46TH TEST GROUP/GD	1644 VANDERGRIFT ROAD	HOLLOMAN AFB	NM	88330-7850
MORTON JACK L MR	46TH GUIDANCE TEST SQUADRON/GDMI	1644 VANDERGRIFT ROAD	HOLLOMAN AFB	NM	88330-7850
MOZER G R JERRY MR	21 CAMINO DEL SUR		ALAMOGORDO	NM	88310
MURPHY DANIEL J MR	1625 ZARTHAN AVENUE		ST LOUIS PARK	MN	55416
NADEAU FREDRIC R MR	46TH TEST GROUP/GD	1644 VANDERGRIFT ROAD	HOLLOMAN AFB	NM	88330-7850
NEAL BRENT MR	46TH TEST GROUP/GDMI	1644 VANDERGRIFT ROAD	HOLLOMAN AFB	NM	88330-7850
NEUGEBAUER GEORGE H MR	RESEARCH, DEV & ENGRG CENTER	28850 PEBBLE BEACH DRIVE	SUN CITY	CA	92586
NIEWELA JOHN DR	46TH GUIDANCE TEST SQUADRON/GDTI	AMSEL-RD-C2-TS BLDG 2525	FORT MONMOUTH	NJ	07703-5603
NOVY MICHAEL LT	SYNETICS	1644 VANDERGRIFT ROAD	HOLLOMAN AFB	NM	88330-7850
NOWICKI B RICHARD MR	US ARMY, CECOM	23272 MILL CREEK DR STE200	LAGUNA HILLS	CA	92653-1655
OLSON PAUL MR	DELCO ELECTRONICS CORP	304 TIMBERLINE PL	BRICK	NJ	08723
OMDALEN CARL W MR	46TH GUIDANCE TEST SQUADRON/GDSS	8767 HOLLISTER AVENUE	GOLETA	CA	93117
ORTEGA ELIZABETH MS	MC DONNELL DOUGLAS CORP DEPT 318	1644 VANDERGRIFT ROAD	HOLLOMAN AFB	NM	88330-7850
PALMER RICHARD H MR	46TH GUIDANCE TEST SQUADRON/GDSS	PO BOX 518 MS 1065425	SAINT LOUIS	MO	63166
PARRA RAUL O LT	WL/AAAS-3 BLDG 835	1644 VANDERGRIFT ROAD	HOLLOMAN AFB	NM	88330-7850
PASCHALL RANDY MAJ	LITTON GUIDANCE & CONTROL	2185 AVIONICS CIRCLE	WRIGHT-PATTERSON	OH	45433-7301
PATTERSON RALPH MR	STEWIS-ID-SG	5500 CANOGA AVE MS 7	WOODLAND HILLS	CA	91367-6698
PAYEN OSCAR MR	ROCKWELL INTERNATIONAL	865 E SEPULVEDA BLVD	WMSR	NM	
PECK R STEVE MR	ARINC RESEARCH CORP	2250 E IMPERIAL HWY #450	CARSON	CA	90745
PENNLIN RICHARD MR	NORTHROP CORP ESD NORWOOD	100 MORSE STREET M/560000	EL SEGUNDO	CA	90245
PERLMUTTER MICHAEL MR	HONEYWELL INC NAVD/GNO MS 838-M	11801 ROOSEVELT BLVD	NORWOOD	MA	02062
PETERSEN MARK E MR	NORTHROP CORP ESD	1961 TAMARACK ROAD	ST PETERSBURG	FL	33716-2202
PETERSON ELDON E MR	HONEYWELL, INC.		NEWARK	OH	43055
PETERSON MARK E.	C S DRAPER LABORATORY INC	555 TECHNOLOGY SQ MS 53	CAMBRIDGE	MA	02139-3563
PETROVICH ANTHONY MR	THE PROTEUS CORP	10010 INDIAN SCHOOL NE	ALBUQUERQUE	NM	87112
PODESNY JOHN J MR	LRBA	DGA	27207 VERNON CE FRANCE		
POMMELLET PIERRE ERIC MR	46TH TEST GROUP/PRX	872 DE ZONIA ROAD	HOLLOMAN AFB	NM	88330-7716
POPOVICH ANTHONY P CAPT	46TH TEST GROUP/PR	872 DE ZONIA RD	HOLLOMAN AFB	NM	88330-7714
PORTER REX MAJ	CONTRAVES INC.	610 EPSILON DRIVE	PITTSBURGH	PA	15238
PREBEHALLA EDWARD MR	ARMY RESEARCH LABORATORY	2800 POWDER MILL RD	ADELPHI	MD	20783-1145
PRICE JOSEPH K MR	C S DRAPER LABORATORY INC	555 TECHNOLOGY SQ MS-65	CAMBRIDGE	MA	02139-3563
PUBLICOVER JOSEPH MR	HQ USAF/HQ	170 LUKE AVE STE 400	BOLLING AFB	DC	20332-5113
PUTNEY DIANE T DR	46TH TEST GROUP/GDIT	1644 VANDERGRIFT ROAD	HOLLOMAN AFB	NM	88330-7850
RAMIREZ FRANCISCO J MR	DET 4 AFOTEC/GPS	4196 E BIJOU	COLORADO SPRING	CO	80909
RAMSEY ELLEN SENA SGT	BENDIX FIELD ENGINEERING CORP	PO BOX 1261	MESILLA	NM	88040-1261
RANDALL H JACK COL (RET)	46TH TEST GROUP/GDMR	1644 VANDERGRIFT ROAD	HOLLOMAN AFB	NM	88330-7850
RAQUET JOHN F CAPT	HONEYWELL INC	13350 US HIGHWAY 19 N	CLEARWATER	FL	34624-7290
RASMUSSEN RONALD M MR	LITTON G/CS	5500 CANOGA AVE IN528	WOODLAND HILLS	CA	91367
RATKOVIC JOE DR	SMITHS INDUSTRIES	4141 EASTERN AVENUE SE	GRAND RAPIDS	MI	49518-8727
REDMAN WILLIAM A MR	REED GROUP	25 TUCKER ROAD	CHARLTON	MA	01507
REED THOMAS E MR	BRITISH AEROSPACE SYS & EQUIP LTD	CLITTAFFORD ROAD	PLYMOUTH PL6 6D ENGLAND		
REILLY RICHARD MR	46TH GUIDANCE TEST SQUADRON/GDSG	1644 VANDERGRIFT ROAD	HOLLOMAN AFB	NM	88330-7850
RETA MARIA L MS	THE PROTEUS CORP	2511 E TELSHOR	LAS CRUCES	NM	88011
RICE WILLIAM A MR	AFIT/ENG	2850 P STREET	WRIGHT PATTERSON	OH	45433-7765
RIGGINS ROBERT N LTC	ROGERS ENGINEERING & ASSOCIATES	3705 NW 24 PLACE	GAINSVILLE	FL	32605
ROGERS ROBERT M MR	NAVAL AIR WARFARE CENTER	WEAPONS DIV CODE C2196	CHINA LAKE	CA	93555-6001
ROSSO PAUL G DR	HONEYWELL INC	2800 RIDGWAY PARKWAY	MINNEAPOLIS	MN	55440
ROUSE GORDON F MR	LITTON GUIDANCE & CONTROL	5500 CANOGA AVENUE MS 99	WOODLAND HILLS	CA	91367-6698
ROZELLE DAVID M MR	46TH TEST GROUP/GDMR	1644 VANDERGRIFT ROAD	HOLLOMAN AFB	NM	88330-7850
RUFF DEREK A MR					

NAME	COMPANY	STREET	CITY	STATE	ZIP CODE
RUFFIN PAUL DR	US ARMY MISSILE COMMAND	ANSMI-RD-GC-L	REDSTONE ARSENA	AL	35898-5264
SAFFLE CHARLES F MR	AGMC/MISSILE ATE BRANCH	813 IRVINGWICK DRIVE W	NEWARK AFB	OH	43057-0005
SAGE BRAD B MR	SYSTRON DONNER COMPANY	2700 SYSTRON DRIVE	CONCORD	CA	94518
SAPUPPO MICHAEL S MR	MS SAPUPPO & ASSOCIATES	7 REGIS ROAD	ANDOVER	MA	01810
SAVAGE JAMES ZLT	ASC/SNEP		WRIGHT-PATTERSO	OH	45433
SCHERNERS FRANK MR	SMITHS INC	4141 EASTERN AVENUE SE	GRAND RAPIDS	MI	49518-8727
SCHNEIDER ROBERT MR	GEC-MARCONI ELEC SYS	150 PARISH DR MS 18A79	WAYNE	NJ	07470
SCHOENFELD HERBERT MR	NGCOSC MR&D	CODE 4013	WARMINSTER	PA	18974-0591
SCHREIBER FRED MR	46TH TEST GROUP/GDMT	1644 VANDERGRIFT ROAD	HOLLOMAN AFB	NM	88330-7850
SCOTT DAN MR	46TH GUIDANCE TEST SQUADRON/GDSS	1644 VANDERGRIFT ROAD	HOLLOMAN AFB	NM	88330-7850
SEIPEL HAKAN MR	SWEDISH AIR FORCE/FMW	AIR MATERIEL DEPT S-115 88	STOCKHOLM	SWEDEN	
SHEARER JAMES A MR	C S DRAPER LABORATORY INC	555 TECHNOLOGY SQ MS 65	CAMBRIDGE	MA	02139-3563
SHILOH SUSAN MSGT	46TH GUIDANCE TEST SQUADRON/GDM	1644 VANDERGRIFT ROAD	HOLLOMAN AFB	NM	88330-7850
SHOAF ROBERT B MR	46TH TEST GROUP/GDMR	1644 VANDERGRIFT ROAD	HOLLOMAN AFB	NM	88330-7850
SIMPSON PHILIP B MR	46TH GUIDANCE TEST SQUADRON/GDSG	1644 VANDERGRIFT ROAD	HOLLOMAN AFB	NM	88330-1117
SINHA PRASUN DR	INTERMETRICS INC	PO BOX 1117	HOLLOMAN AFB	NM	88330-1117
SISAK JOHN W MR	ERIM	PO BOX 134001	ANN ARBOR	MI	48113-4001
SITOMER JAMES L MR	C S DRAPER LABORATORY INC	555 TECHNOLOGY SQ MS 79	CAMBRIDGE	MA	02139-3563
SMITH ARNOLD J MR	CONSULTANT	386 APPLETON STREET	ARLINGTON	MA	617-648-32
SHODGRASS F BRITT CAPT	46TH TEST GROUP/GDTI	1644 VANDERGRIFT ROAD	HOLLOMAN AFB	NM	88330-7850
SPRING SAM S MR	ROCKWELL INTL LITTLE MT TEST FACIL	12000 W 12TH STREET	OGDEN	UT	84404
SPRINGER TOM MR	RETIRED	PO BOX 1205	CLOUDCROFT	NM	88317
STEPHENS ROBERT MAJ	ASC/ENAE		WRIGHT-PATTERSO	OH	45433-6503
STEVENS CHRIS A MR	NAWC AIRCRAFT DIVISION	CODE FW 42	PATUXENT RIVER	MD	20670-5304
STEWART FRANK MR	DYNACORP LAND-AIR DIVISION	PO DRAWER R	HOLLOMAN AFB	NM	88330
STONEKING DON MR	46TH GUIDANCE TEST SQUADRON/GDMT	1644 VANDERGRIFT ROAD	HOLLOMAN AFB	NM	88330-7850
STROING CRAIG MR	NGCOSC NISE WEST	PO BOX 80337 CODE 3131	SAN DIEGO	CA	92138
STROUD ROBERT CAPT	586TH TEST SQUADRON/SC	1644 VANDERGRIFT ROAD	HOLLOMAN AFB	NM	88330-7850
STURDEVANT REESE C MR	46TH GUIDANCE TEST SQUADRON/GDTN	1644 VANDERGRIFT ROAD	HOLLOMAN AFB	NM	88330-7850
STUTZ DERRYL L MR	46TH TEST GROUP/GDMR	1644 VANDERGRIFT ROAD	HOLLOMAN AFB	NM	88330-7850
SUGERMAN LEONARD COL (RET)	NEW MEXICO STATE UNIVERSITY-PSL	3025 FAIRWAY DRIVE	LAS CRUCES	NM	88001
TAYLOR SCOTT W MR	46TH TEST GROUP/GDMR	1644 VANDERGRIFT ROAD	HOLLOMAN AFB	NM	88330-7850
TAZARTES DANIEL MR	LITTON GUIDANCE & CONTROL	5500 CANOGA AVENUE	WOODLAND HILLS	CA	91367
TEHRANI MOHAMMAD M MR	LITTON GUIDANCE & CONTROL	5500 CANOGA AVENUE MS 19	WOODLAND HILLS	CA	91367-6698
TEITT ROBERT MR	LITTON GUIDANCE & CONTROL	2211 W NORTH TEMPLE	SALT LAKE CITY	UT	84116
THIELMAN LEROY O DR	HONEYWELL INC	2800 RIDGWAY PARKWAY	MINNEAPOLIS	MN	55413
THOMPSON GEORGE MR	6595 TEG/TS BLDG 8500	1515 ICELAND STE A	VANDENBERG AFB	CA	93437-5320
TRUNCALE ANGELO MR	ROCKWELL INTERNATIONAL	3370 MIRALOMA BLVD	ANAHEIM	CA	92803-3150
TRUNZO ANGELO MR	46TH GUIDANCE TEST SQUADRON/GDSS	1644 VANDERGRIFT ROAD	HOLLOMAN AFB	NM	88330-7850
UPADHYAY TRIVENI N DR	MAYFLOWER COMMUNICATIONS CO INC	80 MAIN ST	READING	MA	01867
URIBE DANIEL CAPT	46TH GUIDANCE TEST SQUADRON/GDTI	1644 VANDERGRIFT ROAD	HOLLOMAN AFB	NM	88330-7850
VAN KARSSEN KENNETH MR	US ARMY ELECTRONIC PROVING GROUND	STEEP-MT-O	FT HUACHUCA	AZ	85613
VARTY GUY TOM MR	LITTON GUIDANCE & CONTROL	5500 CANOGA AVENUE	WOODLAND HILLS	CA	91367
VENTURONE FREDERICK A MR	NAWC	BLDG 2109 SYD4CN	PATUXENT RIVER	MD	20670
VESTGARD BERIT K MS	SWEDISH AIR FORCE/FMW	AIR MATERIEL DEPT S 115 88	STOCKHOLM	SWEDEN	
VON HUSEN RAY MR	46TH TEST GROUP/GDTN	1644 VANDERGRIFT ROAD	HOLLOMAN AFB	NM	88330-7850
VON KARSSEN KEN MR	US ARMY ELECTRONIC PROV GND	STEEP-MT-O	FT HUACHUCA	AZ	85613
WALKER DORA B MS	46TH GUIDANCE TEST SQUADRON/GDXP	1644 VANDERGRIFT ROAD	HOLLOMAN AFB	NM	88330-7850
WALKER RALPH E MR	C S DRAPER LABORATORY INC	555 TECHNOLOGY SQUARE	CAMBRIDGE	MA	02139-3563
WARD CHUCK MR	INTERMETRICS INC	PO BOX 1117	HOLLOMAN AFB	NM	88330-1117
WESTFALL JEFF MR	STEWIS-ID-SG		WSMR	NM	
WESTOVER FREDERICK L COL	ASC/SMA BLDG 46	1895 FIFTH STREET	WRIGHT PATTERSO	OH	45433 7200
WHITEHEAD DENNIS P MR	ACUTRONIC USA INC	139 DELTA DRIVE	PITTSBURGH	PA	15238
WIEDENER MICHAEL P COL	SNC/GZ	2435 VELLA WAY STE 1613	LOS ANGELES AFB	CA	90245-1613
WIETSTRAK ERIC CAPT	46TH GUIDANCE TEST SQUADRON/GDTN	1644 VANDERGRIFT ROAD	HOLLOMAN AFB	NM	88330-7850
WILK LEONARD S MR	C S DRAPER LABORATORY INC	555 TECHNOLOGY SQ MS 37	CAMBRIDGE	MA	02139 3563
WILLIFORD JAMES H MR	HONEYWELL INC MS 961M	11601 ROSEVELT BLVD	ST PETERSBURG	FL	33716 2202

NAME	COMPANY	STREET	CITY	STATE	ZIP CODE
WINELL KEN MR	KEARFOTT GUIDANCE & NAVIGATION CORP	150 TOTOWA ROAD	WAYNE	NJ	07474-0946
WONG CHRISTI L MS	46TH GUIDANCE TEST SQUADRON/GDMT	1644 VANDERGRIFT ROAD	HOLLOMAN AFB	NM	88330-7850
Y BLOOD WILLIAM T MR	HQ USAF/HQ	170 LUKE AVE STE 400	BOLLING AFB	DC	20332-5113
YERION DALE SSGT	46TH GUIDANCE TEST SQUADRON/GDSG	1644 VANDERGRIFT ROAD	HOLLOMAN AFB	NM	88330-7850
ZETOCHA PAUL MR	PL/VTES		KIRTLAND AFB	NM	87117-5776

347 rows selected.

**THIS PAGE LEFT BLANK INTENTIONALLY**